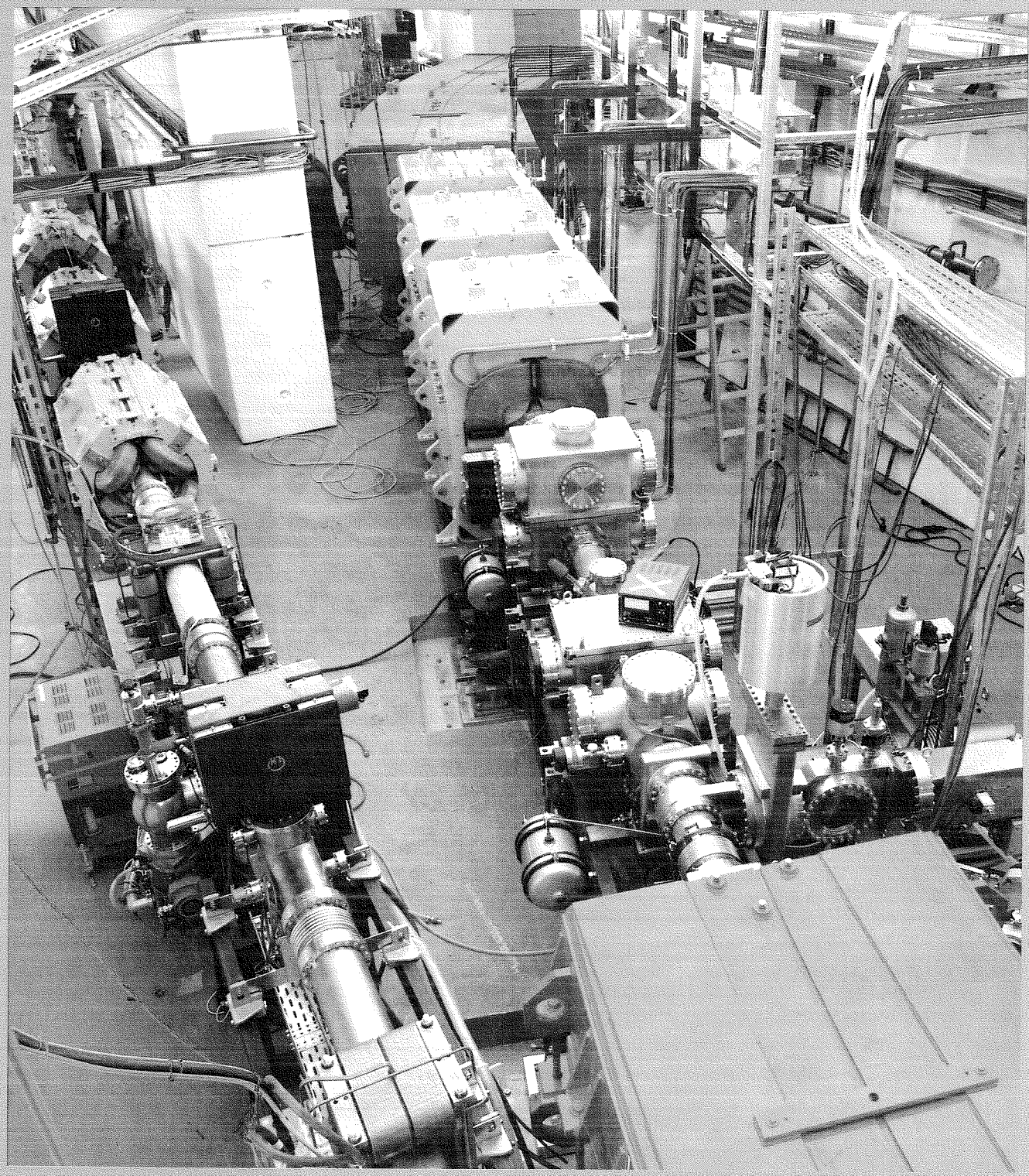
GSI

GSI 90-1
MARCH 1990
ISSN 0174 - 0814

SCIENTIFIC REPORT 1989



GESELLSCHAFT FÜR SCHWERIONENFORSCHUNG mbH
DARMSTADT

Cover Picture

Beamline to the ESR and the Target Hall (left hand side) and first elements of the projectile fragment separator (right hand side), containing the vacuum window (10μ titanium foil), the target area with two target stations, a quadrupole triplet and the first 30° dipole magnet.
Beams of relativistic instable light fragments have already been separated with this section of the fragment separator.

SCIENTIFIC REPORT 1989

Publisher: Gesellschaft für Schwerionenforschung mbH
(Mitglied der AGF)
Postfach 11 05 52
6100 Darmstadt

Editor: U. Grundinger

Print: Druckerei G. Preuß, 6100 Darmstadt

ISSN 0174-0814

Commissioning of our new heavy ion synchrotron SIS started in April 1989. Already on May 18, 1989 our accelerator group succeeded in acceleration of a $^{132}Xe^{21+}$-beam injected from the UNILAC into SIS to an energy of 100.8 MeV/u. On October 31 the final goal was achieved. A beam of $^{238}U^{72+}$ was accelerated in SIS to the highest possible energy: 1 GeV/u. Slow extraction of such beams was developped in December 1989, so that a new area of heavy ion research in the GeV energy range was opened at the GSI. The assembly of the ESR cooler ring was also brought close to the end.

The construction of the other major experimental facilities took a fast progress. Aladin was put with air cushions on a glittery "dancing floor". The frame for the installation of the plastic forward wall of the 4π-detector was put in Cave B. KAOS, the new kaon spectrometer arrived and was used as speaker platform for our Christmas party. The target station and the first quarter of the fragmentseparator FRS was connected with the SIS extraction lines. The installations of the beam lines to the ESR and Cave B are far advanced.

During the first quarter of 1989 the UNILAC was used for an intensive experimental program with very heavy beams. Starting from April 1989 two successful parallel programs, SIS injection at 11.5 MeV/u and UNILAC target hall beams at energies between 3.6 to 20 MeV/u with switching times of 15 ms between both acceleration modes, were offered. The very successful atomic physics program at 1.4 MeV/u in the stripper hall of the UNILAC was terminated after 15 years to provide space for the installation of the new high charge state injector, which is under construction.

The nuclear structure program reports results on such interesting topics like the strength of Gamov-Teller transitions, parity violation, light particle associated fission, measurements of transient magnetic fields and especially on the new results from the search for two-octupole phonon states in ^{208}Pb. Many interesting reaction studies at UNILAC energies are reported including the fusion of the heaviest symmetric system (^{110}Pd + ^{110}Pd), multinucleon transfer reactions, the production and decay of highly excited nuclei. At higher energies first studies on fission and complex fragment emission are reported. Interaction cross sections for neutron rich Li isotopes were measured.

Many interesting results from NA35 and WA80 collaborations on ultrarelativistic heavy ion collisions studied at the CERN SPS are reported including an enhancement of the strange and antistrange particle production in central ^{32}S-^{32}S-collisions at 200 GeV/A.

The experimental programs are supported by vigorous theoretical efforts on low energy properties of heavy nuclei, particle and fragment flow, photon, dilepton and subthreshold particle-production at SIS energies as well as some interesting topics relevant for high energy nucleus-nucleus collisions.

In the field of atomic physics experimental progress in the study of e^+e^- pair production in heavy ion collisions is reported. Energy and angular correlation studies of e^+-e^- pairs reveal several narrow sumenergy lines but a complex angular emission pattern. Bhaba scattering and e^+-annihilation in flight experiments reveal no resonances with a very small limit for the resonance strength ($\Gamma < 8.8 \times 10^{-5}$ eV).

Several very exciting spectroscopy results on highly ionized atoms are reported, including Lambshift studies fine structure splitting measurements and two photon decay spectra. First results on the capture of free electrons in U^{28+} ions, on dielectronic recombination and laser cooling at the TSR are reported. On the theory side, there are interesting contributions on the positron puzzle, various ionization problems and spectroscopic properties of few electron systems.

The large effort to study radiation effects in biological systems continued and a first status report of a heavy ion therapy project is given. Radiation effect studies in solids comprise an increasing number of contributions on ion implantation and ion sputtering, ion beam induced modifications, nuclear tracks and applications of nuclear track filters.

The report contains contributions on chemical separation techniques and chemical properties of heavy elements. Many interesting developments concerning experimental set-ups, detectors, data acquisition, computing mass spectroscopy and accelerators are reported.

In the application of heavy ion beams for the generation of high energy density in matter considerable progress in the study of the interaction of ions in a plasma was made.

The results presented in this report were obtained in close cooperation of scientists from GSI and many universities and research institutes of Germany and all over the world. As SIS is ready now for experimental programs we hope that the international science community makes the best use of this new facility.

P. Kienle

CONTENTS

	PAGE
SURVEY OF EXPERIMENTS AT GSI IN 1989	VII
1. NUCLEAR PHYSICS / NUCLEAR CHEMISTRY	1
1.1 Nuclear Structure	
1.1.1 Exotic Nuclei	11
1.1.2 Nuclear Spectroscopy and High Spin States	17
1.2 Nuclear Reactions	
1.2.1 Nuclear Reactions at UNILAC Energies	22
1.2.2 Reactions at S I S Energies	47
1.2.3 Reactions at Relativistic Energies	52
1.3 Theory of Nuclear Properties and Reactions	
1.3.1 Low Energies	78
1.3.2 Intermediate Energies	89
1.3.3 High Energies	109
1.3.4 Miscellaneous	122
2. ATOMIC PHYSICS	125
2.1 Positron Production in Strong Fields, Bhabha Scattering and Atomic Reaction Mechanism	129
2.2 Few Electron Systems: Spectroscopy and Interaction with Electron and Photons	143
2.3 Theory	155
3. RADIATION EFFECTS	169
3.1 Biophysical Experiments	
3.1.1 Radiation Effects in Biological Systems	175
3.1.2 Preparations for Radiotherapy	200
3.2 Radiation Effects in Solids	
3.2.1 Ion Implantation and Ion Sputtering	202
3.2.2 Ion Beams Induced Modifications	210
3.2.3 Nuclear Tracks and Etching	219
3.2.4 Application of Nuclear Track Filters	229
4. CHEMISTRY	237
4.1 Development of Separations	239
4.2 Chemical Properties	245

5. DEVELOPMENTS 249

5.1 Experimetal Set-ups for SIS and ESR 255

5.2 Detectors 378

5.3 Data Acquisition 302

5.4 Computing Centre 317

5.5 Mass Spectroscopy, Sources, Beams and Targets 330

6. ACCELERATORS 333

6.1 UNILAC Operation and Development 335

6.2 New Accelerator Projects
6.2.1 S I S 347
6.2.2 E S R 352
6.2.3 Beam Dynamics 362

7. HEAVY ION BEAMS FOR THE GENERATION OF HIGH ENERGY DENSITY IN MATTER 367

8. ANNEX 377

8.1 Scientific Activities Outside GSI
8.1.1 Publications 379
8.1.2 Conference Contributions 388
8.1.3 Seminars at Other Institutes 400
8.1.4 Lectures and Courses 403

8.2 Scientific Activities Within GSI
8.2.1 Meetings, Workshops and Research Seminars 404
8.2.2 Seminars at GSI 404
8.2.3 GSI-Reports 408
8.2.4 GSI-Preprints 409
8.2.5 Visiting Groups at GSI 413

8.3 Scientific Committees, Directorate and Personal 414

8.4 Scientific Cooperations 416

8.5 Author Index 418

Survey of Experiments in the Experimental Area in 1989

NUCLEAR PHYSICS/NUCLEAR CHEMISTRY

EXP. NR.	SPEAKER	AFFILIATION	EXPERIMENT TITLE	ION SPECIES	BEAM TIME(d)
311	H. Backe	Univ. Mainz	Kontaktzeiten	^{238}U	12.6
334	v. Oertzen, Schüll	HMI Berlin, GSI	Paarungseffekte	^{208}Pb	5.1
341	S. Polikanov	GSI	Superheavy Relics	^{238}U	3.2
351	Münzenberg	GSI	Überschw. Elemente	^{40}Ar,^{54}Cr, ^{58}Fe	3.0
352	Schädel	GSI	Superheavy Elements	^{40}Ar	5.2
362	Kankeleit, Laubach	TH Darmstadt	Mößbauer Spectr.	Xe	5.6
396	Oeschler	TH Darmstadt	Kontaktzeiten	^{208}Pb	6.0
399	Hass, Heßberger	Rehovot, GSI	Tilted Foil	^{40}Ar,^{65}Cu	1.7
405	Wollersheim	GSI	Two Phonon Excitation	^{208}Pb	7.8
413	Freiesleben	Univ. Bochum	Primäre Wirk.querschn.	^{116}Sn	5.2
416	Kleinheinz	Jülich	Neutr. Def. Lanthanides	^{58}Ni	8.5
417	Speidel, Wollersheim	Garching, GSI	Transient Fields	^{62}Ni	3.8
419	Marinov	Jerusalem	Superheavy Elements	^{88}Sr,^{86}Sr	1.6
420	Egelhof	GSI	(d,p)Reactions	^{124,136}Xe	9.1
422	Hessberger	GSI	Fusion at High Energies	Ar-Ge	4.1
425	Ninov	TH Darmstadt	gasfilled Separat.	^{16}O, ^{22}Ne	11.4
426	Hofmann	GSI	Vorber. Synth. 110	^{40}Ar, ^{48}Ca, ^{50}Ti	3.7
427	Schmidt-Ott	Univ. Göttingen	Very Neutr.-Rich Isot.	^{20}Ne	2.4
428	Olmi	Firenze	Dissip. Coll.	^{120}Sn	6.5
432	Kratz	Univ. Mainz	Excitat. Energy Sharing	^{50}Ti	2.4
434	Hagel		Photon Production	^{120}Sn	9.4
435	Zylicz, Roeckl	Univ. of Warsaw, GSI	Beta-Decay	^{58}Ni	3.8

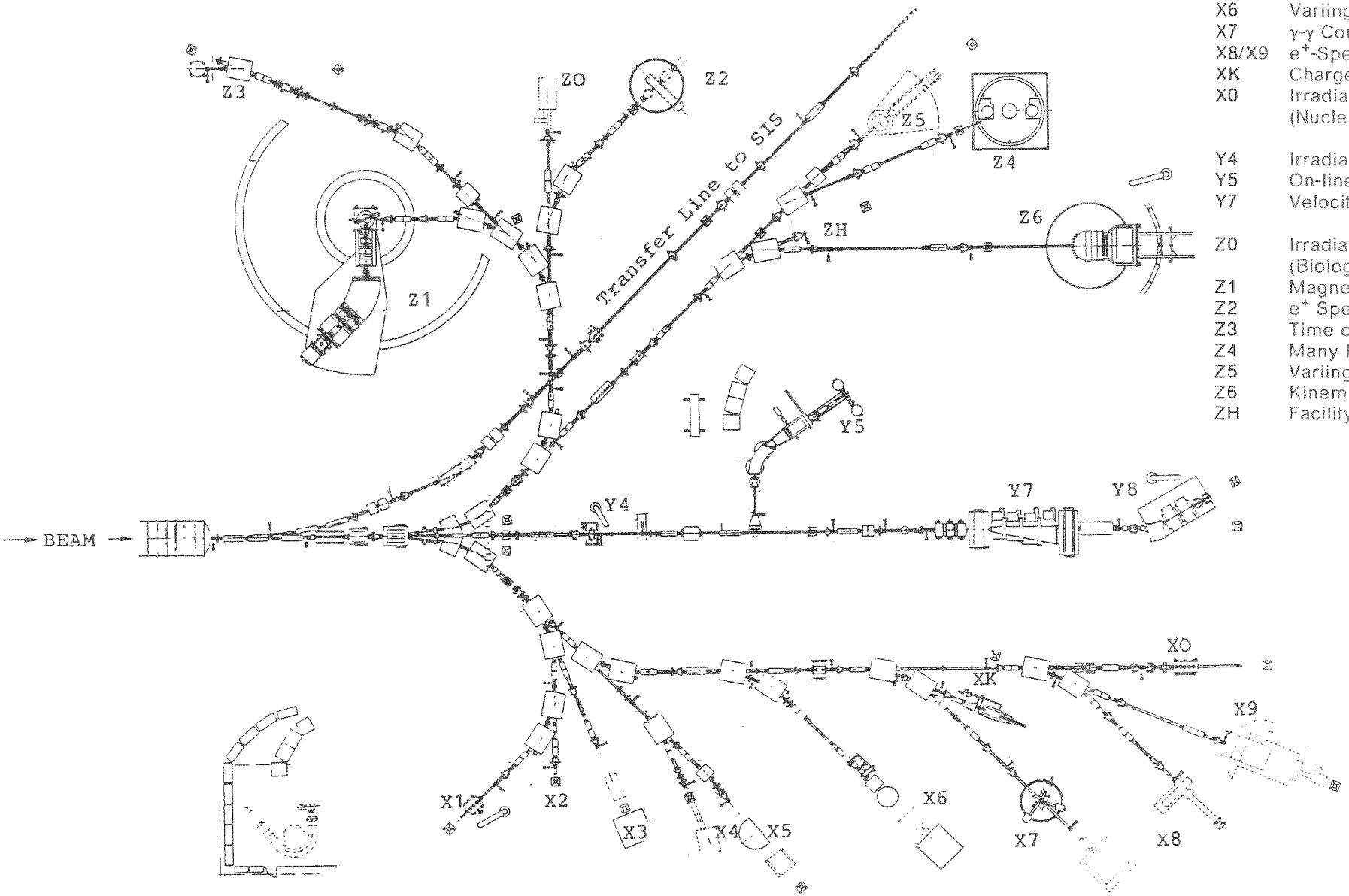
ATOMIC PHYSICS

325	A. Ulrich	TH München	HI-Pumped Laser	^{40}Ar,^{238}U	3.6
354	Dietrich, Mokler	Livermore,GSI	X-Ray-Spectr.	Pb^{71+}	2.5
397	Kienle, Kozhuharov	GSI	Positron-Spectrosc.	^{238}U	17.0
410	Träbert, Mokler	Cambridge, GSI	forbidden Cross-overs	Xe	1.5
421	Deslattes, Beyer	Gaithersburg,GSI	Accur. Spectrosc.	Ni^{28+}	3.3
433	Livingston	Notre Dame	He-like Heavy Ions	Kr^{35+}	4.1

SOLID STATE PHYSICS and APPLIED HEAVY ION RESEARCH

383	Steinhof	GSI	Acc. Mass Spectr.	^{40,41}Ca, ^{41}K	2.4
423	Jousset	CIRIL Caen	Electr. Stopp. Power	U	2.7
436	Dunlop	Palaiseau	Low Temp. Irrad.	U	1.0
var.	Coordinator: Kraft	GSI	Biology	diff. proj.	9.2
var.	Coordinator: Vetter	GSI	Nuclear Tracks	diff. proj.	0.6

EXPERIMENTAL AREA



X1	Irradiation Experiments
X2	Variing Equipment
X3/4	Set-ups for Atomic Physics
X5/XL	Set-ups for Atomic Physics
X6	Variing Equipment
X7	γ-γ Correl. Measurements
X8/X9	e^+-Spectrometer
XK	Charge Changing Processes
X0	Irradiation Facility (Nuclear Tracks)
Y4	Irradiation Experiments
Y5	On-line Isotope Separator
Y7	Velocity Separator 'SHIP'
Z0	Irradiation Experiments (Biology)
Z1	Magnetic Spectrometer
Z2	e^+ Spectrometer
Z3	Time of Flight Telescope
Z4	Many Particle Telescope
Z5	Variing Equipment
Z6	Kinem. Coincidence Telescope
ZH	Facility for Polarized γ's

NUCLEAR PHYSICS / NUCLEAR CHEMISTRY

Some of the results included here are progress reports of research projects and therefore should be considered as preliminary communications.

Several University projects were funded by the Federal Ministry for Research and Technology (BMFT); they are marked with a 'B' after the title. In addition GSI supported external groups with certain recources for development of methods and facilities which are of general interest, this is indicated by a 'G' in the title.

1. NUCLEAR PHYSICS / NUCLEAR CHEMISTRY

PAGE

1.1 NUCLEAR STRUCTURE 11

1.1.1 Exotic Nuclei

Gamow-Teller Strength of the Beta Decays of ^{102}Cd and ^{98}Pd 11
K. Rykaczewski, R. Barden, H. Gabelmann, I. Grant, H. Keller, R. Kirchner, O. Klepper, A. Kolasinski, M. Pfützner, A. Plochocki, E. Roeckl, D. Schardt, J. Szerypo, J. Zylicz,

The Beta-Decay of ^{48}Mn: Improved Data on Gamow-Teller Quenching 12
J. Szerypo, D. Bazin, B.A. Brown, D. Guillemaud-Mueller, H. Keller, R. Kirchner, O. Klepper, D. Morrissey, E. Roeckl, D. Schardt, B. Sherrill

Parity Violation in the 17/2$^-$ Isomer of ^{93}Tc 13
M. Hass, C. Broude, G. Goldring, N. Takahashi, S. Hofmann, F.P. Heßberger, V. Ninov

Study of the ^{88}Sr + ^{184}W Reaction at 5.1 MeV/u 14
A. Marinov, S. Gelberg, H. Folger, D. Kolb, W. Oelert

Alpha Particle Associated Fission of ^{236}U, ^{240}Pu and ^{252}Cf 15
P. Heeg, M. Mutterer, S. Oberstedt, J.P. Theobald, G. Barreau, N. Carjan, B. Leroux

Light Charged Particle Associated Fission of ^{236}U 16
W. Baum, A. Göpfert, M. Mutterer, U. Nast-Linke, J.P. Theobald, C. Zöller, T. Doan, G. Barreau, B. Leroux, A. Sicre

1.1.2 Nuclear Spectroscopy and High Spin States

Two-Nucleon Excitations in $^{148}_{66}Dy_{82}$ from Gamow-Teller Decay of the $^{148}_{67}Ho_{81}$ (6$^-$) Isomer 17
B. Rubio, J.L. Tain, P. Kleinheinz, D. Schardt, R. Barden, J. Blomqvist,

Measurements of Transient Magnetic Fields on Single-Electron Ni-Ions 18
K.-H. Speidel, J. Cub, M. Knopp, H.-J. Simonis, H.-J. Wollersheim, P. Egelhof, H. Emling, H. Grein, W. Henning, R. Holzmann, R.S. Simon, R. Schmidt, N. Gollwitzer

β^+-Endpoint Measurements of Neutron-Deficient Nuclei Near ^{100}Sn and ^{146}Gd 19
H. Keller, R. Kirchner, O. Klepper, E. Roeckl, K. Rykaczewski, D. Schardt, R.S. Simon, P. Kleinheinz, W. Meczynski, R. Menegazzo, C.F. Liang, P. Paris, J. Zylicz

Quadrupole Collective Dynamics in ^{128}Xe 20
J. Srebrny, W. Karczmarczyk, P. Napiorkowski, T. Czosnyka, Ch. Droste, H.J. Wollersheim, H. Emling, H. Grein, R. Kulessa, D. Cline, C. Fahlander

Search for Two-Octupole Phonon States in ^{208}Pb 21
H.J. Wollersheim, P. Egelhof, H. Emling, W. Henning, P. Holzmann, R. Kulessa, R.S. Simon, J. de Boer, E. Hauber, K. Kaiser, P. von Brentano, R. Reinhardt, R. Wirowski, C. Fahlander, R. Julien

1.2 NUCLEAR REACTIONS 22

1.2.1 Nuclear Reactions at UNILAC Energies

Cold Fusion Reactions with ^{48}Ca 22
H.W. Gäggeler, D.T. Jost, A. Türler, P. Armbruster, W. Brüchle, H. Folger, F.P. Heßberger, S. Hofmann, G. Münzenberg, V. Ninov, W. Reisdorf, M. Schädel, K. Sümmerer, J.V. Kratz, U. Scherer, M.E. Leino

Fusion in the Reactions $^{110}Pd + {}^{110}Pd$, ^{104}Ru 23
W. Morawek, D. Ackermann, T. Brohm, H.-G. Clerc, U. Gollerthan, E. Hanelt, M. Horz, W. Schwab, B. Voss, K.-H. Schmidt, F.P. Heßberger

A Comparative Study of Angular Momentum Distributions in the Sub-Barrier Fusion Reactions $^{32}S + {}^{100}Mo$ and $^{36}S + {}^{96}Mo$ 24
H.-J. Hennrich, G. Breitbach, W. Kühn, V. Metag, R. Novotny, D. Habs, D. Schwalm

Angular Distributions of Fissionlike Products for 5.2 MeV/u $^{40}Ar + {}^{165}Ho$ 25
M. Knaack, B. Jäckel, R.A. Esterlund, H. Schulte, W. Westmeier, P. Patzelt

Reactions of ^{40}Ar with ^{233}U, ^{235}U and ^{238}U at the Barrier 26
U.W. Scherer, W. Brüchle, M. Brügger, C. Frink, H. Gäggeler, G. Herrmann, J.V. Kratz, K.J. Moody, M. Schädel, K. Sümmerer, N. Trautmann, G. Wirth

1n-Transfer Reactions in Collisions of U + Au and Au + Au near the Coulomb Barrier 27
G. Wirth, W. Brüchle, F. Wo, E. Jäger, K. Sümmerer, F. Funke, J.V. Kratz, N. Trautmann

Multi-Nucleon Transfer in U + U and U + Au Collisions below and near the Coulomb Barrier 28
F. Funke, J.V. Kratz, N. Trautmann, G. Wirth, W. Brüchle, F. Wo, E. Jäger, K. Sümmerer

Isotope Production in Fast Fission of ^{20}Ne and ^{238}U 29
W.-D. Schmidt-Ott, F. Meissner, P. Koschel, U. Bosch, H. Folger, R. Kirchner, O. Klepper, E. Roeckl, K. Rykaczewski

Indication of In-Flight Separated Evaporation-Nuclei Like α-Emitter from Bombardments of ^{72}Ge, ^{76}Ge with ^{120}Sn at E/A = 14.5 MeV/u at SHIP 30
F.P. Heßberger, V. Ninov

Investigation of Reactions Leading to Highly Excited Compound Nuclei $75 \leq Z_{CN} \leq 82$ 31
F.P. Heßberger, V. Ninov, A. Lüttgen, D. Ackermann, W. Morawek

Investigation of Evaporation Residues from Highly Excited Heavy Compound Nuclei 32
F.P. Heßberger, V. Ninov, A. Lüttgen, D. Ackermann, W. Morawek

Evaporation Residues at E ≃ 400 MeV 33
S. Beiersdorf, R.A. Esterlund, M. Knaack, B. Jäckel, W. Westmeier, P. Patzelt, F.P. Heßberger, V. Ninov

Investigation of the (d,p)-Reaction on ^{132,136}Xe Using the Methode of Inverse Kinematics 34
G. Kraus, P. Egelhof, H. Emling, E. Grosse, W. Henning, R. Holzmann, P. Senger, H.J. Wollersheim, R. Kulessa, W. Walus, Ch. Schiessl, H.J. Körner, W. Wagner, J.P. Schiffer

Trajectory Determination and Entrance Channel Effects in Heavy Ion Collisions at 12.0 MeV/u 35
R. Barth, E. Ditzel, H. Friedemann, E. Kankeleit, G. Klotz-Engmann, V. Lips, Ch. Müntz, H. Oeschler, A. Piechaczek, W. Polai, M. Rhein, I. Schall

Evidence for Non-Equilibrated Fission in Dissipative Collisions at 20 MeV/u 36
G. Casini, A.A. Stefanini, M. Bini, P.R. Maurenzig, A. Olmi, G. Poggi, R.J. Charity, R. Freifelder, A. Gobbi, K.D. Hildenbrand, N. Herrmann, M. Tanaka, J. Wessels

Emission of Complex Fragments in Deeply Inelastic Collisions 37
J. Wessels, R. Bock, R.J. Charity, R. Freifelder, A. Gobbi, N. Herrmann,, K.D. Hildenbrand, H. Stelzer, M. Gnirs, D. Pelte, D. Reimold, G. Casini, P. Maurenzig, A. Olmi, A.A. Stefanini, M. Petrovici

Pre-Equilibrium Light Particle Emission in Deep-Inelastic Reactions 38
R.J. Charity, J. Wessels, R. Freifelder, A. Gobbi, N. Herrmann, K.D. Hildenbrand, F. Rami, H. Stelzer, P.R. Maurenzig, A. Olmi, A.A. Stefanini, M. Petrovici, M. Gnirs, D. Pelte, D. Reimold, J.C. Adloff, B. Bilwes, R. Bilwes, G. Rudolf, J. Galin, D. Guerreau, U. Jahnke

Emission of Light Particles in the Symmetric Reaction ^{100}Mo + ^{100}Mo 39
M. Gnirs

Light Particle Emission in Central Heavy Ion Collisions of Mass Symmetric Systems 40
A. Oberstedt, P. von Neumann-Cosel, A. Richter, W. Rösch, G. Schrieder, D. Bellm, R. Gentner, K. Keller, L. Lassen, W. Cassing, D. Hilscher, M. Lehmann

Production and Decay of Hot Nuclei Observed in the Reaction 15 MeV/u ^{86}Kr + ^{58}Ni, ^{27}Al 41
R. Mühlhans, G. Breitbach, W. Kühn, V. Metag, R. Novotny, D. Pelte, U. Winkler, A. Gobbi, K.D. Hildenbrand

Emission of High Energy Photons in the Reaction ^{136}Xe + ^{48}Ti at 18.5 MeV/u 42
G. Enders, K. Hagel, W. Kühn, V. Metag, R. Novotny, O. Schwalb, A. Gobbi, K.D. Hildenbrand, R. Freifelder, R. Charity, J. Wessels, W. Henning, R. Mayer, R.S. Simon, A. Olmi, A.A. Stefanini

Limiting Excitation Energy in Si + Si Reactions 43
R.J. Meijer, P.F. Box, P. Decowski, E. Gierlik, R. Kamermans, G.J. van Nieuwenhuizen, K.A. Griffioen, H.W. Wilschut, A. Giorni, C. Morand, A. Demeyer, D. Guinet

Nuclear Isomers Produced (and Stopped) in a Thin Au Target by ^{74}Ge at 18.8.MeV/u 44
I.V. Anicin, A.H. Kukoc, P.R. Adzic, D. Toprek, R.B. Vukanovic, M.T. Zupancic, D.M. Krmpotic

Interaction Study of 15 MeV/nucleon U on Au Target 45
U. Kimoundri, M. Zamani, M. Debeauvais, J. Ralarosy, S. Jokic, F. Fernandez

Multifragment Emission in Reaction of Kr on Ag and Au at 17.7, 27 and 35 MeV/nucleon 46
M. Zamani, M. Debeauvais, J. Ralarosy, J.C. Adloff, F. Fernandez, S. Jokic, D. Sampsonidis

1.2.2 Reactions at SIS Energies

Transient Times of Fission in ^{40}Ar + ^{232}Th Pheripheral Collisions 47
E.-M. Eckert, A. Kühmichel, J. Pochodzalla, K.D. Hildenbrand, U. Lynen, W.F.J. Müller, H.J. Rabe, H. Sann, H. Stelzer, W. Trautmann, T. Trockel, R. Wada, C. Cerruti, P. Lhénoret, R. Lucas, C. Mazur, C. Ngô M. Ribrag, E. Tomasi, A. Demeyer, D. Guinet

Fragment Emission in the Reaction ^{40}Ar + ^{197}Au at E/A = 30 and 220 MeV 48
U. Milkau, E. Berdermann, B. Berthier, C. Cerruti, A. Demeyer, E.-M. Eckert, D. Guinet, K.D. Hildenbrand, P. Kreutz, G.J. Kunde, S. Leray, P. Lhénoret, R. Lucas, U. Lynen, C. Mazur, W.F.J. Müller, C. Ngô, C.H. Pinkenburg, J. Pochodzalla, H.J. Rabe, G. Raciti, M. Ribrag, H. Sann, H. Stelzer, E. Tomasi, W. Trautmann, R. Trockel, R. Wada

Interaction Cross Section Measurements of the Neutron-Rich Isotopes ^{8,9,11}Li at 100 MeV/u 49
B. Blank, J.-J. Gaimard, H. Geissel, K.-H. Schmidt, H. Stelzer, K. Sümmerer, H.-G. Clerc, E. Hanelt, M. Steiner, B. Voss, D. Bazin, R. Del Moral, J.-P. Dufour, A. Fleury, F. Hubert

Emission Temperatures in ^{40}Ar + ^{197}Au Reactions at E/A = 200 MeV 50
G.J. Kunde, J. Pochodzalla, C.H. Pinkenburg, E. Berdermann, B. Berthier, C. Cerruti, C.K. Gelbke, J. Hubele, P. Kreutz, S. Leray, R. Lucas, U. Lynen, U. Milkau, C. Ngô, G. Raciti, H. Sann, W. Trautmann

Formation of Delta-Resonances in P-Nucleus Collisions 51
M. Trzaska and DIOGENE-Group

1.2.3 Reactions at Relativistic Energies

Pion Interferometry in Nucleus-Nucleus Collisions at 200 GeV/nucleon 52
J. Bächler, J. Bartke, H. Bialkowska, R. Bock, R. Brockmann, S.I. Chase, C. de Marzo, I. Derado, V. Eckardt, J. Eschke, C. Favucci, D. Ferenc, M. Gazdzicki, H.J. Gebauer, E. Gladysz, C. Guerra, O. Hansen, J.W. Harris, W. Heck, M. Hoffmann, T. Humanic, K. Kadija, S. Kabana, A. Karabarbounis, R. Keidel, J. Kosiec, M. Kowalski, A. Kühmichel, M. Lahanas, J. Lee, M. LeVine, A. Ljubicic, S. Margetis, E. Nappi, G. Odyniec, G. Paic, A.D. Panagiotou, A. Petridis, J. Pfennig, F. Posa, H.G. Pugh, F. Pühlhofer, G. Rai, A. Ranieri, W. Rauch, R. Renfordt, D. Röhrich, H. Rothard, K. Runge, A. Sandoval, E. Schmitt, N. Schmitz, I. Schneider, L.S. Schroeder, G. Selvaggi, P. Seyboth, J. Seyerlein, E. Skrzypczak, P. Spinelli, R. Stock, H. Ströbele, L. Teitelbaum, A. Thomas, S. Tonse, G. Vassileiades, G. Vesztergombi, D. Vranic, S. Wenig

Negative Particle Spectra in S + S Collisions at 200 GeV/nucleon 53
H. Rothard, S. Wenig, E. Schmidt, A. Kühmichel, D. Röhrich, H. Ströbele, R. Stock and NA35 Collaboration

Proton Rapidity Distributions in $^{32}S + ^{32}S$ Collisions at 200 GeV/nucleon 54
S. Wenig, H. Rothard, D. Röhrich, R. Renfordt, H. Ströbele, R. Stock and NA35 Collaboration

Enhanced Strange and Antistrange Particle Production in Central S + S Collisions at 200 GeV/A 55
S. Kabana, A. Thomas, R. Stock, H. Ströbele, M. Gazdzicki, O. Hansen, I. Derado, P. Seyboth, K. Kadija and NA35 Collaboration

Particle Identification of Charged Kaons in the Na35 Streamer Chamber 56
J.-Y. Lee, S. Kabana, D. Röhrich, H. Ströbele, R. Stock and NA35 Collaboration

The Frankfurt Image Processing System for NA35 Streamer Chamber Pictures 57
D. Röhrich, J. Kosiec, A. Kühmichel, J. Pfennig, G. Roland, E. Schmidt, I. Schneider, R. Stock and NA35 Collaboration

The Time Projection Chamber for the NA35 Experiment at CERN 58
V. Eckardt, W. Rauch, N. Schmitz, P. Seyboth, J. Seyerlein, R. Bock, R. Brockmann, R. Renfordt, R. Stock, J.W. Harris, H. Pugh and NA35 Collaboration

Tests with Laser Beams in the Aleph TPC90 at CERN 59
R. Brockmann, H. Gutbrod, B. Kolb, T. Przybyla, R. Schmidt, R. Renfordt and NA35 and WA80 Collaboration

A 50x50 cm^2 RICH Detector Prototype for Ultrarelativistic Heavy Ion Collisions 60
J. Bächler, R. Bock, W. Dominik, A. Gougas, J. Eschke, W. Heck, M. Hoffmann, T. Hernandez-Benavides, A. Karabarbounis, M. Koncul, M. Le Vine, A. Ljubicic, Jr., G. Millon, M. Mongelli, E. Nappi, G. Paic, A. Panagiotou, A. Petridis, A. Posa, A. Sandoval, E. Schmoetten, P. Spinelli, R. Stock, G. Vasileiadis, M. Vasiliou, D. Vranic, M. Wensveen, N. Zaganidis

Automatic Measurement of NA35 Streamer Chamber Pictures 61
R. Keidel, A. Piper, F. Pühlhofer and NA35 Collaboration

Automatic Streamer Chamber Event Reconstruction 62
M. Fuchs, B. Fleischmann, J. Kosiek, A. Kühmichel, J. Pfennig, D. Röhrich, A. Sandoval, R. Stock, G. Vesztergombi and NA35 Collaboration

Transverse Energy Distributions in Central S-Nucleus Interactions at 200 GeV/Nucleon 63
W. Heck, S. Margetis, C. Guerra, R. Stock, H. Ströbele and NA35 Collaboration

Improving the Momentum Distribution in the Analysis of NA35 Streamer Chamber Data 64
A. Piper, R. Keidel, F. Pühlhofer and NA35 Collaboration

Photon Transverse Momentum Distributions in Ultrarelativistic Heavy-Ion Collisions at the CERN-SPS 65
WA80 Collaboration (GSI-LBL-LUND-Münster-ORNL)

Transverse Energy Production in the Target Fragmentation Region and the Formation Time of Secondary Hadrons 66
WA80 Collaboration (GSI-LBL-LUND-Münster-ORNL)

Statistical Moments of Transverse Energy, Charged Particle Multiplicity and Forward Energy Distributions 67
WA80 Collaboration (GSI-LBL-LUND-Münster-ORNL)

Correlations of Charged Pions in 200 A GeV O + Au Collisions 68
WA80 Collaboration (GSI-LBL-LUND-Münster-ORNL)

Calorimetry Results from WA80 69
WA80 Collaboration (GSI-LBL-LUND-Münster-ORNL)

Energy-Density Estimates from ^{16}O- and ^{32}S-Induced Reactions 70
WA80 Collaboration (GSI-LBL-LUND-Münster-ORNL)

Global and Local Fluctuations for Central Ultra-Relativistic Heavy-Ion Interactions 71
WA80 Collaboration (GSI-LBL-LUND-Münster-ORNL)

KNO-Scaling of Charged-Particle Multiplicity Distributions in ^{16}O + Au-Reactions at 60 and 200 A GeV 72
WA80 Collaboration (GSI-LBL-LUND-Münster-ORNL)

Transverse Momentum Distributions of Neutral Pions from Heavy-Ion Collisions 73
WA80 Collaboration (GSI-LBL-LUND-Münster-ORNL)

Upper Limit for Direct Photon Production in Heavy-Ion Reactions 74
WA80 Collaboration (GSI-LBL-LUND-Münster-ORNL)

Determination of the Reaction Plane in Relativistic Heavy-Ion Collisions 75
H.H. Gutbrod, K.H. Kampert, B.W. Kolb, A.M. Poskanzer, H.G. Ritter, R. Schicker, H.R. Schmidt

Energy Dependence of the Squeeze-Out Effect in Relativistic Heavy-Ion Collisions 76
H.H. Gutbrod, K.H. Kampert, B.W. Kolb, A.M. Poskanzer, H.G. Ritter, R. Schicker, H.R. Schmidt

Rapidity Distributions of Ca + Ca, Nb + Nb and Au + Au at Bombarding Energies from 250 to 650 MeV/Nucleon 77
H.H. Gutbrod, K.H. Kampert, B.W. Kolb, A.M. Poskanzer, H.G. Ritter, H.R. Schmidt

1.3 THEORY OF NUCLEAR PROPERTIES AND REACTIONS 78

1.3.1 Low Energies

Ground-State Properties of Heavy Nuclei 78
Z. Patyk, A. Sobiczewski

Deformations of Heavy Nuclei 79
Z. Patyk, A. Sobiczewski

Fission Half-Lives of the Heaviest Nuclides 80
Z. Patyk, J. Skalski, A. Sobiczewski

Numerical Treatment of Fission Dynamics 81
H. Klein, D. Schnabel, J.A. Maruhn, W. Greiner

An Advanced Geometry for the Description of General and Especially Strong Asymmetric Fission 82
W. Renner, D. Schnabel, H. Klein, M. Haffner, J. Maruhn, W. Greiner

New Developments in the Geometric Collective Model 83
D. Troltenier, S. Butorac, J.A. Maruhn, W. Greiner

Dynamical Diabatic Hindrance of Heavy-Ion Fusion 84
P. Rozmej, W. Nörenberg

A Variable Barrier Fusion Model 85
D. Kolb, A. Marinov

Nuclear Landau-Zener Effect in the Scattering of ^{17}O on ^{13}C 86
Ch. Borchert, W. Greiner, W. Scheid, A. Thiel

Dissipative Nuclear Fluid Dynamics 87
G. Wu, R. Feng, W. Nörenberg

Reflection-Asymmetric Shapes in Transitional Actinides 88
S. Cwiok, W. Nazarewicz

1.3.2 Intermediate Energies

An Improved Nuclear Fragmentation Model 89
J.-J. Gaimard, K.-H. Schmidt, M.S. Pravikoff

Properties of Particles from the High Density Region 90
C. Hartnack, H. Stöcker, W. Greiner

Fragment Flow in the Relativistic BUU Model 91
V. Koch, B. Blättel, W. Cassing, U. Mosel, K. Weber

K^+-Production at Subthreshold Energies 92
G. Batko, W. Cassing, K. Niita, G. Wolf

Resonances in Particle Production 93
M. Schäfer, A. Engel, T. Vetter, T.S. Biro, W. Cassing, U. Mosel

Dilepton Production in Heavy-Ion Collisions 94
G. Wolf, G. Batko, W. Cassing, U. Mosel, K. Niita, M. Schäfer

Relativistic Kinetics of Nuclear Collisions 95
M. Schönhofen, M. Cubero, B.L. Friman, W. Nörenberg

Thermodynamical Analysis of Relativistic Heavy-Ion Collisions 96
A. Lang, B. Blättel, W. Cassing, V. Koch, U. Mosel, K. Weber

Retardation and Radiation Effects in the RBUU-Model 97
K. Weber, B. Blättel, V. Koch, A. Lang, W. Cassing, U. Mosel

A Relativistic Effective Interaction for Heavy-Ion Collisions 98
B. Blättel, V. Koch, W. Cassing, U. Mosel

Intermediate Energy Heavy Ion Collisions with G-Matrix Potentials and Cross Sections 99
J. Jaenicke, J. Aichelin, N. Ohtsuka, R. Linden, A. Faessler

Photon Production in Heavy Ion Collisions at Intermediate Energies 100
N. Ohtsuka, M. El Shabshiry, M. Ismail, A. Faessler, J. Aichelin

Relativistic Approach to Intermediate Energy Heavy Ion Reactions 101
T. Maruyama, N. Ohtsuka, A. Faessler, J. Aichelin

Relativistic Effects in Molecular Dynamics Simulations of Heavy-Ion Collisions 102
H. Feldmeier, B. Kämpfer, O. Knospe, R. Schmidt

Fermionic Molecular Dynamics 103
H. Feldmeier

Effect of 3α-Like States in ^{12}C - ^{12}C Scattering 104
G. Pantis, R. Linden, N. Ohtsuka, A. Faessler

Quasiclassical Studies of Equation of State for Inhomogeneous Nuclear Matter 105
G. Peilert, H. Stöcker, W. Greiner, J. Randrup

Relativistic Hartree Fock with Skyrme Type Interactions 106
B.A. Nikolaus, D.G. Madland, D.D. Strottman, T. Hoch, P. Manakos

Bounds on the Coupling Parameters for Vector Mesons in the Relativistic Random Phase Approximation 107
G. Heyer, P. Manakos, T. Mannel, T. Ohl

Improving the Soliton Bag for Nuclear Matter Modeling 108
Ch. Derreth, W. Greiner

1.3.3 High Energies

Nuclear Stopping in Heavy Ion Collisions at AGS Energies 109
H. Sorge, A. von Keitz, R. Mattiello, H. Stöcker, W. Greiner

Pair Creation in a Flux Tube 110
Th. Schönfeld, A. Schäfer, B. Müller, K. Sailer, J. Reinhardt, W. Greiner

Space-Time Effects in the Decay of Strings by Pair-Creation 111
M. Herrmann, J. Knoll

Flavour Kinetics II, Extensions and New Results 112
H.W. Barz, B.L. Friman, J. Knoll, H. Schulz

Evaporation of Hadrons from Quark-Gluon Plasma Globs 113
H.W. Barz, B.L. Friman, J. Knoll, H. Schulz

Production of Supersymmetric Particles in Ultrarelativistic Heavy-Ion Collisions 114
J. Rau, B. Müller, W. Greiner, G. Soff

'Soft' Coherence in Bose-Einstein Correlations 115
I.V. Andreev, R.M. Weiner

Transverse Energy Distributions in High Energy Collisions 116
S. Raha, R.M. Weiner, G. Wilk, Z. Wlodarczyk

Information Entropy and the Multiparticle Production Processes 117
G. Wilk, Z. Wlodarczyk

Number of Sources in Multiparticle Production 118
R.M. Weiner, G. Wilk, Z. Wlodarczyk

Self-Similar Structures in Multiparticle Production and KNO Violation 119
S. Raha, R.M. Weiner, G. Wilk

Diquarks in Nuclear Medium in the Few Mode QCD 120
L. Polley, M.H. Wendel

Massive Gluon Matter 121
T.S. Biro, U. Kalmbach

1.3.4 Miscellaneous

Magnetic Neutrino Scattering by Crystal Lattices 122
J. Augustin, B. Müller, W. Greiner

Comparing Grid Techniques for Nuclear Hartree-Fock Calculations 123
V. Blum, J.A. Maruhn, W. Greiner, G. Lauritsch, P.-G. Reinhard

New Algorithms to Solve the Hydrodynamic Equations 124
U. Katscher, B. Waldhauser, V. Schneider, J. Maruhn, W. Greiner

Gamow-Teller Strength of the Beta Decays of ^{102}Cd and ^{98}Pd

K.Rykaczewski[1,2],R.Barden[1],H.Gabelmann[3], I.Grant[3], H.Keller[1],R.Kirchner[1],O.Klepper[1], A.Kolasiński[4], M.Pfützner[1,2],A.Płochocki[2], E.Roeckl[1],D.Schardt[1], J.Szerypo[1,2],J.Żylicz[2]

[1]GSI,Darmstadt,FRG; [2]Warsaw University,Warsaw,Poland; [3]CERN,Geneva,Switzerland; [4]Astronomical Observatory,Frombork, Poland

Studies of $\pi g_{9/2} \rightarrow \nu g_{7/2}$ Gamow-Teller (GT) transitions in the neighbourhood of the doubly magic ^{100}Sn were continued with the on-line mass separators at GSI and Isolde/CERN. The relatively simple decays of even-even nuclei in this region are serving, e.g., as a test of the reliability of nuclear-structure model approximations, which are required for estimating of double beta decay rates [1,2,3]. As the impact of measured GT strength values B_{GT} on the model parameters depends strongly upon the experimental accuracy, the attempt was made to improve the data of ^{102}Cd and ^{98}Pd decays.

In the cases of ^{96}Pd [4],^{100}Cd [5] and the even tin isotopes [6], the accuracy of the B_{GT} values was mainly limited by the errors of measured decay energies Q_{EC}. This holds also for ^{102}Cd, as experimental data compilations recommend decay energies of 2.9 MeV [7] and 2.36 ± 0.21 MeV [8], despite the reported measurement of $Q_{EC} = 2550 \pm 60$ keV [9]. Using the fusion-evaporation reaction ^{58}Ni (5 MeV/u) + ^{50}Cr (3.5 mg/cm^2) and a β-endpoint spectrometer at the GSI on-line mass-separator, the Q_{EC} value was remeasured to be 2587 ± 8 keV [10] in agreement with [9], but with a precision improved by an order of magnitude. The distribution of the GT strength for the ^{102}Cd decay was investigated in an experiment with a 9 MeV/u ^{16}O beam on a ^{92}Mo target (34 mg/cm^2, enriched to 97.4 %) with a γ-γ-X detector set-up at the GSI on-line mass-separator. Transitions to excited levels in ^{102}Ag at 1965,1727 and 1449 keV were found, simultaneuosly rejecting earlier reported ones [7] to 630,540 and 370 keV levels. Also the accuracy of the half-life value was improved, $T_{1/2} = 345 \pm 8$ s, in comparison to the earlier measured value of 330 ± 30 s. Conversion-electron measurements for the transitions following beta decay of ^{102}Cd were performed with a mini-orange spectrometer attached to the ISOLDE on-line mass-separator at CERN [5]. Distribution of GT transition strength found in ^{102}Cd decay is given in fig.1. The total obseved strength in ^{102}Cd decay is now $B_{GT} = 1.51 \pm 0.04$, compared to earlier quoted value of $1.50 \pm {}^{0.26}_{0.19}$.

The decay energy Q_{EC} and the half-life of ^{98}Pd are known with good accuracy to be 1867 ± 25 keV [8] and 17.7 ± 0.3 min [11], respectively. The main source of the uncertainty of B_{GT} was expected to result from the decay scheme i.e. the GT strength distribution. Indeed, a reinvestigation of the ^{98}Pd decay with the γ-γ$_X$-X detector set-up at the GSI on-line mass-separator (using 4.7 MeV/u ^{40}Ar on 3.1 mg/cm^2 ^{63}Cu reactions) allowed to identify three new $0^+ \rightarrow 1^+$ transitions to excited levels in ^{98}Rh at 1007, 1112 and 1262 keV, see fig.1 . The preliminary analysis gives a total GT strength, measured for the ^{98}Pd decay, of 1.16 ± 0.06 compared to the earlier value of $1.21 \pm {}^{0.10}_{0.14}$ based on an entirely wrong strength distribution [11].

Comparison of the measured B_{GT} values for ^{102}Cd and ^{98}Pd decays to the calculations of Suhonen et al. [12] allows to derive the particle-particle interaction parameter g_{pp} by demanding the reproduction of the observed strength, g_{pp} to be 0.92 ± 0.01 and 1.08 ± 0.02, respectively. These g_{pp} values are outside of the ranges suggested for ^{102}Cd and ^{98}Pd from the calculations and systematics in [12].

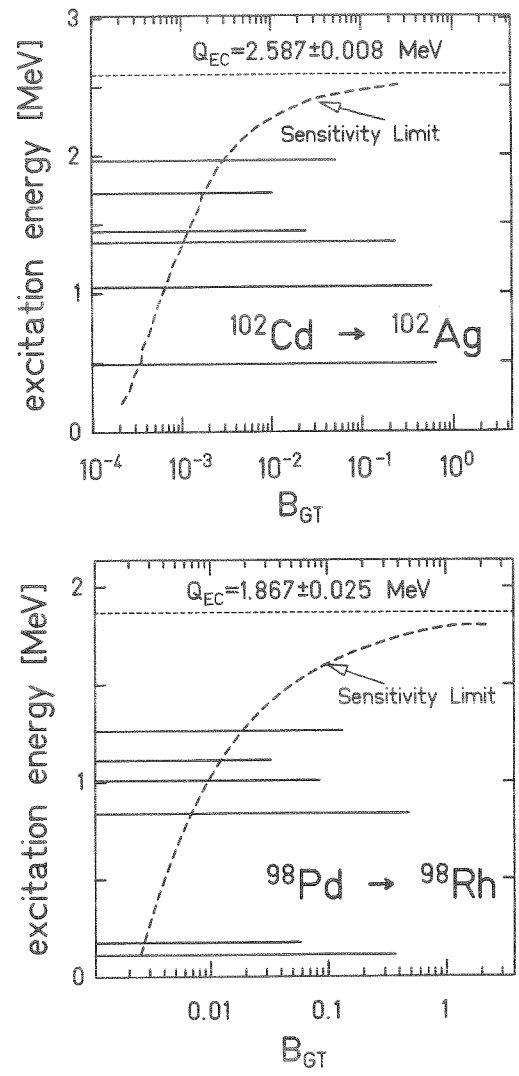


Fig.1: Gamow-Teller strength distribution and experimental sensitivity limits for observation of $0^+ \rightarrow 1^+$ transitions in the decays of ^{102}Cd and ^{98}Pd.

[1] P.Vogel et al.,Phys.Rev.Lett.57(1986)3148
[2] A.Faessler,Phys.Bl.45(1989)321
[3] K.Muto et al.,Z.Phys.A334(1989)187 and references therein
[4] K.Rykaczewski et al.,Z.Phys.A322(1985)263
[5] K.Rykaczewski et al.,Z.Phys.A332(1989)275
[6] R.Barden et al.,Z.Phys.A329(1988)319
[7] P.de Gelder et al.,NDS 35(1982)443
[8] A.H.Wapstra et al., ADNDT 39(1988)281, ed.E.Haustein
[9] L.Westgaard et al.,AMCO-4 Proc.,Teddington 1971,p.94
[10] H.Keller et al.,GSI Scientific Report 1989,in print
[11] H.-W.Müller et al.,NDS 39(1983)467
[12] J.Suhonen et al.,Nucl.Phys.A486(1988)91

The Beta-Decay of ^{48}Mn: Improved Data on Gamow-Teller Quenching

J. Szerypo [a,b], D. Bazin [c], B.A. Brown [d], D. Guillemaud-Mueller [e], H. Keller [a], R. Kirchner [a], O. Klepper [a], D. Morrissey [a,f], E. Roeckl [a], D. Schardt [a], and B. Sherrill [d]

[a] GSI Darmstadt - [b] Warsaw University, Institute of Experimental Physics - [c] CEN Bordeaux - [d] Michigan State University, Department of Physics and Astronomy - [e] GANIL Caen - [f] Michigan State University, Department of Chemistry

Beta-decay studies of very proton-rich nuclides have found renewed interest recently, since they allow, as a competing tool to charge-exchange reactions, to investigate the phenomenon of quenching of Gamow-Teller (GT) transitions. The quenching factor, defined as the ratio between measured and calculated GT transition strength, is used for a renormalization of the weak axial-vector coupling constant or of the calculated GT matrix elements; it therefore covers effects such as second-order configuration mixing, meson exchange, and isobar excitations, which are usually not taken into account in the underlying shell-model calculations. Relevant to this question is, e.g., the first measurement [1] of the beta decay of the very proton-rich fp-shell nuclide ^{48}Mn, which yielded, based on shell-model calculations including 1p-1h excitations, an average GT quenching factor of 0.53(17) for a 0-5.3 MeV interval of excitation energies in the daughter nuclide ^{48}Cr.

In a reinvestigation of the ^{48}Mn decay, we produced this isotope through ^{12}C (^{40}Ca,p3n) reactions and applied γ and proton spectroscopy at the GSI On-Line Mass Separator. From a least-squares analysis of the decay characteristic of the 752 keV γ-line, the ^{48}Mn half-life was determined to be 158.1(8) ms, which is considerably more accurate than the previous value of 150(10) ms (ref.1). The γ singles and $\gamma\gamma$ coincidence measurements lead to a more complete scheme of 9 excited ^{48}Cr levels including a new, tentatively assigned state at an excitation energy of 5608 keV. Furthermore, an improved energy spectrum of beta-delayed protons was obtained (see Fig. 1), and the branching ratio for this decay mode was determined to be 0.280(37)%. Two known γ transitions of 58.3 and 87.6 keV were observed in coincidence with protons, corresponding to a dominant proton feeding of 68(12)% to the 7/2$^-$, 146 keV level in ^{47}V.

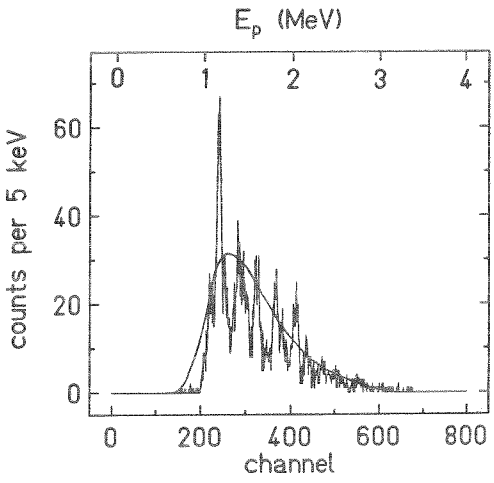


Fig. 1: Measured energy spectrum of beta-delayed protons from the decay of ^{48}Mn, obtained by summing coincident events from a telescope of ΔE (15.6μm, 150mm^2) and E (531μm, 450mm^2) detectors. The energy spectrum from a statistical model calculation [2] is also shown.

The GT transition strength B(GT), deduced from the measured half-life and branching ratios and from an estimated ^{48}Mn Q-value of 13600(100) keV (ref.3), is confronted in Fig. 2 with shell-model predictions including 1p-1h excitations. In deducing B(GT) for ^{48}Cr excitation energies between 8.9 and 11.6 MeV, it was assumed, that all the beta-delayed protons from the ^{48}Mn decay (and not only 68(12)%) feed the 146 keV level of ^{47}V. The resulting GT quenching factors, averaged over ^{48}Cr excitation-energy intervals of 0-5.6 and 8.9-11.6 MeV, are 0.53(6) and 0.53(20), respectively. These values are in agreement with the large majority of quenching-factor data obtained in the sd- and fp-shell regions.

1. T. Sekine et al., Nucl. Phys. A467, 93 (1987)
2. B. Jonson et al., in Proc. 3rd Intern. Conf. on Nuclei far from Stability, Cargese, France, CERN 76-13 (1976), 277
3. A.H. Wapstra and G. Audi, Nucl. Phys. A432, 1 (1985)

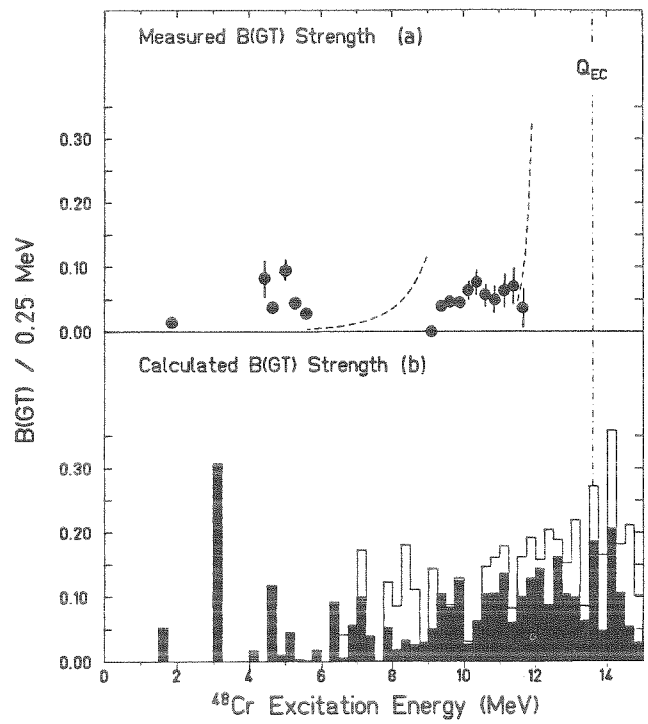


Fig. 2: Comparison of experimental and calculated B(GT) strength for the ^{48}Mn decay. The measured strength is shown in part (a). The dashed lines give the estimated experimental sensitivity limits, below which B(GT) strength escaped observation in this experiment. Part (b) shows the calculated strength [2]. The B(GT) strength is integrated over 250 keV excitation-energy intervals, even though level energies up to 5.6 MeV were measured with 0.2-0.7 keV accuracies. The dash-dot line marked Q$_{EC}$ represents the upper energy limit of the ^{48}Mn β^+/EC decay.

PARITY VIOLATION IN THE $\frac{17}{2}^-$ ISOMER OF ^{93}Tc

M. Hass,* C. Broude, G. Goldring and N. Takahashi**
The Weizmann Institute of Science, Rehovot, Israel
S. Hofmann, F.P. Hessberger and V. Ninov
GSI, Darmstadt

The ^{93}Tc nucleus has two states of spin 17/2 but opposite parity spaced by only 310 eV. Parity violation (PV) would lead to an abnormal $\tilde{E}2$ in the $17/2^- \rightarrow 13/2^+$ 751 keV transition; with polarized $17/2^-$ isomers, the $\tilde{E}2-M2$ interference would result in a forward-backward asymmetry of the decay γ-rays with respect to the polarization direction. The Tc isomers were polarized by passing through a stack of tilted foils. The ionic polarization induced at the exit surface of each foil is progressively transferred to the nuclei by hyperfine interaction in the space between foils[1].

Earlier work at GSI is described in ref. 2. In the present experiment [3], improved statistical accuracy and higher polarization have considerably enhanced the sensitivity.

A nuclear ensemble with polarization p_I introduces an asymmetry which is a function of the transition matrix elements of the two levels and their energy spacing and is proportional to the PV matrix element. Using values from ref. 4, and the mean life of the $\frac{17}{2}^+$ state $\tau(\frac{17}{2}^+) = 38.6(76)\,ps$ [5] the PV matrix element is:

$$|\langle \frac{17}{2}^- |H_{PV}| \frac{17}{2}^+ \rangle| = 91(28) \times \frac{|A|}{p_I Q_1} \text{ meV} \qquad (1)$$

where A is the measured asymmetry and Q_1 is the geometrical attenuation coefficient of the detectors.

The UNILAC provided a beam of $\sim$ 1 pμA ^{52}Cr at 170 MeV. The isomer produced in the reaction $^{45}Sc(^{52}Cr, 2p2n)^{93}Tc$ passed through the SHIP velocity separator. Foils in front of the tilted foils slowed the recoils to optimize the polarizing interaction. The polarizing foils were made of 3 $\mu g/cm^2$ collodion with 3 $\mu g/cm^2$ of carbon on the exit side providing a surface known to yield a large polarization. The tilt angle was 70° w.r.t. beam. The transit time through SHIP ensured that only isomeric transitions were observed from the lead stopper.

The stack was rotated periodically to switch the polarization between left and right. Gamma-rays were measured in two 70% Ge detectors placed on the axis of polarization, shielded from radiation from the collimator and foils. The ratio ρ is:

$$\rho = \sqrt{\frac{W_l(r)}{W_l(l)} \cdot \frac{W_r(l)}{W_r(r)}}$$

where $W_\ell(r)$ is the intensity in the right detector in the left polarization state. The ratio ρ eliminates instrumental asymmetries fixed in space, e.g. differences in detector solid angle, chamber wall absorption, etc.. Asymmetries associated with the rotation e.g. asymmetric γ-ray absorption and recoil energy loss in rotating parts were evaluated from a double ratio of other isomer lines.

The following values were obtained:

$$\rho(751\ keV) = 0.99627(92) \quad \rho(\text{other isomer lines}) = 0.99862(30)$$

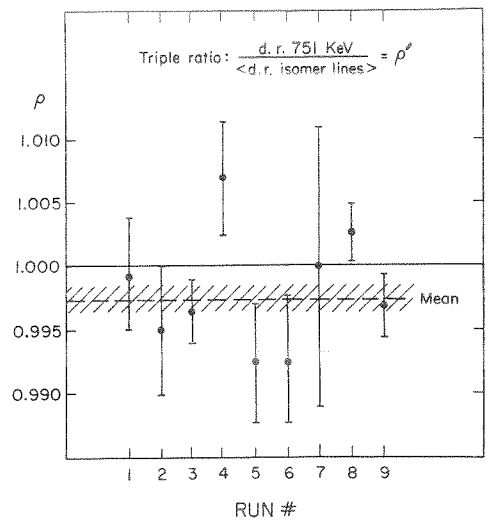
$$\rho' = \rho(751\,\text{keV})/\rho\ (\text{other isomer lines}) = 0.99765(95)$$

The ρ' values for individual runs are shown in the figure.

The asymmetry A is:

$$A = \frac{1-\rho}{1+\rho} = +1.18(48) \times 10^{-3}$$

The polarization was measured[6] at the recoil mass spectrometer of NSRL, University of Rochester, from the time dependent perturbed angular distribution of γ rays from a polarized ^{92}Mo 8^+ isomer in a single crystal of Zr. The amplitude is a measure of the nuclear polarization[7] as $|Q|$ and V_{22} are known. As the quadrupole interaction of Tc in any single crystal is unknown, the neighbouring isomer was measured under nearly identical



conditions. The result, p_I=0.15(3), has been used in evaluating the matrix element in the ^{93}Tc experiment. This is larger than for earlier stacks[8], reflecting the improved conditions when using recoil selectors.

With p_I=0.15(3) and $Q_1 \sim 0.85$, we get from (1):

$$|\langle \frac{17}{2}^- |H_{PV}| \frac{17}{2}^+ \rangle| = 0.8(4)\ meV$$

The ^{93}Tc isomer now appears to allow a definitive PV measurement and the nuclear structure problem does not appear insoluble. It could provide information on the non-strange part of the nuclear weak Hamiltonian. More sensitive measurements are planned at SHIP.

We appreciate the loan of the Ge detectors by K.H.Schmidt and H.J. Wollersheim, GSI. Author N.T. thanks the Israel Association for International Scientific Relations, the Japan Society for Promotion of Science, and the Ministry of Education (Tokyo) for the Grant in Aid of Scientific Research. Support was received from the Deutsch-Israelisches Komitee-Minerva.

1. Goldring, G. and Niv, Y., Hyp. Interact. 21, 209 (1985).
2. Hass, M. et al, GSI Scientific Report 1987, 32 (1988)
3. Broude, C., Goldring, G., Hass, M., Takahashi, N., Hofmann, S., Hessberger, F.P. and Ninov, V., Proc. of the First International Conference on Radioactive Beams, Berkeley, 1989 (in press) and submitted to Z.Phys.
4. Brown, B.A., Häusser, O., Faesterman, T., Ward, D., Andrews H.R. and Horn, D. Nucl. Phys. A306, 242 (1978).
5. Bendahan, J., Ph.D. thesis, The Weizmann Institute of Science (1988).
6. Hass, M., Satteson, M., Wu, C.Y., Broude, C. and Benczer-Koller, N., BAPS, 34, 1809 (1989).
7. Hass, M., Dafni, E., Bertschat, H.H., Broude, C., Davidovsky, F., Goldring, G. and Lesser, P.M.S., Nucl. Phys. A414, 316 (1984).
8. Bendahan, J., Broude, C., Dafni, E., Goldring, G., Hass, M., Naim, E. and Rafailovich, M.H., Hyp. Interact. 34, 139 (1987).

* On leave at NSRL, University of Rochester, Rochester, NY
** On leave from Osaka University, Toyonaka, Japan

Study of the $^{88}Sr+^{184}W$ Reaction at 5.1 MeV/u

A. Marinov[a,b], S. Gelberg[a], H. Folger[c], D. Kolb[d] and W. Oelert[b]

[a] Racah Institute of Physics, The Hebrew University, Jerusalem, Israel.

[b] Institut für Kernphysik, KFA Jülich GmbH.

[c] Gesellschaft für Schwerionenforschung mbH (GSI) Darmstadt.

[d] Department of Physics, Kassel University.

The study of the $^{88}Sr+^{184}W$ reaction is motivated by the consistent interpretation given[1] to the secondary reaction experiments in W targets which were irradiated with 24 GeV protons. It has, for instance, been shown[1] that the measured masses of the fissioning nuclei are consistent with various molecules of element 112 with about 160 neutrons. It has also been pointed out[1] that in principle, under the experimental conditions of the secondary reaction experiments the compound nucleus can be produced at very low excitation energies. The Q value for, for instance, the reaction $^{88}Sr+^{184}W \rightarrow {}^{272}_{112}X_{160}$ is -282.4 MeV[2] while the Coulomb barrier is about 285 MeV. Thus, the radiative capture and the 1n processes, may be possible.

Preliminary experiments using parasitic ^{116}Sn beam were performed to check the durability of the ^{184}W target, the Ta degrader and the C catcher foils to the heavy ion beam. In addition, the background for fission fragments was measured for all together 33 C catcher foils during 48 to 87 days and gave zero results. In another experiment the volatile radioactive nuclei ^{205}Po, ^{209}At and ^{210}Rn were produced and imbedded in C catcher foils via the $^{16}O+^{197}Au$ reaction at 81.4 MeV using the Pelletron accelerator in Rehovot. One of the C foils was then irradiated with 10 pnA of 121 MeV ^{79}Br beam which gives about the same energy loss as 5.1 MeV/u of ^{88}Sr. Alpha and gamma ray activities were studied and no significant loss was found for ^{205}Po and ^{209}At, while for ^{210}Rn a loss of $8.7\pm1.3\%$ and $14.5\pm6.3\%$ was found after 3 and 6 hours of irradiation, respectively.

The $^{88}Sr+^{184}W$ reaction has been studied using 5.1 MeV/u ^{88}Sr beam provided by the UNILAC accelerator in GSI. A stack consisted of 2.0 mg/cm^2 enriched (96.3%) ^{184}W target, followed by 5.0 mg/cm^2 Ta degrader foil and 20 150 µg/cm^2 C catcher foils were irradiated with 5 to 10 pnA ^{88}Sr beam with a total dose of 5.8×10^{15} particles. Under these conditions the expected excitation energies of the compound nucleus are between 0 and 21 MeV[2], it should be stopped[3] in between catcher foil No. 7 and No. 11 and the radiative capture and the 1n reactions are in principle possible. In the first experiment polycarbonate foils covered all the catcher foils for about 24 hours. The search for fission fragments during this period gave negative results with an upper limit on the cross section of 10 nb for halflife of about 14 days. In the second experiment all the catcher foils except No. 7 and No. 9 were covered with polycarbonate foils for about 46 days and did not show any fission fragment. Foil No. 9 was situated for 58 days in between two Si surface barrier detectors for measuring spectra of alpha particles and fission fragments and coincidences between two particles with a resolving time of 5 microsecond. Foil No. 7 was situated, also for 58 days, in between a Si surface barrier detector and a thin window Ge(li) detector for measuring particles versus X and γ rays coincidences with a resolving time of 1 microsecond. Two results which may be significant have been obtained. One coincidence event has been found between an alpha particle of $12.16\pm^{0.3}_{0.1}$ MeV and a fission fragment of $45.8\pm^{20}_{0.4}$ MeV. (The large uncertainties toward the higher energies reflect the thickness of the catcher foil and the large solid angle. The effect of pulse height defect[4] in the silicon detector may increase the energy of the fission fragment by about 10% to about $50\pm^{20}_{0.4}$MeV). The energy of the alpha particle fits with the predictions [2,5] made for element 112 with 159 or 160 neutrons, and the energy of the fission fragment fits with the energy of the low energy group found in the secondary reaction experiments[1].

In the particle versus X-ray coincidence measurement, a coincidence event has been found between 3.8 MeV particle and X or γ ray of 163.7±1.0 keV. 163.7 keV fits with the predictions (163.5 keV according to Carlson and Nestor[6] and 164.1 according to Fricke and Soff[7]) made for the $K_{\alpha 1}$ X-rays of element 112. A possible interpretation of this result may be, for instance, that an isomeric state in $^{271}_{112}X$ or in $^{272}_{112}X$ was formed and decayed by internal conversion (which followed by characteristic X-ray of element 112) to another excited state of the same isotope, which then decayed by emitting a proton of 3.8 MeV. Background measurements under identical conditions were measured during 60 days. Large regions around the positions of the above mentioned coincidence events are entirely clean. Thus the probability of these events being background or spurious events are very small.

We would like to thank Prof. G. Herrmann, Dr. M. Schädel and the chemistry group of GSI for helping us with the irraditions.

1) A. Marinov, S. Eshhar, J.L. Weil and D. Kolb, Phys. Rev. Lett. 52 (1984) 2209; 53 (1984) 1120 (E).

2) S. Liran and N. Zeldes, At. Data Nucl. Data Tables 17 (1976) 431.

3) L.C Northcliffe and R.F. Schilling, Nucl. Data Tables, 7 (1970) 233.

4) H.W. Schmitt, W.E. Kiker and C.W. Williams, Phys. Rev. 137 (1965) B 837.

5) Moller and Nix, Moller et al., Tachibana et al., and Spanier and Johannson, in The 1986-1987 Atomic Mass Predictions, P.E. Haustein Editor, At. Data and Nucl. Data Tables 39 (1988) 185.

6) T.A. Carlson and C.W. Nestor, Jr., At. Data Nucl. Data Tables 19 (1977) 153.

7) B. Fricke and G. Soff, At. Data Nucl. Data Tables 19 (1977) 83.

Alpha Particle Associated Fission of $^{236}U^*$, $^{240}Pu^*$ and ^{252}Cf [B]

P. Heeg, M. Mutterer, S. Oberstedt, and J.P. Theobald
Institut für Kernphysik der Technischen Hochschule Darmstadt
G. Barreau, N. Carjan, and B. Leroux
Centre d'Etudes Nucléaires de Bordeaux Gradignan

With the annular position sensitive detector system DIOGENES, a quarter section of which is shown in figure 1 and which is described in detail in ref.)[1], we have investigated thermal neutron induced (on ^{235}U and ^{239}Pu) and spontaneous (on ^{252}Cf) fission associated with the emission of alpha particles. DIOGENES allows to measure the kinetic energies and relative angular distributions of the three reaction products. Alpha particle yields for equatorial as well as for polar emission regimes have been obtained simultaneously as function of the emission angle $\theta_{\alpha L}$ with respect to the light main fragment's flight path and of the masses and kinetic energies of the two main fission fragments. Figure 2 is a two dimensional display of the integral alpha particle yield as function of emission angle $\theta_{\alpha L}$ and α particle energy for the case of ^{252}Cf (s.f.). Data evaluation has been performed with the computer facilities of GSI and a wealth of correlations between the observables has been deduced. They are discussed in refs.)[2,3,4,5,6]. However, only a few results will be presented, which are of particular importance for forthcoming ternary fission theories.

Figure 3 shows for the case $^{235}U(n,f)$ the ternary fission yield as function of the total kinetic energy of the three reaction products TKE = $E_{ff} + E_\alpha$ (E_{ff} = fragment kinetic energy, E_α = α kinetic energy) and of the mass M_H of the main heavy fragments together with mean values and maximum Q values. For comparison, a corresponding plot is shown for binary fission with TKE = E_{ff}. It is obvious that ternary fission is characterized by lower excitation energies of the main fragments as compared to binary fragmentation. Cold fragmentation occurs in a broader mass range than in binary fission. As a concequence, ternary fragments are less deformed than binary ones. Polar alpha particle emission has a different characteristic. Here the average total excitation energy TXE = TKE - Q is higher than in the case of equatorial emission. Nevertheless, there are distinct shell effects on the mass distribution of the main fragments in particular around mass M_H = 132. This is typical for cold fragmentation. From this observation, we can conclude that polar emission is associated with an asymmetric partition of deformation energy between the two main fragments. Model calculations for particle emission are at present going on.)[7]

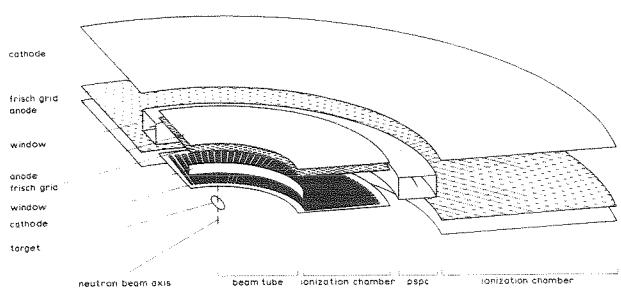


Fig. 1 The kinematic spectrometer DIOGENES

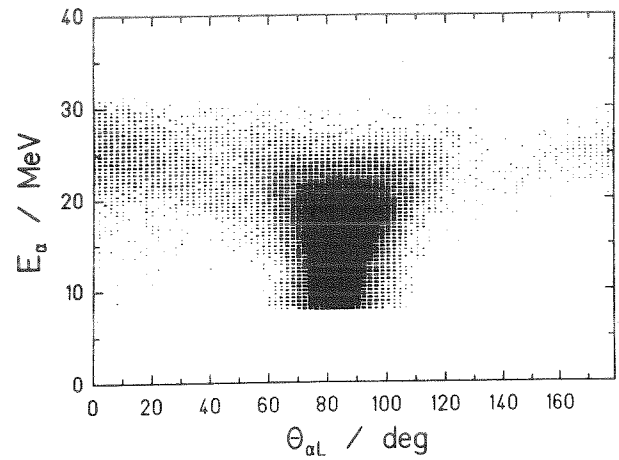


Fig. 2 Two-dimensional α-particle yield distribution of $^{252}Cf(sf)$ as function of $\theta_{\alpha L}$ and E_α

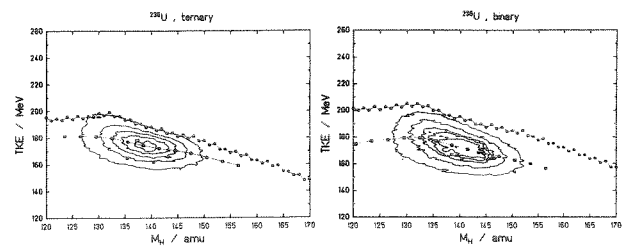


Fig. 3 The sum TKE of the main fragments and alpha particle energies as function of the heavy fragment mass together with the average <TKE> and maximum Q value. For comparison <TKE> = E_{ff} for binary fission.

References

1) P. Heeg et al.
NIM A278 (1989) 452
2) P. Heeg et al.
Proceedings of the XVII Intern. Symposium on Nuclear Physics, Dresden, Nov. 21-25 (1988) in press
3) J. Theobald et al.
Nucl. Phys. A502 (1989) 343c
4) P. Heeg et al.
Proceedings of the Int. Conf. 50 Years with Nuclear Fission, Washington/Gaithersburg, April 25-28, (1989), 299
5) J. Theobald
Proceedings of the Intern. School Seminar on Heavy Ion Physics, Dubna, USSR, Oct. 3-9 (1989) in press
6) M. Mutterer et al.
Proceedings of the Int. Conf. 50th Anniversary of Nucl. Fission, Leningrad, USSR, Oct. 15-20 (1989) in press
7) N. Carjan et al. ibid, 285

Light Charged Particle Associated Fission of ^{236}U [B]

W. Baum, A. Göpfert, M. Mutterer, Ute Nast-Linke, J.P. Theobald, and C. Zöller
Institut für Kernphysik der Technischen Hochschule Darmstadt
T. Doan, G. Barreau, B. Leroux, and A. Sicre
Centre d'Etudes Nucléaires de Bordeaux Gradignan

With the electromagnetic fission product separator LOHENGRIN at the high flux reactor of the Institute v. Laue-Langevin in Grenoble light charged particle yields as function of their kinetic energy have been determined by a large focal plane $\Delta E/E$ telescope with a sensitivity of 10^{-8} - 10^{-9} per binary fission event. For more frequent particles their ionic charge distributions could be recorded,for rare species only one charge state could be measured because of low count rates. The ionic charge distributions for these originally fully stripped particles have been calculated using a new method, which takes also electron shell effects into account.

The experimental results are presented in the table. The data evaluation and model calculations of relative particle yields and mean particle energies have been performed with the computer facilities of GSI.

For the particle yields the double neck rupture model of V.A. Rubchenya and S. G. Yavshits)[1] has been applied. This model is based on the assumption that a first neck rupture separates the heavy fragment from a dinuclear system composed of an initial light fragment and a nascent preliminary light charged particle. Before the second rupture which releases the final light particle, a statistical nucleon exchange between the two parts of the double nuclear system is going on. Calculated particle yields are displayed in figure 1 together with our experimental data and data of A.A. Vorobyov et al)[2]. For the calculation two parameter sets, shown below the figure, have been applied, one of the original paper)[1] and a second one, prefering the even -Z neighbour of the nascent main light fragment introduced by the authors. With the aid of post-scission point charge trajectory calculations it is possible to find appropriate initial conditions for the description of the mean energies of the light charged particles, which could fairly well be reproduced as shown in figure 2. Details of these calculations will be published elsewhere.)[3]

	<E> / MeV	FWHM / MeV	Yield / 10^{-4} α
^{4}He	15.90 ± 0.10	9.80 ± 0.10	10^{4}
^{6}He	10.73 ± 0.03	9.50 ± 0.50	169.00 ± 2.00
^{8}He	8.60 ± 0.20	10.40 ± 0.90	7.40 ± 0.80
^{10}He			< 5 * 10^{-4}
^{7}Li	13.68 ± 0.31	13.56 ± 1.07	2.74 ± 0.25
^{8}Li	12.30 ± 0.37	13.11 ± 0.98	1.43 ± 0.13
^{9}Li	12.51 ± 0.42	14.09 ± 1.37	2.27 ± 0.25
^{9}Be	18.90 ± 0.50	18.50 ± 1.70	4.20 ± 0.40
^{10}Be	17.20 ± 0.10	17.80 ± 0.30	32.00 ± 0.07
^{11}Be	16.30 ± 0.70	16.20 ± 1.70	2.96 ± 0.35
^{12}Be	15.40 ± 0.80	14.30 ± 1.60	1.45 ± 0.20
^{12}B	20.30 ± 1.30	15.00 ± 1.00	0.24 ± 0.04
^{13}B			< 0.01
^{13}C			0.40 ± 0.15
^{14}C	22.30 ± 0.50	21.50 ± 1.30	9.80 ± 0.70
^{15}C	21.90 ± 0.50	18.10 ± 0.90	1.85 ± 0.16
^{16}C	20.70 ± 0.70	17.60 ± 1.10	1.55 ± 0.20
^{18}C			0.05 ± 0.02
^{20}O	24.24 ± 1.59	21.22 ± 3.23	0.18 ± 0.04
^{21}O			< 0.12

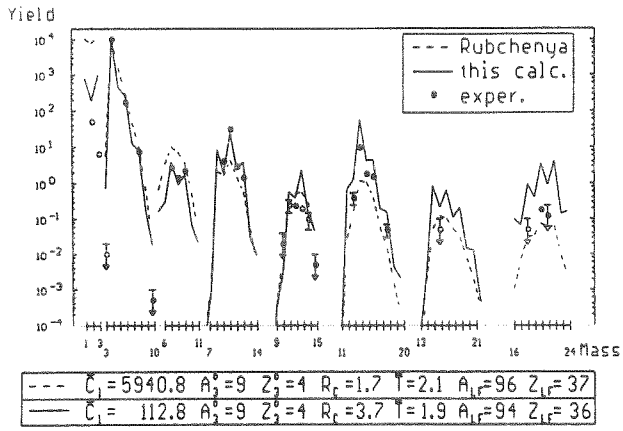


Fig. 1 Relative yields of light charged particles predicted by the double neck rupture model)[1]. The calculations assuming an unpaired nuclear charge of the initial light fragment (dotted lines) and paired nuclear charge (solid lines), respectively, are compared to our experimental results and data from ref.)[2]

The main conclusions of the experiment are:

1. Light charged particles with even proton and with even neutron numbers are emitted preferably.
2. Down to a yield level of 5 x 10^{-8} / emitted alpha particle the double magic nucleus ^{10}He could not be observed. It is particle unstable.
3. The kinetic energies of all particles have a nearly gaussian shape, with some deviations at low energies.
4. The average particle energies have a nearly linear dependence on particle mass and nuclear charge.

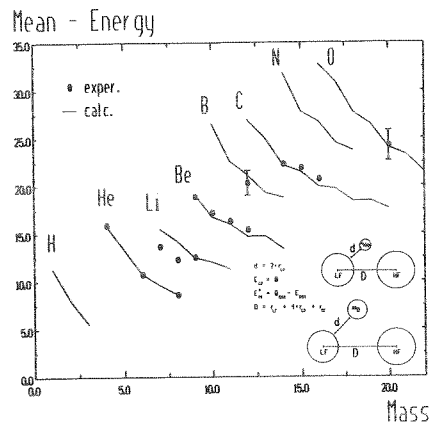


Fig. 2 Mean energies of LCPs as function of mass. Solid lines are the results of trajectory calculations.

References

1) V.A. Rubchenya and S.G. Yavshits
Z.f.Phys. A 329 (1988) 217
2) A.A. Vorobyov et al.
Phys. Lett. 40 B (1972) 102
3) W. Baum
Thesis, Darmstadt 1990, in preparation

Two-Nucleon Excitations in $^{148}_{66}Dy_{82}$ from Gamow-Teller Decay of the $^{148}_{67}Ho_{81}$ (6$^-$) Isomer

B. Rubio[1,2], J.L. Tain[1], P. Kleinheinz[2], D. Schardt[3], R. Barden[3] and J. Blomqvist[4]
[1]IFIC Valencia, [2]IKP,KFA Jülich, [3]GSI Darmstadt, [4]MSI Stockholm

The dominant configuration of the $^{148}Ho_{81}(6^-)$ isomer [1] must involve a proton in the $h_{11/2}$ negative parity orbital coupled to one neutron hole either in the $s_{1/2}$ or in the $d_{3/2}$ positive parity levels. Beta decay to low-lying states in ^{148}Dy can provide valuable information about the the $^{148}Ho_{81}(6^-)$ configuration. Since ^{148}Dy has two protons outside the ^{146}Gd core, these states might also give direct information about proton-proton residual interactions in this region.

Previous knowledge about low-lying ^{148}Dy levels stems mainly from in-beam γ-measurements [2] which established the complete $\pi h_{11/2}^2$ multiplet, the 3$^-$ octupole state, and the $(\pi h_{11/2}s_{1/2})5^-$ and $(\pi h_{11/2}d_{3/2})7^-$ excitations. A previous study of the ^{148}Ho(6$^-$) decay [3] gave one extra level energy at 2.854 MeV. After completion of our study we learned about a similar work on ^{148}Ho(6$^-$) decay [4]; these data are however less complete and did not give any new I^π assignment.

The ^{148}Ho activity was produced by bombarding ^{96}Ru, ^{92,94}Mo, and ^{93}Nb metal targets with 5 MeV/u ^{58}Ni beams from the UNILAC. The reaction products were investigated at the GSI on-line mass separator, using a thermal ion-source. The A = 148 activity was collected during 16 s on a tape and periodically transported to the measuring site between two large-volume coaxial germanium detectors in close geometry. The detection limit was 3×10^{-3} per parent decay at 3 MeV γ-ray energy.

Our measurements resulted in a ^{148}Ho(6$^-$) decay scheme [5] containing twentyfive ^{148}Dy excited states, where six were known [2] from the in-beam work. The ^{148}Ho(6$^-$) half-life was determined as 9.59(15) s. Below 3.5 MeV there are only three states populated with significant strength, among them the previously identified $(\pi h_{11/2}s_{1/2})5^-$ level at 2.350 MeV, which proves that $\pi h_{11/2}\nu s_{1/2}^{-1}$ must have a large amplitude in the ^{148}Ho(6$^-$) parent state. The 2.854 MeV level which is also strongly populated we identify as the 6$^-$ member of the $\pi h_{11/2}s_{1/2}$ configuration, consistent with its γ-decay exclusively to the 5$^-$ multiplet member through the fast 504 keV spin-flip M1 transition. The 5$^-$ state mixes strongly with a state at 2.970 MeV for which only $I^\pi = 5^-$ is compatible with our data. This suggestion is in accord with the expected $B_{GT}(6^-)/B_{GT}(5^-) = 7/11$ ratio. An independent support for the interpretation of the three states mentioned above comes from comparison of the total observed GT-strength, log ft = 5.1(1), with the known log ft value of 5.3(1) for the ^{147}Dy(1/2$^+$ g.st.) $\rightarrow$ ^{147}Tb(1/2$^+$ g.st.) decay.

A similar consideration yields a rather stringent limit for a possible $\pi h_{11/2}\nu d_{3/2}^{-1}$ admixture in the ^{148}Ho(6$^-$) ground-state. Theory predicts for the decay of $(\pi h_{11/2}\nu d_{3/2}^{-1})6^-$ that 53% of the strength should go to the $(\pi h_{11/2}d_{5/2}^{-1})7^-$ daughter state. For possible 7$^-$ candidates between 2.7 and 3.5 MeV the lowest apparent log ft value is 6.1, giving a limit of well below 10% for this admixture. Between 2.9 and 3.5 MeV one should find the remaining members of the $\pi h_{11/2}d_{3/2}$ and the $\pi h_{11/2}d_{5/2}^{-1}$ multiplet. Only these configurations could be reached in β-decay from an even small $\pi h_{11/2}\nu d_{3/2}^{-1}$ admixture in the ^{148}Ho(6$^-$) ground-state. Our interpretation of the observed levels is given in Fig.1 where we have exploited the branching ratios, the fast intra-multiplet γ-decay and the energy systematics. The relative energies of the multiplet members as well as the absolute interactions are found to be similar to those in ^{146}Gd.

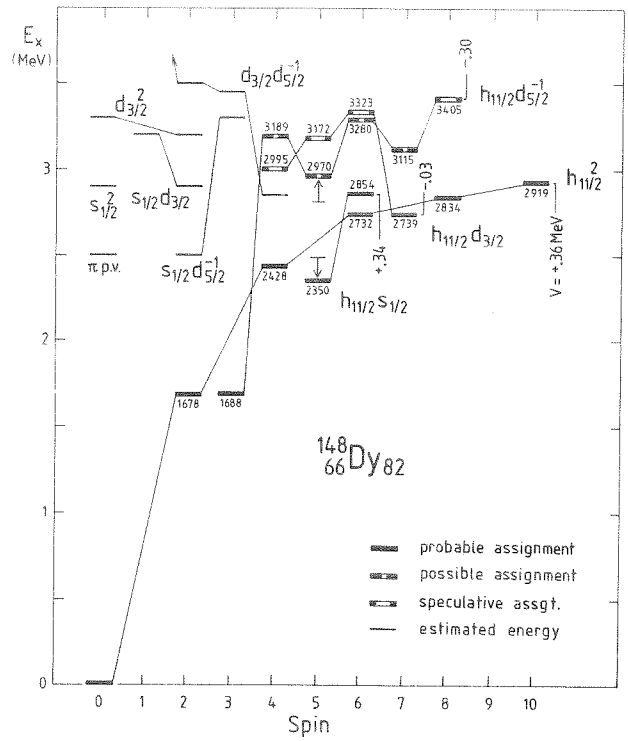


Fig.1: Low-lying two-proton multiplets in ^{148}Dy formed by the two valence protons in $h_{11/2}$, $s_{1/2}$, $d_{3/2}$, and $d_{5/2}^{-1}$. Observed states are labelled with excitation energies. The two-body interaction energies V are specified for the maximum-aligned multiplet members.

The decay of the odd $h_{11/2}$ proton of the ^{148}Ho(6$^-$) isomer should proceed to the $(\nu h_{9/2}s_{1/2}^{-1})5^-$ excitation at about 4.5 MeV, while decay of a $(\pi h_{11/2}^2)0^+$ pair would lead to 4 qp states with 5$^-$, 6$^-$, and 7$^-$ that lie 1 to 3 MeV higher in energy. We observe a group of levels above 4 MeV which probably are populated by the former decay and therefore are assigned as 5$^-$. Our data show that the $(\nu h_{9/2}s_{1/2}^{-1})5^-$ excitation mixes intensely with other 5$^-$ levels.

1. R. Broda et al., Z. Phys. A316,125 (1984)
2. P. Daly et al., Z. Phys. A298,173 (1980)
3. K.S. Toth et al., Phys. Rev. C19,482 (1979)
4. K.S. Toth et al., Phys. Rev. C37,1196 (1988)
5. J.L. Tain et al., Z. Phys. A333,29 (1989)

Measurements of Transient Magnetic Fields on Single-Electron Ni-Ions[G+B]

K.-H. Speidel, J. Cub, M. Knopp
Technische Universität München, Physik-Department, Garching
H.-J. Simonis
Institut für Strahlen- und Kernphysik, Universität Bonn
H.-J. Wollersheim, P. Egelhof, H. Emling, H. Grein, W. Henning, R. Holzmann, R.S. Simon, R. Schmidt
GSI, Darmstadt
N. Gollwitzer
Ludwig-Maximilians-Universität München, Sektion Physik, Garching

Transient magnetic fields (TF) of several kTesla in magnitude act on nuclei when ions penetrate polarized ferromagnets [1]. They are atomic in nature, associated with the polarization of bound s-electrons of the moving ion through spin dependent interactions with the polarized electrons of the ferromagnet [2]. TF have been widely used in measurements of g-factors of short-lived nuclear states in the ps-lifetime range and shorter. In general, one would expect a steady increase of the TF with ion velocity as the ionization proceeds from outer to the inner shells of the ion reaching a maximum value at the Bohr velocity $v = Z \cdot v_0$ ($v_0 = c/137$) where the unique strength of 1s electron ions dominates.
In this situation the TF is well described by [2]

$$B_{TF} = p_{1s}(v,Z,host) \cdot q_{1s}(v,Z,host) \cdot B_{1s}(Z)$$

where $B_{1s} = 16.7 \cdot Z^3$[T] is the Fermi contact field, q_{1s} the ion fraction with 1s electron and p_{1s} its degree of polarization. From systematics of light ions it is evident that the velocity dependence of TF is mainly determined by that of q_{1s} while p_{1s} values are rather constant and large. Whether this feature holds also for heavier ions at correspondingly higher velocities was the main motivation for the present measurements.

The first 2^+ state in ^{62}Ni at 1.173 MeV (τ=2.1 ps, g=0.34(7) [3]) was Coulomb excited by scattering a $^{62}Ni^{26+}$ beam of 18 MeV/u from a ^{208}Pb target giving rise to a mean velocity of $\simeq 25\ v_0$ to the Ni ions in Fe which is so far the highest velocity at which TF measurements were ever performed. Beams of $\simeq$ 0.2 pnA intensity on the target were provided by the UNILAC. Targets consisted of 14 mg/cm^2 thick ^{208}Pb, deposited on a 7 mg/cm^2 thick Fe foil which was backed by a Cu layer of 1 mg/cm^2 thickness. The Fe thickness implies an interaction time of the ions of t_{eff} = 0.15 ps. For magnetization an external field of 0.05 T was applied. In these conditions where a fraction of single electron ions of $q_{1s} \simeq 0.5$ is expected, a precession angle $\Phi \simeq 65$ mrad was estimated using $p_{1s} = 0.14$ and $B_{1s} = 367$ kT.

The γ-rays were measured with four Compton suppressed BGO/Ge-detectors in coincidence with Ni projectiles registered in an annular parallel plate avalanche gas counter at scattering angles $7^\circ \leq \Theta_{Lab} \leq 24^\circ$ and $0^\circ \leq \Phi \leq 360^\circ$.
The γ-detectors were placed at angles $\Theta_\gamma = \pm 24, \pm 150$ relative to the beam corresponding to maximum slopes of the particle-γ-angular correlation. For suppression of background radiation five 6"x6" NaI(Tl) scintillators were operated as multiplicity filter.

Detailed particle-γ-angular correlations have been measured as a function of the azimuth angle Φ defined by the appropriate sections of the gas counter. The correlation was determined from counting rate ratios of two γ-detectors at angles $\Theta_\gamma = \pm 24^\circ$; Fig. 1 shows the measured angular correlation together with COULEX calculations [4] including attenuations due to hyperfine interactions (HFI) of electron configurations of the ions on recoil into vacuum [5]. The attenuation coefficients deduced from the fit to the data are

$$G_2^{exp} = 0.79(2) \quad \text{and} \quad G_4^{exp} = 0.30(4).$$

The observed hard-core attenuations can be understood by including to the 1s electron ion fractions the HFI of Li-like ions in their ground-state and excited He-like ions [5]. In addition, also a contribution from quadrupole interactions between the small quadrupole moment of the ^{62}Ni(2^+) state with predicted very strong transient electric field gradients [6,7] during the ions' traversal through the target, cannot be completely excluded.

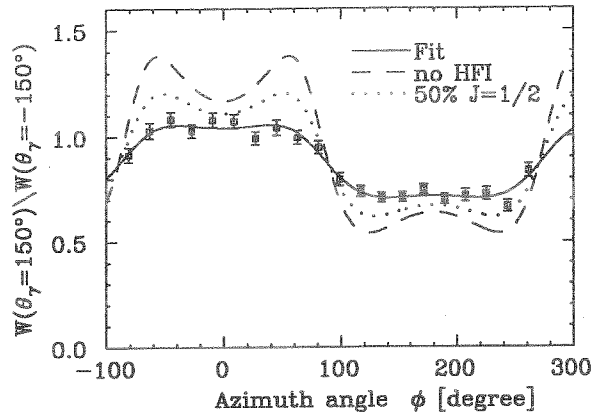


Fig. 1 Measured particle-γ-angular correlation with least-squares fit to the data.

Clear evidence for this phenomenon, however, requires experimental conditions where the magnetic interactions are less dominant.

Precession angles Φ derived from double ratios R of coincident counting rates from two detector pairs, at angles symmetric to the beam direction, with applied fields in the "up" and "down" directions are given by [3]

$$\Phi = \frac{\sqrt{R}-1}{\sqrt{R}+1} \Big/ \frac{1}{W} \cdot \frac{dW}{d\Theta_\gamma} = g \cdot \mu_N / \hbar \cdot B_{TF} \cdot t_{eff}.$$

With the slopes derived from the measured angular correlation at the appropriate angles

$$\left| \frac{1}{W} \cdot \frac{dW}{d\Theta_\gamma} \right| = 0.62(1)$$

we obtained a precession angle

$$\Phi = (4.8 \pm 5.3) \text{ mrad.}$$

This value corresponds to a TF which is by a factor (5-10) smaller than expected.

Such large attenuations of TF had been recently observed for lighter ions and are attributed to dynamic perturbations of ferromagnetism induced by heavy ion beams [3,8]. At present we are considering further measurements using Gd as host for which these attenuations were found to be considerably smaller [8].

[1] N. Benczer-Koller et.al., Ann. Rev. Nucl. Sci. 30 (1980) 53
[2] H.-J. Simonis et.al., Z. Phys. D7 (1987) 233
[3] K.-H. Speidel et.al., Z. Phys. A331 (1988) 29
[4] A. Winther and J. de Boer, in "Coulomb excitation" ed. K. Alder and A. Winther, Acad. Press, N.Y., 1966
[5] G. Goldring in "Heavy Ion Collisions", Vol. 3, p. 483, ed. R. Bock
[6] H. Ernst et.al., Phys. Rev. C26 (1982) 2039
[7] K.-H. Speidel, Hyp. Int. 34 (1987) 167
[8] K.-H. Speidel, et.al., Phys. Lett. 227B (1989)16

β^+-Endpoint Measurements of Neutron-Deficient Nuclei Near ^{100}Sn and ^{146}Gd

H. Keller, R. Kirchner, O. Klepper, E. Roeckl, K. Rykaczewski*, D. Schardt,
R. S. Simon (GSI Darmstadt), P. Kleinheinz, W. Meczynski, R. Menegazzo (KFA Jülich),
C.F. Liang, P. Paris (CSNSM Orsay), J. Żylicz (Warsaw University).

A β^+-endpoint spectrometer[1], where positrons are observed in an 11 mm thick silicon detector in coincidence with subsequent γ-rays in a germanium detector, and where the summing of annihilation radiation is prevented by detecting both 511 keV quanta in opposite segments of a BGO ring, has been installed at the GSI on-line mass separator. This setup was used to improve the determination of Q-values for Gamow-Teller (GT) β decays during four beamtimes in 1988 and 1989. Transitions of the type $\pi g_{9/2} \rightarrow \nu g_{7/2}$ and $\pi h_{11/2} \rightarrow \nu h_{9/2}$ were studied in the regions near ^{100}Sn and above ^{146}Gd, respectively.

Accurate Q-value measurements are important for the determination of the experimental GT β-strength and for the comparison of this quantity with results from model calculations (GT quenching). Furthermore, mass measurements of N=82 and N=83 isotones in the rare earth region enable mass determinations of far unstable nuclei up to the mercury-lead region on the basis of α-decay links.

As an example, Fig. 1 shows the data analysis in the case of ^{150}Er, using different coincidence modes of the spectrometer. The suppression of summing effects due to the 511 keV - 511 keV coincidence requirement is clearly demonstrated by comparing spectra (b) and (c).

The resulting pure β^+-spectrum (c) is very well reproduced by the following shape

$$N'(k) = \sum_E R(E,k) \cdot N(E)$$

where k is the channel number and E is the kinetic energy of the positrons. $R(E,k)$ is the detector response function which was established by combining conversion electron data and measurements[2] using monoenergetic electron and positron beams from the Gießen Linear Accelerator. The theoretical shape of the β^+-spectrum with radiative corrections[3] up to the order of $\alpha/2\pi$ is given by

$$N(E) = c \cdot p \cdot W \cdot (W_0 - W)^2 \cdot F(Z,W) \cdot [1 + \frac{\alpha}{2\pi} \cdot g(W, W_0)]$$

where c is a constant factor, dependent only on the counting statistics; p and W are the relativistic linear momentum and energy of the positrons corresponding to the kinetic energy E; $F(Z,W)$ is the Fermi-function including effects of the finite nuclear size and the screening by atomic orbital electrons as tabulated by Behrens and Jänecke[4]. In the case of a multi-component beta spectrum N(E) has to be replaced by

$$N_\Sigma(E) = \sum_m A_m N_m(E)$$

The determination of the amplitudes A_m for the different branches requires well established decay schemes.

The factor c and the endpoint energy $E_0 = W_0 - m_e c^2$ are the only free parameters of the fit. The $11/2^-$ isomer of ^{149}Tb with a well known endpoint energy[5] of E_0=1854(7) keV served as a test for the whole calibration and fitting procedure which gives E_0=1852(10) keV.

Q_{EC}-values derived from such endpoint determinations are compiled in table 1 and compared to literature values (EC/β^+-ratio measurements[6,7,8,9] and endpoint measurements[10,11]). In all cases, except the ^{149}Tb test case, the experimental uncertainties were significantly reduced. As a remarkable result, our Q-values for the $11/2^-$ nuclei ^{149}Ho and ^{151}Tm are higher by approximately 700 keV and 1000 keV, respectively, than values from EC/β^+-determinations,where the β-decay to high-lying three-quasiparticle states was not taken into account.

Nucleus	Q_{EC}/keV	
	This work	Literature values
^{102}Cd(0^+)	2587(8)	2550(60)[6]
^{104}Sn(0^+)	4515(60)	$4550(^{+350}_{-250})$[7]
^{147}Tb($11/2^-$)	4660(15)	$4600(^{+150}_{-110})$[8], 4620(60)[9]
^{148}Dy(0^+)	2678(10)	$2810(^{+120}_{-70})$[6], 2680(30)[9], 2700(60)[10]
^{149}Tb($11/2^-$)	3671(10)	3672(7)[5]
^{149}Dy($7/2^-$)	3812(10)	3930(150)[10]
^{149}Ho($11/2^-$)	6010(20)	$5320(^{+110}_{-90})$[6], 6040(50)[11]
^{150}Er(0^+)	4110(15)	$4090(^{+90}_{-60})$[8]
^{151}Tm($11/2^-$)	7030(50)	$6020(^{+150}_{-140})$[8]

Table 1: Results of Q_{EC} determinations from β^+-endpoint measurements performed at the GSI on-line mass separator and, in the case of ^{148}Dy, at ISOCELE/Orsay.

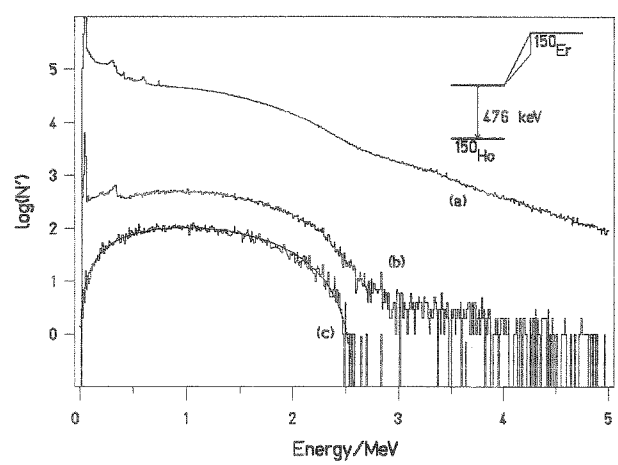


Figure 1: β^+-spectra obtained at mass 150 from the ^{58}Ni + ^{96}Ru reaction : (a) singles spectrum, (b) coincidence with the 476 keV γ-line, (c) additional coincidence with 511 keV pair detection. The solid line in spectrum (c) represents the fitted shape.

[1] H. Keller et al., GSI Report 89-1, 329 (1989)
[2] H. Keller et al., Strahlenzentrum Justus-Liebig-Univ. Gießen, Tätigkeitsbericht 1988, 77
[3] A. Sirlin, Phys. Rev. 164 (1967) 1767
[4] H. Behrens and J. Jänecke, Numerical Tables for Beta-Decay and Electron Capture, Landolt Börnstein Tables, Group I, Vol. 4 (Springer, Berlin,1969)
[5] A. H.Wapstra et al., At. Nucl. Data Tables 39, 289 (1988)
[6] L. Westgaard et al., in Proc. AMCO-4 Conf., Teddington (1971), p.94
[7] R. Barden et al., Z. Phys. A 329, 319 (1988)
[8] W. Habenicht et al., in Proc. AMCO-7 Conf., Darmstadt-Seeheim (1984), p.257
[9] U. J.Schrewe et al., Z. Phys. A 320, 595 (1985)
[10] G. D. Alkhazov et al., LNPI Preprint No. 820, Leningrad, (1982)
[11] G. D. Alkhazov et al., Z. Phys. A 310, 247 (1983)

* on leave of absence from Warsaw University

Quadrupole Collective Dynamics in ^{128}Xe

J. Srebrny, W. Karczmarczyk, P. Napiorkowski, T. Czosnyka, Ch. Droste (Univ. Warsaw)
H.-J. Wollersheim, H. Emling, H. Grein, R. Kulessa* (GSI Darmstadt)
D. Cline (Univ. Rochester) and C. Fahlander (Univ. Uppsala)

During the last decade various theoretical investigations of the mass region in the middle of the N=50-82 shell have been performed. The predictions resulting from these calculations range from prolate or oblate deformation, shape coexistance of different deformations to the strong asymmetric ground-state deformation. The most sensitive measures of the collectivity of nuclei are their electric quadrupole properties, which preferably are studied using Coulomb excitation. The almost complete set of E2 matrix elements for low-lying collective states can be determined from the observed γ-transitions yields as a function of a large range of projectile scattering angle.

In this paper we present the preliminary results of the ^{128}Xe multiple Coulomb excitation. The experiment /1/ was performed at the UNILAC accelerator in Darmstadt using inelastic scattering of 4.3 MeV/u ^{128}Xe nuclei on a ^{208}Pb target. We already analyzed part of the data using the coupled channel Coulomb excitation least-squares code GOSIA /2/. The level scheme of ^{128}Xe used in calculations is shown in Fig. 1. The scheme is based on refs. /3,4,5,6,7,8/ and references given therein. We obtained B(E2) values and static moments as well as relative signs and magnitudes of intraband E2 matrix elements for ground and 2^+_2 bands.

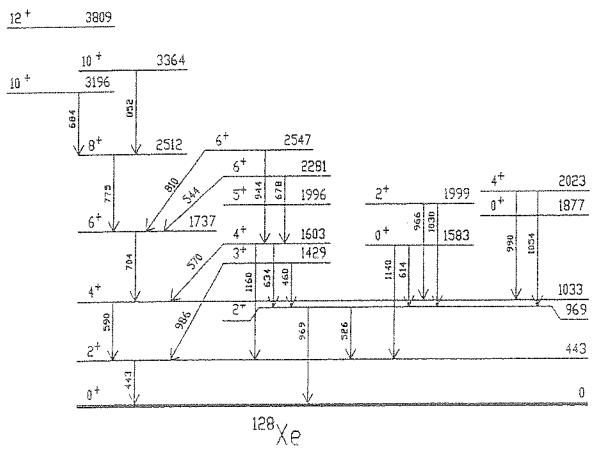


Fig. 1: The level scheme used in the analysis for ^{128}Xe. All γ-transitions observed in the present experiment are shown.

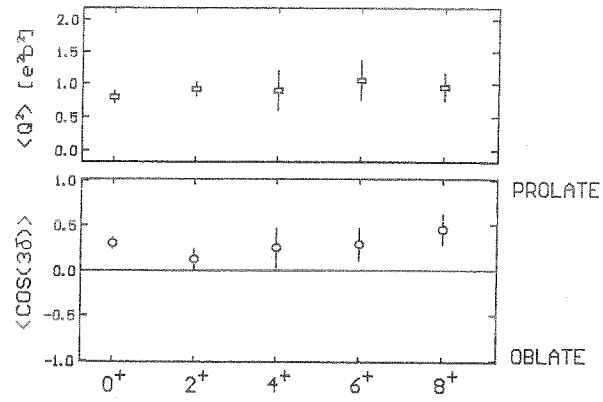


Fig. 2: Expectation values of $<Q^2>$ and $<\cos(3\delta)>$ for the ground state band of ^{128}Xe.

Using all the determined E2 matrix elements we applied the non-energy-weighted sum rules technique /9/ to calculate the expectation values of quadrupole collective degrees of freedom $<Q^2>$ and $<\cos(3\delta)>$ for the ground state band levels (see Fig. 2).

As can be seen from the Fig. 2 $<Q^2>$ and $<\cos(3\delta)>$ are nearly constant within ground state band. Presented values correspond to narrow range of Bohr-Mottelson deformation parameters $\beta=0.19$-0.21 and $\gamma=30^0$-25^0. This suggests β-stiffness for ^{128}Xe. Since the mean value of γ is close to 30^0 γ-stiffness and γ-softness are equally possible. Further analysis will be concentrated on this open question.

This work was partially sponsored by Polish Ministry of Education under project CPBP.01.06.

References

/1/ J.Srebrny et al., GSI Annual Report 1987, p.36.
/2/ T.Tzosnyka et al., BAPS 28(1983)745 and to be published.
/3/ Ch.Droste et al., Z.Phys. A277(1976)167.
/4/ L.Goettig et al., Nucl.Phys. A357(1981)109.
/5/ R.Reinhardt et al., Z.Phys. A329(1988)507.
/6/ L.Goettig et al., Warsaw University Nuclear Physics Laboratory Ann. Report 1986, p.39.
/7/ L.-O.Edvarson and L.-O.Norling, Uppsala Univ. Rep. UUIP-895(1975).
/8/ H.J.Wollersheim et al., GSI Annual Report 1977.
/9/ D.Cline, Ann.Rev.Nucl.Part.Sci. 36(1986)683.

* permanent address: Jagiellonian Univ., Cracow, Poland.

Search For Two-Octupole-Phonon States In ^{208}Pb

H.J. Wollersheim, P. Egelhof, H. Emling, W. Henning, R. Holzmann, R. Kulessa*, R.S. Simon (GSI Darmstadt)
J. de Boer, E. Hauber, K. Kaiser (LMU München), P. von Bretano, R. Reinhardt, R. Wirowski (Univ. Köln)
C. Fahlander (Univ. Uppsala), R. Julien (Univ. Jyväskylä)

The first excited states of most magic nuclei have spin-parity 3^- and are interpreted as one-phonon vibrations of octupole character. The collective nature of these states is inferred from the observed enhancement of the transition probabilities to the ground states. In the particular case of ^{208}Pb the enhancement over the single-particle value is of the order of 30.

This picture of the lowest-lying 3^- levels in magic nuclei seems unimpeachable although the multi-phonon states, whose existence is implied by this description, remain unobserved. The search for such excitation is therefore of great interest as their observation would provide a direct check on the degree of harmonicity of the associated vibrational motion.

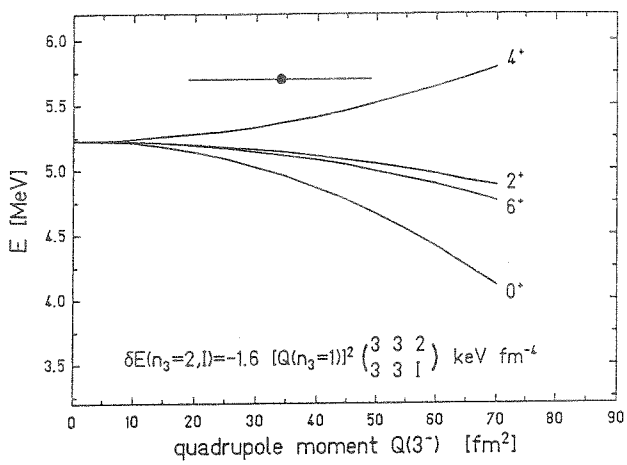


Fig. 1: Energy splitting of the 2-octupole-phonon vibrational states as a function of the quadrupole moment Q of the first excited 3^- state in ^{208}Pb. The measured quadrupole moment[7] is indicated.

The purpose of the present experiment was a new attempt to locate some of these 2-octupole-phonon states in ^{208}Pb using electromagnetic excitation with heavy ions. In a first approximation, one expects a quadruplet of states of two-phonon $(3^-\otimes 3^-)_I$ octupole vibrations with spins and parities $0^+,2^+,4^+$ and 6^+ at about twice the energy of the 3^- state, i.e. at $2\hbar\omega$ = 5.23 MeV. Only a few states with positive parity are known below 6 MeV excitation energy, but in spite of several attempts [1-3] it has not been possible to identify any good candidates for the 2-phonon multiplet. The energy of the 2-phonon states have been estimated by a number of authors[4-6]. In the first place, Blomquist[5] pointed out that the observed large quadrupole moment Q=-0.34(15)[7] of the collective 3^- state in ^{208}Pb implied a departure from harmonicity due to the coupling between the quadrupole and octupole motions which would give rise to a substantial splitting of the two-octupole phonon quartet. Fig. 1 shows the effect of the quadrupole moment on the energy splitting. Other calculations[4,6] showed that the effect of including the interaction with the two-phonon pairing vibration modes are also not negligible but amounts to about the same energy shift in the opposite direction. Those discrepancies illustrate the importance attached to the identification of these two-phonon octupole vibrational states.

A possible way to excite the two-phonon octupole vibration is to use electromagnetic excitation with ^{208}Pb projectiles. We have calculated the inelastic cross section leading to the $(3^-\otimes 3^-)_I$ states and have found that at least the 6^+ state should be observed in a suitable arranged particle-γ experiment.

The search for the 2-phonon states was carried out by bombarding a 1 mg/cm^2 ^{208}Pb target with 6.2 MeV/A ^{208}Pb projectiles. The recoiling target nuclei and scattered projectiles were detected in an arrangement of position-sensitive parallel-plate avalanche gas counters. The coincident emission of γ-rays was observed in eight Ge detectors (all of them Compton suppressed) positioned at angles of 30° (Ge1-Ge4) and 150° (Ge5-Ge8) with respect to the beam direction. In addition a multiplicity filter of six NaI detectors located at 90° was used to select events of high γ-multiplicity. The information about the scattering angle of the excited nuclei allowed to correct for the large Doppler shifts of the emitted γ-rays due to the high recoil velocities (up to ~10% c). Moreover, the measurement of the scattering angles provided the impact parameter dependence of the γ-ray yields.

Fig. 2 (top) shows the summed γ-spectrum of all Ge detectors, after Doppler-shift correction and suppression of the Compton background. The peak at 2.485 MeV (marked with an asterisk) just below the $3^-\rightarrow 0^+$ transition is identified as a transition between higher spin states because of its γ-multiplicity measurement. The most probable decay branch of the 2-phonon state can be assigned to a $6^+\rightarrow 5^-$ transition. Fig. 2 (bottom) shows the result of a $\gamma\gamma$-measurement between Ge and NaI detectors with a gate set on the $5^-\rightarrow 3^-$ transition (E_γ = 583 keV) in the NaI spectrum. The unidentified transition is clearly seen in the Ge-spectrum and it also appears in a γ-spectrum gated on the $3^-\rightarrow 0^+$ transition. However, the bad energy resolution of the NaI detector, mainly due to the large Doppler broadening, did not allow to separate the $5/2^-\rightarrow 1/2^-$ transition in ^{207}Pb (E_γ = 570 keV) so that also γ-transitions in ^{207}Pb and ^{209}Pb, produced by transfer reactions, are identified.

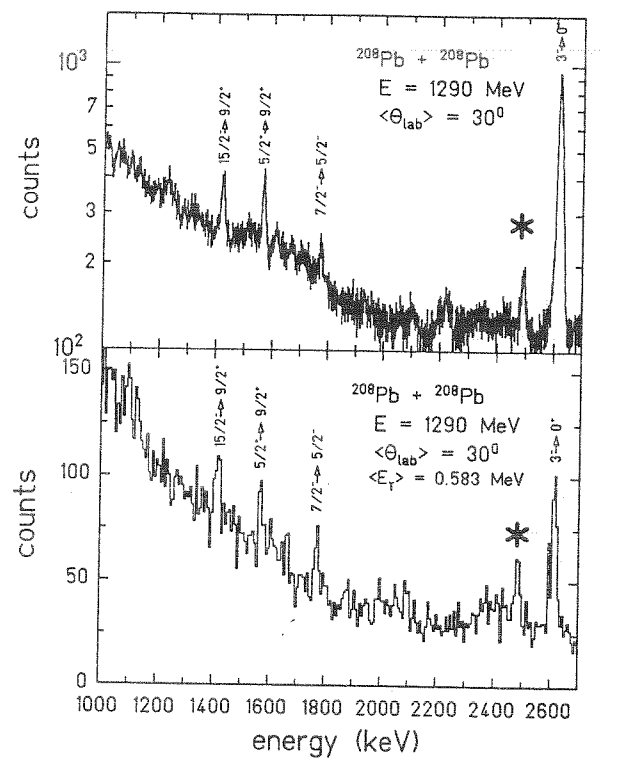


Fig. 2: Doppler-corrected γ-spectrum obtained for the ^{208}Pb+^{208}Pb system at 6.2 MeV/A. Transitions in ^{207}Pb and ^{209}Pb resulting from transfer are also indicated (top). Doppler-corrected $\gamma\gamma$-spectrum between Ge and NaI detectors with a gate set on the $5^-\rightarrow 3^-$ transition in the NaI spectrum (bottom).

The intensity of the γ-transition at 2.485 MeV is approximately a factor of 2 larger than the cross section calculated in the harmonic vibrator limit. The effects of nuclear excitation and simultaneous excitation of projectile and target nucleus are not included in the semi-classical Coulomb excitation calculations.

In summary: Both results - the decay pattern and the measured collectivity of the observed γ-transition - seem to indicate that we have found a possible candidate for the 2-phonon-octupole multiplet in ^{208}Pb. The 2.485 MeV γ-ray which has been seen in the present HI experiment is most likely the decay of the 6^+ state of 2-phonon octupole vibrations to the 5^- state (E=3.198 MeV) resulting in a level energy of E_6=5.683 MeV.

1. M.A.J. Mariscotti et al., Nucl. Phys. A407 (1983), 98
2. P.R. Christensen et al., unpublished, quoted in Phys. Lett. 70B (1977) 292
3. R. Julin et al., private communication
4. J. Hamamoto, Phys. Rep. 10 (1974), 63
5. J. Blomquist, Phys. Lett. 33B (1970), 541, and Phys. Lett. 208B (1988), 331
6. R.A. Broglia et al., Phys. Lett. 37B (1971), 159 and 257
7. R.H. Spear et al., Phys. Lett. 128B (1983), 29

Cold Fusion Reactions with ^{48}Ca

H.W. Gäggeler, D.T. Jost
Paul Scherrer Institute, CH-5232 Villigen Switzerland
A. Türler
Laboratorium für Radiochemie, Universität Bern, CH-3000 Bern, Switzerland
P. Armbruster, W. Brüchle, H. Folger, F.P. Hessberger, S. Hofmann, G. Münzenberg, V. Ninov, W. Reisdorf, M. Schädel, K. Sümmerer
Gesellschaft für Schwerionenforschung bmH, D-61 Darmstadt, Fed.Rep.of Germany
J.V. Kratz, U. Scherer
Institut für Kernchemie, Universität Mainz, D-65 Mainz, Fed.Rep. of Germany
M.E. Leino
Department of Physics, University of Helsinki, Finland

Fusion reactions of ^{48}Ca projectiles with ^{180}Hf, ^{184}W, ^{197}Au, ^{208}Pb and ^{209}Bi were studied. All experiments were performed at the SHIP velocity filter. As target 300 to 400 µg/cm^2 thick metallic foils were used which were either mounted on a rotating target wheel (^{208}Pb, ^{209}Bi, ^{197}Au) or used as single targets (^{180}Hf, ^{184}W). Evaporation residues were detected via their α-decay. In case of the reaction with ^{208}Pb evaporation residues from the 1n and 2n channel were also detected via their grand-daughter nuclides using chemical techniques[1].

All results are summarized in the Table 1[2]. For the heavier systems ^{197}Au, ^{108}Pb and ^{209}Bi the data can be well reproduced with the code HIVAP assuming no (or only a small) hindrance of fusion, i.e. Extra-Extra-push $E_{xx} \leq 5$ MeV. Fig. 1 summarizes (E_{xx}) values from the literature and from this work.

Surprisingly, for the lighter systems (^{180}Hf, ^{184}W) the measured cross sections (3n-channel) were more than two orders of magnitude smaller than expected (HIVAP). At present we have no explanation for this discrepancy. Agreement between experimental and calculated values can only be obtained by reducing the macroscopic fission barries of the compound nuclei by 30 to 40 %. Fig. 2 depicts a schematic of how evaporation residue cross sections evolve for compound nuclei between Th and Lr.

[1] H. Gäggeler et al. GSI-scientific report 1988, GSI-89-1, p.18.
[2] H. Gäggeler et al. Nucl.Phys. A502, 561c (1989).

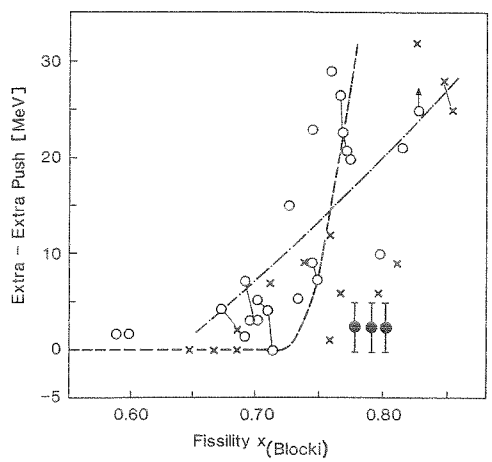


Fig. 1: Extra - extra push values from the literature (open circles and crosses) and from this work (closed circles) as a function of the fissility parameter[12].

Table 1: Experimental cross sections

Reaction	Incident Energy [MeV/u]	Excitation Energy[a] [MeV]	1n [nb]	2n [nb]	3n [nb]
$^{48}Ca + ^{208}Pb$	4.34	13.2	≤ 27	≤ 27	
	4.42	16.3		212 ± 58	
	4.42[b]	16.7	260 ± 30	420 ± 50	
	4.44[b]	17.4		730 ± 150	
	4.50	19.3		2344 ± 544	
	4.50[b]	19.7	180 ± 53	3385 ± 310	
	4.50[b]	19.7		3110 ± 480	
	4.57	21.9		1845 ± 435	
	4.65	25.2		418 ± 114	$37 \pm ^{34}_{20}$
	4.74	28.8		39 ± 19	109 ± 33
$^{48}Ca + ^{209}Bi$	4.38	13.7	≤ 4.5		
	4.46	17.6	61 ± 20	12 ± 7	
	4.53	19.6	20 ± 11	437 ± 96	
	4.61	22.7	≤ 7.5	324 ± 75	
	4.69	25.8		38 ± 11	9 ± 5
	4.76	29.4			28 ± 11
$^{48}Ca + ^{197}Au$[c]	4.42	27.6		40 ± 15	
	4.48	30.0		42 ± 17	
	4.63	35.6		36 ± 15	
$^{48}Ca + ^{184}W$	4.20	34.4			$4 \pm ^{10}_{4}$
$^{48}Ca + ^{180}Hf$	4.24	36.0			128 ± 59

[a] In the middle of the target (chemistry) or at 2/3 of the target (SHIP). Energy width within target ± 1.2 MeV (chem.) and $\pm ^{1.6}_{0.8}$ MeV (SHIP). Additional energy uncertainty from UNILAC ± 0.8 MeV.
[b] Results from chemisty, all other data from SHIP.
[c] Sum of 2n and 3n channel (see text).

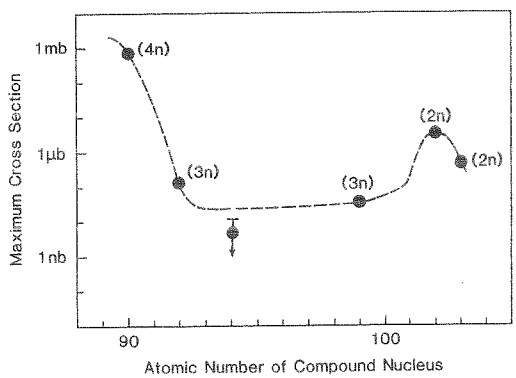


Fig. 2: Maximum cross sections for the main xn channels from ^{48}Ca induced fusion reactions.

Fusion in the reactions ^{110}Pd + ^{110}Pd, ^{104}Ru ^{B}

W. Morawek, D. Ackermann, T. Brohm, H.-G. Clerc, U. Gollerthan, E. Hanelt, M. Horz, W. Schwab, B. Voss
Inst. für Kernphysik TH Darmstadt
K.-H. Schmidt, F.P. Heßberger, GSI Darmstadt

In continuation of our experimental program on the fusion of massive nuclear systems [1,2,3] we reported already on the observation of evaporation residues in the reaction ^{110}Pd + ^{110}Pd [4]. This is the heaviest symmetric system for which fusion has been observed. Along with this system we investigated also the reaction ^{110}Pd + ^{104}Ru. The total evaporation-residue cross section for ^{110}Pd + ^{104}Ru as function of the excitation energy is shown in figure 1. In both reactions the cross section is dominated by evaporation channels with α-particles. In the reaction ^{110}Pd + ^{110}Pd no xn-channels had been observed, while in the reaction ^{110}Pd + ^{104}Ru a small fraction of xn-channels was detected. The cross section for the sum of the xn-channels is also shown in figure 1.

To extract the fusion probability from the measured data, evaporation calculations are necessary, which take the fission competition in the statistical deexcitaion process into account. These calculations were found to be not able to explain the neutron-evaporation cross section and the cross sections for charged particle channels at the same time. The relative emission rates of charged particles with respect to neutrons were found to be much higher than calculated.

Therefore we compared our measured xn-channels of the system ^{110}Pd + ^{104}Ru with the system ^{124}Sn + ^{90}Zr which leads to the same compound nucleus. Assuming the compound-nucleus hypotheses to be true, the ratio of the cross sections gives directly the ratio of the fusion probabilities averaged over ℓ, independent of any evaporation calculation. In figure 2 the fusion probabilities are shown. The absolut value of the fusion probability was fixed by a calculation adapted to reproduce the xn-channels of asymmetric Ar-induced reactions [5]. The figure also shows calculations for the fusion probability based on a one-dimensional model using the Bass-potential. The fusion probability for ^{110}Pd + ^{104}Ru is about one order of magnitude smaller than for the system ^{124}Sn + ^{90}Zr, which is equivalent to a shift in energy of about 10MeV.

Although both systems have nearly the same value for the product of the nuclear charges of projectile and target $Z_P \cdot Z_T$, the value for the extra-push of ^{110}Pd + ^{104}Ru is predicted to be 5MeV larger than the value for the system ^{124}Sn + ^{90}Zr by a macroscopic extra push model [6]. The Bass-barrier for the more symmetric system is also 2MeV larger. Thus it seems, that the observed shift in the fusion probabilities for the two systems is in fair agreement with the predictions of the macroscopic extrapush model.

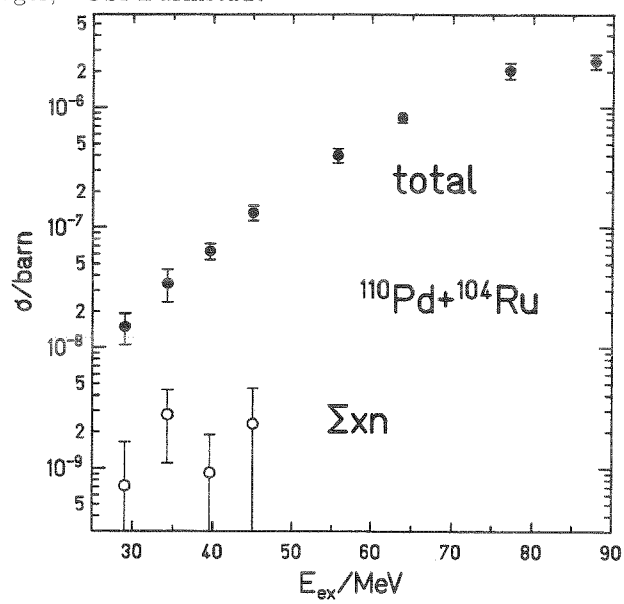


Fig.1 : Evaporation-residue cross sections.

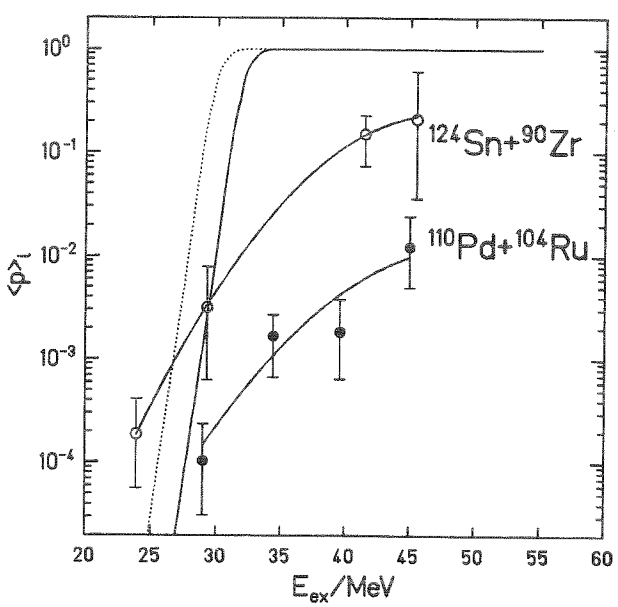


Fig.2 : Fusion probability for central collisions. The lines show the prediction of a model using the Bass-potential (dotted line: ^{124}Sn + ^{90}Zr, solid line: ^{110}Pd + ^{104}Ru). The lines through the data points are drawn to guide the eye.

References:
[1] C.-C.Sahm et al., Nucl. Phys. A441 (1985) 316-343
[2] J.Keller et al., Nucl. Phys. A452 (1986) 173-204
[3] B.Quint, Dissertation, TH Darmstadt (1988)
[4] W.Morawek et al., Scientific Report 89-1 (1988) 38
[5] D. Vermeulen et al., Z. Phys. A318 (1984) 157-169
[6] J.P. Blocki et al., Nucl. Phys. A459 (1986) 145-172

A Comparative Study of Angular Momentum Distributions in the Sub-Barrier Fusion Reactions $^{32}S+^{100}Mo$ and $^{36}S+^{96}Mo$ [G+B]

H.-J.Hennrich, G.Breitbach, W.Kühn, V.Metag, R.Novotny
II.Phys.Inst.Univ.Gießen
D.Habs, D.Schwalm, MPI und Phys.Inst.Univ.Heidelberg

Partial wave distributions for fusion reactions were measured for the systems $^{32}S+^{100}Mo$ and $^{36}S+^{96}Mo$, both leading to the same compound nucleus ^{132}Ce, in the energy range from 7% above to 12% below the classical Coulomb barrier. The evaporation residues have been identified by time-of-flight using an annular PPAC positioned at forward angles. The angular momentum distributions were deduced from γ-ray multiplicity- and angular distributions measured with the Darmstadt-Heidelberg crystal ball. Fig. 1 shows the experimental evaporation residue angular momentum distributions and the deduced fusion probabilities for both systems. The stronger enhancement

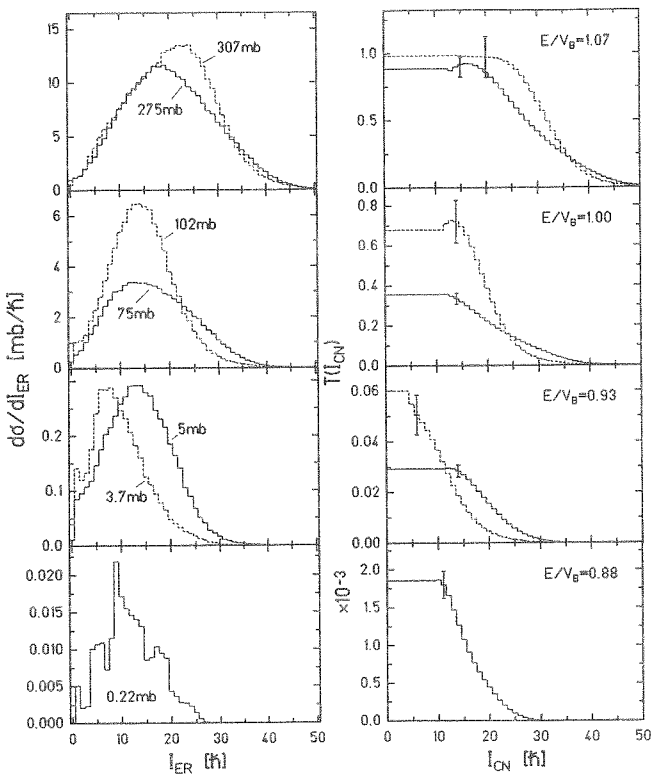


Figure 1: Evaporation residue angular momentum distributions (left) and fusion probabilities (right) for $^{32}S+^{100}Mo$ (full line) and $^{36}S+^{96}Mo$ (dashed line) at different bombarding energies from 7% above to 12% below the Coulomb barrier. The errors in the angular momentum are estimated to 10% for the highest and 15% for the lowest energy. The cross sections are taken from ref.1.

in the sub-barrier fusion cross section in the system $^{32}S+^{100}Mo$ compared to $^{36}S+^{96}Mo$ (ref. 1) is correlated with broader angular momentum distributions

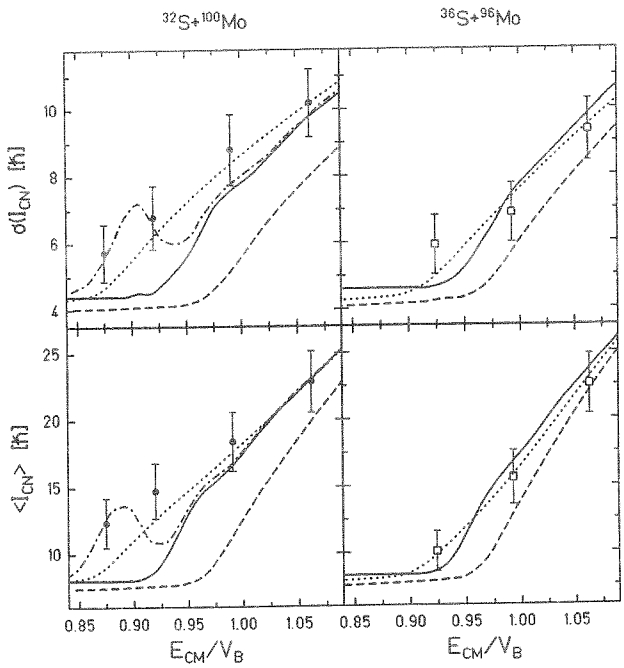


Figure 2: Moments of the angular momentum disributions versus the bombarding energy relative to the barrier. The dashed curves are 1-dim. barrier penetration calculations. The dotted curves include barrier fluctuations (ref. 2) with a relative width of the barrier distribution of σ_B=4.8% for the system $^{32}S+^{100}Mo$ and σ_B=2.8% for $^{36}S+^{96}Mo$, respectively. The full curves represent coupled-channel calculations (ref. 3) including the first two excited states in projectile and target with β_λ-values scaled up by a factor of 1.5 to fit the fusion cross sections. For the system $^{32}S+^{100}Mo$ the 2n-transfer channel with Q=+6.2MeV has additionaly been taken into account (dashed-dotted curves).

for all measured bombarding energies. In Fig. 2 the first and second moments of the angular momentum distributions are compared with different model calculations. The different behavior of the two systems can be described assuming barrier fluctuations with different values for the width of the barrier distribution. Simple coupled channel calculations show that the 2n-transfer channel with Q=+6.2MeV may be important for the broad angular momentum distributions in the system $^{32}S+^{100}Mo$ at sub-barrier energies.

1) R.Pengo et al., Nucl. Phys. A411,255 (1983)
2) W.Reisdorf et al., Phys.Rev.Lett. 49,1811 (1982)
3) C.H.Dasso et al., Comp.Phys.Comm. 46,187 (1987)

Angular Distributions of Fissionlike Products for 5.2 MeV/u ^{40}Ar + ^{165}Ho B

M. Knaack, B. Jäckel, R.A. Esterlund, H. Schulte, W. Westmeier, P. Patzelt
Institut für Kernchemie, Marburg

As part of a systematic program to determine the limits in mass-charge-energy space where dynamic contributions to symmetric fragmentation processes contribute, offline measurements of angular distributions for fission/fissionlike products with exact A and Z identification in the exit channel have been carried out for the reaction of 5.2 MeV/u ^{40}Ar + ^{165}Ho. The measured[1] l_{crit} for symmetric fragmentation at this energy is 67, whereas the rotating-liquid-drop model (RLDM) limit is 76. Furthermore, no dynamic hindrance to fusion is predicted. We determine here the dependence of the angular-distribution anisotropy $A_n = W(0^o,180^o)/W(90^o)$ on the exit-channel asymmetry $\alpha = (A_1-A_2)/(A_1+A_2)$, and investigate whether or not non-equilibrium components (*i.e.*, those exhibiting asymmetry about 90° in the rest frame) are seen in the angular distributions, as has been observed elsewhere[2] in heavier systems.

Natural Ho metal foil targets[3] (0.96 mg/cm^2) in a rotating target-wheel assembly were irradiated with 5.2 MeV/u ^{40}Ar ions from the GSI UNILAC. Scattered reaction products were collected on ten Al catcher foils which covered the moving-frame angular ranges 2.54°-73.30° and 110.55°-178.00°. Offline gamma spectrometry was performed for a period of over 6 months, followed by decay-curve analysis of the observed full-energy photopeaks for product identification and cross-section assay. Conversion from the moving frame to the rest frame was carried out assuming full damping as well as product kinetic energies consistent with observed systematics for fission/fissionlike products.

In Fig. 1, we summarize the results of fitting transition-state theory (TST) calculations to the angular-distribution data. The upper portion of the figure shows the dependence of A_n on $|\alpha|$, and the lower portion displays the deduced dependence of K_0^2. The line labelled TST is the value attained from a transition-state theory calculation for exactly symmetric splittings, using RLDM saddle-point moments-of-inertia and assuming first-chance fission. Compared to our results for heavier systems[2], we observe a significant but relatively weaker dependence of A_n and K_0^2 on α. Moreover, in contrast to our data for heavier systems, *no* significant deviation (on the average) from the A_n and K_0^2 values predicted by the TST is observed.

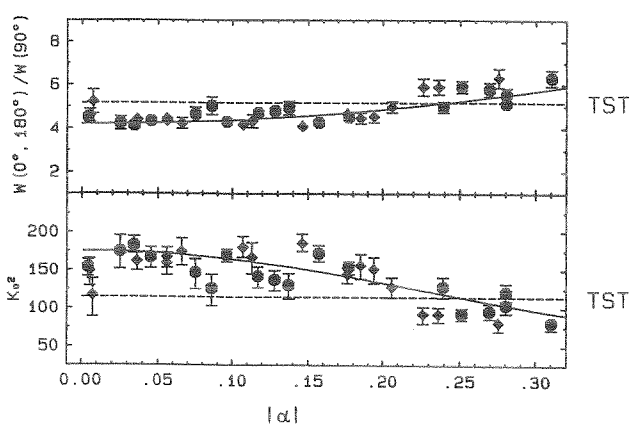


Fig. 1: Angular-distribution anisotropies A_n and deduced K_0^2 values as a function of $|\alpha|$. The line labelled TST *is a transition-state theory calculation.*

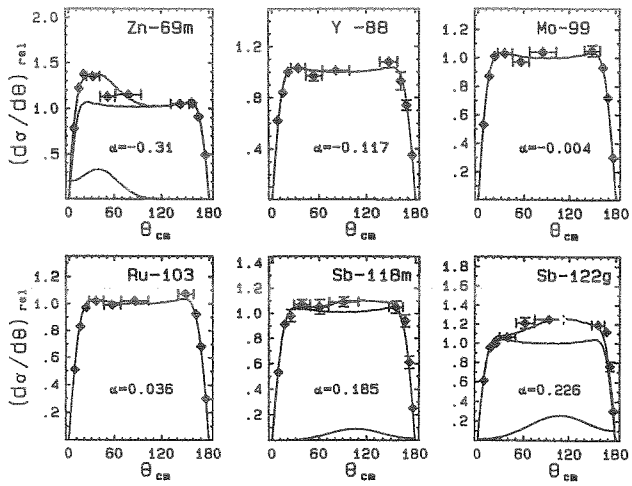


Fig. 2. Selected rest-frame angular-distribution data for the system 5.2 MeV/u ^{40}Ar + ^{165}Ho. All nuclides occupy mass bins in the symmetric component.

Similar to behavior observed[2] in the systems 5.3 MeV/u ^{40}Ar + ^{197}Au and 5.2 MeV/u ^{40}Ar + ^{181}Ta, as we go to increasing α in this system, we observe angular distributions which become increasingly asymmetric about 90° in the rest frame, even though the corresponding mass bins are located well within the symmetric fragmentation component. Selected data are shown in Fig. 2. As in the ^{40}Ar + ^{197}Au system, the asymmetric distributions begin appearing at $|\alpha|$ values greater than *ca.* 0.14. This indicates that dynamic processes contribute to a comparable degree to fission/fissionlike yields in this system. As the deduced A_n and K_0^2 values agree quite well with TST calculations, this result must be considered as unexpected.

[1] C.-C. Sahm *et al.*, Z. Phys. A297, 241 (1980).

[2] H. Schulte *et al.*, Phys. Lett. B232, 37 (1989); M. Knaack *et al.*, GSI Sci. Rept. 89-1, 24 (1989); H. Keller *et al.*, Z. Phys. A326, 313 (1987); K. Lützenkirchen *et al.*, Z. Phys. A320, 529 (1985) and Nucl. Phys. A452, 351 (1986).

[3] Targets supplied by H. Folger and the GSI Target Lab.

Reactions of ^{40}Ar with ^{233}U, ^{235}U, and ^{238}U at the Barrier[B]

U.W. Scherer[1], W. Brüchle[2], M. Brügger[2], C. Frink[1], H. Gäggeler[3], G. Herrmann[1,2], J.V. Kratz[1], K.J. Moody[2,*], M. Schädel[2], K. Sümmerer[2], N. Trautmann[1], G. Wirth[2]

[1]Institut für Kernchemie, Universität Mainz
[2]Gesellschaft für Schwerionenforschung mbH, Darmstadt,
[3]Paul Scherrer Institut, Villigen, Switzerland

The reactions of ^{40}Ar with $^{233,235,238}U$ were investigated at the Coulomb barrier by measuring cross sections for target-like reaction products. The heaviest products detected are isotopes of californium (Z=98). In addition to the quasi-elastic component in the isotopic distributions observed in the vicinity of uranium, there are also relaxed contributions throughout the entire region. For this component, the element yields below uranium are the same within the error limits for the three target isotopes; the yields above the target are higher for ^{238}U than for ^{235}U and lowest for ^{233}U. It is suggested that these trends reflect the gradients of the potential energy surfaces for the three reactions.

As to the centroids of the isotopic distributions at a given value of Z, we find that these, after the transfer of >3 charges, approach closely the minimum of the potential energy valley. This is depicted for $^{40}Ar+^{235}U$ in Fig. 1, where open symbols stand for a bombarding energy $E/E_B=1.0$, and closed symbols for $E/E_B=0.97$. The centroids for the trans-target products coincide at both incident energies; below the target the products seem to be slightly more neutron-rich at the lower-bombarding energy even though this is barely outside the uncertainty limits. In addition to the equi-potential lines, Fig. 1 contains two bold solid lines to the left of the dotted minimum potential energy (MPE) line. These indicate the expected location of the centroids of the post-neutron emission isotope distributions under the assumption of an excitation energy sharing in proportion with the fragment masses. The bold solid line closer to the MPE line is based on the assumption of an exit channel barrier for two touching spheres, whereas the bold solid line further to the left is based on the assumption of Viola kinetic energies. Neither assumption reproduces correctly the observed centroids. For the trans-target products the predicted product locations approach the MPE line for trivial reasons. This is because the Q_{gg} values become increasingly negative (-50 MeV for Cf) with increasing product Z, and the excitation energies become very small. We have to conclude that the experimental data are in conflict with a sharing of the total excitation energy in proportion to the masses, at least for the below-target products, which seem to be much less excited than expected.

This is reminiscent of similar observations in the Ca+Cm reactions[1,2], and in reactions of ^{50}Ti, ^{54}Cr, and ^{58}Fe with Pb[3] at the barrier. In the latter cases, it was found that the projectile-like acceptors of the transferred nucleons carry essentially all of the excitation energy, and the target-like donors stay cold. The condition for this "unusual" excitation energy sharing are the same in the present work and in Refs. 1-3: The bombarding energy corresponds exactly to the Coulomb barrier so that the velocity of the relative motion is zero at contact. Thus, there is no initial friction force and the transfer of nucleons may occur frictionless.

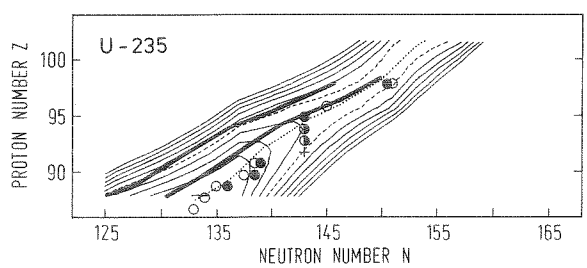


Fig.1 Potential energy surface for $^{40}Ar+^{235}U$. The open and closed dots indicate the locations of the centroids of the experimental isotopic distributions. The bold solid lines are expectations for these locations, see text.

[1] H. Gäggeler et al., Phys. Rev. C33, 1983 (1986)
[2] A. Türler, Doctoral Thesis, University of Bern, 1989
[3] H. Keller et al., Z. Phys. A328, 255 (1987)

1n-Transfer Reactions in Collisions of U + Au and Au + Au near the Coulomb Barrier[B]

G. Wirth, W. Brüchle, Fan Wo, E. Jäger and K. Sümmerer
GSI Darmstadt
F. Funke, J.V. Kratz, and N. Trautmann
Institut für Kernchemie, Universität Mainz

We have investigated nuclear reactions in the collisions of very heavy ions at energies near and below the Coulomb barrier over the last years. One-neutron transfer turned out to be the most probable direct reaction[1]. The excitation function of the 1n-transfer product ^{239}U in the reaction $^{238}U + ^{238}U$ could be well reproduced by a simple semiclassical Sub-Coulomb transfer theory whereas the angular distributions in the same reaction revealed large discrepancies between experiment and theory for the more central collisions. Sequential fission after 1n-transfer did not provide an explanation[2]. Therefore we extended the 1n-transfer measurements to the systems U + Au and Au + Au in order to study possible influences of the static deformation of the collision partners and of the symmetry of the system ("Pauli-Blocking") on the angular distributions.

Since the 1n-transfer measurements in the asymmetric system U + Au were designed to search for deviations from Rutherford trajectories[3] in the same experiments, irradiations were performed at 15 incident energies around the Coulomb barrier yielding a very large number of cross sections for the 1n-transfer products ^{198g}Au, ^{196g}Au and also their isomeric states ^{198m}Au and $^{196m2}Au$. Fig. 1 shows the transfer probabilities versus the reduced distance of closest approach for the 1n-transfer product ^{198g}Au in the reaction $^{238}U + ^{197}Au$. The data are in excellent agreement with the semiclassical theory over 4 orders of magnitude. The slope parameter of the linear fit (1.08 ± 0.02 fm^{-1}) agrees very well with the value expected from neutron binding energies (1.10 fm^{-1}). On the other hand, in the same reaction $^{238}U + ^{197}Au$ the angular distributions of the 1n-stripping transfer product ^{196g}Au show large deviations from the semiclassical theory. This is demonstrated in fig. 2 displaying various angular distributions at the same energy relative to the Coulomb barrier. Similar deviations from the theory are obtained from the analysis of the cross sections of the isomeric states ^{198m}Au and $^{196m2}Au$. In the symmetric reaction $^{197}Au + ^{197}Au$ we measured angular distributions for the already mentioned 1n-transfer products at four energies below the barrier. In all cases the angular distributions of the 1n-transfer products are not in agreement with the semiclassical theory. Similar to the $^{238}U + ^{238}U$ data and most of the $^{238}U + ^{197}Au$ data, the theory fits only to the more peripheral collisions as demonstrated in fig. 2c. It should be noted that the data for the symmetric Au + Au-system have been reduced in a similar way as described in ref. 2 for comparisons to unsymmetrized calculations.

To summarize our experimental 1n-transfer results in very heavy ion collisions at low energies, we find that the ^{198g}Au differential cross sections in the reaction $^{238}U + ^{197}Au$ are the only data that are in complete agreement with the semiclassical theory for all scattering angles excluding the region of trivial absorption. Effects from the static deformation of the collision partners are not observed in the angular distributions, because the 1n-stripping channel in the $^{238}U + ^{197}Au$ system agrees with the theory whereas the complementary 1n-pickup channel does not. In addition, the much less deformed $^{197}Au + ^{197}Au$ system shows deviations from the theory for the central collisions which are comparable with those observed in $^{238}U + ^{238}U$ and most $^{238}U + ^{197}Au$ angular distributions. Pauli-Blocking too seems not to be that important because of the deviations in the angular distributions of most 1n-transfer products in the asymmetric $^{238}U + ^{197}Au$ system.

An interesting correlation of the observed deviations is found with the ground state Q-values (the reaction Q-values were not measured) of the various reactions. ^{198g}Au in the system $^{238}U + ^{197}Au$ is the only 1n-transfer product with a positive ground state Q-value and at the same time the only 1n-transfer product that is in agreement with the theory at all angles.

1. G. Wirth et al., Phys. Lett. **B177**(1986)282
2. G. Wirth et al., Z. Phys. **A330**(1988)87
3. G. Wirth et al. in: Heavy Ion Interactions Around the Coulomb Barrier, Springer 1988, p. 84

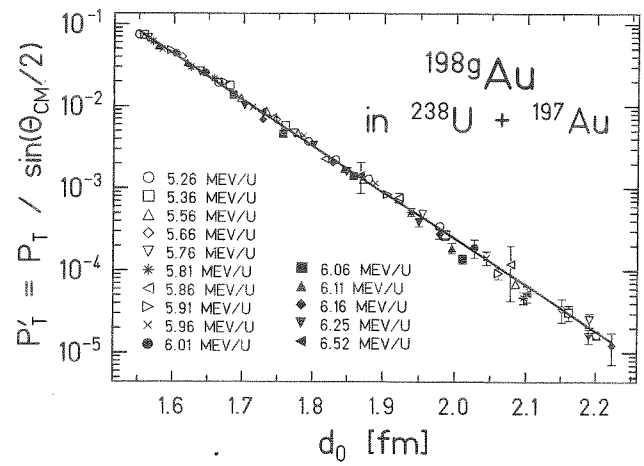


Fig. 1: Transfer probabilities for ^{198g}Au in the reaction $^{238}U + ^{197}Au$. The line is a two-parameter fit of the semiclassical theory to the data. Only data with $d_0 > 1.55$ fm are shown.

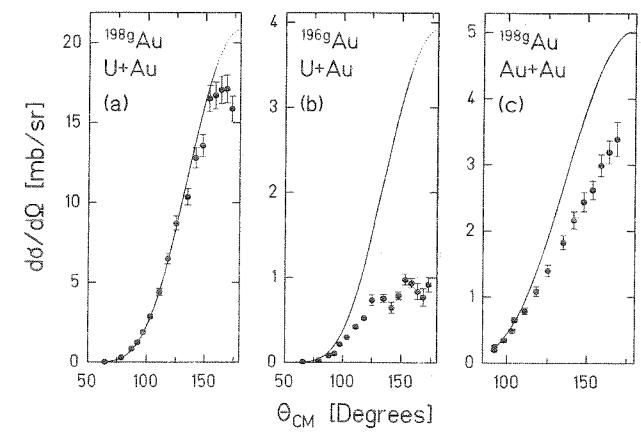


Fig. 2: Angular distributions of 1n-transfer products at 88% of the Coulomb barrier. The lines are fits of the semiclassical theory. The region where absorption, not considered in the theory, sets in ($d_0 < 1.55$ fm), is indicated by a dotted line.

Multi-Nucleon Transfer in U+U and U+Au Collisions [B] below and near the Coulomb Barrier

F. Funke, J.V. Kratz, N. Trautmann
Institut für Kernchemie, Universität Mainz
G. Wirth, W. Brüchle, Fan Wo, E. Jäger, K. Sümmerer
GSI Darmstadt

We have previously reported on the fission excitation function[1] in the U+U reaction. The high fission cross sections exceeding the expected cross sections for Coulomb fission for bombarding energies >0.9xV_c were tentatively attributed to sequential fission following multi-nucleon transfer. The finite fission widths associated with the decay of such multinucleon transfer products requires, for consistency, the observation of surviving products from the transfer of many nucleons. We have measured excitation functions for the formation of several radiochemically accessible Ra, Ac, Th, and Pa isotopes. The excitation functions[2] were found to be very similar to each other suggesting that these isotopes are members of a broad product distribution which is similar in both reactions U+U and U+Au. It has been suggested that these products originate from a small fraction of collisions in which, due to the deformation of one or both collision partners, nuclear contact and the onset of neck formation are established even well below the spherical Coulomb barrier.

Meanwhile, we have studied the systematics of isotope yields for the elements Ra through Pa in both reactions and have arrived at the following conclusions: the yields, see Fig. 1, are consistent with the usual Gaussian systematics and have widths of FWHM≈ 2.8 mass units. The centroids of these Gaussians coincide within the uncertainties with the minimum potential energy (MPE) prediciton, and the position of the centroids does not change with the bombarding energy. These observations suggest that these products have been formed cold, so that neutron evaporation/fission did not play a significant role in their production process. This is consistent with similar results in the $^{40}Ar+^{233}U$, ^{235}U, ^{238}U reactions[3], in reactions of ^{50}Ti, ^{54}Cr, ^{58}Fe with Pb[4], and in the $^{48}Ca+^{248}Cm$ reaction[5]. In all these reactions, as in the present work, the bombarding energy was at (or below) the Coulomb barrier. Thus, the present data add to the conjecture that the donors of the transferred nucleons stay cold and the acceptors carry most of the excitation energy[4], if the collision occurs with relative velocity zero.

From the integrals of the isotopic distributions together with interpolations and extrapolations based on the Wollersheim systematics[6] with parameters adjusted[7] to reproduce the energy dependence of the below-target element yields above the barrier in the U+U reaction[8] we obtain an integral cross section for the surviving below-target multi-nucleon transfer products of 15 mb both for the U+Au and U+U reaction at the barrier. The cross section for sequential fission[1] in the U+U reaction is 100 mb. If we assume that all the heavy complements of the below-target multinucleon transfer products decay by sequential fission, at most 15 mb can be contributed to the sequential fission cross section by multi-nucleon transfer. Fission after 1n-transfer[1] contributes 5 mb. Thus, we have to conclude that the majority of sequential fission processes must occur after the transfer of a few nucleons, i.e. in transfer channels intermediate between one-nucleon and multi-nucleon transfer, for which sufficient cross section should exist. The surviving part of this cross section was not accessible to the radiochemical method.

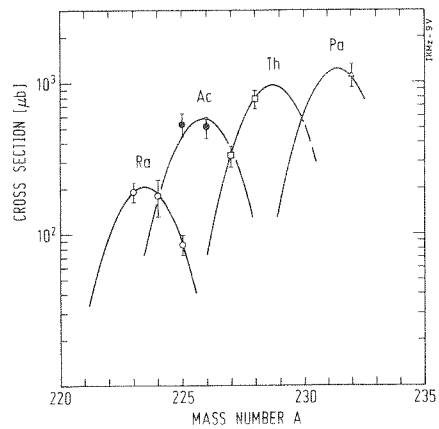


Fig.1 Cross sections for multi-nucleon transfer products in the U+Au reaction at the barrier

[1] G. Wirth et al., Z. Phys. A330, 87 (1988)
[2] G. Wirth et al., GSI Scientific Report 1988, GSI-89-1, p.41
[3] U.W. Scherer et al., Preprint GSI-89-85 (1989) Z. Phys. A, in press
[4] H. Keller et al., Z. Phys A328, 255 (1987)
[5] H. Gäggeler et al., Phys. Rev. C33, 1983 (1986)
[6] H.J. Wollersheim, Report GSI-84-34 (1984)
[7] H. Gäggeler, PSI-Bericht Nr. 14 (1988)
[8] J.V. Kratz et al., GSI Scientific Report 1979, GSI-80-1, p.27

Isotope Production in Fast Fission of ^{20}Ne and ^{238}U [B]

W.-D. Schmidt-Ott, F. Meissner, P. Koschel and U. Bosch, II. Phys. Inst., Univ. Göttingen; H. Folger, R. Kirchner, O. Klepper, E. Roeckl, GSI Darmstadt; K. Rykaczewski, Univ. of Warsaw, Warsaw

In the search for an effective isotope production, especially of light neutron-rich isotopes, we applied the fission reaction to the production of isotopes with $28 \leq Z \leq 31$ and $46 \leq Z \leq 50$. The measurement became feasible after the production of uranium carbide layers[1] which withstood the extreme conditions inside a FEBIAD-H ion source[2] under bombardment with a 120-160 particle-nA ^{20}Ne-beam. The internal target of the on-line mass-separator was composed by layers of uranium carbide and graphite. Graphite was used for the stopping and easy release of the fission products. In beam direction the target-catcher array contained 9.1 mg/cm² graphite, 6.6 mg/cm² UC/UC_2, 13.8 mg/cm² graphite, 13 mg/cm² UC/UC_2, and 21.8 mg/cm² graphite. The energy of ^{20}Ne in ^{238}U ranged from 10.9 to 10.4 and from 7.5 to 4.7 MeV/u. The Coulomb barrier of 5.2 MeV/u was calculated as in ref. 3. The target composition was controlled by proton backscattering[1] giving $^{238}U^{12}C_{1.6-1.8}$. The experimental yields of a number of isotopes are given in fig. 1. At the mass separator tape-stations the collection and measurement cycles were adjusted to the half-life of the shortest-lived isobar. The collected samples were brought in front of calibrated Ge detectors and measured using the known characteristic γ-rays and their branchings[4,5,6,7] in the individual decays. Fig. 1 shows that the respective yields of the heavier elements collected at a given mass are larger by one order of magnitude. Thus, the experimental values can roughly be addressed as primary fission yields.

The positions of maximum yields for copper and indium and the shapes of the yield curves for each element can be compared with earlier results[8]. In these measurements[8] the width (FWHM, in mass units) of the isotopic distributions ranged for rubidium from 3.8 to 5.4 and for caesium from 3.9 to 8.3. For heavier projectiles and at higher bombarding energies broader distributions were observed[8]. The positions of the maximum mass yields for rubidium and caesium[8] were linearly inter- and extrapolated for the neighbouring elements. The expected maxima of the isotopic yield curves for nickel to gallium and for palladium to tin were thus derived. The predicted positions of the maxima for the distribution of the copper and indium isotopes are 69.1 and 119.0, respectively. They are in agreement with the present observation. Distribution curves were fitted to the present yields using the positions of the maxima and adopting the width (in mass units) of 4 (except for copper with 3.3) for the light and 4.4 for the heavy elements. By assuming a uniform overall efficiency of the ion source and the mass-separator, a rough approximation of the fission cross-sections may be derived independent of chemical properties and half-lives of the products. The cross-sections given by the ordinate to the right in fig. 1 were obtained with an adopted efficiency of 10%. Obviously, the fact that copper has a higher peak yield than zinc does not necessarily correspond to a similar situation for the cross-sections. However, the cross-sections for the elements cadmium to zinc in the region of maximum fission yield of 20 to 30 mb are in good agreement with those from earlier measurements[9]. The isotope production by fission can be compared with the one from multinucleon transfer. Fig. 2 shows the yield curves observed for 11.5 MeV/u $^{82}Se+^{nat}W$ (ref. 5) and for 13.5 MeV/u $^{50}Ti+^{nat}W$ (ref. 10). The fast fission in the system $^{20}Ne+^{238}U$ gave less steep yield curves. Fission, therefore, still seems to be an interesting alternative for the production of exotic nuclei.

References

1) D. Kraft et al., Nucl. Instr. Methods A282 (1989) 99
2) R. Kirchner et al., GSI Scientific Report 1987, GSI 88-1, p. 339
3) H. Gäggeler et al., Phys. Rev. C33 (1986) 1983
4) E. Runte et al., Nucl. Phys. A441 (1985) 237
5) U. Bosch et al., Nucl. Phys. A477 (1988) 89
6) C.M. Lederer and V.S. Shirley (eds.), Table of Isotopes, 7th ed. (John Wiley, New York 1978)
7) J.A. Winger et al., Phys. Rev. C39 (1989) 1976
8) M. de Saint-Simon et al., Phys. Rev. C14 (1976) 85
9) L.J. Colby et al., Phys. Rev. 121 (1961) 1415
10) W.-D. Schmidt-Ott et al., subm. to Nucl. Physics A

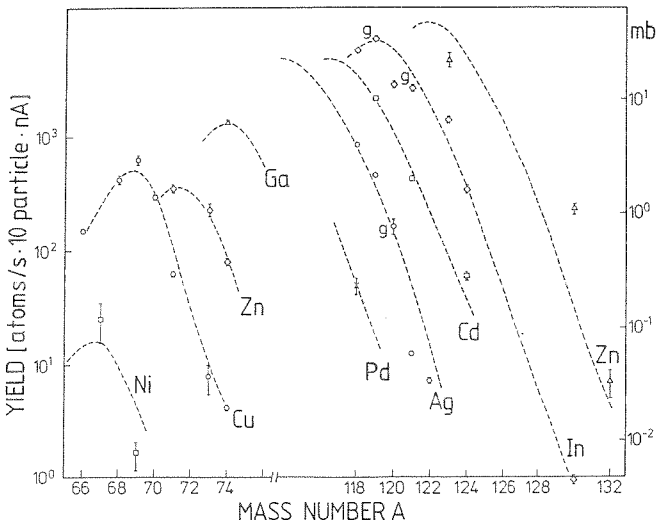


Fig. 1: Measured yields and crudely estimated production cross-section in mb in the fast fission of $^{20}Ne+^{238}U$. Cross-section data from ref. 8 were used to derive approximate yield dependences which were scaled to the present data (dashed curves).

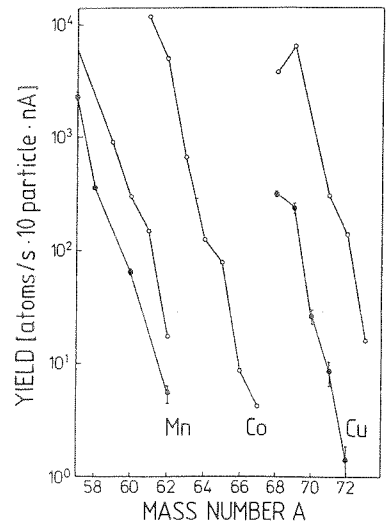


Fig. 2: Yields from multinucleon transfer observed in our earlier experiments. 11.5 MeV/u $^{82}Se+^{nat}W$ (open dots) and 13.5 MeV/u $^{50}Ti+^{nat}W$ (full dots).

Indication of In-Flight Separated Evaporation-Nuclei Like α-Emitter from Bombardments of ^{72}Ge, ^{76}Ge with ^{120}Sn at E/A = 14.5 MeV/u at SHIP

F.P.Heßberger, V.Ninov (GSI Darmstadt)

The positive results concering the observation of evaporation residues (ER) from highly excited nuclei ($E^x = (360 - 400) MeV$) produced in nuclear reactions induced by a high energetic light projectile (^{40}Ar)/1/, encouraged us to investigate the usefulnes of SHIP to separate ER from reactions induced by high energetic heavy projectiles.
A physical motivation to do so, is, that due to the relationship $E^x = E_{CM} + Q$ the highest excitation energies at a given specific beam energy (as long as $E_{CM} >> Q$) are expected for symmetric target - projectile combinations.
From the technical side two aspects are of interest:
a)Due to the higher linear momentum induced by the heavy projectiles the angular spread of the ER due to particle evaporation is smaller compared to reactions with light isotopes; thus the SHIP transmission will be higher.
b)Since the maximum electrical field strength of the high voltage condenser of SHIP is limited to 44 kV/cm, a 'normal' SHIP operation, i.e. 0.1 rad deflection of the ER the condenser, might not be possible due to the high electrical beam rigidity /2/.

The experiment was performed with a 'parasitic' ^{120}Sn beam. The incident beam energy of 19.1 MeV/u was degraded to E/A = 14.5 MeV/u (calculated using stopping powers of ref.3) with a 10 mg/cm² carbon foil.
Since a 'normal' SHIP operation (see above) was not possible due to the high electric beam rigidity of 32.4 MV, and a reduction of the deflection angle increased the background of projectiles to an intolerable extent ($>> 10^5$), we used carbon foils of $\simeq 6$ mg/cm² to reduce the velocity of the ER. After passing SHIP the separated products were implanted into a surface barrier detector (A = 300mm²), which was used to register α decays between the beam bursts.

The results of the α decay measurements are shown in fig. 1.
The isotopes identified range from ^{149}Tb to ^{156}Lu, i.e. isotopes with N = 84,85. They rather represent the 'primary' endproducts of the reaction (after particle emission) than α active endproducts of β decay chains starting with more neutron deficient nuclei. This argument is based on the observed number of α decays of neighbouring N = 84 and N = 85 isobars. In the case of β decay chains the 'mother-daughter' relation $z^t_\alpha / z^m_\alpha = (b^t_\alpha / b^m_\alpha) - b^t_\alpha$ has to be fulfilled. z^t_α, z^m_α, b^t_α, b^m_α represent the counting rate and the α branchings of the N = 85 and N = 84 nuclei. The measured α rates of the N = 85 nuclei however are higher than expected from the formula above.
The maximum intensity of α emitters was observed at a SHIP setting of $v/v_{CN} \simeq 0.85$, i.e. close to the velocity of the composite nuclei. We do not draw any conclusions concerning full momentum transfer from this certain value due to the uncertainties of the energy loss in the thick degrader foils, but state that their velocity distribution is centered close to the CN velocity.
Assuming complete fusion we conclude that the observed α emitters are produced by a massive emission of (ΔA = (41-47) for ^{76}Ge, ΔA = (37-43) for ^{72}Ge) of nucleons or light nuclei from the Highly excited CN $^{196}Pb(E^x = 530 MeV)$ and $^{192}Pb(E^x = 510 MeV)$.
The high survival probabilty of such hot systems is reflected in the formation cross-sections. For the system $^{120}Sn + ^{76}Ge$ we deduced a value for the α-emitter above 4 MeV (not including the long living isotope ^{149}Tb of which only part of the decays was observed in our irradiation times of $\simeq$ 1/2 h) $\sigma \times \varepsilon \simeq 200$ μbarn.
The SHIP transmission can be assumed to 10%. This value is mainly determined by the angular straggling in the 6 mg/cm² carbon foil, and only little sensitive to the energy and number of the neutrons, protons and α particles from the hot composite system, as long as the number of heavier particles (A > 4) can be regarded as negligble. Keeping in mind that the observed α emitters represent only part of the ER distribution, the formation cross section for ER amounts σ > 2 mbarn.

Our experiment showed the applicability of recoil separators for the investigation of ER from reactions using heavy projectiles with inverse kinematic, i.e. $A_p > A_T$. Choosing an appropriate projectile - target - combination part of the reaction products are α-emitters; for these a detailed isotopic distribution can be achieved.
The suppression of the primary beam is only 10^5 and thus considerably lower than in experiments using beam energies close to the fusion barrier (10^{10} - 10^{16}), which leads to serious radiation damage of the detectors after 12 h of operation.
An approvement can be obtained using the additional separator NASE /4/. In a first experiment dealing with this problem, which was performed in May 1989, we investigated the reaction $^{84}Kr(11.6 MeV/u) + ^{102}Pd$. A background reduction by a factor > 100 was achieved. The transmission of NASE, i.e. $Z_{ER}(NASE)/Z_{ER}(SHIP)$ at that special setting was 36%.

References

/1/ F.P.Heßberger et al. GSI-Scientific Report 1986, GSI-87-1,55 (1987) and also this report
/2/ G.Münzenberg, W.Faust, S.Hofmann, P.Armbruster, K.Güttner,H.Ewald: Nucl.Instr.Meth. 161,65(1979)
/3/ F.Hubert, A.Fleury, R.Bimbot, D.Gardes: Annales de Physique 5,1 (1980)
/4/ G.Berthes, Thesis, GSI-Report 87-12 (1987)

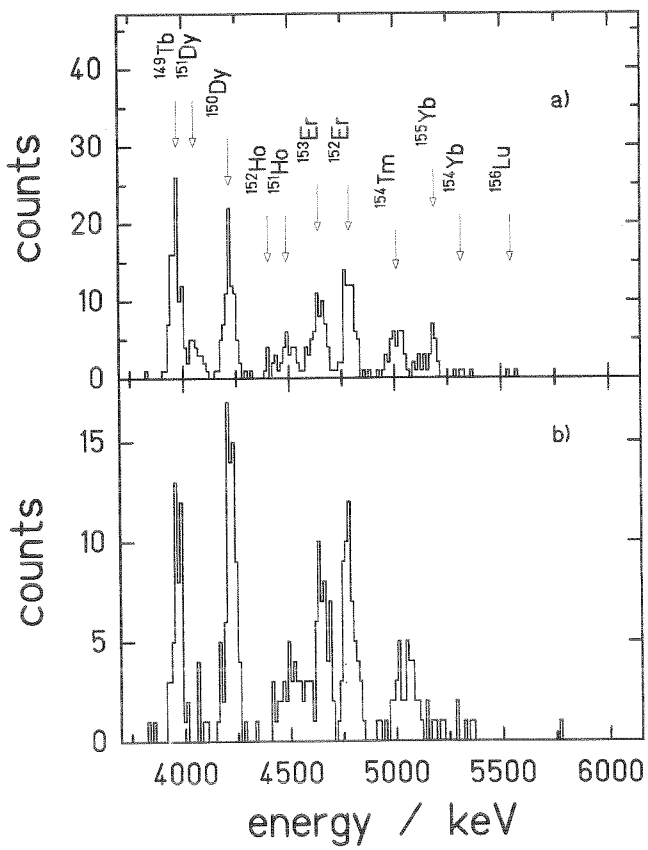


Fig. 1 α-spectra recorded at the irradiations of ^{76}Ge (upper figure a)) and ^{72}Ge (lower figure b)) with ^{120}Sn at 14.5 MeV/u.

Investigation of Reactions Leading to Highly Excited Compound Nuclei $75 \leq Z_{CN} \leq 82$ [B]

F.P.Heßberger, V.Ninov (GSI Darmstadt), A.Lüttgen (Uni Bonn),
D.Ackermann, W.Morawek (TH Darmstadt)

In a previous issue of this report we presented first results on the evaporation residue (ER) production in ^{40}Ar induced reactions leading to compound nuclei (CN) in the region $75 \leq Z_{CN} \leq 80$ with excitation energies of $E^{x} \simeq (360 - 400) MeV$ /1/. Here we want to report on the results of more recent experiments. The relevant reaction data are listed in table 1.

Since the efficiency of SHIP for these kinds of reactions is not well established we will use in the following mostly the 'efficiency weighted' cross-section $\sigma \times \varepsilon$ rather than σ. The 'integral production rates' $(\sigma \times \varepsilon)_{ER}$ were taken from the numbers of implanted nuclei, while the 'differential production rates' (for single isotopes) were taken from the α decay rates.

Reaction	E/A / MeV/u	E^{x} / MeV	$(\sigma \times \varepsilon)_{ER}$ / μb	$\sigma \times \varepsilon(^{152}Er)$ / μb
$^{40}Ar + ^{139}La \rightarrow ^{179}Re$	15	369	-	-
$^{40}Ar + ^{140}Ce \rightarrow ^{180}Os$	14.5	371	860	39
$^{40}Ar + ^{141}Pr \rightarrow ^{181}Ir$	14.5	369	710	36
$^{40}Ar + ^{142}Nd \rightarrow ^{182}Pt$	15.25	384	-	-
$^{40}Ar + ^{144}Sm \rightarrow ^{184}Hg$	14.5	362	650	36
$^{40}Ar + ^{148}Sm \rightarrow ^{188}Hg$	14.5	371	710	18
$^{40}Ar + ^{150}Sm \rightarrow ^{190}Hg$	15.25	400	-	-
$^{40}Ar + ^{154}Sm \rightarrow ^{194}Hg$	14.5	384	631	1
$^{84}Kr + ^{100}Ru \rightarrow ^{184}Hg$	11.6	382	-	-
$^{84}Kr + ^{102}Pd \rightarrow ^{186}Pb$	11.6	376	-	-

Table 1. Reaction parameters and results

As can be seen from table 1, the production rates vary only slightly with the targets. The data indicate a slight decrease with increasing Z and roughly constant values for the Sm-isotopes (Z=62). The center of the mass distribution of the ER varies only slightly with N or Z of the target as can be seen from the ratio $\sigma \times \varepsilon(^{152}Er)/(\sigma \times \varepsilon)_{ER}$. The values are equal within a factor of two for $^{140}Ce, ^{141}Pr, ^{144}Sm, ^{148}Sm$. A 'giant' step to ^{154}Sm is necessary to obtain a significant decrease by a factor of 40 compared to ^{144}Sm.

The mass dependence of the production rates for the N=84,85 isotopes is shown in fig.1 for four reactions ($^{40}Ar + ^{140}Ce, ^{141}Pr, ^{144}Sm, ^{148}Sm$). A steep decrease of the production rates for ER towards higher mass numbers (A=152 to A=157) is seen. The slope of the decrease turns out to be is somewhat steeper for the lighter target isotopes. This effect is more clearly seen in fig.2, where the relative intensities of different ER are plotted versus their atomic number for all investigated reactions leading to compound nuclei with N=104 (see table 1).

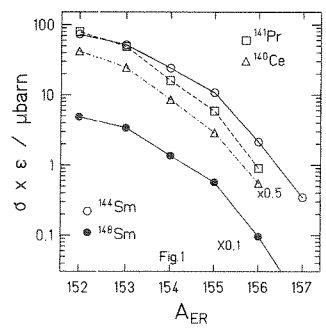
There is only a weak depedence of the relative intensity to the atomic number of CN. A change of the atomic number of the CN by seven units causes only a maximum change in the relative intensity by a factor of six $i(^{156}Lu)/i(^{152}Er)$.

From our data we get a ratio $(\sigma \times \varepsilon)_{\alpha}/(\sigma \times \varepsilon)_{ER} \simeq 0.6$ for $^{40}Ar + ^{144}Sm$ (see fig.3); this high value strongly suggests that the observed α emitters represent the center of the mass distribution of the ER. Thus we can assume that the production rates must decrease rapidly for N > 86. So the center of the mass distribution can be localized by N=84-86 and Z=65-71 (fig.3) The measured 'differential production rates' indicate a rather broad center with a steep decease at the flanks,while a comparison of the different reactions further indicates, that the center is rather stable with respect to variations of Z and N of the CN.

From simulation calculations a rough estimate of 2.5%, which might be reasonable within a factor of two, is obtained for the SHIP efficiency. With this value, the total ER cross section will amount to $\sigma_{Er} \simeq 25 mb$. Taking into account a fusion cross section $\sigma_{fus} = 460 mb$ as obtained using the HIVAP code for $^{40}Ar(14.5 MeV/u) + ^{144}Sm$ one gets a survival probablility of $\simeq$ 5% for the CN at $E^{x} = 362 MeV$, that can be compared with the value of $\simeq$ 20% for the same CN at $E^{x} \simeq 50 MeV$ /5/. So an by an increase of the excitation energy by 310 MeV the survival probability of the CN is reduced by less than one order of magnitude, only.

References

/1/ F.P.Heßberger et al. GSI-Scient. Rep.1986, GSI-87-1, 55
/2/ W.Reisdorf et al. Nucl.Phys. A438,212 (1985)



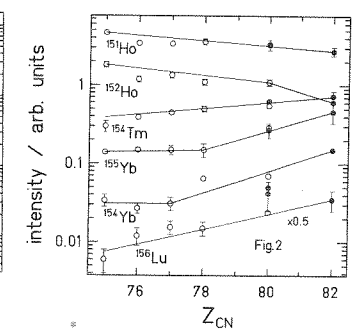


Fig.1: Production rates of N=84+N=85 nuclei in dependeance of A
Fig.2: Relative Intensities of different ER in dependence of Z ($N_{CN} = 104$)

73	Ta	Ta 156	Ta 157	Ta 158	Ta 159	Ta 160
72	Hf	Hf 155	Hf 156	Hf 157 0.36	Hf 158 1.6	Hf 159
71	Lu	Lu 154	Lu 155 0.6	Lu 156 2.1	Lu 157 21	Lu 158
70	Yb	Yb 153	Yb 154 2.7	Yb 155 10	Yb 156	Yb 157
69	Tm	Tm 152	Tm 153 16	Tm 154 21	Tm 155	Tm 156
68	Er	Er 151	Er 152 36	Er 153 36	Er 154 69	Er 155
67	Ho	Ho 150	Ho 151 54	Ho 152 39	Ho 153	Ho 154
66	Dy	Dy 149	Dy 150 40	Dy 151 10	Dy 152	Dy 153
65	Tb	Tb 148	Tb 149 27	Tb 150	Tb 151	Tb 152
64	Gd	Gd 147	Gd 148	Gd 149	Gd 150	Gd 151
		83	84	85	86	87

Fig.3: 'differential cross sections' $\sigma \times \varepsilon/\mu b$ for α emitters produced in the reaction $^{40}Ar(14.5 MeV/u) + ^{144}Sm$

Investigation of Evaporation Residues from Highly Excited Heavy Compound Nuclei [B]

F.P.Heßberger, V.Ninov (GSI Darmstadt), A.Lüttgen (Uni Bonn),
D.Ackermann, W.Morawek (TH Darmstadt)

The high survival probability of highly excited ($E^{\times} \simeq (360-400) MeV$), medium heavy compound nuclei (CN) /1/ encouraged us to search for evaporation residues (ER) from heavier and more fissile CN, since they will deliver most direct information on the stability of highly excited heavy nuclei against prompt fission. For this reason we increased the atomic number of the CN up to Z=110. The reactions we used are listed in table 1.
In order to get a proof to have observed ER we measured the velocity distribution of the registered α active reaction products.
ER-like nuclei have been observed for $^{40}Ar + ^{181}Ta, ^{nat}Pt$ and α decays from transfer products in the reaction $^{40}Ar + ^{209}Bi$. No α decays were found for the heaviest system $^{40}Ar + ^{238}U$. (See table 1 for the production rates).

Target	CN	$E^{\times}$/MeV	$\sigma \times \varepsilon$ / μb
^{181}Ta	^{221}Pa	370	15
^{nat}Pt	^{235}Cm[1]	364[1]	3
^{209}Bi	^{247}Md	355	0.015(α)[2]
^{238}U	$^{278}110$	363	<0.001[3]

[1] for ^{195}Pt
[2] from observed α decays, probably transfer
[3] no α decays observed

Table 1. Reaction parameters and results

In fig.1 we show the α spectrum of reaction products from a ^{40}Ar (14.5 MeV/u) + ^{nat}Pt irradiation. Their ($E_a = (6.0-7.2) MeV$) velocity distribution is shown in fig.2 for two different SHIP settings. The full dots refer to the SHIP setting $\theta = 0.1175$ rad and $q = 0.95 \times q_n$, the circles to $\theta = 0.125$ rad and $q = 0.9 \times q_n$ (θ denotes the deflection angle of the ER in the electrical field, q_n their mean charge charge state calculated according to ref.2).
Both curves show a maximum close to full momentum transfer, thus the α emitters are regarded as 'ER-like'. The behavior of the α emitter (same energy range as above) observed with the Bi-target is quite different; a smooth increase towards higher velocities is indicated.
The α emitters shown in fig.1 differ by ΔZ ≃(9-14) and ΔA ≃ (30-40) from the CN ($^{234-236}Cm$, according to the most abundant natural Pt isotopes), their production rate amounts, $(\sigma \times \varepsilon)_a = 0.5 \mu b$, the total production rate (from counting the implanted nuclei) amounts to $(\sigma \times \varepsilon)_a = 3 \mu b$ The ratio $(\sigma \times \varepsilon)_a / (\sigma \times \varepsilon)_{ER} = 0.17$ indicates that the maximum of the mass distribution of the ER is localized at somewhat lower Z values (most probably non α actitve Bi- and/or Pb isotopes).
A rough estimate of the SHIP efficiency is about 2.5%. Thus one can estimate a total production cross section $\sigma \simeq 600 \mu b$ for $^{40}Ar(14.5 MeV/u) + ^{181}Ta$ and $\sigma \simeq 100$ μb for $^{40}Ar(14.5 MeV/u) + ^{nat}Pt$. These high values are astonishing by two reasons: The value for ^{181}Ta is more than one order of magnitude higher than the sum of the xn, pxn, αxn cross sections measured at a projectile energy close to the Coulomb barrier (4.6 MeV/u) /3/, and b) in ^{40}Ar induced reactions (with targets Z>74) leading to CN with Z > 92 at bombarding energies close to the Coulomb barrier barrier no ER cross sections exceeding ≃ 100 nb, i.e. three ordes of magnitude less, than for $^{40}Ar + ^{nat}Pt$ at E/A = 14.5 MeV/u have been measured so far.

From our measured production rates and isotope yields qualitatively we can draw the following conclusions about the deexcitation of hot nuclei:
a) for CN up to Z = 96, as considered here, particle emission prevails over prompt fission at least in the early stage of deexcitation, and
b)already before fission can compete with particle emission the fissility of the CN must be reduced by emission of charged particles.
Thus we regard these deductions from our data as inline with the conclusion, that fission (or 'scission') will occur at the very end of the deexcitation chain as drawn from neutron measurements in ref.4.

References

/1/ F.P.Heßberger et al. GSI-Scient.Rep.1986, GSI-87-1,55
/2/ V.S.Nikolaev,L.S.Dimitiev Phys. Lett. 28A,277 (1968)
/3/ D.Vermeulen et al. Z.Phys. A 318,157 (1984)
/4/ D.Hilscher et al. Phys. Rev. Lett. 62,10 1099 (1989)

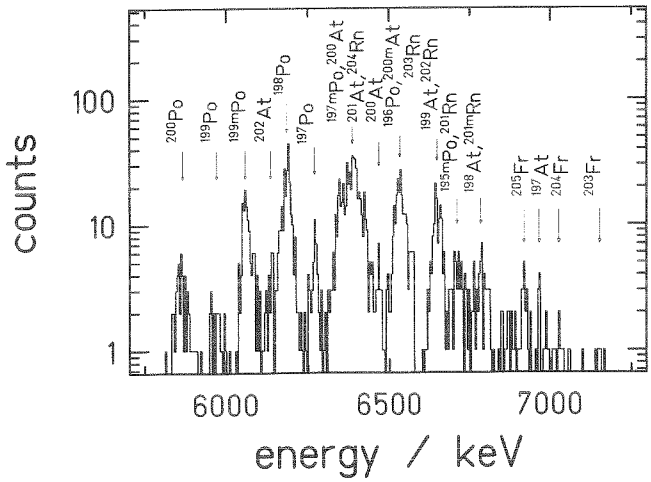


Fig. 1:α-spectrum from the decay of ER produced in the reaction ^{40}Ar (E/A = 14.5 MeV/u) + ^{nat}Pt

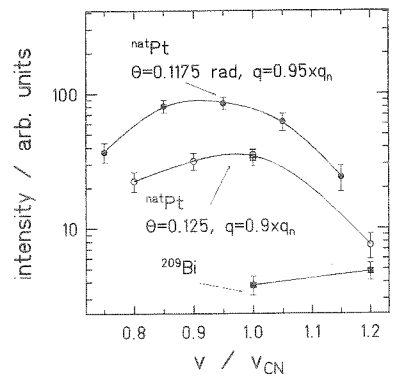


Fig. 2:velocity distribution for isotopes produced in the reactions ^{40}Ar (14.5 MeV/u) + ^{nat}Pt. • SHIP setting: d=0.1175, $q = 0.95 \times q_n$, o SHIP setting: d=0.125, $q = 0.9 \times q_n$ ▪ ^{40}Ar (14.5 MeV/u) + ^{209}Bi.

Evaporation Residues at $E^* \approx 400$ MeV B,G

S. Beiersdorf, R.A. Esterlund, M. Knaack, B. Jäckel, W. Westmeier, P. Patzelt, F.P. Heßberger*, V. Ninov*

Institut für Kernchemie, Marburg and *GSI, Darmstadt

In a series of experiments carried out with the velocity separator SHIP and reported upon elsewhere[1], evaporation-residue-like products have been detected in a number of reaction systems which produce compound nuclei in the A-Z range $184 \leq A \leq 196$ and $80 \leq Z \leq 82$. The compound nuclei all have initial excitation energies of *ca.* 400 MeV, corresponding to temperatures of *ca.* 4 MeV. Online measurement of cross sections for short-lived α-emitters have produced integral evaporation residue (ER) yields (after correction for the SHIP efficiency ϵ) of *ca.* 25 mb.

Since α-decaying products represent only a fraction of the entire ER yield, we deemed it desirable to also determine cross sections for $\beta+$/EC-decaying nuclides. We initially chose the reaction 15 MeV/u ^{40}Ar + ^{154}Sm, for which we performed an offline gamma-spectrometric assay of reaction products caught in an Al catcher foil mounted behind SHIP. Additionally, four Al catcher foils covering the moving-frame angular range 2.0°-33.7° (moving-frame grazing angle ≈ 14°) were positioned in front of SHIP, for the purpose of determining angular distributions of products.

The mass-yield curve obtained from the SHIP foil at $V = V_{cn}$ is shown in Fig. 1, and was constructed under the assumption that cumulative cross sections measured near β- stability constitute a good approximation to the total mass-chain yields. A gaussian curve has been arbitrarily fitted to the data, to guide the eye. The peak at low masses is likely due to the α-decay of higher-mass products which thereby feed lower mass chains. The gaussian centroid $\langle A \rangle \approx 160$ agrees satisfactorily with the calculated value for ER of $\langle A_{ER} \rangle \approx 158$. The measured integrated cross section is *ca.* 1.9 mb, which, when corrected by the calculated SHIP efficiency $\epsilon \approx 0.04$, yields a total deduced ER cross section of *ca.* 48 mb, corresponding to an $l_{ER} \approx 33$.

Empirical systematics for l_{ER} (plateau) as a function of Z^2/A derived from data for much lower energies predict an l_{ER} for this compound nucleus (^{194}Hg) of *ca.* 35, corresponding to an evaporation-residue yield at this energy of *ca.* 52 mb. However, the fact that the observed mass-yield centroid is near the target mass of 154 suggests that a part of our measured ER yield may be contaminated with deep-inelastic transfer (DIT) products. To check this possibility, we have information from four sources:

1) The observed cross sections for genetic decay pairs near β-stability: *e.g.*, we observe no independent formation cross section for ^{160m}Ho, which is the daughter *via* EC decay of ^{160}Er. This indicates that the charge-yield distribution for this mass chain is located in the A-Z plane far to the proton-rich side of β-stability. This is contrary to what would be expected here for a DIT process, suggesting that the mass chain A = 160 is virtually all ER. In contrast, we do observe an independent formation cross section for ^{146}Eu, the daughter of ^{146}Gd, suggesting that DIT processes contribute to yields for this mass chain.

2) The angular distributions measured in foils A-D in front of SHIP: *e.g.*, the observed (moving-frame) $d\sigma/d\Theta$ for ^{160}Er is qualitatively different from that of ^{146}Gd, being relatively narrow and forward-peaked, in contrast to that for the latter nuclide, which exhibits a broad and backward-peaked shape. The former is consistent with an ER origin whilst the latter is consistent with that expected for a target-like DIT product.

3) Mass-yield distributions in the foils A-D: *e.g.*, if mass yields near A ≈ 160 are mostly ER, and those near A ≈ 146 are mostly DIT (see above examples), then the foils without v-separation should exhibit, in contrast to the SHIP foil, a significant increase in the yields about A = 146 relative to those about A = 160.

4) Charge-yield distributions near the target mass in foils A-D: by construction of these curves from the cross-section data, we will follow the evolution of the DIT process in the A-Z plane near the target, and thus hopefully be able to determine quantitatively to what extent such yields intrude upon the ER yield domain.

To the extent that the above procedures are successful, they will also constitute an experimental check on the calculated transmission factor.

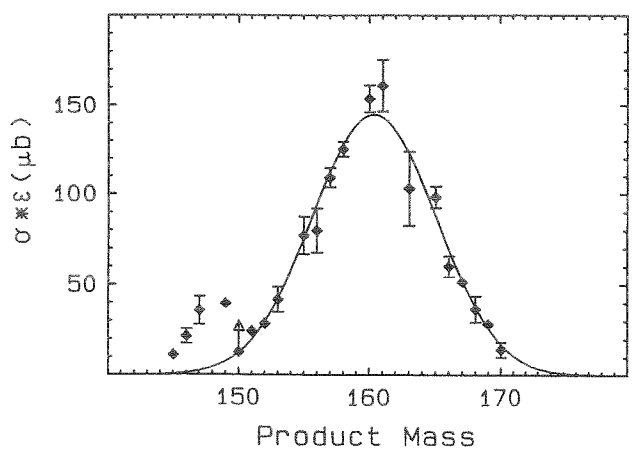


Fig. 1: Mass yields for the ER-like $\beta+$/EC nuclides produced in the reaction 15 MeV/u ^{40}Ar + ^{154}Sm.

[1] F.P. Heßberger *et al.*, GSI Nachrichten (January, 1990); GSI Sci. Rept. 87-1, 55 (1987); GSI Sci. Rept. 88-1, 19 (1988).

Investigation of the (d,p)-Reaction on $^{132,135}Xe$ using the Method of Inverse Kinematics [G]

G. Kraus, P. Egelhof, H. Emling, E. Grosse, W. Henning, R. Holzmann
P. Senger, H.J.-Wollersheim (GSI Darmstadt and University Mainz)
R. Kulessa, W. Walus (University Cracow), Ch. Schiessl, H.J. Körner, W. Wagner (TU München)
J.P. Schiffer (Argonne National Laboratory)

The new GSI-accelerator SIS in combination with the fragment separator FRS and the experimental storage ring ESR will provide cooled beams of relatively short-lived nuclei, extending to isotopes far off stability. These beams may be used for nuclear structure studies in inverse kinematics of nuclei, which are otherwise not accessible for light ion induced reactions[1,2]. For the first phase of SIS/ESR operation the investigation of (d,p), (p,p') and (α,α')-reactions on several nuclei far off stability is planned.

In order to test the experimental conditions for such studies, the reactions d(^{136}Xe, p) $^{137}Xe^*$ and d(^{132}Xe, p) $^{133}Xe^*$ were investigated using stable Xe-beams from the UNILAC accelerator at E = 5.87 MeV/u. For that purpose, a scattering chamber of 90 cm diameter (from MPI Heidelberg) was equipped, tested and installed at the Z6-beamline at GSI. As targets 100 μg/cm^2 deuterized Ti-targets (Ti :D- content 1:1) on a 200 μg/cm^2 Aℓ-backing were used. The detector system consisted of various small solid-angle monitor-detectors (PIN-diodes and conventional surface barrier detectors) and a specially designed large solid angle array consisting of 10x10 PIN-photodiodes[3] with a total active area of 64 cm^2. This corresponds to a solid angle of Ω = 44 msr at 38 cm distance from the target. A semicollective readout allowed to reduce the amount of electronics to 20 channels for 100 detectors. The observed TOF-signals (for particle identification) and energy signals were analyzed using GOOSY. Finally for each run a total of 100 energy spectra and 100 TOF-spectra were available.

Protons from (d,p)-reactions leading to various excited states in ^{133}Xe and ^{137}Xe were detected in the angular range $95^0 < \theta_{lab} < 148^0$. A typical energy spectrum for d(^{136}Xe, p) $^{137}Xe^*$ at $\theta_{lab} = 120.8^0$ is displayed in fig. 1. Peaks corresponding to transitions to the strong single particle levels in ^{137}Xe are clearly visible on a continuous background of light particles from Xe+Ti and Xe+Aℓ-reactions. A more detailed analysis shows that - as expected - the dominating part of this background consists of protons which may not be eliminated by TOF. The observed energy resolution was of the order of $\Delta E = 80$ keV (mainly dominated by the angular resolution), the time resolution was of the order of 1.5 nsec.

In order to deduce the optical-potential parameters of the entrance channel, the cross section for elastic deuteron scattering was measured in addition. As an example the angular distribution for d(^{132}Xe,d) ^{132}Xe is shown in fig. 2. The solid line is the result of the bestfit obtained by optical-model-calculations.

Some typical examples for angular distributions for (d,p)-reactions on ^{132}Xe leading to the groundstate and excited states in ^{133}Xe at $E_x = 1.6$ MeV and $E_x = 3.0$ MeV are displayed in fig. 3. The solid and dotted lines are the results of DWBA-calculations using the code DWUCK with the different transferred angular momenta ℓ indicated. The good ℓ-selectivity of the data is obvious.

From these data excitation energies, spins and spectroscopic factors for a total of 9 energy levels in ^{137}Xe and ^{133}Xe were deduced. The levels in ^{133}Xe at $E_x = 1.6$ MeV and $E_x = 3.0$ MeV were investigated for the first time. In comparison with data obtained from deuteron-induced reactions on Xe-targets[4,5] an overall good agreement is observed, indicating that the method of inverse kinematics is a useful tool to investigate single particle states by (d,p)-reactions on nuclei far off stability.

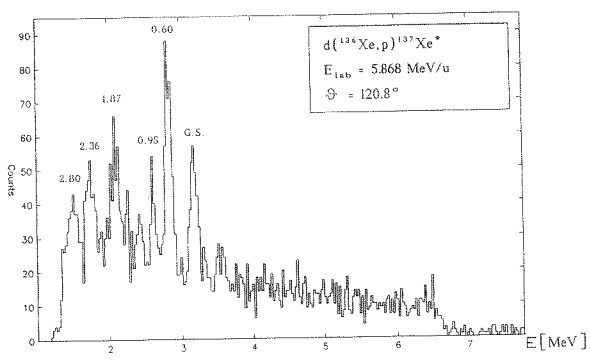


Fig. 1: Energy spectrum for the reaction $^{136}Xe \rightarrow Ti+D$ at $E_{lab} = 5.868$ MeV and $\theta_{lab} = 120.8$. The deduced excitation energies for the strong single particle levels in ^{137}Xe are given in MeV.

1. SIS/ESR-proposal No. 56/New
2. P. Egelhof et al., Technical proposal to proposal No. 56/New
3. J. Friese et al., Contribution to this scientific report
4. E.J. Schneid et al., Phys.Rev. 148(1966)1241
5. P.A. Moore et al., Phys.Rev. 175(1968)1516

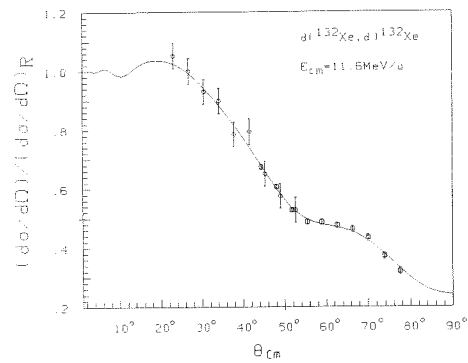


Fig. 2: Angular distribution of the differential cross section (normalized to the Rutherford cross section) for elastic scattering d(^{132}Xe,d)^{132}Xe at $E_{cm} = 11.6$ MeV. The solid line is the result of an optical model calculation.

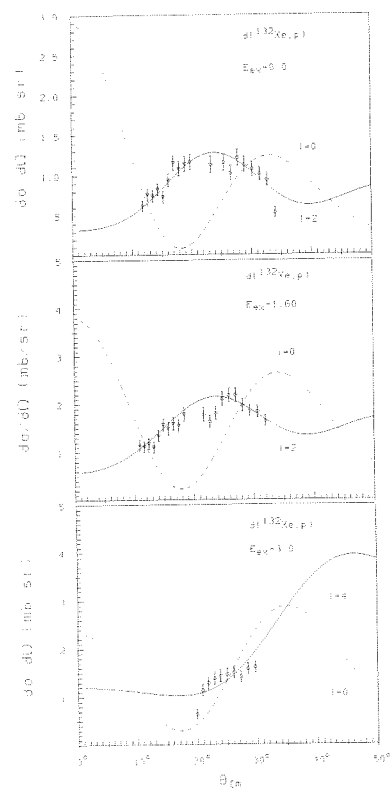


Fig. 3: Angular distributions of the differential cross section for the reaction d(^{132}Xe,p)$^{133}Xe^*$ at $E_{lab} = 5.868$ MeV leading to the groundstate and excited states at $E_x = 1.6$ Mev and $E_x = 3.0$ MeV. The solid and dotted lines are the result of DWBA-calculations for different transferred angular momenta ℓ.

Trajectory Determination and Entrance Channel Effects in Heavy Ion Collisions at 12.0 MeV/u [B,G]

R. Barth, E. Ditzel, H. Friedemann, E. Kankeleit, G. Klotz-Engmann, V. Lips, Ch. Müntz, H. Oeschler, A. Piechaczek, W. Polai, M. Rhein, I. Schall

Institut für Kernphysik, TH Darmstadt

The investigation of the time-scale in dissipative heavy ion collisions by δ-electron spectroscopy is subject of the research program at the TORI-spectrometer [1]. The influence of prolonged nuclear collision times on the δ-electron spectra was shown and a model-independent determination of the nuclear trajectories was developped [2, 3]. In recent years it has been well established that the complex transition amplitude is proportional to the Fourier transform of the function $\dot{R}(t)/R(t)$ [4]. Very similar to formfactor measurements with electron scattering higher lepton energies reveal more detailed informations about short time processes; this is the very fast stopping of the colliding nuclei in the entrance channel. So the knowledge of the spectra at high electron energies allows to gain insight into shorter time scales. For example the slowing down of the colliding nuclei takes place within $\approx 10^{-22}s$; the involved Fourier frequencies lead to electron energies around 7 MeV. For this purpose we have extended the measurable energy range for δ-electrons up to 10.0 MeV by the installation of a new electron detector [5].

For a realistic treatment of extended nuclei R(t) has to be taken as twice the *rms* monopole charge distribution ($R_{rms} = 2\sqrt{< r^2 >}$) [6]. This assumption was verified by comparing the resulting binding energies and wave functions of the electrons calculated by

i): solving the two-center Dirac equation for extended nuclei [7],
ii): assuming pointlike nuclei at the same two-center distance,
iii): assuming pointlike nuclei separated by R_{rms}.

Fig. 1 shows the $1s\sigma$ binding energies calculated under these assumptions for two Pb-ions at a two-center distance of 15 fm. It exhibits the validity of the calculation when treating the nuclei as pointlike at distance $R = R_{rms}$ and was verified also for higher electronic states.

The deceleration of the nuclei can be handled by a new approach, treating the differences of the $\dot{R}(t)/R(t)$ curves for dissipative collisions from the elastic ones. It turns out that the deviations in the entrance-channel can be fitted by a Lorentzian line. Within the reaction model of Schmidt et al. [8] its area is related to the Q-value dissipated in the entrance channel due to radial friction. This opens a new way to determine the radial friction from the expetimental data.

Fig. 2 shows the difference $\dot{R}(t)/R(t)_{Schmidt} - \dot{R}(t)/R(t)_{elastic}$ for Pb+Pb at 8.6 MeV/u and 12.0 MeV/u calculated for b=8.3 fm. The effect on the spectral shape of the δ-electrons is depicted in Fig. 3. The electron yield above 5 MeV differs by one order of magnitude.

To study this behavior we performed an experiment with Pb + Pb at 12.0 MeV/u. Our aims are the comparison with the former 8.6 MeV/u data and the determination of the radial friction parameter. The data analysis is still in progress.

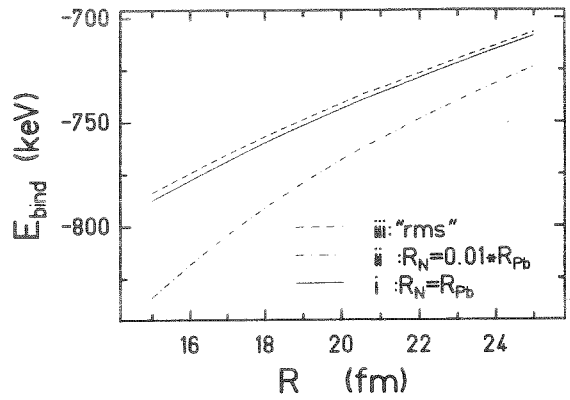


Figure 1: Electron binding energies of the $1s\sigma$-level calculated under the assumptions explained in the text.

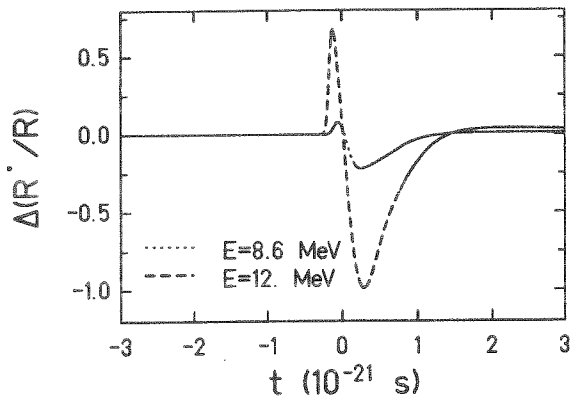


Figure 2: $\dot{R}(t)/R(t)_{Schmidt} - \dot{R}(t)/R(t)_{elastic}$ for Pb+Pb at 8.6 MeV/u and 12.0 MeV/u.

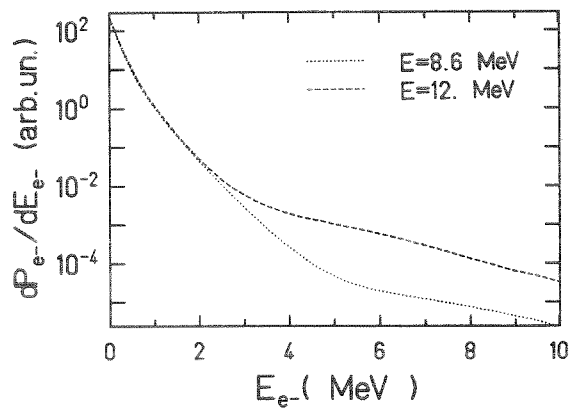


Figure 3: Electron spectra for 8.6 and 12.0 MeV/u and b=8.3 fm.

References

[1] E. Kankeleit et al., NIM A234, 81 (1985).
[2] M. Krämer et al., Phys. Lett. B 201, 215 (1988).
[3] M. Krämer et al., Phys. Rev. C 40, 1662 (1989).
[4] E. Kankeleit, Nucleonica 25, 253(1980).
[5] M. Rhein, Ch. Müntz, this report.
[6] E. Kankeleit, ASI Series "Physics of strong Fields", Maratea, Italy, June 1986
[7] G. Soff et al., Phys. Rev. C 30, 1199 (1984).
[8] R. Schmidt et. al., Nucl. Phys. A311, 247(1978).

Evidence for Non-Equilibrated Fission in Dissipative Collisions at 20 MeV/u

G. Casini, A.A. Stefanini, M. Bini, P.R. Maurenzig , A. Olmi and G. Poggi, University and INFN Florence
R.J. Charity, R. Freifelder, A. Gobbi, K.D. Hildenbrand, N. Herrmann, M. Tanaka and J. Wessels, GSI Darmstadt

Exclusive measurements of two, three and four heavy fragments detected in coincidence for the reaction ^{100}Sn + ^{100}Mo at 19.1 MeV/u have been performed. The experimental setup, largely the same as used in previous experiments at GSI and Ganil[1], consisted of 12 parallel plate avalanche counters mounted in a highly symmetric configuration around the beam axis and covering about 70% of the forward hemisphere (which is practically the only relevant one when using beams of mass heavier or equal to that of the target).
The binary channel is still the dominant one and displays many features which represent a smooth evolution of the characteristic behaviour known in dissipative collisions at lower energies. The ternary events seem to originate, for the most part, from a sequential mechanism, with one of the two highly excited primary products undergoing a scission process.

Excluding the fully relaxed events, the projectile- and target-like fragments of a dissipative collision can be easily recognised on the basis of the Wilczynski diagram. The fission probability P can be obtained[2] with some simplifying assumptions, from the 2-body and 3-body yields in each bin of total kinetic energy loss (TKEL) and for each mass. Using the angular information it is possible to deduce the fission probability separately for the projectile-like fragment (PLF) and for the target-like fragment (TLF). The results are shown in Fig. 1 as a function of the fissioning mass for two TKEL bins . Large differences between the fission probabilities for the PLF and the TLF are apparent.
These results can shed some light on aspects of the equilibrium process, which cannot be studied in a symmetric system. For example, consider a symmetric exit-channel where the PLF has lost and the TLF has gained mass. If the internal degrees of freedom are in equilibration at the end of the dissipative collision, the excitation energy and hence the sequential-fission probability of the two fragments should be, on average, equal. However, this is not the case in Fig. 1 for A = 110. The difference between these two probabilities (not only for A = 110 but also also for all other masses) points to a systematic difference in the populations of the internal degrees of freedom, possibility due to an asymmetric sharing of excitation energy and/or angular momentum.

It can be shown that the results of Fig. 1 are compatible with a simple model[3] where the energy sharing is proportional to the mass transfer (at least on the average for the events which undergo fission).

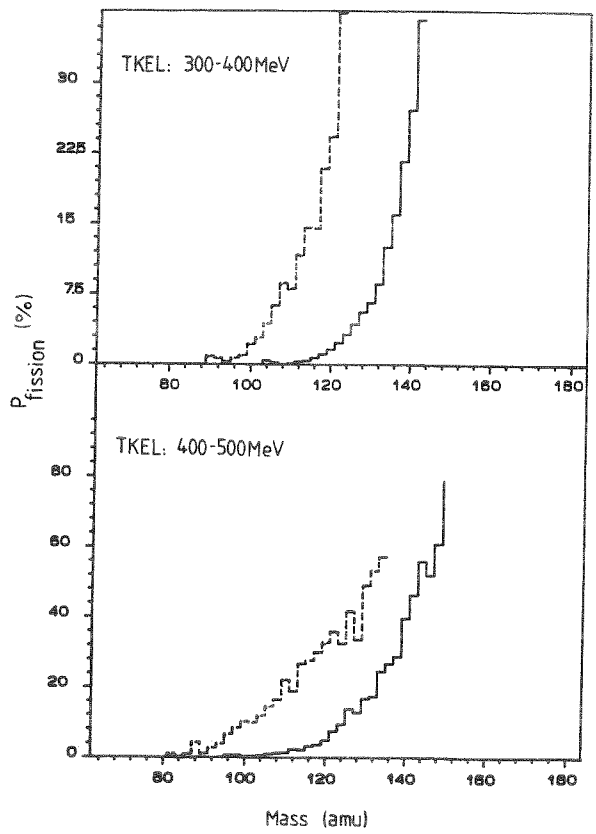


Fig. 1: The absolute fission probability for the target-like (dashed) and projectile-like (solid) fragments as a function of the fissioning mass, for two TKEL bins.

[1] A. Olmi et al., Europhys. Lett. 4 (1987) 1122
[2] G. Casisni, Ph.D. Thesis, University of Florence, unpublished
[3] M. Dakowski, A. Gobbi, W. Nörenberg, Nucl. Phys. A378 (1982) 189

Emission of Complex Fragments in Deeply Inelastic Collisions

J. Wessels, R. Bock, , R.J. Charity, R. Freifelder, A. Gobbi, N. Herrmann, K.D. Hildenbrand, H. Stelzer, GSI Darmstadt
M. Gnirs, D. Pelte, D. Reimold, Univ. Heidelberg
G. Casini, P. Maurenzig, A. Olmi, A.A. Stefanini, Univ. and INFN Firenze
M. Petrovici, IPNE Bucarest

In the collision of two heavy nuclei a large amount of excitation energy is deposited in the two primary fragments formed in a deep-inealstic process. These two highly excited fragments exhibit a long dexcitation chain involving light particles ($A \leq 4$), fission-like products($A \geq 20$) and complex fragments ($4 \leq A \leq 20$). We have studied the reactions ^{100}Mo + ^{100}Mo at energies of 18.7 AMeV and 23.7 AMeV at the UNILAC and at GANIL, with a set-up consisting of 12 parallel-plate avalanche counters (PPAC) and 24 gas-plastic telesopes. The telescopes were capable of mass identification of light paricles and had unity charge resolution for particles with $Z < 40$ [1]. The exit channel of such a collision is composed of 2, 3 or even 4 heavy ($A > 20$) fragments and a large number of light particles. The observations concerning the heavy fragments emerging from such a collision have been described elsewhere [2] [3]. From these observations it was also possible to extract information on the pre-equilibrium light particle emission [4].

In our analysis of the reaction we consider cases where two heavy fragments are observed in coincidence with a complex fragment ($4 < A < 20$). It has been observed that even if a coincident carbon was detected, the two-body kinematics of the heavy fragments is not severely disturbed due to the strong accompanying evaporation. It is thus possible to extract the total kinetic energy loss (TKEL) of the collision with the aid of the kinematical coincidence method [5]. At the same time the two heavy fragments define a separation axis through the centre of mass. Figures 1 a,b show the distribution of the parallel and peprpendicular velocity components of an emitted carbon fragment with respect to the separation axis for different TKEL. The heavy fragments were ordered such that the forward going is taken in right direction. Due to the focussing of the projectile into forward direction at lower TKEL the detection threshold of the telescopes leads to a decreasing yield on the left side.

In order to simulate these distributions we have developed a Monte Carlo code, that simulates the properties of the binary collision and then allows to subsequently evaporate light particles and complex fragments from the accelerated primary fragments. The Coulomb barrier for the complex fragments were adjusted to match the circles from the sequential decay seen in the data at lower TKEL. Figures 2 a,b show the results of the simulation for the same intervals in TKEL, when only sequential decay is allowed. It can be noticed that such simple assumptions are not sufficient to reproduce the large perpendicular velocities obserevd at $v_{||} \simeq 0$.

We conclude that there might be significant emission of complex fragments as heavy as carbon prior to full acceleration of the two primary fragments. The comparison of the calculated lifetime of a nucleus at a given excitation energy [6] with the contact time of the primary fragments [7] shown in figure 3 underline this hypothesis. A quantitative evaluation of these processes is under way.

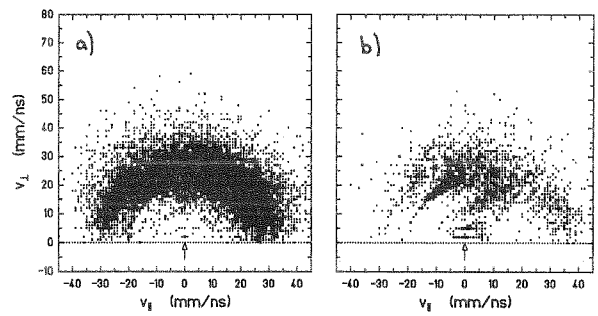


Fig. 1: a) $v_\perp$ versus $v_{||}$ at TKEL = 750 ± 50MeV for a carbon emitted in coincidence with two heavy fragments. The dashed line denotes the their separation axis. b) dto. for TKEL = 430 ± 100 MeV. The structure in the data arises from the fact, that the heavy fragments are strongly focused into forward direction and the telescopes cover only discrete angles.

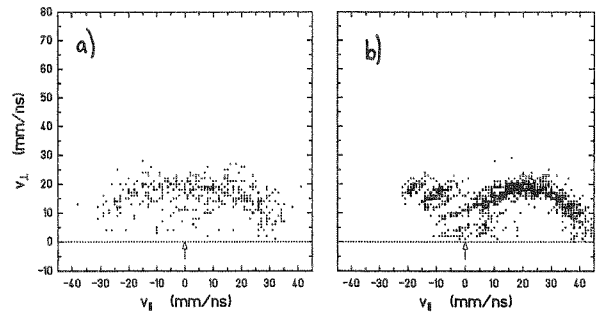


Fig. 2: a) Simulation of the above distribution allowing only sequential evaporation from the accelerated primary fragments at TKEL = 750 ± 50 MeV. b) dto. at TKEL = 430 ± 100 MeV.

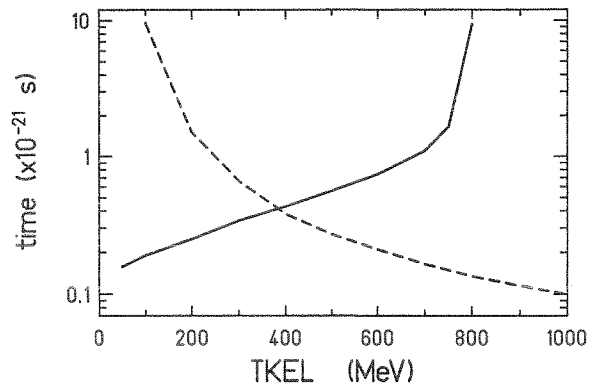


Fig. 3: Comparison of the lifetime of an A = 100 nucleus at various excitation energies (dashed) and the contact time of the system at 18.7 AMeV (solid) calculated with DONA.

[1] J. Wessels, M. Gnirs, GSI Reports 86-16,86-15 resp.
[2] S. Gralla et al., Phys. Rev. Lett. 54 (1985) 1898
[3] A. Olmi et al., Europhys. Lett. 4 (1987) 1122
[4] R. J. Charity et al., this report
[5] G. Casini et al.,NIM A227 (1989) 445 - 457
[6] R. J. Charity, private communication
[7] G. Wolschin, Nucl. Phys. A316 (1979) 146

Pre-equilibrium Light Particle Emission in Deep-Inelastic Reactions

R.J Charity, J. Wessels, R. Freifelder, A. Gobbi,
N. Herrmann, K.D. Hildenbrand, F. Rami H. Stelzer, GSI Darmstadt
P.R. Maurenzig, A. Olmi, A.A. Stefanini, Univ. and INFN Florence
M. Petrovici, IPNE Bucarest
M. Gnirs, D. Pelte, D. Reimold, Univ. Heidelberg
J.C. Adloff, B. Bilwes, R. Bilwes, G. Rudolf, CRN Strasbourg
J. Galin, D. Guerreau, U. Jahnke, GANIL Caen

Most experimental studies of pre-equilibrium light particle (PELP) emission have been made for fusion-like reactions. However, measured quantities obtained in such studies are typically averaged over the relevant distribution of impact parameters. The investigation of PELP emission in deep-inelastic and quasi-elastic collisions allows for the possibility to select on impact parameter. The correlation between the total kinetic energy loss (TKEL) and impact parameter can be obtained from the measured differential cross sections $d\sigma/dTKEL$. We have used the decay properties of the primary heavy fragments to infer the thermalized excitation energy and hence, from energy balance, the energy removed by the PELP.

Our recent investigations[1] of the ^{100}Mo + ^{100}Mo reaction show, that for bombarding energies lower than 19 MeV/nucleon, the probability of producing three heavy fragments via a sequential fission-like mechanism (P_3) is determined predominately from the excitation energy of the primary fragments at scission. This probability thus suggests itself as an excellent "thermometer" for inferring the temperature or excitation energy of the fragments.

The "thermometer" was calibrated using our measurements of P_3(TKEL) at the bombarding energy of E/A = 12 MeV where no PELP emission is expected. From the measured TKEL and the excitation energy of the primary fragments inferred from the thermometor curve, the energy balance in the exit-channel was determined. The PELP energy losses indicated by the hollow symbols in Fig. 1 were obtained assuming the missing energy in the exit-channel is associated only with PELP emission. However, if the deep-inelastic interaction time is long enough, the composite system can also evaporate light particles after the pre-equilibrium emission. The solid symbols in Fig. 1 indicate the PELP energy loss after theoretical corrections for the equilibrium emission were included.

Pre-equilibrium nucleon emission in the model of Bondorf et al.[2] arises from nucleons which are exchanged between the target and projectile, but which subsequently escape from their recipient nucleus. To test the validity of this assumption, the extracted average multiplicity of PELP's (n_{PELP}) was compared the mass-variance of the deep-inelastic fragments which gives a measure of average number of exchanged nucleons. Figure 2 shows the experimental mass-variance for the E/A=23.7 MeV reaction and the extracted values of n_{PELP} suitably scaled to show the similar dependence on the entrance-channel ℓ-wave. A similar finding was also obtained for the E/A=18.7 MeV reaction, thus strongly supporting the main assumption of the Bondorf model.

[1] A. Olmi et al., Europhys. Lett. 4 (1987) 1221 and P.R. Maurenzig et al., GSI Annual Report 1987, p. 63.
[2] J.P. Bondorf et al. Nucl. Phys. A333 (1980) 285.

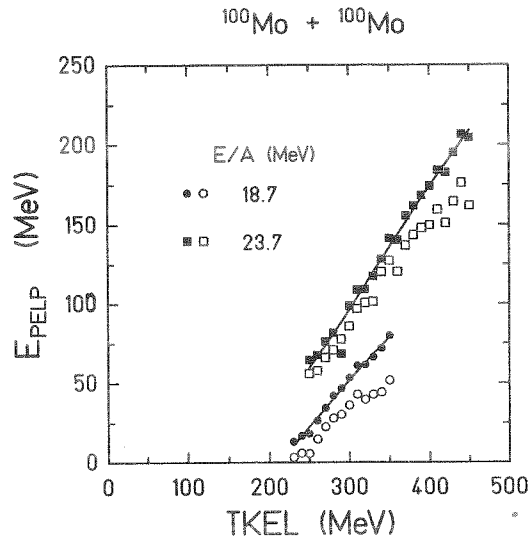


Figure 1: The average kinetic plus binding energy removed by pre-equilibrium light particle emission extracted from experimental sequential-fission probability curves plotted as a function of the total kinetic energy loss.

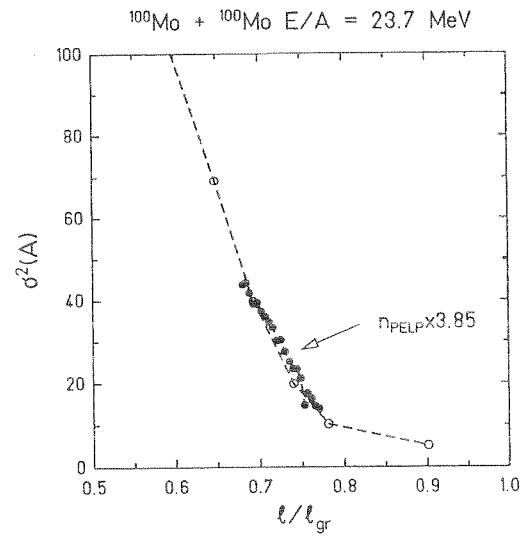


Figure 2: Comparison of the experimental mass-variance of deep-inelastic events to the extracted averge multiplicity of PELP as function of the entrance channel ℓ-wave. ℓ_{gr} is the angular momentum of grazing collisions.

Emission of Light Particles in the Symmetric Reaction $^{100}Mo + ^{100}Mo$ G

Michael Gnirs
Physikalisches Institut der Universität Heidelberg
in collaboration with GSI-Heidelberg and GANIL-Florenz

The analysis of the data taken from the symmetric system $^{100}Mo + ^{100}Mo$ at 18.7 MeV/u and 23.7 MeV/u bombarding energy, was continued[1]. The analysis for reactions with two fragments of nearly equal mass in the exit channel (2- body) is completed. The distributions of light charged particles (Z = 1,2) which were detected in coincidence with the fragments, allowed the identification of the dominant reaction mechanism. The analysis for the 3-body and 4-body reactions has been started.

Because of the geometry of the detectors for the light charged particles (LP) and particularly because of their small solid angle, the interpretation of the LP-spectra is only possible by comparing them to detailed Monte-Carlo simulations. At first it was assumed that the LP dominantly arise from the evaporation of the two highly excited fragments (1. source). A comparison of the measured and the simulated spectra shows that the Z = 1,2 particles are evaporated isotropically in the reaction plane, but that they are strongly anisotropic with respect to the normal-vector of the reaction plane (Fig. 1). If this anisotropy is parametrized with the distribution-function $d\sigma = A\exp(-a^2\cos^2\Theta)$, the anisotropy coefficient a^2 becomes smaller with increasing energyloss in the 2-body reaction (a^2 = 2.5, . . ., 1.0) and is for the Z = 1 evaporation half as big as the given values for the Z = 2 evaporation. In addition, the measured velocity distribution (Fig. 2) of the LP at low energylosses shows that there have to be other processes. The analysis indicates that the LP are emitted from the 'dinuclear system' (projectile + target) before the system breaks up into 2 fragments. It is remarkable that these LP also show an anisotropy with respect to the normal-vector of the reaction plane. The factors a^2 for this anisotropy are (a^2 = 2.3, ..., 1.0) for Z = 1 and Z = 2 particles. For small energyloss the dinuclear component of the LP is isotropic in the reaction plane (2. source), but with increasing energyloss an increasing focussing in beam direction is noticed (Fig. 3), so that at the highest energylosses this process is similar to the fast target- and projectile- breakup (3. source). The total mass of the produced LP in one reaction depends on the energyloss and has a maximum of M(LP) = 40 u at 18.7 MeV/u and M(LP) = 60 u at 23.7 MeV/u bombarding energy. 25 % respectively 50 % originate from the composite system at the lower and the higher bombarding energy.

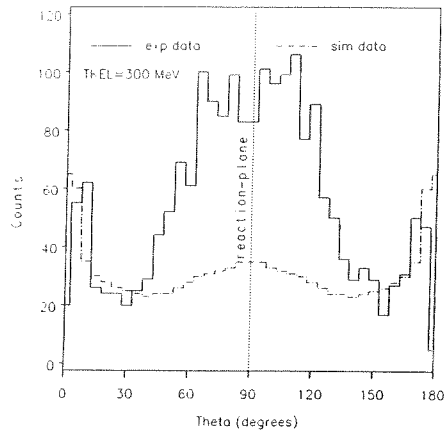


Fig.1: Out-of-plane angelar distribution for alphas. In the simulation the alphas are emitted isotropically from the fragments.

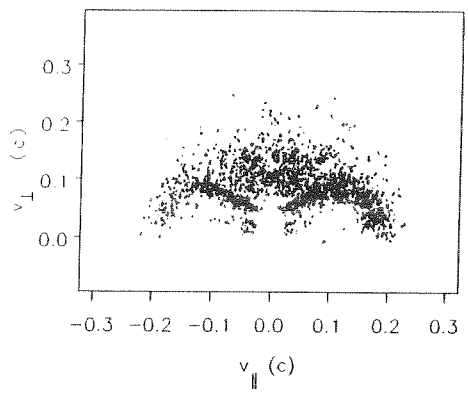


Fig. 2: Measured velocity distribution for alphas in the C.M.-system. $v_\parallel$ = velocity parallel to the separation-axis of the fragments, $v_\perp$ = perpendicular to this axis.

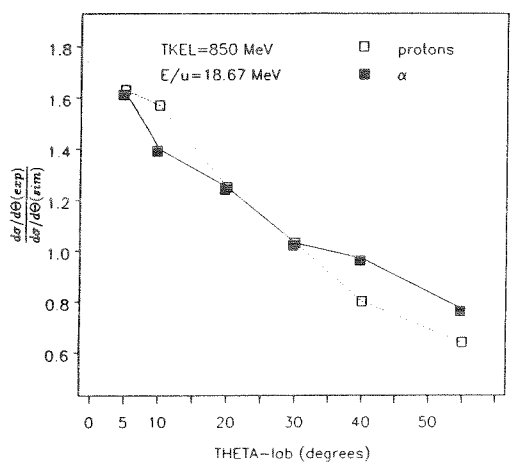


Fig. 3: Cross-section ratio of the measured (exp) and the simulated (sim) data.

[1] R. Freifelder et al. GSI Report-86, 51

Light Particle Emission in Central Heavy Ion Collisions [B,G] of Mass Symmetric Systems

A. Oberstedt, P. von Neumann-Cosel, A. Richter, W. Rösch, G. Schrieder
Institut für Kernphysik, Technische Hochschule Darmstadt
D. Bellm, R. Gentner, K. Keller, L. Lassen
Physikalisches Institut, Universität Heidelberg
W. Cassing, Universität Giessen
D. Hilscher, M. Lehmann, HMI Berlin

As a continuation of former measurements at 20 MeV/u[1] in the mass symmetric system $^{40}Ar + ^{40}Ca$ preequilibrium particle emission in central collisions was studied at E_{lab} = 15 MeV/u[2]. Previous findings at the higher incident energy were confirmed. Neutron multiplicities as well as nuclear temperatures for the equilibrium (EQ) and the pre- equilibrium (PE) component were determined from energy spectra and angular distributions. In the framework of a quantal phase space model[3], which describes successfully the experimental neutron data, the equilibration time yields $\tau \simeq 5 \times 10^{-23}$.

The time-of-flight method allowed the measurement of mass distributions for the evaporation residues (ER). Using the experimental multiplicities as input parameters, a simplified statistical model for the evaporation process[4] leads to an excellent description of the measured ER mass distributions. This means, that light particle emission alone can account for the observed ER masses.

Comparison between the equilibrium temperatures at 15 and 20 MeV/u indicates a soft saturation at $T^{EQ} \simeq$ 5 MeV. This effect is also shown by the energy dependance of neutron multiplicities. A systematics of neutron multiplicities versus incident energy is displayed in Fig.1. The points in the energy range between 4.8 and 6.8 MeV/u were taken from CASCADE calculations, which allowed to reproduce the measured mass spectra[5]. The full symbols represent total multiplicities, the open circles the equilibrium component only. The increasing contribution of PE emission is apparent as the difference of total and EQ multiplicities above 13 MeV/u, corresponding to about 5 MeV/u above the Coulomb barrier in the cm - system.

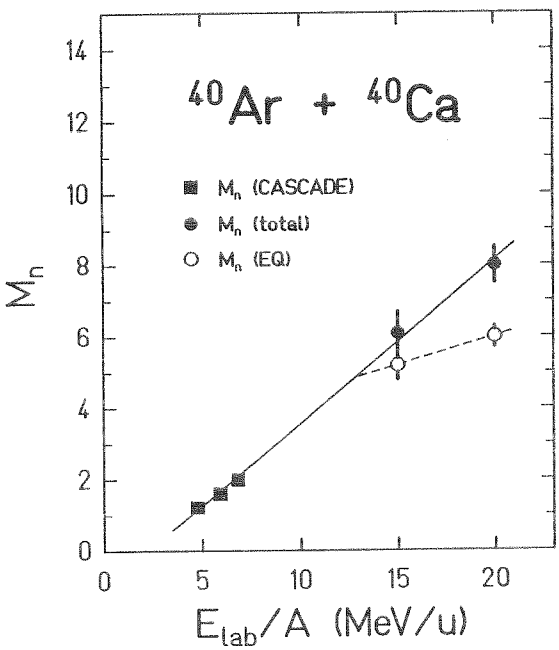


Fig.1: Neutron multiplicities at different incident energies. The lines are guides to the eye.

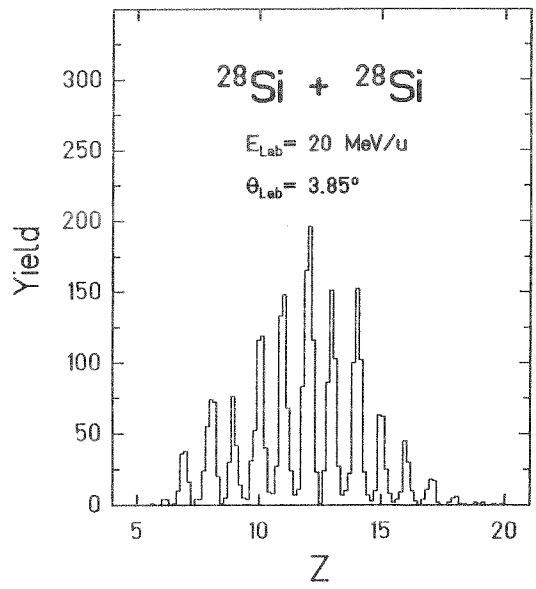


Fig.2: Element distribution of evaporation residues in the system $^{28}Si + ^{28}Si$ at E_{lab} = 20 MeV/u.

In order to study the influence of the compound mass on PE effects additional measurements were performed in the lighter system $^{28}Si + ^{28}Si$ at E_{lab} = 20 MeV/u[6]. For the first time complete mass and element distributions of ER have been measured. First data are plotted in Fig.2. This figure shows the element distribution, detected with a ΔE-E surface barrier telescope at Θ_{lab} = 3.85°. The evaporation residues are separated by their low energies and high masses. The data evaluation of this experiment is under progress.

1 W. Rösch et al., Nucl. Phys. A 496(1989)141
2 GSI scientific report 1988, p.44
3 W. Cassing, Z. Phys. A 327(1987)87
4 H. Wilschut, KVI annual report 1976, p.91
5 J. Carter et al., Z. Phys. A 313(1983)57
6 A. Oberstedt et al., HMI annual report 1988, p.220

PRODUCTION AND DECAY OF HOT NUCLEI OBSERVED IN THE REACTION 15 MEV/U $^{86}Kr+^{58}Ni,^{27}Al$ G+B

R.Mühlhans, G.Breitbach, W.Kühn, V.Metag, R.Novotny
II.Physikalisches Institut Uni. Gießen
D.Pelte, U.Winkler
Physikalisches Institut Uni. Heidelberg
A.Gobbi, K.D.Hildenbrand
GSI, Darmstadt

In the energy range of 10-100 MeV/u there is a gradual transition in the interpretation of heavy ion reactions from a mean field picture to a description in terms of nucleon - nucleon collisions. In this context the study of the production and decay mechanism of hot nuclei is a very interesting question. This demands an experimental setup allowing the determination of the transfered momentum and the coincident detection of all heavy decay products (M>2).

An experiment investigating the reaction $^{86}Kr \rightarrow ^{58}Ni,^{27}Al$ at 15 MeV/u has been performed in inverse kinematics at GSI Darmstadt. The setup comprised two movable large area position sensitive double ionisation chambers positioned on either side of the beam axis to detect heavy particles (Z≥4). A zero degree telescope built of 4 phoswich detectors was used to detect fast charged particles (Z<12) near the beam axis. Kinematical constrains favored coincident detection of strongly damped reactions.

Using conservation laws a 'deficit particle' is introduced in the analysis which represents the integral behavior of all undetected particles. Full and incomplete momentum transfer can clearly be seperated. Reactions with full momentum transfer occur in 36% (Ni) and in only 4% (Al) of the observed reactions. In case of incomplete momentum transfer not all nucleons of the lighter and thereby faster reaction partner in the c.m. system take part in the reaction. The average mass of the target spectator (Ni: 13.4 amu, Al: 11 amu) can be calculated from the momentum ΔP of the 'deficit particle' (similar to the folding angle method) which - according to the massive transfer model - is assumed to move with target velocity.

The relative yield for the ternary to binary decay of the combined system has been determined to 22±10% and 3±2% for the Ni and the Al target, respectively, based on a comparison of the experimental distributions to Monte Carlo simulations assuming sequential fission. In figure 1 the relative yield as a function of the total kinetic energy loss TKEL is shown in comparison to results from $^{100}Mo \rightarrow ^{100}Mo$ obtained at comparable bombarding energies[2]. For both systems the TKEL is calculated as c.m. energy reduced by the Viola energy assuming full damping. In case of incomplete momentum transfer the c.m. system refers to the participating nucleons.

In contrast to the experimental results, a statistical model calculation (HIVAP) based on the assumption of sequential fission underestimates ternary reactions by a factor ≈3-10 in comparison to the experiment as shown in fig. 1. Considering evaporation of light particles from the fused system prior to fission[1] this discrepancy becomes even larger, since the excitation energy of the primary fission fragments is decreased dramatically. This calls for more refined statistical model calculations. On the other hand, non-sequential reaction mechanisms leading to the same kinematical observables in the exit channel can not be fully excluded. Similar discrepancies between experimental results and statistical model calculation have been observed in the $^{100}Mo \rightarrow ^{100}Mo$ system[2].

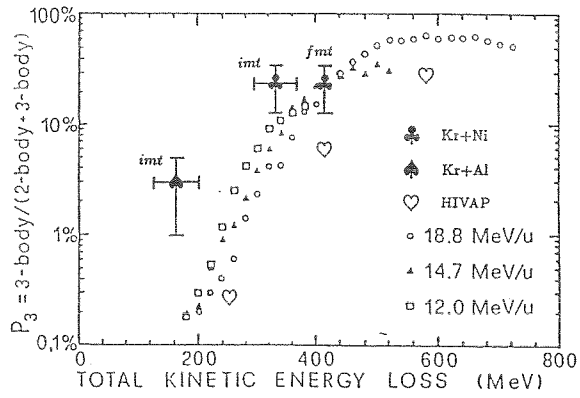


Figure 1: Experimental relative yields for the ternary to the binary decay of the combined system and comparison to calculations with the statistical model code HIVAP. Small data symbols are taken from ref. 2 for the reaction $^{100}Mo \rightarrow ^{100}Mo$ at three different bombarding energies.

[1] D.J.Hinde et al., Nucl.Phys.A502(1989)497c
[2] A.Olmi et al., Nucl.Phys. A471(1987)97c

Emission of high energy photons in the reaction $^{136}Xe+^{48}Ti$ at 18.5 MeV/u^{B+G}

G.Enders, K.Hagel, W.Kühn, V.Metag, R.Novotny, O.Schwalb
(II.Physikalisches Institut Universität Gießen)
A.Gobbi, K.D.Hildenbrand, R.Freifelder, R.Charity, J.Wessels,
W.Henning, R.Mayer, R.S.Simon (GSI Darmstadt)
A.Olmi, A.A.Stefanini (INFN and University of Florence, Italy)

The production mechanism of hard photons at intermediate bombarding energies between 20 and 100 MeV/u is currently of high interest. In an attempt to decide whether the photons are produced during the initial collision stage or at a later time during the de-excitation process we have performed an exclusive experiment. Motivated by two previous measurements (ref. 1), (ref. 2) we used a detector system to get information about the photons as well as the outgoing fragments. An asymmetric projectile-target combination has been studied, since in such systems the source velocity of proton-neutron bremsstrahlung is different from the thermal photon source, formed in deep-inelastic collisions. This leads to different photon angular distributions due to the Doppler-effect.
The reaction $^{136}Xe+^{48}Ti$ was studied at an incident energy of 18.5 MeV/u provided by the UNILAC. High energy photons were measured in coincidence with heavy fragments. Photons were detected in 3 arrays comprising 7, 40 and 19 BaF_2 scintillation counters located at laboratory angles of 50°, 90° and 150°, respectively. We used radioactive sources (^{60}Co, ^{88}Y) and cosmic rays for low and high energy calibration points, respectively. Photons were discriminated against neutrons and charged particles by time of flight and pulse shape analysis, respectively.
Velocity vectors of heavy fragments ($Z \geq 10$) were measured by means of 12 PPAC's covering a solid angle of nearly 2π. Fragment masses and total kinetic energy (TKE) were deduced in a full kinematic reconstruction. Fig. 1 shows the resulting distribution of fragment masses as a function of TKE.
Preliminary photon spectra at the three laboratory angles are shown in Fig.2. The spectra exhibit three major features: statistical nuclear transition below 10 MeV, a bump in the giant-dipole-resonance region between 10 MeV and 20 MeV, and hard photons above 20 MeV. The photon energy spectra were fitted with two exponential functions. The angular dependence of the inverse slope parameter for hard photons indicates emission from a moving source. An accurate determination of the source velocity involving the angular anisotropy in addition is in progress. The observed slope parameter at 90° is consistent with an extrapolation based on systematics (ref. 3).

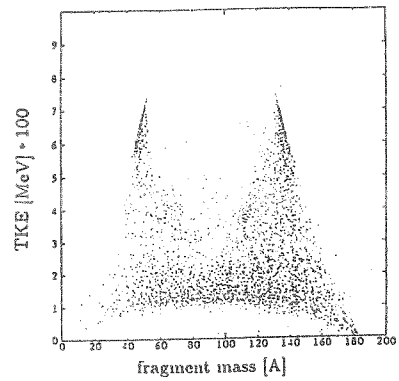


Figure 1: *Diffusion plot*: Distribution of the reconstructed fragment mass (A) and the total kinetic energy (TKE)

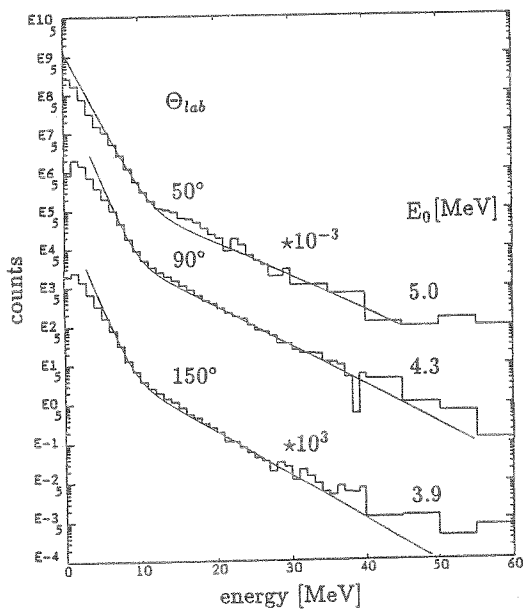


Figure 2: Measured photon spectra at laboratory angles of 50°, 90° and 150°. The cosmic background determined by a delayed time window has been subtracted

(1)G.Breitbach et al. GSI-report, *GSI-87-1*
(2)N.Herrmann et al. *PRL 60(1988)1630*
(3)V.Metag, Nucl.Phys.*A438 (1988) 483c*

Limiting excitation energy in Si+Si reactions

R.J. Meijer[a], P.F. Box[b], P. Decowski[b], E. Gierlik[b], R. Kamermans[b], G.J. van Nieuwenhuizen[b], K.A. Griffioen[c], H.W. Wilschut[d], A. Giorni[e], C. Morand[e], A. Demeyer[f], D. Guinet[f]

[a] GSI Darmstadt, [b] University of Utrecht, [c] University of Pennsylvania, [d] KVI Groningen, [e] ISN Grenoble, [f] University Claude Bernard.

Si+Si fusion reactions at 12.4, 19.7 and 30 MeV/u have been studied with the aim to find the limiting circumstances for which highly-excited nuclei decay via the classical evaporation-mechanism, or, in other words, with the aim to find the conditions for which other, eventually new, decay channels open up [1,2].

The analysis of the events in which light particles (LP) were detected in coincidence with an evaporation residue (ER) yielded results which were at first instance rather puzzling. We found that the ER charge-distribution and the LP multiplicities measured at 19.7 MeV/u are similar to the ones measured at 30.0 MeV/u, although at the highest beam energy the fused systems (FS) can have in principle a much higher excitation energy. Also the small ER cross-section at 30 MeV/u was unexpected since it was a factor of 6 smaller than what we estimated on basis of other experimental results [3].

From the charge- and energy balance of reactions in which protons and α-particles were measured in coincidence with ER's we were able to reconstruct some details of the fusion process. At 12.4 MeV/u the two Si nuclei fuse almost completely, only few nucleons are emitted before equilibrium is reached. Additionally, at 19.7 and 30.0 MeV/u a projectile- and a target-like fragment, with mass number A=6–8 are emitted in opposite directions in the CM system. These fragments have, in the reaction at 30.0 MeV/u, on average a CM velocity which exceeds by 20% the velocity of the projectile- and target nucleus.

Clearly, these details do not explain the puzzling results of the analysis. A hint for the solution of this puzzle was given by the consideration that the velocity distributions of the projectile- and target-like fragments are reflecting the distribution of excitation energies of the nucleus fused from projectile- and target remnants. For example, if the excitation energy of the fused system is lower than the average, then for reasons of energy conservation the kinetic energy of the fragments must be higher than the average. Therefore, the high average velocity of the fragments at 30.0 MeV/u, in reactions in which ER's were produced, indicate that the ER's originate from fused systems that had a lower than average excitation energy. This strongly suggests the existence of a limiting excitation energy $(E^*/A)_{\rm lim}$ above which fused systems decay via other channels in which no ER's are produced.

We have tested this picture of the fusion process with Monte Carlo calculations in which the formation and decay of the fused systems is divided in five steps: 1) At 19.7 and 30.0 MeV/u one fragment of the projectile- and one fragment of the target nucleus with A = 6–8 escape the reaction zone. The velocity distributions of these fragments have a Gaussian shape and are centered around the velocity of the projectile- and target nucleus. 2) Then pre-equilibrium protons and α-particles are emitted. Their multiplicity- and velocity distributions are obtained from parametrisations of experimental distributions [1]. The rest of the target- and projectile nucleons fuse. 3) In the next steps the initial properties of the fused system and its 4) decay by LP evaporation are calculated. In order to avoid the complications in the description of the decay process of highly-excited nuclei, we have also used here parametrisations for the CM angular-distributions of evaporated LP's to obtain the velocities and branching ratios of evaporated LP's [1]. In the last step 5) we update the various spectra with and without the condition $E^*/A_{\rm FS} \leq (E^*/A)_{\rm lim}$. We adjusted $(E^*/A)_{\rm lim}$ in such a way that the experimental observables are reproduced best. The best results were obtained for $(E^*/A)_{\rm lim}$ = 4.3 MeV/u.

Calculations with this model show that the concept of a limiting excitation energy is essential for a good description of the data. In figure 1 we show the calculated distributions of $E^*/A_{\rm FS}$ for the three beam energies. In the reactions at 12.4 and 19.7 MeV/u almost all of the fused systems have an excitation energy which is below $(E^*/A)_{\rm lim}$ = 4.3 MeV/u. However, only about 16 % of the fused systems produced in the reactions at 30.0 MeV/u have an excitation energy which is below $(E^*/A)_{\rm lim}$ and this explains the reduction of the ER cross section at that beam energy. Therefore, the Si+Si data show a clear evidence of a limiting excitation energy for ER formation.

[1] R.J. Meijer, P. Box, P. Decowski, K.A. Griffioen, R. Kamermans, G.J. van Nieuwenhuizen, H.W. Wilschut, A. Giorni, C. Morand, A. Demeyer, D. Guinet, XXVII Winter Meeting On Nuclear Physics, Bormio, Italy (1989).

[2] K.A. Griffioen, B.J. Gluckman, R.J. Meijer, P. Decowski, R. Kamermans, Phys. Rev. C40, 1647 (1989).

[3] M.F. Vineyard, J.S. Bauer, C.H. Gosdin, R.S. Trotter, D.G. Kovar, C. Beck, D.J. Henderson, R.V.F. Janssens, B.D. Wilkins, J.F. Mateja, C.F. Maguire, F.W. Prosser, G.S.F. Stephans, Argonne National Laboratory report 1988-1989.

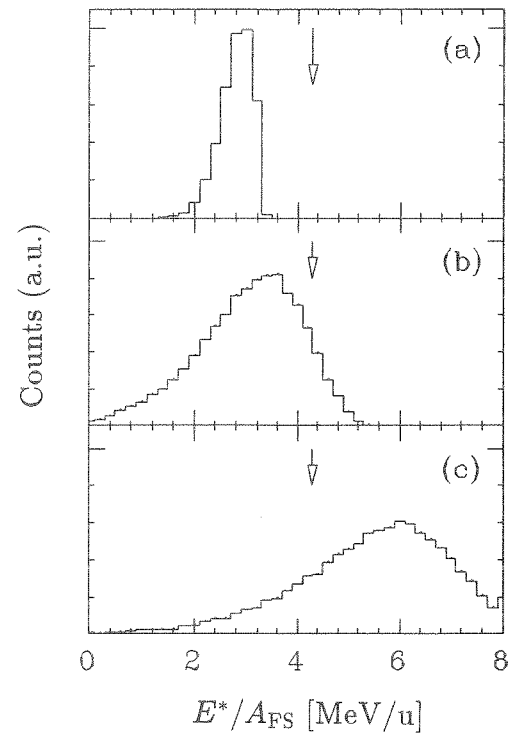


Figure 1: Distribution of initial excitation energy per nucleon of fused systems formed in Si+Si reactions at (a) 12.4, (b) 19.7, and (c) 30.0 MeV/u. The arrow indicates the best value for the limiting excitation energy.

Nuclear isomers produced (and stopped) in a thin Au target by ^{74}Ge at 18.8 MeV/u^{G}

I.V.Aničin, A.H.Kukoč, P.R.Adžić, D.Toprek, R.B.Vukanović, M.T.Župančić and Dj.M.Krmpotić
Boris Kidrič Institute, Vinča, Belgrade, Yugoslavia

For the last five years we have been measuring the gamma-ray spectra of the 500 μg/cm^2 Au target irradiated during 24 hours with 0.3 pnA of ^{74}Ge at 18.8 MeV/u[1]. Among the about 100 isotopes with half-lives from 2 days to 15 years whose yields we have determined there are 8 long-lived isomers which belong to the Z<50 and N<82 islands of isomerism. They fall into the 90<A<140 region where the products of symmetric fragmentation are found. It is known that the yields of fragments which leave the target, vs A/Z, are normally distributed[2]. This opens up an interesting possibility to test the consistency of the abundancies of isomers versus ground state nuclei stopped in the thin target.

Fig.1 presents cross-sections for fragments in ground as well as in isomeric states to remain in the (thin) target as a function of A/Z. Since most of the isomers are actually shielded nuclei with independent yields (eg. note the unique case of ^{121m}Te and ^{121g}Te) our main conclusion is that the whole body of data is satisfactorily consistent with the gaussian centered around $\overline{A/Z}$=2.34 and with FWHM=0.115 (with χ^2=8). Those values correspond to $\overline{A}$≅117 and $\overline{Z}$≅50 meaning that on the average 13 protons and 27 neutrons evaporate altogether to leave the close to the stability line symmetric fragments in the target.

The fact that the high-spin isomers, where they exist, take over the role of ground state nuclei may be interpreted as meaning: a) that most of the fragments which remain in the target, and consequently have negligible TKE's, are indeed formed in comparatively high spin states and b) that, on the average, evaporation in total takes away little angular momentum.

This, together with the obviously high absolute value of the integrated cross-section for the fragments to remain in the target, in our view constitutes an independent confirmation of the heavily damped character of symmetric fragmentation.

[1] A.H.Kukoč et al. GSI SciRep 87-1,60 (1987)

[2] B.Jackel et al. GSI SciRep 84-1,16 (1984)

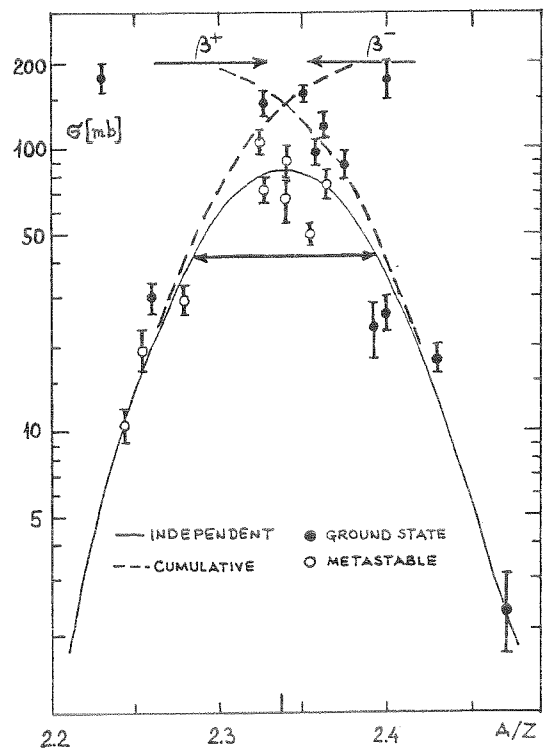


Fig.1. Cross-sections for symmetric fragments to remain in a thin Au target

Interaction study of 15 MeV/nucleon U on Au target

U.KIMOUNDRI[a], M.ZAMANI[a], M.DEBEAUVAIS[b], J.RALAROSY[b], S.JOKIC[c] and F.FERNANDEZ[d]

a) University of Thessaloniki, Thessaloniki, Greece
b) Centre de Recherches Nucléaires, Strasbourg, France
c) University "Svetozar Markovic" Kragujevac, Yougoslavia
d) Universidad Autonoma de Barcelona, Barcelona, Spain

In the inverse reaction U on Au the Solid State Track Detector permits us to visualize all events in correlation in a 4 π space.
In this experiment CR-39 foils were exposed to a flux of $\approx 10^6$ U ions/cm^2 at 15 MeV/n, in GSI (Darmstadt). The $\approx$ 1 mg/cm^2 target was evaporated directly on the detector's surfaces. After ordinary treatment of samples [1] we have detected 3-4-5-6 pronged events. Their partial cross sections are given in Table 1. The total cross section is also shown in the table and it is found to be in agreement with the calculated one of 5050 mb within experimental errors.

Table 1. Reaction cross section σ (in mb)

σ tot	σ 3b	σ 4b	σ 5b	σ 6b
5240	3070	1870	250	50
±340	±260	±210	±70	±30

In this paper we study the characteristics of the 3 body components that represent near 60 % of the total cross section. We measure for each individual event all geometrical parameters of the 3 fragments.
In fig. 1 the correlation between the fragment ranges and their emission angles is shown. We can distinguish one group of fragments with a range of about 20μm at 80° -90° emission angle, corresponding to Au recoil with an energy of about 90 MeV, that represent about 2,5% of the projectile energy.

Each fragment of this group is correlated with two other fragments whose emission angles are preferentially oriented at 15° in the forward direction, thus near the calculated 12°8 grazing angle. These two fast fragments are issued from the same source, that is the fissionning U nucleus. Two types of such correlated forward fragments can be distinguished. On the one hand those whose ranges are of about 120μm and 180μm respectively ; they correspond to near symmetric fission. On the other hand those whose ranges are of about 100μm and 300μm respectively ; the correspond to rather asymmetric fission, the highter framgment having the longer range.

From the characteristics of the 3 body events in this reaction we can conclude that the dominant mechanism is a deep interaction with the recoiling quasi Au target and followed by a in flight fission of the quasi projectile.
The 40 % of events, those with 4, 5 and 6 fragments in correlation have yet been studied. But we remark for the first time a very high 5 and 6 pronged fragments component.

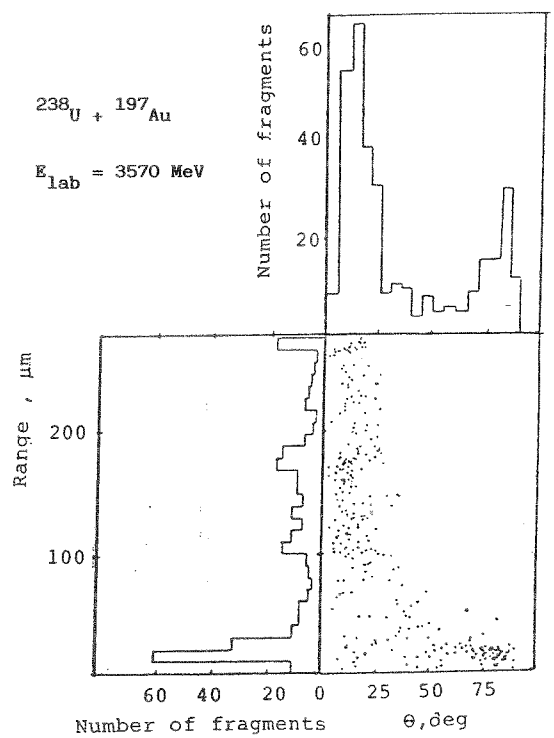


Fig. 1 - Histogramms of fragments ranges as function of their emission angle, for 3 body events in U + Au reaction, at 15 MeV/n.

REFERENCES

(1] M. Debeauvais, M. Zamani, J. Ralarosy, S. Jokic and F. Fernandez
GSI Reports 1987, p. 71

Multifragment emission in reaction of Kr on Ag and Au at 17.7, 27 and 35 MeV/nucleon

M. Zamani[a], M. Debeauvais[b], J. Ralarosy[b], J.C. Adloff[b], F. Fernandez[c], S. Jokic[d] and D. Sampsonidis[a]

a) University of Thessaloniki, Thessaloniki, Greece
b) Centre de Recherches Nucléaires, Strasbourg, France
c) Universidad Autonoma de Barcelona, Barcelona, Spain
d) University "Svetozar Markovic", Kragujevac, Yugoslavia

CR 39 SSNTD have been used to study the reaction products of 17.7, 27, and 35 MeV/nucleon ^{84}Kr on Au and Ag in a near 4π interactions producting two or more correlated intermediate mass fragments in the final state.

The experimental procedure was described elsewhere[1]. Among all events we have selected those with two or more visible fragments issued from the same reaction. We identified the charge Z and the energy of all the fragments and selected all the events that don't correspond to Direct Interaction (DI). We classified as DI all events composed of :

1) one slow fragments corresponding-to the recoil of the quasi target.

2) one or two associated fragments whose the sum of Z and the sum of energies are near the projectile ones and the direction near the grazing angles.

The characteristics of the other correlated fragments are intermediate masses and a few hundred MeV energy for each fragment. That implies that an important amount of energy escapes detection. Only this kind of events was selected in order to establish the multifragment cross section σ_M.

In Fig. 1 and 2 we present the cross sections of 3, 4 and 5 + 6 pronged events in fonction of energy, in reaction Kr on Au and Ag respectively. As we can see, the reaction cross section increases with increasing energy from 17 to 35MeV/nucleon To our knowledge the present cross section results are the first one for high multiplicity of intermediate mass fragments obtained in this energy region.

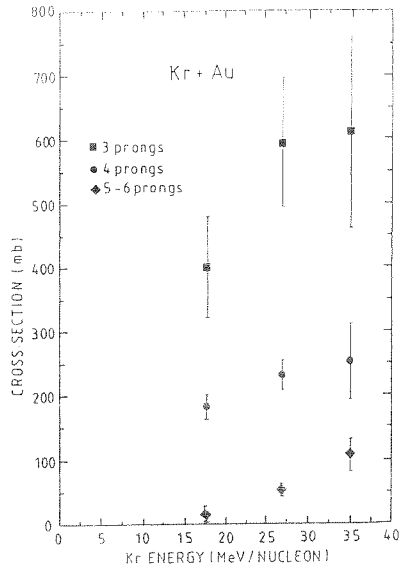


Fig. 1

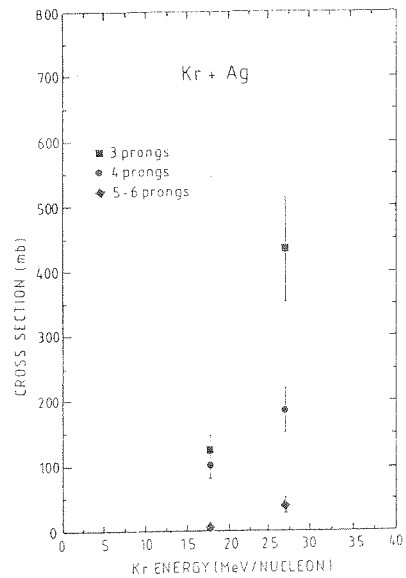


Fig. 2

[1] GSI report 1988 p. 52 et 53

TRANSIENT TIMES OF FISSION IN ^{40}AR + ^{232}TH PERIPHERAL COLLISIONS [G]

E.-M. Eckert, A. Kühmichel, J. Pochodzalla, Universität Frankfurt
K.D. Hildenbrand, U. Lynen, W.F.J. Müller, H.J. Rabe, H. Sann, H. Stelzer, W. Trautmann, R. Trockel, R. Wada
GSI Darmstadt
C. Cerruti, P. Lhénoret, R. Lucas, C. Mazur, C. Ngô, M. Ribrag, E. Tomasi, CEN Saclay
A. Demeyer, D. Guinet, Université Claude Bernard

As reported previously,[1] a fission hindrance was observed for excited target residues produced in peripheral ^{40}Ar + ^{232}Th collisions at a bombarding energy E/A = 30 MeV. The analysis of these data, obtained at the the SARA facility in Grenoble, was further continued, and the measured fission probabilities were used to determine the delay of fission due to the finite transient time that is needed to build up the probability flux across the fission barrier.[2]

A summary of the measured and derived results, listed according to the atomic number Z_{PLF} of the coincident projectile-like fragment, is given in the table. The mean excitation energies $<E_x>$ and spins $<l>$ transferred to the target residues were determined from the linear momenta $<p>$ that were obtained from the measured fission folding angles. The atomic number $<Z_{res}>$ of these nuclei was obtained from a charge balance based on measured multiplicities of light charged particles. The fission probabilities P_f were determined from the measured ratios of inclusive and fission-coincident projectile fragments. They show an unexpected feature as, for $Z_{PLF} \leq 15$, P_f decreases with increasing excitation energy and spin while $<Z_{res}>$ practically does not change.

A comparison to statistical model calculations, performed with the code HIVAP[3], showed that for the lowest excitations (Z_{PLF} = 17) the measured and predicted fission probabilities agree rather well. The calculated values increase, however, as the excitation energy increases and reach values near 100% for $Z_{PLF} \leq 15$, in contrast to the experiment (see table). In order to qualitatively understand this discrepancy we have performed further statistical calculations within the following scheme. We have first used the HIVAP code with the fission probability artificially set to zero in order to determine the most probable evaporation sequences in the absence of fission. Then the fission channel was turned on again, and fission probabilities were calculated for each step n along these sequences, i.e. for the nuclide, energy, and spin reached after n-1 evaporation steps. In Fig. 1 the results are shown for the channels Z_{PLF} = 14, 15, and 16 and for pure neutron cascades starting from excited ^{230}Ac, ^{228}Ra, or ^{225}Fr nuclei. The so determined fission probabilities decrease along the evaporation paths and at some point cross the range of the experimental values. The agreement with the statistical model is thus recovered if fission is assumed to be hindered until the neutron cascades have deexcited the initial target residues to energies in that range. The crossover energies

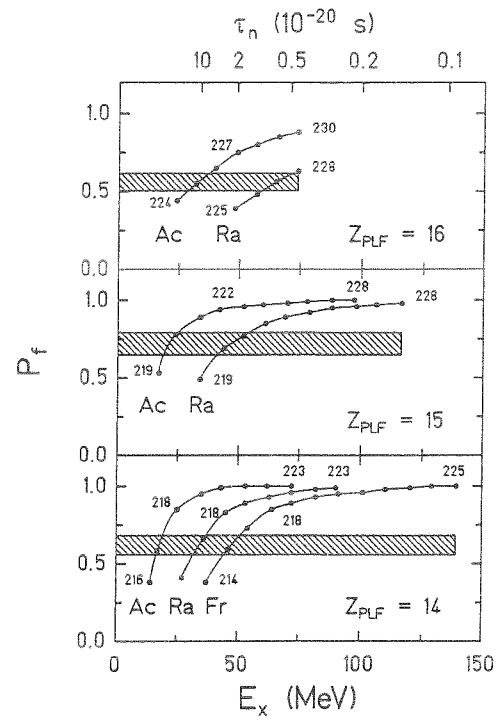


Fig. 1: Calculated fission probabilities along the most probable evaporation paths (see text). Some of the mass numbers are indicated. The hatched areas mark the measured fission probabilities.

are of the order of 50 MeV or less (Fig. 1) which is consistent with the observed onset of the fission hindrance in the Z_{PLF} < 17 channels. An order of magnitude estimate of the transient times may be obtained from the neutron evaporation times which for $E_x \simeq 50$ MeV are of the order of one to several 10^{-20} s (top ordinate scale of Fig. 1). These times are larger than present estimates for saddle-to-scission times of several 10^{-21} s which implies that the transient time is the dominant contribution to the total time elapsing before scission.

[1] E.-M. Eckert et al., GSI Scientific Report 1987, p. 65
[2] P. Grangé et al., Phys. Rev. C27, 2063 (1983)
[3] W. Reisdorf et al., Nucl. Phys. A444, 154 (1985)

Z_{PLF}	$<p>$ (GeV/c)	$<\Delta p>$ (GeV/c)	$<\Delta Z>$	$<Z_{res}>$	$<E_x>$ (MeV)	$<l>$ ($\hbar$)	P_f
17	0.39	0.6±0.1	2.5±0.6	88.5±0.6	49	14	0.52
16	0.59	1.0±0.1	3.5±0.7	88.5±0.7	74	20	0.56
15	0.92	1.4±0.2	4.3±0.8	88.7±0.8	116	31	0.72
14	1.10	1.7±0.2	5.1±1.0	88.9±1.0	139	36	0.62
13	1.45	2.3±0.3	6.4±1.2	88.6±1.2	183	47	0.55
12	1.74	2.5±0.4	7.3±1.4	88.7±1.4	219	55	0.44

Fragment Emission in the Reaction ^{40}Ar + ^{197}Au at E/A = 30 and 220 MeV [G]

U. Milkau[a], E. Berdermann[a], B. Berthier[b], C. Cerruti[b], A. Demeyer[c], E.-M. Eckert[d], D. Guinet[c], K.D. Hildenbrand[a], P. Kreutz[d], G. J. Kunde[e], S. Leray[b], P. Lhénoret[c], R. Lucas[b], U. Lynen[a], C. Mazur[b], W.F.J. Müller[a], C. Ngô[b], C. H. Pinkenburg[d], J. Pochodzalla[d], H.J. Rabe[a], G. Raciti[f], M. Ribrag[b], H. Sann[a], H. Stelzer[a], E. Tomasi[a], W. Trautmann[a], R. Trockel[a], R. Wada[g]

[a] GSI Darmstadt, [b] CEN Saclay, [c] Univ. Claude Bernard, [d] Univ. Frankfurt,

[e] Univ. Heidelberg, [f] Univ. Catania, [g] Texas A&M University

One of the genuinely new features of heavy ion collisions in the intermediate range of bombarding energies between several tens and several hundreds of MeV per nucleon is the production of intermediate mass fragments (IMF's) with large cross section. Our studies[1,2] of ^{40}Ar induced reactions on ^{197}Au, performed at the SARA facility in Grenoble and at the SATURNE facility in Saclay with beams of E/A = 30 MeV and 220 MeV, respectively, span this energy regime. The double-differential cross sections derived from the measured inclusive spectra are generally of the shape characteristic for those bombarding energies. The main difference between the spectra taken at the two different energies is apparent from the example of carbon production shown in Fig. 1. The cross section maxima at E/A = 220 MeV, usually associated with the Coulomb repulsion from the emitting composite system, appear at energies roughly one third of those at E/A = 30 MeV. This may indicate that the emitting system has expanded, that its charge is reduced, or that large dynamical fluctuations have washed out the Coulomb minima.

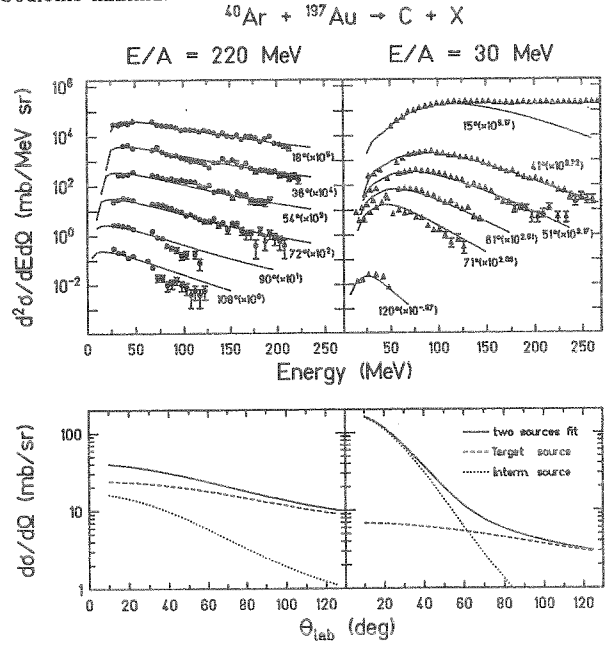


Figure 1: *Top: Double-differential cross sections for carbon ions(Z=6) produced at E/A = 220 MeV (left-hand side) and 30 MeV (right-hand side). The points and triangles represent the experimental data. The lines are the results of the moving-source fits described in the text. Note the scaling by factors of ten (top left) and by factors adjusted to give an equivalent angular representation (top right).*
Bottom: Differential cross sections as a function of the laboratory detection angle as obtained from the moving-source fits. The dotted and dashed lines represent the individual contributions from the intermediate-rapity and the target sources, respectively.

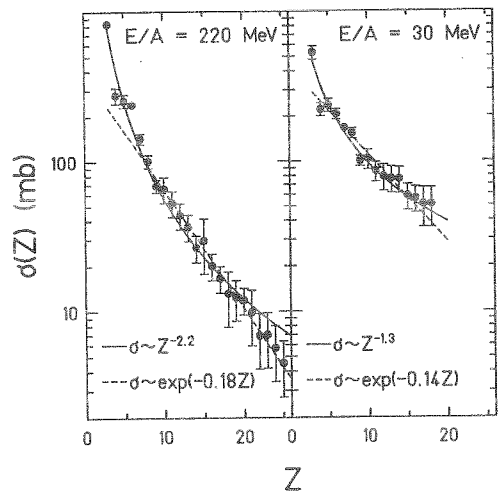


Figure 2: *Integrated cross sections $\sigma(Z)$ of IMFs at the two bombarding energies. The solid and dashed lines represent the results of a power law and of an exponential fit, respectively. The deduced fit parameters are indicated.*

Satisfactory descriptions of the data were obtained with fits employing two Maxwellian sources moving in beam direction and emitting isotropically in their rest frames (solid lines in Fig. 1), apart from the spectra measured at E/A = 30 MeV and $\Theta_{lab} = 15°$, where a projectile-source component contributes to the cross sections at higher energies. The individual contributions of the two sources as a function of Θ_{lab} are shown in Fig. 1, bottom. At the lower energy the slowly moving so called target source is mainly needed to reproduce the backward-angle data while the strong forward peaking of the cross sections at $\Theta_{lab} < 90°$ is well represented by the faster intermediate source. At E/A = 220 MeV the cross sections are considerably more isotropic which means a larger intensity for a target source with a rather low velocity. The moving-source parameters were used to generate total cross sections $\sigma(Z)$, shown in Fig. 2. They reach values up to several hundred mb for smaller IMF's and, generally, are of similar magnitude for the two energies. Fits to the elemental cross section distributions were achieved with both, exponential and power law descriptions except for the lightest IMFs which seem to favour a power law fit. The total IMF-production cross sections are very similar at the two energies. We obtain $\sigma_{IMF} = 2.1$ barn at E/A = 30 MeV and $\sigma_{IMF} = 2.2$ barn at E/A = 220 MeV with an error of about 25% in both cases. This saturation either indicates that the avarage IMF multiplicity remains small as at E/A = 30 MeV (see ref. 3) or that an increase in multiplicity with bombarding energy is counterbalanced by a decrease in the cross section of those reaction processes leading to IMF emission.

[1] R. Trockel et al., GSI Scientific Report 1985, p.93
[2] U. Milkau et al., GSI Scientific Report 1988, p.58
[3] R. Trockel et al., Phys. Rev. C 39 1989, 729

Interaction cross section measurements of the neutron-rich isotopes ^{8,9,11}Li at 100 MeV/u [G,B]

B. Blank, J.-J. Gaimard, H. Geissel, K.-H. Schmidt, H. Stelzer, K. Sümmerer (GSI Darmstadt); H.-G. Clerc, E. Hanelt, M. Steiner, B. Voss (TH Darmstadt); D. Bazin, R. Del Moral, J.-P. Dufour, A. Fleury, F. Hubert (CEN Bordeaux-Gradignan)

In the past, nuclear reaction studies were restricted to stable nuclei. The availability of high-quality radioactive beams provides new possibilities to investigate the properties of exotic nuclei far from stability. Nuclear interaction studies of neutron-rich isotopes at high energy have been initiated at the BEVALAC. Unexpected large reaction cross sections have been observed. In particular, ^{11}Li measurements have been performed at Berkeley between 400 MeV/u and 800 MeV/u [1]. At intermediate energies experiments have been carried out at RIKEN and GANIL [2]. Theoretically the existence of a neutron halo was proposed. This could give rise to a 'soft giant dipole resonance' consisting of an oscillation of the two loosely bound neutrons with respect to the more closely bound charged core which explains both the large radius of ^{11}Li as obtained with low-Z targets and the large electromagnetic dissociation cross section obtained with high-Z targets [3]. According to this picture a significant variation of the cross section with the incident projectile energy is expected.

An experiment to observe this effect has been carried out at the SATURNE synchrotron in Saclay, France. Using the spectrometer SPES I tuned as a momentum-loss achromat [4], isotopically pure secondary beams of ^{8}Li, ^{9}Li and ^{11}Li have been separated from the other projectile fragments of a ^{15}N primary beam of 150 MeV/u. At the exit of the separator these monoisotopic beams have had an energy of about 100 MeV/u.

Near the final focus of the spectrometer a very compact set-up was mounted for the determimation of the secondary reaction rates. It consisted of a first 3 mm thick plastic scintillator which was used to count the number of incoming Li isotopes, followed by the secondary target. Different target materials ranging from carbon to lead have been used. Behind the target a telescope consisting of five plastic scintillators of a thickness of 1 cm each has been mounted. The target thickness has been ajusted in order to implant the non-interacting Li isotopes in the fourth (^{8}Li, ^{9}Li) or fifth detector (^{11}Li), respectively. A 3 mm thick scintillator at the end of the telescope could be used as a veto counter. The acceptance of the set-up was defined by a thick lead diaphragm. For each secondary beam, the targets have been replaced for one run by scintillation material of equivalent thickness in order to correct for reactions occuring in the scintillator telescope. Two different electronic chains have been used to measure the energy loss of the nuclei as well as the beta decay of the radioactive isotopes in the same detectors.

The total interaction cross sections may be obtained from the β-decay measurements. Comparing the number of incident particles with the number of registered, efficiency corrected β-decays one gets the number of interactions in the target and the telescope. After correcting for the reactions in the scintillators one can calculate the total interaction cross section. Fig. 1 shows the measured β-decay spectrum for a secondary ^{11}Li beam on a carbon target. The fitted line includes not only the decay of ^{11}Li, but also a non-negligible contribution of ^{9}Li. This shows that a strong two-neutron-removal cross section exists.

In the ΔE-E plots this reaction channel can also clearly be seen. Besides this, other reaction products can be distinguished. For example, the one-proton removal in the target leads to a significantly lower energy loss in the first detector.

The off-line analysis of the recorded data is still in progress. The results should include the total interaction cross sections and charge-changing cross sections for ^{8}Li, ^{9}Li and ^{11}Li as well as some other specific pronounced reaction channels (e.g. ^{11}Li -> ^{9}Li + 2n) .

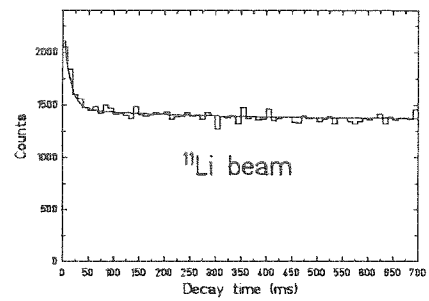


Figure 1: β-decay time spectrum for a ^{11}Li beam. The solid line is a fit using the known decay times of ^{11}Li and ^{9}Li as well as a constant background.

References

[1] I. Tanihata et al. Phys.Rev.Lett 55 (1985) 2676
T. Kobayashi et al., Phys.Rev.Lett. 60 (1988) 2599
T. Kobayashi et al., Phys.Lett. B232 (1989) 57

[2] M.Fukuda et al., preprint RIKEN AF-NP-81
W. Mittig et al., Phys.Rev.Lett. 59 (1987) 1889
M.G. Saint-Laurent et al., Z.Phys. A332 (1989) 457

[3] P.G. Hansen et al., Europhys.Lett. 4 (1987) 409
C. Bertulani et al., Phys.Rep. 163 (1988) 299

[4] J.P. Dufour et al., NIM A248 (1986) 267
K.-H. Schmidt et al., NIM A260 (1987) 287
B. Blank et al., NIM A286 (1990) 160

Emission Temperatures in ^{40}Ar + ^{197}Au Reactions at E/A = 200 MeV [G]

G.J. Kunde[a], J. Pochodzalla[b], C.H. Pinkenburg[b], E. Berdermann[a], B. Berthier[c], C. Cerruti[c], C.K. Gelbke[d], J. Hubele[a], P. Kreutz[b], S. Leray[c], R. Lucas[c], U. Lynen[a], U. Milkau[a], C. Ngô[c], G. Raciti[e], H. Sann[a], W. Trautmann[a],

[a] GSI Darmstadt, [b] Univ. Frankfurt, [c] CEN Saclay,

[d] MSU-NSCL East Lansing [e] Univ. Catania,

The internal excitation energy of fragments produced in energetic nuclear reactions is one of the rare signatures of the primary fragmentation process. Moreover, many other observables are modified by sequential decays of particle unstable nuclei. Measurements of the emission temperature are, therefore, useful in order to quantify these distortions.

The relativ level population of nuclear fragments $2 \leq Z \leq 4$ produced in heavy ion induced reactions at energies below E/A $\approx$ 100 MeV shoiwed a surprising insensitivity to the incident energy. No significant deviation of the emission temperature from T $\approx$ 5 MeV has been observed in various experiments[1]). In order to extent these measurements towards higher energies, we have measured the population of unstable fragments in ^{40}Ar + ^{197}Au reactions at E/A = 200 MeV. The experiment was performed at the SATURNE facility. A compact, highly efficient hodoscope was used to detect the decay products of particle unstable nuclei. The detection array consisted of 16 quadrant silicon ΔE - detectors and 64 individual CsI(Tl) scintillators read out via photodiodes. The total active area of the hodoscope was about 400 cm^2. The detection system was mounted at a distance of 1 m from the target at an laboratory angle of 40°.

Unfortunately, feeding from higher lying particle unbound states can alter the primary populations. Therefore, emission temperatures can be associated with large uncertainties whenever the level separations are smaller than the emission temperatures[2]). The most accurate determinations of the temperature can be made from the relative populations of widely separated states which e.g. can be found in ^{4}He and ^{5}Li. For these fragments mean emission temperatures of $\langle T \rangle_{^4He} = 5.4\ ^{+1.8}_{-1.2}$ MeV and $\langle T \rangle_{^5Li} = 6.4\ ^{+1.1}_{-1.1}$ MeV, respectively, were found in the present study.

Fig. 1 summarizes the presnt information about the mean emission temperaturs of ^{4}He and ^{5}Li fragments in heavy ion induced reactions on gold targets. It is important to note, that in all measurements the quoted errors are dominated by the rather similar systematic uncertainty which is associated with the shape of the uncorrelated background. Statistical uncertainties are smaller than 0.5 MeV. It can be seen, that in particular the ^{5}Li data, which according to statistical calculations are not influenced by sequential processes, exhibit an interesting dependence on the beam energy per nucleon.

We also studied the dependence of the emission temperature on the kinetic energy of the outgoing fragments. Significantly higher temperatures were found for more energetic fragments. For example, increasing the kinetic energy of the ^{4}He fragments from $E_{^4He} \approx 60$ MeV to $E_{^4He} \approx 240$ MeV, the emission temperature increases by about 2.5 MeV. This dependence may either reflect the energy dependence of sequential decays contributions or it may be a consequence of the temporal evolution of the emitting system: slower fragments may be emitted at a later and cooler phase of the reaction.

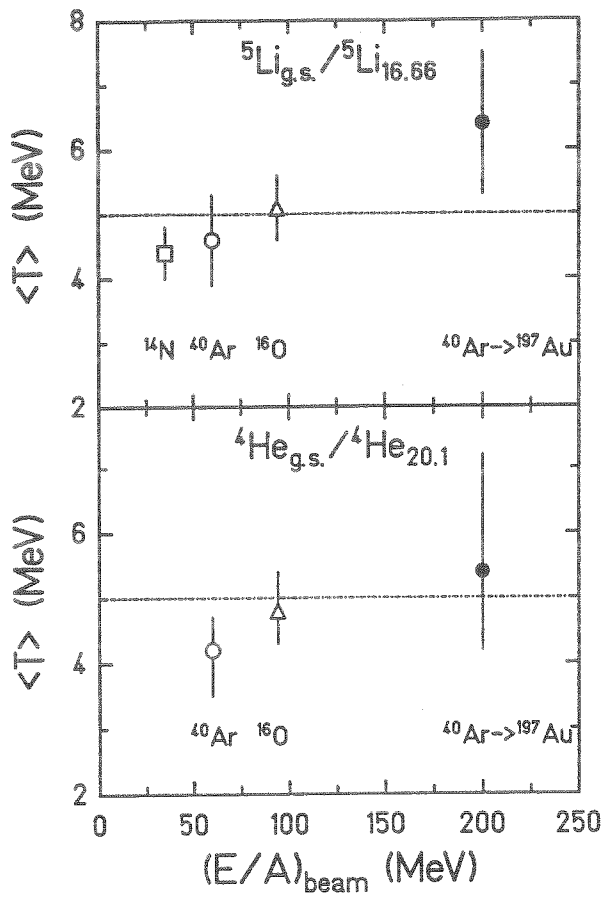


Figure 1: *Dependence of the mean emission temperature of ^{4}He and ^{5}Li fragments emitted in heavy ion induced reaction on ^{197}Au on the beam energy per nucleon.*

1) Z. Chen *et al.*, Phys. Lett. B **199**, 171 (1987)

2) J. Pochodzalla *et al.*, Phys. Rev. Lett. **55**, 177 (1985)

Formation of Delta-Resonances in P-Nucleus Collisions [G]

Martin Trzaska
Physikalisches Institut der Universität Heidelberg
In collaboration with DIOGENE-group (DPhN/ME Saclay, LNS Saclay, CRN Strasbourg, LPC Clermont-Ferrand, IPN Orsay)

Subject of these investigations is the detection of DELTA (1232) excitation in nuclear matter. This first excited state of the nucleon is populated via p-A collisions, with three different targets (A = C, Nb, Pb) and two bombarding energies (0.8 and 1.6 GeV).

The experiment has been performed at SATURNE-synchrotron (Saclay) with the quasi 4 π-detector DIOGENE, a cylindrical drift chamber[1]. This detector is originally designed for higher multiplicity (M ≤ 30) relativistic heavy ion collisions and therefore it is well suited for the detection of the low multiplicity (M ≤ 7) p-A events, where predominantly protons and pions are measured in an angular range of Θ = 15° - 140° .

The main Delta-signal is expected to be seen in events with only one proton and one pion. The invariant mass spectrum of the (π, p) -system should yield a characteristic Lorentz-peak with peak position and -width related to mass and lifetime of the excited DELTA state. As proton and pion are not necessarily related to a DELTA decay, there will be a broad background in addition.

A common method to extract the amount of true correlations relative to the background contributions is given by the 'event-mixing-method': pions and protons from different events cannot be correlated but must obey a more general distribution given mainly by the reaction kinematics. This should yield the desired background distribution.

The tacit assumption in this procedure is that background spectra with (π, p) from the same event are not different from mixed (π, p) pairs. This means that there are no other correlations present which should be due for instance to energy and momentum conservation. Monte Carlo calculations, especially with Cugnon's code[2] have shown, that secondary correlations are neglegible for all investigated systems; i.e. the simple event-mixing method is a valid procedure to disentangle DELTA (π, p) pairs from background pairs.

Figure 1 shows the extracted DELTA-resonance-curve for the p + C (800 MeV) system. The peak position is about 1205 MeV which has to be compared with a free DELTA's 1232 MeV. There is a clear shift in the mass while there seems to be no significant change in the width. This has been observed for all measured systems as shown in Fig. 2. Whether the effect can be regarded as a modification due to the surrounding medium or is just of kinematical origin is still a matter of debate. The latter point of view is supported by the CASCADE calculations which use no inherent medium effect.

Further insight to this subject may be gained by looking at the higher multiplicity data, which correspond to slightly more central collisions. Figure 3 shows the acceptance modified impact-parameter distribution for two event classes with a proton multiplicity of NPRT = 1 (NPRT = 2) and at least one pion present. This broad distribution shows that the observed DELTAs (NPRT = 1) must also have a contribution from reactions inside the nucleus and are surely not of pure peripheral character.

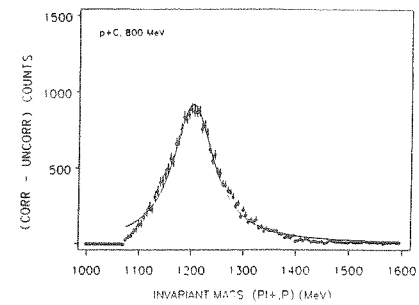


Fig. 1 Extracted DELTA mass distribution for an event-class with one proton and one pion (NPRT = 1).

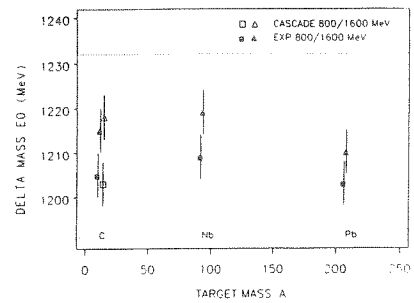


Fig. 2: Effective DELTA masses E0 for all investigated systems including two CASCADE calculations.

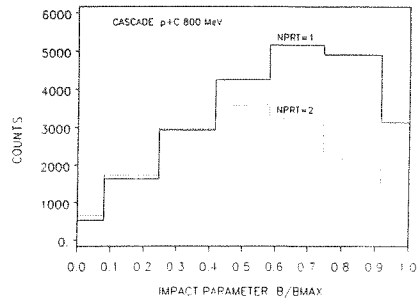


Fig. 3: Impact parameter distribution for the two event-classes: proton multiplicity NPRT = 1 and NPRT = 2 and one pion in addition.

[1] Alard et al. NIM A261 (1987) 379
[2] Cugnon et al. Nucl.Phys. A379 (1982) 553

Pion Interferometry in Nucleus-Nucleus Collisions at 200 GeV/nucleon

J. Bächler[8], J. Bartke[5], H. Bialkowska[12], R. Bock[6], R. Brockmann[6], S. I. Chase[3], C. de Marzo[2], I. Derado[10] V. Eckardt[10], J. Eschke[7], C. Favucci[2], D. Ferenc[13], B. Fleischmann[6], M. Fuchs[6], M. Gazdzicki[12], H. J. Gebauer[10] E. Gladysz[12],O. Hansen[7], J. W. Harris[3], W. Heck[7], M. Hoffmann[8], T. Humanic[6], K. Kadija[13], S. Kabana[7] A. Karabarbounis[1], R. Keidel[9], J. Kosiec[7], M. Kowalski[10], A. Kühmichel[7], M. Lahanas[7], J. Lee[7], M. LeVine[7] A. Ljubicic[13], S. Margetis[7], E. Nappi[2], G. Odyniec[3], G. Paic[13], A. D. Panagiotou[1], A. Petridis[1], J. Pfennig[4], A. Piper[9] F. Posa[2], H. G. Pugh[3], F. Pühlhofer[9], G. Rai[3], A. Ranieri[2], W. Rauch[3], R. Renfordt[7], D. Röhrich[7], H. Rothard[7] K. Runge[8], A. Sandoval[6], E. Schmidt[7], N. Schmitz[10], I. Schneider[7], L. S.Schroeder[3], G. Selvaggi[2], P. Seyboth[10] J. Seyerlein[10], E. Skrzypczak[11], P. Spinelli[2], R. Stock[7], H. Ströbele[7], L. Teitelbaum[3], A. Thomas[7], S. Tonse[3] G. Vassileiades[1], G. Vesztergombi[10], D. Vranic[13], S. Wenig[7]

[1]Physics Dept., Univ. of Athens; [2]Dipartimento di Fisica, Univ. di Bari and INFN Bari; [3]Lawrence Berkeley Laboratory Berkeley; [4]CERN, Geneve; [5]Inst. of Nuclear Physics Cracow; [6]GSI, Darmstadt; [7]Fachbereich Physik, Univ. Frankfurt [8]Fachbereich Physik, Univ. Freiburg; [9]Fachbereich Physik, Univ. Marburg; [10]Max-Planck-Institut für Physik, München [11]Inst. for Experimental Physics, Univ. of Warsaw; [12]Inst. for Nuclear Studies, Warsaw; [13]Rudjer Boskovic Institut Zagreb

HBT is a direct method of obtaining experimentally information about the space-time structure of the pion emitting source.

Establishing the properties of the system formed in the collision of two atomic nuclei at ultrarelativistic energies during freeze-out it may be useful to understand the behaviour of compressed nuclear matter. In a previous report results of HBT in O+Au at 200 GeV/nucleon were presented [1].

A large source for center-of-mass rapidity pions was the surprising result of the analysis whereas in the fragmentation region a much smaller size was measured. In this report first preliminary results of pion interferometry for S+S at 200 GeV/nucleon are presented. 408 events taken with a central trigger which represents 2% of the total inelastic cross section were analysed. S+S is a symmetric configuration in contrast to O+Au . Thus measuring the correlation for S+S in the rapidity range from 0.5 to 3.0 is equivalent to the range 0.5 to 5.5 (which represents practically full acceptance) due to the reflexionsymmetry at y= 3.0. Fig. 1 shows the correlation function for pion pairs with opposite charges, which is reproduced by the correlation calculated from the Coulomb attraction.

The results for like sign pions are shown in Fig. 2a+b together with fits of a gaussian parametrization of the source distribution. No significant variation of the size of the system for two different rapidity intervals are observed in contrast to the O+Au finding. However, we cannot exclude a larger size for midrapidity pions, because significant deviations from the gaussian parametrization for small momentum differences make the fits unreliable. A two gaussian form describes the data much better, a phenomenon observed in p-p and e^+ - e^- interactions [2].

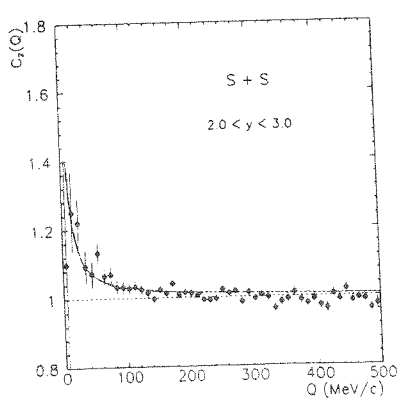


Figure 1: Correlation of pairs of opposite charge due to Coulomb attraction.

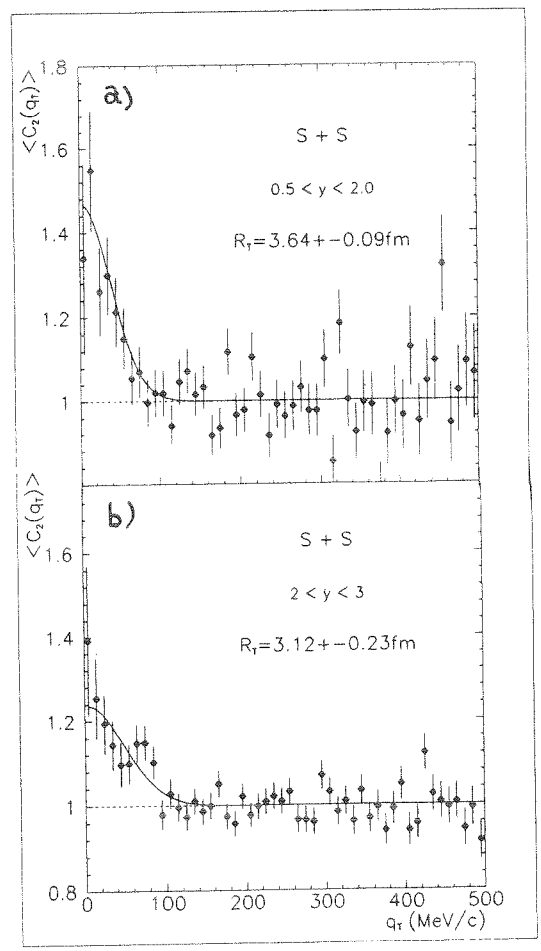


Figure 2: Projected transverse momentum correlations for S+S a) in the rapidity interval 0.5 <y< 2.0, b) 2.0 <y< 3.0.

References

[1] T. Humanic et al., GSI Scientific Report 1987,p. 78
[2] T. Akesson et al., Phys. Lett. B187,(1987)420

Negative Particle Spectra in S+S Collisions at 200 GeV/nucleon[B]

H. Rothard, S. Wenig, E. Schmidt, A. Kühmichel
D. Röhrich, H. Ströbele und R. Stock
Institut für Kernphysik,Universität Frankfurt
and NA 35 Collaboration

S+S collisions at 200 GeV/nucleon were studied with the NA 35 streamer chamber using two different trigger modes : A central trigger representing 2% [1] and a minimum bias trigger corresponding to about 90% of the total inelastic cross section, allowing thus essentially all impact parameters. 457 events of the central and 348 events of the minimum bias trigger sample were analyzed by measuring all charged particle tracks and by assuming that they are all pions. In order to study effects that may depend on the centrality of the collisions the minimum bias sample is divided into two subsamples with approximatley the same statistical significance representing "peripheral" ($10 \leq n_{ch} \leq 100$) and "semi-peripheral" ($n_{ch} > 100$) collisions.

Fig.1 shows the rapidity distributions $1/N_{ev}(dn/dy)$ of negatively charged particles for central and peripheral collisions. The rapidity distributions should be symmetric with respect to midrapidity ($y_{mid} = 3$) due to the symmetric target-projectile system. Because the reconstruction efficiency decreases for rapidities $y > 3.5$ with increasing multiplicities,we focus our analysis on the backward hemisphere $y \leq 3$,essentially representing full phase space.

The rapidity distributions become slightly narrower as the multiplicity (i.e. centrality) increases, a tendency that has also been observed for $\alpha + \alpha$ collisions at the CERN ISR [2].The width of the distribution for central S+S collisions and p+p collisions at the same beam energy is the same within the errors [1].

In order to compare the pt-distributions of two different data samples (1,2) in detail, one usually looks at the ratio $R(pt) = (dn/dpt)_1/(dn/dpt)_2$ (as a function of pt).A significant excess of high pt,first reported for hadron + nucleus collisions [3], and low pt particles has also been observed when comparing p+Au, O+Au [4] and (central) S+S [1] to p+p data. No such excess is seen in the ratio of central S+S collisions to peripheral or semi-peripheral S+S collisions (up to now) [5],whereas such an effect has been observed in the ratio of high multiplicity to low multiplicity events in $\alpha + \alpha$ collisions [2].

Since there are no significant differences in the shape of the pt-distributions we will focus here on the pt-distribution $1/N_{ev}(1/pt)(dn/dpt)$ in the rapidity range $2 \leq y \leq 3$ for central events to compare the data to a thermal and a radial flow model [6] (see fig.2). A satisfying fit to the data can be obtained from a radial flow model [6] wich assumes a thermal fireball with a superimposed isentropic expansion ($\beta = 0.78$, $T = 112 \pm 4$ MeV for central and $T = 110 \pm 7$ MeV for peripheral collisions), whereas a simple thermal model does not describe well the data (dashed line, $T = 138 \pm 3$ MeV for central and $T = 139 \pm 5$ MeV for peripheral events).

References

[1] R.Renfordt et al,GSI Report 1988,68

[2] W.Bell et al, Z.Phys C27 (85) 191

[3] J.W.Cronin et al, Phys.Rev.D11 (75) 3105

[4] H.Ströbele et al, Z.Phys.C38 (88)) 89

[5] H.Rothard,Diploma Thesis.1990

[6] K.S.Lee, U.Heinz, Z.Phys.C43 (89) 425

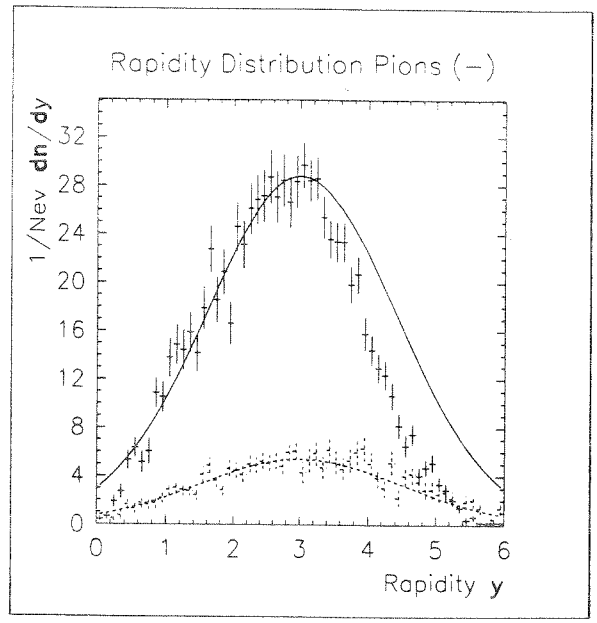


Figure 1: Rapidity distributions for peripheral and central collisions

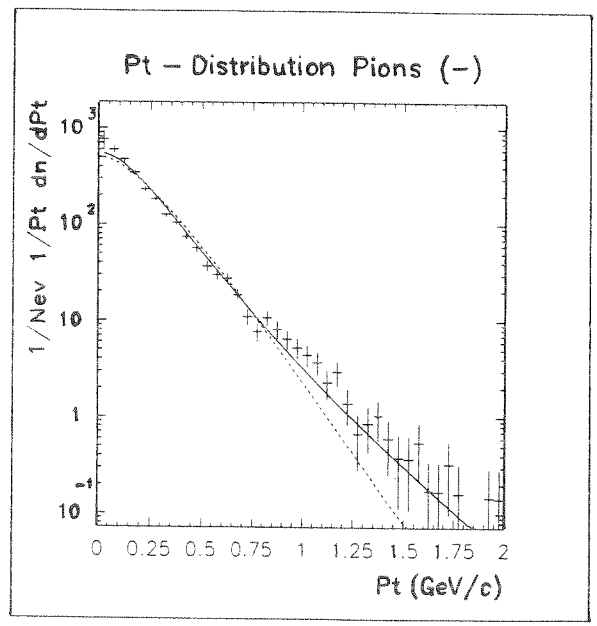


Figure 2: pt-distribution for central collision , $2 \leq y \leq 3$

Proton Rapidity Distributions in ^{32}S-^{32}S Collisions at 200 GeV/nucleon^{B}

S.Wenig, H.Rothard, D.Röhrich, R.Renfordt, H.Ströbele, R.Stock
Institut für Kernphysik, Univ. Frankfurt
and NA35 Collaboration

The rapidity distribution of participating nucleons in nucleus-nucleus reactions reflects the stopping power (i.e. energy loss) of the colliding nuclei and the baryon- and energy density achievable in such collisions along the rapidity axis. With the streamer chamber detector of the NA35 experiment at CERN the rapidity distribution of participating protons in ^{32}S-^{32}S collisions at 200 GeV/nucleon can be determined on a statistical basis by assigning the proton mass to all particles and subtracting the rapidity distribution of negative particles from the one of positive particles. Since the ^{32}S-nuclei are isospin scalars the contribution of the wrongly treated pions cancel out, as well as the produced nucleon-antinucleon pairs. After a correction for the decay tracks of strange particles and a correction for the enhanced production of positive Kaons compared to negative Kaons one finally is left with the rapidity distribution of participating protons excluding those resulting from the decay of hyperons. Because of the isospin scalar property of the ^{32}S-nuclei this distribution is equivalent to the one of neutrons and thus represents the rapidity distribution of all participating nucleons.

In Fig. 1 the rapidity distribution of protons is shown for peripheral ^{32}S-^{32}S collisions at 200 GeV/nucleon. The fitted curve reveals an exponential decrease of the rapidity loss, a behavior which is well known from p-p collisions [1] and results in a mean rapidity loss for these collisions of $\langle y \rangle_{per} = -1$.

In Fig. 2 the rapidity distribution of protons is presented for central ^{32}S-^{32}S collisions at 200 GeV/nucleon. A significant broadening of the distribution is seen, which is very well described by the RQMD-Model [2] represented by the histogram. The resulting mean rapidity loss $\langle y \rangle_{cen} = -1.5$ clearly shows that multiple nucleon-nucleon collisions are occuring in these nuclear reactions. In addition it reflects the characteristics of p-nucleus collisions [3] and central alpha-alpha and d-d collisions [4]. A mean energy loss in the cm-system of 60% per participating nucleon can be deduced from the distribution. Using a simple thermodynamic model [5] a baryochemical potential at midrapidity of $\mu_B = 150-200$ MeV can be extracted from the nucleon density at $y = 3.0$ being the first information for theorists in order to judge whether the assumption of a vanishing baryochemical potential in lattice QCD calculations is justified.

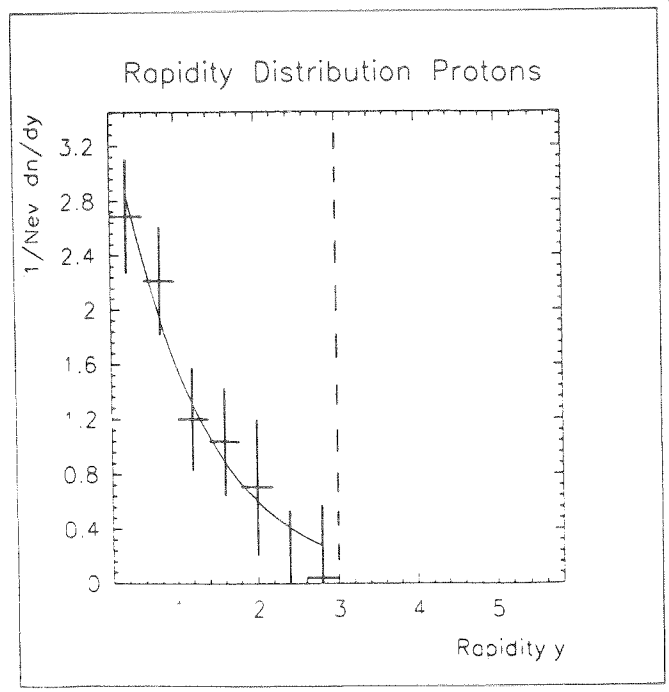


Figure 1: Rapidity distribution of protons for peripheral ^{32}S-^{32}S collisions at 200 GeV/nucleon. Only the backward hemisphere is shown.

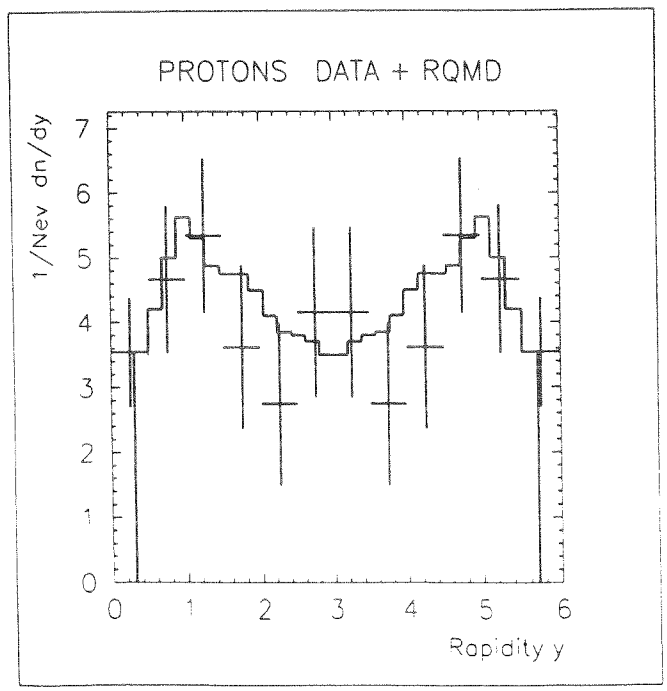


Figure 2: Rapidity distribution of protons for central ^{32}S-^{32}S collisions at 200 GeV/nucleon.

References

[1] W.Busza, A.S.Goldhaber, Phys.Lett. 139B (1984) 235

[2] H.Sorge et al., contribution to this report

[3] W.Busza, R.J.Ledoux, Ann.Rev.Nucl.Part.Sci. 38 (1988) 119

[4] W.Bell et al., Z.Phys. A325 (1986) 7

[5] B.Müller, Lecture Notes in Physics 225, Springer (1985)

Enhanced Strange and Antistrange Particle Production in Central S + S Collisions at 200 GeV/A [B,G]

S. Kabana, A. Thomas, R. Stock, H. Ströbele, Inst. für Kernphysik, Univ. Frankfurt; M. Gazdzicki, Inst. Nucl. Phys., Warsaw University; O. Hansen, BNL Brookhaven; I. Derado, P. Seyboth, MPI für Physik und Astrophysik, München, K. Kadija, Rudjer Boskovic Institute, Zagreb;
NA35 COLLABORATION

We measured rapidity and transverse kinetic energy distributions[1] of neutral strange particles Λ, $\bar{\Lambda}$ and K^0_S, produced in p + S and S + S collisions in the NA35 Streamer Chamber at the CERN SPS. We also determined the mean multiplicities of those particles, along with the multiplicity $\langle h^- \rangle$ of negative hadrons. Minimum bias p + S collisions and central S + S collisions were selected by suitable triggers.

Fig. 1 shows transverse kinetic energy spectra ($T_T = m_T - m_o$; $m_T = (p_T^2 + m_o^2)^{1/2}$) of Λ, $\bar{\Lambda}$ and K^0_S. The central S + S collision data (upper curves) refer to the intervals $0.8 < y < 2.0$ ($1.4 < y < 2.7$) for Λ, $\bar{\Lambda}$ (K^0_S). The intervals of the p + S data are $0.8 < y < 4.2$ ($1.7 < y < 4.2$). The data are described by exponential curves $\exp(-T_T/B) = \text{const.}\ \exp(-m_T/B)$ where B ranges from 180 to 200 MeV for Λ (K^0_S). Within statistics all spectra look similar, providing no indication of different production mechanisms.

Rapidity distributions for neutral strange particles from central S + S collisions are shown in Fig. 2. Note a lower cutoff in p_T at 0.5 (0.62) GeV/c for Λ, $\bar{\Lambda}$ (K^0_S). Data at $y > 3$ are reflected from $y < 3$. The $\bar{\Lambda}$ and K^0_S yield is peaked at midrapidity whereas the Λ yield shows a broad plateau. This shape can be approximated well by symmetrizing our measured Λ data in p + S (not shown) about y = 3: no strong hint of a different mechanism in central S + S collisions.

However, all production rates of Λ, $\bar{\Lambda}$ and K^0_S are strongly enhanced in central S + S collisions. The tab. gives the total mean multiplicities obtained from a yield extrapolation[1] to full phase space, along with our p + S results and p + p data at this energy. In the step from p + p to p + S collisions, all multiplicities increase uniformly by about 1.7. However, from p + S to central S + S collisions the negative hadron multiplicity $\langle h^- \rangle$ increases by 21 whereas <u>all</u> neutral strange particle multiplicities grow by an average factor of about 40. The relative strange and antistrange to negative hadron content of central S + S collisions thus is enhanced about twofold.

1) J. Bartke et al., NA 35, to be published in Z. Phys. C

Fig. 1

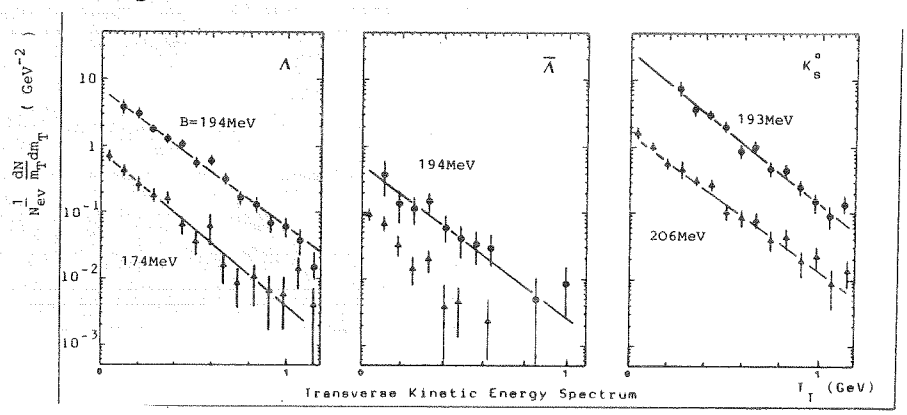


Fig. 2

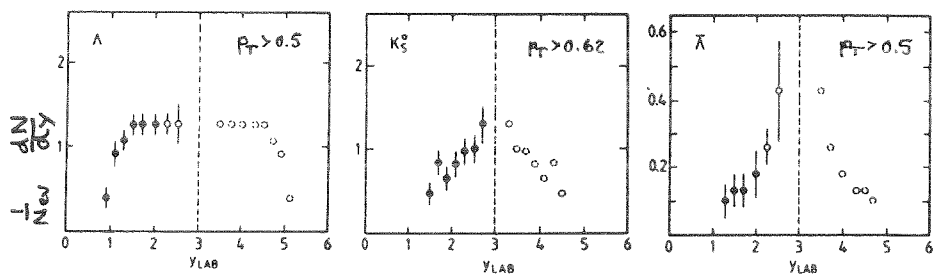


Table:

	$\langle h^- \rangle$	$\langle \Lambda \rangle$	$\langle \bar{\Lambda} \rangle$	$\langle K^0_S \rangle$
p + p	2.85±0.04	0.95±0.015	0.013±0.004	0.17±0.01
p + S	5.0 ±0.6	0.22±0.03	0.028±0.09	0.28±0.04
S + S cent.	103 ±5	8.2 ±0.9	1.5 ±0.4	10.7±1.8
SS/pp	36 ±4	86 ±18	115 ±39	63 ±11
SS/pS	21 ±3	37 ±6	53 ±18	38 ±9
pS/pp	1.7 ±0.2	2.3 ±0.4	2.1 ±0.7	1.6 ±0.4

Particle identification of charged Kaons in the NA35 Streamer Chamber[B]

J-Y. Lee, S. Kabana, D. Röhrich, H. Ströbele and R. Stock
Institut für Kernphysik,Universität Frankfurt
and NA 35 Collaboration

The production of charged particles in nucleus-nucleus collisions at 200 GeV/nucleon was studied in the NA35 streamer chamber at the CERN-SPS accelerator. In the streamer chamber pictures we can also observe the decays of both neutral (Λ, K^0) and charged particles - as for example the three-body (τ) and two-body decay (kink) of charged kaons (fig. 1). In view of obtaining charged kaon spectra one has to distinguish between kaons and other decaying charged particles (Σ^+,π^+). In order to develop a procedure that detects kaons we simulated 10000 central S+S events with the FRITIOF event generator. The produced charged particles were traced into the fiducial volume of the streamer chamber and allowed to decay according to their life-time in the lab system and branching-ratio (table 1) taking into account an appropriate measurement error for the momentum. Even though the kaons live rather long, a reasonable fraction of kaon decays (3%) can be seen in the chamber.

Table 1: decay mode table (two-body decay)

particle	decay-mode	mean-life [cm]	branching-ratio [%]	Q-value [MeV/c]
K^+	μ^+, ν	370.9	63.5	236
K^+	π^+, π^0	370.9	21.2	205
Σ^+	p,π^0	2.4	51.6	189
Σ^+	n,π^+	2.4	48.3	185
π^+	μ^+, ν	780.3	100.0	30

As we see in the table, the kaon can be clearly distinguished from the sigma by its life-time and from the pion by the Q-value. A cut in the life-time (2% of the life-time of the kaon) rejects most of the sigmas (more than 95%). In order to remove the pions from our sample, we then applied a cut to the projected decay angle. The decay angle is the angle between the tracks of the decaying particle and the charged decay product and depends on the Q-value and the rapidity of the particle. We rejected decays with an angle smaller than 2 degrees. The decays were fitted kinematically, and only those particles with a fit-probability greater than 0.02 were retained.

Table 2: FRITIOF 200 GeV/nucleon, S+S, central collision

particle decay products	K^+ μ^+, ν	K^+ π^+, π^0	Σ^+ p, π^0	Σ^+ n, π^+	π^+ μ^+, ν
events	10000	10000	10000	10000	10000
particles	112216	112216	7411	7411	1168920
decay in chamber	2587	821	52	51	13840
after life-time cut	2181	695	1	2	9425
after fit cut	2025	207	1	2	1485
after angle cut	1663	131	0	1	115

There are hardly any sigma decays to be seen in the streamer chamber pictures because these particles have a very short life-time, and therefore most of them decay before reaching the streamer chamber since the target is positioned 8 cm in front of it. In the chamber pions decay 3 times more often than kaons, but it is difficult to find pion decays in the pictures, because of their narrow decay angles. As a result we can expect to obtain kaon spectra with less than 10% contamination of pions (table 2). At the moment scanning and measuring of kinks is underway. Up to now we have measured 457 central S+S events on high-resolution graphics workstations; we found 43 candidates for charged kaon decays, which have to be analyzed.

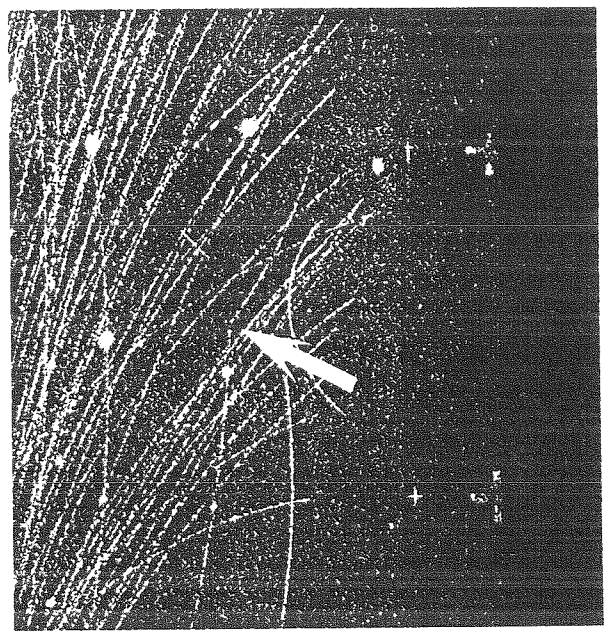


Figure 1: A part of a streamer chamber picture showing a decaying particle (kink)

The Frankfurt Image Processing System for NA35 Streamer Chamber Pictures[B]

D. Röhrich, J. Kosiec, A. Kühmichel, J. Pfennig, G. Roland, E. Schmidt, I. Schneider, R. Stock
Institut für Kernphysik,Universität Frankfurt
and NA 35 Collaboration

At the University of Frankfurt we developed a computer environment for analyzing NA35 streamer chamber data. The hardware configuration allows us to measure films, digitize pictures, process them automatically and analyse the results.

The environment consists of two sections: an UNIX environment for working with the digitized images and a VMS-VAX environment for data evaluation, both connected via a ETHERNET-network running TCP/IP- and DECnet-protocol simultanously.

The images are digitized by a high resolution 4096 pixel line-scan CCD-camera controlled by a 68030-VME-Bus system under the operating system UNIX V.3. The images (4k × 2k) are stored on streamer tapes or are transfered to a computing server (C3000) for further processing.

We are planning to add an optical disk server to the TCP/IP-net to store large amounts of image data (up to 2 TBytes). The computing server, a fast RISC processor (MIPS R3000, 3.6 Mflops, 20 MIPS) has enough computing power to process an event (3 images, 6 MBytes each) by algorithms described in [2] within approximately 20 minutes. The images are then displayed on high resolution graphics workstations for the evaluation of the results of the automatic algorithms.

The workstations are connected to a VAX by RS-232C lines to support the operator with an online space reconstruction program.

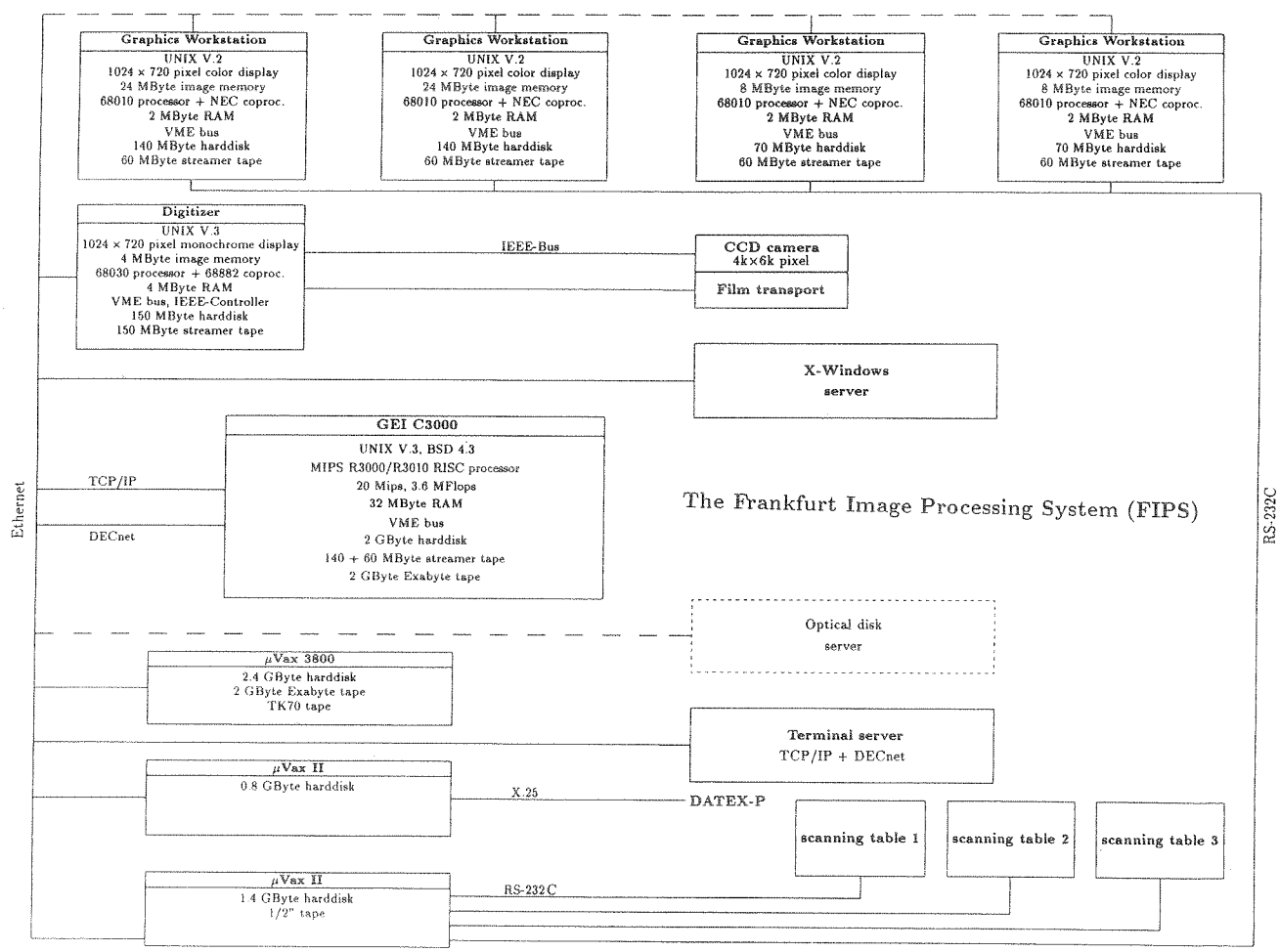
The upgrade of the graphics workstations (68030/68882, 4 MBytes memory, ETHERNET, UNIX V.3) is underway and we will soon be able to connect the workstations to the TCP/IP network.

The final results of the image processing are then transfered to the VAXes for physics data analysis. The VAXes are also employed in the film measurement on 3 scanning tables (2 projection tables with digitzing tables and 1 measuring table controlled by a LSI 11/2 processor in a camac crate).

By upgrading our automatic image processing and pattern recognition software [2] we are going to speed up the film analysis by an order of magnitude.

References

[1] GSI Annual Report 1986, p.76;
J. Pfennig, Dissertation 1989, Univ. Frankfurt.
[2] F. Pühlhofer, D. Röhrich, R. Keidel,
Nucl. Instr. Meth. **A 263** (1988) 360;
cf. also various contributions to this annual report.



The Time Projection Chamber for the NA35 Experiment at CERN[G+B]

V. Eckardt, W. Rauch, N. Schmitz, P. Seyboth, J. Seyerlein
MPI für Physik und Astrophysik, München
R. Bock, R. Brockmann
GSI, Darmastdt
R. Renfordt, R. Stock
IKF der Universität Frankfurt
J. Harris, H. Pugh
Lawrence Berkeley Laboratory, Berkeley

NA35 COLLABORATION

NA35 is the only experiment of the CERN Heavy-Ion Program which provides nearly 4π coverage with momentum measurement for charged particles. However, the high particle density in the forward hemisphere makes it difficult in S+Nucleus reactions to analyse particles forward of mid-rapidity in the Streamer Chamber. A Time Projection Chamber (TPC) is under construction and will be installed downstream of the vertex magnet (Fig. 1), where it will complement the acceptance of the Streamer Chamber.

The TPC will also serve as a developmental prototype for a larger solid angle detector envisaged for the future Pb-program. In particular it will be possible to study the performance with respect to tracking accuracy, two track resolution and dE/dx measurement in a high multiplicity-no magnetic field environment using pad readout only.

A sketch of the NA35-TPC[1] is shown in Fig.2. The overall dimensions are 2500x1000x1400 mm^3, with a vertical drift length of 1000 mm. The six independent readout modules are placed at the top of the field cage and cover an area of 2370x1260 mm^2. The design of the readout modules is based on the ALEPH-TPC design[2]. The pad plane (768x680 mm^2) is completely covered with 5.5x39.5 mm^2 pads with 0.5 mm gaps between them. There are 128 pads in a row and 15 rows for a total of 1920 pads per chamber module, in total the TPC is read out by 11.520 pads. From the experience gained in the production of the ALEPH-TPC we expect a precision of +/-30 µm for the pad positions and dimensions and similar values for the planarity of the pad plane and parallelism between the sense wire plane and the pad plane or cathode grid.

The gas mixture in the chamber will be 91 % NE / 9 % CH4, this selection has been made because of its performance in double track-resolution and its energy-loss behaviour in the region of the relativistic rise. With laserbeams in the ALEPH Prototype TPC-90[3] and with particle beams in a small NA35 prototype TPC we have demonstrated that we can achieve : a measurement accuracy of 200 µm along the pad/wire row, 300 µm in the drift direction, two track separation of 0.4 cm along the pad/wire row and 1.2 cm in drift direction. The dE/dx resolution that we measured with the prototype was around 6 %.

To read out the pad signals we are going to use the ALEPH electronic chain[2]. The chain consists of a preamplifier card on the readout module with 16 channels, approx. 30 m cable to the control room, the Time Projection Digitizer (TPD) including shaper, Flash ADC (8bit) and 2k memory (8bit) for each channel, 64 channels per TPD, the Time Projection Processor (TPP) and the ALEPH - Event-Builder. The FWHM of the shaper is 180 ns and the clock frequency for sampling is 15 MHz. The TPD's, the TPP's and the ALEPH-Event-Builder are Fastbus-Moduls. A Fastbus crate houses 8 TPD's and 1 TPP. One Aleph-Event-Builder reads out 12 Fastbus crates.

We assume 20 central triggers per second during the spill. With about 200 tracks in the TPC each central event contains, after zero suppression, about 150 kbytes of information. For a 4 second spill this amounts to 12 Mbytes which must be buffered and read out during the 14 second cycle time of the accelerator. The input rate of 3 Mbytes/sec is easily handled by Fastbus. While the 750 kbytes/s write speed of standard high performance 6250 bpi tape drives would match the output rate if two tape drives were used, the 200 Mbytes capacity of the tapes is unacceptable. We therefore plan to use four helical-scan 8mm tape drives each with a write speed of 250 kbytes/s and a capacity of 2 Gigabytes.

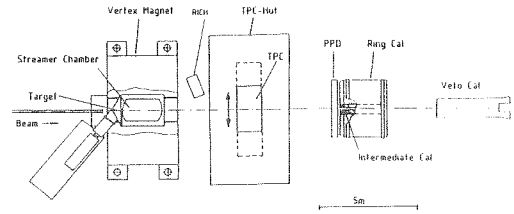
The NA35 TPC will be installed and commissioned at CERN in June/July 1990, first data taking is planned for the Ion-Run in August '90.

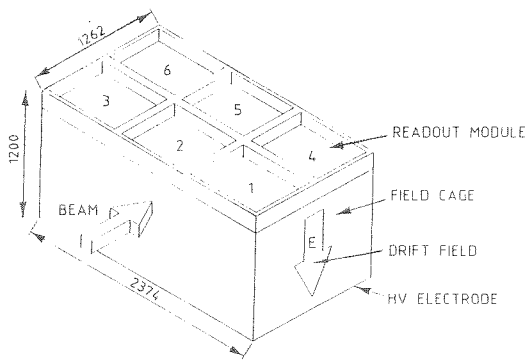
References

[1] Memorandum to the SPSC ..., CERN-SPSC-89-17
[2] The Aleph Handbook, W. Blum Editor, Aleph 89-77, Note 89-03
[3] TPC-90 Tests, this annual report.

Figure Caption

1 Experimental Set-up NA35
2 NA35 TPC





TESTS WITH LASER BEAMS IN THE Aleph TPC90 AT CERN [B]

R. Brockmann, H. Gutbrod, B. Kolb, T. Przybyla, R. Schmidt
GSI, Darmstadt
R. Renfordt
University Frankfurt

NA35 - WA80 COLLABORATION

For the preparation of future Heavy Ion Experiments at CERN a study of the effects of high track densities on the measurement of the energy loss (dE/dx) in a Time Projection Chamber (TPC) is under way. The detailed experimental setup using the Aleph TPC90 has been described in last years annual report. Here the first measurements and results are presented including a comparison between Ar/9% Methane and Neon/9% Methane.

Eight laser beams are generated by a set of semitransparent mirrors so that they are exactly in a plane parallel to the drift direction. The mirrors are arranged in a way to create a 'fanning out' pattern thus allowing to study the effects on gas amplifiation of tracks arriving at the same location of the amplification wire but with different time intervals between arrivals. Reading out different wires (running perpendicular to the direction of the Laser beams) any change in amplitude as a function of distance between the laser beams can be determined. In figure 1 the drift time as a function of wire number (4mm distance) is shown.

The varying distance of the laser beams is clearly visible. In figure 2 the amplitude as function of time for wire 12 is shown using Ne/CH4 gas. The separation is very good considering the rather small distance between tracks. In figure 3 the same is shown for Ar/CH4 gas. Due to the higher drift velocity of the electrons the peaks move closer together.The widths of the peaks on the other hand stay constant. This is due to the fact that the longitudinal diffusion is very similar for the two gases (see table 1). The comparison between figure 2 and 3 clearly shows the advantage of Ne/CH4 over Ar/CH4 in a high track density environment.

The analysis of the pulse heights of consecutive tracks hitting the amplification wire at the same spot has so far not shown any loss of gain due to positive ions still being close to the wire. In order to exaggerate this effect we tried to increase the gas gain so that the ionization of the laser track was 5 to 8 times higher than minimum ionizing (the normal situation). This revealed a known defect of the electronics chain: the shaper saturates if pulses come too close together in time (< 2 μsec corresponding to 6 cm in space for Ne/CH4). It is planned to repeat the tests with a modified version of the shapers in order to find the onset of saturation effects.

Table 1:

Diffusion (sigma) and drift velocities for different gases.
The errors are +-10%.

gas	diffusion transverse	diffusion longit.	drift vel.
Ar/CH4	710 μ/√cm	390 μ/√cm	5.1 cm/μs (113 V/cm)
Ne/CH4	420 μ/√cm	390 μ/√cm	3.2 cm/μs (210 V/cm)

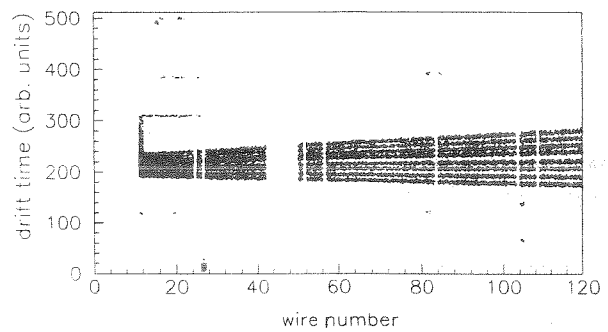


Figure 1:

Scatter plot of drift time as function of wire number. The distance between laser beams on the left side is 1.9 cm and on the right side 5 cm. The gaps are due to missing preamplifier channels. The distance between wires is 4 mm.

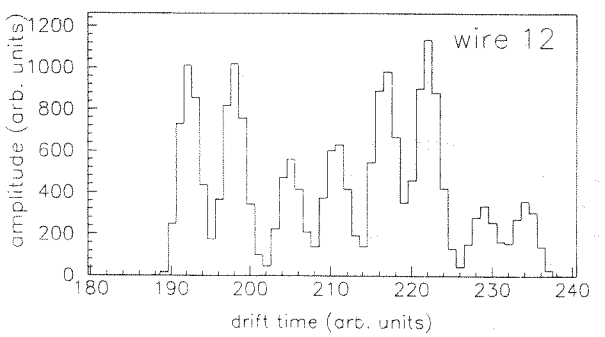


Figure 2:

Amplitude as function of time for wire 12. The average distance between tracks is 1.9 cm. The gas is Neon with 9% Methane.

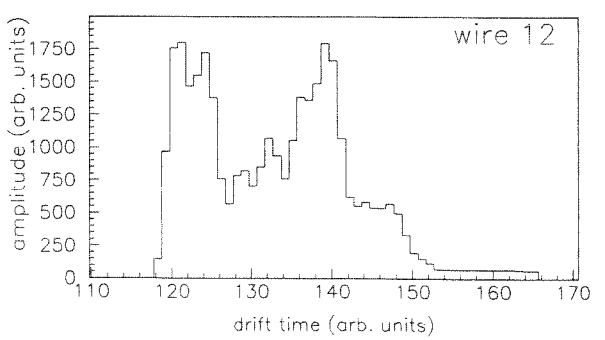


Figure 3:

Same as figure 2 but with Argon gas with 9% Methane.

A 50 x 50 cm^2 RICH detector prototype for ultrarelativistic heavy ion collisions[B]

J. Bächler[5], R. Bock[6], W. Dominik[3], A. Gougas[3], J. Eschke[4], W. Heck[4], M. Hoffmann[5], T. Hernandez-Benavides[6], A. Karabarbounis[1], M. Koncul[7], M. Le Vine[4], A. Ljubicic Jr[7]., G. Millon[3], M. Mongelli[2], E. Nappi[2], G. Paic[6,7], A. Panagiotou[1,3], A. Petridis[1], A. Posa[2], A. Sandoval[6], E. Schmoetten[5], P. Spinelli[2], R. Stock[4], G. Vasileiadis[1], M. Vasiliou[1], D. Vranic[7], M. Wensveen[6], N. Zaganidis[3].

Univ. Athens[1], INFN Bari[2], CERN[3], Univ. Frankfurt[4], Univ. Freiburg[5], GSI Darmstadt[6], Ruder Boskovic Inst., Zagreb[7].

Data from the test at the CERN PS accelerator of a single module RICH detector[1)] with hadrons at energies 1.5, 2.0, 2.5 and 3 GeV have been analyzed[2)]. Algorithms for the treatment of the CCD pictures were developed. The identified photons have then been reconstructed assuming that the conversion occurs 4 mm behind the quartz window and that the emission is taking place midway between the point of incidence in the radiator and the mirror surface. The distribution of reconstructed Cherenkov angles are shown in Fig.1 for 2.5 GeV hadrons (solid line) compared with the result of the reconstruction program, applied under the same conditions to simulated events (dashed line). The mean number of detected photons per ring is $< N_{ph} > = 15$.

Concurrently with the analysis of the single module test, a 50 x 50 cm^2 prototype RICH detector was constructed, designed as a array of hexagonally shaped spherical mirrors closely packed on a planar support, so that all mirrors define a common focal plane at the position of the conversion layer of the photon detector. During 1989 the following elements of the system were constructed and successfully tested :

- The radiator vessel with a capacity of 22 mirrors. The mirrors have a radius of curvature of 16 cm and a dish diameter of 13 cm.
- The multistep avalanche chamber (MSAC).
- The complete liquid freon circulation system with heating, purification and pressure control.
- The gas circulation with the TMAE bubbler.
- The monitoring and control of temperatures using the CERN MAC - 64 system.
- The optical imaging system, consisting of a Thomson 7863 CCD camera with 288 x 384 pixels, a two stage image intensifier of 18 mm diameter and a 35mm f/1.4 lens.
- The card to digitize the CCD signals on a PC/AT computer.

Test runs at different stages of the construction were conducted at the PS and SPS accelerators at CERN. Operation at a TMAE temperature of 43°C was achieved with the detector temperature at 46°C.

Cherenkov rings were observed demonstrating the single photon detection capacity of the 50 x 50 cm^2 MSAC.

In Fig.2 we show typical examples of rings obtained during the SPS run.

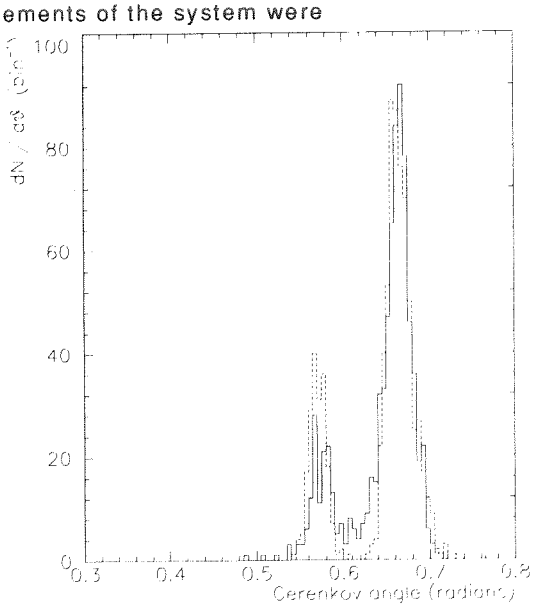


Fig. 1

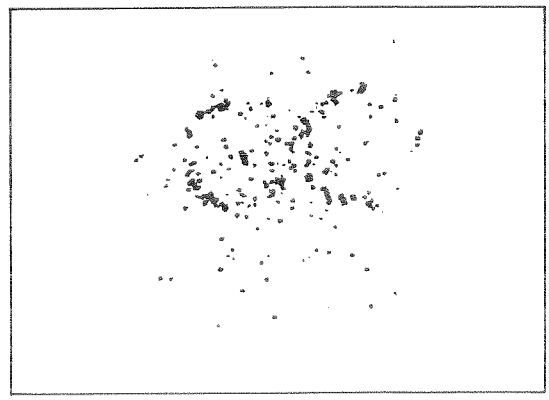


Fig. 2

[1.] *A. Sandoval et al. Test of ring imaging Cherenkov counter GSI Scientific report 1988 GSI 89-1, p.72.*

[2] *G. Vasileiadis et al. CERN EP report 89-107 and proceedings of the 4th Pisa meeting on advanced detectors May 21-26 1989.*

Automatic Measurement of NA35 Streamer Chamber Pictures [G]

R. Keidel, A. Piper, F. Pühlhofer Fachbereich Physik, Univ. Marburg
CERN NA35 Collaboration

The analysis of NA35 streamer chamber pictures is very manpower consuming. Several hundred tracks per event must be measured by an operator on a computer display.

We implemented and tested a method[1]) for an automatic analysis using an image processing computer. This procedure can be subdivided into the following steps:

1. Film digitization by a CCD camera
2. Image pre–processing (filtering)
3. Distortion correction
4. Local track recognition (Hough transform)
5. Global track recognition
6. Verification of tracks
7. Inter–image track assignment
8. Reconstruction in space.

The output is the momentum vector and the sign of the charge for each particle.

The *image pre–processing* of a digitized grey value picture (1.5k * 2k * 8bit) employs a spatial convolution acting as low pass filter and a special "streamer operator"[2]) in order to improve the signal to noise ratio. A discrimination leads to a binary image.

The *distortion correction* is applied to the binary image, which is more economical than to do it with the original image. The correction is calculated with a calibration grid taken from time to time during the run.

The *local track recognition* determines track segments within a moving window of a size of 128^2 pixels. Straight lines are detected by means of a Hough transformation technique.

The *global track recognition* uses the fact that nearly all particles are produced in the target. Due to the magnetic field in the streamer chamber the track form circle with the curvature κ and the target emission angle ϕ. Every recognized track piece has a distinct κ,ϕ–value and can be collected in a common plane. This yields an intensity distribution with κ,ϕ–values corresponding to circular tracks.

For matching and reconstruction the x,y coordinates of several points on each track are needed. Streamer positions are taken from the binary or original image (*verification*). Especially the streamers closest to the streamer chamber wall (end points) are of interest.

The *inter–image track assignment* (finding of corresponding tracks) is solved by using these end points. Their space coordinates are determined from the known positions of the streamer chamber wall. They can therefore be projected into the other two views in order to find corresponding tracks.

The *reconstruction* of the tracks in space is done by a special geometry program (HYDRA, CERN) using the streamer coordinates of the fitting tracks.

A worst case comparison between the results of this automatic method and "hand measured" events yields the following figures: 70% of the hand measured tracks in the individual views can be found with the automatic procedure. Finally 35% of the automatic measured tracks can be matched and reconstructed. The reason for this descent is the difficult detection of the weak end points yielding to a incomplete inter–image assignment. A tuning of the algorithm can be done after implementing the program code on high performance computers. Efforts to develop similar procedures on high performance computers are in progress at Institut für Kernphysik, Univ. Frankfurt am Main and at CERN, Geneva.

1 F. Pühlhofer, D. Röhrich, R. Keidel, Nucl. Instr. Meth. A263 (1988) 360

2 R. Keidel, Automatische Auswertung von Teilchenspurbildern ulatrarelativistischer Kern–Kern–Stösse, Dissertationsschrift, Marburg 1989.

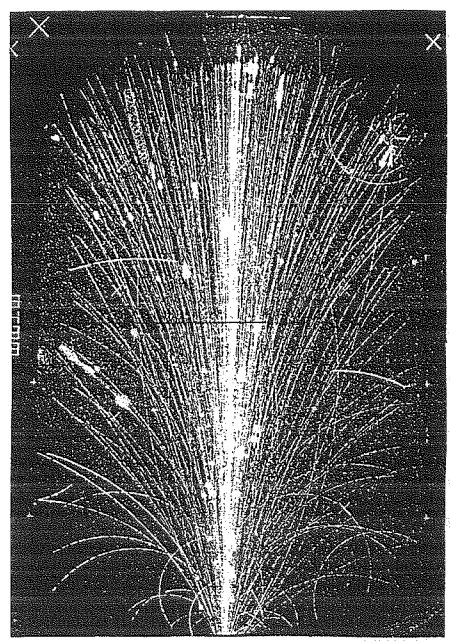


Fig 1: Typical streamer chamber picture (approximately 200 tracks, ^{32}S + ^{32}S, 200 GeV/n, central trigger)

Automatic Streamer Chamber Event Reconstruction B

M. Fuchs[1], B. Fleischmann[1], J. Kosiek[2], A. Kühmichel[2], J. Pfennig[3], D. Röhrich[2], A. Sandoval[1], R. Stock[2], G. Vesztergombi[4]

[1]GSI Darmstadt, [2]Frankfurt University, [3]CERN Geneva, [4]MPI München

CERN NA35 Collaboration

At present the full event analysis of ultrarelativistic heavy ion collisions, recorded by the NA35 Streamer Chamber, is done by operators measuring tracks with computer assistance in digital workstations. Working on digitized film, several hundred tracks per event are routinely being measured with 95% efficiency for central ^{32} S + S collisions. The required 2 remeasurements take between 10 to 14 hours/event.

In order to increase the yield of measured events, algorithms for automatic measurement and reconstruction are being developed. The initial efforts utilizing image processing techniques showed the validity of the approach[1,2], but the efficiency and speed of correctly reconstructed tracks was not high enough. Based on these experiences a new analysis scheme has been developed, that replaces whenever possible the track finding with a statistical criterion in the kappa-phi plane by an heuristic algorithm and introduces more iterations at all levels of the analysis in order to obtain a more robust track identification. The track matching in all 3 stereo views is done with help of conformal mapping.

After filtering and distortion corrections, the 2K x 3K gray level image is subdivided into overlapping patches of 128 x 128 pixels. Utilizing a Hough transform in a recursive way all straight pieces of tracks (match-sticks) are found (Fig. 1).

A cleanup step takes out of consideration all match-sticks that can't belong to a track. Then the sticks are sorted according to their slope and their distance to the vertex and to the beam axis in order to speed up the global track finding. Starting from one of the downstream corners, the sticks are searched for the ones that connect to circles. Circle pieces are then connected to each other if they belong to the same circle passing through the vertex. Using more stringent criterions, several iterations are done in which sticks are added or removed from the circle fits. Again circle pieces in different parts of the Streamer Chamber are connected if they belong to the same track, circles with less than three sticks are removed and the leftover sticks are inspected anew in the same manner. After two iterations all charged tracks outside a predefined cone of too high track density are found (Fig. 2).

The matching of tracks in the 3 views is done with help of a conformal mapping of each of the projections into the space

$$x' = \frac{x}{x^2+y^2} \qquad y' = \frac{y}{x^2+y^2}$$

which corresponds to the reflection of the image around the circle of radius 1 centered on the vertex. In this new space (Fig. 3), circles that pointed back to the target are transformed into straight lines. This property allows a very simple projections of a space track on all the 3 views. The matching is done by predicting where a given track in view 3 would lay in view 2. The requirement, that the last measured stick in view 3 lays within the Streamer Chamber fiducial volumen restricts the range of dip angles of the space track and therefore also of the possible projections in view 2 as is indicated by the hatched regions in Fig. 3. All possible projections are straight lines in the conformal mapping space of view 2 that cross each other in a well defined point, restricting the possible candidates further to have the right slope within the allowed region. By requiring self consistent predictions in all 3 views and using iterative methods, 98% of the measured tracks can be matched.

This analysis chain has been implemented in C and running on a MIPS IGE C 3000 under UNIX. It takes 15 min/event starting from the raw data to the final matched tracks.

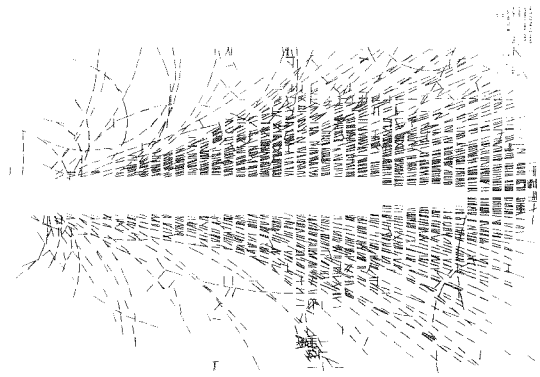


Fig. 1 Local track reconstruction.

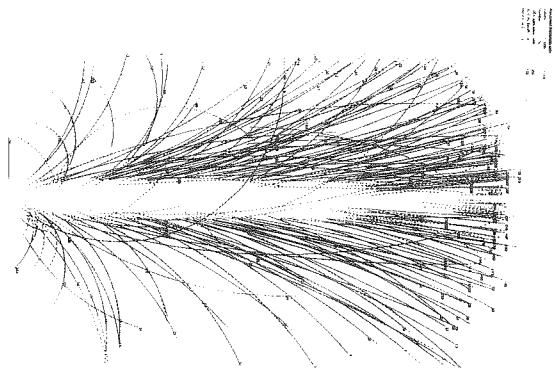


Fig. 2 Global track reconstruction.

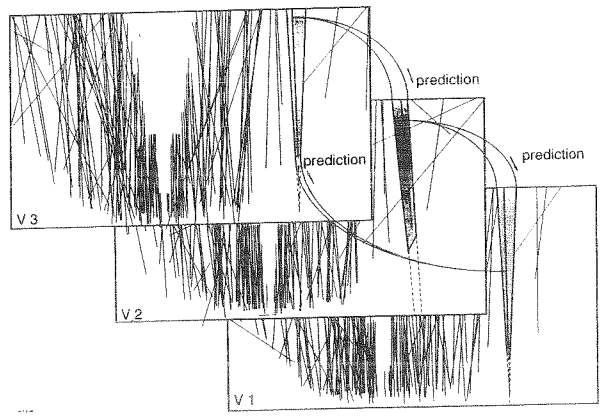


Fig. 3 Track matching in the conformal mapping of the 3 Streamer Chamer views.

[1]F. Pühlhofer, D. Röhrich, R. Keidel, Nucl. Instr. Meth. A 263 (1988) 360.

[2]R. Keidel, Automatische Auswertung von Teilchenspurbildern Ultrarelativistischer Kern-Kern Stösse, Dissertationsschrift, Marburg 1989.

TRANSVERSE ENERGY DISTRIBUTIONS IN CENTRAL S-NUCLEUS INTERACTIONS AT 200GeV/Nucleon [G]

W. Heck, S. Margetis, C. Guerra, R. Stock, H. Ströbele
Inst. für Kernphysik, Univ. Frankfurt

NA35 COLLABORATION

Central Nucleus-Nucleus collisions at 200 GeV per nucleon projectile energy, produce high energy densities over extended volumes as a precondition for new phenomena to occur. In the NA35 experiment at CERN we have systematically studied with our calorimeters, the transverse energy flow around mid-rapidity as well as the forward going energy. Those results have been reported in the GSI reports of the last two years and in ref. [1]. Extensive studies to calibrate the calorimeters and to correct for effects like non-linear response to low energy particles, shower leakage between the modules and inhomogeneties across them, were performed resulting in a rescaling of the transverse energy by a factor roughly 25% towards lower energies. All these corrected spectra will be published soon in a forthcoming publication.

In this report we present the corrected (fitted) pseudorapidity distributions for the electromagnetic component of the Et in central collisions S + Au, Ag, RbBr, Cu and S (Fig. 1). Also we present the same plot for the reaction S + Au were different lines represent different bands in transverse energy (Fig. 2). By central collisions, we mean that we select according to a simple geometrical picture reactions with high transverse energy and a cross-section corresponding to complete overlap of the two nuclei, or in other words, reactions where all the projectile nucleons participate in the reaction. Different bands of transverse energy are correlated with different impact parameters. So, the lower band reflects peripheral collisions as the higher one refers to very central events.

In Fig. 1, one sees that the reaction S + S is nicely symmetric around midrapidity (ymid. = 3). Also as the target gets heavier the peak moves backward to lower pseudorapidities reflecting the shift of the centre of mass rapidity. Indeed, as one goes from 32 + 32 nucleons in the system S + S to 32 + 85 in the case of S + Au, the centre of mass rapidity shifts from 3 in the first case to 2.6 in the latter one. The fact that we have pseudorapidity instead of rapidity does not play any role as the electromagnetic energy comes mostly from gammas, for which rapidity equals pseudorapidity.

A similar behaviour is seen for S + Au collisions, if rapidity distributions are considered in different Et bands. In peripheral collisions we essentially have few nucleons interacting with each other, giving rise nearly symmetric distributions, whereas in central collisions the asymmetry becomes more pronounced due to the difference in projectile and target participant nucleons.

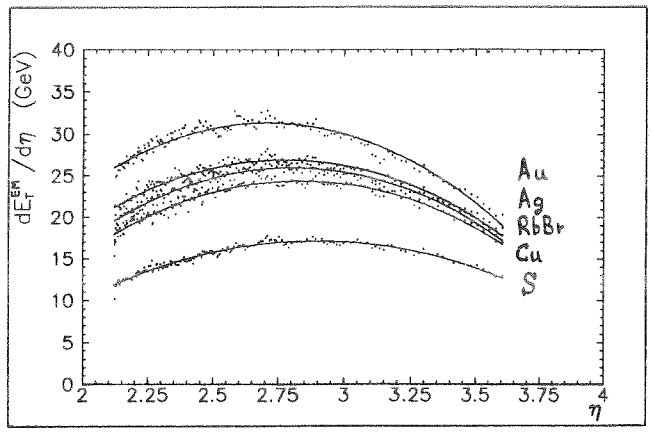


Fig. 1 : Pseudorapidity distributions of the electromagnetic component of the transverse energy for different targets.

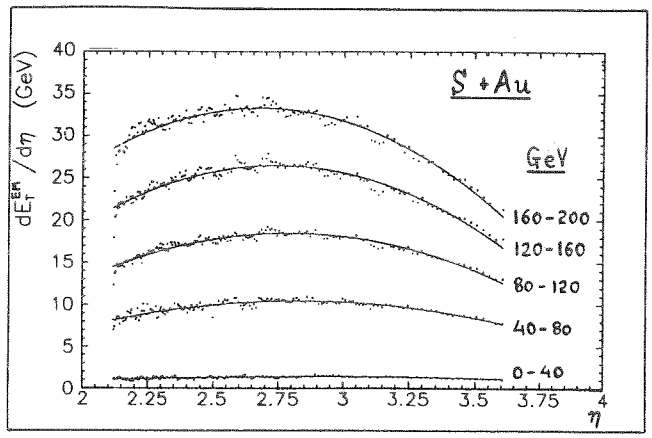


Fig. 2 : Pseudorapidity distributions of the electromagnetic component of the transverse energy for the system S + Au in different Et bands. The numbers refer to the Total Et of the event.

Although these observations reflect simple geometrical correlations, the calorimetric information is a very usefull tool to understand the collision geometry and select a class of interesting events by triggering on the energy measured by the calorimeters. Further information on calorimetric measurements from NA35 can be found in Ref. [1], [2] and [3].

References

1. NA35 Collaboration A. Bamberger et. al. Phys. Lett. B 184(1987)271
2. Quark Matter 1987 Z.Phys.C 38(1988)
3. S.Margetis PhD Thesis, Univ. Frankfurt 1990

Improving the Momentum Distribution in the Analysis of NA35 Streamer Chamber Data [B,G]

A. Piper, R. Keidel, F. Pühlhofer, Fachbereich Physik, Univ. Marburg
CERN NA35 Collaboration

In the NA35 experiment at CERN a streamer chamber is used for detecting the charged particles emitted in relativistic heavy ion collisions. The events are read out by three photographic cameras. The pictures are then digitized by a CCD camera and analyzed by operators or automatically in order to obtain the track coordinates and from them the momentum vectors of all produced particles. In some cases the accuracy with which these momentum vectors can be determined, plays a particularly crucial role. This holds for the study of two pion correlations (HBT effect) or for the statistical identification of unstable particles via measurements of the invariant mass of pairs. We therefore developed a method for improving the accuracy of the present measurements by applying digital image processing techniques.

We start with pictures in which the tracks have been premeasured either manually or automatically. Our method now consists in localizing the brighter streamers along these 'first approximation' tracks and to determine their position as precise as possible. Working with digital images of 1536 * 2048 pixels 8 bit deep and using an image processing computer the streamers are detected on a 5 * 5 pixels wide area and selected according to the following criteria:

1. general threshold in intensity,
2. local maximum in intensity,
3. shape of the intensity distribution around the maximum,
4. selection of streamers brighter than the mean on an individual track.

In detail, the third criterium compares the intensity of a local maximum to that of the surrounding pixels in the following way:

$$\begin{array}{ccccc} & & C_1 & C_2 & C_3 \\ & C_{12} & B_1 & B_2 & B_3 & C_4 \\ & C_{11} & B_8 & A & B_4 & C_5 \\ & C_{10} & B_7 & B_6 & B_5 & C_6 \\ & & C_9 & C_8 & C_7 \end{array}$$

The condition to be fulfilled is

$$A > K_1 \sum_{i=1}^{8} B_i / 8 > K_2 \sum_{j=1}^{12} C_j / 12 \quad ,$$

with K_1, K_2 being adjustable parameters.

Finally the centroids of the streamers are determined with an accuracy of about a tenth of a pixel. The track points obtained in this way for the three perspective views of the event are then read into the program which performs the spatial reconstruction of the events in the usual way.

The quality of the measurement can be judged by means of the deviation between the projections of the reconstructed tracks and the actual track points. For a sample of 160 tracks in one event we obtain for the standard deviation (transformed back to film dimensions)

32 μm for the usual operator results,

24 μm when using the streamer detector,

22 μm when including the streamer centroid measurement.

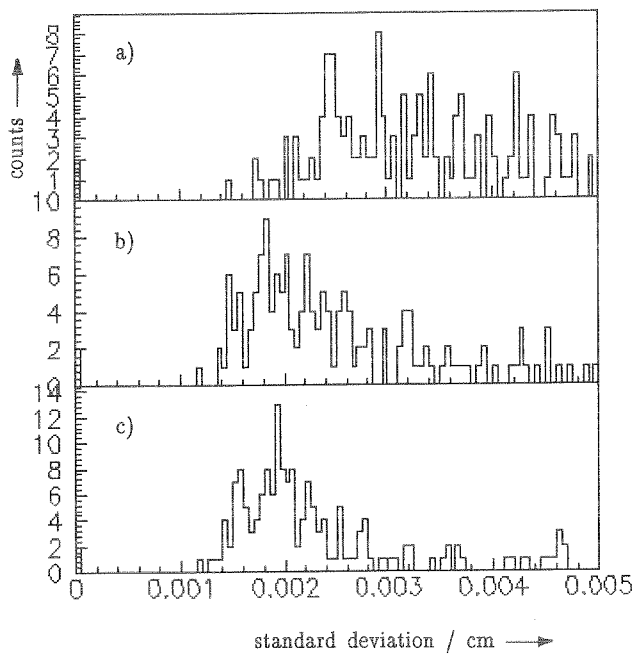


Fig. 1: Standard deviation between the projection of the reconstructed tracks and the actual track points for 160 tracks of one event (1536 * 2048 pixels) **a)** for initial measurements, **b)** after using the streamer detector, **c)** including the streamer centroid measurement.

Photon Transverse Momentum Distributions in ^{G,B} Ultrarelativistic Heavy-Ion Collisions at the CERN-SPS

WA80-collaboration
GSI-LBL-Lund-Münster-ORNL

In the WA80 experiment [1], photons are measured with the lead glass spectrometer SAPHIR [2], which covers the pseudorapidity range from $1.5 \leq \eta \leq 2.1$ and about 1/6 of the azimuthal ring. The analysis of the transverse momentum distributions of inclusive photons [3] could be refined by means of a superimposition test to correct for the effects of the high particle densities in central reactions.

For this test, peripheral 200 A·GeV $^{16}O + Au$ events with low multiplicity were superimposed by adding the ADC values. The range of the multiplicity in these artificial events could be selected by the number of superimposed events; the multiplicities were 6.2 ± 4.3, 11.7 ± 6.0, 16.5 ± 6.7, and 20.1 ± 6.8 for 1 (no) superimposition, 2, 3, and 4 events.

Comparing the input and the output from the analysis of the superimposed events, the showers could be divided into three groups: Those which were not affected by the superimposition or were found changed by less than 3%, those with one or more parameters (energy or position) changed by more than 3%, and those which were completely lost. From the p_T distributions of these showers one can calculate the ratios

$$R_p(p_T) = \frac{\text{number of unchanged showers}}{\text{number of showers in the peripheral events}} = \frac{A_i}{A_p}$$

$$R_s(p_T) = \frac{\text{number of unchanged showers}}{\text{number of showers in the superimposed events}} = \frac{A_i}{A_s}$$

Since the numerators are equal, this yields $A_p = A_s \cdot R_s/R_p$, and a way to correct the effects of the high particle densities by the correction function $K(p_T) = R_s/R_p$, which transforms the the p_T spectrum measured at high particle densities A_s to the spectrum that would have been measured in a low-density environment A_p. For the three ranges of multiplicity in the superimposed events, the function $K(p_T)$ is shown in fig. 1. The curves are fitted by a third-order polynomial in the range $0 \leq p_T \leq 1.75$ and by a straight line above this value. These corrections tend to increase the tails of the p_T distributions and thus to change the slope parameters of the exponential distributions. The corrected p_T distributions for central events are shown in fig. 2. The spectra contain about 10% of the minimum bias cross section after a selection of events with the highest charged particle multiplicity. Also shown is the prediction of the FRITIOF model for the system 200 A·GeV $^{16}O + Au$ and the results of the parametrization $dN/dp_T \sim \exp(p_T/T)$, which was fitted to the data. The slope parameters T for the different reaction systems and for the distributions from peripheral events are given in table 1. Due to the correction, the parameters for the most central systems are about 15 MeV/c higher than stated in earlier publications and thus even farther off the FRITIOF prediction. This rules out the possibility that the observed differences between the data and the FRITIOF prediction are generated by detector effects due to the high particle density.

[1] H. H. Gutbrod et al., *Study of Relativistic Nucleus-Nucleus Collisions at the CERN-SPS*, GSI preprint GSI-85-32 and CERN SPSC/85 – 39/M406 (1985)

[2] H. Baumeister et al., *Design and Performance of the SAPHIR Lead Glass Spectrometer*, submitted to Nucl. Instr. and Meth.

[3] WA80 Collaboration, Phys. Lett. **B 201** (1988) 390–396

System	T(MeV/c)	
	central	peripheral
200 A·GeV $^{16}O + Au$	247.3 ± 2.4	190.2 ± 1.6
60 A·GeV $^{16}O + Au$	230.2 ± 2.1	183.0 ± 1.9
200 GeVp + Au	214.3 ± 3.0	184.1 ± 3.6
200 A·GeV $^{16}O + C$	200.2 ± 3.0	182.9 ± 2.8
FRITIOF	161.0 ± 1.1	160.2 ± 3.1
200 A·GeV $^{16}O + Cu$	216.0 ± 1.5	
200 A·GeV $^{32}S + Al$	227.1 ± 2.4	
200 A·GeV $^{16}O + Ag$	241.2 ± 3.2	
60 A·GeV $^{16}O + Ag$	228.9 ± 3.1	

Table 1: Slope parameters for different reaction systems.

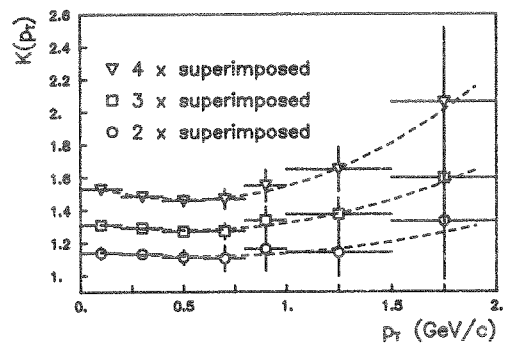


Figure 1: Correction function $K(p_T)$ with the polynomial fits

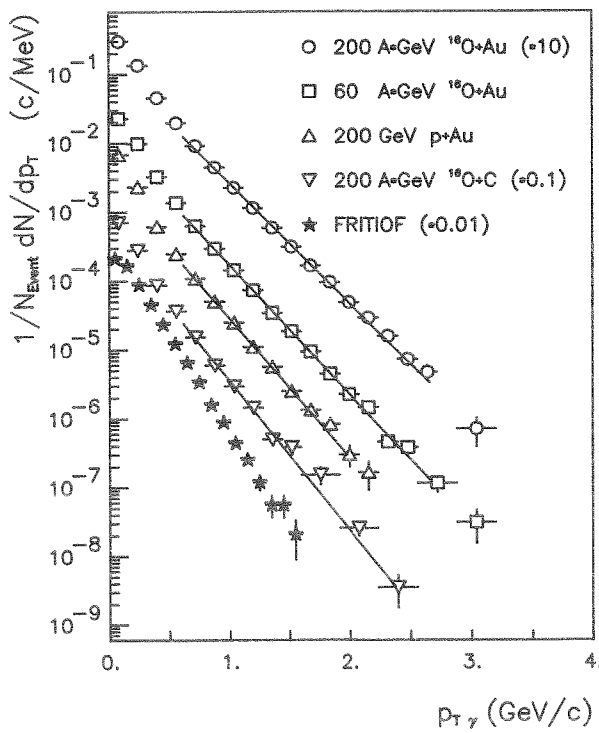


Figure 2: p_T distributions for photons from central events

Transverse Energy Production in the Target Fragmentation Region and the Formation Time of Secondary Hadrons [G,B]

WA80-collaboration
GSI-LBL-Lund-Münster-ORNL

Nucleon-nucleus and nucleus-nucleus collisions at ultrarelativistic energies offer the interesting opportunity to investigate the space-time development of the formation of secondary hadrons because the nucleons in a nucleus serve as detectors of the products of the initial collision. It has been observed in hadron-nucleus collisions [1] that an excess of particles over the predictions from linear string models exist in the backward rapidity region. It was only recently that string models have been combined with intra-nuclear cascading [2,3]. In these models a phenomenological parameter, τ, which has to be determined from experiment, controls the formation time of secondaries and hence the strength of the coupling of the participant matter to the target spectator matter. Measurements in the target fragmentation region might therefore also serve to extract fundamental information about the time scale of hadron creation.

The present data were measured employing the Plastic Ball detector. This detector, which was formerly employed as a 4π-detector at the BEVALAC at Berkeley, has been incorporated into the WA80 experiment in order to cover the target rapidity region.

We compare our experimental result with model calculations done with Ranft's Multi-Chain Fragmentation Model (MCFM) [2], which is modified by a leading order formation zone cascade. The transverse energy distribution of baryons at backward rapidities is strongly influenced by the cascading of secondary particles in the traget spectator, i.e. it is sensitive to the choice of the formation time parameter entering the model calculations.

Fig. 1 shows transverse energy distributions of baryons for O+Au, Ag and Cu in the range $-1.7\leq\eta\leq0.6$. The circles and crosses represent calculations for τ_0=5 and 10 fm/c. In neither case are the data at all reproduced. The calculation for τ_0=10 fm/c underestimates $\langle E_t^{central,baryon}\rangle$ by a factor of 5; for τ_0=5 fm/c the data are still underestimated by a factor of 2. The failure of the model to reproduce the data even for very small values of τ_0 can be traced back to the observation that the model already can't to reproduce the slope of the proton momentum spectrum as shown in Fig. 2 The experimental spectrum is much flatter than the simulated one.

It has to be left to further theoretical investigations if a full intra-nuclear cascade [3], which includes all subsequent collisions of hadrons created in turn in the secondary collisions and so on, will better agree with the data.

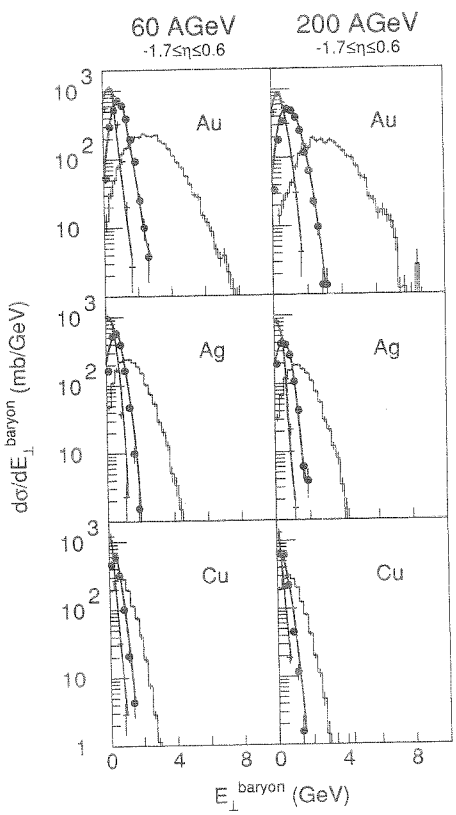


Fig. 1 Transverse energy spectra of baryons in the range $-1.7\leq\eta\leq0.6$ The histogram represents the measured data while the circles and crosses show calculations within Ranft's MCFM assuming formation zone parameters τ_0 of 5 and 10 fm/c, respectively. The solid lines are to guide the eye.

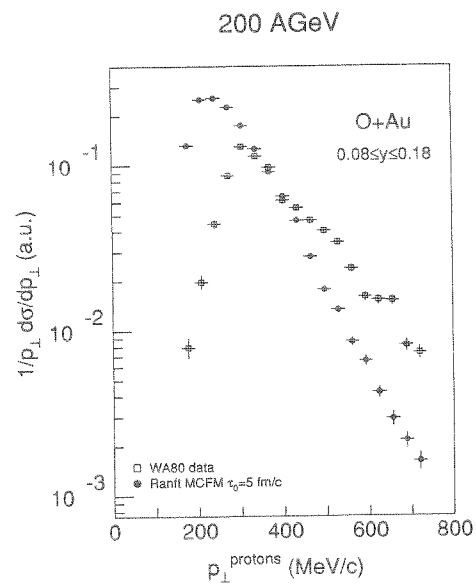


Fig. 2 Invariant cross section $1/p_t\ d\sigma/dp_t$ of protons in the range $0.08\leq y\leq0.18$. The open squares represent the measured data and the filled circles the calculations within Ranft's MCFM assuming a formation zone parameter τ_0=5 fm/c.

[2] J. Ranft, Phys. Rev. D37 (1988) 1842
J. Ranft, preprint CERN-TIS/Rp 219/PP (1988), submitted to Z. Phys. C

[1] W. Busza and R. Ledoux, Ann. Rev Nucl Part. Sci. 38 (1988) 119

[3] V.D. Toneev, private communication (1989)

Statistical Moments of Transverse Energy, Charged Particle Multiplicity and Forward Energy Distributions[G,B]

WA80-collaboration
GSI-LBL-Lund-Münster-ORNL

One of the main features of the WA80 experiment is its nearly 4π coverage for an ultrarelativistic heavy ion event. The WA80 experiment measures the forward energy (E_{ZDC}) close to the beam (η>6, η=-ln(tan(ϕ/2))), the charged particle multiplicity (CPM) between -1.7<η<4.0, and the transverse energy (E_T) between 2.4<η<5.5.

In several publications [1] correlations between E_{ZDC} and E_T, E_{ZDC} and CPM or E_T and CPM have been shown. (The latter should give a measure of the average p_T per particle.) Narrow correlations are observed among these quantities. If these three quantities are related, it seems reasonable to study a simultaneous analysis of all three. This can overcome certain shortcomings of analyzing them only pairwise. For example, if the CPM is analyzed as a function of E_{ZDC} and the width of the CPM distribution is measured, one in effect takes slices parallel to the E_{ZDC} axis from the 3-D ellipsoid of E_{ZDC} vs. CPM vs. CPM and projects the distribution onto the CPM axis. If the E_{ZDC} window is wide, this slicing can disturb the tails of this projection, resulting in wrong interpretations of the data.

Preliminary results of an analysis measuring the widths of the ellipsoid are presented using the information from all three variables simultaneously. The range 2.4<η<4.0 is covered for CPM and E_T. This analysis was stimulated by recent claims [2] that the widths of the CPM and E_T distributions seen in heavy ion collisions are too wide to be explained by an independent source model and that therefore coherence has to be assumed. However, detector effects, such as inefficiencies and resolutions, were not taken into account in the analysis described in [2]. Inclusion of these effects significantly modifies the concluisions drawn. In addition, a more detailed analysis by the WA80 collaboration [3] shows that this effect is not so large as predicted by [2] and can be, within the present limits, understood by "string" models without assuming coherent effects .

The analysis described here takes the full information of all three variables simultaneously and analyzes the widths of the ellipsoid by an eigenvector analysis and compares the results to the Monte Carlo code Fritiof.

For simplicity in the following, CPM is referred to as X, E_T as Y, and E_{ZDC} as Z. The total number of events analyzed in the sample is called N. After the dataset is transformed into it's "Center of Gravity":

$$c_\alpha = \overline{x_\alpha} = \frac{1}{N}\sum_{i=1}^{N} (x_i)_\alpha \ , \alpha = x,y,z$$

a dispersion matrix D is constructed by:

$$\tilde{D} = \begin{pmatrix} \frac{1}{N}\sum_{i=1}^{N} x_i x_i & \frac{1}{N}\sum_{i=1}^{N} y_i x_i & \frac{1}{N}\sum_{i=1}^{N} z_i x_i \\ \frac{1}{N}\sum_{i=1}^{N} x_i y_i & \frac{1}{N}\sum_{i=1}^{N} y_i y_i & \frac{1}{N}\sum_{i=1}^{N} z_i y_i \\ \frac{1}{N}\sum_{i=1}^{N} x_i z_i & \frac{1}{N}\sum_{i=1}^{N} y_i z_i & \frac{1}{N}\sum_{i=1}^{N} z_i z_i \end{pmatrix}$$

This matrix is then transformed into diagonal form, where the elements in the diagonal, which are now eigenvalues, are labelled λ_i. These values represent the variance of the point distribution along these new axes. The correlation observed among the new coordinates are minimal. The direction of these axes are given by the eigenvector equation :

$$\tilde{D} \cdot \vec{a_i} = \lambda_i \vec{a_i} \ , \ i=1,..,3$$

The eigenvalues are ordered so that $\lambda_1 > \lambda_2 > \lambda_3$. Then the a_1 axis represents the direction in which the variance (λ_1) of the pointdistribution is largest.

The point distribution is then transformed into the new coordinate system and the width of the new distribution along the a_2 and a_3 axes is analyzed by making four slices along the first axis.

In order to understand the width of this distribution, it is compared to Fritiof simulations. Figure 1 shows the average and "standard deviations" (σ) of the ellipsoid along axis a_2 and a_3 for the four cuts made along axis a_1. On the left are the results from Fritiof without detector effects, in the middle are the results from Fritiof with those effects included, and on the right are the data from the WA80 experiment. These diagrams show how the data can be accurately reproduced when taking the detector effects into account.

The analysis will be continued for different projectile and target combinations. It will finally tell us more about the correlations involved in the measured quantities.

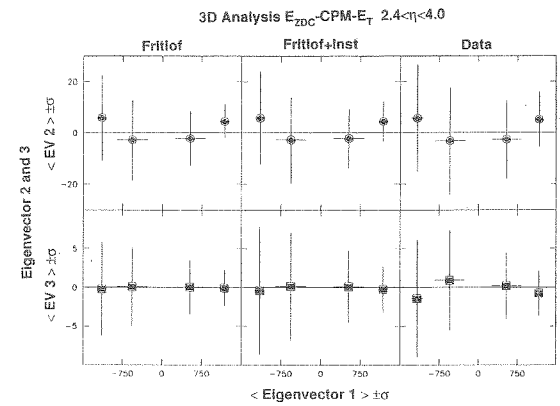


Fig. 1 Average and standard deviation of the pointdistribution for "pure" Fritiof (left), Fritiof including detectoreffects (middle), WA80 data (right).

[1] See e.g. "Proceedings of QuarkMatter 87", Zeitschrift fur Physik C 38, 3-14; or "Proceedings of Nucleus Nucleus Collisions III", Nuclear Physics A448 (1988) 651c-644c; or Phys. Lett. B199, 297-303 (Dec.1987); or Phys Lett. B 202, 596-602 (Mar. 1988).

[2] "Fluctuations and Coherence in Ultrarelativistic Heavy-Ion Collisions", Gordon Baym et al., LA-UR-88/3964

[3] "Global and Local Fluctuations in Multiplicity and Transverse Energy for Central Ultrarelativistic Heavy-Ion Reactions", R.Albrecht et al., submitted to Zeitschrift fur Physic C.

Correlations of Charged Pions in 200 A GeV O + Au Collisions [G,B]

WA80-Collaboration
GSI - LBL - Lund - Münster - ORNL

Two particle correlations have been investigated in the WA80 experiment in 200 A GeV O + Au reactions at the CERN SPS. For this analysis π^+ measured with the Plastic Ball detector [1] in the target rapidity region ($\eta \leq 1.3$) are used. Stopped pions ($E_{kin} \leq 150$MeV) can be identified by their sequential decay $\pi^+ \rightarrow \mu^+ \rightarrow e^+$. From the decay time spectrum the contamination of misidentified particles is estimated to be of the order of 5%.

The two-particle correlation function:

$$C_2 = \frac{d^6\sigma/dp_1^3dp_2^3}{d^3\sigma/dp_1^3 \cdot d^3\sigma/dp_2^3}$$

is evaluated in dependence of the absolute value of the four-momentum difference $Q = \sqrt{-(p_1 - p_2)^2}$ of the two pions by calculating the ratio of the two-particle distribution with a background distribution. This background distribution is obtained by taking pions from different events (event mixing), where both events have the same pion multiplicity.

The lower limit of the measurable momentum differences imposed by the module size is $Q_{min} \approx 8$MeV. To correct for the granular structure of the detector the position of incidence of the particles is smeared randomly over the surface of the individual modules. The correlation functions are then corrected for the final state Coulomb interaction with the so-called Gamow-factor.

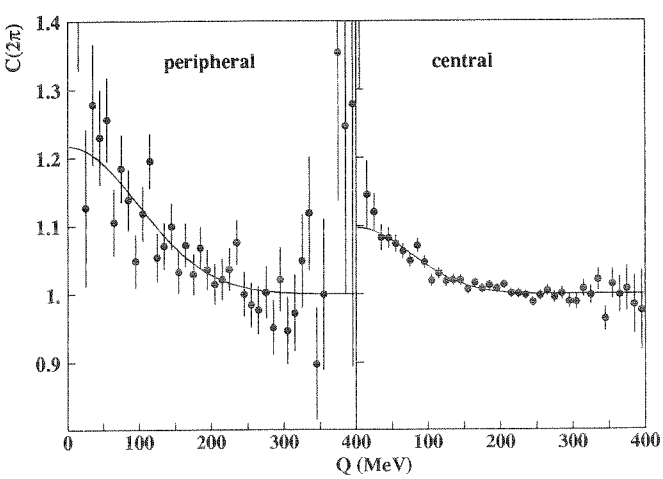
In the WA80 experiment a centrality selection can be obtained with the help of the Zero-Degree Calorimeter. We divide our data sample into peripheral and central collisions according to the energy deposited in the Zero-Degree Calorimeter and investigate the correlation function separately. The figure shows correlation functions extracted for peripheral and central O + Au reactions.

In both cases a rise can be seen for small relative momenta, which can be interpreted as being caused by Bose-Einstein interference [2]. Assuming a Gaussian source distribution we can fit the following expression to the correlation function:

$$C_2 = N \cdot (1 + \lambda e^{-\frac{1}{2}Q^2R^2}),$$

where the normalization N, the correlation strength λ and the correlation length R are free parameters. The fits were obtained using a maximum-likelihood method. The fits are also shown in the figure, fit parameters are given in the table below. It can be seen, that the R-parameter is slightly larger in the central collisions and, on the other hand, that the correlation appears to be much stronger in the peripheral collisions.

	N_{pairs}	R (fm)	λ
peripheral	45000	2.0 ± 0.4	0.22 ± 0.02
central	850000	2.6 ± 0.2	0.10 ± 0.01



[1] A. Baden et al., Nucl. Instr. Meth. 203 (1982) 189

[2] R. Hanbury-Brown and R.Q. Twiss, Nature 178 (1956) 1046; G. Goldhaber et al., Phys. Rev. 120 (1960) 300; G.I. Kopylov and M.I. Podgoretskii, Sov. J. Nucl. Phys. 15 (1972) 219; 18 (1974) 336

Calorimetry Results from WA80 [G,B]

WA80-collaboration
GSI-LBL-Lund-Münster-ORNL

The main purpose of the Midrapidity Calorimeter (MIRAC) in the WA80 setup is to provide a reliable measure of the transverse energy, E_T, generated in high-energy nuclear collisions. E_T is an approximate Lorentz-invariant quantity defined as

$$E_T' \equiv \Sigma E_i \sin\vartheta_i$$

where E_i and ϑ_i are the energy and scattering angle of the i^{th} particle. The sum runs over all produced stable particles. Since hadronic calorimeters in high multiplicity environments are not able to resolve individual particles, the usual experimental approach has been to extract E_T as

$$E_T \equiv \Sigma E_i c_i$$

where E_i is the total energy recorded in the i'th subsection of the calorimeter and c_i is a coefficient adjusted from simulations so $\langle E_T \rangle = \langle E_T' \rangle$. Ci will typically be close to $\sin\vartheta_i$, where ϑ_i is the azimuthal angle of the i'th subsection. In MIRAC the smallest unit is the phototube. It is, however, not only the total integrated E_T impinging on the calorimeter which is of interest. In addition, the more detailed information concerning the angular distribution of the produced transverse energy and its division between hadrons and "electromagnetic" (EM) particles (= electrons + photons and photons from the decay of neutral pions) is of considerable interest. This information can conveniently be expressed in terms of the pseudorapidity distributions, $dE_T/d\eta$, for both hadrons and EM particles.

Considerable effort has been invested in investigating different procedures for extracting $dE_T/d\eta$ from the MIRAC data. Most work has gone into methods based on various unfolding techniques. If α is an index running over a suitable set of pseudorapidity η-bins for both hadrons and EM particles, and if i runs over all 720 tubes of MIRAC, then the average signal S_i in the i^{th} tube can be expressed as

$$S_i = \sum R_{i\alpha} E_\alpha \qquad (1)$$

where E_α is the energy carried by particles in η bin α and $R_{i\alpha}$ is the η-response function of MIRAC. The matrix R can be calculated from simulation of MIRAC's parameterized response to various particles. This response to single particles is known from extensive calibration measurements at CERN. In matrix notation, Eq. (1) can be written

$$\mathbf{S} = \mathbf{R}\,\mathbf{E}$$

and the $dE_T/d\eta$ distribution can, therefore, in principle, be found either by directly inverting R,

$$\mathbf{E} = \mathbf{R}^{-1}\,\mathbf{S}$$

or by utilizing various linear unfolding techniques. The outcome of these investigations, however, have been negative in the sense that no unfolding algorithm was able to produce reasonable $dE_T/d\eta$ distributions when applied to the experimental data. A more conventional and conservative approach which is based on reproducing the average behavior of the data has, therefore, been selected. The core of the method consists of creating the η-distribution coefficients, $D_{\alpha i}$, defined as the fraction of the calibrated signal e, originates from the η interval α. $D_{\alpha i}$ is calculated as

$$D_{\alpha i} = \frac{\langle E_{\alpha i} \rangle_{events}}{\langle S_i \rangle_{events}}$$

where the average is taken over a large number of simulated events from a Monte-Carlo event generator (in our case either FRITIOF or VENUS). S_i is the calibrated signal in the i^{th} tube, and $E_{\alpha i}$ is the energy in the i^{th} tube originating from η-interval α. $dE_T/d\eta$ can now be calculated as

$$\frac{dE_T}{d\eta}(\alpha) = \frac{\sin\vartheta_k}{N_k \Delta\eta_k} \sum_j D_{\alpha j} S_j$$

on an event-by-event basis. ϑ_k is the scattering angle corresponding to η-interval α; $\Delta\eta_k$ is the η-width of that interval; and finally, N_k is the fraction of the total energy emitted in α recorded by MIRAC. N_k will vary from 5-10% at η = 1.6-2.0 to 100% at η = 3.0-4.0. A potential disadvantage of this method using the distribution function D is that the results might be sensitive to the event topology of the event generator. The algorithm has, therefore, been tested for several different event topologies. It was found that different distribution functions had to be used for 60- and 200-A-GeV reactions, but distribution functions for various projectile-target-event-generator cases did not differ much at a fixed bombarding energy.

Figure 1 shows a preliminary dE_T/d_h distribution for 200-A-GeV ^{16}O + ^{197}Au based on WA80 minimum-bias data. Note the differences in the centroids for the electromagnetic and hadronic energy.

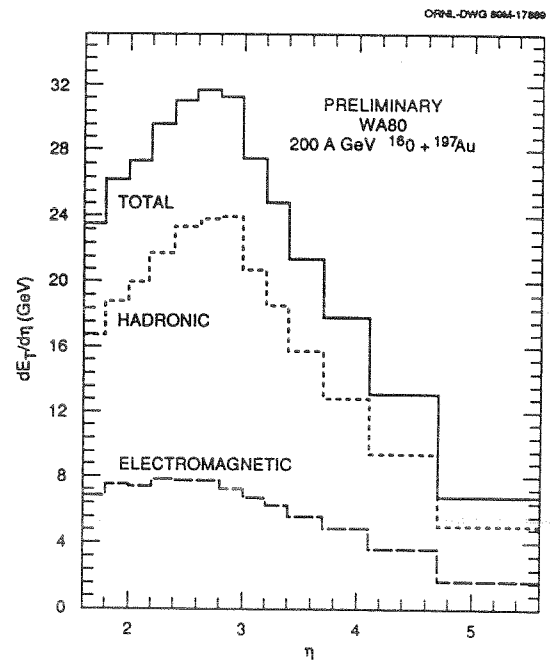


Fig. 1. Preliminary results from WA80 minimum-bias data for $dE_T/d\eta$ for 200-A-GeV ^{16}O + ^{197}Au. The three histograms shown from the top and down: total, hadronic, and electromagnetic $dE_T/d\eta$. Statistical and systematic errors are currently being evaluated.

Energy-Density Estimates from ^{16}O- and ^{32}S-induced reactions [G,B]

WA80-collaboration
GSI-LBL-Lund-Münster-ORNL

Energy-density estimates might be obtained based on the measured E_T since this should directly reflect the amount of thermalized energy. The major source of uncertainty is then to obtain a reliable estimate of the volume over which the observed energy was initially available. The most commonly used method to estimate the energy density is the following relationship first suggested by Bjorken[2],

$$\varepsilon = \frac{1}{F\tau}\frac{dE_T}{d\eta}\bigg|_{\eta_{max}} \qquad (1)$$

in which the differential transverse energy $dE_T/d\eta(\eta=\eta_{max})$ observed at midrapidity is associated with a differential volume of transverse area F corresponding to the area of nuclear overlap and thickness τ related to the particle formation time.

An alternative method is motivated by the observation that, for central collisions, the total transverse energies observed account for a large fraction of the energy available in the center of mass, and therefore indicate a large degree of nuclear stopping. In this case an integral estimate of the energy density may be made as

$$\varepsilon = \frac{1}{FL}\int d\eta \frac{1}{\sin\vartheta_{cm}}\frac{dE_T}{d\eta} \qquad (2)$$

where the total available energy has been obtained by integrating a gaussian $dE_T/d\eta$ distribution fitted to the forward η region. The total volume in the center of mass is given by the transverse area F times L, the total Lorentz contracted length of the stopped system, as seen in the center-of-mass frame. Most estimates have assumed that the initial conditions are such that the smaller projectile is stopped within the target volume[3,4] as suggested many years ago by Landau[5], and have assumed L to be the contracted target length. Alternatively, one may imagine initial conditions as suggested by Bjorken[2] in which, as in the capacitor-plate analogy, after passing through one another, the receding nuclei are nearly stopped due to the energy stored in the intervening color fields. In this case the appropriate total length might be the sum of projectile and target lengths plus the intervening stopping distance LS.

The systematic dependence of these various energy-density estimates on the total nucleon thickness $A^{1/3} + A^{1/3}$ is shown in Fig. 1. It is seen that estimates based on the assumption of Landau-stopping, in which the projectile is completely stopped within the target volume, give estimates roughly 3-6 times larger than estimates based on the Bjorken-type initial conditions. Moreover, the fact that the energy density decreases with increasing thickness of the system is difficult to interpret, given that the stopped energy fraction is observed to be nearly constant but less than one. On the other hand, it is observed that the integral and differential estimates assuming Bjorken-type initial conditions show a systematic increase with increasing thickness of the system, as might be expected for overlapping color strings. A stopping distance of LS = 4 fm gives values consistent with those obtained for a 1 fm/c formation time at about 2-3 GeV/fm^3 for the heavy systems. This is similar to recent calculations[1]. It also may be observed that the average energy density is not expected to increase significantly for reactions of Pb + Pb; however, the core energy density and volume is expected to increase substantially.

In addition to the observation that the total E_T/participant is constant when integrated over the forward pseudorapidity region $2.4 < \eta < 5.5$, it is similarly found that $dE_T/d\eta(\eta=\eta_{max})$/participant is also constant with a value of about 1 GeV/participant for all systems and impact parameters. Using this information we may generalize upon Eq. 1 and calculate the radial energy density profile according to the participant nucleon profile. The result is shown in Fig. 2 for zero impact parameter collisions of O, S, and Au on Au at 200 GeV/nucleon. The comparison between the different systems is now much more dramatic than the volume average comparison in that one expects a 30% higher central energy density for Au projectiles. In fact, it is seen that if the energy density necessary for the phase transition corresponded to 3 GeV/fm^3 on the indicated scale, then reactions of Au on Au would provide a cylindrical volume about 10 fm across significantly above the critical energy density while the other projectiles would fall below the critical energy density.

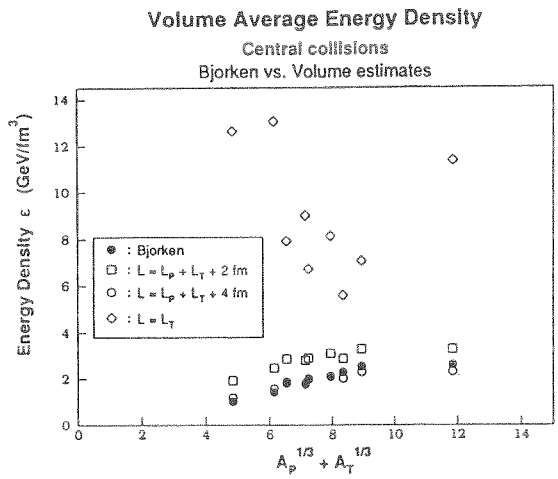


Fig. 1. Energy-density estimates by various methods for 200-GeV/nucleon ^{16}O- and ^{32}S-induced reactions as a function of the total thickness of the interacting system. The Pb + Pb points are based on an extrapolation of the observed E_T scaling.

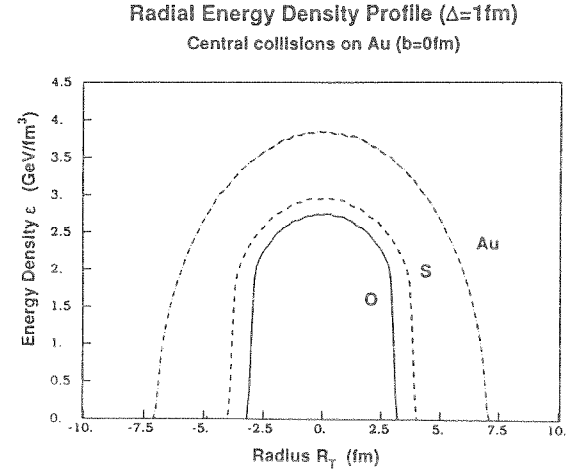


Fig. 2. The estimated energy density profile for zero impact parameter collisions of O, S, and Au on Au at 200 GeV/nucleon based on Eq. 1 and the observed scaling of the transverse energy.

[1] K. Werner et al., Phys. Lett. B 219, 111 (1989).
[2] J. D. Bjorken, Phys. Rev. D 27, 140 (1983).
[3] A. Bamberger et al., Phys. Lett. B 184, 271 (1987).
[4] J. Stachel and P. Braun-Munzinger, Phys. Lett. B 216, 1 (1989).
[5] L. D. Landau, No. 88, Izv. Akad. Naul. SSSR, Ser. Fiz. 17, 51 (1953).

Global and Local Fluctuations for Central Ultra-Relativistic Heavy-Ion Interactions [G,B]

WA80-collaboration
GSI-LBL-Lund-Münster-ORNL

The results of the 200 A GeV oxygen and sulphur runs at the CERN SPS indicate that central collisions give rise to multiplicity and transverse energy distributions of Gaussian shape[1]. The results from ^{16}O+Au are displayed in figure 1. E_{ZDC} is the energy deposited in a narrow forward cone

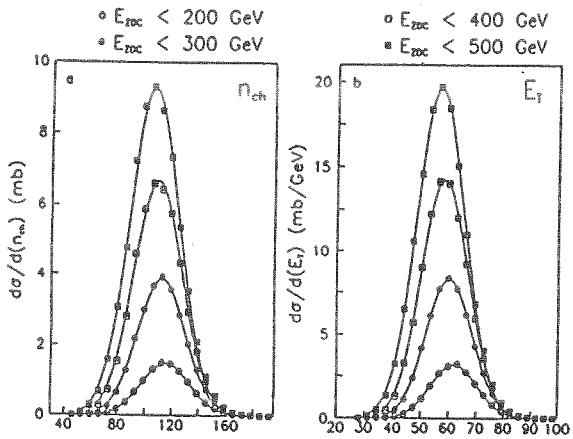


Fig. 1. a) multiplicity and b) transverse energy distributions for ^{16}O+Au at 200 A GeV. The data have been fitted by gaussians.

as measured by the WA80 zero degree calorimeter. A smaller amount of energy in this cone relates to more central collisions. E_{ZDC} < 400 GeV corresponds to about 10% of the minimum bias cross section.

It is believed that the width of the multiplicity and transverse energy distributions contain information about the reaction mechanism as well as the nuclear geometry involved. Baym et al.[2] have shown that the variance of a distribution can be divided into four terms and each of these terms can be given a physical interpretation. With the help of a Monte Carlo event simulator it is possible to calculate these terms for different centrality cuts. The model used in this analysis was the Fritiof Monte Carlo code which has been frequently used to compare with experimental data. The outcome of the analysis was that the number of sources in a collision gives the most important contribution independent of if they were chosen to be the participants or the number of binary collisions. This was particularly clear when a minimum bias sample was considered. Energy degradation was shown to be only of minor importance.

The region of observation also influences the widths of the measured distributions. The smaller region of phase space we use in our analysis the larger are the fluctuations and hence the widths. If the fluctuations are of a purely statistical nature the normalized variance, Ω, of a distribution can be related to the width of the observation window, $\Delta\eta$, and the mean charged particle density in that window, $\langle\rho\rangle$;

$$\Omega - (\Delta\eta\cdot\langle\rho\rangle)^{-1} = \text{constant} \qquad (1)$$

Figure 2 contains the results both from the WA80 data and from the Fritiof model.

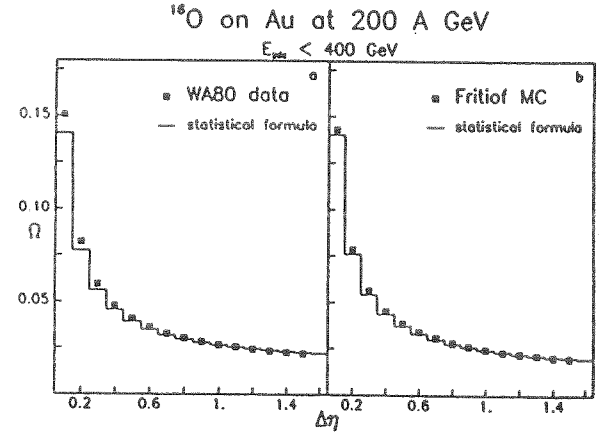


Fig. 2. The normalized variance, Ω, as a function of $\Delta\eta$ for a) the WA80 data and for b) a Fritiof sample.

The constant in formula 1 has been normalized to the data at $\Delta\eta$=1.0. The formula describes the data well except at low $\Delta\eta$ which can be explained by contributions from two-particle correlations. This demonstrates that the observed local fluctuations to a large extent are determined by the underlying global ones.

References

1. R Albrecht et al., Z Phys C45(1989)31 and references therein.
2. G Baym et al., Phys Lett B219(1989)205.

KNO-Scaling of Charged-Particle Multiplicity Distributions[G+B] in $^{16}O + Au$-Reactions at 60 and 200 A GeV

WA80-Collaboration

GSI-LBL-Lund-Münster-ORNL

The streamer-tube detectors of the WA80-collaboration [1,2] allow the measurement of charged-particle multiplicity distributions in the pseudo-rapidity interval $1.2 \leq \eta \leq 4.2$ with good position resolution. Due to the very low energy detection threshold secondary particles (mostly pions) as well as protons are counted. The multiplicity distributions and particle densities in pseudo-rapidity for different targets, energies and centralities are discussed in [3]. The probability P_n to observe n charged particles in a reaction is given by the partial cross-section σ_n normalized to the minimum-bias cross-section σ_{MB}. The mean $< n >$ of the multiplicity distribution with up to N charged particles can be calculated by :

$$< n >= \sum_{n=1}^{N} n P_n \qquad (1)$$

The minimum-bias data for 60 and 200 *A GeV* $^{16}O + Au$-reactions have also been investigated by looking for a scaling law of the two distribubion in the mean $< n >$. Such a behaviour (*KNO-scaling*) was predicted [4] and experimentally confirmed [5] for *pp*-reactions in the same beam-energy range. To compare the different curves the transformations :

$$\begin{aligned} n \quad &\rightarrow \quad z \quad = \quad \frac{n}{< n >} \text{ and} \\ P_n \quad &\rightarrow \quad \Psi(z) \quad = \quad < n > P_n \end{aligned} \qquad (2)$$

are applied.

The requirement in the minimum-bias trigger to take only collisions with an energy in the Zero-Degree Calorimeter (E_{ZDC}) of less than 88 % cuts out the very peripheral reactions and therefore the events low multiplicities. This leads to an estimate of the mean value, which is higher than the unbiased number. The shift of the center-of-mass center, going from 60 to 200 *A GeV*, and the fixed position of the ZDC results in a stronger bias for the higher energy. This effect has been corrected for by sampling the distributions with different upper cuts in E_{ZDC} and extrapolating to the "true" minimum-bias mean of E_{ZDC} = 100%. The error of this procedure was estimated with the event generators FRITIOF [6] and VENUS [7], where the trigger effect can be simulated, and was found to be less than 7 %.

Fig. 1 shows the charged-particle distribution of the $^{16}O + Au$-system for the two energies in *KNO* variables. Except for the very low multiplicities which are strongly distorted by the trigger cut, the scaling seem to be valid for the produced particles and the participants. Such a finding has also been reported for the negative particles [8] and the charged secondaries [9].

For the *pp*-case the *KNO*-scaling is derived from the limited fragmentation and Feynman scaling. The shape of the multiplicity distributions in heavy-ion collisions is mainly determined by the geometry of the reaction system, which should be independent of the energies. The combination of both results in the picture of independent nucleon-nucleon collisions could explain the existence of the scaling in heavy-ion reactions.

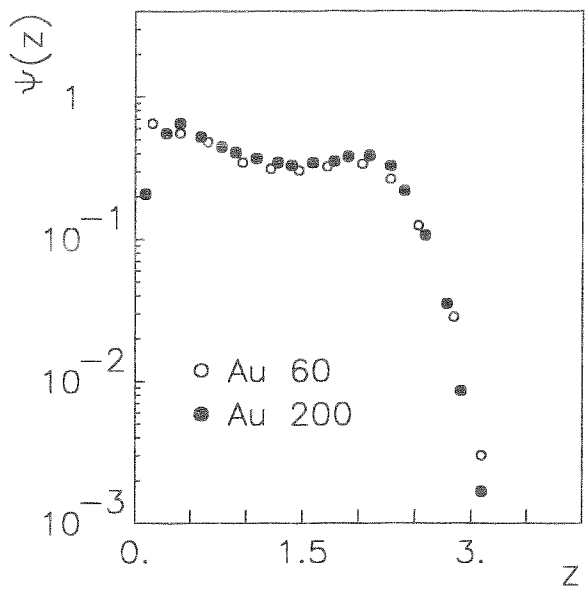


Fig. 1: Charged-particle multiplicity distributions for $^{16}O + Au$-reactions at 60 (o) and 200 *A GeV* (•) in *KNO* variables.

References

[1] R. Albrecht et al., Aug. 1985, Study of Relativistic Nucleus-Nucleus Collisions at the CERN-SPS, preprint:CERN-SPSC/85-39 and GSI-85-32.

[2] R. Albrecht et al., Nucl. Instr. and Meth. **A276** (1989) 131–139

[3] R. Albrecht et al., Phys.Lett. **B202** 1988 596–602

[4] Z. Koba, H. Nielsen, and P. Olesen, Nucl. Phys. **B40** (1972) 317–334.

[5] P. Slattery, Phys.Rev.Lett. **29** (1972) 1624–1626.

[6] B. Nilsson-Almqvist and E. Stenlund, Comput. Phys. Commun. **43** (1987) 387-397.

[7] K. Werner, Z. Phys. C – Particles and Fields **C42** (1989) 85.

[8] A. Bamberger et al., Phys.Lett. **B205** (1988) 583–589.

[9] M. Adamovich et al., Phys.Lett. **B223** (1989) 262–266.

Transverse Momentum Distributions of Neutral Pions from Heavy-Ion Collisions

G+B

1.2.3

WA80 COLLABORATION
GSI-LBL-Lund-Münster-ORNL

The production of neutral pions by the interaction of 200 A GeV p, ^{16}O, and ^{32}S projectiles with different targets has been studied with the highly segmented lead glass detector SAPHIR [1] in the pseudorapidity range $1.5 \leq \eta \leq 2.1$.

Neutral pions are identified by their decay photons ($\pi^0 \rightarrow \gamma\gamma$) and p_T distributions are obtained by accumulating invariant mass spectra for different bins of $p_T(\gamma\gamma)$. The combinatorial background below the invariant mass peak was fitted by a polynomial and subtracted from the spectrum, leading to a gaussian π^0 mass peak. Finally, these momentum distributions have been corrected for the geometrical acceptance, obtained by Monte Carlo simulations, and the total γ reconstruction efficiencies [2].

In Fig. 1 invariant π^0 cross sections are plotted for minimum bias events. Following a suggestion by Hagedorn [3], the $E\,d^3\sigma/dp^3$-spectra were parameterized by the expression :

$$E\frac{d^3\sigma}{dp^3} = \begin{cases} A\ \exp(-m_T/T) & \text{for } p_T \leq 0.8\,GeV/c \\ C\ \left(\frac{p_0}{p_T+p_0}\right)^n & \text{for } p_T \geq 0.8\,GeV/c \end{cases}, \quad (1)$$

where A, T, C, p_0 and n are parameters and m_T is the transverse mass ($m_T = \sqrt{p_T^2 + m^2}$). The first expression is an approximation to a thermal distribution; the second is an empirical formula, inspired by QCD. The requirement that in both expressions the values and the slopes match at $p_T = 0.8$ GeV/c leaves three free parameters, e. g. A, T, and n. The fit results are also shown in Fig. 1. Variations are found for the parameter n, indicating that the spectra show different behaviour in the p_T range above 0.8 GeV/c. However, as already mentioned in Ref. [3], the parameters p_0 and n are highly correlated and hence no obvious interpretation can be given for n. Nevertheless, for the parameter T no significant change for the different data sets is observed. As T also largely determines the mean transverse momentum this finding is consistent with results from Ref. [4], where nearly no variation of the mean transverse momentum for charged pions as a function of centrality and for different systems has been found.

The variation in the shape of the p_T spectra is even more pronounced by normalizing the π^0 spectra from peripheral and central ^{16}O+Au collisions to the $\pi^\pm$ cross sections from inclusive p+p reactions [5] (see Fig. 2). There is a remarkable similarity of the pion cross sections from peripheral ^{16}O+Au and p+p reactions, while the difference between the π spectrum from central ^{16}O+Au and p+p events is obvious. The ratio with central ^{16}O+Au data increases with p_T up to $p_T \approx 1.8$ GeV/c and becomes flat or even decreases at higher transverse momenta. Therefore, it appears that the hard-scattering component of the elementary p+p interactions, starting at about $p_T \approx 1.8$ GeV/c, survives in peripheral heavy-ion collisions, but in the present p_T range it is strongly obscured by nuclear effects in central collisions.

[1] H. Baumeister et al., submitted to Nucl. Instr. and Methods 1989, *Design and Performance of the SAPHIR lead glass calorimeter.*

[2] L. Dragon, *Produktion neutraler Pionen und direkter Photonen in ultrarelativistischen Schwerionenreaktionen*, Doctoral thesis, Institut für Kernphysik, WWU Münster, 1989.

[3] R. Hagedorn, Rivista del Nuovo Cimento **Vol. 6** (1983) 1.

[4] T. Åkesson et al., CERN-EP/ **89-111** 1989, submitted to Z. Phys. **C** .

[5] B. Alper et al., Nucl. Phys. **B 100** (1975) 237.

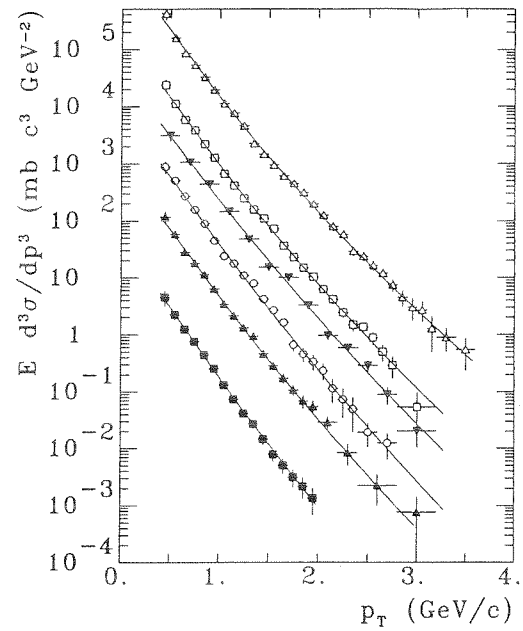


Figure 1: Invariant π^0 cross sections for six different systems as a function of transverse momentum. The lines represent fits to the data with Eq. 1. From the top to the bottom there are the following systems : 200 A GeV ^{16}O + Au (×10), 60 A GeV ^{16}O + Au, 200 A GeV ^{32}S + Al, 200 A GeV ^{16}O + C, 200 GeV p + Au (×0.1) and 200 GeV p + C (×0.1).

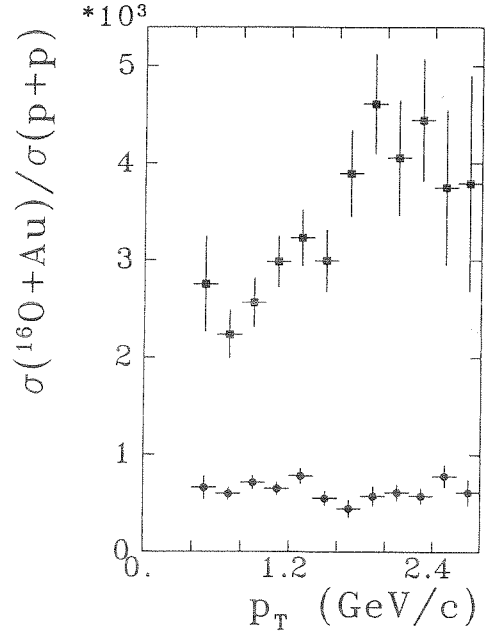


Figure 2: Ratio of the π^0 p_T spectra from central (squares) and peripheral (circles) ^{16}O + Au collisions normalized to the $\pi^\pm$ spectrum from minimum-bias p + p events [5].

Upper Limit for Direct Photon^{G+B} Production in Heavy-Ion Reactions

WA80 COLLABORATION
GSI-LBL-Lund-Münster-ORNL

Results in ultrarelativistic heavy ion collisions indicated that in central ^{16}O+Au reactions energy densities are reached, sufficient for a phase transition from normal nuclear matter to the Quark-Gluon-Plasma. Thermal, direct photons (p_T < 3 GeV/c) are considered a unique signal of the Quark-Gluon-Plasma as they are only very little influenced by the dynamics of the reaction because of their electroweak interaction [1]. This means that they will carry information about the plasma phase.

The lead-glass detector SAPHIR [2] of the CERN WA80 experiment can measure photons and reconstruct π^0 and η mesons with good efficiency and resolution. The dominant part of identified photons result from meson and baryon decays. Those *trivial* photons are calculated by Monte Carlo Simulations. The ratio of direct photons to neutral pions can be estimated by:

$$\frac{\gamma_{direct}}{\pi^0} = \frac{N_\gamma}{N_{\pi^0}} \frac{A_{\pi^0}}{A_\gamma} - (R_{\pi^0} + R_\eta + R_x) \qquad (1)$$

Here N_{γ,π^0} denotes the reconstructed γ, π^0 distribution, A_{γ,π^0} the geometrical acceptance folded with the photon detection probability and R_i the ratio of photons from the decay of particle i to the π^0 spectrum. It has been found [3], that the following 4 decays contribute most to the γ/π^0 background: $\pi^0 \rightarrow \gamma\gamma$, $\eta \rightarrow \gamma\gamma$, $\omega \rightarrow \gamma\pi^0$, and $\eta' \rightarrow \gamma\gamma$. Whereas the π^0 distributions are known in the p_T region 0.4 GeV/c < p_T < 3 GeV/c, the p_T distributions from the other 3 mesons have to be calculated by the following m_T scaling law [4,5] :

$$f(m_T; h) = f(m_T; \pi^0) \qquad (2)$$

with $m_T = \sqrt{m^2 + p_T^2}$. Here is $h = \eta, \omega, \eta'$ and m denotes the respective restmasses. The η meson has been reconstructed for 200 A GeV ^{16}O+Au reactions in a limited p_T region and the result agrees with the value from Tab. 1. The values in Tab. 1 are taken from p+p reactions and serve as normalization points for equation 2. *Trivial* photons from weak decays like $K_S^0 \rightarrow \pi^0\pi^0$ have been estimated and found to be of minor importance [3].

In Fig. 1 the γ/π^0 ratio is shown for central and peripheral 200 A GeV ^{16}O+Au reactions as a function of p_T, the histogram denotes the Monte Carlo calculation whereas the data are represented by the open squares (□). This analysis has also been carried out for the systems : 200 GeV p+C, 200 GeV p+Au, 200 A GeV ^{16}O+C, and 60 A GeV ^{16}O+Au under minimum bias trigger conditions. Within the error limits all created photons can be accounted for by the known hadronic decays. For γ_{direct}/π^0 ratio the data now set an upper limit of ≈ 15%. With better statistics a limit of ≈ 5% is feasible and a detection of direct photons even in heavier systems achievable.

	p_T (GeV/c)	value	reference
η/π^0	5	0.55	[6]
η'/π^0	5	1.	[7]
ω/π^0	5	1.	[7]

Table 1: Normalization points for the meson ratios and the corresponding references.

[1] M. Neubert, Z. Phys. C - Particles and Fields **42** (1989) 231–242.

[2] H. Baumeister et al., submitted to Nucl. Instr. and Methods 1989, *Design and Performance of the SAPHIR lead glass calorimeter.*

[3] L. Dragon, *Produktion neutraler Pionen und direkter Photonen in ultrarelativistischen Schwerionenreaktionen*, Doctoral thesis, Institut für Kernphysik, WWU Münster, 1989.

[4] E. V. Shuryak, Phys. Rep. **61** (1980) 71–158.

[5] J. Bartke et al., Nucl. Phys. **B 120** (1977) 14.

[6] T. Åkesson et al., Phys. Lett. **B 178** (1986) 447.

[7] M. Diakonou et al., Phys. Lett. **B 89** (1980) 432.

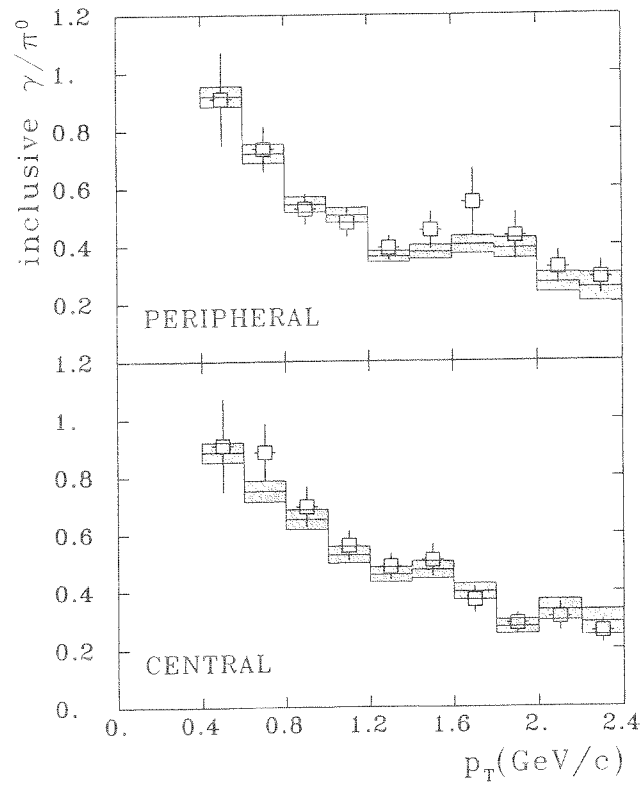


Figure 1: Experimental γ/π^0 ratio for peripheral and central 200 A GeV ^{16}O+Au reactions (□). In addition the Monte Carlo calculations of the γ/π^0 ratio are displayed (histogram).

Determination of the Reaction Plane in Relativistic Heavy-Ion Collisions [B]

H.H. Gutbrod[(a)], K.H. Kampert[(c)], B.W. Kolb[(a)], A.M. Poskanzer[(b)], H.G. Ritter[(b)], R. Schicker[(b)], and H.R. Schmidt[(a)]

(a) Gesellschaft für Schwerionenforschung, Darmstadt, West Germany
(b) Lawrence Berkeley Laboratory, Berkeley, USA
(c) University of Münster, Münster, West Germany

The determination of the reaction plane is the first step in a global analysis of relativistic heavy-ion collisions. The true reaction plane can only be approximated due to the finite multiplicity of charged particles in each event. The two methods which have been used for determining the reaction plane are the sphericity method [GF82] and the transverse momentum method [DO85]. We have investigated both methods in order to get an estimate of the achievable accuracy. Projections of observables on to the reaction plane need to be corrected upward due to the nonzero dispersion in the determination of the reaction plane. The correction factor for the mean of an in-plane projection is $1/ < \cos\phi_\delta >$, where ϕ_δ is the angle between the estimated and the true plane. This factor is estimated by randomly subdividing the full event into two subevents each containing one half of the particles. The reaction planes determined for the two subevents will in general not coincide due to the nonzero dispersion. The mean of the distribution of the cosine of one half the azimuthal angle between the two subevent reaction planes is an estimate for $< \cos\phi_\delta >$. The reduction by the factor of one half has two sources: a factor $1/\sqrt{2}$ comes from the change from the two sampling variables to one, and another factor of $1/\sqrt{2}$ from the increase in multiplicity for the whole event.

Fig.1 shows $< \cos\phi_\delta >$ for both the sphericity and the transverse momentum methods as a function of the normalized multiplicity. The error bars are derived by assuming that the only contribution is the statistical uncertainty in the individual data points of the distribution. The factors are in the numerical range of approximately 0.7 to 0.9, increasing with the number of particles and then decreasing as the event becomes more spherical. A higher value implies a better determination of the reaction plane since the factor will have a value of 1.0 in the limiting case of zero dispersion. Fig. 2 shows that the two methods generate factors which are within one standard deviation at low to medium multiplicity. At high multiplicity, the transverse momentum method gives a slightly better determination of the reaction plane. The overall similarity of the factors determined by the two different methods indicates, however, that the two methods generate very similar dispersion for the reaction plan.

The mean angle of deviation from the true reaction plane can not be trivially derived from $< \cos\phi_\delta >$. Therefore, in Fig. 2, we also show $< |\phi_\delta| >$ as a function of normalized multiplicity. It is estimated from the correlation of the reaction planes of the two subevents as described above.

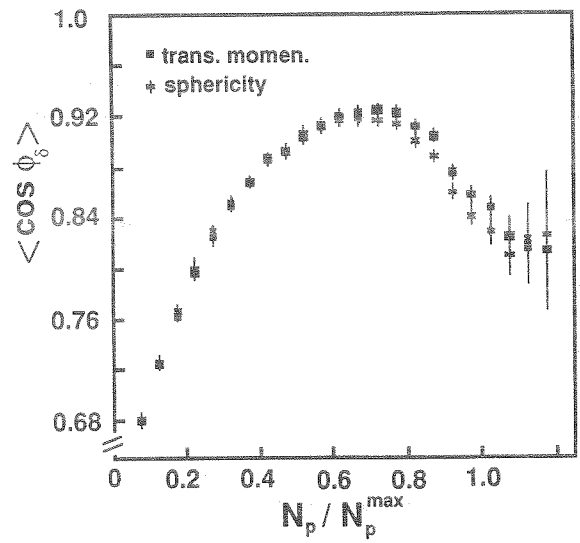


Fig. 1 The mean cosine of the azimuthal difference between the estimated and the true reaction planes calculated from the correlation of the two subevents. Both the sphericity and the transverse momentum method are shown for the system Au+Au at 400MeV/nucleon as a function of the normalized multiplicity.

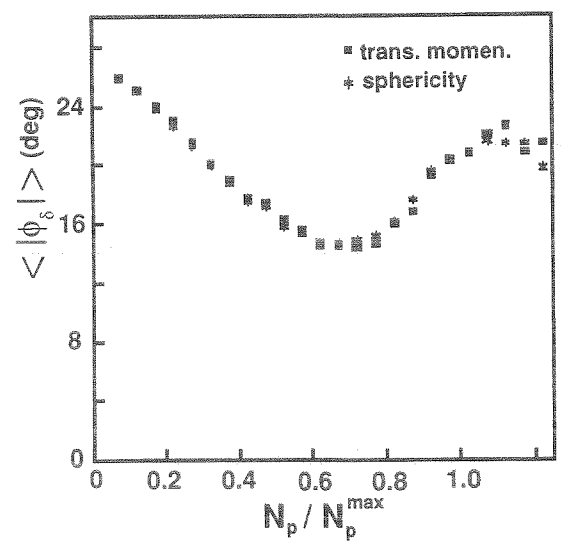


Fig. 2 The mean value of the absolute azimuthal difference between the estimated and the true reaction planes for the system Au+Au at 400MeV/nucleon for the sphericity method and the transverse momentum method as a function of the normalized multiplicity.

[GF82] M. Guylassy, K.A. Frankel and H. Stöocker, Phys.Lett. 110B (1982) 185

[DO85] P. Danielewicz and G. Odyniec, Phys. Lett. 157B (1985) 146

Energy Dependence of the Squeeze-Out Effect in Relativistic Heavy-Ion Collisions [B]

H.H. Gutbrod[(a)], K.H. Kampert[(c)], B.W. Kolb[(a)], A.M. Poskanzer[(b)], H.G. Ritter[(b)], R. Schicker[(b)], and H.R. Schmidt[(a)]

(a) Gesellschaft für Schwerionenforschung, Darmstadt, West Germany
(b) Lawrence Berkeley Laboratory, Berkeley, USA
(c) University of Münster, Münster, West Germany

Squeeze-out, a component of the collective flow of nuclear matter, is the preferential emission of particles out of the reaction plane. Using the sphericity method the out-of-plane/in-plane ratio of the kinetic energy flow has been analyzed as a function of multiplicity and beam energy for Ca+Ca, Nb+Nb and Au+Au collisions measured with the Plastic Ball detector at the Bevalac [GK90].

The sphericity method reduces the information contained in the 4-momenta of all the measured charged particles to a set of six variables, i.e. the three eigenvalues describing the shape of an ellipsoid and a set of three Euler angles describing the absolute orientation of the ellipsoid. The plane spanned by the beam-axis and by the eigenvector $\vec{e}_3$ is identified as the reaction plane. ($\vec{e}_j$ is the eigenvector generated by the eigenvalue λ_j with $\lambda_1 \leq \lambda_2 \leq \lambda_3$.) Since any azimuthal dependence of parameters is only relevant with respect to the reaction plane, the azimuth of $\vec{e}_3$ is chosen to be 0° for each event. This transformation reduces the three Euler angles to a set of two angles which unambiguously characterizes the orientation of the ellipsoid. The two angles are chosen to be the polar angle of $\vec{e}_3$ identified as the flow angle, θ_{flow}, and the angle ψ_{sq} referred to as the squeeze angle. The squeeze angle is used to describe the orientation of $\vec{e}_1$ and $\vec{e}_2$ around the flow axis relative to the reaction plane. Precisely, ψ_{sq} is chosen to be the angle by which $\vec{e}_2$ needs to be rotated around the $\vec{e}_3$ axis in order to be transformed into the reaction plane.

Quantitatively, the in-plane flow is determined for each event by forming the ellipse spanned by $\vec{e}_1$ and $\vec{e}_2$ and by calculating its intersection point with the reaction plane as shown in Fig. 1. The resulting length between the center of the ellipse and the intersection point is a quantity characterizing the in-plane flow. The out-of-plane flow is determined similarly but using the intersection between the ellipse and the perpendicular to the reaction plane through the origin. The mean of the ratio of the out-of-plane to in-plane values is given the name *sphericity squeeze-out ratio*, and the symbol R_λ. The quoted uncertainty in R_λ is calculated by assuming that only the statistical uncertainty in the number of events contributes to the uncertainty of the mean.

The energy dependence of R_λ shown in Fig. 2. was obtained by taking the peak values of R_λ and their error bars and plotting them as a function of beam energy for the three systems measured. The two heavier mass systems clearly show a steep increase in R_λ from the lowest energy of 150 MeV/nucleon to the maximum R_λ at around 250 MeV/nucleon with a subsequent smooth decrease with increasing energy. The lighter system Ca+Ca does not show any significant energy dependence at the two energies measured.

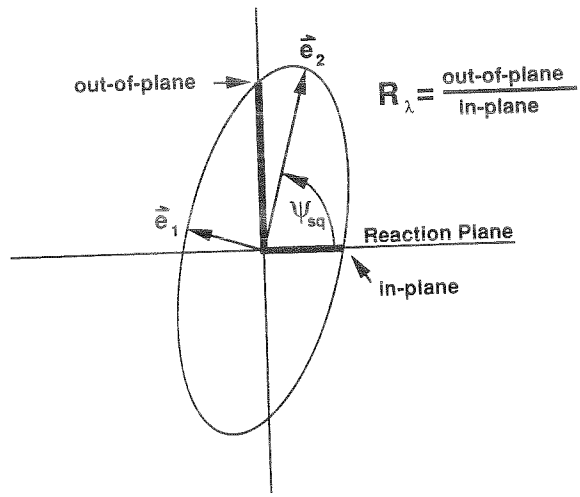


Fig.1 The plane perpendicular to the flow axis through the origin, showing how R_λ is calculated from the two smaller eigenvalues and the reaction plane.

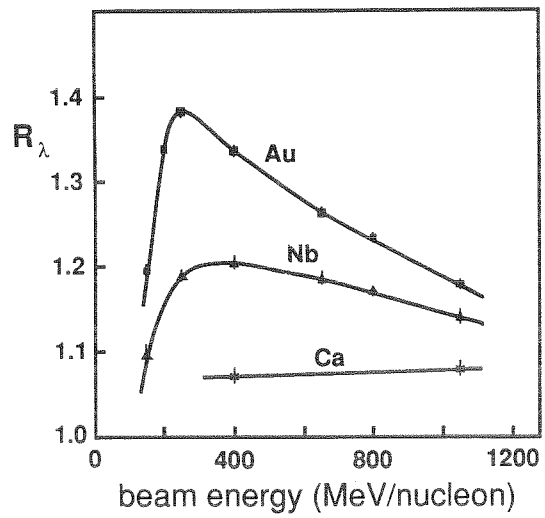


Fig. 2 The peak values of the sphericity squeeze-out ratio in the three systems Au+Au, Nb+Nb and Ca+Ca. The values are shown for all the beam energies at which the systems were measured.

[GK90] H.H. Gutbrod, K.H. Kampert, B. Kolb, A.M. Poskanzer, H.G. Ritter, R. Schicker and H.R. Schmidt, submitted to Phys. Rev. C

[DG86] K.G.R. Doss, H.A. Gustafsson, H.H. Gutbrod, K.H. Kampert, B. Kolb, H.Löhner, B. Ludewigt, A.M. Poskanzer, H.G. Ritter, H.R. Schmidt and H. Wieman, Phys. Rev. Lett. 57 (1986) 302

Rapidity Distributions of Ca+Ca, Nb+Nb and Au+Au at Bombarding Energies from 250 to 650 MeV/Nucleon [B]

H.H. Gutbrod[(a)], K.H. Kampert[(c)], B.W. Kolb[(a)], A.M. Poskanzer[(b)], H.G. Ritter[(b)], and H.R. Schmidt[(a)]

(a) Gesellschaft für Schwerionenforschung, Darmstadt, West Germany
(b) Lawrence Berkeley Laboratory, Berkeley, USA
(c) University of Münster, Münster, West Germany

Rapidity distributions give a qualitative estimate on the degree of stopping in heavy-ion collision. They can furthermore help to remove ambiguities in model calculations due to in-medium effect [PS89].

Figs. 1 and 2 show the projectile-target and bombarding energy dependence, respectively, of the rapidity distributions[GK90].The data were obtained employing the 4π Plastic Ball spectrometer. Fig. 1 shows the rapidity distributions for 400 MeV/nucleon Ca+Ca, Nb+Nb and Au+Au for the fifth multiplicity bin. No remnants of the spectator peaks are observed for any of the systems. Fig. 2 shows the reaction Au+Au for 250, 400 and 650 MeV/nucleon incident energy, again for the fifth multiplicity bin. In all three cases no spectator remnants are left.

A simple gaussian, centered at mid rapidity, is superimposed onto the data. The shape of the rapidity distributions is qualitatively reproduced by this gaussian shaped curve. In addition, detector inefficiencies are clearly visible, e.g. the apparent shift of the distribution at 650 MeV/nucleon away from midrapidity which is probably due to the detector effects such as multiple hits and a degraded energy determination for punch-through particles. We want to stress here again that a comparison with model predictions requires appropriate filtering of the simulated events.

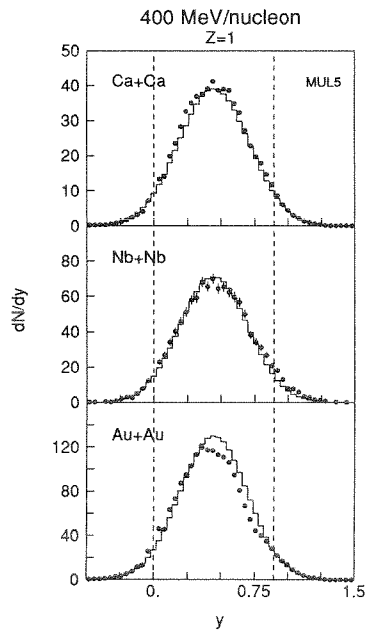


Fig. 1 Rapidity distribution for Z=1 particles from the reaction Ca+Ca (top), Nb+Nb (middle) and Au+Au (bottom) at 400 MeV/nucleon, selected for the fifth multiplicity bin. A gaussian with its center fixed at mid rapidity is superimposed onto the data. The vertical dashed lines are at target and beam rapidity.

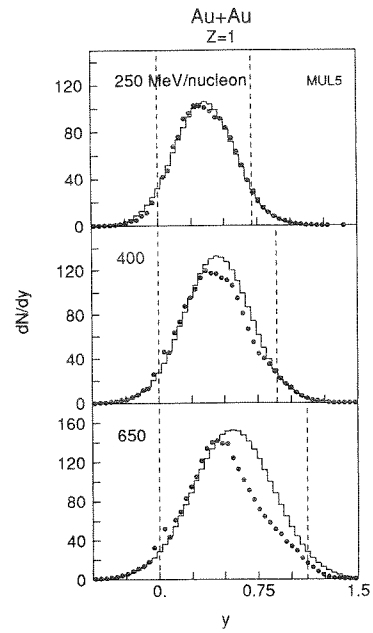


Fig. 2 Rapidity distribution for Z=1 particles from the reaction Au+Au at 250 (top), 400 (middle) and 650 (bottom) MeV/nucleon, selected for the fifth multiplicity bin. A gaussian with its center fixed at mid rapidity is superimposed onto the data. The vertical dashed lines are at target and beam rapidity.

We conclude from the experimentally measured rapidity distributions a high degree of baryon stopping in central relativistic heavy-ion collision in the energy range considered.

[PS89] G. Peilert, H. Stöcker, W. Greiner, A. Rosenhauer, A. Bohnet, and J. Aichelin, Phys. Rev. C39 (1989) 1402

[GK90] H. Gutbrod, K.H. Kampert, B.W. Kolb, A.M. Poskanzer, H.G. Ritter and H.R. Schmidt, submitted to Z. Phys. A

Ground-state properties of heavy nuclei

Z. Patyk and A. Sobiczewski

Soltan Institute for Nuclear Studies-Warsaw and GSI-Darmstadt

The following properties: mass M, alpha-decay energy Q_α and alpha-decay half-life T_α of heavy nuclei are analyzed. They are studied in the three-dimensional deformation space $\{\beta_\lambda\}$ ($\lambda = 2,4,6$), where β_λ are usual deformation parameters. It has been shown [1] that the deformation of multipolarity degree $\lambda = 6$, β_6, may increase the binding energy of a heavy nucleus by up to about 1.5 MeV, significantly influencing some of its ground-state properties.

The potential energy is calculated in the macroscopic-microscopic approach, as described in [1]. The zero-point energy is obtained in the adiabatic and harmonic approximation for the lowest vibrations in the considered degrees of freedom. The mass parameters are calculated by the cranking method. Even-even nuclei with the proton number Z = 90-114 and the neutron number N = 136-168 are considered.

Fig.1 gives the shell correction E_0 to the ground-state energy. One can see that it systematically increases (in absolute value) from about 2 MeV, at the beginning of the region, up to about 7 MeV, for nuclei around the nucleus $^{270}108$. Then, it starts to slowly decrease. The heaviest nuclei (with the mass number A≥262) are indicated by crosses. It is seen that they profit from the shell correction by about 5-6 MeV, in their binding energy (which is then reduced by the zero-point energy of about 1.5 MeV). Fig.2 shows the shell correction to the mass, for these nuclei for which this quantity has been measured. $\tilde{M}$ denotes here the smooth part of the mass (obtained by the Yukawa-plus-exponential model [2]). The theoretical value of the mass is taken as: $M = \tilde{M} + E_0 + E_{zp}$, where E_0 is the shell correction given in fig.1 and E_{zp} is the zero-point energy. One can see that the experimental values are reproduced by the calculations within the average accuracy of about 200 keV.

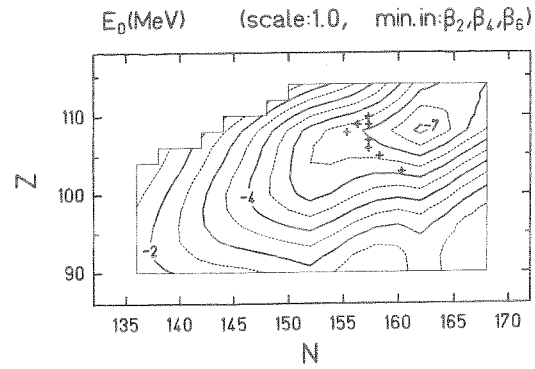


Fig. 1

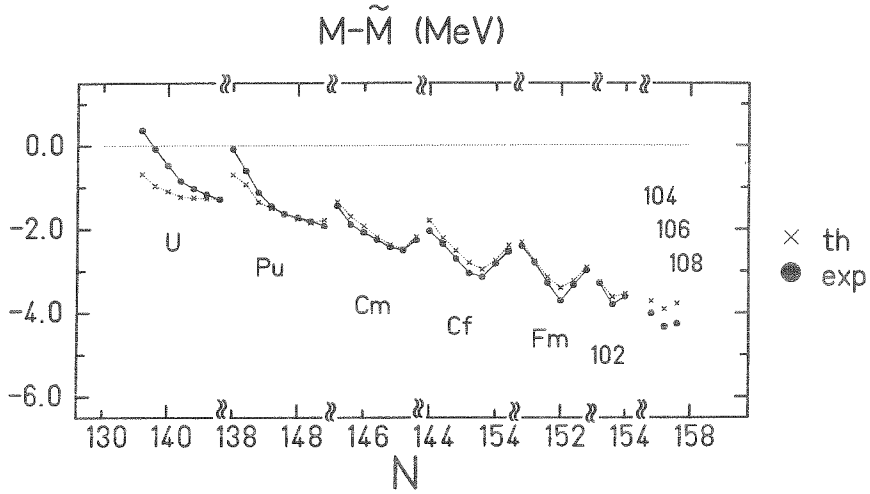


Fig. 2

More detailed results will be presented elsewhere.

References

1. Z. Patyk and A. Sobiczewski, "Deformations of heavy nuclei", this GSI-Report

2. H.J. Krappe et al., Phys. Rev. C20 (1979) 992

Deformations of heavy nuclei

Z. Patyk and A. Sobiczewski

Soltan Institute for Nuclear Studies-Warsaw and GSI-Darmstadt

Ground-state deformations have been calculated in a number of papers (e.g. [1,2]), for various regions of the heaviest nuclei. They were analyzed in a two-dimensional deformation space, usually $\{\beta_\lambda\}$ or $\{\varepsilon_\lambda\}$, $\lambda = 2,4$. The objective of the present study is to extend the analysis to a more dimensional space, similar as has been done for lighter nuclei around radium and barium [3]. It is found in the present study that the deformation of the multipolarity degree $\lambda = 6$, β_6 , may increase the binding energy of a heavy nucleus by up to about 1.5 MeV, influencing significantly its (calculated) properties. Simultaneously, the effect of still higher multipoles, $\lambda > 6$, is found to be small (of the order of the inaccuracy of the calculations). Thus, the three-dimensional space seems to be sufficient for the analysis of the ground-state properties.

Even-even nuclei with the proton number Z = 90-114 and the neutron number N = 136-168 are considered. The potential energy is calculated by the macroscopic-microscopic method with the Yukawa-plus-exponential model taken for the macroscopic part and the Strutinski shell correction (based on the Woods-Saxon single-particle potential) used for the microscopic part of the energy. The equilibrium shape of a nucleus is found by minimization of the energy in the three-dimensional deformation space $\{\beta_\lambda\}$ ($\lambda = 2,4,6$), where β_λ are the usual deformation parameters.

Figs. 1, 2 and 3 show contour maps of the equilibrium deformations β_2^0 , β_4^0 and β_6^0, respectively. One can see that the quadrupole deformation β_2^0 is large. Its largest value ($\beta_2^0 \approx 0.24$) is obtained for nuclei around the nucleus ^{254}No, i.e. around the center of the studied region. The hexadecapole deformation decreases with the increasing N and Z, being small ($\beta_4^0 \approx 0$) around the center of the region. The deformation β_6^0 is negative and it is largest (in absolute value) in the center of the region, increasing the effectiveness of the deformed shell at N = 152. Fig.4 illustrates the shapes of the nuclei. All considered nuclei are well deformed. For almost all of them, the deformation energy E_{def} (i.e. the gain in energy of a nucleus due to its deformation), not shown in this contribution, is larger than 2 MeV. Its largest value ($E_{def} \approx 11$ MeV) is obtained for nuclei around the center of the region and is probably the highest value that can be obtained for known nuclei.

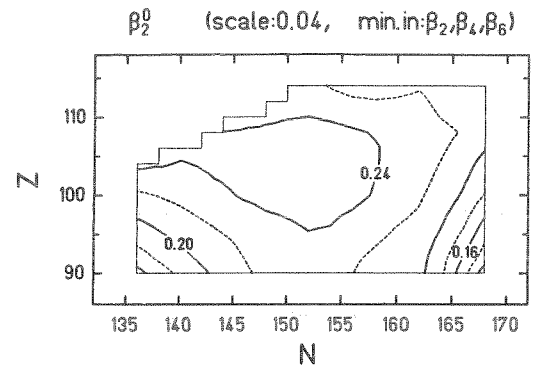


Fig. 1

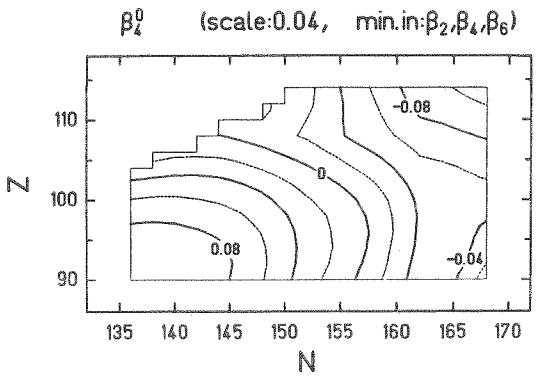


Fig. 2

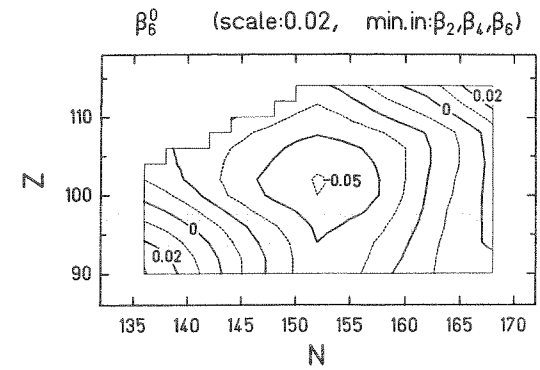


Fig. 3

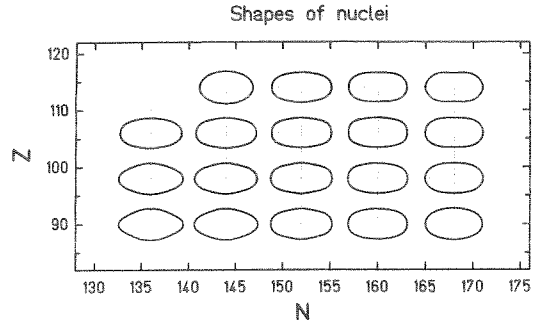


Fig. 4

References

1. S. Cwiok et al., Nucl. Phys. A410 (1983) 254
2. R. Bengtsson et aql., Phys. Scr. 29 (1984) 402
3. A. Sobiczewski et al., Nucl. Phys. A485 (1988) 16

Fission half-lives of the heaviest nuclides

Z. Patyk, J. Skalski and A. Sobiczewski,
Soltan Institute for Nuclear Studies-Warsaw and GSI-Darmstadt

The spontaneous-fission half-lives are studied in a multidimensional deformation space. They are analyzed in a dynamical way (cf. e.g. [1,2]), i.e. when the fission trajectory is chosen so, as to minimize the action integral, and not only the potential energy. Even-even nuclei with Z = 100-112 and N = 140-168 are considered. The potential energy is calculated by the macroscopic-microscopic method with the Yukawa-plus-exponential model taken for the macroscopic part and the Strutinski shell correction (based on the Woods-Saxon single-particle potential) used for the microscopic part of the energy. The mass parameters are obtained in the cranking approximation. The four-dimensional deformation space $\{\beta_\lambda\}$ ($\lambda = 2,3,4,5$) is taken, where β_λ are usual deformation parameters.

Fig.1 gives an example of the potential energy surface calculated for the nucleus ^{254}No. One can see that two valleys are obtained, similar to previous calculations (e.g. [3]). One corresponds to elongated shapes (ES) of the nucleus and the other to its compact shapes (CS). The latter valley becomes more and more pronounced when one increases the neutron number N to N = 164, which corresponds to nucleus with two magic (N = 82) fragments [3]. The dynamical fission trajectory, L_{dyn}, is shown. One can see that it has a tendency to be a straight line or to be composed of pieces of a straight line, to minimize the action integral. Fig.2 shows logarithm of the spontaneous-fission half-life T_{sf} (given in seconds), both: calculated (dashed line) and experimental (solid line), for isotopes of fermium. One can see that the theoretical results reproduce experiment rather well. In particular, they reproduce the large drop (by about 10 orders of magnitude) in T_{sf} when one passes from ^{254}Fm to ^{258}Fm. This drop is due (according to the calculations) to the disappearance of the second hump in the fission barrier. The failure of the present calculations is that they predict this disappearance of the second hump for too light (by two neutrons) isotopes of the Fm (dashed line) and also No elements. It is also seen in fig.2 that the calculations predict the second increase in T_{sf}, when the neutron number N increases from N ≈ 158. This also applies to nobelium. Recent measurement of T_{sf} for ^{262}No [4] seems to support this prediction.

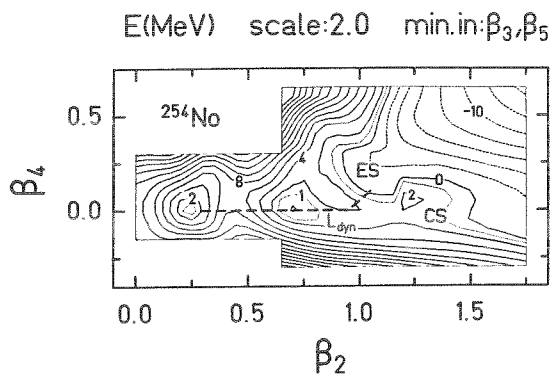


Fig. 1

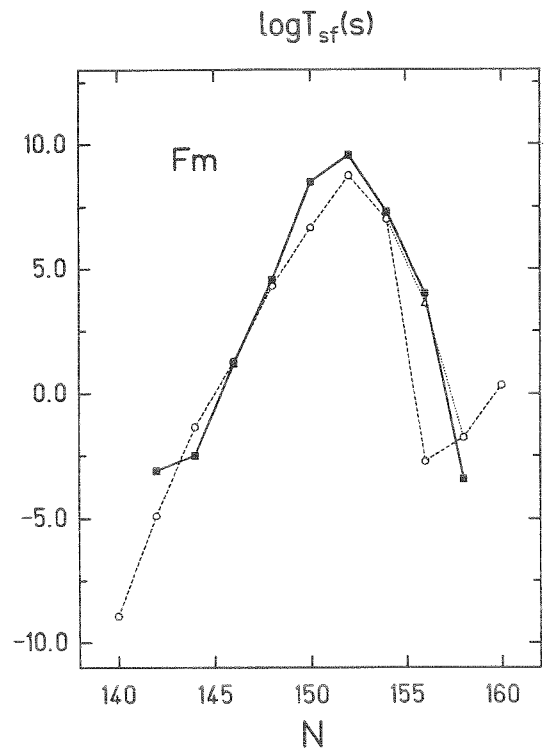


Fig. 2

References

1. T. Ledergerber and H.C. Pauli, Nucl. Phys. A207 (1973) 1
2. A.Baran et al., Nucl. Phys. A361 (1981) 83
3. S. Cwiok et al., Nucl. Phys. A491 (1989) 281
4. R.W. Lougheed et al., LLNL Annu. Rep. UCAR 10062-88 (1988) p.135

Numerical Treatment of Fission Dynamics [G]

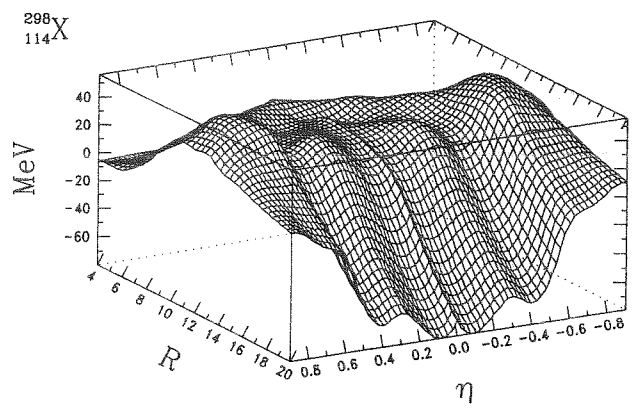
H. Klein, D. Schnabel, J.A. Maruhn, W. Greiner
Institut für Theoretische Physik, Universität Frankfurt

In order to determine the life times of nuclei in a quantum mechanically consistent way a dynamical treatment of the Pauli quantized collective Schrödinger equation has to be done. The time dependent wave function has to be observed and the part which is passing the fission line of the potential energy surface (PES) has to be measured. The PES is calculated by means of the macroscopic-microscopic method: The Yukawa plus exponential model[1] is used for the macroscopic part whereas the microscopic part is given by folding a Yukawa function over a shape parametrized by the Three Spheres Model[2]. An example of a PES is shown in the figure for the superheavy element $^{298}_{114}$X in the collective coordinates R and η. It shows valleys in η for $A_2,Z_2 = 88,34$ and $A_2,Z_2 = 136,52$. Negative values of η contain the same physics as the positive ones. The half life time is reached if $\int \psi_{coll}\psi^*_{coll}\cdot dRd\eta$ over the scission area reaches $\frac{1}{2}$. In order to quantize the Schrödinger equation (SE) correctly one also needs the metric tensor $B_{q_iq_j}$ of the collective coordinates q_i which is determined by the Werner-Wheeler-Method.

The resulting partial differential equation (PDE) will be solved by means of a finite element (FE) method[3]. The spatial part of the PDE is discretized by conforming Bogner-Fox-Schmit-elements assuring that the numerical solution will satisfy all continuity requirements of the SE and thus will converge to the exact solution if the area of the largest finite element tends to zero. By means of the FE method the PDE is transformed in a system of first order ordinary differential equations of the form $D\cdot\dot{u} = H\cdot u$ where u represents the vector containing the knot variables of the wave function and D and H are the combined FE matrices compiled by using the above specified elements. D and H are block matrices containing only constant coefficients and only 45 diagonals of each block are occupied. They can therefore be stored fully core optimized in compressed diagonal storage mode[4,5]. The analytic solution of this equation is $u_t = u_0\cdot\exp(D^{-1}H\cdot t)$. Of course this equation is of no practical importance since a) in calculating D^{-1} one would destroy the sparsity structure of the matrix and b) the Neumann series would converge too slowly. Therefore the above system has to be solved by an adaptive ordinary stiff differential equation solver (IMSL routine DIVPAG).

Each evaluation of $\dot{u}$ now requires a matrix vector multiplication and the solution of a system of linear equations. In order to preserve the sparsity structure of the combined element matrices the evaluation of $\dot{u}$ can only be based on matrix vector multiplications. Therefore the system of linear equations is solved by means of a conjugate gradient method. All routines for the function evaluation are thus provided by the ESSL of the IBM 3090 at GSI. The resulting computer code is therefore fully core optimized, dynamically highly vectorized (>85%) and uses the multitasking facility (52% main task, 48% sub task).
Calculations are in progress and will be shown in future publications.

PES of $^{298}_{114}$X in the collective coordinates
R (center separation) and η (mass asymmetry)



[1] M. Bolsterlie, E.O. Fiset, J.R. Nix, J.C. Norton, Phys. Rev. C 5 (1972) 1050-1077
[2] K. Depta, Ph.D. Thesis, Frankfurt 1989
[3] H.R. Schwarz, Methode der finiten Elemente, B.G. Teubner Stuttgart 1984
[4] W. Schönauer, Scientific Computing on Vector Computers, North Holland 1987
[5] ESSL, Guide and Reference, Rel. 3, IBM 1988

An advanced geometry for the description of general and especially strong asymmetric fission [G]

W. Renner D. Schnabel H. Klein M. Haffner J. Maruhn W. Greiner
Institut für Theoretische Physik der Universität Frankfurt

Because the geometry of the Asymmetric-Two-Center-Shell-Model proved to be disadvantageous for the treatment of strong asymmetric fission, the Three-Ball-Model was indroduced. This TBM-model consists of two spheres connected with a neck defined by a third imaginary sphere rolling in contact with the two fragment spheres. For a centerdistance Δ up to Δ_V the radius A_2 is fixed to A_{2F}. Then the definition changes to the demand of fixing the volume separated by Z_3 in the final ratio. This definitionchange results in unwanted discontinuities of the masses. To avoid the discontinuities the DKM-model (The names have no deeper meaning) was invented. Hereby the volume separation holds from the beginning. But the volumes are functions of Δ now:

$$V_1, V_2 = \frac{V_0}{2}(1 \pm D \cdot \eta) \qquad D = \frac{1}{2}\left[1 - \cos\left(\pi \frac{\Delta - \Delta_H}{\Delta_S - \Delta_H}\right)\right]$$

(Here is Δ_H zero. But later with TSM Δ_H in D is the regular Δ_H like in figure 2 shown.) This newer DKM-model yields smooth masses. But the nearly constant fragmentradius is lost and the Potential-Energy-Surface (PES) shows unfavorable properties for $C_{A_3} \to 0$.

After some thinking now a third geometry TSM is invented. Now the radius A_2 is fixed until the scissionpoint Δ_S with the smooth interpolation $A_2 = A_{2F} + (A_{2S} - A_{2F}) \cdot D$. The PES and the obeying of the cluster-idea is satisfied like with TBM. But the masses will be smooth.

As an further improvement the three spheres can be three spheroids now. This means the three spheres can be elliptical deformed in z-direction, with the deformation parameters Q_1, Q_2 and Q_3.

The masses are most sensitive on the definition of the geometry. They can be calculated in a practicable way with the hydrodynamical Werner-Wheeler formalism:

$$M_{ij} = \pi\sigma \int_a^b P^2(z)\Big\{ A_i A_j + \frac{P^2(z)}{2} C_i C_j \Big\} dz \quad C_i = -\frac{1}{2}\frac{\partial A_i}{\partial z}$$

$$A_i = -\frac{1}{P^2(z)}\frac{\partial}{\partial q_i}\int_a^z P^2(z')dz' = \frac{1}{P^2(z)}\frac{\partial}{\partial q_i}\int_z^a P^2(z')dz'$$

Where $P(z)$ is the shaperadius and q_i are the generalized coordinates, which are in our case the mass-asymmetry $\eta = \frac{NA1-NA2}{NA1+NA2}$, the centerdistance Δ, the neckcurvature C_{A_3}, the initial deformation Q_0, the final deformations Q_{1F}, Q_{2F} , and the neckspheroid deformation Q_{3in}. (negative neck curvature is also possible).

The A_i expressions of the WW-masses contain integrals I derivated with respect to the generalized coordinates q_i. This integrals are functions of the values:

$$x_l = \eta, \Delta, A_3, Q_1, Q_2, Q_3 \qquad y_k = A_1, C_1, Z_3, \rho_3, C_2, A_2$$

(with $l, k = 1 \ldots 6$) Therewith the derivative results into

$$\frac{\partial I}{\partial q_i} = \left\{ \sum_{k=1}^{6} \frac{\partial I}{\partial y_k}\frac{\partial y_k}{\partial q_i} + \sum_{l=1}^{6} \frac{\partial I}{\partial x_l}\frac{\partial x_l}{\partial q_i} \right\} \quad \left(\frac{\partial y}{\partial q}\right) = \begin{pmatrix} \frac{\partial y_1}{\partial q_1} & \cdots & \frac{\partial y_1}{\partial q_7} \\ \vdots & \ddots & \vdots \\ \frac{\partial y_6}{\partial q_1} & \cdots & \frac{\partial y_6}{\partial q_7} \end{pmatrix}$$

The matrix $\left(\frac{\partial x}{\partial q}\right)$ can be calculated straight forward. But $\left(\frac{\partial y}{\partial q}\right)$ can only be obtained with a tricky use of the sentence about implicit functions. Six functions $F_n(y_k(q_i), x_l(q_i), q_i) = 0$ are given as conditions of the geometrical properties. With them we get:

$$\left(\frac{\partial y}{\partial q}\right) = -\left(\frac{\partial F}{\partial y}\right)^{-1} \cdot \left\{ \left(\frac{\partial F}{\partial x}\right) \cdot \left(\frac{\partial x}{\partial q}\right) + \left(\frac{\partial F}{\partial q}\right) \right\}$$

Because the program is not yet fully finished, there are in this moment no results to show.

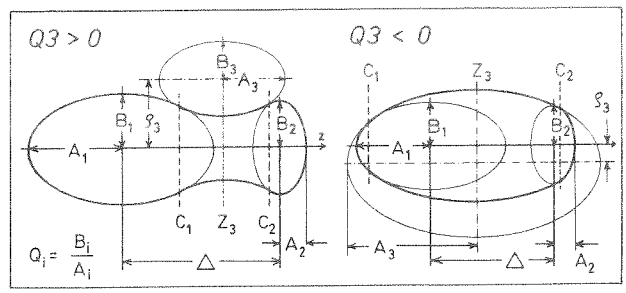


Figure 1: The geometrical proportions

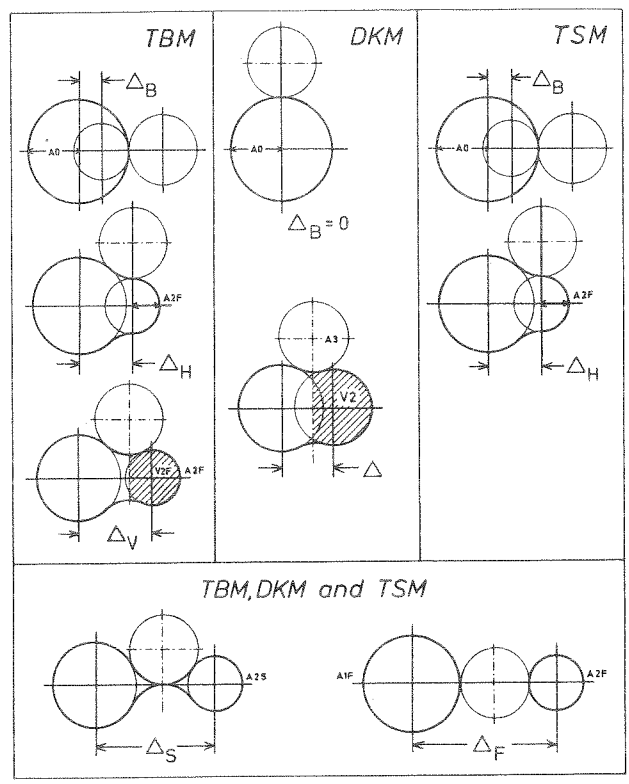


Figure 2: Special geometry points for positive neckcurvature

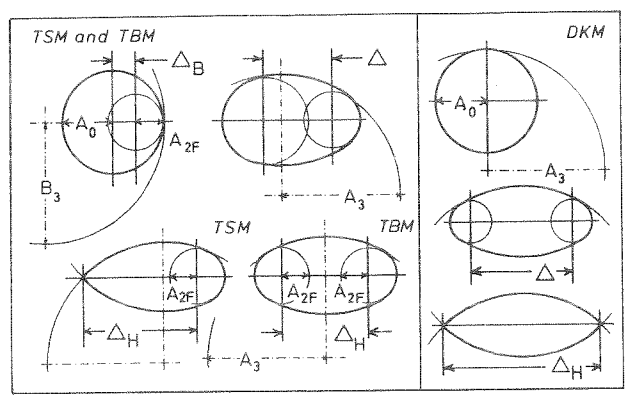


Figure 3: Special geometry points for negative neckcurvature

New Developments in the Geometric Collective Model [B]

D.Troltenier, S.Butorac, J.A.Maruhn, W.Greiner

Institut für Theoretische Physik, J.W. Goethe-Universität, Frankfurt/M, W.-Germany

In this report we want to focus on two new developments in the geometrical treatment of excitations of even-even nuclei:
First we present here some new results from a well-documented, easy-to-use, easy-to-learn code which calculates excitation energies, $B(E2)$-values and quadrupole moments up to spin $I = 10$ for a given potential energy surface. Provided some standard auxilliary programs, e.g. from the IMSL or NAG library, it performs automatic fitting to experimental data and generates thus the corresponding PES. This code is freely available and informations can be obtained by one of us. [1] The Hamiltonian used in this code is given as:

$$\hat{H} = \hat{T} + V(\alpha)$$

with

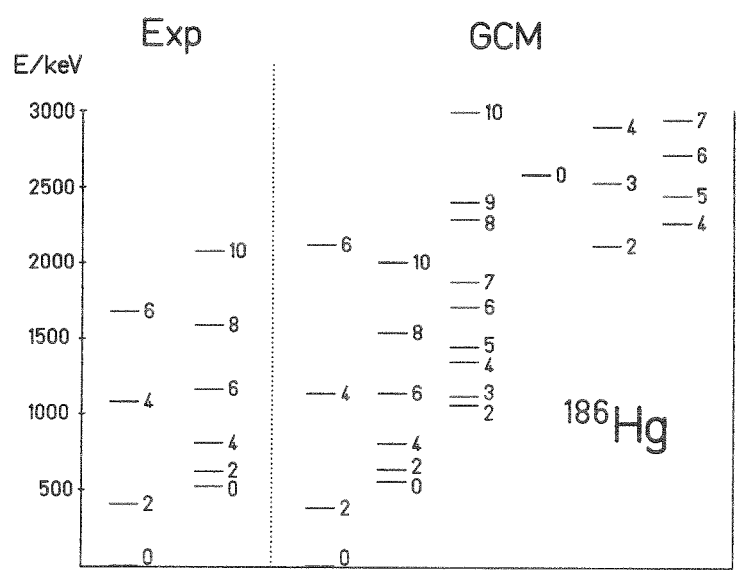
$$\hat{T} = P_2 \left[\hat{\pi} \times \hat{\pi}\right]^{[0]} + P_3 \left[\left[\hat{\pi} \times \alpha\right]^{[2]} \times \hat{\pi}\right]^{[0]}$$

and

$$\begin{aligned} V(\alpha) = {} & C_2 \left[\alpha \times \alpha\right]^{[0]} + C_3 \left[\left[\alpha \times \alpha\right]^{[2]} \times \alpha\right]^{[0]} \\ & + C_4 \left(\left[\alpha \times \alpha\right]^{[0]}\right)^2 + C_5 \left[\left[\alpha \times \alpha\right]^{[2]} \times \alpha\right]^{[0]} \left[\alpha \times \alpha\right]^{[0]} \\ & + C_6 \left(\left[\left[\alpha \times \alpha\right]^{[2]} \times \alpha\right]^{[0]}\right)^2 + C_7 \left(\left[\alpha \times \alpha\right]^{[0]}\right)^3 \end{aligned}$$

where P_2, P_3 are kinetic energy parameters and C_i, $(i = 2, ...7)$ are potential parameters defining the potential energy surface. This potential corresponds to the Gneuss–Greiner potential which contains all important terms [He 80].
We adjusted the Hg–chain from $A = 184$ to $A = 100$ and give below an example for the energy spectrum of ^{186}Hg of our code (GCM) in comparison to experiment (Exp). In general we get a satisfying agreement between the experimental data and our fits, which will as a whole be published elsewhere.
The second point we wanted to report is that we wrote a code which calculates the wavefunctions for arbitrary potentials by solving the corresponding (β, γ)–dependent partial differential equation numerically. Making a difference to former publications on this field (e.g. [KB 66], [RD 77]) we want to concentrate besides on the low energy properties of ee-nuclei, on the high spin states and the strongly deformed nuclei. The calculations are still in progress, but we hope to present first results soon.

[1] D. Troltenier, Inst. f. Th. Physik, R.-Mayer Str 10, D-6000 Frankfurt/M 11



References

[KB 52] K.Kumar, M.Baranger Nucl. Phys. **A92**, (1967) 608

[RD 77] S.G. Rohozinski, J.Dobaczewski Nucl. Phys. **A292**, (1977) 66-87

[HS 80] P.O.Hess PhD Thesis , J.W. Goethe - Universität, Frankfurt/Main, W.-Germany

Dynamical diabatic hindrance of heavy–ion fusion

P. Rozmej * and W. Nörenberg
GSI Darmstadt

The fusion process for heavy nuclei has been extensively studied within a generalized formulation of the diabatic approach to collective nuclear motion [1]. It was shown that coupled equations of motion decouple during the approach if appropriate diabatic channels are used. Thus the mean value and the variance of the fusion barrier are completely determined from the ensamble of diabatic barriers being defined by initial correlations. The mean shift ΔB with respect to the adiabatic barrier and the variance σ_B^2 have been calculated from the splitting of the diabatic single particle levels at the barrier and the initial occupation probabilities given by the pairing wavefunctions of the separated nuclei.

The microscopic model applied in [1] reproduces both the general (smooth) dependence of the mean shift ΔB on the mean fusibility parameter x_m and the strong opposite isotopic dependence due to shell structure present in experimental data [2, 3]. The accuracy of the theoretical predictions decreases, however, with the increasing fusibility. This is a signature that the existing theoretical model does not contain a physical mechanism which becomes important for heavier systems and sets on for $x_m \gtrsim 0.75$.

The model used in [1] can be considered as the diabatic limit. Barrier shifts and fluctuations are calculated under the assumption that the single–particle motion during the approach phase of the collision is purely diabatic. For heavier systems, as an overlap of the colliding nuclei at the barrier distance increases with fusibility, one can expect the increacing influence of two–body collisions. These collisions produce dissipation that generally broadens the barrier distribution. The mean shift is also increased because the additional energy ('diabatic extra–push') is required by the system to reach the fusion configuration. Two–body collisions are incorporated in DDD theory (Dissipative Diabatic Dynamics) [4]. The present paper aims to formulate DDD in convenient way to describe the fusion process of heavy nuclei. Limiting our considerations to only one collective degree of freedom q (in our case it is the distance between centers of colliding nuclei) we can write the equation of the collective motion as

$$B\,\ddot{q} + \frac{1}{2}\left(\frac{dB}{dq}\right)\dot{q}^2 = F_\nu(t)\,, \qquad (1)$$

where B is mass parameter and $F_\nu(t)$ is the force for the particular channel ν. At the time $t = 0$ the force is given by the derivative of the potential that is the sum of adiabatic part and diabatic shift.

$$F_\nu(t=0) = -\frac{d}{dq}\left(V^{\rm ad} + \Delta V_\nu^{\rm diab}\right). \qquad (2)$$

The mean value of diabatic shift and its distribution is taken from the previous paper [1]. Figure 1 shows the initial distribution of the fusion barriers obtained in static approach [1].

Due to two–body collisions the force $F_\nu(t)$ is driven to its thermal equilibriun value and fluctuates. These features can be conveniently describe in terms of Langevin–type equation

$$\frac{\partial F_\nu}{\partial t} = -\frac{1}{\tau_{\rm loc}}\left(F_\nu - \overline{F}\right) + F_\nu^{\rm fluct}\,, \qquad (3)$$

where $\tau_{\rm loc}$ denotes local equilibration time and depends on the excitation energy (which is related to the temperature) and $\overline{F}$ stands for the adiabatic force. The fluctuating force can be related to the diffusion coefficient D of the corresponding Fokker–Planck equation. Using the prescription of [5] one writes :

$$\frac{\partial F_\nu}{\partial t} = -\frac{1}{\tau_{\rm loc}}\,F_\nu^{\rm fluct} = \sqrt{D}\,\sqrt{\tau}\,\omega(t) \qquad (4)$$

and

$$D = \frac{2}{\tau_{\rm loc}}\,\overline{\sigma_F^2} \;\simeq\; \frac{2}{\tau_{\rm loc}}\sum_\alpha \left(\frac{\partial(\varepsilon_\alpha - \mu)}{\partial q}\right)\overline{n}_\alpha\,(1-\overline{n}_\alpha)\,. \qquad (5)$$

Here τ is a time step and $\omega(t)$ is a gaussian distributed random number, such that $\langle\omega\rangle = 0$ and $\langle\omega^2\rangle = 2$. The ε_α are the diabatic single–particle energy, μ is the chemical potential and $\overline{n}_\alpha(q,\mu,T)$ are equilibrium occupation numbers according to Fermi distribution.

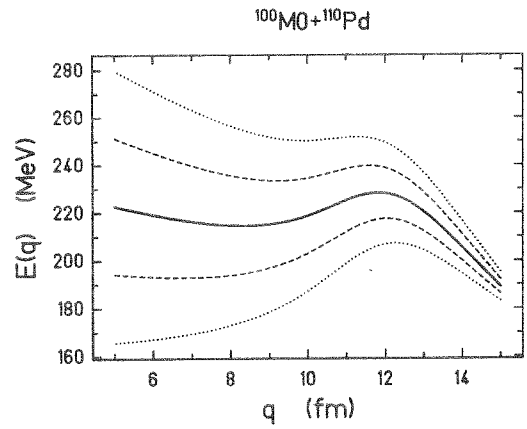


Fig. 1. Initial distribution of fusion barriers for the ^{100}Mo+^{110}Pd system. The thick solid line displays the mean barrier and the outer (dotted) lines correspond to 2 standard deviations.

Numerical calculations of the fusion probability are not finished yet for the dynamical model. Preliminary results (which estimate the mean dynamical shift of the fusion barrier) idicate that the dynamics of the process can indeed be responsible for the previous discrepancy between the theoretical and experimental results.

References

[1] D. Berdichevsky, A. Lukasiak, W. Nörenberg and P. Rozmej, *Nucl. Phys.* **A499** (1989) 609.

[2] J. G. Keller et. al., *Nucl. Phys.* **A452** (1986) 173.

[3] A. B. Quint, Thesis, *Report* GSI–89–22.

[4] W. Nörenberg, in New vistas in nuclear dynamics, ed. P.J. Brussard and J.H. Koch (Plenum, New York, 1986 p. 91).

[5] P. Fröbrich and S. Y. Xu, *Nucl. Phys.* **A477** (1988) 143.

*Permanent address: Institute of Physics, UMCS, 20–031 Lublin, Poland

A Variable Barrier Fusion Model

D. Kolb, A. Marinov[1]

Fachbereich Physik, Universität Kassel

[1] Racah Institute, Hebrew Univ.,Jerusalem,Israel

By a barrier passing model transmission coefficients T_l for angular momentum values l were calculated leading to the fusion cross section

$$\sigma_{fus} = \pi \lambda\!\!\!^{-2} \sum_l (2l+1)\, T_l$$

with $\lambda\!\!\!^{-} = \hbar / \sqrt{2mE}$

Target(1) and projectile(2) be deformed, their major axex forming angles θ_1 and θ_2 respectively with the connection line of their centers of mass. As the rotational collective motion is slow compared to typical reaction times we may integrate over contributions for fixed orientations.

The Coulomb interaction potential includes terms up to quadrupole deformations of target and projectile[1]. For the nuclear interaction potential we used the Bass fusion potential[2]

$$V_{N,l}(r,\underline{\theta}) = -V_o(\underline{\theta}) \exp - \frac{r - R_{12}(\underline{\theta})}{d} + \frac{\hbar^2\, l(l+1)}{m\, 2\mu\, r^2}$$

$$V_o(\underline{\theta}) = r_1 r_2 a_s\, d/(r_{12}\, r_o^2)$$

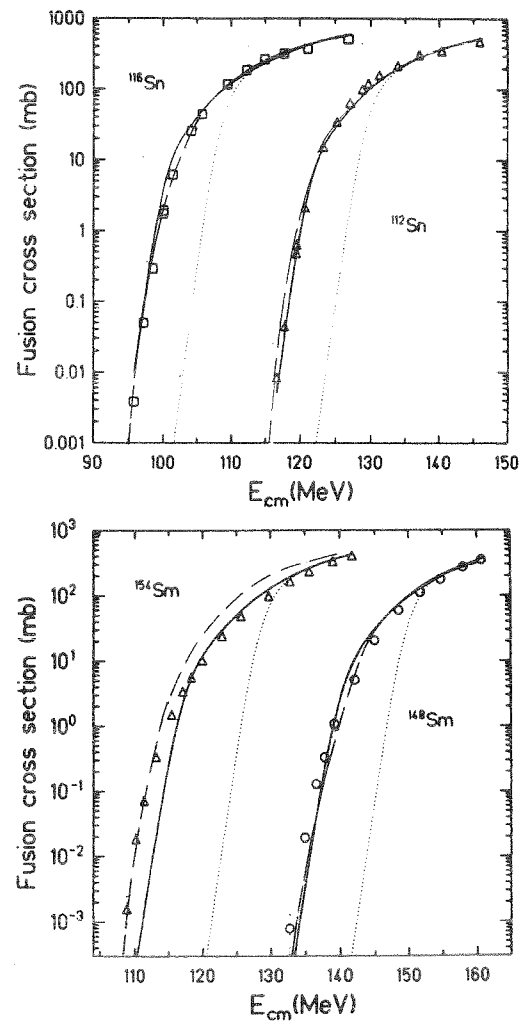
a_s,d,r_o are 17MeV,1.35fm,1.07fm respectively.

$R_{12}(\underline{\theta}) = R_1(\theta_1) + R_2(\theta_2)$, $r_{12} = r_1(\theta_1) + r_2(\theta_2)$ $R_i(\theta_i)$ being the nuclear radii and $r_i(\theta_i)$ the curvature radii, $\mu = A_1A_2/(A_1+A_2)$ the reduced mass. This model deviates from present standard treatments of deformation effects by a $V_o(\underline{\theta})$ counterbalancing the deformation dependence of the exponential term in $V_{N,l}(r, \underline{\theta})$ to some extent; deformation effects tend to be underestimated.

From the l and $\underline{\theta}$ dependent WKB integrals the transmission coefficients $t_l(\underline{\theta})$ follow by extended WKB formulas of Miller[3]. Thus far the shell structure of target and projectile and barrier fluctuations due to excitations are ignored. We therefore added a barrier spread, simulated geometrically by a dipole parameter b. This automatically limits the barrier height distribution to a finite interval. Integrating the $t_l(\underline{\theta},\underline{b})$ over $\underline{\theta}$, $\underline{b}$ finally gives the transmission coefficients T_l. Even though a constant V_o may simulate the average effect of $V_o(\underline{\theta},\underline{b})$, subbarrier cross sections are sensitive.

We fitted a number of experimental excitation functions and found a rather week mass dependence of b.

The fit quality in particular in the subbarrier energy region is remarkable (fig 1 and 2). Using adapted Gaussian integrations one thus has a very fast way (seconds on the GSI computer) to compute excitation functions and study potential parameter influences quite reliably because major physical dependences are accounted for despite the simplicity of the model.



Projectile ^{40}Ar, targets as shown. Solid curves are coupled-channel calculations, dotted curves the no coupling limit[4], dashed curves the present calculations.

[1] K.Alder, A.Winther Nucl.Phys. A132,1(69)

[2] R.Bass Nucl.Phys. A231, 45 (1974)

[3] W.H.Miller J. Chem. Phys. 48,1651(1968)

[4] W.Reisdorf et al Nucl.Phys. A438,212(85)

Nuclear Landau-Zener Effect in the Scattering of ^{17}O on ^{13}C

Ch. Borchert, W. Greiner,
Institut für Theoretische Physik der Johann Wolfgang Goethe-Universität, Frankfurt am Main,
W. Scheid,
Institut für Theoretische Physik der Justus Liebig-Universität, Gießen,
and A. Thiel,
Department of Physics, North Carolina State University, Raleigh, U.S.A.

The collision of ^{17}O on ^{13}C has been investigated in coupled channel calculations within the molecular particle-core model[1] and compared to data observed by Haas et al.[2]. This model decomposes the above scattering system into two cores, ^{16}O and ^{12}C, and two valence neutrons. The valence neutrons are described by the eigenfunctions of the asymmetric two-center shell model[3] (TCSM) in adiabatic approximation. No core excitations have been considered. The relative movement of the nuclei is treated quantum mechanically.

The channels explicitly taken into account in the calculations are the elastic and inelastic channels ($^{17}O^*(\frac{1}{2}^+, 0.871MeV) + ^{13}C(\frac{1}{2}^-)$) and a transfer channel ($^{16}O + ^{14}C$ or $^{18}O + ^{12}C$). In the elastic channel the two valence neutrons occupy the $1d_{\frac{5}{2}}$- and $1p_{\frac{1}{2}}$-levels which correspond asymptotically, r (relative distance) $\rightarrow \infty$, to ^{17}O and ^{13}C, respectively, whereas in the inelastic channel the ^{17}O-valence neutron occupies the $2s_{\frac{1}{2}}$-state. In the transfer channels both valence neutrons belong to one nucleus. They occupy the ground state level ($1p_{\frac{1}{2}}$, or $1d_{\frac{5}{2}}$ for ^{14}C or ^{18}O resp.) and their spins are assumed to be paired to zero. To account for the pairing energy the Q-values of the reactions $^{17}O + ^{13}C \rightarrow ^{16}O + ^{14}C$ (or $^{18}O + ^{12}C$), 4.032MeV (3.098MeV) are subtracted from the real effective potential in the transfer channel.

The TCSM potential parameters are taken from Abe et al.[4] and reproduce the experimental neutron single-particle energies of the nuclei near the Fermi level. Besides the parameters of the TCSM the optical potential has to be specified for the calculations. The employed Woods-Saxon potential has a steeper slope and is much deeper than the one previously used in $^{17}O + ^{12}C$ calculations[5]. The parameters are chosen to reproduce the experimental elastic angular distributions measured by the Straßburg group[2].

In the TCSM level diagram two avoided level crossings are found which affect the cross sections. A close one is at about $r = 7.9fm$ where the $1d_{\frac{5}{2}}(|\Omega| = \frac{1}{2})$- and the $2s_{\frac{1}{2}}$-level approach. This avoided level crossing causes a strong narrow peak in the radial coupling of the inelastic channel due to a nuclear Landau-Zener effect. The second avoided level crossing appears between the $1d_{\frac{5}{2}}(|\Omega| = \frac{1}{2})$- and $1p_{\frac{1}{2}}$-levels of ^{17}O and ^{13}C at about $9fm$, and is giving a contribution to the transfer channel although it is not as close as the first one.

The figure shows the calculated angular distributions for an incident energy of $E_{c.m.} = 18.29MeV$ (corresponding to $E_{lab} = 42.2MeV$). The calculated elastic and inelastic cross sections are compared to the experimental data[2] (triangles). For the transfer channel no experimental data are availiable. We note that the oscillatory behaviour of the experimental data between $\Theta_{c.m.} = 45^o$ and 95^o is well reproduced for the elastic channel. The inelastic channel is underestimated for small scattering angles but lies in the vicinity of the error bars of which some are shown in the figure. The cross sections for the transfer channel ($^{16}O + ^{14}C$) are larger than those for the inelastic excitation. They are large in the forward direction and show a plateau in the backward angles.

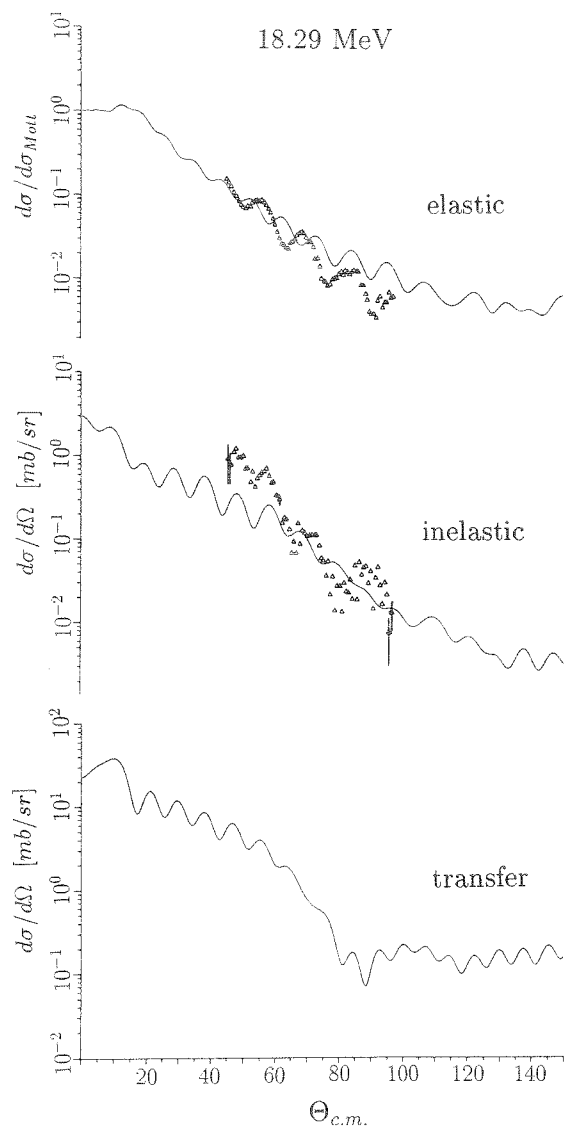


Fig. : Angular distributions of the differential cross sections for elastic and inelastic scattering of ^{17}O on ^{13}C and the $^{16}O + ^{14}C$ transfer. The full curves are the calculations as described in the text and the triangles denote the experimental data observed by Haas et al.[2].

References

[1] J. Y. Park et al., Phys. Rev. **C6**, 1565 (1972); ibid. **C20**, 188 (1979)

[2] F. Haas et al., private communication (1988)

[3] J. Maruhn et al., Z. Phys. **251**, 431 (1972)

[4] Y. Abe et al., Phys. Rev. **C28**, 2316 (1983)

[5] A. Thiel, Thesis, Universität Frankfurt (1988)

Dissipative Nuclear Fluid Dynamics

G. Wu*, R. Feng† and W. Nörenberg
GSI Darmstadt

The attractive feature of dissipative fluid dynamics, as proposed by Bertsch[1], is the possibility of describing the nuclear many-body problem in heavy-ion collisions by a few time-dependent fields, i.e. the density, the velocity and the stress tensor. These fluid-dynamical equations are derived by taking moments with respect to momentum of the Landau-Vlasov equation. In this approach equilibration is described by a relaxation term for the stress tensor which is due to the collision integral. The relaxation time depends on the local excitation in the fluid.

We have modified this approach by assuming that the stresses, which are built up in the direction of the velocity, spread with Fermi velocity over the whole system. For the collisions up to ca. 12 MeV/u this spreading (not the equilibration in all directions!) is fast compared to the collective velocities. This has been demonstrated in TDHF calculations by Köhler[2] and is due to higher moments which are disregarded in the fluid-dynamical approach.

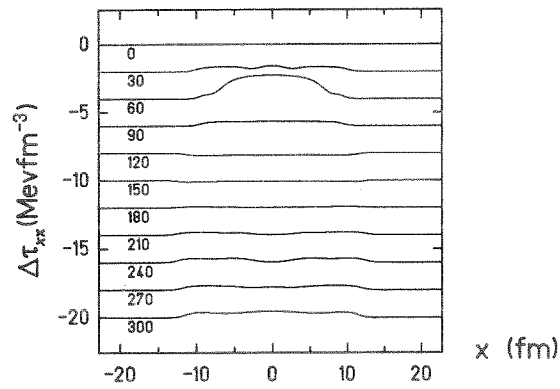


Fig. 1: Time evolution of the momentum-flow tensor component τ_{xx} with respect to the g.s. value for $E_{lab} = 10 MeV/u$.

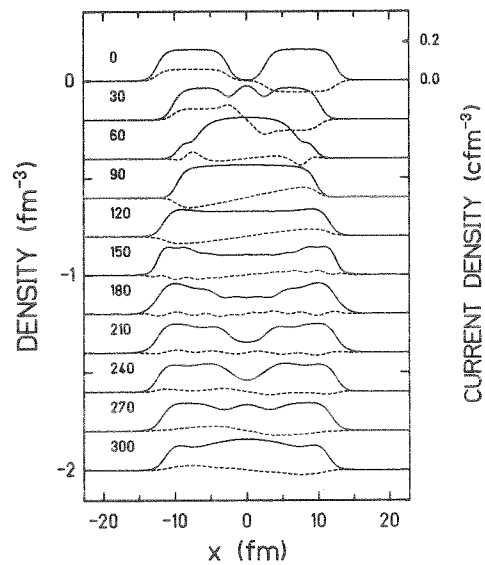


Fig. 2: Time evolution of the particle density (—) and the current density (– –) for $E_{lab} = 10 MeV/u$.

*on leave from the Institute of Modern Physics, Lanzhou, China

†on leave from the Institute of Atomic Energy, Beijing, China

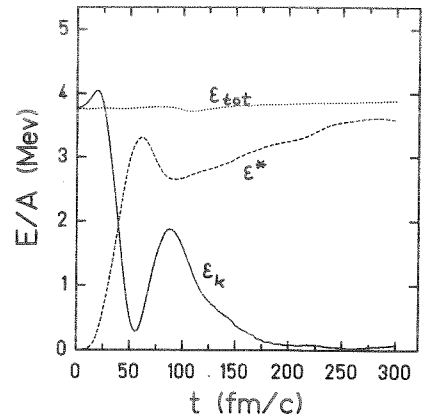


Fig. 3: Time evolution of total collective (ϵ_k) and excitation (ϵ^*) energy per particle for $E_{lab} = 15 MeV/u$. Also shown is the degree of total energy conservation in the numerical treatment.

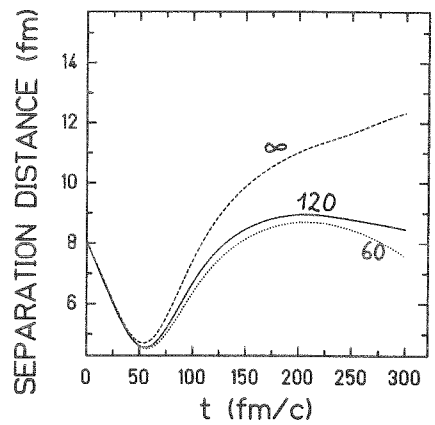


Fig. 4: Time evolution of the slab-slab separation distance for different relaxation times $\tau_{relax} = \tau_o/\epsilon^*(MeV/u)$ with $\tau_o = 60, 120$ and $\infty\, fm/c$.

Here we present some characteristic results from calculations[3] for slab-slab collisions at lab energies between 2 and 15 MeV/u (corresponding to 0.5 and 3.8 MeV/u CM energies). Fig. 1 illustrates how the stress is built up in the beam direction during the initial compression phase. This "pressure" in the beam direction yield additional repulsion which drives the two slabs apart (c.f. Fig. 2). During the later stages of the collision these stresses are equilibrized with respect to all directions (only the thermal pressure survives). Fig. 3 illustrates how the total intrinsic excitation energy ϵ^* and the total collective kinetic energy ϵ_K per particle change with time. Characteristically for the fluid-dynamical approach is the intrinsic excitation energy ϵ^*, which is to a large extent given by the deformation of the local Fermi sphere, is partially converted back into collective kinetic energy and gives rise to an elastoplastic behaviour. Finally, Fig. 4 illustrates the influence of different relaxation times on the slab-slab collisions. The repulsion increases with increasing relaxation time.

[1] G.F. Bertsch, Progr. Part. Nucl. Phys. 4 (1980) 483
[2] H.S. Köhler, Nucl. Phys. A378 (1982) 159
[3] G. Wu, R. Feng and W. Nörenberg, to be published

REFLECTION-ASYMMETRIC SHAPES IN TRANSITIONAL ACTINIDES

S. Ćwiok[a,b] and W. Nazarewicz[b]

[a]GSI, D-6100 Darmstadt, Fed. Rep. Germany

[b]Institute of Physics, Warsaw Institute of Technology, PL-00662 Warsaw, Poland

The suggestion that intrinsic reflection symmetry can be spontaneously broken in ground (and excited) states of atomic nuclei has been supported by increasing experimental evidence and theoretical calculations. An octupole component of the mean field deformation affects some single particle orbitals in ways that should be clearly manifested by the spectroscopy of odd-A nuclei. Experimental fingerprint of octupole deformation in odd-A nuclei is the presence of parity doublets with very distinct rotational properties and unusual electromagnetic moments [1,2]. A beautiful example of such structure are rotational "quasimolecular" bands of alternating parity states in ^{221,223}Th [3]. Because of strong fragmentation of single-particle wave function octupole deformation can influence many quantities which can be established experimentally, like the single-particle parity contents, Coriolis matrix elements, spectroscopic amplitudes, decoupling parameters, transition rates, magnetic moments, etc.

The main objective of the present study is to analyse the excitation energies and deformation properties of one-quasiparticle states in the neutron-deficient nuclei in the Ra-Th region. Detailed calculations of single-particle band-heads have been made for the odd-A isotopes of Rn, Fr, Ra, Ac, Th and Pa with neutron numbers $129 \leq N \leq 139$. We used the shell correction approach with the Woods-Saxon single-particle hamiltonian and the Yukawa-plus-exponential mass formula for the macroscopic energy. The residual interaction was assumed to be of the monopole-pairing form and it was treated by means of an approximate particle-number projection in the version developed by Lipkin and Nogami. The nuclear surface has been define by means of standard axial β_λ parametrisation, $\lambda = 2,3,4,5,6,7$. The assumption of axial symmetry allows us to label single-particle orbitals with one quantum number $K = \Omega$ (the intrinsic parity is violated by the presence of odd-multipole distortions). Levels belonging to the same Ω-family have been distinguished by means of additional quantum number, n_K, ordering single-particle states energetically counting from the bottom of the potential well. Selected results for Th isotopes has been published in a short letter [4] where more details about the method used can be found.

As a representative example, theoretical band-head energies for a sequence of Ac isotopes are shown in fig. 1 versus the mass number. According to the usual convention particle states are plotted above the ground state (at zero energy) and hole states are plotted below. The ground state of ^{219}Ac is a spherical $h_{9/2}$ state. For the nuclei ^{221,223,225}Ac there are two low-lying parity doublets with $K=\frac{3}{2}$ and $K=\frac{5}{2}$ predicted by the calculations and observed experimentally, cf. discussion in [2]. The nuclei ^{227,229}Ac are expected to be very octupole-soft in the low-lying 1-q.p. configurations, see fig. 2 below.

The calculated asymmetry energies for the lowest band-heads in $^{219-229}$Ac isotopes are shown in fig. 2. It is seen that they depend systematically on the structure of blocked orbital and, in particular, on its position with respect to the Fermi level. Therefore, it is very difficult to say, without any detailed calculations, whether octupole instability is present in a given 1-q.p. state or not. The calculated asymmetry energies in odd-A nuclei are usually larger than those calculated for the neighbouring even-even cores. The main contribution to this odd-even staggering are the specialization energy and the pairing energy [4].

In summary, predicted ground state properties of transitional odd-A light actinide nuclei are consistent with available experimental data. In most cases, our calculations reproduce the excitation pattern of low-lying 1-q.p. states. New equilibrium deformations will be used in the Coriolis coupling calculations within the reflection-asymmetric rotor-plus-quasiparticle model [2].

This work was supported in part by the Polish Ministry of National Education through contract CPBP 01.09.

References

[1] G.A. Leander and R.K. Sheline, Nucl. Phys. **A413** (1984) 375

[2] G.A. Leander and Y.S. Chen, Phys. Rev. **C37** (1988) 2744

[3] M. Dahlinger et al., Nucl. Phys. **A484** (1988) 337

[4] S. Ćwiok and W. Nazarewicz, Phys. Lett. **B224** (1989) 5

[5] A. Sobiczewski, Z. Patyk, S. Ćwiok and P. Rozmej, Nucl. Phys. **A486** (1988) 16

[6] S. Ćwiok and W. Nazarewicz, Nucl. Phys. **A469** (1989) 367

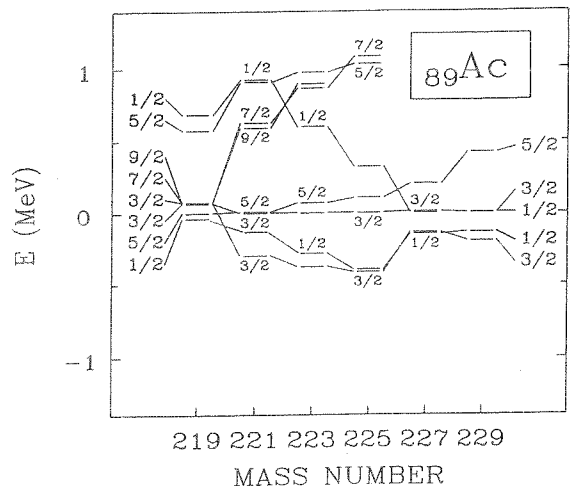


Fig. 1

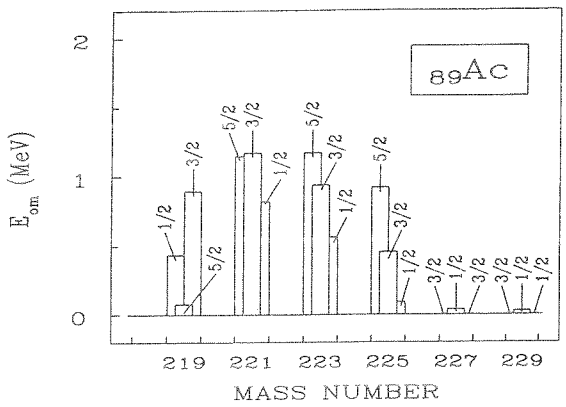


Fig. 2

An Improved Nuclear Fragmentation Model

J.-J. Gaimard, K.-H. Schmidt (GSI D-6100 Darmstadt)
M.S. Pravikoff (CENBG/IN$_2$P$_3$ F-33170 Gradignan)

Nuclear fragmentation (spallation and deep spallation) at relativistic energies is a two-step mechanism[1]. In our study of peripheral nucleus-nucleus collisions, we selected the classical abrasion model[2] for the first step (the spontaneous nuclear interaction step) and Campi and Hüfner's macroscopic evaporation model[3] for the second step (the deexcitation step). In this later model, evaporation is described as a diffusion process. The authors have developed a simple formalism for this complex phenomenon, which has a transparent physical meaning. The isobaric cross section is connected to the mass yield in the following way:

$$\sigma(A,I) = c(A)\times\frac{\Omega(A,I,E_t(A,I))}{\Omega(A,I_S,E_t(A,I_S))}\times\left[\exp\frac{-(I-I')^2}{2\times\tau_2\times(A'-A)/\alpha}\right]\times\sigma(A). \quad (1)$$

A, A', I and I' are the masses and excess neutron numbers of fragments and prefragments, i.e. the end-products and the nuclei formed in the first reaction step, resp. $c(A)$ is a normalization constant and $\Omega(A,I,E_t)$ the level density of the fragment taken at the energy of the lowest particle threshold $E_t(A,I)$. The subscript S stands for the most bound isotope. α is the mean value of the number of nucleons lost at each step of the evaporation process and τ_2 the corresponding mean-square change for the number of neutron-excess loss. In eq.1, the ratio of level densities only depends upon the final observable fragments. It is called *level-density factor*. On the chart of nuclides, this factor induces a corridor named *equilibrium residue corridor*[5]. The gaussian part of the formula (in brackets) memorizes some of the prefragment properties. It originates from a diffusion equation and is called the *memory factor*.

In the formulation of Campi and Hüfner, the relative rates of evaporated neutrons, protons and alpha particles are assumed to be constant. As a consequence of this rough approximation, this model fails to correctly reproduce the evaporation process for prefragments far away from the equilibrium residue corridor. Moreover, the authors treat the microscopic effects (shell corrections and pairing effects) in a non-consistent way when they handle level densities for the Fermi gas model.

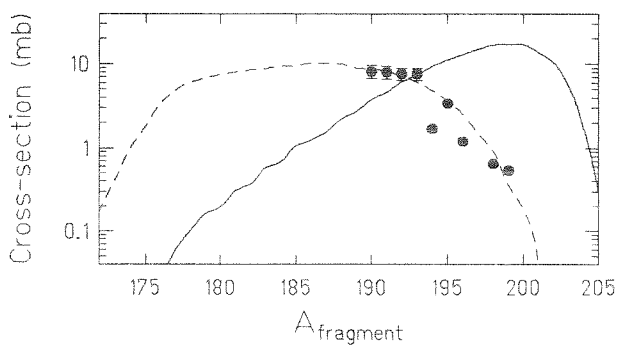


Figure 1: Experimental cross-section values for Au isotopes[4] (black circles) in the $^{12}C(0.4GeV/n)+Bi$ reaction; calculations with the model of Campi and Hüfner (solid line) and with our modified model (dashed line).

In our modified model, the mass distribution is connected to the prefragments distribution, according to:

$$\sigma(A) = \frac{dA'}{dA}\times\sigma(A') \quad (2)$$

where the relation between the fragment (mass A) and the prefragment (mass A'), with E' excitation energy, is:

$$A = A' - \sum_{i=1}^{i_{max}}\alpha_i \qquad \text{with} \qquad \sum_{i=1}^{i_{max}}\epsilon_i \simeq E'.$$

Another important modification of eq.1 is relevant to the memory factor which in our model becomes:

$$\left[\exp\frac{-(I-(I'-\sum_{i=1}^{i_{max}}\tau_{1i}))^2}{2\times\sum_{i=1}^{i_{max}}\tau_{2i}}\right]. \quad (3)$$

α_i, τ_{1i}, τ_{2i} and ϵ_i are, resp., the mean nucleon number, the mean neutron-excess number, its mean-square change and the mean energy loss for the i^{th} evaporation reaction step, calculated with the statistical model. Experimental data are compared to calculations with both the original and the modified model in fig.1. Experiment is only reproduced by the modified model. In fig.2, our calculation for the fragmentation of ^{209}Bi shows that all deexcitation paths for all prefragments eventually lead to the equilibrium residue corridor.

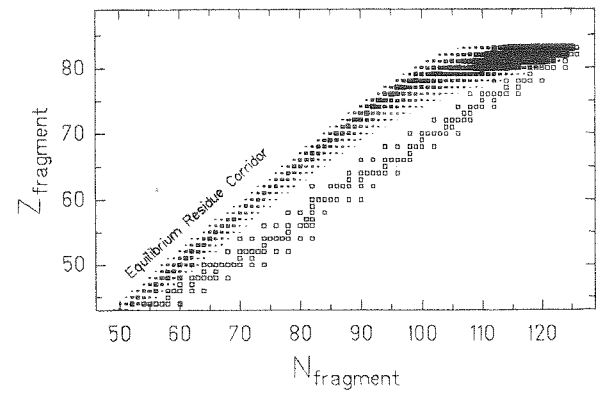


Figure 2: Calculated residue distribution for the $^{209}Bi(0.4GeV/n)+^{20}Ne$ reaction. Open squares indicate β stable isotopes.

To summarize, with the modifications made, we have a performing model for the nuclear fragmentation process to our disposal, where the physics clearly shows up, and for which the calculation times are very short.

References

[1] R.Serber: *Phys. Rev. 72 (1947), 1114*

[2] J.D.Bowman et al.: *LBL Report Nr.LBL2908, 1973*

[3] X.Campi and J.Hüfner: *Phys. Rev. C24 (1981), 2199*

[4] K.Aleklett et al.: *Phys. Rev. C23 (1981), 1044*

[5] J.P.Dufour et al.: *Nucl. Phys. A387 (1982), 157c*

Properties of particles from the high density region

C. Hartnack, H. Stöcker, and W. Greiner
Institut für Theoretische Physik, Universität Frankfurt, Germany

The idea of the nuclear equation of state is to learn something about the properties of hot dens nuclear matter. In high energetic relativistic heavy ion collisions this high density region can be obtained by inertial confinement of the nuclear matter. The key mechanism for this is the formation of shock waves, which was predicted by the hydrodynamical model [1] and confirmed by experiment [2]. The stiffnes of the equation of state controls the compressibility of the nuclear matter. A hard equation of state yields a stronger repulsion of the compressed matter whereas a soft equation of state is less repulsive and thus allows higher compression at a given compressional energy.
In this contribution we will show an analysis of the system Nb on Nb at 1050 MeV using the VUU model [3]. Similar results are also obtained by IQMD calculations. Fig. 1 shows the multiplicity distribution of the maximal density $(\rho/\rho_0)_{max}$ the regarded particle reached during the whole calculation. We see that in the calculation using a soft equation of state (dashed line) higher maximal densities are reached than in the calculation with a hard one (full line). Note that there is only a small number of particles reaching very high densities. Most of the particles reached densities up to $(\rho/\rho_0)_{max} \approx 1$–$2$.
Now let us focus on the kinetic properties of the particles from the different density regions. We distinguished three density regions: particles that come from low density ($(\rho/\rho_0)_{max} < 1.2$, dashed line), particles coming from very dens regions ($(\rho/\rho_0)_{max} > 2.8$, dash-dotted line) and the particles of the intermediate region ($1.2 < (\rho/\rho_0)_{max} < 2.8$, dotted line). Fig. 2 shows the rapidity distribution for the different density components. While the distribution of the particles from the low density region peaks at projectile and target rapidity ($\approx \pm 0.7$ in the NN-frame for the used system), the particles from the high density region are stopped to a peak at CM rapidity. For the particles of the intermediate region, we see a superposition both components. Fig.3 shows the flow $< p_X(Y) >$ for the three components. Here the flow is dominated from the particles of the low density region while for the particles coming from high densities $< p_X(Y) > \approx 0$. This corresponds to the results from the analysis of fragments. "Cold" fragments are less stopped and show larger flow than the "hot" single particles [4]. Therefore the analysis via tranverse flow does not tell so much about the particles of the high density region but about the rather cold matter repelled from that region. For analysis of higher density regions observables corresponding to the stopped matter, e.g. the azimuthal distibution at Y_{CM} and the so-called "squeeze-out" are more interesting. But also here the particles of very high density region show tendencies to isotropy[5].

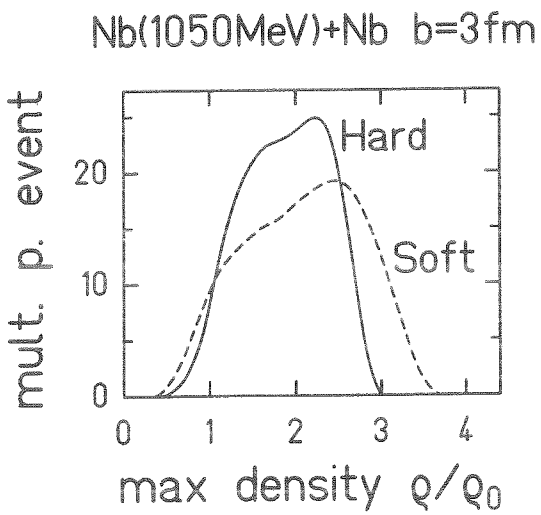


Fig.1: Multiplicity distribution of the maximal density $\left(\frac{\rho}{\rho_0}\right)_{max}$ the particle has reached during the calculation.

References

[1] W. Scheid, H. Müller, and W. Greiner, Phys. Rev. Lett. 21 (1974) 741
H. Stöcker, J.A. Maruhn and W. Greiner, Phys. Rev. Lett 44 (1980) 725
G. Buchwald et al., Phys. Rev. Lett 52 (1984) 1594.

[2] H.A. Gustafsson, H.H. Gutbrod, B. Kolb, H. Löhner, B. Ludewigt, A.M. Poskanzer, T. Renner, H. Riedesel, H.G. Ritter, A. Warwich, F. Weik and H. Wieman, Phys. Rev. Lett. 52 (1984) 1590.

[3] H. Kruse, B.V. Jacak and H. Stöcker, Phys. Rev. Lett. 54 (1985) 289.
H. Stöcker and W. Greiner, Phys. Rep. 137 (1986).

[4] G. Peilert, Thesis, University of Frankfurt (1988).
G. Peilert, A. Rosenhauer, J. Aichelin, H. Stöcker, and W. Greiner, Phys. Rev. C39 (1989), 1402
K.H. Kampert, Ph. D. Thesis, University of Münster (1986)

[5] C. Hartnack, Thesis, University of Frankfurt (1989).

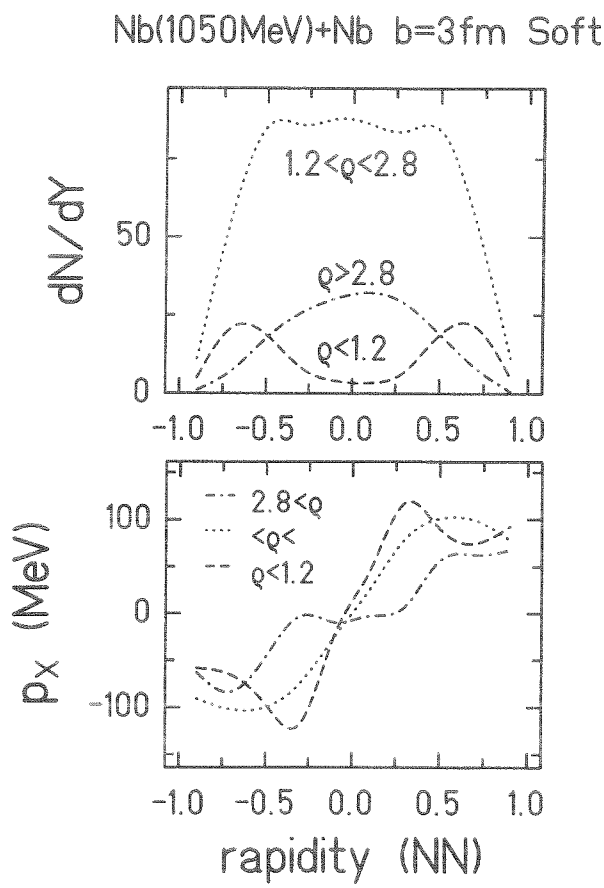


Fig.2: Rapidity distribution for particles with low, high and intermediate $\left(\frac{\rho}{\rho_0}\right)_{max}$.

Fig.3: $< p_X(Y) >$ for particles with low, high and intermediate $\left(\frac{\rho}{\rho_0}\right)_{max}$.

FRAGMENT FLOW IN THE RELATIVISTIC BUU MODEL[B,G]

V. Koch, B. Blättel, W. Cassing, U. Mosel and K. Weber
Institut für Theoretische Physik, Universität Gießen

A recent experiment of the Plastic Ball Group [1] found that the in–plane transverse momentum per nucleon [2] is larger for intermediate size fragments than for single nucleons. Furthermore, the momenta of the fragments are found to be much more focussed into the reaction plane than those of the single nucleons. Calculations based on the QMD model [3], which fitted these experiments, concluded that the formation of intermediate fragments sets in rather early and therefore may influence the whole reaction dynamics. As a consequence, the results of a BUU type calculation would not be conclusive anymore. The validity of this conclusion rests, of course, on the ad–hoc assumption that QMD provides a realistic description of n–body correlations.

Here we will show that the observed difference in transverse momentum can also be explained by simple final state interactions and that nucleons and fragments experience the same reaction dynamics.

We model the final state interaction with a coalescence prescription, where one assumes that particles within a certain distance in momentum space form a cluster. As an effect of the transverse flow there is a certain asymmetry in the occupation of momentum space: at positive rapidity, more particles with positive in–plane transverse momentum (p_x) exist than with negative p_x. Therefore, in the coalesence model more fragments with positive than with negative p_x are created at positive rapidity. Thus the fragments will aquire a high average p_x per nucleon, while the remaining positive p_x of the single nucleons will be cancelled to some extent by nucleons with negative p_x, leading to a smaller net p_x per nucleon.

We have used the covariant BUU model [4] in order to investigate this picture numerically. Experimental data for the flow of fragments are available for the reaction $^{197}Au+^{197}Au$ at 200 MeV [1]. Our calculations are based on 300 parallel ensembles which were subjected to the acceptance filter program [1].

Fig. 1 shows our result together with the experimental data for the p_x/A distribution. Especially in the forward region, where the data and the calculation are most reliable, we find reasonable agreement with experiment. Particularily the higher p_x/A for the fragments is reproduced. In Fig. 2 we show the p_x/p_t distribution, which is a good meassure for the projection of the transverse momentum into the reaction plane. Again we find agreement with experiment.

The coalescence picture thus serves to explain the differences in the transverse momentum distributions between fragments and single nucleons observed in experiment as being due to final state interactions. As a consequence one may average over the p_x/A data of all fragments because in a given rapidity bin the number of nucleons and the total in–plane transverse momentum does not change due to final–state interactions. The average p_x, therefore, should be comparable directly with the result of a BUU calculation without the uncertainty of a fragment description. A detailed presentation of this work can be found in ref. [5].

References:
1) H.H. Gutbrod et al., Rep. Prog. Phys **52** (1989) 1267
2) P. Danielewicz and G. Odyniec, Phys. Lett. **B157** (1985) 146
3) G. Peilert et al., Phys. Rev. **C39** (1989) 1402
4) B. Blättel et al., Phys. Rev. **C38** (1988) 1767
5) V. Koch et al., submitted to Phys. Lett. B

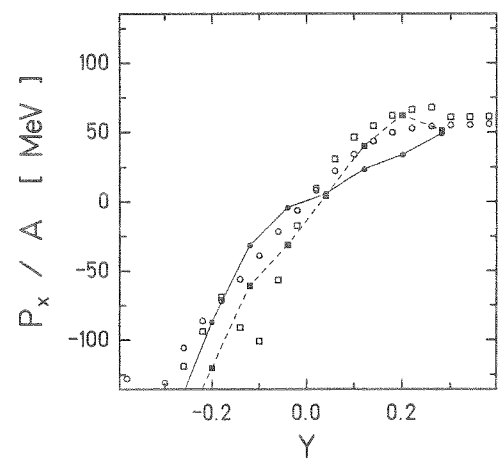


Fig. 1 P_x/A versus rapidity Y for A=1,2 (open circles) and A=3–4 (open squares) particles. The experimental data correspond to full circles and full squares respecitively. The lines are drawn to guide the eye.

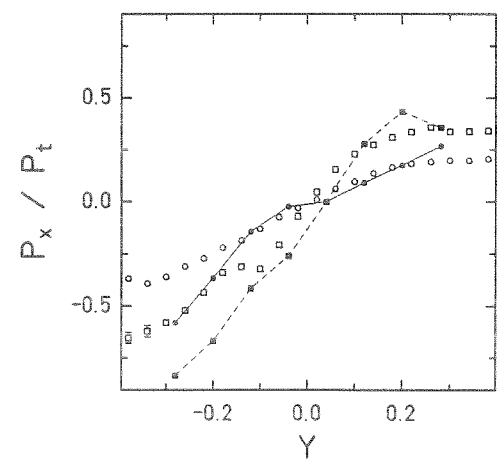


Fig. 2 P_x/P_t versus rapidity Y. Labeling as in fig. 1.

K^+-Production at Subthreshold Energies[B,G]

G. Batko, W. Cassing, K. Niita, Gy. Wolf
Institut für Theoretische Physik, Universität Gießen

The production of K^+-mesons at bombarding energies far below the free NN threshold is expected to provide a clear information either about cooperative phenomena or about high momentum components of the nuclear many-body wavefunction since the interaction with the baryonic environment is smaller than for other mesonic probes due to strangeness conservation. Furthermore, the kaons emitted in this regime may provide a signal for hot and dense nuclear matter[1].

The model is based on the VUU transport theory in which the kaons are produced perturbatively and all production vertices are treated on-shell[2]. The differential particle multiplicity emerging from a heavy-ion reaction at a fixed impact parameter b is given by

$$E_K \frac{d^3N_K(b)}{d^3p_K} = \sum_{\substack{NN \\ coll}} \int \frac{d\Omega}{4\pi} \frac{1}{\sigma_{NN}} E'_K \frac{d^3\sigma_{NN\to K}}{d^3p'_K} [1-f_1]$$

$$+ \sum_{\substack{NN \\ coll}} \int \frac{d\Omega}{4\pi} \int \frac{d^3p_\pi}{E'_\pi} \frac{1}{\sigma_{NN}} \cdot E'_\pi \frac{d^3\sigma_{NN\to NN\pi}}{d^3p'_\pi} [1-f_3]\cdot[1-f_4] \times$$

$$\frac{1}{\mathcal{N}} \sum_{\substack{N_1 \\ |r_0-r_1|<\lambda}} \frac{1}{\sigma_{\pi N_1}} \cdot E'_K \frac{d^3\sigma_{\pi N_1\to \Lambda K}}{d^3p'_K} \qquad [1]$$

The first term represents the contributions corresponding to primary baryon-baryon collisions. $\sigma_{NN}(\sqrt{s})$ is the free nucleon-nucleon total cross section[2] and Ω is the solid angle of the relative momentum $\mathbf{p}_3-\mathbf{p}_\Lambda$. The primes denote quantities in the center of mass system of the baryon-baryon collision. The second term represents the contribution due to secondary pion-nucleon collisions while $\sigma_{\pi N}$ denotes the corresponding total cross section. The internal sum runs over all nucleons $\mathcal{N}$ contained inside a sphere of radius $\lambda=[\sigma_{\pi N}(\sqrt{s})\cdot\rho_0]^{-1}\approx 2$ fm around the point r_0 at which the pion has been created. This procedure is equivalent to fold the pion distribution with the local momentum distribution.

The total cross section for $BB\to BYK^+$ as well as for $NN\to NN\pi$ production processes are adopted from refs. 1 and 3, respectively, while the differential cross sections are parametrized as a function of the maximum momentum $p_{max}(\sqrt{s})$. The cross section for the process $\pi N\to \Lambda K^+$ is taken from the parametrization of Cugnon[4] and averaged over the processes $\pi^0 p\to K^+\Lambda$ and $\pi^+ n\to K^+\Lambda$. Inclusive cross sections, finally, are obtained by integration over impact parameter.

The inclusive cross section for K^+-production in $p+^{12}C$ is shown in Fig. 1 as a function of the bombarding energy E_{lab} of the proton in comparison to the data of Koptev et al[5]. The results corresponding to secondary processes (full line) are in quite remarkable agreement with the experimental yield while

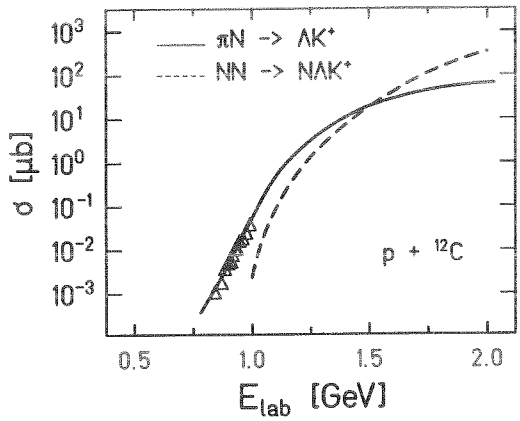


Fig. 1

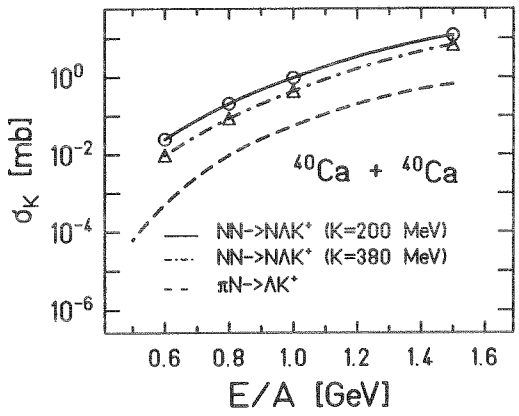


Fig. 2

the contribution from primary processes (dashed line) misses the data completely. The theoretical estimate of the K^+-yield for the system $^{40}Ca+^{40}Ca$ as a function of the bombarding energy per nucleon E/A (Fig. 2) shows that the contribution emerging from BB processes is about a factor 10 larger than the secondary πN yield throughout the whole energy range. In addition we find a sensitivity of about a factor of 2 to 2.5 in the kaon cross section for a change in the nuclear compressibility K from 200 to 380 MeV.

We conclude that in p+A reactions below 1 GeV kaons originate from secondary pion-nucleon inelastic scattering while in A+A reactions the K^+-yield is dominated by baryon-baryon production processes even at low energies.

1) B. Schürmann and W. Zwermann, Mod. Phys. Lett. A3 (1988) 1441.
2) W. Cassing, V. Metag, U. Mosel and K. Niita, Phys. Rep., in press.
3) B. J. Ver West and R. A. Arndt, Phys. Rev. C25 (1982) 1979.
4) J. Cugnon and R. M. Lombard, Nucl. Phys. A422 (1984) 635.
5) V. P. Koptev et al, Sov. Phys. JETP 67 (1988) 2177.

Resonances in particle production[B,G]

M. Schäfer, A. Engel, T. Vetter, T. S. Biró, W. Cassing, U. Mosel
Institut für Theoretische Physik, Universität Gießen

In several models for particle production in heavy–ion collisions the yield is calculated by incoherent superposition of the production from individual nucleon–nucleon collisions. Therefore one needs the elementary nucleon–nucleon production cross sections. As in the case of elastic pion–nucleon scattering, where the main contribution is produced by the virtual Δ in the s–channel, we expect for particle production at higher bombarding energies a dominant contribution from the respective baryon resonances. The calculations are performed by using an effective One–Boson–Exchange potential. The coupling constants and cut–off factors of the exchanged mesons (π, ρ, σ, ω) are obtained by fitting the elastic nucleon–nucleon scattering amplitude.

In the case of pion production the most important resonance is the $\Delta(1232)$. The coupling constant $f_{N\Delta\pi} = 1.85$ is fitted to the experimental data[1]. Using this constant we obtain a decay width for the $\Delta \rightarrow N + \pi$ reaction of $\approx$100 MeV, which is 10% smaller than the experimental value. In Fig. 1 we show our results for the reaction pp $\rightarrow$ pnπ^+ at 800 MeV. Employing only the Δ propagator (full line) the calculation agrees nicely with the data, while a strong interference between Δ – and N – propagator leads to a sizable overestimation for high proton momenta (dashed line).

The most important resonance for the production of η's is the N*(1535). From the reaction π N $\rightarrow$ η N we get $g_{NN^*\pi} \cdot g_{NN^*\eta} = 1.65$. Without any free parameter we calculate p p $\rightarrow$ p p η at several energies (Fig. 2). We find a good reproduction of the experimental data[2].

Pions and η's have the disadvantage that they are reabsorbed in the nuclear medium. Clean information can therefore only be obtained from electromagnetic probes like dileptons (e^+e^- pairs). In addition to our previous calculation[3] we include now the virtual Δ resonance and gauge the formfactors. The coupling constant $f_{N\Delta\gamma} = 0.36$ was fitted to the decay $\Delta \rightarrow N + \gamma$. At a beam energy of 2 Gev the Δ's are found to increase the yield by roughly a factor of two for proton–neutron scattering.

1) J. Hudomalj–Gabitzsch et al, Phys. Rev. C18 (1978) 2666

2) V. Flamino et al, CERN HERA report 84–01

3) M. Schäfer, T. S. Biro, W. Cassing, U. Mosel, Phys. Lett. B221 (1989) 1

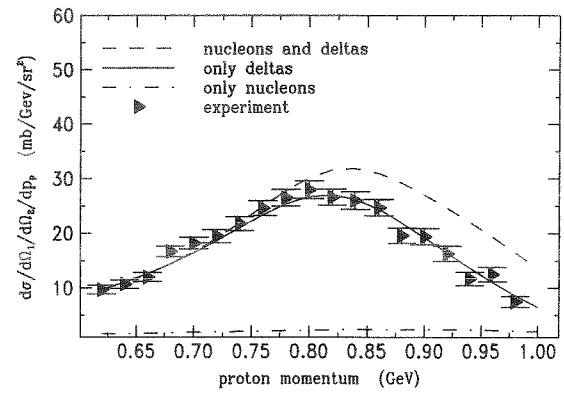


Fig. 1: Comparison between the experimental data for the reaction pp$\rightarrow$ pnπ^+ at 800 MeV and the results of the calculation with nucleon (dash–dotted), delta propagator (solid) and the coherent sum of both (dashed).

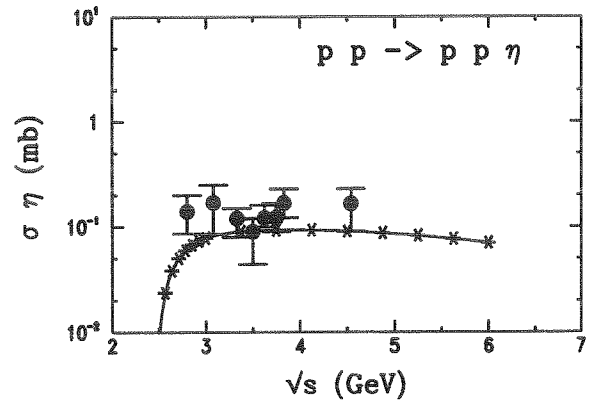


Fig. 2: Comparison between the experimental data for the reaction pp$\rightarrow$ ppη and our results including the N* resonance.

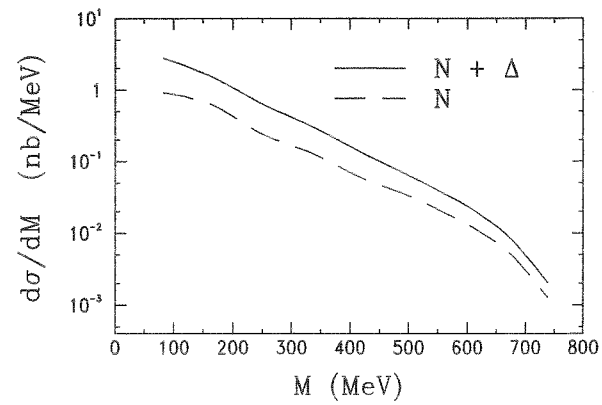


Fig. 3: Dilepton production at 2 GeV with and without virtual Δ–exitation.

Dilepton Production in Heavy-Ion Collisions[B,G]

Gy. Wolf, G. Batko, W. Cassing, U. Mosel, K. Niita and M. Schäfer
Institut für Theoretische Physik, Universität Gießen

We study pion and dilepton production on the basis of a microscopic model of the BUU type. As a new feature, in this model the pions are also explicitly propagated as well as the $\Delta(1232)$ and N*(1440) resonances with their isospin degrees of freedom. The effect of the medium on the resonance peak and width is neglected and free values are used. For the resonance production we used a nonisotropic cross–section with an angular dependence fitted to experimental data. This gives about 20% less stopping at 2 GeV/A than for isotropic production. The isospin degrees of freedom are explicitly included and the isospin dependence of the cross–sections is taken into account, too. Furthermore, an approximately covariant collision prescription is implemented. This model is found to correctly reproduce the nucleon and the pion transverse energy spectra from 400 MeV/A to 2 GeV/A, as well as the total pion yield.

We apply this model additionally to dilepton production by considering $\pi^-\pi^+$ annihilation, proton–neutron and pion–nucleon bremsstrahlung and the Dalitz–decay of the Δ as elementary processes. The calculations are performed for p+^{9}Be and ^{40}Ca+^{40}Ca at 1 and 2 GeV/A respectively, where we can compare with the data of the DLS collaboration[1]. For each system the calculations are in conflict with the data at small invariant masses (fig.1 and fig.2.). Above 300 MeV dilepton invariant mass we obtain a quite good agreement. At small invariant masses, M, the Δ–decay and pn bremsstrahlung dominate, while for M $\geq$ 400 MeV the $\pi^-\pi^+$ annihilation dominates in ^{40}Ca+^{40}Ca collisions in agreement with our earlier findings[2]. From the present inclusive data we cannot extract any detailed information on the pion–dispersion relation $\omega_\pi(k_\pi)$ that has been proposed to be reflected in the dilepton yield for M $\geq$ 300 MeV[3]. The $\pi^-\pi^+$ annihilation yield, however, scales differently with impact parameter b than the pn bremsstrahlung contribution (fig.3.). This suggests to select high multiplicity events as a trigger for central collisions which has the additional advantage of triggering on high density events where possible dispersion relation effects are expected to be strongest.

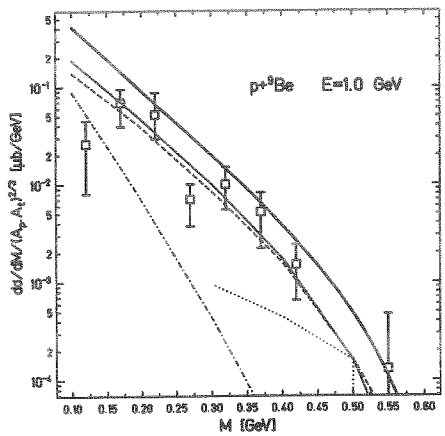


Fig. 1: Dilepton invariant mass spectrum for p+^{9}Be at 1 GeV bombarding energy. Solid line: pn bremsstrahlung; dotted–dashed: π–nucleon bremsstrahlung; dotted: $\pi^+\pi^-$ annihilation; dashed: Δ–decay; the thick solid line: sum of all contributions.

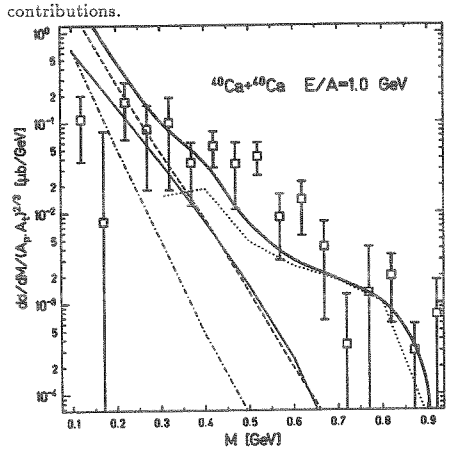


Fig. 2: Dilepton invariant mass spectrum for ^{40}Ca+^{40}Ca at 1 GeV/A bombarding energy. Solid line: pn bremsstrahlung; dotted–dashed: π–nucleon bremsstrahlung; dotted: $\pi^+\pi^-$ annihilation; dashed: Δ–decay; the thick solid line: sum of all contributions.

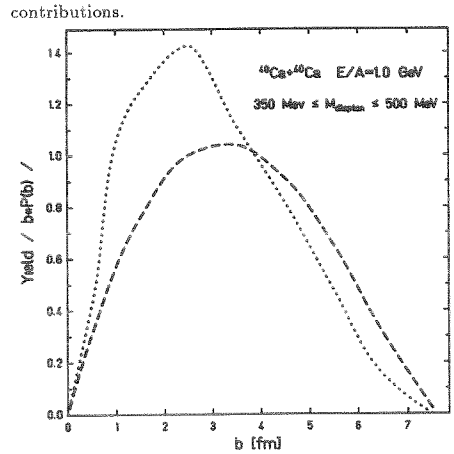


Fig. 3: Impact parameter dependence of the pn bremsstrahlung contribution (dashed line) and the $\pi^+\pi^-$ annihilation (dotted line) for ^{40}Ca+^{40}Ca at 1 GeV/A.

References

1) G. Roche et al., Phys. Rev. Lett., 61 (1988) 1069
C. Naudet et al., Phys. Rev. Lett., 62 (1989) 2652
G. Roche et al., Phys. Lett., B226 (1989) 228

2) G. Batko, T.S. Biro, W. Cassing, U. Mosel, M. Schäfer and Gy. Wolf, in: Proc. NATO ASI The Nuclear Equation of State (Peniscola, Spain, 1989) ed. W. Greiner

3) C. Gale and J. Kapusta, Phys. Rev., C35 (1987) 2107

Relativistic Kinetics of Nuclear Collisions [G]

M. Schönhofen, M. Cubero, B. L. Friman and W. Nörenberg
GSI Darmstadt and Institut für Kernphysik, TH Darmstadt

Starting from the non-equilibrium Green function formalism of Kadanoff and Baym [1] we derive covariant kinetic equations for Quantum Hadrodynamics [2]. We perform the gradient expansion for the Green functions and self-energies [1] assuming that the conditions for quasi classical motion are satisfied, i.e., assuming that the system varies slowly enough in space and time. Furthermore we use the quasi-particle approximation, neglecting the real part of the selfenergy functions, but including the real Hartree selfenergy. In this approximation the spectral function of the nucleons is assumed to be proportional to the delta-function $\delta(p^{*\mu}p^*_\mu - m_N^{*2})$, where p^* is the kinetic momentum of the nucleons $p^{*\mu} = p^\mu - g_V\langle\omega^\mu\rangle$, and m_N^* the nucleon effective mass $m_N^* = m_N - g_S\langle\Phi\rangle$ in the Hartree approximation. The collision integral is calculated in second order perturbation theory (Born approximation) with mean-field quasi-particle states.

The resulting quasi-classsical kinetic equations for the phase-space distribution function of the nucleons [3] are solved numerically for spatially homogeneous systems.

The parameters of the model are the masses of the nucleons and mesons and the coupling constants of the vertices. The coupling constants are determined by fitting the free, elastic, differential nucleon-nucleon cross-section at a beam energy of 1 GeV [4], with the help of form factors $F(q^2)$, where q is the momentum transfer at the meson-nucleon vertices $(F(q^2) = \Lambda^2/(\Lambda^2 - q^2)$, $g_S = 5.74, g_V = 6.00, g_\pi = 13.45, \Lambda_S = 975$ MeV, $\Lambda_V = 706$ MeV, $\Lambda_\pi = 693$ MeV). In figure 1 we show the mean collision time $\tau_{col} = 1/(2Im\Sigma)$ calculated in our model for a nucleon incident on nuclear matter in the groud state. Below $E_{lab} = 150$MeV the Pauli exclusion principle principle is responsible for the very

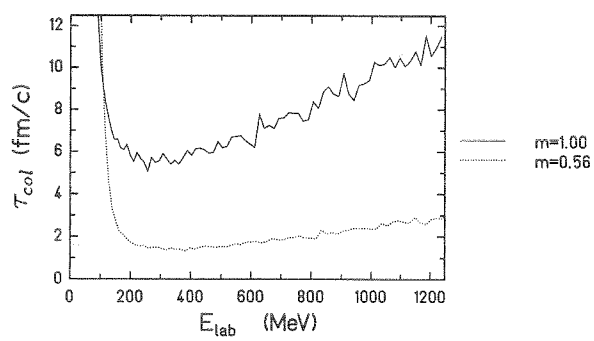


Figure 1: Mean time between two successive elastic nucleon-nucleon collisions for a nucleon incident on the ground state of nuclear matter as a function of the nucleon kinetic energy.

long collision time. Near the Fermi surface most of the scattering events are forbidden. Between $E_{lab} = 200$ MeV and 500 MeV the mean collision time reaches its minimum (≈ 5 fm/c). The importance of the Pauli principle is decreased and the nucleon-nucleon cross-section is still fairly isotropic. At higher energies the elastic cross-section is strongly forward-backward peaked. This implies that many of the final states are blocked since one of the nucleons would be within the Fermi sphere. The net result is an increase of τ_{col} to 9 fm/c at $E_{lab} \simeq 1$ GeV. For $m_N^* = 0.56 m_N$ the effect on the collision time is much weaker. This is mainly due to a larger and more isotropic cross-section.

The time evolution of a symmetric nucleus-nucleus collision with a beam energy of 1 GeV per nucleon, modelled by counter-streaming nuclear-matter, is displayed in figure 2 for different times, where $\tau_0 = 1.8$ fm/c is the mean collision time for free nucleons. Only ellastic collisions are taken into account. The initial condition is achieved by boosting two Fermi spheres with $v_z = \pm 0.6$ c. The mass of the nucleons is $m_N^* = m_N$ and the influence of the mean meson fields is neglected. During the early stage

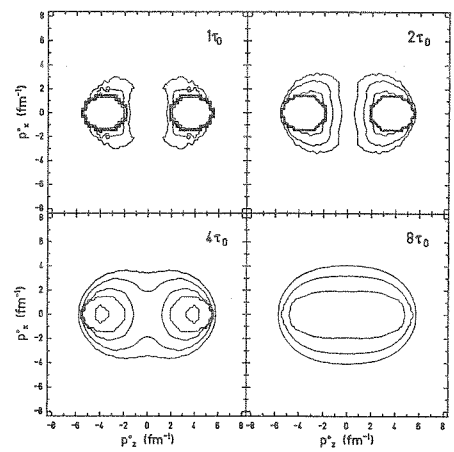


Figure 2: Evolution in momentum space of two Fermi ellipsoides at different times of the collision. The contour lines are: 0.02, 0.04, 0.08, 0.16, 0.32 and 0.64.

of the collision the first nucleon-nucleon collisions should fill a shell in momentum space because of energy and momentum conservation at each vertex. At these energies the cross-section is strongly forward peaked and therefore, only the momentum states near the original Fermi ellipsoides will be occupied by first collisions. Finally after 12 τ_0 the system reaches thermodynamical equilibrium.

[1] L.P. Kadanoff and G. Baym, 1962, Quantum Statistical Mechanics (Benjamin, New York)
[2] B. Serot und J. D. Walecka, Adv. Nucl. Phys. **16** (1986) 1, Plenum Press, New York
[3] Q. Li, Q. Wu and C. M. Ko, Phys. Rev. C **39** (1989) 849
[4] J. Cugnon, T. Mizutani und J. Vandermeulen, Nucl. Phys. **A352** (1981) 505

Thermodynamical Analysis of Relativistic Heavy-Ion Collisions[B,G]

A. Lang, B. Blättel, W. Cassing, V. Koch, U. Mosel, K. Weber
Institut für Theoretische Physik, Universität Giessen

In view of the new GSI SIS-facility we have tried to estimate in a fully covariant transport approach [1] the amount of isotropy in momentum-space reached in heavy-ion collision at an energy of 1 AGeV. This question becomes very important when one tries to relate the highly excited reaction phase to an equation of state (EOS). To learn more about sensitive observables to the EOS, we have choosen three parametrisations of the underlying Lagrangian density which differ in the value of the nuclear compressibility K and the effective mass m^*/m that determines the momentum dependence of the interaction. In shorthand notation we will refer to these as: QHDI (K = 540 MeV, $m^*/m = 0.56$), NL1 (K = 380 MeV, $m^*/m = 0.83$) and NL2 (K = 210 MeV, $m^*/m = 0.85$).

In fig. 1 we show the time evolution of the momentum-space distribution in the central volume element ($\sim$ 27 fm^3) during the high density phase for a collision of ^{93}Nb $\rightarrow$ ^{93}Nb at 1 AGeV and impact parameter b = 2.72 fm. The upper row refers to QHDI and the lower row to NL2. In comparing these two parametrizations, one notices easily a striking difference which manifests itself in a large distortion of the Fermi-sphere in the NL2 case even in the last time step shown. So nuclear compressibility and momentum-dependence play a major role in the equilibration process.

The quantity which contains most information about the local properties of a system is the energy-momentum tensor $T^{\mu\nu}$ defined for an arbitrary Lagrangian density $\mathcal{L}(x)$ as

$$\tilde{T}^{\mu\nu}(x) = \frac{\partial \mathcal{L}}{\partial(\partial_\mu \phi_i)} \partial^\nu \phi_i - g^{\mu\nu}\mathcal{L}. \qquad (1)$$

The symmetrized form of the energy-momentum tensor for the nonlinear σ-ω model reads in phase-space representation assuming the local density approximation:

$$T^{\mu\nu}(x) = \int \frac{\mathrm{d}^3\Pi}{\Pi^0}\, \Pi^\mu \Pi^\nu f(x,\Pi) + m_V^2 \omega^\mu \omega^\nu + \frac{1}{2} g^{\mu\nu}\left(m_S^2 \Phi^2 + \frac{2}{3} B\Phi^3 + \frac{1}{2} C\Phi^4 - m_V^2 \omega^\rho \omega_\rho \right), \qquad (2)$$

where $f(x,\Pi)$ denotes the quasi-particle phase-space distribution, Φ and ω_μ are the scalar and vector meson fields, respectively, and $g^{\mu\nu}$

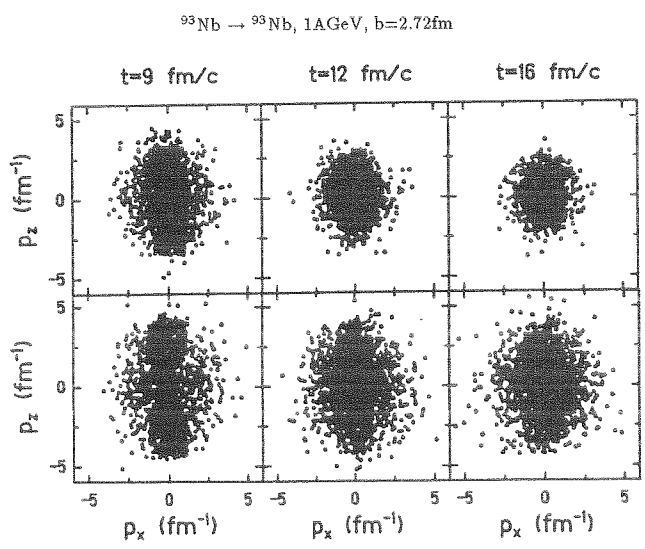


Figure 1: Momentum distribution in the central volume

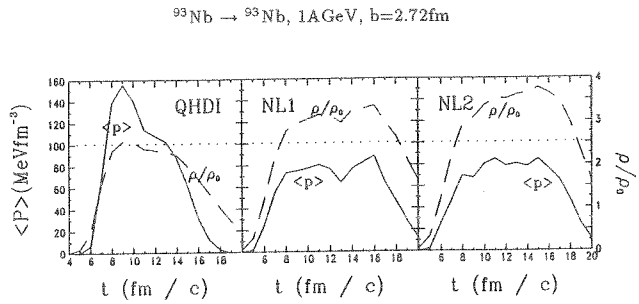


Figure 2: Comparison for different EOS

denotes the metric tensor. The energy-momentum tensor for an ideal liquid moving with four velocity u^μ evaluates to

$$T^{\mu\nu}(x) = (e(x) + p(x))\, u^\mu u^\nu - g^{\mu\nu} p(x) \qquad (3)$$

and reduces in its local rest frame to $T^{\mu\nu}(x) = \mathrm{diag}(e, p_1, p_2, p_3)$. Here $e(x)$ denotes the energy-density and $p_1(x) = p_2(x) = p_3(x) = p(x)$ is the hydrodynamical pressure. In order to compare this with our simulation we divide the whole reaction volume in small cells of 1 fm^3 each which are then transformed to their local rest frame. This gives the local four-velocity u^μ while a diagonalization of $T^{\mu\nu}$ in this frame provides the energy-density $e(x)$ and three eigenvalues for the pressures $p_i(x)$ which are not neccesarily the same.

In fig. 2 we show the time evolution of the average pressure $\langle p \rangle = \frac{1}{3}\sum p_i$ as well as the baryon density ρ_B. It should be noted that there is almost no compression achieved for the QHDI parametrization, which is indicated by the dotted line. The latter corresponds to the density of two overlapping Lorentz-contracted nuclei i.e. $\rho_B = 2\gamma\rho_0$. We obtain about the same average pressure for NL1 and NL2, but nearly twice as much for QHDI. So the most sensitive parameter is not the nuclear compressibility but the momentum dependence of the interaction.

To obtain the local temperatures we have adopted the extension of the Walecka-model for finite temperature T [3]. This provides a relation between the baryon density ρ_B, temperature T and equilibrium pressure p. Since the density ρ_B and the pressure p are calculated locally, we can extract the temperature T. Here it should be emphasized again that it is very important to achieve local equilibrium. From fig. 1 we already know that this is rather poorly fulfilled. So we obtain quite different "temperatures" dependent on the pressures $p_i(x)$ we choose [2]. Local temperatures thus appear to be rather ill defined for heavy-ion collisions at 1 AGeV.

References

[1] B. Blättel, V. Koch, W. Cassing and U. Mosel, Phys. Rev. C 38 (1988) 1767

[2] A. Lang, B. Blättel, V. Koch, K. Weber, W. Cassing and U. Mosel, Preprint UGI-90-4

[3] B. S. Serot and J. D. Walecka, Adv. Nucl. Phys. 16 (1986) 1

Retardation and Radiation Effects in the RBUU-Model[B,G]

K. Weber, B. Blättel, V. Koch, A. Lang, W. Cassing and U. Mosel
Institut für Theoretische Physik, Universität Giessen

We simulate relativistic heavy-ion collisions in the relativistic BUU-approach [1] concentrating on the validity of approximate solutions for the meson field equations.

Whereas the nucleon phase-space density is propagated by a transport equation similar to the nonrelativistic BUU-equation [2], the meson fields obey inhomogenous Klein-Gordon equations of motion:

$$\frac{\partial^2}{\partial t^2}\sigma - \vec{\nabla}^2\sigma + m_s^2\sigma = g_s\rho_s \quad (1)$$

$$\frac{\partial^2}{\partial t^2}\omega^\mu - \vec{\nabla}^2\omega^\mu + m_v^2\omega^\mu = g_v j^\mu \quad (2)$$

where ρ_s and j^μ are the scalar density and the baryon four current, respectively.

Equations (1) and (2) are solved by a predictor-corrector scheme of variable order. The results from this full solution (FS) are compared to those from the local density approximation (LDA), where all space-time derivatives in (1) and (2) are neglected. We further investigate the quasistatic approximation (QSA), where one approximates the time derivative by the value for an undisturbed field moving with constant velocity v in z-direction. For symmetric systems in the center-of-mass frame this yields $\partial_t^2 = v^2\partial_z^2$. The resulting equations are solved using fast Fourier transformation techniques.

We performed calculations for the systems $^{16}O + {}^{16}O$, $^{40}Ca + {}^{40}Ca$ and $^{197}Au + {}^{197}Au$ at projectile energies ranging from 0.6 to 14 AGeV, both with and without collision term. It turned out that up to 5 AGeV the limits LDA as well as QSA yield results very similar to those of the FS both in pure Vlasov calculations and with collision term. In figure 1 we show as an example the transverse flow for $^{40}Ca + {}^{40}Ca$ at 1 AGeV and b = $2fm$. Only at 14 AGeV some differences can be found between LDA on one and QSA and FS on the other hand which are due to the neglect of finite range effects in the case of the LDA.

A phenomenon which cannot be reproduced by the local density approximation is retardation. The quasistatic approximation yields the correct field for sources moving at constant velocity, but fails to reproduce nontrivial retardation effects due to some acceleration of the system or dynamical changes in the source densities. To explore these effects, we compare the field amplitudes calculated in the limits QSA and FS. We find almost no differences for the ω-field whereas clear evidence of retardation can be seen in the σ-amplitude at a projectile energy of 14 AGeV. In Fig. 2 we compare the σ-amplitude calculated using QSA and FS for the collision $^{40}Ca + {}^{40}Ca$ at 14 AGeV. Some timesteps during and after the collision are shown. It can be seen very clearly that during the first three time steps the amplitude of the FS 'follows' the one of the instantaneous QSA with some delay. For later times we observe oscillations in the baryon-free space between the nuclei even after they are well separated again. These die out quite slowly in time.

Although retardation leads to substantial differences in the field amplitude, it obviously has no detectable influence on the reaction dynamics. Note that the effect shown in Fig. 2 is particular to Vlasov calculations; in calculations including the collision term it will not occur due to the sizeable stopping of the nuclei.

Another feature of the FS is the occurence of radiation in the meson fields. This can either be collective bremsstrahlung due to the deceleration of the system or it can be produced by dynamical changes in the source densities. Since Vlasov calculations exhibit almost no stopping, whereas the inclusion of the collision term leads to nearly total stopping, one would expect the amount of energy produced to be much higher when including the collision term.

We find free oscillations in the meson field-amplitude, but, especially for light systems, their amplitude is very small. To get an estimate of the amount of energy contained in this radiation we use a very large grid (65 × 65 × 85) and calculate the total energy content of all grid cells which have zero baryon density and whose neighboring cells have zero baryon density, too. Table 1 shows the maximum radiation energy reached for collisions of $^{40}Ca + {}^{40}Ca$ and $^{197}Au + {}^{197}Au$ at 1, 5 and 14 AGeV. Because of the large numerical errors involved, these should be understood only as estimates of the upper limit for the radiation energy produced. Surprisingly, inclusion of the collision term does not lead to a significantly enhanced radiation. It seems that the characteristic stopping time of roughly 5 - 12 fm, depending on system and energy, is too large to lead to sizeable radiation. We note that the characteristic frequency of changes in the system has to be larger than the meson mass to produce free radiation (in contrast to near zone fields). Inserting the masses of $2.79fm^{-1}$ for the σ- and $3.97fm^{-1}$ for the ω-meson yields an upper limit for the characteristic time of $2.3fm$ and $1.6fm$, respectively. The main source of the radiation, therefore, seems to be the sudden change in the scalar density at the beginning overlap of the nuclei which is independent of the inclusion of the collision term.

Projectile Energy	1 AGeV	5 AGeV	14 AGeV
^{40}Ca, Vlasov	0.4	0.1	0.15
^{40}Ca, CT	0.5	0.1	0.15
^{197}Au, Vlasov	1.1	0.3	0.4
^{197}Au, CT	2.1	0.3	0.4

Table 1: Maximum field energy in the density free region for the systems $^{40}Ca + {}^{40}Ca$ and $^{197}Au + {}^{197}Au$ at different projectile energies with collision term and without collision term. The units are MeV per nucleon.

[1] B. Blättel et al., Phys. Rev. **C38** (1988) 1767

[2] G. Bertsch and S. Das Gupta, Phys. Rep. **160** (1988) 189

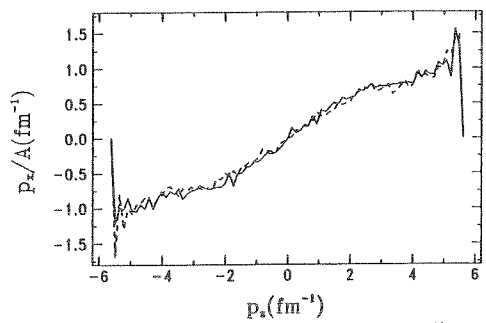


Figure 1: Final transverse momentum per particle for $^{40}Ca + {}^{40}Ca$ at 1 AGeV and $b = 2fm$. Solid: FS; dashed: LDA. The collision term is included in this calculation.

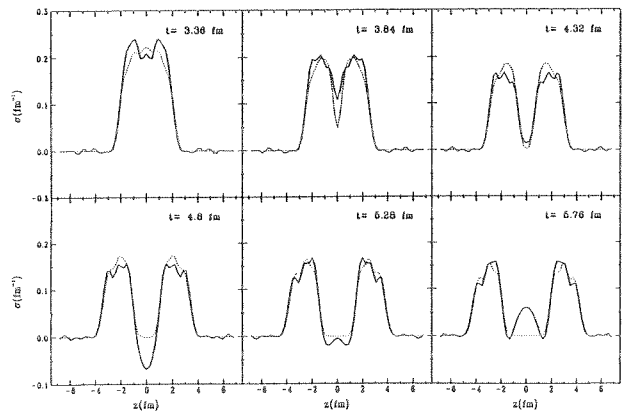


Figure 2: Amplitude of the σ-field during and after the collision for $^{40}Ca + {}^{40}Ca$ at 14 AGeV and $b = 0fm$. Solid: FS; dotted: QSA.

A Relativistic Effective Interaction for Heavy-Ion Collisions[B,G]

B. Blättel, V. Koch, W. Cassing and U. Mosel
Institut für Theoretische Physik, Universität Giessen
6300 Giessen, West Germany

Relativistic transport theories are a promising tool for the investigation of heavy-ion collisions in the SIS-energy regime. For a quantitative comparison with experiment it is important that the two ingredients of the transport description, the mean-field and the collision term, agree with the experimental information that one can extract from other scenarios, e.g. nucleon-nucleus scattering etc. Especially, the momentum dependence of the mean-field affects many observables strongly. At nuclear saturation density it can be characterized by the real part of the nucleon-nucleus optical potential. Unfortunately, in the commonly used relativistic mean-field models, the optical potential depends linearly on energy, whereas experimental analyses show a saturation at about 300 MeV kinetic energy [1].

We therefore propose a modified relativistic mean-field model, which includes an additional momentum dependence motivated in its structure by an exchange-term. To obtain a parametrization of the momentum dependence, which agrees with experiment, we introduce a modification of the exchange term.

The scalar $U_s(x,p)$ and the vector part $U_v^\mu(x,p)$ of the resulting relativistic potential are given as follows:

$$\begin{aligned} U_s(x,p) &= -g_s\sigma_H(x) - g_s\sigma_F(x,p) \\ U_v^\mu(x,p) &= g_v\omega_H^\mu(x) + g_v\omega_F^\mu(x,p) \end{aligned} \tag{1}$$

with the Hartree-fields

$$\begin{aligned} \sigma_H(x) &= -g_s\int d^4y\,\rho_s(y)\,D_\sigma(x,y) \\ \omega_H^\mu(x) &= -g_v\int d^4y\,j^\mu(y)\,D_\omega(x,y) \end{aligned} \tag{2}$$

and the exchange-fields

$$\begin{aligned} \sigma^F(x,\Pi_1) &= -g_s\int\frac{d^3p_2}{\Pi_2^0}\,D_\sigma^f(\Pi_2-\Pi_1)\,m^*(x,\Pi_2)\,f(x,\Pi_2) \\ \omega^{F,\nu}(x,\Pi_1) &= -g_v\int\frac{d^3p_2}{\Pi_2^0}\,D_\omega^f(\Pi_2-\Pi_1)\,\Pi_2^\nu\,f(x,\Pi_2). \end{aligned} \tag{3}$$

In contrast to an exact exchange contribution, we have replaced the mixture of the scalar- and vector-field contribution to U_s, U_v^μ by a single term for each potential. The most important modification is, however, the use of different meson masses m_s, m_v and m_s^f, m_v^f in the direct and the exchange part, as well as additional strength factors f_s, f_v in the Fock-term. Thus, the meson-propagators in momentum space used for the exchange fields (3) are

$$D_{\sigma,\omega}^f(\Pi_2,\Pi_1) = \frac{f_{s,v}}{(\Pi_2^0-\Pi_1^0)^2-(\vec{\Pi}_2-\vec{\Pi}_1)^2-{m_{s,v}^f}^2}. \tag{4}$$

where the kinetic momentum is given by

$$\begin{aligned} \Pi_0 &= \sqrt{m^*(p)^2+\vec{\Pi}(p)^2} \\ \vec{\Pi} &= \vec{p}-g_v\vec{\omega}(p). \end{aligned} \tag{5}$$

Along with these potentials goes the relativistic Vlasov-equation

$$\begin{aligned} &\Big\{\Big(\Pi_\mu-\Pi_\nu(\partial_\mu^p U_v^\nu)-m^*(\partial_\mu^p U_s)\Big)\,\partial_x^\mu \\ &+\Big(\Pi_\nu(\partial_\mu^x U_v^\nu)+m^*(\partial_\mu^x U_s)\Big)\,\partial_p^\mu\Big\}\,f(x,p)=0 \end{aligned} \tag{6}$$

which can be derived in the Hartree-Fock approximation [2].

The important point for this effective interaction is that even with the modified exchange-propagators a conserved energy-momentum tensor can be derived from the transport-equation (6)

$$\begin{aligned} T^{\mu\nu} &= \int d^4p(\Pi^\mu-\Pi_\alpha\partial_p^\mu U_v^\alpha-m^*\partial_p^\mu U_s)p^\nu f \\ &+\Big\{\frac{1}{2}m_s^2\sigma_H^2+\frac{1}{2}g_s\int d^4p\,m^*\,\sigma^F f \\ &-\frac{1}{2}m_v^2\omega_\nu^H\omega_H^\nu-\frac{1}{2}g_v\int d^4p\,\Pi_\alpha\,\omega^{\alpha,F}f\Big\}\,g^{\mu\nu}. \end{aligned} \tag{7}$$

In fig. 1 we show three different equations of state fitted with our effective interaction. The corresponding optical potentials in fig. 2 (as defined e.g. in [3]) are compared with Dirac-phenomenological fits to experiment by Cooper et al. [1]. We see that all three parametrizations are within the uncertainties given by experiment, in contrast to what one could achieve in the pure Hartree-limit. Besides this important adjustment of the momentum-dependence, the effective exchange term also allows for a large variation of the compressibility (MD1: K = 230 MeV, MD2: K = 305 MeV, MD3: K = 405 MeV), which in the Hartree-limit is only possible via the inclusion of a nonlinear σ-selfenergy or 1-loop-corrections.

In fig. 3 we show the density dependence of the relativistic potentials at k_F. The comparison with the results from a Dirac-Brueckner-Hartree-Fock calculation [4] shows, that the proposed interaction can also be used as a parametrization of the G-matrix following from these microscopic calculations. In contrast to simple parametrizations in terms of density or energy-dependent coupling constants, the effective interaction allows for an application to heavy-ion collisions by respecting the essential conservation laws.

[1] E.D. Cooper et al. Phys.Rev.**C36**, 2170 (1987)

[2] B. Blättel, PhD thesis, University of Giessen, (1990), unpublished.

[3] M. Jaminon and C. Mahaux. Phys.Rev.**C40**, 354 (1989)

[4] B. ter Haar and R. Malfliet. Phys.Rep.**149**, 207 (1987)

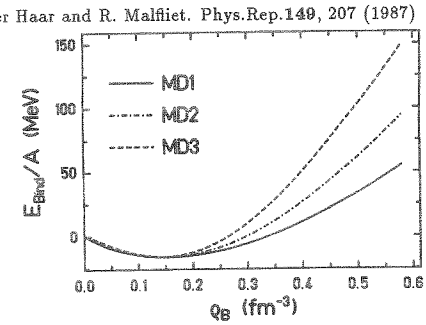


Figure 1: EOS obtained with the effective interaction

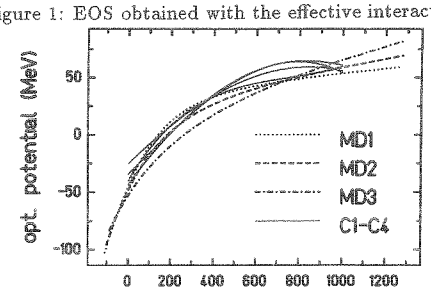


Figure 2: Real part of the Schrödinger-equivalent optical potential compared to experimental results (C1-C4) from [1]

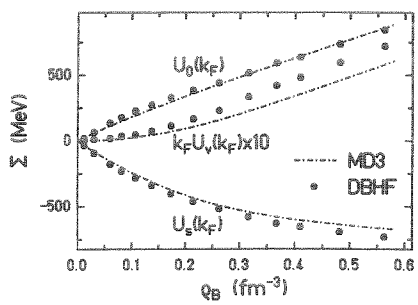


Figure 3: Density dependence of the relativistic optical potentials for MD3, compared to DBHF-results from [4]

Intermediate Energy Heavy Ion Collisions with G–Matrix Potentials and Cross Sections^{G+B}

J.Jaenicke[1], *J.Aichelin*[1,2],
N.Ohtsuka[3], *R.Linden*[3] *and A.Fässler*[3]
[1] *Institut für Theoretische Physik der Universität, Heidelberg, D-6900 Heidelberg, Germany*
[2] *Max-Planck-Institut für Kernphysik, D-6900 Heidelberg, Germany*
[3] *Institut für Theoretische Physik, D-7400 Tübingen, Germany*

Heavy ion collisions at energies between 100 MeV/nucl. and 1 GeV/nucl. have been studied by several groups. One of the primary goals was to obtain informations about the nuclear equation of state (EOS). Because nuclear matter is not available as a probe in our world heavy ions, although surface dominated, are the only source of informations which is at our disposal. With the advent of models which are able to describe the time evolution of a heavy ion reaction, like BUU, LV, VUU and QMD[1], the following strategy has been adopted to approach this goal: simple parametrizations of the nuclear equation of state (usually depending on one or two parameters only) together with the free nucleon–nucleon cross section were used as input of these calculations and the dependence of observables on the parameters was investigated. By comparison with experiments one hoped to be able to fix the EOS.

However, it is not obvious that a two parameter description is sufficient to describe the nuclear potential in the (ρ, p) plane. Furthermore, it turned out that only few observables depend on the EOS. All of them depend also on other quantities. Therefore it is certainly worthwhile to start the opposite approach. Instead of parametrizing the EOS we start out with a n–n interaction adjusted to n–n phase shifts and use it as an input for a G–matrix calculation[2]. The real resp. imaginary part of the G–matrix gives then the potential and the n–n cross section consistently. Since there is no free parameter, this formalism predicts the observables.

The G–matrix interaction automatically gives also the momentum dependence of the potential, which is not needed in nuclear matter calculations due to the equivalence of density and Fermi momentum. G–matrix calculations are numerically much more demanding than those using Skyrme type potentials. Therefore presently we cannot keep cold nuclei stable for times longer than 60 fm/c. Nevertheless, we are able to calculate observables like the momentum transfer which have reached their asymptotic value at that time.

Fig. 1 shows the central density and the transverse momentum as a function of the reaction time for the G–matrix calculation and for a static hard EOS of the Skyrme type. We observe that the G–matrix approach gives a smaller central density and the asymptotic value of $\langle p_x^{dir} \rangle$ is lower for this case. Due to the momentum dependence of the interaction the particles are accelerated in transverse direction much earlier than for the static Skyrme potential. Thus the nuclei are never compressed more than to normal nuclear matter density (0.17 fm^{-3}), though the compressibility is rather small (K = 182 MeV) and it would cost only little energy to compress them. This is a consequence of the strong momentum dependence of the G–matrix potential[3].

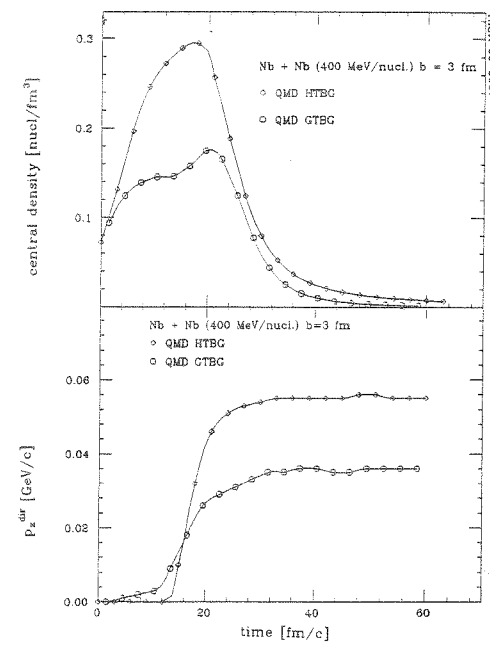


Fig. 1: The central density and the directed transverse momentum as a function of the reaction time. The reaction considered here is Nb + Nb at 400 MeV/nucl. with an impact parameter of b = 3 fm. We compare the QMD-results using a Skyrme type interaction with a static hard equation of state and the G–matrix cross section (QMD HTBG) with a QMD-calculation using G–matrix potentials and cross sections (QMD GTBG).

If these results are confirmed by other reactions and at other energies they would question the possibility to use heavy ion reactions as a source of informations about the EOS.

REFERENCES

1. G.F. Bertsch, H. Kruse and S. DasGupta, Phys. Rev. **29** (1984) 673.
H. Stöcker and W. Greiner, Phys. Rep. **137** (1986) 277.
J. Aichelin and H. Stöcker, Phys. Lett. **B176** (1986) 14.
J.Aichelin et al., Phys. Rev. **C37** (1987) 2451
G. Peilert, A. Rosenhauer, J. Aichelin, H. Stöcker and W. Greiner, Phys. Rev. **C39** (1989) 1402
2. A. Bohnet, N. Ohtsuka, J. Aichelin, R. Linden and A. Fäßler, Nucl. Phys. **A494** (1989) 349
3. J. Jaenicke, J. Aichelin, N. Ohtsuka, R. Linden and A. Fäßler, to be published

Photon production in heavy ion collisions at intermediate energies[G]

N. Ohtsuka, M. El Shabshiry[†], M. Ismail[‡] and Amand Faessler
Institut für Theoretische Physik der Universität Tübingen
J. Aichelin
Institut für Theoretische Physik der Universität Heiderberg

Due to the weakness of the electromagnetic interaction, energetic photons produced in heavy-ion collisions are expected to provide us clean informations about the nuclear equation of state. It has been realized that the main source of energetic photons is the incoherent proton-neutron bremsstrahlung. We study the effect of different equation of states to the photon cross section employing the Quantum Molecular Dynamics (QMD) to describe the collision of two heavy-ions. For this purpose, we use the classical expression for the number of photons produced in a $p-n$ collision:

$$\frac{d^2N_{pn\gamma}}{dE_\gamma d\Omega_\gamma} = \frac{\alpha}{12\pi^2 E_\gamma}(2\beta_f^2 + 3\beta_i^2 \sin^2\theta)$$

where $\beta_{i,f}$ is the relative velocity of two nucleons in the initial (final) state. The photon production cross section in the heavy-ion collision is given by

$$\frac{d^2\sigma}{dE_\gamma d\Omega_\gamma} = \int db^2 \sum_{coll} \int \frac{d\Omega}{4\pi}\frac{E_\gamma}{E'_\gamma}\frac{d^2N'_{pn\gamma}}{dE'_\gamma d\Omega'_\gamma} P(\mathbf{p}_3, \mathbf{p}_4)$$

where primed quantities are in the nucleon-nucleon c.m. frame and unprimed quantities are in the nucleus-nucleus reference frame. $P(\mathbf{p}_3, \mathbf{p}_4)$ is the Pauli-blocking factor for the final nucleons with momenta $\mathbf{p}_3$ and $\mathbf{p}_4$. For the mean field potential, we use the Skyrme type form

$$U(\rho) = \alpha\frac{\rho}{\rho_0} + \beta(\frac{\rho}{\rho_0})^\gamma$$

with parameters $\alpha = -356$ MeV, $\beta = 303$ MeV and $\gamma = 7/6$ (K = 200 MeV) for the soft equation of state and $\alpha = -124$ MeV, $\beta = 70.5$ MeV and $\gamma = 2$ (K = 380 MeV) for the hard equation of state. Numerical calculations have been done for ^{12}C on ^{12}C and ^{40}Ca on ^{40}Ca at $E_{lab} = 84$ and 200 MeV/A. The medium dependent nucleon-nucleon scattering cross section derived from the G-matrix is used to describe the NN-collision in the nuclear medium.

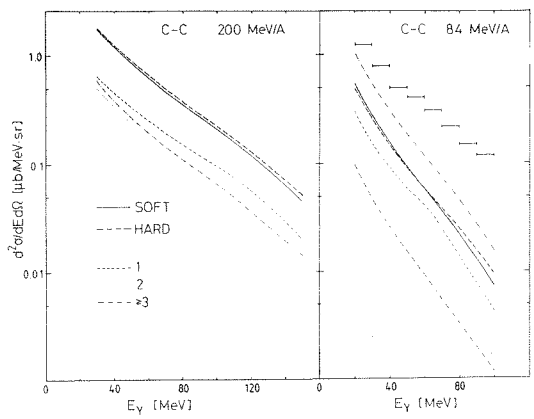


Fig. 1: Photon production cross section at $\theta_\gamma = 90°$ in the C–C collision with $E_{lab} = 84$ and 200 MeV/A. Solid and long dashed lines show the results for the soft and hard equation of state, respectively. Short dashed, dotted and dash-dotted lines show the contributions from the first, second and more than third collisions, respectively. The dash-dot-dot line shows the result with larger Fermi momentum. The experimental data at 84 MeV are taken from ref. 1.

The results for C–C case at $\theta_\gamma = 90°$ are shown in Fig. 1. It can be seen that the first-collision contribution is dominant at 84 MeV but multi-collision contributions are also important at 200 MeV. The different equation of states do not give significant difference in the photon cross section. It has been found that the hard equation of state gives higher maximum density at earlier stage of the collision due to the stopping but gives lower density at later stage due to the faster dissipation. Therefore the number of NN-collision is larger for the hard equation of state at earlier stage but smaller at later stage leading to the almost same number of collision in total. This fact again leads to almost the same photon cross section for both soft and hard equation of states. The result is about an order of magnitude smaller than the experimental data of ref. 1. This is partly due to the too small Fermi momentum ($\sim$ 200 MeV/c) for the initial momentum distribution in a nucleus given in the QMD program to obtain the binding energy of $\sim$8 MeV/A. The result with a larger Fermi momentum of $\sim$260 MeV/c is given by the dash-dot-dot line. It is also known that microscopic calculation of $np \to np\gamma$ process gives larger cross section for high energy photons.

The results for Ca–Ca case is shown in Fig. 2. We can see that the first-collision contribution is still dominant at 84 MeV but less so than in the C–C case. At 200 MeV, the multi-collision contribution is larger than the first-collision one. In the Ca–Ca case, the soft equation of state gives significantly larger cross section than the hard equation of state. For Ca, the stopping works similarly for both soft and hard equation of states and the maximum density at early stage of the collision is similar for both equation of states. At later stage, the hard equation of state gives lower density distribution due to faster dissipation and thus smaller number of collision, which leads to smaller cross section for the photon production.

[1] E. Grosse et al., Europhys. Lett. 2(1986)9

[†] Permanent address: Faculty of Science, Ain-Shams University, Cairo

[‡] Permanent address: Department of Physics, Cairo University, Egypt

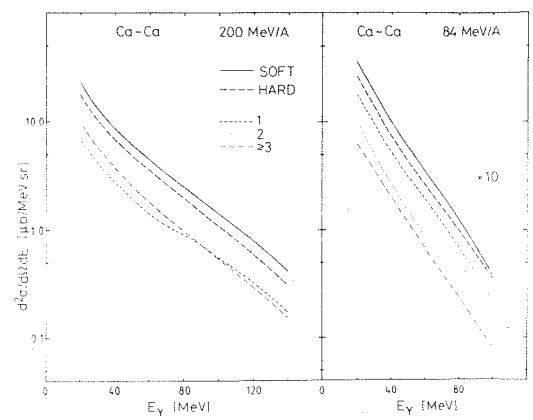


Fig. 2: Same as Fig. 1 but for the Ca–Ca case.

Relativistic Approach to Intermediate Energy Heavy Ion Reactions[G]

T. Maruyama, N. Ohtsuka and Amand Faessler

Institut für Theoretische Physik der Universität Tübingen

J. Aichelin

Institut für Theoretische Physik der Universität Heidelberg

Recently it has become very interesting field in nuclear physics to study the equation of state (EOS) of the hot and dense nuclear matter using intermediate or high energy heavy ion reactions. At high energy region, the relativistic treatment of heave ion reaction is required. We adopt the Relativistic Quantum Molecular Dynamics (RQMD) approach which has been developed by Sorge et.al.[1]. In this approach the equation of motion is constructed in a fully Lorentz covariant way based on 8n-dimensional Poincare invariant Hamiltonian Dynamics[2], and has several important features as follows. a) Time coordinates of the two particles are chosen to be equal in their center of mass system (c.m.s). b) Not only the kinematics, but also the nuclear interactions are treated in a Lorentz covariant way, which is not taken into account in the usual Quantum Molecular Dynamics (QMD). c) As a result of the above feature, the phase space distribution of initial nuclei is Lorentz contracted, whilch is not the case in the usual QMD.

We study the ^{12}C-^{12}C collisions at E_{lab} = 84 and 800 MeV/n, both in the relativistic and nonrelativistic QMD approaches. For the mean field potential in the relativistic case we use the one given by Ref.1 which is a Lorentz scalar and corresponds to the Skyrme type potential in the nonrelativistic limit[2]. Two kinds of parameter sets which correspond to hard (K=380MeV) and soft (K=210MeV) EOS are consider. As the nucleon-nucleon cross section we take the 40mb isotropic cross section for E_{lab} = 84 MeV case while we use the parametrization of Cugnon et.al.[3] including the Δ excitation for E_{lab} = 800 MeV/n case. In the latter case all Δ particles are considered to decay into pions and nuleons at the final stage.

The total inclusive cross sections of proton, deutron, ^3H+^3He and pion are given in Table 1 at E_{lab} = 84 MeV/n and in Table 2 at E_{lab} = 800 MeV/n. One can see that the difference between the relativistic and the nonrelativistic approaches is larger than the difference between hard and soft EOS especially in the case of E_{lab} = 800 MeV/n. The final rapidity distributions in c.m.s. of total nucleons at an impactparameter b = 1 fm are given in Fig.1. A more pronounced dip and peak structure appear in the relativistic case.

For the results we report here the difference between the relativistic and nonrelativistic QMD approach is not very large, but relativistic effect cannot be neglected in the study of the EOS in the intermediate energy region. In the future we will study in more detail the energy and angular distribution of particles and fragments in both the relativistic and nonrelativistic QMD approach with the hard and soft EOS.

[1] H. Sorge, H. Stöcker and W. Greiner, Ann. Phys. 192 (1989) 266

[2] For Example, J. Samuel, Phys. Rev. D26 (1982) 3475, 3482 and reference therein.

[3] J. Aichelin and H. Stöcker, Phys. Lett. B176 (1986) 14

[4] J. Cugnon, T. Mizutani and J. Vandermeulen, Nucl. Phys. A352 (1981) 505

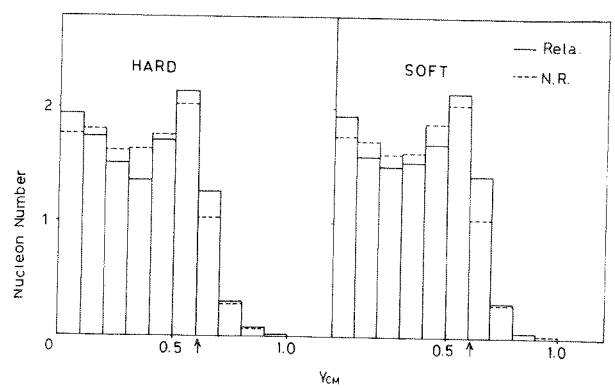


Fig. 1: The final rapidity distibutions in the center of mass system in the C-C collision with b = 1 fm at E_{lab} = 800 MeV/n. The left and right figures display the hard and soft EOS, respectively. Solid (dashed) line shows the results of the relativistic (nonrelativistic) approach. The allows show the rapidity of initial nuclei.

TABLE 1

Particle	HARD		SOFT	
	Rela.	N.R.	Rela.	N.R.
p	4203	3580	3504	3394
d	1476	1257	1622	1335
^3H+^3He	622	547	695	584

Table 1: Total inclusive cross section for particle emission in the C C collision at E_{lab} = 84 MeV/n. The left and right columns display the hard and soft EOS

TABLE 2

Particle	HARD		SOFT	
	Rela.	N.R.	Rela.	N.R.
p	3556	3281	3682	3035
d	640	515	648	568
^3H+^3He	213	183	251	194
π^-	351	358	350	345

Table 2: Same as Table 1 but at E_{lab} = 800 MeV/n.

RELATIVISTIC EFFECTS IN MOLECULAR DYNAMICS SIMULATIONS OF HEAVY-ION COLLISIONS

H. Feldmeier, B. Kämpfer*, O. Knospe†, R. Schmidt†
GSI Darmstadt

It is an interesting question to what extent relativistic effects influence the results of molecular dynamics simulations of high-energy heavy-ion collisions. The formulation of a fully relativistic invariant description of an interacting many-particle system meets conceptual problems which are expressed in the no-interaction theorem [1]. There are many ways to avoid a conflict with the no-interaction theorem. Here we replace the requirement of Lorentz invariance by approximate Lorentz invariance. Such an approximate relativistic theory has been analysed in ref. [2], and we make use of this formulation. As long as one is interested in the influence of relativistic effects in reactions with beam energies $E_{lab} <$ 1 GeV A an approximately invariant theory should be justified. In order to derive an approximate relativistic hamiltonian one can expand an invariant action which contains a Lorentz-scalar and a Lorentz-vector interaction between classical pointlike particles in powers of c^{-1} following ref. [2]. Then one gets the following hamiltonian, when keeping only terms up to order c^{-2}

$$\mathcal{H}(\vec{r}_1(t),..\vec{p}_1(t),..) = \sum_{i=1}^{N}\left(\frac{\vec{p}_i{}^2}{2m} - \frac{\vec{p}_i{}^4}{8m^3c^2}\right) + \sum_{\substack{i,j=1\\ i<j}}^{N} V(\vec{p}_i,\vec{p}_j,\vec{r}_{ij}), \quad (1)$$

$$V(\vec{p}_i,\vec{p}_j,\vec{r}_{ij}) = V_S + V_V - \tfrac{1}{2m^2c^2}((\vec{p}_i\vec{p}_j)(V_S+V_V)+$$
$$(\vec{p}_i-\vec{p}_j)^2 V_S - (\vec{p}_i\vec{r}_{ij})(\vec{p}_j\vec{r}_{ij})\tfrac{1}{r_{ij}}\tfrac{\partial}{\partial r_{ij}}(V_S+V_V)),$$

where the static potentials $V_{S,V}$ depend only on the distances $r_{ij} = |\vec{r}_i - \vec{r}_j|$ between particles i and j. V_S denotes the scalar potential and V_V is the sum of the electromagnetic and the vector potential. In the actual calculations we use [3]

$$V_S(r) = V_S^0 e^{-\mu_S r} r^{-1},\ V_V(r) = V_V^0 e^{-\mu_V r} r^{-1} + e^2 q_i q_j r^{-1},$$

where V_S^0 = -2569 MeV fm, μ_S = 2.469 fm^{-1}, V_V^0 = 6529 MeV fm, μ_V = 3.358 fm^{-1}, e^2 = 1.44 MeV fm, and q_i denotes the charge of the ith particle. The chosen parameters reproduce the nucleon-nucleon transport cross section [4, 5]. The scalar potential V_S and the vector potential V_V give rise to different types of momentum dependent corrections due to the different transformation properties of scalar and vector fields in relativity. Even at small momenta, there is a considerable momentum dependence of the potential. With increasing relative momentum the effective interaction becomes more repulsive [3, 5].

As an example we analyse the reaction $O^{16} + O^{16}$ at an impact parameter of b = 1 fm. In fig. 1 the calculated average transverse momenta in the reaction plane $< p_x >$ as function of the cms parallel momentum $p_{||}$ to the beam axis are displayed for different bombarding energies. The results of the relativistic calculation are strikingly different from the nonrelativistic ones in case of higher bombarding energies. The transverse flow is about two times larger in the relativistic calculation as compared to the nonrelativistic one at E_{lab} = 600 MeV A. These large effects result from the momentum dependence of the two-body potential in eq. (1). Its influence on the transverse flow is larger than a typical change obtained with a stiff or a soft equation of state. The momentum dependence of the relativistic interaction mimics a much stiffer equation of state as actually realized in nuclear matter.

[1] D.G. Currie, T.F. Jordan and E.C.G. Sudarshan, Rev. Mod. Phys. **35** (1963) 350 and J. Math. Phys. **4** (1963) 1470
J.T. Cannon and T.F. Jordan, J. Math. Phys. **5** (1964) 299
H.Leutwyler, Nuovo Cimento **37** (1965) 556

[2] H.W. Woodcock and P. Havas, Phys. Rev. **D6** (1972) 3422
J. Stachel and P. Havas, Phys. Rev. **D13** (1976) 1598

[3] A.R. Bodmer, C.N. Panos and A.D. MacKellar, Phys. Rev. **C22** (1980) 1025

[4] G.S. Anagnostatos, C.N. Panos, Phys. Rev. **C26** (1982) 260

[5] R. Schmidt, B. Kämpfer, H. Feldmeier, O. Knospe, Phys. Lett. **229B** (1989) 197
B. Kämpfer, H. Feldmeier, R. Schmidt, O. Knospe, Proc. Int. Workshop on Gross Properties of Nuclei and Nuclear Excitations XVIII, Hirschegg 1990, (Ed.) H. Feldmeier

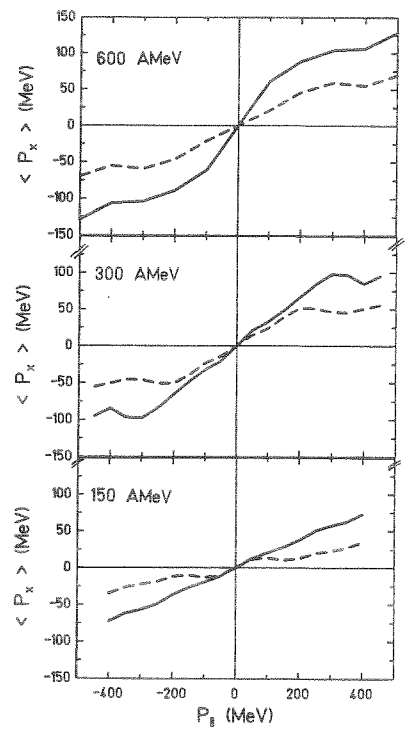


Figure 1: The calculated average transverse momenta in the reaction plane $< p_x >$ as a function of the cms parallel momentum $p_{||}$ for the reaction $O^{16} + O^{16}$ (impact parameter b = 1 fm) at different bombarding energies (solid lines: approximate relativistic model, dashed line: nonrelativistic model).

*present address: JINR Dubna, 101000 Moscow, Head Post Office, P.O.B. 79, USSR; permanent address: Zentralinstitut für Kernforschung Rossendorf, 8051 Dresden, PF 19, GDR
†TU Dresden, Sektion Physik, Mommsenstr. 13, DDR-8027 Dresden, GDR

FERMIONIC MOLECULAR DYNAMICS

H. Feldmeier
GSI Darmstadt

In the Fermionic Molecular Dynamics (FMD) model [1] the quantum variational principle

$$\delta \int_{t_1}^{t_2} dt \, \langle Q(t) | \, i\frac{d}{dt} - \underset{\sim}{H} \, | Q(t) \rangle \; = \; 0 \qquad (1)$$

is applied to an antisymmetrized many body state This state is parametrized by a set of time-dependent parameters $Q(t) = \{ q_\nu(t), \; \nu = 1, 2, \cdots \}$ which are regarded as the generalized coordinates of the system. The variation has to be performed with respect to all $q_\nu(t)$. $\underset{\sim}{H}$ denotes the total hamiltonian of the system and t the time. Let us define a Lagrange function by

$$\mathcal{L}\left(Q(t), \dot{Q}(t)\right) := \langle Q(t) | \, i\frac{d}{dt} - \underset{\sim}{H} \, | Q(t) \rangle \qquad (2)$$

in which $\dot{Q}(t) = \{ \dot{q}_\nu \equiv d\dot{q}_\nu/dt, \; \nu = 1, 2, \cdots \}$ is the set of generalized velocities. The variation (1) leads to the Euler-Lagrange equations

$$\frac{d}{dt}\frac{\partial \mathcal{L}}{\partial \dot{q}_\nu} = \frac{\partial \mathcal{L}}{\partial q_\nu} \quad \text{with} \quad \nu = \{k, j\} \, , \qquad (3)$$

which are the FMD equations of motion for the parameters where $k = 1, 2, ..., N$ enumerates the particles and j denotes the different parameters for each single particle state. These FMD equations may be non-linear and they need not resemble at all a Schrödinger equation. They can be regarded as semi-quantal equations of motion which for special cases may turn into classical molecular dynamics equations.

The general idea is to find a parametrization which contains the essential degrees-of-freedom of the system. Classical molecular dynamics describes the motion of point-like particles under the influence of mutual interactions. Fermionic Molecular Dynamics extends this picture in a natural way towards quantum mechanics by introducing for each molecule (here each nucleon) a wave packet $|q(t)\rangle$ which is localized in phase space. For convenience we take a gaussian form

$$\langle \vec{x} | q(t) \rangle = \exp\left\{ -\frac{(\vec{x} - \vec{b}(t))^2}{2a(t)} + \eta(t) \right\} \begin{pmatrix} \cos\frac{\chi(t)}{2} \\ \sin\frac{\chi(t)}{2} e^{i\phi(t)} \end{pmatrix} . \qquad (4)$$

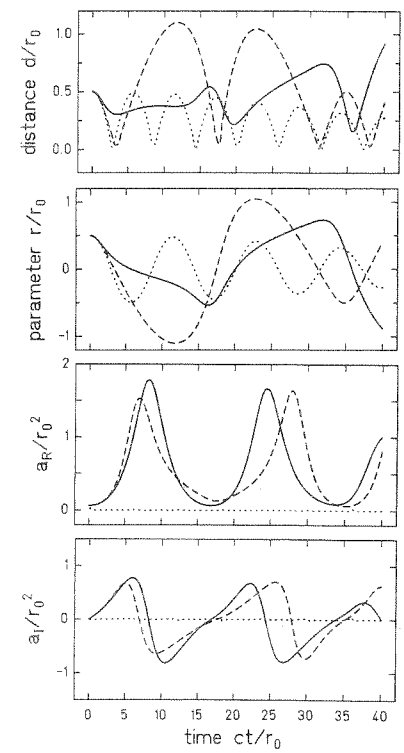
The time dependent parameters $q(t) = \left\{ \vec{b}(t), a(t), \eta(t), \chi(t), \phi(t) \right\}$ define the wave packet uniquely. The parameters $\vec{b}(t), a(t)$ and $\eta(t)$ are complex. $\vec{b}(t) = (\vec{r}(t) - a_I(t)\vec{p}(t)) + ia_R(t)\vec{p}(t)$ contains the the mean position $\vec{r}(t)$ and the mean momentum $\vec{p}(t)$ while $a(t) = a_R(t) + ia_I(t)$ describes the spreading. $\eta(t)$ takes care of the normalization and contains the phase. The spin of the fermion is represented by a two-component spinor where the real polar angles $\chi(t)$ and $\phi(t)$ denote the direction of the spin.

For identical fermions the most simple ansatz for the parameterized many body wave function $|Q(t)\rangle$ is a single Slater determinant built from N different single-particle wave pakets $|q_k(t)\rangle$. As the single-particle states are in general not orthogonal the many body state has to be normalized. Nevertheless it is completely antisymmetric with respect to particle exchange and thus a proper wave function for identical fermions.

As a first application we solve the FMD equations (2) for the relative motion of two fermions which are bound together by an attractive Gaussian potential $V(\vec{r}) = V_0 \exp\{-(\vec{r}/r_0)^2\}$ where $V_0 = -0.5$ $\hbar c$/fm, $r_0 = 4$ fm and the reduced mass $\mu = 2.5$ $\hbar$/(cfm). The fermions are initially at rest with a mean distance of 2 fm and an initial width parameter of $a(t{=}0) = 1$ fm^2, so that they have only little overlap in phase space.

In the figure we display the time evolution of the parameters which define the relative wave function but are not observables, and the measurable observable d which is the distance between the fermions defined by the root of the quadrupole moment along the $\vec{r}$-direction. $d = \left\langle \frac{3}{2}\left(\underset{\sim}{\vec{x}}\frac{\vec{r}}{|\vec{r}|}\right)^2 - \frac{1}{2}\underset{\sim}{\vec{x}}^2 \right\rangle^{1/2}$ For particles with a distance larger than the width of the packet $d = |\vec{r}|$ (classical limit). In the upper part of the figure one sees that as a result of the Pauli principle the fermions with equal spins (solid line) do not get close in space, while the particles with opposite spin (dashed line) oscillate through $d = 0$. At variance with d the parameter $\vec{r}(t)$ goes through zero even for equal spins. The dotted line is for the case where the mass and the potential strength are hundred times larger. Here, the time dependence of $\vec{r}(t)$ is almost identical to the purely classical trajectory which is not shown. The lower part of the figure displays the oscillations in the real and imaginary part of the width parameter $a(t)$.

This example demonstrates that classical molecular dynamics cannot be used in nuclei because quantum mechanics does not allow to localize the nucleons sufficiently. The FMD model may serve as a foundation and an improvement of existing molecular dynamics models.



Measurable distance and parameters of the wave packet as function of time for two fermions oscillating in an attractive potential. Full lines are for parallel spins, dashed lines for antiparallel spins (no Pauli principle), and dotted lines are for heavy particles with antiparallel spins (classical trajectory).

[1] Preprint GSI-89-86 submitted to Nuclear Physics A

Effect of 3α - like states in ^{12}C to^{12}C - ^{12}C scattering[G]

G. Pantis[+], R. Linden, N. Ohtsuka and A. Faessler

Institut für Theoretische Physik der Universität Tübingen

The polarization potential arising from the excitation of 3α-like 0_2^+ (7.66 MeV), 2_2^- (10.3 MeV) states and 3α breakup states in ^{12}C are calculated using the transition densities to these states which are obtained by Kamimura[1] in the 3α resonating-group method. The polarization potential is non-local and is given by

$$\Delta U(\mathbf{r},\mathbf{r}') = \sum_{(m,n)\neq(0,0)} V_{mn}^{*}(\mathbf{r}) G_{mn}(\mathbf{r},\mathbf{r}') V_{mn}(\mathbf{r}')$$

where m and n denote the eigenstates of isolated target and projectile nuclei and G_{mn} is the Green's function. The coupling potential V_{mn} is given in terms of the one-body transition density ρ as

$$V_{mn}(\mathbf{r}) = \int d\mathbf{r}_1 d\mathbf{r}_2 \rho_{m0}^{T}(\mathbf{r}_1) \mathcal{V}(\mathbf{r}_1 - \mathbf{r}_2 + \mathbf{r}) \rho_{n0}^{P}(\mathbf{r}_2).$$

In the numerical calculations, we localize ΔU by the Perey-Saxon method[2]:

$$\Delta\tilde{U}(\mathbf{r}) = \int d\mathbf{r}' \int \frac{d\mathbf{k}}{4\pi} \Delta U(\mathbf{r},\mathbf{r}') e^{i\mathbf{k}\cdot(\mathbf{r}-\mathbf{r}')}$$

where we take the local momentum approximation for k. As the effective nucleon-nucleon interaction $\mathcal{V}$, we consider following 3 sets parametrized as a sum of Gaussians:

$$\mathcal{V}(r) = \sum_{i=1}^{2} v_i \exp(-r^2/s_i^2)$$

with

Potential I $v_1 = -12.7$, $s_1 = 1.54$, $v_2 = -6.1$, $s_2 = 1.78$,
Potential II $v_1 = -v_2 = 11.3$, $s_1 = 1.01$, $s_2 = 1.80$,
Potential III $v_1 = 616$, $s_1 = 0.542$, $v_2 = -195$, $s_2 = 0.942$,

where V_i and s_i are in units of MeV and fm, respectively. It is found that the contribution from the 3α breakup states is roughly the same as that from the bound states (0_2^+ and 2_2^+). The contribution from 0^- states has a peak in magnitude much larger than that of 2^- states, while the position of the peak is at larger R for 2^+ states.

Adding these polarization potentials to the microscopic optical potential of Ohtsuka et al.[3] obtained in the nuclear matter approach, the elastic and inelastic cross sections for the ^{12}C-^{12}C scattering at E_{lab} = 360 and 1016 MeV are calculated including the 2_1^+ (4.44 MeV) and 3_1^- (9.64 MeV) states in the coupled channel formalism. The result for 360 MeV is shown in Fig. 1. It can be seen that the polarization potential reduces the cross section considerably at $\theta \geq 20^{\circ}$ and improves the agreement with the experiment.

The result for 1016 MeV is shown in Fig. 2. At this energy, the imaginary part of the microscopic optical potential which comes from the excitation of 2-particle 2-hole configurations is very large and the excitation of the 3α-like states play a less important role. Thus the good agreement with the experiment is retained.

[1] M. Kamimura, Nucl. Phys. A351(1981)456
[2] F.G. Perey and D.S. Saxon, Phys. Lett. B10(1964)107
[3] N. Ohtsuka, R. Linden, A. Faessler and F.B. Malik; Nucl. Phys. A465(1987)550; N. Ohtsuka, R. Linden and A. Faessler; Phys. Lett. B199(1987)325
[4] M. Buenerd et al., Phys. Lett. B102(1981)242; Phys. Rev. C26(1982)1299; Nucl. Phys. A424(1984)313

[+] Permanent address: Department of Physics, University of Ioannina, Greece

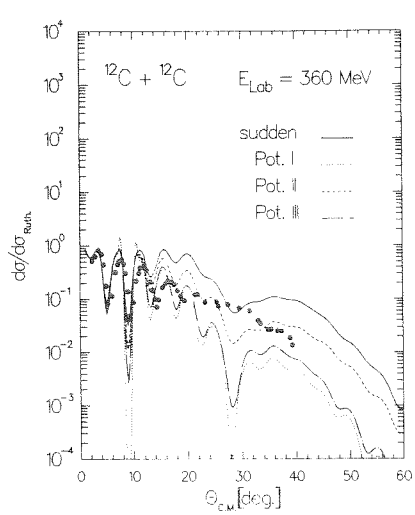


Fig. 1: Elastic differential cross section at E_{lab} = 360 MeV. The solid, dotted, dashed and dot-dashed lines show the results without the polarization potential, with the polarization potential with the effective interaction I, II and III, respectively. The experimental data are taken from ref. 4.

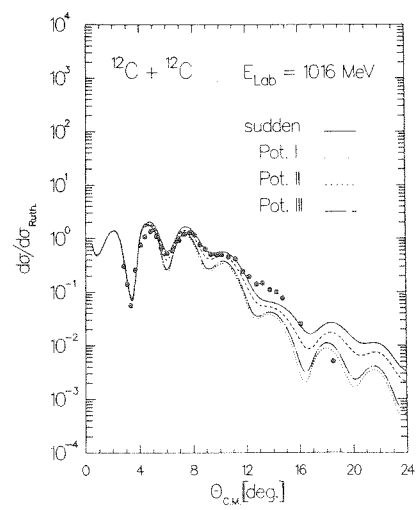


Fig. 2: Same as Fig. 1 but at E_{lab} = 1016 MeV.

Quasiclassical Studies of the Equation of State for Inhomogeneous Nuclear Matter [B,G]

G. Peilert, H. Stöcker, W. Greiner
Institut für Theoretische Physik der Universität, Frankfurt
J. Randrup
Lawrence Berkeley Laboratory, Nuclear Science Division

One of the basic problems of the present microscopic models of heavy ion collisions is the fact that the nucleons are Fermions and the Fermi motion is, up to now, not explicitly incorporated in those models. This affects mostly those models which are able to describe the fragment formation in such reactions, hence the fragments produced have somewhat unrealistic properties, which makes the interpretation of the results difficult. In particular, in the groundstate the nucleons have vanishing momenta. It was proposed already in 1977 by Wilets et al. [1] to remedy this problem by simulating the Fermi motion of the nucleons by a quasiclassical momentum-dependent Pauli potential. Later on also other forms of this potential have been developed [2,3].

We use the Paulipotential of Dorso et al. [3], which has been adjusted so that the total energy compares to the kinetic energy of the free Fermi gas. The total energy of an ideal fermigas is in our model given as

$$E_{tot} = \sum_i \frac{p_i^2}{2m} + \frac{1}{2} \sum_{i,j;j\neq i} V_P^0 \left(\frac{\hbar}{q_0 p_0}\right)^3 exp\left[-\frac{1}{2}(r_{ij}^2/q_0^2 + p_{ij}^2/p_0^2)\right]$$

with:

$$V_N^0 = 29\,\mathrm{MeV}, q_0 = 3\,\mathrm{fm}; p_0 = 120\,\mathrm{MeV/fm}.$$

The interaction used to describe nuclear systems is taken from the QMD model [4] and includes a two- and three-body Skyrme-type interaction, Coulomb and Yukawa interactions, plus an asymmetry term. Because we wish to describe finite nuclei and nuclear matter with the same procedure we do not use the long range Coulomb interaction but a screened Coulomb interaction with a screening length of the order of the radius of large nuclei. For nuclear matter calculations we also include the interaction of the protons with an uniform electron background.

The total energy is given by

$$\begin{aligned} E = \; & E_{kin} + E_{Pauli} + E_{Yuk} + E_{Coul} \\ & + \tfrac{\alpha}{2}\tfrac{\rho}{\rho_0} + \tfrac{\beta}{\gamma+1}\left(\tfrac{\rho}{\rho_0}\right)^{\gamma} + \tfrac{\omega}{2}\lambda_i \tfrac{\rho_p - \rho_n}{\rho_0} \end{aligned}$$

with

$$\lambda_i = \begin{cases} +1 & \text{for protons} \\ -1 & \text{for neutrons} \end{cases}$$

The parameters α, β and γ are adjusted in order to reproduce the properties of infinite nuclear matter with a compressibility constant $K = 380 MeV$.

Fig.1 shows now the equation of state calculated with this interaction in a Metropolis sampling procedure for the temperature $T = 0.5 MeV$, which should be a good approximation of cold nuclear matter. The simulation was first done under the constraint of a uniform gas, which was simulated by placing the nucleons randomly in the box and averaging over several initial configurations. The result is shown with the full line. Next we give up the constraint of the uniform gas and show with the full circles the eos for the full problem with all degrees of freedom. Note that for $\rho > \rho_0$ the energy is lowered slightly. This results from the fact that the random initialization does not minimize the energy and the nucleons will rearrange themselves to their real ground state if they are allowed to move in real space as well. At subsaturation densities, however, the situation changes dramatically. Now the energy is considerably lower than that of a uniform gas, because at low densities the system can lower its energy by clustering into finite nuclei. Therefore for $\rho \to 0$ the energy approaches that characteristic of finite nuclei while in the regime between $\rho = 0$ and $\rho = \rho_0$ the energy lies somewhere between nuclear matter and that of finite nuclei.

References

[1] L. Wilets, E.M. Henley, M. Kraft and A.D. Mackellar, Nucl. Phys. A282 (1977) 341.

[2] D.H. Boal and J.N.Glosli, Phys. Rev. C38 (1988) 1870, Phys. Rev. C38 (1988) 2621.

[3] C. Dorso, S. Duarte and J. Randrup, Phys. Lett. B3 (1987) 287 and Phys. Lett B4 (1988) 611.

[4] G. Peilert, A. Rosenhauer, J. Aichelin, H. Stöcker and W. Greiner, Mod. Phys. Lett. A3 (1988) 459 and Phys. Rev. C39 (1989) 1402.

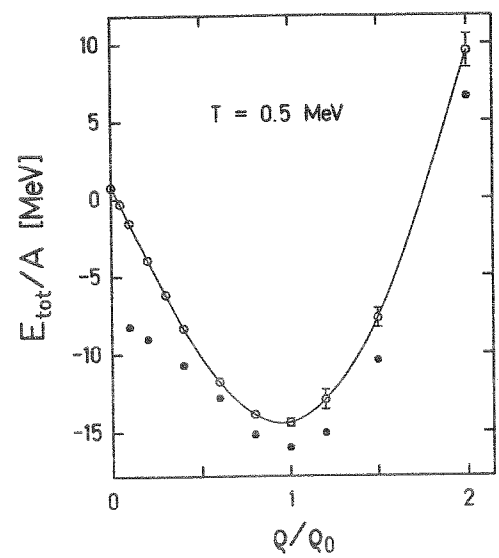


Figure 1: Equation of state for cold ($T = 0.5 MeV$) nuclear matter. The line represents the eos for a homogeneous gas, while the symbols represent the energy of a real gas were inhomogenities are allowed to grow.

Relativistic Hartree Fock with Skyrme Type Interactions

B. A. Nikolaus D. G. Madland D. D. Strottman
Los Alamos National Laboratory

T. Hoch* P. Manakos
Institut für Kernphysik der Technischen Hochschule Darmstadt

Relativistic models for nuclear matter and finite nuclei have attracted increasing attention in recent years [1,2]. Furthermore, simple and efficient relativistic models are very desirable tools for the study of the motion of nuclear matter in relativistic heavy ion collisions. Mean field models containing scalar and vector meson fields which are coupled to the nucleon fields have been very popular and successful. Hartree calculations based on these models could fit with few parameters the ground state properties of finite nuclei (binding energies and radii) and nuclear matter. With the same set of parameters they also yield the right spin orbit splitting of single particle spectra. However, serious deficiencies appear when one goes beyond the tree approximation.

We investigate a relativistic Skyrme type interaction model in Hartree Fock (HF) approximation. This is a generalization of a previously suggested model [3] which contained a manifestly nonrenormalizable four fermion point coupling. The present model additionally contains six and eight fermion point couplings and is defined by the Lagrangian density

$$\begin{aligned}\mathcal{L}(x) &= \bar{\psi}(x)\left(i\gamma_\nu\partial^\nu - M\right)\psi(x) \\ &\quad - \frac{1}{2}\sum_K \alpha_K \left(\bar{\psi}(x)\mathcal{O}^{(K)}\psi(x)\right)\left(\bar{\psi}(x)\mathcal{O}^{(K)}\psi(x)\right) \\ &\quad - \frac{1}{3}\beta_S(\bar{\psi}(x)\psi(x))^3 - \frac{1}{4}\gamma_S(\bar{\psi}(x)\psi(x))^4\end{aligned} \tag{1}$$

Here $\mathcal{O}^{(K)}\otimes\mathcal{O}^{(K)}$ for $K = S, V, T, P, A$ denote the well-known invariant combinations

$$\begin{aligned}&S : 1\otimes 1 \qquad V : \gamma^\mu\otimes\gamma_\mu \qquad T : \sigma_{\mu\nu}\otimes\sigma^{\mu\nu} \\ &P : \gamma_5\otimes\gamma_5 \quad A : \gamma^\mu\gamma_5\otimes\gamma_\mu\gamma_5\end{aligned} \tag{2}$$

This Lagrangian leads to the following HF equations:

$$\begin{aligned}(i\partial_\mu\gamma^\mu - M)u_n(x) &= \Bigg(\sum_K \alpha_K\rho_K(x)\mathcal{O}^{(K)} \\ &\quad + \beta_S\rho_S^2 + \gamma_S\rho_S^3 - \text{ exchange terms }\Bigg)u_n(x)\end{aligned} \tag{3}$$

where

$$\rho_K(x) = \sum_{0\le\epsilon_n\le\epsilon_F} \bar{u}_n(x)\mathcal{O}^{(K)}u_n(x) \tag{4}$$

The exchange terms for the four fermion coupling in (3) may be absorbed in the direct terms by exploiting Fierz relations [4]. This results in a redefinition of the coupling constants α_K. The exchange terms of the higher order expressions in the scalar density given in (3) are also of Skyrme type. In the case of nuclear matter and closed shell nuclei in the sum in (3) only the scalar and vector densities survive.

For nuclear matter the selfconsistency equations for the scalar density and the effective mass M^* are very similar to those of the Walecka model [5]:

$$\begin{aligned}\rho_S &= \frac{M^*}{\pi^2}\left[k_F\sqrt{k_F^2+M^{*2}} - M^{*2}\ln\left(\frac{k_F+\sqrt{k_F^2+M^{*2}}}{M^*}\right)\right] \\ M^* &= M + \alpha_S\rho_S + \beta_S\rho_S^2 + \gamma_S\rho_S^3\end{aligned} \tag{5}$$

where k_F is the Fermi momentum. The binding energy per nucleon is given by

$$\begin{aligned}\frac{E}{A} = \frac{1}{\rho_V}\Bigg\{ &\frac{1}{4\pi^2}\Bigg[k_F\sqrt{k_F^2+M^{*2}}(2k_F^2+M^{*2}) \\ &- M^{*4}\ln\left(\frac{k_F+\sqrt{k_F^2+M^{*2}}}{M^*}\right)\Bigg] \\ &- \frac{1}{2}\alpha_S\rho_S^2 + \frac{1}{2}\alpha_V\rho_V^2 - \frac{2}{3}\beta_S\rho_S^3 - \frac{3}{4}\gamma_S\rho_S^4\Bigg\}\end{aligned} \tag{6}$$

If the higher order coupling constants β_S and γ_S are set to zero one gets exactly the same equations as in the Walecka model, since there is no space dependence of the meson fields in the nuclear matter case. Comparing with an extension [2] of Walecka's model which contains higher order terms in the scalar meson field we find that the dependence of the binding energy on the Fermi momentum can be reproduced very well by fitting our parameters $\alpha_S, \alpha_V, \beta_S$ and γ_S.

We developed a computer implementation of the selfconsistent eqs. (3) to test the model in the case of finite nuclei. We found that for vanishing β_S and γ_S the HF iteration does not converge but leads to a "collapsing" nucleus. This is due to the local interaction in contrast to the Walecka model. The instability is removed by the higher order terms in (1). Our model parameters are adjusted to reproduce simultaneously the experimental ground-state binding energies, charge radii and spin-orbit splittings of doubly-magic nuclei [6]. Here we also included the Coulomb potential not contained in (1). The results can be further improved by adding terms to (1) which depend on the derivatives of the densities. By doing so one can mimic the effect of the finite range of the force in mesonic models.

These calculations do not include the Dirac sea. A renormalization scheme for including the Dirac sea in the Skyrme interaction model has been developed [4].

*Supported by Deutsche Forschungsgemeinschaft

References

[1] B. D. Serot and J. D. Walecka, Adv. in Nucl. Phys. **16** (1986) 1 and references quoted therein

[2] P.-G. Reinhard, Rep. Prog. Phys. **52** (1989) 439 and references quoted therein

[3] P. Manakos and T. Mannel, Z. Phys. **A 330** (1988) 223

[4] P. Manakos and T. Mannel, Z. Phys. **A 334** (1989) 481

[5] J. D. Walecka, Ann. Phys. **83** (1974) 491

[6] B. A. Nikolaus and D. G. Madland, to be published

Bounds on the Coupling Parameters for Vector Mesons in the Relativistic Random Phase Approximation

G. Heyer[1], P. Manakos[1], T. Mannel[1,2], and T. Ohl[1]
[1] Institut für Kernphysik der Technischen Hochschule Darmstadt
[2] Lyman Laboratory of Physics, Harvard University, Cambridge, Massachusetts, USA

There is currently much interest in field-theoretically inspired models for low and medium energy properties of nuclear matter, finite nuclei, and heavy ion collisions [1]. These models treat nucleons and mesons as elementary quantum fields. Going beyond the mean field approximation immediately raises questions of consistency, even in a modest, phenomenological approach.

Recently [2] we have translated the Relativistic Random Phase Approximation (RRPA) into an exactly soluble quantum field theory, attributed to Zachariasen [3].

This model allows to handle the large values of the coupling constants which are needed to fit nuclear properties and to derive upper bounds thereof from consistency conditions. This question is of some importance since coupling parameters lead to the apparition of unphysical poles (ghosts) in the relevant mass region.

We examine by this method the popular σ - ω model consisting of nucleon, scalar and vector meson fields with the Lagrangean

$$\begin{aligned}\mathcal{L} &= \bar{\psi}\left(i\gamma_\mu\partial^\mu - M\right)\psi - \frac{1}{2}\phi\left(\Box + m_S^2\right)\phi \\ &\quad -\frac{1}{4}\left(\partial_\mu V_\nu - \partial_\nu V_\mu\right)\left(\partial^\mu V^\nu - \partial^\nu V^\mu\right) + \frac{1}{2}m^2 V_\mu V^\mu \\ &\quad - g_S\phi\bar{\psi}\psi + g_V V^\mu\bar{\psi}\gamma_\mu\psi\end{aligned} \tag{1}$$

To translate the RRPA into the model we replace the interacting currents $\bar{\psi}\psi$, $\bar{\psi}\gamma_\mu\psi$ by the generalized free fields J, J_μ with c-number commutators. These are taken equal to the vacuum expectation values of the commutators of the original composite fields:

$$\begin{aligned}\left[J_\mu(x), J_\nu(y)\right] &= \langle 0|\left[:\bar{\psi}(x)\gamma_\mu\psi(x):, :\bar{\psi}(y)\gamma_\nu\psi(y):\right]|0\rangle \\ &= -\int_0^\infty ds\rho^2(s)\left(g_{\mu\nu} + \frac{\partial_\mu\partial_\nu}{s}\right)i\Delta(x-y;s)\end{aligned} \tag{2}$$

where current conservation has been exploited to obtain the above Lehmann representation. The spectral weight function $\rho(s)$ may either be calculated in perturbation theory or viewed as a phenomenological non-perturbative input.

Due to the charge conjugation invariance of the vacuum with zero baryon number the commutator $[J, J_\mu]$ vanishes. Thus scalar and vector mesons are decoupled and can be studied separately. The scalar sector has been treated previously [2], so we shall focus on the vector meson sector.

The generalized free fields J_μ are conveniently expressed as a superposition of new spin one fields $j_\mu(x;s)$:

$$J_\mu(x) = \int_0^\infty ds\rho(s)j_\mu(x;s) \tag{3}$$

$$\left[j_\mu(x;s), j_\nu(y;s')\right] = -i\delta(s-s')\left(g_{\mu\nu} + \frac{\partial_\mu\partial_\nu}{s}\right)\Delta(x-y;s) \tag{4}$$

with the following kinetic term in the Lagrangean

$$\begin{aligned}\mathcal{L}^j_{kin} &= \int ds\,\Theta\left(s-4M^2\right)\times \\ &\quad \left(-\frac{1}{4}\left(\partial_\mu j_\nu - \partial_\nu j_\mu\right)\left(\partial^\mu j^\nu - \partial^\nu j^\mu\right) + \frac{1}{2}s j_\mu j^\mu\right)\end{aligned} \tag{5}$$

It is easily seen [2] that the field $j_\mu(x;s)$ corresponds to nucleon-antinucleon pairs with spin one and invariant mass $\sqrt{s}$, this establishes the connection to the RRPA.

The Lagrangean of the model is

$$\begin{aligned}\mathcal{L} &= -\frac{1}{4}\left(\partial_\mu V_\nu - \partial_\nu V_\mu\right)\left(\partial^\mu V^\nu - \partial^\nu V^\mu\right) + \frac{1}{2}m^2 V_\mu V^\mu \\ &\quad + \mathcal{L}^j_{kin} + g_V V^\mu J_\mu\end{aligned} \tag{6}$$

and the resulting equations of motion for field operators can be solved exactly [2], yielding the following relation between the field operator renormalization constant Z_3 of the vector field and the renormalized coupling constant g_V:

$$Z_3 = 1 - g_V^2\int\frac{ds}{s}\frac{\rho^2(s)}{s-m^2}\,. \tag{7}$$

Here m denotes the renormalized mass of the vector meson.

This relation is a most essential result with respect to the derivation of bounds for the coupling constants. The apparition of ghost states is equivalent to Z_3 becoming negative [2]. Thus for consistency we obtain the following upper bound for the renormalized coupling constant.

$$g_V^2 \le (g_V^2)_{max} = \left(\int_0^\infty ds\frac{\rho^2(s)}{s(s-m^2)}\right)^{-1} \tag{8}$$

The two point function of the vector meson is built up by superposing propagators of the free fields V_μ and j_μ or from the commutators via a dispersion relation. However care must be exercised, as is well known from free vector boson propagators, to assure covariance and transversality. We end up with

$$\begin{aligned}iD^{(C)}_{\mu\nu}(q) &= \frac{1}{q^2+i\epsilon}\left(q^2 g_{\mu\nu} - q_\mu q_\nu\right) \\ &\quad \times\left(\frac{1}{q^2-m^2+i\epsilon}\frac{1}{f_R(q^2+i\epsilon)} + \frac{1}{m^2}\frac{1}{f_R(0)}\right)\end{aligned} \tag{9}$$

$$f_R(z) = 1 + g_V^2 z\int\frac{ds}{s}\frac{\rho^2(s)}{(s-m^2)(s-z)} \tag{10}$$

Note that (9) has no pole at $q^2 = 0$.

The one loop contribution to the spectral density is given by:

$$(\rho^2)_{(0)}(s) = \frac{1}{2\pi^2}\theta(s-4M^2)\sqrt{1-\frac{4M^2}{s}}(s+2M^2) \tag{11}$$

In this case the integral on the RHS of eq. (8) fails to converge and we end up with $(g_V^2)_{max} = 0$. We can avoid this trivial model by the indroduction of suitable form factors in the s-channel as discussed in [2]. Finally we find:

$$\frac{1}{(g_V^2)_{max}} = \int ds(\rho^2)_{(0)}(s)\frac{\Lambda^4}{(s-\Lambda^2)^2+\Gamma^2\Lambda^2} \tag{12}$$

where Λ and Γ parametrize the form factors.

In field theoretical models of nuclear physics commonly used values are around $g_V^2 = 80$. From eq. (12) we find that a cut-off $\Lambda = 1450$ MeV is required to avoid the ghost states. Similar values of Λ have been obtained for the scalar meson coupling [2]. It turns out that under such circumstances the width parameter Γ has practically no effect on the resulting bounds.

Our essential conclusion is that in both cases, scalar and/or vector mesons, a strong suppression of $\overline{N}$-N-states is required to avoid the apparition of ghost states in the relevant mass region.

References

[1] B.D. Serot and J.D. Walecka, Adv. in Nucl. Phys. **16** (1986) 1, P.G. Reinhard, Rep. Prog. Phys. **52** (1989) 439

[2] T. Mannel, T. Ohl, P. Manakos, Z. Phys. A (in press)

[3] F. Zachariasen, Phys. Rev. **121**, p.1851 (1961), W. Thirring, Phys. Rev. **126**, p.1209 (1962)

Improving the Soliton Bag for Nuclear Matter Modeling [G]

Ch. Derreth and W. Greiner
Institut für Theoretische Physik der Universität Frankfurt

In recent years numerous authors have made efforts to reproduce nuclear properties from the quark structure of the nucleons. Especially the EMC effect gives evidence that nucleons may not be considererd as elementary particles inside nuclei when probed by deep-inelastic scattering. A QCD-level desciption of nucleons is expected to render nuclei as nucleon molecules bound by gluonic interactions. Up to today bag models habe been used as approximations to QCD in nuclear matter studies.

Our goal is to simulate a heavy nucleus as a cluster of bags. As a first step towards the bag cluster we considered infinite nuclear matter, i.e. a crystal. As our working model we chose the Friedberg-Lee bag[1]. In it quarks are bound in a well of a scalar field σ which assumes a nonzero vacuum value outside the bag. There are neither gluons nor pions in the most simple version of this model. The σ field simulates the non-perturbative long-wavelength QCD effects (gluon condensate).

We calculate the energy band of quarks in the soliton bag crystal in reciprocal space using a band structure method from solid state theory. Our method is the relativistic LMTO[2]. It is well suited for our purpose since it is designed for relativistic systems and can be modified to work in coordinate space (i.e. for a cluster). Since it applies the variational principle to a partial-wave basis it is also computationally fast. We use the fcc crystal structure since it has maximal density and is nearly isotropic.

Fig. 1 shows the energy per baryon lattice cell as a function of density ($\rho_0 = 0.17 fm^{-3}$). The total energy decreases monotonically which means that bag matter is unstable. This in mostly due to the widening of the band. Since the band is only 1/4 filled the occupied part of it moves down from the free bag eigenvalue. The unphysical behaviour of the mass vs. density relation is attributed to deficiencies of the bag model: We neglected the spurious center-of-mass motion because it is not easy to include it into a many-bag problem. Gluonic and pionic degrees of freedom have been neglected as well.

As a first attempt to include residual interactions Ref. 3 proposes a phenomenological ansatz: assume that they mix all states in a band completely, i.e. occupy the whole band with occupation number $f = 1/4$. After subtracting an estimate of the colour-magnetic energy we obtain Fig. 2. It shows that the residual interactions are overestimated leading to a repulsion between bags.

In order to improve on this we started with a calculation of the one-gluon magnetic exchange energy. A self-consistent treatment is possible for free bags, however, we at first tried to add gluons perturbatively[4]. Gluons are confined to the bag by an inhomogeneous dielectric function $\kappa(\sigma)$ which approaches zero as $\sigma \to \sigma_{\text{vacuum}}$. In a colour singlet ground state the total colour electric (exchange and self) energy vanishes. Furthermore, we neglect the magnetic self interaction and approximate the quark source field to be spherical. The static gluon propagator is determined from the solution of the generalised Laplace equation

$$-y'' + (\ln\kappa)'y' + \left[\frac{2}{r} + (\ln\kappa)''\right] y = 0.$$

The strong coupling constant is then fit to the N-Δ split for various parameterisations of κ. However, we could not yet find a satisfactory result for the density dependence of nucleon states in the crystal due to the uncertainty in the functional parameterisation of $\kappa(\sigma)$.

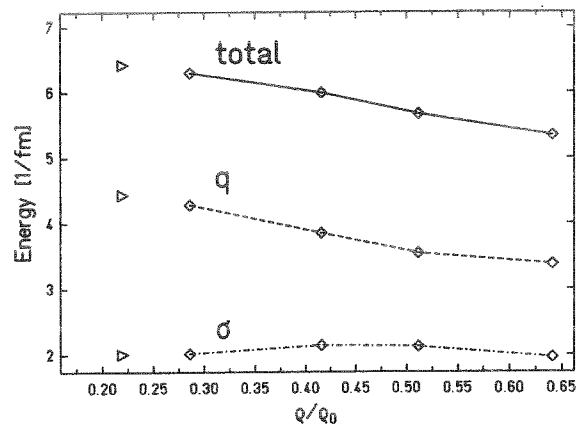


Fig. 1: Soliton field energy, quark energy, and total energy for different densities. Free bag values indicated by ▷.

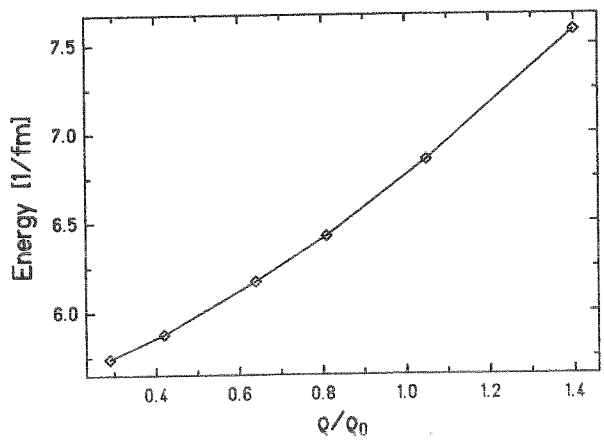


Fig. 2: The total energy including residual interactions phenomenologically.

[1] R. Goldflam, L. Wilets, Phys. Rev. D 25 (1982) 1951
[2] O. K. Andersen, Phys. Rev. B 12 (1975) 3060
[3] M.C. Birse, J.J. Rehr, L. Wilets, Phys. Rev. D (1988) 359
[4] M. Bickeböller et al., Phys. Rev. D 31 (1985) 2892

Nuclear Stopping In Heavy Ion Collisions At AGS Energies

H. Sorge, A. von Keitz, R. Mattiello,

H. Stöcker and W. Greiner

Inst. f. Theor. Physik, Universität Frankfurt

In the last few years much theoretical and experimental effort has been devoted to the study of AA collisions in an energy range beyond the "Bevalac energies" around $1GeV$ per projectile nucleon. At BNL silicon beams have been accelerated up to 14.6 $AGeV$ and at CERN oxygen and sulfur beams up to 200 $AGeV$. The main goal of these experiments is the exploration of the nuclear stopping and thermalization in such light ion induced reactions. It sets the stage for massive beams ($A > 200$) which will become available in the 1990's. Those will enable the search for the quark gluon plasma, a state in which the partons are no longer confined into individual hadrons, but can propagate nearly freely over large distances.

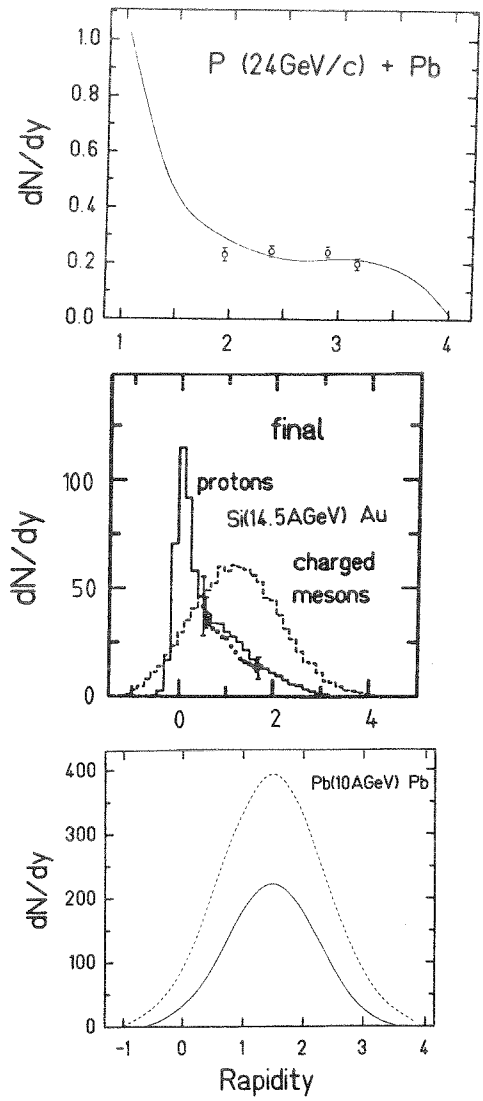
The AGS energy seems to be very promising to achieve nuclear stopping: Experimental data for pA collisions indicate that a nucleon suffers a mean rapidity loss of $\Delta y \sim 2$ in a high energy collision with a heavy nucleus like lead, which is large compared to the rapidity gap of 3. Furthermore, secondary rescattering is important at these energies, because most of the produced hadrons are formed inside the original nuclei. Detailed calculations within the relativistic quantum molecular dynamics approach (RQMD) actually have confirmed that the additional meson-nucleon collisions lead to a nonnegligible contribution to the total interaction and therefore enhance the stopping of the nucleons [1,2]. RQMD combines the classical propagation of the hadrons with stochastic binary scattering and decay of unstable hadrons. This approach has been used for the subsequent calculation.

In Fig.1 we show proton momentum distributions for pA and AA collisions in the AGS energy region. They are directly compared to experimental data [3,4]. Both the calculated and the measured proton rapidity distribution in the Si on Au reaction show a strong deceleration of the projectile. This confirms a high degree of projectile stopping. Essentially no nucleons are left over at projectile rapidity in the calculations for central collisions. This has recently been supported by the E814 group [5]. Experiments with heavy symmetric systems (e. g. Pb on Pb) are planned at the AGS booster in the near future. Fig.1 also shows the RQMD predictions of the final nucleon and meson rapidity distributions for 10$AGeV$ Pb + Pb ($b = 1.3fm$). Both nuclei stop each other. There are no spectator remnants left. The nucleon rapidity distribution in light ion reactions, however, exhibits a dip at midrapidity and maxima near the original target and projectile rapidities. This indicates incomplete stopping.

Just after the collision has started the local maximum baryon and energy densities are simply given by an addition of the projectile and target densities in the observer frame in which projectile and target frame have the same speed, i. e. for the $10AGeV$ collision we expect an initial maximum local baryon density of 5 up to 6 times groundstate nuclear matter density. However, these baryon densities and the associated energy densities are relevant for macroscopic processes (like a phase transition) only if these two matter currents do indeed stop each other in a time which is short compared to the expansion time scale.

In the reaction Si on Au this "kinematic limit" for the local baryon density can be reached in the early stage of the collision. In contrast, the baryon density in the reaction Pb(10$AGeV$) on Pb exceeds its kinematic limit by far. This can be understood as a shock compression due to multiple collisions with a density pile up. The achieved thermal eqilibration can be quantified by computing the degree of anisotropy locally which can be expressed by the ratio $R = \frac{<p_t^2>}{2 \cdot <p_l^2>}$. An isotropic momentum distribution would lead to $R = 1$. For both systems it lasts typically $5fm/c$ until R jumps to values above 0.5. Due to the larger lifetime of the high density region in the Pb on Pb reaction the matter becomes nearly equilibrated while the region of high density is still existing [6].

Finally we would like to point out that thermal matter at such high baryon densities has probably not been produced since the big bang. Therefore we are looking forward for an exciting future with the AGS Booster experiments.



References

[1] H. Sorge, A. von Keitz, R. Mattiello, H. Stöcker and W. Greiner: Proceedings of the NASI school "The Nuclear Equation Of State" Peniscola (Spain) 1989, to be publ. by World Scientific (Singapore)

[2] R. Mattiello, H. Sorge, H. Stöcker, W. Greiner: Phys. Rev. Lett. 63(1989) 1459; H. Sorge, H. Stöcker, W. Greiner: Ann. Phys.(USA) 191 (1989) 266

[3] T. Eichten et al.: Nucl. Phys. B44 (1972) 333; W. Busza, R. Ledoux: Ann. Rev. Nucl. Part. Sci. 38 (1988) 119

[4] M. Sarabura et al. (E802): Nucl. Phys. A498 (1989) 409; T. Abbott et al. (E802): subm. to Phys. Rev. Lett. (1989)

[5] J. Barrette et al. (E814): subm. to Phys. Rev. Lett. (1989)

[6] H. Sorge, A. von Keitz, R. Mattiello, H. Stöcker and W. Greiner: subm. to Phys. Rev. Lett. (1990)

Pair Creation in a Flux Tube

Th. Schönfeld*, A. Schäfer†, B. Müller‡, K. Sailer§, J. Reinhardt* and W. Greiner*

*Institut für Theoretische Physik, Johann Wolfgang Goethe Universität, Frankfurt
†Max-Planck-Institut für Kernphysik, Heidelberg
‡Department of Physics, Duke University, Durham, USA
‡Institute for Theoretical Physics, Kossuth Lajos Tudományegyetem, Debrecen, Hungary

Hadrons of very high excitation can be very well described in the string model[1]. The fission of such strings can be described by assuming a homogeneous chromoelectric field along the string and by considering spontaneous pair creation within this field. For the case of a homogeneous electric field of infinite extension the pair creation rate is given by the Schwinger-formula:

$$\mathcal{W} = \frac{(e\mathcal{E})^2}{4\pi^3} \cdot \sum_{N=1}^{\infty} \frac{1}{N^2} \exp\left(-N\pi \frac{m^2}{e\mathcal{E}}\right) .$$

In the case of strings the field is however restricted to a flux tube of finite radius. We have calculated how the Schwinger-formula must be altered, if this finite extension is taken into account.

Our strings are modelled as cylinders of infinite length and finite radius R. The particles which are created must of course fulfill the equations of QCD in a certain approximation, which is here given by the MIT bag model. Thus the equations to be solved are the Dirac equation which in the case of a homogeneous field of strength $\mathcal{E}$ in z-direction reads

$$(\gamma_\mu \hat{\Pi}^\mu - m)\psi = 0$$

where $\hat{\Pi}^\mu := -i\partial^\mu - eA^\mu$ and $A^\mu = (0,0,0,-\mathcal{E}t)$, and the linear MIT boundary condition (in our case $(n^\mu = (0,\vec{e}_\rho))$)

$$(i\gamma_\rho + 1)\psi(R,\varphi,x_3,t) = 0 \qquad \forall \varphi, x_3, t .$$

Note that the quadratic MIT boundary condition must not be taken into account, since it determines the bag shape which, however, in our case is fixed externally. The Dirac equation is solved by the functions[2]

$$\psi_{1/2} = \left[\left(\gamma\hat{\Pi}\right) + m\right] \frac{1 \pm \alpha_3}{2} E_{\tilde{m}}(x) \ , \ \tilde{m}^2 = m^2 \pm ie\mathcal{E} \ .$$

where $E_m(x) = N \cdot e^{ip_3 x_3} e^{i\mu\varphi} J_\mu(k\rho) D_{\nu \pm \frac{1}{2}}[\tau \cdot (i-1)], \tau = \sqrt{e\mathcal{E}} \cdot (t + p/e\mathcal{E})\nu = (i\lambda - 1)/2$ and $\lambda = (p_1^2 + p_2^2 + m^2)/e\mathcal{E} = (k^2 + m^2)/e\mathcal{E}$. J_μ are the Bessel functions and D_ν are the parabolic cylinder functions.

The linear MIT boundary condition after some calculations leads to the quantisation of the transverse momentum k:

$$0 \stackrel{!}{=} kR \cdot \left(J_{\mu+1}^2(kR) - J_\mu^2(kR)\right) - 2mRJ_\mu(kR)J_{\mu+1}(kR) .$$

If we regard our solutions at both positive and negative time infinity, and if we compare to semiclassical WKB solutions, we find that it behaves like

$$\begin{aligned} \psi &\longrightarrow B_i \left|\bar{a}\right\rangle \quad (\tau \to -\infty) \\ \psi &\longrightarrow A_f \left|a\right\rangle + B_f \left|\bar{a}\right\rangle \quad (\tau \to +\infty) , \end{aligned}$$

i.e. for $\tau \to -\infty$ there are only antiparticles, whereas for $\tau \to +\infty$ there is a mixture of particles and antiparticles. The pair creation rate is then given by

$$W = \tfrac{1}{2} \cdot (B_f^2 - B_i^2 - (A_f^2 - A_i^2)) = \exp\left\{-\pi \frac{k_{n\mu}^2 + m^2}{e\mathcal{E}}\right\}$$

The probability for no creation of any pair is therefore

$$|\langle 0_+ | 0_- \rangle| = \prod_{n,\mu,p_3} (1 - W_{n\mu}) = \exp\left\{\int \frac{dp_3}{2\pi/L} \sum_{n\mu} \ln(1 - W_{n\mu})\right\} .$$

On the other hand, according to Schwinger we know that

$$|\langle 0_+ | 0_- \rangle| = \exp\{-2\Im m\mathcal{L} \cdot \pi R^2 LT\} ,$$

The pair creation rate is then given by the imaginary part of the Lagrangian $\Im m\mathcal{L}$:

$$\begin{aligned} 2\Im m\mathcal{L} = \mathcal{W} &= -\frac{1}{TL\pi R^2} \int \frac{dp_3}{2\pi/L} \sum_{n,\mu} \ln\left(\bar{W}_{n,\mu}\right) \\ &= -\frac{e\mathcal{E}}{2\pi^2 R^2} \sum_{n,\mu} \ln\left(1 - \exp\left\{-\pi \frac{k_{n\mu}^2 + m^2}{e\mathcal{E}}\right\}\right) \\ &= \frac{e\mathcal{E}}{2\pi^2 R^2} \sum_{n,\mu} \sum_N \frac{1}{N} \exp\left\{-N\pi \frac{k_{n\mu}^2 + m^2}{e\mathcal{E}}\right\} \\ &= \frac{(e\mathcal{E})^2}{4\pi^3} \sum_N \frac{1}{N^2} \exp\left\{-N\pi \frac{m^2}{e\mathcal{E}}\right\} \times C_{n\mu}^N \end{aligned}$$

with

$$C_{n\mu}^N = \sum_{n,\mu} \exp\left\{-N\pi \frac{(k_{n\mu} \cdot R)^2}{e\mathcal{E}R^2}\right\} \to 1, \text{if } R \to \infty .$$

Thus for $R \to \infty$ Schwinger's formula is reproduced.

In Fig. 1 we have shown the ratio of the pair creation rate at finite radius to that according to Schwinger ($R \to \infty$) for different field strengths $e\mathcal{E}$. The created particles are assumed to be massless. Observe that all the curves tend to one for large R. Note also, however, that for small radii (≤ 1 fm) in most cases there are considerable corrections to the Schwinger formula, especially for weak fields. This means that the pair creation rate in hadronic strings due to the Euler-Heisenberg-Schwinger mechanism is strongly suppressed.

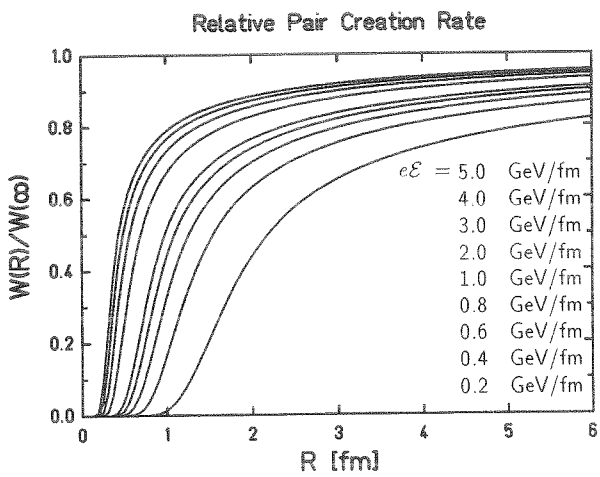


Fig.1: The ratio of the pair creation rate (massless particles) in finite cylinders to that of the Schwinger formula.

[1] K. Sailer, B. Müller and W. Greiner: UFTP preprint 230/1989
[2] Th. Schönfeld et al. UFTP preprint 242/1990

Space-Time Effects in the Decay of Strings by Pair-Creation

M. Herrmann and J. Knoll
GSI

The formation and fragmentation of jets induced by e^+-e^- or hadron-hadron collisions has been successfully described by a number of phenomenological models like the string models or parton models. While for these processes the description can entirely be formulated in momentum space, employing parton distribution functions, the extension to hadron - nucleus and nucleus - nucleus collisions, however, demands a detailed knowledge of the space-time evolution. In this respect the string models offer a pragmatic way to study the space time behavior of the particle production mechanism.

In order to access the space-time behavior one commonly employs Schwinger's pair-creation formula [1]. It applies for an infinitely extended constant electric field. Consequently it predicts a constant pair production probability per unit space-time volume, which in the case of three space dimensions results to

$$W := \frac{\gamma(e\mathcal{E})^2}{(2\pi)^3} \sum_{n=1}^{\infty} \exp\left(-\frac{n\pi m^2}{e\mathcal{E}}\right) . \qquad (1)$$

Here e and m are the charge and the mass of the particle under consideration. γ is the spin degeneracy and $\mathcal{E}$ the strength of the electric field.

However, this formula is derived for an infinite homogeneous and static electric field. This clearly does not apply to the case of two receding quarks, i.e. a quark and an antiquark or a quark and a diquark, as the source of the field. One notices the following essential differences to the Schwinger case:

1. in the vicinity of the source quarks the field is not constant but Coulomb-like
2. the field is bounded in transverse direction
3. in longitudinal direction it is limited by *moving* boundaries
4. the thus created particles screen the field in between them.

In our approach we want to study the effects of moving longitudinal boundaries[2, 3]. The starting point of our calculations is the filled Dirac sea. During a finite time an external potential is switched on. After this time evolution one can in principle calculate the number of produced particles. To get a scheme where most of the necessary steps can be performed analytically we restrict the problem to massless fermions in 1+1 dimension. If one tries now to calculate the number of produced particles in the field, whose space-time distribution is shown in fig. 1, one encounters severe problems. They are connected to a theorem by Hermaszewski and Streater[4] which states, that for 1+1 dimensional massless fermions the S-matrix is unitary, iff

$$\Phi = \int_0^T dt \int_{-\infty}^{\infty} dx \mathcal{E}(t,x) = 2\pi n, \quad n = 0, \pm 1, \ldots \qquad (2)$$

where $\mathcal{E}(t,x)$ is the electric field. That means in our case that the number of produced particles is only finite for a discrete set of switch-off times. This problem is intimately connected to the strict zero mass case which we considered up to now. As we do not intend to describe massless particles but only very light particles with respect to their typical energies we use a small mass approximation. The initial and final states are taken to be solutions of the 1+1 dimensional Dirac equation with a mass comparable to the current mass of the light quarks (m = 20 MeV = 0.1 fm^{-1}). The time evolution in the field is performed without a mass term.

In fig. 2 we show the number of produced particles per available space-time volume. The full line gives the results which we gained by using the small mass approximation. The crosses show the calculable values in the strict zero mass case. For large T this production rate approaches a constant which coincides with the result from the Schwinger formula. For small T, however, a strong suppression of the rate is observed. This means that the string will not break in very early stages. So the density of equilibrated particles in an ultra relativistic heavy ion reaction may be smaller than one would estimate from the Schwinger formula.

References

[1] J. Schwinger; Phys. Rev. **82** (1951) 664.

[2] M. Herrmann; Diplomarbeit TH-Darmstadt, GSI report 1989.

[3] M. Herrmann, J. Knoll; Phys. Lett. **B 234** (1990) 437

[4] Z. J. Hermaszewski, R. F. Streater; J. Phys. **A 16** (1983) 2801.

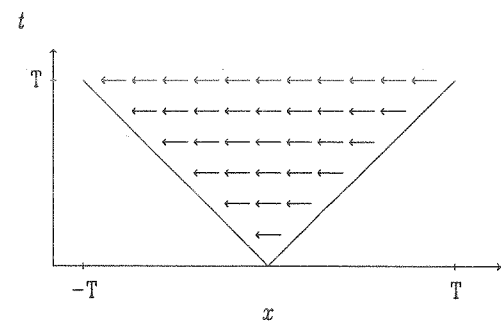


Fig. 1 Space-time configuration of the field of the two receding quarks.

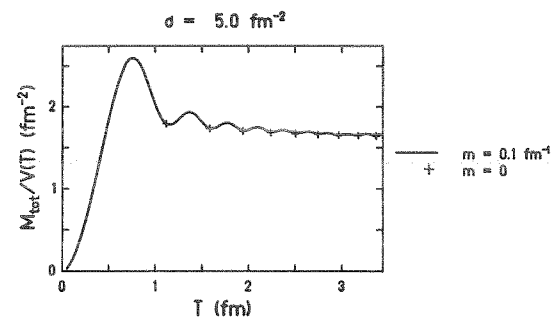


Fig. 2 Number of produced particles per unit volume and unit time for the potential of the two receding quarks as a function of the switch-off time T for m = 20 MeV (full line). The crosses give the exactly calculable values in the massless case.

Flavour Kinetics II, Extensions and New Results[G]

H. W. Barz[a,b], B. L. Friman[b,c], J. Knoll[b] and H. Schulz[a,b]

[a] Zentralinstitut für Kernforschung, Rossendorf, Dresden,
[b] Gesellschaft für Schwerionenforschung, Darmstadt,
[c] Institut für Kernphysik, Technische Hochschule Darmstadt

Non-equilibrium aspects of the rehadronization of the quark-gluon plasma have previously been studied in a flavour kinetic model [1]. This model has been improved in several aspects: (a) all members of the lowest flavour SU(3) multiplets of baryons and mesons are included; (b) the expansion of the system, which in the earlier version of the model was parametrized as a function of time, is now obtained by solving the hydrodynamic equations of motion; (c) fast particles may leave the interaction zone by evaporation from the surface.

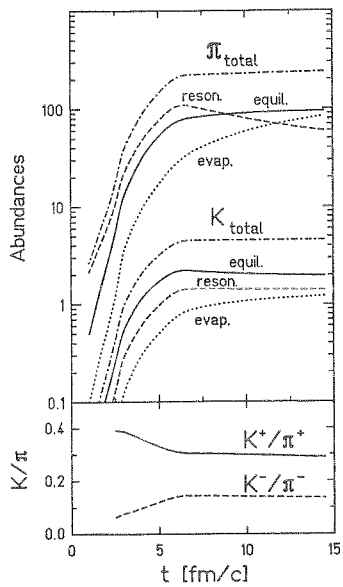


Figure 1: Upper part: Time evolution of the number of pions and kaons ($K^+ + K^0$) in the hadronic phase (*equil*) and those evaporated from the surface (*evap*) of the blob. The curves labelled *reson* give those pions and kaons which will be produced when the hadronic resonances decay. The curve labelled *tot* include all three contributions.
Lower part: Ratios of the total yields K^+/π^+ and K^-/π^- as a function of time.

In fig. 1 we illustrate the production of pions and kaons for a baryon rich plasma. Pions formed in the hadronization of a quark-gluon plasma can either remain in chemical equilibrium in the hadronic phase (π_{equil}) or leave the system as evaporated particles (π_{evap}). Another important contribution to the final pion yield π_{reson} originates from the decay of resonance particles (ρ, Φ, K^*) and exited baryonic states (Δ, Σ^*). After break-up, the decay products will add to the total number of pions π_{tot}. One sees from the fig. 1 that all three contributions to the total pion yield are important. The situation is rather similar for the kaons. In the lower part of the fig. 1 we show the K^+/π^+ and K^-/π^- ratios as a function of time.

The K/π-ratios have been measured in ^{28}Si + Au collisions at 14.5 GeV/c per nucleon by the E802 collaboration [2]. For central collisions it was found that $K^+/\pi^+ \approx 20\%$ and a $K^-/\pi^- \approx 4\%$. At CERN in ^{32}S on S collisions at 200 GeV per nucleon neutral strange particles have been observed[3]. Extrapolating the mean number in the respective acceptance to full phase space one obtains $\Lambda = 8 \pm 2$ and $K^0 + \overline{K}^0 = 22 \pm 5$.

Predictions of the flavour kinetic model are shown in fig. 2. If we assume that the experimental situation for the Si on Au collision at 14.5 GeV/c per nucleon can be simulated by a single fireball containing an energy of about 2.6 GeV per baryon, our model overshoots the experimental K^+/π^+ ratio by about 30% while the K^-/π^- ratio is well reproduced.

For CERN energies of 200 GeV per nucleon the full stopping scenario, which would imply that the energy in the fireball is approximately 10 GeV per nucleon, is unlikely. Assuming that the available thermal energy per baryon is about half of the maximum value, we obtain $(\Lambda + \Sigma^0)/\pi^- = 0.085$ in good agreement with the data and $(K^0 + \overline{K}^0)/\pi^- = 0.4$ which is about twice the measured value.

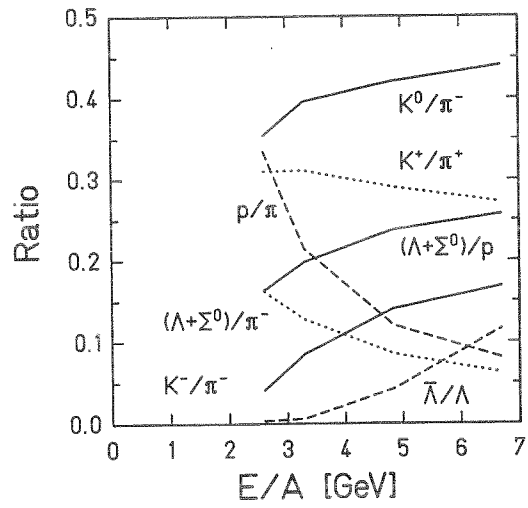


Figure 2: Ratios of particle abundances for several values of the initial energy per baryon. The estimated values for the energy per baryon at AGS (14.5 GeV⋆ A) and CERN-SPS (200 GeV⋆ A) are 2.6 and 4.6, respectively.

References

[1] H.W. Barz, B.L. Friman, J. Knoll and H. Schulz, Nucl. Phys. A484 (1988) 661.

[2] P. Vincent et al., (E802 Collaboration), Nucl. Phys. A498 (1989) 67c.

[3] M. Gazdzicki et al., (NA35 Collaboration), Nucl. Phys. A498 (1989) 375c.

Evaporation of Hadrons from Quark-Gluon Plasma Globs[G]

H. W. Barz[a,b], B. L. Friman[b,c], J. Knoll[b] and H. Schulz[a,b]

[a] Zentralinstitut für Kernforschung, Rossendorf, Dresden,
[b] Gesellschaft für Schwerionenforschung, Darmstadt,
[c] Institut für Kernphysik, Technische Hochschule Darmstadt

Hadronization of a quark-gluon plasma in a cascade type model was explored by Bertsch et al. [1], who considered of plasma globs interacting with pions. We study the relativistic hydrodynamic evolution of a single plasma glob coupled to various decay channels, including the evaporation of pions, strange hadrons (kaons and hyperons) and nucleons. The motion of the glob is represented by a selfsimilar spherical velocity field $u(r,t) = rU(t)/R$, where R is the radius, u is the radial component of the four-velocity, which is connected with the ordinary three-velocity v via $u = \gamma v = v/\sqrt{1-v^2}$ and $U(t) = u(R,t)$ is its value at the surface. The matter density and temperature inside the glob is assumed to be constant. In the equation of state for the plasma phase gluons, massless up and down quarks and strange quarks are included, while the vacuum energy is represented by a bag constant B. The rate for the evaporation of particles from the surface of the glob is estimated following the arguments of Weisskopf for neutron evaporation from a compound nucleus [2].

To illustrate the results we disregard for the moment the oscillatory motion of the glob surface by setting the pressure p equal to zero and neglecting the mass of the strange quarks. In fig. 1 we show the corresponding $p = 0$ isobars in the temperature-density plane for several values of the bag constant. When a pion is emitted the associated loss of energy causes a decrease of the volume, which, since the baryon number of the glob remains unchanged, implies an increase of the baryon density. Thus, irrespective of the initial condition the emission of a pion leads to a cooling of the glob. On the other hand, when a nucleon is emitted the situation is more involved, because both the energy and baryon number of the glob are diminished. The change in the baryon density is approximately

$$\Delta n_B \cong \frac{1}{4BV}\left[\langle E_N\rangle n_B(\mu_q, T) - 4B\right], \qquad (1)$$

where $\langle E_N\rangle$ is the average energy of a nucleon. For sufficiently large values of the vacuum pressure $B \gtrsim \frac{1}{4} m_N n_B$, the change in baryon density Δn_B is always negative and consequently the plasma glob is heated up when a nucleon is emitted. Cooling of the plasma glob by baryon emission is possible only for relatively low values of the bag constant and low initial temperatures. The corresponding initial values of temperature T and baryon density n_B are shown in fig. 1 by the hatched area. The boundary line of this area is determined by solving eq. (1) for vanishing pressure of the plasma. However, for values of the bag constant less than $B^{1/4} \approx 150$ MeV, where the glob is can cool by emitting baryons, quark matter is more bound than nuclear matter. Since there is no sign of a transition to quark matter in low-energy heavy-ion collisions, the bag constant is most likely quite a bit larger. Thus the formation of a strangelets, by cooling of plasma globs is very unlikely in heavy ion collisions.

In fig. 2 we show pressure, temperature and radius of the glob as well as the number of emitted hadrons as a function of time. For a low initial temperature, the glob emits nucleons and heats up, as we discussed above. As the temperature rises, the pion emission rate goes up, and eventually the cooling by pion emission offsets the heating by nucleon emission. The glob then remains at this temperature, radiating off the remaining energy, strangeness and baryon number in the form of pions, kaons, nucleons and lambdas. For a high initial temperature again, cooling by pion emission dominates until the steady state temperature is reached. The calculation is stopped once the glob radius has shrunk below 1 fm, since at this point the quark content corresponds to approximately one hadron.

References

[1] G. Bertsch, M. Gong, L. D. McLerran, V. Ruuskanen and E. Sarkkinen, Phys. Rev. D37 (1988) 1202.

[2] V. F. Weisskopf, Phys. Rev. 52 (1937) 252.

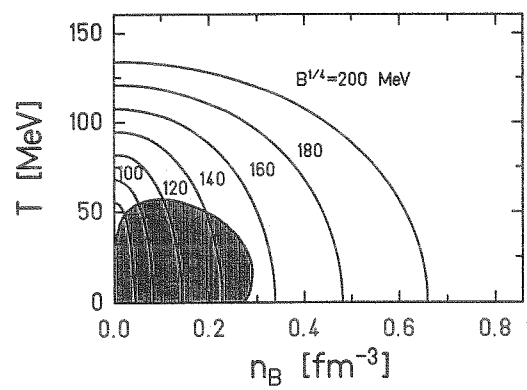


Fig. 1: Isobars in the density-temperature plane for vanishing pressure of the quark-gluon phase for different values of the bag constant.

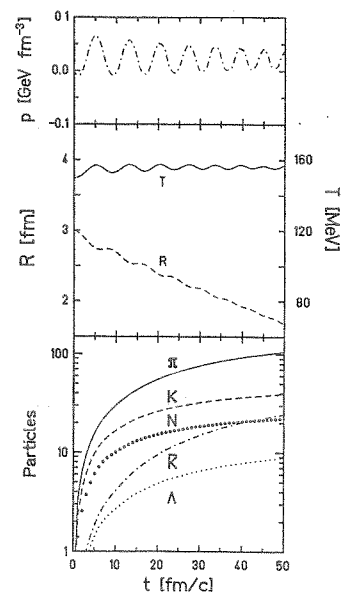


Fig. 2: Pressure, temperature and radius of the glob as well as the number of emitted hadrons as a function of time. The initial baryon content is $N_B = 36$ and the bag constant is $B^{1/4} = 235$ MeV.

Production of Supersymmetric Particles in Ultrarelativistic Heavy-Ion Collisions

J. Rau, B. Müller, W. Greiner, G. Soff
Institut für Theoretische Physik, Universität, D-6000 Frankfurt am Main
and GSI, Darmstadt

Heavy ions with energies of some TeV per nucleon can be considered as carriers of intense photon fields. In peripheral collisions elementary particles with masses up to a few 100 GeV can be produced via two-photon processes. We evaluated total cross sections for the formation of charged supersymmetric particles, namely sleptons and winos, in Pb + Pb collisions. At LHC energy $E_{ion} = 3.5$ TeV/u and for rest masses around $m = 50$ GeV we obtain $\sigma_{\tilde{W}^+\tilde{W}^-} \simeq 10$ nb and $\sigma_{\tilde{l}^+\tilde{l}^-} \simeq 1$ nb.
Recently it was pointed out that elementary particles with masses up to 200 GeV may be produced with measurable cross sections in peripheral collisions of heavy nuclei at TeV per nucleon energies [1]. Future accelerators will allow to probe this energy range, with energies up to 3.5 TeV per nucleon at the CERN Large Hadron Collider (LHC) and up to 8 TeV per nucleon at the Superconducting Supercollider (SSC) in Texas.
Very rapidly ($\gamma \gg 1$) moving ions can be considered as carriers of intense photon fields. A simple estimate for the maximum photon energy yields

$$\hbar\omega_0 = \frac{\hbar c\gamma}{R} \simeq 100 \text{ GeV} \quad (220 \text{ GeV}) \quad ,$$

assuming a Lorentz contraction factor $\gamma \simeq 3500$ (8000) at the LHC (SSC) and a nuclear radius $R \simeq 7$ fm for a lead nucleus. Hence exotic particles with masses up to a few 100 GeV can be produced via two-photon processes. Recently cross sections for intermediate vector boson and Higgs boson production in U + U collisions were predicted to be in the nanobarn range [1].
Here we would like to draw attention to the fact that also supersymmetric particles may be produced in ultrarelativistic heavy-ion collisions. Supersymmetry is one of the most promising attempts to unify all fundamental forces in nature. It involves a symmetry between bosons and fermions which allows for a unified description of matter, built of fermions, and interactions, carried by bosons.
As we consider production of sparticles in heavy-ion collisions, i.e. by virtue of electromagnetic interaction, it is obvious to focus on charged sparticles. In particular, we compute the production cross section for sleptons $\tilde{l}$ and winos $\tilde{W}$. Since global supersymmetry and conventional internal symmetries decouple, internal quantum numbers like charge, weak isospin etc. remain unaffected by supersymmetry transformations. Therefore the interaction of charged sparticles with the electromagnetic field can be described by minimal coupling as usual. Especially sleptons behave like ordinary charged scalars and winos like ordinary charged Dirac fermions in the electromagnetic field.
Using the Weizsäcker-Williams method we computed the total production cross section of sleptons and winos in Pb + Pb collisions as a function of the beam energy, varying the sparticle mass between 50 GeV and 200 GeV. Figures 1 and 2 show the results [2]. For rest masses $m = 50$ (100) GeV and LHC energy $E_{ion} = 3.5$ TeV/u we obtained $\sigma_{\tilde{W}^+\tilde{W}^-} = 10$ (0.15) nb and $\sigma_{\tilde{l}^+\tilde{l}^-} = 2$ (0.03) nb. Considerations of accelerator-technological aspects indicate that a heavy-ion luminosity $L \simeq 10^{28}$ cm^{-2}s^{-1} can be achieved for Pb ions at 3.5 TeV/u. Requiring a signal of at least 10 events/yr leads to the condition $\sigma > 0.03$ nb for the cross section to be measurable. At LHC energy sleptons and winos with masses up to 100 GeV could be detected. Given the same luminosity, at SSC energy the accessible mass region could be extended to 200 GeV.
Corresponding results for proton - proton collisions at $E = 40$ TeV are $\sigma_{\tilde{W}^+\tilde{W}^-} \leq 0.1$ nb and $\sigma_{\tilde{l}^+\tilde{l}^-} \leq 0.01$ nb for masses around $m = 100$ GeV. The disadvantage of lower luminosity of a heavy-ion beam may well be compensated by the low-multiplicity topology of the events predicted for peripheral heavy-ion collisions without direct hadronic interaction.

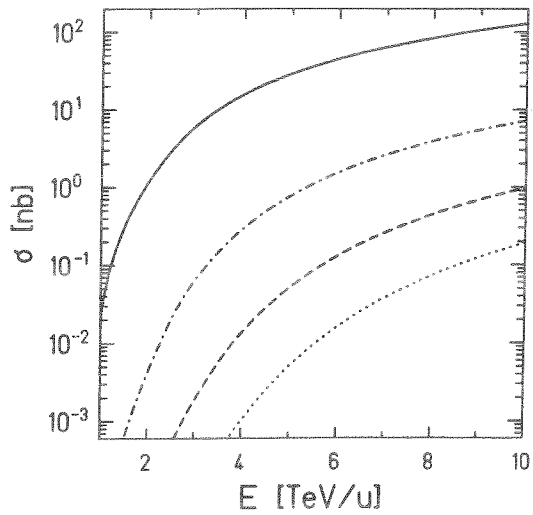


Fig. 1: Production cross section of winos $\tilde{W}^{\pm}$ as a function of the ion energy E for Pb + Pb collisions. For the rest mass of the sparticles we assumed 50 GeV (solid line), 100 GeV (dashed-dotted line), 150 GeV (dashed line) and 200 GeV (dotted line).

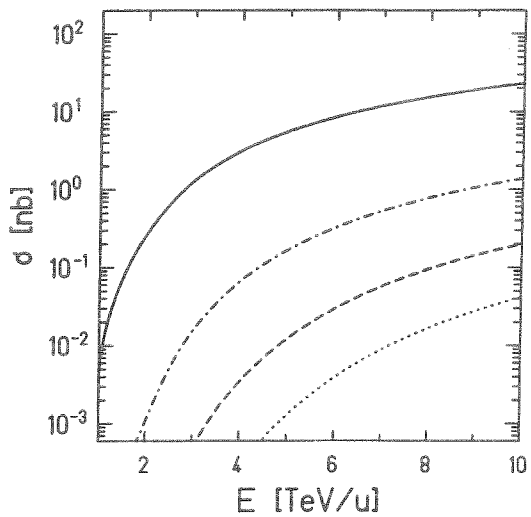


Fig. 2: The same as in fig. 1 for the production of sleptons $\tilde{l}^{\pm}$.

[1] M. Grabiak, B. Müller, W. Greiner, G. Soff, P. Koch, J. Phys. G15 (1989) L25
E. Papageorgiu, Phys. Rev. D40 (1989) 92; Nucl. Phys. A498 (1989) 593c
M. Drees, J. Ellis, D. Zeppenfeld, Phys. Lett. 223B (1989) 454
G. Soff, J. Rau, M. Grabiak, B. Müller, W. Greiner, preprint GSI-89-55 (1989)

[2] J. Rau, B. Müller, W. Greiner, G. Soff, J. Phys. G16 (1990) 211

"Soft" coherence in Bose-Einstein Correlations[G]

I.V. Andreev[1] and R.M. Weiner[2]

1) Lebedev Institute, Moscow, USSR
2) Physics Dept., Univ. of Marburg, FRG

There are various theoretical reasons why one expects that coherent states play a significant role in hadronic reactions (cf. e.g. [1]). Experimentally effects of coherence should be seen among other things in Bose-Einstein correlations (BEC). Unfortunately the simplest way to look in BEC for coherence, namely in the intercept $C_2(0)$, does not work satisfactorily, because of other effects which might mimic the effect of coherence. Here C_2 is the two body correlation function for identical particles

$$C_2(y_1,y_2)=P(y_1,y_2)/\left[P(y_1)\ P(y_2)\right] \qquad (1)$$

where y_i are kinematical (multi-component) variables which characterize the state of a particle and P the corresponding two particle and single particle probabilities. If C_2 depends only on $|y_1-y_2|$, then the value $C_2(0)$ is strongly dependent on whether the particles are in a coherent state ($C_2(0)=2$), but to disentangle this dependence on coherence from other effects like final state interactions, insufficient resolution on $|y_1-y_2|$ etc. is at the present stage quite difficult. However, it has been printed out recently[1] that another "signal" for coherence may be available through the fact that, contrary to the empirical parametrization of $C_{(2)}$ by one exponential

$$C_{(2)}=\sim 1+\tilde{\lambda}\exp(-|y_1-y_2|^2\cdot\tilde{R}^2) \qquad (2)$$

where $\tilde{\lambda}$ is an ad hoc "incoherence" factor and $\tilde{R}$ the source "radius", a quantum statistical (QS) treatment of BEC leads to a two exponential formula of the form

$$C_{(2)}=1+2p(1-p)\exp(-|y_1-y_2|^2R^2)+ \\ +p^2\exp(-2|y_1-y_2|^2\cdot R^2) \qquad (3)$$

where p is the chaoticity:

$$p=\langle n_{ch}\rangle/\langle n\rangle,\quad \langle n\rangle=\langle n_{ch}\rangle+\langle n_c\rangle$$

$\langle n_{ch}\rangle$ and $\langle n_c\rangle$ are the mean numbers of particles in the chaotic and coherent states respectively and $\langle n\rangle$ is the total mean multiplicity.

Here R is the inverse of the coherence length of the chaotic fields in y space. Given the importance of the implications of eq. (3) it seems desirable to see under what conditions it can be reobtained in a different formalism, namely that of currents in the space-time representation.

The result is

$$C_2(K_1,K_2)=1+2p(1-p)\cdot \\ \cdot\exp\left\{-\frac{1}{4}(\tilde{R}^2-R_\lambda^2)\left[K_1^2+K_2^2+\frac{1}{2}(K_1-K_2)^2\right]\right\}\ A+ \\ +p^2\ \exp\left[-\frac{1}{2}(\tilde{R}^2-R_\lambda^2)(K_1-K_2)^2\right]\cdot A$$

with

$$A^{-1}=\left\{p+(1-p)\exp\left[-\frac{1}{2}(\tilde{R}^2-R_\lambda^2)K_1^2\right]\right\}\cdot \\ \cdot\left\{p+(1-p)\exp\left[-\frac{1}{2}(\tilde{R}^2-P_\lambda^2)K_2^2\right]\right\} \qquad (4)$$

where $\tilde{R}$ is the radius of the source $R_\lambda=\tilde{R}^2\lambda^2/\tilde{R}^2+\lambda^2$ and λ is the coherence length of the chaotic currents in <u>real</u> space-time. K_i are 4-momenta and the metric is enclidian.

When comparing this result with eq. (3) we see among other things that now the mixed term $2p(1-p)$ contains an additional factor $e^{-1/4(K_1^2+K_2^2)(\tilde{R}^2-R_\lambda^2)}$ which means that this term is strongly damped and thus the two exponent form survives only for soft particles when K_i are small. This could serve as a supplementary signal for coherence. It also follows that the coherent component in most experimental fits where no cuts in K_i are done is highly underestimated.

<u>References</u>

1) R.M. Weiner, Phys.Lett. <u>B232</u>, 278 (1989).

Transverse Energy Distributions in High Energy Collisions[G,B]

S. Raha[1], R.M. Weiner[1], G. Wilk[2] and Z. Wlodarczyk[3]

1) Fachbereich Physik, Philipps-Universität, Marburg, FRG
2) Soltan Institute for Nuclear Studies, Warsaw, Poland
3) Institute of Physics, Pedagogical University, Kielce, Poland

Multiplicity distributions (MD) constitute the most characteristic property of strong interaction dynamics. Of late, however, measurement of transverse energy distributions (TED) is also gaining great importance. On the other hand, such measurements are essential to identify the class of events where the Quark-Gluon Plasma may be produced. More importantly, with increasing beam sizes (heavy ions) as well as increasing beam energies, the multiplicity of particles is expected to be so large that detection of individual particles may tax the technology beyond limits. Calorimetric measurements may then provide the only avenue to pursue.

It is therefore important to understand the relation between TED and MD. The probability $P(E_T)$ of finding a certain transverse energy E_T can, in principle, be related to $P(n)$ in the obvious manner[1]:

$$P(E_T) = \sum_n \omega(E_T/n)\ P(n) \quad \ldots \qquad (1)$$

where $\omega(E_T/n)$ is the conditional probability of obtaining a transverse energy E_T in a certain event with a given multiplicity n. Equivalently, one can invert this relation to obtain $P(n)$ from a knowledge of $P(E_T)$:

$$P(n) = \sum_{E_T} \tilde{\omega}(n/E_T)\ P(E_T) \quad \ldots \qquad (2)$$

On the other hand, these quantities may be calculated within presently available phenomenological models of multiparticle production. Furthermore, at currently accessible energies, where both TED and MD are measurable, these conditional probabilities are also measurable. We therefore suggest a new strategy in the investigation of the relationship between TED and MD which might ultimately lead to a method for determining MD from the measurement of TED. The idea is to compare at present energies the experimental $\tilde{\omega}(n/E_T)$ with that calculated from theoretical models and then to tune these models so that they can be expected to work satisfactorily at higher energies where measurements of MD (and $\tilde{\omega}(n/E_T)$) would not be possible.

In this work, we report some progress along these lines based on*) Model[2,3]. We have developed a Monte Carlo (MC) event generator program incorporating the basic premises of the IGM. Details of the MC event generator have been given elsewhere[4]. For our present purpose, the principle is firstly to identify events with a certain E_T. For each such event, the number of sources is also given by the routine[5].

These sources (mini-fireballs) are then allowed to decay (hadronize) under the constraint that the associated multiplicity would correspond to maximum information entropy. The resultant distribution is naturally a function of E_T and by definition, this is the desired conditional probability $\tilde{\omega}(n/E_T)$.

The $\tilde{\omega}(n/E_T)$ thus calculated is then convoluted with the experimental $P(E_T)$ to yield $P(n)$. For $P(E_T)$, we take the data of UA1-collaboration[6] for $|\eta|<6$ at 200, 546 and 900 GeV $p\bar{p}$ collisions. In Fig. 1 we show the KNO curves for the $P(n)$ thus obtained at these energies from our calculations. It can be readily seen that they are in good agreement with the KNO curve of UA1 for $|\eta|<2.5$. Application to hA and AA cases is in progress.

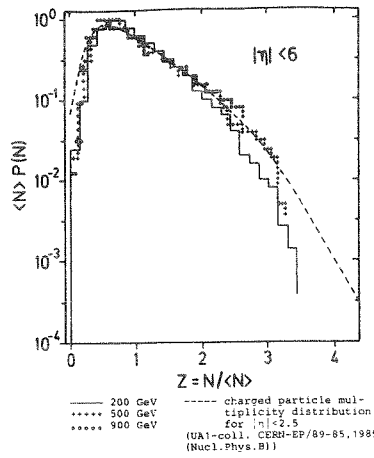


Fig. 1

References

1) M. Plümer and R.M. Weiner, Phys.Rev. D37, 3136 (1988).
2) G.N. Fowler, R.M. Weiner, G. Wilk, Phys. Rev.Lett. 55, 173 (1985).
3) G.N. Fowler et al., Phys.Rev. D35, 870 (1987).
4) G. Wilk, in: Multiparticle Production (eds. R. Hwa, G. Pancheri and Y. Srivastava, p. 455, World Scientific Publ., Singapore, 1989).
5) G. Wilk, Z. Wlodarczyk, R.M. Weiner, to be published.
6) UA1-collaboration, CERN-EP/89-85 (1989), to appear in Nucl.Phys. B.

*) the Interacting Gluon

Information Entropy and the Multiparticle Production Processes[G,B]

G. Wilk[1,2] and Z. Wlodarczyk[1,3]

1) Physics Department, University of Marburg, Marburg, F.R.G.
2) Soltan Institute for Nuclear Studies, Warsaw, Poland
3) Institute of Physics, Pedagogical University, Kielce, Poland

The multiparticle production processes dominate collision experiments where "soft" particles are produced. Usually only single-particle inclusive distributions $Ed^3\sigma/d^3p$ and multiplicity distributions $P(n)$ are extracted from data.

There exists so far no satisfactory theory which would allow to calculate these observables directly from first principles. Instead a number of models was developed which can fit data reasonably well starting from quite different dynamical inputs. Such a situation resulted in an idea of resorting to the information entropy as a guiding principle[1] in constructing the least biased distributions based on the limited experimental information available. It was already shown[2] that fixing only $\langle p_T\rangle$ and the inelasticity K of the reaction as constraints exhausts the dynamical information contained in the data (of this period). Similarly, taking as a constraint only the mean multiplicity $\langle n\rangle$ results in the $P(n)$ of geometrical type, whereas allowing additionally for k independent sources of emission changes it to distribution of the Negative Binomial type[3].

Here we present the least biased single particle inclusive distribution from a fireball of mass M, which decays unisotropically (i.e. with limited $\mu_T=\sqrt{y^2+p_T^2}$) into a fix number n of secondaries of mass μ each. We are then looking for a distribution

$$f_n(y,p_T)=\frac{Ed^3\sigma_n}{\sigma_n d^3p}=\frac{d^3\sigma_n}{\sigma_n dy d^2p_T} \quad \text{such that}^4:$$

$$\int \frac{d^3p}{E}\cdot f_n\cdot(y,\mu_T)=n \quad \text{(normalization)} \tag{1}$$

$$\int\frac{d^3p}{E}\cdot\mu_T\cosh y\cdot f_n(y,\mu_T)=M \quad \text{(energy conservation)} \tag{2}$$

$$\int\frac{d^3p}{E}\,\mu_T\, f_n\,(y,\mu_T)=\langle\mu_T\rangle \quad \text{(cut-off in } p_T) \tag{3}$$

Minimizing the information entropy

$$S_I=-\int\frac{d^3p}{E}\, f_n(y,\mu_T)\ln\left|f_n(y,\mu_T)\cdot\mu^2\right| \tag{4}$$

subject to constraints (1)-(3) we get

$$f_n(y,\mu_T)=\frac{1}{Z}\exp\left|-\alpha\mu_T-\beta\mu_T\cosh y\right|. \tag{5}$$

Although the formula (5) coincides with the one used in thermodynamical models[5] it has some distinct features:

(i) The parameters α and β ("temperatures" in (5)) are not free but fixed (together with normalizeation Z) by the values of M, n and $\langle\mu_T\rangle$ (if the agreement with data is poor it only means that there is more information left, which should be explored to find a better f).

(ii) Approximately: $\alpha\cong\frac{2}{\langle\mu_T\rangle}$ and (for large n) $\beta\cong\frac{2n}{M}$.

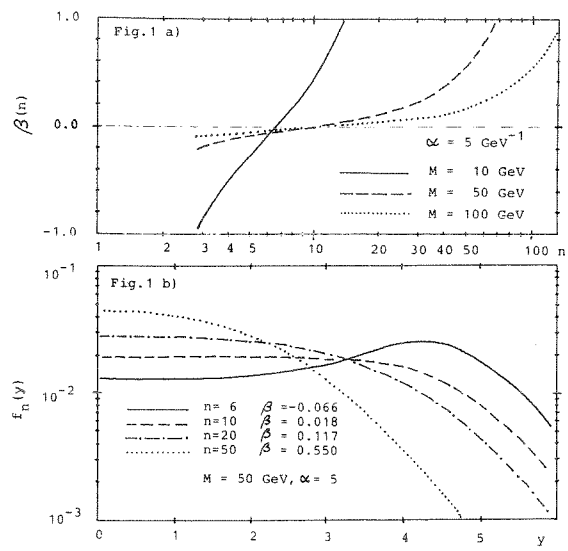
(iii) Unlike in thermodynamical models now $\beta\in(-\infty,+\infty)$:

$\beta\to-\infty$ if $n\to2$ $(\to f\to\delta(y\mp y_{max}))$;

$\beta=0$ if $n=n_0\cong2\ln\left|\frac{M-(n-2)}{2\mu}\right|$;

$\beta\to\infty$ if $n\to\frac{M}{2\mu}$ $(\to f\to\delta(y))$.

(iv) There does not exist factorization between rapidity y and p_T (except for $n=n_0$; here one has a strict plateau in y).



In Fig. 1 we present examples of $\beta=\beta(n)$ for different M and $f_n(y)$ for different n (for $\alpha=5$ GeV/c).

References

1) E.T. Jacques, Phys.Rev. 106, 620 and 108, 171(1957); cf. also A. Katz, "Principles of Statistical Mechanics" (W.H. Freeman and Co., San Francisco, 1967).

2) Y.-A. Chao, Nucl.Phys. B40, 475 (1972).

3) B. Carazzo and A. Gandolfi, Lett.Nuovo Cim. 15, 553 (1976).

4) Simplified one-dimensional analysis (i.e. with p_T fixed) was presented by: F. Tahagi and T. Tsakamoto, Phys.Rev. D38, 2288 (1988).

5) Cf. for example: E.L. Feinberg, Sov.Phys. Usp. 26, 1 (1983).

Number of Sources in Multiparticle Production[G,B]

R.M. Weiner[1], G. Wilk[2], Z. Wlodarczyk[3]

1) Department of Physics, University of Marburg, Marburg, FRG
2) Soltan Institute for Nuclear Studies, Warsaw, Poland
3) Institute of Physics, Pedagogical University, Kielce, Poland

The number of sources k which contribute to multiparticle processes (MPP) is an important ingredient in almost all phenomenological descriptions. As is well known the number k influences strongly the multiplicity distributions P(n) and its energy dependence has been the subject of recent studies in connection with the observed dependence of P(n) on the c.m. energy $\sqrt{s}$.[1)]

In the present note we discuss a method for the determination of $\langle k\rangle$, namely one based on the inelasticity distribution $\chi(K)$ which determines the source number distribution f(k). In our model for $\chi(K)$, the "Interacting Gluon Model" (IGM) (cf. refs. 2,3 for details), two highly energetic hadrons interact mainly through their gluon components. The interacting glue produces then in a given event a number k of sources (mini-fireballs, MF). On the average we have

$$\sigma^{in}_{hN}(s)\langle k\rangle = \int_0^1 dx \int_0^1 dy\,\theta(K^2_{min}-xy)\,\sigma_{gg}(s,y)\,G_h(x)\,G_N(y) \qquad (1)$$

where $\sigma^{in}_{hN}(s)$ is the hadronic inelastic cross section for c.m. energy of reaction $\sqrt{s}$; $K_{min}=\frac{2\mu}{\sqrt{s}}$ is the minimal inelasticity corresponding to the lightest MF produced, G(x) is the gluonic structure function and $\sigma_{gg}(x,y)$ is the gluon-gluon cross section. This last quantity is parametrized as follows:

$$\sigma_{gg}(x,y) = \begin{cases} \sigma^{in}_{hN} \text{ for } K^2_{min}<xy=\frac{M^2}{s}<K^2_0=\frac{M^2_0}{s} \\ \sigma^{in}_{hN}\left(\frac{M^2_0}{s}+\delta\ln\frac{M^2}{M^2_0}\right) \text{ for } K^2_0<xy=\frac{M^2}{s}<1 \end{cases} \qquad (2)$$

There are 3 parameters in the model: μ which defines the phase space, M_0 which gives the scale at which $\sigma_{gg}=\sigma^{in}_{hN}$ decreases and δ which fixes the asymptotic growth of σ_{gg} with $M^2=xys$. Different terms in σ_{gg} determine different energy dependences of $\langle k\rangle$:

$$\begin{aligned} \sigma_{gg}\cong\ln\frac{M^2}{M^2_0} &\to \langle k\rangle \sim \frac{\ln^3 s}{\sigma^{in}_{hN}(s)} \\ \sigma_{gg}\cong\text{const.} &\to \langle k\rangle \sim \frac{\ln^2 s}{\sigma^{in}_{hN}(s)} \\ \sigma_{gg}\,\frac{1}{M^2} &\to \langle k\rangle \sim \frac{\ln s}{\sigma^{in}_{hN}(s)} \end{aligned} \qquad (3)$$

In Fig. 1 we plot the mean inelasticity $\langle K\rangle$ versus the mean number of MF's $\langle k\rangle$ for different energies. Fig. 2 illustrates four particular scenarios for the s-dependence of $\langle K\rangle$:

I. $\langle K\rangle$ decreases continously.[4)] In this case $\langle k\rangle$ at first increases and then levels off at a value $\langle k\rangle = 7\div 8$ (this value coincides with that found in ref. 1 on completely different grounds).
II. $\langle K\rangle$ is constant = 0.5.
III. $\langle K\rangle$ is constant = 0.3. In these both cases $\langle k\rangle$ increases continously.
IV. $\langle K\rangle$ first decreases between $\sqrt{s}=20$ and $\sqrt{s}=500$ GeV from $\sim$0.5 to $\sim$0.3 and then remains constant. In this case $\langle k\rangle$ changes its slope at $\sqrt{s}$ 200-600 GeV but continues to grow indefinitely.

A corollary of these results is that if the saturation of $\langle k\rangle$ at the value $7\div 8$ derived in ref. 1 is to be taken seriously, the decrease of the inelasticity with energy is a necessary consequence.

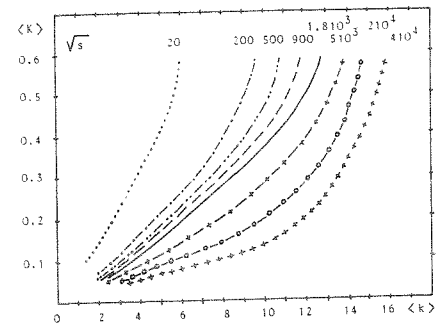


Fig. 1

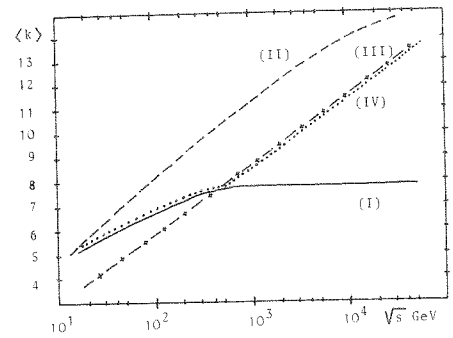


Fig. 2

References

[1] G. Ekspong, Proc. 18th Int. Symp. on Multipart. Dynamics, Kiryat Anavim, 1985, ed. J. Grunhaus Edition Front., Gif-sur-Avette, 1985, p.309; A. Giovannini and L. van Hove, Z. Phys. C30, 391 (1986) and Acta Phys. Polon. B19, 917 and 931 (1988).

[2] G.N. Fowler, R.M. Weiner, G. Wilk, Phys. Rev. Lett. 55, 173 (1985); G.N. Fowler et al., Phys. Rev. D35, 870 (1987); G.N. Fowler et al., Phys. Rev. C40, 1219 (1989).

[3] G. Wilk, in: Proc. Perugia Workshop on Multiparticle Production, Perugia, 1988, eds. R. Hwa et al., World Scientific 1989, p. 455; G. Wilk and Z. Wlodarczyk, V. JSVHECRI, Lódź, Poland, 1988, Univ. Lódź Pub., 1988, p. 171.

[4] J. Wdowrczyk, A.W. Wolfendale, Nature 306, 347 (1983), Nuovo Cim. 45A, 433 (1979), J. Phys. G10, 257 (1983); E. Friedlander, R.M. Weiner, Phys. Rev. D28, 2903 (1983); UA5-collab., G.J. Alner et al., Z. Phys. C33, 1 (1986); Y.T. Chou and C.N. Yang, Phys. Rev. D32, 1692 (1985); K. Watanabe, S. Tone, Phys. Rev. D39, 195 (1989).

Self-Similar Structures in Multiparticle Production and KNO Violation[G]

S. Raha[1], R.M. Weiner[1] and G. Wilk[2]

1) Dept. of Physics, University of Marburg, Marburg, F.R.G.
2) Soltan Institute for Nuclear Studies, Warsaw, Poland

There has been a recent surge of interest in possible self-similar structures in multiparticle production processes[1]. The so-called phenomenon of "intermittency" is an apt example[2]. It has, however, been argued in the literature[3] that the power-like growth of the normalized factorial moments as the rapidity interval δy goes to zero need to require a self-similar structure and may be explained by conventional quantum statistics. Indeed, Dias de Deus[4] has observed that in the case of intermittency, a self-similar structure, if any, can only arise as $s \to \infty$ and thus evidence for fractal structure at constant and finite s is meaningless. On the other hand, Sarcevic and Satz[5] argue that fractal structure would emerge as $s \to \infty$ provided all measured rapidity intervals δy are bigger than the rapidity correlation Δy_{res} imposed by the resonances. The self-similarity will manifest itself through the following behaviour of the moments:

$$C_\ell \underset{Y\to\infty}{\sim} \left(\frac{Y}{\delta y}\right)^{(\ell-1)\lambda_\ell} \quad , \lambda_\ell > 0 \ \ldots \qquad (1)$$

To obtain a fractal structure, Sarcevic and Satz assumed that Δy_{res} is independent of s. This implies that the resonance masses excited in high energy collisions do not increase with s, in opposition e.g. to the Hagedorn statistical bootstrap model which predicts an exponential mass spectrum.

Even if Δy_{res} is independent of s, there are other correlation lengths involved in multiparticle production processes which increase with s. A specific example is the field correlation length ξ which arises naturally in the Quantum Statistical framework[3,6] as well as in most phenomenological approaches to soft strong interactions:

$$\langle \pi^+_{chaotic}(y)\ \pi_{chaotic}(y') \rangle \sim \exp(-|y-y'|/\xi) \qquad (2)$$

If the multiplicity distribution in rapidity is stationary, a realistic assumption in view of the observed plateau structure, then this leads to a scaling model where all the factorial moments can be written in form:

$$\mu_1 = \bar{n}^q \left| (q-1)!\ p^q B_q + q!\, p^{q-1}(1-p)\bar{B}_q \right| \qquad (3)$$

where $\beta = \delta y/\xi$. B_q and $\bar{B}_q$ are analytical functions of [6], p is the relative amount of chaoticity in the field . KNO broadening (violation) implies that p and ξ both increase with s, the increase in ξ with s being faster than ln s[7]. In fact, if one insists on a fully chaotic field configuration ($p \sim 1$), ξ should increase even faster.

The feature of increasing correlation length is not particular to the QS model. The clan model of Giovannini and Van Hove[8] has a similar property. From ISR to SPS, the average size of the clan (rapidity span as well as average multiplicity of a clan) increases quite substantially; the pseudorapidity extent of a clan is 1.5 at ISR and 3.5 at SPS. Given the fact that to establish a fractal structure in a process, the domain of analysis must be free of all other scales, the increasing correlation length with energy should inhibit the onset of a self-similar behaviour in high energy collisions.

Thus, if the broadening of the KNO curve continues at the present rate, then to establish the self-similar behaviour in the sense of Sarcevic and Satz, one would have to look at rapidity regions which become progressively narrower with energy because Y goes like ln s whereas ξ increases faster.

We therefore conclude that a self-similar cascading at high energy processes would imply a slow-down and perhaps a complete stopping of the KNO violation. That such a possibility exists has already been argued in the literature on the basis of independent arguments[9].

References

[1] I. Dremin, Sov.Phys.Usp. 30, 649 (1987); P.Carruthers in: Multiparticle Production (eds. R.Hwa, G. Pancheri and Y. Srivastava), World Scientific Publishing, Singapore, 1989.
[2] A. Bialas and R. Peschanski, Nucl.Phys. B273, 703 (1986); B308, 803 (1988).
[3] P. Carruthers et al., Phys.Lett. 222B, 487 (1989).
[4] J. Dias de Deus, in: Festschrift Leon Van Hove (ed. W. Kittel), World Scientific Publishing, Singapore (in press).
[5] I. Sarcevic and H. Satz, Phys.Lett. 233B, 251 (1989).
[6] G.N. Fowler and R.M. Weiner, Phys.Rev. D17, 3118 (1978); G.N. Fowler et al., Phys.Rev. D37, 3127 (1988).
[7] G.N. Fowler et al., Energy dependence of multiplicity distributions in the quantum statistical approach, Univ. of Marburg preprint 1989.
[8] A. Giovannini and L. van Hove, Z.Phys. C30, 391 (1986).
[9] G.N. Fowler, E.M. Friedlander, R.M. Weiner and G. Wilk, Phys.Rev.Lett. 56, 14 (1985); I. Sarcevic, Phys.Rev. Lett. 59, 403 (1987).

Diquarks in nuclear medium in the few mode QCD[G]

L. Polley, M.H. Wendel
FB Physik, Universität Oldenburg, FRG

1.3.3

The chromomagnetic interaction of quarks (CMI) plays an important role for a variety of resonance and transition phenomena in a rather broad energy range. This covers the nuclear Δ-resonance, the formation of multiquark states (where the famous H-dibaryon is the prominent candidate) up to the possible formation of a diquark condensate[1] as an intermediate state of hadronic matter in the phase transition region. On the other hand it relies on the basic notion of pair interaction of quarks via colour and spin which emerges naturally in a Fock-space evaluation of the quantum field theoretic spectrum of QCD. In the literature up to now only a semiclassical picture –based on phenomenology– is given for CMI. This phenomenological CMI is given by the product of two colour-magnetic moments of two quarks (i,j) multiplied by a negative (coupling-) constant, that is

$$- V_{ij} (\lambda^a \sigma^k)^{(i)} (\lambda^a \sigma^k)^{(j)} \qquad (1)$$

In our model we started with a Hamiltonian formulation of QCD in temporal gauge and elliminated the remaining gauge degrees of freedom by chossing in addition the axial gauge. We restricted ourselves to a discussion of dynamics taking place only in colour and spin degrees of freedom, i.e. using a finite mode representation of the quark and gluon field operators. Interaction of quarks then is essentially carried by a Bogoliubov-type transformation involving the relevant gauge field modes as dynamic quantities. As a result of these studies we could reproduce the colour systematics whereas for the correct representation of colour-spin levels (as compared to phenomenological findings) the inclusion of the Gauss-law was found to be of crucial importance.

We thus reexamined our model using the charge representation introduced by Pottinger and Warner[2]. In this representation the field operators are decomposed with respect to squares of the total colour charge, the fermion and gluon colour charge respectively. Pottinger and Warner found above some critical coupling constant that a colour octet quark-antiquark pair coupled to a colour octet carried by a single gluon became energetically favoured with respect to a quark-antiquark-singlet.

In our model an expression for the effective quark interaction in nuclear medium then is given by all contributions to the few-mode Hamiltonian containing at least two quark creation and annihilation operators projected on a colour-neutral subspace of configurations. There are two types of contributions to this effective part: the transformed chromoelectric field (due to the transformation depending on the quark fields) and the transformed Dirac (quark) field (which enters the energy via the Gauss-law). These two parts read

$$U_B^\dagger(g') E^a U_B(g') = E^a + i\rho_S \left(\theta\ ,\ \partial_{\bar\theta}\right) \mathcal{E} \begin{pmatrix} \partial_\theta \\ \bar\theta \end{pmatrix} \qquad (2)$$

with the matrix $\mathcal{E}$ given by

$$\mathcal{E} = \int_0^{g'} \mathrm{d}g' \begin{pmatrix} C\lambda^a S - S\lambda^a C & C\lambda^a C + S\lambda^a S \\ -C\lambda^a C - S\lambda^a S & C\lambda^a S - S\lambda^a C \end{pmatrix}$$

and

$$U_B^\dagger(g')\Psi^\dagger(\vec r)\lambda^a \Psi(\vec r) U_B(g')$$

$$= (j_0^2 + j_1^2)\left(\theta\ ,\ \partial_{\bar\theta}\right) C_1 \begin{pmatrix} \partial_\theta \\ \bar\theta \end{pmatrix} \qquad (3)$$

$$+ \ i(j_0^2 - j_1^2)\left(\theta\ ,\ \partial_{\bar\theta}\right) C_2 \begin{pmatrix} \partial_\theta \\ \bar\theta \end{pmatrix} \qquad (4)$$

$$+ \ 2j_0 j_1 \left(\theta\ ,\ \partial_{\bar\theta}\right) C_3\, \hat r \cdot \vec\sigma \gamma_5 \begin{pmatrix} \partial_\theta \\ \bar\theta \end{pmatrix} \qquad (5)$$

with the following abbreviations

$$C_1 := \begin{pmatrix} C\lambda^a C + S\lambda^a S & S\lambda^a C - C\lambda^a S \\ C\lambda^a S - S\lambda^a C & C\lambda^a C + S\lambda^a S \end{pmatrix}$$

$$C_2 := \begin{pmatrix} C\lambda^a S - S\lambda^a C & C\lambda^a C + S\lambda^a S \\ -C\lambda^a C - S\lambda^a S & C\lambda^a S - S\lambda^a C \end{pmatrix}$$

$$C_3 = \begin{pmatrix} S\lambda^a C + C\lambda^a S & C\lambda^a C - S\lambda^a S \\ C\lambda^a C - S\lambda^a S & C\lambda^a S + S\lambda^a C \end{pmatrix}$$

(where ρ_s denotes the overlap factor between the gluon mode and the quark modes which are given by spherical bessel function; θ (∂_θ) and $\bar\theta$ ($\partial_{\bar\theta}$) denote quark and antiquark creation (annihilation) operators[3]; S and C are essentially sin and cos functions of the gauge field times ρ_s).

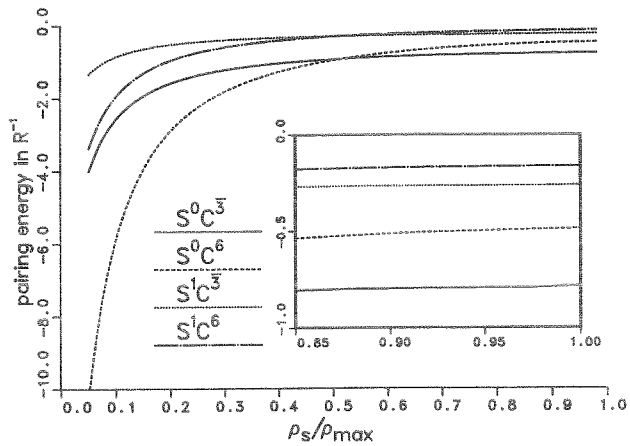
All contributions to effective quark interaction in our model are given then by normal ordered (which includes the influence of the sea quarks) squares of all transformed quantities given above[4].

From the above construction one can easily deduce that the only term surviving in a colour neutral medium (where the total colour charge density vanishes) is given by the square of the upper left element in C_3

$$(S\lambda^a C + C\lambda^a S)_{cc'} (S\lambda^a C + C\lambda^a S)_{dd'} \vec\sigma_{mm'} \cdot \vec\sigma_{nn'} \delta_{p,-p'} \delta_{q,-q'} \times \theta_{cmp}\theta_{dnq}\partial_{\theta_{d'n'q'}}\partial_{\theta_{c'm'p'}}$$

(where the quark operators carry colour, j_z and parity (or –since we are dealing with massless quarks– helicity) indices).

The energy of two quarks in our model is calculated according to a classification scheme respecting different quantum number configurations (colour, spin and helicity (the latter permits asymmetric, symmetric and configurations with equal helicity)). A renormalization procedure for the coupling constant is introduced such that the n-Δ splitting is reproduced. We find a support for the phenomenological chromomagnetic interaction hypothesis which means that we are able to reproduce the *ad hoc* ansatz for the colour-spin interaction of quarks within 7% accuracy (see fig.1)



[1] J.F.Donoghue and K.S.Sateesh, Phys.Rev. **D38**, 360 (1988).
[2] D.Pottinger and R.C.Warner, Phys.Lett. **114B**, 349 (1982); Nucl.Phys. **B216**, 336 (1983). Phys.Lett. **B67**, 175 (1977).
[3] F.A. Berezin, The Method of Second Quantization, Academic Press: New York 1966.
[4] M.H.Wendel, Quark Interaction in One-Mode QCD, PhD thesis, University of Oldenburg, Oldenburg 1989 (in German).

Massive Gluon Matter[B,G]

T.S. Biró and U. Kalmbach
Institut für Theoretische Physik, Universität Gießen

We compare hadronic matter, ideal quark gluon plasma and non–perturbative, massive quark gluon matter through Gibb's criteria.

There is an outstanding research activity on quark gluon matter formation in relativistic heavy ion collisions. The basic argument for the quark gluon plasma formation relies on the thermodynamical comparison of nuclear matter with a massless quark gluon ideal gas supported by a bag constant through which non–perturbative vacuum effects should be taken into account [1] [2].

In order to use a model which can offer an insight into non–perturbative QCD phenomena without the extended work of a lattice Monte Carlo simulation one should choose the key quantity to look for. In the following we argue that besides the bag constant a non–perturbative gluon mass should be taken into account.

Comparing the normalized pressure, p/p_{SB}, ($p_{SB} = 8\pi^2T^4/45$) as a function of the temperature [3] with the same quantity for massive gluons one realizes an impressive drop of the gluon mass around the deconfinement temperature (cf. Fig1).
Unfortunately the error bars were not published in [3] , but they are certainly huge for $T/\Lambda_L \leq 40$.

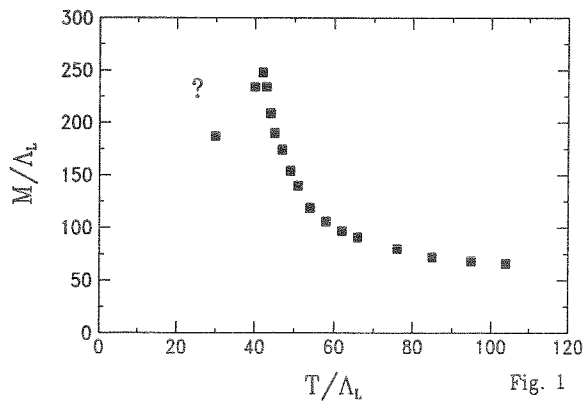


Fig. 1

A non–perturbative model including massive gluonic modes without explicit color confinement should answer the following two questions:

i) How to generate a gluon mass in QCD?
ii) How large it is?

In a variational approach to QCD an effective Lagrangian with background parameter fields Φ_a and quasi gluon fields was obtained [4]. The variational minimum of the effective theory appears at a non–zero value of the gluon condensate and generates

i) quasi gluon mass: $M^2 \approx g^2(\Phi^a\Phi_a)$
ii) varying bag constant: $B(M) = M^4 \cdot f(M/M_0)$
iii) a suppression of thermal excitations: $p_m = T^4 \cdot f(M/T)$

Accepting anyhow that gluonic modes are massive the thermodynamical analysis can easily be done in the independent particle (1–loop) approximation. We get

$$p = -\frac{T\ell nZ}{V} \approx -T \cdot tr\ [\ell n(1-e^{-E_k/T})] \qquad (1)$$

The variation

$$\frac{\delta}{\delta M}\left\{ -p(M,T) + p(0,T) \right\} = 0 \qquad (2)$$

after the renormalization of the vacuum fluctuation contribution $B(M)$ leads to the following constraint equation

$$\frac{1}{\pi^2}\left\{ M^2\ell n(M^2/M_0^2) + 8\cdot\sum_{n=1}^{\infty}\frac{MT}{n^2}K_1(nM/T) \right\} = 0 \qquad (3)$$

The solution of this constraint equation is a temperature dependent, self–consistent gluon mass. Fitting the bag constant $B_0 = B(M_0)$ (160–240)^4 MeV^4 one obtains values of M_0 = (650–950) MeV.

We compare a pure gluon sector with a pion gas. The three respective pressures are

$3\cdot p(m_{\rm pion},T)$ for the pion gas,
$16\cdot p(M(T),T) + B(M) - B(M_0)$ for the massive gluonic vacuum and $p_3 = 16\cdot p(0,T) - B(M_0)$ for the traditional gluon plasma.

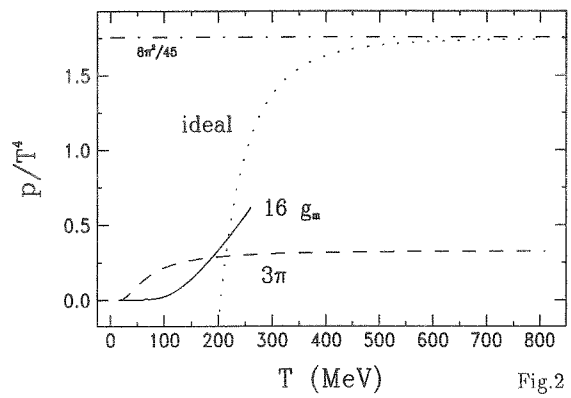


Fig.2

Inspecting Fig.2 one concludes that with a bag constant of (235 MeV)^4 a possible non–hadronic and non–ideal gluon phase arises in the temperature interval about 180–220 MeV.

In conclusion we would like to draw the attention to the possibility of a deconfined phase containing non–perturbative quark and gluon quasi particles. The consequences for quark–gluon plasma signatures in heavy–ion collisions, such as lepton or strangeness production in this phase will be the subject of future work.

1) J.Kuti, B.Lukacs, J.Polonyi, K.Szlachanyi, Phys.Lett. B43 (1979) 1292
2) T.S.Biro, J.Zimanyi, Proc. of the 6th Int. Balaton Topical Meeting on High Energy Nuclear Physics, Lake Balaton, Hungary, June 5–11, 1983, Ed. J.Ero.
3) J.Engels, J.Fingberg, K.Redlich, H.Satz, M.Weber, BI–TP/88–23
4) T.S.Biro, Ann.Phys. (N.Y.) 191 (1989) 1

Magnetic neutrino scattering by crystal lattices [B]

J. Augustin, B. Müller and W. Greiner
Institut für Theoretische Physik der Universität Frankfurt

The question about neutrino magnetic moments is still open. On the one hand the available direct measurements give an upper limit of about $\mu_\nu \leq 10^{-10}\mu_0$, μ_0 being the electron Bohr magneton [1]. Magnetic moments of this magnitude could provide an explanation of the solar neutrino problem [2]. Other authors give stronger limits of about $\mu_\nu \leq 1 - 10 \times 10^{-13}\mu_0$ (cf. [3] and references in [1]) due to astrophysical considerations, but their analysis depends on several assumptions. On the other hand an extension of the standart electroweak model to massive neutrinos yields $\mu_\nu = 3.2 \times 10^{-19}(m_\nu/1eV)\mu_0$. It would therefore be very helpful to find possibilities for more accurate measurements of μ_ν.

Such a process could be coherent scattering of highly energetic neutrinos on crystals. It is well known that channeling of ultrarelativistic particles in crystals provides very strong electromagnetic fields in the rest frame of the particle due to Lorentz contraction of the crystal fields [4]. Assuming a neutrino mass of the order $m_\nu = 1eV$ and neutrino energies in the TeV region, i.e. SSC-energies, one obtains huge Lorentz factors. Therefore large cross sections for neutrino-crystal interactions are conceivable despite the small coupling constant μ_ν.

This idea in mind we investigate the electromagnetic scattering of a massive neutrino by a cubic array of atoms employing the Dirac equation

$$\left(i\gamma^\mu\partial_\mu - m_\nu + \frac{\mu_\nu}{2}\sigma^{\mu\nu}F_{\mu\nu}\right)\psi = 0 \ . \qquad (1)$$

Describing the atomic fields by Thomas-Fermi type potentials (cf. [5] for details), the T-matrix T_{if} for a neutrino-atom collision can be evaluated analytically in first order Born approximation. For the parameters Z=32 (Germanium), $\mu_\nu = 10^{-11}\mu_0$ and a neutrino energy of 10 TeV this yields a total elastic cross section of the order 10^{-19} barns. An electron-neutrino cross section at the same energy caused by weak interactions has a value of 10^{-17} barns [6]. If all atoms in the lattice are described by identical potentials, the T-matrix for scattering by the whole crystal takes the form

$$\left|T_{if}^{tot}\right|^2 = |T_{if}|^2 \cdot \left|\sum_\ell e^{i\vec{q}\cdot\vec{R}_\ell}\right|^2 \ . \qquad (2)$$

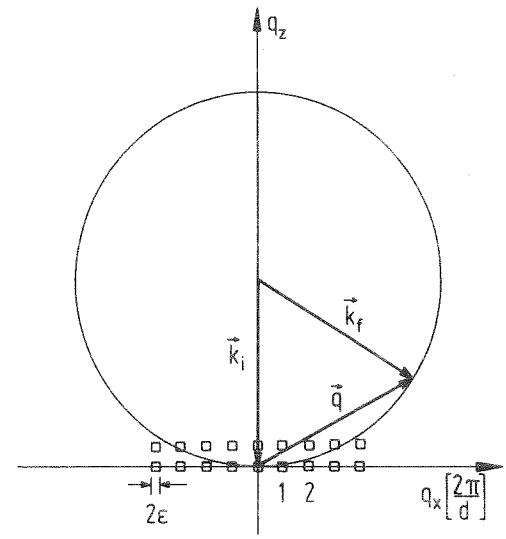
$\vec{q}$ denotes the momentum transfer of the collision and the $\vec{R}_\ell$ are the position vectors of the lattice atoms. The sum in eq. (2) does not reduce to δ-functions, because we consider a finite lattice. In order to derive a total cross section from (2), a manageable approximation of that sum is required. One can write [5]

$$\left|\sum_\ell e^{i\vec{q}\cdot\vec{R}_\ell}\right|^2 = \begin{cases} \frac{1}{8}N^2 & \text{if } \vec{\tau} - \vec{\epsilon} < \vec{q} < \vec{\tau} + \vec{\epsilon} \\ 0 & \text{otherwise} \end{cases} \ , \qquad (3)$$

N being the total number of atoms in the array, d the lattice constant and $\vec{\epsilon} = (\epsilon, \epsilon, \epsilon)$ with $\epsilon = 2\pi/N^{1/3}d$. $\vec{\tau}$ denote the reciprocal lattice vectors. With eq. (3) the necessary solid angle integration over the directions $\vec{k}_f$ reduces to a counting problem. One has to count how many reciprocal lattice points are hit by the sphere defined by k_i and k_f (cf. figure). The contribution of each point to the cross section is given by $|T_{if}(q)|^2$. Using the numbers $d = 1\mathring{A}$ and $N^{1/3} = 10^7$ one gets for the total elastic cross section (Z, μ_ν and the neutrino energy are the same as above)

$$\frac{\sigma_{tot}}{N} \approx N^{\frac{1}{3}} \times 1.8 \times 10^{-20}b = 1.8 \times 10^{-13}b \ . \qquad (4)$$

Obviously an amplification of the neutrino-atom cross section due to coherence occurs, but the absolute values are still quite small. Therefore a direct observation of the helicity changing elastic collision would be very difficult even under ideal experimental conditions.



Solid angle integration in q-space

References

[1] P. Vogel and J. Engel, Phys. Rev. D **39**, 3378 (1989)

[2] M.B. Voloshin, M.I. Vysotskii and L.B. Okun, Sov. Phys. JETP **64**, 446 (1986)

[3] J.M. Lattimer and J. Cooperstein, Phys. Rev. Lett. **61**, 23 (1988)

[4] J.C. Kimball and N. Cue, Phys. Rep. **125**, 69 (1985)

[5] J. Augustin, B. Müller and W. Greiner, Phys. Rev. D, in press

[6] P. Becher, M. Böhm and H. Joos, Eichtheorien, Teubner, Stuttgart 1981

Comparing Grid Techniques for nuclear Hartree-Fock calculations [B]

V. BLUM, J.A. MARUHN, W. GREINER,
Institut für Theoretische Physik, Universität Frankfurt

G. LAURITSCH, P.-G. REINHARD,
Institut für Theoretische Physik, Universität Erlangen

Hartree-Fock and time-dependent Hartree-Fock calculations are a widely used microscopic access to nuclear and heavy-ion dynamics. The solution is particularly easy-to-handle and flexible if the single particle wave functions are represented on a coordinate-space grid. Most coordinate-space techniques use finite-difference schemes and the representation can be optimized by using "variation on the grid" [1]. These techniques have also been successfully applied in relativistic nuclear models [2]. However, a detailed analysis of potential energy surfaces computed in a relativistic mean field model showed that the accuracy-to-expense ratio of the finite difference scheme in coordinate space is not satisfying [3, 4]. The reason is the extremely strong variation of the effective mass in a relativistic model which requires a better representation of the kinetic energy on the grid. In the following we will report our considerations on the way to more precise and nonetheless efficient gridding techiques.

Three possibilities for an improved precision on the grid have been investigated. *First*, one can stay with finite difference schemes and use higher order formulas for the first and second derivative. However, this procedure becomes critically sensitive to round-off errors with rising order. Thus as a *second* option, we study a basis-spline (Bspline) representation which provides more robust derivative formulas with higher orders [5]. Bsplines still allow a representation in terms of coordinate space, but derivatives immediately become a full matrix multiplication on the grid. As a *third* alternative, we evaluate the derivatives on the grid by Fourier transformation. This is usually the optimal definition of a derivative on an equidistant grid. Note that the Fourier-definition of derivatives can be handled in two ways: either one can express the derivative by matrix multiplication in coordinate space, or one uses the fast Fourier transformation forth and back.

In order to have a realistic test of these three gridding techniques for all possible nuclear physics applications, we have investigated the Schrödinger equation with the following test Hamiltonian $\hat{H} = \hat{p}B(r)\hat{p} + V(r)$ and $B, V \propto (1 + A_0 \cos(kr))/(1 + e^{(r-R)/\sigma})$, where the box radius R, the surface thickness σ, the amplitude of shell fluctuations A_0, and the overall strength V_0 and B_0, are chosen to represent typical nuclei.

In fig. 1 we show the results of a spherical calculation within the above model. The Bspline representation as well as the Fourier techniques are clearly superior to the finite difference schemes if one aims at high precision. In particular the finite difference scheme with three point precision converges so slowly that an extremely small grid spacing, far below $\Delta r = 0.1$ fm, would be required to obtain a decent precision. But such fine spacings run into numerical problems with computing time, storage and round-off errors, particularly in higher dimensions. Bspline and Fourier techniques offer obviously promising alternatives. We have studied the effects of grid spacing also in axially symmetric two dimensional and three dimensional cartesian calculations. We find results which are quantitatively comparable to fig. 1. The precision depends only on the numerical representation and not on the dimensionality.

Considerations of precision alone, as displayed e.g. in fig. 1, cannot distinguish between these two approaches. Thus in the next step, we will compare the speed of both. In the Bspline scheme, the derivative operators are represented by a full matrix on the grid, to be more precise: on the grid in the direction of the derivative, either the x- or the y- or the z-direction in case of a three-dimensional calculation. The Fourier definition of the derivatives, on the other hand, allows the choice between a matrix multiplication in x-, y-, or z-direction or the explicit use of a momentum-space representation and the use of the fast Fourier transformation (FFT) forth and back. Thus we have to compare a representation of the wave function in coordinate space together with matrix multiplication for the momentum operators, on the one side, with a representation in momentum space and fast Fourier transformation to coordinate space where the local operators $V(r)$ and $B(r)$ are evaluated, on the other side. The computing times for one action of the above Hamiltonian in case of a fully three dimensional calculation are given in table 1. We find that the matrix multiplication technique is advantageous, whereby the advantage decreases with increasing grid sizes. The fast Fourier technique would take over for larger grids. The relative effects are comparable on both machines such that the conclusion may hold for every vector machine. The equilibrium is shifted towards the Fourier technique on a scalar machine. Anyway, for typical nuclear grid sizes we can conclude that the matrix technique is advantageous. It is unavoidable anyway if one works in noncartesian representation, as in spherical or axially symmetric grids. This conclusion, however, can change if further aspects come into play. For example, the momentum space representation becomes clearly advantageous if the mass is constant because then the kinetic energy can be evaluated completely in momentum space. A further argument in favour of the momentum space representation is that one can easily implement a cut-off in kinetic energy which is sometimes justified and which brings large savings in storage.

References

[1] P. Hoodbhoy, J.W. Negele, Nucl.Phys. **A288**, 23 (1977)

[2] S.J. Lee, J. Fink, A.B. Balantekin, M.R. Strayer, A.S. Umar, P.-G. Reinhard, J.A. Maruhn and W. Greiner, Phys. Rev. Lett.57, 2916 (1986), E: Phys. Rev. Lett.57, 1171 (1987)

[3] J. Fink, Ph.D. thesis, Universität Frankfurt, (1988)

[4] V. Blum, Diploma thesis, Universität Frankfurt, (1988)

[5] C. Bottcher, M.R. Strayer, Ann.Phys. **175**, 64 (1987)

	IBM 3090		CRAY X-MP	
$N_x \times N_y \times N_z$	FFT	Matrix	FFT	Matrix
$16 \times 16 \times 64$	13	4	3	1
$32 \times 32 \times 128$	78	46	24	12

Table 1:
Relative computing times for one action of the Hamiltonian above, evaluated for two typical nuclear grid sizes on two vector computers using the system routines for fast Fourier transformation or matrix multiplication in each case.

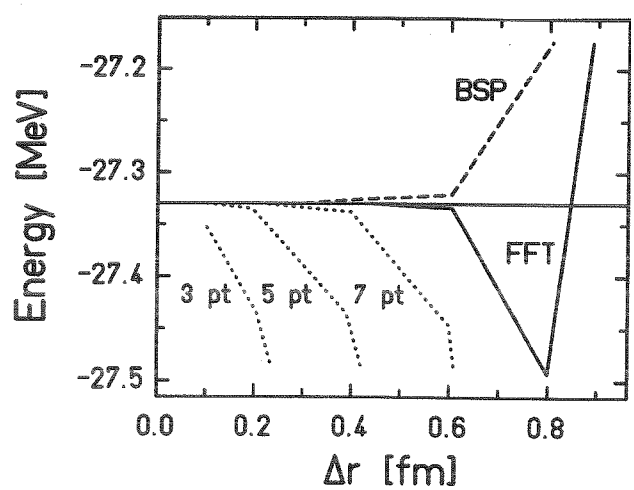


Figure 1:
The binding energy of the lowest 1s-state as function of the grid distance Δr for finite difference schemes at various orders as indicated, for Bsplines of 9. order, and for the Fourier definition of the derivatives.

New Algorithms To Solve The Hydrodynamic Equations[B]

U.Katscher, B.Waldhauser, V.Schneider, J.Maruhn, W.Greiner
Institut für theoretische Physik Frankfurt/Main

Since hydrodynamics are used for describing heavy ion collisions, problems arised how to solve the hydrodynamic equations of mass, momentum, and energy conservation

$$\frac{\partial \rho}{\partial t} + \frac{\partial \rho v}{\partial x} = 0 \quad (1)$$

$$\frac{\partial m}{\partial t} + \frac{\partial m v}{\partial x} = -\frac{\partial p}{\partial x} \quad (2)$$

$$\frac{\partial e}{\partial t} + \frac{\partial e v}{\partial x} = -\frac{\partial p v}{\partial x}, \quad (3)$$

which are strongly coupled especially in the relativistic case by the energy momentum tensor $T_{\mu\nu}$ and the four current:

$$e_{\mathrm{LAB}} = \gamma^2(e+p) - p \quad (4)$$

$$m^k = \gamma^2(e+p)\beta^k \quad (5)$$

$$\rho_{\mathrm{LAB}} = \gamma\rho \quad (6)$$

To close the system of equations, you have to implement the equation of state of nuclear matter, connecting pressure, mass and energy.

Parallel to three dimensional computations of Waldhauser [1], we tested extensively one dimensional problems and compared our results with analytical solutions. The algorithms we used are called SHASTA [2], LCPFCT [3], and RHLLE [4]. The first two of them are flux corrected differencing schemes, the latter one is a Godunov type algorithm in an extended version [4]. Both SHASTA and LCPFCT start by the three point formula

$$\rho_j^{n+1} = \tfrac{1}{2}Q_-^2 \cdot (\rho_{j-1}^n - \rho_j^n) + \tfrac{1}{2}Q_+^2 \cdot (\rho_{j+1}^n - \rho_j^n) + (Q_+ + Q_-) \cdot \rho_j^n + \delta t \cdot s_j^{n+\frac{1}{2}} \quad (7)$$

with $\rho = \rho(t = n\delta t, x = j\delta x)$, S: source term, and $Q_\pm = Q_\pm(v\frac{\delta t}{\delta x})$. To eliminate the implicit diffusion of eq. 7 Boris and Book added a fourth order antidiffusion. This antidiffusion is flux corrected, i.e. it is not possible that antidiffusion generates new extrema nor accentuates existing extrema. It is proportional to the gradient of mass density with a factor μ_i. In SHASTA μ_i are constant, while in LCPFCT they are velocity dependent.

On the other hand, RHLLE divides a density shape in a number of local Riemann problems, where the signal velocities are of main importance: they describe the radius of maximal influence of each Riemann problem.

$$v_+ = \frac{v + c_s}{1 + v c_s} \quad (8)$$

$$v_- = \frac{v - c_s}{1 - v c_s}, \quad (9)$$

c_s is the isentropic sound velocity. With these signal velocities the nonrelativistic HLLE [4] algorithm gets a explicit relativistic form, creating the "R" before "HLLE".

We use two testproblems. In the Riemann problem we initialize a step of 10 : 1 in pressure and 8 : 1 in mass density. For $t > 0$ this discontinuity causes a rarefaction wave behind and a shockwave before the contact discontinuity [5]. Our second testproblem is the shockmodel described by the Rankine - Hugoniot - Taub - adiabate: two colliding slabs produce a region of high compression [5]. Below there are two pictures comparing analytical and numerical solution of the testproblems. We see, that each of our algorithms work rather perfect. There are obviously no large differences between them. A detailled study shows that RHLLE is somewhat better than the flux corrected algorithms: in the case of the shockmodel, the error after 100 iterations ($\gamma = 10$, center of mass system) is 0.8 % (LCPFCT), 0.5 % (SHASTA), and 0.2 % (RHLLE). Additionally, our algorithms are so simple in structure, that they easily can be used for three dimensional computations. Other algorithms which are similar in accuracy have a much more complicated structure and therefore are not usable for two or three dimensional calculations.

[1] B. Waldhauser, Ph. D. thesis, 1990.
[2] J.P. Boris and D.L. Book, J. Comput. Phys. 11 (1973), 38.
[3] J.P. Boris and D.L. Book, "LCPFCT", preprint 1988.
[4] V. Schneider et al., UFTP preprint 1990;
for the nonrel. HLLE see references therein.
[5] L.D. Landau and E.M. Lifschitz, Theoretische Physik Bd.VI, Akademieverlag Berlin.

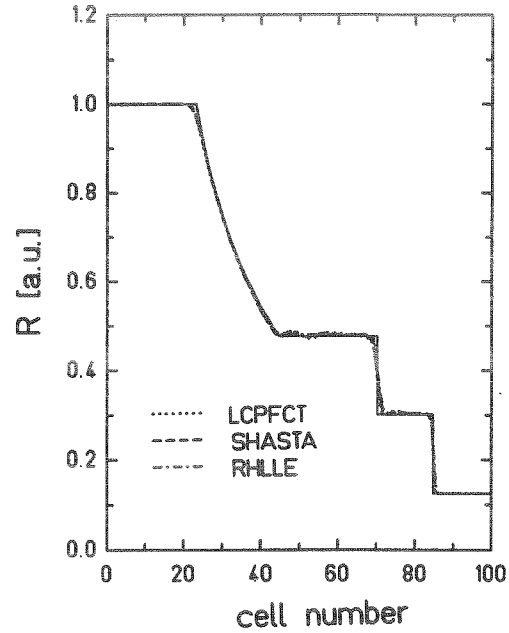


Figure a: The analytical solution (full line) of the Riemann problem compared with three numerical solutions after 100 iterations. The equation of state is that of an ideal relativistic gas: $p = (\Gamma - 1)(e - n)$, $\Gamma = 1.4$.

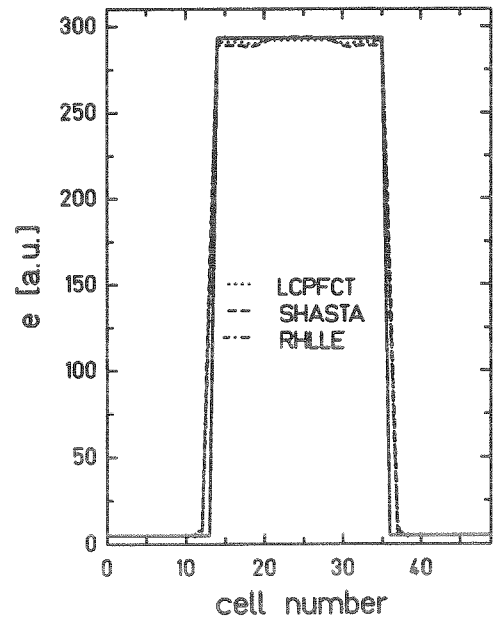


Figure b: The analytical solution (full line) of the shockmodel compared with three numerical solutions after 100 iterations. The equation of state is that of an ideal ultrarelativistic gas: $p = (\Gamma - 1)e$, $\Gamma = 4/3$.

ATOMIC PHYSICS

2. ATOMIC PHYSICS

PAGE

2.1 POSITRON PRODUCTION IN STRONG FIELDS, BHABHA SCATTERING AND ATOMIC REACTION MECHANISM 129

Energy and Angular Correlation of e^+e^- Emission in Heavy Ion Collisions 129
E. Berdermann, F. Bosch, T. Ishikawa, P. Kienle, I. Koenig, W. Koenig, C. Kozhuharov, A. Schröter, H. Tsertos

On the Behaviour of the Narrow Electron Positron Sum Energy Lines 130
H. Bokemeyer, H. Folger, K. Bethge, D. Kraft, K. Sakaguchi, K.E. Stiebing, T. Cowan, J.S. Greenberg, J. Schweppe, H. Backe, D. Schwalm, P. Salabura

Sensitive Search for Long-Lived e^+e^- Resonances Around 1.8 MeV/c^2 131
H. Tsertos, P. Kienle, S.M. Judge, B. Krusche, K. Schreckenbach

Limits for Two Photon- and e^+e^--Decay Widths of Bhabha Scattering Resonances from 1.78 to 1.92 MeV/c^2 132
F. Bosch, K. Maier, E. Widmann, J. Major, S. Connell, A. Seeger

Search for Resonances in Positron Annihilation in Flight 133
J. Kramp, J. Gerl, D. Habs, D. Schwalm, P. Thirolf

On the Decay $e^+e^- \rightarrow 4\gamma$ 134
Th. Schulze, G. Enders, J. Gerl, D. Habs, D. Schwalm,

Single and Double Electron Capture in $Ge^{31+} \rightarrow Ne$ Collisions 135
Th. Stöhlker, Ch. Kozhuharov, E.A. Livingston, P.H. Mokler, R.E. Olson, A. Szymanski, Z. Stachura, A. Warczak

Evidence for Resonant Two Electron Capture and Excitation in Collisions of H-like Ge with Ne 136
Th. Stöhlker, C. Kozhuharov, A.E. Livingston, P.H. Mokler, S. Reusch, A. Warczak, A. Szymanski, Z. Stachura

L-Shell Excitation in Heavy Ion-Atom Collisions as Function of the Impact Parameter 137
Z. Stachura, W. Warczak, D. Liesen, P.H. Mokler, L. Bing, B. Cleff

Spectroscopy of Delta-Electrons in U - Rare Gases Collisions with Impact Energies Between 0.4 MeV/u and 1.4 MeV/u 138
C. Kelbch, S. Hagmann, R. Koch, G. Kraft, R.E. Olson, H. Schmidt-Böcking

Population of He - 4^1D Magnetic Sublevels Excited by 1.4 MeV/u Ne^{6+}-, Cr^{15+}- and Sn^{23+}-Impact 139
M. Anton, K.-H. Schartner

Single and Double Ionisation of Helium by Fast and Heavy Ions 140
H. Berg, R. Dörner, O. Jagutzki, C. Kelbch, J. Ullrich, H. Schmidt-Böcking, S. Hagmann, P. Richard, M. Prior, A.S. Schlachter, D. Loyd, J. Pedersen, R.D. DuBois, J.A. Tanis

Multiple Ionisation Collision Dynamics for High-Energy Highly-Charged Ion Impact 141
R.E. Olson, J. Ullrich, R. Dörner, E. Forberich, H. Schmidt-Böcking

Angular Scattering of Fast Protons by Helium 142
R.E. Olson, J. Ullrich, R. Dörner, H. Schmidt-Böcking

2.2 FEW ELECTRON SYSTEMS: SPECTROSCOPY AND INTERACTION WITH ELECTRONS AND PHOTONS 143

Measurement of the 1s Lambshift in Hydrogen-like Nickel 143
H.F. Beyer, R.D. Deslattes, P. Indelicato, K.D. Finlayson, D. Liesen

Measurement of the Fine Structure Splitting in Helium-Like Ag^{45+} 144
R. Marrus, A. Simionovici, P. Indelicato, D.D. Dietrich, P. Charles, J.-P. Briand, K. Finlayson, F. Bosch, D. Liesen, F. Parente

Two-Photon Decay of the $1s2s\,^1S_0$ State in $_{36}Kr^{+34}$ Produced by Resonant Transfer and Excitation 145
E.A. Livingston, Ch. Kozhuharov, P.H. Mokler, Th. Stöhlker, J. Ullrich

The $2s^2\ ^1S_0$ - $2s2p\ ^3P^0_1$ Intercombination Transitions in Xe^{50+} 146
G. Möller, E. Träbert, C. Wagner, P.H. Heckmann, J.H. Blanke, A.E. Livingston, P.H. Mokler

The GSI 5m Grazing Incidence Spectrometer: First Beam-Foil Measurements at 1.4 MeV/u 147
B. Kraus, K.-H. Schartner, F. Folkmann, A.E. Livingston, P.H. Mokler

Capture of Free Electrons into U^{28+} Ions: a Merged Beams Experiment at the UNILAC 148
S. Schennach, A. Müller, M. Wagner, J. Haselbauer, O. Uwira, W. Spies, N. Djuric, B. Jelenkovic, E. Jennewein, R. Becker, M. Kleinod, U. Pröbstel, I. Müller, N. Angert, W. Enders, J. Klabunde, P.H. Mokler, K. Poppensieker, P. Spädtke, M. Terasawa, B.H. Wolf

Dielectronic Recombination of H-like and He-like Ions at the TSR 149
G. Kilgus, D. Habs, E. Jäschke, D. Krämer, D. Schwalm, M. Steck, A. Wolf, R. Schuch, A. Müller, M. Wagner

Electron Beam Diagnosis Using Dielectronic Recombination 150
G. Kilgus, D. Habs, E. Jäschke, D. Krämer, D. Schwalm, M. Steck, A. Wolf, R. Schuch, L.H. Andersen

Collective Noise Enhancement During Laser Cooling of $^9Be^+$ Ions at the TSR 151
W. Petrich, V. Balykin, C. Ellert, A. Faulstich, D. Habs, G. Huber, E. Jäschke, R. Klein, D. Krämer, M. Kristensen, T. Kühl, M. Music, R. Neumann, S. Schröder, D. Schwalm, P. Sigray, B. Wanner, A. Wolf

Laser Cooling in $^7Li^+$ Ions Stored in the TSR 152
S. Schröder, M. Gerhard, R. Grieser, G. Huber, R. Klein, M. Krieg, N. Schmidt, T. Kühl, R. Neumann, V. Balykin, W. Petrich, D. Habs, D. Schwalm, B. Wanner, A. Wolf and the TSR Group

Precision Spectroscopy on Stored $^{7}Li^{+}$ Ions 153
R. Klein, M. Gerhard, R. Grieser, G. Huber, M. Krieg, N. Schmidt, S. Schröder, T. Kühl, R. Neumann, V. Balykin, D. Habs, W. Petrich, D. Schwalm, B. Wanner, A. Wolf and the TSR Group

Lasers Pumped by Heavy Ion Beams 154
A. Ulrich, B. Busch, H.-J. Körner, W. Krötz, R. Paffenberger, G. Ribitzki, J. Wieser, D.E. Murnick

2.3 THEORY 155

Angular Correlations of Coincident Electron-Pairs in Heavy-Ion Collisions 155
O. Graf, J. Reinhardt, B. Müller, W. Greiner, G. Soff

e^{+}-e^{-}-Angular Correlation in Internal Pair Conversion 156
Ch. Hofmann, J. Reinhardt, B. Müller, W. Greiner, G. Soff

Strongly Bound Bipositronium States in QED ? 157
D.C. Ionescu, B. Müller, W. Greiner

Crystal Assisted Production of Composite Particles 158
S. Graf, J. Augustin, J. Reinhardt, B. Müller, W. Greiner

Electron Excitations in Relativistic Ion-Atom Collisions 159
K. Rumrich, W. Greiner, G. Soff, G. Mehler

The Coupled Channel Equations and Gauge Transformations 160
K. Rumrich, B. Müller, W. Greiner, G. Soff

Coupled-channel Analysis of Inner-shell Ionisation in Relativistic Heavy Ion Collisions 161
K. Momberger, N. Grün, W. Scheid

Ionization of an Atom in Nuclear Decay 162
G. Scheitler, M. Kleber

Radiative Muon Capture in Light Atoms 163
G. Soff, J. Rafelski

Many Electron Dirac-Fock-Slater Coupled Channel Calculations for 16 MeV S^{16+} on Ar 164
P. Kürpick, B. Thies, W.-D. Sepp, B. Fricke

Inter-Nuclear Potential of the System Si-Si Calculated with the Finite-Element-Methode 165
S. Hackel, B. Fricke, D. Heinemann, D. Kolb, L. Yang

Spin-polarized Hartree-Fock-Slater Calculations for Atoms and Diatomic Molecules with the Finite Element Methode 166
D. Heinemann, B. Fricke, D. Kolb, A. Rosen

Wavelengths and Lifetimes of Doubly Excited Few-Electron Ions 167
J.H. Blanke, B. Fricke, P.H. Heckmann

Ionization Potentials and Radii of Atoms and Ions of Elements 104 and Hafnium (2+) from MCDF-Calculations 168
E. Johnson, B. Fricke, O.L. Keller, Jr., C.W. Nestor, Jr., T.C. Tucker

Energy and Angular Correlation of e^+e^- Emission in Heavy-ion Collisions

E. Berdermann, F. Bosch, T. Ishikawa, P. Kienle, I. Koenig, W. Koenig, C. Kozhuharov, A. Schröter*, and H. Tsertos

GSI Darmstadt - *TU München

Using the double-Orange β-spectrometer at GSI a series of e^+e^--coincidence measurements has been carried out, investigating the collision systems U+Pb at a beam energy of (E/A)= 5.9 MeV/u, U+U at (E/A)= 5.8, 5.9, 6.0 MeV/u, and recently U+Ta at (E/A)=6.3 MeV/u. Because of an individual readout for each of the 120 Si detectors, the energy resolution in the sum-energy spectra was improved, resulting in a FWHM of ~10 keV. The opening angle $\theta_{e^+e^-}$ of the detected e^+e^- pairs was determined in the range $40° \leq \theta_{e^+e^-} \leq 180°$ (lab.). A subdivision of this broad interval into 4 bins centered around $\theta_{e^+e^-} = 70°$, 90°, 130°, and 180° with $\Delta\theta_{e^+e^-} \sim \pm 20°$ (FWHM) [1] allows to study e^+e^- emission as a function of the opening angle.

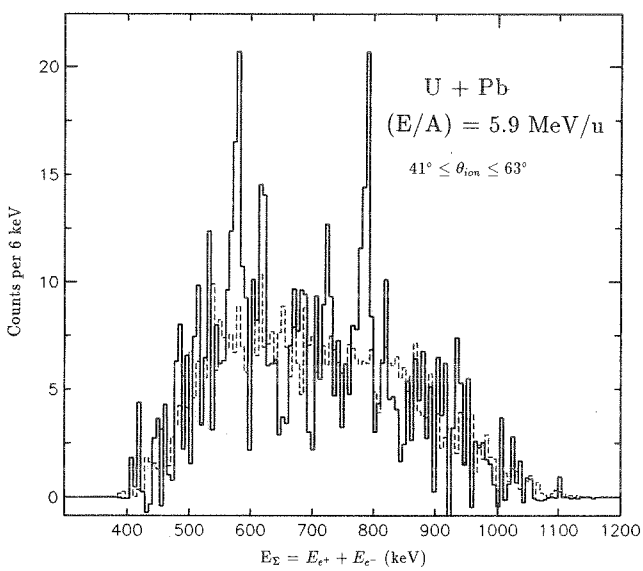


Fig. 1: The (e^+e^-)-sum-energy spectra obtained for U+Pb collisions at 5.9 MeV/u, integrated over negative energy differences (-100 keV $\leq E_\Delta \leq 34$ keV). The full-line histogram corresponds to the opening-angle bin of $(180 \pm 20)°$, while the dashed-line histogram displays the remaining opening-angle range of observation. The latter was adjusted in the height (see text).

The full-line histogram in Fig.1 shows the (e^+e^-)-sum-energy spectrum obtained from U+Pb collisions for opening angles $\theta_{e^+e^-} = (180 \pm 20)°$ and for energy differences $E_\Delta = (E_{e^+} - E_{e^-})$ in the range: -100 keV $\leq E_\Delta \leq 34$ keV. Positrons and electrons were measured in coincidence with the heavy ions, detected in the angular range: $41° \leq \theta_{ion} \leq 63°$; it corresponds to a c.m. interval of $53.5° \leq \theta^*_{ion} \leq 151°$. Two narrow sum lines were observed with energies centered at $E_\Sigma = E_{e^+} + E_{e^-} = (575 \pm 4)$ keV and (787 ± 5) keV. Their widths of (15 ± 4) keV (FWHM) are consistent with the expected experimental resolution. The corresponding spectra, gained for opening angles not containing the 180° bin, show no structures and follow the continuous background as indicated by the dashed-line histogram. The latter was adjusted in the heigth in order to fit the measured spectrum apart from the small regions in which the lines appear. The statistical significance of the lines amounts to ~4 and ~5 standard deviations, respectively, assuming the dashed line to be the background. This behaviour is consistent with a two-body decay of an emitter being essentially at rest in the c.m. system of the colliding ions. Under this assumption, the differential cross sections of the lines, $(d\sigma/d\Omega^*_{ion})$, were found to be ~0.07 and ~0.11 μb/sr, respectively, in agreement with our previous results [1].

The investigation of the collision system U+U at three beam energies with comparable statistics revealed a more complex picture, as that observed in U+Pb collisions. At 5.9 MeV/u, we found again a sum line at ~815 keV, which exhibits a 180° characteristic as reported [1], even though its intensity is reduced appr. by a factor of two. At the other two beam energies (5.8 and 6.0 MeV/u), the intensity of the line is reduced below the level of statistical significance. The shift in the line energy of ~25 keV, when going from U+Pb to U+U collisions, points to a dependence of the line energy on the heavy-ion system. In this context, the effect of the difference in target thickness [Pb (~900 μg/cm^2), U (~400 μg/cm^2)], apart from the negligible difference in the energy loss of the leptons, is not clear presently.

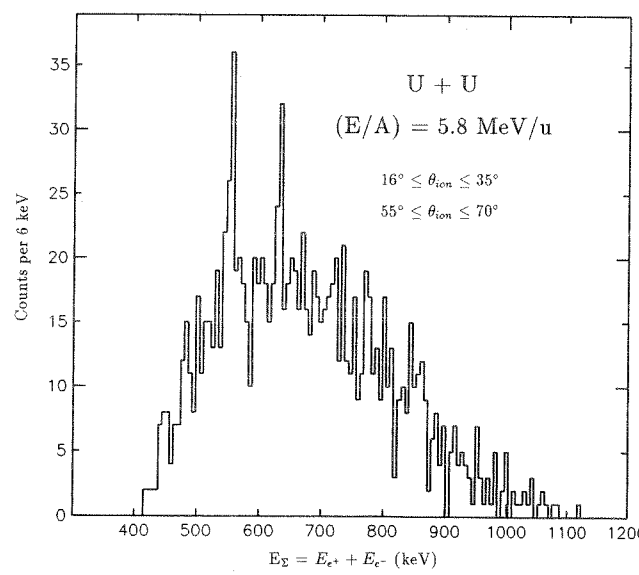


Fig. 2: The (e^+e^-)-sum-energy spectrum obtained for U+U collisions at 5.8 MeV/u, within the whole angular range of $\theta_{e^+e^-}$ and for energy differences in the range: -80 keV $\leq E_\Delta \leq 35$ keV.

In addition, a sum line at E_Σ ~555 keV was also seen, predominantly at 5.8 MeV/u (Fig. 2). Another one is indicated at E_Σ ~630 keV. They appear, however, at all opening angles $\theta_{e^+e^-}$ of observation, in disagreement with the scenario of a back-to-back decay. These features underline that rather complex production mechanisms must be involved in the observed phenomenon, and that all lines found do not have to be necessarily of the same nature.

Monte Carlo studies, fitted to our experimental setup, show that indeed, under certain kinematical conditions, internal pair creation (IPC) from one nucleus can lead to narrow lines in the measured sum spectra, even at small opening angles ($\theta_{e^+e^-} \sim 70°$). Their position and width depend on the emission angle $\theta_{e^+e^-}$. However, none of the lines observed fits to the typical signature investigated within this scenario. The latter fails, furthermore, to reproduce narrow single positron lines. Further Monte Carlo studies as well as the evaluation of the system U+Ta are presently in progress.

References

[1] W. Koenig et al., Phys. Lett. **B 218**, 12 (1989).

On the Behaviour of the Narrow Electron Positron Sum Energy Lines [B]

H. Bokemeyer, H. Folger (GSI); K. Bethge, D. Kraft, K. Sakaguchi, K.E. Stiebing (Univ.Frankfurt);
T. Cowan, J.S. Greenberg, J. Schweppe (Yale University);
H. Backe (Univ. Mainz); D. Schwalm (Univ. Heidelberg); P. Salabura (Univ. Krakow)

The group of sharp electron-positron sum-energy lines at energies around 600 keV, 750 keV and 800 keV found both in $^{238}U+^{232}Th$ and $^{238}U+^{181}Ta$ collisions with the EPOS spectrometer [1,2] has further been analyzed with additional emphasis on their dependences on the lepton emission and the ion scattering angles. In fact the experimental observation of narrow sum-energy lines always associated with a broad structure in the difference-energy spectra excludes conventional nuclear internal pair conversion. Instead, with this experimental pattern resembling a back-to-back emission of the two leptons, speculations were raised on the existence of a neutral object decaying in flight into these lepton pairs. A close inspection of the lepton emission angles, as measured by the transport time of the leptons, can however only support such a simplified picture for the ~800-keV lines.

Utilizing in addition the direct correspondence between the detection of the lepton in the respective subdivided parts of the Si(Li) detectors and its emission into either the forward or backward hemisphere with respect to the beam, the overall hemisphere correlation can be determined. This feature, which was first available for the U+Ta experiment, offers a more direct test of the back-to-back hypothesis. Although still on a poor statistical basis, the results for the 805-keV and the 620-keV lines [2] are consistent with emission in opposite directions (see fig. 1a, b).

For the 748-keV line in $^{238}U+^{181}Ta$ a better statistical quality was obtained which there allowed for a more close inspection of the various dependences. We find, that the asymmetric energy partition between the leptons [2] could still be interpreted within the particle scenario as a Coulomb repulsion effect from the positively charged ions at the time of emission. However, its hemisphere correlation shows, that the electrons contributing to the peak are predominantly observed in the forward hemisphere irrespective of the positron emission direction (fig. 1c, d). This clearly disagrees with a back-to-back emission of the lepton pair, even if a delayed emission off from the solenoid axis by a few mm in beam direction - which could in fact be inferred from this behaviour - is assumed: a high emitter velocity ($\geq$0.2 c) and a particular process which forces the electron to be preferentially emitted forward would then have to be considered which is in contrast to the observed narrowness of the sum-energy line. The latter argument also excludes internal pair conversion in one of the heavy reaction products as a source of this line.

With U+Ta being a sufficiently asymmetric collision system in order to distinguish between the close and the distant elastic collision branch, the impact parameter dependence of the 748-keV sum-energy line could now also be investigated. Fig. 2 (left) shows the result as a function of R_{min}, where the two kinematic branches, after being completely separated by means of the differences in the time-of-flight of the two scattered ions, were added correspondingly. Obviously, the line production probability is strongly correlated with the impact parameter and is maximal for values of R_{min} around 19 fm, i.e. close to the interaction radius for this system. A distinctive ion angular distribution has also been obtained for the other members of the sum-energy line family (an example is given in fig. 2 (right)) and after a very detailed re-analysis [3] also for the singles positron lines reported previously. Because of less asymmetry in these collision systems, a distinction between close and distant collisions is not possible. Assuming, however, the close collision branch to be associated with the line production as it may be inferred from the dependence of the U+Ta 748-keV line, a mean R_{min}-value can be derived for each of the lines which are summarized in the table. Again the deduced values are close to the respective interaction radii of the deformed nuclei. Thus the production of the lines seems to be connected with a particular situation obtained for closely colliding nuclei, although the orgin(s) for the lines still remains an open question.

[1] T. Cowan et al., Phys.Rev.Lett. 56 (1986)444.
[2] H. Bokemeyer et al., GSI An. Rep. 1988, GSI-89-1, p. 158 and P. Salabura et al., to be published.
[3] K. Sakaguchi, PhD-thesis, Univ. Frankfurt 1989.

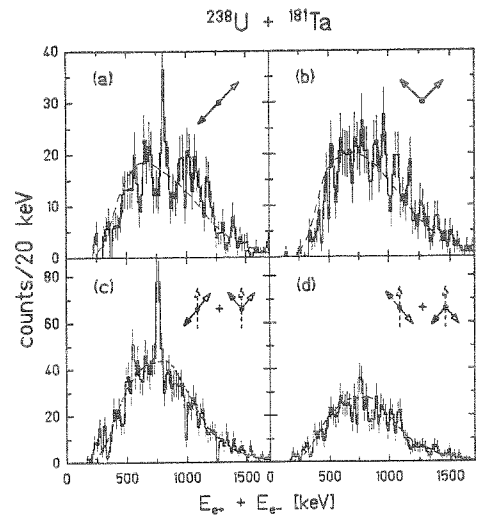


Fig. 1: Hemisphere correlations of the leptons measured for $^{238}U+^{181}Ta$. (a), (b): 805-keV line with the positron and electron of the pair emitted either in opposite or equal hemispheres, respectively. (c), (d): 748-keV line with only the electron selected to be emitted forward or backward, respectively.

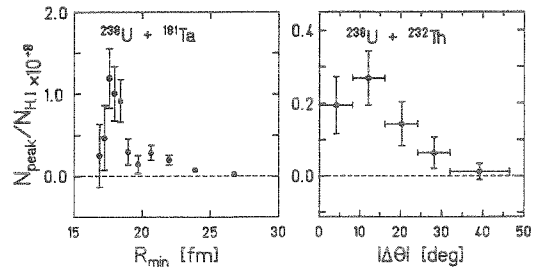


Fig. 2: R_{min} and ion angular dependence of the 748-keV ($^{238}U+^{181}Ta$) (left) and the 805-keV ($^{238}U+^{232}Th$) (right) sum-energy lines, respectively. $\Delta\theta$ is defined as the difference between the individual ion scattering angles.

System	~610 (~320°) keV	~750 keV	~810 (~440°) keV
U+Cm*	20.9±0.6		19.9±0.5
U+Th	19.8±0.7		19.3±0.6
Th+Th*	20.2±0.5		19.6±0.4
U+Ta		18.1±0.5	

Table 1. : Mean R_{min} values in fm for the (e^+, e^-) sum-energy and the e^+ single (*) line families, respectively [3].

Sensitive Search for Long-lived e^+e^- Resonances Around 1.8 MeV/c^2

H. Tsertos and P. Kienle (GSI Darmstadt)

S.M. Judge, B. Krusche, and K. Schreckenbach (ILL Grenoble)

The study of positron-electron scattering (Bhabha scattering) provides a model-independent method to test experimentally suggestions that explain the e^+e^- lines, found in heavy-ion collisions at GSI [1], as being due to the e^+e^- decay of a neutral composite system [2]. In a series of measurements at the high-flux reactor of the ILL, the excitation function for the scattering of monoenergetic positrons on bound electrons has been measured precisely at MeV energies [3]. No evidence was found for the existence of neutral resonances in this mass range, and the lower limit of $\tau^* > 3.5\times10^{-13}$ s was established for their lifetimes [3]. The latter are presently limited between 3.5×10^{-13} and 10^{-10} s [3]. Following on from these results, the experimental arrangement has been modified to improve the sensitivity for long-lived particles.

As in the previous experiments [3], a beam of monoenergetic positrons was produced using the ILL β spectrometer (BILL). Using a modified production target, the beam intensity was increased by a factor of two, i.e., to $\sim3\times10^6$ e^+s^{-1} within an energy interval of ~30 keV [4]. The e^+ beam was focused onto a 4.6-mg/cm^2-thick Be foil, which was suspended along the focal plane of the spectrometer at an angle of 30° relative to the beam. The previous high-resolution detector device [3] was used to detect possible e^+e^- pairs emitted in the decay of a long-lived neutral particle. As the particle would be produced with a velocity of ~0.8c, it would leave the Be foil within 5×10^{-14} s, so, for the lifetimes of interest, the particle would decay outside of the foil. An active-shadow technique was used in order to eliminate the high background from prompt Bhabha scattering within the Be foil, by interposing a plastic scintillator between the foil and one of the detector arrays. In this way, only e^+e^- pairs which originated outside of the foil could reach both detector rows (for details see Ref. 4).

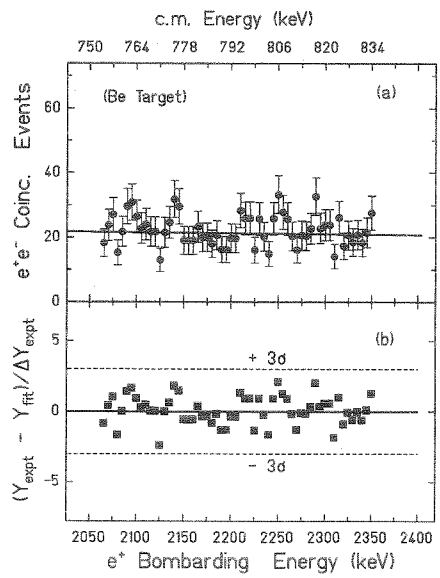


Fig. 1: Number of coincident events observed in the total count time of 10800 s as a function of the incident energy (lower scale) and the c.m. excitation energy (upper scale). The solid line is the result of fit of a first-order polynomial to the data [(a)]. The standard deviations from the fitted curve are displayed in (b).

Fig. 1(a) shows the measured number of the coincident events as a function of the incident energy. The e^+e^- decay of a long-lived resonance would appear as a peak superimposed on this continuum, with a width of ~28 keV (FWHM) [3]. However, no peak was observed and the data can be fitted ($\chi^2/f = 1.04$) by a straight line [Fig. 1(a) solid line]. Fig. 1(b) shows the standard deviations from the fitted curve, lying within $\pm3\sigma$. The maximum peak height for a possible resonant contribution was determined to be $\leq$ 25% (95% C.L.) relative to the fitted curve at 810-keV c.m. energy. From this, a limit can be estimated for the energy-integrated total cross section for the formation of the particle [4].

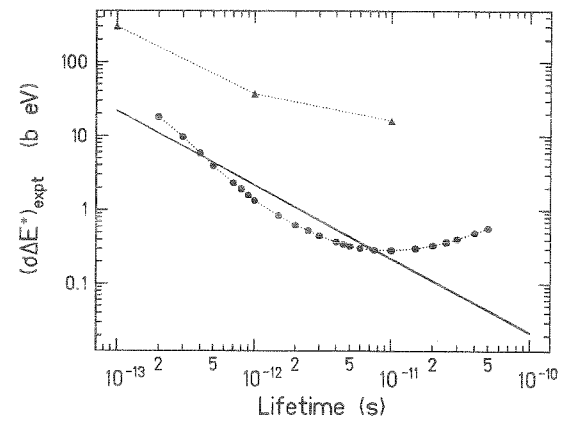


Fig. 2: The upper limits (95% C.L.) for the energy-integrated total cross section for the formation of a neutral particle with an invariant mass of 1.832 MeV/c^2, as a function of the lifetime of the particle (dots). The solid line shows the model-independent total cross section of a spinless (J=0) resonance at 1.832 MeV/c^2 in the unitarian limit. Also shown is the result (triangles) from a less sensitive measurement of van Klinken et al. [5].

Figure 2 shows the result (dots) of the calculated limit (95% C.L.) for the energy-integrated total cross section as a function of the lifetime of the hypothetical resonance. Also shown are the result (triangles) from a measurement of van Klinken et al.[5], and the expected total cross section of a spinless (J = 0) resonance with an invariant mass of M_R = 1.832 MeV/c^2 in the unitarian limit (solid line). As can be seen, the limit on the cross section for the formation of the particle lies below the unitarian limit for a lifetime between 4.5×10^{-13} and 7.5×10^{-12} s. Comparable limits can also be set within the whole mass range investigated (1.776-1.856 MeV/c^2).

Our experiment achieved the sensitivity to detect possible long-lived resonances formed in e^+e^- scattering around the invariant mass of 1.8 MeV/c^2. No particles were detected with a lifetime between 4.5×10^{-13} and 7.5×10^{-12} s (95% C.L.). If the decay of an unknown free neutral particle is responsible for the series of e^+e^- sum lines found in heavy-ion collisions, its lifetime has to be between 7.5×10^{-12} and 10^{-10} s. The limit $\tau^* > 7.5\times10^{-12}$ s ($\Gamma^*_{e^+e^-} < 8.8\times10^{-5}$ eV), set for new particles, is an improvement on that derived from the (g-2) factor of the electron by approximately two orders of magnitude, and can be considered to be a new experimental constraint for the validity of perturbative QED in this mass region.

References

(An asterisk refers to quantities in the c.m. sytem.)

[1] see contributions to this report.

[2] S. Graf et al., J. Phys. G 15, 1467 (1989).

[3] H. Tsertos et al., Phys. Rev. D 40, 1397 (1989).

[4] S.M. Judge et al., to be published.

[5] J. van Klinken et al., Phys. Lett. B 205, 223 (1988).

Limits for Two Photon- and e^+e^--Decay Widths of Bhabha Scattering Resonances from 1.78 to 1.92 MeV/c^2

F. Bosch
GSI Darmstadt
K. Maier, E. Widmann, J. Major, S. Connell, A. Seeger
MPI für Metallforschung Stuttgart

Precise measurements of the excitation function of elastic e^+e^--scattering [1, 2, 3] and, in particular, the Grenoble experiment [1] set a new upper limit

$$\Gamma_{ee}^2/\Sigma\Gamma \leq 2\,meV \qquad (1)$$

(with $\Sigma\Gamma$ the total and Γ_{ee} the e^+e^--decay width) for a neutral resonance within 1.78 to 1.86 MeV/c^2. If e^+e^--decay is the dominant decay-mode (i.e. $\Sigma\Gamma \approx \Gamma_{ee}$), equation (1) corresponds to a lower limit for the life-time $\tau_{Res} \geq 3 \cdot 10^{-13}$.

A corresponding upper limit for the two photon decay-channels can be derived from the limit for the energy-integrated resonance cross section of in-flight two-photon annihilation quoted in [4] (~ 15 b $\cdot$ eV) as

$$\Gamma_{ee} \cdot \Gamma_{\gamma\gamma}/\Sigma\Gamma \leq 5 \ldots 6\,meV \qquad (2)$$

In the last year we performed a series of e^+e^--scattering experiments aiming to improve substantially both the limits (1,2) using the monoenergetic e^+-beam of the Stuttgart Pelletron accelerator [2].

The excitation function (Fig. 1a) for in-flight two-photon annihilation was measured several times for invariant masses from 1.77 to 1.92 MeV/c^2 by using a small energy loss in a 380 μ thick "active" scintillator target as trigger and 4 large-volume BGO detectors for recording the coincident photons.

In a second series of experiments we searched for delayed emission of correlated e^+e^--pair in a "time-window" from $\sim 10^{-13}$ s to $\sim 10^{-11}$ s. For this purpose we designed a special arrangement, consisting of two "active" scintillator targets (T_1 = 380 μ, T_2 = 1000 μ), separated by 4 mm and followed by stop-detector(s). A neutral resonance (of about 1.8 MeV/c^2), formed in the very first part of T_1, passing through T_1 with negligible enery loss and decaying just between T_1 and T_2 shows the quite unusual combination of both a very small energy loss ΔE_1 in T_1 and of a large energy loss ΔE_2 in T_2 (due to the lepton-multiplicity of 2 in T_2), and might be distinguished by these highly specific characteristics from all other processes like elastic e^+e^--scattering, Mott-scattering, etc). The basic assumption in this scenario is, however, that the moving resonance shows only a negligible energy loss in the target.

The calculated detection efficiency $\epsilon(\Sigma\Gamma)$ in our geometry scaled up to 4π is shown in Fig. 2 (for a resonance with $T_{Res} = T_0 - 20$ keV at incident energy T_0 = 2200 keV, assuming isotropic emission of the e^+e^--pairs), as function of the total decay width $\Sigma\Gamma$ (respectively the life-time τ). The influence of systematical errors (target inhomogenities ...) is indicated by the dashed lines.

The measured "delayed" e^+e^--events per 10^8 incident e^+ are shown in Fig. 1b, for energy losses ΔE_1 = 10 to 20 keV (black dots) and ΔE_1 = 20 to 30 keV (open circles); the mean energy loss of the e^+-beam in T_1 is 68 keV. With our conditions the prompt e^+e^--"background" is suppressed by more than 10^4.

The deviations from the best fits in units of the statistical errors are shown in Fig. 1c for both the $\gamma\gamma$- (asterisk) and the Bhabha experiment (same symbols as in Fig. 1b). A resonance should appear — in both systems — as a structure of $\sim$ 8.3 keV FWHM (= Compton profile in the e^+e^--frame, chosen in Fig. 1), superimposed onto the smooth backgrounds. No structures above the 2σ-level can be observed. From F-tests we got for all masses upper limits (95 % C.L.) for the energy-integrated cross section of the two photon as well as for the e^+e^--decay channel of a resonance. According to

$$\left(\int(\sigma dE)\right)_{exp} = \frac{\pi^2}{2}\lambda\!\!\!^{-2}(2J+1)\frac{\Omega}{4\pi}\left\{\begin{array}{l}\Gamma_{ee}\Gamma_{\gamma\gamma}/\Sigma\Gamma \\ \Gamma_{ee}^2/\Sigma\Gamma \cdot \epsilon(\Sigma\Gamma)\end{array}\right. \qquad (3)$$

we derived from these numbers limits for $\Gamma_e\Gamma_\gamma$ / $\Sigma\Gamma$ and Γ_e^2 / $\Sigma\Gamma \cdot \epsilon(\Sigma\Gamma)$, as shown in Fig. 3.

With $\epsilon(\Sigma\Gamma)$ given in Fig. 2 ($\epsilon(\Gamma)$ only marginally depends on energy within the region investigated) and assuming that only Γ_{ee} and $\Gamma_{\gamma\gamma}$ are the important decay channels, we get for each mass a plot Γ_{ec} vs. $\Gamma_{\gamma\gamma}$, showing the excluded and still allowed regions for both partial widths.

Assuming $\Gamma_{\gamma\gamma} = 0$, we can exclude (for J = 0) by our measurements for *all* masses investigated, Γ_{ee}-values between 0.2 to 2.8 meV (corresponding to $\tau = 2.3 \cdot 10^{-13}$ to $3.3 \cdot 10^{-12}$ s). We can, however, *not* exclude by our data Γ_{ee} and $\Gamma_{\gamma\gamma}$-values which are *both* in the range of $\sim$ 0.5 to $\sim$ 2 meV.

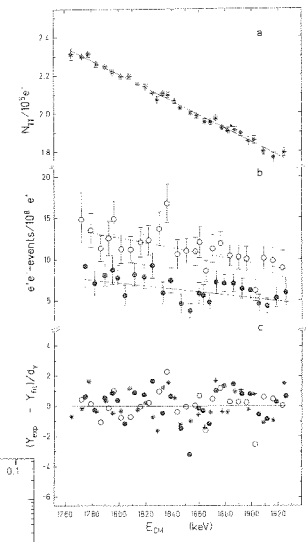


Figure 1: Excitation function for in-flight two-photon vs. total energy in the e^+e^--c.m. system (a); "delayed annihilation" e^+e^--events (b); deviations from fit curves in units of the statistical error for $\gamma\gamma$ annihilation (asterisk) and delayed e^+e^- (c).

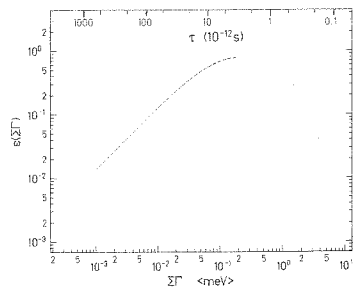


Figure 2: Detection efficiency of our set-up for delayed emission of e^+e^--pairs (scaled up to 4π) as function of the total decay width $\Sigma\Gamma$.

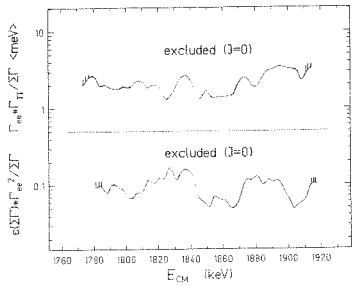


Figure 3: Upper limits for $\Gamma_{ee}\Gamma_{\gamma\gamma}$ / $\Sigma\Gamma$ (upper line) and Γ_{ee}^2 / $\Sigma\Gamma \cdot \epsilon(\Sigma\Gamma)$.

[1] H. Tsertos et al., Phys. D40 (1989) 1397

[2] K. Maier et al., Z. Phys. A330 (1989) 173
and K. Maier et al. in: Proc. of the VII Int. Conf. on e^+e^--Annihilation, Gent 1988 (World Scientific 89)

[3] J. van Klinken et al., Phys. Lett. B205 (1988) 223

[4] W. Heitler, The Qunatum Theory of Radiation[3], V, §27, Eq. (6)

[5] J. Kramp et al., GSI-Scientific Report 1988, p. 161

Search for Resonances in Positron Annihilation in Flight[B,G]

J. Kramp, J. Gerl, D. Habs, D. Schwalm, P. Thirolf
Physikalisches Institut der Universität and
Max-Planck-Institut für Kernphysik, Heidelberg

We have investigated Positron–Annihilation–in–Flight occuring during the deceleration of positrons in a small Al/Plastic sphere mounted in the center of the Darmstadt–Heidelberg Crystal Ball to search for possible resonances in $e^+e^- \rightarrow n\gamma$. Within the c.m. energy region investigated, which overlaps the region where the narrow e^+e^- sum energy peaks have been found in heavy ion collisions, no resonances have been found.

The analysis of an experiment [1] performed in the Crystal Ball to search for resonances in the reaction $e^+e^- \rightarrow n\gamma$ with n=2,3 has been completed. Within the investigated energy region, which corresponds to invariant masses between 1.1 and 2.1 MeV, no resonances have been observed in either of the two annihilation channels. For the $e^+e^- \rightarrow 2\gamma$ channel, where resonances within a charge parity of C= +1, that is with an even total spin J can be seen, we could improve the upper limit for the corresponding integrated resonance cross-section (see fig. 1a) by a factor of about 10 as compared to an earlier measurement [2]. From this we can deduce for each even J-value an upper limit for the width ratio $\Gamma_{e^+e^-} \cdot \Gamma_{\gamma\gamma}/(\Gamma_{e^+e^-} + \Gamma_{\gamma\gamma})$ assuming that the resonances can only decay in e^+e^- or photons. Fig. 1b displays this limit for J=0.

For the 3-photon channel, in which resonances with C= −1, i.e. odd spins could decay, we were able for the first time to determine an upper limit for the integrated resonance cross-section (fig. 2a), which is of the same order as that of the 2-photon channel. The corresponding width ratio for J=1 is shown in fig. 2b.

From the result of the present measurement together with those from Bhabha scattering experiments (see e.g.[3]), where upper limits for the ratio $\Gamma^2_{e^+e^-}/(\Gamma_{e^+e^-} + \Gamma_\gamma)$ are obtained, one is able to deduce for all J-values in a model independent way upper limits for the resonance width $\Gamma_{e^+e^-}$. At an invariant mass of 1.832 MeV, which corresponds to one of the most prominent e^+e^- sum energy peaks observed in heavy ion collisions [4], an upper limit of $\Gamma_{e^+e^-} \leq 12$ meV (3σ) for e.g. J=0 is obtained. Starting from these limits one can deduce under additional assumptions the possible coupling strength of sofar unknown particles to the lepton field and compare it to that deduced from other experimental quantities. (see e.g. [5]).

[1] J. Kramp et al., GSI annual report 1988
[2] S.H. Connell et al., Phys. Rev. Lett. **60** (1989) 373
[3] H. Tsertos et al. Phys. Lett. **207B** (1988) 273 und Z. f. Phys. **A331** (1988) 103
[4] H. Bokemeyer et al., GSI annual report 1988, p. 173
[5] A. Schäfer, J. Phys. **G15** (1989) 373

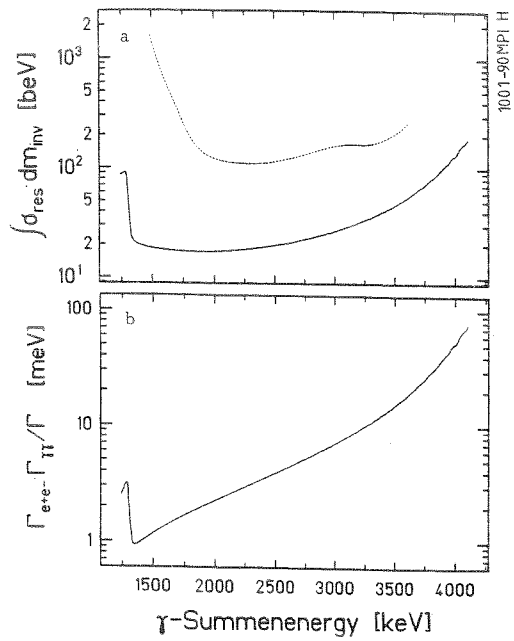


Fig. 1. a) Upper limit (3σ) for the cm-integrated resonance cross-section for the 2γ-channel. The dashed curve is from ref. [2] $(m_{inv} = (2m_e E_\gamma^{sum})^{1/2})$.
b) Upper limit (3σ) for the corresponding reduced decay width of a resonance with spin J=0 $(\Gamma = \Gamma_{e^+e^-} + \Gamma_{\gamma\gamma})$.

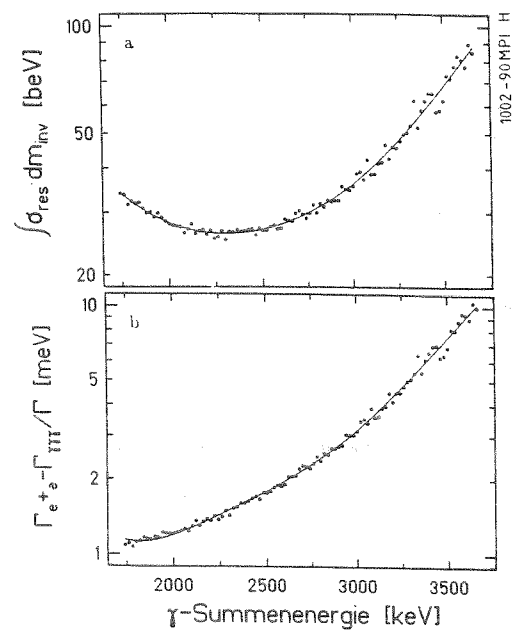


Fig. 2a) Upper limit (3σ) for the cm-integrated cross-section for the 3γ channel. (b) Upper limit for the corresponding reduced decay width of a resonance with spin J=1.

On the decay $e^+e^- \rightarrow 4\gamma$ [B,G]

T. Schulze, G. Enders*, J. Gerl, D. Habs, D. Schwalm

Physikalisches Institut der Universität Heidelberg and

Max-Planck-Institut für Kernphysik, Heidelberg

Elektrons and positrons may annihilate on collision to yield γ rays. Depending on the spin J of the system one expects an even number of photons for the singulet and an odd number for the triplet. So far only the 2γ and 3γ decays have been observed experimentally. For the much weaker 4γ mode QED predicts a branching ratio of 1.5×10^{-6} [1]. With the Darmstadt-Heidelberg Crystal-Ball two experiments with a ^{22}Na source (170×10^3 Bq) have been made to observe the rare decay and improve the upper limit of 7×10^{-6} for the branching ratio.

The identification of the 4γ intensity is difficult because compton scattering in the standard 2γ and 3γ decays, which can be decreased by a spherical lead collimator in the crystal ball, can also produce events with 4γ signature. Several analyzing conditions are employed to reduce their intensities. The straightforward requirements of 4 active detectors and the conservation of energy and momentum are not sufficient and therefore combined with cuts in the theoretical 4γ phase space that particularily affect the standard decays. With Monte-Carlo-Simulations we studied the reduction of the different decay channels [2], but the possible contributions of the standard decays could not be determined with the necessary accuracy.

Thus the experimental scattering pattern of single 511keV photons was used to generate 2γ events with 4γ signature, giving a sufficient reduction for the 2γ decay of more than 4×10^{-9} while the probability for the detection of a 4γ decay under these conditions decreases to $3.5\% \cdot \Gamma_{4\gamma}/\Gamma_{2\gamma}$. This leaves the 3γ decay as the main background with a contribution of $5.4 \cdot 10^{-8}$ given by the natural $3\gamma/2\gamma$ Branching ratio of 1/372 and a experimental reduction of $2.0(1.4) \cdot 10^{-5}$. With its upper limit it can still explain all 35 potential candidates of 4.2×10^8 decays in a test experiment.

A further improvement can be achieved by the investigation of a parameter $\sin(\theta_0)$ which measures for an event with 4γ signature the deviation of coplanarity, which is characteristic for the 3γ decay. θ_0 is here the minimum angle between one of the active counters and the plane given by two others and the center of annihilation. Fig.2 shows the distributions of this parameter for 3γ and 4γ decays with 4γ signature, which can be determined with good accuracy from the simulations. An analysis of least squares to fit these distributions to the experimental data yields 8 ± 4 4γ events corresponding to a branching ratio $\Gamma_{4\gamma}/\Gamma_{2\gamma} = 0.6 \cdot 10^{-6}$. The statistical error might be accompanied by a systematic error of so far unknown size caused by overestimation of scattering in the source. This can be avoided by choosing a cut for the parameter $\sin(\theta_0)$ leaving definitely no significant 3γ contribution without reducing the probability of observing a 4γ decay below 10^{-8}. An experiment, where several conditions are employed already online would then allow to compare the branching ratio with the theoretical prediction.

* Present adress: Phys. Inst. der Universität Giessen

[1] G.P.Lepage, P.B.Mackenzie, K.H.Streng, P.M.Zerwas, Phys. Rev. A 28 p.3090 (1983)

[2] G.Enders et al., GSI annual report 1986, p.171

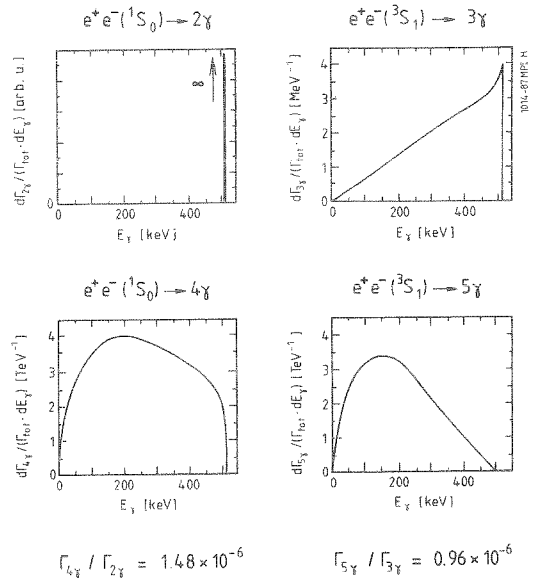


Fig.1 Theoretical energy distributions and branching ratios for the different decay modes of e^+e^-.

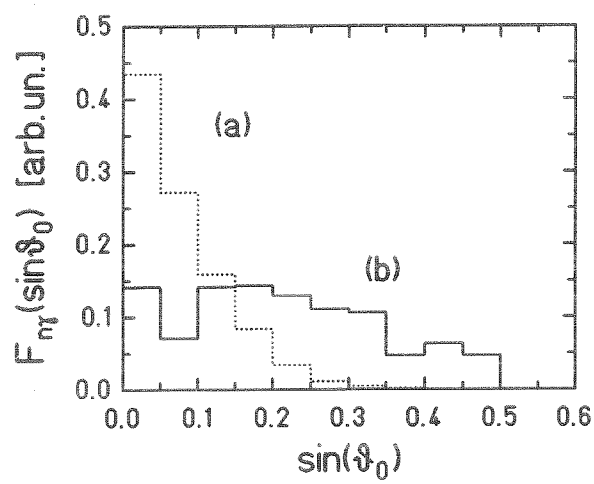


Fig.2 Distribution $F_{n\gamma}$ of the parameter $\sin(\theta_0)$ measuring the deviation of an event with 4γ signature from coplanarity for 3γ (a) and 4γ decays (b). It can be used to seperate these modes after the successful reduction of the dominant 2γ decay by several other conditions.

Single and Double Electron Capture in Ge^{+31} → Ne Collisions

Th. Stöhlker[†], Ch. Kozhuharov, E.A. Livingston[*], P.H. Mokler[‡], R.E. Olson[‡](GSI Darmstadt)
A. Szymanski, Z. Stachura, A. Warczak (University and Inst. of Nuclear Physics, Kraków)

We measured single and double electron capture into hydrogenic $_{32}Ge^{+31}$ ions colliding with Ne gas atoms at beam energies between 4.5 MeV/u and 11.5 MeV/u [1]. The experimental results are compared with CTMC calculations.

Figure 1 shows cross sections for one- and two-electron capture from Ne into hydrogenic Ge ions as a function of ion energy. The triangles represent the measured data points. We estimate the absolute and systematic errors for the single capture measurement to be less than 50 % and for double capture less than 20 %.

The cross sections for single and double capture are in good agreement with theoretical calculations using the CTMC code according to Ref. 2 (see full points). The single capture cross sections agree also with the prediction of Schlachter et al. [2] (see full line).

The fact that for double capture the CTMC calculation predicts a slightly higher cross section compared to the measurement may be explained by Auger processes not included in the calculations. As the CTMC calculation describes the observed capture processes quite well we calculated also the impact parameter dependent capture probabilities at small impact parameters relevant for non-resonant electron capture and simultaneous projectile excitation (NTE). Figure 2 shows these probabilities for single, double, and total electron capture at two different energies (4.56 and 10 MeV/u) for Ge^{+31} → Ne collisions. It is interesting to note that in such close collisions (b < 0.2 a.u.) and at low energies (less than 7 MeV/u) the double capture is calculated to dominate the total capture probability although the single electron capture cross section is about a factor of 7 larger than the double capture. At higher energies (higher than 7 MeV/u) also the single capture probability is the dominant contribution to the total capture probability.

Based on these results we calculated NTE cross sections for $_{32}Ge^{+31}$ → Ne collisions [1]. NTE is a competing process to RTE (resonant electron transition and excitation) which contributes to the measured excitation function for double RTE [1]. The cross section for this process is given by $\sigma = 2\pi \int_0^\infty P_{cap}(b) P_{exc}(b)\, b\, db$ where P_{exc} is the impact parameter dependent K-shell excitation probability, calculated analytically using the SCA-method [4] and the electron capture probability $P_{cap}(b)$ from above.

Figure 3 presents the calculated single NTE (associated with the capture of one electron) and double NTE cross sections (associated with the capture of two electrons) together with the cross section for total NTE. The excitation function for double NTE has a flat maximum at energies where we expect resonances of double RTE and decreases slowly with increasing ion energy. This behaviour is mainly determined by the capture probabilities for two electrons. The cross section for total NTE as a function of beam energy is calculated to be nearly constant over the whole energy region from 4.5 MeV/u to 11.5 MeV/u.

In order to compare these values to measurements one has to correct the results for electron screening effects of the target atom (~ 0.8), fluorescence yield (~ 0.5 – 0.8), metastable states (~ 0.3).

References

[1] A. Warczak et al., GSI Report 89-58 (1989)

[2] R.E. Olson, in Electronic and Atomic Collisions (Elsevier, Amsterdam, 1989), pp. 271 – 285

[3] A.S. Schlachter et al., Phys. Rev. A27, 3372 (1983)

*on leave from Notre Dame University, Notre Dame, Indiana 46556
†associated with University Gießen
‡University of Missouri-Rolla, Humboldt Award Fellow

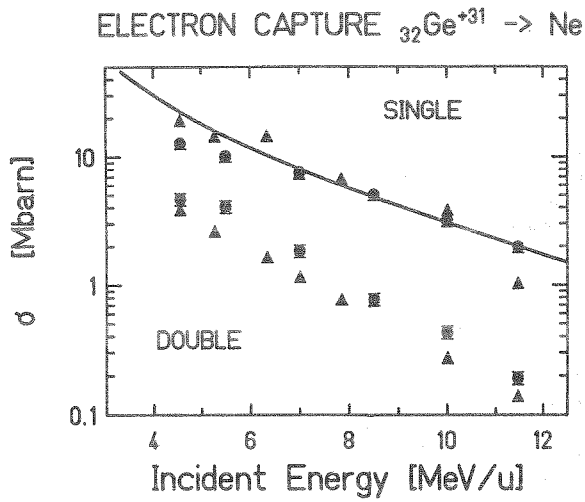


Figure 1:

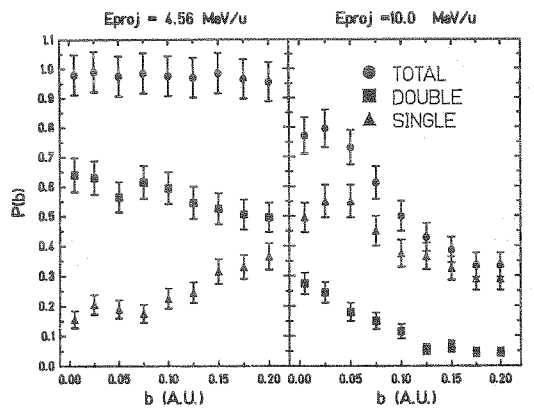


Figure 2:

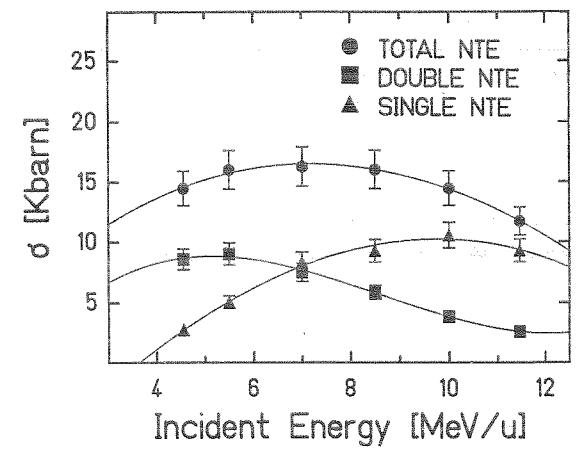


Figure 3:

Evidence for Resonant Two Electron Capture and Excitation in Collisions of H-like Ge with Ne

Th. Stöhlker†, C. Kozhuharov, A.E. Livingston‡, P.H. Mokler †, S. Reusch †, (GSI Darmstadt),
A. Warczak, A. Szymański, (Uniwersytet Jagielloński, Kraków),
Zb. Stachura (Instytut Fizyki Jądrowej, Kraków)

The capture of a quasi-free target electron into, e.c. the L-shell of a H-like projectile and the simultaneous excitation of its K-shell electron is a resonant process, investigated intensively for various collision systems [1], and referred to as RTE (resonant transfer and excitation). Qualitatively, the RTE is a time reversed Auger process with a consecutive radiative stabilization of the doubly excited intermediate state.

Similarly, since the double Auger process is a known phenomenon, a consideration of an invariance under time reversal leads to a new process: resonant capture of two (or more) electrons with a simultaneous excitation of a projectile electron; i.e. double (or multiple) RTE.

We performed, therefore, first experiments aiming at the identification of double RTE in collisions of H-like Ge with Ne gas as a target. The results, a preliminary part of them was shown in the last Scientific Report[2], were elaborated further.

The double RTE process is expected to exhibit a characteristic enhancement of its excitation function in the vicinity of the resonant incident energies and its observable signature is, for incomming hydrogenic projectiles, the coincidence between two x-rays from the decay of the intermediate multiply excited state associated with double charge exchange. No sharp resonancies are expected, however, since the momentum distribution of the bound target electrons lead to large broadenings.

The triple coincidence yield, normalized to the collected number of projectiles and to the target thickness, provided us with the excitation function, $\sigma_{KKQ2}(E_{proj})$, for double electron capture (Q2) associated with a successive emission of two Ge-K-x-ray (KK), as plotted in Fig. 1a. The error bars are of statistical origin. The data exhibit an enhancement of σ_{KKQ2} below 7.5 MeV/u. Thorough checks of the other (simultaneously and independently) measured parameters ruled out the existence of systematic errors. Hence, the observed enhancement was not artificially produced by erratical fluctuations. Because of the modest statistics, a simple step-like function was fitted to the data points (solid line with shaded areas for the errors of the fitted constants). This least square fit shows an increase of σ_{KKQ2} at the lower energies by a factor of 5.77 ± 1.02, i.e. there is indeed a 4.68σ effect.

Having established the statistical significance of the observed effect we note that the position of the enhancement is in accordance with the resonance locations as indicated by the vertical arrows in Fig. 1a (Auger notation). The horizontal bars (Fig. 1a, top) represent the broadening (FWHM) due to the Compton profiles of the target electrons. The expected effect is superimposed, however, on a broad background originating from the double NTE process (non-resonant transfer and excitation). This backgrond is also present at bombarding energies outside the region of expected resonances. Details of its dependence on the bombarding energy are given elswhere [3].

The data, restricted solely to the Ge-K_α transitions, were analysed in a similar way. The results for the tripple coincidence ($K_\alpha K_\alpha Q2$) are shown in Fig. 1b, whereas Fig. 1c displays the data with a double coincidence requirement only ($K_\alpha K_\alpha$). Additionally to the contributions from the double RTE and from the double NTE processes the data in Fig. 1c include also contributions from the single NTE process. The enhancement of the data point at 11.5 MeV/u in Fig. 1c signals the onset of the single RTE process with a maximum at 13 MeV/u [4].

The relevant information was extracted (by means of a least square fit) from all the measured data as well as from the results of calculations on the single as well as on the double NTE as a function of the bombarding energy [3]. The cross section for double RTE amounts to (1.32 ± 0.65) kbarn, whereas the cross section for double NTE—to (0.91 ± 0.44) kbarn at the lower bombarding energies, and to (0.37 ± 0.19) kbarn at the higher energies, resp. (The cross sections are not normalized to the number of target electrons.)

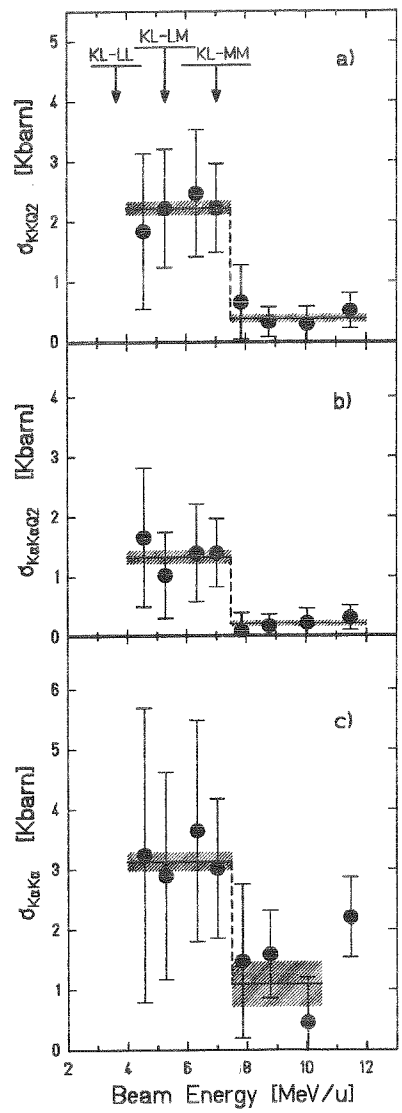


Fig. 1: Measured excitation function, extracted from the tripple coincidence (KKQ2 in Fig. 1a, and KαKαQ2 in Fig. 1b, resp.) as well as from the double coincidence (KαKα in Fig. 1c). The horizontal lines are results of least square fits to the data points, the shaded areas represent the errors of the fitted constants. The vertical arrows (top) indicate the positions of the expected double RTE maxima. The horizontal bars show the expected resonance widths (FWHM).

† and Universität Gießen
‡ on leave from University of Notre Dame

References

[1] A. Warczak et al. GSI 89-58, and referencies cited therein.
[2] A. Warczak et al. GSI 89-1, Scientific Report 1988, p. 167
[3] Th. Stöhlker et al., contribution to this Report
[4] S. Reusch et al., XV ICPEAC, Brighton, Abstr. p. 642

L-Shell Excitation in Heavy Ion - Atom Collisions as Function of the Impact Parameter *

Z. Stachura, A. Warczak (Jagiellonian University and Inst. of Nuclear Physics, Kraków, Poland)
D. Liesen, P.H. Mokler (GSI Darmstadt)
Liu Bing (Inst. of Modern Physics, Academia Sinica, Lanzhou, PR China)
B. Cleff (Univ. of Münster)

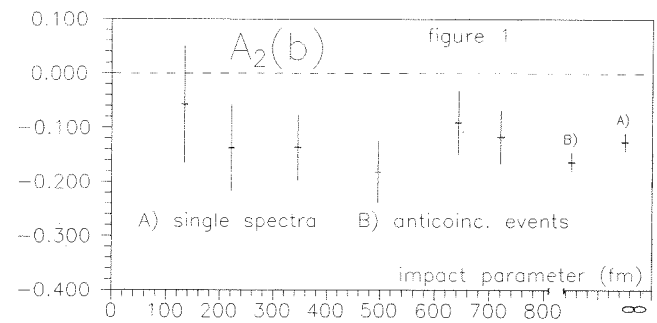
The primary aim of the experiment was to investigate the impact parameter dependence of L-shell alignment in collisions of heavy ions with atoms, where x-rays are produced by MO excitation processes. A collision system of 1.4 MeV/u U → Cu was chosen, where a relatively large alignment in the integral measurement was reported [1]. Two Si(Li) detectors placed at a position of 90^0 and 135^0 with respect to the beam detected x-rays in coincidence with scattered particles registered with a position-sensitive parallel plate avalanche detector [2]. The particle detector registered all uranium ions scattered between 0.92^0 - 6.41^0 lab. angle, corresponding to an impact parameter range of 720 down to 98 fm. In addition, anti-coincident x-ray spectra were also measured, thus allowing an integral measurement for all impact parameters larger than 720 fm.

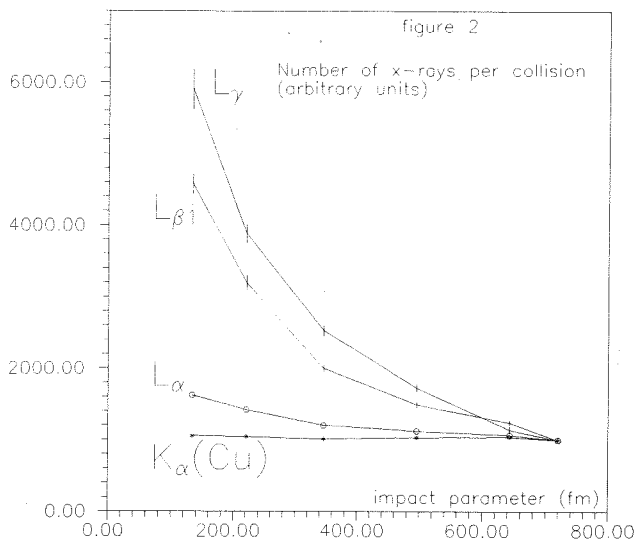
The anisotropy $\lambda_2(b)$ of the L_ℓ line (M_1 - L_3 transition) is presented in Fig. 1. In contrast to measurements reported for systems in which the L shell is excited by direct Coulomb excitation [3, 4], the anisotropy $\lambda_2(b)$ is flat in the whole range of investigated impact parameters: Within the error bars $\lambda_2(b)$ is equal to the integral value evaluated both from anticoincident spectra (λ_2 for $b > 720$ fm) and from single x-ray spectra (λ_2 for all values of b).

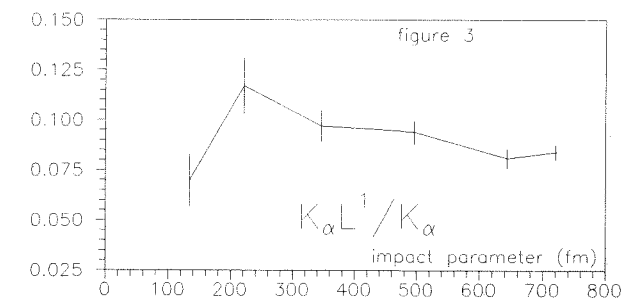
This behaviour is consitent with the assumption that L_3 vacancies are created mostly by $3d\sigma$ excitation via a pseudo-crossing at large interatomic distances during the outgoing part of the trajectory. Thus, the ratio of $L_3(m_j = 1/2)$ to $L_3(m_j = 3/2)$ population is not affected much by other couplings, active at closer distances.

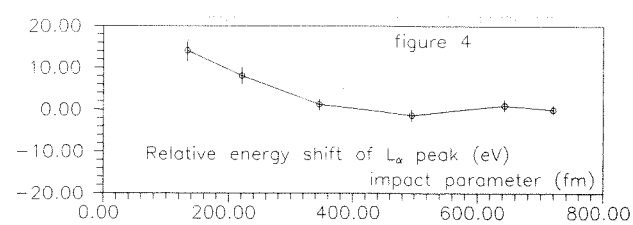
In addition to the alignment the experiment delivered information on cross sections of single and multiple excitation processes which we present here by the experimental results leaving their theoretical interpretation for a forthcoming publication. The relative yield of several strong components of the x-ray spectrum is presented in Fig. 2. The cross section for K-vacancy production in Cu is constant within the investigated range of impact parameters. The number of L_3 vacancies in U is increasing for closer collisions, as seen from the rise of the L_α component. This rise is still larger for components originating from L_2 vacancies ($L_{\beta 1}$ line) or $L_2 + L_1$ vacancies (L_γ line).

The experiment enabled also a study of the impact parameter dependence of the satellite structure in the x-ray spectra. The intensity of the $K_\alpha L^1$ peak of Cu relative to K_α is presented in Fig. 3. In the L spectrum the energy resolution of the detectors did not permit to separate satellite peaks and information on the average number of M spectator vacancies accompanying the L vacancy was obtained from the energy shift of the lines. The absolute value of the energy for strong components in the single spectra is consistent with a mean value of 6 - 7 spectator M vacancies, comparing with calculations by Uchai et al. [5]. The relative shift in the coinicdent spectra (measured with an accuracy of a few eV for strong lines) indicates a rise not larger than for one additional M vacancy for closest collisions observed here (see Fig. 4 for the L_α line).









References

[1] Z. Stachura et al., J. Phys. B: At. Mol. Phys. 17 (1984) 835

[2] B. Liu et al., Nucl. Instr. Meth. A240 (1985) 139

[3] J. Konrad et al., Phys. Rev. Lett. 52 (1984) 188

[4] S. Zehendner et al., MPI Heidelberg, preprint (1984)

[5] W. Uchai et al., At. Data Nucl. Data Tables 34 (1986) 201

*Parially supported by the SFB-216: Polarisation und Korrelation in atomaren Stoßkomplexen

Spectroscopy of Delta-electrons in U - rare gases collisions with impact energies between 0.4 MeV/u and 1.4 MeV/u [*]

C. Kelbch#, S. Hagmann$, R. Koch#, G. Kraft&, R. E. Olson$, H. Schmidt-Böcking#

#) Institut für Kernphysik, Universität Frankfurt,D-6000 Frankfurt/M, FRG
$) Physics Department, University of Missouri-Rolla, Rolla,MO 65401, USA
#) Physics Department, Kansas State University, Manhattan,KS 66506, USA
&) GSI Darmstadt, FRG

Systematic studies have been started to investigate the double differential cross sections for the emission of delta-electrons, differential in emission energy E_e and -angle ϑ_e in U - rare gases collisions. These studies have been performed in a projectile energy range between 0.4 MeV/u and 1.4 Mev/u. The energy spectra for different emission angles show unexpected structures in the region of the binary encounter peak[1], which vary strongly with the emission angle ϑ_e and projectile energy E_p. These structures appear e.g. at $\vartheta_e \approx 40°$ for an impact energy E_p/A of 1.4 MeV/u, at $\vartheta_e \approx 32.5°$ for E_p/A = 1 MeV/u and at $\vartheta_e \approx 22.5°$ for E_p/A = 0.5 MeV/u.
It has been reported[2], that electron-electron interactions may play an important role in these scattering systems. Therefore, to gain more insight into the ionisation process, we have started first electron-electron coincidence measurements at these heavy collision systems. Since electron spectrometers have usually a small solid angle which limits the coincidence count rate drastically, we used a "retarding grid" spectrometer that detects the integrated count rate from a lower energy limit $e \cdot U_R$, given by the retarding voltage U_R, up to the highest emitted electron energy. The second electron was energy analyzed by a cylindrical sector analyzer under an emission angle of $\vartheta_e = 0°$.
Figure 1 shows an example of the 0°-energy single spectrum and 0°-electrons in coincidence with electrons emitted under $\vartheta_e \approx 60°$ with different retarding voltages U_R. The single spectrum shows the expected shape: the well-known cusp-peak and a shoulder near the binary encounter peak energy. However, the coincident spectra show a surprising contribution at energies between cusp energy and binary encounter energy. This broad peak shifts to higher electron energies with increasing retarding voltage, i.e. higher mean electron emission energies under 60°. The comparison of our data with calculations in the Classical Trajectory Monte Carlo- approach (CTMC)[3] gives hints, that the electron loss of the projectile might have a contribution to the energy spectra at electron energies between the cusp energy and BE-energy. This high-energy contribution could be explained by the kinematics of loss electrons, especially a double scattering of projectile loss electrons where the loosely bound outer electrons of the U^{11+} are first deflected at the target nucleus and then scattered at the projectile nucleus, thus gaining energy from the momentum of the projectile nucleus.
Electron-electron as well as electron-projectile coincidence experiments are presently in preparation to obtain more information on the mechanisms of electron ejection in such heavy ion-atom collisions.

1) C. Kelbch et al.
Phys. Lett. A 139 (1989) 304
2) R.E. Olson et al.
J. Phys. B 12 (1979) 1834 and private Comm.
3) C. Kelbch et al, GSI scientific report 1988

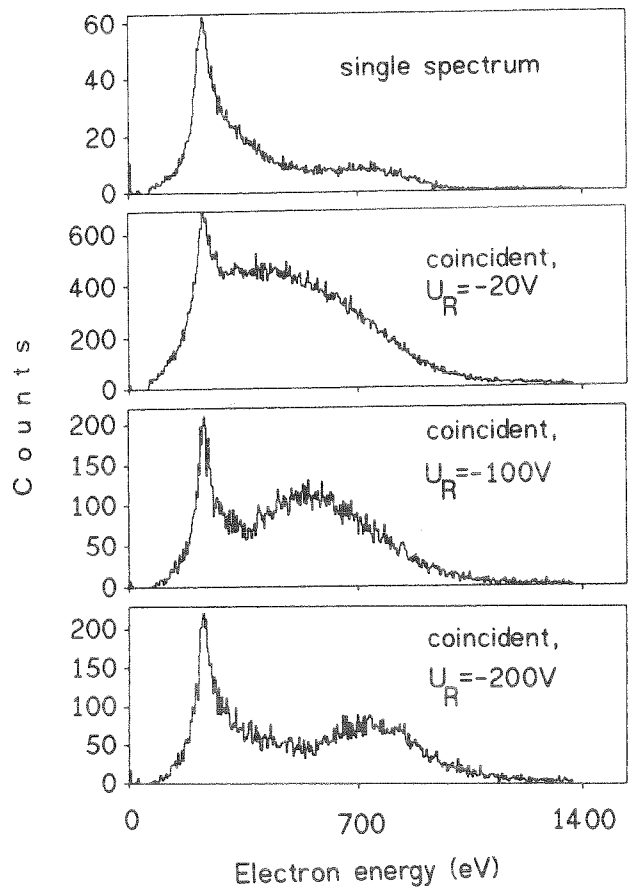


Figure 1 (see text)

POPULATION OF $He-4^1D$ MAGNETIC SUBLEVELS EXCITED BY $1.4MeV/u$ Ne^{6+}-,Cr^{15+}- AND Sn^{23+}- IMPACT

M.Anton and K.-H. Schartner

I.Physikalisches Institut der Universität Gießen

Investigations by Reymann *et al.* [1] on excitation of He by heavy ion impact have been continued using level crossing techniques for the determination of cross sections σ_m for the population of 4^1D -magnetic sublevels. So far two quantities have been determined, the total excitation cross section σ_{1D}

$$\sigma_{1D} = \sigma_0 + 2\sigma_1 + 2\sigma_2$$

and the polarisation fraction $\Pi = I_\parallel - I_\perp / I_\parallel + I_\perp$ of the $4^1D \rightarrow 2^1P$ transition. $I_\parallel$ and $I_\perp$ denote the intensities of the fluorescence radiation with electric field vector parallel and perpendicular to the ion beam axis, respectively. Π depends on the sublevel cross sections σ_m in the following way:

$$\Pi = \frac{3(\sigma_0 + \sigma_1 - 2\sigma_2)}{5\sigma_0 + 9\sigma_1 + 6\sigma_2}$$

For the determination of σ_m a third physical quantity has to be known which can be extracted from magnetic depolarisation signals in a constant electric field [2]. When such a field E_z is applied parallel to a magnetic field B_z, several levelcrossings arise due to the combination of Stark and Zeeman splittings. For our experimental geometry, i.e. with the field directed perpendicular to the ion beam and the direction of observation perpendicular to field *and* ion beam axes, only levelcrossings with $\Delta m = \pm 2$ can be observed for $I_\parallel$. So the well-known Hanle-signal splits up into three components, as shown in fig.1.

The ratio of their amplitudes $\Delta I_{m,m'}$ depends on σ_m according to

$$X := \frac{\Delta I_{-1,1}}{\Delta I_{-2,0}} = \frac{\Delta I_{-1,1}}{\Delta I_{0,2}} = \frac{2\sigma_2 - 2\sigma_1}{\sigma_2 - \sigma_0}$$

yielding the third quantity required for the derivation of σ_m.

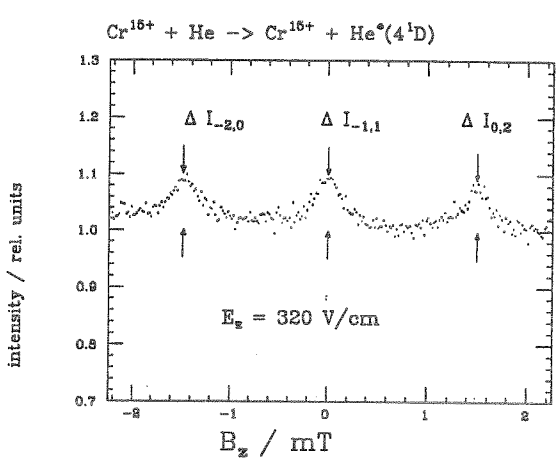


Figure 1: Magnetic depolarization signal in a constant electric field of $320V/cm$. $Cr^{15+} + He^+, E_{Cr^{15+}} = 1.4MeV/u$.

The intention of the experiments is to gain a deeper understanding of the excitation mechanism for heavy ion impact on light target atoms, especially to test the applicability of a scaling relation, observed for the total cross section σ_{1D}, to σ_m, a quantity which may be more sensitive than the total cross section. The scaling relation

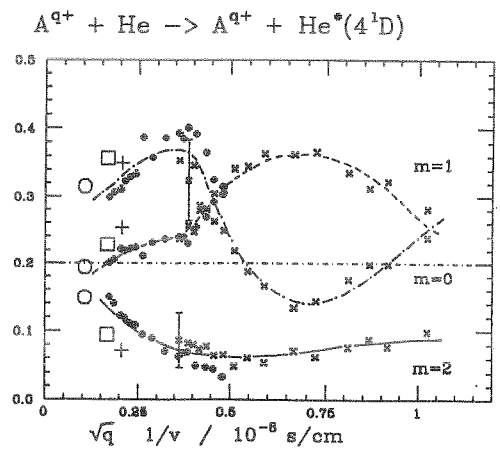


Figure 2: Relative sublevel cross sections σ_m/σ_{1D} for excitation by A^{q+}-projectiles (○ : Ne^{6+}, □ :Cr^{15+}, + :Sn^{23+}, • :He^+ ⁎ :Ne^+) versus $\sqrt{q}/v$

$$\frac{\sigma}{q} = f\left(\frac{v^2}{q}\right)$$

seems to hold for the total cross section, q being the effective charge of the projectile. According to this scaling one expects a universal behaviour of the relative cross section $\sigma_m/\sigma_{1D} = \tilde{f}(v^2/q)$.

Figure 2 contains the experimental data for $\sigma_m/\sigma_{1D}(m = 0, 1, 2)$, obtained for $Ne^{6+}-$, $Cr^{15+}-$ and $Sn^{23+}-$ impact at $1.4MeV/u$. The data are given as a function of the reciprocal projectile velocity multiplied by $\sqrt{q}$. Fig.2 also contains cross section ratios for Ne^+- and He^+- impact excitation which have been measured at a $1MeV$- Van-de-Graaff accelerator with projectile energies between $80keV$ and $800keV$ [3]. It can be seen that the reported measurements for highly charged heavy ion impact, scaled in the discussed way, are not much different from the results for He^+- impact at energies in the $200keV/u$-range. This is in accordance with the expectations. The Ne^+- data are only shown for comparison, a discussion of their behaviour is not within the scope of this report.

References

[1] K.Reymann, K.-H. Schartner, B. Sommer and E. Träbert Phys.Rev. A **38** (1988) 2290

[2] W.Schilling, G.v.Oppen, W.D.Perschmann and D.Szostak J. Phys. B **14** (1981) 2611

[3] M. Anton, Diplomarbeit 1989, I.Physikalisches Institut der Universität Gießen

Supported by the **Deutsche Forschungsgemeinschaft**

Single and Double Ionisation of Helium by Fast and Heavy Ions[G,B]

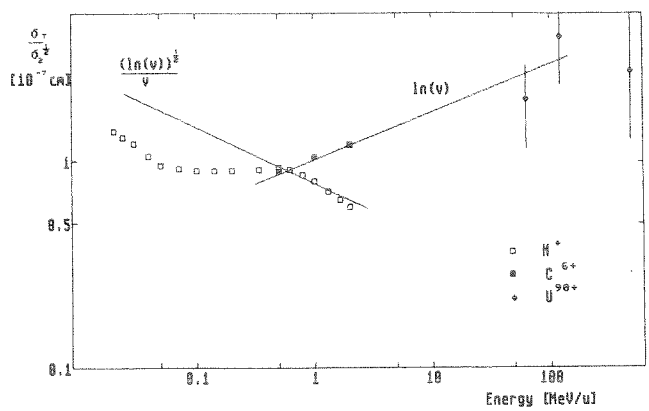
H.Berg[1], R.Dörner[1], O.Jagutzki[1], C.Kelbch[1], J.Ullrich[2], H.Schmidt-Böcking[1], S.Hagmann[3], P.Richard[3], M.Prior[4], A.S.Schlachter[4], D. Loyd[5], J.Pedersen[6], R.D.DuBois[7], J.A.Tanis[8]

1 Institut für Kernphysik,Universität Frankfurt,D6000 Frankfurt,FRG
2 Gesellschaft für Schwerionenforschung GSI,Darmstadt,FRG
3 Kansas State University,Manhattan,Kansas 66506, USA
4 Lawrence Berkeley Laboratory,Berkeley,California 94720, USA
5 Angelo State University,St. Angelo,Texas, USA
6 University of Aarhus,Aarhus,Denmark
7 Pacific Northwest Laboratory,Richmond,Washington 99352
8 Western Michigan University,Kalamazoo,Michigan

supported by: BMFT, GSI, NATO (grant RG85/0501), DOE

As published recently by DuBois and Toburen [1] the investigation of the velocity dependence of single and double ionisation of helium is an important tool to enhance our understanding of the basic principles of ion atom collisions. Helium is often studied as it is the simplest case where multiple ionisation occurs and also because no Auger decays complicate the collision problem.
For the double ionisation of helium McGuire [3] has shown that two processes should contribute: A single step process, where the projectile interacts with one of the target electrons, and the ejection of this electron induces the ionisation of the second one. An indication of this mechanism is that the double ionisation cross section σ_2 is proportional to the single ionisation cross section σ_1 and to the total electron production cross section σ_T ($\sigma_T = \sigma_1 + 2\sigma_2$).
In the two step process the projectile interacts with the two electrons independently, which means that the Independant Electron Model (IEM) is appropriate for describing this process.
Both mechanisms yield different velocity dependencies [1,3]. In the single step process the ratio $\sigma_T/(\sigma_2)^{\frac{1}{2}}$ behaves like $v^{-1}(\ln(v))^{\frac{1}{2}}$, while in the two step interaction picture $\sigma_T/(\sigma_2)^{\frac{1}{2}}$ is expected to behave like $\ln(v)$ for large v. That means studying the velocity dependencies of the cross section ratios can indicate which mechanism is dominant in which velocity regime.
While DuBois and Toburen [1] have investigated light ions like H, He, Li, C at low energies and low charge states (< 2MeV/u), we contribute valuable information for uranium at the high velocities of 60, 120, and 420 MeV/u (description of experiment in [6]). The figure shows that in the upper velocity regime the data for proton impact [5] behave approximately like $(\ln(v))^{\frac{1}{2}}/v$. In this regime the single step process is dominant.
For higher projectile charges (C^{6+}: ref [2] and [4]) the dependence at the same velocity is more like $\ln(v)$, which indicates that the double step process becomes more important due to the stronger coulomb force. The transition between these two regimes appears to be at higher velocities for higher charge state of the projectile [1].
The present data for uranium show that, although the impact energy is almost relativistic, the single step regime has not yet been reached due to the high Z of the projectile. Thus the interaction time is still long enough to result in a two step process.
For further studies more absolute cross sections σ_1 and σ_2, which the new SIS-ESR facility at GSI can provide, will be extremely valuable to get a more detailed picture of the ionisation process. Especially the fact that the system provides bare uranium from 5 MeV/u up to 500 Mev/u is very important. Experiments to measure these cross sections are under preparation.

[1] R.D.DuBois,L.H.Toburen,Phys Rev A 38, pp3960 (1988)
[2] J.H.McGuire,A.Müller,B.Schuch,W.Groh, E.Salzborn,Phys Rev A 35, pp2479 (1987)
[3] J.H.McGuire, Phys Rev Let 49, pp1153 (1982)
[4] H.Knudsen,L.H.Andersen,P.Hvelplund, G.Astner, H.Cederquist,H.Danared, L.Lijleby,K.G.Rensfeld J Phys B 17, pp3545 (1984)
[5] M.B.Shah,H.B.Gilbody,J Phys B 18, pp899 (1985)
[6] H.Berg,R.Dörner,C.Kelbch,S.Kelbch, J.Ullrich,S.Hagmann,P.Richard, H.Schmidt-Böcking,A.S.Schlachter, M.Prior,H.J.Crawford,J.M.Engelage, I.Flores,D.Loyd,J.Pedersen,R.E. Olson,J Phys B 21,pp 3929 (1988)



$\sigma_T/\sigma_2^{\frac{1}{2}}$ for several bare projectiles on helium

Multiple Ionisation Collision Dynamics for High-Energy Highly-Charged Ion Impact

R.E. Olson*, J. Ullrich
GSI Darmstadt
R. Dörner, E. Forberich, H. Schmidt-Böcking
Universität Frankfurt

For the 1.4 MeV/u U^{32+} + Ne collision system extended calculations were performed in the n-body classical trajectory Monte-Carlo approach [1] (nCTMC) in order to elucidate the dynamics of multiple ionisation in energetic, heavy-ion-atom collisions.

The nCTMC method directly includes all target electrons. The classical treatment is designed to reproduce the quantum-mechanical hydrogenic momentum distribution for the electrons, and uses spectroscopic energy levels to determine the initial electron distributions. All pairwise Coulomb interactions of the projectile and the target nuclei with each other and the electrons are explicitely included in the calculations. This allows a direct determination of the energy and angular differential cross sections for the ejected electrons, the outgoing projectile and recoil-ion without any additional assumptions for a scattering potential. In Fig. 1 calculated differential cross sections in dependence of the relative transverse momentum transfer $p_\perp/p_\parallel$ ($p_\perp$,$p_\parallel$: momentum transverse and parallel to the beam direction) to the recoil-ion (solid line) are shown for different recoil-ion charge states, and reasonable agreement with experimental data (full circles) is observed. Also shown are the theoretical differential cross sections for the projectile scattering (dashed line) which differ by orders of magnitude from the recoil-ion differentials at small momentum transfers i.e. distant collisions (note, for the projectile, $p_\perp/p_\parallel$ equals the projectile laboratory scattering angle and the cross sections are the usual angular differential cross sections). This difference is due to the high degree of ejected electron asymmetry towards the projectile side providing evidence for the importance of explicitely considering the electron momenta for the calculation of the heavy particle scattering. Only for the close collisions at high momentum transfers, where preferentially highly charged target ions are produced, the differential recoil-ion and projectile scattering cross sections do become similar. This indicates that for small impact parameters the ejected electron momenta are of increasingly less importance for the heavy particle deflection. A detailed discussion can be found in Ref. [2].

Calculations for 500 MeV/u U^{92+} on Ne show a similar behaviour: A high degree of ejected electron asymmetry and a strong influence on the heavy particle trajectories. For more than 90 % of all ionizing collisions negative deflection angles of the 120 GeV uranium projectiles are predicted. In order to establish these theoretical results experimentally we have improved the resolution of our spectrometer and transverse momenta corresponding to recoil-ion transverse energies of few meV can be determined [3]. For the collision system above, this sensitivity would be equivalent to an angular measurement of the scattered projectiles with a resolution of 10^{-8} rad (a 10 mm deflection over a distance of 1000 km !). In addition, first coincidence measurements between the emitted electrons and the recoil-ion have been performed and will give direct information on the asymmetry of the electron ejection. Work is in progress to design and assemble the atomic physics external target area for these experiments and first tests of the apparatus will be early next year in Heidelberg and at the UNILAC.

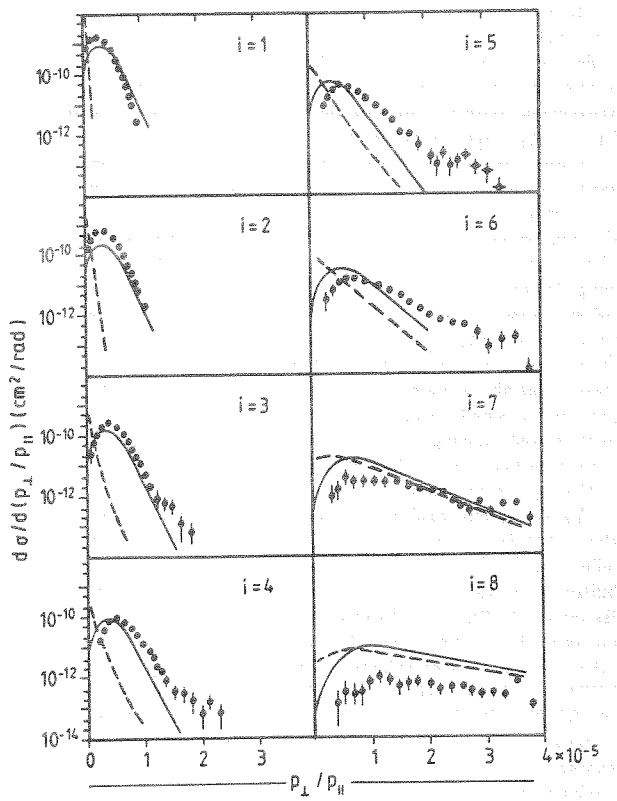


Figure 1: Differential cross sections for the transverse momentum $p_\perp$ of the recoil-ion (full circles: Experiment, solid line: Theory) and the projectile (dashed line: Theory) devided by the parallel momentum of the projectile $p_\parallel$ for different recoil-ion charge states i.

References

[1] R.E. Olson, in "Electronic and Atomic Collisions", edited by H.B. Gilbody, W.R. Newell, F.H. Read, and A.C.H. Smith (Elsevier, Amsterdam, 1988), 271

[2] R.E. Olson, J. Ullrich, H. Schmidt-Böcking, Phys. Rev. A39 (1989) 5572

[3] R. Dörner, J. Ullrich, H. Schmidt-Böcking, R.E. Olson, Phys. Rev. Lett. 63 (1989) 147

*University of Missouri-Rolla, Humboldt Award Fellow

Angular Scattering of Fast Protons by Helium

R.E. Olson*, J. Ullrich,
GSI Darmstadt
R. Dörner, H. Schmidt-Böcking
IKF Frankfurt

Recent experimental data by Giese and Horsdal [1] have displayed a distinct peak at a H^+ scattering angle of ~ 0.9 mrad for the ratio of double to single ionization in MeV H^+ on He collisions. The peak position was found to be independent of the projectile velocity and was unexpected, since it is outside the maximum deflection of 0.545 mrad for a H^+ by a stationary electron.

Several reasons have been given to explain such a peak. In one paper [2] it is postulated that on either side of the maximum the H^+ is deflected by the He nucleus with small momentum transfer with an electron, while at the peak the cross section is dominated by large momentum transfer to an electron; calculations by Reading, Ford and Fang realized a peak at ~ 0.5 mrad. Another model [3] uses a triple-collision hypothesis, H^+-electron, electron-electron, followed by H^+-electron scattering to predict a sharp peak at 0.96 mrad. However, cross-section calculations were not performed by the author. In contrast to the above, we give a simple explanation which is that near the peak and at smaller angles, the double ionization is dominated by two uncorrelated ionizing collisions with the electrons at large impact parameters where the H^+ deflection by the He nucleus is small compared to that by the electrons.

To verify our explanation, we have employed three successive classical-trajectory Monte Carlo (CTMC) calculations [4]. They are as follows: 1CTMC — one-electron calculation with the transition probabilities evaluated within the independent electron model to reflect the He target, 2CTMC — a two-electron calculation where both electrons are explicitly included, but the electrons are independent of one another as in a Hartree calculation without the $1/r_{12}$ interaction, and bCTMC — a two-electron calculation within the Bohr model where the full Hamiltonian with the $1/r_{12}$ electron-electron repulsion is incorporated. The 1CTMC and 2CTMC calculations are similar to one another in that the impact parameter dependence of the single- and double-ionization transition probabilities are the same. However, proton deflection by the second electron will be explicitly included in the 2CTMC model, while not in the 1CTMC model. Calculations with the Bohr He atom, bCTMC, further include the electron-electron dynamical correlation. This latter interaction is required by the model of Vegh [3] in order to obtain a peak in the ratio of double to total ionization. Thus, if the Vegh model is correct, the peak will only be present in the bCTMC results.

The calculated double-ionization fraction for 1.0-MeV collisions from the various calculations are compared to the experimental results (solid line) of Giese and Horsdal [1] in Fig. (1). In Fig. 1(a) are shown the coupled-channel results of Reading, Ford, and Fang [2] (dashed line). The overall magnitude of this calculation is in good agreement with the data, but the peak is incorrectly predicted at ~ 0.5 mrad.

Figure 1(b) presents two sets of independent electron calculations. In the first, the 1CTMC method, the conventional one-electron independent particle model is used to calculate double-ionization transition probabilities from the single-ionization values. A very slight peak around 0.5 mrad is observed before the ratio rises to a constant value for $\theta > 1.0$ mrad (open circles).

Also shown in Fig. 1(b) are the two-electron 2CTMC results (solid circles). Although the large-angle values are similar since there is a direct relationship between impact parameter and scattering angle, there are major differences with the 1CTMC calculations at $\theta < 1.5$ mrad. It should be reemphasized that the single- and double-ionization transition probabilities are identical as a function of impact parameter for both the 1CTMC and 2CTMC calculations. Thus, differences in the angular scattering directly reflect the additional electron-scattering center. We find the second electron leads to an enhancement in the ratio around ~ 1.0 mrad giving rise to a peak, and a decrease at $\theta < 0.2$ mrad. An electron-electron $1/r_{12}$ interaction is not required in order to realize the maximum. Thus, the model of Vegh [3] is not supported by these calculations. To complete our study, the Bohr He model was also used to calculate the ratio, Fig. 1(c), and the maximum is again realized. In Fig. 1, all the classical results have been divided by three in order to normalize the $\theta > 2.0$ mrad data ($b \rightarrow 0.0a_0$).

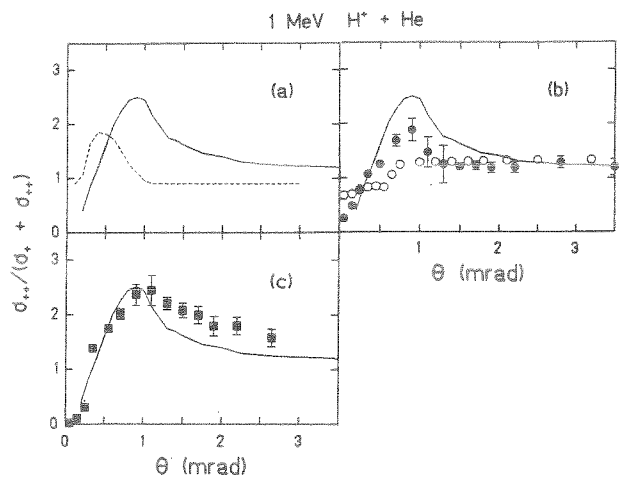


Figure 1: Fraction of double ionization to total ionization as a function of H^+ scattering angle. The solid line in each of the figures is the fit by Giese and Horsdal to their experimental data (Ref. 1).

In conclusion, the classical calculations presented here indicate that a peak at ~ 0.9 mrad in the angular fraction of double ionization to total ionization is realized within a simple model of an uncorrelated collision of the H^+ with the He atom's two electrons. The results strongly suggest that complicated scattering processes or quantal interference mechanisms are not necessary to understand the collision dynamics. The results demonstrate the invalidity of a central potential approach to ionization reactions at intermediate collision energies, and the necessity of including both the heavy particles and the electrons in determining their transverse momentum balance.

The correct calculation of the peak position is an important test and demonstrates the capability of the CTMC method to describe the collision dynamics of multiple target ionisation. The results underline previous predictions on the importance of the projectile target – electron scattering for the deflection of GeV uranium ions in collisions with rare gas targets. Experiments are prepared in order to investigate such processes at the new SIS facility at GSI.

References

[1] P. Giese and E. Horsdal, Phys. Lett. 60, 2018 (1988)

[2] F. Reading, A.L. Ford, and X. Fang, Phys. Rev. Lett. 62, 245 (1989)

[3] L. Vegh, J. Phys. B22, L35 (1989)

[4] R.E. Olson, J. Ullrich, R. Dörner, and H. Schmidt-Böcking, Phys. Rev. A40, 2843 (1989)

*University of Missouri-Rolla, Humboldt Award Fellow

Measurement of the 1s Lambshift in Hydrogen-like Nickel

H.F. Beyer*, R.D. Deslattes+, P. Indelicato+, K.D. Finlayson* and D. Liesen*
*GSI Darmstadt and +NIST Washington D.C.

In the past several years, the measurement of radiative corrections in highly charged heavy ions has gained an increasing interest. The 1s Lambshift which is the largest QED correction, was measured by Wieman and Hänsch [1] in the hydrogen atom by double-laser spectroscopy. It has been measured in hydrogen-like iron [2] and krypton [3] using beam-foil spectroscopy, for chlorine in a Tokamak [4], and for argon recoil ions [5]. Previously, also decelerated bare chlorine ions were used [6].

Here, we report on an experiment using decelerated bare nickel ions. This technique conceptually avoids spectator-electron contamination by making use of a prevailing one-electron transfer in a thin target gas. The Doppler effect, which presents a severe problem when observing x rays from a fast source, is brought under control by measuring the x-ray spectra at four different ion-beam velocities.

Nickel ions are accelerated in the UNILAC up to a specific energy of 11.4 MeV/amu and are then stripped in a 650 μg/cm^2 thick carbon foil giving a naked fraction, Ni^{28+}, of about 10 %. The single-resonator structures at the end of the UNILAC are used to decelerate the beam down to final specific energies which for the bare ions are 8.4, 6.7, 5.2, and 3.1 MeV/amu. The Ni^{28+} ion beams are magnetically selected and directed to a long straight experimental section. There a 15 m long time-of-flight measuring device [7] allows a measurement of the ion-beam velocity with a precision of $\frac{\Delta\beta}{\beta} \lesssim 5 \cdot 10^{-4}$. The ion beam collimated to a divergence of less than 0.7 mrad passes through a differentially pumped gas cell containing argon target gas at a pressure of about 0.2 mbar. The ion current ranges from 150 to 600 particle nA. The 2p states of interest in hydrogen-like Ni^{27+} are populated by one-electron capture mainly into higher-n states followed by cascade transitions.

The x rays of about 8 keV energy are diffracted in second order by a Ge220 crystal bent cylindrically to a radius of 976 mm. As an x-ray detector, a two-dimensional position-sensitive proportional counter with a split back-gammon type cathode is used. The x-ray spectra originating from the fast ion beam are steadily compared to the Cu Kα spectrum serving as a wavelength standard. This is achieved by placing the Cu anode of a 15 keV x-ray generator close to the gas cell. A chopper wheel synchronized to the time structure of the UNILAC beam transmits copper x rays only during the 15 ms long off periods of the pulsed ion beam.

The pattern of the x-ray image in the Johann geometry, as used in the present experiment, was studied in detail previously [8] for both a stationary and a fast-beam x-ray source. In that study an analytical formula for the position of the x-ray image in the detector's x-y plane was given and was shown to agree with detailed Monte Carlo ray-tracing calculations on the 1 ppm level of wavelength accuracy.

The figure shows the Lyman $\alpha_{1,2}$ lines of Ni^{27+} relative to the Cu Kα_1 line at the four different beam energies. Going from low to high beam energy the Lyman α doublet moves towards lower x (corresponding to lower x-ray energy) due to the Doppler effect at $\sim 90^0$ observation angle. Also shown is the result of a simultaneous fit to the Lyman α_1 and α_2 lines according to the analytical formula. From the fit the Lyman α_1 wavelength is obtained

$$\lambda_{Ni\alpha_1} = 1.530336(15)\text{Å}$$

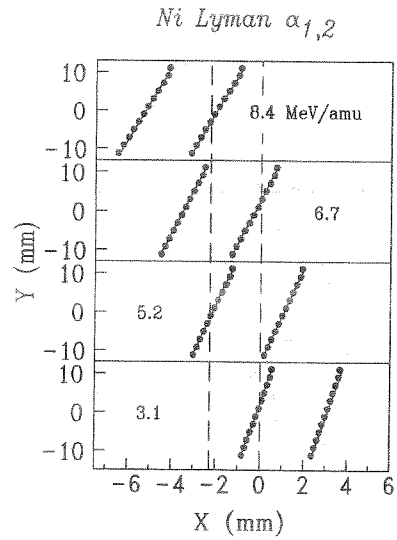


Figure 6: The two-dimensional image of the Lyman $\alpha_{1,2}$ doublet of Ni^{27+} at four different beam energies.

The corresponding experimental 1s Lambshift is 5.07(8) eV which agrees well with the theoretical value of 5.096(4) calculated by Johnson and Soff [9].

References

[1] C. Wieman and T. Hänsch, Phys. Rev. A22 (1980) 192

[2] J.P. Briand, M. Tavernier, P. Indelicato, R. Marrus and H. Gould, Phys. Rev. Lett. 50 (1983) 832

[3] M. Tavernier, J.P. Briand, P. Indelicato, D. Liesen and P. Richard, J. Phys. B18 (1985) L327

[4] E. Källne, J. Källne, P. Richard and M. Stöckli, J. Phys. B17 (1984) L115

[5] H.F. Beyer, R.D. Deslattes, F. Folkmann and R.E. LaVilla, J. Phys. B18 (1985) 207

[6] R.D. Deslattes, R. Schuch, and E. Justiniano, Phys. Rev. A32 (1985) 1911

[7] H. Geissel, Y. Laichter, R. Albrecht, T. Kitahara, J. Klabunde, P. Strehl and P. Armbruster, Nucl. Instr. and Meth. 206 (1983) 609

[8] H.F. Beyer and D. Liesen, Nucl. Instr. and Meth. A272 (1988) 895

Measurement of the Fine Structure Splitting in Helium-like Ag^{45+}

Richard Marrus,(1) Alexandre Simionovici,(2) Paul Indelicato,(3) Daniel D. Dietrich,(2) Pierre Charles, Jean-Pierre Briand,(4) Keith Finlayson, Fritz Bosch, Dieter Liesen(5) and Fernando Parente(6)

(1) *University of California, Berkeley*; (2) *LLNL*; (3)*NIST, Washington*; (4)*Université P. et M. Curie, Paris*; (5) *GSI*; (6)*Universidade de Lisboa, Portugal*

The fine-structure splittings of the $(1s)(2p_{1/2})2^3P_J$ states ($\Delta E_{J-J'}$) of helium-like ions are determined by the electron-electron interaction. The measurement of these splittings therefore provides a test of the theory of this interaction in the simplest atomic system where it can be observed. We have performed an experiment measuring the absolute value of ΔE_{0-1} based on the hyperfine-quenched lifetime of the 2^3P_0 state of He-like Ag.

Hyperfine quenching of the 2^3P_0 state in He-like ions results from mixing with the 2^3P_1 by the hyperfine interaction, which can then decay approximating an E1 transition to the 1^1S_0 ground state. For He-like silver, the 2^3P_1 and 2^3P_0 levels are nearly degenerate and lie relatively far away from other levels making the following an excellent approximation:

$$\begin{vmatrix} E_0 + i\Gamma_0/2 - \lambda & W_{10} \\ W_{10} & E_1 + W_{11} + i\Gamma_1/2 - \lambda \end{vmatrix} = 0 \ , \quad \text{(Eqn. 1)}$$

where $W_{10} = \langle 2^3P_0 | H_{hfs} | 2^3P_1 \rangle$, $W_{11} = \langle 2^3P_1 | H_{hfs} | 2^3P_1 \rangle$ and H_{hfs} is the hyperfine Hamiltonian. The real and imaginary parts of $\lambda_0(\lambda_1)$ are the perturbed energy and lifetime of the $2^3P_0(2^3P_1)$ level respectively. It is possible to calculate W_{10}, W_{11}, Γ_0, Γ_1 with good accuracy, and with a knowledge of the 2^3P_0 lifetime, the fine structure splitting $|\Delta E_{0-1}|$ can be extracted.

The experiment was performed using a 18.6 MeV/u ^{107}Ag beam from the UNILAC. The apparatus that was employed is illustrated in Fig. 1: The beam of the H-like Ag (entering from left) passes through a "dressing" foil (250 $\mu g/cm^3$ carbon) to produce excited He-like Ag. Radiation from the subsequent decay of the excited states is detected downstream of the foil by two Si(Li) detectors mounted on opposite sides of the beam. One of the detectors is fixed while the other is moveable, the time of flight data being obtained by measuring the ratio of counts in the movable detector relative to the counts in the fixed detector as a function of the position of the movable detector. This arrangement allows normalization directly to the ion population in the excited state of interest and has the additional advantage of being insensitive to changes in the shape and state of the dressing foil during the experiment.

A sample spectrum that was obtained with the fixed detector is shown in Fig. 2. The large peak is composed of the unresolved M1 $2^3S_1 \rightarrow 1^1S_0$ and the hyperfine-quenched $2^3P_0 \rightarrow 1^1S_0$ transitions. The peak also exhibits a small high-energy shoulder arising from counts due to the cascade-fed transitions $2^3P_2 \rightarrow 1^1S_0$ and $2^1P_1 \rightarrow 1^1S_0$. A double-humped peak arising at energies around 4.10 keV is also in evidence and is due to $n=3 \rightarrow n=2$ transitions resulting from cascades down the yrast chain.

The analysis of the data for each position of the movable detector proceeded as follows: The $2 \rightarrow 1$ peak was deconvoluted into two gaussians so that unwanted counts from the high-energy shoulder could be removed. The remaining line consisted of counts from the hyperfine-quenched $2^3P_0 \rightarrow 1^1S_0$ transition and the M1 transition $2^3S_1 \rightarrow 1^1S_0$, plus background counts (long lived cascades to the 2^3S_1 level appeared as a contribution to the constant background). The counts in the remaining line were then normalized to the counts in the fixed detector and the ratio plotted versus position of the movable detector to obtain a decay curve. Various ways of fitting the decay curve were tried. The most successful used two exponentials plus a constant background, the results of which are shown in Fig. 3. This yielded values of 207±62 and 666±15μm for the decay lengths of the 2^3P_0 and 2^3S_1 states, respectively. Using the measured beam velocity the following lifetimes were obtained:

$\tau(2^3P_0) = (3.551 \pm 1.06) \times 10^{-12}$ sec ; $\tau(2^3S_1) = 1.14(2) \times 10^{-11}$ sec.

The measured 2^3S_1 lifetime agrees well with that given by the theory of relativistic M1 decay as 1.117×10^{-11} sec. From the measured value for $\tau(2^3P_0)$ and using Eqn. 1, the fine structure splitting was calculated as:

$$|\Delta E_{0-1}| = 0.74^{+0.16}_{-0.19} \text{ eV}$$

A theoretical value of $|\Delta E_{0-1}| = 0.753$ eV has been calculated based on the MCDF method[1] and also Drake has reported a value of $|\Delta E_{0-1}| = 0.933$ eV based on variational methods[2]. The experimental result is in good agreement with the MCDF value and in fair agreement with the variational value. Further experiments are planned which should lead to a substantial reduction in the error. It is however notable that the error in the $|\Delta E_{0-1}|$ splitting is already much smaller than the natural linewidth of 1.06 eV ($=\Gamma_1$) associated with this interval.

[1] P. Indelicato and J. P. Desclaux (private communication)

[2] G. W. F. Drake, Can. J. Phys. 66, 586 (1988)

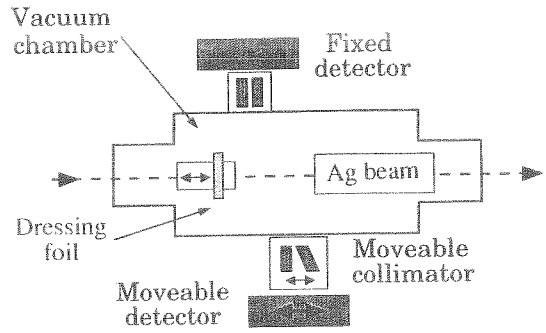


Fig. 1 Schematic of the apparatus

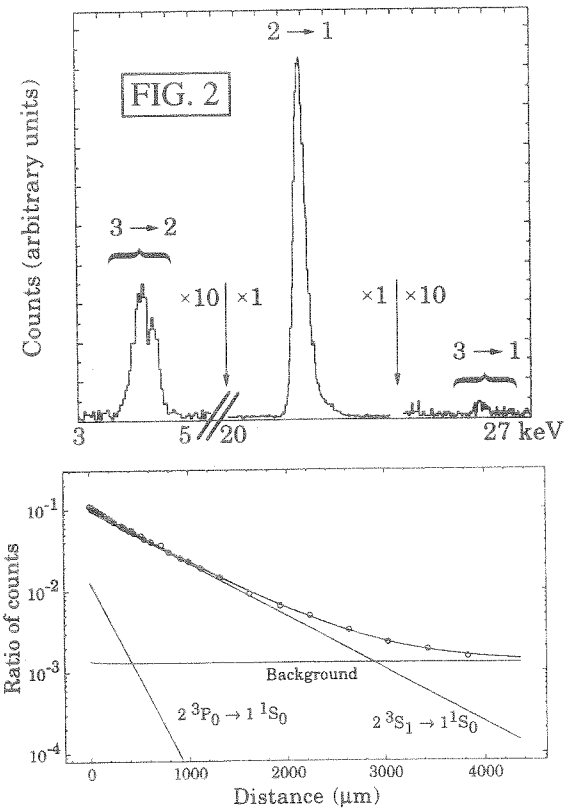


FIG. 3. Decay curve showing the various contributions to the total fit.

Two-Photon Decay of the $1s2s^1S_0$ State in $_{36}Kr^{+34}$ Produced by Resonant Transfer and Excitation

E.A. Livingston*, Ch. Kozhuharov, P.H. Mokler†, Th. Stöhlker†, J. Ullrich
GSI Darmstadt

The $1s2s^1S_0$ state in helium-like ions can only decay to the ground-state via a 2E1 transition, i.e. a simultaneous emission of two photons with continuous energy distributions and the sum energy given by: $\hbar\omega_1 + \hbar\omega_2 = E_i - E_f = K_\alpha$. The spectral distribution of the continuum is influenced by relativistic effects and electron correlations. Measurement of the excitation function for Resonant Transfer and Excitation (RTE) in $_{32}Ge^{+31} \rightarrow H_2$ collisions has shown that RTE is an effective method to populate the $2s2p^1P_1$ level and to study the two-photon decay [1].

In order to determine the various contributions at a higher Z system we measured the two-photon decay of the 2^1S_0 state in Kr^{+34} using the x-ray/x-ray/particle (X/X/P) coincidence technique [1]. This state was produced in $Kr^{35+} \rightarrow H_2$ collisions at the KLL-resonance (16.7 MeV/u) associated with the capture of one electron by the projectile. The cluster plot of two coincident photons is shown in Fig. 1. All events with the same sum energy equal $K_\alpha = 13.4$ keV appear on the diagonal. Under this energy condition the resulting spectral distribution of the 2E1 decay for one detector is shown in Fig. 2 together with the expected theoretical lineshape [2] which is folded with the detector and the electronic response function.

In addition to the expected continuum the spectral distribution shows sharp lines at low energies and broadened structures at the high energy side. All these structures can be explained by radiative electron capture (REC) into outer shells (M,N,O,...) and a following cascading of the electron into the L shell which leads to a coincident emission of two x rays. Because of the KLL-resonance condition for the beam energy (adiabaticity parameter $\eta = 0.5$) the sum energy of both photons also equals K_α as is illustrated in Fig. 3b.

REC into outer shells and following radiative decay directly into the K-shell can also be seen in the cluster plot at the diagonal with $E_x = 2\ K_\alpha$ (compare Fig. 3a). (This diagonal includes the $K_\alpha - K_\alpha$ coincidence events.) These contributions are cut off at an energy which corresponds to REC into high Rydberg states.

For higher Z it should be possible to separate more clearly the REC contributions from the 2E1 decay spectrum. Moreover, we like to point out that the X/X/P coincidence method is quite sensitive to trace rare processes like K-REC and simultaneous K- to L-shell excitation (see the faint structures in Fig. 1).

Further measurements are planned to study the 2E1 decay for medium as well as for high Z helium-like ions at UNILAC- as well as at ESR-energies.

References

[1] P.H. Mokler et al., Radiation Effects and Defects in Solids, Vol. 110 (1989) pp. 39 - 43 and
S. Reusch GSI-88-19 (1988)

[2] G.W.F. Drake, private communication

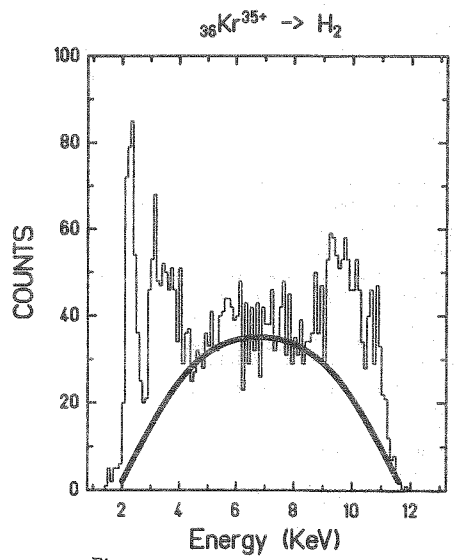


Figure 2:

*on leave from Notre Dame University, Notre Dame, Indiana 46556
†associated with University Gießen

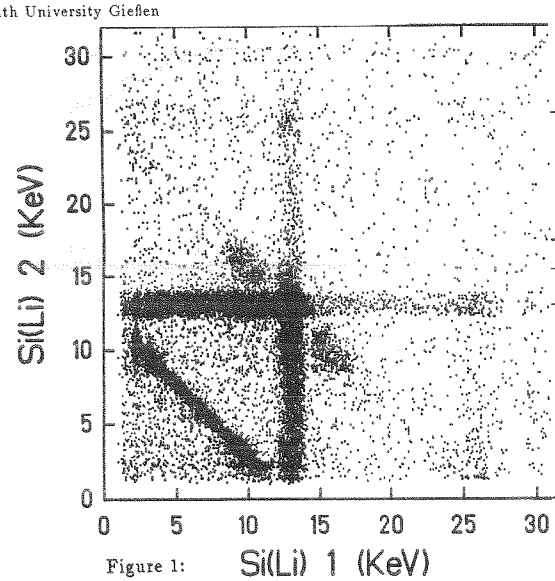


Figure 1:

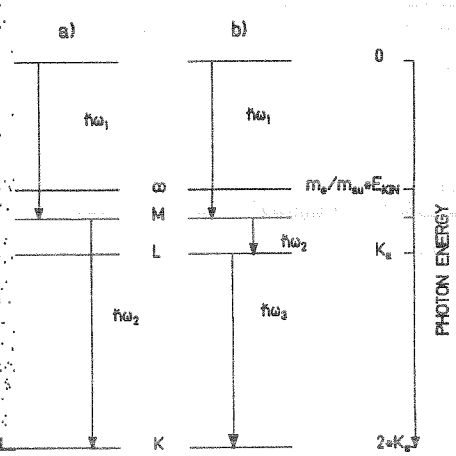


Figure 3:

The $2s^2\ ^1S_0$ - $2s2p\ ^3P^o_1$ Intercombination Transition in Xe^{50+} [B]

G. Möller, E. Träbert, C. Wagner, P.H. Heckmann
Experimentalphysik III, Ruhr-Universität Bochum
J.H. Blanke
Fachbereich Physik, Universität Kassel
A.E. Livingston
University of Notre Dame, Indiana (USA)
P.H. Mokler
GSI Darmstadt

The previously described experiment [1] on forbidden (M1) and intercombination (E1) transitions in highly charged Xe ions has been continued with a $^{132}Xe^{30+}$ ion beam of energy 14.7 MeV/u. This higher energy, compared to 11.5 MeV/u in the previous experiment, was chosen to increase the relative abundance of Be-like ions (Xe^{50+}) after passage through a 700 µg/cm² thick C-foil.
As a result of this measurement, the wavelength of the $2s^2\ ^1S_0$ - $2s2p\ ^3P^o_1$ intercombination transition could be determined to (9.79 ± 0.04) nm. An isoelectronic comparison between theoretical predictions and experimental measurements of energy differences of the $2s^2\ ^1S_0$ - $2s2p\ ^3P^o_1$ intercombination transition is shown in fig. 1.

It is obvious that the nonrelativistic calculations [2,3] underestimate the $2s^2\ ^1S_0$ - $2s2p\ ^3P^o_1$ term difference for Z ≥ 18, whereas a relativistic MCDF calculation in which the Lamb shift is neglected [3], overestimates it for the whole range of nuclear charge Z. Only the MCDF calculations by Cheng et al. [4], which include the Lamb shifts of the $1s_{1\ 2}$, $2s_{1\ 2}$ and $2p_{1\ 2}$ electrons, seem to converge to the experimental values for increasing Z in the range 6 ≤ Z ≤ 29. This convergence may be related to the decreasing influence (electron correlation) of the neglected configurations with n ≥ 3.
Although the experimental values for the higher nuclear charges (Z = 36,42,54) agree with the calculations by Cheng et al. [4], it is not yet possible to establish a reliable trend of the (o-c)-values in this Z region. More data points with smaller error bars are evidently necessary.
Concerning the $2s^2\ ^1S_0$ - $2s2p\ ^3P^o_1$ transition probabilities, there are only very few experimental values (for C (using an ion trap), Fe an Kr (using fast ion beams), see fig. 2). The present measurement for Xe, yielding a transition probability of A = (2.13 ± 0.23)·10⁹ s⁻¹, can clearly distinguish between the different theoretical values [2,3,4] and agrees only with the MCDF calculations by Cheng et al. [4].

[1] G. Möller et al., GSI Scientific Report 1988, 171
[2] A.W. Weiss, in Sellin and Pegg (eds.) "Beam-Foil Spectroscopy", Vol. 1, 51, Plenum Press, New York (1976)
[3] L. Armstrong et al., Phys. Rev. A14, 1114 (1976)
[4] K.T. Cheng et al., At. Data Nucl. Data Tables 24, 111 (1979)
[5] B. Edlén, Phys. Scr. 28, 51 (1983)

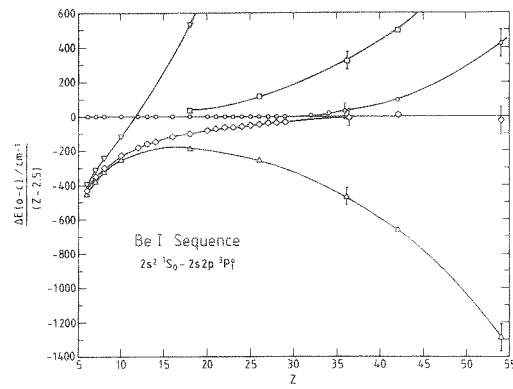


Fig. 1: Scaled observed - calculated (o-c) energy differences of the $2s^2\ ^1S_0$ - $2s2p\ ^3P^o_1$ intercombination transition in the BeI isoelectronic sequence (6 ≤ Z ≤ 54)

Theory:
(□) intermediate coupling — Weiss[2]
(▽) MCHF + BREIT — Armstrong et al.[3]
(△) MCDF + BREIT + — Armstrong et al [3]
(◇) MCDF + BREIT + LAMB — Cheng et al.[4]

semiempirical approach:
(o) Edlén [5]

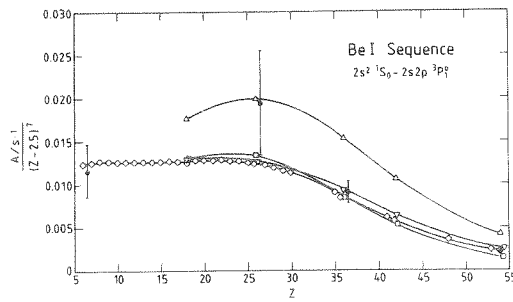


Fig. 2: Scaled transition probability of the $2s^2\ ^1S_0$ - $2s2p\ ^3P^o_1$ intercombination transition in the BeI isoelectronic sequence (6 ≤ Z ≤ 54)

Experiment:
(●) (Z = 50 this work)

Theory:
(□) intermediate coupling — Weiss [2]
(△) MCDF + BREIT, velocity form — Armstrong et al. [3]
(▽) MCDF + BREIT, length form — Armstrong et al. [3]
(◇) MCDF + BREIT + LAMB — Cheng et al. [4]

The GSI 5m grazing incidence spectrometer: First beam-foil measurements at 1.4 Mev/u [G]

B. Kraus and K.-H. Schartner
1. Physikalisches Institut, Universität Gießen
F. Folkmann
Institute of Physics, University of Aarhus, Denmark
A. E. Livingston* and P. H. Mokler
GSI Darmstadt

The GSI 5m grazing incidence spectrometer contains originally a double scan detector which is clamped on a chassis beam (Fig. 1.)[1]. Additionally we have equipped the spectrometer with a two dimensional position sensitive detector (PSD). It can be positioned along the Rowland circle by stepmotor driven translation and rotation stages. The position relative to the instrument beam is controlled by position encoders[2].

We have recorded beam foil spectra of Xe, Ni, Ar and Ne at the GSI Stripperhalle. The measurements include both position sensitive and scanned spectra in the wavelength range 40-350Å. The beam foil exitation at 1.4 MeV/u produces atomic transitions in ionization stages ranging from hydrogenlike Ne^{9+} to titaniumlike Xe^{32+}.

Fig. 2 shows a neon beam foil spectrum assembled sequentially from 9 exposures with the position sensitive detector. It was produced by Ne^{6+} impinging on a carbon foil of thickness 25µg/cm². Lines involving n=2-n=3 and n=2-n=4 transitions in hydrogenlike, heliumlike and lithiumlike neon are dominating in the wavelength range 48-110Å. This spectrum establishes the capabilities of the spectromter for detecting low wavelengths.

The beam foil spectrum of highly ionized xenon was observed between 85-270Å, as shown in fig. 3. This spectrum, also assembled from 9 position sensitive spectra, is dominated by transitions between low lying Rydberg states with Δn=1 and Δn=2.

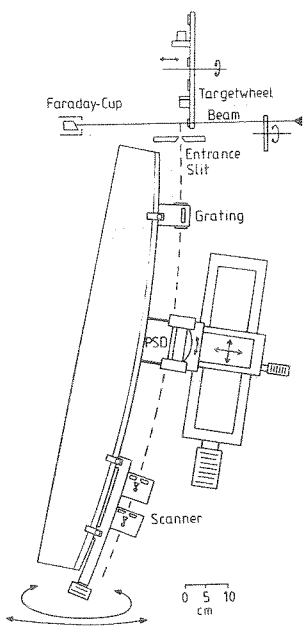


Fig. 1. Scheme of the GSI 5m grazing incidence spectrometer

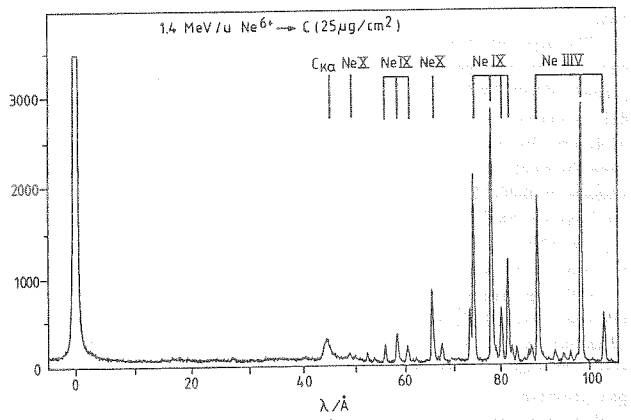


Fig. 2. Beam foil spectrum of 1.4 Mev/u neon

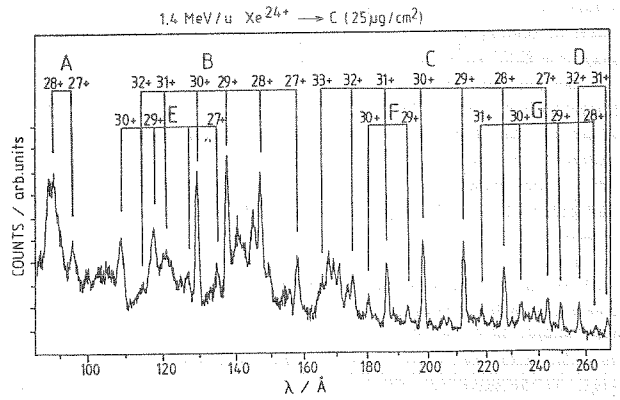


Fig. 3. Beam foil spectrum of 1.4 Mev/u xenon. The letters on the group peaks correspond to the following transitions: A: n=5-6, B: n=6-7, C: n=7-8, D: n=8-9, E: n=7-9, F: n=8-10, G: n=9-11.

The spectrometer is currently prepared for measurements of Δn=0 transition energies in very heavy heliumlike and lithiumlike ions in order to test theoretical calculations of relativistic, QED and electron correlation contributions to these fundamental atomic structures.

1 R. J. Speer, Space Sci. Instrum. 2, pp. 463-488 (1976).
2 B. Kraus, K. - H. Schartner, F. Folkmann, A. E. Livingston and P. H. Mokler, Proc. SPIE 1159 (1989).

* On leave from: Department of Physics, Notre Dame University, Indiana, USA.

Capture of Free Electrons into U^{28+} Ions: A Merged Beams Experiment at the UNILAC [G,B]

S. Schennach, A. Müller, M. Wagner, J. Haselbauer, O. Uwira, W. Spies, N. Djurić*, B. Jelenković*
Institut für Kernphysik der Universität Gießen
E. Jennewein, R. Becker, M. Kleinod, U. Pröbstel, I. Müller
Institut für Angewandte Physik der Universität Frankfurt
N. Angert, W. Enders, J. Klabunde, P.H. Mokler, K. Poppensieker, P. Spädtke, M. Terasawa†, B. Wolf
GSI Darmstadt

During the last year, the electron-ion merged beams setup [1] at the UNILAC has been completed. The "electron target" was installed and during a parasitic beam time first measurements could be carried out.

The electron target is a dense electron beam produced inside a super-conducting solenoid with a field of up to 1 Tesla. The cathode is placed off axis inside the solenoid so that a strong transverse magnetic field is needed to bend the electron beam onto the axis. Over a length of 45 cm electron and ion beams are merged. Behind this interaction zone the electrons are deflected into a water cooled collector by a second transverse field. The transverse magnetic fields are so strong that even ion beams with UNILAC energies are deflected considerably and a correction becomes necessary. This correction can be accomplished with three magnetic steerers before and three behind the electron target.

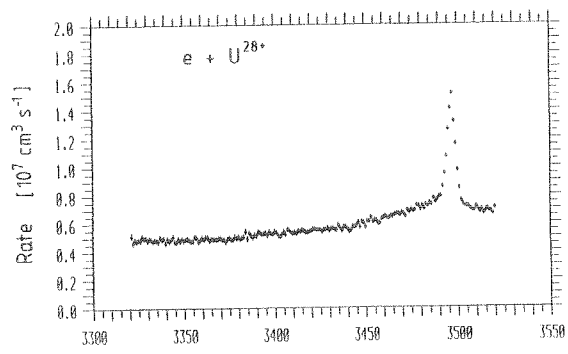
Although the electron beam is extremely dense (up to 10^{10} cm^{-3}) the event rates in interacting particle beams are usually so small that experiments can only be performed under ultra-high-vacuum conditions. The setup of the beamline (Z3) was planned to provide residual gas pressures in the 10^{-10} mbar range. During the test experiments with both beams "on" pressures around 1×10^{-10} mbar were obtained over a distance of about 15 m of beam line. Proper performance of the six steering magnets needed to merge and demerge the beams could also be demonstrated. This was controlled by collimating the ion beam with two apertures before and behind the interaction region (3 mm maximum diameter, 450 mm apart) and observing the position of an attenuated ion beam with a position sensitive detector. Bending of the beam by increasing the solenoid current (and hence also the transverse magnetic field) could be compensated by using the (rotatable) steerers.

The position sensitive detector is based on a chevron assembly of microchannel plates. Instead of a normal voltage of about 2200 V across the two plates needed for detection of slow single electrons, the energetic ions from the UNILAC need only 2/3 of this voltage for an efficient detection. At a voltage of 1400 to 1500 V across the plates, background from low-energy electrons or photons is almost completeley suppressed.

In the test experiment, a beam of 6.3 MeV/u U^{28+} ions was merged with an electron beam of energies between 3325 eV and 3525 eV. The electron density amounted to 4×10^8 cm^{-3}. By scanning the electron energy back and forth between the above limits a spectrum was recorded with the number of U^{27+} ions versus electron laboratory energy. At the same time the parent ion current was monitored and the charge accumulated per energy interval was also stored in a spectrum.

Figure 1 shows the experimental rate $< v\sigma >$, i.e. electron capture cross section times relative velocity, averaged over the experimental velocity distribution as a function of electron laboratory energy. Background, e.g. from residual gas collisions is not subtracted.

At an electron energy of about 3500 eV electrons and ions travel at the same speed which results in zero energy $E_{c.m.}$ in the center-of-mass (c.m.) frame. When $E_{c.m.} = 0$ eV the cross section for radiative electron capture (REC) is infinite whereas the observed maximum rate depends on the energy spread in the experiment. The rate measured in this experiment with U^{28+} exceeds that expected [2] for a completely flattened 0.2 eV energy distribution in $e + U^{92+}$ collisions by a factor 2.5. The unexpected size might be due to a very strong dielectronic recombination resonance at $E_{c.m.} \approx 0$ eV. Another explanation would be an energy spread considerably smaller than 0.2 eV in the experiment. The peak in the experimental (laboratory frame) spectrum is about 5.3 eV wide. Under the assumption that this width is only due to spreads in the longitudinal components of beam velocities the width transforms to less than 1 meV in the c.m. frame. If there is also a transverse velocity spread contributing to the observed 5.3 eV, the longitudinal energy spread in the c.m. frame is even less, however, the transformation does not influence the energy spread due to a transverse velocity distribution. For the transverse energy spread one expects 0.1 eV at best for a cathode operating at a temperature of roughly 1100 K. The next beam time will hopefully bring a clarification of some of the open questions. In particular we hope to measure the radial energy spread in the electron beam by observing dielectronic recombination resonances at non-zero energies.



References

[1] A. Müller, S. Schennach, W. Spies, N. Djurić, R. Becker, E. Jennewein, M. Kleinod, K. Pröbstel, D. Brill, I. Müller, N. Angert, H. Emig, W. Enders, J. Klabunde, P.H. Mokler, K. Poppensieker, P. Spädtke, B. Wolf, GSI Scientific Report 1988, GSI-89-1, p. 363

[2] D. Liesen and H.F. Beyer, "On the Radiative Capture of Free Cooling Electrons: Total and Differential Recombination Coefficients", GSI-ESR/86-04 (1986)

*Permanent address: Institute of Physics, P.O. Box 57, 11001 Belgrade, Yugoslavia

†Permanent address: Himeji Institute of Technology, 2167 Shosha Himeji Hyogo 671-22, Japan

Dielectronic Recombination of H-like and He-like ions at the TSR[B,G]

G.Kilgus*, D.Habs, E.Jaeschke, D.Krämer, D.Schwalm, M.Steck and A.Wolf
Physikalisches Institut der Universität Heidelberg and Max-Planck-Institut für Kernphysik
R.Schuch
Manne-Siegbahn-Institute, Stockholm, Sweden
A.Müller and M.Wagner
Institut für Kernphysik, Universität Giessen

At the Test Storage Ring in Heidelberg, investigations of dielectronic recombination (DR) of low Z hydrogen- and helium-like ions have been performed, employing the electron cooling device as a target of free electrons. In particular, absolute rates of charge changed ions due to DR of O^{7+}[1], C^{5+} and C^{4+} have been measured with high energy resolution. The charge changed ions were separated from the main beam in the first bending magnet downstream of the cooler, and detected with a 20mm diameter microchannel plate. Typically, 5×10^7 ions have been stored and cooled by matching the ions and electrons velocities. Then the electron energy was increased to fulfill the resonance condition for DR and varied in small steps while the corresponding ion rate was recorded. After about 30s the electron energy was lowered again to recool the beam. A new beam was injected after three cycles of DR measurement and cooling. Fig.1a shows the resulting spectrum for the O^{7+} case, where the background due to electron capture in the residual gas has already been subtracted. According to the reaction

$$O^{7+}(1s) + e^- \rightarrow O^{6+}(N\ell n\ell') \rightarrow O^{6+}(1s^2) + h\nu$$

the prominent structures belong to a Rydberg series of doubly excited states, where the inner electron occupies the $N = 2$ shell and the outer electron occupies the same or a higher n shell up to the series limit. Smaller structures appear at higher energies, which are due to resonances with $N \geq 3$. Owing to the low energy spread of the electrons, compared to other setups [2], individual states of the $Nn = 22$ resonances could be resolved for the first time. The width of the measured peaks of $\approx$ 2eV originates in the size of the ion beam (6mm during DR measurement) within the space charge potential of the electron beam. Fig.1b shows a theoretical calculation of the DR cross section convoluted with a 2eV Gaussian [3]. The Hartree-Fock calculation which uses intermediate coupling and allows for configuration mixing, nicely reproduces the energetic positions as well as the absolute height of the spectrum, although there are small deviations at the low lying Rydberg states (23...25).

The resonance strength of the high Rydberg states can be predicted with a simple scaling law. The DR cross section is proportional to $\sigma_{DR} \propto A_a A_r/(A_a + A_r)$, where A_a and A_r are autoionization and radiative width, respectively. Considering that the autoionization width strongly decreases beyond a certain orbital momentum ℓ_0 and using the relation $A_a(n,\ell) \propto n^{-3}$ for $\ell \leq \ell_0$ and $A_r(n) = const$, one gets $\sigma \propto (n^3 + n_0^3)^{-1}$, where the parameter n_0 is defined by $\Sigma_\ell A_a(n_0,\ell) = A_r$. A superposition of resonance curves according to this scaling law fits the measured rate perfectly. Due to the drastic decrease of the cross section as function of n, only states up to $n_{max} \approx 35$ contribute to the measured rate. The experimental conditions allowed for the detection of all resonances because the limit for the maximum observable n due to field ionization was estimated to be $n_{max} = 69$.

The helium-like ion C^{4+} exhibits a quite different behaviour. For the $N = 2$ series the presence of the additional $1s$ electron causes the formation of four Rydberg series corresponding to the four possible configurations $1s2s(^{1,3}S)$ and $1s2p(^{1,3}P)$ of the two inner electrons. The ^1P series dominates the spectrum (fig.2) because the stabilizing radiative transition $1s2p(^1P) \rightarrow 1s^2(^1S)$ is favoured. It is remarkable that the measured cross section drops off when approaching the series limit, while - based on the measured C^{5+} spectrum - one would have expected an increase. The decrease is probably due to the interaction of the resonance states with continuum states of the other Rydberg series, which enhances the autoionization probability of the intermediate states and thus reduces the recombination cross section. Detailed calculations of the cross section are in progress.

[1] G.Kilgus et al., submitted to Phys. Rev. Lett.
[2] D.R.Knappet et al., Phys. Rev. Lett. **62**, 2104 (1989).
[3] D.C. Griffin and M.S. Pindzola, priv. communication; Phys. Rev. A **35**, 2821 (1987).

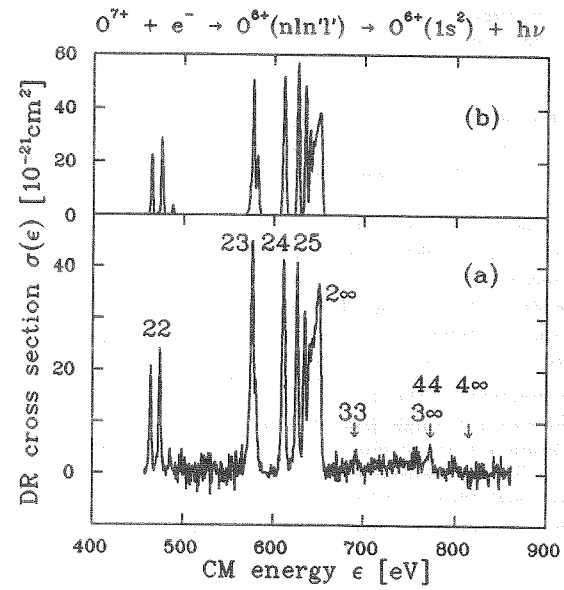


Fig.1 a) Measured spectrum of DR-resonances due to doubly excited states in O^{6+}. Resonances are marked with Nn according to the principal quantum numbers of the inner and outer electron, respectively.
b) Theoretical calculation of the cross section [3] convoluted with the experimental resolution

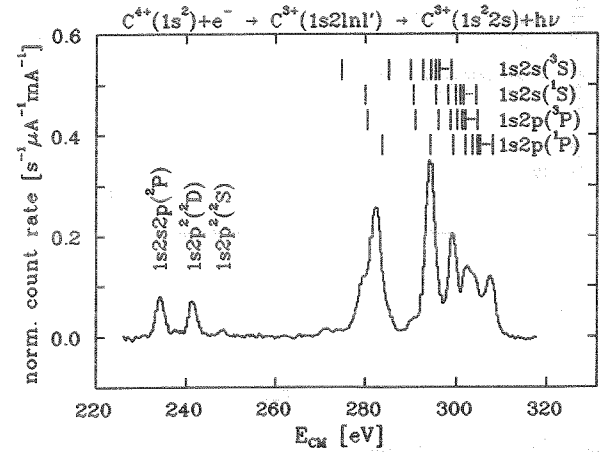


Fig.2 Measured spectrum of DR-resonances due to doubly excited states in C^{3+}. Marked are the configurations of the low lying resonances as well as the Rydberg series that are built upon the various configurations of the inner electrons.

Electron Beam Diagnosis using Dielectronic Recombination [B,G]

G.Kilgus*, D.Habs, E.Jaeschke, D.Krämer, D.Schwalm, M.Steck and A.Wolf
Physikalisches Institut der Universität Heidelberg and Max-Planck-Institut für Kernphysik
R.Schuch
Manne-Siegbahn-Institute, Stockholm, Sweden
L.H.Andersen
Institute of Physics, University of Aarhus, Aarhus, Denmark

At the Test Storage Ring (TSR) in Heidelberg experiments aiming at the diagnosis of the energy spread in the electron cooler have been performed, using strong resonances in the charge changing cross section due to dielectronic recombination (DR). Longitudinal and transversal electron temperatures, which are defined by $T_{\parallel,\perp} = \langle(\delta v_{\parallel,\perp})^2\rangle/2m$, with $\delta v_{\parallel,\perp}$ being the velocity deviations and m the electron mass, can be clearly deduced from the line shape of the resonance, if its natural width is negligibly small. The resonance condition can be written as $(v_0 + \delta v_\parallel)^2 + (\delta v_\perp)^2 = v_R^2 = 2E_R/m$ with E_R being the fixed resonance energy in the ion's rest frame. Neglecting the transversal temperature ($\delta v_\perp \equiv 0$) one gets an image of the longitudinal velocity distribution by varying v_0. On the other hand, if ($\delta v_\parallel \equiv 0$) the resonance condition cannot be fulfilled if $v_0 > v_R$ and only if $v_0 \leq v_R$ the resonance probes the the transversal velocity distribution. Provided that $T_\parallel \ll T_\perp$, which is expected for good electron coolers[1] one will thus observe an asymmetric line shape, whose high energetic part is determined by the longitudinal temperature, while the low energy part is dominated by the transversal temperature. The asymmetry of the line shape is most pronounced at low resonance energies fulfilling $v_R\delta v_\parallel \ll (\delta v_\perp)^2$, as can be seen from the resonance condition with $v_0 \approx v_R$. Fig.1 elucidates this dependence by varying the transversal temperature at fixed longitudinal temperature and vice versa, assuming a gaussian distribution of velocities $v_\parallel$ and $v_\perp$.

Measurements of the line shape of a DR resonance have been performed in a single pass experiment, which means that the ion beam is stopped after having passed through the electron target. This procedure serves two purposes. On the one hand it suppresses dynamical effects of the electron beam on the ion beam. On the other hand it allows to work with metastable ions, where suitable low lying DR resonances can be found[2]. In the presents investigations the resonance

$$C^{4+}(1s2s(^1S)) + e^- \rightarrow C^{3+}(1s2p(^1P)9\ell) \rightarrow C^{3+}(1s^29\ell) + h\nu$$

at $E_R \approx 0.8$eV has been used which is based on the metastable 1s2s (^{1}S) state of C^{4+}. This reaction is characterized by a large cross section and the absence of overlapping resonances within the expected experimental line width. Fig.2 shows the measured rate of charge changed ions due to this resonance (background subtracted), for two different settings of the electron cooler, together with theoretical line shapes obtained by adjusting $T_\parallel, T_\perp$ and E_R. The resulting temperatures are also given in fig.2. The transversal temperature observed in fig.2a is close to the limit of 0.1eV corresponding to the temperature of the cathode, whereas the longitudinal temperature is larger than expected. This is probably caused by the width of the ion beam and the effective energy spread of the electron beam due to its space charge. To study this effect, in fig.2b the electron current has been reduced by a factor of four. The longitudinal temperature decreased by one order of magnitude, now being only a factor of two away from the theoretical limit. However, in order to reduce the electron current, the potential of the first anode of the electron gun and consecutively the radial focusing potential was altered; this probably caused the evident increase of the transversal temperature in this measurement.

In conclusion, the electron beam of the TSR cooler does exhibit a strongly flattened velocity distribution with $kT_\parallel \ll kT_\perp$ and values, which probably can be brought even closer to the design values by a more careful adjustment of the cooler parameters.

[1] G.I.Budker and A.N.Skrinsky, Sov. Phys. Usp. 21(1978), 277-296
[2] L.H.Andersen and J.Bolko, Phys. Rev. A in press

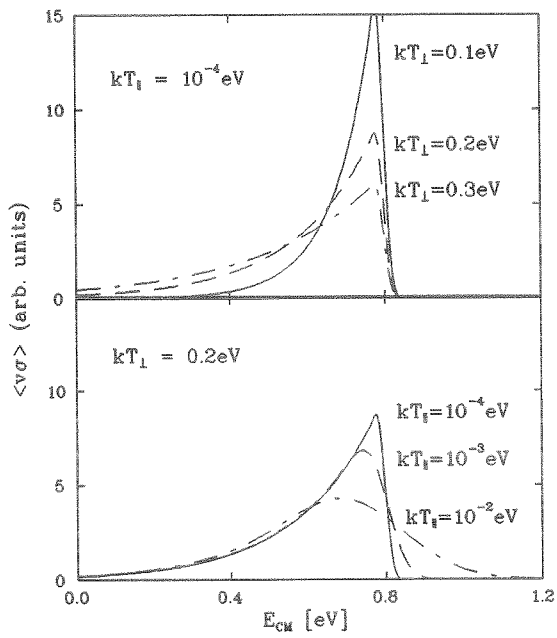


Fig.1 Calculated line shapes of the rate coefficient for a DR resonance having negligible natural width as a function of the c.m. energy of the electrons with different longitudinal and transversal electron temperatures. The resonance energy was set to E_R=0.8eV.

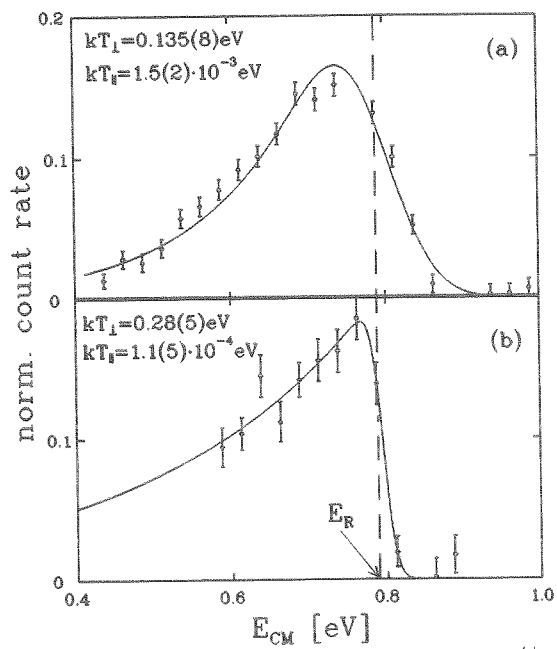


Fig.2 Measured rate of charge changed metastable C^{4+} ions as function of the electron energy in the CM frame for two different setting of the electron cooler. The solid line shows the theoretical line shape, where longitudinal and transversal temperatures have been fitted to the data.

Collective Noise Enhancement During Laser Cooling of $^9Be^+$ Ions at the TSR [B]

W.Petrich[1], V.Balykin[7], C.Ellert[1], A.Faulstich[1], D.Habs[1], G.Huber[4], E.Jaeschke[1], R.Klein[4], D.Krämer[1], M.Kristensen[6], T.Kühl[3], M.Music[1], R.Neumann[2], S.Schröder[4], D.Schwalm[2], P.Sigray[5], B.Wanner[1], A.Wolf[1]

[1] Max-Planck-Institut für Kernphysik, Heidelberg

[2] Physikalisches Institut der Universität Heidelberg

[3] Gesellschaft für Schwerionenforschung, Darmstadt

[4] Physikalisches Institut der Universität Mainz

[5] Manne-Siegbahn-Institute, Stockholm, Sweden

[6] Institute of Physics, University of Aarhus, Denmark

[7] Institute of Spectroscopy, Academy of Sciences of the USSR, Troitsk, Moskow

At the Heidelberg Test Storage Ring TSR laser cooling of a relativistic $^9Be^+$ ion beam has been observed for the first time. At a velocity of $\beta = 4.2 \cdot 10^{-2}$ the intense 300.2 nm line of an Ar^+ ion laser ($\bar{P}_i \approx 100$ mW) was used to excite the $^2S_{1/2}$ (F=1,2) $\longrightarrow$ $^2P_{3/2}$ (F=0,1,2,3) transitions (λ_0 =313 nm) via the Doppler shift [1]. At an intensity of I_{sat} =230 mW/cm^2 these transitions can be saturated. As the singly - charged beryllium ions can be excited from their stable 2s $^2S_{1/2}$ ground state (and not from a metastable state, like in the $^7Li^+$ case [2]) *all* of the ions can be cooled in principle. Thus, investigation of collective phenomena such as plasma waves are not restricted by the presence of a remaining, uncooled distribution like in the experiments on $^7Li^+$ ions [3].

In order to collect $^9Be^+$ ions at a certain velocity and thus to compress the velocity distribution by means of the accelerating radiation pressure force, deceleration due to collisions with the residual gas was used to shift the ions across the resonantly excited velocity class. This deceleration independently was measured to be 150 eV/s at a pressure of p$\approx 5 \cdot 10^{-10}$mbar, which is in agreement with theoretical estimates. Fig. 1b shows a Schottky noise spectrum, where the uncooled distribution displays a width of $\Delta p/p = 3.0 \cdot 10^{-4}$, corresponding to a temperature of T_i = 3800 K. The theoretically expected velocity distribution of $^9Be^+$ ions after a laser interaction of 1.5 s is plotted in fig. 1c. Here, all ions which reach the resonant velocity region of the laser are assumed to be trapped in the laser field. The rather sharp velocity peak at maximum contains 7% of all ions, assuming perfect collection. In contrast to fig. 1c, a much more intense peak develops in the Schottky noise spectrum (fig. 1a), when the $^9Be^+$ beam is overlapped with the laser beam. The peak width is limited by the bandwidth of the spectrum analyser.

However, the measured signal does not reflect the theoretically expected velocity distribution: Assuming, that the narrow peak (fig. 1a) is due to incoherent particle fluctuations, the ratio of cooled to uncooled ions is obtained after squaring the Schottky noise amplitude. The ratio of $\int_{peak} A^2(f)df / \int_{hot} A^2(f)df = 4$ would mean, that 80% of all ions are in the cold peak, while at most 7% of all ions can be collected by the laser. This already proves a strong signal enhancement in the region of the narrow peak (f_0 =225.4 9kHz) by at least a factor of 11. However, a direct comparison of Schottky noise spectra with (fig. 1a) and without (fig. 1b) laser interaction shows, that also the total frequency integrated power spectrum is enhanced by a factor of 5.

These findings are similiar to the behavior observed during laser cooling of $^7Li^+$ [3], but they are in contrast to the result of strong Schottky noise suppression observed for electron cooling. While in the $^7Li^+$ experiments indirect arguments were necessary to prove a signal enhancement [3], a direct measurement of this enhancement has been possible for $^9Be^+$.

In a different measurement, local deceleration was achieved by the use of two high voltage tubes installed in the middle of the TSR cooling section. The spectra shown in fig.2 were taken 0.6 s (fig. 2a) and 2.7 s (fig. 2b) after injection. The intense peak could be shifted to *any* wanted position as a function of applied voltage. After sweeping over the complete uncooled distribution, it seems that all ions are collected in the cooled peak (fig. 2b); within errors, at most 30% may still remain in the uncooled distribution.

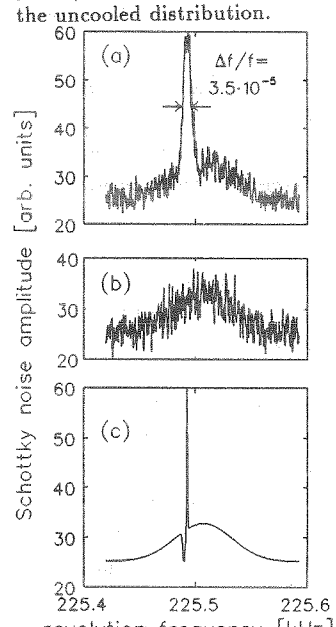


Fig. 1. Collecting part of the uncooled distribution by means of residual gas deceleration (collection time: 1.4 s). Fig. 1b shows the uncooled distribution, whereas fig 1a is taken after approx. 1.5 s of laser interaction. Fig. 1c gives a schematic plot of the expected velocity distribution. The data was taken at the 29th harmonic of the plotted revolution frequency.

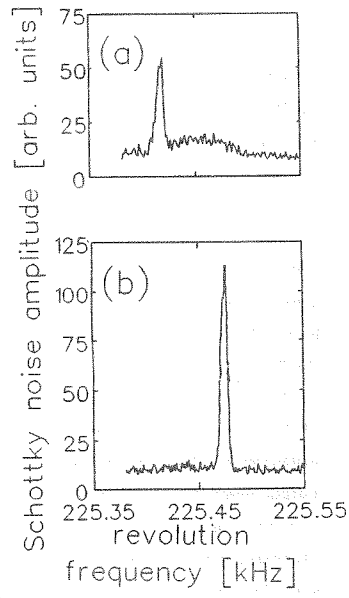


Fig. 2. Time evolution of the velocity distribution while laser cooling with the high voltage scan method. Fig. 2a is taken 0.6 s after injection, whereas the measurement shown in fig. 2b is started 2.7 s after injection. The widths of the peaks are determined by the apparative resolution.

At present, the unexpected noise enhancement with extremely stable properties seems to be a maser like exitation of longitudinal plasma waves. Theoretically, strong Landau growth is expected for a very narrow phase velocity region for an ion velocity distribution depicted in fig. 1c, which is typical for a two stream instability in plasma physics. Theoretical investigations by I. Hofmann [4] show, that only a very small, broad distribution has to be present together with a narrow peak in order to create an intense collective excitation in Schottky noise. This agrees with the above mentioned upper limit of 30%.

In future experiments simultaneous beam diagnostics in a separate section of the storage ring by means of fluorescent light will enable a proper determination of the beam velocity distribution and thus, the described collective effects can be investigated as a function of the ion distribution parameters.

[1] W.Petrich, MPI - K report H 1989 - V 42, Heidelberg
[2] S.Schröder et al., annual report GSI 1989
[3] S.Schröder et al., submitted to Phys. Rev. Lett.
[4] I.Hofmann, priv. communication and annual report GSI,1989

Laser cooling of $^7Li^+$ ions stored in the TSR [B,G]

S. Schröder, M.Gerhard, R.Grieser, G.Huber, R.Klein, M.Krieg, N.Schmidt
Institut für Physik der Universität Mainz

T.Kühl, R.Neumann
Gesellschaft für Schwerionenforschung, Darmstadt

V.Balykin, W.Petrich, D.Habs, D.Schwalm, B.Wanner, A.Wolf and the TSR group
Physikalisches Institut der Universität Heidelberg und Max-Planck-Institut für Kernphysik, Heidelberg

A 13.3 MeV $^7Li^+$ ion beam stored in the TSR has been cooled longitudinally by laser interaction. A compression of the momentum spread of the beam by a factor of 10 to a value of $\Delta p/p = 6 \cdot 10^{-6}$ has been achieved.

Two laser beams of 1 cm diameter were merged with the stored beam co– and counterpropagating the ions. Both laser frequencies are tuned almost resonant with the $^3S_1(F = 5/2) \longrightarrow {}^3P_2(F = 7/2)$ transition of the metastable Li ion in the moving frame. The geometrical overlap and the definition of the merging angle between ion and laser beams were defined by two 18 mm diameter apertures inserted in the experimental section of the TSR.

At the ion velocity of $\beta = 0.064$ the Doppler shifted transition frequency of the above two level system coincides with the green 514.5 nm line of an argon ion laser for the copropagating geometry and can be reached with high output power from a cw ring dye laser at 584.8 nm respectively. In this experimental situation two oppositely directed longitudinal cooling forces are present and the cooled ions can be 'trapped' in momentum or frequency space between the two laser frequencies.

For laser cooling of the metastable ions stored in the TSR the Ar^+ laser was set at a fixed frquency some GHz apart from the original Doppler profile and the yellow 584.8 nm dye laser was scanned across the velocity distribution towards the green frequency. Fig. 1a shows a fluorescence spectrum where the dye laser is scanned even across the green frequency (from right to left). In the moment of almost equal frequencies in the ions rest frame the accumulated and cooled ions produce a high and narrow peak in the spectrum.

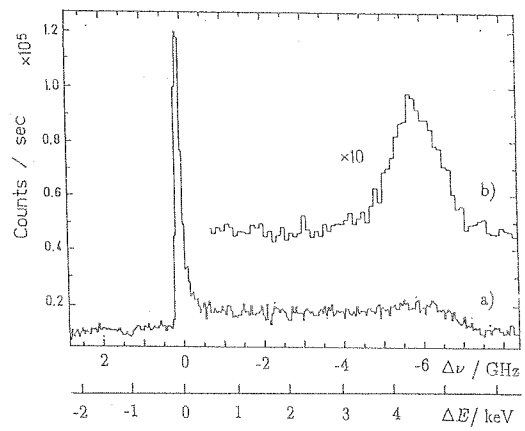


Fig. 1: Fluorescence spectrum of a laser cooled velocity distribution.

In fig. 1b the original uncooled Doppler profile of the ion beam is shown, as it has been measured by reverse scanning, where the cooling effect is absent.

In this not really ideal probing situation the fluorescence is a highly nonlinear responce of laser powers and frequencies. Thus the minimum width of the laser cooled distribution of 200 MHz corresponding to a beam temperature of 2.9 K only gives an upper limit for the real momentum spread of the cooled ions.

Performing laser cooling scans where the dye laser stopped before it crossed the Ar^+ laser frequency in the ions rest frame, the longitudinal Schottky noise of the stored ion beam was recorded. As Schottky noise measurement does not distinguish between ions in the triplet and singlet state, data from all ions is observed as shown in fig. 2.

Pictures a),b) and c) are recorded at the 18. harmonic of the revolution frequency ($f_o = 6.211 MHz$) with a resolution bandwidth of the rf spectrum analyser of 100 Hz, while for the spectrum d) the resolution was tuned almost to its maximum at 14 Hz. This spectrum has been taken at the 36. harmonic and scaled down to f_o. Therefore its amplitude may not be compared directly. a) shows a Schottky spectrum of the stored $^7Li^+$ ion beam taken with a delay of 2.5 s after beam injection. Applying the above mentioned laser cooling scheme reveals spectrum b) and c), where the cooled ions are decelerated to lower revolution frequencies. The width is in this case limited by the resolution of the spectrum analyser, while in trace d) 25 Hz are evaluated. The signal from the cooled ions is strongly enhanced, which might be a result of longitudinal coherent density waves in the ion beam. In this case the width is not correlated directly to a beam temperature.

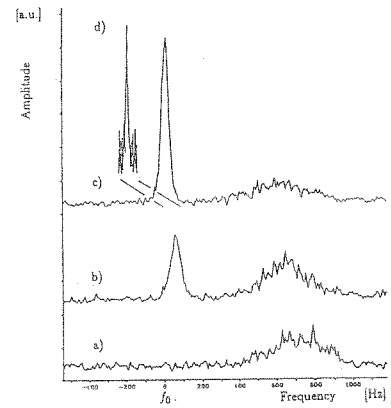


Fig. 2: Longitudinal Schottky noise spectra of the uncooled (a) and the cooled ion beam (b,c,d).

While these data were taken at typical laser powers of 200 mW up to 1 W in a beam of 0.7 cm diameter, it has turned out, that the cooling effect could be achieved even with very low laser powers. as shown in trace b) of fig. 2 (2.1 and 5 mW).

The achieved progress in improving the quality of a stored ion beam by laser cooling marks an important step towards precision experiment on stored fast ions [1].

[1] R.Klein et al.:Precision spectroscopy on stored $^7Li^+$, this report

Precision Spectroscopy on Stored $^7Li^+$ Ions ^{B,G}

R.Klein, M.Gerhard, R.Grieser, G.Huber, M.Krieg, N.Schmidt, S. Schröder
Institut für Physik der Universität Mainz

T.Kühl, R.Neumann
Gesellschaft für Schwerionenforschung, Darmstadt

V.Balykin, D.Habs, W.Petrich, D.Schwalm, B.Wanner, A.Wolf and the TSR group
Physikalisches Institut der Universität Heidelberg und Max-Planck-Institut für Kernphysik, Heidelberg

The new storage rings TSR at the MPI für Kernphysik in Heidelberg and the ESR at GSI in Darmstadt allow a new generation of precision experiments at relativistic velocities. At the TSR in Heidelberg a $^7Li^+$ ion beam stored at a velocity $\beta = 0.064$ was laser cooled and the momentum spread was decreased to $\Delta p/p = 6 \times 10^{-6}$ [1]. Such a high quality ion beam is a suitable candidate for a new precision measurement of the relativistic Doppler shift.

The ion beam was merged with two counterprogagating laser beams. The ions' restframe resonance λ_0 is shifted according to the well known Doppler formula to $\lambda_\pm = \lambda_0\gamma(1 \mp \beta)$. The ion velocity β was chosen that the Doppler shifted resonance of the copropagating laser beam λ_+ coincided with the 514.5 nm Ar^+laser line. A cw dye laser with $\lambda_- = 584.8$nm was used for excitation from the onward direction. Fig. 1 shows a fluorescence signal of the laser cooled distribution as obtained by a single scan within 2.5 seconds. As a next step it is planned to create a Lamb dip in this narrow distribution allowing to determine the absolute value of λ_+ and λ_- to a high degree of accuracy. Besides the closed two level transition $^3S_1(F = 5/2) \rightarrow ^3P_2(F = 7/2)$ used for laser cooling the transition $^3S_1(F = 5/2) \rightarrow ^3P_2(F = 5/2)$ could be used to deplete the $^3S_1(F = 5/2)$ metastable ground state of a certain velocity class by optical pumping. First Lamb dip measurement with the uncooled ion beam in this scheme have shown the suitablility of this method.

Once obtained the absolute frequency values for these two Doppler shifted resonances at different daytimes or at different seasons allows a new and more accurate test of the isotropy of space within the framework of a well developed theoretical test theory [2]. Renewed interest in this question has risen since the detection of an unisotropy in the 3K cosmic radiation [3].

A schematic drawing of the experimental setup under discussion is shown in Fig 2. A special device for adjusting and monitoring the parallelism of the two laser beams has been designed and tested allowing a precision in angle of 10^{-5} rad. Two apertures in the interaction section of the TSR facilitate merging the laser beams with the ion beam and thus minimizing the uncertainty in frequency due to misalignment.

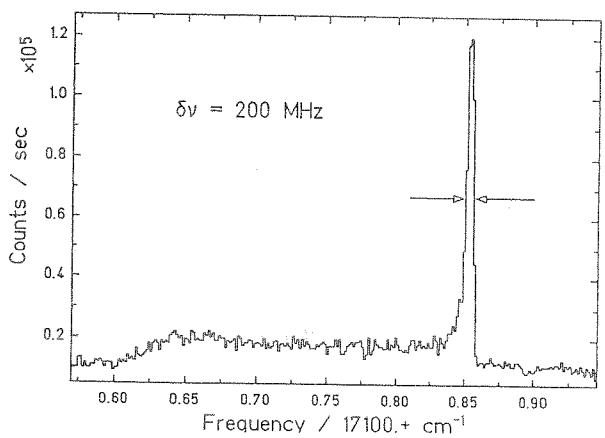


Fig. 1: Laser cooled velocity distribution. This fluorescence spectrum was obtained by setting the Ar^+ laser to a fixed frequency slitely apart from resonance, while the dye laser was scanned towards resonance to compress the momentum distribution via photon momentum transfer. Just for the purpose of revealing the cooled velocity distribution the laser was scanned further through resonance.

The Ar^+ laser was stabilized to the transition curve of a 300 MHz Fabry-Perot resonator. A short time stability of $\Delta\nu/\nu \approx 1.4 \times 10^{-9}$ was achieved. The next step will be to lock the Fabry - Perot resonator length to an iodine molecular resonance. So a long time stability of the laser frequency will be gained. At the same time the molecular iodine hyperfine transition serves as a secondary frequency standard. Also the dye laser has to be frequency locked an iodine molecular resonance using a rf offset method to maintain the laser tunable.

Performing this type of experiment at the ESR in Darmstadt will allow ion velocities upto $\beta = 0.42$ in the future [4].

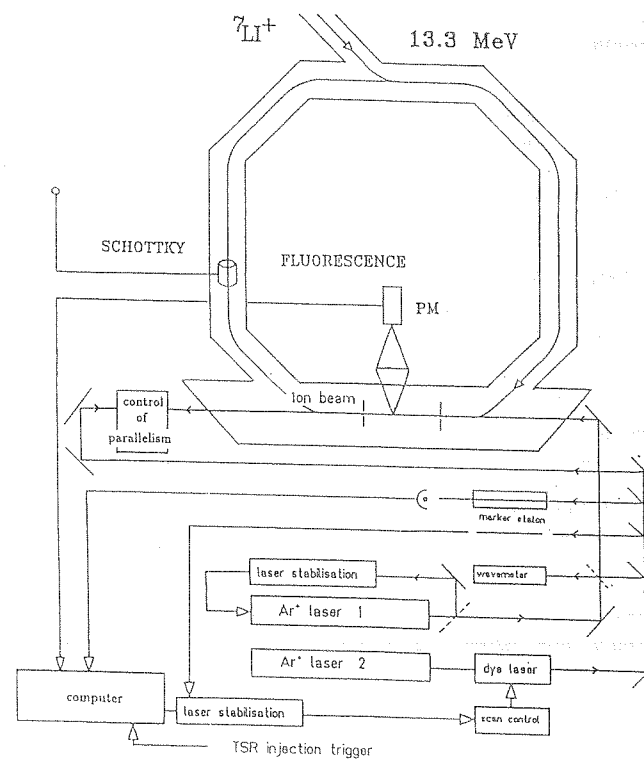


Fig. 2: Experimental setup. Two counterpropagating laser beams merged with the stored ion beam are used for laser cooling as well as saturation spectroscopy. The laser frequencies are to be stabilized to molecular iodine transition lines.

References

[1] S.Schröder et al.:Laser cooling of $^7Li^+$ ions stored in the TSR, this report
[2] R.Mansouri and R.Sexl, General Relativity and Gravitation, 8, (1977) 497
[3] N.Kaiser and J.Silk, Nature (London)324 (1986) 529
[4] G.Huber et al.: Proposal # 111, GSI 1988

Lasers Pumped by Heavy Ion Beams[B,G]

A. Ulrich, B. Busch, H.-J. Körner, W. Krötz, R. Pfaffenberger, G. Ribitzki, J. Wieser
Technische Universität München, D 8046 Garching
D.E. Murnick
Rutgers University, Newark, NJ 07102, USA

Neon gas targets at pressures of 200mbar, 900mbar and 2bar were excited with a pulsed argon beam at the UNILAC accelerator. The 1ns micropulses of the beam consisted of $4 * 10^5$ particles each with a particle energy of 590MeV in the target region. Population densities of excited levels in neon atoms and ions were determined by measuring the intensity of spectral lines. The detecting system, consisting of a normal incidence VUV grating monochromator with 30cm focal length and a photomultiplier with a MgF_2 window, had a known spectral response. Light emission was measured by photon counting over a 5ns time window prompt with the micropulses. Spectra were scanned in the wavelength range from 110nm to 620nm. Population densities of selected levels in a 200mbar neon target are shown in tab.1 in comparison with data obtained from excitation with a 60MeV ^{32}S beam. A factor F=0.2 can be expected for the population densities ($n_{Ar,590MeV} = F * n_{S,60MeV}$) from the Bethe formula $\sigma \sim \frac{Z^2 M}{E} ln(b\frac{E}{M})$[1]. The ratio n_{Ar}/n_S=F_e found experimentally is consistent with F within the experimental error of about 30% .

	wavelength [nm]	level	n_1 [10^7/cm^3]	n_2 [10^7/cm^3]	n_2/n_1
NeI	585.25	$3p'[1/2]_0$	500	120	0.24
	616.36	$3p'[1/2]_1$	100	23	0.23
	352.05	$4p'[1/2]_0$	30	6	0.19
NeII	337.83	$3p^2P^0_{\frac{1}{2}}$	5	1	0.19
	356.85	$3p'^2F^0_{\frac{7}{2}}$	1	0.18	0.18
NeIV	202.22	$3p'^2D^0_{\frac{5}{2}}$	0.1	0.02	0.2

Table 1: Population densities of neon atoms and ions in selected levels are listed. The neon gas was excited with 60MeV ^{32}S ions (n_1) and 590MeV ^{40}Ar (n_2) ions, respectively.

A time integrated Ne spectrum at 2bar target gas pressure excited with a 450MeV ^{40}Ar beam is shown in fig.1. Continuum radiation was found in addition to the spectral lines about 40ns after the beam pulses. A conclusive assignment of this continuum is not yet obtained. A similar continuum was also observed in recent experiments at the Munich Tandem van de Graaff accelerator.

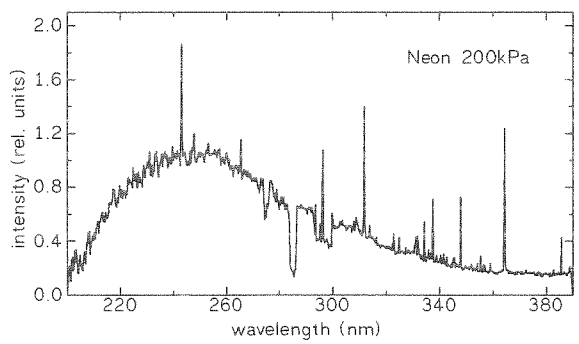


Fig.1: A time integrated spectrum of a 2bar Ne gas target excited with a 450MeV Ar beam is shown.

The excitation of solid xenon with high current pulses from the RFQ accelerator MAXILAC at GSI was studied in continuation of the experiment described in the scientific report 1988[2]. The spatial and temporal distribution of emitted excimer light was measured using the setup shown in fig. 2. A 3.7 MeV, 3mA Kr-beam (B) was focused onto a solid xenon target (T). Light emitted from the solid xenon and xenon evaporated by the beam was focused with a MgF_2 lens (L). The target cell was sealed with a MgF_2 window (W). A VUV filter (F) ($\lambda_0 = 172$nm, $\Delta\lambda = 55$nm) was used to select excimer light. The image was scanned by a photomultiplier (P) with an aperture (A) of 0.5 mm diameter. In fig. 3 the spatial distribution of the time integrated light emission is shown. The distance x was measured perpendicular to the target surface. Most of the light was emitted from a 1 mm thick layer. The time structure of the emission followed the microstructure of the beam over the distance scanned.

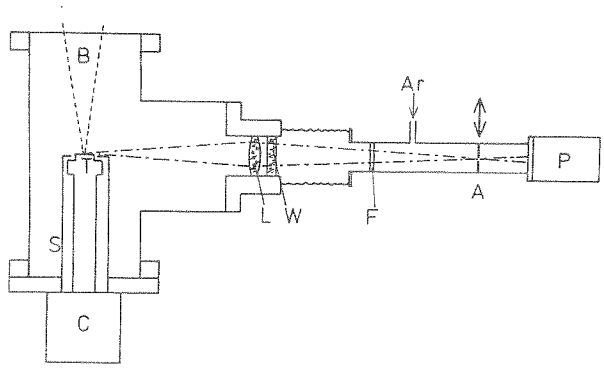


Fig. 2: Experimental setup for measuring the spatial and temporal distribution of the light emitted from the solid xenon target. The components are explained in the text.

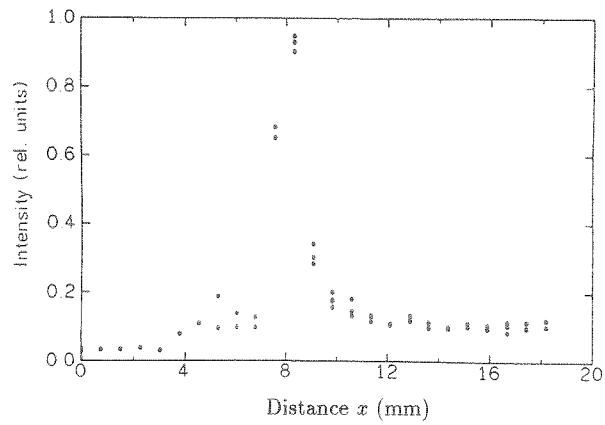


Fig. 3: The spatial distribution of time integrated emission of excimer radiation is shown. The target surface is at $x = 7$ mm.

[1] H. Bethe, Ann. Phys. 5 (1930), 325

[2] A. Ulrich et al., Lasers pumped by Heavy Ion Beams, Scientific Report GSI Darmstadt (1988), 181

Angular correlations of coincident electron - pairs in heavy ion collisions

O. Graf, J. Reinhardt, B. Müller, W. Greiner,

Institut für Theoretische Physik, Universität Frankfurt

G. Soff,

GSI Darmstadt

We calculate angular correlations between coincident e^-e^- pairs in heavy ion collisions. Within a semiclassical coupled channel formalism in monopole approximation [1] we obtain the following expression [2,3]:

$$\begin{aligned} N_{\vec{p}_i\vec{p}_j} &= (4\pi)^{-2} \cdot \left\{ 4 \cdot \left(N_{E_i}^{(-)} + N_{E_i}^{(+)} \right) \cdot \left(N_{E_j}^{(-)} + N_{E_j}^{(+)} \right) \right. \\ &- \left(2 \left| \sum_{r<F} a_{rE_i}^{(-)} a_{rE_j}^{(-)*} \right|^2 + 2 \left| \sum_{r<F} a_{rE_i}^{(+)} a_{rE_j}^{(+)*} \right|^2 \right. \\ &\left. \left. + 4 \cos\theta_{ij} \cdot Re \left[\sum_{r<F} a_{rE_i}^{(-)*} a_{rE_j}^{(-)} a_{rE_i}^{(+)} a_{rE_j}^{(+)*} \right] \right) \right\} \end{aligned}$$

The superscripts $(\pm)$ classify the angular momentum channels taken into account $\kappa = \pm 1$, the subscripts E_i, E_j the energies of the observed electrons and θ_{ij} the angle included by their momenta $\vec{p}_i$, $\vec{p}_j$. The expression is invariant against permutation $i \leftrightarrow j$. As a second condition it has to fulfill Pauli's exclusion principle. Two electrons must not be in the same state $|\vec{p}_i\lambda_i\rangle$, i.e. $N_{\vec{p}_i\lambda_i,\vec{p}_i\lambda_i}$ must vanish:

$$N_{\vec{p}_i\vec{p}_i} = (4\pi)^{-2} \cdot \left(4 \cdot \left(N_{E_i}^{(+)} + N_{E_i}^{(-)} \right)^2 - 2 \cdot \left(N_{E_j}^{(+)} + N_{E_j}^{(-)} \right)^2 \right)$$

Thus from the 4 possible spin combinations entering the statistical term only the two corresponding to antiparallel alignment remain. The angular correlation can be written in the following form:

$$N_{\vec{p}_i\vec{p}_j} = a_{E_iE_j}^0 \cdot (1 - a_{E_iE_j}^1 \cos\theta_{ij})$$

Numerical results for central collisions of the system Pb + Pb at 6.2 MeV/u are shown as contour plots in figure 1. Nuclear effects are not taken into account. The coefficient $a_{E_iE_j}^0$ decreases strongly with increasing electron energy and exhibits the behaviour known from single electron emission rates. The anisotropy coefficient $a_{E_iE_j}^1$ is allways positive, so coincident e^-e^- emission occurs anticorrelated. It obtains its maximum $a_{max}^0 \approx 0.33$ for equal energies $E_i - E_j = 0$, which can be understood from the Pauli principle. The value of a_{max}^0 corresponds to a ratio of antiparallel emission to parallel emission of $K \approx \frac{1+1/3}{1-1/3} = 2:1$, as it has to be expected, because due to Pauli's principle twice as much spin combinations contribute to antiparallel electron emission as to parallel emission. Indeed one obtains $K \approx 2$ up to small corrections steming from differences in the contributions of the angular momentum channels:

$$K = \frac{N_{\vec{p}_i,-\vec{p}_i}}{N_{\vec{p}_i\vec{p}_i}} = 2 - \left(\frac{N_{E_i}^{(+)} - N_{E_i}^{(-)}}{N_{E_i}^{(+)} + N_{E_i}^{(-)}} \right)^2$$

Generally angular correlations of concident e^-e^- pairs should be measureable and could yield a sensitive test for the theoretical description of dynamical excitations in heavy ion collisions.

Fig. 1a

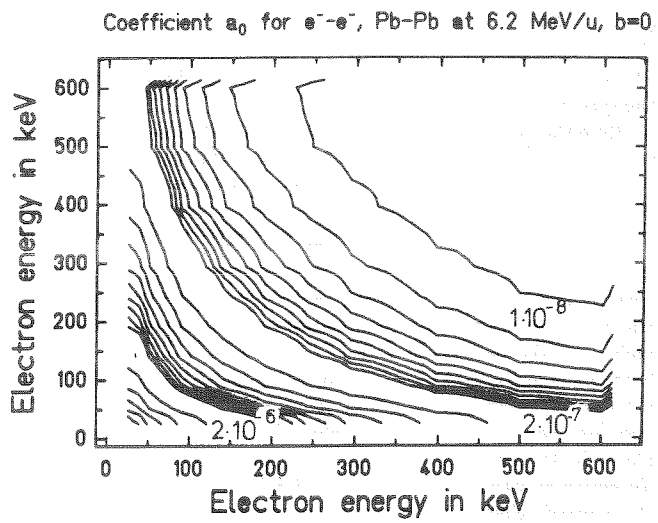
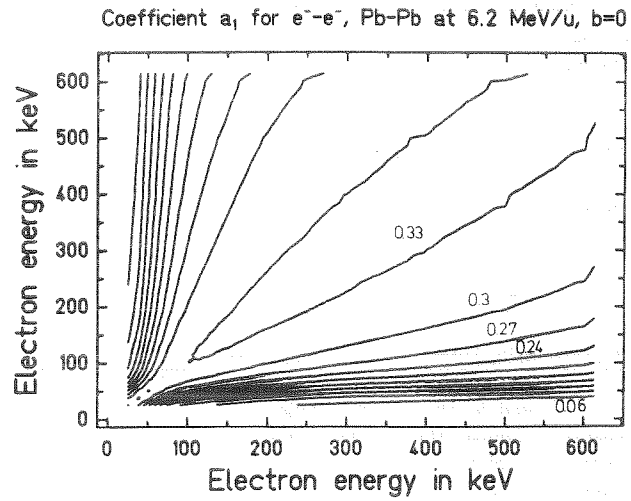


Fig. 1b



References

[1] J. Reinhardt, B. Müller, W. Greiner, Phys. Rev. A 24, 103 (1981)

[2] O. Graf, J. Reinhardt, B. Müller, W. Greiner and G. Soff, Phys. Rev. Lett. 61, 2831 (1988)

[3] O.Graf, Diploma thesis, GSI-Report GSI-88-24

$e^+ - e^-$-Angular Correlation in Internal Pair Conversion

Ch. Hofmann, J. Reinhardt, B. Müller, W. Greiner,
Institut für Theoretische Physik, Universität Frankfurt,
and G. Soff,
GSI Darmstadt

Several groups at GSI have measured electron and positron spectra which show narrow peak structures at some definite energies in the sum energy spectra. The experiments have been modified in the last years due to the measurement of the angular correlation of these electrons and positrons. To interpret these experiments it is important to understand in which way e^+e^--pair emitting processes contribute to the background of the spectra.

Here the angular correlation of electrons and positrons emitted in internal pair conversion is considered. We have calculated [1] the doubly differential pair conversion coefficient

$$\frac{d^2\beta}{dE\, d\cos\theta} = \frac{d^2 P_{e^+e^-}/(dE\, d\cos\theta)}{P_\gamma} \quad ,$$

with respect to positron energy E and angle θ between electron and positron direction. $P_{e^+e^-}$ denotes the pair conversion probability, P_γ the probability of emitting a photon instead. This holds for a multipolarity $L > 0$ of the nuclear transition. (In the case of electric monopole conversion, which is not treated here, one has to calculate an analogous expression with P_γ replaced by the emission probability of a bound state electron [1].) To derive an expression for $d^2 P_{e^+e^-}/(dE\, d\cos\theta)$ we considered the S-matrix element in second order perturbation theory in the fine structure constant α. The matrix element is evaluated using distorted scattering waves as electron wave functions which are deformed by the Coulomb potential of the nuclear charge. These wave functions are given in their partial wave decomposition. Neglecting the penetration effects [2] which come from the overlap of the electron density with the nuclear charge density the matrix element separates into an electronic part M and a nuclear part V

$$S \propto V\, M \quad .$$

The square of the S-matrix element gives the doubly differential pair conversion probability. Dividing by P_γ which is essentially the square of the nuclear matrix element V the final expression for the angular distribution

$$\frac{d^2\beta}{dE\, d\cos\theta} = \frac{d\beta}{dE}\left(1 + \sum_{I>0} a_I P_I(\cos\theta)\right) \qquad (*)$$

becomes independent of $|V|^2$. The $P_I(\cos\theta)$ are the Legendre polynomials, the anisotropy factors a_I are computed numerically. They depend on the nuclear charge Z, the nuclear transition energy ω, and on the positron energy E. As an example the dependence of several a_I's ($I = 1, \ldots, 6$) on Z for the nuclear transitions $E1$ and $E2$ for the transition energy $\omega = 2046$ keV and positron energy $E = 511$ keV is depicted in Fig. 1 ($E1$) and Fig. 2 ($E2$). In the region of overcritical nuclear charges the angle dependent part of $(*)$ is supressed, the angular distribution is therefore isotropic. In some interval the anisotropy factors can be negative. The angular distribution peaks then around $\theta = 180°$ instead of $\theta = 0°$ caused by the changing phase shift of the positron wave function at the resonances in the Dirac sea. Fig. 3. shows the angular distribution itself for a uranium like nucleus assuming $\omega = 2046$ keV, $E = 511$ keV. The dashed curve is obtained within Born approximation normalized to the same $d\beta/dE$ and is more strongly peaked at $\theta = 0°$.

Taking plane waves as electron wave functions (Born approximation) which are not deformed by the Coulomb potential we would be led to charge independent coefficients a_I, which is considerably inaccurate in the case of strongly charged nuclei like uranium.

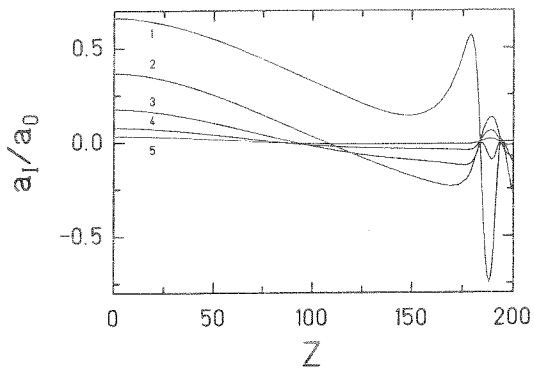


Fig. 1: Anisotropy-factors in dependence of the nuclear charge assuming $\omega = 2046$ keV, $E = 511$ keV for $E1$-transition. The numbers at the curves denote the coefficient a_I.

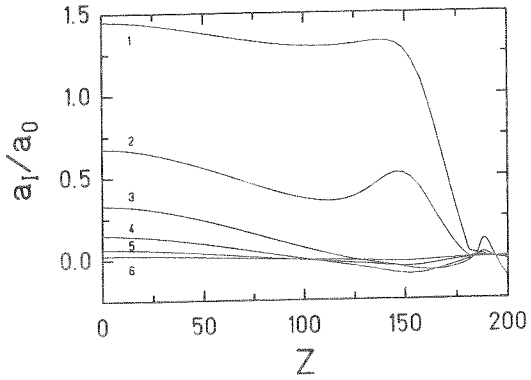


Fig. 2: Same as in Fig. 1 for $E2$-transition.

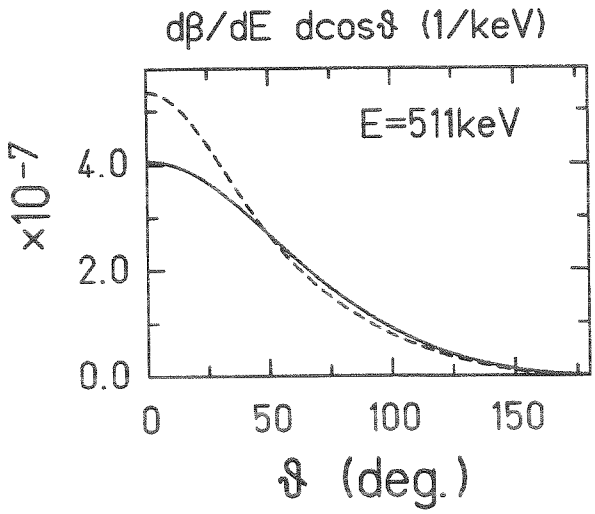


Fig. 3: Angular distribution assuming an $E2$-transition in a uranium like nucleus with $\omega = 2046$ keV, $E = 511$ keV.

References

[1] Ch. Hofmann, diploma thesis, GSI-89-31 (1989)
[2] E. L. Church, J. Weneser, Ann. Rev. Nucl. Sci. **10**, 193 (1960)

Strongly Bound Bipositronium States in QED ? [B]

D. C. Ionescu, B. Müller, W. Greiner
Institut für Theoretische Physik der Universität Frankfurt

Motivated by the yet unexplained peak-like structures observed in the spectra of positrons and electrons emitted in heavy-ion collisions [1, 2] at GSI, we investigateed the question whether electron-positron clusters consisting of two electrons and two positrons can be strongly bound due to the electromagnetic interaction. The two body decay of the hypothetical bound system $(e^+e^-)^2$, which represents a particular member of the family of "polypositronia" [3] $(e^+e^-)^n$, would constitute a source of monoenergetic positrons and electrons with energies independent of the formation process. In a recent work [4] we investigated bound states of particle-antiparticle clusters due to Fermi-type contact interactions in the Dirac-Hartree-Fock approximation. The main result found in [4] was that the coupling constants required to support bound states exceed by several orders of magnitude the limits posed by the precision spectroscopy of heavy atoms. It also has been argued [5] that the spin-orbit interaction could provide an attraction of the order of 100 keV in the $(e^+e^-)^2$-system. However, the crucial point is whether the electromagnetic interaction in this system is strong enough to provide fermion orbits of the size of the Compton wavelength, such that the spin-orbit interaction is large.

Our starting point is the following second quantized Hamilton operator

$$\begin{aligned} \hat{H} &= \int d^3\vec{x} : \hat{\psi}^+(\vec{x})(\vec{\alpha}\cdot\vec{p} + \beta m)\hat{\psi}(\vec{x}) : \\ &+ \frac{e^2}{2}\int d^3\vec{x}\, d^3\vec{y} : \hat{\bar{\psi}}(\vec{x})\gamma^\mu\hat{\psi}(\vec{x})\,\Delta(\vec{x},\vec{y})\,\hat{\bar{\psi}}(\vec{y})\gamma_\mu\hat{\psi}(\vec{y}) : \end{aligned} \tag{1}$$

where $\hat{\psi}(\vec{x})$ and $\hat{\psi}^+(\vec{x})$ represent the fermion field operators and $\Delta(\vec{x},\vec{y})$ is the instantaneous photon propagator. Note that the considered Hamiltonian contains the full current-current interaction. We expand the fermion field operators in a complete orthonormal single particle basis and specify the variational ground state of the bipositronium system which is assumed to contain two electrons and two positrons in the same s or p state:

$$|\,\tilde{0}\,> \;=\; b^+_{e_1}\, b^+_{e_2}\, d^+_{p_1}\, d^+_{p_2}\,|\,0\,> \quad . \tag{2}$$

Next we evaluate the expectation value of the Hamiltonian with respect to the ground state of the system and after inserting the explicit form of the s, p electron and positron wavefunctions in the energy functional we perform the angular integrations and minimise the energy expectation value with respect to the radial functions which are subjected to the normalisation constraint. The variational problem $\delta < \tilde{0}\,|\,\hat{H}\,|\,\tilde{0} > \;=\; 0$ provides the following coupled equations for the radial functions:

$$\begin{aligned} \frac{dg}{dr} &= -Q(r)\cdot g(r) + [\omega + m - V_1(r)]\cdot f(r) \;, \\ \frac{df}{dr} &= \left[-\frac{2}{r} + Q(r)\right]\cdot f(r) - [\omega - m - V_2(r)]\cdot g(r) \end{aligned} \tag{3}$$

where we substituted

$$V_1(r) = -2\alpha\int_0^\infty dr'\frac{(r')^2}{r_>}\left\{2\left[\frac{1}{3}+\frac{2}{15}\left(\frac{r_<}{r_>}\right)^2\right]\cdot f^2(r') + g^2(r')\right\}$$

$$\begin{aligned} V_2(r) &= -2\alpha\int_0^\infty dr'\,\frac{(r')^2}{r_>}\left[2\,g^2(r') + f^2(r')\right] \;, \\ Q(r) &= 2\alpha\int_0^\infty dr'\,r_<\left(\frac{r'}{r_>}\right)^2 f(r')\,g(r') \;, \end{aligned} \tag{4}$$

In order to estimate the maximal attraction in the system we evaluate upper bounds for $|V_1|$, $|V_2|$ and $|Q|$ and obtain the following estimates [6]

$$\begin{aligned} -\frac{2\alpha}{r} &< V_1(r) < 0 \;, \\ -\frac{4\alpha}{r} &< V_2(r) < 0 \;, \\ -\frac{\alpha}{r} &< Q(r) < \frac{\alpha}{r} \;, \end{aligned} \tag{5}$$

which are valid for $s_{1/2}$ and $p_{1/2}$ states. From this bounds it is evident that these attractive potentials can never provide fermion eigenenergies ω lower than energy eigenvalues of K-shell electrons in atoms with charge $Z = 2, 3, 4$ as given by the Sommerfeld fine structure formula. In addition, the radial extension of the system never shrinks below the value of the K-shell radius in such atoms. As a consequence, spin-orbit splitting will be weak, and certainly cannot attain values of the order of 100 keV, as suggested in ref. [5]. Consequently, strongly electromagnetically bound bipositronium states cannot be seriously considered as possible explanation of the GSI data.

[1] Cowan T et al, 1985, Phys. Rev. Lett. **54**, 1761

[2] Koenig W et al, 1989, Phys. Lett. **218B**, 12

[3] Müller B, Reinhardt J, Greiner W and Schäfer A: 1986, J. Phys. G: Nucl. Phys. **12**, L109

[4] Ionescu D C, Reinhardt J, Müller B, Greiner W and Soff G: 1988, J. Phys. G: Nucl. Phys. **14**, L143

[5] Griffin J J: 1989, submitted to J. Phys. G: Nucl. Phys.

[6] Ionescu D C, Müller B and Greiner W : 1989, J. Phys. G: Nucl. Phys. **15**, L103

Crystal assisted production of composite particles

S. Graf, J. Augustin, J. Reinhardt, B. Müller, W. Greiner

Institut für Theoretische Physik, Universität Frankfurt

1 The Model

In a recent publication [1] we discussed the consequences of a new hypothetical composite particle X^0. It has been described in terms of a phenomenological nonrelativistic potential model introducing a scalar potential of the form:

$$V(r) = \begin{cases} \sigma r & r > r_0 \\ V_0 & r < r_0 \end{cases} .$$

The long range linearly rising part guarantees confinement of the two electrically charged fermionic constituents f^+, f^-. Since $\sigma \approx 50\text{keV/fm}$ is small, it leads to a large spatial extension, dense level spacing and fast radiative deexcitation by emission of soft photons.

The short range repulsion, modifying the wavefunction at small relative distances, was found to be essential in order to avoid contradiction with results from with various high energy or precision experiments.

2 Results

Since the constituents are assumed to be electrically charged, the X^0 will be preferrably created in the presence of strong fields. Apart from heavy ion collisions, which provided the motivation for this model, we consider here the process of X^0-production in the channeling of ultrarelativistic particles through oriented crystals [2,3]. We restrict ourselves to axial channeling with perfect alignment. Similar to the calculations performed in [1], we neglect the linear confinement and simulate the hard core repulsion core by an appropriate Gamov suppression factor G.

This enables us to apply the well established calculations for e^+e^--pair creation in channeling processes to our problem (substituting $m_e \rightarrow m_f$).

Considering an aligned photon-beam, homogeneous in the transverse direction with energy $E_\gamma = \hbar\omega$, we average over the transverse plane to obtain a f^+f^- pair creation rate $\bar{W}(E_\gamma)$ using the uniform field approximation [2].

In case of an aligned electron beam, the rate $\bar{W}(E_\gamma)$ has to be folded with the photon spectrum $\eta(E_{e^-}, E_\gamma)$, which has been calculated using the Weizsäcker-Williams method. We then obtain the rate

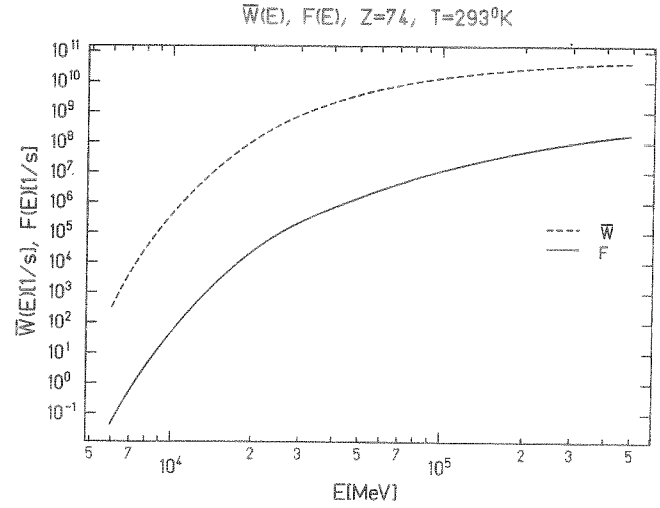
$$F(E_{e^-}) = \int dE_\gamma \eta(E_{e^-}, E_\gamma) \bar{W}(E_\gamma) .$$

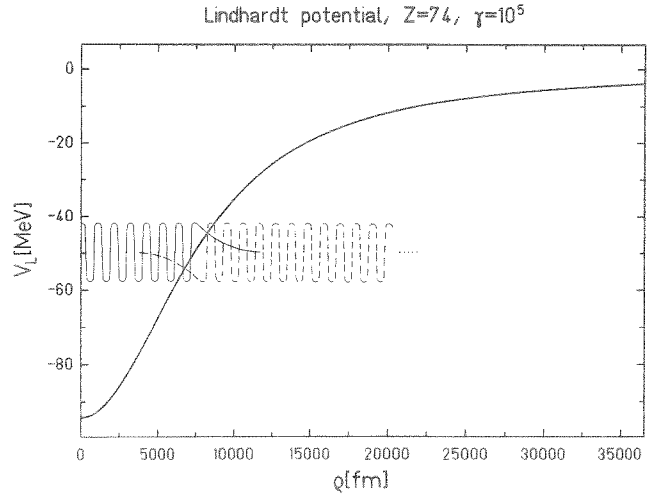
The results shown in Fig.1 correspond to channeling along the $\langle 111 \rangle$-axis of tungsten at room temperature. Fig.2 depicts the transverse Lindhardt potential [4] in tungsten (same axis), as it is seen by an ultrarelativistic particle with a Lorentz factor $\gamma = 10^5$. The wavefunctions of the $f^\pm$, deformed by the action of the strong potential, are shown only scematically.

Considering the available beam energies ($\approx$250GeV) and particle flux ($\phi \approx 10^7 e^-/s$) at CERN, as well as the time of flight τ through a 1mm tungsten crystal and a Gamov factor $G \approx 10^{-3}$, we obtain a considerable X^0-production rate per second:

$$G\tau\phi\bar{W}(E_\gamma = 250\text{GeV}) \approx 10^3 \quad , \quad G\tau\phi F(E_{e^-} = 250\text{GeV}) \approx 1 .$$

The produced X^0 will be highly excited as soon as they emerge from the crystal. Due to their lifetime against decay into a cascade of photons followed by an e^+e^--pair and the corresponding Lorentz factor outside the crystal, we expect a decay length of 30m-300m in the laboratory frame. These e^+e^--pairs should be well distinguishable from those being created directly in the crystal.





References

[1] S. Graf et. al, J. Phys. G15, 373 (1989)

[2] J. C. Kimball, N. Cue, Phys. Rep. **125**, 69 (1985)

[3] J. Augustin et. al, submitted to Z. Phys. A (1990)

[4] D. S. Gemmell, Rev. Mod. Phys. **46**, 153 (1974)

Electron Excitations in Relativistic Ion-Atom Collisions

K. Rumrich and W. Greiner
Institut für theoretische Physik der Universität Frankfurt

G. Soff
GSI Darmstadt

G. Mehler
Robert Bosch GmbH Stuttgart

In order to calculate electron excitation and ionisation rates in ion-atom collisions we solved the time-dependent Dirac equation. For this purpose several authors used the coupled channel equations with different basis states [1 – 3]. Expansion of the wave function in terms of target-centered, time-independent basis states results in [3]

$$\dot{a}_f \;=\; -i \sum_k a_k \, \langle \phi_f | \hat{V} | \phi_k \rangle \, e^{i \Delta E_{fk} t}$$

The matrix elements $\langle \phi_f | \hat{V} | \phi_k \rangle$ contain the electromagnetic potentials of the bypassing charged projectile. Since we are interested in relativistic collisions with kinetic energy up to a few GeV/nucleon, magnetic field and retardation effects may not be neglected. We assume a fixed target atom and the projectile ion following a straight line, both very good approximations for high velocities. Thus, the electromagnetic potentials can be calculated by a Lorentz transformation of the Coulomb potential in the projectile frame into the target frame.

Screening effects can be taken into account by the use of Dirac-Fock-Slater wave functions as basis states. This requires a numerical calculation of the basis states and thus the matrix elements are computed by a numerical integration in coordinate space. While the finite size of the target nucleus can be taken into account the projectile is assumed to be pointlike.

When the multipole expansion of the electromagnetic potentials is transformed from the projectile frame into the target frame, the spheres on which the multipoles are defined are deformed to ellipsoids. For that reason, standard spherical operator techniques cannot be applied to perform the angular integration needed for the calculation of the matrix elements [3].

In figure 1 we present the time evolution of the occupation probabilities $|a_k(t)|^2$ of some atomic states during a collision of Pb on Pb with impact parameter $b = 12$ fm and velocity $v = 0.9$ c ($E = 1200$ MeV/nucleon). For $t \to -\infty$ only the 1s-state is occupied with one electron. At $t = 0$, the time of closest approach, strong excitations of higher states occur. The decrease of the content of the 1s-state shows that probability is conserved and that perturbation theory is unsuitable for high-Z projectiles.

Figure 2 shows the comparison between the electron spectra calculated using first-order perturbation theory and the full coupled channel equations.

Considerable differences in the spectra are obvious. Using the coupled channels, due to continuum-continuum interactions the spectrum is shifted towards higher electron energies. In addition, the relative contribution of the different angular momenta changes, which results in different angular distributions of the emitted electrons.

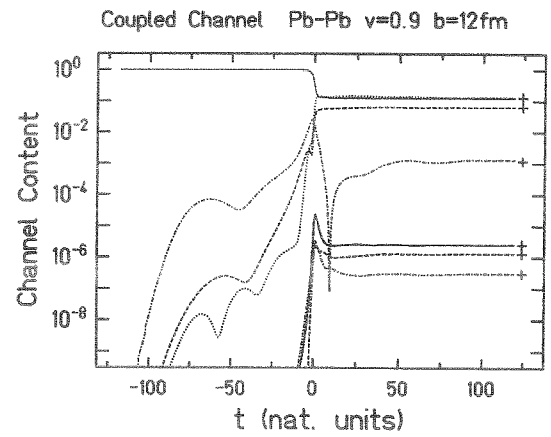


Figure 1: Time evolution of the channel contents $|a_k(t)|^2$ of some atomic states (solid lines: 1s, dashed lines: 2s, dashed-dotted lines: 2p, dotted line: continuum s-state with $E = 1.1$) during a collision of Pb on Pb with impact parameter $b = 12$ fm and velocity $v = 0.9$ c.

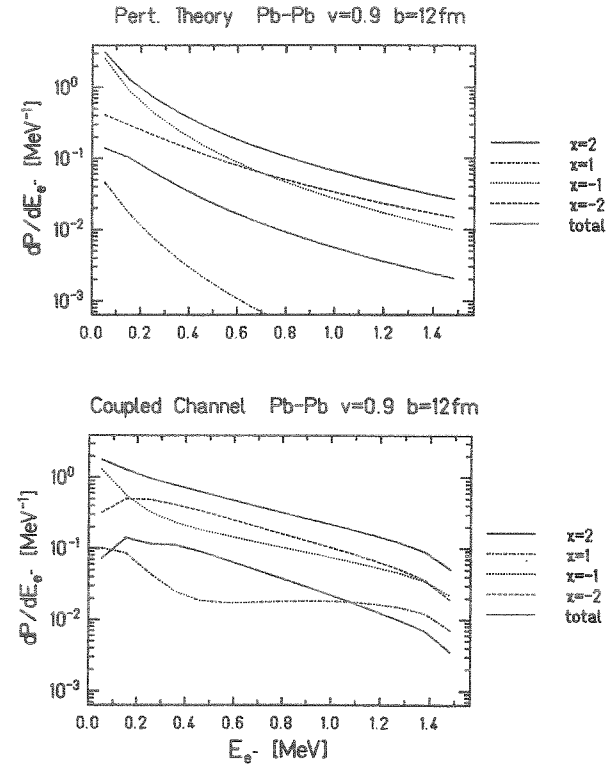


Figure 2: Electron spectrum for collisions of Pb on Pb with impact parameter $b = 12$ fm and velocity $v = 0.9$ c. Different angular momentum contributions are denoted by the quantum number κ. (a) First-order perturbation theory. (b) Coupled channel calculation.

[1] U. Becker, N. Grün, K. Momberger, W. Scheid: NATO ASI Series B, Phys. Vol. **153**, 609 (1987)

[2] N. Toshima and J. Eichler: Phys. Rev. A**40**, 125 (1989)

[3] G. Mehler, G. Soff, K. Rumrich, W. Greiner: Z. Phys. D**13**, 193 (1989)

The Coupled Channel Equations and Gauge Transformations

K. Rumrich, B. Müller and W. Greiner
Institut für theoretische Physik der Universität Frankfurt

G. Soff
GSI Darmstadt

We investigate whether the representation of the time-dependent Dirac equation in terms of coupled channels is gauge invariant if the set of basis states is truncated for numerical reasons. The coupled channel equations read [1]

$$\dot{a}_f = -i \sum_k a_k \, \langle \phi_f | \hat{V} | \phi_k \rangle \, e^{i \Delta E_{fk} t} \tag{1}$$

with

$$\hat{V} = e \vec{\alpha} \cdot \vec{A} - eV, \qquad \Delta E_{fk} = E_f - E_k \tag{2}$$

and time-independent basis states ϕ_k. Inserting the gauge transformed electromagnetic potentials

$$\hat{V}' = \hat{V} - e \vec{\alpha} \cdot \vec{\nabla} \chi - e \partial_t \chi \tag{3}$$

we obtain

$$\begin{aligned} \dot{a}'_f &= -i \sum_k a'_k \, \langle \phi_f | \hat{V} | \phi_k \rangle \, e^{i \Delta E_{fk} t} \\ &\quad + i \sum_k a'_k \, \langle \phi_f | e \vec{\alpha} \cdot \vec{\nabla} \chi + e \partial_t \chi | \phi_k \rangle \, e^{i \Delta E_{fk} t}. \end{aligned} \tag{4}$$

Using the continuity equation for the transition current of the basis wave functions ϕ_i it is easy to show that

$$\langle \phi_f | \chi^n \vec{\alpha} \cdot \vec{\nabla} \chi | \phi_k \rangle = \frac{i \Delta E_{fk}}{n+1} \, \langle \phi_f | \chi^{n+1} | \phi_k \rangle \, . \tag{5}$$

This relation is used for $n = 0$ and we end up with

$$\begin{aligned} \dot{a}'_f &= -i \sum_k a'_k \, \langle \phi_f | \hat{V} | \phi_k \rangle \, e^{i \Delta E_{fk} t} \\ &\quad + ie \sum_k a'_k \, \partial_t \langle \phi_f | \chi e^{i \Delta E_{fk} t} | \phi_k \rangle \, . \end{aligned} \tag{6}$$

Since the additional term from the gauge transformation is a total time derivative we find the result that in first-order perturbation theory

$$a'_f(t = \infty) = a_f(t = \infty) \quad \text{if} \quad \chi(t = \pm\infty) = 0. \tag{7}$$

In order to go beyond first-order perturbation theory we consider the case $\hat{V} = 0$. In the following we omit the primes at the transformed amplitudes a_i. Now the coupled channels simply reduce to

$$\dot{a}_f = i \sum_k a_k \, \dot{\chi}_{fk} \tag{8}$$

with the abbreviation

$$\chi_{fk} = \langle \phi_f | \chi e^{i \Delta E_{fk} t} | \phi_k \rangle \, . \tag{9}$$

We want to show that with the initial condition

$$a_f(t = -\infty) \;=\; \delta_{fi} \tag{10}$$

the solution in j^{th}-order perturbation theory reads

$$a_f^{(j)} = \sum_{n=0}^{j} \frac{i^n (\chi^n)_{fi}}{n!} \, . \tag{11}$$

For $j = 0$ this is evident since $a_f^{(0)} = \delta_{fi} = \langle \phi_f | e^{i \Delta E_{fi} t} | \phi_i \rangle$. Now we assume that (11) is true for a certain value for j. Then using (8) the next order $j + 1$ reads

$$\dot{a}_f^{(j+1)} = i \sum_k a_k^j \, \dot{\chi}_{fk} = i \sum_{n=0}^{j} \frac{i^n}{n!} \sum_k \dot{\chi}_{fk} \, (\chi^n)_{ki} \tag{12}$$

Making use of (5) we get

$$\begin{aligned} \dot{a}_f^{(j+1)} \;=\; & i \sum_{n=0}^{j} \frac{i^n}{n!} \sum_k \langle \phi_f | \vec{\alpha} \cdot \vec{\nabla} \chi + \partial_t \chi | \phi_k \rangle \, e^{i \Delta E_{fk} t} \\ & \langle \phi_k | \chi^n | \phi_i \rangle \, e^{i \Delta E_{ki} t} \, . \end{aligned} \tag{13}$$

Now, only if the basis set $\{\phi_k\}$ is complete, i.e. $\sum_k |\phi_k\rangle\langle\phi_k| = 1$, we may proceed further:

$$\begin{aligned} & \dot{a}_f^{(j+1)} = \\ & = i \sum_{n=0}^{j} \frac{i^n}{n!} e^{i \Delta E_{fi} t} \left[\langle \phi_f | (\vec{\alpha} \cdot \vec{\nabla} \chi) \chi^n | \phi_i \rangle + \langle \phi_f | (\partial_t \chi) \chi^n | \phi_i \rangle \right] \\ & = i \sum_{n=0}^{j} \frac{i^n}{n!} e^{i \Delta E_{fi} t} \left[\frac{i \Delta E_{fi}}{n+1} \langle \phi_f | \chi^{n+1} | \phi_i \rangle + \frac{1}{n+1} \langle \phi_f | \partial_t \chi^{n+1} | \phi_i \rangle \right] \\ & = \sum_{n=0}^{j} \frac{i^{n+1}}{(n+1)!} \, \partial_t \langle \phi_f | \chi^{n+1} e^{i \Delta E_{fi} t} | \phi_i \rangle \\ & = \sum_{n=0}^{j} \frac{i^{n+1}}{(n+1)!} \, \partial_t (\chi^{n+1})_{fi} \end{aligned} \tag{14}$$

where in the second line again (5) has been employed. It is easy to integrate this equation. Paying attention to the initial conditions (10) and $\chi(t = -\infty) = 0$ we get

$$\begin{aligned} a_f^{(j+1)} \;&=\; \sum_{n=0}^{j} \frac{i^{n+1}}{(n+1)!} \, (\chi^{n+1})_{fi} + \delta_{fi} \\ &=\; \sum_{n=0}^{j+1} \frac{i^n}{n!} \, (\chi^n)_{fi} \, . \end{aligned} \tag{15}$$

Now, for $j \to \infty$, the final result reads

$$a_f = \left(e^{i \chi} \right)_{fi} = \langle \phi_f | e^{i \chi} \, e^{i \Delta E_{fi} t} | \phi_i \rangle \xrightarrow{t \to \infty} \delta_{fi} \, . \tag{16}$$

This is not very surprising since in this derivation we made use of the completeness of the basis set and we demonstrated only the gauge invariance of the Dirac equation in the representation by coupled channels.

But the completeness of the basis states was rather essential for this proof and thus we can conclude that the gauge invariance of the coupled channel equations is violated if the basis set is truncated.

[1] K. Rumrich, W. Greiner, G. Soff and G. Mehler: this report

Coupled-channel analysis of inner-shell ionisation in relativistic heavy ion collisions [B]

K. Momberger, N. Grün and W. Scheid
Institut für Theoretische Physik der Justus-Liebig-Universität Giessen

We performed calculations of cross sections for K-shell ionisation in relativistic collisions of high-Z ions. The formalism is based on the semiclassical picture, i.e. the nuclear motion is treated classically by a straight-line trajectory, while the electron is described by the time-dependent Dirac equation. This equation is solved with a wave function expanded in a set of bound and continuum wave functions centered at the target.

$$\Psi(\vec{r},t) = \sum_{\substack{k\in \text{bound}+\\ \text{continuum states}}} a_k(t)\,\phi_k \exp(-iE_k t) \qquad (1)$$

The continuum functions are discretized by means of time-dependent relativistic wave packets:

$$\phi_k(\vec{r},t) = \frac{1}{\sqrt{\Delta E_k}} \int_{E_k-\frac{\Delta E_k}{2}}^{E_k+\frac{\Delta E_k}{2}} dE\; \phi_E(\vec{r})\exp(i(E_k-E)t). \qquad (2)$$

Inserting this ansatz into the time-dependent Dirac equation and projecting on the various states, we obtain the following system of coupled channel equations

$$id\, a_k/dt = \sum_n \langle\phi_k|V|\phi_n\rangle \exp(i(E_k-E_n)t)a_n. \qquad (3)$$

Here, V denotes the time-dependent perturbation by the projectile:

$$V(\vec{r},t) = e\,\vec{\alpha}\vec{A} - e\,\phi\ .$$

The system of coupled differential equations is solved under the initial condition that the electron occupies the $1s_{1/2}$ state at the target nucleus for $t\to-\infty$. For the calculation of the elements of the coupling matrix we use the momentum-space method: The projectile potential is transformed into momentum space and then a multipole expansion is carried through. For hydrogenic Coulomb-Dirac wave functions it is possible to integrate over the spatial coordinates analytically. However, a two-dimensional integration in momentum space remains to be performed numerically. Although our theory is based on the single-particle interpretation of the Dirac-equation, we can also describe the K-shell vacancy production of many-electron ions if electron-correlation effects are negligible.

Experimental data in the relativistic regime have been measured by Anholt and coworkers at the Bevalac in Berkeley. In this connection Anholt et al.[1] investigated the range of validity of a scaling law for the K-shell ionisation cross section given by

$$\sigma(Z_P,Z_T,v_P) = \frac{Z_P^2}{Z_T^4} F\left(\frac{v_P}{Z_T},\frac{Z_P}{Z_T}\right). \qquad (4)$$

Z_P and Z_T are the nuclear charges of the projectile and target ion, respectively, and v_P is the incident velocity of the projectile.

Experimental results of Anholt et al.[1)] for the collision systems Z_P+Xe^{52+} at 82 MeV/nucl. and Z_P+U^{90+} at 430 MeV/nucl. are shown in Fig.1.(Anholt et al.[1] scattered Xe^{52+} and U^{90+} ions on various target atoms.) Since v_P/Z_T is approximately the same for both systems, identical values should be expected for $\sigma\cdot(Z_T^4/Z_P^2)$ as a function of Z_P/Z_T. However, the scaled experimental data deviate from one another at larger values of Z_P/Z_T.

For both collision systems we carried out coupled channel calculations. The theoretical results shown in Fig.1 are in qualitative good agreement with the experimental data. They are generally too low at small values of Z_P/Z_T and can not explain the experimentally found breakdown of the scaling law at higher values of Z_P/Z_T. The reason for this unsatisfactory agreement may be due to the method of Anholt et al.[1] in correcting the experimental data for the anti-screening effect which is the contribution to the ionisation of the projectile electrons induced by the field of the electrons of the target.

[1] R. Anholt et al., Phys.Rev. A36, 1586 (1987)

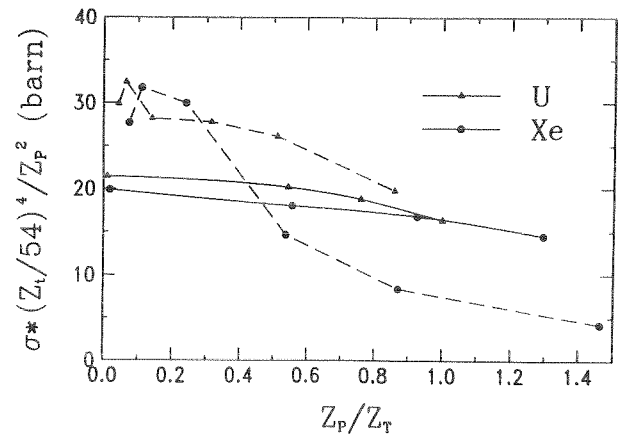


Fig.1: Scaled ionisation cross sections for one K-shell electron of the systems Z_P+U^{90+} and Z_P+Xe^{52+} at E_{lab}= 82 MeV/nucl. as a function of Z_P/Z_T. The cross sections have been multiplied by the scaling factor $(Z_T/54)^4/Z_P^2$. The experimental data of Anholt et al.[1] are shown by triangles for Z_P+U^{90+} and by full dots for Z_P+Xe^{52+} connected by dashed curves. The theoretial values are connected by solid curves.

Ionization of an Atom in Nuclear Decay[B]

G. Scheitler and M. Kleber

Physik Department, TU München, D-8046 Garching

We discuss the old problem: How do the electrons react when a nucleus decays into two pieces (fission, α-decay)? We have found[1] the analytic solution for the collinear decay under the following assumptions:

i) The relative motion of the (heavy) nuclear fragments is treated classically. The two fragments are assumed to separate from each other at $t = 0$ with relative velocity $2v$.

ii) We use the single-electron-approximation, neglecting the electron-electron interaction. The electron under consideration is assumed to move in the two zero-range potentials

$$V(x,t) = -\alpha\,\delta(x - vt) - \beta\,\delta(x + vt)\,. \tag{1}$$

At $t = 0$, the electron is bound to the zero-range atom with binding energy $-(\alpha+\beta)^2/2$ which will be taken from experiment. Also, the ratio α/β is fixed by the ratio of the effective nuclear charges of the fragments.

The problem now is to calculate the probabilities for an electron to travel with one of the fragments or to end up in a continuum state after the fragments have separated ($t \to \infty$).

Assuming sudden decay at $t = 0$ we have

$$\psi(x,t) = \int_{-\infty}^{\infty} dx'\,K(x,t \mid x',0)\,\psi(x',0)\,, \tag{2}$$

where K is the (retarded) time dependent propagator for the transient two center problem (1). It turns out that the propagator can be written in the form

$$\begin{aligned} K(x,t \mid x',0) &= U_0(x - x';t) \\ &+ i\alpha\,D^-(x,x',t)\int_0^{\infty} dy\,f^-(y,x')\,U_0(\mid x - vt \mid + \mid x' \mid + iy;t) \\ &+ i\beta\,D^+(x,x',t)\int_0^{\infty} dy\,f^+(y,x')\,U_0(\mid x + vt \mid + \mid x' \mid + iy;t)\,. \end{aligned} \tag{3}$$

Here $D^{\pm}$ are velocity dependent phase factors and $U_0(x - x';t)$ is the free particle propagator. The non trivial part are the $f^{\pm}$ which can be expressed in terms of Bessel functions. The result is

$$\begin{aligned} f^+(y,x') &= e^{-ivx'}\,e^{-v(1-d)y}\,. \\ &[\,C_1\,J_{\nu^+}(-h(y,x')) + C_2\,J_{-\nu^+}(-h(y,x'))\,] \end{aligned} \tag{4}$$

and

$$\begin{aligned} f^-(y,x') &= \frac{1}{i}\sqrt{\frac{\beta}{\alpha}}\,e^{ivx'}\,e^{-v(1-d)y}\,. \\ &[\,-C_2\,J_{\nu^-}(-h(y,x')) + C_1\,J_{-\nu^-}(-h(y,x'))\,]\,. \end{aligned} \tag{5}$$

In (4) and (5) we have introduced the Bessel functions of the first kind with non integer indices

$$\nu^{\pm} = (1 \mp \frac{i(\alpha-\beta)}{2v})/2\,, \tag{6}$$

together with

$$h(y,x') = \frac{\sqrt{\alpha\beta}}{2v}\,e^{2iv(|x'|+iy)} \tag{7}$$

and

$$d := \frac{i(\alpha+\beta)}{2v}\,. \tag{8}$$

The C_1 and C_2 are functions of x' and are determined from the condition

$$f^{\pm}(0,x') = 1\,. \tag{9}$$

Instead of discussing the general case we have a look at the symmetric decay $\alpha = \beta$ (see also[2]). Then, the $x-$even and $x-$odd parts of $\psi(x,0)$ develop independently from each other. For $x-$even wave functions the propagator is given by

$$\begin{aligned} &K(x,t \mid x',0) = U_0(x - x';t) \\ &+ i\alpha\,\cos(vx')\,e^{-iv^2t/2}\int_0^{\infty} dy\,e^{i\alpha y}\,\exp[ig(y,x')]\,\Phi(x,x',y,t)\,, \end{aligned} \tag{10}$$

where

$$\begin{aligned} \Phi(x,x',y,t) &= e^{ivx}\,U_0(\mid x - vt \mid + \mid x' \mid + iy;t) \\ &+ e^{-ivx}\,U_0(\mid x + vt \mid + \mid x' \mid + iy;t) \end{aligned} \tag{11}$$

and

$$g(y,x') = \frac{\alpha}{2v}\,\left(1 - e^{-2vy}\right)\,e^{2iv|x'|}\,. \tag{12}$$

There is a similar expression for the time evolution of $x-$odd wave functions.

Let us mention that despite its simplicity the model retains important physical properties of the three dimensional world. It reproduces the Stueckelberg oscillations for quasiresonant charge transfer[3] and the $v/2$ electron emission[4] in ion-atom collisions. In the latter two cases the model simulates scattering processes. In such a situation one has to specify the initial wave function before the collision ($t \to -\infty$). The needed transition probabilities can then be calculated from $\psi(x,t=0)$ and it is not necessary to determine $\psi(x,t>0)$, in contrast to the present problem.

[1] G. Scheitler and M. Kleber, preprint

[2] S. K. Zhdanov and A. S. Chikhachev, Sov. Phys. Dokl. **19**, (1975) 696

[3] W. Däppen, J. Phys. **10**, (1977) 2399
H. Danared, J. Phys. **B17**, (1984) 2613

[4] J. Burgdörfer, J. Wang and A. Barany, Phys. Rev. **A38**, (1988) 4919

Radiative Muon Capture in Light Atoms

G. Soff and J. Rafelski
GSI, Darmstadt and Department of Physics,
University of Arizona, Tucson, Arizona 85721, USA

We evaluated total cross sections for radiative muon capture into inner shells of light atoms [1]. One important problem in muon catalyzed fusion (MCF) is the determination of the muon capture rate into hydrogen or helium. This capture rate is an essential ingredient for the number of possible fusion cycles per muon. Muon capture can proceed either by Auger transitions, by three-body collisions incorporating neighbouring atoms or by radiative transitions. Here we concentrate on the evaluation of the cross section for the latter process which can be measured independently.
In first-order perturbation theory we can employ Fermi's golden rule to represent the radiative capture cross section from an initial continuum state Ψ_i to a final bound state Ψ_f with principal quantum number n and orbital angular momentum quantum number l as

$$\sigma_{nl} = \frac{V}{v}\frac{\alpha}{2\pi}\frac{\omega}{\mu^2 c^2}\sum_{\alpha=1,2}\int\left|\left\langle\Psi_f|e^{-i\mathbf{Q}\cdot\mathbf{r}}(\varepsilon_\alpha\cdot\hat{\mathbf{p}})|\Psi_i\right\rangle\right|^2 d\Omega_{\mathbf{Q}}$$

ε_α with $\alpha = 1,2$ denote the two orthogonal polarization vectors of the emitted photon which are perpendicular to the photon momentum $\mathbf{Q}$, i.e. $\varepsilon_\alpha\cdot\mathbf{Q} = 0$. $\hat{\mathbf{p}}$ is the momentum operator acting on the initial continuum state Ψ_i. The direction of the impinging muon with momentum $\hbar\mathbf{q} = \mu\mathbf{v}$ is chosen to be the quantization axis (z-axis); $v = |\mathbf{v}|$. After angular integration it results for the muon capture into a bound state with the quantum numbers n and l

$$\sigma_{nl} = \frac{16}{3}\pi\alpha\frac{c}{v}\frac{1}{q^2}\left(\frac{\hbar\omega}{\hbar c}\right)^3\left[l\left\{\int_0^\infty R_{nl}\,F_{l-1}(-\eta;qr)\,r^2\,dr\right\}^2 + (l+1)\left\{\int_0^\infty R_{nl}\,F_{l+1}(-\eta;qr)\,r^2\,dr\right\}^2\right]$$

with the radial bound state wavefunction R_{nl} and the regular Coulomb wavefunction F_l. $\hbar\omega$ is the photon energy. Restricting ourselves to the 1s-state one can perform the radial integrals analytically. The capture cross section into the 1s-state finally reads

$$\sigma_{1s} = \frac{256}{3}\pi^2\alpha^3\frac{E_{1s}^3}{(\hbar\omega)^2(\hbar\omega - E_{1s})}\frac{\exp\{-4\eta\,\arctan(1/\eta)\}}{1-\exp\{-2\pi\eta\}}a_0^2\,.$$

The dashed lines in figs. 1 and 2 display the total cross section σ_{1s} for radiative muon capture into the 1s-state of the the atoms H, He, C, Ne and Ca. Kinetic muon energies in the domain 0.1 keV $\leq E \leq$ 100 keV are considered.
Now we turn the discussion to radiative capture into arbitrary bound states being characterized by n and l. The total cross section for radiative capture summed over all bound states reads

$$\sigma = \sum_{n=1}^{n_{max}}\sum_{l=0}^{n-1}\sigma_{nl}\,.$$

We have chosen $n_{max} = 14$ for the maximum principal quantum number. For still higher values of n screening effects may no longer be neglected. They tend to reduce drastically capture cross sections.
The total capture cross sections are depicted by the solid lines in figs. 1 and 2 [1]. For high kinetic muon energies E the total cross section is dominated by capture into the K-shell whereas for lower values of E also the higher bound states become significantly important.

1. G. Soff, J. Rafelski, Z. Physik D14 (1989) 187

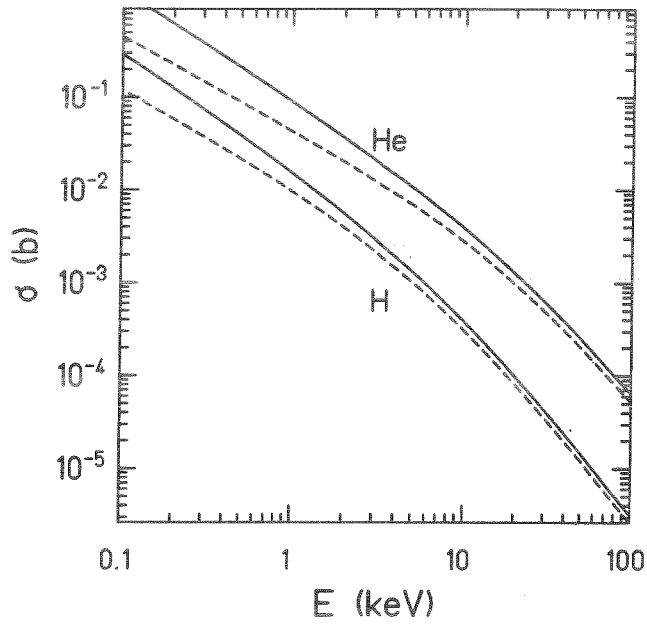


Fig. 1: Dashed lines: Total cross section σ in units of barn for radiative muon capture into the 1s-state of hydrogen and helium, respectively. Solid lines: Total cross section σ for radiative muon capture into all bound states summed up to the principal quantum number $n_{max} = 14$. σ is plotted versus the initial kinetic muon energy E in units of keV.

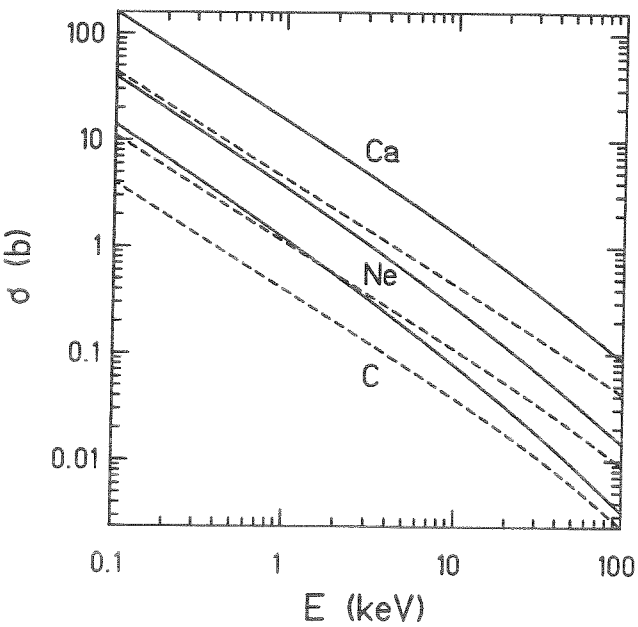


Fig. 2: The same as in fig. 1 for target atoms with Z = 6, 10, and 20, respectively.

Many Electron Dirac-Fock-Slater Coupled Channel Calculations for 16 MeV-S^{16+} on Ar[G]

P. Kürpick, B. Thies, W.-D. Sepp, B. Fricke
Fachbereich Physik, Universität Kassel

During the last few years we developed a fully ab initio Dirac-Fock-Slater (DFS) Coupled Channel-Code to study heavy ion scattering processes [1,2]. It is of interest to test these programs on heavy-ion collision systems which contain a large number of electrons and where more than one electron is transferred within the various levels. In the literature the most complete experimental results[3] to be found are on the system 16 MeV-S^{16+} on Ar. This experiment was carried out to answer the following questions:
How large is the probability of finding:

1. One electron in Ar 1s and one electron in S 1s? (P_{sa})
2. Two electrons in Ar 1s ? (P_{aa})
3. Two electrons in S 1s ? (P_{ss})

We performed a large number of selfconsistent static DFS calculations of the quasi-molecular system S^{16+} - Ar at all internuclear distances to obtain the adiabatic energyeigenvalues as well as the d/dR and d/dθ coupling-matrix elements with an occupation according to the asymptotic occupation of the separated atoms in the incoming channel. In the coupled-channel code we included the 20 lowest relativistic channels (8 non relativistic channels) and asked for the amplitudes of the two lowest molecular levels which form the separated Ar 1s and S 1s levels after the collision. To evaluate the many particle probabilities P_{ss}, P_{aa}, and P_{sa} a complicated sum and product of one-electron amplitudes[4] calculated with the coupled channel code must be used. Figs. 1 and 2 show the answers i.e. P(b)-curves for the questions 1 to 3 .

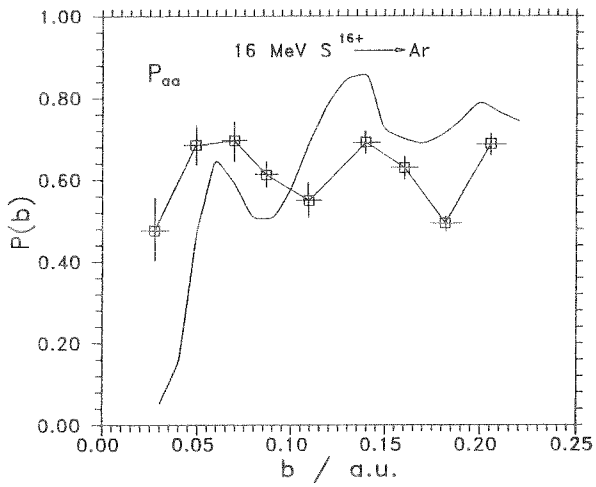


Fig.1 P_{aa}(b) curves for two electrons in Ar 1s. Experimental values : Ref.3; full line: this work.

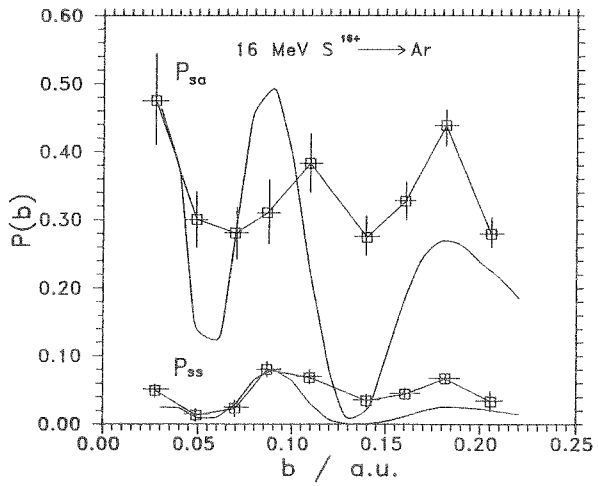


Fig.2 P_{sa}(b) curves for one electron in Ar 1s and one electron in S 1s. P_{ss}(b) curves for two electrons in S 1s. Experimental values: Ref.3; full line: this work.

1 W.-D. Sepp et al., Phys.Rev. A33 3679 (1986)
2 B. Thies, Dissertation, Kassel (1988)
3 Schulz et al., J.Phys. B: At. Mol. Phys. 20 (1987) 2057
4 Reinhardt et al., Phys. Rev. Lett. 43 (1979) 1307

Inter-Nuclear Potential of the System Si-Si calculated with the Finite-Element-Method[G]

S. Hackel, B. Fricke, D. Heinemann, D. Kolb, L. Yang
Fachbereich Physik, Universität Kassel

Using the Finite-Element-Method[1] (FEM) to solve the Hartree-Fock-Slater equations one achieves very accurate energy eigenvalues, total energies and wavefunctions for diatomic molecules. Up to now only small diatomic molecules have been calculated with this method. Improvements in the grid-point distributions[2] now allow the calculation of heavier systems.

Sputtering processes are studied with the help of Monte-Carlo simulations[3]. For these simulations potential energy curves are needed as input for the systems of interest. To provide such potential energy curves, and to check the quality of the semiempirical or fitted potentials used so far[4], the system Si-Si was calculated as an example.

For our FEM-calculations we use the prolate-spheriodal coordinate system with 1369 grid points, for the radial coordinate a logarithmic and for the angular coordinate a linear point distribution. The internuclear distance is varied from 0.4 a.u. to 4.1 a.u., this being the region of interest for sputtering simulations[3].

Results of these calculations are the correlation diagram for the one-electron energies (fig. 1), and the total energy curve of the groundstate of the system Si-Si. In figure 2 the resulting potential energy curve is plotted and compared with other potential energy curves[4]. The numerical accuracy is approx. 0.05 eV. For small distances up to 1.0 Å it shows good agreement with the Molière-, KrC-, and "Universal"- potential energy curves[4], above 1.0 Å it behaves like a normal groundstate potential energy curve with negative values for very large distances. All other curves plotted here do not contain this behaviour.

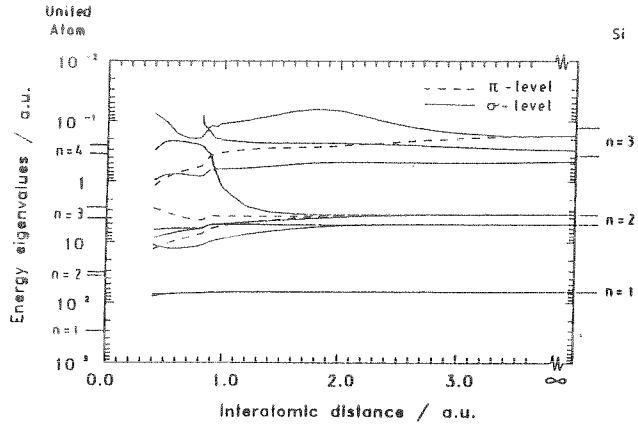


Fig 1.: Correlation diagram of the groundstate of the system Si-Si

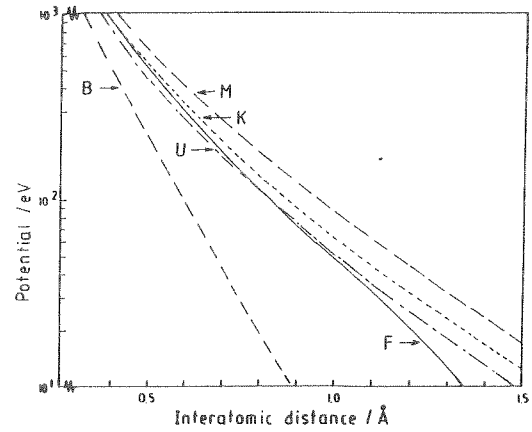


Fig. 2: Potential energy curves of the groundstate of the system Si-Si as calculated in this work (F; solid) in comparison to the Molière- (M; dashed), KrC- (K; dotted), "Universal"- (U; dotted-dashed) and Bohr-potential (B; dashed)

1 D. Heinemann et al., Phys. Rev. A38, 125 (1988)
2 D. Heinemann et al., GSI-Rep. 1988, p. 198
3 J.P. Biersack, Nucl. Inst. Meth. B27, 21 (1987)
4 J.F. Ziegler, The stopping and range of ions in solids, Vol. 1, Pergamon, New York, 1985

Spin-polarized Hartree-Fock-Slater Calculations for Atoms and Diatomic Molecules with the Finite Element Method[6]

D. Heinemann, B. Fricke, D. Kolb
Fachbereich Physik, Universität Kassel
A. Rosén,
Department of Physics, Chalmers University of Technology

In recent years there has been an increasing interest in the use of numerical methods for the self-consistent solution of the Hartree-Fock-Slater (HFS) equations[1,2] as a complement to basis-set oriented approaches. With the finite element method (FEM) calculations with an accuracy of up to 10^{-8} a.u. have been performed for closed shell systems like CO, N_2 and BH. In order to extend the applicability of the method to open shell systems a program version was developed capable to solve the spin-polarized HFS equations with the FEM. These equations read:

$$(-1/2\,\nabla^2 + V^s(r))\,\phi_i^s(r) = e_i\,\phi_i^s(r)$$

with:

$$V^s(r) = V_{nuc}(r) + V_c(r) + V_x^s(r)$$

$$V_x^s(r) = -3\alpha(3/4\pi\,\rho^s(r))^{1/3}$$

where $V_{nuc}(r)$ is the nuclear Coulomb potential of nuclei 1 and 2 with charges Z_1 and Z_2 at position r_1 and r_2. $V_c(r)$ is the electronic Coulomb potential, and $V_x^s(r)$ the remaining exchange correlation contribution of the electron-electron interaction in Slater approximation. The superscript s denotes the spin quantum number. For open shell systems this equations result in different exchange potentials for the spin-up and the spin-down electrons.

The computational approach was tested by calculating some atomic systems. Table 1 compares the results for the ^3P state of the Oxygen atom with those of a 1-dimensional calculation. The values for the total energy and the eigenvalues agree within 10^{-5} a.u. using about 260 grid points for the 2-dimensional approach.

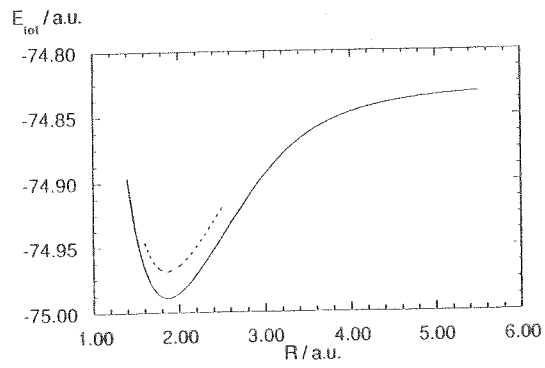
For a first application to diatomic molecules the radical OH was selected. Figure 1 shows the potential energy curve between 1.4 and 5.5 a.u. including a comparison with the result from a non-polarized HFS calculation. The spin-polarized calculation results in a lowering of the total energy of approx. 0.02 a.u. The numerical accuracy of the total energy is approx. 10^{-6} a.u., and is achieved by using 1389 grid points.

From the potential energy curve we calculated a bond length of r_e = 1.86 a.u., a binding energy of E_b = 4.43 eV and a vibrational energy w_e = 3714 cm^{-1}. Agreement with experimental values[3] r_e = 1.83 a.u., E_b = 4.392 eV, and w_e = 3737.76 cm^{-1} is very good.

Table I :
Total energy E_{tot} and orbital energies e_i of the ^3P state of the atomic Oxygen. All values in a.u. 1D denotes the 1-dimensional calculation.

	1D	this work
E_{tot}	-74.3565	-74.35651
$e_{1s\uparrow}$	-18.79722	-18.79722
$e_{1s\downarrow}$	-18.73319	-18.73318
$e_{2s\uparrow}$	-0.898507	-0.898506
$e_{2s\downarrow}$	-0.749675	-0.749670
$e_{2p\uparrow}$	-0.362628	-0.362627
$e_{2p\downarrow}$	-0.221280	-0.221276

Figure 1 :
Comparison of potential energy curves for the OH radical with spin-polarized (full curve) and non-polarized HFS potenial (dotted curve) with α = 0.7.



[1] L. Laaksonen, D. Sundholm, P. Pyykkö, Comp. Phys. Rep. 4, 313 (1986)

[2] Numerical Determination of the Electronic Stucture of Atoms, Diatomic and Polyatomic Molecules, Eds. M. Defranceschi and J. Delhalle, NATO ASI Series C. Vol. 271, Kluwer Academic Publishers, Dordrecht Boston London 1988

[3] K. P. Huber and G. Herzberg, "Constants of Diatomic Molecules", Van Nostrand Reinhold, New York (1979)

Wavelengths and Lifetimes of Doubly Excited Few-electron Ions[G]

J.H.Blanke, B.Fricke

Fachbereich Physik, Universität Kassel

P.H.Heckmann

Inst. für Experimentalphysik III, Ruhr-Univ. Bochum

Doubly excited three-electron quartet and doubly excited four-electron quintet states are stable against autoionization and decay to singly excited states. Therefore optical transitions should be readily observable. We use the Multi-Configuration Dirac-Fock Method[1] (MCDF) to calculate transition wavelengths for such transitions. For the three-electron quartet transitions there exist experimental values to compare with for the elements[2] Li to F. The transitions are of the form $1s2s2p\ ^4P^o$ - $1s2l3l\ ^4L$ or $1s2p^2\ ^4P$ - $1s2l3l\ ^4L^o$. The limitation of our theoretical approach is that we leave out part of the correlation energy. In Figure 1 we have plotted the difference between the experimental and calculated transition energies. This difference is linear in Z for all transitions in question. Therefore an extrapolation to higher Z is possible so that we are able to predict very good wavelengths for such transitions in Mg, Al and Si. Beam-Foil experiments do confirm these expectations. Spectra are taken by a 2.2 m grazing-incidence spectrometer in Bochum. Examples for Mg are given in Table 1.

Furtheron we formulated an addition to the MCDF-approach that enables us to calculate transition probabilities for dipole transitions. Initial and final states are calculated independently. The consequent nonorthogonality of the orbitals is partly corrected by multiplying the transition matrix elements with the overlaps of the non active orbitals. For the three-electron quartet states there exist some experimental data and a model potential calculation by Laughlin[3]. Comparison is given in Table 2, as example. This method will be used to confirm our tentative identifications of quintet lines of the form $1s2s2p^2\ ^5P$ - $1s2s2p3l\ ^5L^o$ along the isoelectronic sequence.

It should be mentioned that such doubly excited states give rise to satellite lines that cause problems to some high Z Lamb shift experiments and that they are also important for diagnostic methods in plasma physics.

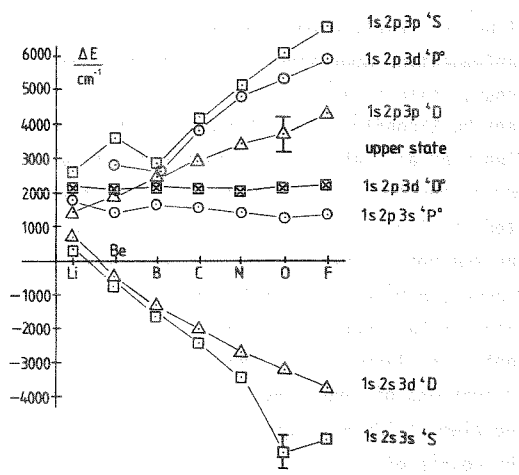


Fig. 1: Deviation between experiment and MCDF

Tab.1: Wavelengths of quartet trans. for Mg

Transition	MCDF /nm	Corrected /nm	Exp. /nm
$1s2s2p\ ^4P^o$			
- $1s2s3s\ ^4S$	5.821	5.847(2)	5.849(3)
- $1s2s3d\ ^4D$	5.547	5.5635(10)	5.562(2)
$1s2p^2\ ^4P$			
- $1s2p3s\ ^4P^o$	6.027	6.023(2)	6.020(3)
- $1s2p3d\ ^4P^o$	5.719	5.684(1)	blended
- $1s2p3d\ ^4D^o$	5.734	5.726(1)	5.726(1)

Table 2: Partial lifetimes of doubly excited three-electron quartet states as calculated with MCDF

	$1s2s3d\ ^4D$		
Z	Model Pot.(Ref.3) /ps	MCDF /ps	Experiment[4] /ps
6	29.7	27.8	
7	13.2	12.4	11.9±1.4
8	6.7	6.3	8.4±0.9
9	3.8	3.6	2.7±0.9

	$1s2p3d\ ^4D^o$		
Z	Model Pot.(Ref.3) /ps	MCDF /ps	Experiment[4] /ps
6	29.0	29.2	30.8±3.0
7	12.5	12.5	8.2±2.3
8	6.2	6.2	5.7±0.6
9	3.5	3.4	3.6±0.7

1. J.P.Desclaux, Comp.Phys.Comm. 9, 31 (1975)
2. S.Mannervik, Phys. Scr. 40, 28 (1989)
3. C.Laughlin, Z.Phys. D9, 273 (1988)
4. J.H.Blanke, P.H.Heckmann, and E.Träbert, Phys.Scr. 32, 509 (1985)

Ionization Potentials and Radii of Atoms and Ions of Elements 104 and Hafnium (2+) from MCDF-Calculations [G]

Elijah Johnson and B. Fricke
Theoretische Physik, Universität Kassel
O.L. Keller, Jr., C.W. Nestor, Jr., and T.C. Tucker
Chemistry Division, ORNL, Oak Ridge

According to the normal continuation of the periodic table element 104 is expected to be a group 4 element below Ti, Zr, and Hf with a ground state configuration of $6d^2 7s^2$. Early Dirac-Fock calculations in the single configuration approximation[1] indicate that indeed the ground state is $6d^2 7s^2$, but now we confirm the more recent Multiconfiguration-Dirac-Fock (MCDF) results of Glebov et al.[2] which give the ground state as $6d^1 7s^2 7p^1$. During the last year we have re-calculated and re-evaluated the first four ionization energies of element 104. The theoretical method was the relativistic Multiconfiguration-Dirac-Fock (MCDF) method[3,4]. The results presented in last year's GSI report were preliminary ones containing large errors. Now we are able to present good evaluations of "experimental" ionization potentials for the element 104 with only a very small error margin. In the course of this evaluation we realized that the experimental ionization potential of Hf^{2+} has probably been measured poorly. We are now able to give an improved value (see Table I).

The actual calculations done by us were MCDF calculations including all configurations which can be constructed from the outer s, d, and p wave functions. All ionization states, and all possible angular momenta have been calculated. For the known elements all experimentally known ground states are reproduced correctly. The extrapolation - which yielded good "experimental" ionization potetials - has been improved drastically to correct for the errors in the calculated values. This method is based on a consistent and automatic extrapolation of double-differences between calculated and experimental values in two ways: first, along the same ionization potential but with increasing element, and, second, along the increasing ionization state of the same element. Both procedures give the same result and make allowance for a very small error[5].

Table I lists the experimentally known or extrapolated ionization potentials as well as the calculated ones for the group IVb elements.
Table II presents the radii of the group 4 elements plus ions, Ti, Zr, Hf, and 104 from the MCDF calculations.

[1] B. Fricke, Structure and Bonding 21, 89 (1975) Springer Verlag, New York
[2] V.A. Glebov, L. Kasztura, V.S. Nefedov, and B.L. Zhuikov, Radiochimica Acta 46, 117 (1989)
[3] J.P. Desclaux, Computer Phys. Comm. 9, 31 (1975)
[4] I.P. Grant, Advances in Physics 19, 747 (1970)
[5] E. Johnson, B. Fricke, O.L. Keller, Jr., C.W. Nestor, Jr., and T.C. Tucker, to be published in J.Chem.Phys.
[6] C.C. Moore, Aromic Energy Levels, NSRDS-NBS-35, Washington, D.C., 1971

Table I: Calculated and experimental[6] ionization potentials in eV.

Ion	calc. value	exp. value
Ti	6.41	6.82
Zr	6.13	6.63
Hf	6.10	6.82
104	5.54	(6.5+0.1)
Ti^{1+}	12.94	13.58
Zr^{1+}	12.26	13.13
Hf^{1+}	13.82	14.9
104^{1+}	13.47	(14.8+0.2)
Ti^{2+}	26.55	27.49
Zr^{2+}	22.31	23.11
Hf^{2+}	21.55	(22.4+0.2)
104^{2+}	22.94	(23.8+0.3)
Ti^{3+}	42.23	43.27
Zr^{3+}	33.42	34.42
Hf^{3+}	32.26	33.37
104^{3+}	30.59	(31.9+0.1)

Table II: Calculated radii in nm

	Ti	Zr	Hf	104
0	0.161(4s)	0.173(5s)	0.161(6s)	0.178(7p)
1+	0.150(4s)	0.163(5s)	0.149(6s)	0.145(7s)
2+	0.052(3d)	0.083(4d)	0.0872(5d)	0.138(7s)
3+	0.049(3d)	0.080(4d)	0.0831(5d)	0.135(7s)
4+	0.047(3p)	0.062(4p)	0.0626(5p)	0.0706(6p)

RADIATION EFFECTS

3. RADIATION EFFECTS PAGE

3.1 BIOPHYSICAL EXPERIMENTS 169

3.1.1 Radiation Effects in Biological Systems

Comparison of Geometrical Nuclear Cross Sections of Synchronous V79 Chinese Hamster Cells with the Corresponding Inactivation Cross Sections of 5.1 MeV/u Uranium Ions 175
M. Scholz, M. Wannenmacher, W. Kraft-Weyrather, G. Kraft, F. Kraske, G. Lenz, H. Penninger, S. Ritter, Th. Rothmann, S. Thiel

Cell Cycle Delays after Irradiation of Synchronous V79 Chinese Hamster Cells with 5.1 MeV/u Uranium Ions 176
M. Scholz, M. Wannenmacher, W. Kraft-Weyrather, G. Kraft, F. Kraske, G. Lenz, H. Penninger, S. Ritter, Th. Rothmann, S. Thiel

Induction of Polyploidy and Persistent Chromosome Aberrations in V79 Cells after Heavy Ion Irradiation 177
S. Ritter, E. Kehr, W. Kraft-Weyrather, K. Füssel, M. Scholz, G. Kraft

Split Dose Effects after Heavy Particle Irradiation with 15 MeV/u Argon Ions in Human Carcinoma Cell-lines 178
M. Flentje, J. Bühler, M. Scholz, M. Wannenmacher

Cell Survival as a Function of Defined Number of Passed Ions and Impact Parameter 179
F. Kraske, M. Scholz, S. Ritter, M. Schneider, D. Schall, H. Penninger, G. Lenz, C. Wiese, T. Rothmann, G. Kraft, E. Kankeleit

Recovery Experiments with V79 Cells after Heavy Ion Exposure 180
H. Rink, J. Heilmann

Measurement of Haemolysis Erythrocytes as an Indication of Radiation Induced Membrane Damage 181
W. Schön, H. Gärtner, G. Bartosz, G. Kraft

Molecular Analysis of Syrian Hamster Embryo-Cell Lines Transformed by 8 MeV/u Carbon Ions 182
K. Trutschler, L. Hieber, A.M. Kellerer

In-situ Hybridization of Human Chromosome 11 in Human-Hamster Hybrid Cells 183
R. Greinert, J. Smida, A.M. Kellerer,

Mutation Induction in V79 Cells by Accelerated Heavy Ions 184
T. Kranert, E. Schneider, J. Kiefer

Biological Dosimetry of Radiation-Induced Chromosome Aberrations in Interphase and Metaphase of Human Lymphocytes by Chromosomal in Situ Suppression Hybridization 185
S. Popp, T. Cremer, B. Remm, C. Cremer

Repair of DNA Double Strand Breaks in Mammalian Cells: an Experimental Approach 186
G. Taucher-Scholz, C. Wiese, J.A. Stanton, M. Schneider, G. Kraft

Heavy Ion Induced DNA Double Strand-Breaks in Yeast: Preliminary Results 187
T. Akpa, K.J. Weber, J. Kiefer, M. Frankenberg-Schwager, R. Harbich, D. Frankenberg

Induction of DNA Double-Strand Breaks in Vegetative Cells of Bacillus Subtilis and Escherichia Coli 188
U. Micke, M. Schäfer, G. Horneck, H. Bücker, H.D. Mennigmann

The Effect of Heavy Ion Radiation on SV40 DNA Under Different Experimental Conditions 189
J. Stanton, M. Schneider, G. Taucher-Scholz, C. Wiese, G. Kraft

Heavy Ion Induced Free Radical Formation in Nucleic Acid Constituents: Quantitative Electron Spin Resonance Investigations 190
A. Schäfer, J. Hüttermann, G. Kraft

Laser Spectroscopic Investigation of Heavy-ion Induced DNA Strand Breaks 191
N. Hellmann, Th. Kühl, G. Kraft, R. Neumann

A Model System to Detect Heavy Ion Induced Mutations in Mammalian Cells 192
B. Stahlhacke, J. Thiermann, H. Appelhans, H.G. Gassen

Biological Action of Single Heavy Ions on Individual Yeast Cells 193
M. Kost, E. Schneider, J. Kiefer, G. Lenz

Chemical Protection of Bacterial Cells Against Heavy Ion Irradiation 194
M. Schäfer, C. Schmitz, H. Bücker

Influence of Growth Conditions on the Survival of Deinococcus Radiodurans Exposed to Ionizing Radiation 195
M. Schäfer, C. Schmitz, H. Bücker

Effects of HZE-Irradiation in Arabidopsis Pollen 196
M. Pickert, U. Bork, A.R. Kranz

Irradiation-Induced Tumors in Xiphophorus (Pisces, Teleostei) 197
M. Henze, F. Anders, A. Luboeinski

A Scanning Tunneling Microscope for the Investigation of Technical Surfaces and Biological Objects 198
W. Mayer, R. Stephan, H. Gärtner

δ-electron Spectroscopy from Fast Heavy Ion Collisions 199
U. Ramm, H. Schmidt-Böcking, G. Kraft

3.1.2 Preparation for Radiotherapy

Status of the Heavy Ion Therapy Project 200
G. Kraft, N. Angert, K. Blasche, D. Böhne, B. Fischer, B. Franczak, H. Geissel, T. Haberer, W. Kraft-Weyrather, B. Langenbeck, G. Münzenberg, S. Ritter, D. Schardt, Th. Schwab, H. Stelzer, G. Gademann, M. Wannenmacher, G. Hartmann, W.J. Lorenz

Computer Simulations of Beam Scanning Strategies for the Radio-Therapy-Project 201
T. Haberer, K. Blasche, D. Böhne, B. Fischer, G. Kraft, B. Langenbeck, M. Wannenmacher, W.J. Lorenz

3.2 RADIATION EFFECTS IN SOLIDS 202

3.2.1 Ion Implantation and Ion Sputtering

High Dose Iron Implantation into Silicon and Metals 202
G. Müller, G. Klingelhöfer, P. Schwalbach, E. Kankeleit

Mößbauerspectroscopy after ^{57}Fe-Implantation into Semiconductors and Insulators
M. Hartick, E. Kankeleit, B. Keck, G. Klingelhöfer, S. Laubach, P. Schwalbach, B. Stahl 203

MeV-implantation of Kr^+ into Ti 204
H. Volkmann, K. Thoma, H. Gärtner, D.M. Rück

Simulation of Particle Reflection During Ion-implantation 205
S. Saler, R. Kassing

Novel Chromium Layers Formed by Nitrogen Ion Implantation of Conventional and ABCD Electrodeposited Films 206
H. Ferber, G.B. Hoflund, C.K. Mount, S. Hoshino, D.M. Rück

Recent Progress Using Ion Beam Techniques for Materials Modification 207
P. Ballhause, W. Ensinger, W. Fischer, G.K. Wolf, D.M. Rück

Surface Analysis by Spontaneous Desorption of Ions 208
S. Metzger, B. Fischer

Sputtering of Gold by Uranium Ions with UNILAC Energies 209
Yu.N. Cheblukov, D.G. Koshkarev, A.R. Peuto, I.V. Rudskoygh, N.A. Vasiliev, V.M. Nazarov, R. Bock, D.H.H. Hoffmann, R.W. Müller, J. Vetter

3.2.2 Ion Beam Induced Modifications

Study of Radiation Effects of Heavy Ions in Microelectronic Devices 210
W. Heinrich, O. Geschke, A. Noll, R.H. Sorensen, J. Vetter

Swift Heavy Ions Induced Effects in Matter 211
CIRIL

The Stability of the Silicon Against the High Electronic Excitation Induced by ^{238}U Ion Irradiation 212
M. Toulemonde, S. Bouffard, P. Mary, P. Bogdanski, R. Spohr, J. Vetter

Enhancement of Defect Creation Yield in Organic Metals for Swift Heavy Ion Irradiation 213
S. Bouffard, M. Toulemonde, R. Spohr, J. Vetter

Magnetic Insulators 214
F. Studer, C. Houpert, H. Pascard, M. Toulemonde, R. Spohr, J. Vetter

Effects of Electronic Energy Loss in Amourphous Fe-B Alloys Irradiated with High Energy Heavy Ions 215
A. Audouard, E. Balanzat, J.C. Jousset, G. Fuchs, D. Lesueur, R. Spohr, J. Vetter, L. Thomé

A Short Introduction to the Motivations of the Low Temperature Irradiations of Metallic Targets with GeV Heavy Ions 216
A. Dunlop

High Electronic Excitations and Damage Production in GeV Ion Irradiated Metals 217
A. Dunlop, D. Lesueur, J. Morillo, J. Dural, R. Spohr, J. Vetter

Partial Amorphization of Crystalline Ni_3B Induced by High Electronic Excitations 218
A. Audouard, E. Balanzat, S. Bouffard, A. Chamberod, A. Dunlop, G. Fuchs, J.C. Jousset, D. Lesueur, R. Spohr, J. Vetter, L. Thomé

3.2.3 Nuclear Tracks and Etching

Structure of Heavy-Ion Tracks in Zircon 219
G. Braunshausen, L.A. Bursill, J. Vetter, R. Spohr

Diffraction Contrast Imaging of Heavy-Ion Tracks in Zircon at 400 keV 220
G. Braunshausen, L.A. Bursill, J. Vetter, R. Spohr

Latent Tracks Induced by High Electronic Ecitations in a Metallic Compound ? 221
A. Barbu, A. Dunlop, R.S. Averback, R. Spohr, J. Vetter

Response of CR-39 to ^{238}U Ions 222
J. Raju, S. Gosh, A. Saxena, K.K. Dwivedi

Tracks of ^{132}Xe in CR-39 223
S. Gosh, J. Raju, K.K. Dwivedi

Tracks of ^{132}Xe Through Polymer Stacks 224
P.P. Chaubey, J. Raju, S. Gosh, K.K. Dwivedi

Comparison of High Sensitivity Polymeric Track Detectors 225
B. Grabez, P. Vater, R. Brandt

Direct Visualization of Heavy Ion Tracks in Evaporated Se-Films 226
J. Düring, F. Granzer, K.O. Groeneveld

Etching and Technical Parameters of Polyvinylidene Flouride for the Production of Nuclear Track Microfilters 227
C.-D. Zhao, P. Vater, R. Brandt

Production of Thick Nuclear Track Filters Using 8.5 MeV/u ^{208}Pb Ions 228
H.A. Khan, S.-L. Guo, Y.L. Wang, T.C. Zhu

3.2.4 Applications of Nuclear Track Filters

Searching for the Superfluid Josephson Effect 229
C. Trautmann, R. Spohr, J. Vetter, Y. Hirayoshi, G. Eska, S. Lang

On the Investigation of Solid Pollution Particles in the Pleisse-River (DDR), Using PVDF Nuclear Track Microfilters 230
E. Köber, E.-J. Langrock, B. Plisch, M. Rommel, D. Molzahn, P. Vater, R. Brand

An Semi-Automatic Device for Erythrocyte Deformability Measurement with Nuclear Track Membrane 231
X.-H. Hao, Z.-J. Fan, S.-L. Guo, Y.-L. Wang, R. Brandt, P. Vater, M. Ganz

Determination of Solute Concentration with Nuclear Track Microfilters 232
S.-L. Guo, Y.-L. Wang, X.-H. Hao, T.-C. Zhu, H.A. Khan, G. Hussain, R. Brandt, P. Vater, M. Ganz

On the Purification of Certain Industrial Oils with the Help of Kapton Track Micorfilters 233
M. Ganz, C.-D. Zhao, P. Vater, R. Brandt

Bacteria Free Drinking Water Using Kapton Particle Track Microfilters 234
E.U. Khan, R. Tahseen, K. Mansoor, A. Sher, W. Ahmad, P. Vater, R. Brandt, F. Durrani

Isolation of Allergen-Containing Fractions from Housedust Mites Using the Cascade Particle Fractionator with Track Microfilters 235
C.-D. Zhao, P. Vater, R. Brandt, E. Bischoff

On the Surface Charging of Nuclear Track Filters 236
S.K. Chakarvarti, P. Singh

Comparison of geometrical nuclear cross sections of synchronous V79 Chinese hamster cells with the corresponding inactivation cross sections of 5.1 MeV/u Uranium ions

M. Scholz, M. Wannenmacher (Strahlenklinik der Universität Heidelberg)
W. Kraft-Weyrather, G. Kraft, F. Kraske, G. Lenz,
H. Penninger, S. Ritter, Th. Rothmann, S. Thiel (GSI Darmstadt)

Recent measurements of the cell cycle dependent radiosensitivity of mammalian cells to heavy ion irradiation yielded significant differences compared to the effects of X-rays. Especially, sensitivity increases from G_1 to S and G_2-cells for particle irradiation[1], whereas for X-rays the sensitivity of S-cells is minimal[2]. In addition, the variation of sensitivity throughout the cell cycle is lower for particle irradiation than for X-rays.

Because the cell nuclei are assumed to be the sensitive target for inactivation effects, one contribution to the increasing sensitivity could be the growth of the cell nuclei during the cell cycle, which leads to an increasing geometrical cross section with increasing cell age. This simply means, that the probability to hit a G_2-cell is higher than that to hit a G_1-cell. Therefore, the geometrical nuclear cross sections of synchronous V79 Chinese hamster cells have been measured. Cells have been synchronized by the centrifugal elutriation method. At 6 time points after synchronization the size distributions have been measured. Therefore, the cell nuclei have been stained by a DNA specific fluorescent dye (HOECHST 33258) and microscopic photographs have been taken. These photographs were analyzed by means of an automatic image processing system (TAS, Leitz).

The size distributions are shown in fig. 1a, the corresponding DNA spectra, showing the cell cycle distribution, in fig. 1b. From the size distributions $w_i(s_i)$, the fraction of cells which are not hit at a given particle fluence F can be derived using the Poisson statistics for each size interval s_i:

$$(1) \qquad p_0(F) = \sum_i w_i \cdot \exp^{-s_i \cdot F}$$

Although the probability function $p_0(F)$ shows a weak curvature in a logarithmic scale, it can be approximated with sufficient accuracy by a pure exponential function

$$(2) \qquad p_0(F) \simeq \exp^{-\sigma_{hit} \cdot F}$$

assumed that the size distribution is not to broad. This function is described by a hitting cross section σ_{hit}, which is not equal to the average geometrical nuclear cross section σ_{geom}, but is always smaller. This is due to the exponential weighting in (1), which favours the small cell nuclei. In fig. 2, these hitting probability cross sections σ_{hit} are compared with the measured inactivation cross sections σ_{inact} of an experiment performed with 5.1 MeV/u Uranium ions. In addition, the average geometrical cross sections are shown. Obviously, the hitting probabilities, described by σ_{hit}, and the inactivation probabilities, described by σ_{inact}, are very similar throughout the whole cell cycle. Assuming, that track structure effects play a minor role at this low energies, it can be concluded, that in the case of 5.1 MeV/u Uranium ions a single hit is sufficient to kill a cell. Therefore, the observed cell cycle dependence of the radiosensitivity is mainly due to the different geometrical sizes, that means different hittting probabilities in different cell cycle stages.

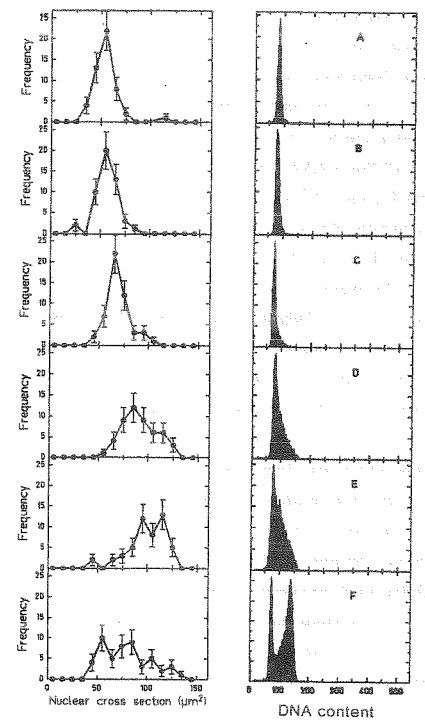


Fig. 1
a.Size distributions for cell nuclei of synchronous V79 cells for different times after synchronization in G_1-phase
b.DNA content distribution for the populations shown in fig. 1a

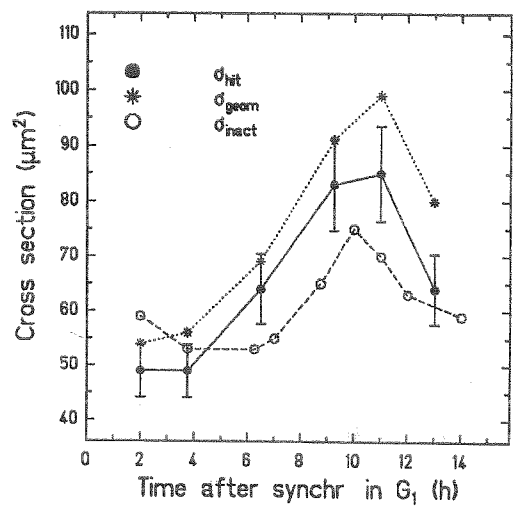


Fig. 2
Comparison of hitting probability cross sections with inactivation cross sections of an experiment performed with 5.1 MeV/u Uranium ions.

REFERENCES

1) Kraft-Weyrather,W. et al., GSI Report 89-1, 230 (1989)
2) Sinclair,W.K. and R.A.Morton, Rad.Res.29, 450-474 (1966)

Cell cycle delays after irradiation of synchronous V79 Chinese hamster cells with 5.1 MeV/u Uranium ions

M. Scholz, M. Wannenmacher (Strahlenklinik der Universität Heidelberg)
W. Kraft-Weyrather, G. Kraft, F. Kraske, G. Lenz,
H. Penninger, S. Ritter, Th. Rothmann, S. Thiel (GSI Darmstadt)

Previous experiments have shown, that heavy ion irradiation of mammalian cells leads to drastic cell cycle perturbations. These experiments have been extended to very heavy ions like Pb und U in order to clearly demonstrate the effects of high LET radiation on the proliferation capacity of cells.

Because of the marked cell cycle delays after irradiation, the observation time for each experiment has been extended from 24 to 48 hours, which corresponds to 4 complete cycles of unirradiated control cells; during this time, samples have been taken every 1.5 hours. Cells have been synchronized by centrifugal elutriation in G_1-, S- and G_2M-phase and plated immediately after synchronization. They were incubated for about 2 hours to attach to the petri dishes and were then irradiated with a fluence of $3x10^6$ particles/cm² of 5.1 MeV/u Uranium ions (LET: 15.000 keV/μm). The corresponding survival level were between 10% and 20%. In fig. 1c the proliferation of a synchronous cell population is shown, which was irradiated in G_1-phase. For comparison, the proliferation of unirradiated control cells and of X-ray irradiated cells is shown in fig. 1a and 1b, respectively. (For the X-ray experiment, a dose was chosen to give a similar survival level as in the particle experiment.) For each experiment, the progress in cell cycle can be derived from the respective fractions of the cell population in G_1-, S- and G_2M-phase as a function of time after irradiation.

The most pronounced differences after heavy ion irradiation compared to X-rays are:

1. The exit from the G_1-compartment is slowed down by a factor of about 2 compared to the control cells; for X-rays, however, no significant delay can be observed in G_1-phase.
2. There is a drastic delay of cells during the passage through S-phase, which leads to a shift of the entrance in G_2M-phase of about 9 hours.
3. Many cells are blocked in S-phase and G_2M-phase up to 48 hours after irradiation and do not divide. There is almost no increase observed in the G_1-fraction after reaching the first minimum.

In general, the proliferation of cells irradiated in S-phase or in G_2M-phase is similar to those irradiated in G_1-phase, i.e. they also show a drastic delay in S- and G_2M-phase and a large fraction of cells which do not divide up to 48 hours after irradiation.

Therefore, it is suggested, that the damages induced by 5.1 MeV/u Uranium ions are quite severe, and that these damages and the corresponding delays are not reversible, i.e., the observed cell cycle delays can be probably correlated with cell death within the first cell cycle after irradiation. This assumption is supported by microscopic observation of the cells, which showed large fractions of pyknotic cells already 24 hours after irradiation. In contrast, X-ray irradiation causes more moderate damages, which lead to cell death not before 1 or 2 additional cell cycles have been completed after irradiation. This difference can be explained by the completely different energy deposition pattern for both types of radiation. Whereas after X-rays the energy deposition is quite uniform and the local damages are comparably small, the high ionisation density inside a Uranium particle track leads to severe local damages. These damages can probably not be repaired, so that the replication of DNA cannot be completed and a division of the cell is inhibited.

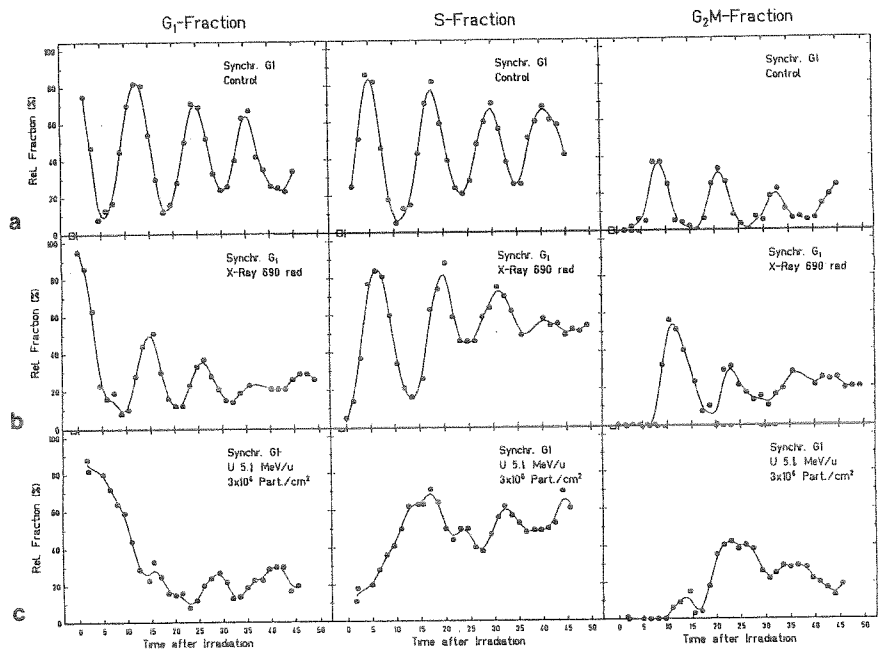


Fig. 1
Effect of irradiation on the proliferation of V79 cells synchronized in G_1-phase by centrifugal elutriation:
a. Proliferation of untreated synchronous G_1-cells
c. Proliferation of G_1-cells after X-ray irradiation
d. Proliferation of G_1-cells after irradiation with 5.1 MeV/u U-ions.

Induction of polyploidy and persistent chromosome aberrations in V79 cells after heavy ion irradiation*

S. Ritter, E. Kehr, W. Kraft-Weyrather, K. Füssel, M. Scholz and G. Kraft
GSI, Darmstadt

Numerical and structural chromosome aberrations can be observed after the exposure of cells to ionizing radiation or chemicals. Many of these aberrations result in the death of the injured cell, others are transmitted to further cell generations. These persistent aberrations are dangerous. They may result in a pathological defect, for example tumor formation. Since many years it is well known, that aberrations can initiate cancer. This point of view is supported by the observation that chromosomes of tumor cells are often abnormal (1). In connection with the proposed radiotherapy at GSI the induction of persistent chromosome aberrations by heavy ions has to be studied as an indicator of long-term genetic effects.

For the experiment V79 Chinese hamster cells with a cell cycle time of 12 hours and a chromosome number of 2n = 22 were used. Asynchronous and synchronous V79 cells were irradiated with 45 Mev/u Ca ions ($2x10^6/cm^2$, $5x10^6/cm^2$) at Ganil, Caen. Cells were allowed to grow for 2 weeks before chromosome preparations were made.

In all irradiated samples the amount of tetraploide cells was 2-3 times higher than in unirradiated controls, i.e. 9% instead of 2.5%. Only in one sample (cells irradiated in G_1-phase with $2x10^6$ particels/cm^2) even an higher amount of tetraploid cells (18%) was found. Up to now the induction of polyploid cells has been investigated only for short periods (4 days) after irradiation (2). Our long-term experiment demonstrates that at least a portion of polyploid cells is able to devide and form a stable subpopulation in culture. The reason for this radiation effect is yet unknown. As a possible mechanism the disruption of the spindle fibers or the fusion of cells is suggested.

In heavy ion irradiated samples also a slightly increased rate of aberrant cells was found. Mainly deletions in the arms the large hamster chromosomes and exchange-type aberrations (dicentric chromosomes, ring chromosomes and translocations) were observed as shown in table 1. No significant difference between asynchronous and synchronous cells was found. But in all cases the number of aberrant cells increased slightly with particle fluence. In fig. 1 a typical radiation induced persistent chromosome aberration (dicentric chromosome) is shown. In controls 1 to 2 % of cells show chromosome aberrations - usually chromatid breaks. Exchanges, however, are very rare events in control samples. Up to now, in 10000 unirradiated cells scored, only 1 dicentric chromosome was found. The increase in cells showing structural chromosome aberrations indicates that some damaged cells are able to survive despite this damage. Usually aberrant cells are lost from the population - i.e. these cells die after the first or second post-irradiation mitois because of a loss or a gain of genetic material. In cultured human lymphocytes the rate of loss is estimated at 40 - 50% per division. Our data indicate, however, that several aberrant cells survive for at least 2 weeks - this corresponds to 28 cell divisions in control cultures.
In further experiments we will use higher particle fluences in order to avoid problems related with the statistics of particle irradiation (a fraction of cell nuclei is not hit at low particle fluences). Especially light particles with higher energies will be used, because these data are interesting for the application of particles in radiotherapy.

References:
(1) Nowell, P., In: German, J. (ed), Chromosomes and Cancer, J. Wiley and sons, pp268-285, 1974
(2) Lücke-Huhle, C., Mutation Res. 119, 407-413, 1983

---

* Experiments were performed at Ganil, Caen.

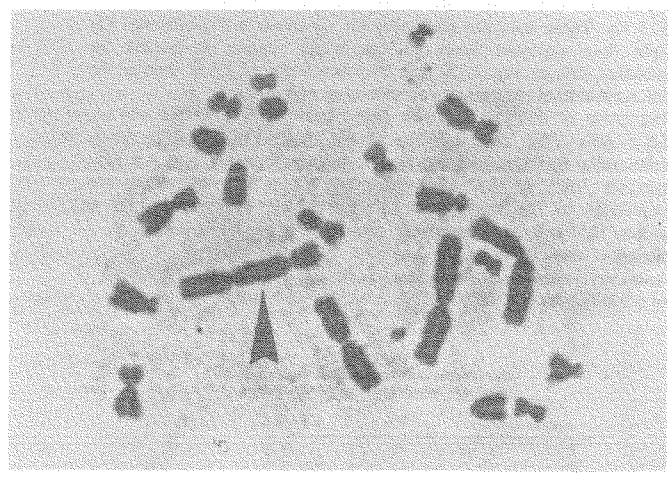


Fig. 1: Heavy ion induced chromosome aberration (dicentric chromosome) found two weeks after irradiation with 45 MeV/u Ca ions.

	Fluence (part/cm^2)	Aberrant cells (%)	Chromatid breaks per 100 cells	Deletions per 100 cells	Exchanges per 100 cells
Control	0	2	2	0	0
Asynchronous cells	$2 * 10^6$	5	2	0	3
	$5 * 10^6$	7	2	1	4
G_1-cells	$2 * 10^6$	3	2	0	2
	$5 * 10^6$	6	2	2	3
Late S-cells	$2 * 10^6$	5	1	1	3
	$5 * 10^6$	6	2	1	4

Tab 1: Persistent chromosome aberrations found two weeks after irradiation with 45 MeV/u Ca ions.

Split dose effects after heavy particle irradiation with 15MeV/u argon ions in human carcinoma cell-lines.

M.Flentje, J.Bühler, M.Scholz[2], M.Wannenmacher
Dept.of Radiology, Univ.of Heidelberg, and Sect. of Radiobiology GSI, Darmstadt[2] ' FRG

Fractionation modifies the biological effects of radiation. After low LET-irradiation (x-rays) recovery from sublethal damage is observed for most cells and tissues(2). Recovery is decreasing with increasing LET (1). However, with very high LET's even enhancement of radiation injury has been observed mostly using neutrons. Experiments are reported comparing the effects of Argon 15 MeV/u ions to low LET ^{60}Co-gamma rays.

MATERIALS AND METHODS

The CASKI and LX-I CELL lines (Courtesy Tumorbank German Cancer Research Foundation) are recently established human carcinoma cell lines of the cervix and lung. Plating efficiencies are about 40 % in monolayer culture. The cell cycle time (BdUrd-Method) is 23 and 16 hrs, respectively. **Irradiation** of exponentially growing cells was carried out at a ^{60}Co-Gammatron (240 cGy/min) and at the UNILAC for heavy particle experiments. The setup for heavy particle irradiation has been described before (5). After irradiation cells are trypsinized and plated at appropriate concentrations for determination of colony survival.
For **Cell Cycle Analysis** cells were fixed after different intervals post irradiation. Analysis of **DNA-Distributions** is done using DNA-staining by RNAse/ Propidium Iodide (60ug/ml) and a FACScan or Hoechst 33258 and a PHYWE ICP 22. Cell cycle distributions were estimated using squared rectangle approximations.

Results

Fig.1 shows the typical shouldered dose response of the Caski cells to Low-LET ^{60} Co irradiation. For a single dose exposure survival at 2 Gy is 0.58. Linear quadratic fitting gives a alpha/beta Quotient of 19.5 Gy. These data are consistent for squamous cell carcinomas (3). Split dose exposure leads to cytotoxicity sparing attributable to sublethal damage repair. A dose recovery factor of 1.3 is seen at the 1% survival level after a split course interval of 14 hours.
Irradiation of this cell-line with Argon (13.4 MeV) particles and of LX-I cells (Fig 2a,b) give a linear logarithmic dose response relationship for clonogenic survival at fluences between 1 to 7 x 10^6 particles /cm^2. At the energy used this means exposure of the cell monolayer to the Bragg peak of the particle path at an LET of around 1000 keV/ and a statistical probability of one hit/nucleus at a fluency of about 0.5 to 1 x 10^6 /cm^2.
Sensitivity is expressed in nuclear cross section giving the probability of cell killing for one particle.

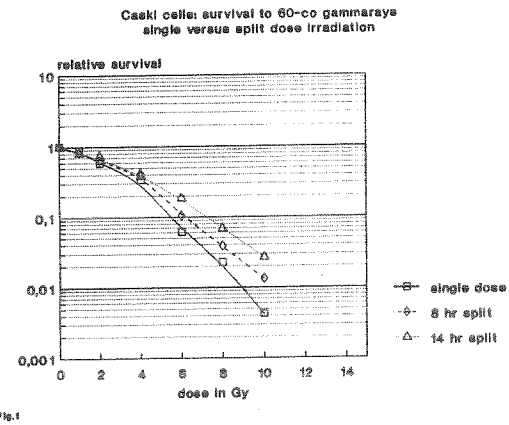
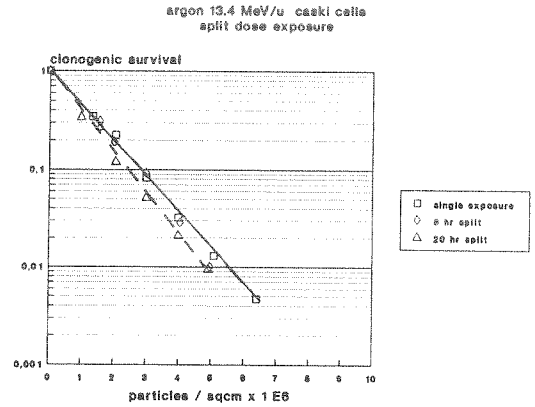
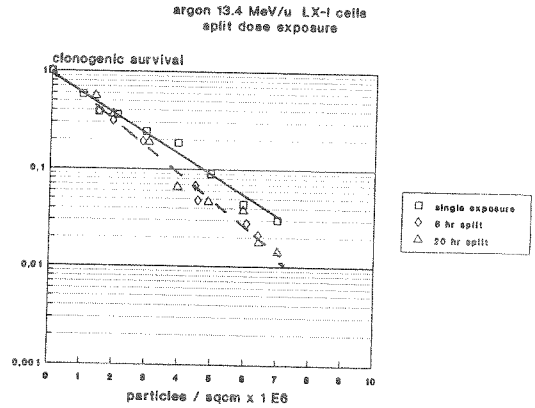


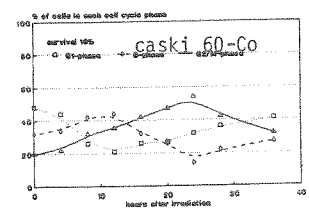
Fig.1

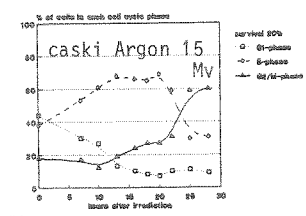
Split dose exposure to argon particles gives enhanced cytotoxicity with dose modification factors of 1.1 and 1.9 Marked differences in sensitivity are between the two lines.

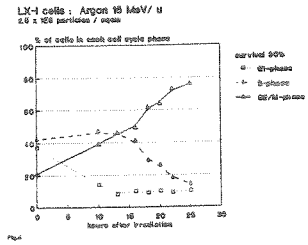




Sequential DNA-flow cytometry after irradiation with either gamma rays or heavy particles (Figs.4 and 5) show cell cycle perturbations with accumulation of cells in S- and G^2/M-phase. For comparative levels of overall survival progression delay , especially in S-phase is more pronounced after heavy particle exposure. As cell flux through S-Phase is mainly compromised, the appearance of cell cycle perturbations is influenced by the duration of G_1-phase. Cells with a shorter G_1-phase (LX-I) show earlier changes compared to Caski-cells. Moreover, the data suggest that, contrary to Low-LET irradiation, a considerable ratio of the cells do not complete cell division and suffer premitotic death.
Accumulation of cells in S-phase seems to be correlated with the finding of enhanced sensitivity for a splitdose irradiation.







Cell survival as a function of defined number of passed ions and impact parameter

F. Kraske, M. Scholz, S. Ritter, M. Schneider, D. Schall, H. Penninger, G. Lenz, C. Wiese, T. Rothmann, G. Kraft
E. Kankeleit*
GSI Darmstadt, TH Darmstadt*

Using the Mini-Beam set-up as described in the last annual report, we were able to irradiate mammalian cells with a preselected number of ions. The aim of this experiment was to study the influence of the spatial distance of two incoming ions passing through the cell nucleus on cell survival. This is done to test the theoretical approach according to which two neighbouring and correlated events could interact and yield more complex chemical, and hence biological, damage[1].

Up to now possible interaction mechanism has been studied in the molecular beam experiment[2] using a beam of deuterium molecules. In this experiment, fast physical interaction dominants the effect but biological interaction could not be expected to be present because of the low biological efficiency of the single deuteron ion. The experiments with molecular beams are restricted to light ions because of the difficulties to accelerate charged molecules to higher energies. In the minibeam experiment, the ions are not correlated in time but only in space, therefore the fast physical interaction will not influence the measured effect but the interaction on a biological scale which are much slower. An advantage of this experiment is the possibility of using very heavy ions up to uranium. The particles above Ne with an energy of 1.4 MeV/u cover an LET range from 500 - 12,000 keV/μm, where the track diameter is in the order of 1 μm. Therefore many ionization events occur within a track. The occurence of many ionizations in a short distance increase the probability of interaction effects.

With this set-up, cells were irradiated under atmospheric pressure with individual ions which are counted with the surface barrier detector. Fig. 1 shows the pulse height spectrum of a collimated beam of an approximately 1.3 μm^2 sized hole. At about 100 ions impinging on a detector area of $\approx$ 100 μm^2 the pulse height is reduced by 10%. Using such a detector for monitoring the number of incoming ions the effects of radiation damage have to be taken into account. After a pre-selected number of one or two passing ions was reached, a control unit interrupted the beam.

The spatial resolution of the minibeam was measured with nuclear track detectors. The spots were produced after the reduction of the beam spot size to very small values to get a well defined impact parameter. It is then calculated to 1 $\pm$ .5 μm (fig. 2) after the analysis of many spot pictures.

For the cell exposure, V79 Chinese hamster cells were placed directly behind the mica aperture of 1.1 μm in diameter and exposed sequentially to single ions, while the rest of cells served as controls. The positioning of cells were done by hand, so that only about 20 samples, each with approx. 20 cells, could be irradiated during 10 hours of beam time. After exposure, the cells were incubated under normal conditions and the progression of irradiated cells was observed in 6-12 hour intervals. For each time interval we obtained about 40 pictures, i.e. 10 MBytes of data. The last image was used to find the same position in a petri dish in order to get the next picture after a defined time period. All the data were then copied via an Ethernet card to the VAX and then via Hyperchannel to an IBM 3090 computer, which is used as a high storage capacity and for data analysis. New programs have been written in order to transduce the microscope image to the screen of a work station for a subsequent analysis.

With this set-up descriped above it was possible for the first time to irradiate single cells with individual ions. Up to now the analysis procedure was tested using stochastic exposed cell samples, yielding comparable results to experiments with standard methods. Control cells grow with a purely exponential function (fig. 3) whereas the cells with 6 hits in average in the cell nucleus were not able to divide.

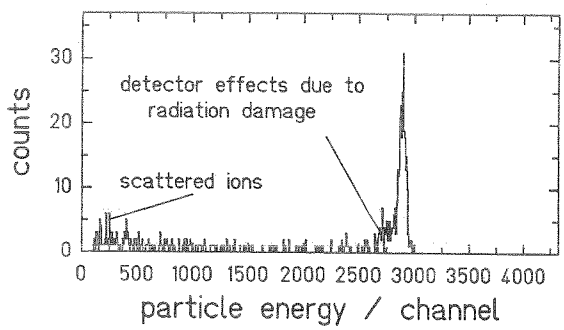


Fig. 1 : Energy spectra of 1.4 MeV/u uranium-ions collimated by a 15 μm^2 mica hole measured with a surface barrier detector

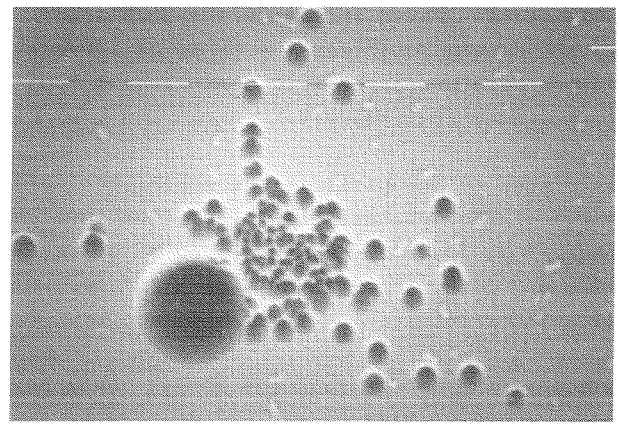


Fig. 2 : Directed irradiation of glass slides for dosimetry purposes in order to optimize the beam quality and the hitting accuaracy. The aim was to set the beam spot at the position of the big hole (each black and white bar represents 1 μm)

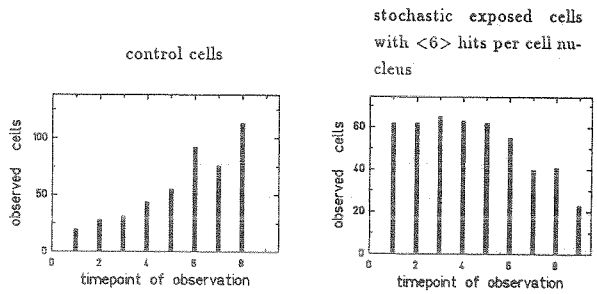


Fig. 3 : growth curves : observed V79 cells irradiated with uranium-ions are plotted versus timepoint of observation

[1] Kellerer, A.M. and Rossi, H.H., 'The theory of dual radiation action.', Current Topics in Radiation Res. Quart. 8, 85-158 (1972)

[2] Rossi, H.H. et al The molecular ion experiment, Proc. 6th Sym. on Microdosimetry Vol. II, 937-947 (1978)

[3] O. Hug, A.M. Kellerer, Stochastik der Strahlenwirkung, Springer-Verlag (1966)

Recovery Experiments with V79 Cells after Heavy Ion Exposure [G]

H. Rink, J. Heilmann
Institut für Strahlenbiologie
Sigmund-Freud-Str. 15, D-5300 Bonn 1

Although RBW values of accelerated heavy particles are low in the energy range provided by the UNILAC facility, the resulting damage on the molecular and biological level has been reported to be drastic. The ratio of DSB/SSB is much higher than with sparsely ionizing radiation [1,2] and the resulting chromosome damage also reveals severe aberrations [3].

In order to survey the effect of heavy ion induced damage on the cellular level, recovery experiments were performed. Cells were held under non growth conditions after irradiation, and colony forming ability was tested after selected time intervals (up to 24 h). Irradiations were performed with ions ranging from 11 MeV/u Ne to 5 MeV/u U.

With most of the particles no enhancement of survival could be detected even after more than 12 h. There is an indication of minute recovery after irradiation with $3*10^6$ Ar (9 MeV/u, Fig. 1).

With $5*10^6$ P/cm² Ni-ions (16 MeV/u) the apparent recovery (Fig. 2) was accompanied by a parallel loss of cells detaching from the culture surface (Fig. 3). Therefore, only survivors were scored and the net survival remained constant.

These results are consistent with other survival data such as lack of a shouldered dose response curve. A slight recovery potential with lighter particles cannot be excluded. The possibility of cell loss following post irradiation incubation might be important for the evaluation of experiments depending on cell cultivation after irradiation (e.g. mutation induction).

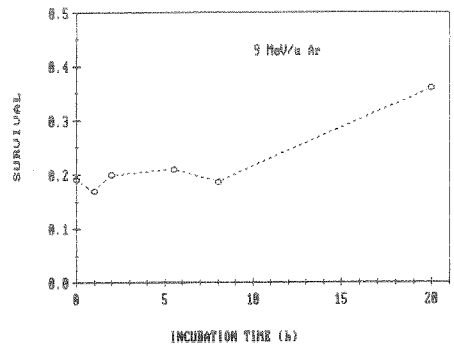


Fig.1: Survival as function of postirradiation incubation time with $3*10^6$ P/cm² Ar-ions (9 MeV/u)

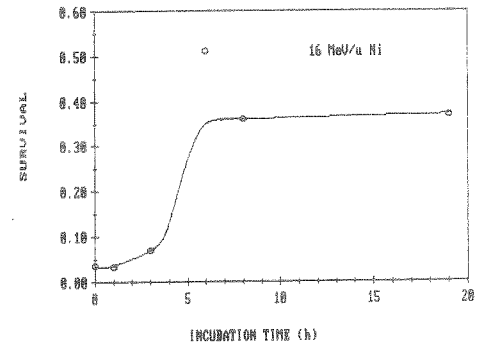


Fig.2: Survival versus incubation time after irradiation with $5*10^6$ P/cm² 16 MeV/u Ni-ions

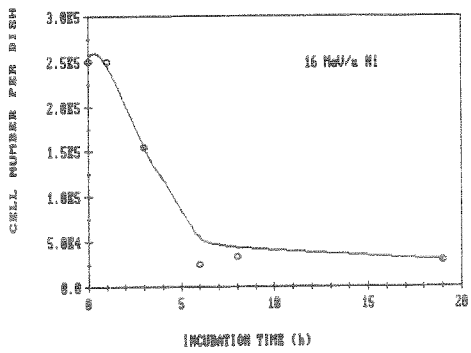


Fig.3: Cell number as function of incubation time from experiment in Fig. 2

[1] E.Aufderheide et al., Int.J.Radiat.Biol. 51 779-790 (1987)
[2] J.Heilmann, GSI 87-20 (1987)
[3] L.Sabatier et al., D19 GSI Report 87-11 (1987)

Measurement of haemolysis of human erythrocytes as an indication of radiation induced membrane damage [G]

W. Schön, H. Gärtner

Experimentalphysik III, Fachbereich Physik der Gesamthochschule Kassel, D-3500 Kassel

G. Bartosz

Department of Biophysics, Institute of Biochemistry and Biophysics,

University of Łódź, Poland

G. Kraft

Gesellschaft für Schwerionenforschung, D-6100 Darmstadt

In order to investigate the effect of heavy ions on membranes, human erythrocytes (red blood cells) have been used as targets for heavy ion exposure.

Mature red blood cells do not contain a nucleus or mitochondria. Therefore, erythrocytes are suitable systems for membrane investigations.

Radiation induced haemolysis was investigated i.e. the loss or damage to the red cell membrane leading to liberation of the intracellular hemoglobin. Erythrocytes were isolated from citrated pheripheral human blood and were washed free from plasma proteins by suspension in phosphate buffered saline (PBS), followed by centrigugation [(1)].

After irradiation the red cell suspension was centrifuged and haemolysis was determined by measuring the hemoglobin concentration in the supernantant [(2),(3)]. This was done by reading the absorbance at 540 nm using a Shimadzu UV-200 Photometer. Human erythrocytes were irradiated with X-rays (250kV / 20mA) at doses up to 1000 Gy and with 13.8 MeV/mu Pb up to 1200 Gy. The release of hemoglobin was measured over a period of 5 days.

In figure 1 the percentage of haemolysed cells is given as a function of time after exposure. For particle irradiation the cells undergo haemolysis within a few minutes after exposure, while X-irradiated cells with the same dose reach the 80% level only after several days. Therefore Pb ions are much more efficient at inducing haemolysis.

This is also demonstrated in figure 2, where the time to reach a level of 50% haemolysis as function of dose is compared for X-ray and Pb exposure. The X-ray curve is shifted by a factor of ten to higher doses. This is in strict contrast to other radiobiological measurements in which the measured effect depends on the integrity of the cellular DNA. In DNA related measurements the relative biological efficiency of Pb radiation is two orders of magnitude below that of X-rays. This difference of three orders of mangitude indicates a different mechanism for the production of DNA lesions compared to membrane damage.

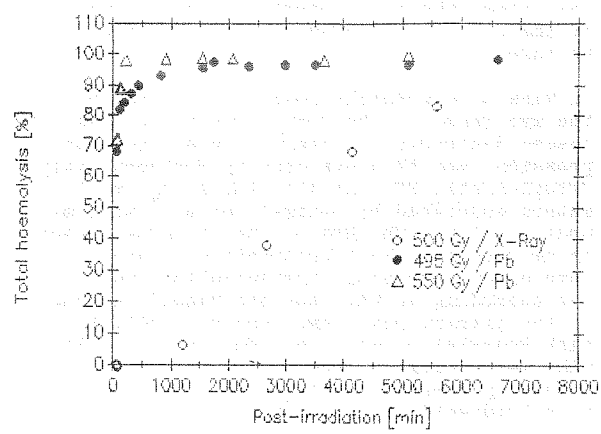


Fig.1:
Time dependence of haemolysis after irradiation with 13.8 MeV/mu Pb-ions and 250 kV X-rays.

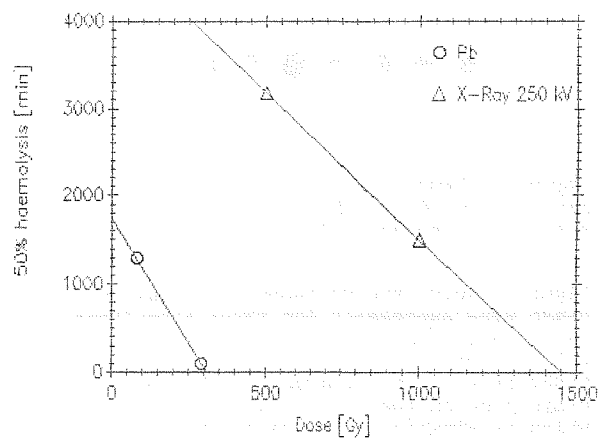


Fig.2:
Time dependence of 50% haemolysis as a function of dose.

REFERENCES

1. A.H. Ross and H.M. McConnell; Biochemistry 14; pp. 2793 (1975)
2. W.G. Zijlstra and E. van Kampen; Clinica chim. Acta 5; pp. 719 (1960)
3. G. Bartosz and W. Leyko; Int.J.Radiat.Biol. 39; p. 39-46 (1981)

MOLECULAR ANALYSIS OF SYRIAN HAMSTER EMBRYO-CELL LINES TRANSFORMED BY 8 MeV/u CARBON IONS[6]

K. Trutschler, L. Hieber, and A.M. Kellerer
Institut für Medizinische Strahlenkunde der Universität Würzburg

Syrian Hamster Embryo (SHE) cells have been neoplastically transformed by exposure to different doses of 8 MeV/u carbon ions. Tumor-cell lines were then established from tumors in athymic mice, that had been injected with radiation transformed cells. These cell lines were used for a study of the molecular mechanisms underlying cell transformation. As previously shown, the radiation transformed and tumor-cell lines exhibit a distinct growth advantage that is recognized through higher plating efficiencies, shorter doubling times, and increased cloning efficiencies in semi-solid medium[1]. Three transformed and the related tumor-cell lines showed a modestly elevated expression of the c-Ha-ras oncogene by factors of about two to three[2].

In view of a possible joint role of the ras and the myc genes in the transformation process, it seemed desirable to determine also the c-myc expression, and this was done by Northern analysis. Cytoplasmatic RNA was isolated according to the method described by Chirgwin et al.[3] with minor modifications. The RNA preparations were separated by agarose gel electrophoresis and were blotted onto nylon membranes. Hybridizations were carried out according to Williams and Mason[4]; a fragment of the plasmid pSV-c-myc1 radioactively labeled by nick translation was used. The amount of the c-myc mRNA was estimated from autoradiograms of the membranes by comparison the c-myc signals with those of hybridizations of the the same filters with an α-actin standard.

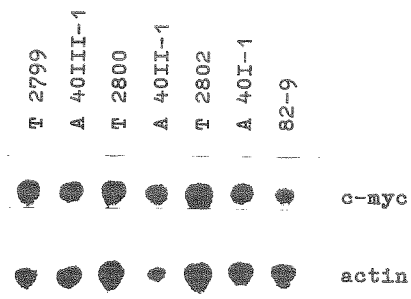


Figure 1: Expression of the c-myc gene (tumor-cell lines T2799, T2800, T2802; C-ion transformed cells A 40 I-III; primary SHE cells 82-9).

Figure 1 shows the Northern blot analysis of the c-myc gene expression for three transformed and three tumor-cell lines in comparison to primary untransformed SHE cells. The transformed and tumor-cell lines revealed an enhancement of the c-myc gene expression by factors of two to four, which is similar to the result that was found for the c-Ha-ras gene. The slightly increased expression of these two cellular oncogenes appears not to be primarily responsible for the transformation event; however, it may reflect the increased proliferative capacity of the transformed cells.

Since the ras genes are most frequently activated by point mutations, we performed a sequence analysis of the gene to study this possibility. The cellular Ha-ras gene was amplified using the polymerase chain reaction (PCR) according to Saiki et al.[5]. In brief, two oligonucleotide primers, homologeous to the flanks of the target DNA to be amplified, were annealed to heat-denatured, genomic DNA. Then the primers were extended by the enzyme Taq-polymerase with the single-strand target DNA as template. This three-step cycle (heat denaturation, primer annealing, and DNA replication) was repeated 35 times resulting in more than 10^8 copies of the target DNA. By this method the c-Ha-ras genes of three tumor-cell lines have been amplified, and they have then been analysed by direct sequencing according to Sanger et al.[6] and with the use of a modified T7 DNA polymerase[7].

Figure 2: Wild-type DNA-sequence of the Syrian Hamster Ha-ras gene (codon 8-15)

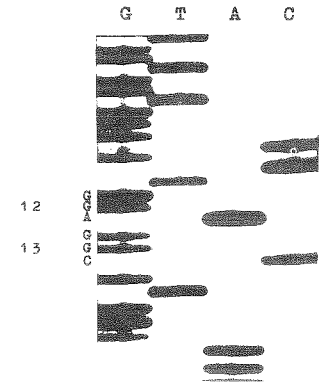


Figure 2 shows a segment of the autoradiogram that is part of the sequence analysis. In three tumor-cell lines, derived from carbon ion transformed cells, no mutations in the codons 12, 13, 59 and 61 were present. The regions adjacent to these codons, too, exhibited no changes in the sequence of the Ha-ras gene. The results that are here reported for studies with carbon ions are consistent with findings we determined with tumor-cell lines from cells that have been transformed by other types of ionizing radiation, such as γ-rays or α-particles. In none of these experiments point mutations in the region of the Ha-ras gene that has been mentioned above were seen.

In conclusion, there are only minor alterations of the expression of the ras and the myc genes and there are no mutations in those codons of the Ha-ras gene that have been reported to activate this gene; this appears to imply that cell transformation by ionizing radiation is not directly linked to the activation of these genes. However, one can not exclude the possibility that the Ha-ras gene might be activated by mutations at different sites. It is also possible that neoplastic transformation by ionizing radiation may involve the activation of some other oncogenes or that it may be due to the loss of certain tumor suppressor genes.

[1] GSI Scientific Report 1987
[2] GSI Scientific Report 1988
[3] Chirgwin et al., 1979, Biochemistry 18, 5294
[4] Williams & Mason, 1987, in Nucl. Acid Hybridization (Hames & Higgins eds.) 139-160
[5] Saiki et al., 1988, Science 239, 487
[6] Sanger et al., 1977, PNAS, 74, 5463
[7] Tabor & Richardson, 1988, PNAS 84, 4767

IN-SITU HYBRIDIZATION OF HUMAN CHROMOSOME 11 IN HUMAN-HAMSTER HYBRID CELLS[G]

R.Greinert, J.Smida and A.M.Kellerer
Institut für Medizinische Strahlenkunde der Universität Würzburg,
Versbacher Straße 5

Major advances in cytogenetics have been attained due to methods which permit a distinction between different types of chromosomes. In-situ hybridization techniques for sensitive detection and localization of specific nucleic acid sequences in metaphase or interphase cells are becoming more and more important[1]. Because of these techniques it is possible to label human metaphase or chromosomes in human-hamster hybrid cells.

In our institute we are using cells of the A_L hybrid, formed by fusion of human amniotic fluid fibroblasts and the gly^- A mutant of the Chinese hamster ovary CHO-K1 cell; This hybrid has been constructed by Puck and coworkers[2] and has been kindely provided by Dr. Waldren (Eleonor Roosevelt Institute for Cancer Research, Denver, Colorado, USA).
The cells contain in addition to the standard set of CHO-K1 chromosomes the human chromosome 11, which contains the information for 3 surface antigenes termed a_1, a_2, a_3. They offer the opportunity to determine radiation induced mutations in an immunological test, that is 200 times more sensitive than the widely used hgprt-test.

Critical studies of this immunological test are accompanied in our group by investigations of chromosomal translocations due to ionizing radiation. This is to provide a basis for the correlation between translocations and mutations.

In context of this work we have synthezised a hybridization probe against the human chromosome 11 in A_L hybrids.
The hybridization probe consists of plasmids pBlur8 (kindely provided by Dr.Kaina, Kernforschungs-Zentrum Karlsruhe, Inst. f. Genetik) that contain alu-sequences, which are highly specific for the human chromosmes. The plasmid is transfected to a HB101 E-Coli - host, enriched and harvested. After linearization of the plasmid (EcoRI) and denaturation, single stranded DNA of the plasmid is random primed with oligonucleotides (N_6) in the presence of dCTP which is ^{32}P labeled at the α-phosphorus. Thus we obtaine a radioactive hybridization probe, that is highly specific for the human chromosome 11 (see Fig.1).

In other experiments random priming of single stranded plasmid DNA is done in the presence of BrdU instead of thymidine, or the alu-hybridization probe is tailed with a BrdU using the enzyme terminal transferase.
Under either of these conditions the human chromosome 11 in A_L hybrid cells can be detected after in-situ hybridization of metaphase chromosomes with the BrdU-probe. This is done by addition of a fluorescent anti-BrdU-antibody to A_L chromosomes after they are spread on microscope slides (see Fig.2). With this sytem, we will be able to measure chromosomal translocations (by detecting parts of the radioactive or fluorescent human chromosome 11 in hamster chromosomes) after exposure to ionizing radiation (heavy ions). The use of the human chromosome 11 in A_L hybrid cells is of special interest because this chromosome contains the human h-ras-oncogene, which is known to play an important role in the context of chromosomal translocations and cell transformation, which are suspected to be critical for carcinogenesis in general.

The study of gene rearrangement and activation is of central importance in investigations of radiation carcinogenesis and it is therefore particulary desirable to extend such studies to densely ionizing radiations.

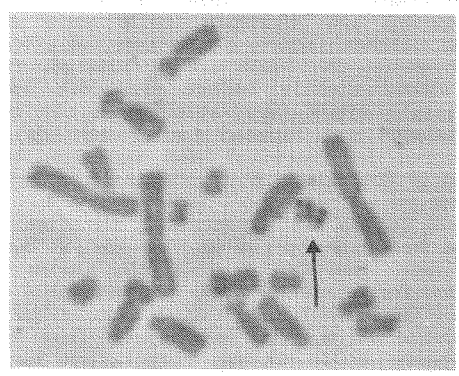


Fig.1: Autoradiographic detection (see arrow) of human chromosome 11 in A_L cells after in-situ hybridization with radioactive (^{32}P) alu-sequences.



Fig.2: Detection of human chromosome 11 in A_L cells using BrdU-tailed alu-sequences for in-situ hybridization and a fluorescent (FITC) anti-BrdU-antibody.

[1] Hopman,A.H.N., Wiegant,J. & van Duijn, A. Exp.Cell Res. 169, 357 (1987)

[2] Wuthier,P., Jones,c. and Puck,T.T., J.Exp. Medicine 138, 229 (1973)

Mutation Induction in V79 Cells by Accelerated Heavy Ions[G]

T. Kranert, E. Schneider, J. Kiefer

Strahlenzentrum der Justus-Liebig-Universität Gießen

It has been shown recently that accelerated heavy ions are able to induce mutations at the HGPRT-locus (resistance to 6-thioguanine) in V 79 Chinese Hamster cells over the whole range of LETs available[1-5] (0.1 - 15 700 KeV/µm).
To ensure well defined and constant conditions during transport from Gießen to GSI in Darmstadt and during ion exposure, cells were seeded in special dishes with a bottom of "MYLAR"-foil though which the cells are irradiated. The dishes were closed tightly before transport and opened immediately after irradiation when the cells were trypsinized and spread according to standart procedures for survival and mutation tests. The method is described in more details in references 1 to 5.
Survival curves are exponential, mutation induction curves are linear (fig. 1) for UNILAC irradiation conditions (see tab. 1). From the slopes the cross sections for inactivaton σ_i and mutation induction σ_m can be calculated. Fig. 2 summarizes the LET dependence of σ_m. It is obvious from the graph that there is an unique correlation for σ_m with LET[7] for LET values smaller than about 200 KeV/µm while for higher LETs the curves for different ions seperate.
In contrast to the inactivation cross section, which decreases for each ion with increasing LET in this region[6], σ_m increases with increasing LET. This may be due to the fact that most cells which receive a hit with higher specific energy rather die than survive what can be seen also from σ_i-values which are close to the geometrical cross section of about 120 µm². Nevertheless the data show that a certain fraction of hit cells which survives and expesses a mutation. It is not clear whether the different behaviour of the neon curve is real or an experimential artefact. Further experiments are obviously needed.
Mutagenicity, defined as σ_m/σ_i, is shown in fig. 3. Althouhg there are not sufficent data to draw general conclusions, a tendency to a smaller mutagenicity with increasing LET and with increasing atomic mumber of the ions can be seen. The physical irradiation parameters and the cross sections for mutation induction and inactivation are summarized in Tab. 1.

Ion	E/M at cell surface (MeV/u)	LET (H_2O) (keV/µm)	Z^{*2}/β^2	Penumbra-radius (µm)	σ_i (µm²)	σ_m (10^{-4} µm²)	σ_m/σ_i (10^{-5})
O	8.2	311	1394	2.2	50±4	20 ±4	4.0±0.8
Ne	8.9	448	4821	2.5	48	4.6	1.16
	12.0	360	3665	4.2	42	15	3.5
Ar	8.8	1296	13965	2.4	63	6.8	1.08
Ca	14.1	1170	11510	5.5	46±7	7.0±0.4	1.5±0.25
Ti	4.4	2544	11538	0.76	54±3	14 ±1	2.6±0.3
	14.8	1341	13133	6.0	50±6	8.6±1.6	1.7±0.38
Ni	9.0	2673	28620	2.6	65±2	8.3±1.2	1.3±0.18
	14.6	1866	21830	5.45	87±5	5.7±1.8	0.65±0.05
Xe	10.6	6661	69282	3.4	70*	12.0±2.5	1.7±0.36
Pb	15.6	10483	101646	6.6	88±8	9.2±2.6	1.1±0.33
U	4.7	15166	192541	0.86	79±4	6.9±0.9	0.84±0.12
	5.1	15637	187757	1.0	76±8	6.0±2.3	0.78±0.36
	5.1	15673	187757	1.0	71	21	2.1
	10.6	13738	140359	3.4	105±10	8.8±1.5	0.81±0.16
	14.1	12494	123515	5.5	90±9	4.5±2.0	0.50±0.20
X-ray 300kV							3.1±0.4-

Tab. 1:Physical irradiation parameters and cross sections for the experiments discussd. (σ_i: inactivation cross section, σ_m cross section for mutation induction)
(* taken from ref. 6)

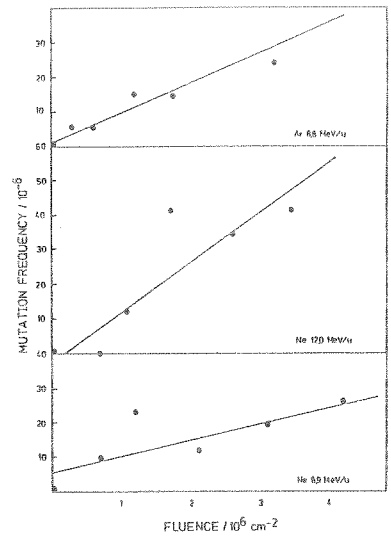


Fig. 1: Induction of resistance to 6-TG in V79 cells after exposure to Ne- an Ar-ions

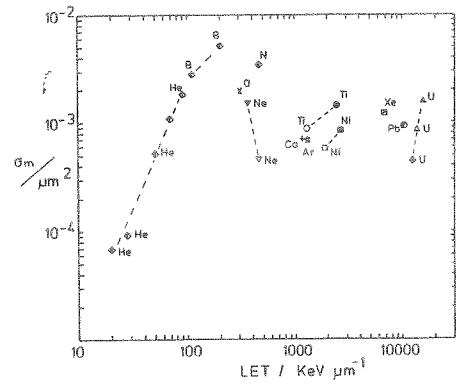


Fig. 2: Dependence of mutation induction cross section (σ_m) on LET. ◆ data taken from Thacker et al. 1979 (ref.5), final slopes

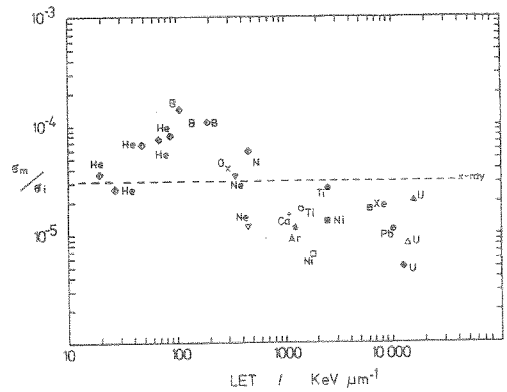


Fig. 3: Let dependence of the "mutagenicity" of various heavy ions in V79 cells. ◆ data calculated from final slopes taken from ref. 5

[1]Kranert T., Schneider E., Kiefer J., GSI-Report 87.1 (1987) 233
[2]Kranert T., Schneider E., Kiefer J., GSI-Report 88.1 (1988) 228
[3]Kranert T., Schneider E., Kiefer J., GSI-Report 89.1 (1989) 223
[4]Kranert T., Schneider E., Kiefer J., Proc. 21st. Annu. Meet. Radiat Biol (1989) (in press)
[5]Thacker J., Stretch A., Stephens M. A. Int. J. Radiat Biol 36 (1979) 137
[6]Wulf H.,Kraft-Weyrather W., Miltenburger M. G.,Blackely E. A. K, Tobias C. A., Kraft G., Radiat Res 104.2 (1985) 122
[7]Goodhead D.T., Munson R.J., Thacker J., Cox R., Int.J.Radiat Biol 37 (1980) 135.

BIOLOGICAL DOSIMETRY OF RADIATION-INDUCED CHROMOSOME ABERRATIONS IN INTERPHASE AND METAPHASE OF HUMAN LYMPHOCYTES BY CHROMOSOMAL IN SITU SUPPRESSION HYBRIDIZATION[G]

S.POPP, T.CREMER
Institut für Humangenetik und Anthropologie, Universität Heidelberg

B.REMM, C.CREMER
Institut für Angewandte Physik I, Universität Heidelberg

The visualization of specific chromosomes or parts of chromosomes both in metaphase spreads and interphase nuclei (1-4) has provided an new approach to biological dosimetry of radiation induced chromosome aberrations in human cells (5,6).

Peripheral human lymphocytes (46,XY) were irradiated with ^{60}Co-gamma-rays five hours after PHA-stimulation. After additional 67 hours of cultivation, slides with metaphase spreads and interphase nuclei were prepared.

Specific chromosomes (#1,7) were visualized by CISS-hybridization and FITC fluorescence (2,3). In other cases, a subregion (1q12) on chromosome #1 was labelled (4,8). These procedures allowed an easy microscopic detection of a large spectrum of chromosome aberrations (e.g. monocentrics with translocations and inserts; deletions and fragments; dicentrics.

Fig.1 shows dose-effect relationships obtained for metaphase chromosomes. A linear increase of the percentage of specifically stained aberrant chromosomes was observed when plotted as a function of the square of the dose. The same increase was also observed for the percentage of interphase nuclei with an aberrant chromosome pattern (Fig 2).

Presently, procedures are being developed for an automated analysis of the aberrations. A program, using the C language, was written and has been tested with digitized images of metaphase spreads which previously had been evaluated visually. The program allows automatic segmentation, counting and size determination of labelled chromosome regions. On this basis the cell is automatically classified as "normal", "aberrant" or "segmentation error", the error rate being small (presently about 1%). Using an AT-386 Computer, evaluation time required per cell was about 1-2 sec. This is considerably shorter than the time required for image analysis of homogeneously stained metaphase spreads (9).

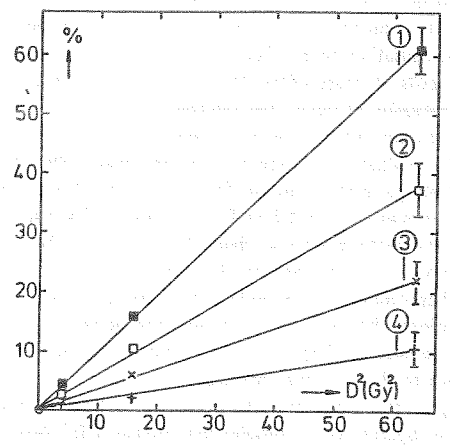


Fig.1: Dose-effect relationships for ^{60}Co-γ-ray induced aberrations of human lymphocyte metaphase chromosomes as detected by fluorescence hybridization (from ref. 7).
Abscissa: Square (D^2) of the dose D (Gy)
Ordinate: Accumulated percentages of
(▩) all types of aberrant chromosomes;
(□) monocentrics with translocations and inserts;
(x) deletions and fragments
(+) dicentrics
The bars at D^2 = 64 Gy^2 (8 Gy) indicate the 99% confidence intervals. For Details see ref 7.

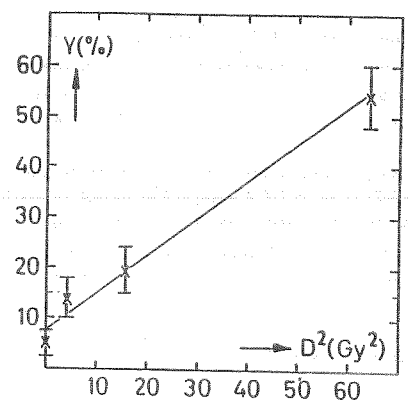


Fig.2: Dose-effect relationship for ^{60}Co-γ-ray-induced aberrations of chromosomes 1 and 7 in human lymphocyte interphase nuclei as detected by fluorescence hybridization (from ref. 7).
Abscissa: Square (D^2) of the dose D (Gy)
Ordinate: Percentage of nuclei with aberrant chromosome patterns of chromosomes 1 and 7.
The bars indicate the 99% confidence ranges.
For details see ref. 7.

LITERATURE

1) Cremer T. et al., Hum Genet 74 (1986),346
2) Lichter P. et al., Hum Genet 80 (1988),224
3) Cremer T. et al., Hum Genet 80 (1988),235
4) Cremer T. et al., Exp Cell Res 176 (1988),199
5) Cremer C. et al., GSI Scientific Report 1987,234
6) Popp S. et al., GSI Scientific Report 1988,229
7) Cremer T. et al., Cytometry 11 (1990), in press
8) Emmerich P. et al., Exp Cell Res 181 (1981),126
9) Lörch Th. et al., in: Automation of Cytogenetics (C.Lundsteen, J.Piper, Eds.), 19. Springer Verlag (1989)

Repair of DNA double strand breaks in mammalian cells: an experimental approach

G. Taucher-Scholz, C. Wiese, J.A. Stanton, M. Schneider and G. Kraft
GSI Darmstadt

The DNA double strand break (DSB) is considered to be the critical lesion leading to chromosomal aberrations and ultimately to cell death. The induction and repair of DSBs by heavy ions in mammalian cells has been examined in various systems (1,2). However, techniques like filter elution or sedimentation gradients, which are widely used to measure DSB induction in mammalian cells, show technical limitations at low radiation doses. For DSB repair studies it is of interest to irradiate cells at doses within the range of cell survival in order to assure the integrity of repair mechanisms.

In order to accomplish this we are developing a new experimental approach to evaluate DSB repair in mammalian cells. It is based on pulsed field gel electrophoresis (PFGE) which allows us to resolve DNA fragments as large as 1.5 million base pairs. The use of a similar electrophoretic technique for studying X-ray induced DNA DSBs and repair of yeast chromosomes has been reported (3). In this case, breakage of chromosomes is seen by a decrease in intensity of ethidium bromide stained chromosome bands and the appearence of a broad smear of chromosomal fragments. Following DSB repair chromosome bands return to their original intensity.

Intact genomic DNA must be prepared by lysis of cells in situ, embedded in agarose (4). Complex mammalian DNA does not enter the gel, but restriction with low frequency restriction enzymes yields a smear of chromosome fragments in the range of 200 - 1500 kb (Fig.1). In order to visualize individual bands, we first transferred the DNA to nylon membranes by Southern blotting and hybridized to a 300 base pair Alu probe purified from a Blur2-pUC vector plasmid (5,6). A non-radioactive detection assay using digoxigenin-labeled probes was applied (7). Only human DNA fragments containing repetitive Alu sequences can be detected as hybridizing bands by this procedure.

However, as can be observed in Fig.(2), a conventional Southern blot of total human EcoRI restricted DNA hybridized to the Blur2 Alu probe shows a few distinguishable bands over a background smear of hybridizing DNA due to the large amount of repetitive sequences dispersed in the human genome. For this reason, we chose to use a hybrid hamster-human cell line containing only the long arm of human chromosome 21 (corresponding to 0.5% of the genome) as a translocation in a Chinese Hamster Ovary (CHO) background (8). A discrete banding pattern of Alu-hybridizing DNA is expected for this cell line.

The retention of human material in the hamster hybrid was verified by dot blot hybridization of DNA prepared by standard methods to the Blur2 Alu vector (5). In addition, the hybrid cell line was characterized for its radiosensitivity. Fig.(3) shows the survival curves obtained after exposure to X-rays and to accelerated Pb ions. The low effectivity of the very heavy particles becomes apparent in this comparison: the Pb survival curve is less steep than the X-ray curve but does not exhibit a shoulder. For 4.5 MeV/u Pb ions a cell inactivation cross section of 116 μm^2 was calculated.

[1] Aufderheide,E. et al., Int. J. Radiat. Biol. 51, 779-790 (1987)
[2] Heilmann, J., diploma thesis, University of Bonn (1987)
[3] Mortimer,R. et al., Biophys. J. 49, 103a (1986)
[4] Gardiner,K. et al.,Somat. Cell Mol. Genet.12, 185-195 (1986)
[5] Maniatis,T. et al., Molecular Cloning, Cold Spring Harbor Lab., CSH, N. Y. (1982)
[6] Deininger, P. et al., J. Mol. Biol. 151, 17-33 (1981)
[7] Boehringer Mannheim, Biochemica, Nonradioactive DNA labeling and detection (1989)
[8] Gardiner,K. et al., Somat. Cell Mol. Genet. 14, 623-638 (1988)

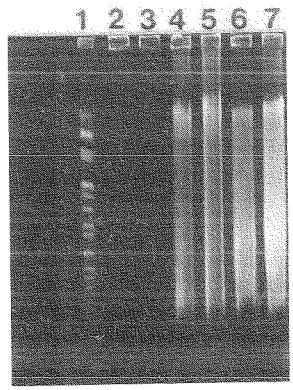


Fig.1: Ethidium bromide stained gel showing the resolution range of PFGE. Lane 1 is S.cerevisiae DNA; lanes 2 and 3 are controls of undigested CHO DNA; lanes 4,5 and 6,7 are CHO DNA digested with SacII and SalI, respectively. The gel is 1% agarose,run for 18 h with 60 sec. pulse time starting at 250 V.

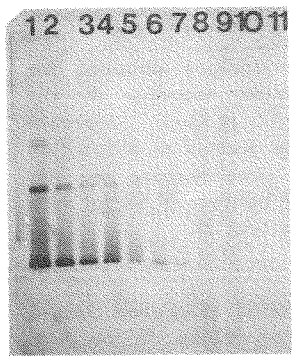


Fig.2: Detection of Alu sequences using a digoxigenin labeled Blur2-pUC plasmid probe. Lanes 1-7 contain 5000, 1000, 500, 300, 100, 50, 10 pg respectively of the Blur2-pUC vector; lanes 8, 9 contain 10 μg EcoRI digested human placenta DNA; lanes 10, 11 contain 4 μg EcoRI digested V79 hamster DNA.

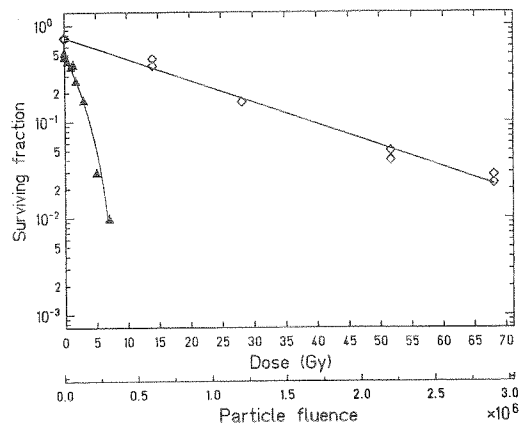


Fig.3: Surviving fraction of hybrid CHO-human chromosome 21 cells as a function of dose after exposure to(▲) 250kVp X-rays (2 keV/μm) and to (◇) 4.5 MeV/u (14680 keV/μm) Pb ions.

Heavy ion induced DNA double strand-breaks in yeast: preliminary results [G]

T. Akpa, K.J. Weber, J. Kiefer
Strahlenzentrum der Justus-Liebig-Universität, Gießen

M. Frankenberg-Schwager, R. Harbich, D. Frankenberg
Abteilung für Biophysikalische Strahlenforschung der GSF, Frankfurt

It is a widely accepted view that DNA double-strand breaks represent crucial lesions in cellular ionizing radiation action but only with yeast lethal damage from low LET irradiations could conclusively be identified with this lesion type. DNA double strand breaks are also assumed to correlate with the effects of heavy ion exposure on cells. Despite the qualitatively similar dependence of DSB production cross-sections and e.g. inactivation cross-sections on heavy particle physical parameters, however, direct experimental evidence for this hypothesis is missing.

Here, first results on DSB induction in diploid wild-type yeast (Saccharomyces cerevisiae, strain 211*B) from exposure to accelerated charged particles are presented. Details of the irradiation setup and of the experimental protocol for DSB measurement by sedimentation velocity analysis in neutral sucrose gradients have been described, earlier[1,2].

The physical data of heavy ions together with the DSB production rates derived from the respective fluence dependences (figure 1) and the corresponding inactivation cross-sections (from final slopes of the survival curves measured in parallel) are summarized in table 1.

table 1

ions	E/m (MeV/u)	LET (KeV/μm)	DSB induction (DSB/10^9D/μm^{-2})	inactivation cross-section (μm^2)
Ar	14.0	964	0.62	0.52
Ar	8.8	1296	0.47	0.51
Pb	12.7	11080	2.08	2.08

A comparison of the argon data indicates a dependence of DSB production rates on particle velocity rather than LET similar to what is found when measuring survival of these cells. Before further analysis can be attempted, however, more data are needed.

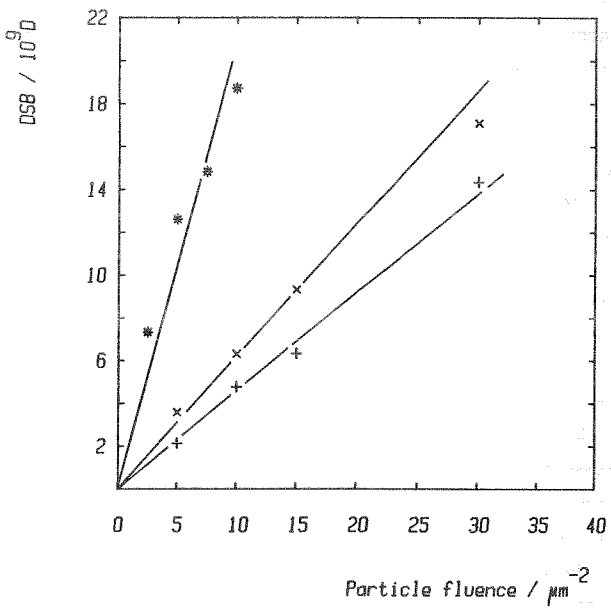


Fig.1: Number of DNA double-strand breaks per 10^9D as function of heavy particle fluence (x: Ar, 14.0 MeV/u; +: Ar, 8.8 MeV/u; * Pb, 12.7 MeV/u).

[1] F.Schöpfer et al., Radiat. Res. 92, 30 (1982)

[2] M.Frankenberg-Schwager et al., Int. J. Radiat. Biol. 36, 261 (1979)

Induction of DNA Double-Strand Breaks in Vegetative Cells of Bacillus subtilis and Escherichia coli

U. Micke, M. Schäfer, G. Horneck, H. Bücker

DLR, 5000 Köln 90

H. D. Mennigmann

Universität Frankfurt/M., Institut für Mikrobiologie, 6000 Frankfurt, Main

DNA represents an important and sensitive biological target concerning ionizing radiation. Besides base damage DNA strand breaks are the major events in bacterial genomes exposed to ionizing radiation. DNA double strand breaks are considered to be one of the main reason for lethal events in bacterial cells. In E. coli K 12 1.3-1.4 double strand breaks per cell were observed to be lethal[1] and in Bacillus subtilis[2] 5-6 double strand breaks per cell were necessary for inactivation. Difficulties to determine induced double strand breaks in long DNA molecules of 4.5×10^6 bp of E. coli or B. subtilis genomes with the widely used sucrose gradient centrifugation technique arise by appearing of DNA destruction by shear forces. To overcome this problem the new technique of pulsed field agarose gel electrophoresis[3] was applied to investigate DNA double strand breaks in bacterial genomes after irradiation with different heavy ions and X-rays. Cells embedded in small agarose blocks were lysed with enzymes and detergents. The remaining purified DNA in matrix was treated by low voltage in alternating fields. Whereas an intact circular bacterial genome does not move, the linear DNA fragments resulting from one or more double strand breaks move gently through the agarose, the smaller the faster. After staining with ethidium bromide, the distribution of DNA was fluorometrically determined. The mean number of double strand breaks per genome will be calculated from the degree of degradation of the intact genome[4].

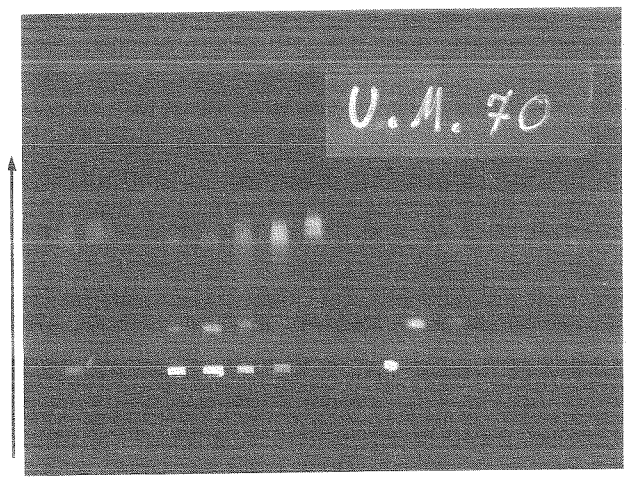


Fig. 1 Photo of a gel showing DNA of vegetative cells of Bacillus subtilis (TKJ 8431) separated after irradiation (Pb 15 MeV/u) with increasing fluences.

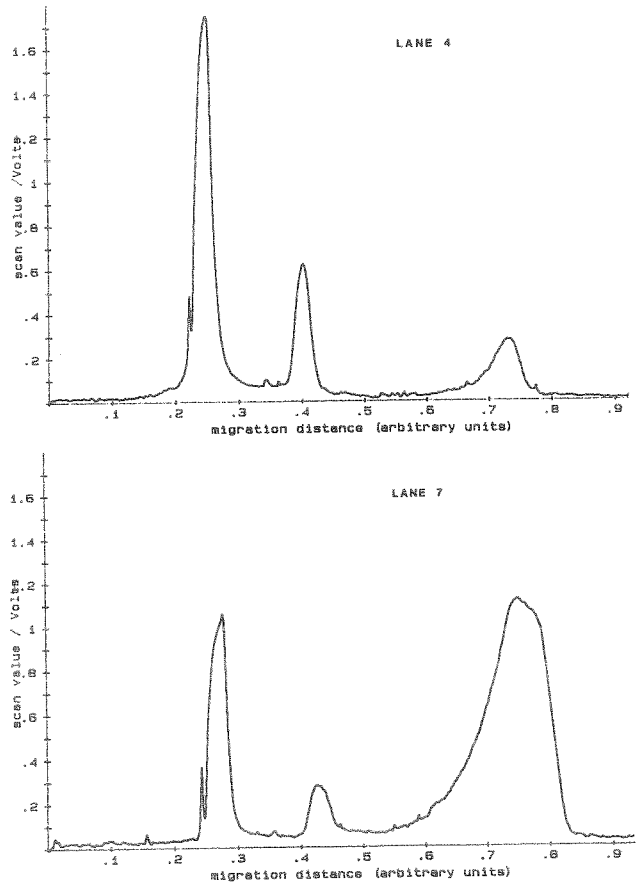


Fig. 2 Scan plot of lane 4 (control) and lane 7 (10^8 particles/cm^2) of Fig. 1.

[1] Bonura, T., Town, C.D., Smith, K.C., Kaplan, H.S., The influence of oxygen on the yield of DNA double strand breaks in X-irradiated Escherichia coli K 12, Radiat Res. 63, 567-577 (1975)

[2] Kampf, G., Die Erzeugung von DNS Strangbrüchen durch ionisierte Strahlung unterschiedlicher Qualität und ihrer Bedeutung für die Zellinaktivierung, ZfK 504, 1-66, Zentralinstitut für Kernforschung Rossendorf, Dresden, 1983.

[3] Cantor, C.R., Smith, C.L., and Mathew, M.K., Pulsed-field gel electrophoresis of very large DNA molecules, Ann. Rev. Biophys. Chem. 17, 287 (1988)

[4] Kuhnlein, U.R.S., Penhaet, E.E., and Linn, S., An altered apurinic DNA endonuclease activity in group A and group D xeroderma pigmentosum fibroblasts, Proc. Nat. Acad. Sci. USA 73, No. 4, 1169-1173 (1976) Biochemistry

The effect of heavy ion radiation on SV40 DNA under different experimental conditions

J. Stanton, M. Schneider, G. Taucher-Scholz, C. Wiese and G. Kraft
Darmstadt, GSI

SV40-virus has been used at GSI to investigate the damaging influence of accelerated heavy ions on DNA. One of the advantages in using such a viral probe is that it provides the possibility to irradiate SV40 either *in vivo* or *in vitro*. In *in vitro* studies we irradiated SV40 in TE-buffer (10mM Tris pH 8, 1MM EDTA). For experiments using radioprotective compounds Tris(hydroxymethyl)aminomethane (Tris, 200mM) or 2-Mercaptoethanol (Met, 100mM) was incorporated into the TE-buffer system prior to irradiation. Samples were irradiated using the track segment method as previously described[1].

To study heavy ion radiation effects in a more natural environment, we irradiated SV40 infected CV-1 cells. Irradiations were performed on monolayers of CV-1 cells 36 to 48 hours after infection with SV40 virus. Preparation of SV40 DNA was carried out according to Hirt[2].

After irradiation, SV40 DNA was analysed by agarose gel electrophoresis. Using this method it is possible to detect three DNA configurations: supercoiled or undamaged DNA, nicked-circular resulting from a single strand break (SSB) and linear DNA which results from a double strand break (DSB). The relative proportion of each form per sample was than determined using a transmission densitometer as described elsewhere[3]. Cross sections (σ) were determined by dose effect curves (an example is shown in figure 1); biological efficiencies were calculated in breaks per dose and molecule weight.

The absolute biological efficiency of heavy ions depends on the chemical environment of SV40. As expected the DNA shows the highest susceptibility in TE-buffer both for single and double strandbreaks.

Using radical-scavengers, here Met or Tris, the radiation efficiency is diminished. Tris and Met protect DNA by scavenging OH radicals arising from water radiolysis during irradiation. In theory, any damage at sufficiently high concentrations of either radioprotector should only result from direct ionization of the DNA molecule. The concentrations used here were determined experimentally and gave approximately the same scavenging capacity (K_S × scavenger concentration) . From our data it is apparent that the degree of protection differs. We have attributed this to the damaging effect of the Tris-radical arising from the scavenging reaction.

The intracellular situation is far more complex than that *in vitro*. However when the absolute biological efficiencies are compared, it is obvious that the cellular environment is a protective one.

Our data are compared with results obtained by Christensen et al.[4] who used a cocktail of different protecting agents. We can see that our experimental points lie close to his (Figure 2a,b), despite differences in radiation method (track-segment versus thick mixed sample). It is difficult to draw final conclusions as Christensen's data is taken from the mid-LET region while ours is concentrated in the high LET range. Further studies at the new SIS facility may help to fill the gap between the two sets of data.

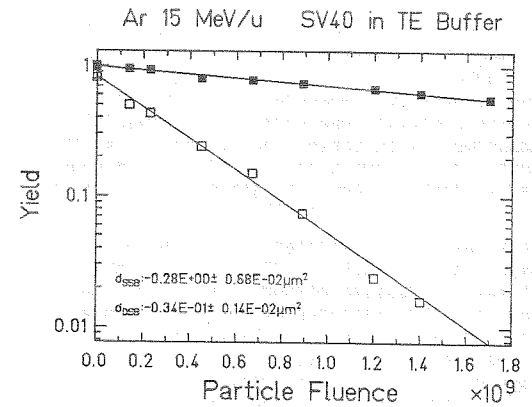


Figure 1: Dose effect curves used to calculate cross sections for single and double strandbreaks.

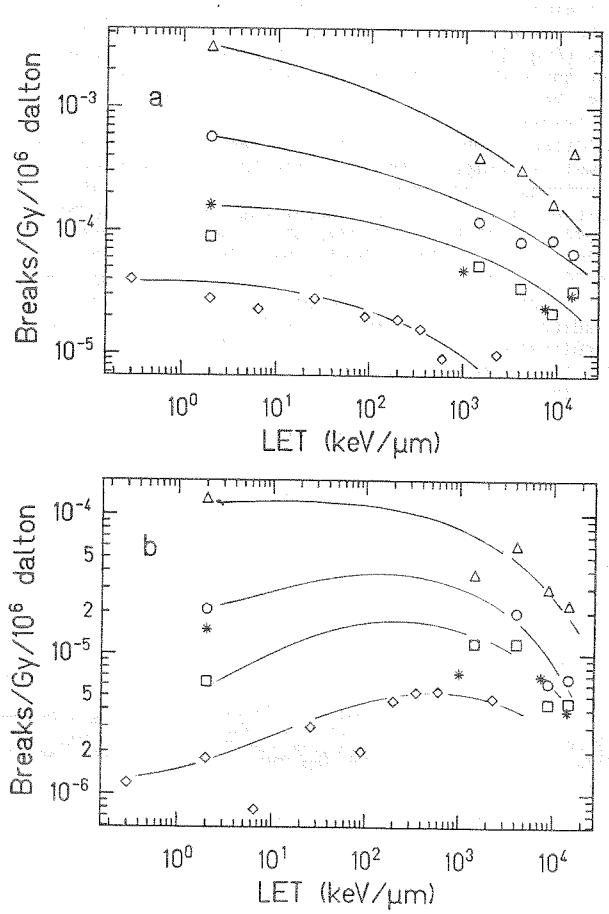


Figure 2: The absolute biological efficiency for
a) single strandbreaks (SSB) and
b) double strandbreaks (DSB);
△ - TE-buffer, ○ - 200mM Tris-buffer, □ - 100mM Met-buffer, ∗ - intracellular, ◇ - data from Christensen[4].

References

1 W. Kraft-Weyrather et al. (1989) Nucl. Instr. and Meth. in Phys Res. (in press)

2 B. Hirt (1964) J. Mol. Biol.26, 365.

3 J. Stanton et al. (1989) Radiat. Protection Dos. (in press)

4 R. Christensen et al. (1972) Int. J. Radiat. Biol. 22: 457-477.

Heavy ion induced free radical formation in nucleic acid constituents: Quantitative Electron Spin Resonance investigations[G]

A. Schaefer, J. Hüttermann

Fachrichtung Biophysik, Univ. d. Saarlandes, Homburg

G. Kraft

GSI, Darmstadt

In order to study the molecular pathways of cellular radiation damage the formation of free radicals induced by heavy ion bombardment in solid, polycristalline pellets of DNA-constituents was measured using ESR-spectroscopy. First results comprised measurement of dose-yield curves after bombardment with various heavy ions (^{40}Ar 15 MeV/u ^{238}U 6 MeV/u) at T = 300 K and T $\leq$ 100 K. A discussion of structural features could be attempted within the limitations set by powder type ESR-spectra /1/.

In the last report we presented additional measurements on 2'deoxycytidine (2'CdR) at 300 K using combined heavy ion and X-ray irradiation methods. In a first analysis, these suggested the existence of molecular processes in which free radicals produced by heavy ions are transformed or destroyed by X-rays.
Irradiation of 2'CdR with different heavy ions (^{40}Ar, ^{132}Xe, ^{238}U) subsequently X-irradiated yielded higher radical concentrations (Fig. 1) and changed ESR-spectra (Fig. 2) /2/.

Here we report on continuing experiments dealing with this aspect. As is shown in Fig. 2 irradiation of 2'CdR using either X-rays (Fig. 2 c) or heavy charged particles (Fig. 2a) yields two different spectral patterns. Thus the spectral change upon subsequent X-irradiation (Fig. 2b) is tried to be explained in terms of a radical transformation.
Employing techniques of specific radical formation /3/ as well as computer manipulation the different radical structures formed upon low- and high-LET irradiation could be identified: Upon heavy charged particle bombardment a pattern is formed which can be assigned to radical sites at the cytosine base (H-addition to C5 and C6) and to a special radical site at the sugar moiety (radical pattern R_i) whereas X-ray irradiation yields a radical which is known in the literature to be the deprotonated cation of the cytosine base /4/ together with the formyl radical formed by oxidation of the sugar ring (radical pattern R_X).

After heavy ion bombardment and additional X-irradiation the spectra don't contain any concentration of R_i but only R_X, transformation $R_X \rightarrow R_i$ however is energetically very improbable /5/. For these reasons the measurements confirm the assumption that X-rays simoultanously produce and destroy radicals during irradiation.

In order to study a possible dependence of the destruction rate on radiation quality samples of 2'CdR preirradiated with X-rays (saturation dose) have been bombarded with heavy ions (^{40}Ar, ^{208}Pb). The quantitative results are presented in Fig. 3:
- Upon bombardment with ^{40}Ar 14 MeV/u and ^{208}Pb 15 MeV/u an increase in radical concentration with increasing particle dose is measured whereas ^{208}Pb 6.3 MeV/u yields a first decrease.
- Additionally the corresponding spectra change with increasing particle dose (Fig. 4). This spectral change can be explained by a destruction of R_X and a simoultanous production of R_i.
Fig. 5 presents the radical concentration assigned to R_X as a function of additional particle dose. The values for ^{208}Pb 6.3 MeV/u are only rough estimates because the range of the particles is lower than the thickness of the samples. To decide if the destruction process is first or second order further measurements have to be made.

/1/ Hüttermann J., Schaefer A., Kraft G., Adv. Space Res. Vol 9, Nr. 10, 35, 1989
/2/ Hüttermann, J., Schaefer A., to be published in Int. J. Radiat. Appl. Instr. Part A
/4/ Sevilla et al, J. Phys. Chem. 85, 1027, 1981
/3/ Dainton F. S., Jones F. T., Trans. Faraday Soc., 61, 1681, 1965
/5/ Schulte-Frohlinde D., private communication, 1989

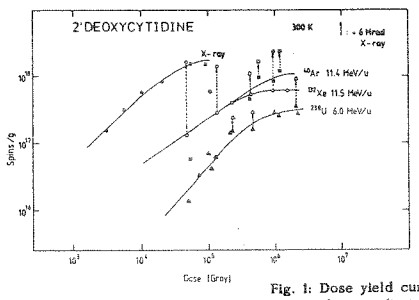


Fig. 1: Dose yield curves of 2'CdR after irradiation with X-rays (●), with ^{40}Ar-ions (■), with ^{132}Xe-ions (○) and with ^{238}U ions (▲). Points marked by arrows show increase of radical yield by additional X-ray irradiation.

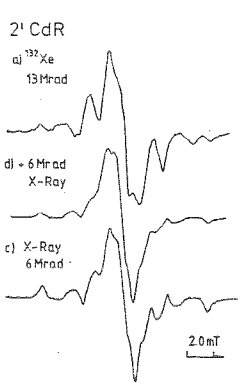


Fig. 2: Spectra of 2'CdR after low- and high-LET irradiation. Irradiation with: a) ^{132}Xe-ions 11.5 MeV/u b) ^{132}Xe-ions and subsequently X-ray irradiation c) X-rays.

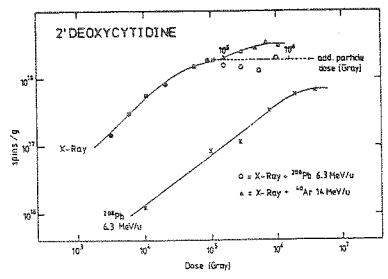


Fig. 3: Dose yield curves of 2'CdR after irradiation with X-rays (●) and after additional heavy ion bombardment with ^{40}Ar 15 MeV/u (△) and with ^{208}Pb 6.3 MeV/u (○).

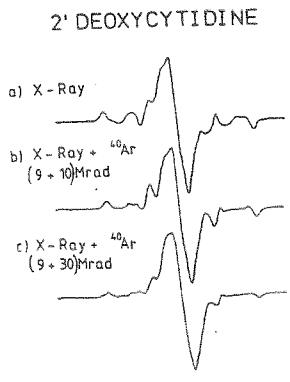


Fig. 4: Spectra of 2'CdR after irradiation with: a) X-rays b), c) X-rays and subsequently bombardment with ^{40}Ar ions of 10 Mrad dose (b) and 30 Mrad dose (c).

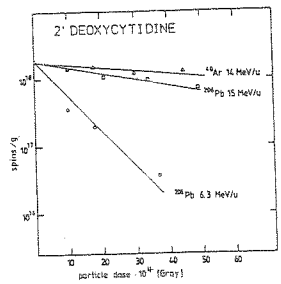


Fig. 5: Radical concentration assigned to R_X as a function of additional particle dose of ^{40}Ar 14 MeV/u-ions (△), ^{208}Pb 15 MeV/u-ions ([]) and ^{208}Pb 6.3 MeV/u -ions (○).

Laser spectroscopic investigation of heavy-ion induced DNA strand breaks

N.Hellmann,Th.Kühl,G.Kraft,R.Neumann

GSI Darmstadt

Electro-optical properties of DNA enable the development of a very fast method of measuring heavy-ion induced strand breaks in DNA molecules . The technique is based on the Kerr-effect: the molecules become aligned in an electric field via their phosphate groups. The resulting orientation of the purine and pyrimidine rings causes birefringence. The originally linear polarisation of the passing laser-light is therefore changed to elliptical. The resulting change of intensity behind an analyzer in crossed position referred to the linear polarization is detected by a photodiode (fig. 1). After switching off the electric field the orientation of the molecules decreases, leading to an exponential decay of the change in intensity. The field-free deorientation is determined by rotational diffusion and depends on size and form of the molecules and the viscosity of the buffer.

In the experiment circular plasmid DNA is used in a supercoiled form (replication form RFI, fig.2). A single strand break causes the DNA to relax into a ring (RFII). One double strand break finally leads to a linear form (RFIII).

The three types of conformation are of the same molecular weight, but are different concerning rotational diffusion : the very compact form RFI rotates faster than the nicked circle. In addition there is also the possibility of variations of the internal flexibility of the DNA molecules. Therefore, the field-free decay of the polarisation signal consists of at least three components for each conformation :

$I(t) = a_1 \exp^{-t/\tau_1} + a_2 \exp^{-t/\tau_2} + a_3 \exp^{-t/\tau_3}$. (fig. 3)

The analysis of the spectrum of an irradiated sample yields the occurring conformation via the time-constants τ_i and the relative portions via the corresponding factors a_i . After exposure to difference doses a variation in the coefficients a_i has been observed, which has been attributed to the induction of single strand breaks. (fig. 4)

The main advantage of this method is the short analysis time. Therefore, it is especially suitable for on-line experiments in order to detect the kinematics of induction processes.

Reference :

(1) G.Kraft and R.Roots, Analysis of Gamma and Neon Irradiated SV 40 DNA by Electrooptical Methods, Rad. Environ. Biophysics 19, 296 (Abstract) 1981

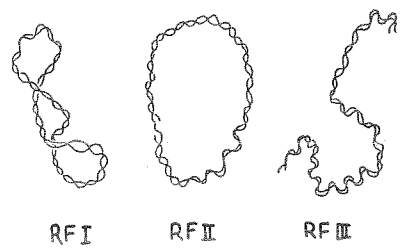


fig.2 conformations of DNA-molecules

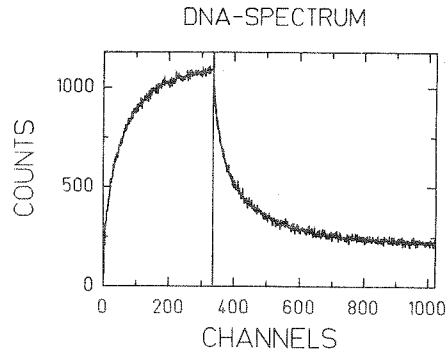


fig.4 time dependence of the polarisation signal at a Kerr-voltage of 800 V and a duration of 800 μs (performed with PHY118 plasmid DNA)

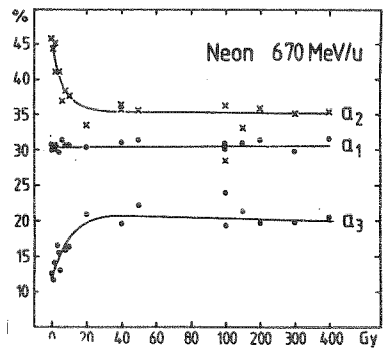
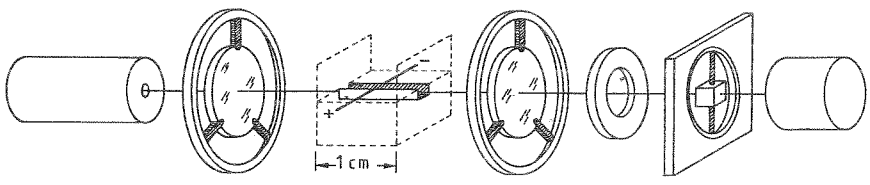


fig.3 dose dependence of the coefficients a_i (1)



laser lense I Kerr-cell lense II λ/4plate analyzer photodiode

fig. 1 optical set-up

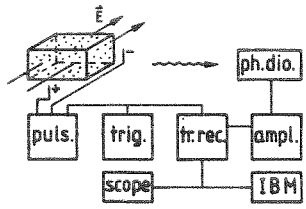


fig. 1a electronical set-up (pulser, trigger,transient recorder, amplifier,photodiode)

A Model System to Detect Heavy Ion Induced Mutations in Mammalian Cells[G]

B. Stahlhacke, J. Thiermann, H. Appelhans, H. G. Gassen

Institut für Biochemie, Technische Hochschule Darmstadt

Damage occurs in living cells after irradiation with heavy ions. Lesions in DNA molecules consist mainly of single and double strand breaks, base excisions or deletions of DNA fragments. For mending of these lesions various repair systems exist in procaryotic as well as in eucaryotic cells. However, mutations can still be detected.

We have developed a model system to investigate the molecular nature of mutations arising after exposure to heavy ions. It allows detection of mutations within a certain gene and the flanking regulatory regions since the DNA sequence is known. We constructed the shuttle vector pJTE9 which contains all regulatory units required for the expression of a gene in pro- and eucaryotes[1]. The gene for chloramphenicol acetyl transferase (CAT) was inserted into this vector. The resulting plasmid[2] was designated pJT215. The human breast tumor celline MCF7 was transfected with this vector. Transient expression of CAT was detected by measuring CAT activity[2]. In this system the loss of the CAT gene due to its extrachromosomal location was an evident disadvantage. The gene thus could not be transmitted to daughter cells.

In order to guarantee the transmission of the CAT gene to the following generations of the cells the vector pJT215 was chromosomally integrated into the host cell genome. To accomplish this the CAT gene was cotransfected with the gene for resistance to antibiotic G418. To do this the vector containing the G418 gene was ligated to the CAT gene vector in a molar ratio of 1:10 to increase the probability of integration of the CAT gene when G418 resistance is observed. Stable transfectants were then selected in medium containing G418. We isolated 21 cell clones which expressed the CAT gene permanently.

For detection and characterization of mutations after heavy ion radiation MCF7 cells will be transfected with an inactivated CAT gene. Inactivation of the CAT gene in the N-terminal region was achieved by exchange of thymine in position 24 to an adenine. This exchange resulted in a stop codon at this position thus preventing CAT expression. To introduce the adenine we used oligonucleotide-directed mutagenesis[3] (Fig. 1). The mutated gene was again inserted in the vector pJTE9. For stable integration the resulting vector pTS21 will be cotransfected with the G418 gene as described above.

Any revertants obtained after exposure to heavy ions will be selected in medium containing chloramphenicol since the resistance is regained by an active CAT gene. Mutations in the CAT gene will be investigated on the molecular level by sequencing the reverted gene.

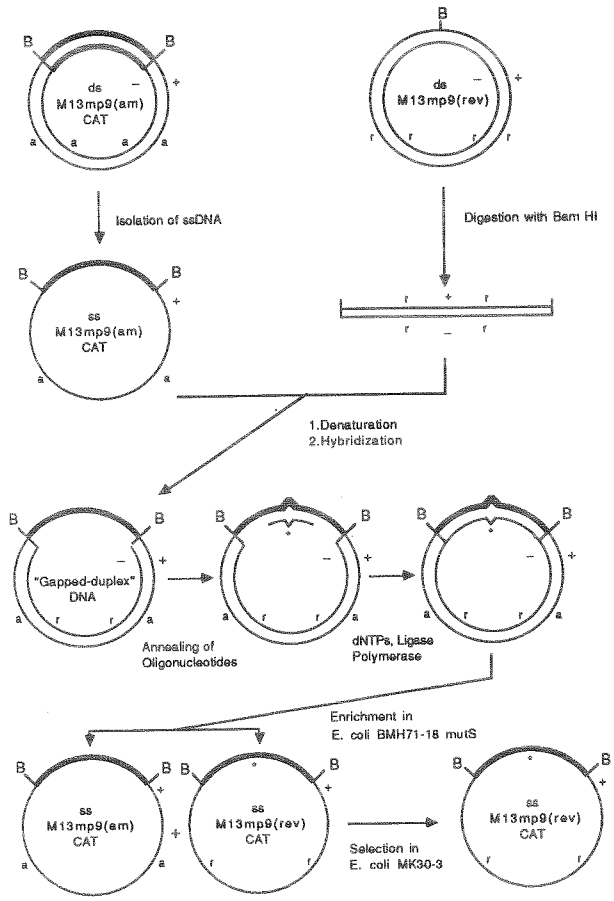


Fig.1: Schematic representation of the "gapped duplex" DNA method used for the construction of CAT mutants[3]

B = Bam HI; a (am) = amber codon; r (rev) = reverted (wild type codon) ▬ = CAT gene; * = point mutation

[1] J. Thiermann et al. (1986) GSI Scientific Report, 211.

[2] J. Thiermann et al. (1987) GSI Scientific Report, 222.

[3] W. Kramer and H.-J. Fritz (1987) Methods Enzymol. 154, 350-367.

Biological action of single heavy ions on individual yeast cells [G]

M. Kost, E. Schneider, J. Kiefer
Strahlenzentrum der Justus-Liebig-Universität Gießen

G. Lenz
GSI Darmstadt

Heavy ions (HZE-particles) constitute an important part of radiation in space. Although their number is small the high amount of energy transferred by individual particles may cause severe biological effects[1]. Their investigation requires special techniques which were tested by experiments performed at the UNILAC at the GSI. As reported already in previous GSI-Reports[2,3] we used diploid yeast which is a suitable eucaryotic test system for space experiments because of its resistance to extreme conditions like dryness and vacuum. The method of analysis has already been described in detail, the most recent experimental improvements are concerned with the use of high resolution and high-quality image analysis equipment. As track detectors 200 μm polycarbonate "LEXAN" foil is employed, which is capable of detecting tracks of ions with Z_{eff}/β greater than 230 and values of Z greater than 8 [4]. Its advantages are good mechanical rigidity and easy handling. Irradiation was performed with about 10^6 particles per cm^2, the cell density on the surface of the detector foil was 3 x 10^6 per cm^2.

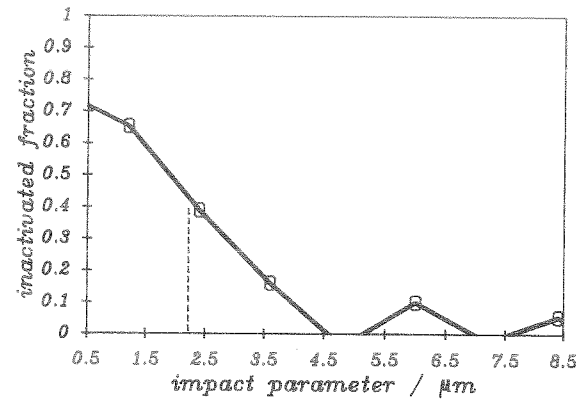


Fig. 1: Normalized inactivated fraction of yeast cells for individual track parameters after irradiation with 8.5 MeV Argon ions.

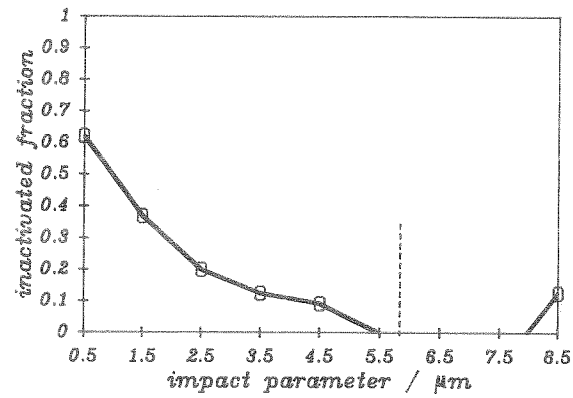


Fig. 2: Normalized inactivated fraction of yeast cells for individual track parameters after irradiation with 14.5 MeV Argon ions.

Results

In previous GSI-Reports we reported data derived from Argon Xenon and Uranium beam times. The curves given therein were based on analyzed cell numbers between 200 to 600. The following data are taken from two beam times, one with 8.5 MeV/u Argon and the other with 14.5 MeV/u Argon ions. A third experiment providing 13 MeV Lead ions is still under analysis. About 600 to 800 cells per experiment were analyzed with respect to colony forming ability. The normalized inactivated fractions for each track parameter value are plotted in figures 1 and 2 for the 8.5 MeV/u Argon- and the 14.5 MeV/u Argon-ions, respectively. The decrease of the curve for the inactivated cells is to be expected as already seen from previous experiments. The dashed lines at the track parameters of 2.4 μm in the 8.5 MeV/u Argon-curve and of 5.8 μm in the 14.5 MeV/u Argon-curve mark the penumbra radius of these specific ions calculated according to Kiefer and Straaten[5]. The considerable scatter to be seen at larger track parameters is mainly due to the comparatively small number of cells which can be analyzed with very high track parameter values. One tentative attempt to sum up all so far available results in one graph is shown in figure 3. The integral over the area under the dead fraction-impact parameter curve is taken as a measure for the total inactivation capability of the respective ion and its secondary particles around the primary particles path. If this value is plotted in arbitrary units versus LET one obtains a representation which is similar to a σ-vs-LET plot. There are, however, not yet sufficient data to draw any general conclusions.

Since the method allows to analyze large samples with comparatively little effort but utmost accuracy it may contribute to a better statistical foundation of heavy ion experiments with respect to the action of single particles on individual cells.

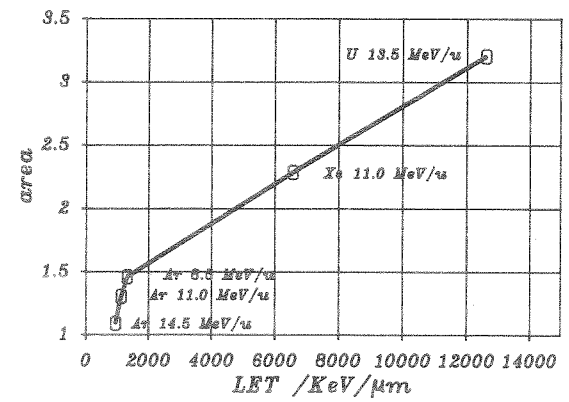


Fig. 3: Area under respective 'inactivated fractions vs impact parameter'-curves as function of LET.

[1] H. Buecker, R. Facius, Acta Astronautica 8:1099, 1981
[2] M. Kost, J. Kiefer, GSI-Report 1987
[3] M. Kost, E. Schneider, J. Kiefer, GSI-Report 1988
[4] H.A. Khan, GSI-Report 1986
[5] J. Kiefer, H. Straaten, Phys Med Biol 31:1201, 1986

Chemical Protection of Bacterial Cells Against Heavy Ion Irradiation

M. Schäfer, C. Schmitz, H. Bücker
DLR, Institut für Flugmedizin, 5000 Köln 90, FRG

There is a large number of chemical compounds that can reduce radiation damage if present during the irradiation. Among them sulphydryl compounds, or thiols, are the most effective agents for bacteria[1]. These effects are under investigation for heavy ion radiation. We used a strain of E. coli (K-12 λ_s) which gives a large protection effect for X-rays after treatment with dithiothreitol (DTT). It is the aim of these experiments to measure the influence of DTT on cell survival as a function of radiation quality in terms of physical particle parameters, such as LET, charge and energy and to compare this with sparsely ionizing radiation. Stationary cells are treated for at least 30 min. with DTT in buffer solution. Irradiation was performed on membrane filters in the presence of DTT. Cells are then resuspended in buffer solution which reduces the concentration of DTT in the cells by more than a factor of 5 (dependent on the survival level).

Fig. 1 shows the results for E. coli cells after irradiation with 150 KV X-rays exposed to different concentrations of DTT. For low concentrations we find a steep increase in the protecting effect while for higher concentration only a slight increase could be observed. Apparently, there is a trend towards a saturation value. However, further increasing the concentration above 0.5 M DTT is toxic for the cells. The maximum protection factor reached is about 5.

First experiments with Ar-ions demonstrate that protection of DTT (0.5 M) can also be observed for high LET radiation. Fig. 2 shows the results of irradiations using Ar with different energies under the experimental conditions described above. The protection factor, P, is determined as the quotient of the slopes of survival curves. The protection factor increases as a function of energy and reaches the highest value of 2.5 at 12 MeV/u. This is half the value obtained from X-ray irradiation. In principal, this indicates that for increasing particle energies the δ-electrons can be considered, to a certain degree, as a sparsely ionizing component. This qualitatively corresponds with other findings[2].

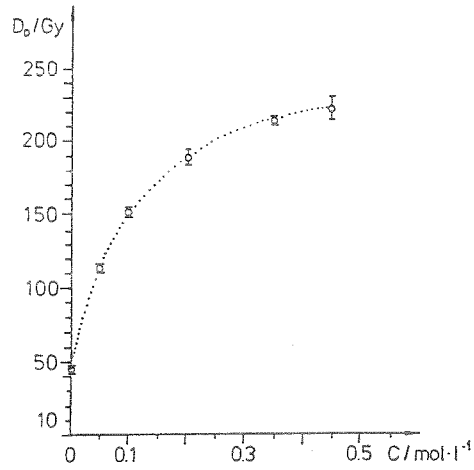


Fig. 1 D_0-values (dose at 37% survival) after X-ray irradiation as a function of DTT concentration.

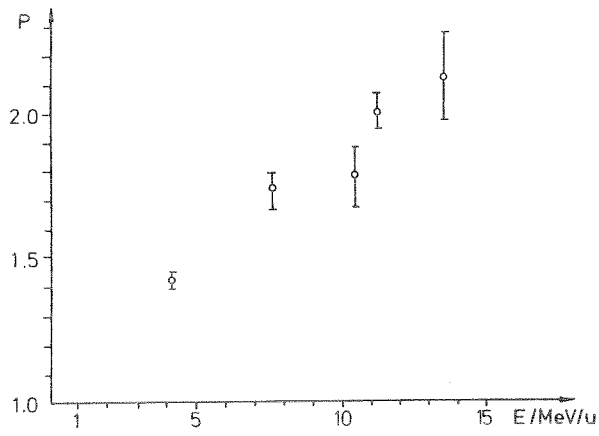


Fig. 2 Protection factor P (determined as a quotient of the inactivation cross sections with and without DTT) as a function of the energy of Ar-ions.

[1] T. Alper, Cellular Radiobiology, 1979, Cambridge University Press

[2] K. Baltschukat et al., GSI Scientific Report 1984, pp. 239 and 243

Influence of Growth Conditions on the Survival of Deinococcus radiodurans Exposed to Ionizing Radiation

M. Schäfer, C. Schmitz, H. Bücker
DLR, Institut für Flugmedizin, 5000 Köln 90, FRG

It was reported in earlier experiments[1] that the survival curves of the radiation resistant Deinococcus radiodurans strain R1 showed small shoulders after heavy ion radiation while there is a large shoulder obtained after X-ray irradiation. It was assumed that growth conditions[2] could be responsible for these effects. Therefore, detailed studies with Am-α-particles and heavy ions were performed under controlled growth conditions.

Growing cells normally reach a stationary phase characterized by a constant cell number. In this phase the response of the cells to ionizing radiation is the same, independent of the time spent in stationary phase. For cells of Deinococcus radiodurans we find contrary results. Fig. 1 demonstrates that survival curves differ greatly depending on the incubation time. For all curves the cells were grown in TYG-medium, starting with the same cell concentration of 10^3 cells/ml, reaching a maximum concentration (30^oC after 2 days) of about 10^8 cells/ml which remained constant for up to 4 days. Only at 37^oC the cell number is reduced to 10^6 cells/ml. In the stationary phase of strain R1 processes alter the cells, drastically influencing survival after irradiation. Increasing incubation time reduces the shoulder of the curves (this effect being most remarkable at 37^oC). We point out that the sensitivity, measured from the slope of the exponential part of the curve, is not influenced by these conditions.

One explanation for this effect could be that the cells exhibit a higher number of genomes when they reach the stationary phase. The longer the time spent in stationary phase the fewer genomic copies are present.

Only two experimental results with Ar and U ions have been obtained for comparison. Fig. 2 also demonstrates a reduction of the shoulder for heavy ions while the slope of the curves are nearly the same. From these experiments we can conclude that if we are only interested in the slope of the curves we find no influence on our results by changing the experimental conditions. However, they have a high influence in performing the experiment.

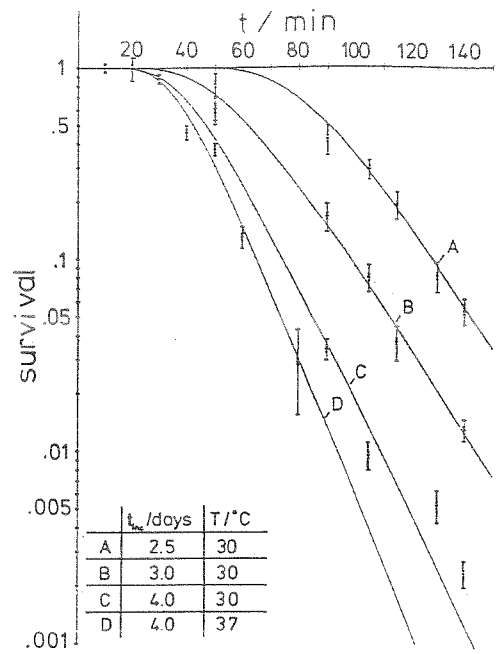


Fig. 1 Survival curves after Am-α-particle irradiation for different temperatures and incubation times (dose given in time units (t) for an Am-source with a constant dose rate).

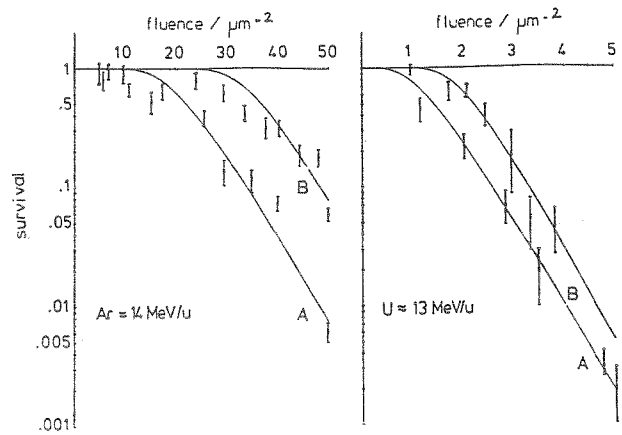


Fig. 2 Survival curves after heavy ion irradiation of Deinococcus radiodurans cells under different growth conditions.
(A: 4 days, 37°C; B: 2.5 days 30°C)

[1] M. Schäfer, H. Bücker, GSI Scientific Report 1987, p. 225

[2] B.E.B. Moseley, in: Photochemical and Photobiological Reviews, Vol. 7, 1983, ed. K.C. Smith, Plenum Press, New York, London

Effects of HZE-Irradiation in Arabidopsis Pollen[G]

M.Pickert, U. Bork, A.R. Kranz

Botanisches Institut, J.W. Goethe-Universität, Frankfurt am Main

Former experiments with Arabidopsis seeds irradiated with heavy ions made by accelerators have shown a correlation between the radiation damages and the level of cellular ploidy. Dry seeds of diploid wild type Enkheim (2n) and its autotetraploid line (4n) were irradiated and the results compared (1).

The male gametophytes of plants, the so called pollen grains, are in general haploid (n). Now, the use of pollen for radiobiological experiments allows investigations of this ploidy level. The whole trinucleate pollen of Arabidopsis thaliana is only 20 µm in diameter. The mean volume of the three nuclei is about 12 μm^3 (2). We calculated with this value, though new computer aided 3D-measurements of crucifer pollen nuclei (3) particular for Arabidopsis are needed.

In our experiment monolayers of dried pollen grains spread on petridishs and covered with Mylar foil, have been exposed to Uranium ions (15.9 MeV/u), Argon ions (14 MeV/u) and Lead ions (13.6 MeV/u). The "Kraft machine" for irradiation of biological objects was used. After irradiation, pollen vitality was investigated by fluorescence staining (fluorescein diacetate, FCR-Test) and with in vitro germination on synthetic media. The seed set on nonirradiated malesterile mother plants crossed with the irradiated pollen, and the frequency and kind of mutants in the following generations are also parameters for the genetic radiation damage induced in pollen grains.

Table 1.: Cross sections of biological endpoint (μm^2) pollen germination in vitro

ions	σ (μm^2)
U 15.9 MeV/u	6.2
Pb 13.6 MeV/u	2.2
Ar 14.0 MeV/u	1.4

Figure 1 illustrates the effect of three different heavy ions on the survival of pollen grains measured by in vitro germination. The exponential regressions and the cross sections σ for the biological endpoint germination (Tab. 1) were calculated. The mean value of the geometrical cross section of one haploid pollen nucleus is about 6.3 μm^2 (for the generative nuclei probable lower), for diploid meristem nuclei about 8.8 μm^2 (4). The cross section σ of biological endpoints of pollen and seed are not comparable, because of the different physiological system of germination. Pollen germination should be understood as a function of all three nuclei so called "male germ unit". It seems that the statistical hit of only one of the three nuclei inhibits the pollen tube elongation totally. This effect is incomparable to the suppression of germination measured for seeds. The radiobiological relevant area of one seed includes only the meristem cells, with seperated nuclei of which the genetic material is presented twofold (diploid). At least two HZE-hits per meristematic cell nucleus are necessary to reduce the seed germination and seedling survival significantly (5).

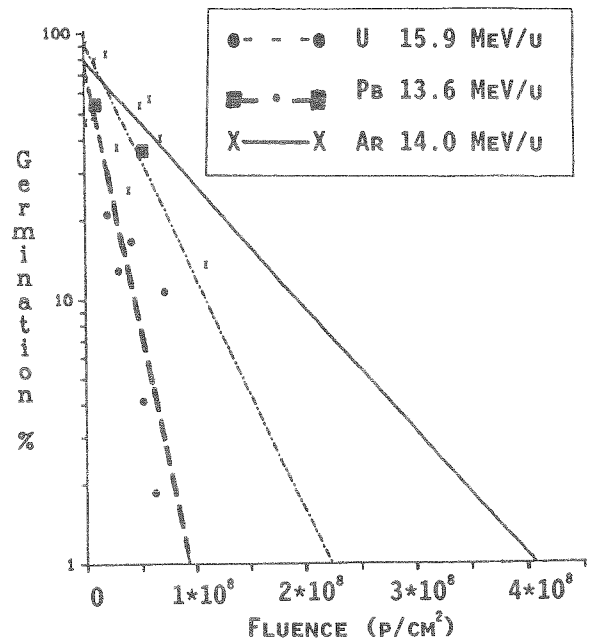


Fig. 1: Fluence-effect-curves (U 15.9 MeV/u; Pb 13.6 MeV/u; Ar 14 MeV/u) for the germination of Arabidopsis pollen grains.

References

1. K.E. Gartenbach, U. Bork, A.R. Kranz, M. Pickert, GSI, Scientific Report, 222 (1988)
2. G. Röbbelen, Z. für Vererbungslehre 93, 127 (1962)
3. C.A. McConchie, S.D. Russell, C. Dumas, M. Tuohy, R.B. Knox, Planta 170, 446 (1987)
4. K.E. Gartenbach, Diplomarbeit, Botanisches Institut der J.W. Goethe-Universität Frankfurt (1988)
5. U. Bork, K.E. Gartenbach, A.R. Kranz, Adv. Space Res. 9 (10), 117 (1989)

Irradiation-induced tumors in Xiphophorus (Pisces, Teleostei)

M. Henze, F. Anders and A. Luboeinski

Genetisches Institut der Universität Giessen

In Xiphophorus the development of tumors depends upon a Mendelian tumor gene (Tu), which is present in all genotypes. Fish from wild populations have coadapted population-specific regulatory (R) gene systems for Tu that protect them from neoplasia[1]. Tu is molecularly associated with a gene related to the human EGF receptor gene (2).

Interspecific hybrids of Xiphophorus maculatus (platyfish) and Xiphophorus helleri (swordtail) are susceptible to neoplasia following the crossing procedures delineated (Fig. 1 - 3). They develop melanoma either "spontaneously" (Fig. 1), or after treatment with mutagenic carcinogenes, e.g. X-rays and UV (Fig. 2), or treatment with tumor promoters such as TPA (12-O-decanoyl-phorbol-13-acetate), steroid hormones, etc. (Fig. 3). X-rays and UV, besides being mutagens, show also promoting effects.

We are now going to treat the fish with heavy particles, because they permit to induce well defined tracks in respect to diameter and energy deposition by appropriate choice of ion mass and energy[3], in comparison to electromagnetic radiation like X-rays.

In comparison to the in vivo experiments, experiments with X-rays and heavy particles upon two cell lines were performed. An established cell line of embryonic origin (A_2) and a transformed cell line (PSM) from melanoma revealed data upon survival and sensitivity: Sensitivity of the fish cells seems to be higher than that of the V79 hamster cells.

A new setup of experiments is in preparation: In parallel with our former experiments with X-irradiated fishes, pregnant individuals will be exposed to heavy particles. Morphological changes in both, the females and the litter, will be studied with respect to tumor incidence. Moreover, interactions of irradiation with heavy particles, pigment cell patterns and restriction length polymorphisms (RLFLPs) of oncogenes will be studied according to methods described by Zechel et al.[3].

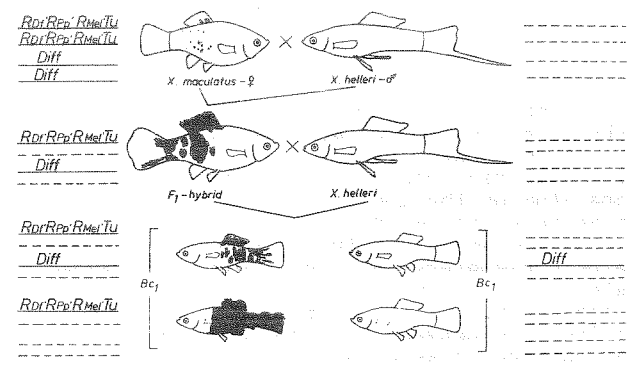


Fig. 1: Crossing scheme displaying the genetic conditions for melanoma development. ---, chromosomes of X.maculatus; - - -, chromosomes of X.helleri; Tu, tumor gene; R_{Mel}, mutated pigment cell specific regulatory gene; R_{Pp} and R_{Df}, mutated compartment specific regulatory genes for the posterior part and the dorsal fin; Diff, powerful posttransformationally acting repressing gene.

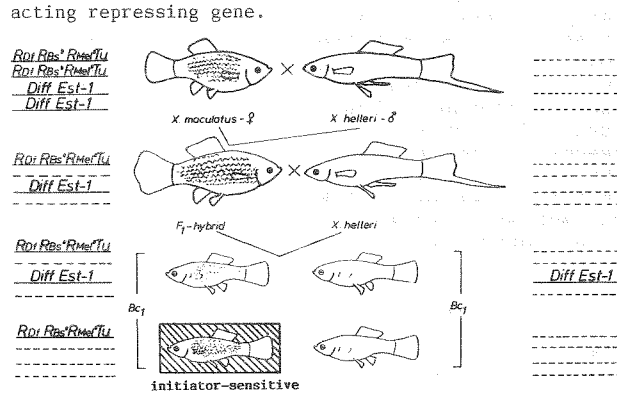


Fig. 2: Crossing scheme displaying the genetic conditions for melanoma development after treatment with carcinogens. Est_1, Esterase-locus-1 of X.maculatus.

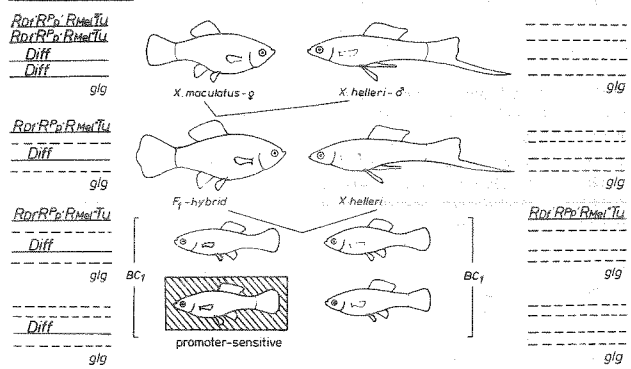


Fig. 3: Crossing scheme displaying the genetic conditions for melanoma development after treatment with tumor promoters. g, golden gene, delays pigment cell differentiation.

[1] A.Anders et al., Biochim. Biophys. Acta 516, 61-95 (1978)

[2] Ch. Zechel et al., Modern Trends in Human Leukemia VIII, 366-385 (1989)

[3] G. Kraft et al., Nucl. Sci. Appl. 3, 1 - 28 (1987)

A scanning tunneling microscope for the investigation of technical surfaces and biological objects [G]

W. Mayer, R. Stephan and H. Gärtner
Fachbereich Physik der Gesamthochschule Kassel
D-3500 Kassel

STMs[1] have become quite popular as a tool for the investigation of surfaces with resolution in the nanometer range.
In the ideal case a sharp metall needle with one atom on the top, is scanned over a conducting material with the utilization of piezoceramic elements in the distance of only some atomic diameters. At these small distances an electrical current will flow by quantum mechanical tunneling if we apply a small potential difference between the sample and the tip.
An applied bias of several tens of millivolts will induce current flows of the order of nanoampere. With $V << \phi$ the tunneling current can be written[2]:

$$I = f(V) * \exp(-\sqrt{\phi} * s)$$

f(V) and $\sqrt{\phi}$ are material properties, ϕ is the average of the barrier height between the two electrodes, f(V) is the average local density of states, s is the gap width.
A feedback control system is adjusted to maintain a constant tunneling current and thus a constant distance between tip and surface.
When the tip is scanned laterally across the surface in a raster pattern an image of surface topography and/or surface electronic structure can be obtained by recording the feedback loop voltage.
The STM in construction is a further development of a operating STM, which is used in air at ambient pressure. Fig.1 shows a STM image of an optical disc, sputtered with Au. The designed STM is capable to reach every position of a 6 mm² large sample. This is feasible by the use of two micrometer screws which shift the sample table for lateral positioning in the x-and y-direction.
A third micrometer screw and a stacked piezo are necessary to bring the tip within tunneling distance. The coarse mechanical motions of the micrometer screws will be motorized by the use of three stepper motors.
The utilization of two piezo systems, three stacked-piezo drivers and a single tube x-y-z scanner[3] makes it possible to measure large objects (The maximum scan area is 12 µm², the maximum vertical displacement is 6 µm) as well as to achieve atomic resolution. By employing both systems one has the possibility to find small biological objects in a large range with the stacked-piezos and to inspect them with the single-tube scanner.
The STM does not use the flow of free electrons between sample and tip, hence measurements are independent of the kind of medium between the two electrodes. So it is possible to investigate biological objects[4] in air at ambient pressure.
Large insulating organic specimens can only be probed with the STM if they are coated with a conductive overlayer. Thin biological objects < 20 Å will only change the electronic properties of the substrate surface. On thicker isolating organic samples > 50 Å measurements are possible by local electric transport properties, which are still not well unterstood.

The STM is built for investigations on biological cell membranes and on DNA molecules, which are damaged by heavy ions bombardment leading to the formation of DNA filament fragments.
On solid state substrates which were irradiated with heavy ions, the interest lies in the shape and size of the produced holes, depending on the host material, the angle of incidence and the energy of the bombarding ions.

[1] G.Binnig, H.Rohrer, STM, IBM Journal of Research and Development, Volume 30, Number 4, July 1986
[2] J.Tersoff, D.R.Hamann, Theory of the STM, Physical Review B, Volume 31, Number 2, 15 January 1985
[3] G.Binnig, D.P.E.Smith, Single- tube three -dimensional scanner for STM, Rev.Sci.Instrum. 57(8), August 1986
[4] G.Travaglini, H.Rohrer, M.Amrein, H.Gross, STM-on Biological Matter, Surface Science 181 (1987) 380-390

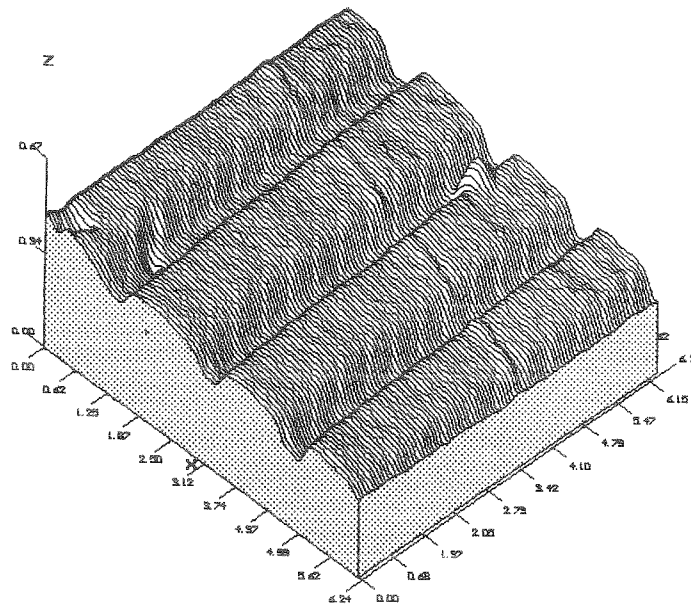


Fig. 1: STM image of an Au-coated optical disc. The total scan range in the x-and y-direction is 6 µm, the lattice constant is 1.6 µm.

δ-electron spectroscopy from fast heavy ion collisions ^{G,B}

U. Ramm, H. Schmidt-Böcking
Institut für Kernphysik, Universität Frankfurt
G. Kraft
GSI, Darmstadt

Heavy ion induced biological damage is due to primary ionization events caused by the projectiles and secondary ionization effects relating to the primarily produced electrons [1]. More than 90% of the radiobiological efficiency of the heavy ions is due to these so called δ-electrons. Therefore the local ionization density and in consequence the energy and also the angular distribution of the δ-electrons are of great interest.

Various models, classical (BEA [2]) and semiclassical (SCA [3], CTMC [4], nCTMC [5]) as well as quantummechanical (PWBA [6]) are existing for calculating double differential cross sections for δ-electron emission. Recent measurements at the UNILAC showed unexpected angular and energy distribution [7] indicating that the assumptions of these models are incomplete. Therefore, measurements have to be continued to obtain greater systematics of the dependence of δ-electron emission on particle parameters like atomic number and energy.

In addition, nothing is known on the electron emission in solids which might be different from gas phase because of a different distribution of the impact parameters caused by Debye screening as well as the possibility of collective effects for the outer target electrons which have only small binding energies. Therefore, electron emission of solid targets shall be studied as well as of gas targets.

Up to now experiments in δ-electron spectroscopy were performed at the low energy beam line of UNILAC ('Stripperhall') [7]. A 1.4 MeV/u U^{33+} beam were collimated to a spot size of 0.5mm^2 penetrating a differentially pumped target gas cell. Electrostatic sector analyzer were measuring electron energy spectra in the range of $200 \leq E_e \leq 4000$ eV, at angles to beam axis Θ_e between 25 and 160° [Fig.1]. A channeltron was mounted behind the focal point to detect the electron emission.

In the last year this setup was transferred to the high energy experimental hall of the UNILAC. Since the energy of the δ-electrons depends on the projectile energy the apparatus had to be modified giving the permission to detect energies of some keV.

This adapted equipment is just installed and tested resently using a 5.9 MeV/u Ne beam according to δ-electrons-energy up to 15 keV. In Fig.2 the yield of electrons (in an arbitrary unit) versus the δ-electron energy is plotted. The angle to beam axis was set to $\Theta_e = 50°$. The plot is showing the exponentially decaying continous spectrum overlapped by the the Binary Encounter Peak. This peak is according to the target electrons-projectile collision which can be described in a classical way.

However the data are up to now not already interpreted but with these data we will be able to describe the damages of organic molecules and in complex biological samples in a more realistic way.

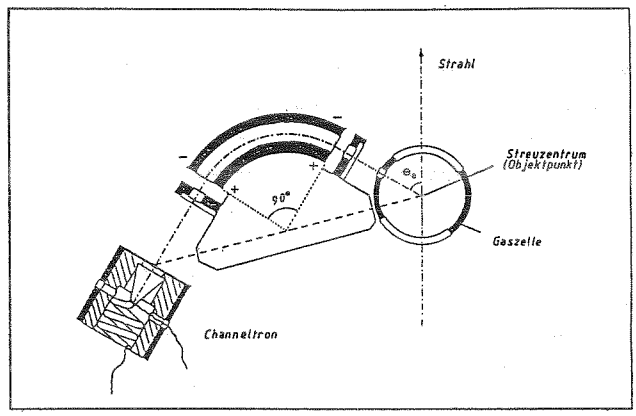


Fig. 1 : Experimental setup.

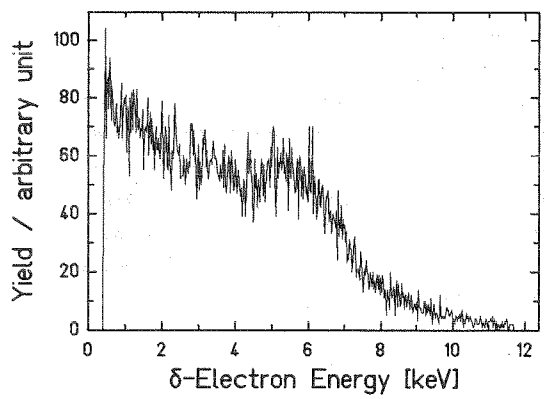


Fig. 2: δ-electron emission for 5.9 MeV/u Ne^{7+} on Nitrogen. Angle of electrostatic sector analyzer to beam axis set to $\Theta_e = 50°$.

[1] G. Kraft, Nucl. Science Appl. 3, 1 (1987)
[2] J.D. Garcia et al., Phys. Rev. 165, 66 (1968)
[3] J. Bang, J. Hansteen,
Med. Fys. Dan. Vid. Selsk. 31, No.13 (1959)
[4] R.E. Olson, A. Salop, Phys. Rev. A 16, 531 (1979)
[5] R.E. Olson, in 'Electronic and Atomic Collisions
H.B. Gilbody (ed.), North Holland, Amsterdam (1987)
[6] H. Bethe, Ann. d. Phys. 5, 325 (1930)
[7] S. Schmidt, Diploma Thesis, Univ. Frankfurt (1987)
[8] M.E. Rudd, in 'Low Energy Electron Spectrometry'
K.D. Servie (ed.), Wiley-Intersience, New York (1972)

Status of the Heavy Ion Therapy Project

G. Kraft, N. Angert, K. Blasche, D. Böhne, B. Fischer, B. Franczak, H. Geissel, T. Haberer, W. Kraft-Weyrather, B. Langenbeck, G. Münzenberg, S. Ritter, D. Schardt, Th. Schwab, H. Stelzer (GSI Darmstadt)
G. Gademann, M. Wannenmacher (Radiologie Heidelberg)
G. Hartmann, W.J. Lorenz (DKFZ Heidelberg)

In January 1989 the installation of an experimental heavy ion radiotherapy unit at the SIS was proposed to the German government by the Radiological Clinic of the University and the German Cancer Research Center (both at Heidelberg) and GSI.

In this proposal the superior depth dose distribution and the enhanced radiobiological efficiency of heavy ion beams shall be used to treat malignant tumors which are either highly radioresistant or which are located in close proximity to radiosensitive or vital organs. For treatment, the lighter ions between carbon and neon are the most favourable. In this range of atomic numbers the physical properties of the heavy ion beam, such as the lateral and range straggling are very small when compared to the lighter ions like protons. The nuclear fragmentation is also still moderate. In addition, the biological efficiency of these ions is essentially increased only at the end of the particle range in the target volume, while full repair capacity is maintained in the normal tissue around the tumor.

For these reasons, radiotherapy will concentrate on the lighter ions. Heavier ions which might be the main interest for physics experiments cannot be used for radiotherapy. For an effective use of the SIS beam, radiotherapy has to be performed by time sharing with the physics experiments, i.e. short periods of light ion beams should be available for therapy once or twice an hour during the course of other experiments. In order to facilitate fast switching of atomic number, the installation of a separate injector for light ions is necessary. This will inject the medical beam directly into SIS without any perturbation of the Unilac injector and to the low energy experiments.

Other installations necessary for radiotherapy are: a dedicated beam delivery system, a treatment room and additional rooms for beam control and for medical preparations. In order to achieve a precise tumor conform treatment, the use of a magnetic deflection system is proposed. This enables irradiation of a tumor volume slice by slice corresponding to different particle ranges with a controlled particle fluence. The scanning system will be controlled by a fast position sensitive detector at the entrance of the beam into the body of the patient. In order to verify the dose distribution in vivo, radioactive beams as for example ^{11}C or ^{19}Ne, will be produced in a special fragment separator and the two 511-keV annhilation quanta of the emerging positrons will be monitored in coincidence by a gamma camera.

The magnetic scanning system combined with the fast energy variation of a modern synchrotron is a novel concept which would allow the treatment of a target volume with ultimate precision. The total costs of this installation, i.e. medical injector, beam delivery system, treatment cave, and medical rooms, has been estimated at 17 Million DM, distributed over a 3 years time span. Treatment of patients could start in the second half of the forth year after commencement of the project and should reach a level of 100 patients per year. This concept of experimental heavy ion therapy was presented in a symposium in March held at Heidelberg and Darmstadt and was well received by the radiotherapy comunity, the accelerator- and nuclear-scientists and by government officials. Simultaneously, a similar concept using heavy ion therapy based on a superconducting cyclotron has been proposed to the European Community by the European Light Ion Medical Accelerator (EULIMA) project committee.

In response to our proposal and in order to explore the possibility of heavy ion therapy and its socio economic relevance, the governmental officials proposed a two year prephase in which the technical feasibility of the different components, the radiobiological aspects, and the clinical relevance should be studied. As a result, a concept for a two year experimental program has been developed using the heavy ion beam of the SIS without major investment. The main points of these studies at GSI are:

- Radiobiological experiments for a biological characterisation of the heavy ion beams.
- The development of a three-dimensional beam scanner using the magnetic scan system in the biophysics cave.
- Measurement of the fragmentation cross section of light ion beams in a thick target.
- Development of fast, position sensitive transmission detectors.
- Production of radioactive, positron emitting beams.
- Experiments with a positron camera in order to verify range profiles.
- Machine experiments at the SIS for the achievment of slow extraction of heavy ion beams with constant intensity.
- Design studies for an hospital based heavy ion therapy unit.

These studies will be performed using the already existing equipment (fragment separator, rasterscan, etc.) but with major support from the German government and from CEC Brussels in close collaboration with the EULIMA project.

First radiobiological experiments, concerning the killing efficiency of heavy ions as a function of cell cycle, fractionation effects, chromosome aberrations as well as a computer simulation of different scan strategies for the magnetic scanning system have commenced and are also presented in this report.

Computer Simulations of Beam Scanning Strategies for the Radiotherapy Project*

T. Haberer, K. Blasche, D. Böhne, B. Fischer, G. Kraft, B. Langenbeck (GSI Darmstadt)
M. Wannenmacher (Radiologie Heidelberg)
W.J. Lorenz (DKFZ Heidelberg)

The specific advantage of heavy ion radiotherapy is the precision of beam delivery. In order to cover the tumor volume with a well defined dose, a magnetic deflection system will be used for beam scanning[1,2].

The tumor volume will be dissected into slices of equal particle range[3] by variation of the beam energy (figure 1). These irregularly shaped areas are sequentially exposed to a homogeneous or a defined inhomogeneous dose of stopping ions. It is the goal at this initial stage of simulations to deliver a constant fluence to an area of any contour. Up to now, using computer simulations the influence of different scan techniques on the produced dose distribution, ie. pixel and raster scan, has been investigated (figure 2).

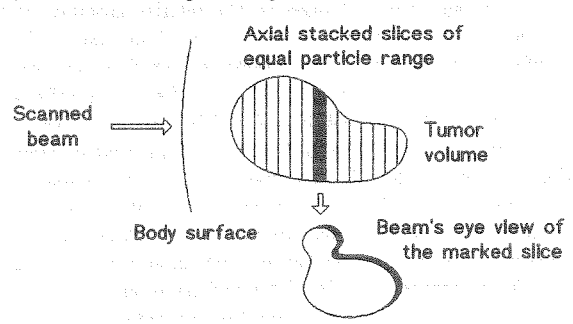


Fig. 1: Dissected tumor volume.

In order to study the influence of line/pixel spacing on dose uniformity both strategies have been applied to a rectangular and an irregular area. Provided the line/pixel spacing is smaller than the FWHM of the beam profile the uniformity will be better than 5 % in both cases (figure 3). This means sufficient uniformity could be realized, and could be documented as line profiles (figure 4). Finally the influence of the beam diameter on minimal structure width was studied. Though the minimum interior diameter of the target area was about 7 mm (FWHM 5 mm), one can clearly see from figure 5 that the field produced fits quite well to the target contour.

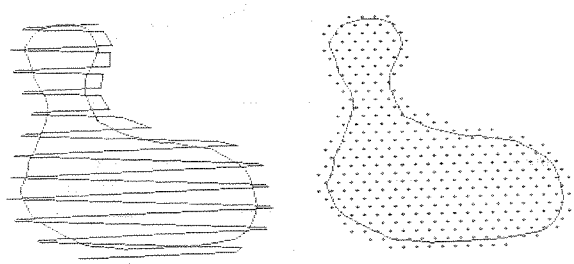


Fig. 2: Raster (left) and pixel (right) scan pattern.

The results of these simulations do not justify the preference of one of the two tested strategies - pixel or raster scan. Both techniques lead to nearly identical results subject to all underlying criteria. Figure 6 shows an isodifference plot of a raster and pixel scan, based on comparable parameters. Differences in dose solely arise outside the boundary of the scanned area.

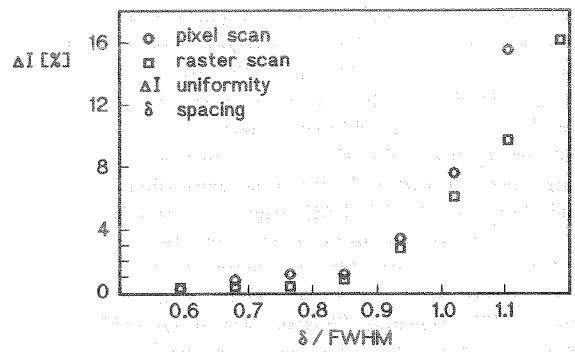


Fig. 3: Relationship of spacing and dose uniformity.

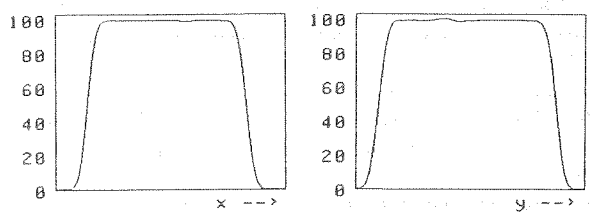


Fig. 4: Horizontal (left) and vertical (right) line profile.

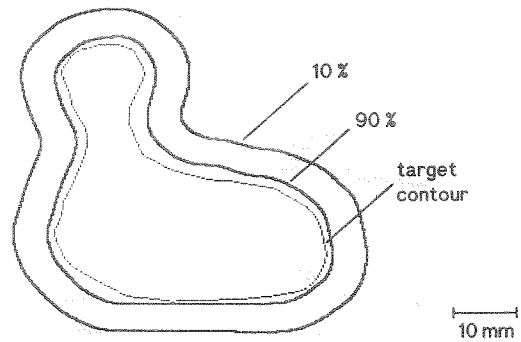


Fig. 5: Shape of the dose distribution applied to an irregular target area.

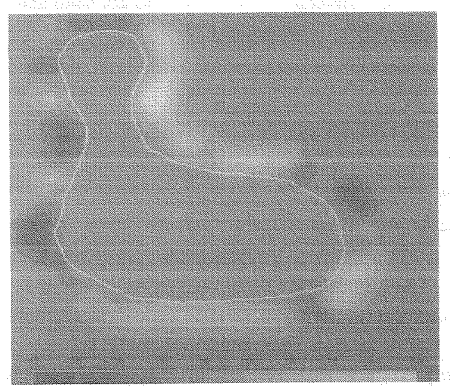


Fig. 6: Comparison of distributions produced by raster and pixel scan in an isodifference plot (therapeutic dose ≙ 100 %).

* This work was supported by the European Light Ion Medical Accelerator (EULIMA) project.

References

[1] G. Kraft et al., GSI Annual Report (1988), p. 324
[2] G. Kraft et al., this report
[3] M. Goitein, Med. Phys. 10 (6), p. 831 (1983)

High Dose Iron Implantation into Silicon and Metals[B,G]

G.Müller, G.Klingelhöfer, P.Schwalbach, E.Kankeleit
Institut für Kernphysik, Technische Hochschule Darmstadt

For high dose implantations of Si and various metals the UNILAC-Injector was employed. Isotope-separated beams of about 20 and 0.2 particle μA of ^{56}Fe and ^{57}Fe are available, respectively [1]. Studies of the transmission and the mass separation of ^{56}Fe and ^{57}Fe at different target positions in the beam line of the injector yield, that for our purposes the only useful target position with a distinct mass separation is just before the injection into the UNILAC itself. The irradiated samples have been characterized using several complementary methods (Mössbauer Spectroscopy (MS), Rutherford Backscattering Spectroscopy (RBS), X-ray diffraction (XRD), Auger electron Spectroscopy (AES), Scanning Electron Microscopy (SEM)). As an example of our work [2] we will discuss the case of Cu briefly.
A 20 μm thick polycrystalline Cu-target (99.0%) was irradiated with a dose of $2\cdot10^{17}$ ^{56}Fe/cm^2 and an ion energy of 610 keV. The equilibrium temperature during ^{56}Fe implantation was 410 K. The ^{57}Fe dose amounts to $8\cdot10^{15}$ Fe/cm^2 and has been implanted in two steps. In the first step half of the ^{57}Fe dose has been implanted with an energy of 610 keV before the ^{56}Fe implantation. After the ^{56}Fe implantation the remaining ^{57}Fe dose was implanted in the second step with an energy of 440 keV. This lower energy was chosen to deposit the ^{57}Fe in the center of the ^{56}Fe implantation profile. Due to the lower current in the ^{57}Fe implantations the temperature did not rise above room temperature. The pressure in the beam line was below $1\cdot10^{-6}$ mbar.

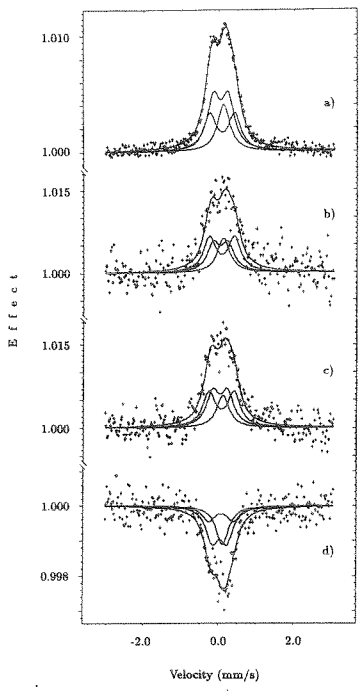


Figure 1:

Mössbauer spectra of Fe implanted in Cu
a) ICEMS spectrum
b) DCEMS spectrum, E=6.9 keV
c) DCEMS spectrum, E=6.6 keV
d) TMS spectrum

In the conventional phase diagram the room temperature solubility of Fe in Cu is smaller than 0.25 atomic % Fe and no intermetallic compounds are known. The maximum available concentration of implanted ions was calculated to be 19 at.% Fe and the sputter yield was calculated to be 5.1. Due to sputtering a surface concentration of 12 at.% Fe is expected. With AES a Fe concentration of ~16 at.% is determined at the surface, in agreement with our calculations. The sample has been investigated by transmission -, integral conversion electron - and by depth-selective conversion electron Mössbauer spectroscopy, (TMS, ICEMS, DCEMS) (fig. 1). DCEMS-spectra have been recorded at electron energies of 6630 eV and 6930 eV, corresponding to a mean depth of about (200 - 250) Å and (300 - 350) Å, respectively, using our orange-type magnetic spectrometer with 2% energy resolution. Since in the X-ray diffraction data no pure Fe-phases are detected at room temperature the Mössbauer spectra are interpreted with three components corresponding to Fe-monomers, Fe-dimers and Fe-polymers, following ref. [3]. Applying ICEMS and DCEMS, which are sensitive to the top 1000 Å of a sample, no significant changes in the relative amounts of the three components are found, unlike ref. [3]. This may be due to the different implantation layer thickness, which in our case is about 3 - 4 times larger than in ref. [3]. After 12 months aging at room temperature an additional ICEMS-spectrum was measured. It indicates a change in the ratio of the relative amounts of the components (fig. 2). The fraction of dimers remains constant, whereas the polymers increase to 54 % at the expense of the monomers. Clustering appears because Fe diffuses in Cu predominantly by a vacancy mechanism with an activation energy of 1 eV at room temperature [4]. This process is supported by the excess of vacancies produced during the implantation.

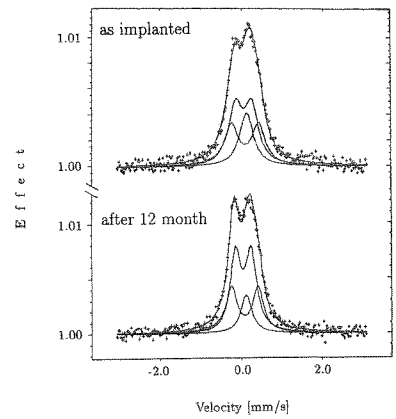


Figure 2: Mössbauer spectra of Fe implanted in Cu
a) ICEMS spectrum as implanted, cf. fig. 1a
b) ICEMS spectrum after 12 month aging

References

[1] G.Müller, G.Klingelhöfer, P.Schwalbach, E.Kankeleit, GSI-Scientific Report 1988, GSI 89-1

[2] G.Müller, G.Klingelhöfer, P.Schwalbach, E.Kankeleit Nucl. Instr. and Meth. B, 1990 in press

[3] T. Shigematsu, S. Staniek, R. A. Brand, W. Keune, R. H. Nussbaum, H.-D. Pfannes, D. Liljequist, D. Longworth, R. Atkinson, Hyp. Int. 15/16(1983)383

[4] S. J. Campbell, J. M. Cadogan, M. J. Yazxhi, P. E. Clark, J. Phys. F: Metal Phys. 9(1979)3793

Mößbauerspectroscopy after ^{57}Fe-Implantation into semiconductors and insulators^{B+G}

M.Hartick, E.Kankeleit, B.Keck*, G.Klingelhöfer, S.Laubach, P.Schwalbach, B.Stahl

*Institut für Kernphysik, TH-Darmstadt und HMI-Berlin**

The aim of our experiments is to study the microscopic surrounding of implanted ions after the implantation into a sample on the 100ns time scale. Especially dynamic annealing effects, e.g. changes of the electronic configuration or in the surrounding lattice geometry, have hardly been observed in situ. We could show recently that the *long range diffusion* of implanted atoms (interstitial Fe in Si, [1,2]) can be studied in favourable cases. In 1989 we have used a beam (333ns pulse separation) of ^{132}Xe ions with an energy of 3.2 MeV/nuc to excite ^{57}Fe ions by Coulomb excitation and implant the excited recoiling nuclei into samples of GaAs, MnF_2, and $LiNbO_3$. Mößbauer spectra were taken with resonance counters. The technique has been described earlier [3,4].

The spectra we find in MnF_2 can be described with two components. Most of the ions ($\sim$ 70%) land as Fe^{2+} ions on Mn sites. About one third represent probably Fe^{3+}. The site of these latter ions, which are associated with a quadrupole dublet with a small splitting, is not clear yet. We analysed a polycrystalline and a single crystal sample. The difference in the shape of the spectra is most probably due to asymmetries in the line intensities of the dominating dublet what may be caused by the orientation of the single crystal. The analysis of the data, including lower temperatures also, is not yet completed.

A first implantation into a GaAs single crystal was made at 160K and 300K. The spectra show a distinct change in shape with temperature, calling for further systematic investigation. Tentatively we can fit the data with two components: a single line and a dublet, found earlier in ^{57}Co-diffusion experiments in GaAs [5] and interpreted as Fe on the substitutional Ga site and in a Fe-vacancy complex, respectively. It is very interesting to note the increase in single-line intensity with temperature, which might point to an annealing process, similar to the one indicated in the case of Si at higher temperatures [1]. The time differential data are in agreement with a dublet decaying by an atomic process into the single line ground state. But due to poor statistics a steady-state description can not be excluded. There is no indication for the interstitial component, accounting for 30% of the intensity in the case of silicon [1].

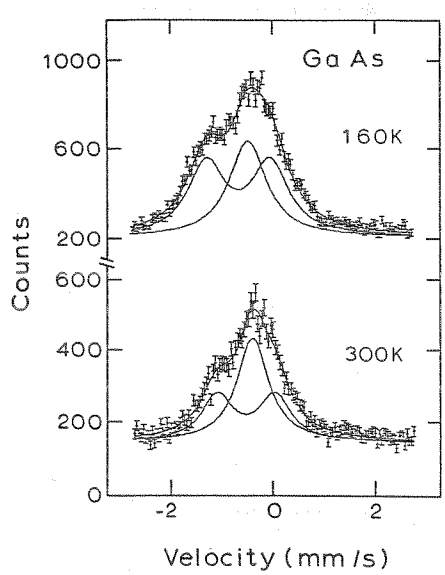


Figure 2: Mößbauerspectra of ^{57}Fe implanted into GaAs

$LiNbO_3$ was implanted in a temperature range of 20K-300K. Fe in $LiNbO_3$ is very interesting because of the potential in electro-optic applications. The implantation of the dopant might be superior to standard diffusion techniques, but has hardly been studied. Our spectra, recorded after implantation into a single crystal, show a strongly asymmetric dublet. The overall shape of the spectrum is almost constant over the whole temperature range. Due to the crystal orientation, we expect only a slight asymmetry of the quadrupole split components. Thus at least two components must be responsible for the resonance. The parameters of substitutional Fe^{2+} in $LiNbO_3$ are known and Fe^{2+} might account for $\sim$ 50% of the intensity, the remaining intensity is presumably due to Fe^{3+}. Whereas the existence of Fe^{3+} can be expected, it is surprising that it does not show up in a paramagnetic hyperfine splitting. A similar effect has been observed in Al_2O_3 [2,4]. This behaviour could be explained with much shorter spin relaxation times than encountered in the steady state - perhaps due to some kind of radiation damage.

[1] P.Schwalbach et al.; accepted by *Phys.Rev.Lett.*

[2] S.Laubach et al.; Hyp.Int. (1990) in print

[3] S.Laubach et al.; *Z.f.Physik B - Condensed Matter* 75(1989)173

[4] M.Hartick et al.; GSI-Report 89-1

[5] P.Seregin et al.; *Phys. Stat. Sol.* (b) 91(1979)35

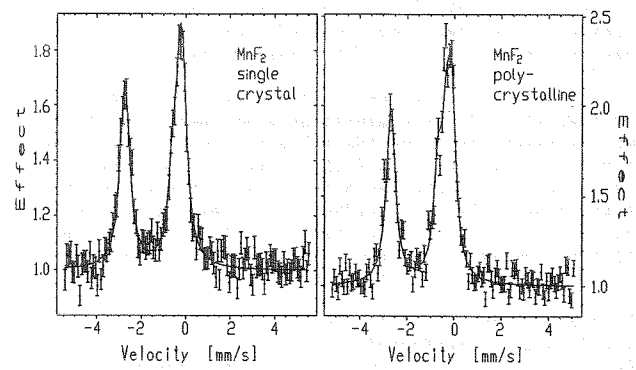


Figure 1: Mößbauerspectra of ^{57}Fe implanted into MnF_2

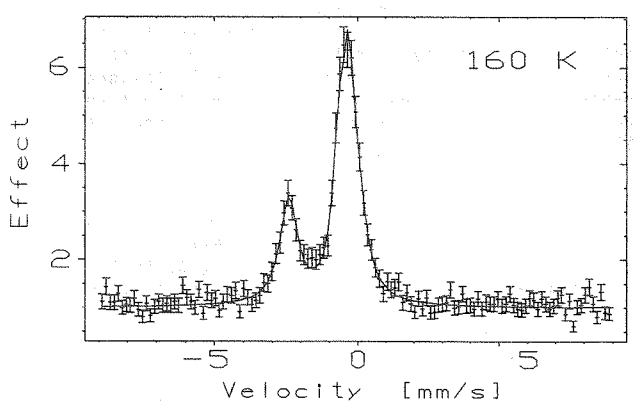


Figure 3: Mößbauerspectrum of ^{57}Fe implanted into $LiNbO_3$

MeV - Implantation of Kr^+ into Ti[G]

H. Volkmann, K. Thoma and H. Gärtner, Fachbereich Physik, Gesamthochschule Kassel
D.M. Rück, GSI Darmstadt

Titanium and its alloys have found widespread use as light weight construction materials. Their resistance against corrosion and wear can be greatly improved by surface treatments, among them ion implantation and related techniques such as ion beam mixing. Commonly, low ion energies in the order of 100 keV are employed and therefore shallow implantation profiles will result.

The use of ions with high energy allows implantation depths of several µm in the base material. In this report we describe ion implantation of Kr^+ ions with a kinetic energy of 3.78 MeV (45keV/amu)into Ti, which was performed with the RFQ accelerator. The implantation of noble gas ions is of interest in itself, since these ions tend to segregate and to form blisters which affect the usefulness of the host material in fusion and nuclear reactors[1].

Ti specimens of 3 mm thickness and 25 mm diameter were cut from sheets of technically pure Ti (Schmiedewerke Krupp- Klöckner, Tikrutan RT 12) and polished by SiC paper and diamond paste to a final roughness of <1 µm. They were exposed in a watercooled target holder to a Kr^+ beam of 16 $\mu A/cm^2$ current density. The doses employed were $3*10^{16}$, $6*10^{16}$, $1*10^{17}$, $2*10^{17}$, $3*10^{17}$, $5.4*10^{17}$, $9*10^{17}$ ions/cm^2.

With increasing dose the ion bombarded surfaces became increasingly rough. Beyond $1*10^{17}$ ions/cm^2 an increase in volume could be measured by a mechanical stylus apparatus (DEKTAK, Sloan). Fig. 1 shows an effective increase of thickness as a measure of the volume increase. The volume growth was not uniform laterally but had the form of a lens with a maximum in the center.

As a function of dose the hardness of the surfaces increased (Fig. 2) as measured by a microhardness tester with a weight of 49 mN (Metalloplan, Leitz). By increasing the weight up to 2 N the Vickers diamond penetrates more deeply into the material and thus allows to discriminate the hard surface layer against the softer volume[2] (Fig. 3). The hardness is a technically important parameter since it determines besides other influences the wear resistance.

In order to see the depth dependence of the implanted ion density we performed x-ray measurements with a Guinier thin- film diffractometer with Seemann-Bohlin focussing. One expects a variation of the lattice constant with the depths below the surface, since the concentration of ions and defects changes. TRIM simulations[3] show the maximum of the density at 1.44 µm. The resolving power of the x-ray diffractometer of about 0.3 µm is therefore sufficient to test the depth profile. The interpretation of the x-ray results is difficult since at the very small glancing angles the roughness and swelling of the samples disturbs the measurements. In order to measure the depth distribution independently Rutherford backscattering experiments are being performed.

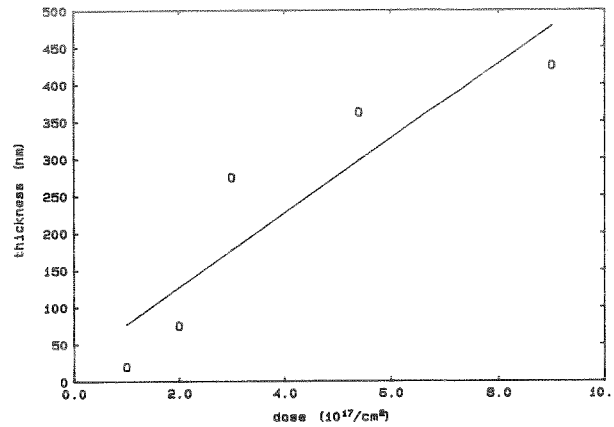


Fig. 1 : Effective growth of layer thickness as a function of dose.

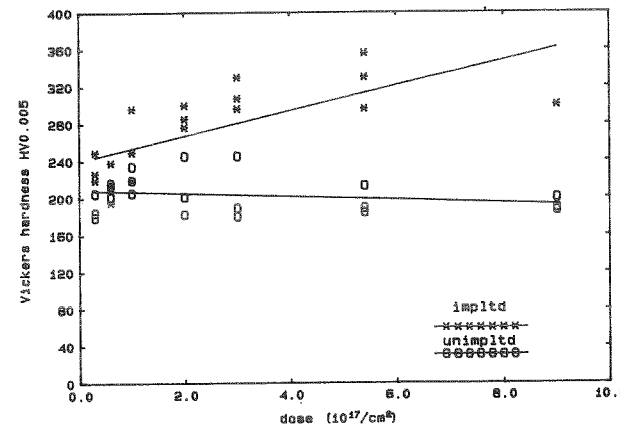


Fig. 2 : Change of Vickers hardness as a function of dose for implanted and unimplanted material.

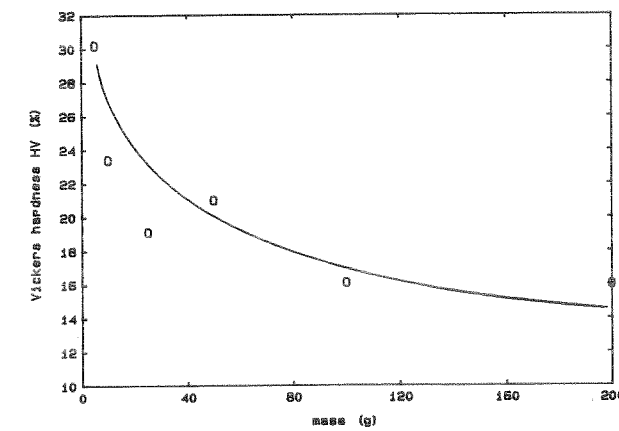


Fig. 3 : Increase of Vickers hardness of the implanted over the unimplanted material in percent as a function of Vickers weight.

[1] D.J.Mazey and J.H. Evans, J. Nucl. Mater.138(1986)16
J.H. Evans and D.J.Mazey, J. Nucl. Mater.138(1986)176
I. Hashimoto et al., J. Nucl. Mater.149(1987)69
I. Hashimoto et al., J. Nucl. Mater.150(1987)100

[2] A.M. Vredenberg et al., Mater.Sci.Eng., A115(1989)297
F.Z. Cui et al., Appl. Phys. Lett. 53(1988)2152

[3] J.F. Ziegler, J.P. Biersack and U. Littmark,
The Stopping and Range of Ions in Solids, Pergamon,
Oxford, 1985

SIMULATION OF PARTICLE REFLECTION DURING ION-IMPLANTATION[G]

S. Saler, R. Kassing
University of Kassel, Institute of Technical Physics
D-3500 Kassel, W. Germany

Ion implantation is a well established tool in VLSI applications. In future device generations three dimensional topographies will certainly become more and more important[1,2]. In order to characterize dopand profiles in 3-D structures, information is needed about the spatial distribution of the reflected particles, making it possible to identify the parts of the structure exposed to indirect implantation by backscattered particles. This information can be obtained by computer simulations[3]. Calculations have been made for the reflection of arsenic, boron and phosphorous from silicon surfaces at various incident angles ant energies.

Because ions usually can travel a long distance through the target before they are reemitted, the reflected particles are distributed over a wide range of emission angles and energy. In Fig. 1 a plot of the reflection coefficient vs. the polar angle of emission is shown for 80 keV As bombardment of Si at several incident angles. The reflected particles are distributed over the entire range from 0° to 90° with the main portion in the interval between 60° and 90°. With increasing angle of incidence (measured from the surface normal) the reflection coefficient increases, too. This mainly leads to stronger reflection into angles above 60°, so there is a smooth transition to a more specular kind of reflection.

Quite similar observations can be made for the azimutal distribution of the reflected particles. In this case the main intensity falls into the interval between -30° and 30°, which is roughly double the width of the polar distribution. Ions which are heavy compared to the target mass (here As) are mainly scattered forward so there is no reflection into azimutal angles larger than 90°.

In contrast changes in the energy of emission with increasing angle of incidence are more distinct. In Fig. 2 a plot of the reflection coefficient vs. energy of emission for several angles of incidence is shown. At an angle of incidence of 72° the maximum energy of emission is about 80% of the primary energy, shifting to a value of about 95% for glancing incidence. But the increase is found in the entire energy range and only for glancing incidence there is a maximum at high energies. In all other cases the maximum value is found at the lower end of the energy scale. Particles backsattered with low energies are emitted into angles not correlated to the angle of incidence, the reason being the loss of energy during their penetration of the target.

Results are very similar for higher particle energies, except for two minor changes. Due to reduced reflection at higher energies, the curves are slightly shifted downward and the special shape of the curves for an angle of incidence of 87° is less developed.

Results obtained from computations for the lighter materials boron and phosphorous follow the general trends stated above. But there are three differences. First, the reflection into small and medium polar angles (0°-60°) is increased. Second, the amount of reflection into azimutal angles larger than 90° is significantly larger. Third, there is a small increase in reflection with low and medium energies of emission. The reflection of these elements therefore is more diffuse than that of As, explainable by the lower mass of the projectiles leading to larger scattering angles and to higher energy loss in a single collision event.

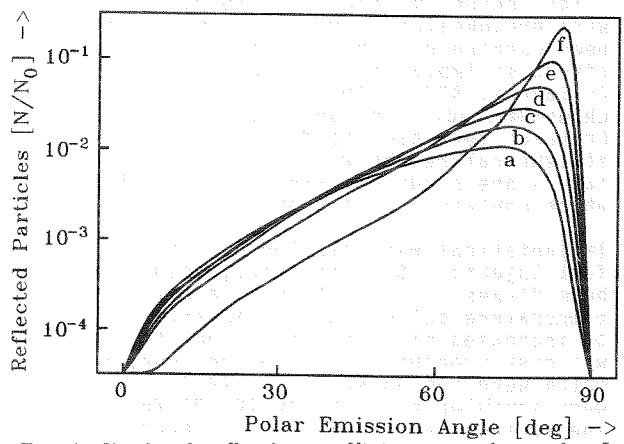


Fig. 1: Simulated reflection coefficient vs. polar angle of emission (integrated over all azimutal angles) for 80 keV As -> Si. Incident angles: a) 72°, b) 75°, c) 78°, d) 81°, e) 84°, f) 87°.

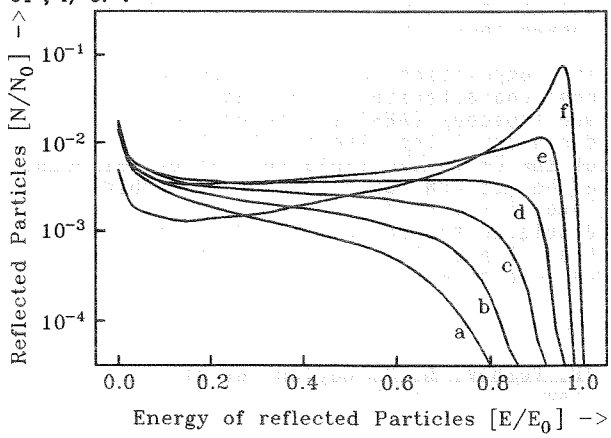


Fig. 2: Simulated reflection coefficient vs. energy of emission for 80 keV As -> Si. Incident angles: a) 72°, b) 75°, c) 78°, d) 81°, e) 84°, f) 87°.

References

[1]K. Kato. IEEE Trans. Electr. Dev. 35, 1820, 1988

[2]T Tokuyama. Nucl. Inst. Meth. B37/38, 744, 1989

[3]S. Saler et al. submitted to Nucl. Inst. Meth.

Novel Chromium Layers formed by Nitrogen Ion Implantation of Conventional and ABCD Electrodeposited Films

Hermann Ferber
Daimler-Benz AG
Gar B. Hoflund and Charles K. Mount
Department of Chemical Engineering; University of Florida
Shigeo Hoshino
Musashi Institute of Technology
Tokyo, Japan
D. Rück
GSI, Darmstadt

Nitrogen implantation into metals can be understood as a special kind of surface nitridation and holds a great potential for the improvement of tribological properties of chromium and Cr-containing steels. Some investigations have been carried out using conventional Cr-layers and this work includes N-implantation experiments using novel ABCD-Cr films in our research. Nitrogen-ion implantation of conventional Cr and amorphous bright chromium deposited (ABCD) films, which were preannealed at various temperatures, has been carried out in order to determine the effect of implantation on hardness of the Cr-layers. ABCD films consist of C-rich chromium and, in contrast to conventional Cr reach very high hardness after annealing at temperatures between 300 and 500 °C. Such layers are produced using a special bath which contains organic oxygen-rich compounds.[1]

Implantations were carried out at the 300 kV-Test-Injektor, GSI Darmstadt, using low ion-beam fluxes in order to maintain a sample temperature below 250 °C. Implantation lead to increased micro hardness, but the extent was most pronounced for conventional films which were not annealed and ABCD films which were annealed at or below 400 °C for 1/2 hour. The surface sensitivity of the hardness measurements was varied by altering the load used during the test. Data obtained in this manner showed that the more surface-sensitive hardness was greater than the more bulk-sensitive hardness for both the implanted and nonimplanted ABCD films and the implanted conventional Cr films.

The compositions of the implanted films have been characterized using Auger electron spectroscopy (AES) in conjunction with sputter depth profiling. These data showed that all of the Cr in the implanted region was bound either as CrN, Cr oxides or Cr carbides at large total N^+ doses. Furthermore, the N displaced the carbon in ABCD films producing N and C profiles which mimic each other in an inverse manner.

[1] H. Ferber, G. B. Hoflund et al., paper given at ECASIA 89, to be published

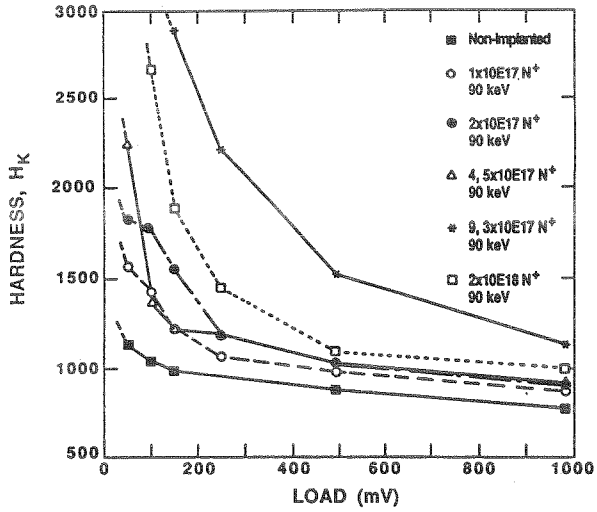


Fig. 1: Knoop-microhardness of implanted conventional Cr-layers vs. indentation load

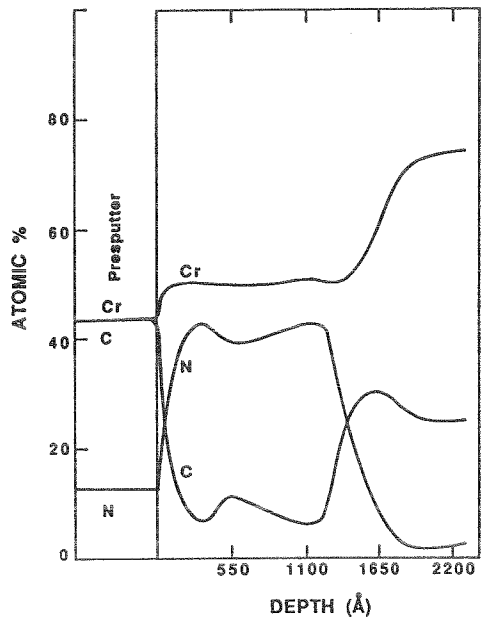


Fig. 2: AUGER depth profile of a N^+-implanted ABCD-chromium layer (80 keV, 8 x 10^{17} N^+/cm^2)

Recent Progress Using Ion Beam Techniques for Materials Modification

P. Ballhause, W. Ensinger, W. Fischer, G.K. Wolf, Physikalische Chemie der Universität Heidelberg, D. Rück, GSI Darmstadt

1. Introduction

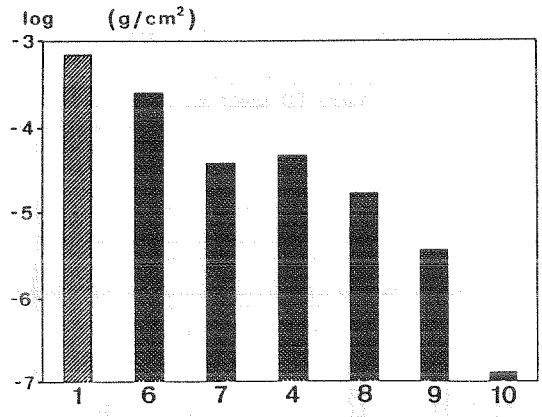
In connection with two "Joint Projects" providing collaborations with industry and other research institutions (1) the low energy accelerators of GSI were used for materials modification. The techniques ion implantation and ion beam mixing of thin surface films were applied for studying wear reduction and corrosion protection of metals, and as a new approach also engineering ceramics. By various analytical methods informations on the microstructure of the modified surface layers were obtained.

2. Microstructure of nitrogen implanted WC/Co

Nitrogen implantation in hard metals like WC with Co-binder results in a substantial improvement of wear resistance of the material (2). Because the mechanism of the improvement is not known accurately until now, a study of the µ-structure of WC/Co samples bombarded with 6×10^{17} N^+/cm^2 was performed (3). The structure was determined by x-ray diffraction under very small incidence angles. The variation of the angles between 0,1° and 5° provides information on structure changes as a function of depth up to 500 nm below the surface. Preliminary results show that the bulk spectrum begins to change around the projected range of the nitrogen ions, indicating smaller grain size and a partial amorphization of WC.
Near the surface a new crystalline phase seems to develop (WN?) the identity of which is not clear yet.

3. Corrosion of titanium modified by tantalum in oxidizing acids

Titanium is widely used as construction material in chemical industry, however, it is not resistant against strong mineral acids and oxidizing acids. Therefore, an attempt was made to modify the titanium surface with tantalum by ion implantation and ion beam mixing (4). The samples were bombarded with 200 keV Ta^+/cm^2, and coated with Ta-layers 100 nm thick which were subsequently mixed with 400 keV Ti^{++}/cm^2. The results of corrosion studies in 45% HNO_3 at 100°C are presented in the figure 1. Ion beam mixed samples showed the lowest corrosion rate, and implantation was just as effective as bulk alloying with 10% Ta. After 15 days only 100 µg/cm² Ti had dissolved from the ion beam mixed Ta/Ti sample compared with 5 mg/cm² from pure Ti.



Amounts of titanium and tantalum respectively, dissolved in 48 h in 45% HNO_3 at 100 °C: 1, titanium; 6, titanium alloyed with 3 at.% Ta; 7, titanium alloyed with 10 at.% Ta; 4, titanium bombarded with 200 keV, 5×10^{16} Ta^+ cm^{-2}; 8, titanium evaporated with 100 nm of tantalum; 9, titanium evaporated with 100 nm of tantalum and ion beam mixed with 400 keV, 5×10^{16} Ti^{2+} cm^{-2}; 10, tantalum.

4. Present studies and future prospects

Systems studied recently involve more and more bombardment with ions of $E > 200$keV. Therefore in addition to doubly charged ions from the 300 keV test accelerator also ions from the RFQ-system are used.
There are mainly two directions of investigations:
a) Engineering ceramics are well known to show improved mechanical properties like hardness, wear resistance and fracture toughness as consequence of ion implantation. In order to maximize these effects ions of higher energies with greater penetration are desirable. However, this causes problems because of high target temperature and difficulties with target charging and dose determination. In preliminary tests a special arrangement for ion current measurements and target manipulation of ceramics were successfully tested. In addition a firstr series of Ti^+-implantations in Si_3N_4 and Al_2O_3 were performed. It could be shown that the surface hardness of the implanted samples increased considerably without loss of flexural strenght. At present Ti^+-implanted samples of Si_3N_4 are undergoing wear and friction tests performed in collaboration with Daimler Benz, Stuttgart.
b) Ion beam mixing for improved adhesion of surface films suffers from the drawback that most ions below 200 keV energy can only penetrate thin films of up to $\approx$100 nm thickness. Many applications, however, require much thicker coatings. Therefore, the RFQ-accelerator is used to bombard samples with films of thicknesses $\gtrsim$1µm. The effectiveness of mixing is studied by adhesion tests. The mechanical and chemical properties of steel substrates modified by TiN-, CrN- and metal films are compared with earlier studies with ions of 60-200 keV.

1. G.K. Wolf, GSI 89-1 (1989) 236.
2. U. König, G.K. Wolf, Surface and Coatings Technology, 33 (1987) 501.
3. P. Ballhause, Thesis, Heidelberg 1990.
4. W. Ensinger, G.K. Wolf, Mat. Sci. Eng A.116 (1989) 35.

SURFACE ANALYSIS BY SPONTANEOUS DESORPTION OF IONS

S. Metzger, B. Fischer (GSI Darmstadt)

In 1985 Della-Negra et al.[1] showed that ions can be desorbed from surfaces without heating the target foil or bombarding it with keV or MeV particles. Only a 'small' electric field (2 - 3kV/mm) between the sample and a grid positioned a few millimeters in front of the sample surface is needed. This type of desorption is called spontaneous desorption (SD). The desorption process is noy yet understood, but Della-Negra et al.[2] suggest that SD is a SIMS effect caused by keV primary ions from the grid by field desorption.

Looking for a method to test a new time of flight (TOF) mass spectrometer for heavy ion induced desorption (HIID) of particles without a fission source or the heavy ion beam itself, it seemed to us that SD was the easiest way to do that. After studing SD in more details we think that SD is a very interesting and useful tool because it is a simple and inexpensive type of mass spectrometry. The experimental set up is shown in figure 1. The spectrometer consists of a tube with a vacuum of $10^{-7}Torr$ inside, a metallic sample foil in front of a thin metallic grid (parallel to the sample foil at a distance of 3mm) and a multichannelplate detector (MCP). A voltage of about -9kV is applied to the sample foil while the grid is grounded. Under these conditions electrons and negative ions are emitted simultaneously from the target. After passing the accelerating field and drifting through the field-free region electrons and negative ions are detected by the same MCP. The signal from the MCP is split. The delayed branch starts the the time-to-amplitude converter (TAC) and the direct signal stops it. That way the fast electrons start the TOF measurement and the slower ions stop it (the delay is longer than the flight time of the electrons) and so the differneces in flight time to the detector of electrons and ions determines the mass of the ions.

Figure 2 shows a negative ion SD spectrum of the amino acid Valine (MW = 117amu). The high mass region is dominated by a peak at m = 116amu which is the deprotonated molecular ion $(M-H)^-$. Also intense peaks are at m = 25 and 26amu (C_2H^- and $C_2H_2^-$). The main differences between SD and HIID spectra appear in the low mass region. For SD masses between 12 and 26amu are more abundant than for HIID. Figure 3 illustrates the large variety of different masses in the range of m = 37 to 83amu (most of them are of the type $C_nH_m^-$) and shows the good mass resolution of $\frac{M}{\Delta M} \leq 900$.

Until now we have studied a number of different samples, e.g. we looked for surface contaminations on a gold foil, for $(CsJ)_nJ^-$-cluster from a CsJ-target, for fragments of a polycarbonate called Lexan etc., by SD mass spectrometry and we are convinced that SD is a good method for analysing surfaces of organic and inorganic samples, if we are able to overcome two problems: 1. it is difficult to identify interesting molecules when there is such a 'underground' of organic surface contaminations as in figure 2 and 3, 2. we didn't succeed in accumulating positive SD spectra because the yield of time-correlated emission of a suitable 'start', i.e. H^+ or alkali$^+$, and positive ions is rather low.

References

1 S. Della-Negra, Y. Le Beyec and P. Håkansson, Nucl. Instrum. Meth Phys. Res B, 9 (1985) 103

2 S. Della-Negra, C. Deprun, Y. Le Beyec, F. Röllgen, K. Standing, B. Monart and G. Bolbach, Int. J. Mass Spectrom. Ion Processes, 75 (1987) 319

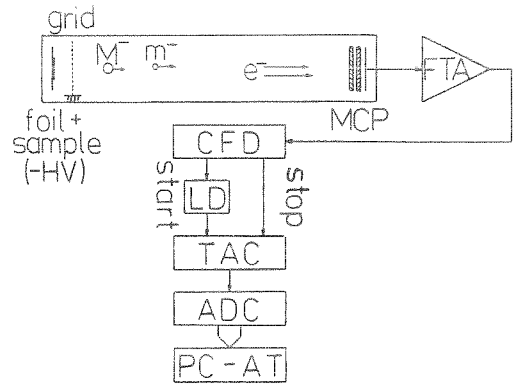


Figure 1: Scheme of the TOF spectrometer. Tube (0.5m long, 0.1m diameter); M^-, m^-, negative ions; e^-, electrons; FTA, fast-timing amplifier; CFD, constant-fraction discriminator; LD, delay; ADC amplitude-to-digital converter.

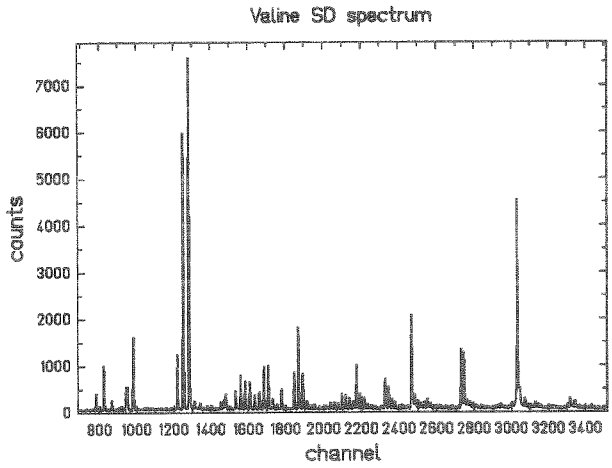


Figure 2: Negative ion SD spectrum of Valine (MW = 117amu).

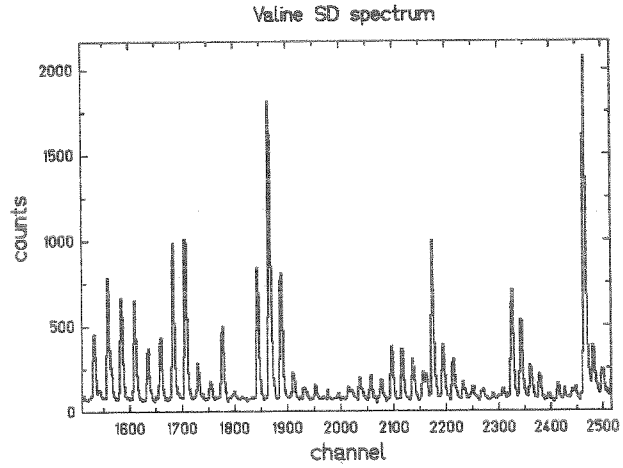


Figure 3: Part of the negative ion SD spectrum of Valine.

Sputtering of Gold by Uranium Ions with UNILAC Energies

Yu. N. Cheblukov, D. G. Koshkarev, A. R. Peuto, I. V. Rudskoygh, N. A. Vasiliev
ITEP, Moscow, USSR
V. M. Nazarov
JINR, Dubna, USSR
R. Bock, D. H. H. Hoffmann, R. W. Müller, J. Vetter
GSI, Darmstadt

The sputtering yield of gold foils by uranium ions in the energy range between 1.25 and 5.5 MeV/u was investigated experimentally with UNILAC beams. These experiments were begun in connection with the necessity of acceleration and storage of high-intensity heavy-ion beams in ring machines.[1] There is some concern that beam instability might be induced by avalanche effects if the sputtering yields at medium and high ion energies are high (>20 atoms/ion).[1] A theory of high-energy sputtering was published recently.[2] According to this theory the sputtering yield for the pair U-Au should be very large (a few hundred atoms/ion) due to inelastic interaction of high energy ions with matter. Also, the sputtering yield should increase when inelastic energy losses of heavy ions increase. The experimental results obtained by us, however, are essentially different from the predictions as well of the high-energy sputtering theory[2] as of the more well-established cascade theory.[3] We propose a possible mechanism of sputtering for the pair U-Au.

In order to obtain data on the energy dependence of the sputtering yield we employed a collection method and a special target that consisted of many alternating layers of gold, carbon and aluminium foils. The carbon foils collect the sputtered atoms of gold. Aluminium foils are used for changing the uranium ion energy. Gold foils with thickness of 0.4 µm were warmed in a vacuum oven at a temperature of 350 °C during four hours to provide a gross grain structure. Sputtering yields strongly depend on the grain size.[4] The target allowed us to take data of the relative sputtering yield of Au foils by U ions of different energies simultaneously. The quantity of sputtered gold on the carbon collectors was determined by activation analysis. The result of one target stack is shown in fig. 1; fig. 2 shows the combined data of four targets. In the first case yields were measured for the forward ("transmission") and backward sputtering, as indicated in figure 1; the yields are not significantly different. The dependence of the sputtering yield on the U ion energy does not correspond with the high-energy sputtering theory[2], but is consistent with the cascade mechanism.[3]

The absolute sputtering yield of Au with a clean surface by U ions was measured. The surface of gold was cleaned by heating. The sputtering yield is equal to (12±2) atoms/ion at the U ion energy of 5.5 MeV/u. This value is too large as compared with the cascade mechanism which predicts ≤ 1 atom/ion for this ion energy. We have to try to interpret our experimental result.

According to the model[2] a heavy ion crossing the gold foil creates a hot cylindrical region around its trajectory, with an electron temperature of 20 to 25 eV. At the same time the metal atoms are cold. It is necessary to notice that the binding energy of atoms in metal is zero if the electron temperature is more than some critical electron temperature. This temperature is ≈4eV for gold.[2] Evaluating the model[2] one can show that the cooling time of the hot expanding cylindrical region to the temperature of ≈4eV is $\approx 10^{-13}$ s, for the pair U-Au with uranium ion energy of 2.1 MeV. The initial radius of the hot region is ≈25 Å, and the initial electron temperature is ≈15 eV. For comparison, the time of transform of the hot electron energy into phonon energy is $\approx 10^{-12}$ s. The model[2] predicts acceleration of surface atoms by an electrical double layer that appears on the material's surface due to high electron temperature and pressure. Our results show that this mechanism must not be so important in our case.

Our experimental results are consistent with the cascade mechanism,[3] but under conditions where the electron system in the metal has a high temperature, and the binding potential of the atoms in the metal is below V_0, the binding potential in cold matter. In this case the surface atoms with energy ≤eV_0 have a finite probability to leave the metal. The time of 10^{-13} s is enough for this. Accordingly, the sputtering yield should be higher than given by the cascade theory for cold metal. For checking our hypothesis we have to extend our experimental investigation to the uranium ion energy region below 1.25 Mev/u, in order to have contact with the energy region where the cascade mechanism for cold metal is applicable. Besides we shall have to measure angular distributions.

The authors wish to thank to Dr. R. Arnold for helpful discussions.

References

1. D. G. Koshkarev, Particle Accelerators 16 (1984), 1
2. Yu. V. Martinenko, Yu. N. Javlinskij, Sputtering by nuclear splinters, preprint IAE-4084/11, 1985 (in Russian)
3. P. Sigmund, Theory of Sputtering, Phys. Rev. 184 (1969), 383
4. I. A. Baranov, Yu. V. Martinenko et al., Usp. Phyz. Nauk 156 (1988), 477

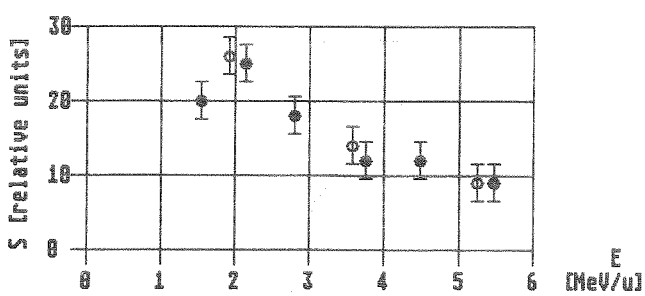


Fig. 1. The dependence of sputtering yield S of gold foils on energy E of incident uranium ions for one target
● backward ○ transmission

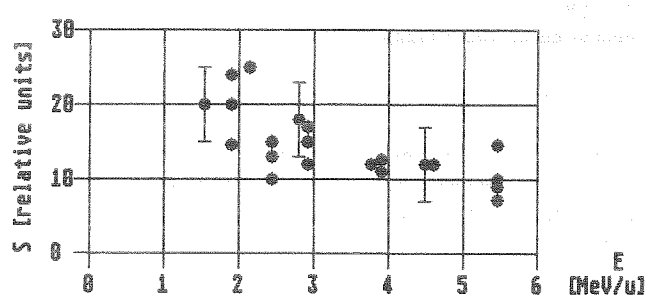


Fig. 2. The dependence of sputtering yield S of gold foils on energy E of incident uranium ions for four targets; backward sputtering only

Study of Radiation Effects of Heavy Ions in Microelectronic Devices *

W. Heinrich, O. Geschke, A. Noll
Department of Physics, Univ. Siegen
R. Harboe Sorensen
European Space Research and Technology Centre, Noordwijk, Netherlands
J. Vetter
GSI Darmstadt

In a number of space missions it has been observed, that a single cosmic ray particle can cause malfunction of a microelectronic device. This phenomenon, called single event upset (SEU), happens when a heavy ion due to its ionization deposits enough charge in the sensitive region of a device causing a change of the logical state.

The expected rate of SEUs can be calculated from measured cross sections for SEUs as a function of deposited charge or of the linear energy transfer (LET) for high energy particles. In general the measured cross sections are increasing from zero at low LET-values to a saturation value at high LETs which is comparable to the geometric cross section area of the sensitive volume.

We intend to expose memory devices to SIS beams to investigate LET-dependences of SEU-cross sections under different experimental conditions. For this purpose we developed a memory test system which is able to test RAM's. It consists of a MC 68000 microprocessor system with an EPROM containing test software and RAM devices to be tested. The RAM's can be loaded with different test patterns (00, FF, AA and 55) and the test software provides adequate identification and localization of errors. The testsystem can be reset and started from a PC which is connected to it by a RS232 interface. Software running on the PC controls and operates the test system.

Additionally we plan to irradiate CCD image sensors to measure the amount of charge deposited inside the sensitive volumes of single picture elements. For this purpose the picture seen by the sensor chips during exposure to a heavy ion beam is digitized and written into the memory of a picture analysis system. Software running on this system allows to identify picture elements which have been hit by a heavy ion and to read out the grey level which is proportional to the charge deposited by the ionizing particle.

The devices to be tested can be moved by a system of stepping motors which is also controlled by the PC. This allows to move devices or detectors into the beam line or to tilt the devices during one run. Additionally devices can be operated at controlled temperatures ranging from 30^0C to 70^0C.

The aim of a first run at beam line X0 was to test the operation of the PC-based electronic test system for RAM's and CCD image sensors. The devices were exposed to a beam of 15.5 MeV/nucleon ^{40}Ar ions extracted through a thin 13.4 µm titan window. After passing through 61 mm of air the ions hit the microelectronic devices with an energy of somewhat above 12.7MeV/nucleon causing an energy loss of about 8500 MeV/(g/cm^2). ^{40}Ar ions of this energy have a range of 180 µm in silicon which is much larger than the depth of the sensitive volume of the device.

The test system was running without any problems. Several spectra of collected charges were measured for the VALVO NXA1011 CCD image sensor. Figure 1 shows a spectrum of the charge values collected in the pixels of the image sensor.

For a calibration of particle fluxes we exposed CR39 track detectors to the beam for several seconds. First cross sections could be determined for the HM61162 2kx8 SRAM device for 12.7 MeV/nucleon ^{40}Ar (LET = 8500 MeV/(g/cm^2) in silicon). This value of about $4*10^{-3}$ cm^2/device is below that one measured with fission particles of a californium source, which is σ_{Cf} = $2.6 *10^{-2}$ cm^2/device. For ^{40}Ar ions impinging under an angle of 45^0 to the device the cross section increased to a value of about $6 *10^{-3}$ cm^2/device due to the longer path of the particles through the sensitive volume. These data show that for the first tests LET values were used for which the cross sections are below the saturation value of geometric cross sections. This is an important result for the planning of future tests at the new SIS facility at Darmstadt. It can be concluded that 1 GeV/nucleon ions heavier than Xe should be used for the tests of SRAM's at the SIS.

* Work funded by ESTEC Contract number 8223/89/NL/RE(SC)

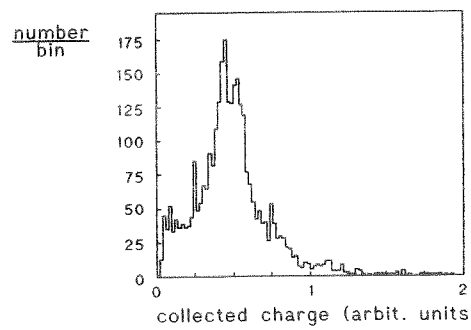


Figure 1: Spectrum of charges collected by the pixels of the VALVO NXA1011 CCD image sensor for 12.7 MeV/Nucleon ^{40}Ar ions

Swift heavy ions induced effects in matter

CIRIL, CAEN

It is well known that the slowing down of swift heavy ions in matter i) occurs almost exclusively by interaction with the target electrons and ii) results in a huge deposit of energy : some tens keV per nanometer. The way the structure of the material accomodates to high and localized electronic excitations will depend on the number of free electrons, their mobility and on the electron-phonon coupling in the target i.e. on the nature of the bombarded material.

By comparison with the efforts made to understand the damage effects due to elastic collisions, the "inelastic" induced effects have not been, much studied so far.

Since 1982, a large range of very different types of targets has been investigated in Caen: insulators, semi-conductors, amorphous and crystalline metallic alloys, organic conductors, pure metals, supraconductors[1]. The experiments reported hereafter have been made with the prospect of studying the effects at the highest electronic stopping power i.e. during the slowing down of U ions. All the experiments have been performed using the CIRIL 's IRABAT facility which allows irradiation at controlled temperatures between 4 K and 500 K and with accurate ion flux measurements.

[1] The main results were published in the Proceedings of the " Swift heavy ions in matter" Symposium, SHIM, Caen 1989 in Radi. Effects and Defects in Solids, 110 n° 1 and 2 (1989).

The stability of the silicon against the high electronic excitation induced by ^{238}U ion irradiation

M. Toulemonde, S. Bouffard, CIRIL, Caen
P. Mary, P. Bogdanski, LERMAT, ISMRa, Caen
R. Spohr and J. Vetter, GSI, Darmstadt

In semiconductors the concentration of mobile electrons is in between the one of the insulators and the one of the metals. It is known since a long time that insulators are sensitive to the high electronic excitation induced by the slowing down of an heavy ion while it is quite recently that pure metals are known to be sensitive (this report and 1). Then how will behave a semiconductor like silicon in an ultimate case ? The damage production in silicon has already been studied using electron [2,3], proton [4], nickel[5], krypton and xenon[6] irradiations. The relative number of defects created in each irradiation can be normalized by the number of displaced atoms by nuclear elastic collisions[7].

In the present experiment of Uranium ion irradiation, the defect production is followed by the increase of the electrical resistance[6] measured at room temperature[3,4]. Typical result for two samples in the same conditions of irradiation is given in the Figure. A critical fluence ϕt_c is deduced for each sample leading to a mean value of $(2.0 \pm 0.5)\ 10^{10}$ U/cm^2. This critical value has to be compared to other values of ϕt_c determined after electron and proton irradiations[3,4]. In order to make the comparison, we calculate the value $Xc = 5\ 10^{22}\ \sigma\ \phi t_c$ /Nd where the atomic density of the silicon is multiplied by the displacement cross section σ and the critical fluence, and divided by the number of donor Nd (see ref. 6). The results are given in :

	ϕt_c(cm^{-2})	Nd(cm^{-3})	σ (cm^2)	Xc
Uranium	$2.0\ 10^{10}$	$3.5\ 10^{15}$	$7\ 10^{-17}$	20
Protons	$4.0\ 10^{13}$	$3.0\ 10^{14}$	$3.3\ 10^{-20}$	22
Electrons	10^{+16}	$3.5\ 10^{15}$	$2.2\ 10^{-22}$	31

Xc is constant within the experimental errors. It indicates that silicon is stable against the ultimate irradiation i.e an uranium irradiation.

From this result silicon is classified in materials which are not sensitive to the high electronic excitation like the insulators MgO and Al_2O_3 or metals like Al and Cu whatever is the number of mobile electrons.

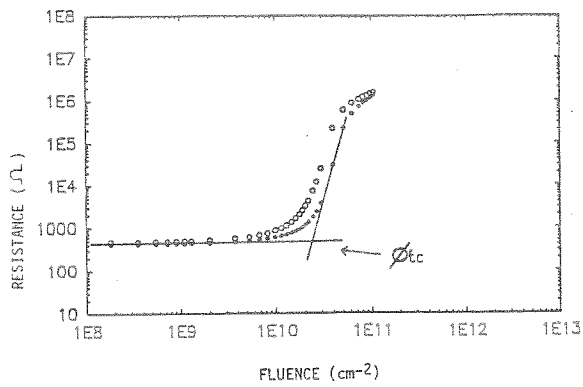


Fig. 1 - Resistance of the silicon versus the Uranium ion fluence.

1 E. Paumier, M. Toulemonde, J. Dural, F. Rullier-Albenque, J.P. Girard and P. Bogdanski
Europhys. Lett. 10 (1989) 555

2 P.M. Mooney and J.C. Bourgoin
Phys. Rev. B29 (1984) 1962

3 T. Wada, K. Yasuda, S. Ikuta, M. Takeda, H. Masuda
J. Appl. Phys. 48 (1977) 2145

4 N. Hayashi, H. Watanabe, I. Sakamoto, K. Kuriyama, H. Kawakara and I. Kohno
Riken Accel. Prog. Rep. 22 (1988) 105

5 E.H. Te Kaat, N. Hecking and J.K.N. Lindner
Deep implants (North-Holland publishing 1989 p 145)

6 M. Toulemonde, J. Dural, G. Nouet, P. Mary, J.F. Hamet, M.F. Beaufort, J.C. Desoyer, C. Blanchard and J. Auleytner
Phys. Stat. Sol. (a) 114 (1989) 467

7 J.P. Biersach and L.G. Haggmark
Nucl. Instr. and Meth. 174 (1980) 257

Enhancement of defect creation yield in organic metals for swift heavy ion irradiation

S. Bouffard, M. Toulemonde, CIRIL, Caen
R. Spohr and J. Vetter, GSI, Darmstadt

Since ten years, it is known that electronic excitations are responsible of the damage created in a particular class of materials which present a metallic character : organic metals[1]. Of course, they are, somewhat particulars since they are constituted by large organic molecules and their conductivities are quasi-one-dimensional. However the number of free electrons is of the order of 10^{21} cm^{-3}.

In spite of this large number of free carriers, these compounds are damaged by the same electronic processes than the usual organic crystals, but they are less sensitive to radiation than the insulating one.

A simple measurement of the variation of the electrical conductivity giving the defect concentration[2], it is then possible to study the evolution of the damage rate as a function of the energy released to the target electrons.

The results of several experiments made with swift heavy ions at GANIL (O, Kr, Xe)[3] at GSI (U) are reported on the figure.

The enhancement of the damage rate for the high stopping power could be explained as follows :

The large molecules have a small probability (~ 1/1000) to convert an electronic excitation or ionization to a stable defect. When the stopping power increases, a given molecule could be excitated several times : the interactions between free radicals increase the probability to create stable defects. This explains the difference between the oxygene which ionizes once the molecules and the krypton which is able to ionize several times the same molecule.

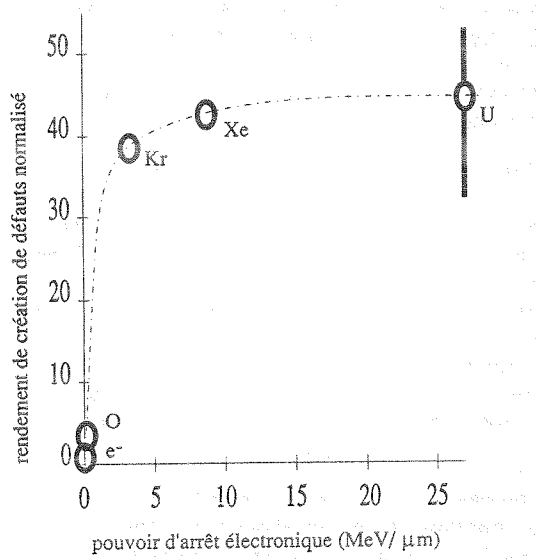


Fig. 1 - Defects creation yield of an organic conductor (TTF-TCNQ) as a function of the electronic stopping power of the incident particule. The damage rate is normalized to the one of the electrons.

1 G. Mihaly and L. Zuppiroli
Phil. Mag. A, 45 (1982) 549

2 L. Zuppiroli, S. Bouffard, K. Bechgaard, B. Hilti and C.W. Mayer
Phys. Rev. B22, (1980) 6035

3 S. Bouffard and E. Balanzat
N.I.M. B32 (1988) 170

Magnetic Insulators

F. Studer and C. Houpert, CRISMAT, ISMRa, Caen
H. Pascard, LSI, Ecole Polytechnique, Palaiseau
M. Toulemonde, CIRIL, Caen
R. Spohr and J. Vetter, GSI Darmstadt

Irradiation of magnetic insulators by high energy heavy ions (Kr : 44 MeV/n and Xe : 27 MeV/n) have been undertaken in GANIL (Caen) in order to correlate high electronic stopping powers, rate of damage and damage morphology.

The high sensitivity of the magnetic properties of ferrimagnetic oxides such as garnet $Y_3Fe_5O_{12}$ and baryum hexaferrite $BaFe_{12}O_{19}$ to any change in bond lengths and/or directions allows a precise determination of the damage by Mössbauer spectroscopy and magnetization measurements. Moreover the morphology of the defects at a given electronic stopping power can be observed by high resolution electron microscopy [1,6].

The results are presented in terms of the rate of damage A, estimated from the Poisson's law $Fd = 1-\exp(-A\,\phi t)$ in which Fd is the amorphous volume fraction calculated from Mössbauer spectra, as a function of electronic energy loss $\left(\frac{dE}{dx}\right)_e$ (see figure). Before the irradiation in G.S.I. (Darmstadt), only one point was known at high electronic stopping power in the garnet due to a previous irradiation by low energy uranium ions (1.4 MeV/a)[7]: this point, together with xenon irradiation above 20 MeV/µm, let us suggest that a change in the slope of the damage rate would occur at high electronic stopping power. Such a result was confirmed by the irradiation of both garnet and baryum hexaferrite with uranium ions of 14 MeV/n. It supposes that, above 20 MeV/µm in the garnet and 22 MeV/µm in the baryum haxaferrite, the damage rate increases linearly with electronic stopping power.

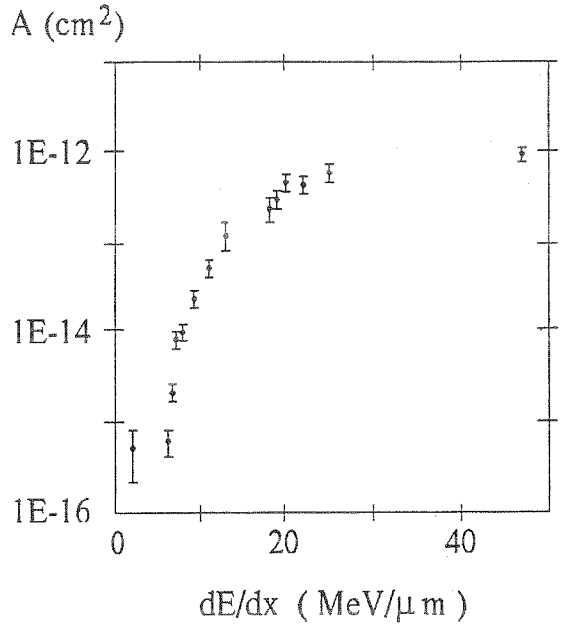


Fig. 1 - Rate of damage versus the electronic stopping power for the $Y_3Fe_5O_{12}$

1 G. Fuchs, F. Studer, E. Balanzat, D. Groult, M. Toulemonde and J.C. Jousset
Europhysics Letters 3 (1987) 321

2 F. Studer, N. Nguyen, G. Fuchs and M. Toulemonde
Hyperfine Interactions 29 (1986) 1287

3 M. Toulemonde, G. Fuchs, N. Nguyen, F. Studer and D. Groult
Phys. Rev. B35 (1986) 6560

4 F. Studer, D. Groult, N. Nguyen and M. Toulemonde
Nucl. Inst. and Meth. B19/20 (1987) 856

5 C. Houpert, M. Hervieu, D. Groult, F. Studer, M. Toulemonde
Nucl. Inst. and Meth. B32 (1988) 393

6 M. Toulemonde and F. Studer
Philisophical Magazine A58 (1988), 799-808

7 A. Timm and B. Strocka
Nucl. Inst. and Meth. B12 (1985) 479

Effects of electronic energy loss in amorphous Fe-B alloys irradiated with high energy heavy ions

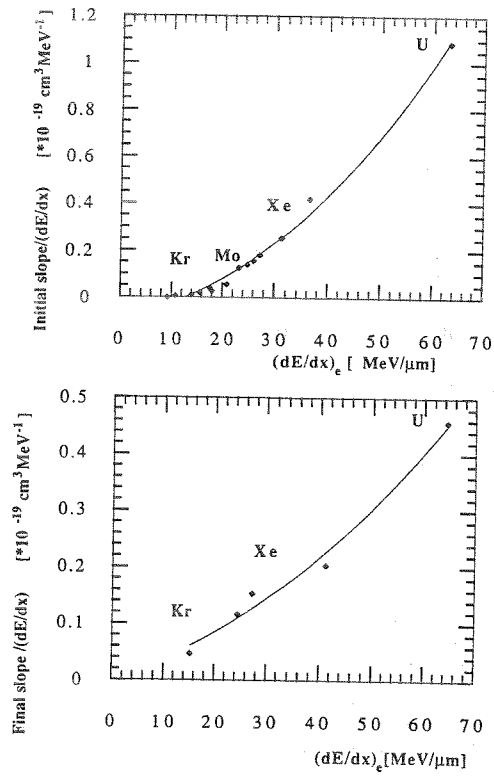
A. Audouard, Université, Nancy
E. Balanzat, J.C. Jousset, CIRIL, Caen
G. Fuchs, Université, Villeurbanne
D. Lesueur, Ecole Polytechnique, Palaiseau
R. Spohr and J. Vetter, GSI, Darmstadt
L. Thomé, CSNSM, Orsay

It was recently demonstrated that electronic energy loss of high energy heavy ions leads to drastic topological modifications in amorphous metallic alloys : i) defect production[1,2,3] with a cross-section two orders of magnitude higher than that of elastic collisions, at the very beginning of the irradiation; ii) large growth[4,5] of the sample dimensions perpendicular to the ion beam direction, above an incubation fluence depending on the material considered.

The possibility to noticeably extend (by a factor of two) the range of the ion electronic stopping power, offered by an irradiation with the 3 GeV U beam of the GSI accelerator, was of prime interest to check the effect of very intense electronic excitation on the above mentioned disordering mechanisms.

Electrical resistance measurements performed in situ at 80 K during U irradiation of amorphous Fe-B ribbons with the experimental procedure described in Ref. 3 (samples mounted with different angles between the beam axis and the normal to the sample length in order to separate the resistivity from the growth contributions in the resistance variation), confirm the results recorded on the same system irradiated with Kr and Xe ions[2,3]. A huge increase of both the alloy resistivity and the sample dimension variations, essentially due to electronic energy loss effects, is clearly evidenced on the figure .

A phenomenological model, based on the assumption that i) an incoming ion creates a cylindrical volume of damaged matter along its path ; ii) part of the created disorder can be annealed by a subsequent ion impact leading to the sample growth, accounts for the structural modifications observed.



Relative electrical resistance variation (normalized to the ion electronic energy loss) of an amorphous Fe-B ribbon irradiated at 80 K with various high energy heavy ions versus the ion electronic energy loss (a) at the beginning of the irradiation (defects production) ; (b) above the incubation fluence (growth region).

1 A. Audouard. E. Balanzat, G. Fuchs, J.C. Jousset, D. Lesueur and L. Thomé Europhys. Lett. 3 (1987) 327

2 A. Audouard. E. Balanzat, G. Fuchs, J.C. Jousset,D. Lesueur and L. Thomé Europhys. Lett. 5 (1988) 241

3 A. Audouard. E. Balanzat, J.C. Jousset, G. Fuchs, D. Lesueur and L. Thomé Nucl. Instrum. Meth. B39 (1989) 18

4 S. Klaumünzer, Ming-dong Hou and G. Schumacher Phys. Rev. Lett. 57 (1986) 850

5 S. Klaumünzer, Changlin Li, S. Löffler, M. Rammensee, G. Schumacher and H.C. Neltzert Rad. Eff. Def. Sol. 108 (1989) 131

A short introduction to the motivations of the low temperature irradiations of metallic targets with GeV heavy ions

A. DUNLOP
Laboratoire des Solides Irradiés, Ecole Polytechnique, F-91128 Palaiseau, FRANCE

The experiments summarized in the following pages are relative to different approaches of a unique problem, i.e. the answer to the question : can high electronic excitations lead to damage creation in metallic crystalline targets ? GeV heavy ions loose their energy via (i) inelastic collisions with the target electrons (electronic stopping power $(dE/dx)_e$) and (ii) elastic collisions with the target atoms (nuclear stopping power $(dE/dx)_n$). Except in the stopping zone of the ions, the inelastic energy losses are predominant : the ratio $(dE/dx)_e$ / $(dE/dx)_n$ is close to 2000.

According to the nature of the target, high excitations of the electrons can lead to various effects :

(i) in insulators, the number of mobile electrons is low, so that the time of excitation of the electronic system is sufficient for interactions between ionized atoms to take place. This leads to the formation of zones in which the atomic arrangement of atoms is strongly perturbed : the latent tracks[1,2] located along the ion trajectories.

(ii) in metals, the number of mobile electrons is very high, so that the excitation of the electronic system disappears very quickly and no target atom has enough time to react to the perturbation.

In order to know whether a metallic system is able to smear out a perturbation of its electronic system, whatever the intensity of the perturbation, we performed irradiations with GeV ions ($(dE/dx)_e \sim 1$ to 8 keV.Å^{-1}) in various metallic targets* and showed that various types of behaviours occured :

- some targets (Cu, Cu_3Au) are insensitive to high electronic excitations,
- in others (Fe, Ni_3Fe, austenites), high electronic energy losses induce a recombination of part of the defects created in nuclear collisions ($(dE/dx)_e$ < 4 keV.Å^{-1}) or can even lead to supplementary damage creation ($(dE/dx)_e$ > 6 keV.Å^{-1}),
- finally high electronic excitations can lead to amorphization (crystalline Ni_3B) or latent track formation ($Ni_{50}Zr_{50}$).

A great amount of work has to be done in order to explain (i) what are the relevant parameters according to which high electronic excitations can induce residual damage in a metallic target and (ii) what are the mechanisms by which the energy is transfered from the excited electrons to the target atoms.

1 R.L. FLEISCHER, P.B. PRICE and R.M. WALKER in Nuclear Tracks in Solids - University of California Press (1975)

2 D. ALBRECHT, P. ARMBRUSTER, R. SPOHR, M. ROTH, K. SCHAUPERT and H. STURMANN Appl. Phys. A 37 (1985), 37

* The detailed descriptions of the experiments follow.

High electronic excitations and damage production in GeV ion irradiated metals *

A.DUNLOP, D. LESUEUR, J. MORILLO
École Polytechnique, Palaiseau, FRANCE
J. DURAL
C.I.R.I.L. Caen, FRANCE
R. SPOHR and J. VETTER
G.S.I. Darmstadt, FRG

The damage induced by high energy heavy ions in metallic targets has been followed in situ at low temperatures (10 or 80 K) by electrical resistivity measurements.

The nuclear elastic collisions between the ions and the target atoms lead to atomic displacements : the concentration of defects corresponding to this process (C_{calc}) can be easily calculated[1]. If the energy transfers to the target electrons do not modify these damage processes, the ratio r of the measured resistivity increase $\Delta\rho$ ($\Delta\rho \propto$ concentration of defects in the target) to the calculated defect concentration should be totally independent of the amount of electronic energy loss $(dE/dx)_e$ of the ions in the target.

This is what happens in Cu_3Au targets (figure 1) in which the nuclear elastic collisions account for the observed damage rate.

In other targets (for example iron, figure 2) when the electronic stopping power of the incident ions increases : (i) at low $(dE/dx)_e$ (< 4 keV.Å^{-1}) the damage efficiency described by the ratio r decreases, whereas (ii) at high $(dE/dx)_e$ (~ 6 keV.Å^{-1}) it increases very strongly. At low $(dE/dx)_e$, electronic excitations induce a recombination of part of the defects created in elastic collisions, whereas at high $(dE/dx)_e$ collective effects in the wake of the ion path induce a large increase of the observed damage production rate. It has been shown moreover that this damage induced by energy transfers between the excited electronic system and the target atoms is located along the ion path, i.e. that the corresponding damage is inhomogeneously distributed in the sample volume.

1 A. DUNLOP, D. LESUEUR and J. DURAL
Nuclear Instruments and Methods B42 (1989) 182

2 A. DUNLOP, D. LESUEUR, J. MORILLO, J. DURAL, R. SPOHR and J. VETTER
C.R. Acad. Sci. Paris 309, série II (1989), 1277 and Nuclear Instruments and Methods B (1990)

* Irradiations performed at GANIL Caen (Ar and Xe ions) and GSI Darmstadt (U ions)

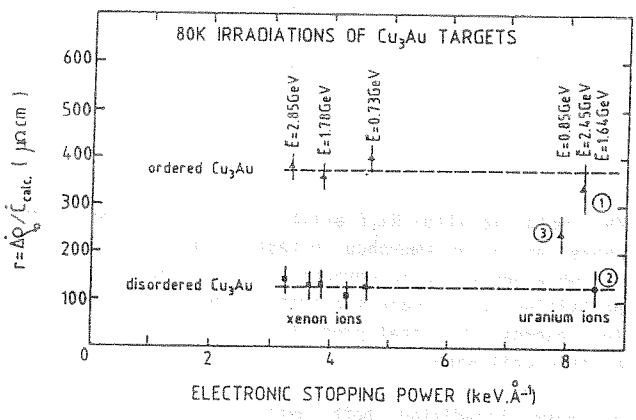


Fig. 1 Evolution of the ratio $r = \Delta\dot{\rho}_0/\dot{c}$ of the measured initial resistivity variation rate to the theoretical rate of defect creation in nuclear elastic collisions as a function of the average electronic energy loss of xenon and uranium ions in chemically ordered and disordered Cu_3Au alloys.

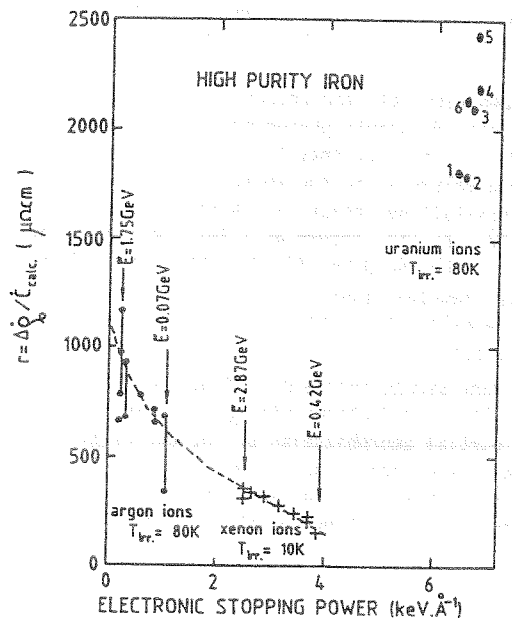


Fig. 2 Evolution of the ratio $r = \Delta\dot{\rho}_0/\dot{c}$ of the measured initial resistivity variation rate to the theoretical rate of defect creation in nuclear elastic collisions, as a function of the average electronic energy loss of the (argon, xenon, uranium) ions in each iron ribbon.

Partial amorphization of crystalline Ni_3B induced by high electronic excitations

A. AUDOUARD [1], E. BALANZAT [2], S. BOUFFARD [2], A. CHAMBEROD [3], A. DUNLOP [4], G. FUCHS [5], J.C. JOUSSET [2], D. LESUEUR [4], R. SPOHR [6], J. VETTER [6] and L. THOME [7]

[1] Physique du solide, Nancy and Toulouse, FRANCE
[2] CIRIL, Caen, FRANCE
[3] D.R.F. Grenoble, FRANCE
[4] Ecole Polytechnique, Palaiseau, FRANCE
[5] Physique des Matériaux, Lyon, FRANCE
[6] G.S.I. Darmstadt, F.R.G.
[7] CSNSM, Orsay, FRANCE

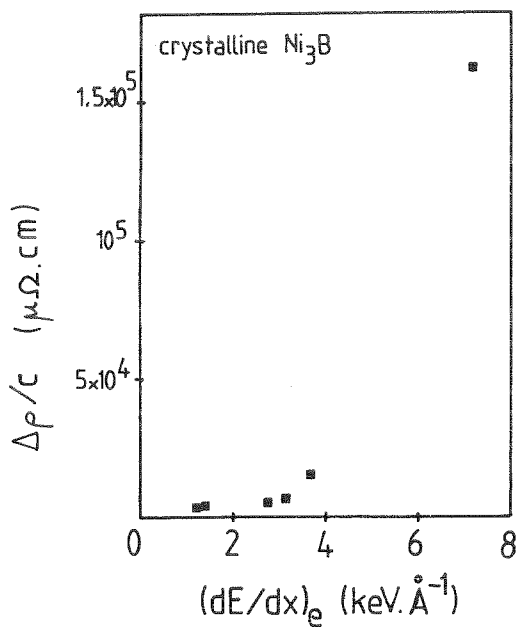
The metallic alloy Ni_3B exists in a stable crystalline phase and in an amorphous metastable phase. The latter is obtained by rapid quenching from the melt, by vapor deposition on a cold substrate or by irradiation with low energy ions that produce displacement cascades by elastic collisions.

We have irradiated both amorphous and crystalline alloys with 3 GeV heavy Kr and Xe ions at GANIL and U ions at G.S.I. The stopping power of these ions in Ni_3B varies between 1.2 and 7.2 keV.Å^{-1}.

Concerning the amorphous alloy, the electrical resistivity measurements confirm the results already obtained with another amorphous alloy Fe_{85} B_{15}. The amorphous alloy is damaged by electronic excitation effects. After an incubation fluence ($\simeq 10^{12}$ ions.cm^{-2}) the growth phenomenon takes place (the growth is a change in the sample dimensions occuring without any volume change : the sample extends perpendicularly to the beam direction and shrinks along the beam direction).

The behaviour of the crystalline alloy is completely different. No growth phenomenon takes places, which can be due to the fact that in crystalline alloys there is no free volume as in the amorphous alloys. Nevertheless the crystalline phase is highly damaged : we have reported on the figure as a function of the ion electronic stopping power $(dE/dx)_e$ the ratio of the resistivity increase (characteristic of the induced damage) to the calculated damage that would result from the sole elastic collisions.

The very strong increase of damage efficiency observed during the irradiations with uranium ions is attributed to a partial amorphization of the the crystalline phase by high electronic excitation effects. This is confirmed by X rays diffraction experiments and electron microscopy observations of the samples.



Evolution of the ratio $r = \Delta\rho/c$ of the measured initial resistivity variation rate to the theoretical rate of defect creation in nuclear collisions as a function of the average electronic energy loss of the ions in the crystalline Ni_3B ribbons.

Structure of Heavy-Ion Tracks in Zircon

G. Braunshausen and L.A.Bursill
School of Phyiscs, The University of Melbourne

J.Vetter and R. Spohr
GSI Darmstadt

Introduction

Observations of heavy-ion tracks proved quite difficult using a 100 kV electron microscope[1]. We have re-examined heavy-ion tracks in zircon using a new 400 keV high-resolution instrument. This has three advantages. First, the higher voltage allows a reduction in electron-induced irradiation effects ($\alpha \frac{1}{E}$). Secondly, much thicker portions of crystal may be penetrated, allowing significant improvement to the number and spatial extent of tracks observed. Finally, this instrument has the highest resolution available commercially (1.7 Å), which ensures higher quality images.

Experimental

Gem quality zircons ($ZrSiO_4$) were irradiated with 14 MeV/u Pb ions at GSI, Darmstadt. The dose was $\leq 10^{11}$ ions cm^{-2} parallel to [100]. Thin fragments were then removed from the ion entrance surface. High-resolution images were obtained using crystals oriented with the incident electron beam exactly parallel to the track direction [100].

Results

Figs. 1-3 show enlargements of three track cores. Facetting occurs parallel to {011} planes of zircon. Note that the disordered regions appear to be entirely confined to the core, having diameter approximately 80Å diameter. Enlargements of dislocation cores, recorded adjacent to the track cores, showed terminating half-planes and it was apparent that the lattice displacements were large relative to any displacement associated with the zircon outside the track core. Dislocation strain fields drop off very slowly with distance (typically ~1/R); thus any strain field associated with the tracks drops off rapidly with distance (say $\leq 1/R^2$). Some bright- and dark-field transmission microscope images are described in another contribution[2].

Discussion

Our observations confirm directly the conclusions of Fleischer, Price and Walker[3], based on track etching and electrical conductivity measurements, that fission or heavy-ion irradiation damage is confined essentially to a 50-100 Å core region of atomically-disordered structure with virtually no damage outside this region. The present observations refer only to the high energy portion of the track; we expect that evidence for cascades (displacement damage) may finally be found in the relatively short low energy portion of heavy-ion tracks. Sectioning techniques are presently being developed to this end.

The total number of atoms involved in a track core (140 μm length, 80 Å diameter) is 6.4 x 10^9, which share the total energy of ~ 14 MeV/u = 2.9 GeV. Thus an average of 4.53 eV per atom of core has been dissipated. This figure is typical of activation or displacement energies for ions in ceramic crystals like zircon. Overall, the available energy is reasonably-well accounted for by the assumption that the track crore has simply undergone a crystalline → glass phase transition.

Acknowledgement

This work was supported by GSI, Darmstadt and the Australian Research Council.

References

[1] Braunshausen, G., Bursill, L.A.,, Vetter, J. and Spohr, R. GSI Scientific Reports, March 1988, Darmstadt, ISSN 0174-0814, (U.Grundinger, Ed.), p237.

[2] Braunshausen, G., Bursill, L.A., Vetter, J. and Spohr, R., GSI Scientific Reports, this volume.

[3] Fleisher, R.L., Price, P.B. and Walker, R.M. (1975) "Nuclear Tracks in Solids", University of California Press, Berkeley.

Fig.1

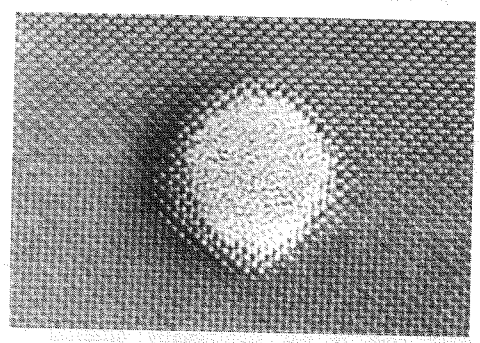


Fig.2

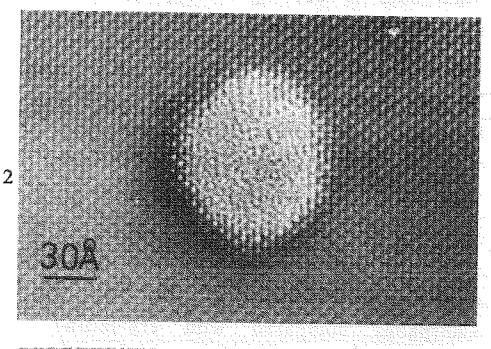
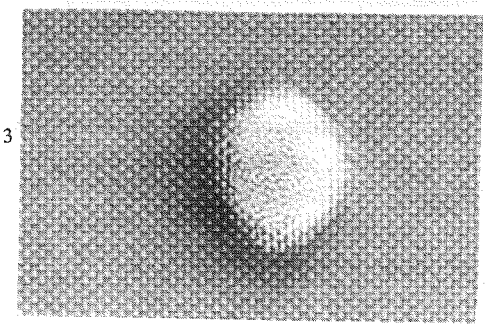


Fig 3



Diffraction Contrast Imaging of Heavy-Ion Tracks in Zircon at 400 keV

G. Braunshausen and L.A. Bursill
School of Physics, The University of Melbourne

J.Vetter and R. Spohr
GSI, Darmstadt

Introduction

A 400 keV high-resolution electron microscope has yielded high quality images of heavy-ion tracks in zircon using conventional bright- and dark-field image modes. High-resolution images of the core structure are reported separately[1].

Experimental

Slices (0.5 mm) of zircon crystal were irradiated with 14 MeV/u Pb ions at GSI, Darmstadt. The dose was $\leq 10^{11}$ ions.cm^{-2} parallel to [100]. Thin fragments were recovered from the ion entrance surface and examined at 400 keV in a JEOL-4000 EX instrument using conventional bright and dark-field imaging techniques[2].

Results

Fig.1 is a bright-field image with approximately a two-beam diffracting condition for reciprocal lattice vector $\underset{\sim}{k}$ ($\bar{1}3\bar{2}$). The surface normal is inclined by 25° with respect to the heavy-ion irradiation direction [100]. The area contains line contrast features consisting of a central strip, width ~80Å, accompanied by periodically-placed pairs of bright- and dark-contrast features. The specimen thickness ranges from 250-2500Å for the area of Fig.1. The observed track density is ~10^{10} cm^{-2}, consistent with the estimated heavy-ion dose of $\leq 10^{11}$ ions.cm^{-2}. Fig.2 shows a bright-field image obtained for surface normal close to [100], i.e. the tracks appear edge-on. Bright contrast occurs at the thin edge, which gradually changes to dark-on-white in the thickest areas. Dark annular contrast occurs for intermediate thickness when detail within the track core is not significantly different to the adjacent background intensity.

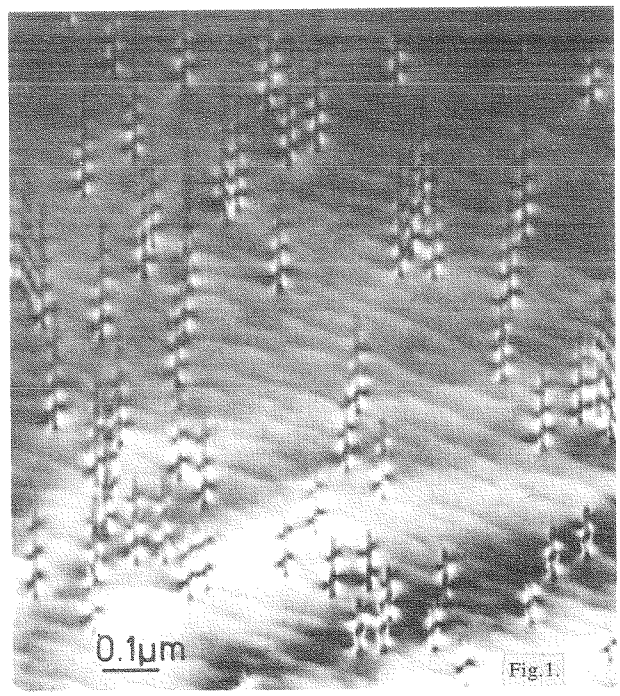


Fig.1.

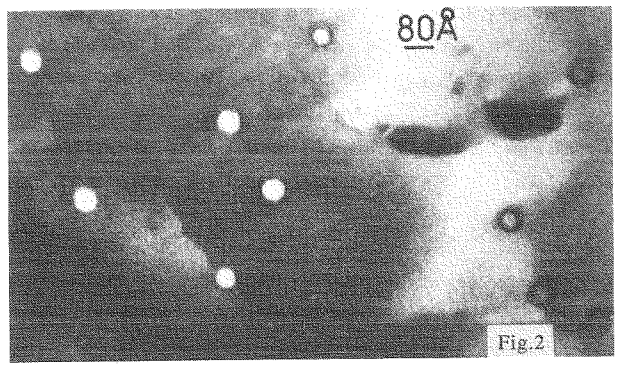


Fig.2

Discussion

(a) Inclined tracks. The periodically-dotted contrast is primarily a diffraction effect; it does not imply that the structure is periodic on the scale of 100'sÅ. High-resolution images showed that the track core was essentially amorphous structure[1]. The central band of contrast represents the projected image of the track core, due to the different effective structure amplitude of amorphous compared with crystalline zircon. The periodically-dotted contrast represents contributions from diffracted beams which have been phase-shifted on crossing the track as well as phase shifts due to any strain field (atomic displacements) of the zircon matrix.

(b) End-on tracks. It appears that strain contrast dominates for the intermediate range of crystal thickness, say 1000-2000Å. For thicker specimens the track contrast is complicated by Fresnel diffraction effects and overlapping images due to slight misalignment of the tracks. For the very thin edges of the crystal edge-on tracks tend to be etched away during observation.

Conclusion

Use of 400 keV, rather than 100 keV, has given a dramatic increase in image quality for heavy-ion irradiation tracks in zircon. Quantitative analysis of the images, using computer-simulations and image-matching[2] should yield values for the track core density as well as elastic strain parameters.

Acknowledgement

This work was supported financially by the Australian Research Council and GSI, Darmstadt.

References

1 Braunshausen, G., Bursill, L.A., Velter, J., and Spohr, R., GSI Scientific Reports, March 1990; this volume.

2 Head, A.K., Humble, P., Clareborough, L.M., Morton, A.J. and Forwood, C.G., 1973, "Computed Electron Micrographs and Defect Identification", North-Holland, Amsterdam.

Latent tracks induced by high electronic excitations in a metallic compound ?

A. BARBU, A. DUNLOP
École Polytechnique, Palaiseau, FRANCE
R.S. AVERBACK
Urbana, Illinois, U.S.A.
R. SPOHR and J. VETTER
G.S.I. Darmstadt, F.R.G.

A few discs of the intermetallic compound Ni_{50} Zr_{50} have been irradiated at 80 K with incident uranium ions at two fluences : 10^{11} and 7×10^{11} ions.cm^{-2}. Except in the zone in which the ions are stopped (i.e. at a depth of 60 μm), the ions mainly interact with the target electrons. The aim of this work is to know if the process of latent track formation occuring in insulators is apt to take place in metallic targets when the level of excitation of their electronic system is very high $(dE/dx)_e \sim 5$ keV.Å^{-1}).

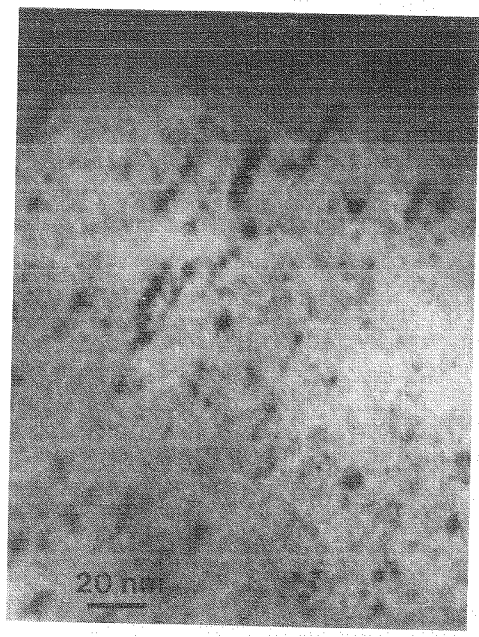
A preliminary study of the microstructure of a sample irradiated with 7×10^{11} ions.cm^{-2} has been started using transmission electron microscopy. These first observations show that in the electronic stopping zone and only in some grains, linear strings of elongated defects that are all aligned in the same direction are visible : figure 1 is a bright field photograph using symetrical multibeam conditions, whereas figure 2 is a high resolution picture along the same orientation of a very thin zone of the sample. The normal to the plate is at about 10° from the normal to the sample, ie. from the incident beam direction. The length and direction of the strings depend of the orientation of the foil, their number is close to the number of incoming ions.

In two beam bright field conditions, whithin the thickness fringes, the defects appear bright in the dark fringes and dark in the bright fringes : this indicates a structure factor contrast originating from chemically disordered or amorphous zones.

Up to now, we cannot say if the fact that these strings are only observed in certain grains comes from an orientation or a crystalline structure effect (Ni Zr presents several orthorhombic phases around the stoechiometry 50-50 that we used).

In conclusion, it is thus probable that these strings materialize the trajectories of the ions and can be considered as latent tracks.

Figure 1



Transmission electron microscopy observations of a Ni_{50} Zr_{50} sample irradiated at 80 K with 3 GeV uranium ions at a fluence of 7×10^{11} ions.cm^{-2} : the observed zone is located at 30 μm depth, ie. in the electronic stopping zone.

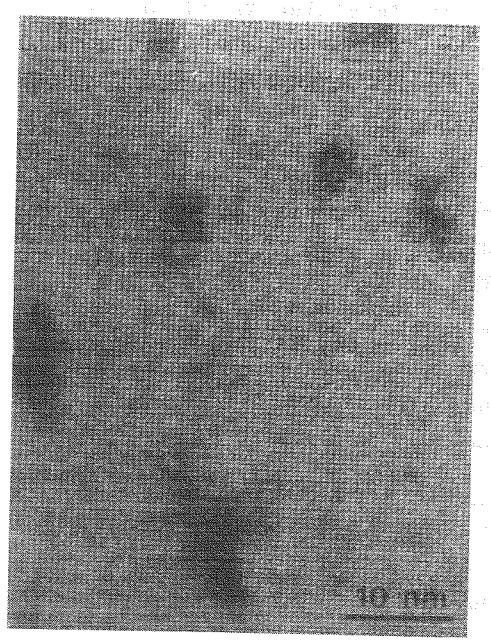


Figure 2

RESPONSE OF CR-39 TO ^{238}U IONS

J.Raju, S.Ghosh, A.Saxena and K.K.Dwivedi.

Department of Chemistry,
North-Eastern Hill University, Shillong 793 003, India.

Various track recording properties[1] have made CR-39 the most sensitive track detector among plastics and hence find wide applications in various fields.An attempt has been made to study the response of CR-39 to ^{238}U ions having three different energies.Emphasis has been made on the study of the energy resolution of the detector. Maximum etchable track lengths have been measured too.

CR-39 detectors were prepared by cutting the commercially available sheets from Homalite Corporation, Wilmington,Del(U.S.A) in to size of 2.0x2.0 cm^2. The detectors were exposed to collimated beam of ^{238}U ions of three different energies (12.0,10.06,4.5 MeV/u) at XO channel of UNILAC, GSI,Darmstadt. The detectors were exposed at an angle of 45° to the surface using an areal dose of $\sim 10^4$ cm^{-2}.The detectors were then etched in 6N NaOH at 55°C till rounded track tips were observed.Successive etching was carried out to determine V_T along the tracks of ^{238}U in CR-39 .

Maximum etchable track lengths were found from the peak centroid of the track length distribution curve (fig. 1). Table 1 lists the maximum etchable track length alongwith the theoretically calculated values. The experimental results support the validity of the computer code 'RANGE'[2] based on the stopping power equations of Mukherji etal.[3-6]. Broadening of the track length distribution peaks for degraded ion energies is due to staggling of the ion with increasing absorber thickness.

Table1

Parameters	12.00(MeV/u)	10.06(MeV/u)	4.5(MeV/u)
Energy(MeV/u)	12.00	10.06	4.5
FWHM(μm)	3.5	4.0	5.0
σ_L (μm)	1.49	1.69	2.12
FWHM(MeV/u)	0.3	0.35	0.40
σ_E(Mev/u)	0.025	0.031	0.041
L_M(μm)			
Experimental	151.0	134.00	72.50
Theoretical	153.0	125.35	75.85
R%	2.4	3.3	8.9

σ :Standard Deviation, FWHM: Full-width Half Maxima

L_m: Most probable Track Length.

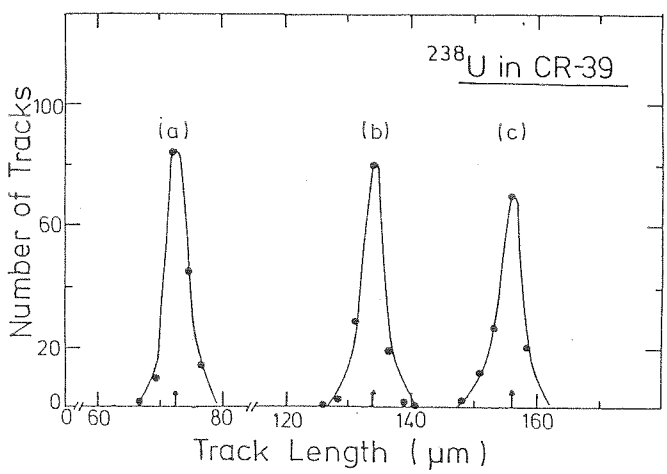


Figure 1.Track length ditribution curves (a)4.5,(b)10.06,(c)12.00 MeV/u

1. B.G.Cartwright,E.K.Shirk & P.B.Price, Nucl.Instr. Meth.,153(1978)457.

2.K.K.Dwivedi,Nucl.Tracks.Radiat.Meas., 15(1988)395.

3.S.Mukherji and B.K.Srivastava, Phys. Rev.B9(1974)3708.

4.B.K.Srivastava and S.Mukherji, Phys. Rev.A14(1976)718.

5.S.Mukherji and A.K.Nayak,Nucl.Instr. Meth.159(1979)421.

6.K.K.Dwivedi and S.Mukherji,Nucl.Instr. Meth.,161(1979)317.

TRACKS OF ^{132}Xe IN CR-39

S.Ghosh, J.Raju and K.K.Dwivedi

Department of Chemistry,
North-Eastern Hill University, Shillong 793 003, India.

Study of etching characteristics of CR-39(SSNTD) is important due to its application in wide ranging fields[1]. To do so theoretical data of range and energy-loss becomes very important. hence the validity of such theoretical information must be varified by experimentally measurable parameters. Present work deals with the study of track length ditribution of ^{132}Xe with various energies in CR-39.Theoretical data used are obtained from computer code 'RANGE'[2] based on the stopping power equations of Mukherji etal.[3-5].

CR-39 detector pieces of size 2.0x2.0 cm^2 were prepared by cutting the sheets commercially available from Homalite Corporation, Wilmington, Del(U.S.A). The detectors were exposed to collimated beams of ^{132}Xe of various energies at an incident angle of 45 to the detector surface with an areal dose of 10^4 cm^{-2} at the XO channel of UNILAC,GSI,Darmstadt. The detectors were then etched successively in 6N NaOH at 55° C.Detectors were scanned in -X and -Y directions under an optical microscope to measure various track parameters. Etching was terminated when rounded track tips were formed.By applying suitable etching corrections maximum etchable track lengths were found out. Table 1 lists the maximum etchable track lengths of ^{132}Xe at various energies in CR-39 determined from the peak centroid of the track length distribution curves.

Table 1 also lists the theoretical track length values calculated by using computer code 'RANGE' based on the stopping power equations of Mukherji etal. It has been observed that the experimentally measured track length values are in fair agreement with the theoretical values supporting the validity of stopping power equations.

Table 1

Energy(MeV/u)	Track Length(μm) Experimental	Theoretical
17.00	227	232
16.08	222	216
15.60	211	214
15.05	197	200
13.18	168	170
12.00	153	154
10.87	142	137
9.83	129	124
8.82	117	112
7.35	94	94
5.82	78	78

1.B.E.Fischer and R.Spohr, Rev. Mod. Phys.,55(1983)907.

2.K.K.Dwivedi, Nucl. Tracks Radiat. Meas.15(1988)345.

3.S.Mukherji and B.K.Srivastava, Phys. Rev.,B9(1974)3708.

4.B.K.Srivastava and S.Mukherji, Phys. Rev.A14(1976)718.

5.S.Mukherji and A.K.Nayak, Nucl. Instr. Meths., 168(1979)317.

TRACKS OF ^{132}Xe THROUGH POLYMER STACKS

P.P.Chaubey, J.Raju, S.Ghosh and K.K.Dwivedi

Department of Chemistry,
North-Eastern Hill University, Shillong 793 003, India.

SSNTDs are widely used for particle identification and for this purpose the detector has be calibrated. Of the various methods ones based on the measurement of maximum etchable track length and relation of track-etch rate (V_T) with various other related parameters are more versatile. V_T can more realistically be measured[1] by exposing a stack of SSNTD with energetic heavy ion beam and then etching all of them under identical conditions than by prolonged etching of the track from start to end of the ion trajectory in the detector.

We have studied the passage of isoenergic ^{132}Xe ions through the stacks Hostaphan(Polyethylene terephthalate) and overhead projector trasperancy(Cellulose triacetate). Our emphasis has been to study the track-etch rate along the trajectory of the ions. As the work on the determination of V_T and related study is in progress we have reported the ranges of the ions in mentioned detectors alongwith the theoretically calculated values. Theoretical data are obtained from computer code 'RANGE'[2].

A Hostaphan stack comprising of five foils each of thickness 50 μm and overhead projector tranperancy(OPT) stack having three foils each of 100 μm were irradiated to 14.5 MeV/u ^{132}Xe ions. The irradiations were carried out at an incident angle of 45° to the detector surface using an areal dose of 10^4 cm^{-2} at XO channel of UNILAC, GSI, Darmstadt. All the foils were etched successively in 6N NaOH maitaining a temperature of 65° C for Hostaphan and 55°C for OPT.

In Hostaphan tracks were observed only in upper three foils. By applying suitable etching corrections the maximum etchable track lengths were found to be 180.38 μm. Theoretically calculated value is 171 μm.

Tracks were observed only in two upper foils of OPT stack. Maximum etchable track length was found to be 204.28 μm. Theoretical value is 218.58 μm.

Thus experimentally measured value of track lengths are in fair agreement with theoretically calculated values within the limits of experimental errors.

1. P.B.Price, R.l.Flischer, D.D.Peterson, D.O'Ceallaigh, D.O'Sullivan and A.Thompson, Phys.Rev.164(1967)1618.
2. K.K,Dwivedi, Nucl. Tracks Radiat. Meas. 15(1988)345.

COMPARISON OF HIGH SENSITIVITY POLYMERIC TRACK DETECTORS

B.Grabež
Institute of Physics, P.O.Box 57, 11001, Beograd, Yugoslavia
F.Vater and R.Brandt
F.B.14, Philipps Universitat, 3550 Marburg, FRG

The many scientific and technological applications of solid state track detectors have stimulated efforts toward finding better recording solid. In 1978 the new solid state track detector CR-39 was introduced by Cartwright et al./1/. Because of its high sensitivity and excellent resolution this detector is used in wide application. The CR-39 detector is now casted under different conditions from CR-39 monomer by various firms. In 1988 /2/ the new polymeric track detector of high sensitivity SR-86 was introduced. It was reported /2/ that SR-86 shows higher sensitivity than that of CR-39 for 6 MeV α-particles. In order to make comparison we studied the characteristics of various kinds of CR-39 detectors and the new introduced SR-86 detector. We investigated the characteristics of CR-39 casted by American Acrylics and Plastics Inc., Stratford (Acrylic Dosimetry grade) and Homalite Company (Wilmington, USA), respectively; MA-ND/p and MA-ND/α detectors produced by Hungarion Optical Works (MOM) and SR-86 detectors. We made measurements on the tracks of ions with low Z/β (α-particles from Am-241 source) and ions with high Z/β (14.5 MeV/u ^{132}Xe).

Samples of all five detectors were exposed to 14.5 MeV/u ^{132}Xe at the GSI, Darmstadt and to α-particles from Am-241 source. The etching was carried out in 6.25 N NaOH at 70°C.Samples irradiated with ^{132}Xe ions were etched for 15 min., 0.5h and 1h, respectively and samples exposed to α-particles were etched for 2h, 4h and 7h, respectively. For each sample measurements were made on the 100 tracks. From the measured track parameters the etched track lenghts relative to the unetched surface (L), the bulk etch rate (V_B) and the etch rate ratio (V_T/V_B; V_T-track etch rate) were determined.

Fig.1. presents the track etch rate ratio (V_T/V_B) versus (Z/β) ratio for various detectors. For ^{132}Xe the mean etch rate ratio (V_T/V_B) along the track is presented. For α-particles the V_T/V_B ratio measured after 4h of etching is shown. From Fig.1. it can be seen that for CR-39 (Acrylics and Homalite),MA-ND/p and MA-ND/α detectors the points coresponding to particles with low and high Z/β are relatively near. Only, it seems that MA-ND/α detector is a little less sensitive than the other detectors. The SR-86 detector has for α-particles higher and for ^{132}Xe lower sensitivity than the other detectors. The result is that V_T/V_B versus Z/β curve is less steep for this detector. For bulk etch rate of SR-86 detector we obtained the value V_B=4.90±0.05μm/h what is about three times higher than that obtained for other detectors. For α-particles it has 1.8-2.2 times higher sensitivity than the other examined detectors. It was observed that for ^{132}Xe ions SR-86 shows higher track etch rate (V_T) than the other detectors but its sensitivity for these ions, as can be seen in Fig.1., is smaller in comparison with other detectors. It seems that for particles with high Z/β this detector is 'faster 'but less sensitive than the other detectors.

References:

1. B.G.Cartwright et al., Nucl.Instr.Meth. 153, 457 (1978)
2. M.Fujii et al., Nucl. Tracks Radiat.Meas. 15, 107 (1988)

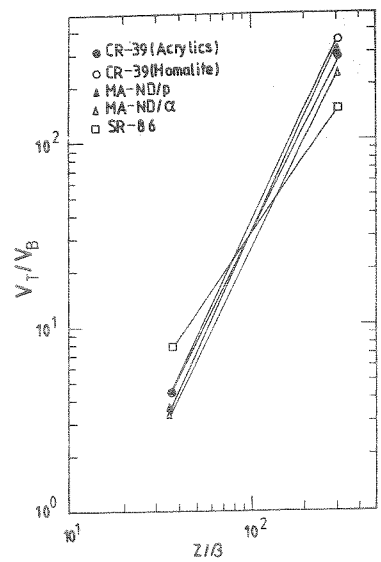


Fig.1. Track etch rate ratio (V_T/V_B) versus Z/β ratio for various detectors

Direct Visualization of Heavy Ion Tracks in Evaporated Se-Films

J. Düring[1], F. Granzer[1] and K.O. Groeneveld[2]

1) Institut f. Angewandte Physik, 2) Institut f. Kernphysik, Universität Frankfurt

If a thin film is exposed to a beam of heavy ions at glancing incidence it should be possible to observe the details of the released tracks in a high resolution transmission electron microscope (TEM). In the case of Selenium films we expected a phase transformation from the amorphous into the crystalline state inside the thermal spike region, surrounding the particle trajectory, as shown schematically in Fig. 1. Assuming a well defined value for the transition temperature T_K (amorphous → crystalline) it should be possible to obtain the

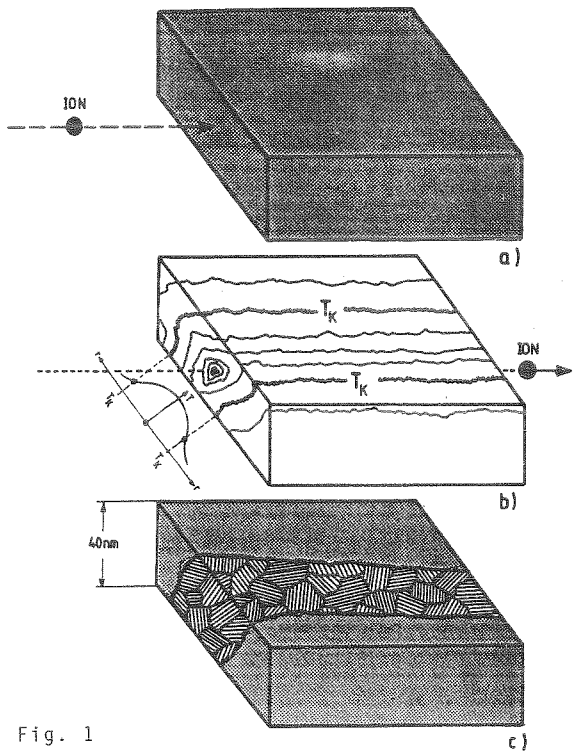


Fig. 1

temperature distribution inside the thermal spike.

Amorphous Se-films with thicknesses ranging between 300 and 400 Å were deposited onto a clean glass substrate by evaporating high purity granulated selenium out of a Mo-crucible at 230° C in a vacuum of 10^{-6} Torr. These films, still on the backing glass substrate, have been exposed to the beam of heavy ions as shown in Fig. 2a. The irradiation dose was about 10^{10} ions/cm^2, the maximum angle of incidence 4°. The preparation of these films for their examination in the TEM is shown in Figs. 2b,c.

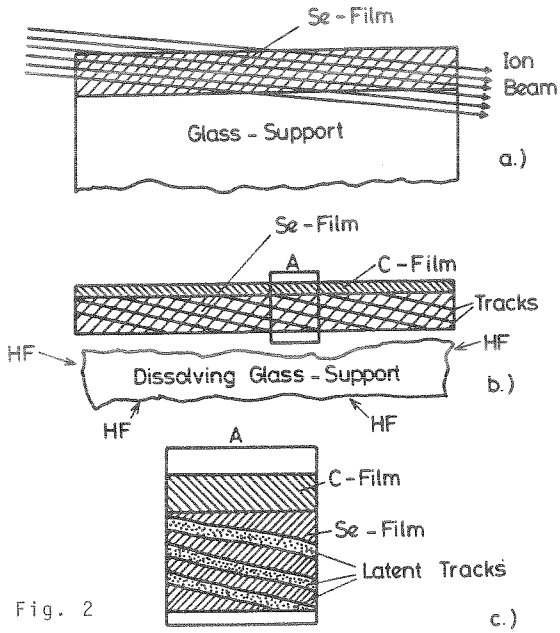
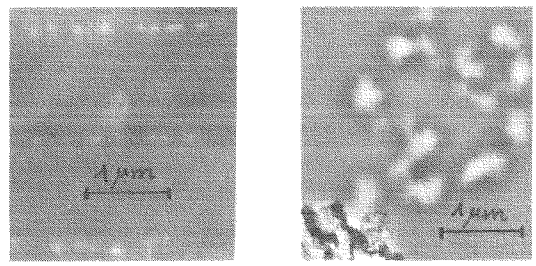


Fig. 2

The interpretation of the phenomena visualized in the electron micrographs of Se-films which have been exposed to 13,6 MeV/u ^{106}Pb (Fig.3a), and to 15 MeV/u ^{238}U (Fig. 3b) is extremely difficult. The intermittent tracks (Fig. 3a) are probably due to displacement-cassades, the origin of the "cluster" in a partly crystallized Se-film (Fig. 3b), however, is unknown.



a b

Fig. 3

There was no evidence at all, that the passage of heavy ions through amorphous Se-films can trigger the phase transition into the crystalline state.

Etching and Technical Parameters of Polyvinylidene Flouride for the Production of Nuclear Track Microfilters

C.-D. Zhao*, P. Vater, R. Brandt

Kernchemie, FB 14, Philipps-Universität Marburg, D-3550 Marburg

Polyvinylidene Flouride (PVDF) is a very useful and attractive material to produce nuclear track microfilters for a wide variety of technological applications due to its highly physical and electrical properties. Some successful efforts have been made to investigate the etching behaviour of PVDF[1,2].

We continued to study systematically the etching behaviour of nuclear tracks in PVDF for the purpose of production of nuclear track microfilters. The PVDF foils were irradiated with several heavy ions (^{50}Ti of 4.96 Mev/N, ^{86}Kr of 17.71 Mev/N, ^{208}Pb of 17.14 Mev/N and ^{238}U of 13.67 Mev/N) perpendicular to their surface at UNILAC (GSI,Darmstadt). Two etching solutions, 6 N KOH + 0.1 FW $KMnO_4$ (we call "0.1 solution") and 6 N KOH + 0.05 FW $KMnO_4$ (we call "0.05 solution"), have been employed. The etching temperature remains at (70±1)°C for both of solutions in order to preserve the electrical properties of PVDF films. A water cooling reflector was used for keeping the concentration of solutions unchanged, and the solutions were stirred with a magnet during the entire etching period.

As other plastic filters (e.g. Kapton), the PVDF filters have the funnel-like holes (the openings at surface being larger than the openings in the middle of holes).

The outer diameter (D) and inner diameter (d) of holes were simultaneously measured by means of an optical microscope. We noticed that, as expected, the etching behaviour of PVDF films depends not only on the etching condition, but also on the track producing heavy ions and their specific energies. Therefore, it is always important in practice to determine V_T before the etching of every batch of foils irradiated with certain heavy ions. One of practical methods is the deduction of V_T by using a plot of outer diameter (D) and inner diameter (d) of etched holes vs. the etching time[3]. V_T is equal to half of the original foil thickness divided by t_o, the time when d starts to grow. Fig. 1 is a plot of the experimental data fitted by using a linear regression for PVDF filters irradiated with ^{238}U of 13.67 Mev/N ions and etched in "0.1 solution" and "0.05 solution", respectively. From Fig. 1, we deduced V_T to be ≈ 0.7μm/hr for "0.1 solution", and ≈ 0.8μm/hr for "0.05 solution", respectively. The radial etch rate of "0.05 solution" is larger than that of "0.1 solution". Although this difference is not that large, it indicates there exsists the interest to seek more suitable solution for etching of PVDF films. At the moment, we prefer "0.05 solution" for etching times less than 100 hours, whereas for etching times longer than 100 hours, we have observed that "0.05 solution" produces more precipitate on the etched foils with the consequence of a reduction of the etching rate. Therefore, for very long etching times the "0.1 solution" seems to be more useful.

In both cases we could get rid of the brownish precipitate by treating the etched filters in a $K_2S_2O_5$ solution for a few hours.

Some preliminary experimental results encourage us to look for even better etching solutions by varying the concentrations of KOH and $KMnO_4$.

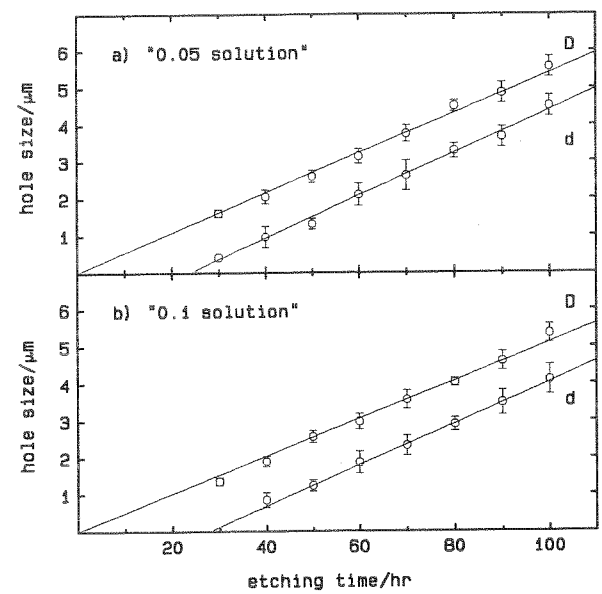


Fig. 1: Outer (D) and inner (d) pore sizes vs. etching time (see text)

The authors thank Drs. R. Spohr and J. Vetter for their help during the irradiation of the foils at GSI. This work was performed under the agreement of China-F.R. Germany scientific collaboration, we thank the International Office, DLR, Köln, for their support.

[1] Y. Komaki, Nucl.Tracks, 3 (1979)33

[2] Khodai-Jopary et al., Nucl. Tracks and Radiat. Meas. 15 (1988)167.

[3] P. Vater et al., GSI Report (1988)243

* Visiting scientist from Institute of Atomic Energy, Beijing, China.

PRODUCTION OF THICK NUCLEAR TRACK FILTERS USING 8.5 MeV/NUCLEON ^{208}Pb IONS

HAMEED A. KHAN

SSNTD-Laboratory, Nuclear Engineering Division, Pakistan Institute of Nuclear Science & Technology (PINSTECH), P.O. Nilore, Islamabad, Pakistan

SHI-LUN GUO, YU LAN WANG, AND T.C. ZHU

Institute of Atomic Energy (IAE),P.O. Box 275(50), Beijing, Peoples' Republic of China

"Nuclear Track Filters" are produced by making microholes in thin sheets of insulating materials by exposing them to collimated beams of different charged particles [1-3]. The latent damage trails so produced can be enlarged to desirable dimensions by etching. In the past, thin track filters were obtained by exposing appropriate track forming materials having thicknesses smaller than the ranges of energetic heavy ions (or fission fragments). Following this method only thin filters could be produced. The so produced filters required a lot of care in their use. Here, we describe a method of producing "thick filters", having thicknesses much larger than the ranges of the track producing particles.

The principle of the technique is as follows: Thick sheets of plastic track detectors are exposed to heavy charged particles having ranges much smaller than those of the plastics. These detectors are then eletrochemically etched. Afterwards, the normal chemical etching is performed which dissolves the core of the electrochemical etched region (the region containing treeing). Further chemical etching can be carried out from one or both the sides. The mode of etching determines the profile and size of the hole so produced.

We exposed 300 um thick sheets of Makrofol-E plastic track detectors to 8.5 MeV/nucleon ^{208}Pb ions at GSI (Darmstadt, F.R. Germany). These ions have a range of less than 150 μm in Makrofol-E, which is smaller than the thickness of the detector. Systematic studies of the profiles of the "through holes" have been carried out by employing different combinations of the applied voltage and the frequency of the alternating electric field. The Scaning Electron Microscopic (SEM)- observations showed that the profile of the electrochemically etched channels varies from a cylinder to a cone, to a funnel like structure; and to a double conical structure. It has been observed that the etched track profile so produced is a strong function of (a) the range of the particle, (b) the frequency of the applied oscillating field, and (c) the applied voltage.

Figure 1 shows profiles of four etched channels, produced by using different combinations of frequency (100 Hz to 3000 Hz) and applied voltage (300V to 1800V). Profile "a" was obtained by enlarging the damage in 6N NaOH solution using a frequency of 200 Hz and a voltage of 450V. Profile "b" was produced under conditions, similar to those employed for Profile "a", however, relatively a higher voltage (1800 V) was employed for the enhancement of the damage. Profile "c" was obtained by enlarging the damage by using 6N KOH + 10% ethyl alcohol at a frequency of 1500 Hz at 600 V. Profile "d" was obtained by etching in 6N KOH, using a frequency of 1500 Hz & an oscillating voltage of 1800 volts. Similar results were obtained by exposing CR-39 sheets to fission fragments from a reactor.

This work has been carried out under the scientific collaboration agreement between the Institute of Atomic Energy (IAE) Beijing , Peoples' Republic of China and Pakistan Atomic Energy Commission (PAEC) Islamabad, in the field of "Nuclear Track Microfilters".

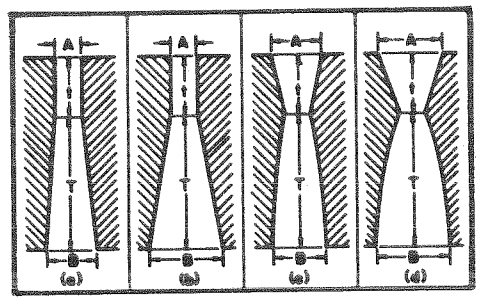


FIGURE 1. Changes in the pore structure due to different combinations of voltage, frequency and the etchants (see the text).

REFERENCES

1. P. Vater, G. Tress, R. Brandt, B. Genswurger and R. Spohr: Nucl. Instr. Methods 173 (1980) 205.
2. W. Hollander, E. Pape, M. Plachky, P. Vater and R. Brandt: J. Aerosol Sci. 17 (1986) 859.
3. G. Tress, P. Vater, H.A. Khan, R. Brandt, and M. Kadner: Staub, Reinhaltung der luft 46 (1986) 147.

Searching for the superfluid Josephson effect[G]

C. Trautmann, R. Spohr, J. Vetter (GSI Darmstadt)
Y. Hirayoschi, G. Eska, S. Lang (Universität Bayreuth)

The analogy of the Josephson effect in superconductors[1] was observed recently in the superfluids ^{3}He and ^{4}He[2,3]. In superfluids the interaction between two reservoirs of superfluid helium has to be a small orifice acting as weak link. As soon as the mass flow through this orifice exceeds a critical velocity[3,4], defined by the size of the aperture, quantized circulation in the form of vortices is generated which can be monitored. The experimental observability depends on the dimensions, diameter and length, of the weak link. They should be roughly comparable to the core radius of a vortex, which is of the order of the coherence length ξ_0 of the superfluid ($\xi_0(^4\text{He})$=0.2 nm, $\xi_0(^3\text{He})$=70 nm). For the production of microscopic apertures the nuclear track technique is a promising alternative to the lithographic technique used until now [5,6]. We exposed 30 µm thick polycarbonate (PC)-foils to single ions (^{132}Xe, 14 MeV/u) which produce latent tracks. In an electrical conductivity cell[7] these tracks were etched to circular pores with diameters of about 100 nm. Although these diameters are in the required range, the thickness of the PC- foils exceeds the proposed pore length by far. To solve this problem a 100 nm thick layer of gold was evaporated on the front side of the foil. With appropriate beam conditions the hole pattern is preserved in the gold layer. In a second etching procedure the foil was floated on a NaOH-solution to increase the pore size in the polycarbonate while the original pore size of about 100 nm was maintained in the gold layer. In addition, a 800-1000 nm thick layer of superconducting lead was evaporated on the back side of the foil. During this process the orifice was shielded in order to avoid the intrusion of the easily diffusing lead. The resulting weak link membrane is shown schematically in fig.1.

For the planned experiments a miniaturized Helmholtz resonator, similar to the one used by Avenel et Varoquaux[2,3], was built up. It will allow a better cooling of the fluid inside the resonator which is enclosed in a cell containing the main superfluid bath (fig. 2). In the first experiments ^{4}He will be cooled down to temperatures below 20 mK by a dilution refrigerator. The resonator chamber is schematically shown in fig. 2.

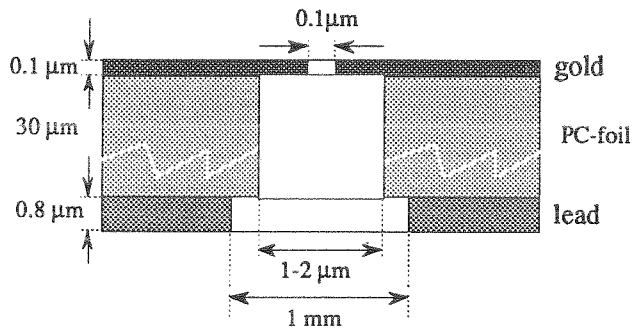


Fig. 1: The weak link membrane with an orifice of 0.1 µm diameter in a 0.1 µm thick gold layer. The figure is not to scale.

In the experiment the flow of superfluid helium through the weak link is induced by a deformation of the flexible membrane generated by an electrostatic force. This force acts between the plates of the capacitor, formed by the lead coated PC-foil and a copper plate at a distance of 30 µm. The resulting motion is detected by a superconducting coil system, which was built analogous to a superconducting accelerometer [8]. A flat coil (L_c) faces the lead side of the foil at a close distance. The moving membrane, coated with the superconductor, modulates the inductance L_c and induces a current in the signal coil of the SQUID. As soon as the critical velocity of the helium is exceeded in the aperture, phase slippage takes place and a sudden jump in the motion of the membane resulting from the dissipation of energy by the system, is observed.

Almost all parts of the setup were successfully tested. They will be assembled in the cryostat within the next month.

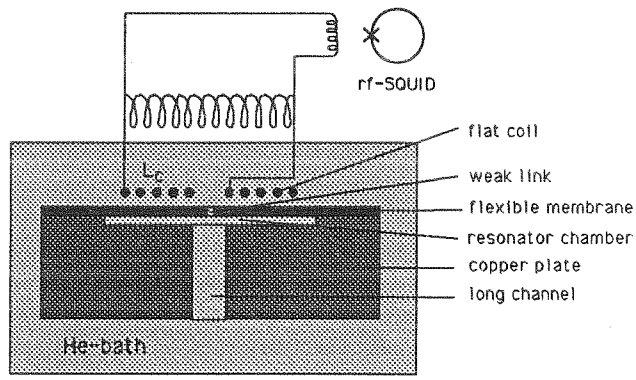


Fig. 2: Schematic view of the planned experimental setup. The resonator chamber is connected to the bath by a long channel and by the microscopic aperture in the PC-foil. The motion of the membrane is monitored by the flat coil.

Acknowledgement

We thank H. Folger for the Au and Pb evaporations.

[1] see D.R. Tilley, J. Tilley, Superfluidity and Superconductivity, Adam Ltd. Bristol (1987)
[2] O. Avenel, et al., Jap. J. App. Phys. 26-3, 1798 (1987)
[3] E. Varoquaux, et al., Physica Scripta T19, 445 (1987)
[4] J.P. Pekola, et al., J. Low Temp. Physics 67, 47 (1987)
[5] P. Sudraud, et al., J. Appl. Phys. 62, 2163(1987)
[6] B.P. Beecken, et al., J. Vac. Sci. Technol. A3, 1839 (1985)
[7] C. Trautmann, et al., GSI Scientific Report 1987, p.246
[8] H.J. Paik, J. Appl. Phys. 47, 1168 (1976)

On the Investigation of Solid Pollution Particles in the Pleisse-River (DDR), Using PVDF Nuclear Track Microfilters

E. Köber, E.-J. Langrock, B. Plisch, M. Rommel

Arbeitsgruppe Radiochemie, Sektion Naturwissenschaft, Technische Hochschule, DDR-7030 Leipzig

D. Molzahn, P. Vater, R. Brandt

Kernchemie, FB 14, Philipps-Universität, D-3550 Marburg

Nuclear Track Microfilters have found some widespread use in a variety of environmental research projects, as has been described for many years in GSI Annual Reports. Here we report on a first and very brief investigation of solid contaminants in the water of the river Pleisse, a highly polluted river in Leipzig (DDR). We used PVDF Nuclear Track Microfilters[1] and a simplified Filtration Cascade[2]. This cascade employed 3 PVDF-filters, having a diameter of 4 cm and pore sizes of 1.2, 6.5, and 7.0 µm, respectively. Our system had a flow-rate of 10^{-2} ml sec^{-1} for distilled water. It turned out, that the water from the Pleisse had to be purified with a very rough filter paper, having large openings (Filtrak 388, DDR), before it could be send through our Filtration Cascade. This rough filter was used to pre-purify 10 l of Pleisse-water. Consecutively, this filter was studied for its gamma-activity. It contained only minute amounts of natural radioactivity due to ^{226}Ra and ^{232}Th (<< 1 Bq/l). 25 ml of the pre-purified water was send through the Filtration Cascade during 24 hours, afterwards the flow-rate became practically nil.

We studied briefly the solid components collected on the surface of the second PVDF filter with the help of a scanning electron microscope (SEM) with attached energy dispersive X-ray analysis (EDXA). Typical solid particles are shown in Fig. 1. The average X-ray spectra of this area is shown in Fig. 2. A point-like EDXA investigation of the particles 1, 2, 3 as indicated in Fig. 2 revails that they consist of Na, Cl; Ca, S; and Fe, Ca, K, respectively, i.e. we could observe, most likely, sodium chloride, gypsum,...

We plan to intensify these studies - and hope to witness in the future a reduction of the amount of solid particles in the Pleisse-River.

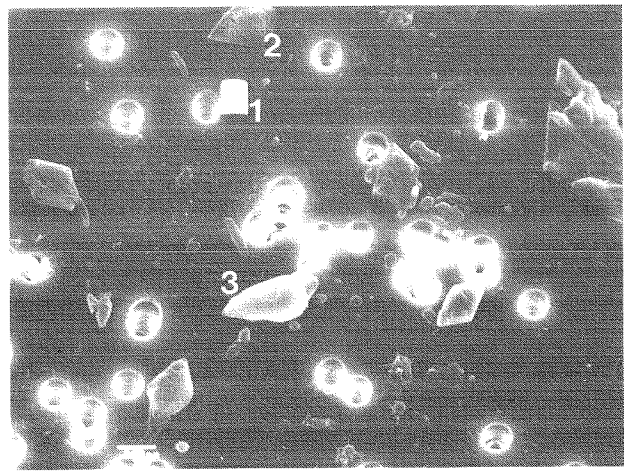


Fig. 1: SEM-picture of the second filter loaded with solid particles from the Pleisse River. The marked particles are mentioned in the text.

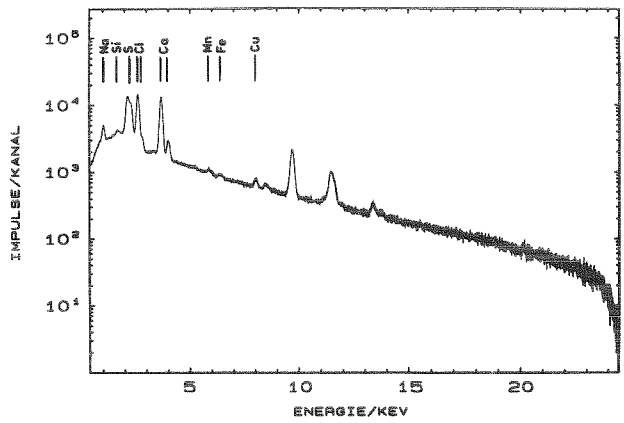


Fig. 2: X-ray spectra of the filter section shown in Fig. 1.

[1] A. Khodai-Joopary, et al., Nucl. Tracks Radiat. Meas. 15, 167 (1988)

[2] G. Tress, et al., Staub 46 , 147 (1986)

An Semi-Automatic Device for Erythrocyte Deformability Measurement with Nuclear Track Membrane

X.-H.Hao, Z.-J.Fan, S.-L.Guo, Y.-L.Wang, R.Brandt* P.Vater,* M.Ganz*.
Institute of Atomic Energy, Beijing 102413, China.
*Kernchemie, Universitat Marburg, Marburg.

The deformability of erythrocytes is an important parameter in many aspects: in the determination of their lifespan, the influence on blood flow in the peripheral circulation and the influence on viscosity of whole blood. It has also been used as one of the bases in diagnosis of some diseases, such as thrombosis, diabetes and peripheral circulation impediments.

In order to extend our research and application of nuclear track membrane to medical science, a vital instrument is required to measure the deformability of erythrocytes. Variety of devices for this purpose have been built with nuclear track membranes. Compared with the devices made by others, ours is more convenient in manipulation, precise in measurement and higher automatic in function.

The whole device consists of the following parts:(1) flow rate device composed of a track membrane and its holder and three electrodes to restrict the volume of blood sample and switch-on and - off the stop-watch ; (2) big syringe used as generator of negative pressure; (3) glass bubble of big volume (> 1 litre) as stabilizer of negative pressure; (4) glass measuring tube for negative pressure;(5) automatic / manual temperature controller with two electric heaters deployed in the upper and bottom part of the device. The whole device is kept in a box retaining constant temperature. Only 3 small holes allow the operator to syringe in the blood sample and turn - on and - off the stop - cocks with a screw driver. The full view of the device is shown in Fig.1.

Makrofol track membranes used in this device are irradiated with heavy ions from the accelerator UNILAC in GSI, Darmstadt or with fission fragments at the Heavy water Research Reactor in the Institute of Atomic Energy, Beijing, and etched in NaOH solution. The membrane has pore size 5μm, pore density $5\times10^5 cm^{-2}$ and effective area $0.8cm^2$ (total area $1.3cm^2$). The operating negative pressure can be set up to 25cm(usually 10cm) column of water. The stop-watch automatically starts and stops in recording the time in which a preset volume of sample(for example,1ml of red blood cell suspension) has passed through the membrane.The precision of time measurement is 0.1second. The adjustable operating temperature ranges from romm temperture to 40°C with long-term stability±1°C for 8 hours. The time and temperature are digitally displayed. Consecutive measurements of flow time with physiological saline show that the flow time does not change after 50times of measurements without cleaning the membrane in the course of measurements (See Fig.2). The statistics (±10.9%) shows that a higher negative pressure should be tried to improve the reproducibility of the measurement than the usual negvtive pressure 10 cm water column by others. This device will be used in testing the quality of nuclear track membranes and in medical research.

The authors thank Dr.R.Spohr and J.Vetter for their help in exposure of nuclear track membrane. This work was performed under the agreement of China - F.R.Germany Scientific Cooperation and was partly supported by the International Atomic Energy, Vienna under the contract No. 4792/RB.

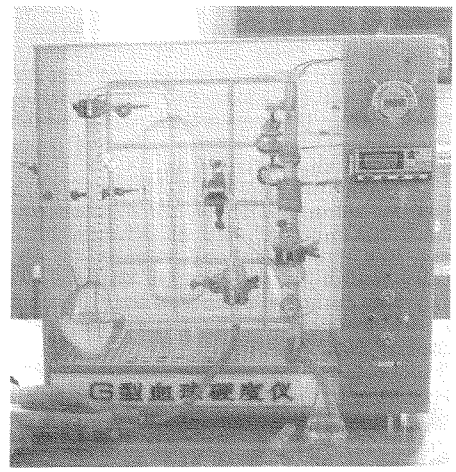


Fig.1. Fall view of the semi - Automatic Erythrocyte Deformability Measuring Device.

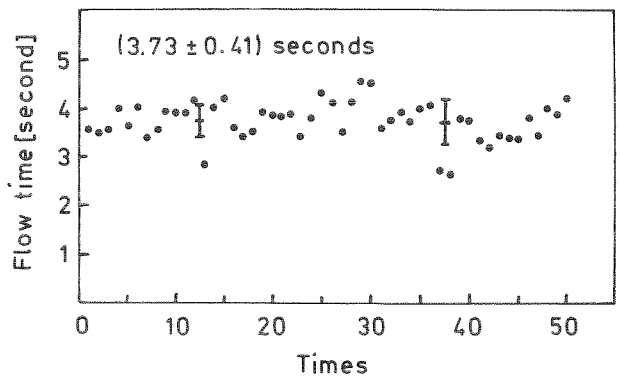


Fig.2. Reproducibility of flow time of physiological saline through the device for100 times

Determination of Solute Concentration with Nuclear Track Microfilters

S.-L.Guo, Y.-L.Wang, X.-H.Hao, T.-C.Zhu
Institute of Atomic Energy, Beijing 102413, China
H.A. Khan, G Hussain
Nuclear Engineering Division, PINSTECH, Islamabad, Pakistan
R.Brandt, P.Vater, M.Ganz
Kernchemie, FB 14, Philipps-Universität, Marburg.

Nuclear track microfilters have been used for various purposes, such as, biomedical Science, Environment study and industrial purification. Here we report a new field of application of nuclear track microfilters - determination of solute concentration in various solutions.

All liquids, in common conditions, have viscosity, which comes from the attractive force between neighbouring molecules and thermal motion of molecules in liquids. The viscosities are different for different liquids because of different composition, structure and electric distribution of the molecules.

The viscosity of a solution is different from its solvent because of the existence of solute molecules. The increment of viscosity is related to the amount of solute in the solution. Therefore, the solute concentration can be determined, in principle, by measuring the viscosity of solution.
In our previous work, we have demonstrated that the viscosity of liquid can be determined with nuclear track microfilter by measuring the flowing time of liquid through the microfilter. Therefore, we expect that the solute concentration can be determined with nuclear track microfilters.

For determination of solute concentration in a solution by using nuclear track microfilters, one should measure the ratio t/ts of the flowing time t of the solution to the flowing time ts of a standard liquid of known viscosity through the same microfilter in the same condition and calibrate the relationship of t/ts versus concentration c of the same kind of solution: $t/ts=f(c)$ as a standard curve. The standard liquid could be water having viscosity 1.006 cp..at 20°C.

For checking the feasibility and precision of this method, we have used two solutions: NaOH and alcohol in water. The nuclear track microfilters were made with Makrofol KG foil irradiated to the beam of heavy ions from UNILAC accelerator at GSI, Darmstadt and fission fragments at Heavy Water Research Reactor at the Institute of Atomic Energy, Beijing and etched chemically. The pore sizes of the filters are 7 μm and 5 μm, respectively. The results of t/ts measurements for NaOH solution are shown in Fig.1. The figure shows that t/ts for NaOH solution changes clearly with changing of the concentration of solution. It means that nuclear track microfilters can be used to determine the NaOH concentration in its solution.

Fig.2. shows the precision of the measurements of the NaOH concentration. It shows that the precision reaches to a few percent above the percentage concentration of 6% and molal concentration of 1.5M. The precision can be improved if one uses an automatic stop-watch to record the flowing time.

The method of measuring solute concentration with nuclear track microfilters can be applied to the on-line control of industrial processes and off- Line examination of product solutions.

This work was partly supported by the collaborations of the Institute of Atomic Energy (IAE), China - PINSTECH, Pakistan, China-F.R.Germany and the International Atomic Energy Agency (IAEA), Vienna under the Contract No. 4792/RB. The authors thank Dr. R.Spohr and J.Vetter for their help in irradiation of the fillter.

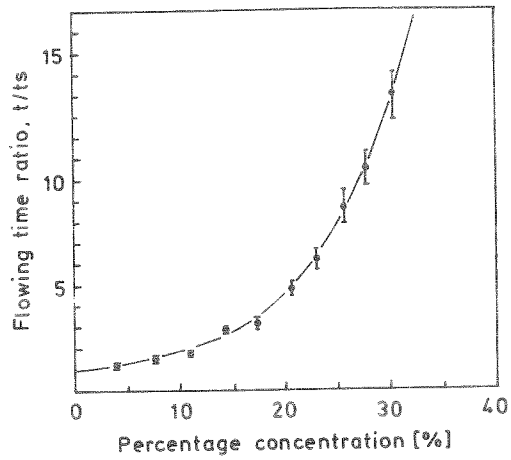


Fig.1. t/ts versus solute concentration in NaOH solution. t - flowing time of NaOH solution. ts - flowing time of water

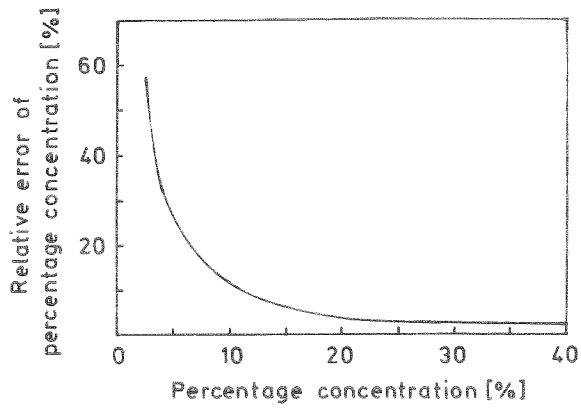


Fig.2. Precision of the measurement of NaOH solute concentration with nuclear track microfilters.

On the Purification of Certain Industrial Oils with the Help of Kapton Track Microfilters *

M. Ganz, C.D. Zhao**, P. Vater, R. Brandt
Kernchemie, FB 14, Philipps-Universität, D-3550 Marburg

Recently, we have developed track microfilters using Kapton as plastic base material[1]. The Kapton track microfilters are very resistent against heat and a large variety of aggressive chemicals[1]. These filters can be used in normal chemical operations as a tool for the separation of two different liquid phases[2]. Now we applied Kapton track microfilters for the first time for a "high-degree" purification of industrial oils used as insulators in certain high-voltage electrical units. In this case, it is quite important to have this industrial oil rather free from small solid components in order to minimize the risk of an electrical current break-through.

For this application, we use Kapton track microfilters with rather large holes, as shown in Fig. 1. The filtration was performed in a cleaned chemical filtration set-up, as shown in Fig. 2.

The oil was sent through two types of filters (d=10.1 µm and 1.5 µm) and collected in special clean glass-bottles. The contamination of the oil with solid particles was measured before and after the filtration with the help of a "Particle Measuring and Analysis System" (PMT-PAMAS). The results are shown in Table 1 (a,b).

They clearly demonstrate, that our Kapton track microfilters have purified the industrial oil quite significantly, in particular the number of relative large impurities has been reduced quite substantially. (The fact of observing sometimes a larger particle number after filtration than before teaches us to use in future experiments an even better cleaned filtration set-up).

[1] T.-C. Zhu, et al., Nucl. Tracks and Rad. Meas. 15 (1988) 771
[2] M. Ganz, et al., Nucl. Tracks and Rad. Meas. 15 (1988) 799

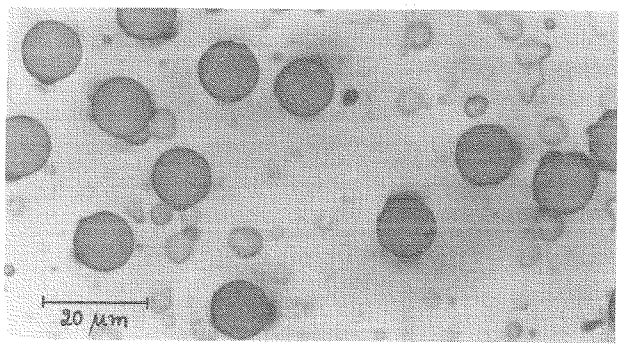


Fig. 1: Microphoto of a Kapton track microfilter having large (~ 10 µm) holes

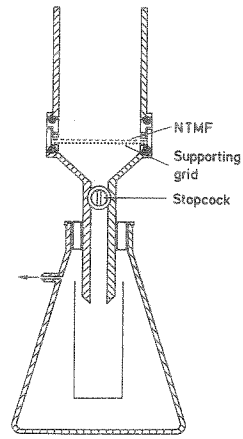


Fig. 2: Filtration apparatus to purify industrial oil with the help of Kapton track microfilters.

Table 1: Purification of industrial oil with the help of:

a) "10.1 µm Kapton track microfilter" for oil type A

size/µm	no of particles	before filtration	after filtration
d > 2.5		$15 \cdot 10^5$	$18 \cdot 10^5$
> 5		13	15
> 15		4.1	3.7
> 25		1.7	0.94
> 50		0.36	0.05
> 100		0.17	0.01
total volume of solid particles		2.13 %	0.23 %

b) "1.5 µm Kapton track microfilter" for oil type B

size/µm	no of particles	before filtration	after filtration
> 2.5		55.300	8.244
> 5		14.500	3.512
> 15		432	608
> 25		88	124
> 50		32	0
> 100		24	0
total volume of solid particles		2.93 ppm	0.21 ppm

* Kapton Track Microfilters can be obtained commercially through: Palas GmbH, Partikel- u. Lasermeßtechnik, Haid-und-Neu-Str. 7, D-7500 Karlsruhe 1

** Permanent adress: Institute of Atomic Energy, Beijing, China

Bacteria Free Drinking Water Using Kapton Particle Track Microfilters

E.U. Khan, R. Tahseen, Khalid Mansoor
Physics Department, Gomal University, D.I. Khan, Pakistan
Alam Sher, Wilayat Ahmad
Pharmacy Department, Gomal University, D.I. Khan, Pakistan
P. Vater, R. Brandt
Kernchemie, FB 14, Philipps-Universität, 3550 Marburg, F.R. Germany
Fakhruddin Durrani
University of Engineering and Technology, Peshawar, Pakistan

Water contamination has been one of the major causes of epidemiology of microbial diseases in underdeveloped and developing countries. Many chemicals and disinfectants have been tried to get drinking water free from living pathogens, but all such compounds are associated either with variable degree of toxicicity or a change in the natural composition and taste of water.

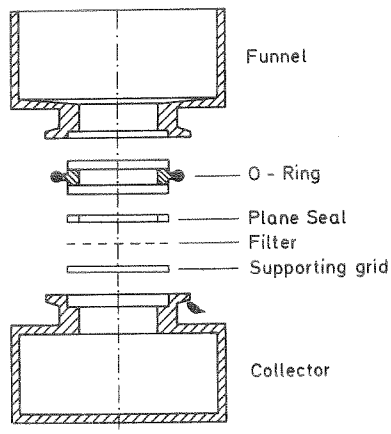
Interest has been developed to explore the physical means of purifying drinking water. The aim of the present work is to try a number of physical filters made of Kapton having various pore sizes for getting bacteria free water which will be more suitable for drinking as compared to the one treated with disinfectants.

Some work has already been reported with Particle Track Microfilters (PTMF) made of Makrofol[1,2]. We have applied Kapton PTMF[3] for this purpose. Kapton sheets were irradiated with heavy ions at GSI and etched with NaOCl-solution at 70 °C for the time required to get holes of needed size.

A simple gadget was fabricated for this experiment as shown in the Figure. Prior to experiment, whole equipment was sterilized in autoclave at 121 °C for fifteen minutes.

In the preliminary study water samples from Gomal University campus were allowed to pass through three Kapton PTMF of various hole sizes. Water was pored from input funnel which, after passing through filters, was received in collector. This water, alongwith unfiltered water (control) was applied to nutrient medium (Mac Conkey agar) and was placed in incubator alongwith nutrient itself (blank) for 48 hours for bacterial growth. Colonies were counted in each sample as shown in the Table.

The results clearly demonstrate a remarkable reduction of the number of bacteria in the filtered water, which is the better, the smaller is the hole size. To remove 100% of bacteria, filters with hole sizes smaller than 1 µm have to be used. This result is in agreement with Ref. 1 and 2.



Schematic diagram of the gadget.

[1] X. Hao et al., GSI-88-1, 257 (1988)
[2] X. Hao et al., GSI-89-1, 258 (1989)
[3] T.-C. Zhu et al., GSI-88-1, 253 (1988)

Table: Colony count of three water samples, unfiltered water (control) and nutrient (Mac Conkey agar, blank) after 48 hours of incubation. Each count is the mean of 3 replicate.

Sample	Pore size of Filters	Porosity of Filters	Dilution	Colony count
Blank	----	----	----	----
Control	----	----	10^{-3}	30
Filtrate I	1.0 µm	2.0 %	Nil	3
Filtrate II	1.5 µm	1.8 %	--do--	5
Filtrate III	3.5 µm	25.0 %	--do--	10

Isolation of Allergen-Containing Fractions from Housedust Mites Using the Cascade Particle Fractionator with Track Microfilters

C.D. Zhao*, P. Vater, R. Brandt
Kernchemie, FB 14, Philipps-University, 3550 Marburg
E. Bischoff
Gesellschaft für hausbiologische Forschung mbH, 6500 Mainz

Last year we described the use of our Cascade Particle Fractionator for the investigation of the dust in normal living rooms[1]. This dust contains also components from housedust mites (Hausstaubmilben).
The allergens which have been located in the mite excreta cause a formidable health problem to a certain fraction of our population. Therefore, the whole problem must be studied thoroughly.
We could show, that our Cascade Particle Fractionator equipped with Kapton track microfilters could be used to collect from dust in air the mites themselves (Fig. 1) and their excreta (Fig. 2)

In continuation of the investigation we tried to enrich mite excreta to be able to perform chemical experiments with them. For this purpuse housedust was suspended in water and separated into components following the principle of the Cascade Particle Fractionator:

1. Suspension of approx. 1g dust in water. Heavy silicates remain at the bottom, organic components form a suspension.
2. Filtration of the suspension through a Mica track filter having a pore size of 50 µm. Large components get isolated.
3. Further filtration of the filtrate through a Kapton track microfilter having a pore size of 8 µm. Particles smaller than 50 µm are collected on the filter surface, among them the mite excreta which have diameters of (10-30) µm. Examples of mite excreta collected on this filter are shown in Figures 3 and 4.

[1] P. Vater, et al., GSI-89-1 (1989), 256

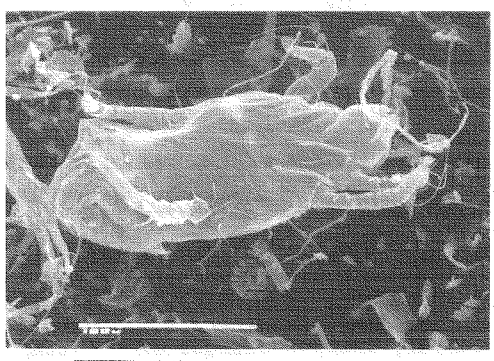


Fig. 1: A mite collected on the first filter (from air)

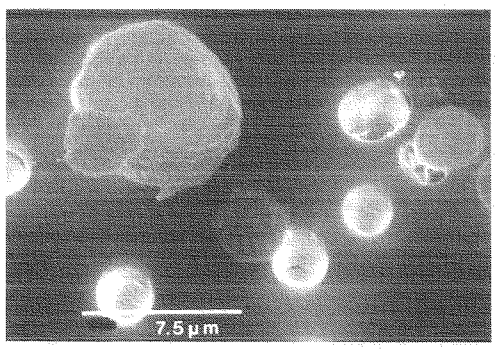


Fig. 2: Mite excreta (~10 µm) collected on the second filter (from air). The "shiny" parts are holes in the filter (d=1.5 µm)

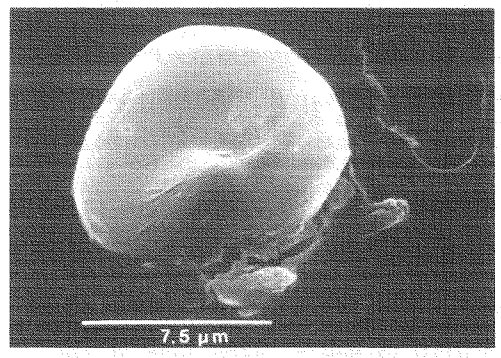


Fig. 3: Possible mite excreta removed by a Kapton filter (d~8µm) from suspension of dust in water.

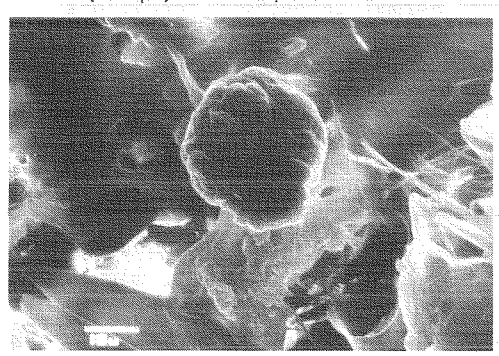


Fig. 4: Similar to Fig. 3

* Permanent address: Institute of Atomic Energy, Beijing, China

ON THE SURFACE CHARGING OF NUCLEAR TRACK FILTERS

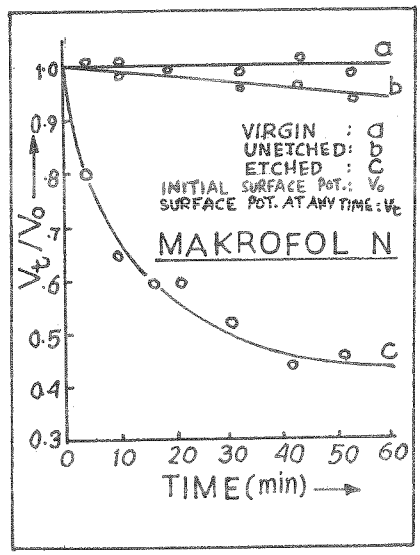
S. K. Chakarvarti and Paul Singh*
Department of Applied Physics, Regional Engineering College, Kurukshetra-132 119, India.
* Department of Chemistry and Bio-Chemistry, Haryana Agriculture University, Hissar, India.

It is well known that electric charging of fibrous and granular filters greatly improves their filtration efficiency/1/. This has found applications in personal protection in situations where a high filter efficiency is required at a low pressure drop e.g., in face masks used in dusty environment, exhaust filters in vacuum cleaners, liquid filtration, air-circulators, flue gases filtration and cleaning of non-conducting fluids/1,2/. The charged particles are captured by Coulomb forces and neutral particles by dielectric forces developed from strongly inhomogeneous electric field around these filters. Even at high gas velocity, electrically enhanced filters show a high collection efficiency because of the fact that electrostatic forces are long range forces in contrast to mechanical capture process and hence it becomes convenient to use more porous filters. While using nuclear track filters (NTFs) in areas of bio-research viz., chemotaxis diagnostic cytology, rehology, virus and protein filtration, microfiltration etc., the surface charging of membranes may also prove to be equally useful because most of the NTFs which are being put to applications are made of polymers which can easily be charged. Thus in filtration of negatively charged small organisms like endotoxins, micoplasma pyrogens and suspended particles in colloidal solutions, a positively charged filter would prove to be better than an uncharged conventional filter.

There are various methods of charging polymer surfaces. The charges can be due to built-in-charges(electret filters) or can be achieved by polarization in an external electric field. Corona charging is a convenient method and corona charged filters are bipolarly charged. In this work an attempt has been made to investigate the charge decay characteristics of corona charged NTFs of polycarbonate foil.

Circular samples of 5 cm dia. and 60 μm thick Makrofol N (Bayer AG, FRG) polycarbonate irradiated with 14 MeV/n, ^{238}U ions at the UNILAC of GSI, Darmstadt, FRG were metallized with vacuum evaporated aluminium on one face whereas the rough surfaces were corona charged in air under normal laboratory conditions using Tesla coil held at a distance of 1 cm from the samples with the polished/coated surfaces grounded. The R.H. and the room temp. were 70% and 23°C, respectively. The surface potential decay measurements were carried out at the room temperature using vibrating electrode method with field compensation/3/. The probe area of the vibrating electrode was about 3 cm^2 and the distance from probe to the sample(non-mettalized surface) NTF was 0.2 cm. The a.c. signals pickedup by the vibrating electrode were measured using a.c. microvoltmeter. Similar trials were also repeated for etched NTFs(6 N NaOH, 70°C) and unirradiated as-received virgin samples.

The following figure shows the decay curves of surface potential(normalized to the initial magnitude of the surface potential) vs time at room temperature.



It is clear from the curves (a) and (b) that the surface potential remains almost unchanged even after a period of 2 days(not shown in the figure). This may be attributed to the fact that charges are trapped in deeper traps and are not depleted at room temperature. However, this property of retaining the charges does depend upon many parameters viz., nature of the material, trapped charges depth, temp, humidity, surface conditions etc. The curve(c) for etched NTF of Makrofol N shows the almost exponential decay of surface potential with a half-life of about 50 min. Polycarbonates are tight polymers and untreated or unexposed foils store charges for a longer time. Nevertheless, a half-life of the order of 50 min is a sufficient time span during which filtration experiments can be finished.

The decay of charges is probably due to leakage from the surface to the ground via pores through walls. The choice of materials like teflon and Kapton may improve the storage properties if used as NTFs.

REFERENCES

/1/. P.H.de Haan, J.Van Turnhout and K.E.D. Wapenaar, Proc.5th Intern.Symp.Electrets, Heildeberg 1985, p.756.

/2/. D.B.Blackford and R.C.Brown, Proc.5th Intern. Symp.Electrets, Heildberg 1985, p.766.

/3/. Reedyk C.W. and M. M. Perlman, J.Electrochem. Soc. 115,49(1978).

CHEMISTRY

4. CHEMISTRY

PAGE

4.1 DEVELOPMENT OF SEPARATIONS 239

Development of Fast α-HIB Separations of Element 105 239
H.P. Zimmermann, W. Brüchle, M.K. Gober, J.V. Kratz, M. Schädel, N. Trautmann

Gaschemical Separations by Selective Desorption from Small KCl Particles 240
A. Türler, D.T. Jost, H.W. Gäggeler, A. Kovacs, W. Brüchle, H. Folger, M. Schädel, M.K. Gober, J.V. Kratz, H.P. Zimmermann

Chemical Separation of Transfer Products in the Reaction $^{22}Ne + ^{238}U$ 241
M.K. Gober, J.V. Kratz, U.W. Scherer, H.P. Zimmermann, W. Brüchle, M. Schädel, B. Schausten

The Deposition of Polonium - A Comparison of Experimental and Calculated Yields 242
M. Schädel, B. Schausten, W. Brüchle

Deposition of Polonium from Hydrofluoric- and Phosphoric Acid 243
B. Schausten, W. Brüchle, M. Schädel

Polonium Content in Hydrochloric- and Hydrofluoric Acids 244
B. Schausten, W. Brüchle, M. Schädel

4.2 CHEMICAL PROPERTIES 245

Gasphase Chemistry Experiments with Element 105 245
D.T. Jost, H.W. Gäggeler, U. Baltensperger, N.-Q. Ya, A. Türler, Ch. Lienert, K.E. Gregorich, C.M. Gannett, H.L. Hall, R.A. Henderson, D.M. Lee, J.D. Li, M.J. Nurmia, D.C. Hoffman, M. Schädel, W. Brüchle, J.V. Kratz, H.P. Zimmermann, U.W. Scherer

Elution of Lanthanides and Actinides with α-Hydroxy-Isobutyrate from Cation Exchange Columns Revisited 246
M.K. Gober, J.V. Kratz, U.W Scherer,

On the Thermoionization in Hot Cavities 247
R. Kirchner

Development of fast α-HIB Separations of Element 105 [B]

H.P. Zimmermann[1], W. Brüchle[2], M.K. Gober[1], J.V. Kratz[1], M. Schädel[2], N. Trautmann[1]

[1] Institut für Kernchemie, Universität Mainz

[2] GSI, Darmstadt

In 1988 we have studied the halide complex formation of element 105 in aqueous solutions by anion exchange separations of 34-s $^{262}_{105}$Ha relative to its homologues niobium and tantalum, and to protactinium [1]. Also, volatile bromides of $^{262}_{105}$Ha have been prepared and separated by isothermal gaschromatography [2].

In the latter experiments evidence was found for the existence of a $\sim$ 10 -s spontaneous fission (SF) activity which might be another isomer or isotope of element 105, possibly the hitherto unknown $^{263}_{105}$Ha. This activity could not be detected in the anion exchange separations because assay of the samples for α-particle and SF activity did not start before 55 s after the end of bombardment.

In order to verify the existence of such a short-lived SF activity, much faster aqueous-phase separations of element 105 and a much faster procedure for sample preparation have to be developed. To this end, we have studied elutions of pentavalent, tetravalent and trivalent metal ions from cation exchange columns in unbuffered solutions of α-hydroxy-iso-butyric acid (α-HIB). α-HIB complexes of the pentavalent group-V elements should immediately be eluted from the resin, while the interferring tetravalent group-IV elements are retained on the column. This is even more the case for the trivalent actinides. Besides providing a faster access to element 105, the method is expected to provide also an independent proof of the 5+ oxidation state of element 105 in aqueous solution, and an improved decontamination from the interferring actinides.

We have manually performed HPLC separations using the cation exchange resin Aminex A6 (particle size $17.5 \pm 2\mu m$) and tracer activities of ^{95}Zr, ^{95}Nb and ^{233}Pa produced at the Mainz TRIGA reactor. The activities were dissolved and stored in unbuffered solutions of various α-HIB concentrations. The columns (1.7×25 mm) were prewashed with solutions of the same α-HIB concentration. The tracer activities were fed onto the columns through a sample loop. Fig.1 shows the elution behaviour of the pentavalent Nb and Pa from the column in 0.075 M α-HIB at a flow rate of 1 ml/min. After the dead volume of about 130 μl ($\sim$ 7s), both activities appear in the effluent and are eluted completely within another $\sim$ 150 μl ($\sim$ 9s). The first activity of the tetravalent Zr is detected after the elution of another 3150 μl ($\sim$ 190 s). By increasing the α-HIB concentration to 0.5 M, zirconium, after the elution of Nb and Pa in 0.075 M α-HIB, can be eluted in 210 μl ($\sim$ 12 s), see Fig.1.

This separation is presently being implemented at the Automatic Rapid Chemistry Apparatus, ARCA II [3], which, itself, was subject to major mechanical improvements. First experiments were performed on the tantalum isotopes $^{168-170}$Ta produced on-line at the UNILAC accelerator, and transported by a He/KCl gas-jet transportation system to ARCA II, where they were deposited on a polyethylene frit. The dissolution of the collected tantalum activity from the frit was investigated as a function of the α-HIB concentration. Because of the smaller column size in ARCA II (1.6 x 8 mm) which might cause an earlier breakthrough of the tetravalent and trivalent metal ions it was desirable to decrease the α-HIB concentration. Even with 34 μl of 0.025 M α-HIB, dissolution of > 75 % of the collected tantalum activity was achieved within 2 s. Due to the smaller column size and to the smaller dead volume of 35 μl, the time required for the complete separation of the element 105 fraction is anticipated to be of the order of a few seconds.

In order to avoid the time consuming preparation of weightless samples for α- and SF counting by evaporation to dryness, the effluent will be eluted directly onto the surface of a large area passivated implanted planar silicon (PIPS) detector as a thin layer ($\sim$ 20 μm). Under these conditions, an energy resolution of FWHM $\simeq$ 40 keV at E_α = 8.8 MeV can be achieved [4].

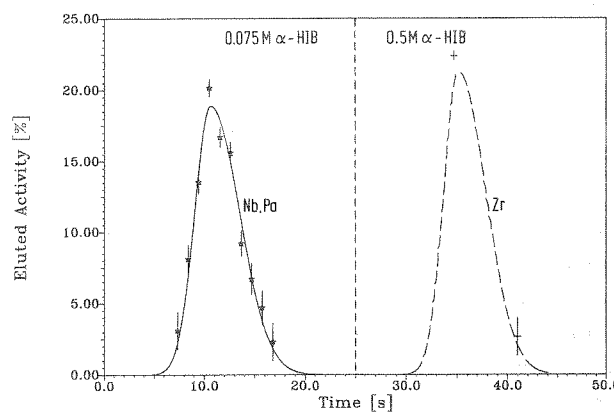


Figure 1.: Elution of Nb and Pa in 0.075 M α-HIB from a 1.7 x 25 mm cation exchange column, followed by the elution of Zr in 0.5 M α-HIB.

[1] J.V. Kratz et al., Radiochim. Acta, 48,121(1989)
[2] H. Gäggeler et al., PSI-Report Nr. 49 (1989)
[3] M. Schädel et al., Radiochim. Acta, 48,171(1989)
[4] F. Haberberger, Diploma Thesis, Mainz (1989)

Gaschemical separations by selective desorption from small KCl particles

A. Türler

Lawrence Berkeley Laboratory, Berkeley, CA

D.T. Jost, H.W. Gäggeler, A. Kovacs

Paul Scherrer Institut, Villigen, Switzerland

W. Brüchle, H. Folger, M.Schädel

GSI - Darmstadt

M. Gober, J.V. Kratz, P. Zimmermann

Institut für Kernchemie, Universität Mainz

For chemical studies of heaviest elements on-line separations in the gas-phase have proven to be very useful and fast. In recent years this technique was applied to search for superheavy elements[1] and to study chemical properties of the heavy elements Lr[2] and 105[3].

So far, the nuclides of interest were transported to the gaschemistry set-up by a gas-jet device, mostly using KCl as transporting species. In the chromatography column (usually quartz or metal) the particles containing the reaction products were stopped on a wool plug which was heated to a fixed temperature of about 1000 to 1100 ^{0}C. Volatile species evaporating from this collecting plug were then separated in a following isothermal section of the oven. Depending on the temperature of this section species of a certain volatility were passing the chromatography column and were then available for counting. For a detailed description of the entire chromatography apparatus see[2,4]. The advantage of this technique is its speed and continuous mode which allows chemical separations within a few seconds[4]. The disadvantage, however, are the rather poor chemical separation factors. Therefore, this technique was applied so far only for separations of groups of elements (as atoms or molecules) with distinctly different volatilities, e.g. in separations of highly volatile trans-actinide halides from the much less volatile actinides halides[3].

In the following we have tried to perform chemical separations using the same gaschromatography device but varying the temperature of desorption of the products from the transporting KCl particles.

A 12.5 mg/cm^2 thick La target, mounted behind a double window system of 3.4 mg/cm^2 Mo and 2 mg/cm^2 Be, was bombarded with ^{40}Ar projectiles of an incident energy of 9.2 MeV/u. This defines an energy range within the target of 8.10 to 6.26 MeV/u. According to a HIVAP calculation for this energy range mainly nuclides from the channels 7n, p7n and α4n to α7n should be produced, all with cross sections above 10 mb.

In the following we have analysed only such nuclides which are mainly produced directly, such as ^{172B}Re ($T_{1/2}$ = 15 s), ^{170}W (2.4 min) or ^{166}Ta (32 s). In addition, we also included into our chemical study ^{99m}Nb which was studied at PSI with the same set-up using its production via fission of ^{235}U at the SAPHIR reactor[4].

For all the above mentioned nuclides the desorption behaviour from small (Ø ≈ 40 nm) KCl particles was studied which were collected on a quartz wool plug. HBr and HCl were used as reactive gas. Typical gas-flow rates were 1 l/min of carrier gas (He) and 100 ml/min of reactive gas which was added to the carrier gas at the postion of the wool plug. The temperature of the isothermal part of the oven was kept at 500 ^{0}C and 600 ^{0}C, respectively, for HBr and HCl. After the column the products were thermalized, attached onto new KCl aerosols and transported along a capillary to a collecting glass fibre filter, mounted on top of a HPGe detector for γ-spectroscopy (for details see[2]).

Fig. 1 shows the result with HBr as reactive gas. 100 % desorption yield represents the maximum value of the chemical yield, which is dependent on the half-life of the nuclide[4]. Typical values for the *absolute* chemical yields are 70 % for ^{170}W and 20 % for ^{172B}Re. Easiest desorption is obtained for Re, followed by W, Nb and Ta. This sequence may be explained by the maximum oxidation states of the corresponding elements. In case of Nb and Ta, both transition elements from group V, easier desorption is observed for Nb as compared to Ta, in agreement with results from isothermal chromatography[3].

With HCl the desorption temperatures are higher than with HBr. This can be explained by a lower volatility of chlorides compared to bromides. Fig. 2 shows, as an example, the data for ^{166}Ta with HBr and HCl. Surprisingly, the desorption curve measured with HCl has a local minimum at about 750 ^{0}C. We attribute this minimum to a melting of the KCl particles (melting point 760 ^{0}C).

[1] P. Armbruster et al., Phys.Rev.Lett., *54*,406(1985)

[2] D.T. Jost et al., Inorg.Chim.Acta *146*, 255(1988)

[3] H.W. Gäggeler et al., Report PSI-49(1989)

[4] Ya Nai-Qi et al., Radiochim.Acta, *47*,1(1989)

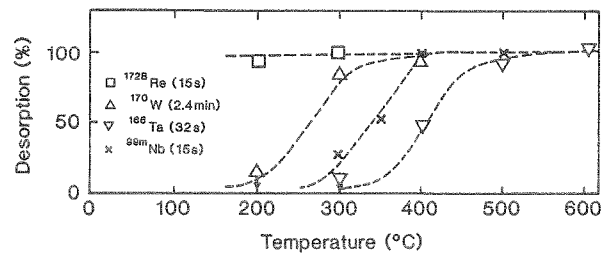


Fig.1 : Relative desorption yields for some elements from KCl particles with HBr as reactive gas.

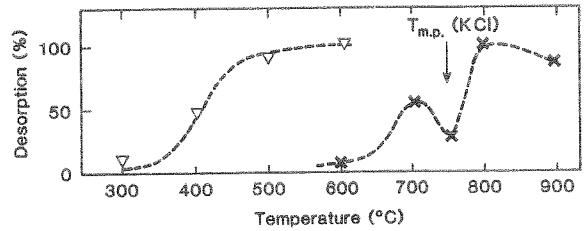


Fig.2: Relative desorption yields for ^{166}Ta from KCl with HBr (triangles) and HCl (crosses).

Chemical Separation of Transfer Products in the Reaction $^{22}Ne + ^{238}U$

M.K. Gober[1], J.V. Kratz[1,2], U.W. Scherer[3], H.P. Zimmermann[1], W. Brüchle[2], M. Schädel[2], B. Schausten[2]

[1]Institut für Kernchemie der Universität Mainz

[2]Gesellschaft für Schwerionenforschung, Darmstadt

[3] presently at Paul Scherrer-Institut, CH-5303 Würenlingen

A chemical separation procedure for the isolation of reaction products with $88 \leq Z \leq 100$ was developed to determine their production cross sections in the reaction of ^{22}Ne with ^{238}U at bombarding energies of 112 resp. 122 MeV. It was also planned to measure the transmission of ^{252}Fm through the gas filled seperator NASE. ^{252}Fm is generated in two different reaction channels:

$$^{238}U\ (^{22}Ne,\ 4n)\ ^{256}No \longrightarrow\ ^{252}Fm$$
$$^{238}U\ (^{22}Ne,\ \alpha 4n)\ ^{252}Fm$$

The excitation function for the 4n-reaction has its maximum at 112MeV and a cross section of 43nb whereas the α4n-reaction has a maximum cross section around 122MeV, while at 112MeV there is $\sigma \approx$ 50nb [1]. Moreover, there is a possibility, that ^{252}Fm is formed in transfer reactions, so that the determination of the systematics of transfer cross sections of heavy target-like reaction products is of considerable interest.

The chemical procedure is based on the one developed by Scherer for the separation of the Actinides and Ra in the $^{40}Ar + ^{233,235,238}U$ reactions. Chemical yields and purity of the different fractions were monitored by radioactive tracers chemically similar to the different elements, except for the light actinides where the yields of two previous tracer experiments where assumed, because most of the potential tracer isotopes were expected to be main reaction products.

In the experiment, a $^{238}UF_4$-target (290μg $^{238}U/cm^2$) on a 39μg carbon backing was irradiated with $^{22}Ne^{8+}$ at 500 pnA. The reaction products were collected in a Ni-catcher foil situated behind the target. Unfortunately, in the first experiment, the target was heavily damaged and partly detached from the target wheel, so that it is not possible to obtain absolute cross sections.

After the end of bombardment the catcher foil was dissolved in concentrated HNO_3, tracers and carriers were added and chemical processing was carried out. The chemical yields of the different steps were between 80 and 99%, except for the $BaCO_3$-Precipitation (30%).

Before the final samples were prepared for counting, the Transplutonium elements (TPE) were cleaned up by means of small cation-exchange columns, with an average chemical yield of 85%. Afterwards, they were electroplated on Ti-disks. The yield of electrodeposition was determined by addition of ^{177g}Lu-tracer, it was around 93%.

Pu and Th were electroplated on Ti-discs, too, but with relatively poor yields compared to the heavy actinides (Pu 70%, Th 60%).

Ra and Ac were eluted together from the HDEHP-column, the fraction was evaporated to dryness on a Ta-disc, γ-counting of the ^{133}Ba gave a yield of 100% in this step.

The samples for γ-counting (Pa - Np, Bk) were prepared by co-precipitation with $Fe(OH)_3$ as carrier and ^{177g}Lu as tracer (quantitative).

The overall chemical yields for all elements after clean-up and sample preparation are shown in the table below. Tracer isotopes and yields designated by a * are from tracer experiments.

We observed no cross contaminations due to incomplete separation. The chemical yields of Ba, Th, Pu and of the heavy actinides are still being optimized.

The fusion evaporation residue 25.4h-^{252}Fm was clearly identified by its 7.04 and 7.0MeV α-radiation. Production rates relative to the ^{252}Fm production rate of target-like transfer-products are being determined.

Element	Tracer	yield	Element	Tracer	yield
Ra	^{133}Ba	26%	Am	^{147}Nd	59%
Ac	^{140}La	85%	Cm	^{151}Pm	66%
Th	^{230}Th*	48% *	Bk	^{152g}Eu	66%
Pa	^{233}Pa*	80% *	Cf	^{153}Gd	53%
U	^{233}U *	80% *	Es	^{160}Tb	72%
Np	^{237}Np*	80% *	Fm	^{88}Y	53%
Pu	^{238}Pu*	56% *			

[1] E.D. Donets et al, Atomnaya Energiya *16*, 195 (1964)

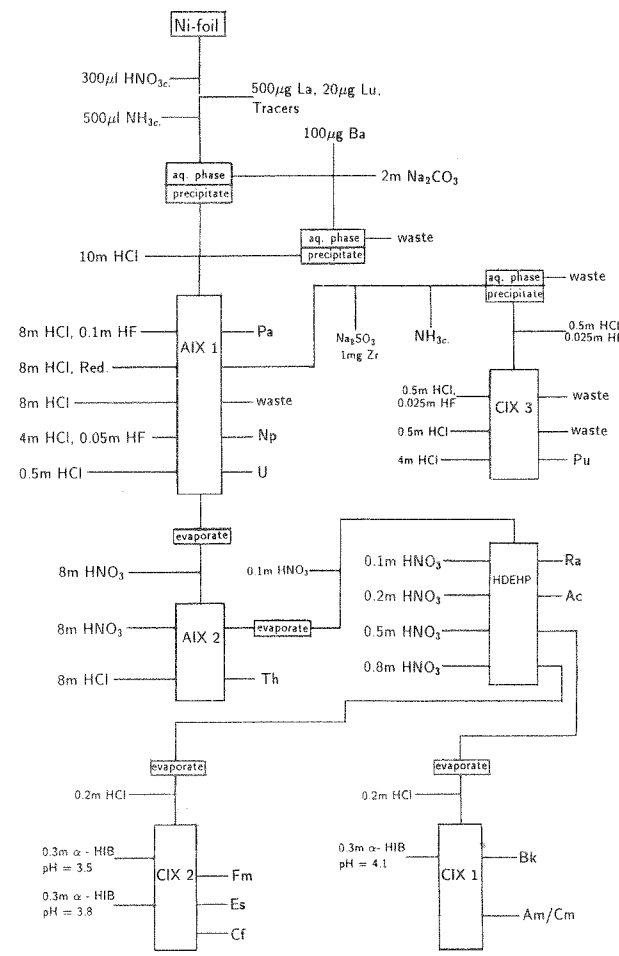


Fig. 1: Separation scheme for target-like reaction products

The Deposition of Polonium - A Comparison of Experimental and Calculated Yields

M. Schädel, B. Schausten, W. Brüchle
GSI Darmstadt

The yield of spontaneous deposition of polonium on silver has been studied[1] as a function of the volume of the solution, and of the time exposure from a hydrochloric acid solution. Fahland, Herrmann and Straßmann[2] have shown that the Nernst-Brunner equation[3]

$$y = a \times (1 - e^{-r \times t}) \qquad (1)$$

which describes the rate of diffusion through a solid-liquid interface, can also be applied to describe the deposition of carrier free isotopes. If necessary, the radioactive growth and decay have to be taken into account as an additional factor in Eq.(1). In the Nernst-Brunner equation the following terms are used:

t duration of the exposition
a number of atoms in the solution at t = 0
y number of atoms on the solid after the time t
F surface area of the exposed solid
V volume of the solution
D diffusion coefficient of the deposited material
i thickness of the interfacial film
k deposition constant
$r = k \times F/v$; $k = D/i$

From the Nernst-Brunner equation, the deposition constant, k, can be determined as:

$$k = \frac{V}{F \times t} \ln \frac{a}{a - y} \qquad (2)$$

These two equations have some nice features to check and plan experiments. The deposition constant, k, can easily be calculated for each individual experiment. Large deviations from a value which has previous by been determined for a specific reaction system and experimental set-up indicates an experimental problem. In a known system the yield of deposition can be calculated for any experimental time, and, if one has to account for radioactive decay, an optimum duration of the experiment can be calculated[2].

A comparison of calculated and experimentally determined yields of the deposition of polonium as a function of time, see Fig. 1, and volume, see Fig. 2, is given below. Details of experimental conditions of the Po deposition on silver from the buffered hydrochlorid acid solution are given in Ref. 1. The good agreement between the calculated and experimental values which can be observed from Figs 1 and 2 provides the confidence to apply the method to a search for Po on very low levels in solutions like laboratory reagents for example[4]. It has been shown that the concentration of the Po in the solution between 10^8 and 40 atoms does not influence the rate and yield of the deposition[5,6].

1. M. Schädel, B. Schausten, W. Brüchle, W. Weber, Scientific Report 1988, GSI 89-1 (1989) p. 265
2. J. Fahland, G. Herrmann, F. Straßmann, J. Inorg. Nucl. Chem. 7, 201 (1958)
3. E. Brunner, Z. Phys. Chem. 47, 56 (1904)
4. B. Schausten, M. Schädel, W. Brüchle, contribution to this annual report
5. F.-J. Reischmann, N. Trautmann, G. Herrmann, Radiochim. Acta 36, 139 (1984)
6. F.-J. Reischmann, B. Rumler, N. Trautmann, G. Herrmann, Radiochim. Acta 39, 185 (1986)

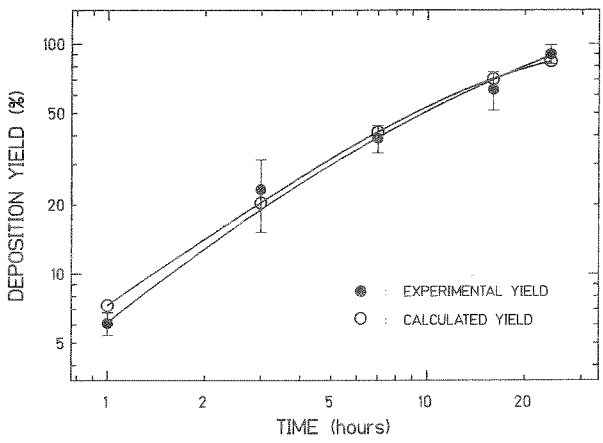


Fig.1:
Comparison of calculated and experimental deposition yields of Po as a function of the exposition time. The error bars represent one standard deviation.

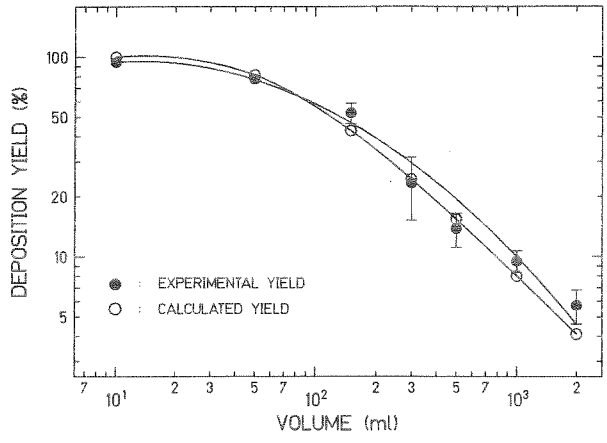


Fig.2:
Comparison of calculated and experimental deposition yields of Po as a function of the volume of the solution.

Deposition of Polonium from Hydrofluoric- and Phosphoric Acid

B. Schausten, W. Brüchle, M. Schädel
GSI Darmstadt

Our first studies to determine the deposition yield of polonium from hydrochloric acid[1] was motivated by the upcoming needs to determine small amounts of α-radioactive impurities in chemicals which are used to fabricate high density random access memories. The α-particle from the radioactive decay looses energy in the silicon and generates particle-hole pairs. As a result the bit state in the memory cell can be upset and altered, a so called soft error[2] occurs.

In producing semiconductors hydrofluoric- and phosphoric acid are commonly used reagents, and therefore we began to include these acids into our investigations. In this first step we again wanted to find out by using ^{210}Po tracer activities how applicable the method of spontaneous deposition from these acids is. To measure the deposition yields as a function of the volume of the solution and the exposure time have been the first goals of our investigation.

We have used the same procedure as described in the previous report[1] to buffer the acids and to prepare the solution for the polonium deposition on a silver plate. Slightly different absolute quantities of the various reagents have been used to adapt for the different acidities. The pH of the solution at the time of the beginning of the deposition, which is known to be an important parameter, was between 4.5 and 5. The solution was kept at boiling temperature under reflux conditions for the time of exposure. For the hydrofluoric acid a chemically inert Teflon destillation flask was used to avoid reaction with the glass walls.

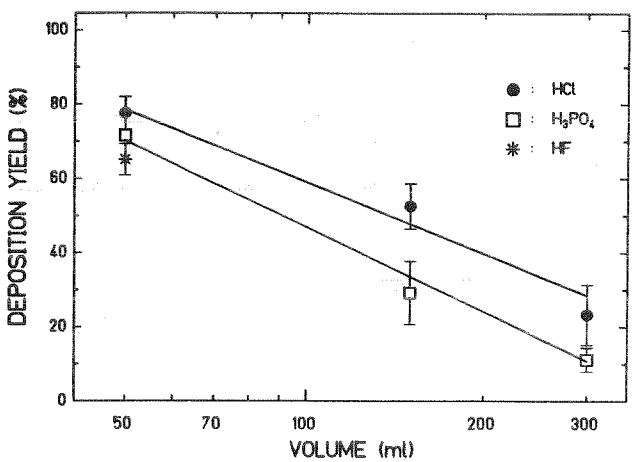


Fig. 1:
Yield of ^{210}Po deposition from hydrochloric- and phosphoric acid on silver as a function of volume. The curves represent fits to the data. The error bars of one standard deviation are given. One data point for hydrofluoric acid is shown at 50 ml.

The volume dependence of the deposition yield of the phosphoric acid in comparison with the data for hydrochloric acid is shown in Fig. 1 together with one data point for hydrofluoric acid. The plating time in all of these experiments was three hours. Because of instrumental limitations presently only one data point with a yield of 65% at a volume of 50 ml is available for the hydrofluoric acid. The deposition yield of polonium from hydrofluoric acid can be increased from 65% to 91% by increasing the plating time from three hours to seven hours. This is in good agreement with the time dependence observed for hydrochloric acid in earlier experiments. The yields are high and reproducible enough to use this method of spontaneous deposition of polonium on silver also for hydrofluoric- and phosphoric acid.

From our discussion of the Nernst-Brunner equation in a separate contribution to this report[3] we can expect to find different absolute yields for phosphoric acid, and also hydrofluoric acid, as compared with hydrochloric acid for a fixed time and volume. This is because of the presence of, most likely, different diffusion coefficients and thicknesses of the interface film at the solid-liquid interface. For the volume dependence of the deposition yields all acids should exhibit the same slope of a straight line in a semi-logarithmic presentation. Within the error bars this behaviour can be observed in Fig. 1 from a comparison of the hydrochloric- and phosphoric acid data. The result of the tracer studies with hydrofluoric- and phosphoric acid makes us confident that the spontaneous deposition of polonium on silver is a very useful method to determine small amounts of polonium impurities in these reagents.

1. M. Schädel, B. Schausten, W. Brüchle, GSI Scientific Report 1988, GSI 89-1 (1989) p. 265
2. T.C. May, M.H. Woods, 16th Ann. Proc. Reliability Physics 1978 (Symp. San Diego) 16, p. 33
3. M. Schädel, B. Schausten, W. Brüchle, contribution to this report

Polonium Content in Hydrochloric - and Hydrofluoric Acids

B. Schausten, W. Brüchle, M. Schädel
GSI Darmstadt

The search for trace amounts of polonium as a source of alpha radioactivity in laboratory reagents was stimulated by the discussion about soft errors [1] in high density random access memories.

The spontaneous deposition of polonium from buffered acid solutions on a silver foil is an establish method [2] for simultaneously separating the polonium and preparing a good sample for α-spectroscopy. From our parameter studies [3,4] and a comparison of experimental and calculated yields [5], we have determined conditions for a routine polonium deposition procedure.

The preparation of the solution is described in Ref. 3. For the hydrochloric acid we used a total volume of 300 ml and a deposition time of 24 hours at boiling point temperature. From the previous tracer experiments [3], we expect a deposition yield of 90% under these conditions. Because of the need to use a chemically inert Teflon apparatus with the hydrofluoric acid only a smaller total volume of 50 ml has been applied for this solution. With such a small volume a deposition yield of 91% can be obtained during an exposure time of seven hours [4]. The concentration of the initially applied hydrochloric - and hydrofluoric acid in this final plating solution was 12.3% and 16.0%, respectively. Each sample has been measured for 24 h with a Au(Si) surface barrier detector with a 36% efficiency. A typical spectrum of such a measurement is shown in Fig. 1.

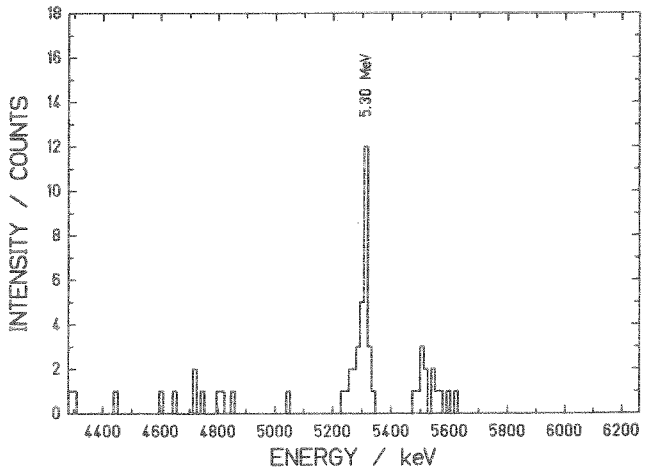


Fig. 1:
Alpha spectrum of ^{210}Po from a hydrofluoric acid solution. The observed activity corresponds to a polonium content of 2×10^{-18} mol/l in the solution.

Above the peak of ^{210}Po at 5.30 MeV with a total intensity of 30 counts a few events between 5.5 and 5,6 MeV from a calibration source can be seen. The background for this specific detector and counting chamber in the energy window 5.2 to 5.4 MeV, which has been used as integration limits for ^{210}Po, was three counts per day. A background of three alphas per day corresponds to a detection limit of about 1×10^{3} Bequerel ^{210}Po per liter or, in different units, 2.5×10^{-20} mol/l for a sample prepared from 300 ml hydrochloric acid solution.

We have started a series of first experiments to determine the ^{210}Po content in commercially available hydrochloric- and hydrofluoric acids of various concentrations and specified purities from various suppliers. The experiments are still in progress, and presently only first preliminary results can be reported.

Hydrochloric acids from three different companies with the specified purities 'technical pure', 'chemically pure', 'extra pure', 'Suprapur' and 'pro analysi' have been assayed. No significant differences, which means deviations of less than one order in magnitude, in the content of ^{210}Po were found in these solutions. On an average the observed activity in the hydrochloric acid has been about 1×10^{-2} Bq/l which corresponds to 3×10^{-19} mol/l. The ^{210}Po content in the hydrofluoric acid has been significantly higher. Again reagents from three different companies with similar specifications of the purities as for the hydrochloric acids has been investigated. The average observed activity was 1×10^{-1} Bq/l or 3×10^{-18} mol/l with an indication for slightly larger deviations of the polonium content between the individual solutions as compared with the hydrochloric acid.

1. T.C. May, M.H. Woods, 16th Ann. Proc. Reliability Physics 1978 (Symp. San Diego) 16, p.33
2. P.E. Figgins. The Radiochemistry of Polonium, NAS-NS 3037, 1961, p. 29
3. M. Schädel, B. Schausten, W. Brüchle, GSI Scientific Report 1988, GSI 89-1 (1989) p. 265
4. B. Schausten, W. Brüchle, M. Schädel, contribution to this report
5. M. Schädel, B. Schausten, W. Brüchle, contribution to this report

Gasphase chemistry experiments with element 105

D.T. Jost, H.W. Gäggeler, U. Baltensperger, Nai-qi Ya; *Paul Scherrer Institut, Villingen, Switzerland*
A. Türler, Ch. Lienert; *Institut für anorganische Chemie, Universität Bern, Switzerland*
K.E. Gregorich, C.M. Gannett, H.L. Hall, R.A. Henderson, D.M. Lee, J.D. Li, M.J. Nurmia, D.C. Hoffman; *LBL, Berkeley*
M. Schädel, W. Brüchle; *GSI Darmstadt*
J.V. Kratz, H.P. Zimmermann, U.W. Scherer; *Institut für Kernchemie, Universität Mainz*

Element 105 is (hahnium (Ha) or nilsbohrium (Ns) depending on the claim of its discovery) so far the heaviest element whose chemical properties have been investigated. Early work on the gas-phase chemistry by Zvara [1] indicated that it behaves similar to a group V element. We have investigated the formation and volatility of the $HaBr_5$ compound using on-line gaschromatography.

The experiments were performed with ^{262}Ha ($T_{1/2}$=35s), produced in the reaction ^{249}Bk(^{18}O,5n) at the 88"-cyclotron at LBL. The gas-jet technique and a gaschromatography set-up similar to the one used in previous experiments [2,3] were employed. The LBL MG-wheel counting device with an 18 second stepping time was used to detect alpha- and fission- events. Pairs of CANBERRA PIPS (passivated ionimplanted planar silicon) detectors were installed in 6 counting positions giving a total counting time of 108 s after the end of the collection. These PIPS detectors proved to be very resistant to the corrosive gases used. Spectroscopic data was recorded event by event. An analysis of all data accumulated in runs using HBr/BBr_3 and temperatures from 300 to 500 ^{0}C give for the alpha events in the energy region of ^{262}Ha and its daughter ^{258}Lr (8.35-8.75 Mev) a half-live of 33±6 s, in good agreement with the literature. Low energy tailing from the neighboring ^{211m}Po at 8.88 Mev contributes less than 40 % giving a lower limit of 160 ^{262}Ha events.

The bromide complexes were formed by adding HBr or HBr which had passed over BBr_3 to the carrier gas at the entrance of the gaschromatograph. Figure 1 shows the chemical yield curves for the Ha and its homologous elements Nb and Ta as a function of temperature. From these curves we conclude that $HaBr_5$ is more volatile than the corresponding tantalum compound since the maximum yield is found at a lower temperature and that $NbBr_5$ is more stable than $HaBr_5$ since it can be formed without adding BBr_3 to the HBr. These findings are in contrast to the volatility sequence Nb>Ta>Ha recently published by Timochin et al. [4] who used HBr/Br_2 but in agreement with Kratz et al. [6] who showed that in aqueous solutions the hahniumhalide complexes are more like the Nb complexes than the Ta ones.

Figure 2 shows the decay analysis of the fission activity of direct catch experiments (no chemistry). A new, so far not identified fission activity with a half live of 14±4 s is clearly visible above the background from the spontaneous fission activity of long lived actinides. This same activity was also found in runs where HBr/BBr_3 was used as bromating agent whereas in runs with HBr alone it was not seen. This suggestes an origin with a similar bromide chemistry as Ha. A fission activity with the 35 s half-live of ^{262}Ha could not be identified.

According to Gregorich et al. [5] ^{262}Ha has a 50% spontaneous fission branch. Taking the above sum of 160 ^{262}Ha events an equal number of sf-events decaying with a 35s half-live should have been seen. Comparing this with 19 events observed in the first 60 seconds we find that the sf-branch is less than 25%.

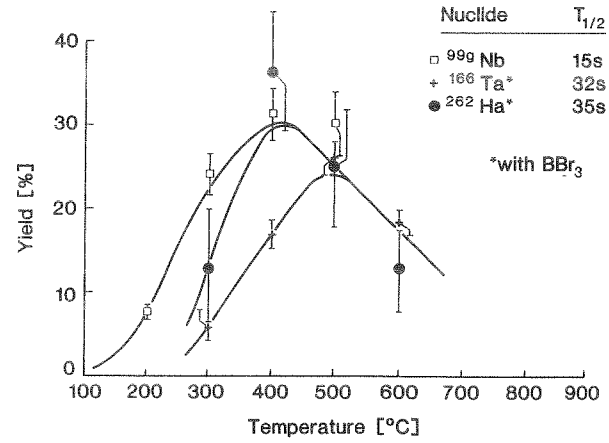


Fig.1: Chemical yields for group V elements Nb, Ta and Ha

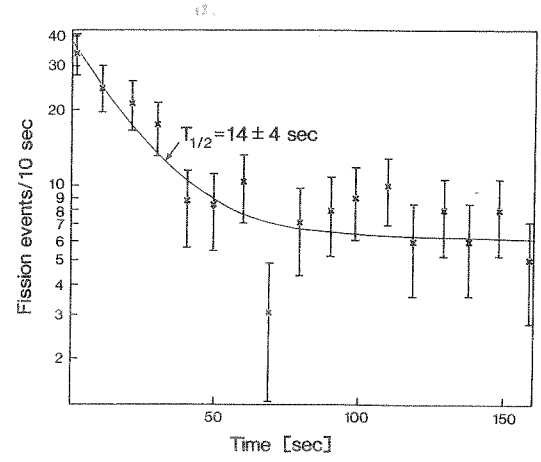


Fig.2: Decay analysis of sf-events in a direct catch experiment with 36s stepping time.

[1] I. Zvara et al., Sov. Radiochem. **18**,328(1976)
[2] D.T. Jost et al., Inorg. Chim. Acta **146**,255(1988)
[3] Nai-Qi Ya et al., Radiochim. Acta, **47**,1(1989)
[4] S.N. Timochin et al., Abstract Int. School Seminar on Heavy Ion Physics, Dubna, Oct. 3-12(1989),p. 20
[5] K. Gregorich et al., Radiochim. Acta, **43**,233(1988)
[6] J.V. Kratz et al., Radiochim. Acta **48**,121(1989)

Elution of Lanthanides and Actinides with α-Hydroxy-Isobutyrate from Cation Exchange Columns Revisited

M. K. Gober[1], J. V. Kratz[1], U. W. Scherer[2]

[1]Institut für Kernchemie der Universität Mainz, [2] presently at Paul Scherrer-Institut, CH-5303 Würenlingen

For ions of the same charge and hydration number in a given chromatographic system the logarithm of the distribution coefficient, $logK_D$, is a linear function of the ionic radius [1]. This linear correlation is expected to break down when the hydration (coordination) number CN is changed. From the measurement of diffusion coefficients for several Ln^{3+} and An^{3+} ions at 25°C it is known [2] that a change of CN from 8 to 9 occurs around Eu^{3+} in the lanthanide series and around Bk^{3+} in the actinide series with the smaller value of CN being associated with the heavier elements in both series. For higher temperatures measurements of CN are not available, and it was argued [3] that the discontinuity might then occur at lower atomic number. This should cause a temperature-dependent discontinuity in the correlation of $logK_D$ *vs.* ionic radius also in α-HIB/CIX separations. The published K_D-values for 87°C [4] and for 25°C [5] are not necessarily compatible with this proposition. Therefore, we have considered it worthwhile to remeasure systematically the elution positions of Ln^{3+} and An^{3+} ions from CIX columns with α-HIB solutions at both room temperature and 87°C.

Lanthanide tracer activities and actinides were either produced by reactor irradiations, obtained commercially, or were produced by heavy-ion bombardements. Mixtures of the tracers were dissolved in ~100μl of a 0.025M α-HIB solution and were added to our standard HPLC system through a sample loop and absorbed on top of a 2×60mm column packed with Aminex A6 cation exchange resin (particle size 17.5 ± 2μm) kept at 25°C or 87°C, respectively. They were subsequently eluted from the column with α-HIB solution. Concentration and pH of the α-HIB solutions were varied, because elution of all Ln^{3+} and An^{3+} ions with the same α-HIB would lead to poor separation of the heavy elements and unreasonably long times for eluting the lighter elements, which would elute in very broad peaks. So the lanthanides and actinides were divided in groups of up to eight elements, each group being eluted at an optimum concentration and pH of the α-HIB. The effluent was assayed for γ- and α-activity in order to determine the distribution of the lanthanide and actinide tracer activities. From the retention volumes associated with the peak maxima of the elution curves the logarithm of the distribution coefficients, $logK_D$, were determined as a function of the ionic radius [6].

As shown in fig.1, for 25°C $logK_D$ is a function of the ionic radius *and* of the negative logarithm of the α-HIB-concentration, pL. The resulting plain has a discontinuity caused by the change of CN and is twisted because the slope of the function $logK_D$ *vs.* r_{ion} is dependent on the pL. The position of the discontinuity also varies: with rising α-HIB concentration it is drifting towards bigger ionic radii. At 87°C the situation is similar (fig.2), but the break in the linear correlation of $logK_D$ *vs.* r_{ion} seems to occur at smaller ionic radii. This explains why the comparision of elution data for the two temperatures obtained at different pL's as in [7] is misleading because here the discontinuity occurs in the same range of ionic radii only by chance [8].

Figure 1

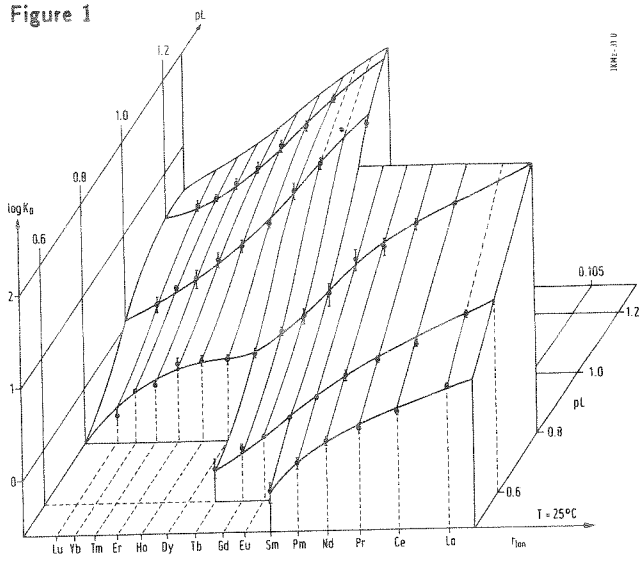
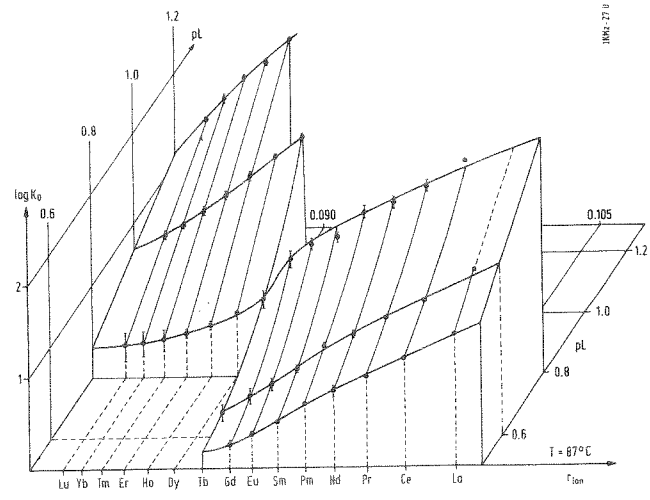


Figure 2



References

[1] Y. Marcus, A.S. Kertes, Ion Exchange and Solvent Extraction of Metal Complexes, Wiley,1969, p. 287

[2] F. David, J. of the Less Common Metals 121,27 (1986)

[3] F. David, private communication

[4] G. H. Higgins, 'The Radiochemistry of the Transcurium Elements', U.S. NAS-NS-3031,1960

[5] H.L. Smith, D.C. Hoffman, J. Inorg. Nucl. Chem., 3, 243 (1956)

[6] D. H. Templeton, C. H. Dauben, JACS 76, 5237 (1954)

[7] M.K. Gober, J.V. Kratz, U.W. Scherer, GSI-Jahresbericht 1988

[8] M.K. Gober, Diplomarbeit, Mainz 1989, p. 51

On the Thermoionization in Hot Cavities

R. Kirchner
GSI Darmstadt

Thermally equilibrated gases of low pressure are characterized by a high degree of ionization at temperatures easily reached with laboratory devices. This property is generally believed to be the principle behind ion sources of the hot-cavity-type, in which a quasi-neutral plasma is formed due to an ambipolar flux of glow electrons and surface-ionized particles from the wall into the volume of the enclosure. In the typical application for isotope separation on-line, where the ions are dominantly due to the vapour of the cavity material including impurities, the electron flux exceeds by far the flux of ions, giving the plasma the character of an ion trough.

If the resulting ensemble were in thermal equilibrium (an assumption in general tacitly made), one would expect the ionization efficiency to increase with decreasing plasma density, but to be **not** (or in a wide range not) dependent on the pressure of the neutral particles, the temperature and the material of the cavity. Detailed investigations, however, have shown[1] that this situation is practically reversed for a realistic cavity ionizer operated at low particle densities, in which the thermalization of the ions is hardly possible. Then the ionization efficiency is in a wide range only little dependent of the plasma density, whilst work function ψ and temperature T of the cavity surfaces (see table) and the density of the neutral particles (figs. 1 and 2) become of decisive significance.

For both these controversal situations the ionization efficiency η_Z of a particular trace element Z is described by the equation

$$\eta_Z = \beta_Z N/\{1 - \beta_Z(1 - N)\} \quad \text{with} \tag{1}$$

$$\beta_Z/(1 - \beta_Z) = \exp\{(\psi - W^*_{iZ})/kT\}, \tag{2}$$

β_Z being the surface ionization efficiency. In case of thermoequilibrium, the amplification factor $N = \exp(-e\Phi_p/kT)$ is quantitatively defined by the plasma potential Φ_p, in case of non-equilibrium phenomenologically described by $N = \omega\kappa$. κ is the mean number of wall collisions of atoms in the enclosure (typically $\approx$ 700) and ω the probability that a surface-ionized particle leaves the cavity as an ion. This probability is measured to be of the order of 0.1-0.2 at low particle densities; values close to unity are reached for neutral densities so high, that mean free path of ions λ_i and cavity dimensions become comparable (figs. 1 and 2). Then a surface-ionized particle can easily loose its excessive energy gained in the plasma boundary sheath and become confined in the volume, instead of falling through the potential trough and recombine at the opposite wall.

Cavity material	ψ [eV]	T [K]	η(Sr) [%]	η(U) [%]	η(Pb) [%]
Re	$\approx$5	2600	-	15 ± 3	-
Re	$\approx$5	2740	-	23 ± 4	0.3 ± 0.05
Re	$\approx$5	2850	82 ± 13	39 ± 6	0.6 ± 0.1
W	4.52	2850	70 ± 11	15 ± 3	0.2 ± 0.03
Ta	4.25	2850	58 ± 9	4.5 ± 07	0.1 ± 0.02

Measured ionization efficiencies of strontium (W^*_{iZ} = 5.5eV), uranium (6.1eV) and lead (7.3eV) as function of cavity material and temperature.

1. R. Kirchner, submitted to Nucl. Instr. Meth. A

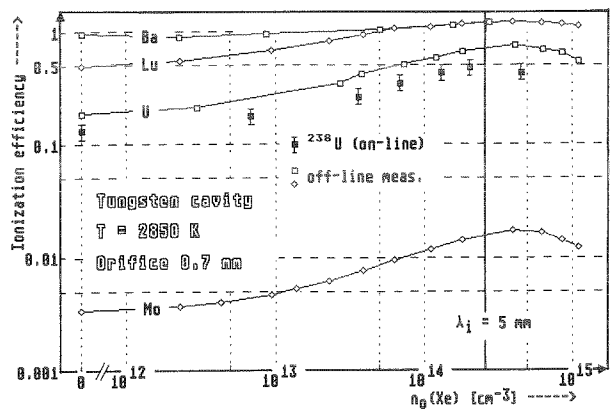


Fig. 1. Ionization efficiencies for various trace elements as function of the neutral density, which is varied and determined by feeding known fluxes of xenon into the cavity. The on-line data were measured using UNILAC beam particles as tracer. Off-line measurements were performed with a cavity contaminated with unknown traces of the chosen elements and thus reveal only the relative dependence; to give the dependence also in these cases in absolute scale, the values for $n_0(Xe) = 0$ are adjusted according to the N = 150-curve in fig. 2. This residual density of neutral particles due to impurities and vapour of the ionizer material is estimated to $5 \times 10^{10}/cm^3$.

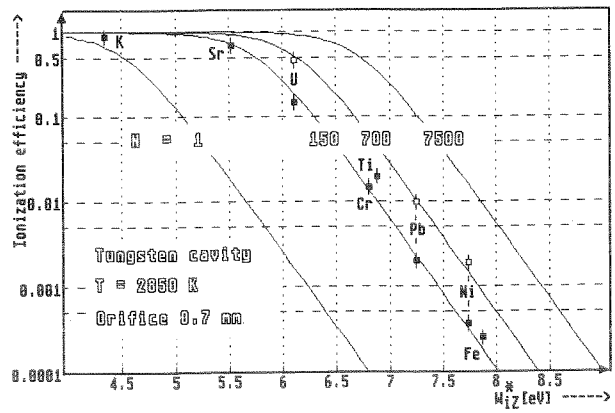


Fig. 2. Ionization efficiencies of various trace elements versus the effective ionization potential W^*_{iZ}, measured in low-pressure operation (full points) or with a xenon density of $\approx 5 \times 10^{14}/cm^3$ (open points). Curves are calculated according to eq. (1) assuming N = 1 (surface ionization efficiency) and N = 150 (exponential fit to full points). The good agreement of the open points with N = 700 indicates that here the wall recombination of particles - once surface-ionized - is effectively suppressed ($\omega \approx 1$). N = 7500, the thermoequilibrium-case, is clearly ruled out.

DEVELOPMENTS

5. DEVELOPMENTS

PAGE

5.1 EXPERIMENTAL SET-UPS FOR SIS AND ESR

255

The Projectile-Fragment Separator Project 255/256
H. Geissel, P. Armbruster, K.-H. Behr, B. Blank, Th. Brohm, A. Brünle, H.-G.Burkard, K.-H. Burkard, M. Chen, H.-G. Clerc, J.-P. Dufour, F. Feuerstrack, H. Folger, B. Franczak, J.J. Gaimard, E. Hanelt, R. Kirchner, O. Klepper, B. Knödler, B. Langenbeck, G. Moritz, F. Nickel, K. Poppensieker, M.S. Pravikoff, M. Pfützner, E. Roeckl, K. Rykaczewski, D. Schardt, K.-H. Schmidt, H.J. Schött, H. Stelzer, Th. Schwab, B. Sherrill, M. Steiner, K. Sümmerer, B. Voss, M. Weber, J. Weckenmann, H. Wollnik, G. Münzenberg

Development of Beam-Profile Monitors with Gas Amplification and Current Readout for the SIS Projectile-Fragment Separator 257
R. Anne, C. Bruske, K. Burkard, M. Fradj, H. Geissel, Y. Georget, R. Hue, R. Johänntges, R. Kirchner, A.C. Müller, E. Roeckl, J. Rasmusson, K. Rykaczewski, M. Weber

The Universal Energy Degrader System for the Fragment Separator 258
E. Hanelt, J. Weckenmann, K.-H. Schmidt, H.-G. Clerc, H. Folger,

On the Energy-Loss Mode of the FRS - An Experiment Using The Energy-Loss Spectrometer SPEG 259
H. Geissel, Th. Schwab, P. Armbruster, A. Gillibert, W. Mittig, R.E. Olson, K.B. Winterbon, H. Wollnik, G. Münzenberg

Precise Energy-Angle Measurements Performed with the High-Resolution Spectrometer SPEG at GANIL 260
Th. Schwab, H. Geissel, P. Armbruster, A. Gillibert, W. Mittig, R.E. Olson, K.B. Winterbon, H. Wollnik, G. Münzenberg

Direct Mass Measurement of Exotic Nuclei at the ESR 261
K. Balog, Y. Fujita, H. Geissel, K. Lindemann, K.E.G. Löbner, G. Münzenberg, H. Seifert, J. Schnell, T. Schwab, J. Trötscher, D. Vieira, Th. Winkelmann, H. Wollnik, J. Wouters

USCHI Trimmed for HDMP 262
E. Schimpf, E. Jäger, K.H. Behr, M. Schädel

Status of the 4π Detector for Charged Particles 263
The 4π Collaboration

The Central Drift Chamber of the 4π Detector 264
A. Glatz, N. Herrmann, D. Pelte, R. Schlesier, M. Trzaska, U. Winkler, H. Wolfenstetter

Present Status of the Cluster Detector for the 4π Facility at SIS/ESR 265
C. Cerruti, J.P. Coffin, I. Combes, R. Ernwein, P. Fintz, G. Guillaume, F. Hornecker, M.O. Hunzinger, F. Jundt, C.F. Maguire, R. Neunlist, F. Rami, M.A. Saettel, R. Tezkratt, B. Tischler, P. Wagner

Simulations of the Response of the Cluster Detector/Scintillator Wall for the 4π Facility at SIS/ESR Using the GEANT Detector Program 266
C. Cerruti, J.P. Coffin, P. Fintz, G. Guillaume, F. Jundt, C.F. Maguire, F. Rami, R. Tezkratt, P. Wagner

The Zero Degree Detector of the GSI-4π Facility 267
J.P. Alard, J. Augerat, N. Bastid, F. Biagi, M. Crouau, F. Daudon, P. Dupieux, L. Fraysse, S. Mayade, G. Montarou, P. Morel, M.J. Parizet, D. Qassoud, A. Rahmani, G. Savinel

Time-of-Flight System for the ALADIN Spectrometer 268
J. Hubele, P. Kreutz, A. Schüttauf, G.C. Adloff, U. Lynen, U. Milkau, J. Pochodzalla, D. Rudolf, G. Rudolf, M. Runne, H. Sann, W. Trautmann, A. Wörner

Status of L.A.N.D. 269
H. Freiesleben, J. Keller, W. Kneissl, R. König, S. Lange, Y. Leifels, R. Kulessa, E. Lubkiewicz, W. Prokopowicz, W. Walus, Th.W. Elze, S. Heerd, H. Klingler, H. Spies, K. Stelzer, P. Egelhof, H. Emling, W. Henning, R. Holzmann, G. Ickert, R. Schmidt, H.J. Wollersheim, T. Blaich, J.V. Kratz, D. Lambrecht, M. Proft

Target Detector Array for L.A.N.D. 270
B. Gugulski, R. Kulessa, E. Lubkiewicz, K. Pena, W. Prokopowicz, W. Walus, and the L.A.N.D. Collaboration

Experimental Study of Soft Coulomb Dissociation in Extremely Neutron-Rich Nuclei 271
P.G. Hansen, F. Humbert, L. Johannsen, B. Jonson, T. Nilsson, G. Nyman, A. Richter, K. Riisager, G. Schrieder, and ALADIN-, FRS- and LAND-Collaboration

γ-Ray Spectroscopy of Relativistic Exotic Fragments with Position-Sensitive Germanium Detectors 272
R. Holzmann, H. Emling, H.J. Wollersheim, and the LAND Collaboration

Status of the Photon Spectrometer TAPS 273
R.S. Simon and the TAPS Collaboration

Status Report: The Kaon Spectrometer at SIS 274
W. Ahner, P. Baltes, D. Brill, R. Brockmann, E. Grosse, W. Henning, H. Jäger, P. Koczon, B. Kohlmeyer, W. Konrad, D. Miskowiec, Ch. Müntz, H. Oeschler, K. Poppensieker, H. Pöppl, F. Pühlhofer, R. Renfordt, A. Sandoval, R. Schicker, B. Schlei, P. Senger, Y. Shin, K. Stiebing, R. Stock, H. Ströbele, K. Völkel, W. Walus

Status of the TOF-Detectors for the Kaon Spectrometer at SIS 275
B. Kohlmeyer, W. Konrad, H. Pöppl, B. Schlei, F. Pühlhofer and the Kaon Spectrometer Collaboration

Event Characterization at the Kaon Spectrometer 276
D. Brill, E. Grosse, D. Miskowiec, P. Senger, Y. Shin, R. Stock, H. Ströbele, W. Walus, and the KaoS Collaboration

A Magnetic Spectrometer for the Detection of 'Knock-On' Electrons from Heavy Ion-Atom Collisions at Relativistic Energies 277
K.E. Stiebing, J. Bernhardt, K. Bethge, A. Hausmann, D. Kraft, H. Schmidt-Böcking, H. Bokemeyer, H. Folger, E. Grosse, W. Henning, R. Mann, P. Senger, J. Ullrich, A. Balanda

5.2 DETECTORS 278

Developments in the Detectorlaboratory 278
H.W. Daues, H. Stelzer

Detector Development for the In-flight Particle Diagnostic at the FRS 279
E. Hanelt, T. Brohm, H.-G. Clerc, B. Knoedler, K.-H. Schmidt, M. Steiner, B. Voss

Residual Gas Beam Profile Monitor for SIS Beams 280
H. Berg, H. Schmidt-Böcking, J. Ullrich, R.E. Olson

Calibration of a Detector System for the Measurement of Target-Like Fragments from $^{116}Sn + {}^{48}Ti$ Reactions 281
J. Kiesewetter, K.-Th. Brinkmann, F.M. Baumann, M. Bergmann, H. Freiesleben, H. Gassel, B. Kohlmeyer, K.D. Hildenbrand, D. Schüll, H. Sohlbach, J. Speer

A Large-Area Multiwire Proportional Chamber for the Kaon Spectrometer 282
P. Baltes, J. Froh, H. Jäger, E. Kankeleit, Ch. Müntz, H. Oeschler, H. Stelzer, and the KaoS Collaboration

A Single Wire Readout System for Multiwire Proportional Chambers 283
J. Friese, H. Hiller, W. Wilhelm

Test of a Multiwire Proportional Chamber for VUV-Photons 284
J. Friese, H.J. Körner, J. Reinhold, K. Zeitelhack

TP-MUSIC III - A New Tracking Detector for the ALADIN Facility 285
R.J. Meijer, Z.A. Liu, J. Lühning, U. Lynen, H. Sann, W. Quick, W. Seidel

A High Pressure Xe-Filled Gas Scintillation Proportional X-Ray-Camera with Fast Timing Properties and High Compton Suppression Capability for $1s\sigma$ - MO Spectroscopy 286
V. Dangendorf, H. Schmidt-Böcking, A. Breskin, R. Chechik, I. Tserruya, P. Mokler

Test of a Subsection of the Large Area Neutron Detector at SATURNE 287
J.S. Lange, H. Freiesleben, J. Keller, W. Kneissel, R. König and the L.A.N.D. Collaboration

A Beamtracking and Particle Identification Detector System for Experiments with L.A.N.D. 288
H. Spieß, S. Heerd, H. Emling, J. Keller, K. Stelzer and the L.A.N.D. Collab.

Test of a TAPS-Sub-Array with Electrons 289
O. Schwalb, G. Enders, K. Hagel, W. Kühn, V. Metag, R. Novotny, K. Hildenbrand, W. Arnold, U. Kneissl, F. Steiper, T. Weber and the TAPS Collab.

Charged Particle Sensitivity of BaF_2 Detectors 290
A.L. Boonstra, H. Löhner, A. Raschke, L.B. Venema, H.W. Wilschut, N. Brummund, and TAPS Collaboration

The Charged Particle Veto Detector CPV for TAPS 291
N. Brummund A.L. Boonstra, H. Löhner, A. Raschke, L.B. Venema, H.W. Wilschut, and TAPS Collaboration

Response Function of a TAPS-Subarray to High Energy Photons 292
M. Appenheimer, W. Kühn, V. Metag, R. Novotny, M. Pfeiffer, A. Baumann, J. Peise M. Schmitz, A.L. Boonstra, H.W. Wilschut and TAPS Collaboration

A Scintillation Counter for High Energy Electrons 293
M. Rhein, Ch. Müntz, W. Arnold, U. Kneissl, Th. Fromhold, R. Göbel

Heavy Ion Detection with a Plastic Scintillator Photodiode Array at the TORI-Spectrometer 294
I. Schall, E. Kankeleit, H. Oeschler, M. Rhein

Detector System for the Z- 110 Experiment 295
S. Hofmann

A Silicon Detector Array for the Investigation of Proton- and Alpha Radioactivity 296
T. Faestermann, A. Gillitzer, F. Heine, M. Köpf, W. Wagner

A Multi Detector Array of PIN Diodes 297
J. Friese, H.J. Körner, C. Schießl, W. Wagner

Calorimetric Cryo-Detectors for Heavy Ions 298
V. Trübenbacher, P. Egelhof, W. Henning, A. v. Kienlin, J. Meier, F. Azgui, K. Shepard

Physical Properties and Transverse Profiles of Electron Showers in Pb/SciFi Calorimeters 299
M. Bahr, F. Berger, G. Clewing, R. Glasow, H.A. Gustafsson, H.H. Gutbrod, D.W. Hertzog, G. Hölker, S.A. Hughes, J. Idh, K.H. Kampert, M. Purschke, R. Santo, R. Schmidt, P. Viyogi

A Multi-PPAC System for the Detection of Reaction Products from Dissipative Very Heavy Ion-Atom Collisions 300
K.E. Stiebing, D. Kraft, K. Bethge, R. Rüschmann, R. Staudte, M. Dahlinger, J. Stroth, H. Backe, P. Kosmadakis, H. Bokemeyer, P. Senger

Dependence of Partially Annealed Volume Tracks on Track Orientation 301
R. Dersch, C.D. Zhao, E.U. Khan, P. Vater, R. Brandt, V.P. Perelygin, S.G. Stetsenko

5.3 DATA ACQUISITION 302

Experimental Electronics Department (Elektronik/Experimente) 302
R. Albrecht, J. Dengler, G. Eidmann, H.G. Essel, R. Fritzsche, H. Hammal, H. Hardel, J. Hoffmann, H.P. Liebold, A. Loos, H.-G. Martens, W. Meufels, K. Mömerzheim, A. Muhn K. Poppensieker, A. Przybyla, D. Quis, M. Richter, D. Schall, H.-G. Schmidt, R. Schulze, H. Sohlbach, W. Spreng, E. Sturm, T. Batsch

Electronic Support for the SIS/ESR Experiments 303
R. Albrecht, H. Hammal, A. Muhn

GOOSY, the Acquisition and Analysis System for Experimental Data 304
H.G. Essel, R. Fritzsche, U. Post, M. Richter, D. Schall, W. Spreng

Computerized Control Systems for Experiments 305
H.G. Martens, W. Meufels, K. Poppensieker

Status of the VME-based Data Acquisition System Interfacing of CAMAC and FASTBUS Systems to VSB 306
J. Hoffmann, M. Richter, D. Schall, H. Sohlbach

Frontend Software in the VME-based Data Acquisition System 307
W. Ahner, H.G. Essel, U. Post, D. Schall, W. Spreng

Ethernet Communication Software for VSM and OS9 308
H.G. Essel, R. Fritzsche, D. Schall

Online Computers and Ethernet at GSI 309
H.G. Essel, R. Fritzsche, M. Meufels, M. Richter, H.-G. Schmidt

AI-based Telecom Equipment Management ATEM 310
M. Richter

Acquisition, Analysis and Control Software for the Experiments in CAVE B 311/312
T. Blaich, R. Freifelder, N. Herrmann, J.G. Keller, P. Koczon, M. Krämer, Y. Leifels, V. Lindenstruth, W.F.J. Müller, R. Schmidt, K. Teh

Development of a Fast Software Trigger for η-Detection 313
F.-D. Berg, W. Kühn, V. Metag, S. Rieß, and TAPS Collaboration

Algorithms for Automatic Streamer Chamber Data Analysis: Inter-View Track Assignment and Reconstruction in Space 314
F. Pühlhofer, R. Keidel, A. Piper, and NA35 Collaboration

Data-Summary-Tape Production Using the ACP Farm 315
WA80 Collaboration

Developments for the Euroball Data Acquisition System and Electronics 316
Ch. Ender, D. Schwalm

5.4 COMPUTING CENTER 317

Computing Center 317-321
H. Egger, S. Glückert, U. Meyer, O. Siart, K. Winkelmann

Experiment Data Processing 322
H. Göringer, P. Kohn, P. Malzacher, U. Post, D. Schall, K. Winkelmann, M. Manns

Parallel FORTRAN 323
M. Krämer, K. Winkelmann, R.J. Lucas

Numerical Classification of Data under Consideration of the Physical Function Type 324
I. Giese, M. Ihorst

VENUS Library Part II and the Vectorized Interpretative Analysis 325
M. Krämer, W. Kynast, U. Post, K. Winkelmann

GIPSY - The GSI Interpreter / Preprocessor SYstem 326
W. Kynast, U. Post

A New Interactive Help System 327
A. Möller, W. Kynast

Graphics 328
I. Giese, P. Malzacher, R. Rittenhouse, C. Pinilla, E. Schindler

Telecommunications 329
U. Meyer

5.5 MASS SPECTROSCOPY, SOURCES, BEAMS AND TARGETS 330

Accelerator Mass Spectroscopy of ^{41}Ca 330
W. Henning, M. Müller, E. Roeckl, D. Schüll, A. Steinhof, J. Speer,
W. Kutschera, M. Paul

Determination of Trace Amounts of Platinum in Glasses Using Rutherford Backscattering 331
E. Stiel, G. Herrmann, J.V. Kratz, K. Lützenkirchen, M. Overbeck,
S. Polikanov, C. Sastri, N. Trautmann

Status of the Utracold Ordered Electron Beam Project 332
P. Krause, S. Zwicker, D. Habs, R. Neumann, D. Schwalm, A. Wolf

The Projectile-Fragment Separator Project [G]

H. Geissel, P. Armbruster, K.-H. Behr, B. Blank[1], Th. Brohm[1], A. Brünle, H.-G. Burkhard, K.-H. Burkard, M. Chen, H.-G. Clerc[1], J.P. Dufour[2], F. Feuerstrack[1], H. Folger, B. Franczak, J.-J. Gaimard, E. Hanelt[1], R. Kirchner, O. Klepper, B. Knödler[1], B. Langenbeck, G. Moritz, F. Nickel, K. Poppensieker, M.S. Pravikoff[2], M. Pfützner, E. Roeckl, K. Rykaczewski, D. Schardt, K.-H. Schmidt, H.J. Schött, H. Stelzer, Th. Schwab[3], B. Sherrill[4], M. Steiner[1] K. Sümmerer, B. Voss[1], M. Weber, J. Weckenmann[1], H. Wollnik[3], and G. Münzenberg

GSI Darmstadt, [1] TH Darmstadt, [2] C.E.N. Bordeaux, [3] Univ. Giessen, [4] Michigan State Univ.

The projectile-fragment separator[1,2], FRS, is a part of the new high-energy heavy-ion facilities at GSI presently in the commissioning phase. This versatile magnetic spectrometer and its different modes of operation have been described in previous GSI scientific reports and in references 1 and 2. In the following, we will give a brief status report and also the first on-line results of the commissioning experiment with the first dipole stage of the FRS carried out in January 90.
We have also performed experiments in France at SATURNE and at GANIL to gain experience for the future operation of the FRS. These experiments are described in different contributions to this report[3,4].

Installation of the first FRS stage

Since the SIS and the first FRS stage have common radiation shielding this part of the spectrometer had to be installed in the November shut-down period of the accelerator. We succeeded in the installation of the target area, the first quadrupole triplet with a hexapole magnet, and the first dipole magnet. A thick shielding wall following this dipole magnet allows now the installation of the other FRS stages indepently of the schedule of the SIS operation. Simultaneously with the construction work, we used the installed FRS stage for first test experiments in January 90. A photographic picture of this FRS section is shown in fig. 1. In the front, the vacuum system of the two target stations is shown followed by a quadrupole triplet, a hexapole and the first dipole magnet. The total length of the system is about 15 m. The vacuum of the target area is separated by a metal window (5 mg/cm^2 Ti) from the ultra-high vacuum system of the SIS. The feed-lock system with the support for the window foil can be recognized in the front part of fig.1. This device has been successfully tested in first SIS commissioning experiments with an extracted neon beam.

For the first FRS experiments a water-cooled linear target holder with 15 positions was successfully tested. Our experiments at SATURNE have demonstrated that the standard target material for isotope production cannot be ordinary carbon due to large thickness inhomogeneities[3]. We plan to measure soon the energy-loss distributions of relativistic ions penetrating through different materials to investigate this target problem.

Magnets

All the FRS dipole, quadrupole and sextupole magnets are delivered as well as the corresponding power supplies. The field measurements are done for the magnets installed and will be continued by the GSI magnet group. The new mapper system with a hall probe for three-dimensional field mapping was used for the first dipole magnet (D_1). The probe heads were temperature stabilized and calibrated with a NMR. The measured field homogeneity of D_1 is shown in fig. 2 for 1.0, 1.2, 1.4, and 1.6 T in radial direction for the midplane. The measured field homogeneity is in accordance with the design values. These measurements will yield a realistic ion-optical description of our separator including the effective lengths and the multipole components of the different magnets.

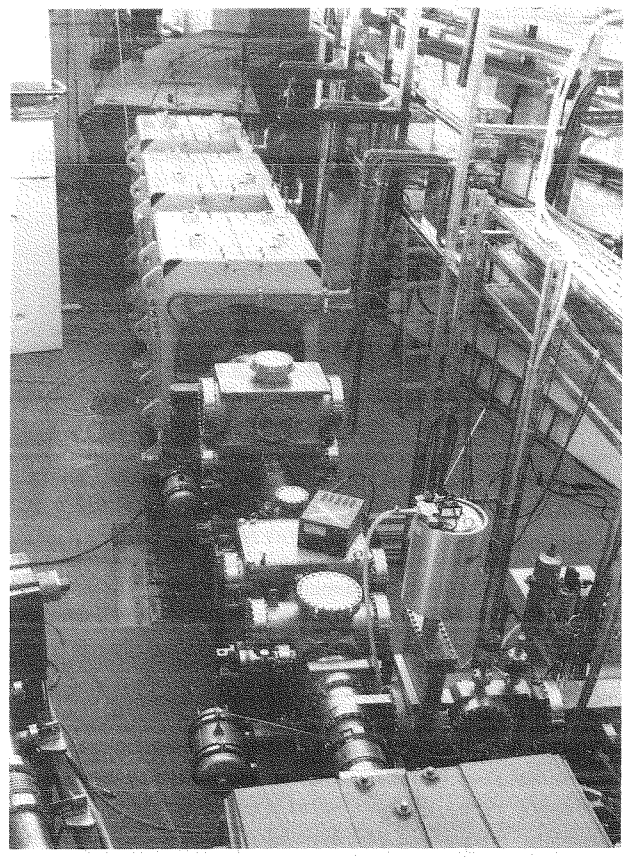


Fig. 1 : View of the target area in front of the presently-installed FRS section. The vacuum chambers for targets and diagnostic instruments and the first quadrupole triplet can be seen in front of the first dipole magnet.

Vacuum System

The FRS vacuum system was designed for a final pressure of better than 10^{-7} Torr and is separated from the ultra-high vacuum system (10^{-11} Torr) of SIS and ESR by the window mentioned above and a differential pumping section, respectively. The turbo-molecular and ionic pumping units, the gate valves and the related control units are delivered. The vacuum chambers for the target area and the chambers for three focal planes are also in house. Feedthroughs and special bellows will be available by March 90.

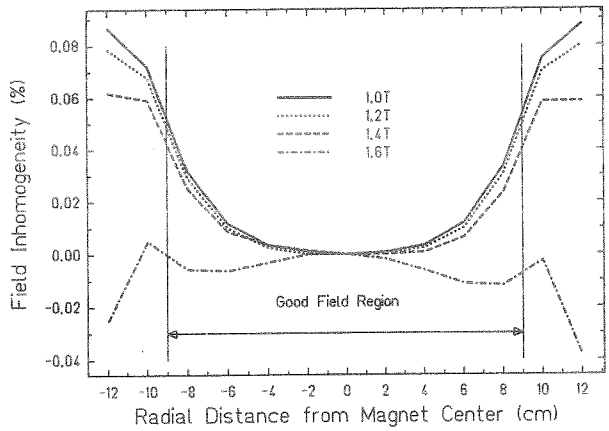


Fig. 2: Measured field homogeneity of the first FRS dipole magnet for 1.0, 1.2, 1.4, and 1.6 T. The results are shown in radial direction for a cut in the midplane.

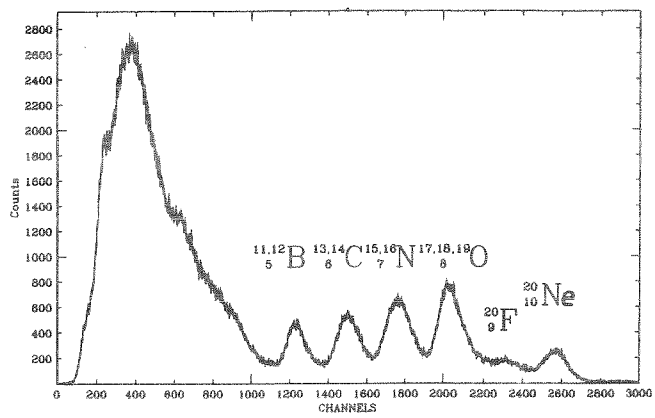


Fig. 3: Energy-loss spectrum of the first neon fragment beam of SIS - FRS produced in a 500 mg/cm^2 thick aluminum target. The fragments are analyzed by their magnetic rigidity, the Z identification is achieved by a 3 mm thick plastic scintillator[8].

Experiments with FRS in the commissioning phase

A first test run of the installed section of FRS, see fig.1, with a 150 MeV/u ^{20}Ne beam has been carried out in January 1990. The beam current was monitored by measuring the yield of secondary electrons emitted in an aluminum foil[5]. The maximum intensity was about 10^8 particles /spill. The SIS was running successfully in both the fast and resonance extraction modes, with extraction times of 1.4 μs and 500 ms, respectively. The ^{20}Ne beam was fragmented in different target materials and thicknesses. The FRS components worked reliably according to their design values which allowed to separate the fragment beams via Bρ-analysis. The current grids, designed and built by GAN-ELEC GANIL and IPN Orsay showed excellent performance[6]. They worked well for both extraction modes. The multi-wire proportional chambers, modified after the first tests at SATURNE, also worked excellently and allowed to measure for the first time the transversal emittance of the slowly extracted SIS beam. We also tested a new more homogeneous position-sensitive micro-strip detector. A MUSIC detector[7] and two scintillators[8] provided the signals for Z identification. Although the separation of the MUSIC ($\delta Z < 0.3$ charge units) was superior the energy-loss information of a 3 mm thick plastic scintillator (8 x 20 cm^2) suffices to provide a Z-identification of the neon fragments, as demonstrated in fig. 3. The magnetic fields were set on a rigidity for $^{20}Ne^{9+}$, which corresponds to the highest energy-loss peak in the spectrum. The other peaks represent fragments having the same magnetic rigidity. In other runs, we succeeded to produce ^{19}Ne beams along with ^{17}F, ^{15}O, and ^{13}N ions, the positron emitters which are most relevant for diagnostic beams[9] to measure online the implantation profile.

Further experiments aim to measure the ion-optical performance of the magnet system, detector properties and the production of radioactive beams. After the installation of the second dipole stage, systematic studies of the kinematics and cross sections of fragments of heavy projectiles are scheduled[10]. The magnetic analysis of the FRS section in combination with Cerenkov detectors, scintillators, PIN diodes, and drift chambers will be used for identification of fragments. When the magnet system is completely installed, we will investigate isotopically separated fragments using a degrader placed in the dispersive focal plane in the middle of the FRS. The selection of α-emitters allows us to use correlation techniques which have been successfully applied at SHIP[11,12]. Coulomb excitation of the separated heavy fissionable fragments in secondary targets at the final focal plane may lead to a new field of investigations of fission barriers.

REFERENCES

1. H. Geissel et al., Projectile-Fragment Separator, A Proposal for the SIS-ESR Experimental Program (1987) ; GSI Report GSI-89-30 (1989).
2. G. Münzenberg et al., GSI Nachrichten 11-87 (1987), GSI Preprint GSI-89-80.
3. B. Blank et al., GSI Preprint 89-54 (1989) and contribution to this report.
4. T. Schwab et al., GSI Preprint GSI-89-79 (1989); and contribution to this report.
5. E. Hanelt et al., contribution to this report.
6. R. Anne et al., contribution to this report.
7. H. Sann et al., Proc. of the Int. Conf. for Heavy Ion Nuclear Research, Oak Ridge (1984)
8. B. Voss et al., GSI Sci. Report 1988, 283, 284 (1989).
9. H. Geissel et al., Abstr. of the 3rd Int. Workshop of Heavy Charged Particles in Biology and Medicine, Darmstadt 1987, GSI-87-11 (1987)
10. J. Friese et al., Proposal for SIS-FRS 1989
11. S. Hofmann et al., Nucl. Instr. and Meth. 223 (1984) 312
12. K.-H. Schmidt et al., Z. Phys. A 316 (1984) 19

Development of Beam-Profile Monitors with Gas Amplification and Current Readout for the SIS Projectile-Fragment Separator [G]

R. Anne [a], C. Bruske [b], K. Burkard [b], M. Fradj [b], H. Geissel [b], Y. Georget [a], R. Hue [a], R. Johänntges [b], R. Kirchner [b], A.C. Mueller [c], E. Roecki [b], J. Rasmusson [b], K. Rykaczewski [b], M. Weber [b]

[a] Ganil Caen - [b] GSI Darmstadt - [c] IPN Orsay

In order to measure spatial distributions of primary and secondary nuclear beams at the Projectile-Fragment Separator (FRS)[1] at the SIS, beam-profile monitors with gas amplification and current readout are developed. The mechanical layout is based on experience gained at GANIL [2,3]. For measuring the horizontal (x) and vertical (y) intensity distribution of a beam, two planes of parallel wires (77 wires/plane) are used, being mounted between metal-foil cathodes in a gas chamber. According to the ion-optical requirements of the FRS, there are five such small-area monitors foreseen at the target position, at the symmetric and the final focal points, and in the transfer line to the ESR. Furthermore, two large-area monitors are planned to be positioned downstream of the first and third dipole, which have 95 wires in one plane for determining the x distribution only. For both types of monitors, the distance between the 20μm thick gold-plated tungsten wires is 1 mm, and the thickness of the stainless-steel cathodes is 10μm. The 100μm thick stainless-steel windows (115 mm $\emptyset$ and 194 × 194 mm^2, respectively) for incoming and outgoing beam allow to use gas pressures between 100 and 1000 mbar, with the gas chamber being mounted in vacuum or in atmospheric pressure.

The x and y wire planes of each small-area monitor are divided into a central region with single-wire readout, and two side regions, where wires are combined, so that the 77 wires of one plane are readout into 48 channels. The large-area monitors are also subdivided into regions of different spatial resolution in order to meet the 48-channel limitation. By means of two FET multiplexers, up to eight monitors can be connected to current amplifiers and the related control unit, which allows to select 2 × 48 channels for simultaneous visualization, to vary the gain between 2nA/V and 10μA/V, and to select integration times of 0.5 ms or 5 ms (ref. 4).

First test measurements were carried out with ^{20}Ne beams of 150 MeV/u (approximately 10^7 ions/bunch), using small-area monitors at the FRS target position and downstream the first FRS dipole. Typical results are shown in Fig. 1, which were obtained using a gas (90% Ar, 10% CH_4) pressure of 760 mbar, a cathode voltage of 200V and an electronic gain of 2 nA/V. For these tests, only 31 channels/plane were used with a 17-mm wide central region with single-wire readout, and two 28-mm wide side regions with four wires connected to one channel. In order to obtain true intensities distributions from the measured profiles, the variation of the spatial resolution (1 mm in the center of a wire plane, 4 mm in the outer regions) and possible saturation effects, especially in the case of fast beam extraction, have to be considered. In order to study the latter phenomenon, investigations of the gas amplification as a function of gas composition, gas pressure, and high voltage are planned for various ions and intensities. Without taking saturation effects into account, the apparent horizontal and vertical widths (FWHM) of the $^{20}Ne^{10+}$ beam spot on the FRS target position were preliminarily determined from Fig. 1 to be 5.9 and 5.7 mm, respectively. A comparison of such values with the corresponding ones measured after the first FRS dipole allows to check the alignment of this FRS section and to verify ion-optical calculations [5]. Assuming spatial beam extensions of a few mm FWHM, and electronic integration times comparable to or larger than the time duration of the beam bunch, the minimum number of detectable 150 MeV/u ^{20}Ne ions is estimated to be approximately 100 ions/bunch. Based on these initial measurements, the beam-profile monitors proved to be a very useful tool for routine control of the beam qualities at the FRS.

1. H. Geissel et al., Projectile-Fragment Separator, A Proposal for the SIS-ESR Experimental Program (1987), unpublished
2. D. Bazin and Y. Bouveret, Etude et mise au point d'une chambre multifils à ionisation pour la détection de faisceaux secondaires au GANIL, GANIL Report 84.03 (1984), unpublished
3. R. Anne and Y. Georget, Chambres à circulation de gaz, etalonnage avec le faisceau GANIL, GANIL Report RA.YG. 627.85 (1985), unpublished
4. M. Fradj, Beschreibung Profilgitter-Meßsystem, Internal GSI-Report (1989), unpublished
5. H. Geissel et al., The Projectile-Fragment Separator Project, contribution to this report.

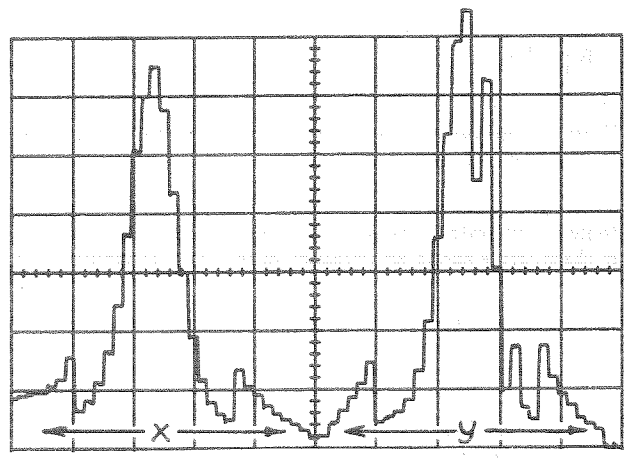


Fig. 1: Horizontal (x) and vertical (y) intensity profiles of a 150 MeV/u $^{20}Ne^{10+}$ beam from SIS, measured at the FRS target position. The bunch width of the slowly extracted beam was approximately 500 ms, and the electronic integration time was 5 ms.

The Universal Energy Degrader System for the Fragment Separator [G]

E. Hanelt, J. Weckenmann, K.-H. Schmidt[1], H.-G. Clerc, H. Folger[1]
TH Darmstadt, [1]GSI Darmstadt

The fragment separator (FRS) presently under construction at GSI will be operated as a momentum-loss achromat using a specifically shaped thick layer of matter as an energy degrader. It has been shown theoretically [1] and experimentally [2] that this degrader works as a high resolution ion-optical instrument. The limitation of the separation quality for projectile fragments due to the energy straggling in the degrader material is in most cases less severe than the ion-optical limit due to the emittance of the primary beam and the aberrations of the magnetic system. Nevertheless, there are some other undesired effects when the fragments are passing the degrader. Most importantly, some of the fragments are lost due to secondary reactions or angular straggling.

For a fixed relative degrader thickness d_0/r_f expressed as a fraction of the fragment range r_f in the degrader material, nuclear reactions are more probable for a low-Z than for a high-Z degrader material. For secondary reactions due to electromagnetic dissociation, the dependence on the degrader material is opposite. The losses due to angular straggling can be important in the case of light fragments and a high-Z degrader material. We investigated the material dependence of these effects theoretically using the model described in reference [1].

The results can be discussed by means of the examples in table 1 which are typical for the operation of the FRS. The beam energies and the degrader thicknesses are a compromise in order to obtain a good separation, to avoid ambiguous charge states behind the degrader and to limit the losses due to secondary reactions. In all cases the target thickness is 10% of the range of the projectiles in the target material.

	fragment	projectile	beam energy MeV/u	degrader thickness d_0/r_f
A	^{234}Ac	^{238}U	1000	0.2
B	^{80}Se	^{86}Kr	500	0.4
C	^{9}Li	^{15}N	200	0.4

Table 1: Some typical cases for the operation of the FRS as chosen for the studies described in the text.

In figure 1 the number of selected fragments at the exit of the fragment separator relative to the number of fragments produced in the target is shown as a function of the degrader mass number.

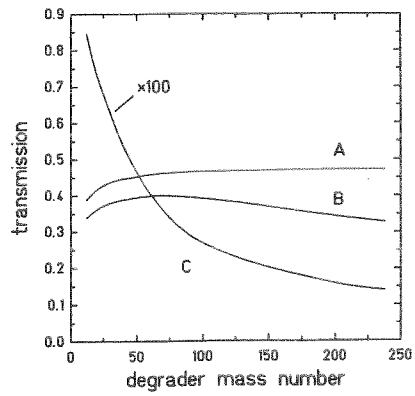


Figure 1: Number of fragments at the exit of the FRS relative to the number of fragments produced in the target for the three cases A,B,C as listed in table 1 .

For the production of a light, a medium or a heavy fragment the ideal degrader material is also light, medium or heavy, respectively. Nevertheless the number of medium or heavy fragments at the exit of the FRS depends only little on the degrader material, whereas for light fragments one can gain a factor of five by using a carbon degrader instead of lead. The reason for the different behaviour of the lithium fragments is the larger angular straggling which for degrader masses greater than 50 already exceeds the angular acceptance of the magnets behind the intermediate focal plane. In addition to the angular straggling the transmission of lithium is also reduced by the large width of the momentum distribution behind the target which is about four times the momentum acceptance of the first magnetic dipole stage. Therefore the amount of lithium fragments at the exit is only in the percent region whereas half of the heavier fragments survive all separation stages.

The material which is best suited for the construction of the intermediate energy degrader of the FRS should be of low Z and should be easy to machine in order to obtain a high mechanical precision. Aluminum is the lightest metal which fulfills these conditions.

The thickness and the shape of the intermediate energy degrader depend on the primary beam, the target, the selected fragment and on the ion-optical properties of the magnetic system. Therefore a universal degrader system for the FRS is in preparation which provides high flexibility ranging from 2 g/cm^2 to 20 g/cm^2 mean thickness with a variation of about 5% to 10% over the full extension of the intermediate focal plane (figure 2). The thickness of the degrader d is approximated by a linear expansion $d(x) = d_0 + d_1 \cdot x$ with the coordinate x in direction of the dispersion. The coefficients d_0 and d_1 must be adjustable within a precision of one per mille of the total thickness. Although the exact degrader profile is curved, an additional quadratic term in the expansion is in the same order of magnitude as the required precision and thus can be neglected.

The coefficients d_0 and d_1 are technically realized in the following way: A ladder with various degrader plates serves for changing the degrader thickness and also its profile in single steps. A continuous variation of the coefficient d_0 is achieved by shifting two identical wedges in opposite directions perpendicular to the beam axis. The coefficient d_1 can be varied continuously by rotating two other identical wedges in opposite directions around the beam axis. The latter includes also a constant contribution to the coefficient d_0 and thus defines the minimum adjustable degrader thickness.

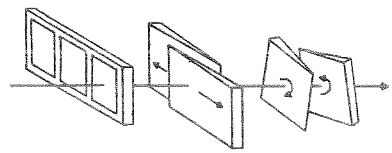


Figure 2: Schematic view of the degrader station (see text)

References

[1] K.-H. Schmidt et al., Nucl. Instr. Meth. A260 (1987) 287 und H. Geissel et al., Nucl. Instr. Meth. A282 (1989) 247.

[2] B. Blank et al., Nucl. Instr. Meth. A286 (1990) 160.

On the Energy-Loss Mode of the FRS--- An Experiment using the Energy-Loss Spectrometer SPEG [G]

5.1

H. Geissel, Th. Schwab[1], P. Armbruster, A. Gillibert[2], W. Mittig[3], R. E. Olson,
K. B. Winterbon[5], H. Wollnik[1], G. Münzenberg

GSI, [1]II. Physikalisches Institut der Universität Giessen, [2]CEN Saclay, [3]GANIL Caen, [5]AECL Chalk River

Matter placed within ion-optical systems offers new possibilities to modify and to control the phase space of high-energy heavy-ion beams [1]. At GSI, the projectile fragment separator FRS is presently under construction to produce and to separate relativistic radioactive beams [2,3,4,5]. Since the isotopic separation principle is based on magnetic rigidity analysis and on atomic energy loss in thick profiled degraders placed in the dispersive focal plane of an achromatic ion-optical system, the angular and energy straggling phenomena are the physical limitations for the resolving power of such a system.

The FRS can also be used as an energy-loss spectrometer which enables precise energy-loss measurements independent of energy fluctuations of the incident beam. Such an energy-loss spectrometer consists of at least two dispersive dipole stages, which form an achromatic system at the final focal plane, i.e., the position and angle resolutions are independent of the momentum spread of the beam at the entrance of the spectrometer and the interaction of the beam with the target is performed at the dispersive intermediate focal plane. Ion-optical calculations on the resolution of the FRS as an energy-loss spectrometer are presented in reference [2].

Such an energy-loss spectrometer for high-energy heavy ions is the SPEG [6] at GANIL which we used to measure precise energy and angular distributions of Ar ions penetrating different solid materials [7].
A 85.38 MeV/u ^{36}Ar beam was provided by the GANIL accelerator. The energy-loss and angular distributions were measured with the high-resolution spectrometer SPEG. This achromatic spectrometer consists of three dipoles, along with quadrupoles and sextupoles for correcting higher-order image aberrations. A diagram of the spectrometer and the experimental set-up are presented in fig. 1. The targets were placed at the dispersive focal plane. The position and angle distributions were measured with two drift chambers (CD1, CD2) at the final focus of SPEG. An ionisation chamber (CI) and a plastic scintillation detector (PL) provided signals for particle identification. The horizontal and vertical angular acceptances and the analyzed momentum range of the spectrometer section following the target are ± 35 mrad and ± 3.5%, respectively. The dispersion at the final focal plane is 8.1 cm/% resulting in a measured momentum resolution of $\Delta p/p \approx 3 \cdot 10^{-5}$. The magnification in the dispersive coordinate is 0.8 in the achromatic operation mode.
Two angle and energy sprectra obtained with and without a gold target positioned in the beam are shown in fig. 2. The high-resolution performance of the spectrometer is clearly reflected in the corresponding spectra demonstrating that the deconvolution of the contribution of the incident beam has only a minor influence on the data reduction.

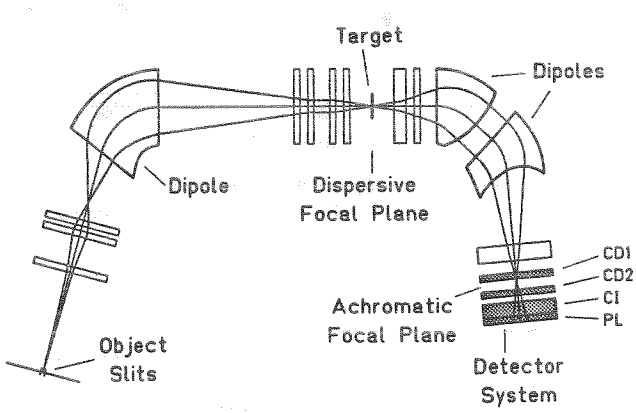


Fig. 1: The energy-loss spectrometer SPEG [6] and the detector system used for the present experiment.

The data are presented in a separate contribution in this report [8]. The stopping-power data agree within 1% with the relativistic Bethe theory with higher-order corrections. The energy-straggling data can be described within 10% with the collision theories based on the Bohr-Titeica formulae. The half-angles of the angular distributions agree within 5% with the extended theory of Sigmund and Winterbon.

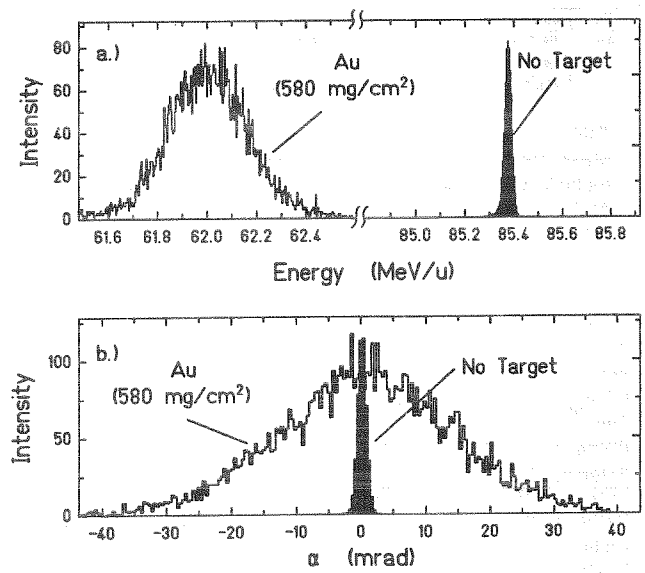


Fig. 2: Measured energy and angle spectra with and without a gold target placed in the 85.38 MeV/u ^{36}Ar beam.

REFERENCES

1. H. Geissel et al., Nucl. Instr. and Meth. A 282 (1989) 247.
2. H. Geissel et al., GSI Report 89-30.
3. G. Münzenberg et al., GSI Report 89-80.
4. K.-H. Schmidt et al., GSI Report 89-78.
5. J.P. Dufour et al., Nucl. Instr. and Meth. A248 (1986) 267.
6. L. Bianchi et al., Nucl. Instr. and Meth. A276 (1989) 509.
7. Th. Schwab et al., GSI 89-79.
8. Th. Schwab et al., this report.

Precise Energy-Angle Measurements performed with the high-resolution Spectrometer SPEG at GANIL [G]

Th. Schwab[1], H. Geissel, P. Armbruster, A. Gillibert[2], W. Mittig[3], R. E. Olson,
K. B. Winterbon[5], H. Wollnik[1], G. Münzenberg

GSI, [1]II. Physikalisches Institut der Universität Giessen, [2]CEN Saclay, [3]GANIL Caen, [5]AECL Chalk River

Heavy-ion cyclotrons and synchrotrons typically provide beams with an energy spread of 10^{-3}. Since the energy-straggling of heavy ions in thin targets contributes nearly the same magnitude, such measurements demand a high-resolution system. In addition, it is essential to eliminate energy fluctuations of the incident beam during the measurement with the stopping medium inserted. To solve these problems, we have chosen for our experiment [1] the high-resolution energy-loss spectrometer SPEG [2] at GANIL which enables precise energy-loss measurements independent of energy fluctuations of the incident beam. The set-up and the method is described in a separate contribution in this report [3]. The target materials used were Al, Pt, and Au. The mean thicknesses determined with an opto-mechanical method were in the range of 100-900 mg/cm^2, see table 1. The accuracy achieved in this measurement was about 0.1 μm. The areal density of the material was checked by weighing well defined target areas.

$Z_1 = 18$, $M_1 = 35.9675$, $E_0 = 85.38 MeV/u$					
Target	x	E	S_e	δE (fwhm)	$\alpha_{1/2}$
	$mg\ cm^{-2}$	MeV/u	$MeV/(mg\ cm^{-2})$	MeV	$mrad$
Al	106.4 ± 0.2	82.23	2.127 ± 0.011	4.17 ± 0.28	2.78 ± 0.12
	108.6 ± 0.3	82.19	2.110 ± 0.013	4.33 ± 0.28	-
	218.7 ± 0.3	78.70	2.196 ± 0.007	6.66 ± 0.23	4.43 ± 0.09
Pt	232.3 ± 0.8	80.96	1.366 ± 0.008	6.68 ± 0.36	7.78 ± 0.26
Au	96.3 ± 0.2	83.55	1.367 ± 0.011	4.35 ± 0.23	4.80 ± 0.18
	580.1 ± 0.9	73.67	1.451 ± 0.004	13.30 ± 0.23	15.80 ± 0.32
	860.1 ± 0.7	66.77	1.556 ± 0.002	17.86 ± 0.28	21.66 ± 0.48

Table 1:
Measured stopping power (S_e), energy straggling (δE), and multiple scattering ($\alpha_{1/2}$) data for 85.38 MeV/u ^{36}Ar ions in Al, Pt, and Au targets. The thickness x is given in the 2nd column.

a) Stopping Powers

Stopping powers of 85.38 MeV/u ^{36}Ar projectiles have been measured in Al, Pt, and Au target materials of different thicknesses. The experimental results are presented in fig. 1 and table 1.
The ^{36}Ar projectiles are nearly fully ionized at 85.38 MeV/u during their penetration through the targets. The measured stopping power values compared with experimental data published by Bimbot et al. [4] and with the modified relativistic Bethe formula [5] are presented in fig. 1. Bonderup shell corrections, the Bloch terms, the Barkas term from Jackson McCarthy, and the Mott correction are incoporated in the theoretical curve (dashed line).

b) Energy Straggling

For completely stripped heavy ions the relativistic Bohr formula with a few corrections due to the binding of the target electrons should give a good description of the measured results. Indeed, the validity of this assumption is confirmed by our measurements as demonstrated in fig. 2. We agree within 10% with the theory based on simple collision models. However, our results are by roughly a factor of two smaller than the corresponding measurements by Herault et al. [6]. Precise microscopic thickness investigations with a laser interferometer, selection of uniform targets, and the use of a high-resolution ion-optical spectrometer are probably the reasons for these measured differences.

c) Multiple Angular Scattering

The multiple angular scattering of 85.38 MeV/u ^{36}Ar projectiles is mainly caused by elastic collisions with the target atoms. The results for the different materials and target thicknesses are listed in table 1. The data agree well with theoretical and semi-empirical formulae [1].

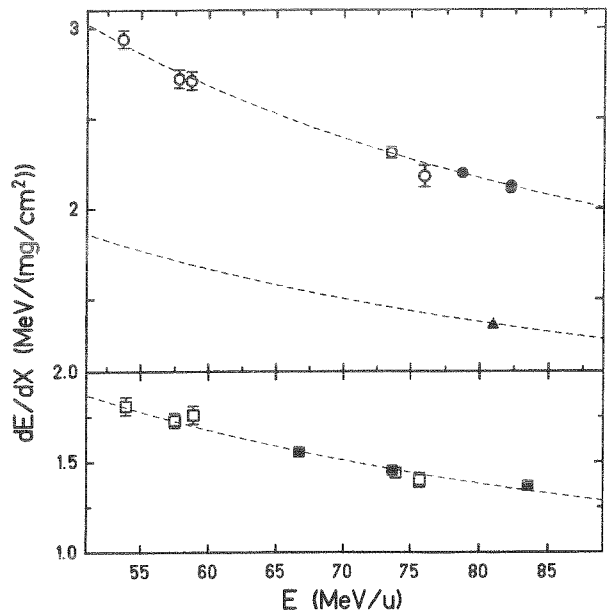


Fig. 1: Measured stopping powers of 85.38 MeV/u Ar ions in solids (Al:●, Pt:▲, Au:■) compared with experimental data of Bimbot et al. [4] (open symbols) and with the modified relativistic Bethe-Ahlen [5] theory (dashed line).

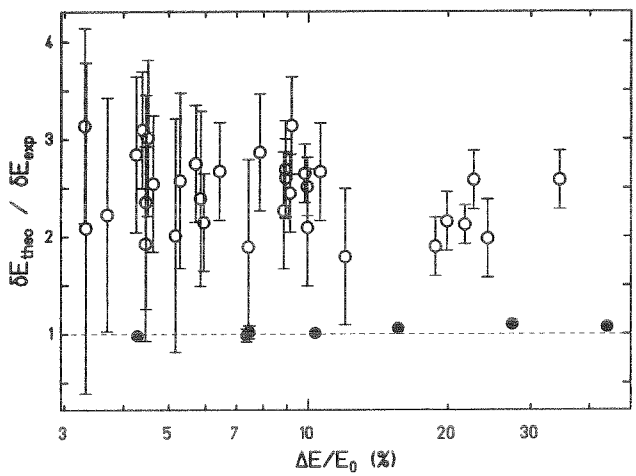


Fig. 2: Energy-loss straggling data (full symbols) compared with the integrated Bohr-Titeica formula (dashed line) and the data of ref. [6] (open symbols).

REFERENCES

1. Th. Schwab et al., GSI Report 89-79.
2. L. Bianchi et al., Nucl. Instr. and Meth. A276(1989) 509.
3. H. Geissel et al., this report.
4. R. Bimbot et al., Nucl. Instr. and Meth. B17 (1986) 1.
5. S.P. Ahlen, Rev. Mod. Phys. 52 (1980) 121.
6. J. Herault et al., J. Phys. C7 (1988) 33.

Direct Mass Measurement of Exotic Nuclei at the ESR [G]

K. Balog[2], Y. Fujita[5], H. Geissel[3], K. Lindemann[1], K. E. G. Löbner[2], G. Münzenberg[3], H. Seifert[1], J. Schnell[1], T. Schwab[3], J. Trötscher[1], D. Vieira[4], T. Winkelmann[2], H. Wollnik[1] and J. Wouters[4]

[1] 2. Physikalisches Institut der Universität Giessen
[2] Sektion Physik der Universität München, Garching
[3] Ges. für Schwerionenforschung mbH, Darmstadt,
[4] Los Alamos National Laboratory, Los Alamos,
[5] College of General Education Osaka University, Japan

For the planned direct mass measurements [1] by using the ESR as a multi–turn time–of–flight mass spectrometer we continued to investigate the ionoptical problems as well as designed a position sensitive timing detector which can be used in the ultra high vacuum. We also investigated the electronic problems occurring with the necessary timing accuracy and the high momentary count rates.

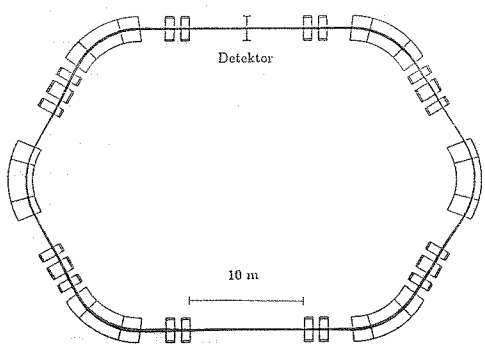


Figure 1: Off-axis calculation of the ESR in an isochronous mode assuming an emittance of $20\,\pi\,mm\,mrad$.

To achieve a high intrinsic time resolution when using the ESR as a time–of–flight mass spectrometer requires to fulfill the energy isochronous and lateral achromatic conditions simultaneously besides the operation of the system as a storage ring. This can be achieved by adjusting the quadrupoles of the ESR. The first ionoptical calculations assumed that the beam follows the symmetry axis of the magnet structure. In reality, the beam is steered away from this axis, because the location of the injection kicker requires the beam to be off–axis (see fig. 1). Using the newest version of the COSY 5.0 program [2], ionoptical calculations could be performed with an off–axis beam showing that this zeroth order distortions modifies the first– and higher– order transfer matrices only slightly.

The relative accuracy of the mass measurements is proportional to the relative accuracy of the time measurement, the accuracy of the isochronicity (i.e. the intrinsic time resolution) and the number of turns of the ions in the ESR. Therefore a time detector and electronics with absolute time resolution of around $100ps$ will be necessary. The timing signal will be obtained from secondary electrons created by the passage of the ions through a thin foil. These electrons will be guided isochronically to a micro channel plate by crossed electric and magnetic fields. The major goals of the new detector are to obtain a time resolution of around $100ps$ [3], a position information of the passing ions – which would help to correct for any non–isochronism – and last not least the new detector must be usable in the ultra high vacuum of the ESR.

For the new detector the geometry of the electrostatic unit has been newly designed. The mounting of the whole detector system inside the ESR is planned in such a way, that it can be removed from the ESR–beam through a vacuum lock without interrupting the ESR–vacuum.

We intend to measure the absolute time–of–flight for each ion and each turn in the ESR. The flight time per turn is about $500ns$ which corresponds to a data rate of 2MHz for a single ion over some ten microseconds. The electronics should be able to handle at least 4 particles simultaneously.

The goal of obtaining a time resolution of $100ps$ at such high data rates requires the development of special data acquisition electronics. A possible electronic layout has been completed which is hoped to achieve an electronic time resolution of about $35ps$ and a pulse pair resolving time of about $5ns$.

To optimize the yield of secondary electrons we tested different types of foils. Using Al_2O_3-foils with Al and CsJ coating we found that the yield of secondary electrons increased by a factor of about ten against foils without the CsJ coating (see figure 2). Measurements with α particles at $5.5MeV$ were done at Los Alamos and Gießen. During a beamtime at the LOHENGRIN mass separator at the ILL in Grenoble the secondary electron yield of C-foils ($19\mu g/cm^2$) with and without layers of CsJ– ($30\mu g/cm^2$) and LiF– ($30\mu g/cm^2$) were tested by monoenergetic α–particles of $2MeV$. Also here it was found that CsJ and LiF layers have much higher electron yields than carbon or SiO– foils. LiF–layers would be especially interesting for use in the ESR because of their low Z. However, in all cases some instabilities were observed due to surface charges. It is hoped that these effects can be avoided by using thinner layers.

Furthermore the measurements at the ILL showed that the timing signal can be taken from the backside of the channel plate (in order to have the anode for position measurements available) without loss of time resolution and efficiency. It should thus be possible to use only one channel plate for time and position measurement.

For the relativistic heavy ions to be measured the electron yield is not known. We expect the emission of electrons by relativistic heavy ions to be similar to those of α–particles in the MeV region. Explicit information is expected from an experiment at the FRS.

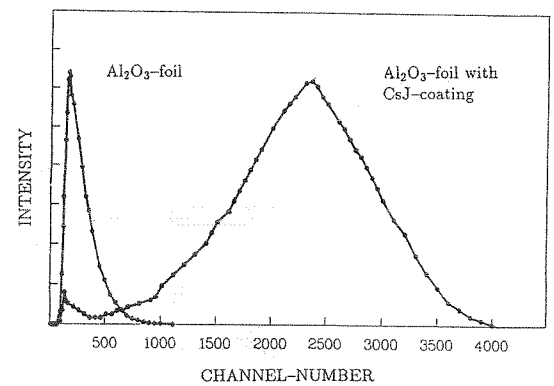


Figure 2: Secondary electron yield of Al_2O_3–foils with and without CsJ coating .

References

[1] T. Schwab, H. Seifert, H. Wollnik, H. Geissel and G. Münzenberg; GSI-Rep. GSI-87-1, 360.
H. Wollnik, T. Schwab, and M. Berz; GSI-Rep. GSI-86-1, 372.

[2] M. Berz, H. C. Hofmann, H. Wollnik; Nucl. Instrum. and Meth. **A258** (1987) 402

[3] R. H. Kraus, D. J. Vieira, H. Wollnik and J. M. Wouters; Nucl. Instrum. and Meth. **A264** (1988) 327

USCHI Trimmed for HDMP

E. Schimpf, E. Jäger, K.H. Behr, M. Schädel
GSI Darmstadt

The scattering chamber USCHI, previously used for Rutherford back scattering experiments[1] in the UNILAC stripperhall has been trimmed for its installation as a manifold usable vacuum chamber for various types of experiments at the high dose multipurpose cave (HDMP) at SIS. Precautions where not only taken to provide a universal and easily accessible chamber for many kinds of irradiation and activation experiments with high beam intensities up to the design value of SIS, but also to furnish a well suited environment for test of detectors, and last, but not least, to investigate such kind of rare reaction channels in nuclear physics experiments in which the use of the highest available beam intensities are a prerequisite. USCHI will be installed at a position 16m downstream the first quadrupole triplett of the FRS in front of the SIS beam dump.

A cross section through the rebuilt chamber and some of the new peripheral parts is shown in Fig. 1. The beam enters and exists the chamber through short beam pipes mounted inside the chamber, see Fig. 2., which optionally can be equipped with beam windows to also allow for irradiations in an atmosphere different from the 'standard' vacuum of $< 1 \times 10^{-6}$ Torr obtained with two turbo molecular pumps (TPU 1500 and TPU 510). A piece of beam pipe to connect, if desired, the open ends inside the chamber is available. The beam traverses the chamber at a height of 312 mm above a removable platform on which the experimental set-up can be mounted. The available height above the beam is 400 mm to the rim of the tank, and additional 400 mm in the middle of the lid. While the inner horizontal diameter of the chamber is 1.5 m the removable platform provides an easy access for set-ups smaller than 850 mm in diameter. An opening of 250×200 mm² in the middle of the platform allows to insert targets and/or detectors through a NW 250 gate value from underneath into the chamber. This gate valves separated the big vacuum tank from a smaller sluice chamber with the inner dimensions of $430 \times 300 \times 300$ mm³ which can be pumped separately. Experimental set-ups of up to 40 kg, can be mounted on a combination of a tilt platform and a translation stage for a precise adjustment ($< 10\mu$m) in the irradiation position. A stepping motor in combination with a shaft decoder provides the vertical movement between the two chambers and the vertical position adjustment.

Two out of six large flanches (400×300 mm²) which are accessible on the chamber furnish 96 electrical (BNC) and 16 gas feed through at present. In addition, a variety of smaller flanches may be used. The chamber will house additional elements for the diagnostics of the size and the position of the beam close to the target.

1. M. Brügger, K. Lützenkirchen, S. Polikanov, G. Herrmann, M. Overbeck, N. Trautmann, A. Breskin, R. Chechik, Z. Fraenkel, and U. Smilansky, Nature 337, 434 (1989)

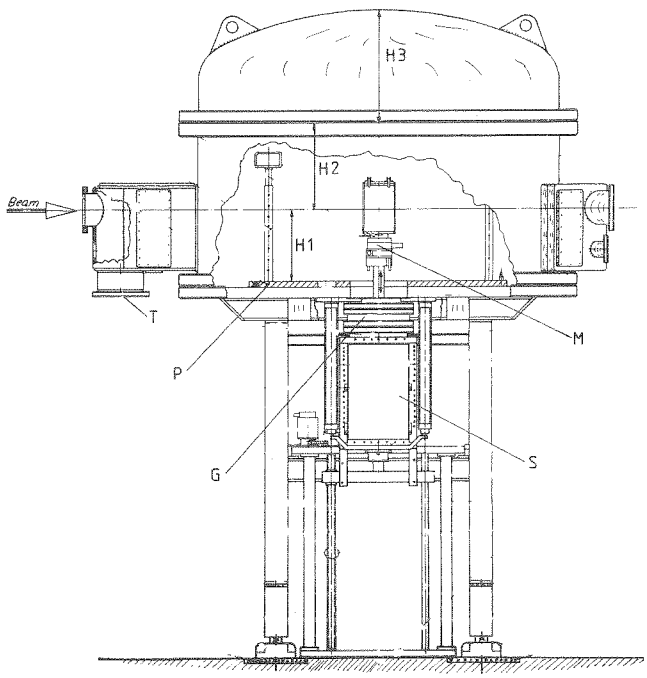


Fig.1: Schematic side view of USCHI.
G = gate valve NW 250, M = translation stage and tilt platform, P = removable platform, S = sluice chamber, T = turbomolecular pump TPU 1500, H1 = 312 mm, H2 = 400 mm, H3 = 400 mm.

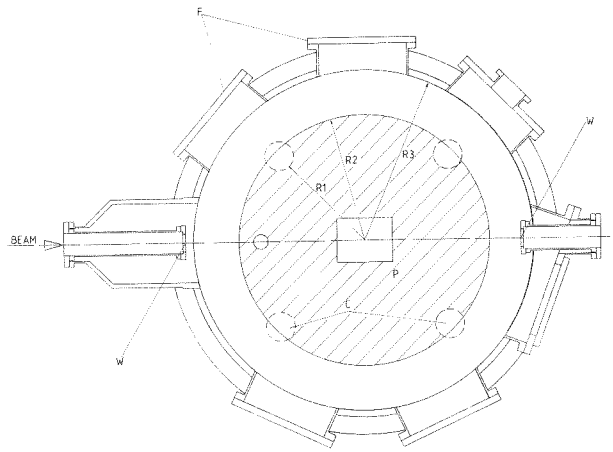
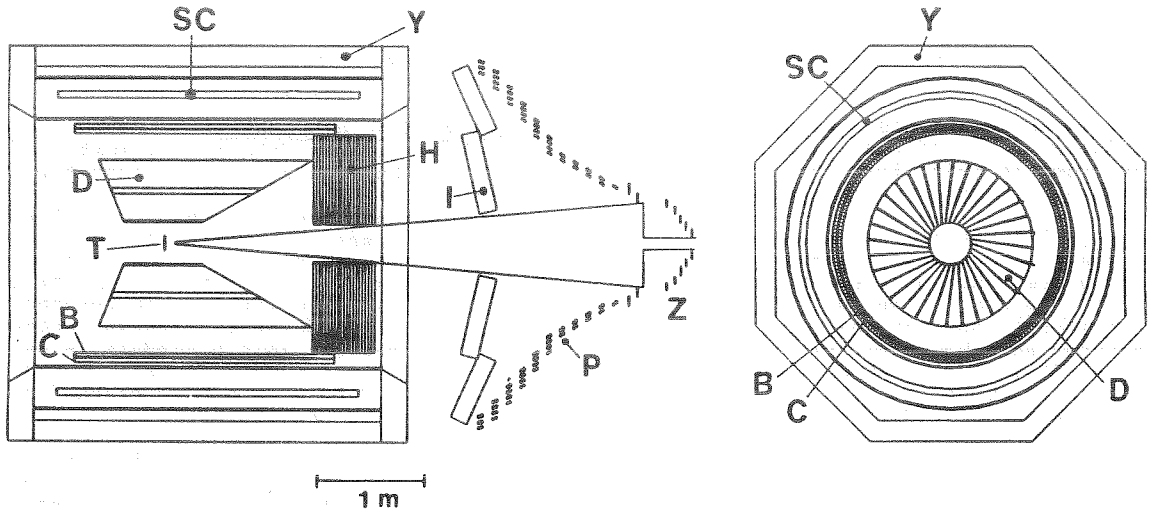


Fig.2: Schematic top view of USCHI.
W = inner beam pipes with NW 100 or beam window, F = large flanches, C = poles to carry the platform with a crane, R1 = 480 mm, R2 = 570 mm, R3 = 750 mm, P = removable platform.

Status of the 4π Detector for Charged Particles [G]

The 4π Collaboration

Darmstadt,Bucharest,Budapest,Clermond-Ferrand,Florence, Heidelberg,Legnaro,Moscow,Strasbourg,Warsaw



The 4π Detector for Charged Particles[1] has been designed for the study of central and semi-central collisions between heavy ions in the SIS energy range. The main components are illustrated schematically in the shown cross section parallel to the beam direction and the vertical cut at the target location with its azimuthal symmetry. The target is located inside a cylindrical drift chamber with conical ends (D) located inside an axial superconducting coil (SC) producing a magnetic field of 0.6 T. Other detectors inside the magnetic field volume are a barrel (B) of plastic scintillator detectors and a barrel of Cerenkov counters (C) and, finally, a radial drift chamber (H), the Helitron. These detectors, all involved in the magnetic field tracking analysis, will not be ready before the middle of 1991('Phase II'). The 'Phase I' detectors primarily cover the angles forwards of 30° and should be ready for first experiments in 1990. They comprise a 'parabola' of ionization chambers (I), a high-granularity plastic wall consisting of an inner part (Z) covering the angles from 1° to 7° and an outer part (P, 7° to 30°). Furthermore, (not shown) there will be a 'Rosace' of 60 thin plastic detectors in front of the inner Plastic Wall and 6 movable Si-CsI Particle Telescopes.

The status of some of the components, Zero Degree Detector[2], Central Drift Chamber[3]., and Cluster Detector[4], is presented in separate reports. Therefore we confine this report to the remaining components.

The External Plastic Wall. All necessary components for the strips have been delivered with exception of 20% of the PM bases. About 400 of the 512 individual strips have been assembled (glueing of light guides/tubes/scintillators), wrapped, and successfully tested, the rest will follow until middle of February 90. Tests have shown that the resolutions obtained in prototype studies[5] are also achieved with the final modules. Mounting of the wall is planned to start by the end of January 90.

The Solenoid. The superconducting solenoid coil is in production at Oxford Instruments. The cryogenic supply has been designed and a He-refrigerator is ordered. The design of the iron yoke was completed and the manufactoring started at the Efremov Institute in Leningrad.

The Helitron. The design studies for the Helitron radial drift chamber have been continued. Extensive calculations about its mechanical rigidity which are summarized in a separate report, show that the mechanical deformations of the proposed structure are negligible. The cathode planes have been designed and tested. Full-sized prototypes of one sector have been assembled and the tests will begin now.

The Plastic Barrel. A close-to-final prototype of the Plastic Barrel modules has been designed by testing different geometries of scintillator plus lightguide and several types of photomultipliers. A position and time FWHM resolution of 5 cm and 400 ps, respectively, was obtained with minimum ionizing particles for strips of BC408 scintillator 0.4 m long and 4 × 4 cm² thick connected to VALVO XP2262B photomultipliers via 1.2 m long and 90° bent plexiglas lightguides.

Electronics and Data Acquisition. The necessary electronics for the inner and outer Plastic Wall are in house. Most of these modules are CAMAC based; All necessary FASTBUS hardware (ADC's and TDC's) has been delivered. The FASTBUS processors and interfaces are available and have been tested. Data transfer from FASTBUS crates and CAMAC crates to a single VME based micro processor has been achieved. Subsequent transfer of the data to the VAX using remote procedure calls has also been successfully implemented.

Data analysis is currently being done on a group of four VAX workstations using standard CERN (i.e. PAW, ZEBRA, etc.) software. The reason for this is the increased portability between the collaborations and their many different computers and the other collaborations in Cave B. It has the additional benefit of ease of integration with the GEANT simulation code.

1. The 4π Collaboration, GSI Scientific Report 1988, p.285
   see also GSI Nachrichten 11-89
2. J.P. Alard et al., contribution to this Report
3. A.-Glatz et al., contribution to this Report
4. C. Cerruti et al., contribution to this Report
5. K.D. Hildenbrand et al., GSI Scientific Report 1988,p.288

The central drift chamber of the 4 π detector[G+B]

A. Glatz, N. Herrmann, D. Pelte, R. Schlesier, M. Trzaska,
U. Winkler, H. Wolfenstetter
Physikalisches Institut der Universität Heidelberg

The work to build and operate the central drift chamber (CDC) of the 4 π-detector was continued in 1989. This includes work on the following subsystems:

Gas system: The gas system which will be used to mix gases in controlled proportions before they are pumped through the CDC was designed and built. The gas system contains a small drift chamber to monitor the drift velocity of electrons and their multiplication in high electrical fields. The gas system has two modes of operation, a purging mode and a circulating mode. In the latter mode, the pressure in the CDC (5 mbar above atmospheric pressure) is stabilized by an electronic feed-back system. The gas system also monitors the oxygen and water contents of the gas which can be reduced by oxygen absorbers and a refrigeration system.

Laser calibration: At the end of 1989 a ND-YAG laser with an output power of 1.4 mJ in 5 ns long pulses at λ = 266 nm was delivered. Development work to construct the optical system for the CDC calibration was started.

Test sector: In the second half of 1989 a full-size test sector of the CDC was delivered from SACLAY. The maximum length of the sector is 2 m and it is equipped with 21 sense wires (compared to 60 of the CDC) and 22 potential wires. The maximum drift length of electrons is 16 cm. In the first test with this sector several problems were encountered. Most severely the required gas purity could not been reached in the circulating mode because of the high outgasing rate of the sector. Therefore the gas has to be purged with a flow of larger than 70 l/h to reduce the oxygen content to lower than 100 ppm. Till the end of 1989 gas mixtures of Ar, CH_4, i-C_6H_{10} in various proportions were studied at various field strengths and the sector performance was measured with ^{56}Fe, ^{90}Sr sources or with cosmic radiation. The Fig. 1 shows the energy loss spectrum of x-rays from the ^{50}Fe source (left). Fig. 1 also displays the drift time resolution of electrons produced by cosmic ray tracks (right). The measured charge division and energy loss resolutions match the values quoted in the detector proposal, the required drift time resolution of σ = 6 ns has not been achieved yet. The reasons for this are still under investigation.

Data Reduction: The VMEbus based multi-processor system with M68020 μprocessors was installed and the software was developed. The system is now used to take data from the monitor drift chamber and the test sector. In addition it is used to study the performance of currently available 8 bit, 100 MHz flash-ADC systems, namely the STRUCK DL312 or DL363 systems. The decision of which system will be ordered for the CDC, partly depends on the outcome of these studies.

Track finding procedures: Since the track identification in high multiplicity (m > 50) environments is a particular problem, the early development of proper track finding algorithms has been started. Two different algorithms were tested with data obtained from Monte Carlo simulations of central Au+Au collisions. The first algorithm is based on a wire to wire search for nearest points, which combine to circular segments of common radius. This procedure is rather fast (1.5s for m = 100 tracks) and has an efficiency of 90 % in a high background environment. The second algorithm performs for a fixed bending radius a simultaneous transformation of all points into straight lines and selects those points which have the identical azimuthal angle. This algorithm is slower by a factor 10 but appears to have higher efficiency. The performance studies of track finding algorithms under different conditions will continue.

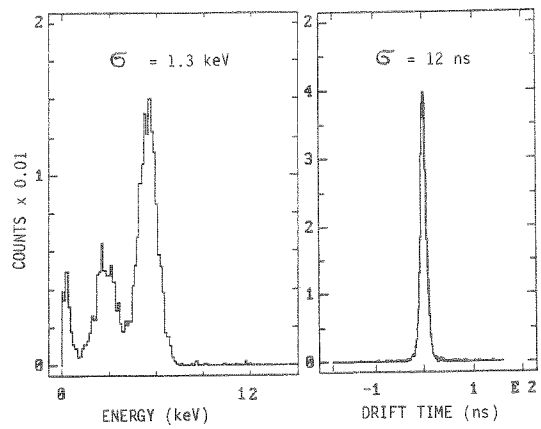


Fig. 1. Energy spectrum from ^{50}Fe (left) and drift time resolution (right).

Present status of the Cluster Detector for the 4π Facility at SIS/ESR

C. Cerruti, J.P. Coffin, I. Combes, R. Ernwein, P. Fintz, G. Guillaume, F. Hornecker, M.O. Hunzinger, F. Jundt, C.F. Maguire, R. Neunlist, F. Rami, M.A. Saettel, R. Tezkratt, B. Tischler, P. Wagner.

CRN, Strasbourg (France)

The construction of the modular cluster detector capable of detecting and identifying charged clusters emitted in heavy-ion collisions at energies from 0.1 to 1 GeV/nucleon in a near-4π geometry is in progress. The external part of the detector, covering polar angles between 6° and 30° and consisting of 128 Ionization chambers has been described previously[1].

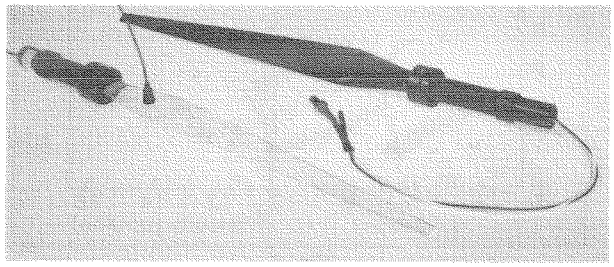


Fig. 1

The central part subtending angles from 1° to 5° is made of 60 modules designed to detect ions ($2 \leq Z < 15$) with energy larger than about 25 MeV/nucleon. Each module consists of a NE102A scintillator with a thickness of 2 mm attached to a Hamamatsu E3478 photomultiplier. Fig. 1 shows two examples of such a device before and after it has been made light-tight. The 60 modules are set side by side in a "Rosace" configuration as shown in Fig. 2. A pulsed laser light conducted through a plastic optic fiber glued to the scintillator (visible in Fig. 1) is used for calibration and control purpose. The Rosace is placed vertically, 4.7 m downstream the target, before the Zero Degree-detector being built by the Clermont-Ferrand Collaboration[2] for light charged particle detection.

The Rosace

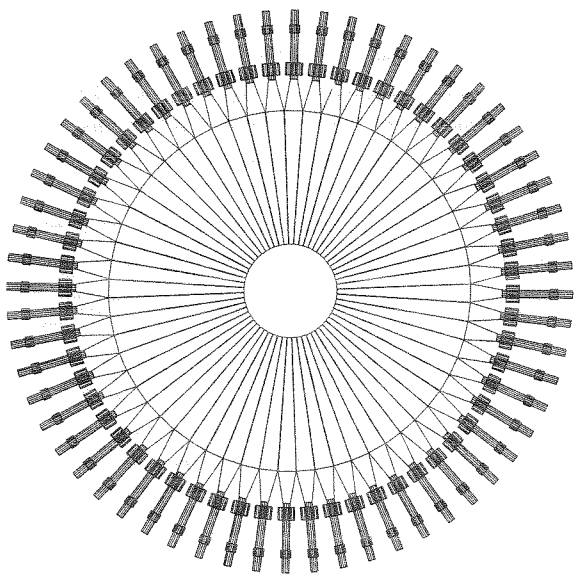


Fig. 2

The energy loss of an ion is measured with the Rosace while the velocity v is calculated from the ion's time-of-flight measured with the Zero Degree-detector. The 2D-representation (ΔE, v) is characteristic of the Z of the ion. An example of data obtained for the $^{20}Ne + ^{12}C$ reaction performed at 38 MeV/nucleon at SARA is shown in Fig. 3. This shows, with E-residual substituting for v, the Z resolution of the Rosace scintillator obtained with a collimated beam of outgoing ions.

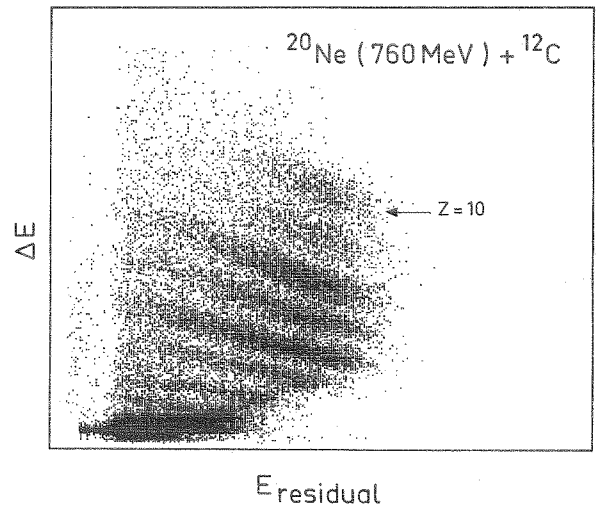


Fig. 3

1 J.P. Coffin et al., GSI Scientific Report 1988, ISSN 0174-0814, p. 289

2 J.P. Alard et al., this report

Simulations of the Response of the Cluster Detector/Scintillator Wall for the 4π Facility at SIS/ESR using the GEANT Detector Program

C. Cerruti, J.P. Coffin, P. Fintz, G. Guillaume, F. Jundt, C.F. Maguire, F. Rami, R. Tezkratt, and P. Wagner.
CRN, Strasbourg (France)

For angles between 7 and 30 degrees the SIS/ESR 4π detector facility will initially be composed of a gas ionization chamber/organic scintillator sub-system whose principle identification method will be based on differential energy loss as a function of particle velocity (Ref. 1). The ionization chamber will contain 128 anode plane sensor strips, and there will be 512 scintillator strips oriented more or less transversely to the anodes. An event reconstruction software is being developed to match the hits in the ionization chamber (primarily low multiplicity $Z \geq 3$ ions) with those in the scintillator wall (primarily high multiplicity $Z = 1$, 2 ions) in order that a correct association be made between energy loss and velocity. This task is complicated because of the large multiplicty difference, because many events in the scintillator wall will be below the detection threshold of the ionization chamber, and conversely, because a number of slow moving heavy ions detected in the ionization chamber will stop in the air gap (80 cm average) in front of the scintillator wall.

In order to simulate the response of the detector combination and the efficacy of the track reconstruction method we have made use of the detector program GEANT (Ref. 2) which incorporates as realistically as possible the actual configuration of the experimental apparatus. Specific effects such as energy loss straggling and thresholds, multiple scattering, finite resolution, and multiple hits in the same detector element are explicitly included. For an event set we have used 3000 FREESCO (Ref. 3) collisions of 200 MeV/amu $^{197}Au + ^{197}Au$; in particular this event set has on average 1.7 $Z \geq 3$ ions, and 38 $Z = 1$, 2 ions in the angular range of interest resulting in a 5% multiple hit rate in the scintillator wall. The FREESCO event set was analyzed in two passes. The first had the scintillator wall see only the $Z \geq 3$ clusters which effectively negates the difficulties associated with the large multiplicity differential. In the second event set pass, all the particles were considered together. The result of pass 1 is that the $Z \geq 3$ ions can be cleanly resolved from one another using realistic assumptions about the intrinsic performance and limitations of the sense elements. The track analysis indicates that 90% of the non-stopped $Z \geq 3$ ions can be traced back to the anode plane by simple geometry. The remainder are projected to have a slight mis-alignment with the true track position, and these may be recovered by a more sophisticated tracking algorithm.

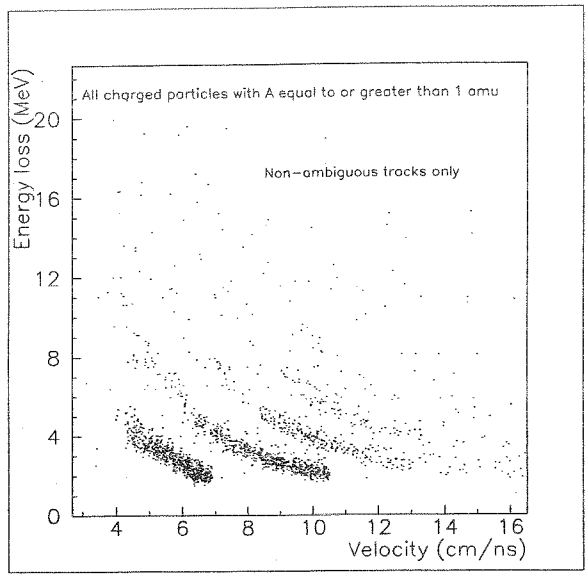


Fig. 1

In the second event set pass, which should be much closer to the actual experience, one can see the effects the multiplicity disparity in Fig. 1. This figure shows all the signals in a given anode strip which can be uniquely identified with a signal in a scintillator strip. It should be noted that "unique" in this case includes both the correctly identified, single hit particles as well as the unambiguous but misidentified particles. There is clearly a background present in Fig. 1 which appears to come from tracks whose velocity parameter is uncharacteristically too fast. This is confirmed by the GEANT track analysis which indicates that these events are primarily caused by heavy particles stopping in the air gap between the detectors but whose ionization chamber has hit has been incorrectly matched to a light particle traversing the same anode strip. These mis-identifications amount to about 20% of the so called "uniquely" identified ionization chamber hits.

Further study of just the scintillator wall energy loss/velocity correlation indicates that it should be possible to remove most of the ambiguities and mis-identifications in the reconstruction of ionization chamber hits. This being the case, one should then be able to determine the reaction plane event-by-event and do a statistically significant flow analysis even for the restricted solid angle coverage of the initial detector system.

References :

1 J.P. Coffin et al., GSI Scientific Report 1988, ISSN 01740814, p. 289
2 GEANT 3.13, CERN Data Handling Division
3 G. Fai and J. Randrup, Comp. Phys. Commun. 42, (1986)385

The Zero Degree Detector of the GSI-4π facility

J.P. Alard, J. Augerat, N. Bastid, F. Biagi, M. Crouau, F. Daudon, P. Dupieux, L. Fraysse
S. Mayade, G. Montarou, P. Morel, M.J. Parizet, D. Qassoud, A. Rahmani, G. Savinel.
L.P.C. Clermont-Ferrand

The Zero Degree Detector is the small angle part $[1\text{-}7]^0$ of the 4π facility[1] which will be installed at GSI and ready for the first SIS beams. The goal is to detect and analyse charged particles up to Z≃7-10. The low energy cuttoff is of the order of 20 MeV for protons due to the different materials between the wall and the target (5 meters). The detector has a very good granularity with 252 modules arranged in 7 rings arround the beam axis (Fig. 1). From a simulation with the Freesco code[2], we estimate a double hit probability of 1% for external ring and 7% for internal one. Two movements are possible : a global one for in-beam energy calibration and a second which gives a separation of the layers in two parts, mainly for mechanical interventions.

The modules are made of 2 cm thick trapezoïdal scintillators (BC404) glued to a short plexiglass light guide and followed by a 2" photomultiplier. All these elements are perpendicular to the beam axis in order to avoid Cerenkov effects and direct hits on the photocathode.

Particle identification is obtained by the combination of time of flight measurements with energy loss in the scintillator. It is well known that we can't separate isotopes by this method. The position is simply given by the number of the hitted module. The wall is able to provide a fast multiplicity signal in order to make a centrality trigger.

The associated electronics is composed mainly of fastbus ADC (two slopes) and TDC.

A nitrogen pulsed laser is used to determine the time calibration offsets. The laser is also used to test the modules before the runs and to verify the stability of the modules during beam time. The UV laser light is shifted in visible light and is carried to the modules by coating plastic fibers of 1 mm diameter.

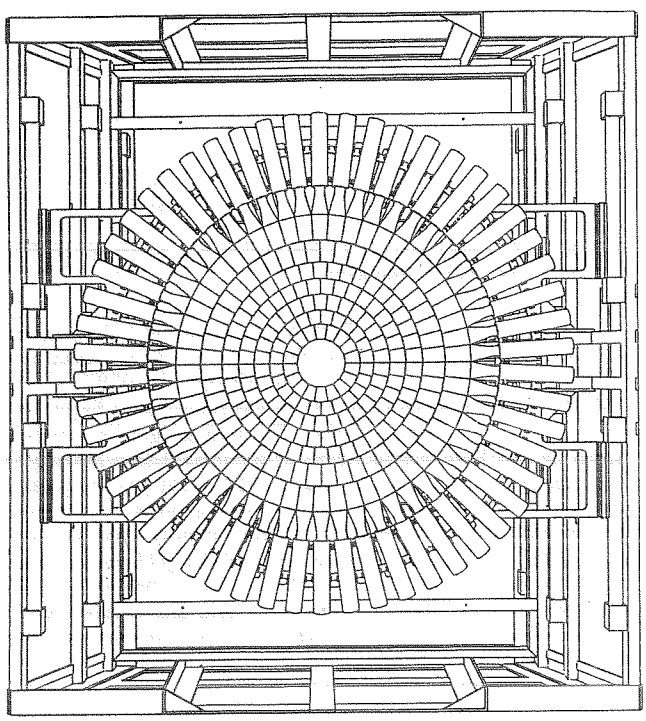


Fig. 1 : View of the Zero Degree Detector (from the target)

As clearly expressed in the proposal of the 4π collaboration[3], there's a clear challenge for studying intermediate mass fragments produced in collisions of massive systems like Au + Au between 100-400 MeV/u.

For instance, the rapidity distributions of these fragments are sensitive to the in-medium scattering cross sections (transparency ...), which are of first interest in our knowledge of excited nuclear matter. It's also clearly pointed out that a good estimate of the impact parameter is needed.

Through QMD calculations[4], it seems that the fragment transverse momenta close to projectile rapidities in almost central collisions are the most sensitive quantity to EOS.

Following this, the quantities that we propose to measure with the ZDD are mainly the fragment multiplicity and charge distributions (correlated to impact parameter, see Fig. 2), the rapidity distributions (in medium effects, phase transition, ..) and the differential cross sections (medical interest too).

Finally we don't forget that the ZDD obsiouly covers a part of the whole detection solide angle and that he is asked as a centrality trigger for the 4π experiments and also for experiments with TAPS[5] and LAND[6].

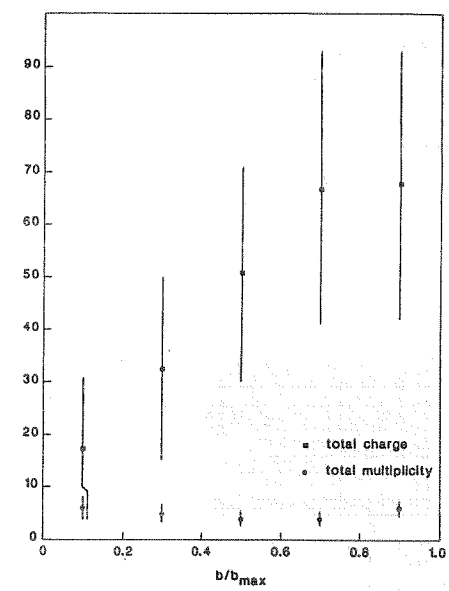


Fig. 2 : Total charge and total multiplicity on the wall versus reduced impact parameter. Data are obtained with the Freesco code.

1 - Technical proposal of the 4π detector for SIS/ESR : GSI report 88-03

2 - G. Fai, J. Randrup, Nucl. Phys A404, 551 (1983)

3 - Composite particle production in central and semi-central collisions of Au on Au : proposal from the 4π collaboration, May 89

4 - G. Peilert et al., Phys. Rev. C39, 1402 (1989)

5 - Technical proposal for a two arms photon spectrometer (TAPS) : GSI report 87-19 and submitted TAPS proposals

6 - Proposal #53 / letter of intent #63 to SIS Program Advisory Commitee, March 87 and March 88 and submitted LAND proposals

Time-of-Flight System for the ALADiN Spectrometer [G]

J. Hubele[a], P. Kreutz[b], A. Schüttauf[b], J.C. Adloff[c], U. Lynen[a],
U. Milkau[a], J. Pochodzalla[b], D. Rudolf[d], G. Rudolf[c],
M. Runne[d], H. Sann[a], W. Trautmann[a], A. Wörner[d]

[a] GSI Darmstadt, [b] Univ. Frankfurt, [c] CRN Strasbourg, [d] GSI Summer Student Program

The time-of-flight (TOF) wall consists of 208 vertical scintillator strips made of BC408. Each slat is 1100 mm long, 25 mm wide and 10 mm thick. They are read out on both sides by photomultiplier tubes. After extensive tests[1] we selected the eight-stage 3/4" tube R3478 from Hamamatsu. This tube has good timing properties and permits a compact design of the modules without light guides and bending. The base is made of a ceramic layer printed circuit with SMD resistors and capacitors[2] and is directly soldered to the connection wires of the photomultiplier tube.

Eight scintillator strips are combined to one module covering a width of 20 cm. The eight tubes on each side of such a "8 - pack" are covered by a common μ - metal box for magnetic shielding. This box also contains all required connectors (Fig. 1). The eight tubes of each module are operated with a common cathode voltage and in addition a common voltage for the first dynode. In this way the gain can be varied by a large factor without worsening the time resolution. In order to minimize the bleeder current booster voltages are provided for the last four dynodes. These voltages are common to all modules. Before glueing the tubes were selected in such a way that the gain spread within each module for a reasonable range of cathode voltages was less than 10% .

The ALADiN TOF wall is arranged in two layers which are displaced by half the width of a scintillator strip. Each layer consists of 13 modules, thus covering a total width of 260 cm. The modules are mounted curtain-like in the rear of the detector chamber, which has a width of 3.2 m. The modules can be moved seperately to the left or right, thus meeting the different experimental requirements.

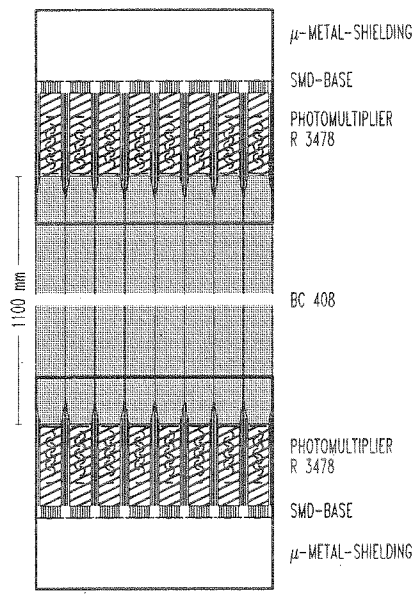


Figure 1: *Schematic sketch of one TOF module.*

The TOF wall will be monitored by means of a laser system which provides a pulsed UV light of 337 nm. The laser pulse is 3 ns long with a risetime of less than 200 ps. This allows to simulate the excitation of the scintillator by real particles making the laser system suitable for amplitude and time calibration as well. We have developed a quartz fiber system which supplies all strips of the detector with the same light intensity within a variation of less than 10 % (see Fig. 2). The laser beam is first split by a 10 % - mirror (glass plate) to branch off some light for a start counter and an intensity monitor supervising the laser longterm stability. The energy reference consists of a scintillator glued on a photodiode which is directly connected to a main amplifier. The energy resolution is about 1 % . After the mirror the light is focused by a lens system into a 1mm quartz fiber which leads via a vacuum feedthrough into the detector chamber. A filter (type UG11) mounted in front of the entrance of the 1 mm fiber protects the scintillators from other than UV light. In the chamber we use black coated fibers with 200μm core diameter. Because of the modular character of our detector - each individual module should be easily exchangeable - we built a serial system which first divides the light into 26 main fibers, each serving one module. In top of each module a second optical system distributes the light of each main fiber to eight secondary fibers which illuminate the scintillator slats.

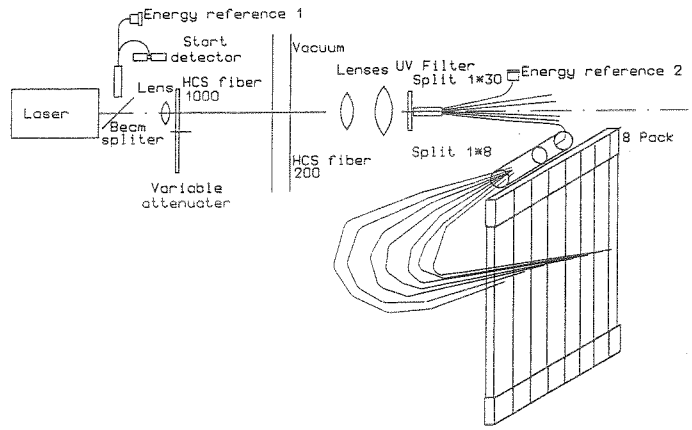


Figure 2: *Schematic view of the laser calibration system of the TOF wall at the ALADiN spectrometer.*

The start signal for the TOF measurements and the position of the incident beam particle at the target will be provided by a START-detector set-up built with scintillator foils of BC418 and NE102a with 100μm to 500μm thickness chosen according to the energy loss of the beam particles. The timing signal will be provided by two Hamamatsu R2083 2"-photomultipliers looking on the scintillator foil under an angle of 45°. The time resolution obtained in tests with a UV-laser (providing pulses of only some picoseconds) was $\sigma = 20ps$ for a laser intensity approximately equivalent to the light intensity expected for gold projectiles of 200 MeV per nucleon. For the position information we use foils of about 3×3 cm^2 directly coupled to four Hamamatsu R3478 photomultipliers. During laser tests of a prototype detector (using R1666 tubes) a position resolution of $\sigma = 0.3$ mm could be achieved for large light deposits in the foil.

[1] P. Kreutz et al., GSI Scientific Report 1988, p. 293

[2] Devellopment of H. Schmitt at CRN Strasbourg

Status of L.A.N.D.[G,B]

H. Freiesleben, J. Keller, W. Kneissl, R. König, S. Lange, Y. Leifels
(Ruhr-Universität Bochum, Institut für Experimentalphysik)

R. Kulessa, E. Lubkiewicz, W. Prokopowicz, W. Walus (Jagiellonian University Cracow, Poland)

Th.W. Elze, S. Heerd, H. Klingler, H. Spies, K. Stelzer (Universität Frankfurt, Institut für Kernphysik)

P. Egelhof, H. Emling, W. Henning, R. Holzmann, G. Ickert, R. Schmidt, H.J. Wollersheim

Gesellschaft für Schwerionenforschung, Darmstadt)

T. Blaich, J.V. Kratz, D. Lambrecht, M. Proft (Universität Mainz, Institut für Kernchemie)

The L.A.N.D. (Large Area Neutron Detector) facility was presented in the previous Scientific Report. The assemblage of the 200 submodules ('paddles') is close to completion, during February/March 1990 they will be inserted into the supporting structure and supplemented with the photomultiplier tubes. Sample tests were performed in order to control the quality of the paddles, in particular with regard to their relative light output, light attenuation and linearity of response. Examples for the sample tests are presented in figs. 1 and 2. In figure 1a we show the distribution of the light attenuation length of samples resulting in a mean value of L=2.4 m, which is even better than the figure guaranteed by the manufacturer of the plastic material (L=2 m). The relative light output measured for cosmic rays is shown in fig. 1b, it represents the quality of the plastic material as well as that of the light coupling between scintillator and phototube by means of a multi-strip plexiglas light guide. The coupling was achieved using 1.5 mm thick pads of Silicon rubber which allowed to compensate mechanical tolerances. Fig. 2 presents the linearity of the paddle response with regard to the position measurement. Again cosmic rays were used for this measurement, the incidence of which was determined by a trigger detector. The deviation from linearity of the measured position was found to be smaller than 1 cm, while an overall position resolution $\lesssim$4 cm (FWHM) was obtained. A subset of the paddles was exposed to high energetic neutrons delivered by the SATURNE accelerator at Saclay. The results fully satisfy our expectations with regard to the detector performance, based on earlier Monte Carlo studies. For example a position resolution of $\lesssim$6 cm was measured when the paddle triggered first by the neutron induced shower is selected. A detailed report on this performance study can be found in a separate contribution to this Scientific Report (S. Lange et al.). In a first application the L.A.N.D. will be installed for an experiment at SIS devoted to the study of inelastic excitations in pheripheral collisions. For that purpose various supplemental detector systems will be required which have been developed meanwhile. For example, various detectors for the identification of the projectile-like fragment and the momentum measurement in conjunction with the ALADIN spectrometer have been constructed and are presently under test with the first SIS beams. Also a charged particle multiplicity filter and a γ-ray calorimeter subtending almost the full solid angle around the target has been built. Detailed reports on the various detector components are presented separately (W. Walus et al. and H. Spies et al.). A schematic view of the entire set-up for this first experiment is given in fig. 3.

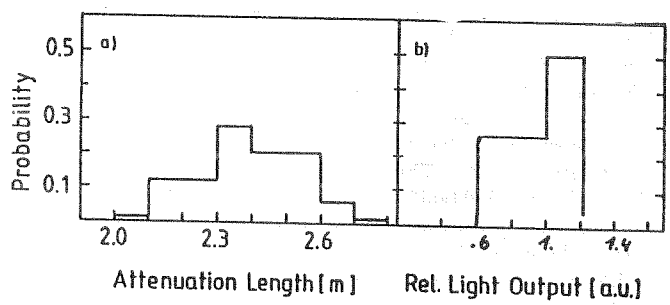


Fig. 1a: Distribution obtained from sample tests for the light attenuation length. b: Same as a) but for the relative light output.

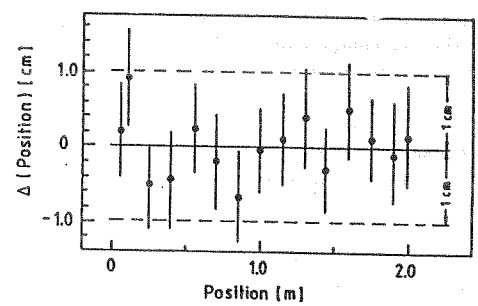


Fig. 2: Deviation from linearity of the position measurement in function of the position along the paddle.

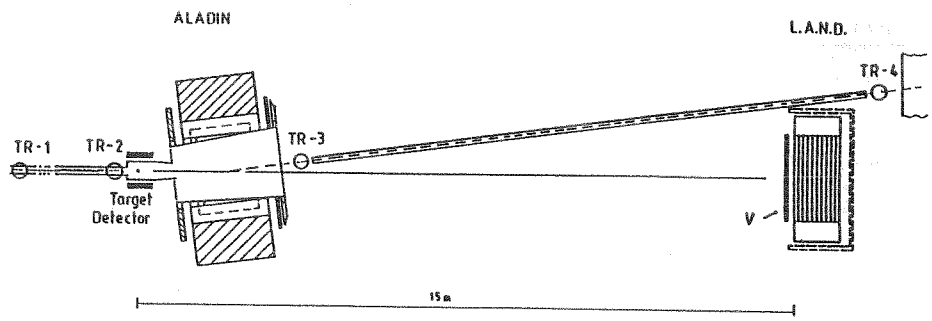


Fig. 3: Schematic view of the set-up as planned for the first measurement using L.A.N.D. at SIS
TR1,TR2: Start and beam defining counters
TR3: position sensitive plastic counter (PPL)
TR4: PPL, ionization chamber, Cerenkov detector
V: charged particle veto counter

Target Detector Array for L.A.N.D [G,B]

B.Gugulski, R.Kulessa, E.Lubkiewicz, K.Pena, W.Prokopowicz, W.Walus[1]
Jagiellonian University Cracow
and the L.A.N.D Collaboration

The neutron measurement after inelastic projectile excitation in peripheral collisions requires a supplemental detector system aside from the neutron detector. Such a detector system should give possibility to separate the central collisions from the grazing collisions with some differentiation for the midimpact collisions. In addition, the total energy released by γ-ray emission after inelastic excitation needs to be measured for a complete event characterization [1]. The target detector therefore involves both, a 4π charged particle detector array and a γ-calorimeter consisting of BaF_2 counters.

The charged particle multiplicity measurement is implemented by means of a 4π counter array (42 modules), a schematic view is shown in fig. 1. The detectors are made of organic plastic material (NE102) with a thickness of 5 mm. They are placed inside a vacuum chamber parallel (12 modules) and perpendicular (30 modules) to the beam axis. The modules parallel to the beam axis have dimensions of 260 mm x 80 mm and cover angles between Θ=40° and Θ=121°. They are read out at both sides via multistrip plexiglas lightguides and phototubes VALVO XP2972. A determination of position of impact is obtained by the time difference of the signals from the two photomultipliers. The detectors which are placed perpendicular to the beam axis cover forward angles between Θ=1.5° and Θ=40° (26 detectors) and backward angles between Θ=120° and Θ=150° (4 detectors) , respectively. All phototubes are placed outside the vacuum chamber. The light output from the plastic detectors was found to be sufficiently high even at the low energy deposit obtained from minimum ionizing particles, it has been tested using a ^{90}Sr β source ($\Delta E \approx 1$ MeV). For the γ-ray measurement an array consisting of 48 BaF_2 modules will be installed. The BaF_2 detectors are of 20 cm length and of hexagonal shape (inner diameter 5.2 cm) and are placed outside the vacuum chamber. The arrangement is schematically shown in fig. 1. The geometry of the BaF_2 detector array allows for a Doppler correction of the measured γ- ray energy.

In order to test to which extent the plastic detector array is sensitive to the impact parameter, heavy-ion collisions have been simulated with the statistical event generator FREESCO [2]. This code uses a fireball prescription to generate three thermal sources, the size of which depends on the impact parameter. The FREESCO parameter x_0 = 0.2, y_0=$exp^{-\sqrt{E_{per}N/125MeV}}$, z_0 = 0.1 and χ=1, which govern the excitation energy and momenta of the sources were used. From events predicted by the simulation and subsequently filtered by the response of the detector system, one can construct different observables. Fig. 2 displays the impact parameter dependence of the detector hit multiplicity for Pb on Pb collisions at a bombarding energy of 800 MeV/u. Obviously, a reasonable selectivity is obtained for the more peripheral collisions.

The target detector array including the vacuum chamber has been developed at the Jagiellonian University in Cracow and is presently installed for experiments at the SIS. The first tests will be performed during February 1990.

[1] present address: GSI Darmstadt

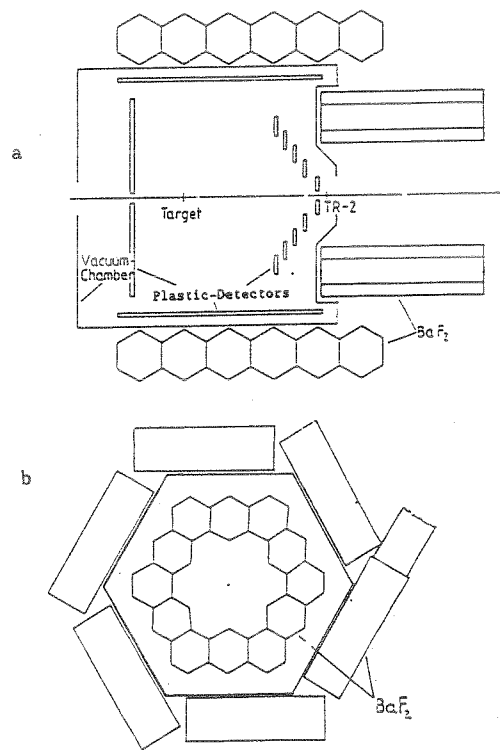


Figure 1: Schematic view of the 4π target detector array
a. along the beam axis and
b. perpendicular to the beam axis (only BaF_2 detectors are presented).

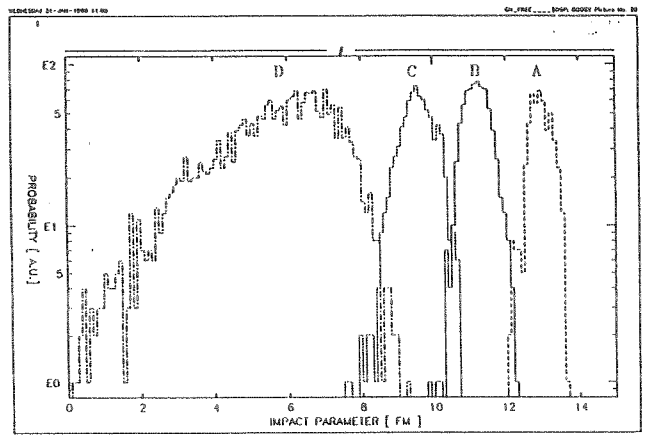


Figure 2: Impact parameter distribution for charged particle multiplicities as predicted by the FREESCO simulation and filtered by the response of the plastic counter array (^{208}Pb + ^{208}Pb at 800 MeV/u). The hit multiplicities $1 \leq M \leq 5$, $11 \leq M \leq 15$, $21 \leq M \leq 25$ and $31 \leq M \leq 36$ were selected and are denoted as A, B, C, and D, respectively.

References

1. SIS Proposal #S038 of the L.A.N.D collaboration, 1989.

2. G. Fai and J. Randrup, Nucl. Phys. **A404**, 551 (1983); Com. Phys. Comm. **42**, 385 (1986).

Experimental study of soft Coulomb dissociation ^{B} in extremely neutron-rich nuclei

P. G. Hansen[1)], F. Humbert[2)], L. Johannsen[1)], B. Jonson[3)], T. Nilsson[2,3)], G. Nyman[3)], A. Richter[2)], K. Riisager[1)], G. Schrieder[2)]

and

Members of the ALADIN-, FRS- and LAND-Collaborations.

[1)]The Institute of Physics, University of Aarhus

[2)]Institut für Kernphysik, Technische Hochschule Darmstadt

[3)]Department of Physics, Chalmers University of Technology, Gothenburg

An experiment to study Coulomb dissociation in extremely neutron-rich nuclei is going to be performed in the second experimental period of 1990 at GSI. The goal is an accurate measurement of the momentum distribution of neutrons and charged fragments which are produced in breakup processes. This will provide further information on the 'neutron halo'[1], which was proposed to surround such nuclei after ^{11}Li was shown to have a remarkably large radius.[2] Together with measurements of the ^{11}Li dissociation cross section it should be possible to prove the predicted existence of soft, low-lying E1 originating from ^{9}Li oscillations relative to the halo.

The new experiment facilities at GSI are very suitable for this kind of experiment. The fragment separator (FRS) will be able to supply about 200 ^{11}Li per sec. At the time for the experiment there will be no direct beamline from the FRS to the experimental area, so the beam will have to be transported through the storage ring (ESR). The experimental set-up will be placed in the 4π-cave.

The set-up has been subject of extensive considerations and simulation programmes have been written to optimize the different parts. A schematic picture is shown in fig.1. The position of the incoming beam is determined by two small (8×8 cm^2) multi-wire drift chambers (MWDC). The second drift chamber trigger also serves as starttrigger for time of flight measurement. The ALADIN magnet is situated close behind the target and is used to deflect the charged fragments, which are analyzed in two larger MWDC's (40×50 cm^2). When the position information from the drift chambers is coupled together with the bending power of the magnet, it is possible to resolve the longitudinal and transversal momentum distribution thoroughly. The dissociation neutrons are detected with the Large Area Neutron Detector (LAND), which is used in two different positions. With the LAND positioned as far away as possible, the transversal and longitudinal momentum resolution is maximized due to good angular resolution and a long TOF distance. To measure neutrons with a transversal momentum greater than 50 MeV/c, the LAND is moved to a closer position (see fig.1). To distinguish between Coulomb dissociation and nuclear reaction breakup, several targets covering a range from very low to very high Z will be used.

At this state of preparations (January 1990), a prototype for the small drift chambers is being under construction. It has been developed following the same ideas as have been used for building drift chambers at TRIUMF[3] (see fig.2).

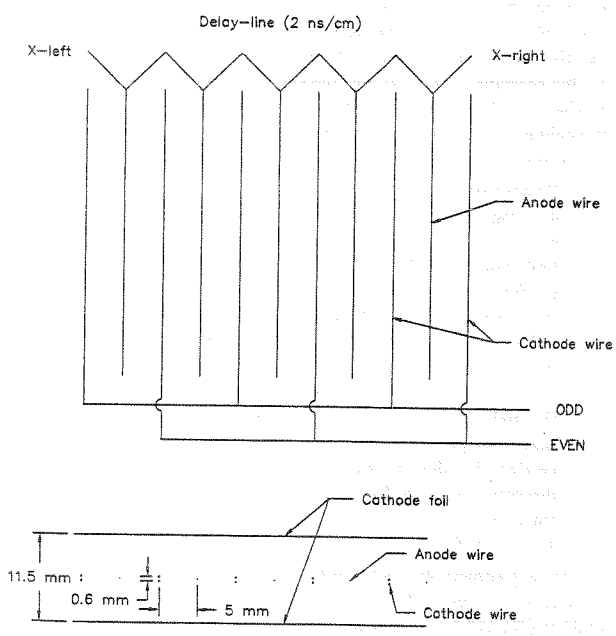


Fig.2: Schematic picture of one wire plane in the MWDC.

The anode readout is done in two directions over a delay-line. The time difference makes it possible to determine which anode wire was triggered. To distinguish between two tracks located at the same distance from, but on either side of the anode wire, the signal induced in the adjacent cathode wire is also used. A single wire read-out is not necessary so alternate cathode wires are bussed out on ODD and EVEN outputs. The double cathode geometry improves the detectors track collection near the cathode. With a satisfying position resolution of the prototype, the larger MWDC's will be built with the same wire geometry.

1 P. G. Hansen and B. Jonson, Europhys. Lett. 4 (1987) 409
2 I. Tanihata et al., Phys. Rev. Lett. 55 (1985) 2676
3 R. S. Henderson et al., Nucl. Instr. and Meth. A254 (1987) 61

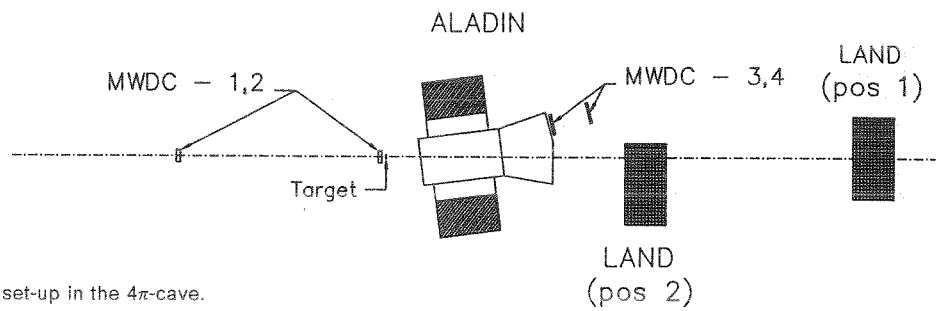


Fig.1: Experimental set-up in the 4π-cave.

γ-RAY SPECTROSCOPY OF RELATIVISTIC EXOTIC FRAGMENTS WITH POSITION-SENSITIVE GERMANIUM DETECTORS[G]

R. Holzmann, H. Emling, H.J. Wollersheim (GSI, Darmstadt) and the LAND Collaboration*

For a long time, apart from neutron transfer, no experimental techniques have been available to investigate highly excited states in very neutron-rich nuclei. Only recently have new methods been explored which are based on the γ spectroscopy of excited fragments from spontaneous [1] or in-beam [2] fission, or from deeply inelastic collisions [3]. The nuclei accessible are largely determined by the mass- and charge distributions characteristic of these processes, and the selectivity critically relies on being able to discriminate unwanted nuclides, e.g. through γ-coincidence techniques.

We describe here an experimental technique which is not hampered by these shortcomings and which can be applied throughout the chart of nuclides. It consists in populating excited exotic nuclei in a three-step procedure :

1. Relativistic projectiles from SIS (with E/A = 100-1000 MeV/u) are fragmented on a production target yielding a distribution of exotic nuclei.
2. Following a method pioneered at Ganil the fast-moving projectile fragments are mass- and charge-separated in a fragment recoil separator (FRS) [4]. With a primary beam intensity of $5 \cdot 10^{11}$ particles/s and a 1 g/cm^2 fragmentation target, one expects production rates of separated exotic nuclei of up to 10^7/s [5].
3. Excited states in the separated fragments are then populated through Coulomb excitation in peripheral collisions on a second, high-Z target [6]. At the beam energies considered here the cross sections for this process can be as high as a few barns. Low-lying discrete states are fed both from the ground state by direct excitation and from high-lying collective states (GDR, GQR) through statistical decay.

For a complete characterization of the peripheral collisions the incoming and outgoing fragments will be tracked through a large dipole magnet (ALADIN) with position-sensitive particle detectors. The mass will be determined from time of flight and magnetic rigidity, and the charge from the ΔE signal in plastic scintillator and Cherenkov detectors. Violent central collisions will be suppressed with a plastic charged-particle veto detector. As rather low-spin states are fed by the two mechanisms at play, γ multiplicities will be small and a detection system consisting of only a limited number (< 10) of efficient Ge detectors will be required.

The extremely high recoil velocities of the relativistic fragments, i.e. v/c = 0.4-0.8, together with the large solid angle required to achieve the high detection efficiency produce an extremely large Doppler broadening of the γ lines, limiting the energy resolution severely. This limitation is however circumvented if one uses position-sensitive detectors to measure the angle of incidence of the γ rays and correct the Doppler effects on an event-by-event basis. This position sensitivity can be achieved by employing planar Ge crystals which have one of their outer contacts segmented. Each segment has to be read out separately, providing the position information, while the energy information is obtained from the unsegmented opposite contact.

Using the computer code GEANT we have done Monte Carlo simulations for a stack of two planar 50x20 mm Ge crystals each divided into vertical stripes. For added realism the simulation included also a BGO anti-Compton shield and a passive lead collimator (Fig. 1). In the calculation monoenergetic γ rays were emitted from a source moving with given velocity and angle to the detector system. Compton-suppressed energy spectra were then generated with and without the Doppler correction applied. Thus, for a photopeak energy of 600 keV, v/c = 0.8 and a detection angle of 45°, the uncorrected spectra give a fwhm resolution of 18 % [Fig. 2(a)]. Correcting with the position information however improves the resolution to 5.1 %, 3.2 % and 1.7 %, with a 5- ,8- and 20-fold segmentation respectively [Fig. 2(b-d)]. This shows that in-beam spectroscopy of relativistic nuclei is feasible with segmented Ge detectors.

A prototype detector consisting of a stack of two planar Ge crystals, each 8-fold segmented, is currently in construction.

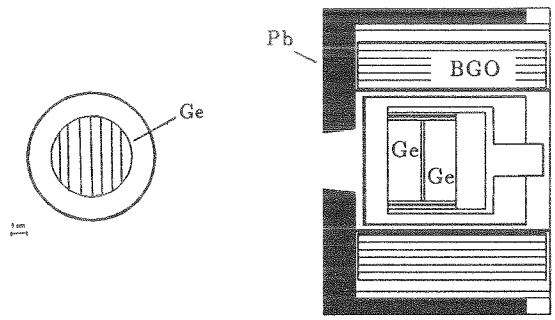


Figure 1: Schematic views of the detector set-up used in the GEANT calculations. An 8-fold vertical segmentation of the Ge crystals is shown.

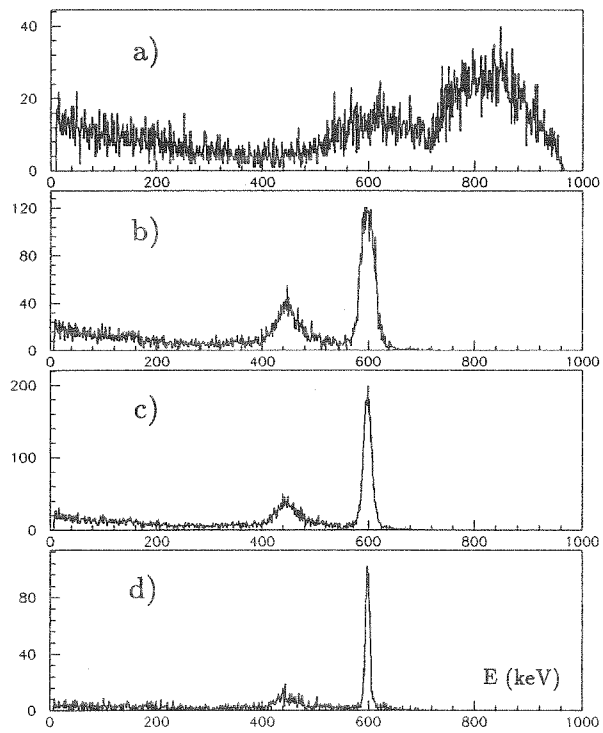


Figure 2: Simulated γ spectra for a source moving with v/c = 0.8 at 45° to the detector, before (a) and after the Doppler correction for a 5-fold (b), 8-fold (c) and 20-fold (d) segmentation.

[1] W.R. Phillips et al., Phys. Rev. Lett. 57, 3257 (1986).

[2] Y. Abdelrahman et al., Phys. Lett. 199B, 504 (1987).

[3] J.X. Saladin in Proc. Conf. on High-Spin Nuclear Structure and Novel Nuclear Shapes, April 13-15 1988, Argonne.

[4] H. Geissel et al., GSI Scientific Report 1987, p. 281.

[5] G. Münzenberg et al., GSI Nachrichten 11-87, 1987.

[6] H. Emling et al., LAND Collaboration, SIS proposal #52, 1987.

* GSI Darmstadt, Univ. Bochum, Univ. Frankfurt, Univ. Krakow, Univ. Mainz

Status of the Photon Spectrometer TAPS [G,B]

R.S. Simon and the TAPS Collaboration

GANIL, University Gießen, KVI Groningen, GSI, University Münster

TAPS is a modular scintillation detector for high-energy γ rays. It is based on BaF_2 for the detection of photons and on NE102 for the registration of charged particles. In the forthcoming experiments at SIS TAPS will comprise 256 individual modules. They will be arranged in blocks of 64 which are mounted on two detector arms[1].

Test experiments that addressed various aspects of the detector response continued throughout 1989. Among these were tests of BaF_2 sub-arrays with electrons in the energy range from 10-43 MeV as well as studies with discrete photons of 4.4, 11.7 and 16.1 MeV and with tagged photons of 186 MeV. Also investigated was the possibility to identify light particles, in particular p,d,t and ^{3}He, ^{4}He, by a combination of TOF information and pulse shape analysis. Part of the results are presented in separate contributions to this scientific report.

The mass production of the detector modules started mid 1989. At present the BaF_2 crystals are delivered by the manufacturer at a rate of approximately 8 per week. More than 80% passed the acceptance tests which for instance check the optical transmission in the UV and visible range from 200-800 nm and which determine the intensity of the fast and slow component of the scintillation light. A groove is cut into the cylindrical base of the crystals to hold the input light fiber of the laser control. The crystals are wrapped in teflon and aluminium foils and then crystal, photomultiplier and base are tightly joined with the help of plastic shrinking tube. The performance of the finished detectors is shown in fig. 1.

Before the experiments begin at Darmstadt TAPS will be used at Caen. The TAPS electronics, the data acquisition hardware and the detectors have recently been transferred to GANIL. For the experimental set-up 12 blocks of 19 detectors each are arranged in close geometry: 6 blocks with TAPS modules, 3 blocks of slightly smaller detectors from GSI and 3 blocks of detectors from ORNL. The laser control system for the TAPS detectors is in operation. At GANIL the TAPS data acquisition and control system serves the 228 BaF_2 detectors as well as the spectrometer SPEG which participates in the experiments. In-beam measurements are planned in the period from mid February to the end of March 1990 using beams of Ar, Kr and Xe.

[1] Technical Proposal for a Two Arm Photon Spectrometer, GSI Report GSI-87-19

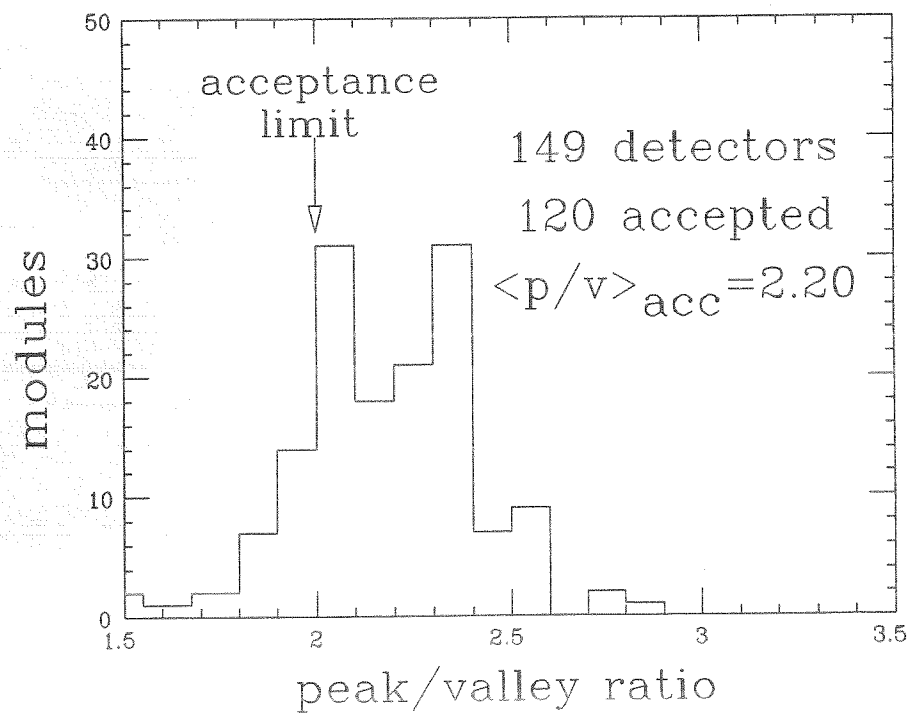


Fig. 1: Distribution of peak/valley ratios for ^{60}Co calibration spectra. The peak/valley ratio corresponds to the maximum intensity of the 1.33 MeV peak relative to the intensity in the valley between this peak and the 1.17 MeV peak below. For the measurements always the same photomultiplier was used.

Status Report: The Kaon Spectrometer at SIS[G]

The KaoS-Collaboration:
W. Ahner[1], P. Balthes[2], D. Brill[3], R. Brockmann[1], E. Grosse[1], W. Henning[1], H. Jäger[2], P. Koczon[1], B. Kohlmeyer[4], W. Konrad[4], D. Miskowiec[1], Ch. Müntz[2], H. Oeschler[2], K. Poppensieker[1], H. Pöppl[4], F. Pühihofer[4], R. Renfordt[3], A. Sandoval[1], R. Schicker[1], B. Schlei[4], P. Senger[1], Y. Shin[3], K. Stiebing[3], R. Stock[3], H. Ströbele[3], K. Völkel[4], W. Walus[1]

[1]GSI, [2]TH Darmstadt, [3]Univ. Frankfurt, [4]Univ. Marburg

The Kaon Spectrometer[1),2),3)], consisting of a dipole and a quadrupole magnet on a movable platform, was built within one year by DANFYSIK A/S and installed in the SIS target-area in December 1989. The "figure-of-eight"-type quadrupole (aperture 30 cm, length 80 cm) is kept free of material between the upper and lower pole at the side of the downstream beam pipe to allow for an easy observation of projectile fragments. The C-shaped dipole yoke (2.4x2.7x2.6 m^2) has a weight of 100 tons and consists of 5 iron blocks clamped together. The gap volume is 0.2 m x 1.8 m^2. At a nominal magnetic field of 1.7 Tesla the magnetic force between the pole shoes (aquivalent to 300 tons) does not deflect the yoke legs by more than 0.1 mm. One large vacuum chamber reaches from the quadrupole entrance to the dipole exit; in the dipole it is formed by inner surfaces of the pole shoes. The large-area exit window (310x40 cm^2), covering two sides of the chamber including a corner, will be made of two 180 μm thick carbon foils and tested for a pressure of 6 bars.

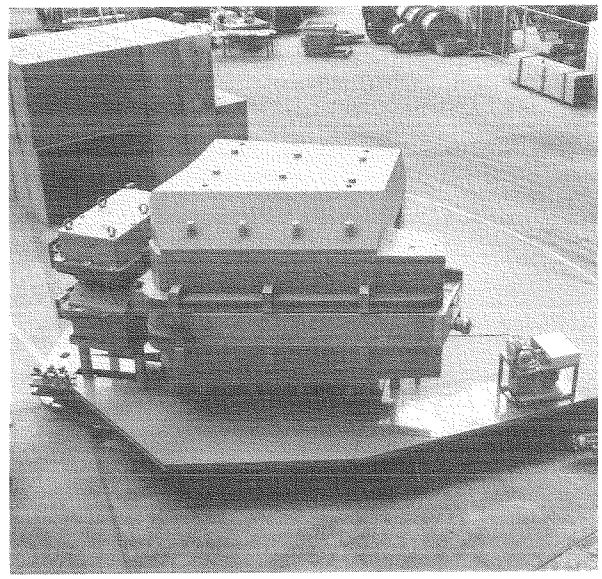
The setup has a total weight of 130 tons and can be rotated around the target position by means of 4 air cushions and a motor drive. Each of the air cushions is able to lift 40 tons by 75 mm with an air pressure of 4.5 bar. The total air consumption is about 6000 l/min for an ideally flat floor. The platform is sitting on the pivot (at target position) and on two "elephant" feet, which are adjustable in height by computer controlled step motors in order to correct for floor ondulations at different angular positions. This in combination with a high accuracy angle encoder allows a positioning of the QD with an accuracy of better than 0.1 mrad. Two different ways of guiding the SIS beam downstream from the target allow mean observation angles from 0^0 to 9^0 and from 19^0 to 120^0 with respect to the beam; due to the large opening angle of the spectrometer all forward angles are accessible in experiments.

The power supplies deliver currents of 2500 A (450 kW) and 1250 A (160 kW), respectively; they will be controlled by GSI standard devices using the modified MIL-STD 1553B. All cables for power and signals as well as the tubes for cooling water and compressed air will be connected to the spectrometer in such a way, that they enter the cave 5 m above the floor and hang down at the pivot position to allow for the rotation of the platform without being stressed.

The target scattering chamber has a double-conical shape (aperture 50-100 mm) and is made of 1 mm thick carbon fibre, so that no special window is needed for the particles going to the spectrometer's entrance. The beam pipe downstream the target is also made of carbon fibre to minimize scattering and secondary reactions of the projectile fragments measured with the Small Angle Hodoscope (see contribution in this report). The 20 ton iron beam dump, designed for an intense beam of 10^{10} Ne-ions, is under construction. It will be movable on rails, as the primary beam is deflected slightly by the strayfield of the quadrupole at measuring angles below 45^0 Provision has been made for the control of the different mechanical movements - as well as the Hall probes, power supplies etc. - by VME modules, which will be operated by special control systems.

Experiments at the spectrometer will investigate small cross sections - like K-production - in the presence of large background rates - mainly from protons and pions. Thus a selective trigger system has to be available already for the first experiments. The signals from the threshold Cerenkov detectors (for low momenta supplemented by start-stop overlap coincidences delayed by the proper time-of-flight) will be used in a first level hardware trigger to start the FASTBUS ADC's and TDC's for the right velocity particles preferentially (e.g. for kaons). A second level trigger is based on the time-of-flight information as digitized in fast CAMAC-FERA modules; a flight path correction (on the basis of a position sensitive transmission scintillator in front of the QD) will be performed on the Motorola 68030 processor in the CVI crate controller. This trigger decision will be made long before the end of conversion and readout in the FASTBUS modules and allows their fast clear and reset for unwanted events. Each of the two trigger levels is expected to reduce the event rate by about one order of magnitude, allowing the study of central collisions at a target rate of 10^6/s corresponding to an average beam intensity of up to 10^9 part/s. In the case of K-production we then expect 0.1 to 10 'good' events per second.

1) GSI Scientific Report 1987 (1988) p.298
2) GSI Nachrichten 05-88 (1988)
3) GSI Scientific Report 1988 (1989) p.310,311



Status of the TOF-Detectors for the Kaon Spectrometer at SIS [G,B]

B. Kohlmeyer, W. Konrad, H. Pöppl, B. Schlei and F. Pühlhofer
FB Physik der Universität Marburg
and the Kaon Spectrometer Collaboration

The time-of-flight (TOF) between the start detector near the target and the stop detector in the Kaon Spectrometer focal plane will be measured with a time resolution of 250 ps FWHM over a flight path of 5m[1].

Covering the momentum range from 0.75 to 1.7 GeV/c the stop detector consists of 60 separate plastic paddles in two rows (fig.1). The design allows to rotate each paddle to a position perpendicular to the central ray (angle of incidence 37° [2]). A paddle consists of a 38x3.7x2cm^3 PILOT F scintillator, two 8cm long light guides and 2" photomultiplier tubes (PMT) on both ends. Compared to the original plans the scintillator height has been reduced from 60cm to 38cm because of problems in building a sufficiently large MWPC in front of the stop detector.

For 2" PMT with good time characteristics[1] the gain shift has been measured by increasing the count rates of a ^{241}Am-source and a light pulser in front of the scintillator (fig.2)[3]. As studied by many investigators the gain shifts to higher values due to the deflection of electrons by charging the insulating materials in the tubes or to the residual gas reacting with the dynode material. The best stability condition up to count rates of 2x10^5 Hz is found for the HAMAMATSU tubes R1828.

Fig.3 shows the measured influence of the magnetic field on the gain of the PMT R1828 screened by a 22cm long and 6cm wide PERMENORM cylinder extending 5cm beyond the PMT front side[3]. For our setup we have chosen 1.6mm thick cylindes in order to shield against magnetic fields in the focal plane up to B_x=147, B_y=154 and B_z=40 Gauss.

As start detector 20cm in front of the quadrupole a segmented setup of 16 96mm long and 2mm thin plastic-strips in one row with curved light guides and 3/8" PMT HAMAMATSU R1635 on both ends is under construction (fig.4). This detector requires magnetic PMT screens of 13mm wide and 0.8mm thick PERMENORM cylinders to shield against the strong quadrupole leakage field as well as a 10x10mm^2 deflection magnet near the target to suppress knock-on electrons up to 3.3 MeV.

Serving for the PMT stabilisation and the energy and time calibration of each detector module a laser calibration system is designed. In order to stimulate scintillations in the plastic material an UV laser VSL337 is chosen, which itself is stabilized by a ^{241}Am-source producing a constant light output in a separate reference start and stop detector paddle.

1. B. Kohlmeyer et al., GSI Annual Report 1988
2. W. Ahner et al., GSI Annual Report 1988
3. B. Kohlmeyer et al., to be published in NIM (1990)

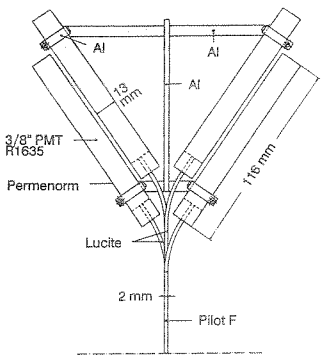


Fig.4: Schematic side-view of the upper part of the start detector.

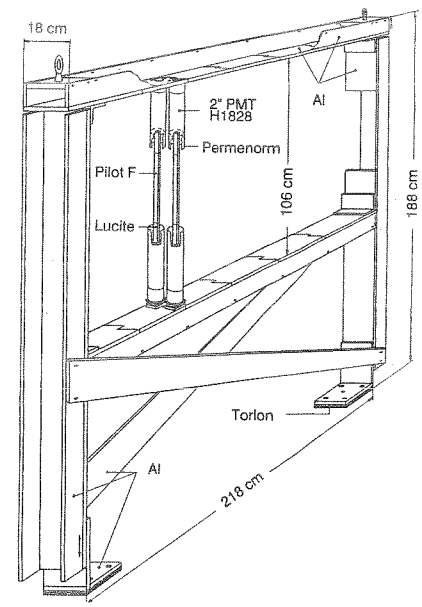


Fig.1: 3-dimensional view of the stop detector (only two modules shown).

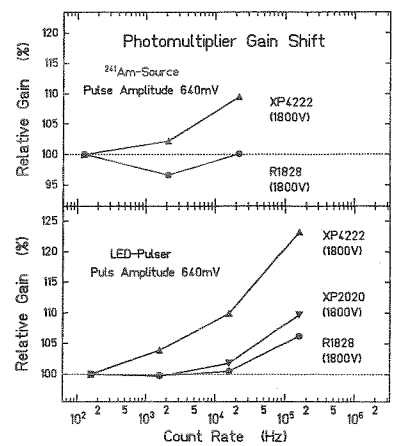


Fig.2: Photomultiplier gain shift as a function of the count rate.

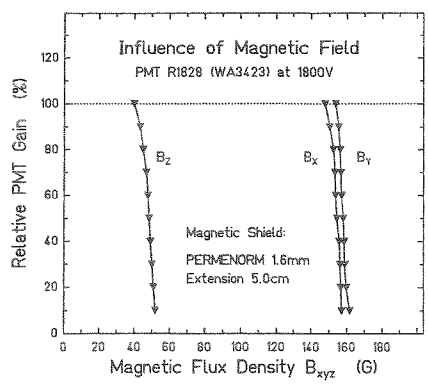


Fig.3: Influence of the magnetic field on the photomultiplier gain.

Event characterization at the Kaon Spectrometer[G]

D.Brill[1], E.Grosse[2], D.Miśkowiec[2,3], P.Senger[2], Y.Shin[1], R.Stock[1],
H.Ströbele[1], W.Waluś[2,3] and the KaoS Collaboration
([1]Univ.Frankfurt,[2]GSI,[3]Univ.Kraków, Univ.Marburg,TH Darmstadt)

In order to determine global event properties like impact parameter and orientation of the reaction plane in the proposed experiments with the Kaon Spectrometer the reaction products will be measured with two scintillator arrays. One of them, the Small Angle Hodoscope, is a planar plastic wall which was used previously at the BEVALAC Streamer chamber facility (see ref. [1],[2]). This hodoscope is located about 7 m downstream of the target and will measure the energy loss and the time of flight of fragments emitted in a forward cone of about 9 degrees opening angle. The hodoscope has an active area of 2.24m x 1.92m and consists of 380 plastic scintillator counters of three different dimensions: the small angle range is covered by $4\times4cm^2$ elements, with an adjacent area of $8\times8cm^2$ and an outer frame of $16\times16cm^2$ modules. In the middle of the small angle area a hole is cut in the scintillator wall for the carbon beam pipe. The material of the 2.54 cm thick scintillators is Bicron BC 408. Each element is coupled on the backside to a photomultiplier (Amperex XP2982 for the small modules, XP2262 for the others) by an aluminium cone. During the run the calibration will be controlled by a laser driven optical system. A coated 1 mm diameter quartz light fibre is fed into each aluminium cone. It illuminates the scintillator backside with light from a pulsed nitrogen laser via a splitter system. The wavelength of the laser's UV radiation is 337 nm corresponding to a photon energy of 3.68 eV which allows a simulation of an ionizing particle going through the scintillator. The anode signals of the photomultipliers are split to charge sensitive Fastbus ADC's (LeCroy 1885F), which record the specific ionization-dependent amplitude, and to leading edge discriminators (Camac: LeCroy 4415) feeding into Fastbus TDC modules (LeCroy 1875) for particle time of flight measurements.

In addition to the forward wall a target counter array (Target Hodoscope) will be installed, as shown schematically in Fig. 1. It consists of 96 detectors arranged in three rings around the beam axis, outside a vacuum chamber made of 1mm carbon fibre. The plastic scintillators (PILOT F) have a thickness of 20 mm and cover angles between $\Theta = 12°$ and $\Theta = 48°$. They are read out via cylindrical light guides of 15 mm diameter and phototubes HAMAMATSU R3478. The light output from the plastic detectors was found to be sufficiently high even at low energy deposited by minimum ionizing particles.

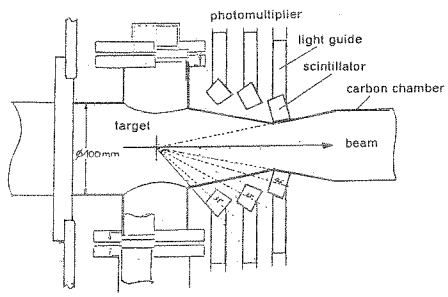


Figure 1: Schematic view of the target counter array

Simulations were performed in order to test the possibility of reconstructing the impact parameter and the reaction plane orientation using the information from the two hodoscopes. FREESCO (Fragmentation-by-Explosion/Evaporation Simulation Code) [3] was used to generate 10^4 events of $^{208}Pb+^{208}Pb$ and $^{40}Ca+^{40}Ca$ at the beam energy 800 MeV/u. These events were treated by the GOOSY analysis, using the detector setup information. The Target Hodoscope covers the angular range where most of participant fragments are emitted at the beam energies of concern. Since the impact parameter is directly correlated with the number of participating nucleons, it can be selected via multiplicity of particles detected in the Target Hodoscope (Fig.2). In semi-central collisions the number of projectile spectator fragments registered in the Small Angle Hodoscope can give additional information about the impact parameter. These fragments have approximately beam velocity and can be separated from participant fragments by their different time of flight.

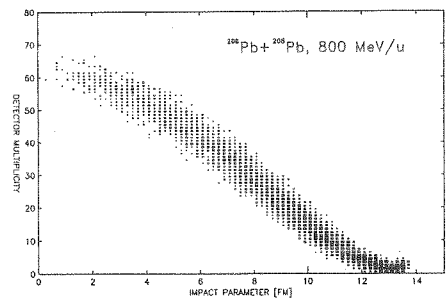


Figure 2: Correlation between the impact parameter and the number of hit scintillators of the Target-Hodoscope ($^{208}Pb+^{208}Pb$ at 800 MeV/u) – simulation.

Heavy fragments of the projectile spectator can be used also to determine the reaction plane. The following procedure was applied to test this assumption: in each event the ϕ (azimuthal angle) distribution of particles detected in the Small-Angle-Hodoscope, weighted with the expected amount of light produced in the scintillator (to enhance heavy fragments), was considered. The centre of gravity of this distribution was compared to the known angle of the reaction plane (Fig.3). The correlation between the width of the ϕ distribution and the multiplicity of the event, as appearing in the simulation, has to be verified in the experimental data in order to justify this method of event characterization.

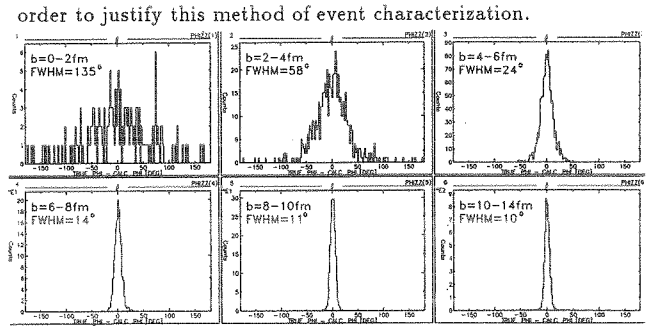


Figure 3: The difference in azimuthal angle between the calculated and true reaction plane for several impact parameter bins ($^{208}Pb+^{208}Pb$ at 800 MeV/u).

References

[1] R. Brockmann et al., GSI Scientific Report 1983; ditto 1984.
[2] W. Rauch, Doktorarbeit, 1986.
[3] G.Fái,J.Randrup, Comp.Phys.Communication 42(1986)385.

A Magnetic Spectrometer for the Detection of "Knock-On" Electrons from Heavy Ion-Atom Collisions at Relativistic Energies

G

5.1

K. E. STIEBING, J. BERNHARDT, K. BETHGE, A. HAUSMANN, D. KRAFT,
H. SCHMIDT-BÖCKING (IKF Frankfurt)
H. BOKEMEYER, H. FOLGER, E. GROSSE, W. HENNING, R. MANN,
P.SENGER, J.ULLRICH (GSI Darmstadt)
A. BALANDA (Univ. Cracow)

A four-gap orange-type magnetic electron spectrometer has been developed and is presently built at the IKF Frankfurt. It is designed for first SIS experiments exploring the emission spectra of energetic δ-electrons from very heavy intermediate-energy and relativistic ion-atom collisions. The concept of this spectrometer is the use of ray tracing *inside* the gas filled gaps of the toroidal magnetic system by means of low-pressure windowless MWP-detectors to determine the leptons energies [1] for a spectroscopy of electrons/positrons in the energy range between 5.0 to 40.MeV. It has been tested in a prototype one-gap version by investigating the reaction ^{11}B(d,p)^{12}B ($E_{(\delta)}$= $13.4 MeV$) at the 2.5MV van de Graaff accelerator of the IKF [2].

In this report we describe an application of the magnetic system for the investigation of the spectrum of energetic "knock on" electrons, i.e. the ionisation of loosely bound atomic electrons from the target (binary encounter electrons) and the projectile (convoi electrons). Depending on mass and energy of the projectile the energies of these electrons reach to 3.0 to 4.0MeV for the highest SIS energies available. However, contrary to the electrons from very strongly bound atomic and quasiatomic levels, the emission of these "quasifree" electrons is focussed into forward angles with highest energies being emitted at 0^o. Therefore the magnet will be used in an arrangement rotated by 90^o with respect to its way of installation for the investigation of δ-electrons. The heavy-ion beam is then passed through two of the four 190. x 245.mm^2 gaps of 30^o opening angle. The first gap is used to clean the beam from accompagnying electrons, whereas the second gap contains the lepton detectors.

In fig.1 a cut at the mid plane of the system through the "down-stream" magnetic gap of the system,along the beam axis is shown. At the range of electron energies of interest here, the concept of ray traycing cannot be applied any more, due to multiple scattering of the electrons in the detector gas and entrance foil. A set of silicon detectors will be used instead.A ΔE/E-detector arrangement is used as electron detection system. In this way a commercially available set of three 20 x 40mm^2 position sensitive silicon detectors with a thickness of .5mm are combined with a large Si(Li)-detector of 7.0mm or 10.0mm thickness, the latter being capable of stopping all electrons. In order to increase the countrate capabilities of the set-up this detector is also subdivided into six independent detector areas of 10 x 40mm^2 each. As the system is designed to measure mainly spectra with exponential shapes (binary encounter electrons) and dynamically broadened structures (convoi electrons), a moderate energy resolution is sufficient and a cooling device (peltier element) mainly serves to keep the detectors at a constant temperature. It is able to cool the whole system down to $T \approx 10.0^o C$. At this temperature the energy resolution of the E-detectors amounts to δE $\approx$ 25.0 to30.0keV.

In fig.1 it is shown, that the electron paths of interest are located well inside the magnetic-gap where the discrepancies of the magnetic field from a truely 1/r-dependence can be neglected [2]. The trajectories displayed in fig.1 therefore are calculated assuming ideal 1/r-field and emission angles of 0^o. The transport efficiency $\epsilon(\theta)$ onto the whole detector area has been calculated as a function of the energy and the emission angle. The emission-angle dependence for three different energies, resembling roughly the bandwidth of the spectrometer at a constant setting of the magnetic field (.6Tesla), is displayed in fig.2. It is demonstrated that the most interesting range of emission angles, i.e. centered around 0^o is completely transported to the detector system ($\Delta\theta \pm (5-7)^o$) at a bandwidth of ΔE/E $\approx \pm 15.0\%$. Emission angles of $\pm(20-25)^o$ are still measured simultaneously with transport efficiencies of $\epsilon(\theta) \geq 10\%$.

Beeing designed for the spectroscopy of an purely electron-emitting process the set-up has been optimized for the detection and background suppression of one species of leptons only (depending on the polarity of the magnetic field). However the opposite ("positron") side of the set up can advantageously be used to discriminate against electrons stemming from nuclear pair creation and bremsstrahlung radiation by identifying coincident positrons. For for this purpose a szintillation detector will be installed.

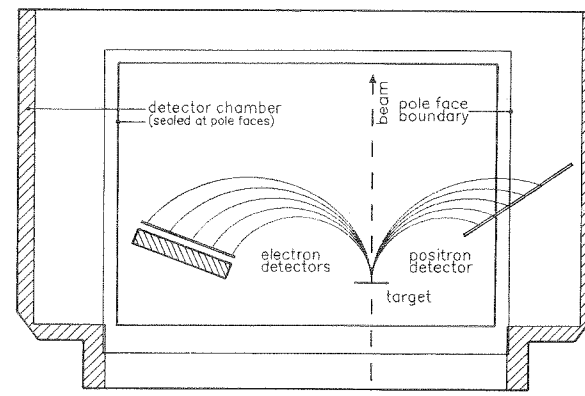


figure 1:schematic drawing of a cut through the "downstream" magnetic gap along the beam axis. Also shown are electron and positron trajectories calculated assuming 1/r-field.

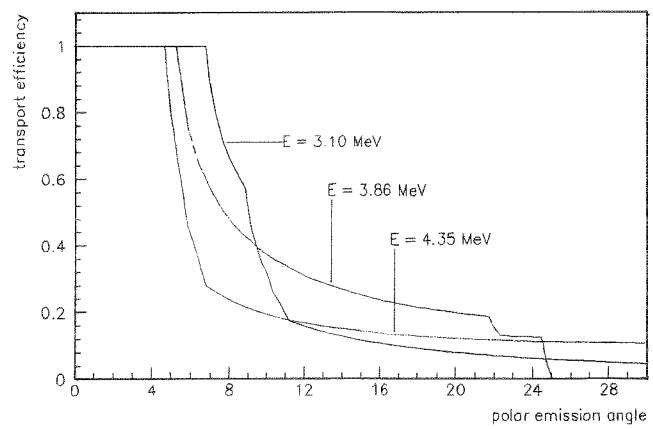


figure 2:emission-angle dependence of the transport efficiency $\epsilon(\theta)$ of the magnetic system for three electron energies, at a field setting of 0.6Tesla.

[1]A. Müller et al., GSI 88-1 ,GSI report, p.306
[2]J. Peter et al., DPG(IV)24, KH-9.3 (1989)

Developments in the Detectorlaboratory

H.W. Daues and H. Stelzer
GSI Darmstadt

In the course of this year the main activities have been concentrated on the assembly and testing of a variety of multiwireproportional chambers for the first experiments at the SIS and ESR. These chambers are all operated with a two-stage gasamplification, the properties of which have been extensively studied in the recent years[1]. The first gas-amplification occurs in the preamplification gap in a homogenous high electric field. The electrons then drift via a transfer gap into an ordinary multiwire proportional chamber and are multiplied again around the anode wires. This two-stage amplification greatly facilitates the operation of these detectors. Furthermore, they exhibit a better time-resolution (10 nsec FWHM for heavy ions) and can record with the same voltage setting minimum and heavily ionizing radiation.

In the beginning, the electrodes of the preamplification gap have been made of 50 μm tungsten wires with a spacing of 0.5 mm. It could be shown that a woven mesh of thin metalized polyester threads is very well suited for a planar electrode. This fabric has a sufficiently high mechanical rigidity and can firmly be stretched and fixed onto a frame. The thickness of the electrodes could thus be reduced by a factor of three. Even more important, especially for measurements at the fragment separator, is the fact that this material is much more homogenous than an electrode made of the formerly used tungsten wires.

A large chamber for the Kaon spectrometer has been built and tested. The performance of this chamber during the test runs was excellent. The tests were done with the beta-particles of a Sr-90 source. The sensitive area is 1190 x 340 mm. To allow for high trigger rates and multiplicities the wires are read-out individually. To allow for a simultaneous determination of the x and y coordinates of the impact point the induced signals on the cathode wires are read-out. The anode wires are also read-out to resolve ambiguities in multi-hit events. Extensive studies have been performed to investigate the shape and distribution of the induced charges onto the cathode wires. The read-out of this chamber with its approximately 500 channels will be performed by a transputer network, which is currently being built and tested by the TH Darmstadt[2].

For the ray-tracing at the fragment separator and for biological irridiation experiments eight counters with a sensitive area of 200 x 200 mm^2 have been built and successfully tested. These counters are equipped with a delay-line read-out. This economic read-out method limits the maximum count rate of the chambers to some 100 Khz. Three of these counters are already installed in a preliminary set-up at the SIS.

A beam-profile monitor with an active area of 90 x 90 mm^2 has been designed and built. It is essentially a multiwire proportional chamber, again with a pre-amplification gap. The wires (or groups of wires) of each cathode plane are connected to a current integrator. The wires of the two planes are orthogonal to each other and by determining the current on the individual wires one gets a beam profile in the horizontal and vertical direction. In the more commonly used read-out methods a puls-amplifier is connected to the cathode wires, which senses the **induced charge** created by the avalanche around the anode wire near the impact point of the particle. In a counter with current read-out, the actual flow of the positive ions to the cathode wires is sensed and amplified. A prototype of such a counter is installed in one of the extraction channels of the SIS and clear beamprofiles could be observed in the fast and slow extraction mode. Due to its two-stage gasamplification, this beam monitor works over a wide range of beam intensities. The lower limit is of the order of 100 Neon particles per pulse, the upper limit is about 10^7 particles per pulse. The read-out of this gas-filled beam profile monitor is performed with the standard current read-out electronics used for the beam profile grids at the UNILAC and the SIS.

In high intensity beams, the aging of the counting gas is a severe problem. In the gas amplification process the gas is cracked and the cracking products are deposited onto the anode wire. The wire gets thus thicker and the gas gain drops. The critical limit, as found in the literature, lies around 1 coulomb of collected charge per cm anode wire. Argon-methane mixtures and iso-butane are especially sensitive to this effect. Unfortunately, they seem to be the best suited counting gases. Tests have been performed and are still under way to find other gas-mixtures with no or at least greatly reduced admixture of hydrocarbon gases.

References:

[1] H. Stelzer et. al., GSI Scientific Report 1986, 1987

[2] P. Baltes et. al., this report

Detector Developments for the In-Flight Particle Diagnostic at the FRS [G,B]

E. Hanelt, T. Brohm, H.-G. Clerc, B. Knoedler, K.-H. Schmidt[1], M. Steiner, B. Voss

TH Darmstadt, [1]GSI Darmstadt

For the operation of the fragment separator (FRS) several diagnostic tools will be necessary in order to tune the separator to select a pure secondary beam and to monitor the conditions of the experiments. In the following we report on new detector systems to be used at the FRS.

Transmission Beam Monitor

For the experiments at the FRS a reliable beam-current normalisation is needed. At relativistic beam energies it is impossible to use a standard Faraday cup. Therefore we constructed a SEcondary-Electron TRAnsmission monitor. This detector type which has been developed at SATURNE as a position-sensitive profile monitor [1] works like a current grid with a sensivity which is increased by several orders of magnitude.

Our prototype which is not yet position sensitive consists of a cylindrical casing, carrying two 10 μm aluminum foils of 110 mm diameter on both sides. In this faraday cage a third foil is mounted, which is insulated against the casing. The casing is held on a potential of +100 V during operation, so that the secondary electrons knocked out from the inner foil are collected on the outer ones. The corresponding current is measured on the inner aluminum foil. This large-area transmission detector is homogeneous and has a small thickness of about 8 mg/cm^2. The detector can mechanically resist to the irradiation with relativistic heavy ions for a long time. Therefore it can be used as a a universal current monitor for SIS beams.

Recently the SEETRAM was successfully tested at the target station of the FRS using a beam of 150 MeV/u ^{20}Ne at an intensity of about 10^8 particles per second. During the fast extraction period of SIS the detector was operated in two modes: Coupled to a charge-sensitive preamplifier, the charges of consecutive bunches extracted with a time difference of 355 ns could be measured (see figure 1). Then the current was read out using a standard current digitizer (CD 1010). The latter operation mode should be preferable with slow extraction.

Two-Dimensional Position-Sensitive Scintillator

All transmission detectors which can be used online between the intermediate focal plane and the exit of the FRS have to fulfill the condition of extreme homogeneity in order not to disturb the ion-optical resolution. A large homogeneous charge- and position-sensitive scintillation detector has already been tested successfully using a 400 MeV/u ^{40}Ar beam at SATURNE [2]. This type of detector has been further improved by a two-dimensional readout. Using one detector in the intermediate focal plane and a second one at the exit of the FRS it will be possible to resolve all fragments up to uranium with a maximum kinetic energy of 900 MeV/u by a time of flight measurement with an expected time resolution of 85 ps FWHM. A test with two of these detectors will be carried out in the near future at SIS.

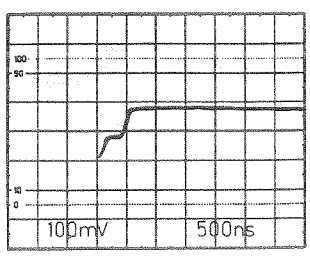


Figure 1: Signal of the SEETRAM during one extraction of SIS (two bunches).

The Influence of MWPCs on the Resolution of the FRS

The standard diagnostic system of the FRS will be supplied with multi-wire proportional counters (MWPC) from the GSI detector laboratory [3]. These detectors have also been tested successfully using the 400 MeV/u ^{40}Ar beam at SATURNE [4]. However, inhomogeneities introduced by tungsten wires and plastic grids deteriorate the ion-optical resolution of the separator when these tracking detectors are introduced. As demonstrated in fig. 2 for light ions at high energies, the detoriation is only small.

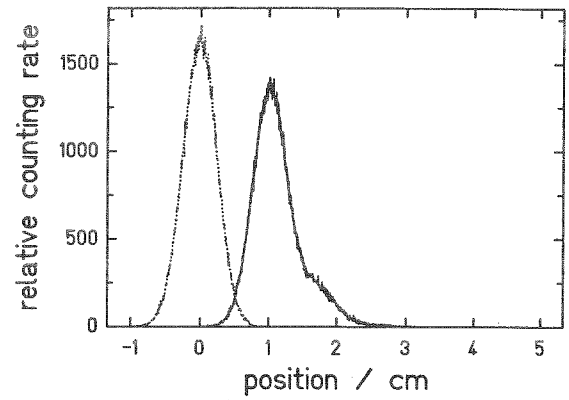


Figure 2: Calculated position distribution of a ^{22}Ne-beam (1 GeV/u) at the exit of the FRS without (dashed line) and with (full line) two MWPC tracking detectors introduced in the intermediate focal plane. The ion-optical resolution in the intermediate focal plane was assumed to 1500.

Microstrip Anode Detector

For the application with heavier ions, a microstrip anode detector system is in preparation, which combines homogeneity, high count-rate capability and good position resolution. This detector originally developed for the detection of neutrons at the ILL Grenoble [5] was tested at SIS in December (We would like to thank A. Oed for his advice and support for the construction and the operation of the detector). It consists of a gas chamber with a nearly homogeneous electric field similar to an ionization chamber. The anode is split into various chromium microstrips on a glas plate with alternate voltages (anode and cathode strips) in order to assure gas amplification of the electrons there. These strips with a width of only a few microns are the essential feature of this detector, as they allow a very high field strength and short drift times for the produced ions to reach the neighbouring strips. In our test with a beam of 100 MeV ^{20}Ne from SIS the detector was used for the detection of high-energy ions for the first time. Although the neon projectiles themselves did not reach the detector, the secondary particles produced in the windows and detectors upstream the beam were used to study the drift times of the electrons and the ions as well as the gas amplification as a function of the applied voltages.

References

[1] R. Anne et al., Nucl. Instr. Meth. 152 (1978) 395.

[2] B. Voss et al., GSI Scientific Report 1988, p.283 .

[3] H. Stelzer, H.W. Daues, GSI Scientific Report 1988, p.326 .

[4] B. Voss et al., GSI Scientific Report 1988, p.284 .

[5] A. Oed, Nucl. Instr. Meth. A263 (1988) 351.

Residual Gas Beam Profile Monitor for SIS Beams

H. Berg, H. Schmidt-Böcking
Universität Frankfurt
J. Ullrich, R.E. Olson*
GSI Darmstadt

A prototype of a beam-profile monitor which determines the profile by detection of ionised residual gas atoms has been developed and successfully tested. Applying this method, profiles and absolute beam intensities can be determined without any perturbation of the beam. Similar developments have been reported by other authors [1].

As illustrated in Fig. 1 an electric field is applied perpendicular to the beam axis accelerating positive residual gas atoms, ionized by the beam onto a two-dimensional position sensitive channelplate detector. Due to the low kinetic energies of the produced recoil-ions [2] below 100 meV, an exact beam profile can be obtained using only small accelerating voltages of about 1 keV/cm, thus avoiding any practical pertubation of the beam itself. In the present design the aperture for the SIS beam is 10 cm × 10 cm and large enough for the penetration of an even poorly focused beam.

To test the apparatus, a 4.8 MeV/u Ar beam of the UNILAC was collimated to a spot of 0.5 mm × 0.5 mm and then led through the monitor at a residual gas pressure of 10^{-7} torr. A trace of recoil-ions along the beam path is observed at the detector, shown in Fig. 2a. The projection of the two-dimensional plot perpendicular to the trace yields the beam profile as illustrated in Fig. 2b. Since only low quality channelplates were available for these first tests, the measurement was influenced by an unusual large amount of background events. By shifting the vertical position of the beam inside the monitor and providing a beam of a well defined size, the overall resolution of the system could be measured. Under optimum conditions a resolution of ± 0.25 mm was obtained. This includes the position resolution of the channelplate detector itself (± 0.05 mm), the spread of the profile due to a small fraction of recoil-ions with higher transverse velocities as well as influences due to inhomogenities of the accelerating electric field.

A set of total ionization cross sections was calculated using the CTMC approach [3] in order to estimate the recoil-ion count rates under SIS conditions. At 1 GeV/u the cross sections range between 10^{-17} cm^2 and 10^{-14} cm^2 depending on the projectile charge state and the composition of the residual gas. For 10^{10} particles/s in the beam and a residual gas pressure of 10^{-10} torr, recoil-ion intensities between 1 and 10^4 particles per seond and cm beampath are expected. Such rates can easily be handled by the channelplate detector. For the case of small cross sections (low charged, high-energy projectiles) the pressure can be increased up to a maximum value of 10^{-6} torr in an area well localized around the detector. Thus, recoil-ion count rates or in other words the time necessary to take a profile, can be continuously increased up to a factor of 10^4. For high-energy projectiles and low charge states, where this amplification will be necessary, the electron capture cross sections are small so that the perturbation of the beam is still negligible.

Presently, the monitor is developed futher in order to be compatible with UHV conditions, and work is in progress to perform first tests with beam from the SIS by the midth of February, 1990.

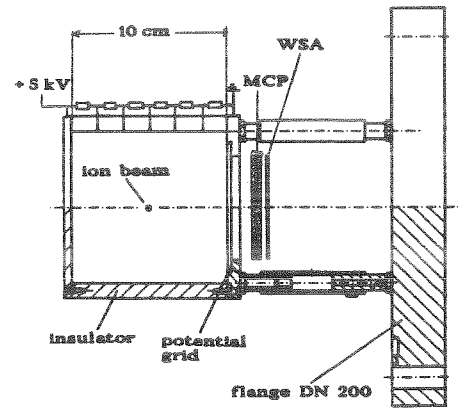


Figure 1: Beam profile monitor. MCP: Multichannelplate detector; WSA: Wedge and strip anode

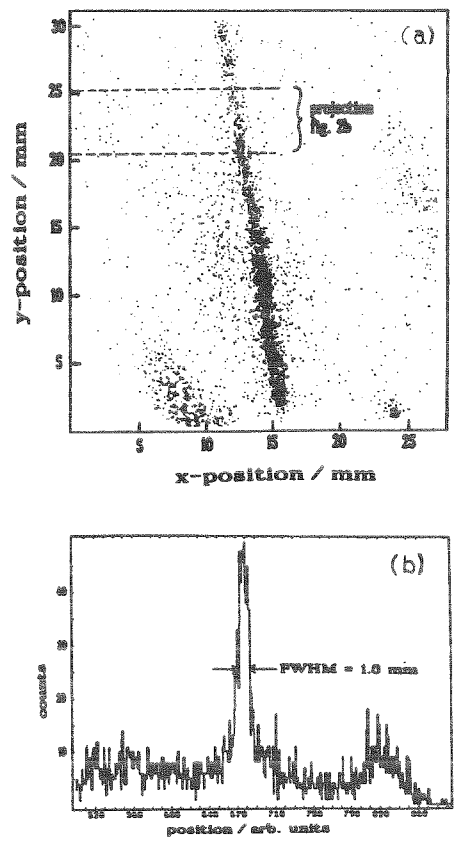


Figure 2: (a) Trace of the beam detected on the two-dimensional position sensitive MCP; (b) Projection onto the x-axis of the part indicated in Fig. 2a.

References

[1] J. Krider, Nucl. Instr. Meth. A278 (1989) 660

[2] R.E. Olson, J. Ullrich, H. Schmidt-Böcking, J. Phys. B20 (1987) L809;
J. Ullrich, R.E. Olson, H. Schmidt-Böcking, S. Schmidt, R. Dörner, V. Dangendorf, H. Berg, Journal de Physique, tome 50, (1989) C1-29

[3] R.E. Olson, J. Ullrich, H. Schmidt-Böcking, Phys. Rev. A39 (1989) 5572

*University of Missouri-Rolla, Humboldt Award Fellow

Calibration of a Detector System for the Measurement of Target-Like Fragments from ^{116}Sn + ^{48}Ti Reactions [B]

J. Kiesewetter, K.-Th. Brinkmann, F. M. Baumann, M. Bergmann, H. Freiesleben, H. Gassel
Institut für Experimentalphysik, Ruhr-Universität Bochum

B. Kohlmeyer
Fachbereich Physik, Universität Marburg

K.D. Hildenbrand, D. Schüll, H. Sohlbach
GSI, Darmstadt

J. Speer
HMI, Berlin

The detector system[1] consisting of an ionization chamber (IC) with an integrated parallel plate avalanche counter (PPAC) was used as coincidence detector at the GSI magnetic spectrometer. The aim of the experiment was to measure quasi-elastic primary cross-sections (yield of both reaction products prior to particle emission) in the system $^{48}Ti(^{116}Sn,x)y$ at E=A·8 MeV. In order to obtain an optimum mass resolution for TLFs of 1-2 MeV/u very thin foils needed to be used. The entrance window consisted of a 35 µg/cm² Formvar-foil[2]. The cathodes of the PPAC were Formvar-foils of 75 µg/cm² on which a 60 µg/cm² Au-layer was evaporated. The size of both the IC and the PPAC together with the particular electrical potential caused by the integrated PPAC results in significant position dependences of energy and time measurements. Their investigation and respective correction in the final data analysis is an essential prerequisite to obtain good Z and A resolution. The position dependences were determined from elastic scattering of ^{16}O on ^{16}O at E_{lab}=28 MeV utilizing the 4 MV tandem-accelerator at Bochum. A 35 µg/cm² SiO_2-target was used. The detector system was placed at d=2.26 m,⟨Θ⟩=45° and was run in coincidence to a surface barrier detector (d=6 cm,⟨Θ⟩=-45°).

In a first step the active area of the detector was divided in the offline analysis into sections of 0.9 cm x 1 cm using the position informations (in plane: X , out of plane: Y). The differences of the effective signal-generation time at different points on the PPACs were evaluated by comparing the measured times of flight with those obtained from kinematics and energy-loss calculations for the centers of these sections. Lines of constant signal-generation time are shown in fig. 1 for one half of the PPAC. These times were parametrized for fixed X by $t_E = aY^2 + BY + C$. The corrections for different values of X were done by interpolating the coefficients A,B,C. The non-linear behaviour of t_E is probably due to an arching of the thin cathodes caused by the strong field of the PPAC.

The dependences of the pulse heights in the ΔE and E_R-sections of the IC on Y appeared to be nearly independent from X. Additionaly, they were found to be proportional to the mean pulse height ⟨P⟩. Hence, a parametrization of the form P(Y) = ⟨P⟩ · (1 + d(Y)) could be chosen. Fig. 2 shows d(Y) for the ΔE section of the IC and the whole IC.

[1] K.-T. Brinkmann et al., GSI Scientific Rep. 1988,p.316
[2] H. Gassel et al., GSI Scientific Rep. 1988,p. 332

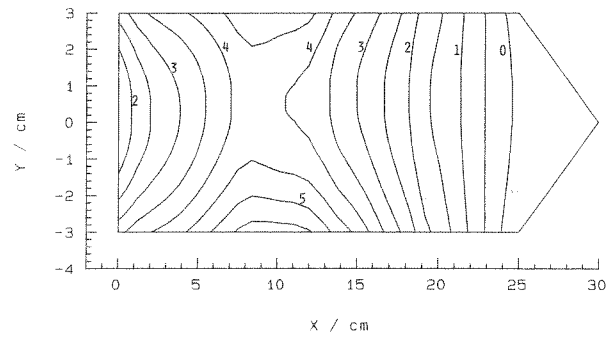


Fig. 1: Lines of constant signal-generation time in one half of the PPAC (values refer to t_E / ns). The signal is taken off at X=30cm.

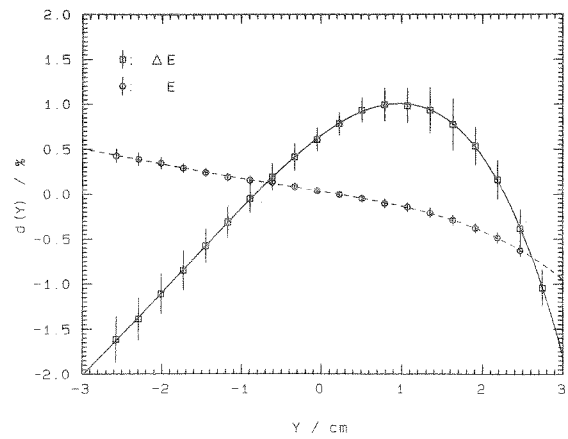


Fig. 2: Y-dependence of pulse heights of the ΔE section and the whole IC (E). The lines represent polynomial fits to the data

A Large-Area Multiwire Proportional Chamber for the Kaon Spectrometer[B,G]

P. Baltes, J. Foh, H. Jäger, E. Kankeleit, Ch. Müntz, H. Oeschler (TH Darmstadt),
H. Stelzer (GSI Darmstadt) and the KaoS Collaboration

A two-stage multiwire proportional chamber [1] for the determination of particle trajectories in the Kaon Spectrometer [2] at SIS has been constructed. A new modular transputer-based data acquisition system for the single-wire read out of 580 channels was designed and various components of it were successfully tested.

The MWPC operating at atmospheric pressure has a sensitive area of 1190 × 340 mm^2. Measurements were performed with minimum ionizing electrons of a ^{90}Sr-source. The operating gas P10(Ar:CH_4=9:1)/C_4H_{10} is used in order to optimize gas amplification and quenching properties. Full efficiency was achieved. Other gas mixtures, P10/CO_2 and particularly Ar/CO_2, show a deterioration concerning quenching.
To design the readout electronic and algorithms the shapes of the influenced cathode charge distributions were studied. Figure 1 shows the distribution of the areas (influenced charge) and FWHM of these distributions: In spite of the large dynamic range the number of neighbouring wires with a signal above pedestal is nearly constant.

To allow for high trigger rates and multiplicities the wires are read out individually. Two cathode planes for x and y determination are used, respectively, where 5 wires are connected together to one amplifier, consisting of a charge-sensitive preamplifier and a linear amplifier with a gaussian filter (100 ns shaping time, gain ≈ 10 V/pC). A 8-Bit Flash-ADC with linear gate and stretcher is used for digitalisation (1.3 μs conversion time). 16 ADCs are connected to one transputer module (s. figure 2). Each of these modules is connected to the neighbouring transputer board by a fast link for communication and data transfer. The center of gravity of the charge distributions is calculated in parallel and processed online in this transputer chain within less than 100 μs. One transputer module (81 × 75 × 8 mm^3, two-sided SMD technique) includes a T222 transputer (INMOS), 64 kByte RAM, link- and I/O-driver and -receiver and I/O-decoder. This module with a computing power of 10 MIPS (Million Instructions Per Second) and the possibility of cross linking represents an universal usable and compact system for data processing, including synchronisation and data analysis. The parallel architecture of the anode and cathode readout is supported by the programming language OCCAM.

One module with 16 ADCs and amplifiers was successfully tested with cathode signals. The discriminators for the pattern readout of the anode wires (reduction of multiple-hit ambiguities) are designed and tests are in progress. A T801-board (floating point processor) is designed and built in order to speed up the data acquisition in an improved transputer network.

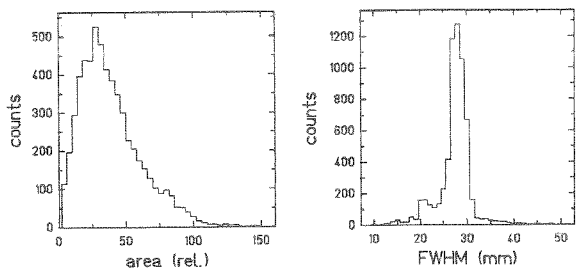


Figure 1: Area (charge) and FWHM of influenced cathode charge distributions.

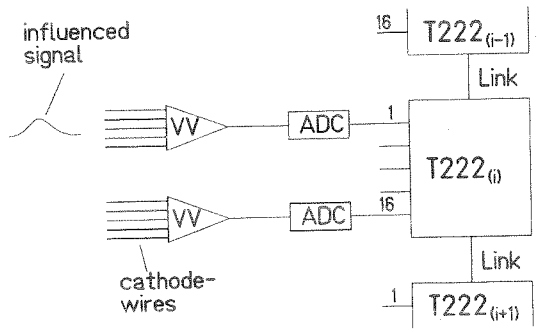


Figure 2: Cathode readout and transputer architecture.

References

[1] Ch. Müntz et al., GSI Scientific Report (1988).

[2] GSI-News 88-5; this report.

A Single Wire Readout System for Multiwire Proportional Chambers G+B

J. Friese, H. Hiller, W. Wilhelm
Technische Universität München

For many applications of multiwire proportional chambers a single wire readout is desirable. In particular for the VUV-photon detector [1] (115 wires) and other larger MWPCs a high speed readout system at reasonable cost is needed. We therefore started the development of a modular, transputer controlled data preprocessing system, in which one modul is designed for 64 channels (Fig. 1).

Each wire is connected to a hybrid charge sensitive preamplifier, a shaping amplifier (gaussian, 250 ns FWHM), and a 8 bit flash ADC with additional discriminator and peak sensing circuitry. The discriminator level can be set commonly for all ADCs. Each ADC contributes one 'valid'- signal as a significant bit to a 64 bit word, which is input to a cluster recognition circuitry. This circuitry examines the input word with respect to the appearance of certain programmable bit clusters and is realized on a specially designed ASIC (Application Specific IC). The ASIC is designed such that the allowed cluster length is programmable. The length $L = UL - LL + 1$ is variable within the limits $1 \leq LL \leq 7$ and $1 \leq UL \leq 15$. Up to 6 clusters (f.i. of length 2 to 5) might be identified simultaneously. Additional bits provide for a fast recognition of invalid events. For each 'allowed' cluster the start address (wire number) and the length (number of neighbouring wires) are stored and given sequentially to a transputer (T800), which in turn addresses only the corresponding ADCs for digital readout (via a 10 Mbit/sec serial link).

The selection of only those wires, which have fired, allows then the transputer to perform a fast online center-of-gravity analysis of the measured pulse height distributions in each cluster. The only numbers transferred to the host computer might then be the centroid <x>, amplitude A(<x>), and variance σ , or others.

Due to the fast timing ($t_{ADC} < 0.5$ µsec, $t_{ASIC} = 3.5$ µsec) and the drastically reduced number of parameters to be transferred, the system should be capable of comparatively high count rates. Depending on the complexity of the analysis software in the T800, rates between 10 to 100 kHz should be accessible. A similar system has already been successfully tested for the Q3D-focal plane detector at the Munich Tandem Laboratory [2] with count rates up to 40 kHz.

A prototype system (hardware and software) is beeing assembled and will hopefully be ready in May 1990. Preliminary tests of a newly developed 4-fold ADC card show encouraging results and the ASIC will be delivered in March 1990. The host of the stand alone prototype system will be an IBM-PC. A rough cost estimate results in less than 250 DM/channel.

[1] J. Friese et al.,
A Particle Identification System for Relativistic Heavy Ions, GSI Scientific Report 1988, p.297

[2] H. Hiller, H. Lindner et al.,
Private communication and
Beschl.Lab. TUM,LMU, Jahresbericht 1989, p..

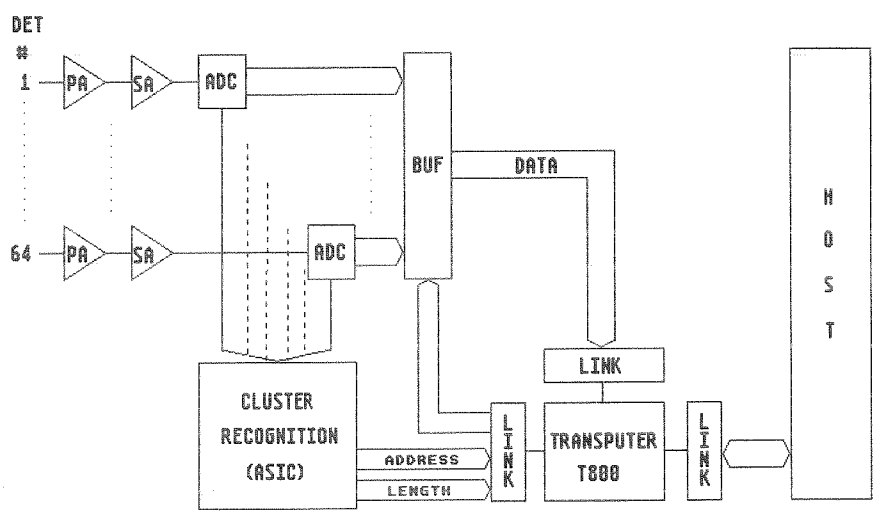


Fig. 1: Block diagram of the readout system for a VUV-photon sensitive MWPC.

Test of a Multiwire Proportional Chamber for VUV-Photons G+B

J. Friese, H.J. Körner, J. Reinhold, K. Zeitelhack
Technische Universität München

The Cerenkov photon detector, which is part of the particle identification system built for the central focal plane of the FRS[1]), has been tested with respect to detection efficiency and position resolution.

The detector is a 30 cm long single stage MWPC (115 wires)[2]) on top of a drift chamber with 5 cm drift length. The measurements have been performed for Ar-CH_4(P10) and Ar-iC_4H_{10} (80/20) with a 0.5% TMAE admixture at 930 hPa. Each wire is read out via a charge sensitive preamp., shaper and peak sensing ADC.

A calibrated, pulsed H_2-flash lamp (700 ± 200 photons/pulse for 170 nm ≤ λ ≤ 230 nm) was used to generate a collimated VUV-photon beam. The image (Ø ≅ 10mm) at the entrance window of the detector simulated the expected 'ear'- like structure of the focussed Cerenkov ring[1]).

The pulse height spectrum (Fig. 1) for the center of typically 7 firing wires corresponds to a primary charge of 20±10 photoelectrons and suggests a lower detection threshhold of 2-3 electrons. The pulse height distribution of all wires (Fig 2.) thus resembles the projection of an equally illuminated spot onto one axis and yields an integrated charge of 60±30 photoelectrons. From that we deduce an overall detection efficiency of ε ~ 9% for VUV- photons, in good agreement with Monte-Carlo calculations performed earlier.

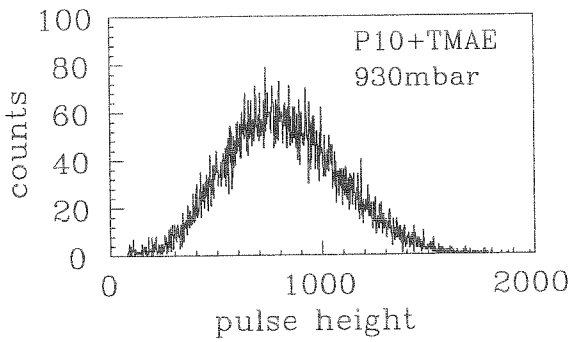


Fig. 1: Pulse height spectrum measured on one wire for a primary charge of 20±10 electrons.

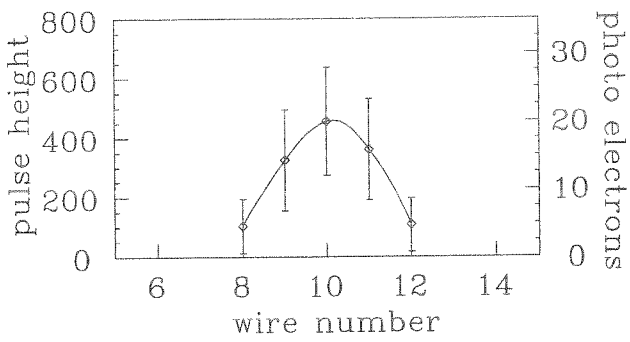


Fig. 2: Pulse height distribution as a function of wire number (wire spacing Δ = 2.6 mm), revealing the projected intensity distribution of the VUV-light spot.

The center position X_{meas} of the light spot was obtained as a weighted average of the measured pulse heights of all neighbouring wires for each single light pulse (Fig. 3). The position resolution is Δx = 1.84 mm (FWHM) for Ar-CH_4 and Δx = 1.55 mm (FWHM) for Ar-iC_4H_{10}. Small position variations of the flash lamp could easily bee measured by the detector, revealing no significant structures due to the discrete wire spacing of 2.6 mm (Fig. 4).

According to the geometry of the detector setup at the FRS these measurements simulate the detection of an ion (Z=30, β=0.815) with a velocity resolution $\Delta\beta/\beta = 2.0 \cdot 10^{-3}$ (FWHM) and a resulting mass resolution of $\Delta A \cong 0.4$ u. For heavier ions these numbers will improve, as the number of emitted Cerenkov photons scales with Z^2 and thus leads to significant larger pulse heights and narrower distributions.

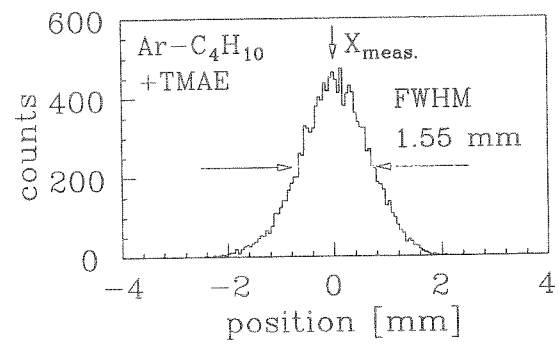


Fig. 3: Variation of the center position of the VUV-light spot as it results from a center-of-gravity analysis for each single light flash.

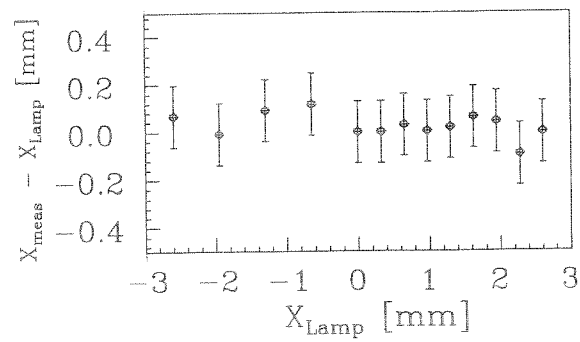


Fig. 4: Difference of measured and true location for various positions of the flash lamp along the detector axis.

[1] J. Friese et al.,
A Particle Identification System for Relativistic Heavy Ions GSI Scientific Report 1988, p.297

[2] E. Berdermann et al.,
A VUV-photosensitive Gasdetector for RICHI
GSI Scientific Report 1987, p.291

TP-MUSIC III- A new tracking detector for the ALADIN facility

R.J. Meijer, Z.A. Liu, J. Lühning, U. Lynen, H. Sann, W. Quick
(GSI Darmstadt)

W. Seidel (Zentralinstitut für Kernforschung, Rossendorf, GDR)

A new ionisation chamber of the TP-MUSIC type is now in the final stages of construction and will replace TP-MUSIC II mid 1990 at the ALADIN facility. The new detector is designed especially to measure the tracks and the atomic numbers of minimum-ionizing particles which pass the ALADIN magnet. TP-MUSIC III will be able to determine the tracks of the particles without relying on position information of other detectors. Research is started to improve the detection of light particles using gas-amplification techniques.

The ionisation chamber is build inside a support structure made from stainless-steel and epoxy-glass rods. This rigid construction allows for the precise positioning of all other parts of the detector. The active volume is 1.80 m along the beam axis (Z-axis), 2.0 m in the bending plane of the magnet (X), and 1.0 m in the direction perpendicular to this plane (Y). The cathode is placed vertically along the beam axis in the center of the detector, and two Frisch-grids will be placed at a distance of 1 m on the left- and right side of it. The stainless-steel frames on which the Frisch-grid wires will be mounted provides also a firm support for the Θ-grids and anodes.

The drift region between cathode and Frisch-grid is surrounded by kapton foils. Aluminium strips of 10 mm wide are evaporated with spacings of 3 mm on both sides of the foils. The spacings on one side of the foil are covered by the strips on the other side. Connected to a voltage-divider chain, the overlapping strips will define the potential on the boundary of the drift region. Furthermore, the pattern of the overlapping aluminum strips mimimizes the influence of external potentials on the field in the drift region. The non-trivial way of connecting the strips to printed-circuit boards was solved satisfactory.

About 45 anodes, each 1 m long and 30 mm broad, will be placed at a distance of 15 mm from both Frisch-grids. The charge of each anode is amplified by a charge-sensitive preamplifier and a shaping (150 ns) main amplifier. The signals of the main amplifier will be digitized by a flash-adc system.

From the drift times of the electron clouds the X-positions of the track are determined. The measurement of the Y-positions will not, unlike the previous versions of the detector, be measured with a separate field cage. Instead Θ-grids, placed between the anodes and the Frisch-grids, and resistive anodes will be used. The new method has the advantage that now, without using information from other detectors, X- and Y-coordinates can be correlated unambiguously in the case of multiple tracks.

The electronic noise in the amplification chain limits the detection of particles with $Z < 5$–6 in the ionisation chamber. In principle gas amplification of the primary electron-cloud would increase the signal of these particles far above the noise level. However, amplifications of large primary electron-clouds, generated by highly-charged particles, can lead to cross talk and space charge problems. To study these problems two small ionisation chambers, in which one of the anodes was replaced by a gas-amplification unit, were build. In the first detector the gas-amplification unit has two amplification sections, each consisting of several wire planes. The amplification of each section is low (100). The first wire plane screens quite efficiently the anode volume from the large signals at the second amplification stage. Also Y-coordinates are measured by the induced charge on wires in the second amplification section.

The second detector employs a 14 μm W-Au wire to create the high fields needed for the gas amplification. In the present detector configuration amplification factors uptil 10^4 at 150 torr argon(90%)-methane(10%) are easily obtained. A delay line is positioned parallel to the wire and from the induced signals the Y-coordinates of the primary electron clouds are deduced. It was found to be very time saving to study cross-talk problems by applying pulser-generated pulses on the proportional wire. The results indicate that small dummy anodes (0.5 cm broad) adjacent to the gas-amplification unit and a fine nickel-evaporated polyester mesh, in the anode plane of the amplification unit, screens the rest of the anodes sufficiently well from the large pulses generated on the proportional wire.

Further research on both amplification techniques will continue in the next year, during which also tests with the TP-MUSIC III detector are foreseen.

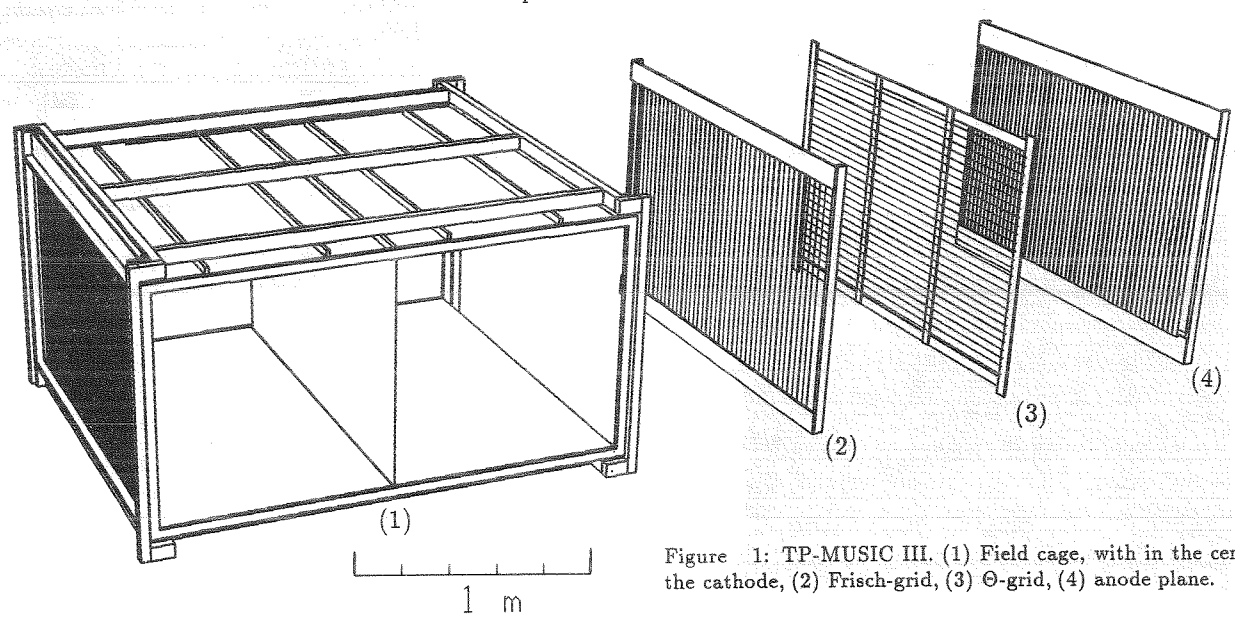


Figure 1: TP-MUSIC III. (1) Field cage, with in the center the cathode, (2) Frisch-grid, (3) Θ-grid, (4) anode plane.

A High Pressure Xe-filled Gas Scintillation Proportional X-Ray-Camera with fast Timing Properties and high Compton Suppression Capability for 1sσ - MO Spectroscopy[G,B]

V. Dangendorf, H. Schmidt-Böcking
Institut für Kernphysik, Universität Frankfurt, 6000 Frankfurt, FRG

A. Breskin, R. Chechik, I. Tserruya
Department of Physics, The Weizmann Institute of Science, Rehovot, Israel

P. Mokler
Gesellschaft für Schwerionenforschung, 6100 Darmstadt, FRG

A prototype high pressure Xe-filled Gas Scintillation Proportional Counter (GSPC) was developed and tested for quasimolecular (1sσ-) X-ray spectroscopy in supercritical heavy ion-atom collisions. Due to the low MO-X-ray yield and the high multiplicity of the simultaneously emitted γ-rays in such experiments, the availability of high energy X-ray detectors (30 - 500 keV) with excellent Compton suppression capability is of great importance. To enable fast X-ray-particle coincidence experiments such a device should exhibit a time resolution of a few ns. An energy resolution of a few percent is required to resolve the expected oscillatory structure in the MO-X-ray spectra. Following the scope of the work as reported in Ref.1, a prototype GSPC was developed and tested for its performance.

ENERGIE (keV)	CSF ^{22}Na	CSF ^{60}Co
40 - 60	15.4	13.5
60 - 80	17.5	15.6
80 - 120	11.5	11.1
120 - 160	10.5	10.8
160 - 200	11.1	10.5

(error ≤ 10 %)

Tab.1: Compton Suppression Factor achieved by application of the K-fluorescence-gating method.

Tab. 1 shows the measured Compton suppression performance of the device under K-fluorescence-gating condition[2] in the energy range between 40 - 200 keV. For lower energies a combined method of pulse-shape analysis and the definition of appropriate effective X-ray conversion layers yielded CSFs of 5 to 10 [2]. A simulation of the γ-absorption processes proved, that with this detector the γ-induced low energy Compton background (below 100 keV) may be reduced by a factor of ~ 70 than compared to a unprotected Ge-detector of similar absorption efficiency. Fig.1 shows the X-ray energy spectrum of an ^{241}Am source as obtained with the GSPC. The resolution of the 30 and 60 keV peaks was measured to be 6.8 resp. 4.3 % (fwhm). The time resolution, which was derived from the primary scintillation emission of the GSPC, could be determined with ~3 ns (fwhm).

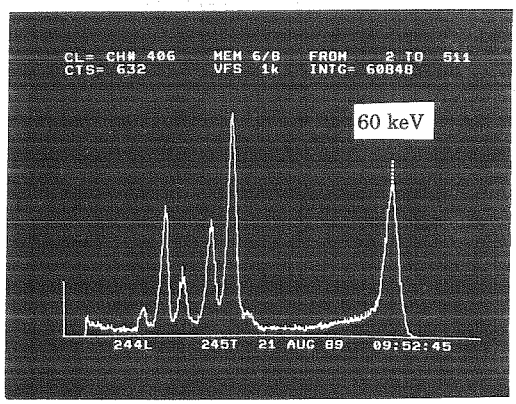


Fig. 1: X-ray energy spectrum of ^{241}Am. measured with the GSPC

However, a "bottleneck" in the present setup is the low efficiency under the complex operating conditions of the detector. In the energy range below 150 keV this is mainly due to the fact, that for absorbed events the probability of detecting primary light and fluorescence radiation after the occurance of a photoabsorption is near 30 %. For higher energies the gas detector suffers from its low photon absorption cross section. To overcome this obstacle, an upscaled version of the GSPC with 300 cm^2 window area and a working pressure of 25 bar is under construction. For such a device a 3-dimensional, multi hit imaging capability would be of great advantage, to separate simultaneously incident γ- and MO-X-ray-events. To investigate such a possibility, we developed a 2-dimensional position sensitive UV-detector for the Gas Scintillation Chamber, based on a low pressure hydrocarbon filled double step multi-wire counter with a solid photocathode[3] (called "SPAC", from Solid Photocathode Avalanche Chamber). A sketch of the present setup, consisting of the GSPC and the SPAC is shown in Fig.2. With this devise we obtained a 3-dimensional imaging capability for the position of the X-ray interaction with a resolution of 2-3 mm.

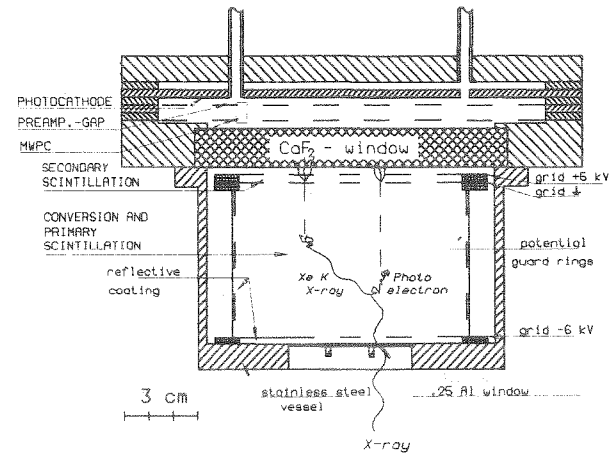


Fig. 2. Scheme of the GSPC - X-ray camera

1) V. Dangendorf, H. Schmidt-Böcking, A. Breskin, R. Chechik, I. Tserruya, GSI-Scientific Report, 1988

2) V. Dangendorf, H. Schmidt-Böcking, A. Breskin, R. Chechik, A contribution to SPIE's 33rd Symposium, San Diego, August 1989

3) V. Dangendorf, H. Schmidt-Böcking, A. Breskin, R. Chechik, "A Gas-filled UV-Photon Detector with CsI-Photocathode for the Detection of Xe Light", to be published in NIM 1990

Test of a subsection of the Large Area Neutron Detector at SATURNE [B.G]

J.S. Lange, H. Freiesleben, J. Keller, W. Kneissl, R. König
Institut für Experimentalphysik, Ruhr-Universität Bochum
and the L.A.N.D. Collaboration

In May 1989 a subsection of the large area neutron detector (L.A.N.D.)[1] was tested at the SATURNE accelerator at Saclay with tagged neutrons. Ten paddles out of 200 of the final design (200 · 10 · 10 cm³, alternating layers of 5 mm Fe/scintillator) were arranged in parallel order symmetrically with respect to the height of the incident beam. A horizontal cut through the setup is shown in Fig. 1:

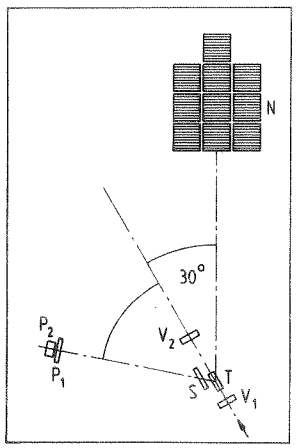


Fig. 1:
Experimental setup

A CH_2-target of 5 cm thickness was irradiated with primary neutrons of 250, 600, and 1000 MeV. The neutron detector subsection was positioned at 30° with respect to the incident beam. Recoiling protons passing through three szintillator paddles (S, P_1, P_2) were identified via time of flight between S and P_1, P_2 (TOF) and energy loss (ΔE) in P_1, P_2 at angles as determined by the kinematics of elastic scattering. Upstream and downstream of the target two scintillator paddles served as veto detectors against charged particles coming along the neutron beam line. Tagged neutrons were defined by the trigger condition $N \cup \overline{V}_1 \cup \overline{V}_2 \cup S \cup P_1 \cup P_2$. All neutron paddles as well as the proton paddles P_1, P_2 were viewed with photomultipliers at both ends such as to allow mean timing and determination of the position of incidence of the incoming particle.

Time calibration was performed via a laser system[2], especially developed for L.A.N.D. For the laser line a time resolution of 150 ps FWHM was achieved.

From the analysis of tagged-neutron events the following results were obtained:

(a) The total efficiency as shown in Fig. 2 is satisfactorily reproduced by Monte-Carlo[3] simulations indicated by the solid line. These predict for the fully assembled L.A.N.D. an efficiency of ≥ 90 % for neutrons with energy ≥ 350 MeV.

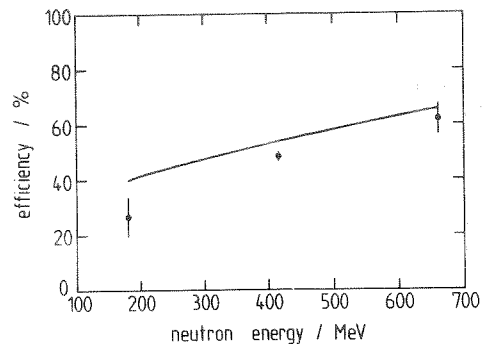


Fig. 2: Efficiency of the L.A.N.D. subsection (dots: measurements, line: simulation)

(b) From the two photomultipliers viewing each L.A.N.D. paddle a position information with a resolution of 5.4 cm is deduced.

(c) For protons impinging on a vertical cut of 5 cm on P_1, P_2 the correlated neutron events showed a TOF resolution of 450 ps (FWHM). This value contains the kinematical broading caused by the rather thick target as well as the time resolution of the proton paddles P_1 and P_2.

(d) The examination of the lengths of the showers induced revealed that 90 % of the showers are contained within a sphere of radius ≈ 20 cm (see fig. 3). Again, these values are reproduced by Monte Carlo simulations.

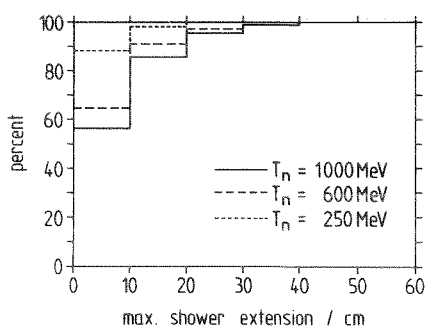


Fig. 3: Maximum shower extension

[1] GSI Scientific report 1988, p. 298
[2] M. Proft, Diploma thesis, Mainz, 1989
[3] W. Kneissl, R. König, Diploma theses, Bochum, 1989

A Beamtracking and Particle Identification Detector System for Experiments with L.A.N.D.[B,G]

H. Spies[2], S. Heerd[2], H. Emling[1], J. Keller[3], K. Stelzer[2]

and the L.A.N.D. Collaboration

([1] GSI Darmstadt, [2] Univ. Frankfurt, [3] Univ. Bochum, Univ. Mainz, Univ. Cracow)

For experiments with the L.A.N.D. facility (see separate contribution to this report) a system of several detectors for beam tracking and identification of projectile-like fragments has been developed and partially tested at GSI. Four position sensitive scintillation counters serve to define the direction of the incoming particle and to measure, in conjunction with the ALADIN spectrometer[1], the momentum transfer in the collision. The nuclear charge of the projectile-like fragment will be measured by means of a Cerenkov detector[2] and a multi-sampling ionization chamber (MUSIC)[3]. The velocity of the fragments will be obtained via time-of-flight measurements or alternatively with a Threshold Cerenkov Counter[2]. The experimental requirements for those detectors are the following:

- velocity resolution $\leq 0.5\%$
- position resolution ~ 1mm
- charge resolution $\sim 1\%$

The velocity resolution will be achieved by fast plastic counters of small size which are spatially separated over distances in the order of 10 m. A test measurement at SATURNE showed, that the number of electrons which is required to reach the respective time resolution (100 psec) can be obtained for heavy ions of high energy.

The position of the particle will be measured by a very thin (100-200 μm) scintillation foil which is coupled via lightguides to 4 photomultipliers as shown in fig. 1. The position of incidence can be derived from the relative pulse heights in the 4 phototubes. A prototype of such a detector (sensitive area 10x10 cm^2; thickness 200 μm) has been tested with a 18.5 MeV/u ^{120}Sn beam at the UNILAC. We observed a position resolution of 3 mm (fig. 2). Meanwhile the detector has been improved and was tested with an UV-laser. Using light pulses which produce about 1000 photoelectrons in the tubes a position resolution of 0.9 mm was obtained (fig. 3). For very heavy ions at high energies a number of 10^4 photoelectrons is estimated. In a test run with this detector using 100 MeV/u Ne ions at SIS in December 1989, the position measurement was hampered because of the still short extraction time (15 ms), which resulted in unresolved multiple hits.

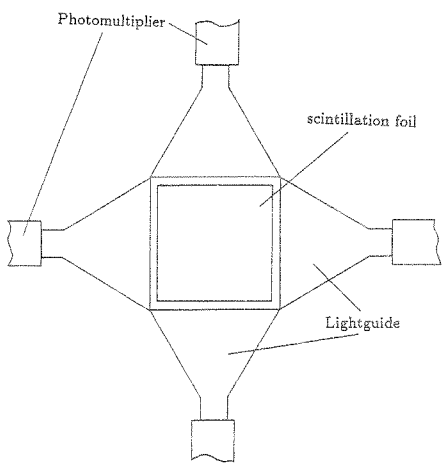


Fig.1: Schematic view of the position sensitive counter

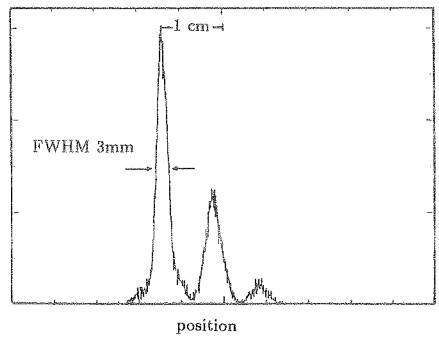


Fig.2: Position resolution measured with a 18.5 Mev/u Sn beam

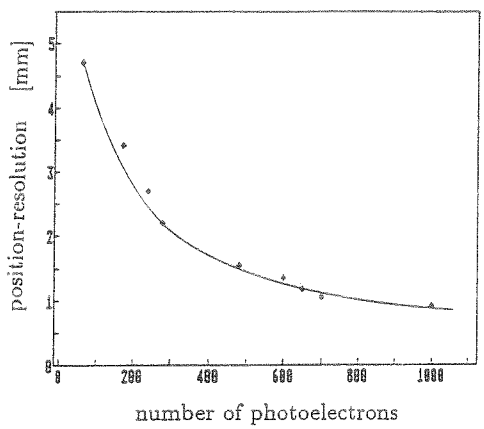


Fig.3: position resolution as a function of the number of photoelectrons

The Cerenkov counters for the charge measurement are built from 1 cm thick lead glass (Schott SF3). These detectors are sensitive to particle energies above 210 MeV/u. To reduce the position dependence of the output signal the radiators are of trapezoidal shape[2]. Estimates show that for a charge-resolution of 1% a number of 5 detected photoelectrons for minimum ionizing particles is necessary. Tests with electrons and cosmic rays resulted in 6(2) photoelectrons in our detector, therefore the required charge-resolution should be achievable.

Our ionization-chamber has been constructed in collaboration with the FRS group . It is of the same type as described by H.Sann et al. (ref.3) but of smaller size. A first prototype has been completed. The chamber has an active volume of 20x20x40 cm^3 and a fourfold divided anode. A theta-grid for an additional position measurement is implemented.

The entire detector setup is presently installed in the SIS experimental area and will be exposed to the first SIS beam presumingly delivered in February 1990.

References:

1. U. Lynen et al., SIS Proposal 1988
2. J.P.Dufour et al., N.I.M. A241 (1985), 491-502
3. H.Sann, Proc. of the Int. Conf. on Instr. for Heavy Ion Nuclear Research, Oak Ridge (1984), p. 27

Test of a TAPS-Sub-Array with Electrons^{G+B}

O. Schwalb, G. Enders, K. Hagel, W.Kühn, V.Metag, R.Novotny
II.Physikalisches Institut Universität Gießen
K. Hildenbrandt
GSI Darmstadt
W. Arnold, U. Kneissl, F. Steiper, T. Weber
Strahlenzentrum Gießen
TAPS-Collaboration:
GANIL - Univ. Gießen - KVI Groningen - GSI - Univ. Münster

A sub-array of seven BaF_2-detectors of the TAPS-geometry was tested at the Gießen electron LINAC with monochromatic electrons in the energy range from 10 to 43.5 MeV. Time- and energy-resolutions were determined. The experimental data are compared to Monte-Carlo-simulations performed with the code GEANT3 which has also been used for calibration.

At electron energies above 20 MeV the time resolution of the central detector has been determined to $\Delta t \approx 170$ ps (FWHM) (Fig.1). The discriminator threshold corresponds to 2 MeV. In a recent measurement at the highest energy using a modified voltage divider circuit a time resolution of $\Delta t \approx 110$ ps (FWHM) was achieved.

The energy deposit in the array was studied in simulations (Fig.2). In the energy range between 8 and 41.5 MeV the main energy leakage out of the central detector obviously occurs through the side faces and thus can be registered by summing the energy deposited in the neighbouring detectors. Fig.3 shows the measured energy resolution of the central detector and the entire array in comparison to GEANT-simulations. The resolution of the central detector can clearly be improved in the described way.

In Fig.4 the influence of the discriminator threshold on the energy resolution of the array is shown. In order to achieve good energy resolution the threshold has to be as low as possible since the mean energy deposited in one individual ring detector is about 3.8 MeV at an electron energy of 43.5 MeV. Summarizing the test shows that the experimental results are in good agreement with the GEANT simulations.

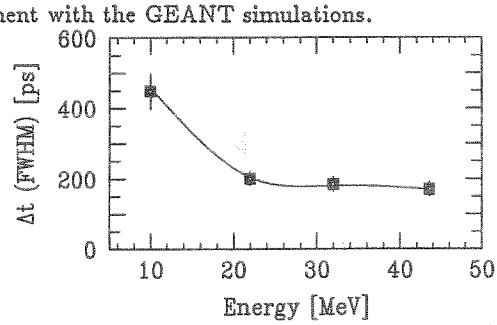


Figure 1: Measured time resolution of the central detector at different electron energies.

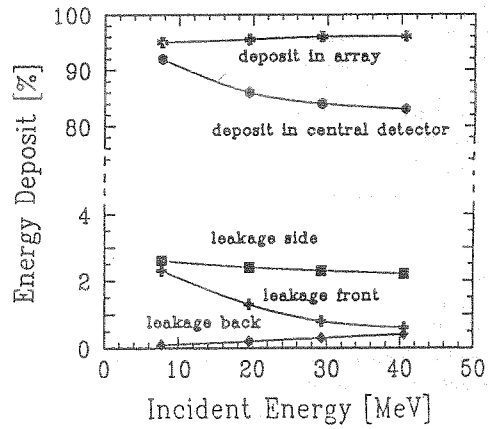


Figure 2: Mean values of deposited energy and leakage at various incident electron energies (GEANT simulation).

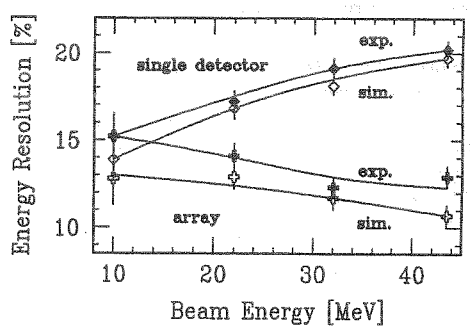


Figure 3: Measured energy resolution of the central detector and the array determined at the Gießen electron linac compared to results of GEANT simulations.

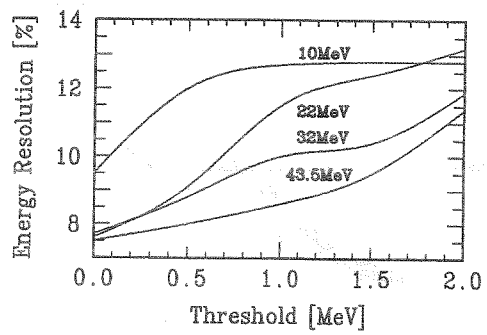


Figure 4: Influence of the discriminator threshold on the energy resolution of the array for different incident electron energies (GEANT simulation).

Charged Particle Sensitivity of BaF_2 Detectors[G]

A.L. Boonstra, H. Löhner, A. Raschke, L.B. Venema, H.W. Wilschut
(KVI Univ. Groningen)
N. Brummund (IKP Univ. Münster)
TAPS Collaboration:
GANIL - Univ. Gießen - KVI Groningen - GSI - Univ. Münster

BaF_2 crystals of TAPS [1] geometry (hexagonal cross section, 25 cm length = 12 X_0, 754 cm^3) have been exposed to light charged particles emitted in p- and α- induced reactions at the KVI cyclotron. Such measurements aimed at new results on the capabilities of the TAPS spectrometer in relativistic heavy ion experiments at SIS. Besides the investigation of new probes like photons and neutral mesons in this energy domain, TAPS could provide an essential contribution to the event characterisation through the analysis of rapidity distributions and transverse momenta (flow) of charged particles at midrapidity.

To this end one BaF_2 detector was mounted outside the 120 cm scattering chamber at a lab. angle of 45° behind a 25 μm Kapton foil. Beams of 55 MeV p and 100 MeV α were used on C, ZnS and Pb targets. Inside the scattering chamber silicon detectors were used as beam monitors and as ΔE detectors in order to provide redundant information on the charged particle separation. A N_2-laser calibration system was installed in order to receive results on the linearity of the phototubes, the dynamic range and the gain stability. In part of the run a 5 mm thick plastic scintillator (charged particle veto prototype) was used in front of the BaF_2.

The BaF_2 phototube signal was fed through a 500 ns delay cable (in order to accomodate the TAPS setup requirement) to a passive 50 Ω split and then to a LRC 2249A and W ADC for integration over 25 ns and 2 μs, respectively, in order to separate the fast and slow scintillation components. A 20 dB attenuation at the wide gate ADC input was used to adjust the dynamic range.

From elastic and inelastic scattering lines in the wide gate spectrum an energy resolution σ_E = 1% for 40 and 55 MeV p, and σ_E = 1.5% for 82 MeV α could be determined. The scatterplot of short and wide gate signals shown in fig. 1 reveals a clean separation between the lines of photons, hydrogen and helium. The projection of these lines after linearization is shown in fig. 2. A Z-resolution of $Z/\sigma(Z) = 6$ is determined from the estimates of the centroids for ^{3}He and t peaks. The latter could be verified with the help of the redundant information from the silicon detectors or from TOF.

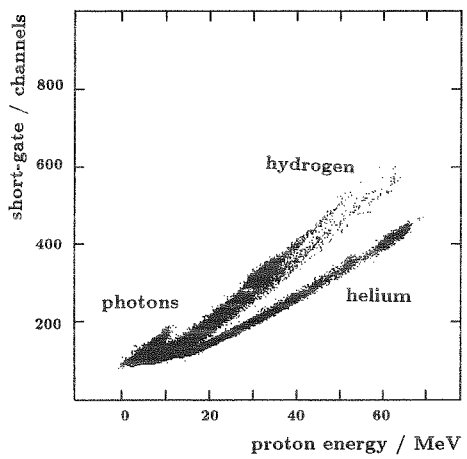


Fig. 1. Scatterplot of BaF_2 short-gate vs. wide-gate signals for reactions induced by 100 MeV α on a ZnS/mylar target. The horizontal axis is calibrated in proton energies with the help of the hydrogen recoil line.

Improved isotope separation could be achieved via TOF. Using the cyclotron RF as time reference, we obtained a time resolution of 1.3 ns. The scatter plot of BaF_2 wide gate signals versus TOF reveals that the mass resolution is spoiled by the fact that the ^{3}He line overlaps partly with the deuteron line due to the Z-dependence of the total light output. Using the pulse shape discrimination first to separate Z's, the TOF information results in the particle spectra shown in fig. 3, which are projections of particle lines from the linearized TOF versus wide gate scatterplot. A mass resolution of $M/\sigma(M) = 5$ is obtained for the p,d separation, 4.5 for d,t and 3 for ^{3}He, α. Since the mass resolution is essentially determined by the time resolution, a factor of at least 3 improvement can be expected from the TAPS experiment where a time resolution of about 400 ps [2] will be achieved on the basis of time-zero determined by photons from the same event in the BaF_2 array.

References

[1] R.S. Simon et al., GSI Scientific Report 1988, p.303

[2] N. Brummund et al., GSI Scientific Report 1988, p.306;
O. Schwalb et al., GSI Scientific Report 1988, p.305

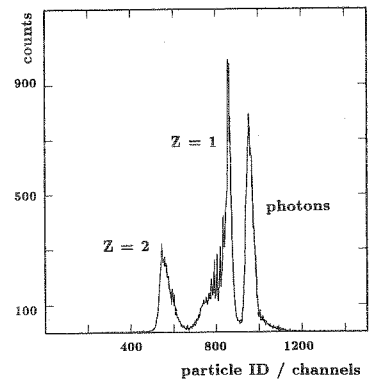


Fig. 2. Linearization of scatterplot in fig. 1.

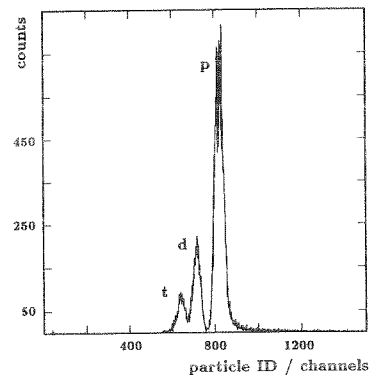


Fig. 3. Linearization of scatterplot of time-of-flight vs. wide-gate signal after selection of hydrogen isotopes from fig. 2.

The Charged Particle Veto Detector CPV for TAPS [B,G]

N. Brummund (IKP Univ. Münster)
A.L. Boonstra, H. Löhner, A. Raschke, L.B. Venema, H.W. Wilschut (KVI Univ. Groningen)
TAPS Collaboration:
GANIL - Univ. Gießen - KVI Groningen - GSI - Univ. Münster

The Two Arm Photon Spectrometer TAPS is designed for operation in heavy ion reactions with projectile energies ranging from 0.1 to 2 GeV/u.

The charged particle veto detector CPV consists of 256 plastic scintillator hexagons which are read out via perspex - lightguides and photomultipliers [1]. It will mainly be used to distinguish charged particles from photons detected in the BaF_2 - modules of TAPS in order to perform an efficient online photon analysis. Therefore the average photon conversion probability in the CPV has to be low (2.5%).

In order to measure the position dependence of the light-output the scintillator hexagon of a CPV module was irradiated with a collimated ^{106}Ru electron source (Fig. 1a). With a low energy threshold in the trigger detector minimum ionizing electrons were selected. It turns out that the energy loss in the 5mm thick NE102A scintillator is sufficient to detect minimum ionizing particles; the electron signal is well separated from noise. The variation of the position dependent light output is within 5% for 80% of the total hexagon area. We observed a maximum deviation of 17% between Position **C** and Position **2** (see Fig. 1b).

The energy-loss signal of the CPV - modules can be used to perform particle identification together with the BaF_2 - modules (Fig. 2). This methode complements the particle identification which can be done via pulse shape analysis by the BaF_2 - modules of TAPS only. With this additional information an improved charged particle analysis can be achieved.

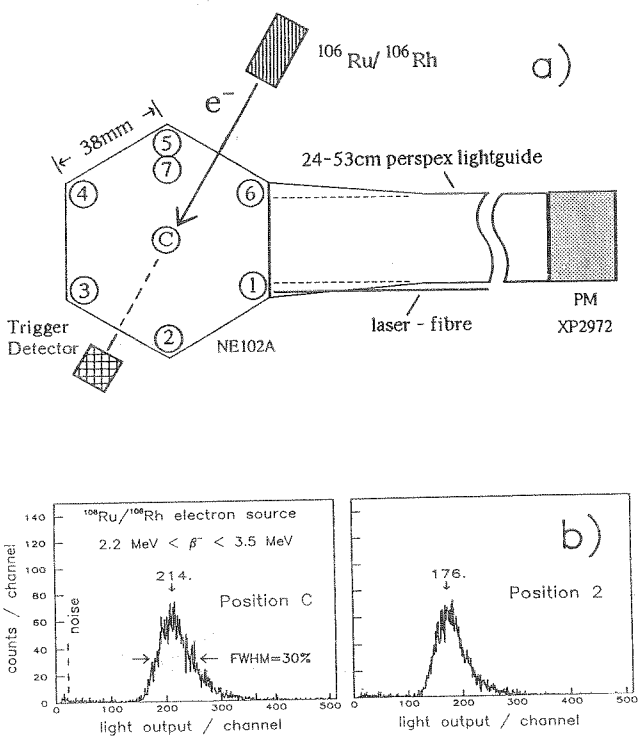


Fig. 1: Setup of the electron source with the CPV detector module (a) and measured position dependence of the light-output in a single CPV detector module (b).

The particle separation is affected by the position dependence of the light output in the CPV module and, in this case in addition, by energy loss due to scattering out since only a single BaF_2 crystal was used. The sum effect is seen from (Fig. 3a) in comparison to (Fig. 3b) where only the central part of the hexagon is irradiated with particles. While the ideal case shows a mass resolution $M/\sigma(M) = 10$ a slightly worse but still satisfactory result of $M/\sigma(M) = 7$ is obtained for the realistic situation.

[1] N.Brummund, GSI Scientific Report 1988, p. 306

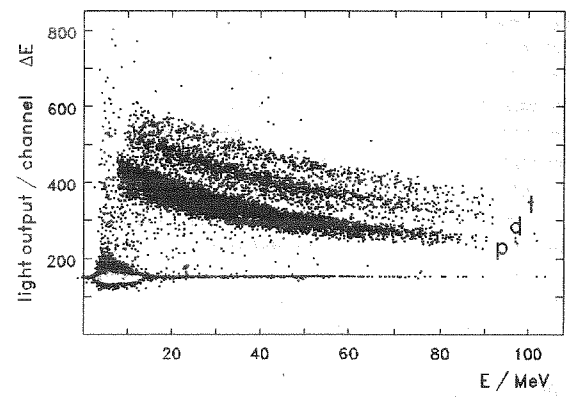


Fig. 2: Hydrogen-isotope separation (a) with a typical CPV-module (ΔE) and a 25cm long BaF_2 - TAPS module (E). The data were taken from the reaction $^4He + ^{208}Pb$ at 25 MeV/u, $\Theta_{lab} = 45°$. The X-axis is calibrated for proton energies.

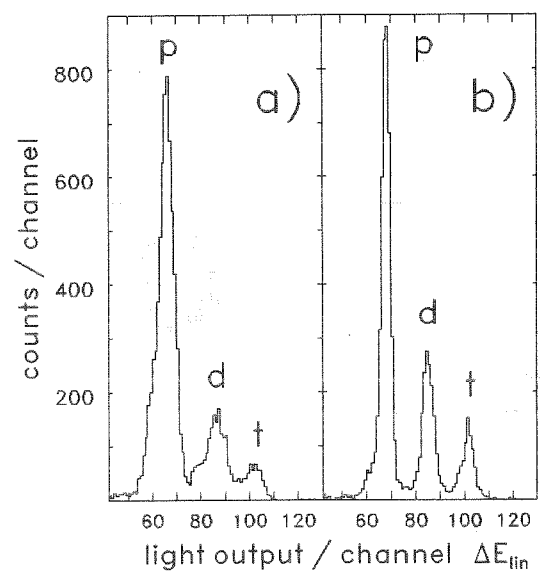


Fig. 3: Linearized projection to the ΔE - axis for the data in Fig.2 (a). The particle separation is improved by irradiating only the central part (diameter = 2cm) of the hexagon (b).

Response Function of a TAPS-Subarray to High Energy Photons[G+B]

M.Appenheimer, W.Kühn, V.Metag, R.Novotny, M.Pfeiffer
(II.Physikalisches Institut Universität Gießen)
A.Baumann, J.Peise, M.Schmitz
(A2 Collaboration; Institut für Kernphysik Univ. Mainz)
A.L.Boonstra, H.W.Wilschut
(KVI Groningen)
TAPS-Collaboration:
GANIL - Univ. Gießen - KVI Groningen - GSI - Univ. Münster

In a test experiment at the Mainz LINAC tagged photons of 186 MeV have been employed to determine the energy response of a detector array of 19 TAPS BaF_2-detectors. A collimated photon beam with a diameter of $\emptyset \approx 1.2$cm illuminated the central detector.
In the analysis the energy information provided by the tagger spectrometer was used to calibrate the spectra. An energy resolution of $\Delta E(FWHM)/E = 7\%$ and 8% is obtained when summing the energy signals of 19 and 7 modules, respectively. The energy resolution of the central detector has been determined to be 18%. Fig.1 shows the energy deposited in the first and second ring. The corresponding mean values are 19 and 7 MeV, respectively. In Fig.2 the spectrum of the central detector and the sum-spectra of 7 and 19 detectors are shown. The peak energies were determined by a gaussian fit to the data.

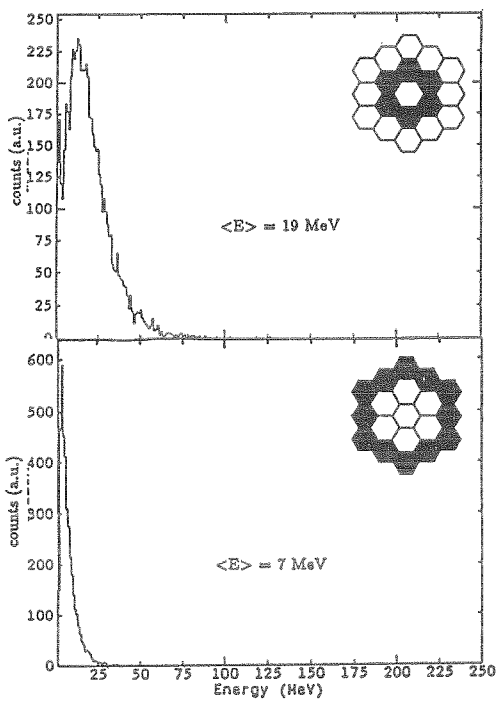


Figure 1: Energy response of the first and second ring to 186 MeV photons

It can not be excluded that electrons from conversion in the collimator contributed to the rather large yield at low energies. The line shape and the energy resolution will be compared to GEANT3 simulations presently in progress.

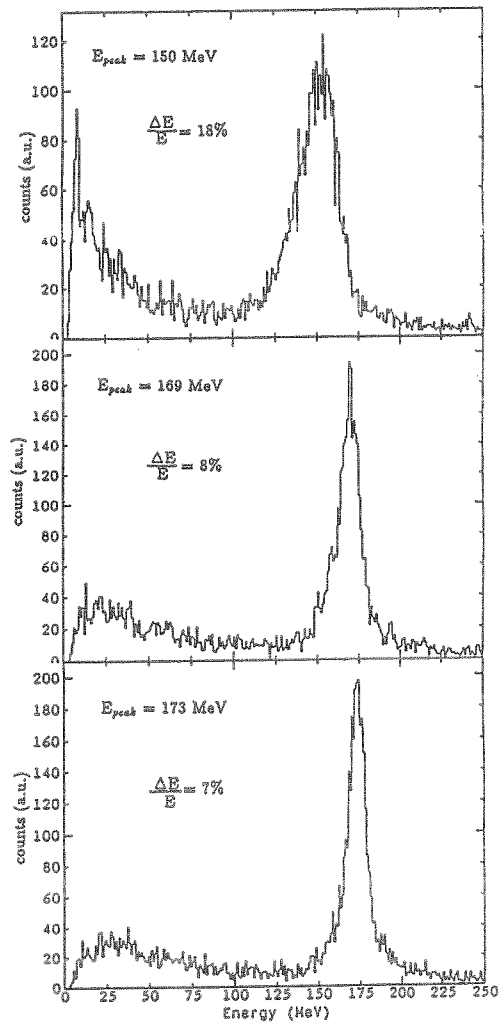


Figure 2: Energy response of the central detector , 7 and 19 detectors, respectively, to 186 MeV photons

A Scintillation Counter for High Energy Electrons [B,G]

M. Rhein, Ch. Müntz
Institut für Kernphysik, TH Darmstadt
W. Arnold, U. Kneissl, Th. Fromhold, R. Göbel
Strahlenzentrum, Univ. Giessen, Giessen

For the TORI-spectrometer [1] a phoswich-type plastic detector was developed to extend the measurable region for δ - electrons up to 10 MeV. Good timing resolution ($\Delta t < 5$ ns) to distinguish electrons from neutrons by their time of flight together with a high supression of γ-rays was requested.

The detector consists of a 500 μm thick surface-barrier detector (7.5 cm diameter), mounted in front of a 5 cm thick plastic block (7.5 cm diameter, NE102) in which electrons with energies up to 10 MeV will be stopped. To reduce the thermal noise the large area Si-detector was cooled down to 8 $°C$. Due to the low sensitivity of the surface-barrier detector to γ-rays it served as a trigger-counter for electrons supressing γ-rays for $E_\gamma > 300$ keV to 10^{-4}. To separate the photomultiplier from the magnetic-field region of the TORI-spectrometer it was coupled with a 1 m long plexiglas light pipe to the scintillator.

The response of the whole system to electrons in the energy range from 1 MeV to 9 MeV was tested at the electron accelerator of the Strahlenzentrum in Giessen. Together with a magnetic deflection system and an anticoincidence plastic-paddle with small angular acceptance the energy resolution of the beam was $\Delta p/p = 0.005$. To reduce pile-up events the beam current was limited to $\approx$ 10 electrons/s.

In figure 1 the electron spectra obtained at 2, 3, 5, 7 and 9 MeV beam energy are shown. The absolute height is normalised to equal counting rates. The energy response is linear up to 7 MeV; for higher energies effects due to bremsstrahlung become visible. Figure 2 shows the peak-to-total values and the energy resolution derived from the measured spectra. The response function of the detector will be obtaind together with Monte-Carlo calculations, taking into account the conditions at the TORI-spectrometer. This detector has been successfully used in an experiment at the TORI-spectrometer with Pb + Pb at 12 MeV/u [2].

We would like to thank H. Stelzer (GSI) for his support concerning the PC-based online-data aquisition system CAMDA.

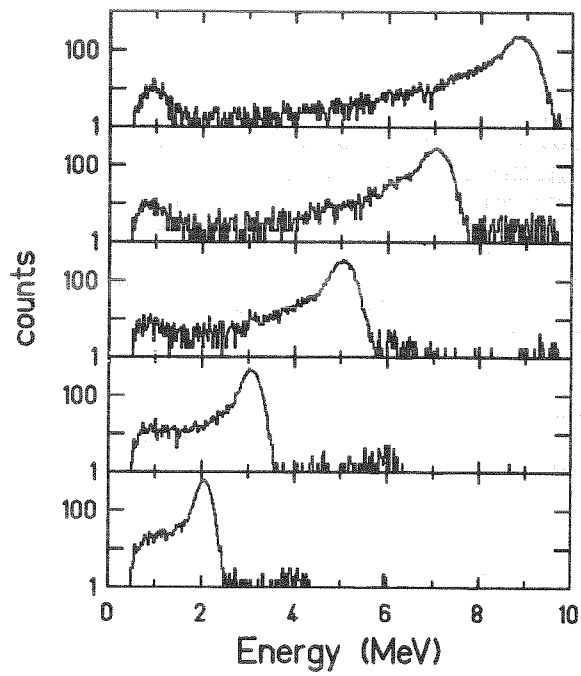


Figure 1: Electron spectra at 2, 3, 5, 7, and 9 MeV beam energy.

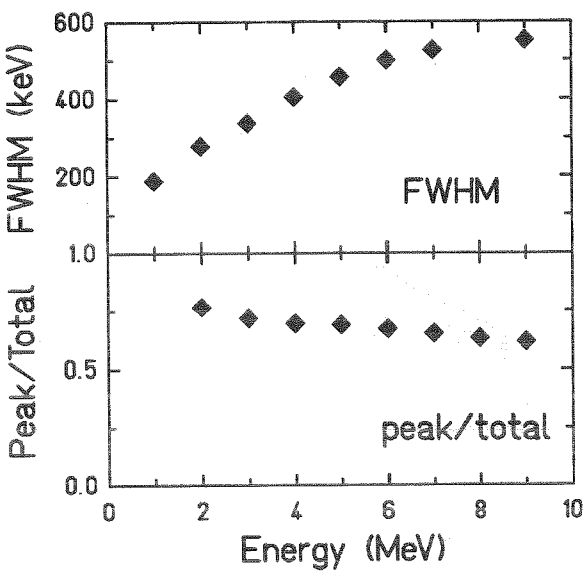


Figure 2: Peak-to-total values and energy resolution as derived from the measured spectra.

References

[1] E. Kankeleit et. al., NIM A234, 81(1985).

[2] R. Barth et. al., this report.

Heavy Ion Detection with a Plastic Scintillator Photodiode Array at the TORI - spectrometer[B,G]

I. Schall, E. Kankeleit, H. Oeschler, M. Rhein (TH Darmstadt)

Recent data have shown that the theoretical predictions of integral atomic positron production in elastic heavy ion collisions underestimate experimental results at short collision times up to a factor two [1, 2]. For further examination at higher incident energy (12 MeV/u Pb + Pb) a new detector system for heavy ions at scattering angles $\theta_{lab} < 12^0$ has been developped. As positron production probability is of the order of 10^{-6}, a most critical point is to measure scattered Pb-Ionen up to a dose of 10^{10} heavy ions/cm^2 detector area. For that reason detection of heavy ions with semiconductors is excluded. Further, elastically scattered Pb-ions have to be distinguish from fission products.

In our new device heavy ions are stopped by thin plastic scintillator plates and the arising lightpulses are detected with a PN - photodiode array by single diode readout. PN - photodiodes were choosen to minimize the γ-contribution, due to their thin depletion depth. We used an array with 38 elements each with an active area of 4.4 × 0.9 mm^2 (Hamamatsu, S2311-38N). The scintillation material was a wavelengthshifted plastic (BC430). Figure 1 shows the schematic view of the detector . A thin slice of alternating aluminium plastic stripes was sawed from an plastic aluminium 'sandwich' block, polished and directly coupled to the photodiode array with a two-component silicon glue.

This arrangement was tested with 8 MeV/u Sn-ions scattered on a Au-target. Additionally carbon foils of different thicknesses lead to desired energy losses. The results are shown in Figure 2. The increasing width is caused by straggling of ions in carbon. The light output as a function of the range from Sn - Ionen in plastic can be seen in Figure 3. This relation is suggested due to high quenching effects. However, the light output of Pb-ions will increase at least as a function of range as depicted in Figure 3. This shows that fission products, at least up to 10.8 MeV/u can be distinguished from elastic scattered Pb-ions in the 12 MeV/u Pb + Pb collisions, as was confirmed in our last experiment.

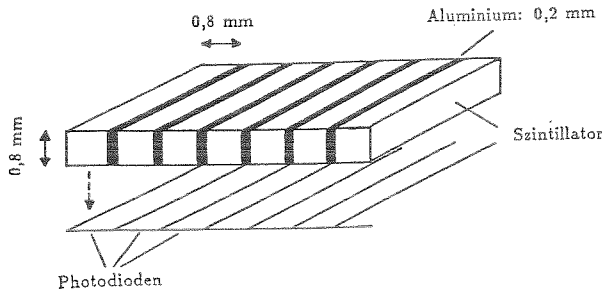


Figure 1: Schematic view of the detector.

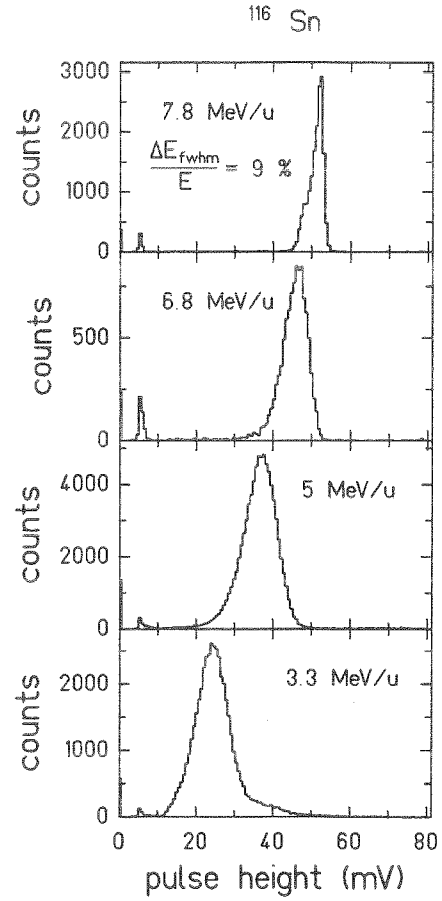


Figure 2: Spectra of Sn-ions detected with the plastic scintillator photodiode array (one segment).

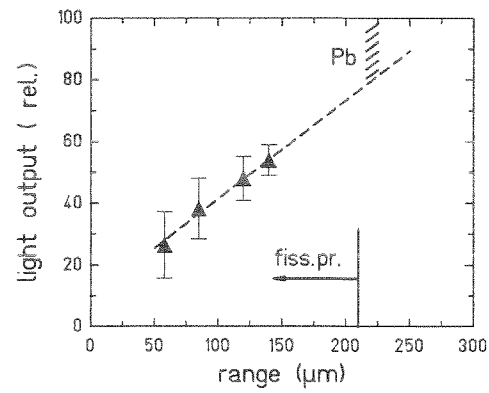


Figure 3: Measured light output of Sn-ions with the plastic scintillator photodiode array as function of their range in plastic.

References

[1] M. Krämer et al., GSI Scientific Report, 163(1988).

[2] M. Krämer et al., submitted to Phys. Lett. B.

Detector System for the Z = 110 Experiment

S. Hofmann

GSI Darmstadt

In the past ten years production cross sections and decay properties of isotopes of heavy elements up to Z = 109 have been measured[1,2]. Extrapolations of the cross sections and of the half-lives towards higher elements give values, which seem to make an experimental proof possible for the element Z = 110 with improved experimental techniques. Part of the improvements concerns the detector system.

The ions after separation are implanted into a solid-state detector; their radioactive decays are measured with the same detector. The implantation has the advantage of being sensitive to α decay as well as fission; branching ratios can be measured directly; half-lives and decay chains can be measured by delayed coincidences; recording the data event by event allows to set the widths of the time windows during the analysis.

The time windows can be tremendously opened if position sensitive detectors are used. In that case, measurement of the *relative* position of the implanted nuclei and of the subsequent decays allows to follow decay chains up to several minutes, at reduced background even hours may become possible. Measurement of the *absolute* position gives the distribution of ions in the focal plane of the separator; in that mode properties of the separator are measured and the field settings are controlled during experiments[3].

The concept for identification of nuclei will be kept in future; however, the old detector array will be replaced by a passivated ion-implanted silicon strip-detector (see Tab. 1). This new detector provides a 31 % gain of active detector area in the center of the beam spot and a finer granulation for measuring the horizontal positions. The total active detector area is increased by 66 %. Also, the resolution for α particles is improved from 20 keV to 14 keV (FWHM) for 241Am α's; detector cooling is not necessary.

Alphas escaping into the backward hemisphere give a time information due to the energy loss signal but the efficiency to measure the full energy is reduced to nearly 50 %. An improvement can be achieved with an arrangement of big area detectors which cover part of the backward hemisphere. It is possible to cover ≈65 % of the backward hemisphere with six detectors of the above type. The detector arrangement is shown in Fig. 1. To reduce the amount of electronics neighboring strips can be connected at a time; with 4 strips connected sufficient information on escaping α's or fission fragments is obtained.

A seventh detector is mounted on a pneumatic drive which moves the detector into the beam facing the stop detector. The active area of the backward hemisphere is then increased to ≈78 %. The pneumatic is triggered electronically, e.g. whenever a high energy implantation signal is measured that can be assigned to an evaporation residue, or when an alpha signal according to the decay of a heavy element is measured.

Simultaneously the stop detector is shielded and decay chains can be measured without implantation of background ions which passed the separator.

Although the same silicon waver can be used for all eight detectors the detector holder has to be different for the stop detector. For this detector a *transmission* mount has been built; the 32 cables are connected at the top and bottom side. For the other detectors the inactive frame around the silicon was minimized; in that case the cables are connected from behind. Both types have been tested and have been used in experiments recently. The whole detector system will be ready in second half of 1990.

The improvements of the new detector system for the Z = 110 experiment are: 1) increase of the active detector area and hence total efficiency by at least 31 %; 2) better energy and position resolution; and 3) high probability for detection of escaping particles.

[1] Armbruster, P.: Ann. Rev. Nucl. Part. Sci. 35, 135 (1985)
[2] Münzenberg, G.: Rep. Prog. Phys. 51, 57 (1988)
[3] Hofmann, S.: Preprint GSI-89-83, (November 1989)

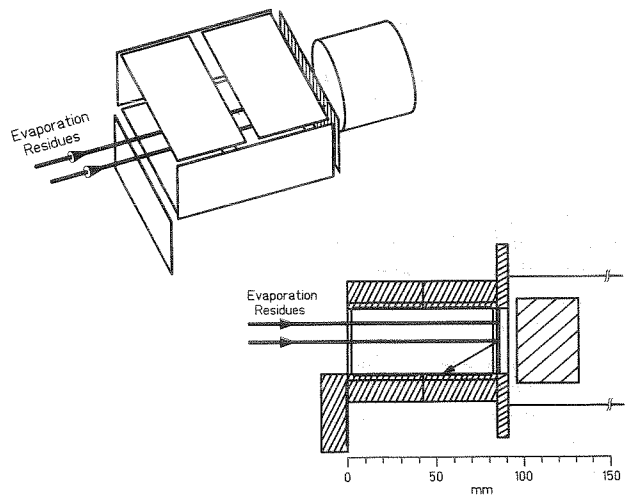


Fig. 1: Detector system for identification of rare nuclei; upper part: parallel projection showing the actual positions of the silicon wavers of the 16-strip stop-detector, the six permanent detectors for escaping α's or fission fragments, the movable detector mounted on a pneumatic drive, and the cylindrical germanium detector; lower part: sectional drawing to scale showing the different types of detector mounts which also support the cables.

Table 1: Detector system for identification of rare decays.

Detector array, old	
7 position-sensitive silicon detectors	
size	87mm broad x 27mm high = 2,349 mm^2
total active area	1,701 mm^2 = 72.4 %
detector size	9 mm broad x 27 mm high x 300 μm thick
frame between detectors	4 mm broad
Strip detector, new	
Passivated ion-implanted	
position-sensitive silicon strip detector	
size	80mm broad x 35.3mm high = 2,824 mm^2
total active area	100 %
number of strips	16
area of 1 strip	5mm broad x 35.3mm heigh = 176.5 mm^2
α resolution	≈14 keV (FWHM) for 241Am α's
Detectors in backward hemisphere	
6 strip detectors	same type as above
opening angle	≈65 % of 2π, permanent
1 strip detector	same type as above, on pneumatic drive
opening angle	≈13 % of 2π, occasional
HPGe detector, n-type	
efficiency	12 % rel. efficiency
size	36 mm x 46 mm Ø
	behind silicon stop detector

A Silicon Detector Array for the Investigation of Proton- and Alpha Radioactivity B,G

T. Faestermann, A. Gillitzer, F. Heine, M. Köpf, W. Wagner
Technische Universität München

In the previous report[1] we described our electrostatic recoil separator, which will be very well suited to investigate the decay of extremely neutron deficient nuclei, that can be produced in fusion reactions by the radioactive beams expected from the SIS-FRS-ESR combination. It combines a large acceptance solid angle (9 msr) with a reasonably good suppression of the background due to beam particles.

As an alternative for the existing gas detector system a large area detector system has been developed, which consists of a position sensitive parallel plate avalanche counter (PPAC) and an array of 10x10 PIN-photodiodes, each with an active area of 1 cm^2. For the readout of the signals the front contacts of the diodes are connected in columns, the backcontacts in rows, as described in the contribution by J. Friese et al.[2]. In order to minimize the efficiency for β-particles we chose the thinnest diodes (220 μm) available. To reduce the noise due to leakage current, diodes of high resistivity (6000 Ωcm) are used and cooled to 5°C. The relatively thick dead layer (1.4 μm Al) is not harmful in this application, because the radioactivities are implanted into the active volume of the detectors.

For heavy ion events, the measurement of their energy with the diodes and of the time-of-flight with either the PPAC or the diodes allows to distinguish evaporation residues from scattered beam particles. The energy of low energetic particles (protons or alpha-particles) is measured in a separate electronic chain both for the rows and the columns. By averaging the two energy informations the electronic resolution, which is mainly determined by the large capacitance of ten detectors in parallel (0.5 μF), is improved. In addition the position of a low energy event can be used to correlate it with a preceeding evaporation residue in space and time. Such a correlation reduces background from decays with comparably long halflives like β-decays.

The setup has been tested with the reaction of 240 MeV ^{58}Ni (from the Tandem-Linac combination in München) with ^{54}Fe. The beam was pulsed with a period of 100 μs and a pulse width of 20 μs. Fig. 1 shows an energy spectrum from the decay of evaporation residues taken during the beam pause. α-lines are observed due to the decay of ^{108}Te (3.320 MeV), ^{109}Te (3.080 MeV) and ^{110}I (3.444 MeV), but the proton line from ^{109}I (0.811 MeV) is hidden among the signals from β-decays. If however only events are accepted which are detected in the same diode and not later than 0.4 ms after an evaporation residue, the proton-line from the decay of ^{109}I ($T_{1/2}$=0.11 ms) is nearly free of background (Fig. 2). For this sum spectrum of 100 diodes we observe an energy resolution of 35 keV.

1) T. Faestermann et al., GSI-Report 89-1, p. 317
2) J. Friese et al., this report

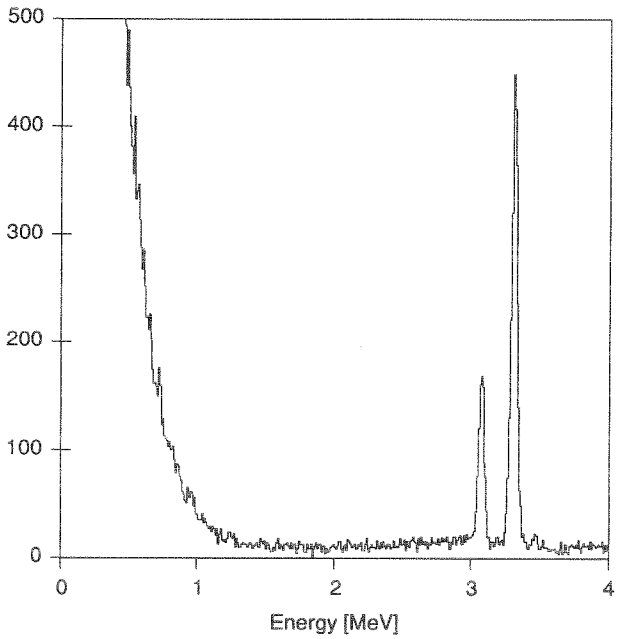


Fig. 1: Summed energy spectra of all diodes from the decay of fusion evaporation residues, produced in the reaction of 240 MeV ^{58}Ni with ^{54}Fe.

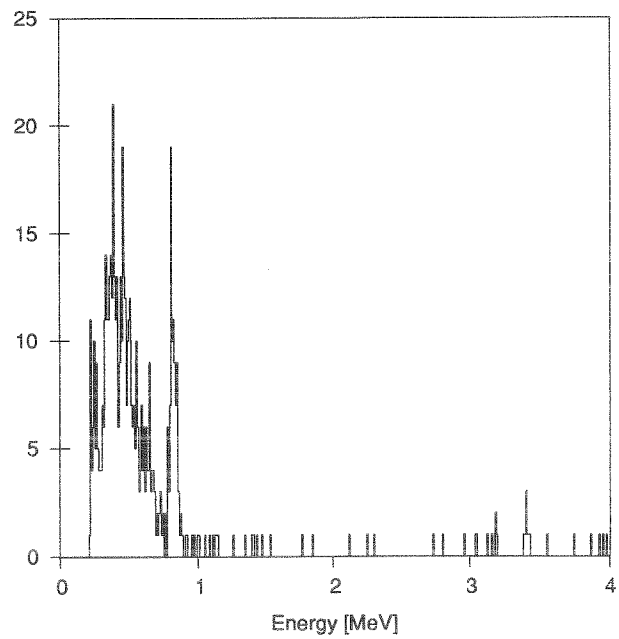


Fig. 2: Same as Fig. 1 but only events within a time span of 0.4 ms after an evaporation residue in the same diode are accepted, featuring the proton line of ^{109}I.

A Multi Detector Array of PIN-Diodes G+B

J. Friese, H.J. Körner, C. Schießl, W. Wagner
Technische Universität München

G. Kraus
Universität Mainz

For the study of (d,p)-reactions in inverse kinematics[1] a large area (100 cm^2) silicon detector has been assembled and tested. It consists of 100 PIN-diodes (SIEMENS F109D) of 500 µm thickness (ρ = 1200 Ω·cm) and an active area of 1 cm^2.

The diodes are arranged in a 10·10 array with matrix signal readout (Fig. 1). The rows were read out via fast timing electronics, the columns via charge sensitive preamps and pulse shaping main amps(τ = 0.5 µsec). Energy and time for any single detector was thus addressable by means of the appropriate column-row coincidence. Each row was supplied independently with a bias voltage of -280V, leading to a depletion zone of 300 µm, a total capacity of 350 pF, and a typical reverse current of 700 nA.

For 5.486 MeV α-particles the energy resolution of a single detector within a column was 30 keV, that of a whole column was 35 keV. The difference is due to fluctuations in the thickness of the diodes' entrance window.

The array was successfully operated in an UNILAC test experiment $^2D(^{136}Xe,^{137}Xe)^1H$ at E_{Lab}= 5.9 MeV/u [2], where the target consisted of a deuterium loaded titanium foil with additional ^1H impurities. Fig. 2 shows a sample set of measured energy spectra for elastically scattered protons and deuterons. Each spectrum represents the calibrated, but uncorrected sum of all diodes in one column (i.e. $\Theta_{Lab} \approx$ const) as it emerges directly from the energy branch. The particles' energy ($E_d \approx 2 \cdot E_p$) decrease with increasing angle is due to the kinematics. The deuterons are not stopped within d=300 µm for column #1, whereas lower level thresholds lead to the disappearance of the protons in column #9 and #10. Heavy target recoils contribute predominantly at these angles. The measured energy resolution ΔE_p = 143 keV(fwhm) and ΔE_d = 286 keV(fwhm)

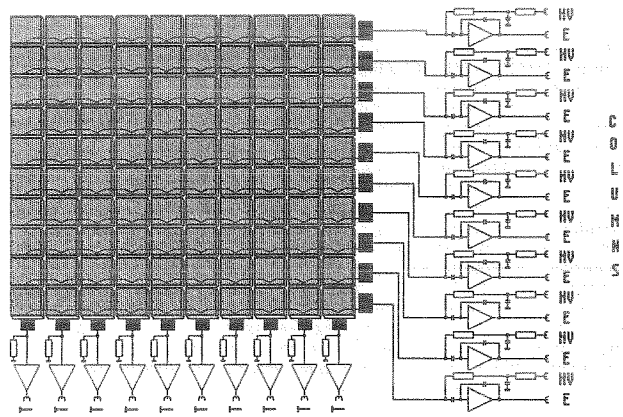


Fig. 1 Schematic diagram of the PIN-diode array with electronic matrix readout.

results from the remaining kinematic shift due to the finite solid angle of one column.

Meanwhile high ohmic PIN-diodes (ρ = 6000 Ω·cm) are available, which promise a full depletion depth over the 500 µm thickness. For future experiments we will assemble multilayer telescope arrays to cover a larger energy range and to provide for particle identification.

[1] P. Egelhof et al.,
Nucl. Struct. Stud. near Closed-Shell-Nuclei far off Stability
A Proposal for SIS-ESR Experiments, GSI 1988

[2] G. Kraus, Diploma Thesis, Univ. Mainz 1989 ,and
G. Kraus et al., this report

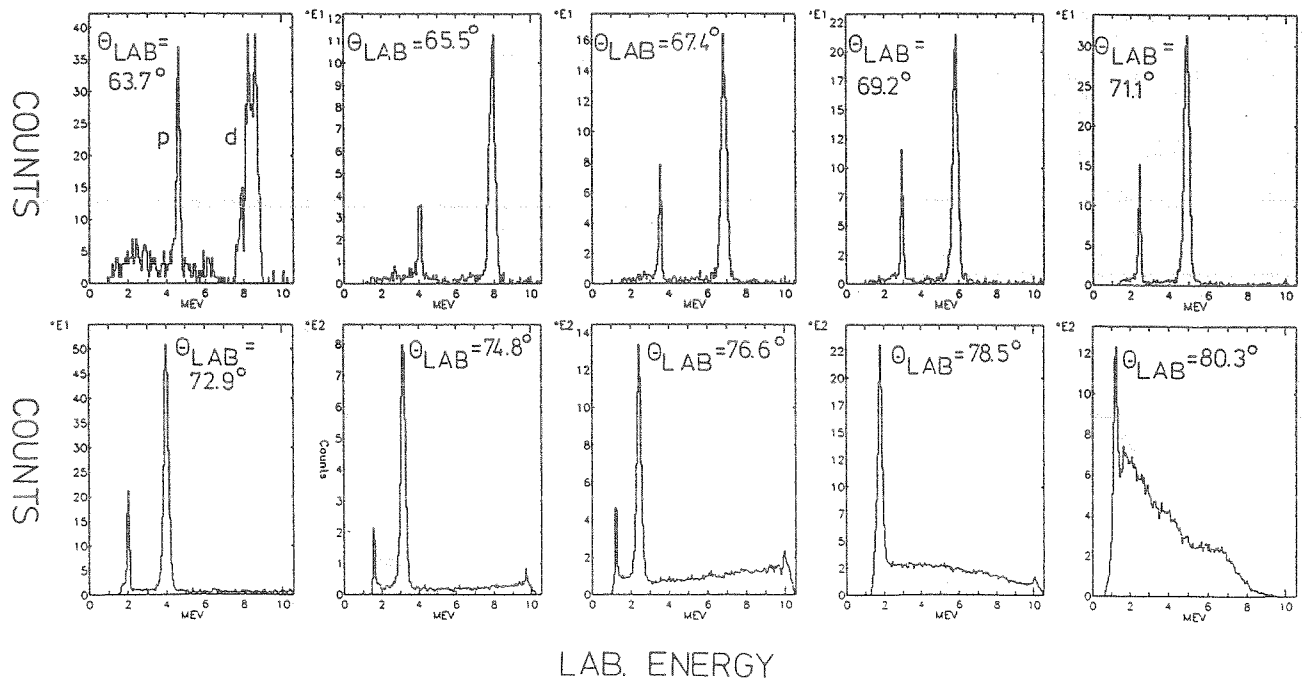


Fig. 2: Energy spectra of elastically scattered protons and deuterons measured simultaneously in one array position. The spectra for columns #1 to # 10 correspond to fixed lab. angles.

Calorimetric Cryo-Detectors for Heavy Ions

V. Trübenbacher, P. Egelhof, W. Henning, A. v. Kienlin,
J. Meier (GSI Darmstadt and University Mainz)
F. Azgui (CDTN Alger, Algeria); K. Shepard (Argonne National Laboratory, USA)

Calorimetric detectors operating at low temperature can provide good energy resolution for the detection of radiation. In the recent past successful tests of cryodetectors have been published for the detection of x-rays, γ-rays as well as β- and α-particles. The purpose of the present project is to investigate the possibilities of using such detectors for high resolution detection of heavy ions up to uranium with energies around 10-20 MeV/nucleon, i.e. total energies of several GeV. Some of the obvious questions concern the scaling of the energy resolution with high incident energies (GeV-range), the dependence of the energy resolution on radiaton damage, the specific technique employed for construction of a bolometer for heavy ions and the choice of detector materials. Presently two types of detectors, a germanium bolometer (consisting of a highly doped Ge-crystal which serves as absorber and thermistor) and a phase-transition thermometer (consisting of a thin superconducting Al-strip on a sapphire substrate), both operating in the temperature range 1.3-4.2 K, are being developed. For first tests a germanium bolometer of 3x1x0.5 mm³ volume was constructed, characterized in its physical properties and tested with α-particles.

In order to characterize the bolometer, systematic measurements of the temperature dependence of the resistance, voltage-current curves, as well as the time response to heating by voltage pulses were performed. The dependence of the resistance on the temperature is displayed on the left side of fig. 1. For almost the full temperature range it is described by the well known exponential relation $R=R_0\exp((T_0/T)^{0.5}$ with the parameters R_0 = 1.06 kOhm and T_0 = 130 K. At the working point around 2.4 K the temperature coefficient $\alpha=1/R\bullet dR/dT$ was 1.5. On the right side of fig. 1 the U(I) curves for three temperatues of the cold bath are shown. From these curves we deduce a thermal conductivity to the cold bath of k=47 μW/K for typical operating conditions of the bolometer. In order to determine the thermal time constant for the coupling to the cold bath, the response of the bolometer to an applied voltage pulse of rectangular form was measured. We observe two time constants, a short one, τ_1, of about 3.7 ms and a long one, τ_2, of about 65 ms. In order to understand this behaviour, the heat-balance differential equation for the system was solved numerically. Only the short time constant τ_1 can be reproduced by such calculations whereas the longer time constant τ_2 is not predicted. Thus we attribute τ_1 to the direct thermal coupling of the bolometer to the heat sink, whereas there is at present no full explanation for the long time constant.

The response of the bolometer to 5.5 MeV α-particles was studied using a conventional charge sensitive preamplifier to read out the signals. For typical operating conditions we observe a signal of about 1.6 mV after the preamplifier corresponding to a temperature rise of the bolometer of about $\Delta T=3$ μK. From that signal height we deduce a heat capacity of $C_{bol}=3.0\times10^{-7}$ J/K for the bolometer which is about twice as high as compared to the values calculated from ref. 1. After amplification of the signals with a shaping amplifier (shapingtime 100 μsec) and read-out by a conventional ADC, the observed pulse height spectrum is displayed in fig. 2. An energy resolution of $\Delta E=1.3$ MeV is deduced from this spectrum after unfolding the three α-lines of the α-source. In a recent test using a bolometer of considerable smaller volume, an energy resolution $\Delta E=320$ keV was measured. These results may be improved by optimizing the readout electronics with respect to the special conditions of the bolometers used. Presently a window-cryostat is under construction which enables to study the bolometer response on energetic heavy ions from the UNILAC.

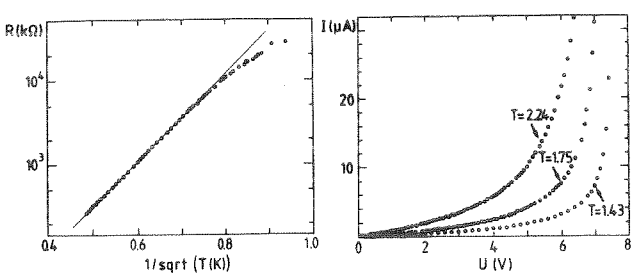


Fig. 1: Temperature-dependence of the bolometer resistance (left side) and U(I)-curves for various temperatures of the cold bath (right side).

The use of superconducting phase-transition thermometers may provide considerably better sensitivities than semiconductor bolometers, due to the strong temperature dependence of the resistance for the transition region between the superconducting and the normalconducting phase. Earlier experiments with thin aluminium films[2], especially their property of having a transition temperature within the operating range of a ^4He -cryostat, led to the decision to investigate their behaviour as thermometers for a composite heavy-ion bolometer.

For first tests thin aluminium films of about 8nm thickness were evaporated onto a glass substrate and covered by a thin layer of Al_2O_3 for protection. Single strips of 40 μm width and 10 mm length were prepared and contacted. Fig. 3 shows a typical transition curve. At a transition temperature of $T_c=1.467$ K a transition width (20-80%) of $\Delta T=8.6$ mK is observed. In order to match the thermometer resistance to the preamplifiers to be used we aim to use a meander - like structure consisting of 100 connected strips of 5 μm width and 1 mm length each, on a sapphire substrate of 1x1mm² size. Prototype detectors of that type are presently under construction.

We would like to thank H. Folger for the careful preparation of the aluminium- films.

REFERENCES

1. P.H. Keesom and N. Pearlman, Phys. Rev. 91 (1953) 1347
2. K. Shepard, W.J. Lai, J.E. Mercereau; Z. Appl. Phys. 46 (1975) 4664

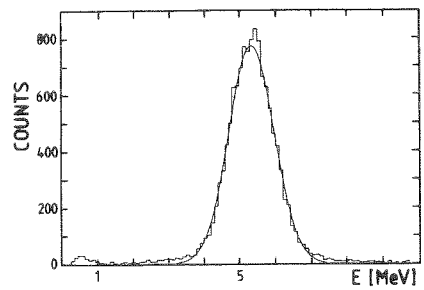


Fig. 2: Energy spectrum observed for bombardment of the germanium bolometer with α-particles.

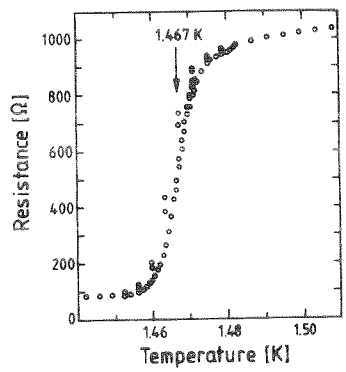


Fig. 3: Phase-transition curve for a superconducting thin (8 nm) Al-strip of 40 μm width and 10 mm length.

Physical Properties and Transverse Profiles of Electron Showers in Pb/SciFi Calorimeters G+B

M. Bahr, F. Berger, G. Clewing, R. Glasow, H.Å. Gustafsson‡, H.H. Gutbrod*, D.W. Hertzog×, G. Hölker, S.A. Hughes×, J. Idh‡, K.H. Kampert, M. Purschke, R. Santo, R. Schmidt, and P. Viyogi+

University Münster, University Lund‡, GSI Darmstadt*, Univ. of Illinois at Urbana Champaign×, VECC-BARC Calcutta+

In recent years there has been large interest in scintillating fibre calorimeters [1]. Massive hadronic calorimeters of this type are being investigated for applications at future colliders like SSC or LHC and have shown already promising results. Other developments in this new field aim for optimizing the fibre material and the composition of active-passive materials for high resolution electromagnetic calorimeters. Such a development, pursued by the *JETSET* group at LEAR, has led to a design of 1 mm diameter fibres imbedded in grooved Pb-foils as sketched in figure 1. The fibre-to-Pb volume ratio of 5:1 results from a compromise between high density absorber material and sufficiently small sampling fluctuations.

The advantages of such fibre calorimeters, like high density (i.e. small shower size), high counting rate capability, radiation resistance, relatively inexpensive, etc. would be attractive also for future large scale applications of high energy photon measurements in ultra-relativisitic heavy-ion reactions. A test of several of that prototype calorimeter modules with a size of about $10 \times 10 \times 20$ cm^3 (ca 15 X_0) has therefore been performed during a two week test run at a DESY electron test beam-line in spring 1989. The available beam energy ranges from 1 – 5 GeV/c. Physical properties like energy and position resolution, photon yield, light attenuation length, lateral shower profiles, etc. were investigated with different read-out techniques.

The obtained energy resolution can be parameterised as:

$$\sigma/E = 1.5\,\% + 6.6\,\%/\sqrt{E/\mathrm{GeV}}$$

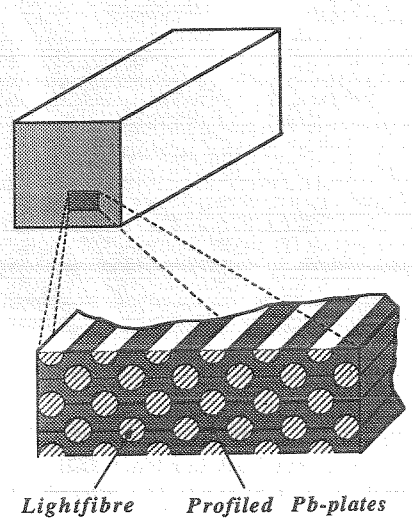


Figure 1: Sketch of a Pb/SciFi module. Fibres are placed along the length of the block. Profiled plates (blowup) are stacked with fibre bundles to form the completed block.

which is in agreement with measurements performed at lower energies ($\sigma/E \cong 7\,\%\sqrt{E/\mathrm{GeV}}$) by the group of the University of Illinois at Urbana Champaign. For *SF5* lead-glass values of $\sigma/E = 0.4\,\% + 6.0\,\%/\sqrt{E/\mathrm{GeV}}$ were obtained under similar conditions.

Another important quantity for the overall capabilities of a photon detector in the high multiplicity environment of ultra-relativistic heavy-ion collisions is the Moliére radius, i.e. the lateral spread of shower energy in the material. This measurement was performed by scanning the electron beam across boundaries of adjacent readout cells and inspecting the relative energy depositions in those cells as a function of electron position. In order to reduce possible systematic uncertainties of this procedure, the same measurements have been done in addition with *SF5* lead-glass modules (35×35 mm^2 cross section) for comparison. From these measurements we extract

$$\frac{R_M(\mathrm{Pb/SciFi})}{R_M(SF5)} = 0.81 \pm 0.06$$

resulting, because of the similar energy reolution – according to $\sigma_x(E) \propto R_M\,\sigma_E(E)$ – to an expected position resolution of only slightly better than of *SF5* lead-glass. Final analyses for extracting absolute numbers of the Moliére radii and position resolution are in progress.

The above given numbers imply that spaghetti calorimeters of this type are comparable or only slightly superior to *SF5* lead-glass, but are definitely worse than *SF6* lead-glass ($\sigma/E \cong 3.5\,\%/\sqrt{E/\mathrm{GeV}}$). Modifications in the Pb-to-SciFi ratio are expected to improve the energy resolution only a little, however, at the cost of enlarging the Moliére radius, as has been shown by thorough GEANT simulations on this point. We expect that spaghetti calorimeters of this type will play an important role in future high-energy experiments, particularly if large solid angle coverage is required but extremely good energy resolution is not mandatory.

References

1. See e.g.: P. Sonderegger, Nucl. Instr. Meth. A257 (1987) 523.

A Multi-PPAC System for the Detection of Reaction Products from Dissipative Very Heavy Ion-Atom Collisions

B

K. E. Stiebing, D. Kraft, K. Bethge, R. Rüschmann, R. Staudte (IKF Frankfurt),
M. Dahlinger, J. Stroth, H. Backe, P. Kosmadakis (Univ. Mainz),
H. Bokemeyer, P. Senger (GSI Darmstadt)

A new detector set-up has been installed at the Z4-experimental site for the use in coincidence experiments exploring the spectrum of high-energy δ-electrons emitted during dissipative very heavy ion-atom collisions[1]. The set-up is displayed in fig.1. It consists of six planar detector chambers forming the frustum of a pyramide and one annular one. A central hole allows to stop the beam far off the target and detector area. In order to determine the absolute times of flight of reaction products, the set-up is positioned at sufficiently large distances from the target. At a distance of 65cm the pyramide covers a scattering angular range from 25^{o} to 65^{o}. In ternary reactions of heavy systems (e.g. U+Au) a substantial amount of the fission fragments ($\approx$ 50%) is focussed into scattering angles smaller than 25^{o}. This region is covered by the central annular detector. Although principally allowing to detect scattering angles as low as $\theta \leq 5^{o}$ a compromise has to be found between the high total trigger rate from distant-collision elastic scattering and highest possible solid angle for fission events in this angular range. This is achieved by means of annular diaphragms, introducing appropriate lower cut-off angles.

The system as a whole can be adjusted in its distance to the target to optimize conditions for the investigation of more asymmetric collision systems like U+Pd or U+Ni. These systems became of particular interest by our finding of an anomalously high production yield for δ-electrons in close collisions [2].

Each of the six detector chambers of the pyramide contains 5 individual PPA-detectors, whereas the annular detector chamber houses 6 PPAC's. This high granularity of altogether 36 detectors (all of a similar sizes of $\approx 600cm^2$) guarantees a high trigger-rate capability of the total set up and at the same time reduces typical problems arising from very large detector areas (e.g. position dependence of the time resolution). The high modularity, using only 4 basic geometrical detector forms, simplifies production and maintainance of the set-up.

Each PPA-detector consists of two stages of 4mm depth each for the detection of the x- and y-position, respectively. Both stages are separated by one common anode formed by a 1.5μm Mylar® foil, which is homogeneously evapoprated on both sides. It provides a fast trigger signal and a common start signal for the delaylines of both detectors. The position detection is achieved by averaging the charges influenced on a pattern of parallel conducting stripes of 1.9mm width separated by .2mm. In the first stage this pattern is evaporated onto a 1.5μm Mylar® entrance foil, whereas in the second stage it is realized as printed circuit. The stripes are coupled to a "meander-type" delayline [3], which is read out on both sides and provides a time delay of 700ps/stripe. The delayline signals of all detectors contained in one vacuum housing are fed out of the scattering chamber via one twisted-pair flat-ribbon cable inside the gas supply system to minimize outgasing in the Z4-vacuum vessel.

High-voltage is supplied to all anodes by means of a 40-channel voltage divider allowing to adjust the individual voltages within $\pm$10% of the basic value given by one common power supply. In addition, each channel is equipped with a current-sensing spark protection circuit.

All signals of the detector system are processed via fast linear- or difference amplifiers (for anodes and delaylines, respectively) and CAMAC-controlled constant fraction discriminators into standard CAMAC front-end electronics (TDC's,QDC's). The read out of the system is enabled by requiring at least two fragments in opposite hemispheres of the system. For this purpose a fast trigger is generated by performing an overlay coincidence between two common OR's, each supplied with the anode signals of one hemisphere of the system. In addition to this, an identification of those detectors is performed by means of fast input registers, which have been triggered by a valid event. In this way only the active channels (i.e. maximal 16 out of 144 processed delayline signals) are selected by the J11 front-end processor and written on tape by the GOOSY data aquisition system.

The system has successfully been employed in a recent beam time investigating mainly the aspects of the unexpectedly high δ-electron yield from asymmetric collision systems. The data analysis of these experiments is in progress.

Acknowledgement: We wish to express our gratitude to those who helped us, especially H. H. Gutbrod for supplying the large number of TDC-channels for the delayline read out.

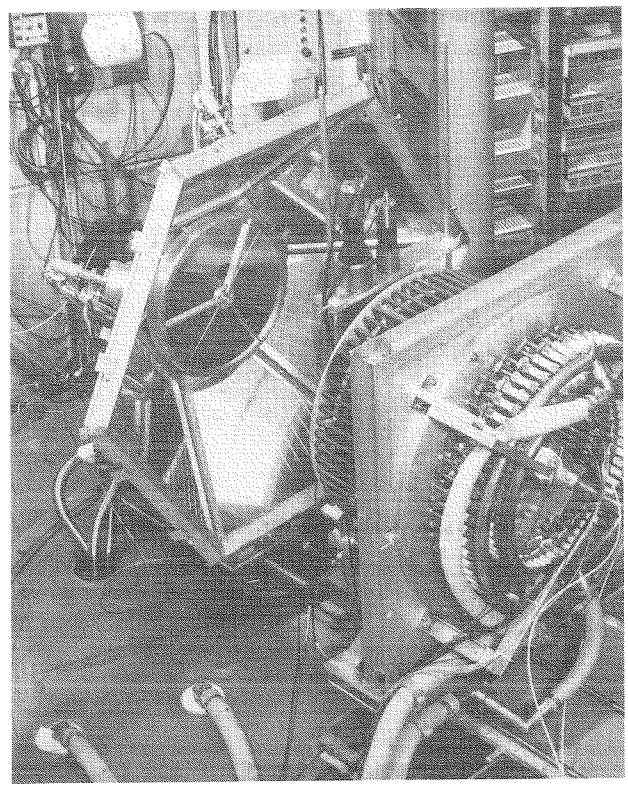


figure 1: experimental set up in the Z4-scattering chamber

[1] P. Senger et al., Physics of Strong Fields, Maratea 1986 (Plenum Press, New York London, p.423)
[2] H. Backe et al., GSI-report 89-1, scientific report 1988, p.162
[3] R. Bosshard IEEE Trans. on Nucl. Sci. NS-22 5(1975)2053

Dependence of Partially Annealed Volume Tracks on Track Orientation

R. Dersch, C.D. Zhao*, E.U. Khan[1], P. Vater, R. Brandt, V.P. Perelygin[2], S.G. Stetsenko[2]

Kernchemie, FB 14, Philipps-Universität Marburg

[1]Physics Department, Gomal University, Dera Ismail Khan, Pakistan

[2]Joint Institute for Nuclear Research, Dubna, USSR

Olivine as a common crystal in meteorites had been used to investigate the heavy component of cosmic rays[1] with nuclear track technique. The total etchable length of the volume tracks corresponds to the atomic number of the nuclei. After partial annealing at 450°C for 32h the resulting length spectrum[1] from Marjalahti meteorite is shown in Fig. 1a. Most of the volume tracks are shorter than 200 µm whereas only few tracks are about 250 µm long. A similar spectrum can be observed at an annealing temperature of 430°C. Here the length of a few very long tracks is about 360 µm, whereas the track length doesn't exceed 260 µm for most other tracks.

For the purpose of calibration, meteoritic crystals were irradiated with about 70 MeV/N ^{238}U ions at BEVALAC (Berkeley) and one crystal at GSI with 13.6 MeV/N ^{208}Pb-ions at 5 various azimuthal directions and an angle of 10° to the surface.

Typical results from the track length measurements of partially annealed (T=430°C) uranium volume tracks from U-irradiations at BEVALAC are shown in Fig. 2. The mean track length is different from crystal to crystal as the total etchable track length depends on the orientation of the tracks with respect to the crystallographic planes. In crystals were the polished surface was nearly parallel to the main crystal plane (010) longer volume tracks were observed (Fig. 2a). In previous experiments we observed in some crystals a mean track length up to 440µm.[2]

At an annealing temperature of 450°C the results from track length measurements of accelerated heavy ions are presented in Fig. 1b and compared with the length spectrum of ancient tracks.

In general the larger dispersion of the measured track lengths within one crystal or of length distributions of different crystals is mainly due to orientation dependent annealing or etching. The results of the measurements in one crystal irradiated at 5 different azimuthal angles (see table 1) indicate that with increasing azimuthal angle the track diameter and so also the mean track lentgh increase.

Table 1: Dependence of track parameters on the orientation of the track with respect to the direction of preferential etching, irradiated with 13.6 MeV/N ^{208}Pb

azimuthal angle	No. of tracks*)	track diameter (µm)	mean track length (µm) (volume tracks)
15°	1 (1)	0.75 (0.5)	55 (5)
45°	16 (5)	1.25 (0.5)	67.5 (10)
49°	23 (6)	1.25 (0.5)	71.2 (10)
63°	19 (12)	2.5 (0.5)	72.5 (11)
85°	24 (12)	2.5 (0.5)	75.8 (6)

*) In brackets: No. of volume tracks

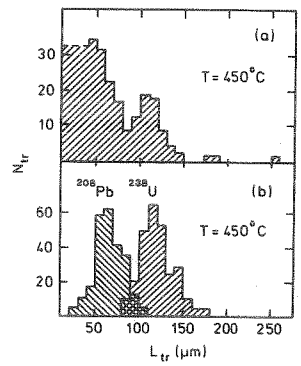


Fig. 1: Length spectrum of ancient cosmic ray tracks (a) and of tracks due to accelerated ^{238}U and ^{208}Pb nuclei (b) in meteoritic olivine crystals partially annealed at 450°C.

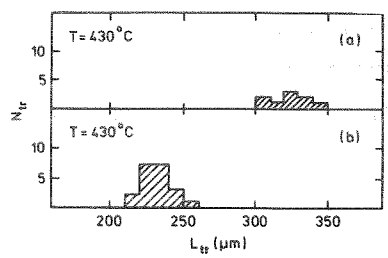


Fig. 2: Length distribution of partially annealed (T=430°C) ^{238}U-tracks in two different meteoritic olivine crystals

[1]V.P. Perelygin and S.G. Stetsenko, JETP Lett., Vol. 49, No.5 (1989)

[2]R. Dersch et al., GSI Scientific Report (1987)

* On leave from Institute of Atomic Energy, Academica Sinica, Beijing, China

Experimental Electronics Department (Elektronik/Experimente)

R. Albrecht, J. Dengler, G. Eidmann, H. G. Essel, R. Fritzsche, H. Hammal, H. Hardel, J. Hoffmann, H. P. Liebold, A. Loos, H.-G. Martens, W. Meufels, K. Mömerzheim, A. Muhn, K. Poppensieker, A. Przybyla, D. Quis, M. Richter, D. Schall, H.-G. Schmidt, R. Schulze, H. Sohlbach, W. Spreng, E. Sturm

GSI Darmstadt

T. Batsch

University of Warsaw, Poland

The Experimental Electronics Department is involved in development, production and maintenance of electronic systems and equipment. These systems are used for data processing and control in experiments at the UNILAC and in the future at SIS/ESR as well as at outside experiments of GSI groups, e. g. at CERN. The activities of the department include analog and digital signal processing, the digital online computer systems (hardware and software), control systems, and the assistance of experimentalists. In addition, we collaborate with the development group of the new synchrotron facility under construction at GSI and with the GSI Computer Center.

Detectors and Signal Processing

In 1989, the production of approximately 1200 CAMAC modules for SIS detector electronics was started. More than 20000 cables with a total length of 35 km were assembled and 7500 printed circuit boards were ordered.

Specific versions of CAMAC Constant Fraction Discriminators CF8102, CF8103, and CF8104 were designed and produced, which included additional leading-edge thresholds, delay-line terminated monoflops and coincidences between neighbouring outputs.

A large amount of 16-channel Leading-Edge Discriminators LE1600, 16-channel Logic Delays with 500 ns DL1600, 48-channel CAMAC ECL Scalers and Relay Multiplexers RM2400 and RM4800 were built. In 1989, 340 NIM modules of former design were ordered.

A 1/25 CAMAC module DP1630 was built to delay 16 analog pulses of a plastic scintillator using 10 hybrids of 50 ns each. This module serves as cable terminal for long connections from a set-up cave to the electronics and splits cables between CFD and ADC.

Approximately 500 fast analog pre-amplifiers with an amplification factor between 1 and more than 1000 and various differentiation and integration time constants were produced for the electronics pool and the prototype of a multiwire proportional chamber for SIS/ESR.

A new linear Fan-Out module was designed. On a small board of 2 cm x 5.4 cm two Fan-Out channels are realized with a DC-coupled input of 1 kΩ or 50 Ω impedance, where inputs can be switched in parallel. With a fixed gain of 1 or 2 the DC-coupled output has an offset less than 3 mV (baseline restorer). The output delivers up to 5 V into 50 Ω (tr = 5 ns). The amplifier can drive high capacitive loads without overshoot, as it is necessary for flash-ADC drivers.

According to the needs of experiments using multi-scaling techniques like X-ray spectroscopy with crystal spectrometers a sophisticated multi-scaling module MSC2000 is ready for production and available on request.

The activities concerning the specific support for the large SIS/ESR experiments including the cooling system and the cabling are described separately in this report.

In 1989, our department continued the support of the accelerator development of SIS/ESR for the kicker magnets. Several layouts of printed circuit boards were also made for the accelerator development.

Computerized Layout System

The computerized system to design and lay out printed circuit boards installed in 1983 (CADE, Laichingen) again was used very successfully in 1989. 78 schematics and printed circuit boards (NIM boards, Euro boards, CAMAC boards, VME boards, 41 double sided, 33 multilayer, and 4 multiwire) have been designed, layed out and documented by our department using the CADES layout system. The data base updates, general command procedures, program documentation, and system updates for the whole GSI are maintained by our department.

Online Computers

In 1989, most UNILAC experiments used the standard data acquisition system GOOSY running on VAX computers. The GOOSY software has been maintained in 1989. New developments are described separately in this report.

The general VAX system management, the expansion of the GSI Ethernet, and new software available for VAX users are described separately in this report. There is also an article about the network management program ATEM initiated and supported by the Hahn-Meitner-Institute, Berlin and the GSI and realized by Digital Equipment.

The frontend processor data readout system for future SIS/ESR experiments was the main focus of the hardware and software data acquisition development. The activities concerning the VME, FASTBUS, and CAMAC hardware and software are described separately in this report.

The activities concerning the control of experimental set-ups are also described separately in this report.

Electronic Support for the SIS/ESR Experiments

R. Albrecht, H. Hammal, A. Muhn
GSI Darmstadt

1. Water Cooling of Electronic Racks

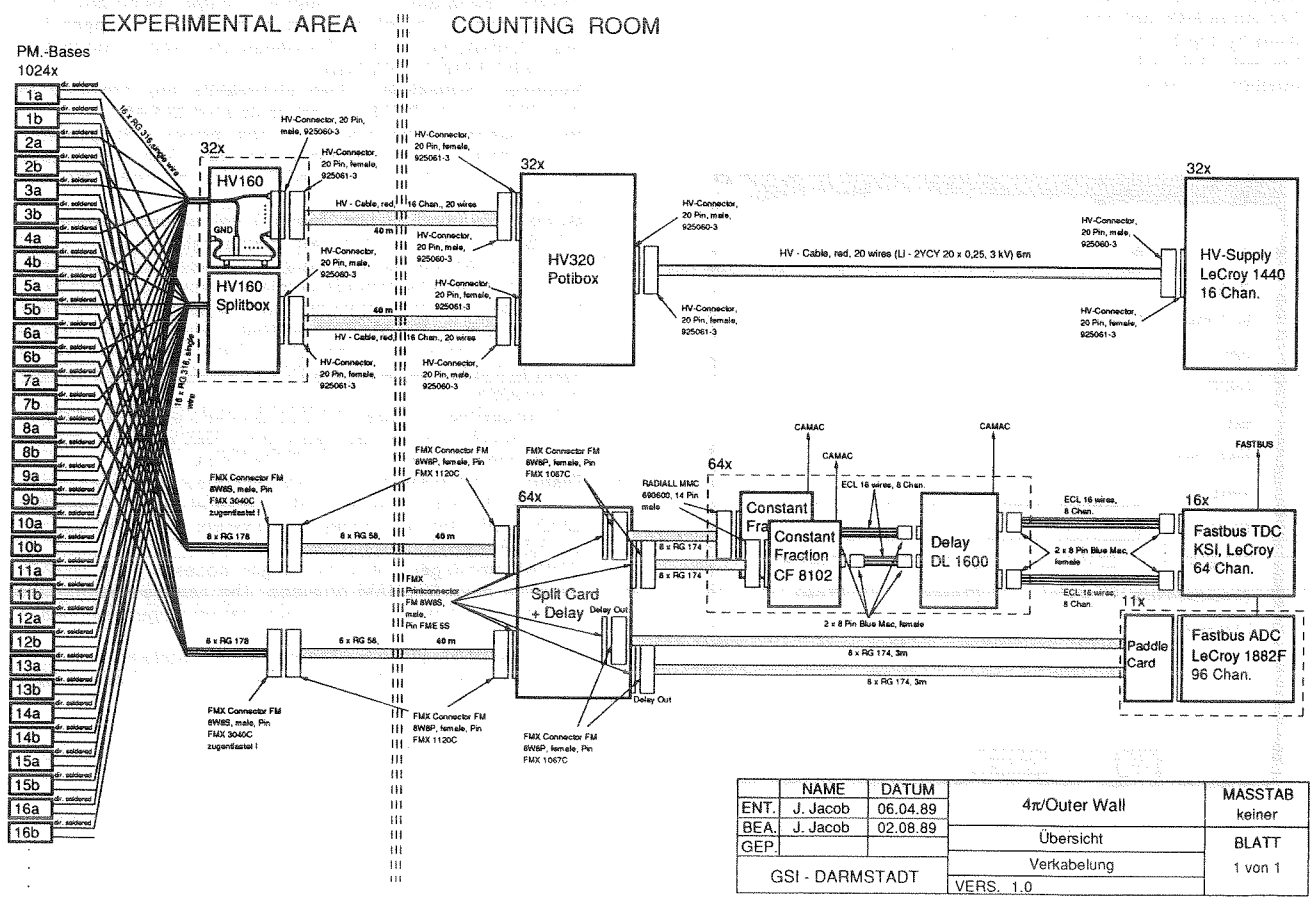
More than 200 kW are necessary to power all electronic data taking equipment for a single large SIS experiment, 10 times the power needed to heat a villa in wintertime. Surface-mounting techniques and dense packing require an extra effort in the cooling techniques.

We decided to install water-cooled racks similar to latest CERN experiments. The cooling air is blown through a complete rack, where NIM-, CAMAC-, FASTBUS- and VME-crates alternate with water heat exchangers for the air. A heat exchanger is always mounted above the crate, thus allowing higher temperature differences. Above the rack the air is emitted into the electronics room to circulate back to the bottom air-inlet of the rack. Thus also some surrounding electronic modules will be cooled in addition.

Precautions have to be made avoiding the condensation of water in the rack. Therefore the cooling water has to have a temperature above the dew point. The central water preparation, an assembly of pump, valves, and tubes, raises the entry temperature of the water up to 16° C and reduces the temperature of the return water down to 12° C, just right for the refrigerator. For high humidity the temperature of the input water will be raised to avoid dew water. An additional heat exchanger directly driven by 6° C water allows the decreasing of the room humidity if necessary. To guarantee the correct air flow in the rack unused crate stations and rack space must be closed by front panels. Free space on the sides and on the back are filled with foam. In addition, fan plug-ins were designed using 11 high efficiency 24 V DC fans per plug-in, distributed over the whole cross section of the rack.

2. Multi-Coaxial Signal Cables

For signal distribution from the detectors to the electronics hut huge amount of cables are necessary. We ordered a special 8 x RG58 multi-coaxial cable for the analog signals from crystal scintillators, plastic scintillators, etc. It is assembled with SubD octal coaxial connectors (FMX) on both sides. 27 km of this cable were needed for experiments in early 1990. The same connectors were used for signal distribution within the electronics together with an specifically ordered 8 x RG174 coaxial cable. High voltage is distributed using a special 20-wire cable with shielding assembled to the block connectors used also in LeCroy HV crates. The figure shows the cabling layout of the plastic wall detector of the 4π experiment.



	NAME	DATUM		
ENT.	J. Jacob	06.04.89	4π/Outer Wall	MASSTAB keiner
BEA.	J. Jacob	02.08.89	Übersicht	BLATT
GEP.			Verkabelung	1 von 1
GSI - DARMSTADT			VERS. 1.0	

GOOSY, the Acquisition and Analysis System for Experimental Data

H.G. Essel, R. Fritzsche, U. Post, M. Richter, D. Schall, W. Spreng
GSI Darmstadt

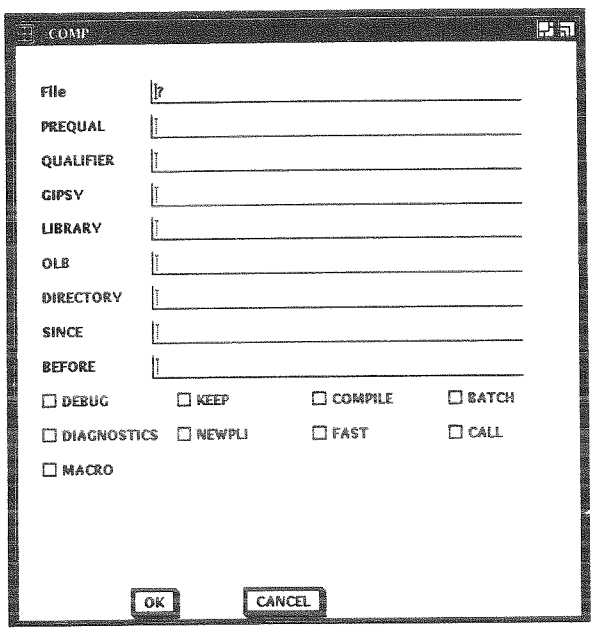
In 1989, GOOSY has been distributed to several laboratories collaborating with GSI, i.e. Texas Cyclotron Institute, GANIL, Frascati, Valencia, Göteborg, München, Groningen, Villigen, and Lyon. Most of the experiments at the UNILAC used GOOSY for data acquisition. Several experiments done at other laboratories used a portable μVAX with GOOSY.

Communication Lines

The main modifications of GOOSY concerned the support of the new VME frontend equipment. The GOOSY transport manager has been reorganized into a set of files. It communicates with the frontend processors via Ethernet and VME net processor (ELTEC E-5). A more detailed description can be found elsewhere in this report(1). For data input the DMA interfaces HVR 8217 (on the VME side) and DRQ11 (on the VAX side) are supported. Data rates of 400 KByte/second have been measured. When writing a tape, the rate goes down to about 320 KByte/second. The interface DRB32 of VAX-BI machines will be supported soon.

Downline Load

The programs for the VME processors (FIC 8230) are compiled and linked on a VAX. By command they are loaded via the net processor to the FIC. The FIC is reset first by software. After a program is loaded into the FIC it starts automatically. The software of the frontends and the event builder are described in more detail elsewhere in this report(2).
The readout tables are written on the VAX as text files. They are compiled and loaded via the transport manager and net processor to the frontend processors. From there they may be distributed to the intelligent readout processors like CVI or AEB.
The list of FICs and their specifications like programs and tables used by the frontend system are kept in text files on the VAX. For each FIC a logical number, its VME crate number and its position in the crate is specified in these files. The transport manager keeps this information in its control data base.



Commands

A first set of commands like INITIALIZE ACQUISITION/VME, LOAD VME TABLE and LOAD VME PROGRAM are implemented in the transport manager. Commands executed in the FICs are implemented to control a test system. These include START/STOP VME, RESET VME, INIT/RESET CAMAC, EXECUTE CNAF. All commands are sent from the transport manager via Ethernet and net processor to the addressed FIC. Commands may be sent to all FICs, a subset or a list of FICs.

Current Status

A system with net processor, event builder, two FEPs with one CAMAC crate each and the DMA interfaces has been tested and first data have been taken. The data buffers and events are written in a standard format. All modules to handle these buffers and events are ready. There will be final adjustments in the VME control commands for the final version of the frontend hardware and software, because the trigger module is not yet available.

GOOSY News

Other general enhancements are summarized below.

- **GOOSY Analysis program**: The user analysis routine may use up to three data bases instead of one.
- **Raw data files**: It is now possible to copy events from input buffers directly into output buffers under control of a user routine.
- **Event spanning**: Events from the VME system may span over buffer boundaries.
- **Random generator**: The internal random generator runs now independently of the interface provided to support foreign frontend equipment. Previously the random generator emulated foreign equipment.
- **Spectrum protection**: Two commands are provided to PROTECT or UNPROTECT spectra against CLEAR.
- **Monte Carlo in analysis**: It is now possible to generate event data in the analysis routine. The commands START/STOP ANALYSIS RANDOM are provided for that purpose.
- **GOOSY menus**: A new menu level is implemented in GOOSY. A question mark will display all keywords of all available commands. Selecting a keyword all commands containing this keyword are displayed. Now a command can be selected and the command menu is activated. There is a new couple of GOOSY prompters which communicate through a mailbox with each other. These prompters will be used to implement a simple DECwindows interface to control GOOSY.
- **DCL procedure menus**: All DCL procedures got a DECwindows interface to be activated from DECwindows menus. The arguments are input in a DECwindow.
- **Display**: The GKS-driver for DECwindows has been implemented. It has, however, still several bugs. Therefore GOOSY will run only under VWS system until the bugs are corrected by the company.
- **GOOSY privileges**: It is no longer necessary for GOOSY users to have SYSNAM privilege. The actions needing this privilege are now executed by special privileged routines.

1) H.G.Essel et al., Ethernet Communication Software.
2) W.Ahner et al., Frontend Software in the VME-based Data Acquisition System.

Computerized Control Systems for Experiments

H.G. Martens, W. Meufels, K. Poppensieker

GSI Darmstadt

The development and maintenance of process control for experimental setups at the UNILAC is an integral part of our department. The control system for the velocity filter SHIP consisting of an LSI-11/23 processor and CAMAC has been working well in 1989. The magnet power supplies for NASE had been integrated into the SHIP control system this year.

Ten 1/25 CAMAC module (CAM1000), supporting the MIL 1553 B, used in several experiments to control power supplies and other equipment have been produced and are available .

Twenty FuG high voltage power supplies for the electron target experiment and for the Electron Cooler have been equipped with the adaptor boards HVN1000 and GSI standard interface boards [1].

It is now possible to perform process control for experiments either from the new data acquisition system GOOSY via CAMAC/VME or with the new SIS/ESR control system using VME. Both systems will support the GSI device bus MIL 1553 B. This work has been done in collaboration with the accelerator electronics department.

For motion control applications in the experimental area eight CAMAC modules DCC1000 and the corresponding servo amplifiers (H-bridges) have been built for the Z1-Spectrometer and will be installed in 1990. The DCC1000 is a two fold dc-motor controller for point to point motions with maximum speed. The current position of the armature is monitored by a gear down potentiometer (for details see manual for this device).

For stepper motor applications the following standard will be supported by our group:

- 5-phase stepper motors from BERGER LAHR (with encoder for rotation control),
- Power supplies type MD5 BERGER LAHR (for three or two axis) for stepper motors,
- Indexer MSC1-VME/D2 (VME module) PROMOTION ELECTRONIC, Karlsruhe.

Motion controllers using dc-motors (commutators- and brushless) with incremental encoder as position sensors which will be used for TAPS are under development.

Also the control system for the KAOS Spectrometer is under development.

The information interchange between the SIS/ESR control system and the data acquisition system GOOSY will play an important part in the light of the new experiments at ESR. For slow or medium speed data communications the GSI device bus (MIL 1553 B) will be a good choice. Therefore a VME module VIB1000 has been developed with the following characteristics:

1. it behaves like a GSI standard interface board (can be handled by GSI SE-68K or CAM1000),
2. it responds to more than one device address,
3. these addresses are under software control,
4. due to the microprocessor firmware it is highly flexible.

Another application is the handling of a complete control system (e.g. a whole VME crate) as a specific device. This module is ready for production.

Again a lot of new terminals had to be installed all over the building. A lot of work had to be done for connecting these terminals. Several kilometers of cables had to be manufactured and installed and over 90 EIA-to-current-loop converters were produced. Obeying a strict scheme of connections the installation of other new terminals will be achieved with less efforts.

[1] P. Spädtke; this report.

Status of the VME-based Data Acquisition Interfacing of CAMAC and FASTBUS Systems to VSB

J. Hoffmann, M. Richter, D. Schall, H. Sohlbach
GSI Darmstadt

More than 50 CAMAC crate controllers (CAV) and 25 VSB interfaces (VSC) have been produced in 1989. They are used in experiments and in test assemblies for software development. A CAMAC dummy display module is used as a necessary accompanying module to CVI and CAV. It is inexpensive replacement for the CAMAC Display Module DMS. A new intelligent CAMAC controller (CVI) with a VSB interface and a FASTBUS to VSB interface have been produced and the prototypes perform successfully. Production in quantities will start soon. A trigger system for CAMAC,FASTBUS and VME has been designed. The CAMAC trigger module has been tested.

The CVI module.

An improved versions of an intelligent CAMAC crate controller with VSB interface (CVI) has been designed and successfully tested in 1989. It contains a MOTOROLA 68030 20 MHZ microprocessor, 16k X 32 bit no-wait-state memory for data and programs, 1Mbit EPROM, a VSB interface, a CAMAC interface, CAMAC LAM logic, a control-status register, two serial I/O ports for terminal and host, and an external port connector. Up to 15 CVI modules can be connected to one VME front-end processor via VSB.

The 68030 CPU can work in parallel with CAMAC cycles. It can trigger a CAMAC cycle and then process the next instructions while CAMAC is running. After completion of the CAMAC cycle the CPU can read the data or proceed if it was a write cycle. This "short" CAMAC cycle (600 nsec) is possible. The CVI module runs pROBE and pSOS.

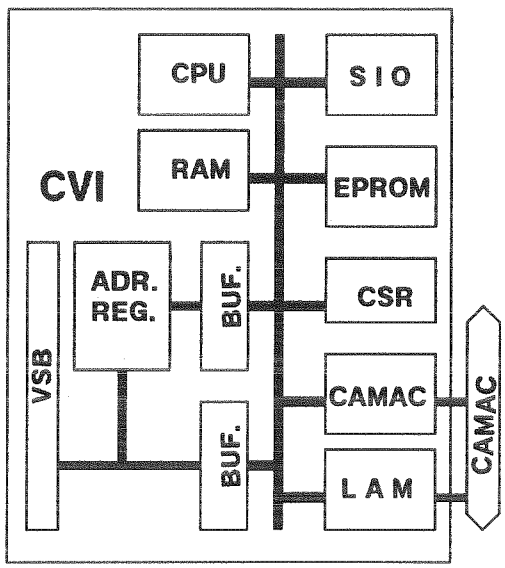


Figure 1. : Block diagram of the intelligent CAMAC controller module (CVI)

The EBI module.

In 1989 two EBI modules have been produced and successfully tested. The EBI is coupled with the ALEPH event builder by the AEB front panel bus connector. It consists of a VSB interface, an AEB interface, 16k X 32 bit dual port memory, a 1K x 32 bit CSR area for command and exchange. The register CSR 0 is reserved for controlling the interrupt mechanism and the external port interface. Both VSB and AEB can set interrupt requests (IRQ) to each other.

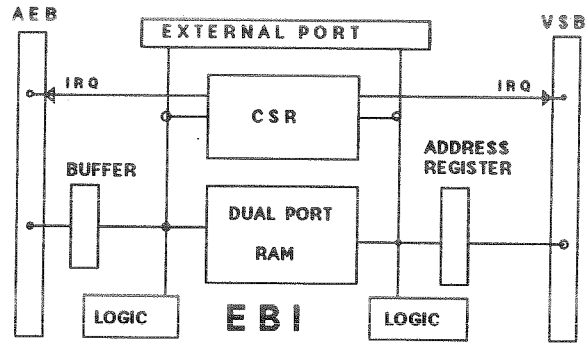


Figure 2. : Block diagram of the FASTBUS to VSB interface module (EBI)

The TRIGGER module.

The CAMAC, FASTBUS and VME TRIGGER modules together with the front-end processors have to guarantee a correct inhibition of ADC gates and TDC starts during conversion and readout time as well as collection of corresponding subevents to the complete event. In every crate should be a trigger module. They are connected together via a trigger-bus. The trigger-bus signals are: Halt/Go, four Master trigger lines, a Hardware Fast Clear, Subevent Invalid, Reset, total dead time, Delay Interrupt and a four bit Event Counter. The CAMAC version of the TRIGGER module has been tested in 1989, the FASTBUS version design is ready now.

Testsoftware

Menu driven testprograms have been written for test and debug of the various functions , the memories of the CAV, CVI and EBI modules and the VSB communication. The software is written in C , time critical parts in the interrupt handlers in 68000 assembler. The programs on the FEPs run with pSOS on the AEB with OS9.

Frontend Software in the VME-based Data Acquisition System

W. Ahner, H.G. Essel, U. Post, D. Schall, W. Spreng
GSI Darmstadt

VME Commands

The VME frontend system is controlled from a VAX through a VME Ethernet processor (Eurocom-5 under OS9). Commands are sent from the VAX to this processor using a specific Ethernet protocol (1). Each command contains a list of destination addresses specifying the VME processors which have to execute the command. The net processor then dispatches the commands to these processors. Until now, the processors write a completion status in their local control base and the net processor waits for command completion. The VME processor gets an interrupt and signals the command through an event flag to the execution task. The task may execute the command itself immediately or may deliver it to the subevent readout loop to be executed between two events. A first set of commands is implemented to control a test system. These include LOAD TABLE, START/STOP/RESET VME, INIT/RESET CAMAC, EXECUTE CNAF.

Program Loading

The programs for the FIC 8230 processors are loaded from the VAX through the net processor into the FIC memory. The LOAD VME PROGRAM command first resets the FIC processor which waits after the bootstrap for input to its FIFO. When the program is loaded and verified, its start address is written into the FIFO and the FIC starts the program execution. The setup of all FICs of the system and the specifications of their software and characteristics are kept in text files on the VAX. These files are used in the LOAD commands. User written routines called at certain points of the event loops can be loaded at any time.

Communication Between Frontend and Readout Processors

The frontend processors (FEP) communicate with the intelligent CAMAC controller (CVI) or the Aleph Event Builder (AEB) (2) through memory which can be accessed from both sides. In the memory, transfer control blocks (TCB) are defined where a message can be deposited. Then a VSB interrupt signals the receiving processor to read the message. There is one TCB for each direction. This method is used to dispatch commands and send messages or data.

Readout Tables

On the VAX the readout tables are text files specifying the modules in the CAMAC or FASTBUS crates. The trigger module provides a 4-bit number set by hardware. For each trigger number a different table can be specified. The tables are compiled into lists of CNAF codes or FASTBUS modules, respectively. They are loaded by commands into the FEPs. If necessary the lists are copied from there to the CVI or to the AEB which do the readout. The files also contain the specifications to reset and init the crates. The init or reset tables can be executed by commands.

CAMAC Readout

The CAMAC readout depends on the CAMAC controller used.

- The CAV generates a VSB interrupt in the FEP from a CAMAC LAM, and the FEP executes the lists itself.
- The CVI polls on a register which is set by the LAM. It reads the crate and interrupts the FEP via VSB. Then the FEP copies the data via VSB to the subevent buffer.

In both cases a user routine may be called to manipulate the data. The readout routines may be provided by the user, if a different readout scheme is needed.

FASTBUS Readout

The FASTBUS readout lists are stored in an internal control data module on the AEB. The readout is done by a task under OS9 on the AEB using the trigger number to select the corresponding list. When the readout is done, a VSB interrupt is signaled to the FEP which then copies the data buffer into the subevent buffer. A default readout routine is provided which currently reads the raw data of the FASTBUS modules into the AEB interface memory (EBI) using the AEB FASTBUS standard routines (2). It may be replaced by a user written routine. Another user routine may be called to manipulate the data after the readout.

DMA Channel to VAX

The Event Builder (EB) collects the subevents from the FEPs into events. The events are stored in buffers. The buffers are sent to the VAX through a parallel DMA interface. On the VME side the HVR 8217 from CES is used, on the VAX side the DRQ11 or the DRB32, depending on the VAX bus system.

Monitor Programs

A monitor program has been written to display the activities on a FIC. It utilizes a locally attached terminal to display various informations selected by menus. Two sources of information are accessed: The process control blocks (PCB) maintained by the pSOS operating system and the control and status region (CSR) maintained by the FIC software. As the CSRs are accessible via VME any FIC may be used to display the CSR information of other FICs. The PCB information, however, is accessible only on the local FIC. The program displays all kind of information about the buffer management, the event statistics, and processes. Optionally two FICs may be monitored simultaneously.
Another monitor module is optionally called during the readout on the AEB. It is activated by pressing any key at a locally attached terminal. It displays information about the loaded readout lists, the subevent data, and the communication path to the FEP.

Data Formats

The formats for the Ethernet messages, the VME command buffers, the readout tables, and the list mode data are specified. All formats fit into the GOOSY buffer scheme. The default buffer type for VME event buffers is 10,1. The default event type is 10,1. Each event header keeps a current number and the trigger number. Each subevent header keeps a logical FEP number specified in the setup file. In case of errors the subevent may be followed by an error element. The subevent type is negative in this case.

1) H.G.Essel et al., Ethernet Communication Software.
2) Aleph Collaboration, CERN

Ethernet Communication Software for VMS and OS9

H.G. Essel, R. Fritzsche, D. Schall
GSI Darmstadt

Purpose

Control information like commands and messages is exchanged between VAX-VMS processes and the VME net processor (Eurocom-5 with OS9) via Ethernet. For that purpose a special Ethernet protocol has been designed. A package of routines for the VMS side and for the OS9 side has been implemented. The package uses Ethernet protocol type 53-80. The basic routines from CERN are used to access the Ethernet and read and write Ethernet frames under VMS and OS9 (1).

Protocol

The protocol is based on links between masters and a slave. In general, all messages sent must be acknowledged by the receiver. The difference between a master and a slave is that the masters open a link to a slave which must be already started. The masters send link control messages to the slave after time intervals which are specified during initialization. When the slave does not acknowledge such a link control message in a certain time interval, a specified number of retries will be done. If no response is received, the link will be declared as broken. The master also may send a link abort message to break the link. When a link is open, the slave may, however, send messages to a master.

Buffer Formats

All Ethernet messages are preceded by a header. Each message has a unique current number and two numbers specifying the message type. There are reserved numbers for link open requests, link close requests, link check messages and the acknowledge messages. Because of the limited size of physical Ethernet frames the logical message buffers are split into several physical frames. Each physical frame sent must be acknowledged. If an acknowledge is not received during a certain time, a number of retries is done. If no acknowledges are received the write operation will be timed out. The physical frames contain information about the logical buffers they belong to, i.e. the total number of fragments and the current fragment number. The receiver copies all fragments belonging to one logical buffer together.

Software Layers

The package is split into a logical and a physical layer. The physical layer controls the link, the acknowledges and send retries if necessary. It writes and receives physical frames. In general read operations are done asynchronously to make sure that a read is outstanding at any time. Write operations are done synchronously in the sense that the sender waits a certain time to receive an acknowledge. During initialization byte swapping can be enabled or disabled. For GOOSY, byte swapping is done on the VAX side.

The logical layer is used in the application program to open/close links, to send/receive logical buffers of any size, and to specify handlers for certain incoming messages specified by the message type numbers. In GOOSY the VME net processor works as slave and the VAX processes as masters. The first master connecting to a slave specifies a link ID (VMS group number). When the first link is established, only link requests with the same ID are accepted.

Logical Layer Routines

The following routines are available:

- **N$LE_INIT** Initialize the package. Specify master/slave mode, maximal logical buffer size and swapping.
- **N$LE_SET** (VAX only) Specify timer values for link control, read and write operations and number of retries.
- **N$LE_HANDLER** (VAX only) Specify handlers for specific message types.
- **N$LE_OPEN** Open a link to a node. As master a link request message is sent. As slave, a read queue is established.
- **N$LE_CLOSE** Send 'close' message.
- **N$LE_READW** Read a logical message of a certain type and wait. All physical frames of the logical buffer must arrive before timeout.
- **N$LE_WRITEW** Write a logical message of specified type and wait until timeout or physical acknowledge.
- **N$LE_TASEND** (VAX only) Write a logical buffer of specified type and wait for a logical acknowledge until timeout. The type of the acknowledge can be specified. In this case, all physical frames must be acknowledged physically and then the message must be acknowledged by a logical message.
- **N$LE_SHOW** Show status and statistics of a link.

1) T.Charity, A Multiport Ethernet Driver for OS9, CERN
1) T.Charity, A Subroutine Library for the VAX Ethernet Interface, CERN

Online Computers and Ethernet at GSI

H. G. Essel, R. Fritzsche, W. Meufels, M. Richter, H.-G. Schmidt
GSI Darmstadt

In addition to the two experiment assigned VAX-8600 running in a Computer Interconnect (CI) based VAXcluster together with a VAX-8700 for accelerator control a new VAX-6310 was installed to support large new SIS experiments. With the new VMS operating system version 5.0 the mixture of CI cluster and Ethernet based Local Area VAXcluster (LAVC) has become possible. 15 new VAXstations 3100 were integrated into this mixed cluster to make use of local computing power and graphic displays for experiment data acquisition and analysis. All of the 15 GBytes of the centralized (HSC connected) disk space is available for each cluster member. The six magnetic tape drives (1600/6250 bit per inch) and four 8mm video tape drives (Exabyte) are available through the HSC-70 controller for the CI connected VAXes. Two additional LAVCs are installed at GSI. One LAVC with two nodes is running for the computer aided design of schematics and printed circuit boards. The other LAVC with 19 nodes supports the accelerator control and operating. Furthermore five Micro VAXes are running autonomously connected to Ethernet, two of them installed in 1989 for ESR and Fragment Separator experiments.

The mixed VAXcluster is used as a disk, file, and printer server via Ethernet for HP Vectra PCs (MSDOS) using the PCSA software. The VAXes are also disk and file servers for several VME (Eurocom-5, -6) and Fastbus (Aleph Event Builder) based MC68020 and MC68030 processor boards running OS-9 together with CERN software (ALEPH) and TCP/IP (VMS Ultrix Connection).

In 1989, a lot of new software products were installed on the GSI VAX systems. Among others:

- RDB, Digital's relational data base system together with:
- CDD/Plus, the common data dictionary,
- SQL, the standard query language, and
- Datatrieve, Digital's query language.
- CMS, the code management system.
- MMS, the module management system.
- PHIGS, a graphics standard.
- NOTES, a communication and conference system.
- OPS5, a language for artificial intelligence applications.
- PCSA, PC server software.
- VMS Ultrix Connection with TCP/IP, Network File System (NFS) and File Transfer Protocol (FTP).
- VAX Image Scanning Application.
- DECwindows, X Window System implementation (VMS V5.1 and 5.2).
- DECwrite, a document processing application.
- Terminal Server Manager.
- LAN Traffic Monitor.
- RABBIT-7, a disk defragmentation utility of RAXCO Inc.

The following compilers are installed:

- VAX-FORTRAN (77),
- VAX-PASCAL,
- VAX-C,
- VAX-PL/I (Subset G),
- Modula,
- VAX-BASIC.

The common CERN libraries together with GEANT and PAW are also available on our VAX systems.

Unfortunately the X Window System device driver for our Graphical Kernel System (GKS) of GTS-GRAL is still not performing correctly. This inhibits presently the use of DECwindows for our data acquisition and analysis system GOOSY.

The Ethernet was expanded in 1989 including fiber optic links to the new SIS/ESR experiments. Over 100 terminal servers, fourteen low cost laser printers (LN03+), one Postscript laser printer (LN03R) and about one hundred VME or Fastbus based processor boards are spread over all buildings connecting directly to Ethernet or to terminal server ports. The Ethernet is available in all rooms at GSI. It now includes seven bridges (DEBET), five repeaters (DEREP), four fiber optic segments (Hirschmann), eight thinwire multiport repeaters (DEMPR) with 35 thinwire Ethernet segments, and 210 DECnet nodes including VAXes, PDP-11, terminal servers, and PCs.

Connections out of GSI are provided with DATEX-P (PSI software), DECnet via 9600 baud modem line to the University of Giessen, and EARN (Bitnet) via a 9600 baud modem line.

AI-based Telecom Equipment Management ATEM

M. Richter
GSI Darmstadt

The support, management, and maintenance of large local area computer networks (LAN) like the Ethernet at GSI demand easy to use computer aided tools. Initiated in 1988 and continuously supported by the Hahn-Meitner-Institute, Berlin, and the GSI the Digital Equipment GmbH (ACT-IS/IT, Dr. D. Bade), Unterföhring, developed a DECwindows and artificial intelligent based telecom equipment management named ATEM. It is successfully in use at GSI since October 1989.

ATEM makes use of a data base (RDB), a common data dictionary (CDD/Plus), image scanning and manipulation software (DECimage SCAN Application), X Window System software (DECwindows), and artificial intelligence programs (OPS5 language).

The user friendly system aids the compilation of the inventory of all network components like computers, terminal servers, Ethernet repeater, bridges, cables of all sorts, connectors, terminals, etc. These components are stored in the data base together with their characteristics like type, part number, color, supplier, value, electrical properties, mechanical properties, etc. The locations like building, floor, room, cable track, wall mounting, etc. are stored, too. In addition, the connections of all data elements are stored.

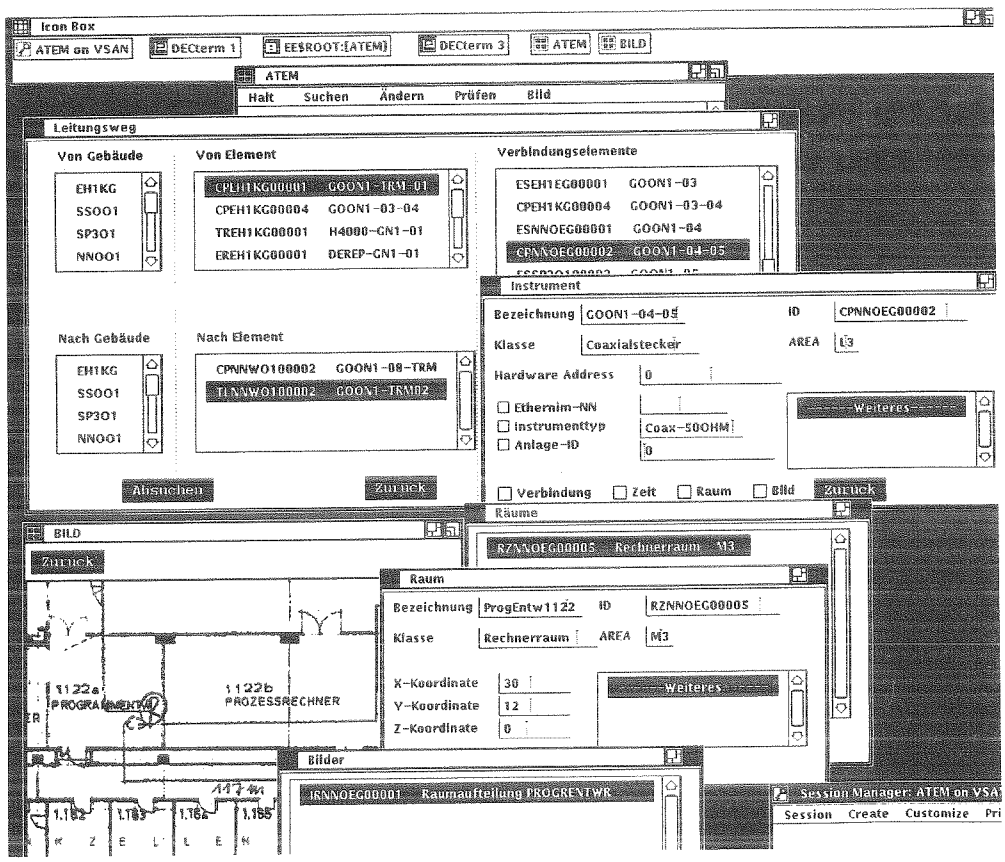
ATEM allows the definition of standard elements, cables, locations, and connections. Together with these standard data definitions the real elements can be acquired easily. The data consists of text, values, and images. The text and the values like length, size, etc. describe the properties and characteristics of the element. The images like the ground-plans of buildings and rooms, the drawings or pictures of locations or schematics may describe the elements more clearly. The images must first be scanned by a black and white 300 dots/inch image scanner hardware. The images can then be manipulated interactively to select parts of the image or to add graphics or text to them. An image can be linked to one or more elements of the ATEM data base.

Existing network data bases, e.g. from the Ethernim application software can be fed into the ATEM data base.

The artificial intelligence component of ATEM allows to find all links between two elements in the data base. It lists all parts in between the elements, e.g. from a terminal to a specific computer. ATEM will find the terminal line to a terminal server, the transceiver cable to a transceiver adaptor H4005, the Ethernet cable, a connecter, another Ethernet cable, an H4000, a transceiver cable, and finally the computer. Each component found can be selected to present all of its information, e.g. which type of terminal server, were it is located, how the location or the ground-plan looks like.

The user interface of ATEM is DECwindows. Pop up menus, subwindows, and simple selection buttons help the user to collect data, to search within the data, and to display the element characteristics and the images.

In further releases the system will test actively the connectivity between two elements to find out possible points of failure. ATEM will also check configuration rules like maximum cable length or maximum number of nodes connected to one segment. At present ATEM is tailored to support mainly Ethernet but it can easily be applied to other networks like wide area networks, cable systems for large experiments, or the internal telephone net.



Acquisition, Analysis and Control Software for the Experiments in CAVE B $^{G+B}$

T. Blaich[b], R. Freifelder[a], N. Herrmann[c], J.G. Keller[d], P. Koczon[a], M. Krämer[a], Y. Leifels[d], V. Lindenstruth[a], W.F.J. Müller[a], R. Schmidt[a], K. Teh[a]

[a)] GSI Darmstadt, [b)] Univ. Mainz, [c)] Univ. Heidelberg, [d)] Univ. Bochum

The Cave B in the SIS target hall houses four large facilities, LAND, ALADiN, the 4π Detector and TAPS. Many of the proposed experiments are based on coincidence measurements which involve two or more facilities. An efficient implementation of these experiments requires that the data acquisition and analysis software of the Cave B facilities be compatible and can indeed cooperate to handle a joint experiment.

To coordinate the various aspects and requirements of the different experiments, a regular meeting was established with participants from all major Cave B collaborations and representatives of the GSI computer center and the GOOSY group to develop a software strategy for these large scale experiments. In addition, working groups were formed to focus on particular topics, define standards and implement software commonly used by Cave B experiments.

This contribution presents the general Cave B software concept and reports on the software jointly developed by members of the KP1, KP2 and KP3 division in trying to realize this concept.

1. Analysis Software

The Cave B experiments effectively form one large multiinstitutional and multinational collaboration. Even though the data taking will mainly take place at GSI, the data analysis will be done at the different institutions with a wide variety of computing environments. This situation leads to the following basic requirements:

- Machine independence of the software.
  Today's offline analysis is likely to be part of tomorrow's online monitoring and might be part of a software trigger in the acquisition system at some later time.
- Portability of programs *and* data.
  Porting a code to another computing environment is of little value unless all associated data (raw data tapes, parameter data bases, reduced data, histograms, graphics,...) can be ported too.
- Inclusion and comparison of simulated data on all levels.

To the best of our knowledge these requirements can currently only be met by using the PAW / ZEBRA software package developed, distributed and maintained by the CERN Data Division. The basic features are:

- The programming language is FORTRAN 77.
- Data are represented by ZEBRA, a memory manager which includes a machine independent I/O package and a low level transportable database.
- An interactive layer (PAW) is available with interfaces to histogramming (HBOOK), plotting (HPLOT), various interpreter and command processor functions (KUIP) and graphics (HIGZ, GKS).
- A versatile multiparameter correlation analysis tool, based on a list representation of n-dimensional spectra (NTUPLE's) and interpreters (COMIS, SIGMA).
- The system is supported on VAX (VMS), IBM (VM/CMS) and a wide variety of UNIX-like systems. A subset is available for OS-9 based frontend systems.
- A frame for Monte-Carlo simulations (GEANT) is available that uses the same data and I/O management (ZEBRA) and can therefore be easily integrated.

2. Control Software

For multiparameter detector systems like the ones under construction for SIS there is the problem of bookkeeping for all setup and calibration parameters. To avoid updating problems all parameters should appear only once. All data should be accessible in a multiprocessor environment (e.g. VAX-Cluster).

Our solution to this problem was a relational database structure based on the CERN package ZEBRA. It allows to store data in a tree-like structure without knowing the final amount of data.

The data is grouped in tables. The columns are called ATTRIBUTES, the lines are called ENTRYS. Each table is declared to the system by giving its name, a description, the number of attributes, and for each attribute the name, type, and its description. The type of an attribute may be character, integer or real. An attribute may also be declared to be a vector of either type integer or real. A single data item is specified by its attribute and its entry. To be able to relate attributes in different tables, it is necessary, that any pairs of attributes are unique and appear only in one table.

Under these restrictions items can be called up by giving their attribute, an attribute and item the selection is based on, and the name of the table where this selection attribute is to be found. The called attribute is found, if there is exactly one common attribute between its table and the selection table. The links between attributes are determined at run time.

The file storage is on ZEBRA direct-access files. As soon as updates are saved on a file, a history for each entry is kept. The files can be simultaneously accessed clusterwide. During usual operation, the whole system is memory based, therefore the performance should be acceptable.

For the handling of the parameters a command interface to the CERN program PAW was written. This interface is completely independent of the experimental setup, and it easily adapts itself to different facilities (e.g. ALADiN, 4 π detector, LAND) by reading information on the geometry, detector types, and electronics from the tables that are part of the database. The package includes an automatic startup for the entire experiment, interactive commands for setting and monitoring discriminator thresholds, high voltages etc. during the run, and control over the database, in particular commands for consistency checks.

3. Acquisition Software

The Cave B experiments will use the VME-based GOOSY data acquisition system. This system has been designed such that the four facilities can either run independently during tests and calibrations or form a combined setup during joint experiments. When it became apparent, that some key software and hardware components for the GOOSY system would not be ready in time for the first SIS runs in February '90, we decided to develop a temporary data acquisition system TDAS. The implementation was done in close coordination with the GOOSY group, uses a minimal subset of the hardware components used in the GOOSY VME-system and produces compatible output data.

In contrast to the GOOSY VME-system, which achieves a high degree of parallelism and configuration flexibility by using 3 layers of CPU's (Event Builder, Front End Processor, Readout Processor) connected by multiple busses, we use a simple master-slave approach with an event builder connected to some slave CPU's via a single VSB bus. This limits the number of connectable crates but is adequate for our commissioning operation.

We have chosen the Eltec E6 processor as the event builder, mainly because it has sufficient memory (4 Mbyte) and interfaces for Ethernet, SCSI and VSB. All CPU's run under OS-9, a simple UNIX-like multi-tasking operating system, and share a common network file system. This allows efficient program development directly on the frontend CPU's and avoids all the problems and extra work associated with cross software and program and data 'down load'. The various components execute as independent OS-9 tasks, communicate through either local shared memory (in data modules) or dual-port memories connected to the VSB-Bus port.

All CAMAC, Fastbus and VME subsystems communicate with the event builder through a differential VSB bus[1], designed as daisy chained cable. An IO/LAM CAMAC module is used as the trigger source while a pattern unit is used to define the various readout types.

The FASTBUS ADC's and TDC's are read out with an Aleph Event Builder (AEB) by means of program calls to the AEB FASTBUS library [2, 3]. This readout program is controlled by the event builder via a control structure defined in their shared memory – the Event Builder Interface (EBI). Event processing such as pedestal subtraction and compression is done locally by the AEB before data is transferred to the master. Some tests were done to estimate the speed of the readout program. A single block read, including setup times, requires 34μsec per 96 channel ADC while pedestal subtract and zero compress requires 2-3μsec per data word.

The data handling in the event builder is done with a cyclic buffer structure with enough capacity to hold all data generated in one SIS spill. We plan to connect an EXABYTE 8mm tape drive to the event builder SCSI bus as mass storage device for event recording.

Online monitoring and analysis programs on any VMS machine can access raw experiment data from the event builder through an interface based on 'Remote Procedure Calls' or RPC's. We are using the CERN-DD RPC package [4] which supports clients and servers under VMS, OS-9 and UNIX and, among others, raw Ethernet and TCP/IP as transport service. In a typical run, various client programs running in the PAW environment on the VAX hosts, usually VS3100 workstations, will issue requests for event data. These requests are served by TDAS access processes running on the event builder CPU.

It is possible to select subclasses or subsets of events, e.g. specific triggers or subevents. This selection is done on the server side and reduces therefore the ethernet traffic and software overhead considerably if rare triggers like scaler dumps or pulser events are to be analysed.

The CAMAC access functions, as defined by the ESONE Standard [5], have been implemented on a VME processor, to be used with the new VME based Data Acquisition and Control Systems for SIS experiments.

The package supports CAMAC crates connected with a CAV or CVI controller and the differential VSB bus [1] to an Eltec E5 or E6 processor running under OS-9. The functions can either be used directly on the E6 or from any VAX with a remote procedure call (RPC) interface. Here a client routine on the VAX performs a remote procedure call to the server task on the E 6.

References

[1] VSC - VME - differential VSB interface, Jan Hoffman, GSI 1989
EBI - AEB - differential VSB interface, Jan Hoffman, GSI 1989
CAV - Camac A1/A2 crate controller, interfacing to differential VSB bus, Jan Hoffman, GSI 1989

[2] Event Builder Users' Guide, A. Marchioro, CERN-ALEPH 88-59, 1988

[3] Aleph Event Builder FASTBUS Library, A.Castro, A. Miotto, CERN-ALEPH 88-11, 1988

[4] T. J. Berners-Lee: RPC Users Manual, Version 2.4, CERN DD/OC, 1989

[5] Subroutines for CAMAC, ESONE Committee, 1978

Development of a Fast Software Trigger for η - Detection[G,B]

F.-D. Berg, W. Kühn, V. Metag, S. Rieß
II. Phys. Inst. Univ. Gießen
TAPS-Collaboration:
GANIL - Univ. Gießen - KVI Groningen - GSI - Univ. Münster

The production of η-mesons is a rare channel in heavy ion collisions. In contrast π^0-production is abundant, typical π^0-multiplicities for U + U at 1.4 GeV/u are 20. For experiments planned with TAPS [1] this leads to high raw data rates of about 1 Mb/s. Therefore, data acquisition is limited by tape writing speed and a selective online software trigger is needed to reduce the raw data rate and the computer dead time. A general problem in designing algorithms for neutral meson detection arises from the large number N_γ of photons and the corresponding combinatorial background proportional $N_\gamma!$. This problem has been avoided by exploiting a multi-level scheme consisting of

(i) an energy test for possible γ's from η-decay

(ii) an opening angle and

(iii) an invariant mass analysis for events passing tests (i) and (ii).

Thereby the number of photons undergoing test (iii) is reduced to typical values ≤ 3. The program has been tested using a Monte Carlo event-generator, running together with the trigger on a hardware configuration consisting of 3 VMEbus CPU's. For event analysis with GOOSY a MicroVAX computer was used. For a typical η-production experiment planned for TAPS the number of stored raw data events is expected to decrease by up to two orders of magnitude as shown in fig. 1.

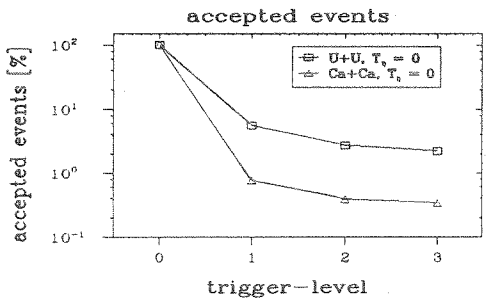


Figure 1: Percentage of remaining events after the individual trigger levels for the systems Ca+Ca at 1 GeV/u and U + U at 1.4 GeV/u and TAPS geometry. The higher background suppression in the Ca-case is a consequence of the lower η-production rate (10 times lower as in U + U).

At the same time the fraction of stored events containing η-mesons increases up to 88% (fig. 2) leading to a drastic supression of the π^0-background in invariant mass spectra (fig. 3). Here it should be noted that less than 1% of events with η are rejected.

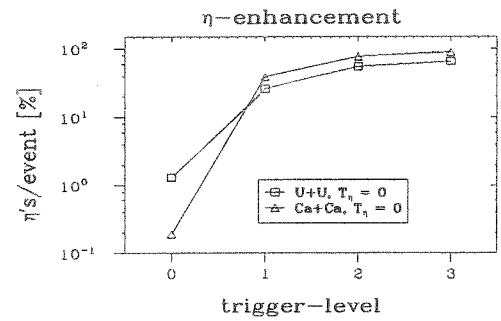


Figure 2: Portion of events containing η-mesons relative to all events triggered.

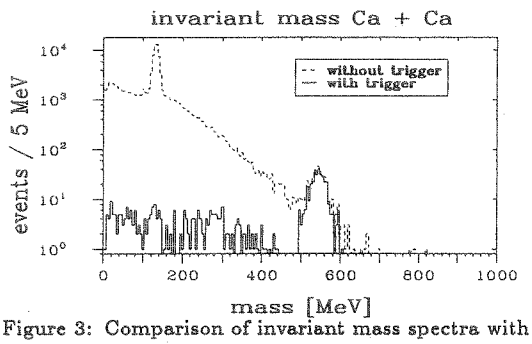


Figure 3: Comparison of invariant mass spectra with and without trigger for the simulated system Ca + Ca at 1.0 GeV/u and TAPS-geometry.

For a 25 MHz MC68020 CPU typical execution times are 35 - 60 μsec per event. Here we did not take into account the time needed for detector calibration and particle discrimination. This time can be minimized by performing a good calibration (energy and time matching) of the detectors prior to the experiment. A realistic estimate assuming a maximum saturated data aquisiton and including the time required to add the energies of neighbouring detectors results still in an increase of the total number of accepted η-events by 50%. This value can be further improved by utilizing the new generation of RISC-CPU's.

[1] High-Energy-Photon Collaboration, Technical Proposal for a Two Arm Photon Spectrometer (TAPS), GSI-Report Nov. 1987.

Algorithms for Automatic Streamer Chamber Data Analysis: Inter-view Track Assignment and Reconstruction in Space [B,G]

F. Pühlhofer, R. Keidel, A. Piper
Fachbereich Physik der Universität Marburg
CERN NA35 Collaboration

In the NA35 experiment at CERN a streamer is used for studying high-energy heavy-ion collisions. Events in this visual track detector are recorded by photographic cameras from three different positions. Their 3-dimensional structure can then be reconstructed from these 2-dimensional projections or views.

Traditionally the pictures are analyzed using manually controlled measuring tables or electronic displays, the operator often being assisted by a computer. Recently, we proposed a method for an automatic track recognition and measurement[1]. After transforming the photographic film into a digital image suitable for numerical processing by a computer the tracks are first detected piecewise or locally. The obtained track segments are then concatenated to tracks using an image transformation technique. This method is based on the assumptions that the tracks originate from a common interaction point in the target and that their shape is circular. The result of this processing is a list of projected tracks, each described by the two parameters κ und ϕ, the curvature and the emission angle relative to the beam.

For the spatial reconstruction tracks from the 3 different perspective views have to be assigned to triples belonging to the same trajectory in space. Characteristic features of the tracks can be used for this. Then a helical trajectory has to be found, whose 3 projections coincide with the hand-measured points along projected tracks. In case of the automatic analysis described above a reconstruction method based on the information given by the global track parameters κ and ϕ is more appropriate. A procedure for doing this was developed and tested using low-multiplicity p-A events obtained in the NA35 streamer chamber at CERN. Fig. 2 shows the κ-ϕ data of the tracks in fig. 1 together with those from the other two views of the same event. The relation between the κ-ϕ points for different projections can be calculated from the known camera positions. There is only one free parameter, the dip angle λ of the helix. It can be fitted to the data as shown in fig. 2, thus establishing the 3 parameters necessary for the description of a helix in space.

A survey of the relationship between the κ-ϕ parameters of the different views is given by the "clock diagram" in fig.3. The crosses mark the positions κ_H, ϕ_H of the assumed helix in space; the circles refer to the parameters κ_3, ϕ_3 of the projection in view 3; the thick hands point to κ_1, ϕ_1, the thinner ones to κ_2, ϕ_2. The drawing holds for the dip angle indicated; in first approximation the lenghts of the hands vary linearly with λ.

The method described here combines the inter-view track matching and the reconstruction in space into one step. It is, however, limited in accuracy due to the fact that the tracks deviate slightly from circles. A typical standard deviation of the dip angle is σ_λ = 10 mrad. In cases where this is not sufficient, the technique can at least serve for matching, leaving the reconstruction task to conventional methods.

References:
1. F. Pühlhofer, D. Röhrich, R. Keidel, Nucl. Instr. Meth. A 263 (1988) 360

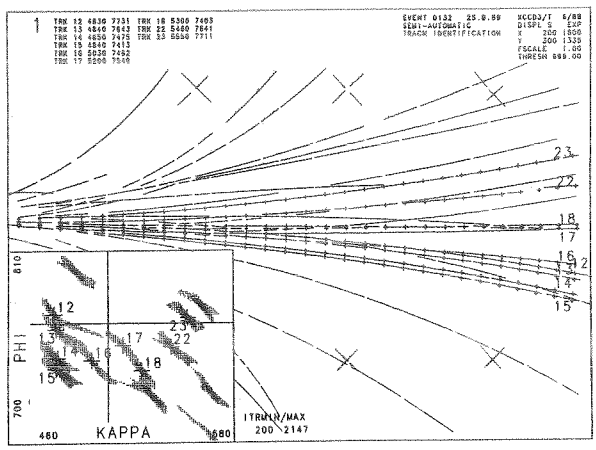


Fig. 1 Streamer chamber picture of a 200 GeV proton-nucleus collision in an intermediate stage of automatic processing (view by camera 3).The central region of the κ-ϕ transform is shown as insert.

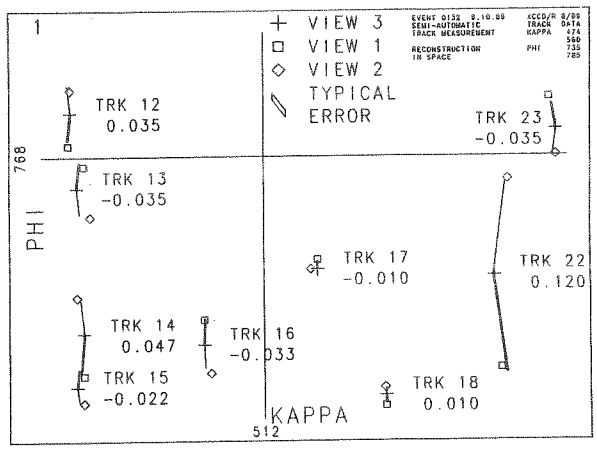


Fig. 2 κ-ϕ data of the event whose view by camera 3 is shown in fig. 1.

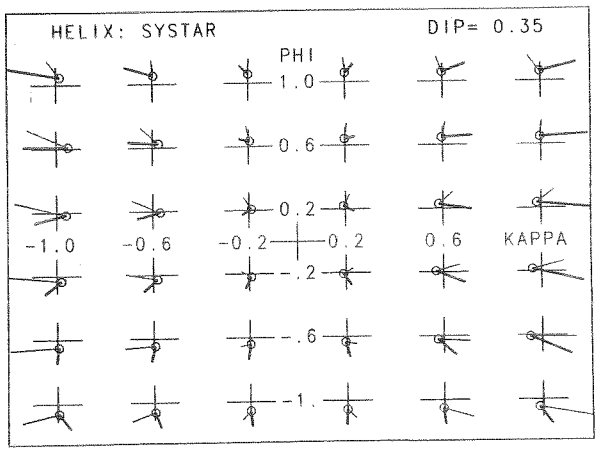


Fig. 3 Systematics of the relation between the κ-ϕ values of helix and projections for a series of κ_H-ϕ_H values (o for view 3, thick hand pointing to view 1, thin one to view 2)

Data-Summary-Tape Production using the ACP Farm [G,B]

WA80-collaboration
GSI-LBL-Lund-Münster-ORNL

The research in ultrarelativistic heavy ion collisions naturally implies large experiments which produce a huge amount of information which must then be processed to correlate the information from the different detector components. The first step in analyzing the experimental data is to process the RAW information, such as ADC and TDC channels numbers, in order to produce so called Data-Summary-Tapes (DSTs). These DSTs contain the information from the event in terms of calibrated physical quantities. This information can then be used for further analysis without having to repeat the time consuming first step of transforming the information from RAW to DST format.

For the WA80 sulfur data we currently need around 15 hours of CPU time on a VAX 8650 to process one 6250bpi tape of ^{32}S + Al data. Heavier targets need even more cpu time. Given that we have over 200 RAW tapes from the sulfur run alone, and given the high costs of CPU time on VAX clusters like the STC VAX 8650 cluster in ORNL or the 8650 cluster in Berkeley, the processing of the experimental data becomes quite expensive. Because every event is independent of the previous or the following one, parallel processing of events is an obvious computer architecture to investigate. We have started to use a multi microprocessor farm of the type developed by the Advanced Computer Program (ACP) at Fermi National Laboratory. Each node of such a farm is a single VME-board, in our case based on an Motorola 68020 32-bit CPU with a 68881 or 68882 floating point coprocessor. Each node has 2MByte of on-board memory with an optional extension to 6MByte via an external card. Each node has the processing power of about 0.8 of a VAX 11/780 or 0.13 of a VAX 8650. The nodes are accessed from a host computer, in our case a DEC VAXstation II/GPX, by a special backbone bus (Branch Bus).

Figure 1 shows the setup currently used by the WA80 group. A VAXstation II/GPX workstation with graphics terminal and two 8mm tapedrives for data input and output is connected by an QVI interface card to the VME Branch Bus Controller (BBC). From here the information is transferred to the different VME crates by the Branch Bus. Each crate contains a VME Resource Module (VRM) to allow bus arbitration and the Branch Bus VME Interface (BVI). Within a crate the information is transferred using the VME buses.

The full setup at ORNL currently consists of 70 CPU's (50 from ORNL and 20 from GSI, Darmstadt, FRG) and 38 4MByte extension cards (18 from ORNL and 20 from GSI). Thirty-five of these CPU's with full memory are used for the DST production. A diagram of this part of the setup shown in Figure 1. The rest of the nodes is connected to another VAXstation II/GPX for program development, running of Monte Carlo event generators, and other analysis.

Several modifications had to be made in our analysis program to make it compatible with the ACP farm. The first obvious change is a split of the program into a HOST and a NODE part. The HOST part handles reading the RAW data from tape, accessing information from on-line databases, transferring the data after some short data-integrity checks to the next available node, and collecting results from the nodes. The NODE part handles processing the data and transforming the RAW information into physical quantities. Because of the limited Fortran compiler running on the nodes, the NODE programs had to be changed to standard Fortran 77 and all "Common Blocks" that need to be transferred from the VAXstation to the nodes had to be separated in ones containing Real or Integer variables.

Estimates based on a limited DST production done last year at the 8650 cluster at Berkeley show that about 4100 hours of 8650 CPU time would be required to process only the WA80 sulfur data. Assuming $30.- for a non prime CPU hour (i.e. nights and weekends) at the STC cluster, this adds up to $123K. This does not include renting disks and analyze the produced DST tapes. Further assuming an availability of around 100 CPU hours a week, the whole DST production would have taken 42 weeks of continuous processing on the STC VAX 8650 cluster at ORNL.

The part of current ACP Farm setup that is dedicated to DST production is equivalent to 28 VAX 11/780 or 4.6 VAX 8650. It is accessible to us all the time. We found that new cluster routines which are much more consumptive of cpu time had to be installed in part of the code to improve the physics analysis. In spite of this, we will be able to produce all DST tapes in less than 30 weeks.

With the Farm fully operational now we are not only able to process our DST tapes, but also to analyze the data afterwards and produce high statistic Monte Carlo runs needed for comparison with our data.

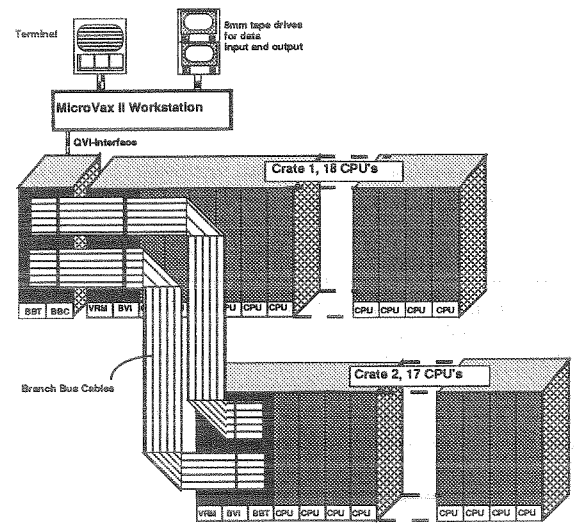


Fig.1 Artist's view of the current ACP Farm setup to produce DST tapes from WA80 RAW data.
BBT = Branch Bus Terminator
BBC = Branch Bus Controller
VRM = VME Resource Module
CPU = ACP CPU
BVI = Branch Bus VME Interface

Developments for the Euroball Data Acquisition System and Electronics

Ch. Ender, D. Schwalm
Physikalisches Institut der Universität Heidelberg

For future high resolution γ-ray spectroscopy arrays with several hundred data acquisition channel a new system is in design[1]. The currently available electronics has to be shrinked in space by at least a factor 20. Also computer setup- and monitor- possibilities to this kind of electronics are new features. This system will be able to handle different detector types (e.g. Germanium, shielding, particle detectors) in an uniform way. It has to improve the functionallity and the reliability.

The system is based on a hierarchical, modular design, which allows the adjustment and selection of components, specially for the front-end electronics — the channel part — to adapt different types of detector systems to the common trigger and readout interface. Each channel has therefore its own digitizers, sending the data to the distributed readout controller (Fig. 1). The event builder receives all data event by event, reformats them to an intermediate structure and forwards this to number crunching processors for event selection, analysis, storage and monitoring. The master trigger receives from each channel of the detector system informations (e.g. CFD signals) on which decisions can be performed. The master trigger sends the trigger signal and the validation back and generates other useful information (number of event, time of event), for further processing.

The Instrumentation system will be the VXIbus system (VMEbus Extention for Instrumentâtion)[2]. It has the advantage of the large module size (D-size 34x36x3cm), shielding, the VMEbus, and a large number of additional signal lines for trigger purpose and private busses (transfer rate up to 400Mbyte/s). A VXIcrate has up to 13 modules. In the new data acquisition system a readout controller module, 10 front end modules, and the space for a special purpose module (e.g. for testing or trigger) is foreseen. Each VXI crate is equipped with an intelligent resource manager – a VXI crate controller – which provides local intelligence for testing, setup, and control.

Each Front-End Module will contain several channels — 8 high resolution (Germanium) or 32 low resolution (BGO) — and the interface to the VXI bus system, trigger, and inspection bus. Common functional blocks to all channels providing such things as a setup, readout, and other central functions.

With the exception of the preamplifier all the electronics is designed to be on small cards (channel building block), which are plugged onto a VXI card. Each channel building block, which can consist of several subchannels (e.g. one for energy and one for time in this example.) contains several replaceable analog processing elements, including the digitization.

Each channel is controlled by a local programmable trigger section, which is responsible for channel timing and the interaction with the main trigger system. It generates all timing signals, status signals (e.g. pileup), and supports a three level pipeline.

The self timing of the channels allows that many events can be processed simultaneously by the data acquisition system. The main trigger signal, which will be formed by the multiplicity and some other fast special detectors (within $2\mu s$), defines in this scheme only the acceptance of signals in the channel. In addition to the master trigger signal, a validation signal is provided, which has to come after a certain programmable time after the main trigger. This allows to incooperate also slow triggers which have to come $\approx 10\mu s$ after the trigger signal. Another task of the trigger system is to provide pattern matching capabilities for the detection of possible Compton scattered gamma rays. Therefore a programmable switch matrix is planned. For monitoring rates information will be provided. The master trigger logic is again computer controlled and programmable.

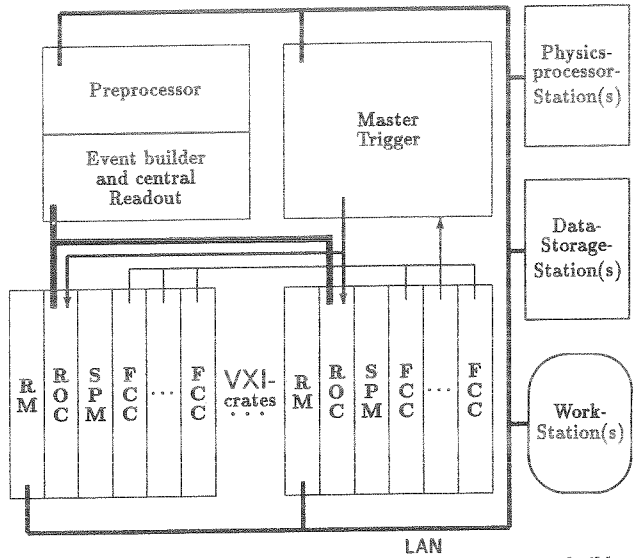


Fig. 1: Top Level System view of the new system. Event builder and Master Trigger are central parts in the hierarchical system. The level below, the crate Level, is formed by several VXI crates with the Front-end Cards and the subsystem-relevant parts (RM – Resource Manager, ROC – Readout controller, with Direct Memory Increment and the Trigger interface, FCC – Frontend Channel Card, SPM – special purpose module). All Systems are connected via a local area network (e.g. Ethernet) together with several workstations for control and monitoring.

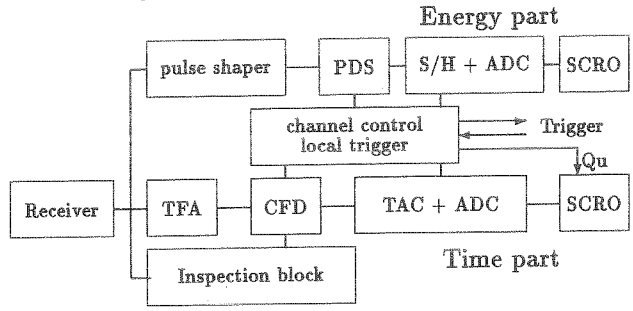


Fig. 2: An example of a channel building block. Shown are a simple channel with an Energy and a Time part. (TFA – timing filter, CFD – constant fraction discriminator, TAC – Time amplitude converter, SCRO - subchannel readout, PDS – peak detection and stretcher, Qu – Qualifier bits)

[1] Ch. Ender et.al.: **A new concept in data acquisition electronics, control, and monitoring for the next generation of nuclear gamma ray spectrometer**, subm to IEEE Trans. Nucl. Scien. 1990

[2] VXIbus Specification Revision 1.2 June 1988, VXIbus Consortium

Computing Center

H. Egger, S. Glückert, U. Meyer, O. Siart, K. Winkelmann
GSI Darmstadt

Heavily increasing demands for computing services arising from simulation and modelling in preparation of the experiments at SIS/ESR have been typical for the whole year of 1989. Because of the nearly fully loaded system already within the last quarter of the previous year these demands could only be fulfilled by reducing the amount of computing services dedicated to the applications of theoretical physics. Especially within the second half of the year, the demand for computing services within the experiment data analysis system SATAN ('System to Analyze Tremendeous Amounts of Nuclear Data') increased significantly. Additional computing power for theoretical physics could be delivered by two additional vector processors ('vector features'), which had been available at GSI within a joint study contract between GSI and IBM Germany. These two processors led to a mainframe configuration consisting of four tightly coupled processors, each of them equipped with a vector feature. The additional vector features had been installed at the end of 1988 and had been used until the scheduled end of the joint study at the end of October, 1989. Some details of the joint study project are covered within a separate report ('Parallel FORTRAN').

Significant steps have been done in order to improve the connectivity of the computer users at GSI within the local as well as the wide area range. Locally, a terminal controller has been equipped with ASCII adapters connected to an Ethernet server. By this way a user at an IBM-terminal has the possibility to connect via a 'hot-key' to a DEC/VAX host without logging off his session at the IBM host. In the wide area range two significant enhancements have been implemented. First, by using a link which connects DESY, Hamburg and CERN, Geneva, within the architecture of the 'AGF-Netz', direct Logon at the CERN computing center and several other research institutes all over Europe and vice versa are possible now. These facilities are heavily used by the members of several collaborating groups. Second, a direct support of two high resolution workstations for CAD-applications at the 'MPI für Kernphysik in Heidelberg has become available. Several interfacing with hardware as well as software was necessary to fulfil the requirement to use the local CATIA CAD-system with a link providing only 48 kbit/sec transfer rate. Details are given in a separate report ('Telecommunications').

Figure 1 gives a general overview of the computing center hardware configuration at December 1989. An overview of the major hardware installation activities of 1989 is given in the following list:

- Replacement of 40 GByte disk storage MRX 3680 HDP and 20 GByte disk storage MRX 3682 by 70 GByte MRX 3890 offering a significantly reduced power and space consumption.
- Installation of two additional vector features within a joint study project with IBM Germany.
- Replacement of eight disk storage control units IBM 3880-3 by four units IBM 3990-2 thus providing a four-path access to all IBM disk storage devices.
- Installation of a MRX-TLX 6890 solid state disk, capacity 128 MByte, 4.5 MByte/sec transfer rate to support very heavily used datasets, e.g. the SATAN- and the ISPF-libraries.
- Replacement of a teleprocessing device IBM 3720 by a processor IBM 3745. It is planned to replace the processor IBM 3725, too, after hard- and software upgrading of the IBM 3745 early in 1990. This will significantly reduce hardware maintenance and software licensing costs.
- Replacement of vector graphic devices Tektronix 4014 by channel attached units Spectragraphics DS 1082 (compatible to IBM 5080-2).
- At the end of the year, the central mainframe IBM 3090-40E/VF2 has been replaced by a six-way-processor IBM 3090-60J/VF6.

Operation and Services

Interruptions of computing services are very limited at the GSI computing center. Only shutdowns of the airconditioning and power supply systems due to maintenance activities and very few preventive hardware maintenance have caused some scheduled interruptions during the year. Development and testing of new versions of the operating systems can be done 'in second level' besides the normal productive operation of the system. This concept using a VM/XA host system has proven to be stable and excellently suited to systems development work. The whole system has been very stable during the year: the meantime between two unscheduled initial program loadings (IPL) was 576 hours.

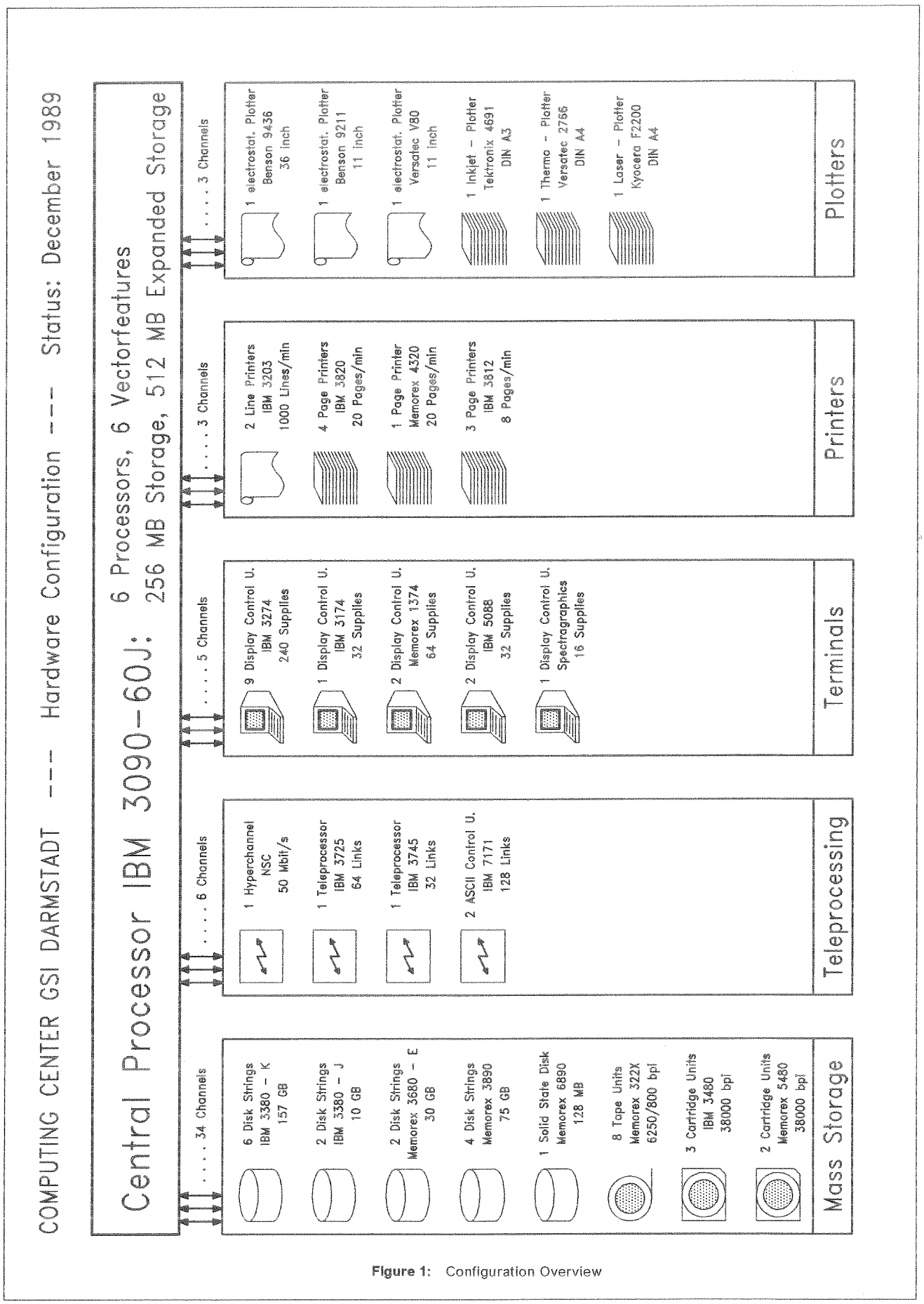


Figure 1: Configuration Overview

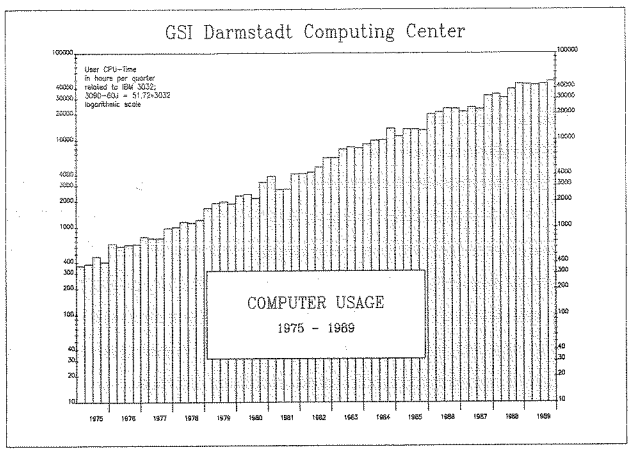


Figure 2: User CPU time from 1975 to 1989 per quarter of the year, semi-logarithmic scaling.

Figure 2 shows the amount of CPU time quarterly from 1975 to 1989 on a semi-logarithmic scale normalized to the power of a processor IBM 3032. At the end of 1988 the user CPU time had reached a value which represented a fully loaded system. So the amount of delivered CPU time could not increase any more during 1989. In December 1989 the central processor has been replaced by a six-way-multiprocessor system fully equipped with vector features (IBM 3090-60J). The processor has been made available by a special offer of IBM Europe within the EASI-program ('European Academic Supercomputer Initiative'). This processor is expected to increase the computing power by about a factor of two compared to the old four-processor system. Due to that installation the amount of delivered CPU time increased in the last quarter of 1989.

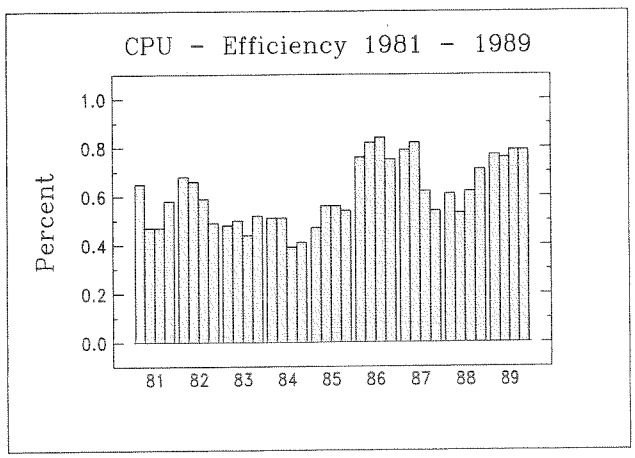


Figure 3: CPU-efficiency from 1981 to 1989 per quarter of the year. CPU-efficiency is CPU time in problem status relative to the achieved production time

Figure 3 shows the CPU efficiency, which is the ratio of user CPU time over CPU availability time. It does not take into account time for operating system test machines, other service machines like remote spooling, remote access facilities, and the central EARN node. A CPU efficiency value greater than 70 percent is excellent for a four-way multiprocessor system, especially if it is heavily used by dialog computing. When running only few numerically intensive applications, which is typical for night shifts and weekends, this value may nearly reach 100 percent.

The data analysis system SATAN, developed at GSI, is still used heavily. Its consumption of CPU time is shown separately in **figure 4**.

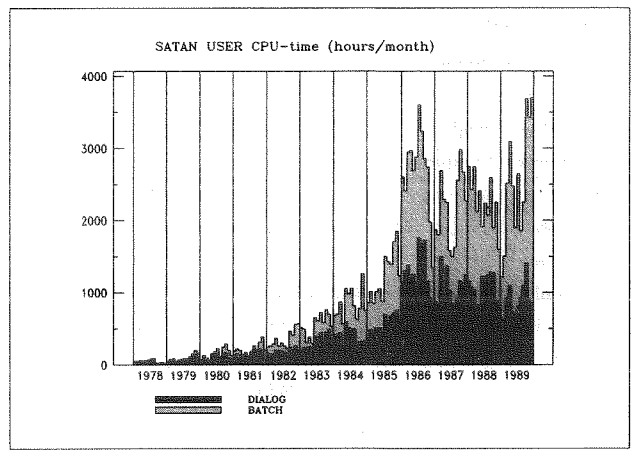


Figure 4: User CPU time for experiment data analysis tasks from 1978 to 1989 per month in batch and interactive mode.

The following table shows a list of software available at the GSI central computing system:

Compilers: VS/Fortran, PL/I Optimizer, Pascal/VS, C/370, VS/Cobol, Spitbol, VS/Assembler.
Interpreter: Plitest, Speakeasy.
Algorithmic Languages: Formac, Reduce, Schoonship.
Mathematical Libraries: Acrith, Eispack, ESSL, Fidisol, IMSL, PL-MATH.
Physics Libraries: CERN-Lib, CPC-Lib, DESY-Lib
Utilities: Fortran-PL/I Converter, CA-Sort, ISPF Full Screen Support, RACF Resource Security Control, DF/DSS Fast Dump and Restore, DFHSM Data Set Migration and Backup, OMEGAMON Operating Support, FASTDASD Disk Utilization Analysis Tool (CA)
Application Programs: SATAN Experiment Data Processing, GNOM Graphics and Numeric System, SYNPLOT Syntaxgraphs, SOAP Parsergenerator, GL Programming System Administration, IIPS Interactive Instruction System, OXYCALC Spreadsheet Program, CATIA CAD-System, GIPSY Interpreter Preprocessor System.
Graphics: Calcomp, GAM, GDDM, RASPAK, GEOPAK 3D-Graphics, GKS, graPHIGS, AGF Plotfile Interpreter.
Text Formatting: SCRIPT/DCF, TeX
Communication Software: ACF/VTAM, EP, NCP, NPSI, NETEX and BFX Hyperchannel-Software, Telex Software, EMS Electronic Mail System, EARN, DFN-SNAPAD.
Open System Interconnect (OSI)-Software OTSS, OSNS, UCLA/Mailer.

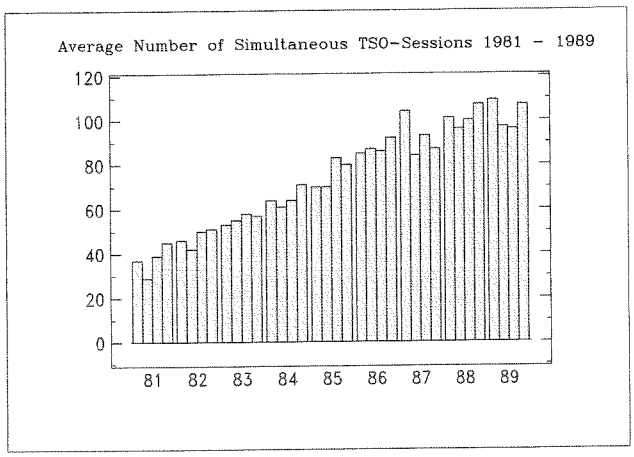


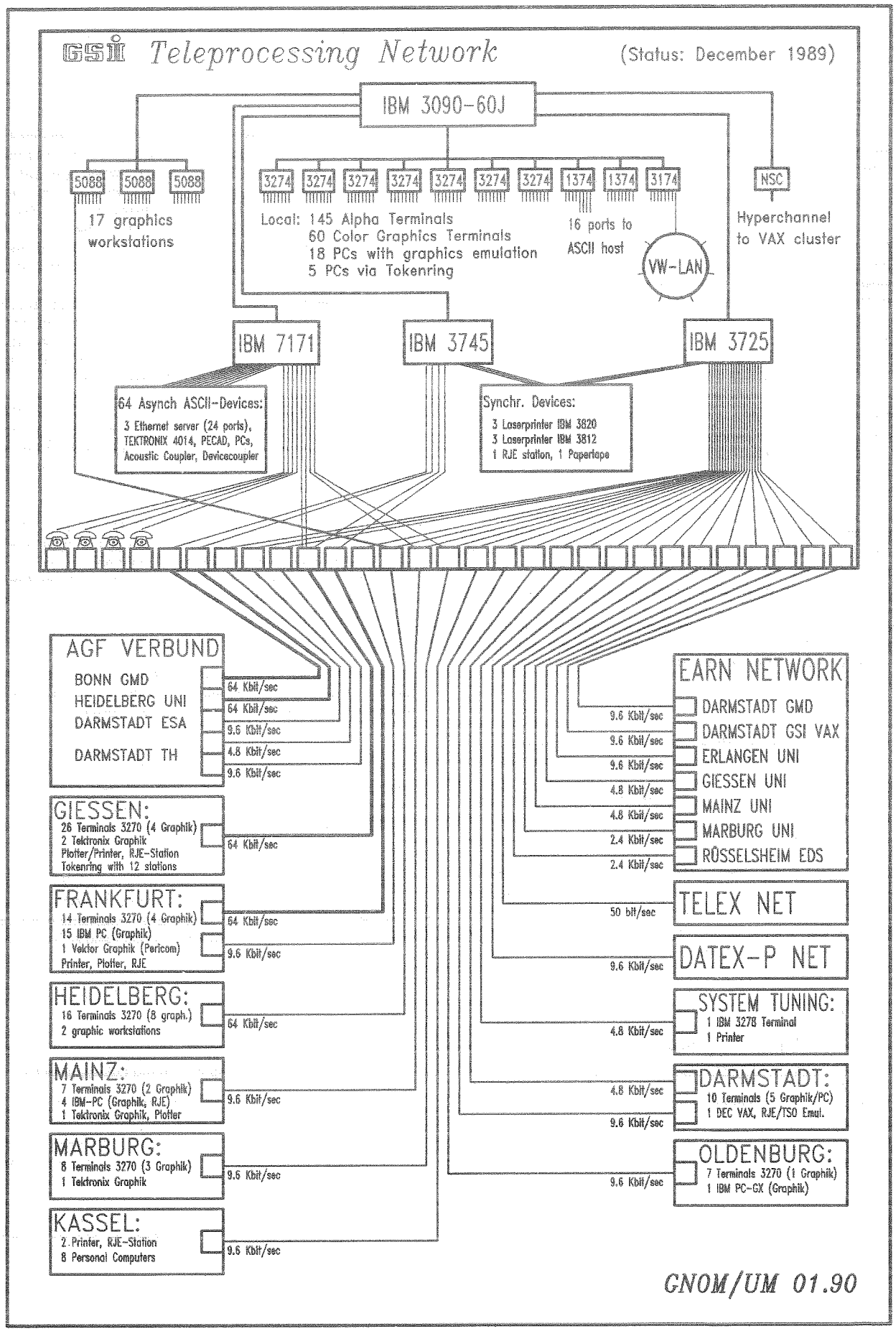
Figure 5: Average number of simultaneously active timesharing sessions during day shift from 1981 to 1989 per quarter of the year.

System Software

In 1989 a major development step in computer software service was the introduction of the Enterprise System Architecture (ESA/370) on the IBM 3090-40E mainframe requiring the installation of the operating system MVS/SP Version 3 (MVS/ESA). This architecture enables very large amounts of data (16k times 2 GByte at maximum) to be addressed in the program providing a very efficient access to that data. Main elements are data-only address spaces, called "data spaces", and "hiperspaces", a new concept to exploit expanded and auxiliary storage.
At the end of the year the levels of basic system software are:

- VM/XA SP 2
- MVS/SP 3.1.0e
- DFP 3.1.1
- JES3 2.1.5
- TSO/E 1.4
- RACF 1.8.1
- DFHSM 2.4.0

Another important feature available in MVS Version 3 is the Data Facility Storage Management Subsystem (DFSMS), realizing the concept of system managed storage. SMS offers an improved management of magnetic disk storage devices. By separating the logical view of data from physical device characteristics it simplifies the use and administration of storage, thus releasing the user from specifying device dependent parameters on allocating data sets like block size or record length. After upgrading the JES3 subsystem the whole system will be prepared to use these new facilities. It is planned to become productive early in 1990 after adapting SMS to the special needs of GSI.


GSI Teleprocessing Network
(Status: December 1989)
IBM 3090-60J
5088
5088
5088
17 graphics workstations
3274
3274
3274
3274
3274
3274
3274
1374
1374
3174
Local: 145 Alpha Terminals
60 Color Graphics Terminals
18 PCs with graphics emulation
5 PCs via Tokenring
16 ports to ASCII host
VW-LAN
NSC
Hyperchannel to VAX cluster
IBM 7171
IBM 3745
IBM 3725
64 Asynch ASCII-Devices:
3 Ethernet server (24 ports), TEKTRONIX 4014, PECAD, PCs, Acoustic Coupler, Devicecoupler
Synchr. Devices:
3 Laserprinter IBM 3820
3 Laserprinter IBM 3812
1 RJE station, 1 Papertape
AGF VERBUND
BONN GMD
HEIDELBERG UNI
DARMSTADT ESA
DARMSTADT TH
64 Kbit/sec
64 Kbit/sec
9.6 Kbit/sec
4.8 Kbit/sec
9.6 Kbit/sec
GIESSEN:
26 Terminals 3270 (4 Graphik)
2 Tektronix Graphik
Plotter/Printer, RJE-Station
Tokenring with 12 stations
64 Kbit/sec
FRANKFURT:
14 Terminals 3270 (4 Graphik)
15 IBM PC (Graphik)
1 Vektor Graphik (Pericom)
Printer, Plotter, RJE
64 Kbit/sec
9.6 Kbit/sec
HEIDELBERG:
16 Terminals 3270 (8 graph.)
2 graphic workstations
64 Kbit/sec
MAINZ:
7 Terminals 3270 (2 Graphik)
4 IBM-PC (Graphik, RJE)
1 Tektronix Graphik, Plotter
9.6 Kbit/sec
MARBURG:
8 Terminals 3270 (3 Graphik)
1 Tektronix Graphik
9.6 Kbit/sec
KASSEL:
2 Printer, RJE-Station
8 Personal Computers
9.6 Kbit/sec
EARN NETWORK
DARMSTADT GMD
DARMSTADT GSI VAX
ERLANGEN UNI
GIESSEN UNI
MAINZ UNI
MARBURG UNI
RÜSSELSHEIM EDS
9.6 Kbit/sec
9.6 Kbit/sec
9.6 Kbit/sec
4.8 Kbit/sec
4.8 Kbit/sec
2.4 Kbit/sec
2.4 Kbit/sec
TELEX NET
50 bit/sec
DATEX-P NET
9.6 Kbit/sec
SYSTEM TUNING:
1 IBM 3278 Terminal
1 Printer
4.8 Kbit/sec
DARMSTADT:
10 Terminals (5 Graphik/PC)
1 DEC VAX, RJE/TSO Emul.
4.8 Kbit/sec
9.6 Kbit/sec
OLDENBURG:
7 Terminals 3270 (1 Graphik)
1 IBM PC-GX (Graphik)
9.6 Kbit/sec
GNOM/UM 01.90

Experiment Data Processing

H. Göringer, P. Kohn, P. Malzacher, U. Post, D. Schall, K. Winkelmann
GSI Darmstadt
Marc Manns, TH Darmstadt

In preparation for the evaluation of SIS/ESR experiments, many SATAN functions have been enhanced or new functions have been developed. The most important highlights are listed in the following.

Raw Data. Due to the increasing storage requirements for list mode data, the 3480 cartridge is implemented in SATAN as alternate storage device. A 3480 cartridge has a write density of 38,000 bpi, compared to 6,250 bpi for a magnetic tape reel. 3480 cartridges contain 200 MByte of data, roughly 10% more than a magnetic tape, but they are much smaller and easier to handle. They have been proved to be as reliable as magnetic tapes, and emerged to a far-spread industrial standard in the meantime.

Besides volumes without label (NL), both, magnetic tapes and 3480 cartridges, can be used in SATAN also with ANSI label (AL) or IBM standard label (SL). Especially AL tapes with raw data written by GOOSY on the VAX are accepted now as standard input to SATAN.

Dataset names on AL volumes convenient for VAX users are allowed in SATAN, though deviating from standard IBM conventions. They may contain, for example, special characters such as '_', and name parts separated by dots may be longer than 8 characters. Taking into account the **GSI raw data naming conventions**, the length of name parts between two underscores ('_') should be smaller than 9, or smaller than 8 if starting with a number. The total length of the complete file name should not exceed 25 characters.

Visualization of many-dimensional Spectra. The accumulation of spectra with several dimensions will be significantly more important in the future. Currently it is convenient to perform many accumulations into one-dimensional spectra under various conditions in order to investigate the correlations between different physical parameters. More-dimensional spectra, however, contain all correlations between the corresponding parameters. In this case normally only one accumulation is necessary, reducing the CPU time for raw data analysis considerably. To facilitate the visualization of many-dimensional spectra, the display environments of SATAN have been enhanced to allow the graphical representations of one- and two-dimensional cuts or projections.

Working with an n-dimensional analyzer spectrum ($1 < n \leq 4$) in the **one-dimensional** display environment, both, the analyzer dimension to be drawn along the x-axis, and the channel limits of the non-displayed dimensions, which will be summed up for the projection or cut, can be specified.
Similarly, in the **two-dimensional** display environment, the two analyzer dimensions to be drawn along the x- and y-axis, and the channel limits of the non-displayed dimensions, which will be summed up for the projection or cut, can be specified.

The whole functionality of the one-dimensional display is available now for projections or cuts of multi-dimensional analyzer spectra. So, for example, the display windows are treated as multi-dimensional objects with as many dimensions as the related analyzer spectrum. The contents of display windows with more than one dimension may be accessed in two ways:

1. In the **dynamic mode**, the display window corresponds to the display window of a one-dimensional spectrum. Its contents is evaluated by summing up the displayed spectrum contents between the window limits of the displayed dimension. The window limits along the **not** displayed dimensions are taken from the actual projection limits of the display. However, you must be aware of the fact that the contents of a display window in dynamic mode is not a constant and depends on the actual display environment.
2. In the **static mode**, the window limits along the non-displayed dimensions are fixed as specified by the last window definition. Therefore the contents of a display window in static mode is a constant, independent of the actual projection limits of the current display environment.

Correspondingly also display points of n-dimensional analyzers are n-dimensional objects. In a similar way they may be accessed in static or dynamic mode, if their dimensionality is larger than one. In the first case, all n coordinates are unique and independent of the actual display environment.

In the dynamic mode, the contents of a display point is taken from the actually displayed projection or cut, that means, evaluated by projection onto the specified coordinate of the currently displayed dimension. As the projection limits are taken from the actual display, also the contents of a dynamic display point depends on the actual display environment.

Calibration in two-dimensional Display Environment. Both, x- and/or y-axis of a two-dimensional SATAN display, can be drawn now with calibrated values and axis descriptions.

Data Analysis. A new keyword 'NOCHECK' is available in the macro $OPTION enabling a faster list mode data analysis without handling of condition flags and analyzer flags.
FORTRAN subroutines can be called in analysis procedures.

Free Form Conditions. Free form ('banana') conditions can be used now to sum up the spectrum contents within a banana condition (command ASUM) or to make projections of the spectrum parts within a banana condition (command APROJECT).

Linearization. The linearization utilities of SATAN are available also in multiple LIVE displays.

Outlook. Work has been done also in the following areas:

- The first prototype of an interpretative vectorized analysis has been developed (see separate report).
- A SATAN test environment has been developed providing the powerful tools of the commercially available UNIRAS raster color graphics for the representation of two- and three-dimensional spectra.
- First investigations have been done to utilize the new features of the MVS/ESA operating system for very large analyzers with sizes $\gg 1$ MByte.

Parallel FORTRAN

M.Krämer, K.Winkelmann, GSI Darmstadt
and R.Jorba Lucas, Fachhochschule Darmstadt

One way to improve performance of software on multiprocessor machines (like the IBM 3090-600J) is to partition programs in such a way that they can be run in parallel on several processors. Parallel FORTRAN is an experimental FORTRAN compiler which supports concurrent execution of parts of a FORTRAN program. With support of IBM in a 12 months joint study project it was investigated how well IBM's Parallel FORTRAN compiler is suited to the scientific environment at GSI.

Two compute intensive problems from GSI's application program library were chosen to study the potential for parallelization and vectorization: a Monte Carlo code to simulate the energy deposition of electrons in a soft tissue (author: M.Krämer) and a theory code to calculate quasimolecular wave functions (Department of Theoretical Physics of the University of Frankfurt, West-Germany). In both cases satisfying speed-ups have been achieved.

The figures show the results from the parallelization and vectorization of the Monte Carlo code. The program is advised via special FORTRAN statements to run on several (1 to 7) 'logical processors', which in our case are then mapped to the physically available six processors. The overhead from parallelization was found to be negligible.

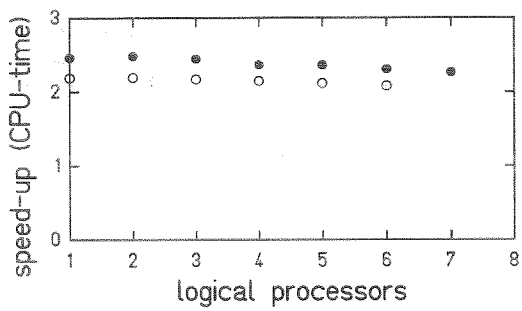
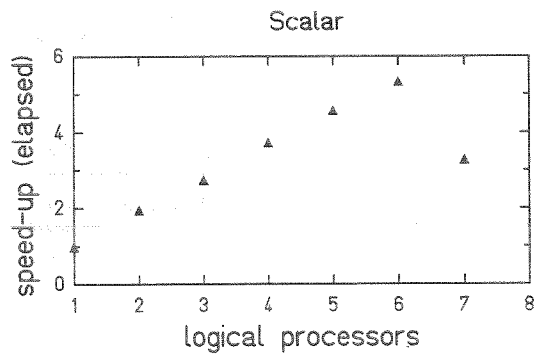


Fig.1 shows that the gain in CPU-time from vectorization lies between a factor of 2 and 2.5. The decrease with increasing number of processors is due to the decreasing vector length when the problem is split into several tasks. The picture also shows the improved vector performance of a 600J model compared to a 400E.



In **fig.2** the performance gain in elapsed time for a parallelized scalar version of the code can be seen. In a six processor run on a dedicated machine the program finishes in roughly the sixth of the time of the serial version. The nearly linear increase with the number of real CPUs shows the absence of serialization bottlenecks.

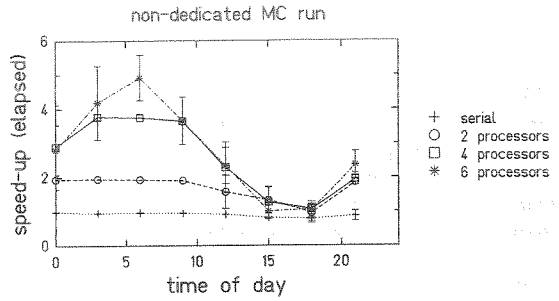


Fig.3 shows that gains in speed-up can also be achieved during times when many interactive users are on the computer: the turnaround time of the parallelized job is most of the time considerably shorter than that of the serial version. Note however that a price has to be paid in memory usage: because of the replication of code and vector data, parallelized programs need significantly more storage than serial ones.

Extensive documentation including tips and hints for efficient parallelization has been developed within the study project [1] [2].

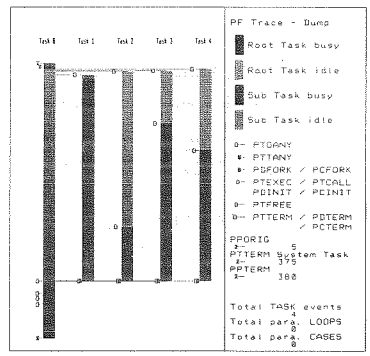


Fig.4: Graphical representation of a Parallel FORTRAN trace with HELP text switched on.

Parallel FORTRAN generates information at run-time of all activities related to task organisation. That trace information is written to a dataset and can later be evaluated to visualize the degree of parallelization and to spot conflicts in execution. Software was developed which converts the trace into a graphical color representation to ease that evaluation. **Fig.4** shows an example.

The functions of the experimental Parallel FORTRAN meanwhile have been further developed and are now incorporated into IBM's standard FORTRAN compiler Version 2 Rel.5 which is planned to be available by the middle of 1990.

References

[1] M.Krämer: 'Experiences with Parallel FORTRAN, a User's Guide', GSI internal documentation.
[2] 'Parallel FORTRAN on the IBM 3090VF', IBM Application Brief.

Numerical Classification of Data under Consideration of the Physical Function Type

I. Giese, GSI Darmstadt
M. Ihorst, FH Darmstadt

Some experiments at GSI create data such as flight time t, energy loss ΔE, rest energy E_{Rest}, and drift time t_{drift} of the particles. From these data the charge and mass of the particles have to be determined. Representing the data in a two-dimensional diagram a rib structure can be recognized. Each rib corresponds to a particle type. After transforming the data from these diagrams into a diagram with linear ribs, the distribution of the masses or charges of the particles found in the experiment can be derived easily by projection. Currently, the form of the ribs has to be defined using graphical input. This is both error prone and time consuming. Within two theses for the Fachhochschule Darmstadt it was tried to find an automatic procedure to solve this problem.

One method to find a structure within data points is the cluster analysis. There are basically two different methods, the partitioning and the hierarchical method. Both methods were examined for suitability in the first paper [Luk]. But the results were not satisfactory: The rib structure could be derived only for almost linear ribs (partitioning method), or the consumption of computing time was too high (hierarchical method).

In the second paper, a new ansatz was investigated [Iho]. Exploiting the low computing time of the partitioning method, the procedure was modified to take into account the physical correlations which are known from the experiment. Very roughly, the algorithm works as follows:

The standard principle, known as k-means principle, searches for a partition P of the data z_i into n clusters which minimizes the function Z(P):

$$Z(P) = \sum_{j=1}^{n} \sum_{i \in C_j} (z_i - \overline{z}_j)^2 \qquad (1)$$

with the mass centers of the clusters C_j:

$$\overline{z}_j = \frac{1}{|C_j|} \sum_{i \in C_j} z_i \qquad (2)$$

That means the data are split up into such clusters, that the sum over all distances to the corresponding mass center of all clusters is minimal. But this algorithm cannot detect elongated clusters. Therefore a so called mass line was introduced and the function Z(P) was extended to minimize the distances to a given mass line function y = f(x) with h_i as the multiplicity of the data pair x_i, y_i:

$$Z(P) = \sum_{j=1}^{n} \frac{1}{|C_j|} \sum_{i \in C_j} h_i [y_i - f_j(x_i)]^2 \qquad (3)$$

From the heavy ion physics theory usually three types of mass line functions are useful: The hyperbolic function for $E_{Rest} - \Delta E$ diagrams, the parabolic function for $t - \Delta E$, and the square root function for $t_{drift} - \Delta E$. The modified algorithm uses one of these functions and determines the two or three parameters for each cluster. This will be done in three steps. The first step determines roughly the main direction of the clusters, the second step computes the cluster mass lines with a linear function, and the last step uses the appropriate function. To evaluate another similar set of data, only the last step is necessary. In all cases the user has to specify the number of clusters and the mass line type.

To calculate the function parameter sets for the mass lines for data points as shown in figure 1, the program takes about 10 seconds of computing time (3788 points). The example shows the classification with a two-parametric parabola:

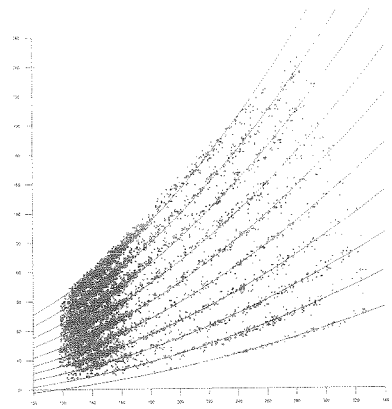


Figure 1: Classification with $y = ax^2 + c$

The second part of the new method linearizes the data on the basis of the function parameters found. Using a function sequence and the interpolation of the parameters a transformation to linear mass lines is possible. Figure 2 shows another set of data after linearization and the corresponding projection:

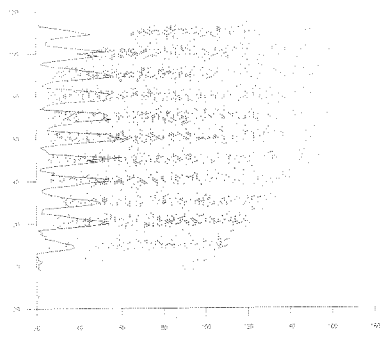


Figure 2: Another spectrum linearized with the classification using $y = \frac{b}{x+a}$, including the spectrum derived by projection

There may arise some problems, if clusters have few data points or if clusters are short compared to the other clusters. This problem sometimes occurs at the first or last clusters. It may be solved using an additional data point, only to hold a mass line in a desired area. The paper shows that usually a two-parametric function is sufficient. It is planned to implement the algorithm in the experiment data evaluation system SATAN and to make it available as a FORTRAN subroutine.

[Luk] Jutta Lukas: "Klassifikation von Datenpunkten aus Schwerionenexperimenten"; Diplomarbeit, FH Darmstadt 1988

[Iho] Martina Ihorst: "Numerische Klassifikation von Daten aus Schwerionenexperimenten unter Berücksichtigung physikalischer Zusammenhänge"; Diplomarbeit, FH Darmstadt 1989

VENUS Library part II and the Vectorized Interpretative Analysis

M.Krämer, W.Kynast, U.Post and K. Winkelmann
GSI Darmstadt

VENUS, the **V**ector Library for **N**uclear Physics **S**upercomputing, is a /370 Vector Assembler subroutine library at GSI. It was developed within a project partly funded by IBM. *VENUS* modules allow the exploitation of the Vector Facility of the IBM 3090. The need for conditional execution and for parallel tasks lead to about 50 additional subroutines covering following areas:

1. measurement of time intervals elapsed and CPU, also task specific,
2. tools for parallelism (serialized accumulation in shared memory locations, serialized random number generators),
3. arithmetic (logical operations, more comparisons, conditional gather/scatter)
4. conditional conversions, convert bit mask to index vector,
5. higher functions (polynomial calibration, interpolation, binary search, vectorized random number generator).

In addition access to the FORTRAN vectorized builtin functions (like SIN, COS, EXP, LOG ...) has been made possible by writing special interface routines so that the speed-up can be exploited from any other language. Most routines have been written with the help of the GSI preprocessor GIPSY (see separate report). The achieved speed-up factors in vector mode, compared to simple PL/I are between 1.5 and 10. The routines are summarized in a manual 'VENUS Library part II'.

A lot of GSI's computing time is spent in data analysis programs of the SATAN or GOOSY type, where vectorization can be exploited when rewriting the event loop so that parameter vectors (of optimal length) instead of parameter scalars are processed: the analysis program works on hundreds of events at the same time. In order to avoid to write loops, a vector notation in the language would be favorable. However no language at hand offers that.
For that reason, GNOM as a basic interpreter system, which knows sequences (vectors) as data elements and allows a vector notation, is used. All arithmetic operations can be done within this interpreter environment. The creation, update and interrogation of SATAN-like data elements are provided by the interpreter language extensions V$AGEN, V$ACDEF, V$AC and V$ANAL. Declaration and input of events can be handled by the statements V$DCLEVENTS and V$GETEVENTS. Note that the interpreter environment allows a high degree of interactivity: analysis programs can be modified in a session and rerun immediately. Simple correlation tests including arithmetics can be made easily without the annoying leave-the-session-edit-compile-restart cycle.
The underlying routines for accumulation and condition setting are written in /370 Vector Assembler.
A common objection against vectorization is, that the slowdown of the conditional execution in sparse vectors destroys the gain of the vectorization. /370 vector systems allow two kinds of conditional execution. Information about valid vector elements can be held in a bit mask (mask mode) or in an index vector (index mode). Investigation showed that mask mode is better for high occupation (many valid elements) and short vectors, index is better for low occupation and long vectors. Our system allows to execute the V$ANAL operation in both ways.
Sample PL/I analysis programs were taken, converted to GNOM syntax and were run on this interpreter system. **Fig.1** shows the speed-up achieved with a sample analysis program (SCHNEIDR). It shows the measured speed-up as a function of vector length for mask and index mode only. The best results can be achieved if the V$ANAL operation works dynamically: if the conditions are valid in less than 70% of all vector elements, index mode is taken, otherwise mask mode. It can be seen that long vectors give the best speed-up over SATAN-PL/I analysis program of more than 2.6 which is a very satisfying result for an interpreter.
The system is currently being modified to be called from SATAN to provide the usual interactive analysis environment.

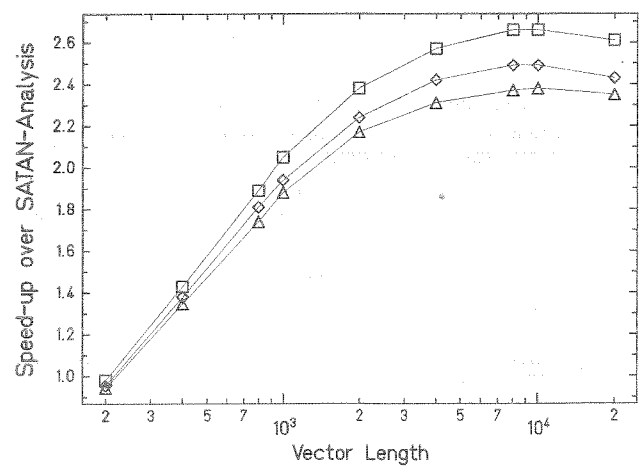


Fig.1: The speed-up of a typical analysis program rewritten for the vectorized interpretative environment over the common SATAN-analysis was measured. Different conditional execution modes have been tried: mask mode only (triangle), index vector mode (diamond) and dynamic mode depending of the number of valid elements (square).

GIPSY – the GSI Interpreter / Preprocessor SYstem

H. Essel, H. Grein, W. Kynast, U. Post, and K. Winkelmann
GSI Darmstadt

GIPSY is a powerful software tool originally developed at GSI as an alternate preprocessor for PL/I and as a GOOSY command interpreter. Inbetween, a whole set of other programming languages is supported by GIPSY. Recently it has been used extensively for the generation of program modules for GNOM (PL/I code), and the VENUS library (/370 assembler).

GIPSY provides the following improvements for coding:

- Achieve a **higher safety of program coding** by replacing
  - numbers (e.g. dimensions),
  - names (e.g. of variables, procedures, labels),

  by the content of GIPSY variables.
- Achieve a more **compact coding** by using
  - loops (also over sequences of strings!),
  - user defined GIPSY procedures and functions,
  - INCLUDE statements

  for similar program segments, i.e. code replication by preprocessing instead of editing. This leads to an additional gain of safety, especially, if the same modification has to be done in these similar segments.
- Generate programs of analogous structure by using INCLUDEd procedures, functions, or segments of GIPSY code. The included text may contain GIPSY variables leading to different programs after their replacement.
- Support of many different programming languages with respect to the substitution of GIPSY expressions in strings and comments: Assembler, ADA, C, CLIST, DCL, FORTRAN, Modula, OCCAM, Pascal, PL/I, REXX, SPITBOL and SQL. As an additional option, the recognition of strings and comments can be turned off in order to process the input text independent of any programming language.
- It is possible to include / exclude single input lines or entire blocks for / from being processed by GIPSY using *tags*. Active tags are specified when GIPSY is invoked in order to include the corresponding lines. This feature is especially valuable to optionally include lines for debugging purpose. These lines are omitted later on, if the tag is not used.
- GIPSY is available on IBM/MVS and VAX/VMS at GSI. Using tags one can keep a single program source for both computers.

In comparison to the standard PL/I preprocessors available at GSI, GIPSY has several advantages:

- First of all, there is an interactive mode, which can be used to enter single GIPSY commands and allows to test GIPSY variables, procedures and functions. The syntax is much more powerful than any of the standard preprocessors.
- The input for both preprocessors sometimes may look slightly confusing. However, GIPSY allows to create a formatted preprocessor output, which can be viewed by the user.
- Loop variables may be strings, too. In the extreme case, this feature allows to loop over a sequence of strings, where each string contains one text line of the code to be generated. Hence, a maximum of flexibility is achievable.
- Many builtin functions for arithmetic operations and string handling.
- Most operators and builtin functions are designed to work with single GIPSY data elements as well as with sequences of them.
- GIPSY variables may substitute only parts of names (variables etc.) occuring in the program code to be generated.

This is a simple example of an input text for GIPSY:

```
%%+DEBUG:
@/* GIPSY-Comp. at @G$TIME(). on @G$DATE("long") */
% var_names = "x","y","z"
% var_dims = 5,10,20
     DCL
       @var_names.(@var_dims.)  BIN FLOAT(21),
       j    BIN FIXED(15);
% FOR (j = 1 TO G$ELEMENTS(var_names) ) DO
     DO j = 1 TO @var_dims(j).;
        PUT SKIP LIST(@var_names(j).(j));
     END;
% END
% EXIT
%%-DEBUG:
```

Processing this by GIPSY yields:

```
/* GIPSY-Comp. at 18:20:53 on WEDNESDAY, 10 JAN 90 */
     DCL
       x(5)  BIN FLOAT(21),
       y(10)  BIN FLOAT(21),
       z(20)  BIN FLOAT(21),
       j    BIN FIXED(15);
     DO j = 1 TO 5;
        PUT SKIP LIST(x(j));
     END;
     DO j = 1 TO 10;
        PUT SKIP LIST(y(j));
     END;
     DO j = 1 TO 20;
        PUT SKIP LIST(z(j));
     END;
```

if the DEBUG tag has been specified.

References

[1] W Kynast and U. Post: GIPSY User Guide, Jan. 1990, available at the Benutzerberatung.

[2] Command "HELP GIPSY" at IBM and VAX computers at GSI.

A New Interactive Help System

A. Möller, W. Kynast
GSI Darmstadt

In extension to a diploma thesis[1] a new interactive help, called XHELP, has been introduced. It has been tested and is in use by selected users since autumn 1989. In spring 1990 it will be available to all users on the IBM-mainframe and will replace later the original IBM-help as online-help.

XHELP offers following additional features:

- Hierarchical structure of the XHELP texts (a tree-structure, see e. g. figure 1),
- Synonyms are possible to each help-item,
- Several possibilities to branch into another help text:
  - Positioning the cursor under a help-item and press the ENTER-key.
  - Editing a new help-item in the appropriate inputfield.
  - Fatherfunction: display of the higher XHELP text in the hierarchical structure.
  - Endfunction: display of the previously shown XHELP text (not previous in the structure). By these means a net of XHELP texts rather then a XHELP-tree can be accessed.
- special subsections of the help text (e. g. syntax, purpose, examples, remarks) can be chosen by PF-keys,
- search for strings in the XHELP text,
- highlighting of important parts of the XHELP text (e. g. words, sentences, paragraphs),
- indexfunction to display all available help-items and to select from them,
- printing of XHELP texts on laserprinters,
- scrolling and browsing through the XHELP text,
- executing of TSO-commands in XHELP,
- executing of TSO-commands for tutorial purpose by positioning the cursor under an item.

To use XHELP, the user needs only one argument – the help-item. If no argument is given, XHELP displays the highest help text in the structure. From any text he can step interactively through help texts to find a solution to his problem.

The sources of the help texts must exist in a special format. They are held in a partitioned dataset. In order to guarantee a fast access via the XHELP-command, help texts are accessed from VSAM-datasets with the maximal keylength of 41 characters.

A fast and safe update of the help texts is crucial for an interactive help. The responsible experts maintain the sources. They may also introduce new nodes in the XHELP-tree. Utilities have been written for:

- conversion of help-source into VSAM-help,
- conversion of IBM- and SATAN[1]-helps in XHELP-format, including the transformation of aliases into synonyms and automatic highlighting,
- notification of the XHELP-administrator of proposed modifications,
- update and visualization of the structure.

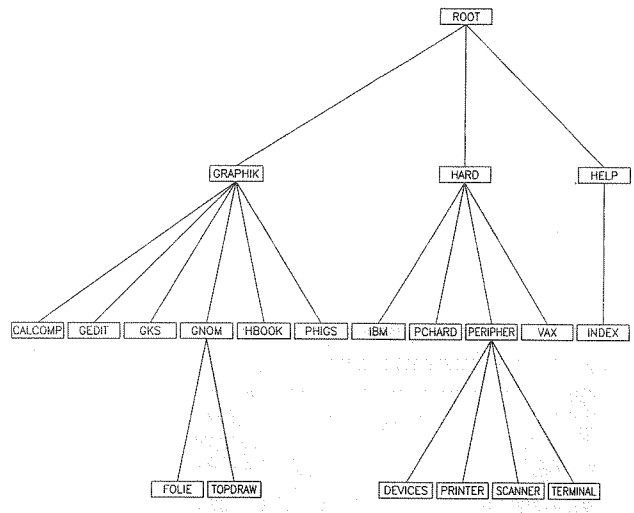


Figure 1: A Section of the XHELP-Tree

The XHELP-structure currently contains approximately 250 nodes and will be extended in 1990 to be used for SATAN[1]-helps. Programs will be implemented to enable a multilingual version of XHELP.

A further utility will visualize the whole hierarchical structure of the help texts in the XHELP-tree (see e. g. figure 1). This will be based on the "structure-dataset", containing the structure of the XHELP-tree. This "structure-dataset" is created by a special XHELP-run.

References

[1] G. Wilhelm:
"Design und Implementierung eines Informationssystems in der TSO-Umgebung",
Fachhochschule Darmstadt

[1] System to Analyze Tremendous Amounts of Nuclear data

Graphics

I. Giese, P. Malzacher, R. Rittenhouse - GSI Darmstadt
C. Pinilla, E. Schindler - FH Darmstadt

The conversion of the old graphics basis using the AGF plotfile interpreter to a new one using a PHIGS implementation is still under work. PHIGS (Programmer's Hierarchical Interactive Graphics System) is the international standard for fast and interactive 2-D and 3-D graphics, including hierarchical graphical data structure creation and editing. PHIGS became ISO standard in April 1989. IBM's implementation graPHIGS does not match exactly the international standard, so it is planned to offer subroutine interfaces both for PHIGS and graPHIGS users. In addition to the user interface routines the GDF file interpreter, used to support non-IBM graphics devices, was extended.

To have all TEX text fonts in this PHIGS based system available, a program was developped to convert the TEX fonts to vector data. Thus it is possible to create filled and hollow proportionally spaced characters using PHIGS polyline or polygon primitives. From the TEX fonts 16 of the most commonly used fonts were converted to allow a large variety of text output in proportional or equidistant form.

In addition new high level graphics subroutines were written or derived from other sources using PHIGS primitives; e.g. a procedure to draw contour lines using polygon primitives, filled with colours, patterns or simply hatched [Preu].

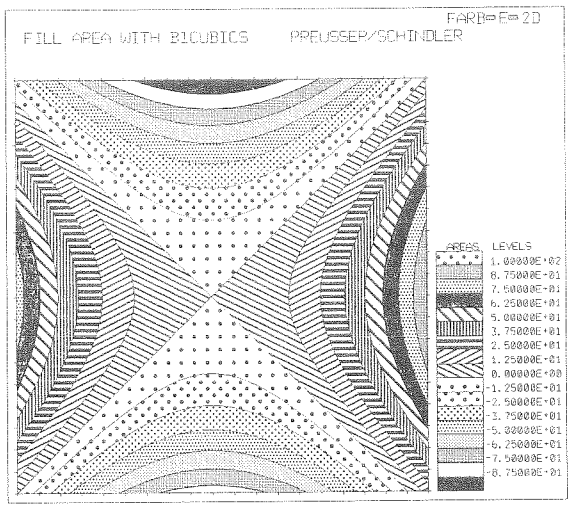


Figure 1: Example for the new contour plot procedure using PHIGS primitives and attributes

Other PHIGS based subroutines are available now for drawing axes with user control for a large amount of parameters, or drawing natural or periodic splines using cubic, rational, or balancing functions. In addition to new facilities, the current status has to be kept. Thus the current line styles, line width types, marker types, and also the current text facilities using special control characters had to be adapted to the new graphics basis.

As another application of PHIGS routines, a set of procedures for the GEANT system was developped. These FORTRAN procedures allow to draw and manipulate threedimensional basic elements like cubes, spheres, or trapezoids to represent parts of detector systems.

The interactive language GNOM was extended and optimized considerably. To get faster procedure execution the parser rules for an interpreted procedure line will be saved in a compressed form, even with evaluated constant expressions. Almost all functions use the mainframe vector facility and are allowed to run under a given mask to evaluate only those values where the corresponding mask bit is on. To have easy access to these facilities a new control structure was implemented in a short (WHERE) and a long (DOWHERE .. ENDWHERE) version, as indicated in the following example:

```
DOWHERE (z = 0)
  a <- x + y
ORWHERE (z > 0)
  a <- x + y/z
ELSEWHERE
  a <- x + y/(z-1)
ENDWHERE
```

Also GATHER and SCATTER functions are implemented to work on parts of array elements, defined by a given mask or index vector. GNOM procedures using all the new facilities are usually faster than compiled PL/1 procedures; this is very remarkable because GNOM is an interpreter.

To serve as a test system for the new PHIGS basis and to be used as a PHIGS tutorial system GNOM was also extended to call all graPHIGS routines directly. For this purpose three-dimensional coordinates were introduced, supported in all functions previously working only for two dimensional coordinates.

Further, some new operators (e.g. NOTIN), functions (e.g. SPLIT) and keywords (e.g. PATTERN) were added to GNOM. A new message system was implemented to offer messages in different languages and for different terminal types, necessary because of the large variety of different codes for highlighting, color, or umlauts. The messages are parameter controlled and reside on a data set. This message facility is generally available for other software systems too.

The GNOM procedure ACADGNOM to convert images from the PC based AUTOCAD system to GNOM objects allowing access to all graphics devices was extended. In particular new GNOM fonts were created (8 and 9) corresponding closely to the standard AUTOCAD fonts, which have different size relations for each character. Thus text positioned at a special place or following a previous text will look very similar on a mainframe output device.

The CAD system CATIA is being used extensively at GSI. There are now about 25 CATIA users working on 14 IBM 5080 and 10 Spectragraphics 1080 GX workstations. During the last 3 years, these users filled 80 model and library files with about 6500 models and library elements (about 2000 MB of disk storage). Some of these models were created on IBM's 6150 workstations and transferred to the CATIA mainframe system. Two of the CATIA workstations are located at the Max Planck Institute in Heidelberg, connected to the GSI mainframe computer.

[Preu] Albrecht Preusser: "FARB-E-2D: Fill Area with Bicubics on Rectangles - A Contour Plot Program"; ACM Transactions On Mathematical Software, Vol. 15, No.1, March 1989

Telecommunications

Udo Meyer
GSI, Darmstadt

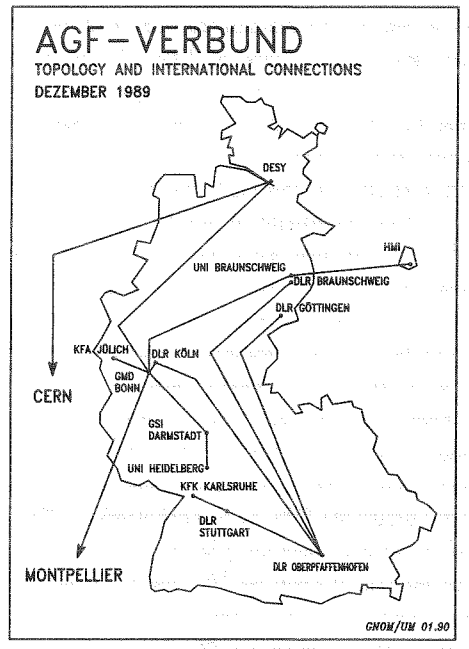
In 1989 one of the major tasks within the networking activities of the GSI computer center was to increase the connectivity.

Two tokenring LANs were installed and got access to host services. One LAN with about 20 attached PS/2 personal computers, some of them with local printers, and a 400 MByte file server with 3 attached printers for central use is dedicated to the GSI purchase and stock-keeping system. 5 stations may connect concurrently to the IBM host via a tokenring adapter of a local IBM 3174 terminal control unit. A remote terminal controller located at the department of theoretical physics in Gießen University, which allows access to the GSI host via a 19.2 Kbit/s channel of 64 Kbit/s multiplexed leased line, was also equipped with a tokenring adapter. 12 PCs of different manufacturers, each of them with two host sessions, may use now the GSI host services including graphics applications.

The connectivity between the IBM mainframe and the DEC/VAX cluster was improved by a new service on the IBM side. A MEMOREX 1374 terminal controller was equipped with two 8 port ASCII adapters. Each of these ports allows to connect one of the attached terminals to a DEC host via Ethernet. The VT100 emulation on the IBM compatible terminal is performed by the 1374 microcode. A hotkey allows switching between the parallel DEC and IBM sessions. A third DEC server was attached to the IBM 7171 protocol converter, supporting the opposite direction, i. e. connection of ASCII terminals on the Ethernet to the IBM host. In total 24 ports are now dedicated to the MVS/TSO access from VAX terminals.

A special data compression software GAMBIT was necessary to allow the CATIA CAD software to be used remotely. With a compression factor of 0.6 to 0.8 depending on the application, two graphic workstations at the MPI in Heidelberg are connected to a local controller, using 48 Kbit/s bandwidth of a 64 Kbit/s multiplexed line. On both sides, a protocol converter transforms the coax output signal of the station control unit respectively the coax input of the remotely placed station to the X.21/V.35 protocol running on the PTT line and vice versa. The two CAD stations replaced TEKTRONIX 4014 graphic devices. They are used for TSO applications with graphic output (SATAN, GNOM) as well as for construction purposes with the GSI local CATIA system.

In the wide area networking range, the mail interchange between different networks and domains has become more and more important. Most of them are connected to EARN/BITNET by means of gateways. So the use of the VM MAILER was an easy way to make them accessible for GSI EARN users. The EARN MAIL panel works as the user interface, which prepares the mail including a header in the MAILER standard (BSMTP and RFC 822). With the TSO standard procedure IEBGENER, the complete dataset is punched from MVS/XA to the MAILER machine on the VM/XA system via a virtual channel to channel connection. The MAILER has access to a domain table, which is periodically updated. This table contains all networks attached to EARN/BITNET with their gateway addresses. The MAILER scans the header for the network name and forwards the mail to the correct gateway. If the adressed network cannot be identified, i.e. it is not part of the domain table, the mail will be resent to the sender with the rejection reason appended. In terms of the ISO/OSI X.400 standard for mail exchange, the MAILER works as a Message Transfer Agent (MTA). A GSI modification of the TSO-RECEIVE command offers an easier handling of incoming mail. Still on the JES3 spool, the mail text can be browsed, directly appended to an existing log dataset or deleted.



The AGF SNA/SNI network became fully operational in 1989. A 64 Kbit/s leased line between the GMD in Bonn and the DLR in Köln enabled the full use of the DLR German backbone network for the AGF traffic. In Germany, currently about 40 hosts are available for interactive access (LOGON). A 64 Kbit/s line between DESY and CERN became operational in November. This line allows the full dialog access to all CERN and CERN connected hosts, which is of special interest due to the cooperations between GSI and CERN research groups. In summary about 20 hosts in Switzerland, France and Italy may be reached via the AGF network.

Accelerator Mass Spectrometry of ^{41}Ca

W. Henning, M. Müller, E. Roeckl, D. Schüll, A. Steinhof (GSI Darmstadt),
J. Speer (HMI Berlin), W. Kutschera (ANL Argonne), M. Paul (U. Jerusalem)

^{41}Ca ($T_{1/2} \approx 10^5$ years) was proposed for radiometric dating [1,2], as solar neutrino detector [3], and for measurements of erosion rates [4]. For these applications one has to determine $^{41}Ca/Ca$ ratios of 10^{-15} and less, which are measurable by accelerator mass spectrometry (AMS). First experiments [4,5] showed, that the UNILAC energy allows a very good identification and separation of ^{41}Ca events against background (mainly ^{41}K ions). The ^{41}Ca concentrations are determined from (i) the number of ^{41}Ca events in the focal plane detector of the GSI magnetic spectrograph, (ii) the ^{40}Ca current in the injection, and (iii) the value of the transmission through the UNILAC. In the first experiments the transmission was determined by measuring a sample with known ^{41}Ca concentration (produced by neutron activation) before and after the measurement of the unknown sample. However this method requires a good stability of the UNILAC transmission, which is not given in long term operation. Therefore we investigated the possibilities of using a ^{82}Kr pilot beam.

The applicability of a pilot beam is based on the fact, that the acceleration as well as the beam transport depends only on the mass to charge ratio M/Q. In case of $^{41}Ca^{q+}$ ions this is fullfilled by $^{41}K^{q+}$ or $^{82}Kr^{2q+}$ ions. With a pilot beam, the transmission is determined from the ratio of its currents at the injection and at the GSI magnetic spectrograph, corrected for stripper efficiencies. Due to admixture of other ion beams in the injection, the smallest current quantitatively measurable is around 100 nA. But such intensities of ^{41}K are excessive, since they produce a ^{41}Ca background by nuclear reactions in the target in front of the magnetic spectrograph; this target is nescessary for the ^{41}Ca detection by full-stripping [6]. (At lower intensity levels these false ^{41}Ca events are well separated by their energy defect due to the nuclear reaction.) Additionally the count rate limitation of the detector would be exceeded due to scattered ^{41}K events [4,5]. In case of a ^{82}Kr pilot beam there is no background problem, because the cross sections for producing ^{41}Ca by induced fission of ^{82}Kr are orders of magnitude smaller than the ones by (n,p)-transfer reactions of ^{41}K. Also the rate of scattered ^{82}Kr events can be kept below the count rate limit by selecting appropriate charge states after the gas stripper at 1.4 MeV/u. In case of $^{82}Kr^{22+}$ the charge state probability is low (0.18 %), while the one for $^{41}Ca^{11+}$ is high (22%). Due to differences in nuclear binding energies, the possible pilot-beam ions have equal M/Q values only to first approximation. In case of ^{82}Kr the relative difference has the value 1.35×10^{-4}. The question was therefore, whether this difference in M/Q or in small angle scattering and/or energy loss in the gas stripper at 1.4 MeV/u are relevant for the transmission.

To simplify the measurement we used a beam of ^{82}Kr and of ^{41}K (instead of ^{41}Ca) with a similar relative M/Q-difference (1.24×10^{-4}), and we determined the transmissions not absolutely. Relative ^{41}K- and ^{82}Kr- transmissions T_K and T_{Kr} were obtained by dividing the events, measured after Rutherford scattering in the magnetic spectrograph, by the respective currents of $^{39}K^{3+}$ and $^{84}Kr^{6+}$ in the injection. The currents were measured in a Faraday cup on the central trajectory after the inflector magnet by switching the extraction and acceleration voltage of the ion source. In this way, the long term stability of the ratio T_K/T_{Kr} was checked. It was found to be stable within ±2.3 % (fig. 1), although the krypton and potassium currents as well as the transmissions varied as much as by one order of magnitude. Additionally the behaviour of T_K and T_{Kr} was investigated with respect to variations of the extraction voltage of the ion source and the HF-amplitude of the first Alvarez tank, which were thought to be the most sensitive accelerator elements. An influence of the velocity difference, connected with the different M/Q and energy loss in the stripper, would lead to a displacement of the T_K and T_{Kr} maximas, but was not observed. Therefore these results mean that, from the technical point of view, natural ^{41}Ca concentrations can now be measured very precisely.

The demand for a pilot beam is not restricted to ^{41}Ca-AMS only, but exists also e.g. for the AMS of ^{205}Pb [7]. For $^{205}Pb^{5q+}$ suitable ions are $^{41}Ca^{q+}$, $^{82}Kr^{2q+}$, $^{123}Sn^{3q+}$, and $^{164}Er^{4q+}$ with relative M/Q-differences of 7.96, 8.07, 9.31, 6.42, and 3.07×10^{-4} respectively. Due to the larger M/Q-differences the use of any of these beams requires further investigations.

1. Y. Yamaguchi, Progr. Theor. Phys. 29 (1963) 567.
2. G.M. Raisbeck, F.Yiou, Nature 277 (1979) 42.
3. W.C. Haxton, G.A.Cowan, Science 210 (1980) 897.
4. A. Steinhof, GSI Report GSI-89-11.
5. A. Steinhof et al., Nucl. Instr. and Meth. B 29 (1987) 59.
6. A. Steinhof et al., Nucl. Instr. and Meth. B 36 (1989) 93.
7. H. Ernst et al., Nucl. Instr. and Meth. B 5 (1984) 426.

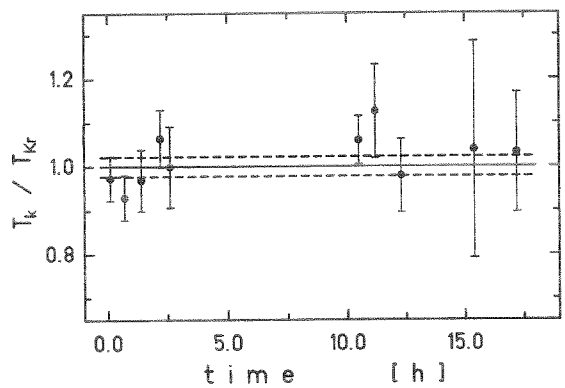


Fig. 1. Measured transmission ratio T_K/T_{Kr} as a function of time. Each data point is the mean value of 5-12 single measurements, the errow bars show the standard deviations. The data are normalized to 1.0 for the weighted mean. The dashed lines indicate the error of the weighted mean of ±2.3 %.

Determination of Trace Amounts of Platinum in Glasses using Rutherford Backscattering

E.Stiel[b], G.Herrmann[b], J.V.Kratz[b], K.Lützenkirchen[b], M.Overbeck[b], S.Polikanov[a], C.Sastri[a], and N.Trautmann[b]

[a] Gesellschaft für Schwerionenforschung mbH, Darmstadt

[b] Institut für Kernchemie, Universität Mainz

Nuclear backscattering has become a valuable tool to analyze samples composed of light to medium mass elements. It is usually performed by using α–particles as projectiles which are backscattered from target samples due to Coulomb repulsion and whose energy after scattering is measured with semiconductor detectors. The energy after scattering E' is related to the initial energy E_o through

$$\frac{E'}{E_o} = \frac{m \cdot cos\theta + \sqrt{M^2 + m^2 \cdot sin^2\theta}}{m + M} \qquad (1)$$

with m and M as projectile and target masses in amu and θ as scattering angle. Thus, by measuring E' one can deduce the mass number of the target atom. The RBS method can also be used for quantitative analyses with accuracies usually in the percent range.

Recently, the problem was raised to determine concentrations of platinum in glasses on the ppm–level. If the platinum concentration increases above a certain value in the ppm–range, the platinum atoms start to form larger aggregates which deteriorates the optical properties of the glass. We decided to test the applicability of RBS for this problem, however, by applying a kind of particle detection more sophisticated than the usual semiconductor–based one, see below.

Another major difference between our experiment and a more traditional RBS experiment is the use of ^{40}Ar–ions as projectiles instead of the usual α–particles. This is quite essential for the determination of platinum, since other heavy elements might be present in the sample. The difference in energy loss of α–particles backscattered from platinum (A=198) on the one hand and from nuclei in the A=100–150 mass region on the other is too small to be reasonably well resolved. This situation improves for heavier projectiles (see eq.1).

As detection device we used the heavy–ion identification system installed at GSI's stripper hall initially set up to search for "strange matter" [1]. The present study was performed by using ion beams from the UNILAC with an energy of 1.4 MeV/u. Scattered nuclei were detected in a system of twelve low-pressure multiwire proportional counters [2] divided into four identical modules each of which consisted of one start and two stop detectors. The ranges of scattering angles covered by this system are 92°–120° and 127°–170° with a total solid angle of 1.15 sr. Detected nuclei are identified by measuring the time-of-flight (TOF) and the specific ionization (ΔE). The scattering angle is obtained from the position measurements in start- and stop-detectors.

In our experiment a glas target with a known platinum concentration of 5 ppm was irradiated. As another heavy element the glas contained 1-3% of barium. The irradiation lasted about one hour with a total of $1.3 \cdot 10^{13}$ projectiles of ^{40}Ar.

In Figure 1 data of part of a detector module are displayed. The TOF of ^{40}Ar is depicted as a function of the laboratory scattering angle θ. One can clearly distinguish two different groups in the figure. The first one is in the range TOF = 45 – 55 ns, the second one in the range TOF = 55 – 80 ns. The solid line is deduced from calculated values corresponding to ^{40}Ar backscattered from ^{195}Pt, the dashed line corresponds to ^{40}Ar backscattered from ^{138}Ba. The bulk of the glas does not contribute to backscattering of ^{40}Ar, since it consists largely of the lighter elements silicon and oxygen.

The sum of all events of Figure 1 corresponding to scattering from ^{195}Pt is 179; in the whole system 1015 events were detected. We assume that in order to identify platinum about 50 events would have been sufficient. Thus, the detection limit in our experiment is 0.3 ppm. By using larger projectile doses even lower concentrations can of course be determined.

References

[1] M.Brügger et al. Nature(London) *337* (1989) 434.

[2] M.Overbeck et al. Nucl. Instr. and Meth., in press.

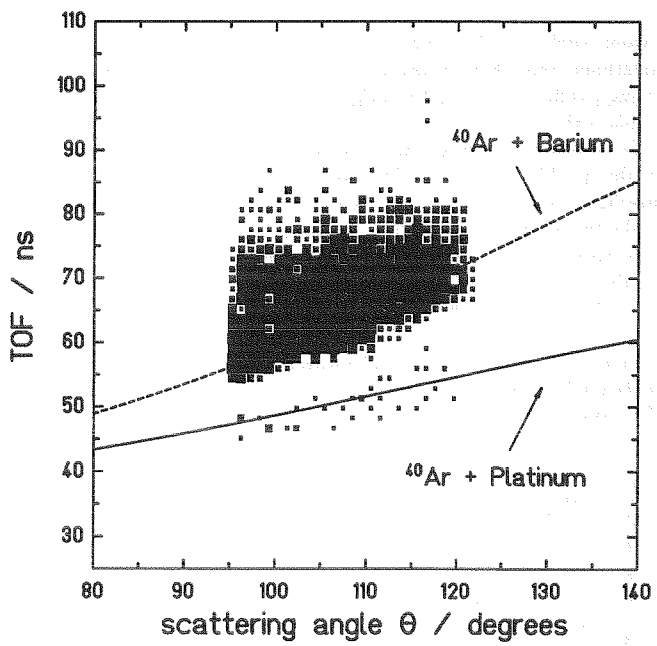


Fig.1: Two - dimensional representation of the time-of-flight of ^{40}Ar–particles backscattered from a glas containing barium and platinum as a function of the laboratory scattering angle θ.
Solid line: Calculated values for ^{40}Ar backscattered from platinum
Dashed line: Calculated values for ^{40}Ar backscattered from barium

Status of the Ultracold Ordered Electron Beam Project[B,G]

P.Krause, S.Zwickler, D.Habs, R.Neumann, D.Schwalm, A.Wolf
Physikalisches Institut der Universität Heidelberg and
Max-Planck-Institut für Kernphysik

By using a cold GaAs photocathode instead of a thermocathode, an ultracold electron beam with a rest-frame energy spread about two orders of magnitude smaller than in present electron cooling devices can be obtained [1]. At heavy ion storage rings like the TSR or the ESR such an electron beam device will be of great use both for electron cooling of ion beams to even lower temperatures and for the study of electron-ion interactions, where narrow resonances can be scanned with high resolution.

The work on the ultracold electron beam has been directed towards the development of the photocathode and towards the design of an adequate beam transport system, which preserves the low energy spread of the electrons.

The circular GaAs crystal (diameter 2mm) is covered with cesium and oxygen leading to a negative electron affinity. Electrons lifted from the valence to the conduction band by infrared laser light (λ =800nm) can leave this cold cathode with a narrow energy distribution. Several crystals have been implemented in the UHV test setup and gave quantum yields between 0.1 and 1% [2]. The value of the quantum yield depends critically on the cleanliness of the surface. Besides the conventional methods of cleaning the crystal by heating it in UHV, it was also observed that surface contaminants such as CO and CH_4 were flash-desorbed by intense infrared laserlight(350mW/mm^2 at 800nm). This will be further investigated.

Another important observation concerns the lifetime of the activated surface. After each activation the lifetime of the photocathode showed a strong dependence on the laser light intensity, independent of the original quantum yield. Figure 1 displays the fast decrease of the quantum yield at a laser power of 100mW which corresponds to a current of 0.8mA. A solution to this problem was found by continuous cesiation; with low laserlight intensity and a Cs partial pressure of $6 \cdot 10^{-11}$mbar in the test setup an equilibrium between cesium desorption and -adsorption was maintained so that a current of 0.1mA could be obtained for several days. This laserinduced cesium desorption effect, already observable at low light intensities, was up to now only examined by Reichert et al.[4]. It will be studied more accurately in a special setup in collaboration with the surface science group (Träger et al.) at the Univ. of Heidelberg (Physikalische Institut).

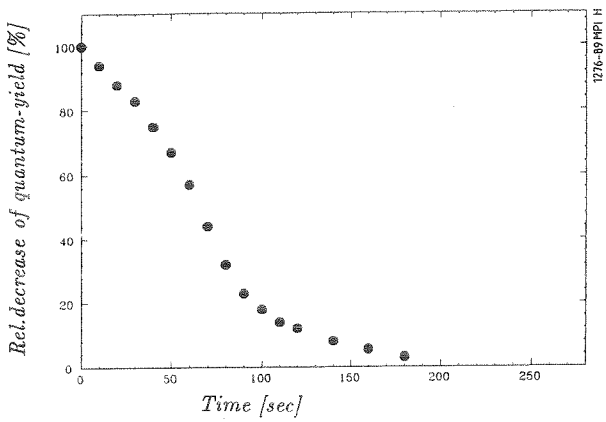


Fig.1 Relative decrease of quantum-yield as a function of illumination time at 100mW laserpower and 0.8mA initial current

In the beam transport system, a low energy spread of the electrons will be maintained by accelerating the electrons adiabatically with respect to the plasma oscillations in the beam [1]. In the final design the electrons are accelerated non-adiabatically to 130 eV at the anode and will be decelerated again to 5 eV. This is the lowest energy possible in view of the space-charge forces in the beam. Adiabatic acceleration then will take place in a NEC acceleration tube. Based on the computer simulations it was decided to enlarge the diameter of all acceleration electrodes to 18 mm. A very smooth electric field gradient along the beam axis is used except for the deceleration section (Fig.2a). In the magnetic field of 2 kG, the transverse electric field creates a very small transverse electron energy of 3 meV at the entrance and below 0.2 meV at the end of the acceleration section (Fig.2b). For comparison, the transverse temperature of the electrons at the cathode is expected to be 1meV. The decrease of the transverse energy during the acceleration is caused by the lowering of the electron density. Since the low transverse energy of this smooth optics is achieved without using resonant focusing, all parameters connected with electric and magnetic fields such as the final beam energy can be chosen independently from each other.
The beam transport and acceleration system will soon be tested in a linear test bench using a thermionic cathode, which will later be replaced by the GaAs cathode. The longitudinal temperature will be measured by varying the decelerating field of an analyzing diaphragm.

[1] D.Habs, J.Kramp, P.Krause, K.Matl, R.Neumann, D.Schwalm, Physica Scripta T22 (1988) 269
[2] S.Zwickler, Diplomarbeit, Heidelberg, 1989
[3] V.A. Lebedev, A.N. Sharapa, Sov. Phys. Tech. Phys. 32(5), (1987), 594
[4] M.Sprenger, Diplomarbeit, Mainz, 1989

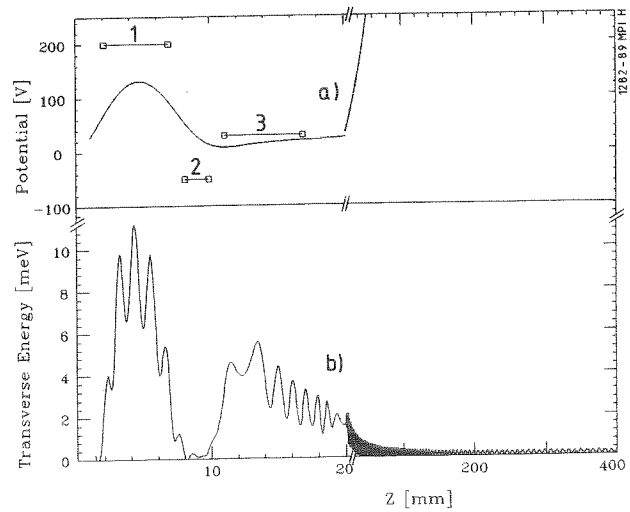


Fig.2 Computer modeling of an electron gun with smooth optics, a.) potential on the axis where the bars numbered 1-3 indicate the length and potential of the first three electrodes, b.) transverse energy at the boundary of the beam, $I_e = 1mA$, $E_{kin} = 7keV$, $B = 2kG$.

ACCELERATORS

6. ACCELERATORS

PAGE

6.1 UNILAC OPERATION AND DEVELOPMENT 335

UNILAC Operation 335
N. Angert, G. Hutter, J. Klabunde, M. Müller, P. Strehl, D. Wilms

UNILAC Injector 336
M. Müller, M.M. Khaouli, J. Bossler, N. Hofmann, M. Stork, H.P. Kurz, H. Krichbaum,
B. Gutermuth

Status of the New 1.4 MeV/u High Charge State Ion Injector 337
N. Angert, J. Bossler, L. Dahl, H. Emig, J. Glatz, K. Graf, J. Klabunde, M.M. Müller, A. Nicklas, U. Ratzinger, H. Deitinghoff, J. Friedrich, H. Klein, A. Schempp

Design of the RFQ-Structure for the GSI 1.4 MeV/u Injector 338
A. Schempp, J. Friedrich, U. Bessler, J. Madlung

Beam Dynamic Calculations for the RFQ Part of the New 1.4 MeV/u UNILAC Injector 339
H. Deitinghoff, A. Schempp

The IH-Cavity for the New 1.4 MeV/u-Injector - Status Report 340
W. Bleuel, B. Langenbeck, U. Ratzinger, R. Stenner

An Improved Drifttube Geometry for the IH-Structure 341
U. Blell, U. Ratzinger

High-Voltage Tests with a 27 MHz-Spiral-RFQ 342
A. Kipper, J. Brutscher, O. Pan, A. Schempp

300kV and 45 kV/u Accelerator 343
H. Emig, D.M. Rück, P. Spädtke, D. Vogt, B.H. Wolf

Ion Beams of Metallic Elements with CHORDIS 344
D.M. Rück, H. Emig, P. Spädtke, B.H. Wolf, B. Torp

Laser Induced Metal Ion Beams 345
M.M. Müller

Ion Source Modification for Ion Beam Assisted Deposition of Work Pieces 346
H. Wituschek, G.K. Wolf, H. Emig, D.M. Rück, P. Spädtke, B.H. Wolf,

6.2 NEW ACCELERATOR PROJECTS 347

6.2.1 S I S

First Results of Schottky Diagnostics at SIS 347
U. Schaaf, K. Beckert, S. Cocher, F. Nolden

Working Line Measurements at SIS 348
S. Cocher, K. Beckert, F. Nolden, U. Schaaf

Status of Geodetic Survey and Component Alignment of New Hall Area, SIS, ESR 349-351
I. Schmadel

6.2.2 E S R

Assembly of the Experimental Storage Ring ESR 352/353
B. Franzke

Status of the Electron Cooler 354
N. Angert, W. Bourgeois, H. Emig, B. Franzke, A. Kritzer, B. Langenbeck, K.D. Leible, G. Moritz, T. Odenweller, H. Schulte, P. Spädtke, B.H. Wolf

Status of the ESR Schottky-Diagnosis-System 355
K. Beckert, S. Cocher, B. Franzke, U. Schaaf

Magnetic Field Measurements of the Electron Cooler 356
P. Spädtke, F. Klos, B. Langenbeck, G. Moritz, K. Zweig

A System to Measure Field Harmonics in the Electron Cooler Solenoid 357
B. Langenbeck, G. Moritz, T. Odenweller, J.-R. Dang, M. Chen

The Linear Test Facility for the Electron Cooler 358
G. Jöst, K. Leible, H. Schulte, P. Spädtke, B. Wolf

Operating Program for the Electron Cooler 359
P. Spädtke

Beam Signal Detection in Stochastic Cooling Systems Using Electrode-Array Pickups 360
P. Raabe, W. Heinrich, H.L. Hartnagel

Beam-Electrode Interactions in Stochastic Cooling 361
F. Nolden

6.2.3 BEAM DYNAMICS

Filamentation of Phase Space and Coherent Noise 362
I. Hofmann

Observation of a Dip in the Momentum Distribution of a Coasting Beam 363
I. Hofmann

A Methode to Determine Momentum Distribution and Impedance for Cooled Beams 364
I. Hofmann, A.N. Talysin, P.R. Zenkevich

Harmonic Dynamics of the Chain of Charged Disks 365
V.V. Avilov, I. Hofmann

Large Amplitude Vibrations of the Coulomb String 366
R.W. Hasse,

Unilac Operation

N.Angert, G.Hutter, J.Klabunde, M.Müller, P.Strehl, D.Wilms
GSI, Gesellschaft für Schwerionenforschung mbH
Postfach 11 05 52, D-6100 Darmstadt, FRG

A new period in the history of the Unilac has begun in 1989. In the first quarter mainly heavy ions and not easy to handle beams were accelerated. At the begin of April beams for the commissioning of the SIS had to be delivered in parallel to the Unilac experimental program. This operation continued throughout all the year, only interrupted by a five week shut-down in summer. From April on, mainly light and medium heavy ions were accelerated in order to achieve sufficient beam intensities for the SIS. Beam energy for SIS was usually 11.5 MeV/u, whereas the parallel running Unilac experiments were provided with beams from 3.6 to 20 MeV/u with switching times of 15 ms between both acceleration modes. During the shut-down in summer the 1.4 MeV/u beam exit to the stripper hall was given up after 15 years of operation in order to provide space for a new high charge state injector to the Alvarez section. The total running time in 1989 was nearly 5000 hours. The efficiency (Fig. 1) was much higher than the year before, mainly due to the fact that referably long runs with only one ion species were scheduled. Table 1 shows the distribution of operation times. The time beam was used in the SIS, is counted like parasitic beam time, because only one pulse out of 50 per second was injected with proper energy into the SIS.

Table 1: Unilac Operation in 1989

Target time, main beam	3509 h	
Target time, parasitic beam		1635 h
Beam injected into SIS		690 h
Accel. exp. and development	192 h	
Beam tune-up	512 h	
Source replacement	185 h	
Unscheduled down time	546 h	
	4944 h	

Due to operation in the first quarter, the distribution of accelerated elements (Fig.2) shows still a large fraction of very heavy elements. In 1989 beams of 17 different isotopes were accelerated for more than 40 Unilac experiments. The beam energies (Fig. 3) ranged from 3 to 20 MeV/u. This graph does not contain the 11.5 MeV/u for SIS injection. The 1.4 MeV/u energy indicates a dedicated beam for the stripper hall before its shut-down. In addition to the fast energy switching, fast beam intensity modulation was introduced at the ion source. This allows to inject high peak intensity beams to SIS and about 10 times lower beam currents for the Unilac experimental hall, thus, avoiding damages and contamination there.

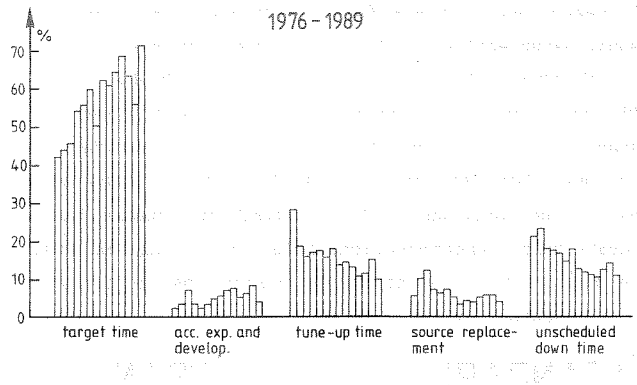


Fig. 1: Statistics of the Unilac operation

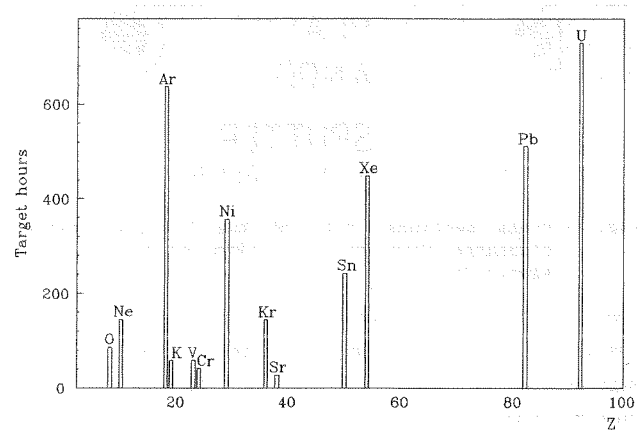


Fig. 2: Statistics of elements in 1989

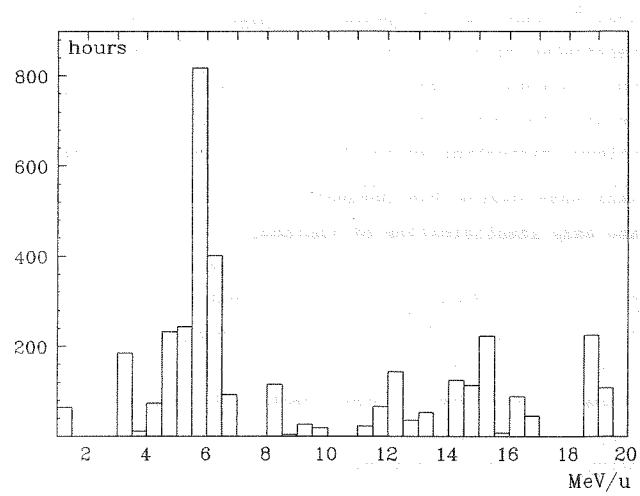


Fig. 3: Distribution of beam energies

UNILAC-INJECTOR

M. Müller, M.M. Khaouli, J. Bossler, N. Hofmann, M. Stork, H.P. Kurz, H. Krichbaum, B. Gutermuth
GSI Darmstadt

To reduce health risks for the ion source service personal sandblasting of Uranium poluted ion source parts was abandoned. For this reason the anode chamber of the PIG ion source was reconstructed and was given the shape of a stainless steel tube, easy to manufacture and much less expensive, thus becoming a throw away part to use only once. The old discharge chamber had a square shaped cross-section, prism (9 x 9) mm; as shown in fig. 1 the new discharge chamber has a circular cross-section, cylinder (8 mm diam).

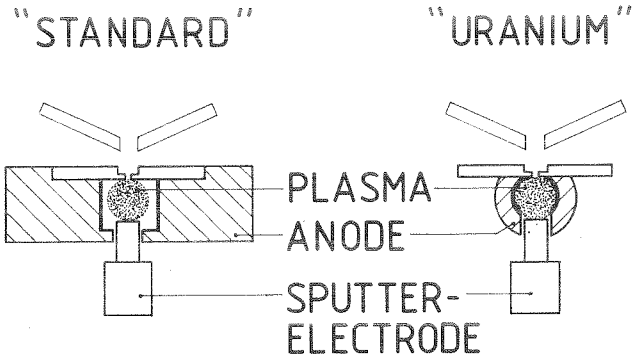


Fig. 1: Cross sectional view of the PIG ion source discharge chambers with extractor and sputter electrode

Shortly after the introduction of this modification, the Unilac operating reported a strong effect in the suppression of beam current oscillations usually observed together with plasma oscillations in the ion source discharge.

The low repetition rate of SIS (1 to 5 per sec) and the 50/s beam of Unilac demands for "Dual" pulse operation of the PIG source, e.g. 49 pulses of moderate intensity are followed by 1 pulse of high intensity. This particular pulse is kicked by a suitable magnet into the SIS transfer beam line. A reasonable current ratio between low rep. and high rep. pulses is about 1 in 10 without disturbing seriously the ion source discharge.

Mass scan device for determination of isotopic ratios and easy identification of isotops.

At the Unilac Injector the beam line from the ion source to the image slit of the magnetic mass spectrometer (77.5 deg) consists out of two accelerating gaps, a series of quadrupole lenses and a dipole magnet spectrometer. Recording a mass spectrum by simultaneously varying the magnetic parameters, the result is unsatisfactory and sometimes difficult to interpret, because the mass range, leaving the preseparating ion source magnet and which is transmitted to the mass analyzer on ground potential, is too narrow to get a full overlook over the isotopic distribution. For a more convenient and quicker beam preparation a mass scanning device was developed and set in operation. The mass spectrum is obtained by recording the ion current beyond the exit slit of the 77.5 degree magnetic dipol spectrometer on ground potential versus ion source extraction voltage (first acc. gap). During the scanning the injector voltage (second acc. gap) is varied proportional, to give to the beam a constant magnetic rigidity. By this way the recorded mass spectrum is very close to the natural isotopic distribution as is shown in fig. 2.

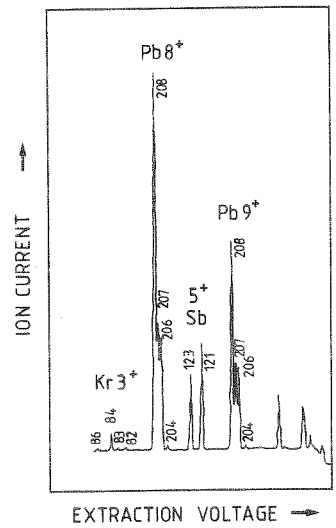


Fig. 2: Mass spectrum of a complex ion beam leaving the PIG source when a Lead/Antimony alloy is sputtered in a Krypton discharge

Sr ion beam.

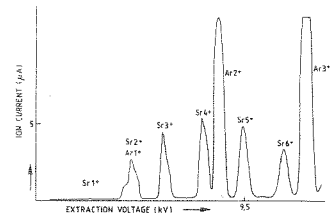


Fig. 3: Charge state spectrum of Sr beam from PIG sputter ion source.

As a new ion species, Strontium joined the list of elements/beams at the Unilac. For sputter electrode pure metalic Sr was used. After the mounting of the electrode the ion source was set under vacuum as soon as possible. The ion source worked very stable with an average lifetime of 15 hours per electrode at a beam current of 20 microamps c.w. for Sr 5+ after mass analysis.

Status of the New 1.4 MeV/u High Charge State Ion Injector

N.Angert, J.Bossler, L.Dahl, H.Emig, J.Glatz, K.Graf, J.Klabunde, M.Müller, A.Nicklas, U.Ratzinger
GSI, Postfach 11 05 52, D-6100 Darmstadt, FRG

H.Deitinghoff, J.Friedrich, H.Klein, A.Schempp
Inst. f. Angewandte Physik, Universität Frankfurt

The new Unilac injector projects were discussed in the 1988 GSI annual report.[1] The conceptual design of the high charge state injector (HSI) was frozen in 1989. The final layout is shown in fig. 1, the major injector parameters are listed in table 1.

The concept of injection into the Alvarez linac was modified as shown in fig. 1. The existing charge state separating system will be mirrored, the last bending magnet will be prepared for pulsed operation in order to inject the beam into the Alvarez linac from the new injector or from the existing prestripper linac and later from the planned high current injector.

All new components of the injector were ordered in 1989. The ECR ion source is being manufactured by IRF Grenoble (R. Geller). In October 1989 the CAPRICE prototype source delivered a current of 10 eμA U^{28+} which is twice the GSI requirement. The delivery of the source is scheduled for spring 1990.

The beam line components of the mass analysis system[2] are already at GSI with exception of the magnets. The mounting on the support has begun. The magnets, a double 135 degree dipol, a quadrupole singlet and triplet and also a solenoid will be delivered successively between March and June 1990, also the necessary power supplies.

Some details of the RFQ and IH structure will be reported in separate contributions of this report.[3,4] Both tanks were ordered and will be expected for copper plating at GSI in March 1990.

Most components of the 180 degree beam transport line connecting the new injector with the Unilac Alvarez section are taken from the former 1.4 MeV/u experimental hall beam transport lines. Four bending magnets have been improved by mounting shims on the pole shoes. Three λ/4 coaxial type bunchers will be copper plated in March, the 2 kW 108 MHz RF transmitters are standard industrial products. An 11 degree kicking magnet serving local experiments and a 30 degree kicking magnet for switching the two injector beams are in production as well as five pulsed quadrupole lenses for matching the beams to the Alvarez accelerator. The necessary power supplies will be manufactured successively in time.

The commissioning of the injector will begin with the ECR ion source and mass spectrometer in June 1990, will continue with the RFQ and IH accelerators and will end with beam parameter measurements in the transfer line to the Unilac in December 1990.

References:

[1] N.Angert et al., A New 1.4 MeV/u Injector for the Unilac, GSI Scientific Report 1988, GSI-89-1
[2] L.Dahl, Th.Schwab, A Mass Separation System for the ECR-Source, GSI Scientific Report 1988.
[3] A.Schempp, J.Friedrich, U.Bessler, J.Madlung, The Design of the RFQ-Structure for the GSI High Charge State Injector, this report
[4] U.Ratzinger et al., An Improved Drift Tube Geometry for the IH-Structure, this report.

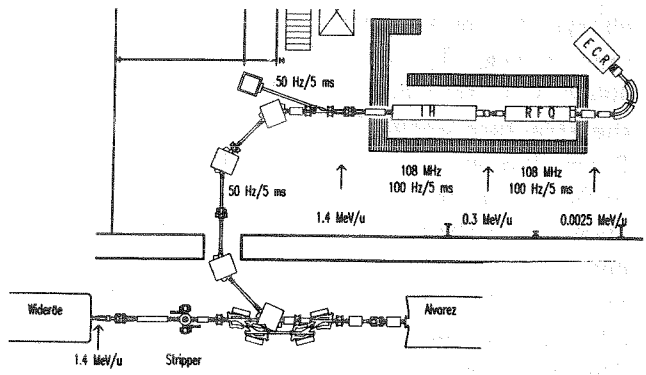


Fig. 1: Layout of the new injector

Table 1: Summary of major injector parameters

Injection	
Ion source	ECR-type, 14.5 GHz
Charge-to-mass ratio	0.105 to 1
Extraction voltage	23.8 kV
Energy	2.5 keV/u (β=0.0023)
Radial emittance (norm.)	0.46 π•mm•mrad
Radial emittance (unnorm.)	200 π•mm•mrad
Mass resolution Δm/m	$3x10^{-3}$
RFQ accelerator	
Structure type	four rod
Energy, input	2.5 keV/u (β=0.0023)
Energy, final	300 keV/u (β=0.025)
Radio frequency	108 MHz
Repetition frequency	100 Hz
Duty cycle	50 %
Max. RF power (for U^{25+})	125 kW
Max. Voltage	90 kV
Length	3 m
Tank diameter	0.5 m
Radial acceptance (norm.)	≥ 0.8 π•mm•mrad
Longitudinal emittance	24 π•keV/u•deg
Energy spread	± 0.8 %
Bunch width	± 0.3 ns (± 10 deg)
IH accelerator	
Energy, input	300 keV/u (β=0.025)
Energy, final	1.4 MeV/u (β=0.055)
Radio frequency	108 MHz
Repetition frequency	100 Hz
Duty cycle	50 %
Max. RF power (for U^{25+})	100 kW
Max. field strength	150 kV/cm
Length	3.55 m
Tank diameter	0.68 m
Shunt impedance	300 MΩ/m
Radial acceptance (norm.)	1.1 π•mm•mrad
Radial acceptance (unnorm.)	45 π•mm•mrad
Longitudinal acceptance	100 π•keV/u•deg
Longitudinal emittance	70 π•keV/u•deg
Energy spread	± 0.5 %
Bunch width	± 0.2 ns (± 8 deg)

Design of the RFQ-Structure for the GSI 1.4 MeV/u Injector

A. Schempp, J. Friedrich, U. Bessler, J. Madlung
Institut für angewandte Physik der Universität Frankfurt/Main
Robert-Mayer-Str. 2-4

A 4-Rod RFQ is being built as a part of the new "High Charge State Injector"(HLI)[1] for the UNILAC. The beam parameters are: charge to mass ratio q/A= 0.1176 (U^{28+}), input energy T_i= 2.5 keV/u, final energy T_f= 300 keV/u, frequency f= 108.5 MHz, length of the structure about 2.9m.

Beam dynamic calculations[2] show that for a sufficient acceptance of 0.8 pimmmrad an electrode voltage of 80 kV is needed. The duty cycle of the RFQ is 25% with an option for 50%. The peak power is appr. 120kW (the average power: 60 kW).

The mechanical design has been made for effective cooling of the structure e.g. direct cooling of the electrodes and the stems.

The 4-Rod-RFQ has circular rod electrodes and a linear array of straight stems as a resonant structure.

The vacuum-tank will be of a coffin like design. The tank has a lid which is along as the whole length which facilitates installation, alignment, and maintenance.

Fig. 1 shows a cross section of the tank of the HLI-RFQ. Fig.2 shows the injection part of the RFQ with a segmented aperture and an integrated Faraday-cup for beam diagnostic. The electrodes are cooled by a parallel tube and screwed to the stems. The baseplate will be used as a tuning element.

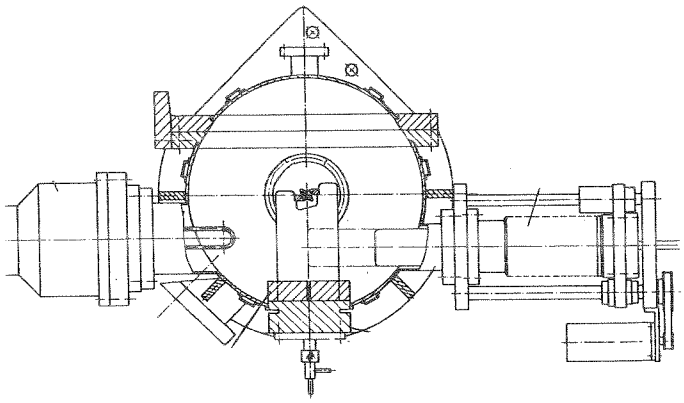


Fig. 1 Cross section of the RFQ

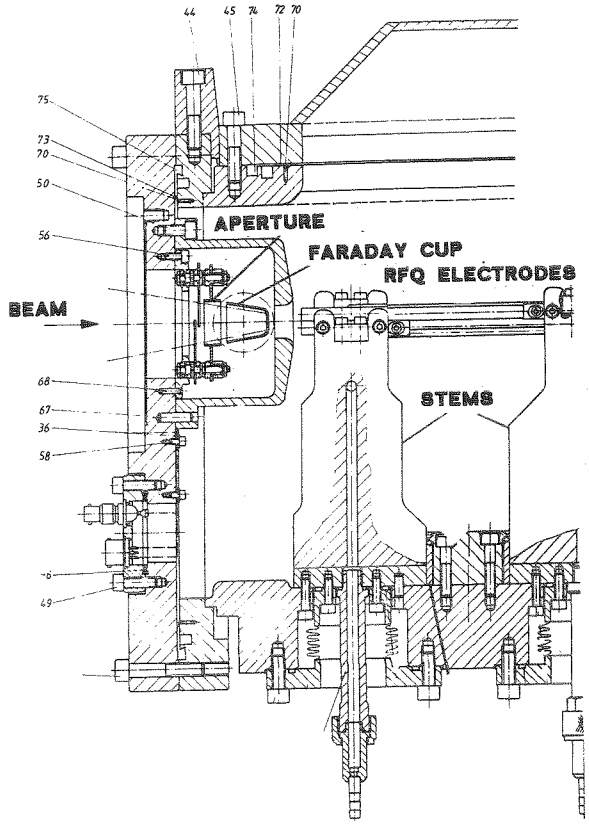


Fig. 2 Injection part

References:

1) **N. Angert et al., GSI-89-1**
2) **H. Deitinghoff, A. Schempp, this report**

BEAM DYNAMIC CALCULATIONS FOR THE RFQ PART OF THE NEW 1.4 MeV/u UNILAC INJECTOR

H. Deitinghoff and A. Schempp
Institut für Angewandte Physik, J. W. Goethe-Universität,
Robert-Mayer-Str. 2-4, D-6000 Frankfurt am Main

A new 1.4 MeV/u injector[1] for the Unilac will be installed in the stripper hall, consisting of an ECR ion source, a 108 MHz Four-Rod-RFQ and an IH structure. The design ion is U^{28+}, the RFQ will accept ions from the ECR source at an energy of 2.5 keV/u and accelerate them up to 300 keV/u. For a good beam quality in all linac parts strong conditions are imposed on the RFQ, which determines the initial beam quality: The transverse emittance growth should be less than 50 % for a normalized input emittance of 0.5 π mm mrad, the longitudinal output emittance has to be smaller than 1 MeV·nsec. With a new design method a solution was found[2], which fulfils the requirements. Fig. 1 shows an RFQ parameter plot, fig. 2 the output emittances at the end flange of the tank[3], fig. 3 the beam behaviour along the RFQ. The transmission is a bit less than 90 %, because only the linear core of the separatrix can be used. Further calculations[4] indicate, that an integrated prebuncher will rise the transmission to 95 %, but add about 20 cm of structure length. Table I gives some beam parameters.

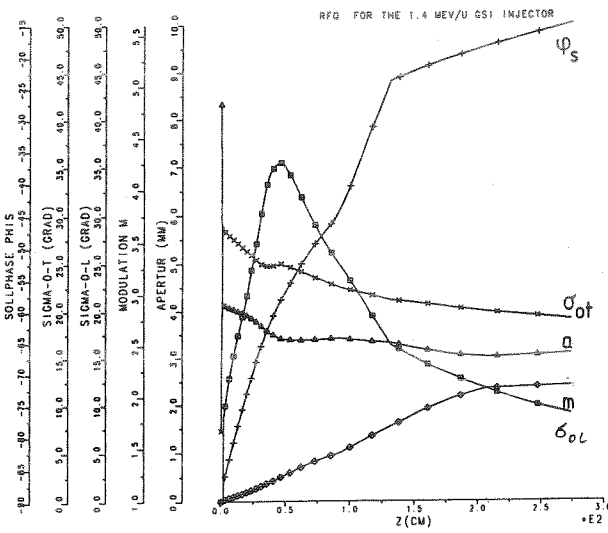


Fig. 1 RFQ parameter vs. length

Table I

Norm. acceptance	0.8 π mm mrad
" input emittance	0.5 π mm mrad
transmission	88 %
norm. output emittance	0.55 π mm mrad
long. output (95 %, rms)	< 20° keV/u
4 radial matching cells in	
2 " " " out	

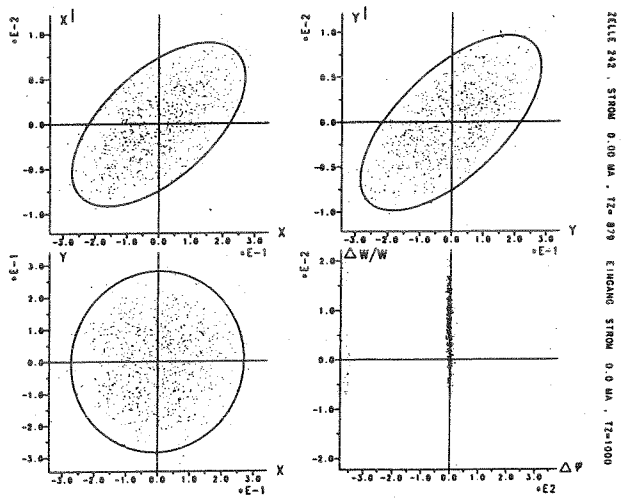


Fig. 2 Output emittances at the end flange

References

[1] N. Angert et al., GSI-Rep. 89-1, p. 372
[2] A. Schempp, Proc. 1989 PAC, Chicago
[3] A. Schempp, J. Friedrich et al., this report
[4] H. Deitinghoff, IAP, Int. Rep. 89-3

Computations have been carried out at the IBM of GSI.

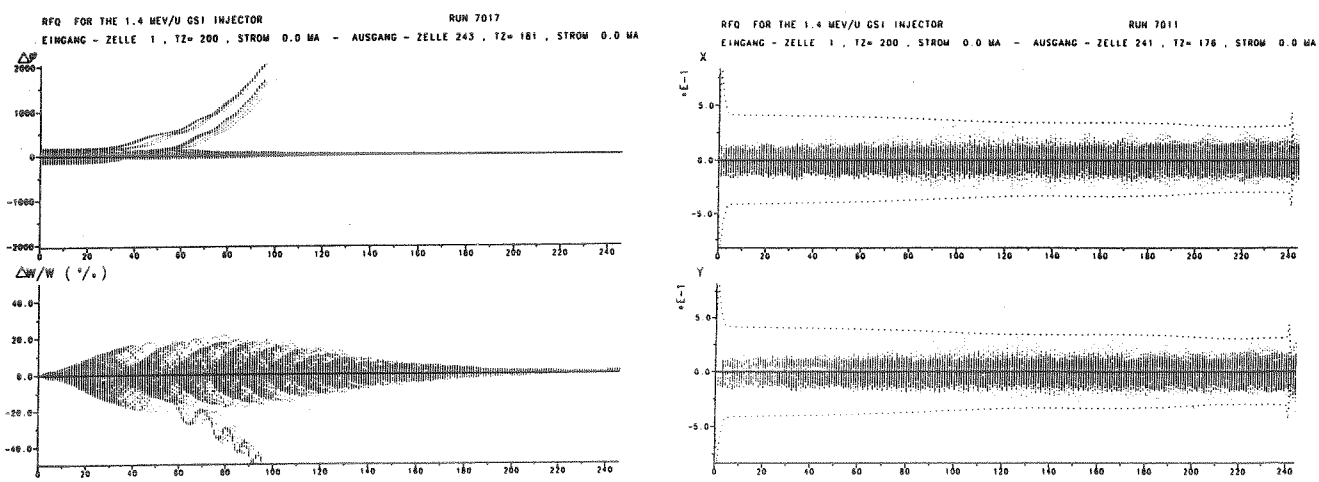


Fig. 3 Examples of longitudinal and transversal beam behaviour along the RFQ

The IH-Cavity for the New 1.4 MeV/u-Injector - Status Report

W. Bleuel, B. Langenbeck, U. Ratzinger, R. Stenner

GSI Darmstadt

Status

The rf-model studies[1] were continued. Finally, it was possible to get a flat electrical field distribution by optimizing the capacity distribution along the tank. Manufacturing of the tank has been started since October 1989.

The drift tube structure including the stems is ready for galvanic copper plating. A special drift tube geometry was developed to suppress the transversal dipole component of the gap field[2].

The two magnetic quadrupole triplets were ordered. Their construction is described in more detail below.

Quadrupole lenses

The lenses inside the IH-tank should be built as short as possible because of two main reasons:

- The axial length of lenses is lost for particle acceleration
- The rebunching of the beam pulse behind the lenses needs more effort with increasing the drift length through the lenses.

The space which is used for the installation of a lense has to be an even multiple of the corresponding period length $\beta \cdot \lambda/2$. In our case, the first lense corresponds to $8 \cdot \beta \cdot \lambda/2$ and has a mechanical length of 375 mm, the second lense corresponds to $6 \cdot \beta \cdot \lambda/2$ and has a length of 370 mm.

In that kind of IH-structure, it is possible to use a very big outer diameter for the lense housings, in our case $\varnothing_a$ = 230 mm. This helps to generate high magnetic field strengths.

The polar cores of the quadrupoles are made of Vacoflux 50, allowing a magnetic flux density up to about 2.2 Tesla. The yokes are made of steel.

By that way, it is possible to get field gradients as high as 78 T/m. The aperture radius of the quadrupoles is 13 mm, the thickness of the vacuum chamber wall is 1 mm.

[1] W. Bleuel, U. Ratzinger, R. Stenner, The IH-Cavity for the New 1.4 MeV/u-Injector - Status and RF-Model, GSI Scientific Report 1988, p. 374

[2] U. Blell, U. Ratzinger, Improved Drift tube Geometry for the IH-Structure, GSI, This report

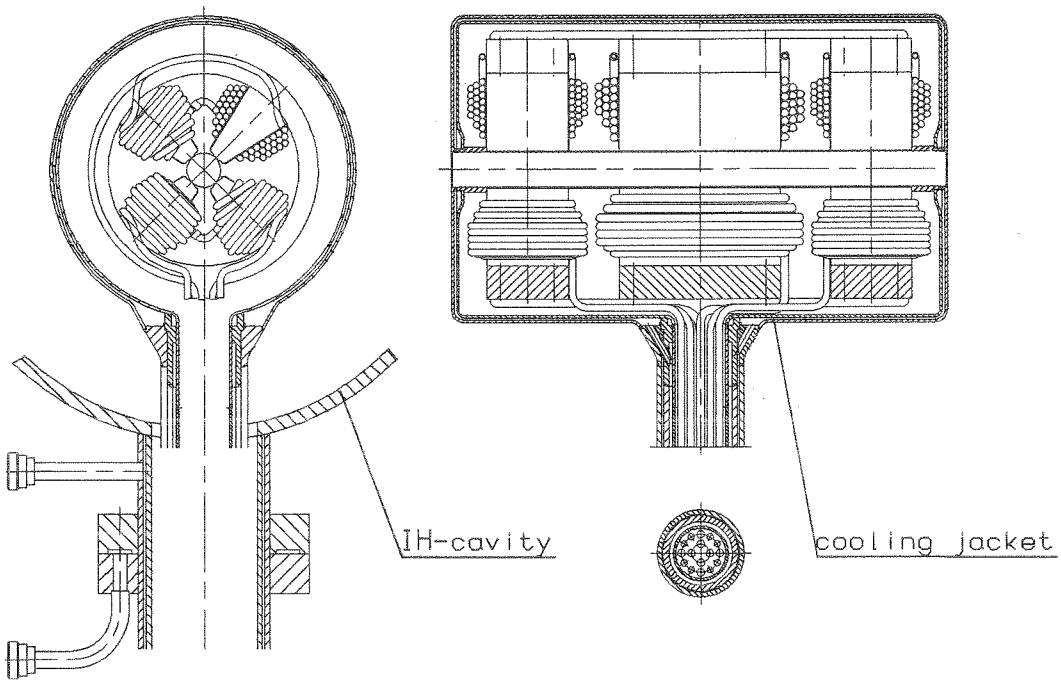


Fig.: Crossections of a quadrupole triplet inside the IH-cavity. The lenses can be adjusted to the beam line separately from the tank

An Improved Drift tube Geometry for the IH-Structure

U. Blell, U. Ratzinger
GSI Darmstadt

The dependence of the shunt impedance on the electrical capacity between the drift tubes is very strong in the case of the IH-structure. The rf power consumption of all $\beta\lambda/2$-drift tube structures can be minimized by using slim drift tube walls and thick, conical shaped drift tube stems to get a low surface current density (fig. 1). The disadvantage of that design is the appearance of an asymmetric, dipole-like component in the electrical gap field distribution[1], which is mainly caused by the electrical capacity between the stems and the neighboured drift tubes.

At a beam energy above 1 MeV/u this dipole component does not have much influence on the beam direction, because the dipole orientation is inverted in each subsequent gap, and the relative energy gain $\Delta W/W$ per gap becomes small. At low energies however, a displacement of the beam can be caused. Quantitatively, the misalignment of the beam mainly depends on the voltage distribution over the first few gaps of the structure.

By the asymmetric shape of the drift tube ends as shown in fig. 1, the dipole component of the electric field lines can be reduced by a factor between 0.2 and 0.4 typically, depending on the actual gap geometry (fig. 2). The improvement of field symmetry is paid off by an 8 %-increase of rf power consumption in the case of the GSI-tank.[2]

Field calculations

The calculations were done with the three-dimensional code PBM3D[3]. This program is solving Maxwell's equation of continuity in the form:

$$\oint_V (\kappa + i\omega\varepsilon_0\varepsilon_r)\,\vec{\nabla}\phi \cdot d\vec{A} = 0;$$

The code is based on the 'method of differences' and can be used to find the field distribution of the capacitive part of a cavity with complicated geometry. The voltage distribution along the drift tube stems is defined by their geometry and conductivity κ. This distribution can be varied in a wide range without significant influence on the gap field distribution. The tank walls are kept on zero potential.

Using a code which solves the complete set of Maxwell's equations for a cavity with an accurately defined gap geometry would take to much computing time. With PBM3D, one calculation needs about 25 min CPU time on the IBM 3090. The number of lattice points is about 100.000 typically. It takes about 200 iterations, to solve the system of linear equations by the SOR-method.

[1] U. Ratzinger et al., Nucl. Instr. and Meth. A 263 (1988) 261-270

[2] N. Angert et al., GSI Scientific Report 1988, p. 372

[3] U. Blell, PBM3D, GSI Darmstadt

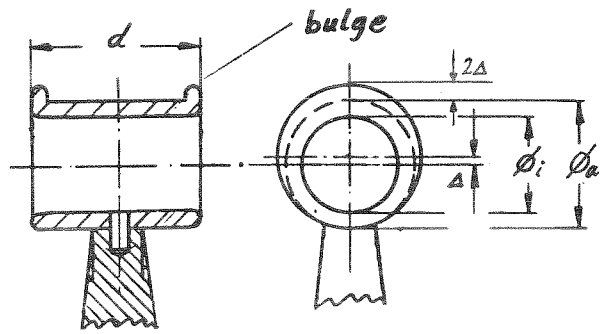


fig. 1: Drifttube geometry with reduced dipole component

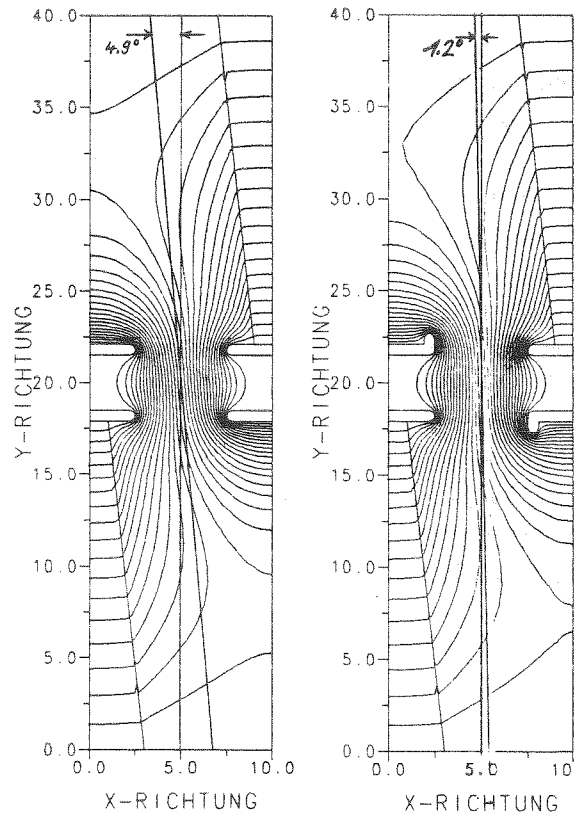


fig. 2: a) without bulges b) with bulges MECHGEN-results of the distribution of the äquipotential lines

High-Voltage Tests with a 27 MHz- Spiral- RFQ [G]

A. Kipper, J. Brutscher, O. Pan, A. Schempp
Institut für Angewandte Physik der Universität Frankfurt/Main
Robert Mayerstr. 2- 4

The Spiral-RFQ is a low frequency high current structure. Results of particle dynamic calculations [1] showed that, at a frequency of 27 MHz, for acceleration of a 25 mA U^{2+} beam an electrode voltage of approximately 180 kV is required. The injection energy can be as low as 2.3 keV/u.

A test resonator has been built for high voltage testing purposes. Its parameters can be seen in table 1. Improvements of mechanical design parameters revealed an even higher stability compared to the first module.[2] The spiral tube diameter is now 25 mm, the aperture diameter 16.8 mm. These values correspond to the forthcoming prototype accelerator.

The rf-voltage has been determined by measurement with a calibrated pick-up loop. Independently the emitted Bremsstrahlung has been recorded with a γ-detector. The peak voltage is given by the maximum photon energy in the γ-spectrum (Fig. 2). The accuracy of this method is about 2%. [3] No sparking could be detected up to an electrode voltage of 205 kV. This corresponds to 2.8 times the Kilpatrick value. Due to the limited output power of the rf-transmitter no higher voltages could be applied. The duty cycle was 5%, clearly higher than the 1% required for the high-current prototype. The operation of the resonator was very stable even up to 15 kW at cw-operation.

A prototype 4 Rod Spiral-RFQ-accelerator[1] designed for bunching and acceleration of a 25 mA U^{2+}beam from 2.3 keV/u to 25 keV/u (length appr. 4.5 m) will be built to study in more detail the emittance growth and possible beam loss sources in the crucial first part. With this prototype the suitability of the Spiral-RFQ-structure for a possible use, as a part of the GSI-High-Current-Project, will be checked.

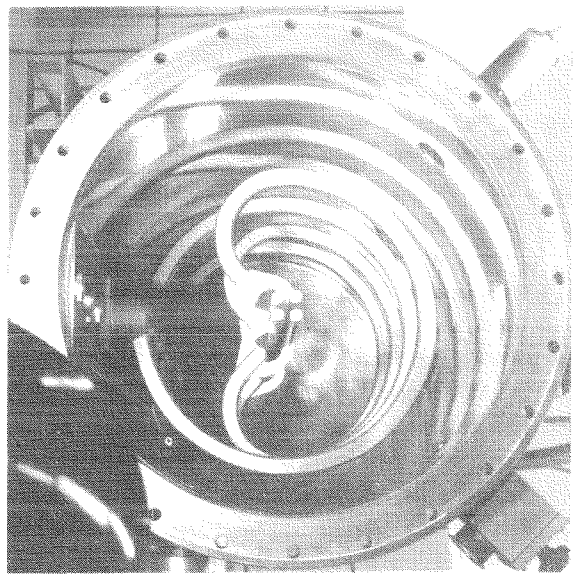


Fig 1 View of the spiral RFQ " sparker "

Electrodes		
aperture	16.8	mm
diameter	14.0	mm
length	710	mm
Spirals		
diameter	25.0	mm
length	1180	mm
Frequency	26.6	MHz
Q_0	3200	
$R_p = U^2/N$	580	kΩ
U (10 kW)	76	kV

Table 1 Parameters of the test spiral RFQ

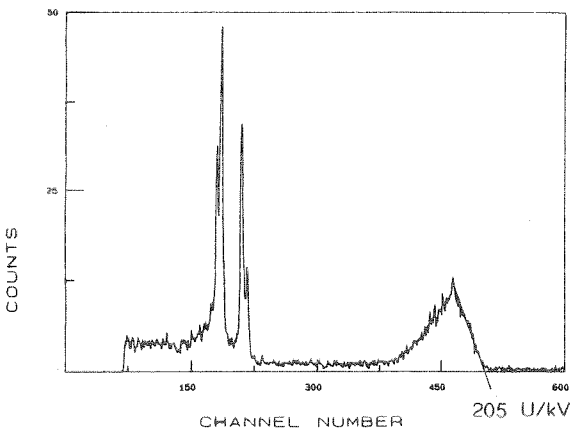


Fig 2 γ-spectrum of the RFQ at 205 kV gap voltage

References:

1) A. Schempp, H. Deitinghoff, A. Kipper, NIM A 278 No. 1 (1989), p. 169
2) A. Kipper, A. Schempp, GSI -89-21, 1989, p. 25
3) A. Gerhard, Dissertation 1989 Uni. Ffm., GSI 89-29

300 kV and 45 kV/u Accelerator

H. Emig, D.M. Rück, P. Spädtke, D. Vogt and B.H. Wolf
GSI Darmstadt

In 1989 the 300 kV accelerator and the Maxilac have delivered ion beams for 133 days in total. Users came from GSI as well as from universities, industry and other research laborartories.
The 300 kV accelerator beam line was used for experiments over a period of 74 days. H^+, D^+, He^+, N^+, N_2^+, Ti^+, Fe^+, Ta^+, ions have been accelerated to energies up to 200 keV. Detector tests with H^+ and D^+ beam have been done by users of GSI [1]. Researchers from the University of Heidelberg used ion beams for implantation and ion beam mixing applications. Implantation of N, N_2 in hard metals increased the wear resistance. Ion implantation of Ta ions into pure Ti and with Ta coated Ti samples improved the corrosion behavior [2]. In a collaboration work between Daimler-Benz AG (FRG), the University of Florida (USA) and the Musashi Institute of Technology in Tokyo (Japan) implantation of N_2 ions into Cr-layer have been done at different energies and doses. That lead to an improvement of the tribological properties of the layer [3]. To detect impurities in thin layers users from TH Darmstadt implanted Fe ions into targets [4]. Investigations in the field of material research for fusion reactor applications have been done by members of the laborartory of the European Community in Italy: ISPRA. Targets have been bombarded with He and D ions at different temperatures at energies 40 kV and 200 kV respectively [5].

The second beam line (Fig. 1), where high current beams are accelerated by the RFQ accelerator Maxilac to 45 keV/u [6] was in operation for 59 days. Mainly Argon and Krypton ions have been accelerated for RFQ beam transport investigations [6]. Within the project "High Energy Density in Matter" experiments with gas puff targets and solid state targets have been performed mainly with Kr-ions [7].
In addition high energy ion implantation with penetration depth of μm have been done with Krypton and Molybdenum ions [8].

References

[1] R. Simon et al, this scientific report GSI 90-1, 1990

[2] G.K. Wolf et al, this scientific report GSI 90-1, 1990

[3] H. Ferber et al, this scientific report GSI 90-1, 1990

[4] U. Scheuer private communication, 1989

[5] O. Gautsch, private communication, 1989

[6] R.W. Müller et al, this scientific report GSI 90-1, 1990

[7] K. Mahrt-Olt, this scientific report GSI 90-1, 1990

[8] H. Gärtner et al, this scientific report GSI 90-1, 1990

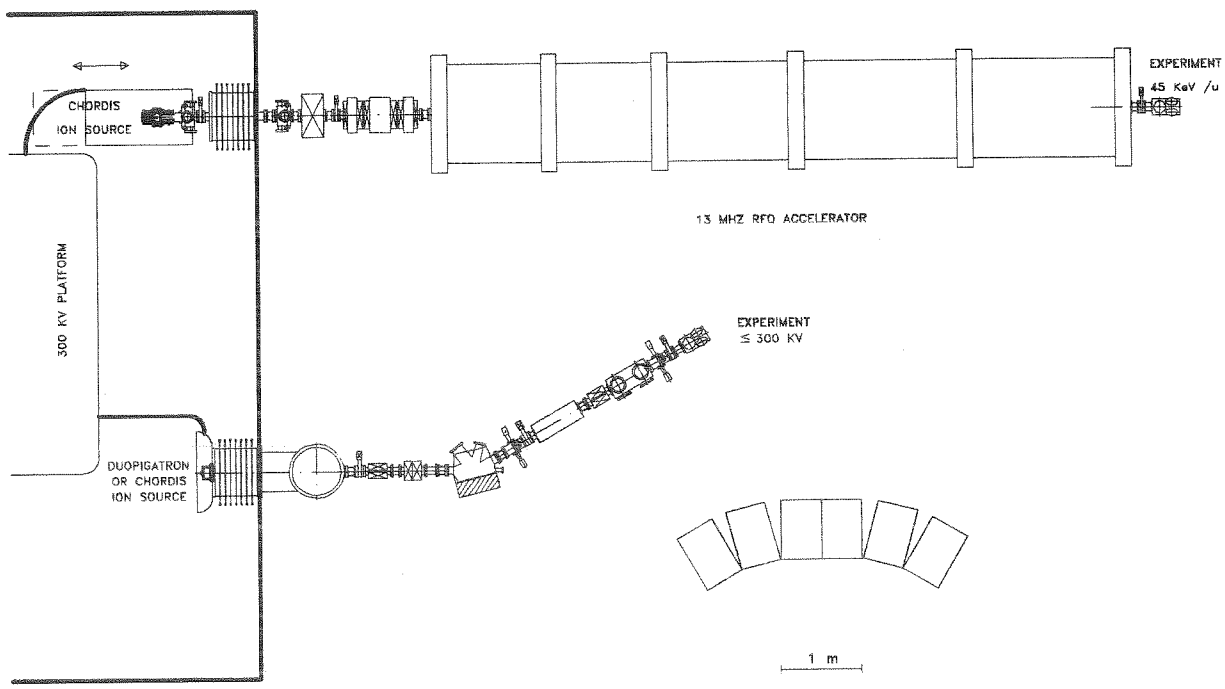
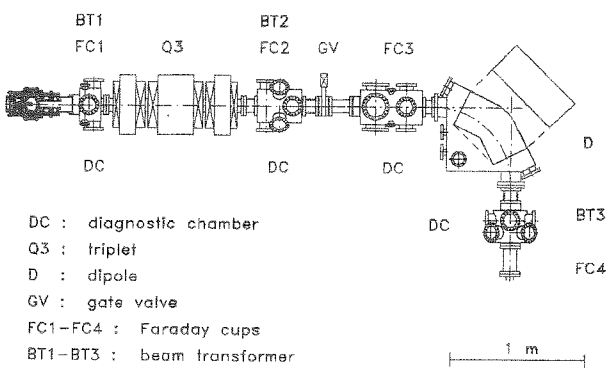


Fig. 1: 300 kV test accelerator with Maxilac beam line

Ion Beams of Metallic Elements with CHORDIS

D.M. Rück, H. Emig, P. Spädtke, B.H. Wolf, GSI Darmstadt
and
Bo Torp, Danfysik, DK-4040 Jyllinge

The investigations on the production of high-current ion beams of metallic elements have been performed at the high current test benches at GSI [1] and at Danfysik [2], shown in Fig.1.



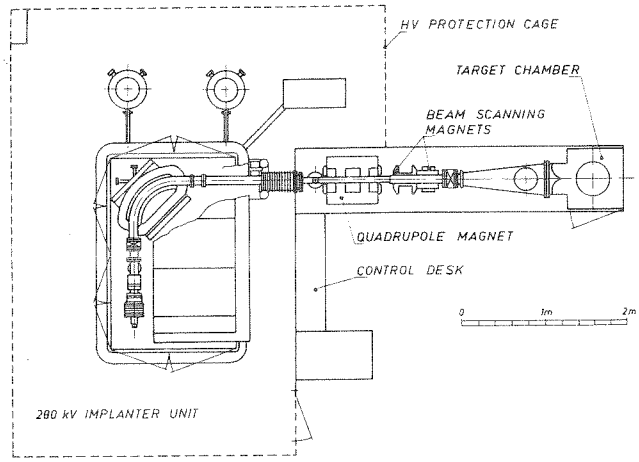


Fig. 1: High current test benches at GSI and at Danfysik

The experiments were done, using both the sputter version and the oven version of the high current ion source CHORDIS [3].
The mechanical and electrical set-up of the sputter version of CHORDIS and the operating parameters are described elsewhere [4].
The produced ion beam currents are summarized in Tab.1 for the dc operation mode. The sputter voltages used are the maximum voltages which can be applied without getting unstable conditions due to local melting of the sputter-electrode.
The stability was measured with maximum current Ta^+- beam to be better than 5 % over 6 hours. The lifetime of the source is determined by the cathode filament and is 40-100 hours depending on the operation conditions. It sometimes happens that metallic flitters shorten the two extraction electrodes after the source was switched off and restarted later again. That of course also limits the lifetime of the source.

Tab.1: Ion beams of metallic elements

Element	I_m	I_s	U_s	U_e	I_e
Ti	300	400	150	20	1130
Cr	160	900	245	30	1390
Fe	1200	1300	230	40	1300
Ni	110	500	245	30	770
Cu	400	600	250	25	1210
Mo	240	750	300	25	1520
Ta	500	500	300	40	500

I_m: measured current of the main isotope (μA), charge state 1^+
I_s: sum of beam current for all isotopes (μA)
U_s: sputter voltage (V)
U_e: extraction voltage (kV)
I_e: I_n extrapolated to 40 kV
The auxiliary gas was Argon in all cases.
One hole extraction system with a 9 mm main gap and an extraction area of 79 mm^2 was used in all cases.
The Cr and Ni currents were obtained using a $Fe_{46}Ni_{33}Cr_{21}$ -alloy. In this case the current I_e are extrapolated to 100 % Cr and 100 % Ni.

The other possibility to obtain ion beams of metallic elements is using the chlorination technique, where one uses a heated oxide with the metal of interest together with carbontetrachloride. The discharge chamber and the extraction system are the same parts used in the other versions of CHORDIS. The oven is indirectly heated by the oven filaments. The oven has to be the coldest part in order to avoid condensation of the compound on its way to the discharge chamber. The temperature is measured in the oven and the maximum temperature which can be obtained is around 1100° C. Furthermore a gas mixture can be let into the ion source through the oven. The reflector on the extraction side and the outlet electrode were redesigned made out of carbon in one whole piece.
As source material Cr_2O_3 was used and the gas mixture consisted of Ar and CCl_4, which could be individually controlled with two needle valves. The best results were obtained at an oven temperature of approximately 700° C. The measured ^{52}Cr current was 400μA at 30 kV extraction voltage, giving a total chromium current of 475 μA. The obtained Chromium beam corresponds to about 2 % of the total extracted ion beam. The lifetime of the source was approximately 10 hours due to the heavy corrosion of the hot metal parts exposed to the chlorine and to buildup of carbon.
Though the obtained chromium current was acceptable, the short lifetime and the required maintenance of the ion source makes this method unfavorable compared to the sputtering technique.

References

[1] P. Spädtke, H. Emig, J. Klabunde, D.M. Rück, B.H.Wolf, I.G.Brown, GSI-88-20

[2] private communication, Danfysik

[3] R. Keller, P.Spädtke and H. Emig, Vacuum 36 (1986) 833

[4] D.M.Rück, H.Emig, P.Spädtke, B.H.Wolf and B.Torp, GSI scientific report GSI 89-1, 1989

Laser induced metal ion beams

Michael Müller

GSI Darmstadt

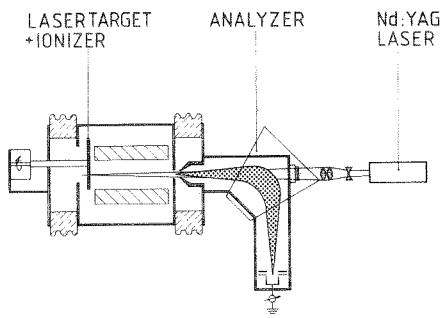


Fig. 1: Schematic of Laser Ion Source Assembly

A Q-Switched cw Nd-Yag Laser was used to investigate the material ablation by lasers for use in ion sources. Compared to the "classical" evaporation of metals with ovens, the laser evaporator might have some advantages as were low average temperature of the vapour source and the pulse operation option which is preferably usefull for pulsed ion sources: The material can be injected precisely timed during the workingtime of the ion source; also the response time of the laser evaporator is very short (microseconds or less) which is an appreciated advantage in the ion source optimalisation business.

An experimental setup as shown in fig. 1 was chosen. A simple magnetic analyser for the ions can easily be combined with existing ion sources and/or laser targets and ionizers. In every case the laser beam travels through the analyser chamber via extractor hole onto the "impact" spot.

The distance between laser and target is about 1.5 m and in TEMoo mode a beam spot size of 0.1 mm diameter can be achieved which leads to power densities of more than 100 MW/cm².

Survey measurements on ablation rates as a function of laser pulse energy for different metals have been done. These measurements showed soon the importance of a special surface control to satisfy the typical ion source demands, like steady material flux. Best results have been obtained when the target was rotating and/or the laser beam was moved radialy in the target plane. This forms a flat valley on the target surface and the shape of surface damages is randomized in such a way, that the ablation rate is constant at the average. The ablation rates are ranging from about 1 ng/laser-pulse up to several hundred ng/laser-puls depending on material properties and laser-pulse energy as well.

The laser induced metal ion source may look as follows: The laser impact target serves as "cathode" of the discharge which is ignited by external circuitry between a cylindrical anode which may also serve as radial confinement. Ions are extracted through a hole in the "anticathode" which also is the entrance port of the laser beam. Thus the ion source looks similar like the high current reflex arc sources.

Preliminary results

As a first step, the direct extraction of ions from the laser impact spot was investigated.

For Al und Fe total currents up to 30 mA pulse, 2 microsec. pulse length have been measured.

Magnetic analysis of the beam at 16 kV extraction voltage, ion currents of

Al 1+ 0.8 mA, (see Fig. 2)

Fe 1+ 0.6 mA,

Fe 2+ 0.06 mA have been observed.

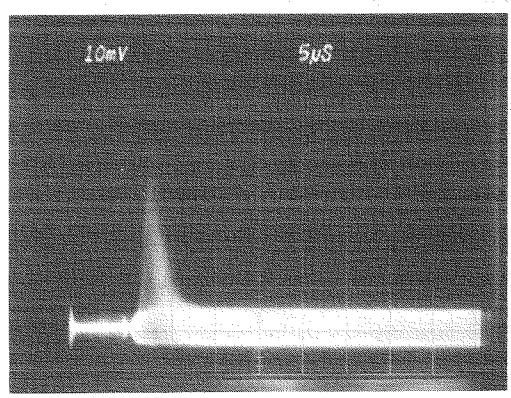


Fig. 2: Current Puls of Al 1+ beam, measured as voltage drop on 50 Ohms

Experiments with the complete source assembly have not yet performed but are projected for near future, the work is focused on the control of the metal plasma with the aim to get longer pulses in the range of several hundred microseconds at least.

Many thanks to Mr. Bossler, Mr. Hofmann and Mr. Khaouli of Unilac Injector Group for their useful help in this work.

Ion Source Modification for Ion Beam Assisted Deposition of Work Pieces

H. Wituschek, G.K. Wolf, Physikalische Chemie der Universität Heidelberg
H. Emig, D.M. Rück, P. Spädtke, B.H. Wolf, GSI - Darmstadt

Introduction

As part of the joint project "Ion Beam Mixing" [2] the development of a broad beam ion source on the basis of the existing MUCIS [1] concept for bombardment of large items and for ion beam assisted deposition (IBAD) was performed. The source is proposed to be attached to an apperatus for IBAD currently under development. The apparatus will consist of a standard vacuum chamber of ≈ 1 m^3 volume equipped with a 6 kW electron beam evaporater, a broad beam low energy ion source and the source described below. It will enable us to condense films of metals, non-metals and alloys under partial or continuous bombardment with ions in the energy range 0.5 - 40 keV. Areas of roughly 20 cm diameter can be processed in one step.

Description of the modified ion source

The ion source consists of a plasma generator with all the basic features of the LBL multi-cusp source [3] and an extraction system based on the one, used for the CHORDIS [5] ion source family.

The source is entirely made of stainless steel. The discharge chamber is 200 mm long and 200 mm in diameter. The confinement is done by 10 line magnets on the cylinder wall, 10 radial magnets arround the outlet and 4 parallel line magnets between two cathode feed-throughs on the other side. Cooling channels below every magnet prevent heating up the cobalt samarium magnets. Each of both cathode blocks is able to carry 4 tantalum filaments.

The original high current accel - decel extraction system, used for injection into an accelerator was optimized earlier to deliver an ion beam with low divergence, low emittance and high brightness. The requirements on the ion beam in an IBAD-System are quite different. Besides an high beam-current, allowing short processing times, large divergence (for big samples) and constant current density all across the substrate are necessary.

Using the Computercode AXCEL [6], it was possible to design an extraction system satisfying these requirements, while keeping most of the mechanical parts unchanged [4]. The insulators are made of polyimide, the electrodes from a tungsten - copper sinter cake and all other parts of copper or stainless steel. The flanges are cooled by water. The gaps and other distances are so wide that the breakdown voltage is more than 40 kV.

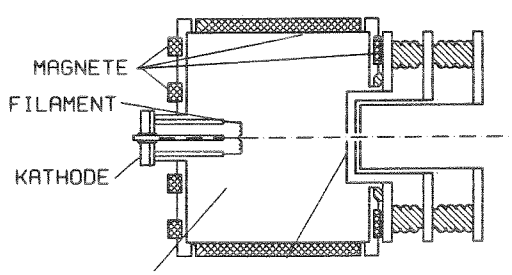


Figure 1: MUCIS with high current extraction

In order to obtain a high current a multiaperture extractor was used. It has 14 holes each 5 mm in diameter. This gives a total extraction area of 275 mm^2. A large divergence was achieved by inclining the axes of the beams proportional to their distance from the middle axis. The three extraction holes of each beam should ideally lie on concentric spherical electrodes, but for the reason of easy manufactering they were projected to plane electrodes.

A new test bench was mounted to perform tests with the extraction. The test bench is capable of measering the current density in an area of 300×300 mm^2 1250 mm downstream the extraction. This is done by four faraday cups, each 5 mm in diameter which were positioned on a grid of 40×40 points. A typical current density profile for argon is shown in figure 2. Further it is possible to evaluate the emittance by a pepper pot device and to measure the over-all current with a faraday cup near the source.

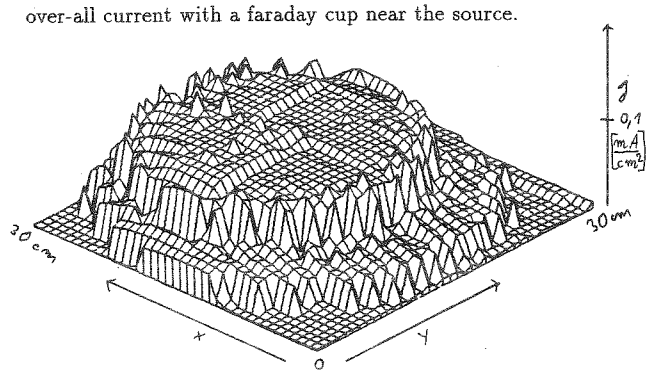


Figure 2: Current density distribution at 25 kV

Preview

A completly revised extraction system is manufactered at present. The main features are exactly spherical electrodes for lower abberation, larger diameter, allowing 22 holes of 5 mm diameter. This extraction area will deliver an over-all current of 130 mA argon at 25 kV.

It will also be necesssary to measure the fraction of neutral particles in the ion beam. This can be done by studying the sputtering by the beam on a tantalum foil which is covered with a thin (a few hundred nm) coating of tantalumoxide. According to the sputter reduction of the oxid thickness the surface changes its colour. A problem to be solved for this measurement is the heating of the surface, which interferes with the sputtering effects.

References

[1] R. Keller, GSI 88-1 (1988) 360

[2] G. K. Wolf, GSI 89-1 (1989) 236

[3] K. W. Ehlers, K. N. Leung, Rev. Sci. Instr. 54, 1296 (1983)

[4] H. Wituschek GSI-Report, GSI-89-26 (1989)

[5] R. Keller, F. Nöhmeier, P. Spädtke, Vacuum 34 1-2 (1984)

[6] P. Spädtke, Axcel-GSI, GSI-Report 83-9, (1983)

First Results of Schottky Diagnostics at SIS

U. Schaaf, K. Beckert, S. Cocher, F. Nolden
GSI-Darmstadt

It has been decided by the end of 1988 to use the powerful Schottky-Scan method to determine various relevant beam and machine parameters at SIS. Measurements have been carried out with different ions (Ar^{10+}, Xe^{21+}, Kr^{16+} and Ne^{10+}) at energies from 10 to 100 MeV/u and bunched as well as coasting beams. By the end of multi-turn injection the beam current reached typically a maximum of some 10 μA. Suitable events from the control system have been used to start the evaluation of a spectrum and then up to 500 spectra of succeeding machine cycles have been averaged to improve the measurement accuracy. In addtion to normal Schottky-scans we analyzed transverse spectra resulting from a short excitation by a magnetic kicker. This method is described in another article [1].

1 Measurement Setup

Figure 1 shows the preliminary hardware arrangement used for measurements in 1989. One of the already installed phase monitors was used as electrostatic pickup to detect the Schottky-noise signals. The electrodes have been made resonant by a shorted cable forming a quarter wave resonator to improve the signal to noise ratio. The spectral analysis was finally done in the main control room with an analog spectrum analyzer as well as with a digital "Fast Fourier Transformer" (FFT), each method having its own advantages (that can't be described here).

2 Results

Figures 2 to 4 show some of the measurements in 1989. A more detailed description of the obtained results can be found elsewhere [2]. Figure 1 shows several longitudinal Schottky-bands of succeeding harmonics of the particle revolution frequency. The effect of the resonant pickup is clearly visible. The shape of each harmonic is a direct image of the particle frequency distribution. That allows us to determine the momentum spread of the beam and the distance of the harmonics gives the average revolution frequency and particle energy respectively. Figure 2 shows the splitting into several synchrotron satellites of a single Schottky-band in the case of a bunched beam. The synchrotron frequency can easily be evaluated by measuring the distance of these satellites. In figure 4, the narrowband time domain measurement shows the integral power of a Schottky-band as a function of time. The beam lifetime (e-folding time) is determined by the slope of this curve.

The following list finally gives a short review of the results obtained in 1989. With Schottky-scan methods, we have been able to measure

- the exact particle revolution frequency and energy
- the particle frequency distribution and momentum spread of the beam
- the synchrotron frequency in the case of a bunched beam
- the average betatron tune Q and moreover the so called "working line" i.e. the variation of the betatron tune across the particle momentum distribution. The slope of this curve defines the chromaticity ξ.
- the variation of the betatron tune Q and the chromaticity ξ in a wider range (across the aperture) by varying the RF-frequency and evaluating the tune at several points.

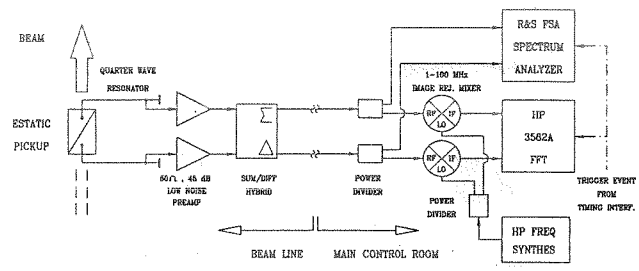


Figure 1: Hardware arrangement for Schottky-scan measurements.

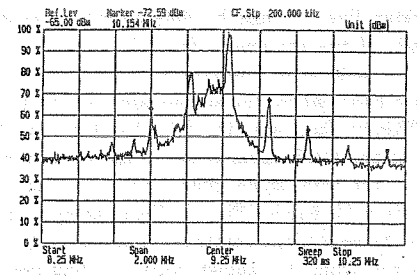


Figure 2: Longitudinal Schottky-bands of a Xe^{21+} beam (11.6 MeV/u) at several harmonics of the particle revolution frequency. The increase of sensitivity due to the pickup resonance around 9 MHz is clearly visible.

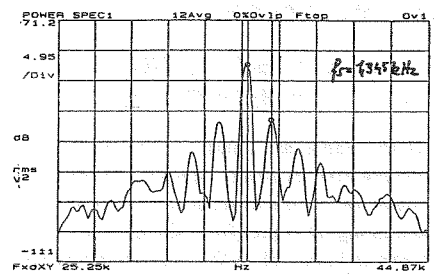


Figure 3: Longitudinal Schottky-band with same beam parameters as above and RF on (bunched beam). The distance of the synchrotron satellites gives the synchrotron frequency of the particles.

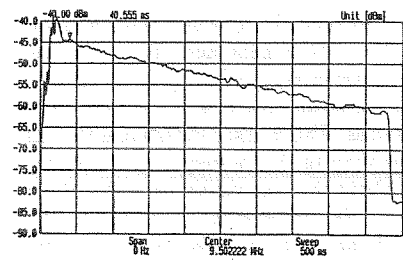


Figure 4: Narrowband timedomain measurement showing the integral power of a Schottky-band as a function of time. From the slope of this curve a beamlifetime of τ= 290 ms can be evaluated.

References

[1] S.Cocher, K.Beckert, F.Nolden, U.Schaaf, *Working Line Measurement at SIS*, GSI Scientific Report 1989

[2] K.Beckert, S.Cocher, F.Nolden, U.Schaaf, *First Schottky-Scans at SIS*, GSI Nachrichten 12-89

Working Line Measurement at SIS.

S.Cocher, K.Beckert, F.Nolden, U.Schaaf.

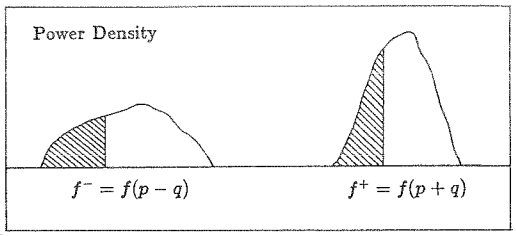


Figure 1: *Corresponding points in slow and fast-wave sidebands.*

The variation of the betatron tune with momentum defines the working line. It can be determined by analysing the two side-bands of the transverse Schottky spectrum. Hereward [1] proposed a method to find corresponding points in the fast and slow wave band where the signals are induced by the same particles. This method uses the fact that the contribution of each particle to the total signal power is the same in each side band. Therefore, the total signal power below corresponding points is identical in both bands (Fig. 1). Using an appropriate computer program the equivalent points are determined by integrating the signal power from two known corresponding points. The edges of the bands could be used, but they are not well defined in most cases. Therefore, the integration is started at the center of the bands where the integrated signal strength equals half of the total power. The fractional part of the tune and the revolution frequency are then defined by

$$\begin{aligned} q &= p(f^+ - f^-)/(f^+ + f^-) \\ f &= (f^+ + f^-)/(2p) \end{aligned}$$

where p is the harmonic number. This method is usually applied to uncorrelated Schottky spectra. In order to improve the signal to noise ratio, the beam has been kicked by a short pulse. The measured signal comes from the collective beam response to the pulse and is identical to the well-known beam transfer function. Although this signal differs in frequency domain from the Schottky power spectrum, we found that the method proposed by Hereward can also be applied to the power spectrum of a kicked beam.

Results obtained with this method are shown in Fig. 2. For calculations we used the measured horizontal betatron sidebands of Fig. 3. They are in good agreement with the results obtained with a complementary method (Fig. 4) which considers the variations of the mean tune of a kicked bunched beam at different RF-frequencies. This method determines the tune with frequency steps larger than the beam frequency spread and doesn't give information about the tune variations within the particle frequency distribution. Nevertheless the chromaticity obtained with these two methods are in good agreement. It is proportionnal to the slope of the tune curves. We found -0.8 with the first method and -1 with the second one.

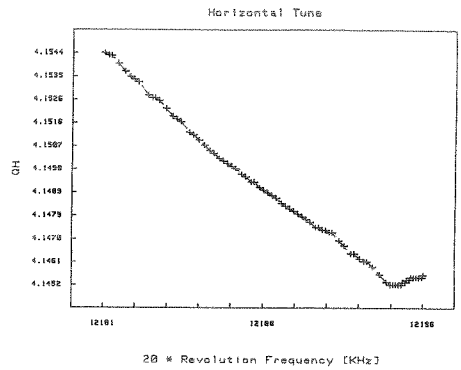


Figure 2: *Horizontal betatron tune distribution vs revolution frequency within the particle frequency distribution.*

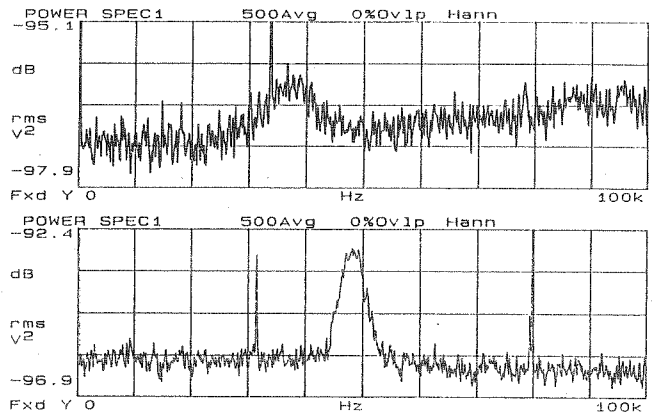


Figure 3: *Fast-wave (a) and slow-wave (b) sideband of a Ar^{10+} coasting beam at 100 MeV/u at the 20th harmonic of the revolution frequency.*

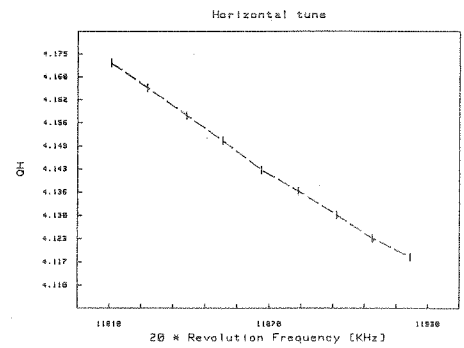


Figure 4: *Mean horizontal betatron tune distribution vs RF-frequency.*

References

[1] S. van de Meer, *Diagnostic with Schottky Noise*, presented at the US-CERN School, October 1988, Capri, Italy.

Status of Geodetic Survey and Component Alignment of New Hall Area, SIS, ESR

Ingobert Schmadel
GSI Darmstadt

Separate geodetic network in the new hall area

Starting in autumn 1988 a geodetic control in the transfer ESR- and target hall area was worked out (see table 1). We developed special brass plates, which were installed in the ground of the hall area. These plates can be used for various purposes. The following can be centered on the cylindrical pivot of the brass plates:
a) target for optical/mechanical plumbing
b) target for horizontal determining of direction
c) reading mark for steel tape
d) sphere for vertical measurements (settlement measurements)
A minimum of 25 μ centering accuracy is guaranteed by the quality of fit of all splits. The standard deviation of the single plumbing by measurings with the electronic high precision theodolite E2 of KERN (Switzerland) is calculated as 0.03 mm, that of the horizontal determining of direction as about 0.01 mm. By using a specially developed levelling device the brass plates could be secured in the ground with not more than 20 ' angle of tilt. In this case the difference in height of about 20 mm between the plumbing centre and the horizontal direction target centre would give less than 0.1 mm inaccuracy in the x-y plane. A conical support in the upper part of the cylindrical centering pivot guarantees the vertical self-centering in the Z-plane by putting a steel sphere in it (as used in ball bearings).
In order to achieve a workable network for the future the allocation of the brass plates was dependent on the position of the shielding walls at that time. We devized these datum positions to be separate from the marks of the beam line axis. This represented the last occasion to observe a geodetic network in the almost empty new hall area. The angles were measured in two faces using two rounds of angles on the E2 of KERN. The measured data was immediatly registered and analysed by an external SHARP PC 1600 data logger. The distance measurements up to approx. 20 m were taken in both directions with high precision steel tape and corrected with respect to temperature and tension. Distances beyond 20 m were observed by measurement with the high precision laser range finder KERN ME 5000. This kind of distance measuring is based on sending out a periodically modulated light signal and measuring the phase of the modulation of the reflected wave. With this information the length of the light path is internal calculated. The firm KERN states that the standard deviation for the measuring of ranges amounts to 0.2 mm + 0.2 ppm within an internal resolution of 10 μ [1] [2]. The ME 5000 measurements were carried out by members of the TU Karlsruhe.
To determine the unknown 114 coordinate and 62 orientation parameters of the geodetic network 381 angles and 153 distances were measured. A least square fit was carried out as a two-dimensional compensating calculation using the program system KATRIN of the Landesvermessungsamt Nordrhein-Westfalen (Bonn/Bad Godesberg). By connecting measurements to three well known SIS pillar centres we obtained the orientation of the SIS coordinate system.
The semi-major-axis of the confidence ellipses of the compensated coordinates amount to an average value of 0.2 mm. It is remarkable that the steel tape measurements correspond to the far more precise ME 5000 scale to within 0.2 mm. The controllability of the compensating calculation of the distances is between 80 % - 90 % and over, that means their influence on the point positions is insignificant. The very small normalized correction demonstrates a high degree of measuring accuracy:
a) average value for the normalized correction = 0.7
b) comperative value = 3.3

It is not possible to orientate the independent geodetic network to the SIS with economic expenditure. We have to take into account the possibility of a twist. But the decisive factor for the range of use is that the high inner accuracy of the network is not touched by the twist.

SIS

For the first time the SIS was surveyed as originally designed [3]. By connecting the surface and the tunnel measuring system a higher geodetic network quality was achieved. The underground geodetic control is formed as a uniform dodecagon (shown in fig. 1). The pillars of the system stand in an eccentric position outside the ideal SIS machine-dodecagon. The geodetic network on the surface is a pentagon. The line of sight between the points (O) and (S) (as shown in figure 1) is obstructed by the transfer-hall building. Vertical line-of-sight pipes connect the two systems. The difference in height between upper and lower centre amounts to approx. 8 m. In both geodetic networks angle measurements with E2 and distance measurements with ME5000 were carried out. The measured data was registered with the MS-DOS-version of the portable PC HUSKY HAWK (BOSTON COMPUTERS), which is very compact and has a high battery capacity. In the surface network all angles and distances were determined except the (O) - (S) connection.
The difference in x and y between collateral points in both systems can be obtained by the measurement of zenith angles from the self-centering KERN-datum on top of the tunnel pillar to the centering target at the end of the line of sight pipe. The vertical angles were measured in two vertical planes, which are perpendicular to each other. That corresponds to 4 horizontal measuring positions (0, 200; 100, 300 gon) with orientation toward one of the adjacent survey points. The height difference between theodolite and target was measured with a steel tape. An accuracy within 10 mm was sufficient because of the favourable x-y positions of both centres. The standard deviation resulted in 0.02 mm for the single coordinate-transfer from the surface to the tunnel level.

A loop traverse was measured in the tunnel. In the same perspective two adjacent loop points of the twelve pillars represented the base to measure horizontal and vertical directions to the entry and exit points of all SIS dipoles and quadrupoles, solving the coordinates by calculating three-dimensional intersections. This information was not overdetermined. We stabilized it by measuring some distances from the pillars to the magnets with ME 5000. It was the first time with direction-measurements in the tunnel that we encountered adverse lateral refraction accumulation. These caused closure errors of the loop traverses of values up to 1 cgon. The reasons were thermic fluctuations especially in the areas of injection, reinjection and extraction. Here we found the largest horizontal thermal gradients with up to 0.6^{o}C/m. The other problem of lateral refraction remains in the horizontal deflection of the line of sight close to warmer objects in particular dipol- and quadrupol power supply cables. In this case some temperature profile tests were measured and estimated according to [4] gives the refraction influence of approx. 0.5 mgon per angle. A good solution for the refraction problems seems to be the vorticity of air spaces with the SIS ventilating system. Subsequent measurements under these conditions revealed essentially better closure errors ($<$ 2 mgon).
All measured information:
a) surface network (stabilization)
b) tunnel network (relation to the magnets)
c) plumbing (connecting the two systems)
were combined together in a free compensating calculation. A fixture of datum exert arbitrary pressure on the least square fit. In our case the different impact of each piece of information necessetates the fixture of datum on the surface network. A separate compensating calculation of this network reinforces the above. The result shows nearly circular confidence ellipses with a radius of 0.02 mm.

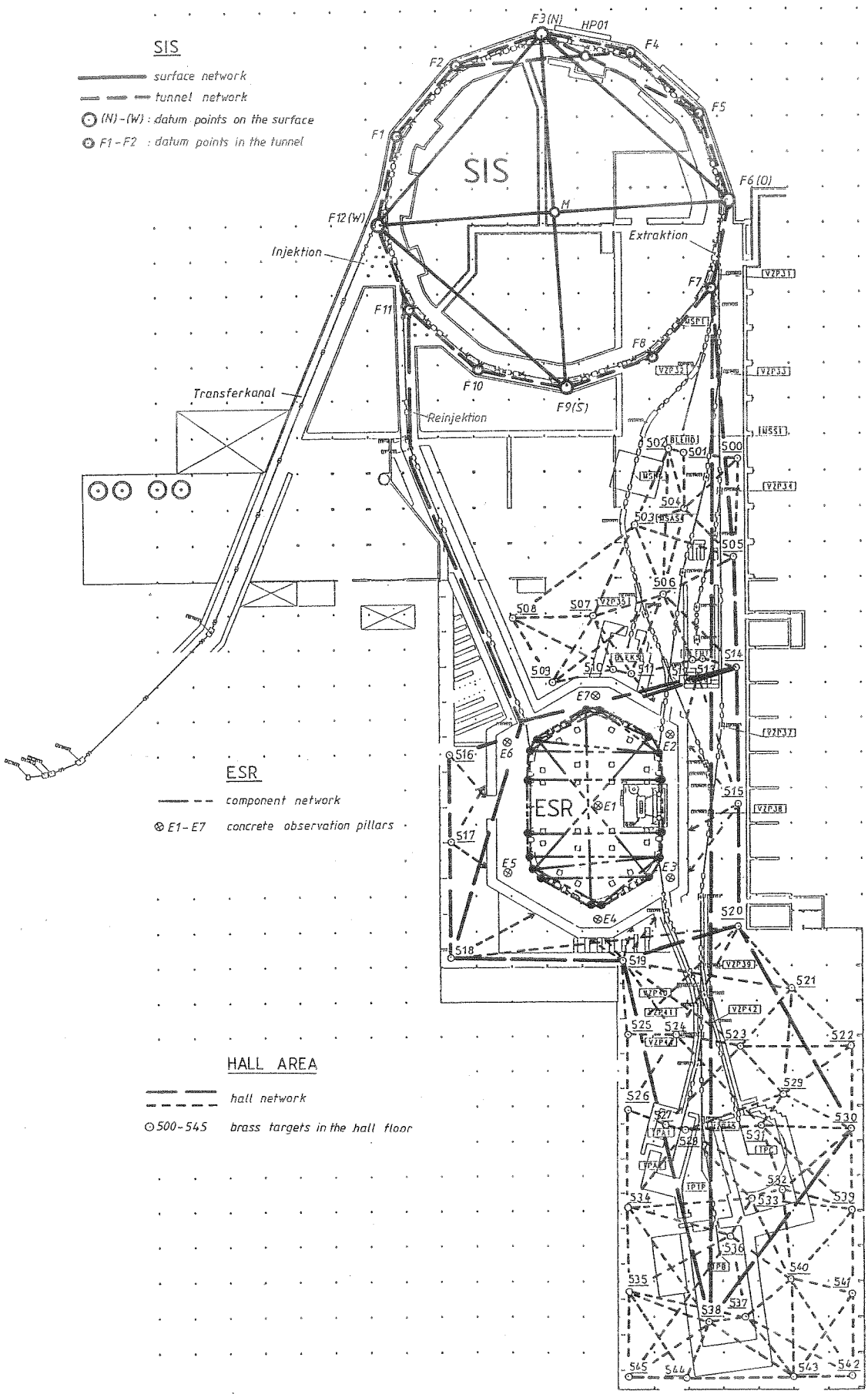


Figure 1: Geodetic network systems of the new accelerator complex

The whole compensating calculation gives average standard deviations (S_L, S_R, S_V) for the magnet position points:
S_L = 0.8 mm longitudinal
S_R = 0.1 mm radial
S_V = 0.1 mm vertical
They have a confidence level of 95 %. A readjustment was not possible in the previous shut down periods. That means that the actual position of the machine has not exceeded the zero-approximation. The absolute required and actual costs accounting lie between values of 1 and 3 mm in the 3 D. The horizontal divergencies result from the lack of the surface network and ME 5000 horizontal scale precision at the time of first adjustment. The vertical differences follow from the time-settlement-reaction of the tunnel building.
The special aspect of SIS geodetic survey is the basic thesis, that none of the geodetic SIS controls can be seen as static because of the movement of the SIS building (see fig. 2). The basic systems have to be measured and calculated before every review, the adjustments are relative.

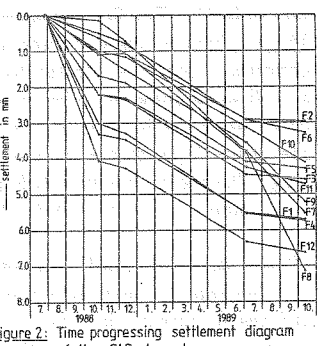


Figure 2: Time progressing settlement diagram of the SIS loop traverse

ESR

The installation of ESR dipoles and quadrupoles was carried out with very little time at our disposal and the requirement that the first adjustment brought the nearest absolute positions and closest final accuracy. It was a disadvantage that the adjustment zone = sighting zone has a height of 3 m above ground. For the short-term massive concrete observation pillars were positioned in the centre and in extension to the outside of the hexagon of the ESR geometry (shown in fig. 1). In this new geodetic control all directions were measured. The high precision of the measurement of angles (0.15 mgon/angle) defines the network excactly in its geometric form. The scale of the network was found by measuring some long ME 5000 distances. The result of the compensating calculation showed nearly circular confidence ellipses < 0.05 mm in the horizontal plane and < 0.08 mm in the vertical plane. The MEKOMETER ranges proved to be extremely precise, which achieved a degree of accuracy of < 0.1 mm standard deviation obtained from the compensating calculation including all the networks (SIS, ESR, hall system).
The concrete pillar network was the basis for the adjustment of the ESR dipoles with the ECDS-System (KERN). This system allows a survey in either a three-dimensional theodolite or object coordinate system using two electronic theodolites in connection with a PC. The quadrupoles were positioned by locking them onto the dipoles with polar measuring elements. The short polar distances were measured with a 1 m-scale-bar.

A second geodetic control was measured directly on top of the magnets in winter 1989 to eliminate external influences and to obtain the best inner-accuracy of the ESR. With adapter devices we could use the adjusting mount on the magnets as stands. The data flow method was similar to the SIS survey:

a) registration and analysis of the measured data on the portable PC
b) transmission to the evaluation PC
c) evaluation and processing of measured data.

The three-dimensional network adjustments (SIS/ESR) were calculated with the PAN 3 D program system from the firm GEOTEC. The remarkable features of this excellent software are its various possibilities such as options and statistical tests and its speed. The ESR system of equations comprised of 693 observations and 294 unknown. It was solved in about 10 minutes with a simple 8 MHZ IBM AT.

The use of trigonometric levelling and compensating calculation in a complete system is not utilized so often in geodetic accelerator surveying but it brings very good results in our usage. The vertical error component was smaller than 0.1 mm. Otherwise the semi-major-axis of the confidence ellipsoids pointing in the direction of the beam line with maximum values of 0.3 mm (confidence level 95 %). These values are surprisingly large and have their foundation as we discovered in special tests in an unsatisfactory construction of the adjustment devices. The devices will be modified. In comparison to these results a diagnostic compensating calculation shows maximum values of 0.15 mm for the semi- major-axis and 0.08 mm for the other axis of the ellipsoid.

Another comparison can be made with the current adjustment positions and their theoretical values. The difference reveal that the setting out with the ECDS system brought high adjacent accuracy but had some orientation error due to the reasons as described before. The average radial differences in between real and theoretical magnet positions amounted to 0.2 mm between the neighbouring magnets. These values are sufficient for the first adjustment.

Acknowledgements

I like to thank the following institutions and people for their friendly assistence:
Prof. Dr.-Ing. Roman Reiser (Labor für Sondervermessung der FH Rheinland-Pfalz), Dipl.-Ing. Michael Petri, Dipl.-Ing. Bernd Padberg, Dipl.-Ing. Meinolf Henkenjohann, Dipl.-Ing. Joachim Franke
Prof. Ing. Franz Löffler, Dr.-Ing. Wilfried Schwarz (DESY Hamburg, Vermessungsabteilung),
Dr.-Ing. Hansjörg Seckel, Dr.-Ing. Wolfgang Zick (Univ. Karlsruhe, Geodätisches Institut/Prof. Dr.-Ing. E. Kuntz),
Dipl.-Ing. Dieter Tengen (Fa. GEOTEC).
Special thanks to Dipl.-Ing. Rolf Schwedhelm and the staff of BT/EA, GSI.

References

[1] Maurer, W.; Schirmer, W.; Schwarz, W.: Wirkungsweise und Einsatzmöglichkeiten des Mekometer ME 5000, Ingenieurvermessung 88, Beiträge zum X. Internationalen Kurs für Ingenieurvermessung, Beitrag A10; Dümmlerbuch 7808, Bonn 1988, ISBN 3-427-78081-3
[2] Meier, D./Loser, R.: Das Mekometer ME 5000 - Ein neuer Präzisionsdistanzmesser, Sonderdruck aus AVN, Heft 5, Mai 1986, Herbert Wichmann Verlag GmbH, Karlsruhe.
[3] Schmadel, I.: Survey System for the SIS, GSI Scientific Report 1986, S. 339, ISSN 0174-0814.
[2] Wilhelm, W.; Matthias, H.J.: Empirische Bestimmung der Seitenrefraktion an 9 Objekten in der Praxis, Kurs für Ingenieurvermessung 88, Band 2, C 6, Dümmler, Bonn.

Assembly of the Experimental Storage Ring ESR.

B. Franzke, GSI - Darmstadt

I. Survey

In the beginning of 1990 the ESR assembly went into its final phase. Mainly the large parts of the ring vacuum chamber were installed with unexpectedly high speed. Now, at the end of January, the nearly 45 m long northern arc of the ESR is complete and leak tested. The southern arc will be in a comparable state within next two weeks, and the straight sections by the end of February. The electron cooler, provided for the eastern straight section, and the internal gas jet target (at the other side) are nearly complete and prepared for the transport to their final position on straight sections. All main dipole and quadrupole magnets and all ring elements for beam injection and extraction are ready for use. Some assembly or cabling still has to be done for correction magnets, rf–cavities, beam diagnosis and beam transfer line between SIS and ESR.

The ESR–cave is built up except some ceiling elements, which would have hindered the assembly of heavy components by means of the crane. All necessary cables between ring and auxiliary building and from there to the main control room have been layed. Some local cabling and connection work still has to be done. The ESR control station in the main control room is sufficiently equipped for the first commissioning steps starting on March 5 with beam injection and transport over one single turn. An intermediate goal is the storage and (hopefully) cooling of totally stripped xenon ions at 200 MeV/u by the end of April.

II. Ring Components

Magnets

Six 60^0-bending magnets and 20 quadrupoles were aligned and connected to power supplies and water cooling. All magnets have been operated already with their power supplies up to maximum field levels. The gap fields of bending magnets were mapped by means of a large 3D-mapper [1] and matched precisely to equal effective lengths at the mean field level of 1 T. The experimental optimization of currents for the 23 pole face windings, provided for shaping the radial profile of the bending field, had to be postponed because of power supply problems (see below). Overlapping field regions between adjacent magnets – quadrupoles on one side and sextupoles or vertical steerers on the other side – have been mapped in order to obtain corrected effective lengths.

The remaining magnets, 8 sextupoles, 8 vertical steerers, and 3 septum magnets are completely installed. Two compensation solenoids and two combined horizontal/vertical steerers are prepared for the installation in the ring together with the electron cooler. The rather delayed beam inflector magnet is complete now and will be in house within coming days.

Magnet power supplies

The eleven main power supplies for bending and focusing magnets have been tested with loads and can be operated by means of computer codes. During commissioning of the power supplies for the pole face windings, non–tolerable current oscillations appeared in the case of operating many of them simultaneously, obviously due to strong inductive coupling. The suppression of oscillations, e. g. by means of suitable matching of the feed back circuits, is being investigated. All other power supplies for steerers, sextupoles etc. are in house and shall be commissioned step by step by the end of February.

Radio frequency cavities

Two pre–assembled rf–cavities had been delivered in September last year, but the final assembly had to wait for beam pipes, accelerating gaps, and heating jackets. Meanwhile, these parts have been tested successfully, included baking at the design temperature of 300^0C. The first cavity is on its final position in the ESR. The mechanical assembly and wiring of the power amplifiers is underway. Low level electronics and driver amplifiers are ready as well as all power supplies for anodes, grids, and ferrite biasing. Power tests are foreseen in the beginning of March 1990. Only one cavity is necessary for the first months of ESR commissioning. The second cavity, which presently is replaced by a simple beam pipe, shall be installed a few month later.

Beam injection and extraction

All elements for beam injection and extraction were assembled and tested outside the ring. In the meantime, the electrostatic septum for slow beam extraction, three ferrite kicker modules for fast beam transfer between SIS and ESR (and vice versa), three septum magnets (one for the injection and two for the extraction channels), and the rotated kicker for betatron tune measurements are in the ring and ready for commissioning.

UHV-system

All parts of the ring vauum chamber were tested systematically, either by manufacturers or at GSI, by means of a 300^0–baking procedure, almost using the final heat jackets. Fortunately, the installation of the six nearly 7 m long dipole chambers and the 12 quadrupole chambers by means of special mounting supports turned out to be less critical than suspected by several outsiders. In parallel to the mechanical assembly mentioned above, local cabling is being completed and systematic testing of components via vacuum control units is taking place. After the complete closure of the ring vacuum, one week of pumping and, eventually, moderate baking is planned before first beam injection.

For the coming months, where parts of the vacuum system might have to be flooded repeatedly for repair work or additional installations, only moderate baking to 150^0C is planned, mainly to remove water from the residual gas. By this way, we hope to attain a base pressure (without ion beam and internal gas jet target) close to 10^{-10} mbar corresponding to a life time in the order of minutes of a partially stripped heavy ion beam above 100 MeV/u. The design pressure of 10^{-11} mbar should be approached step by step after having raised the baking temperature to 300^0C and consecutive pumping with full speed over several weeks.

Beam diagnostics

14 capacitive beam position/phase pickups, a beam current transformer, and three beam scrapers have been assembled, tested, and installed in the ring. Two additional scrapers for the second scraper station shall be installed next. Due to delayed delivery of special parts the completion of the first turn diagnosis, beam profile grids and Faraday cups, is strongly behind schedule. But we are sure now that these components will be available in time for the first beam injection. The coaxial cables from local terminals inside the ESR to the position pickups are in work. Long

distance cables between ESR and final amplifier electronics are layed and cut to identical length.

The Schottky diagnosis for bunched and coasting beams [2] is well prepared, though the provided special pickup station will not be availble for the first time. As an interim solution, the electrodes of the transverse rf-exciter will be amployed for picking up both longitudinal and transverse beam signals. By means of switchable external rf-circuitry the electrodes can be used either for wide band or for narrow band decoupling of beam signals. Most of the planned methods using spectrum analyzer, fast Fourier transformers (FFT) or network analyzer have been applied successfully during commissioning of the SIS.

Computer controls

The controls hardware and software is prepared for starting the storage ring mode with dc operation of magnet power supplies. For the ramped mode, i. e. the synchronous variation of many magnet power supplies and the rf-system during deceleration, there is a lack of control units and interface boards. The full equipment required for this mode is promised within the first half of this year. A preliminary connection to the computer control is necessary also for position pickups and for linear feedthroughs (scrapers, grids etc.), which are driven by stepping motors. All other components can be controlled without restrictions by operating codes. Most of them have been tested and improved step by step over nine month of SIS commissioning.

III. Special Devices

Electron cooler [3]

The major fraction of time in the past year had to be spent for mapping the magnetic fields of the electron cooler [4]. The (expected) inhomogeinity of cooler solenoid field had to be corrected iteratively by means of two pairs of geometrically complicated saddle coils [5]. In addition, the necessary dipole correction coils in the toroids and four sets of steering coils were designed and ordered. Electron gun and collector were tested at the linear test facility [6]. The high voltage stability of the accelerating columns could be raised to 220 kV without electron beam and to 100 kV with a beam current of 2 A. In the latter case, the limit was set by the available electrical power on the high voltage potential.

Meanwhile, the electron cooler is nearly complete. The vacuum test showed that there is neither any leak nor any major pollution. The Faraday cage with high voltage terminal inside the ESR is being equipped with all necessary instruments and cables. An operating code for the electron cooler was developed and successfully tested at the linear test facility. The goal is to get the electron cooler ready to be switched on by the end of March 1990.

Stochastic pre-cooling

Nearly all components of the stochastic precooling system are in house and tested, except the pickup and kicker electrodes. Though the mechanical design of the electrode system had been frozen since half a year, the production had to be postponed, mainly due to the lack of personal capacity. In the meantime, the coupling of simulated beam signals to prototype electrode has been investigated in more detail [8,9]. The meaning of results is still under discussion. Installation and commissioning of the system are now scheduled for the middle of 1991.

Internal target

The gas jet apparatus is completely assembled. Naval nozzle, skimmers and orifices separating the different stages of the differential pumping system were precisely aligned. The leak test was successful as well as a test with gas load and full pumping speed by seven 1000 ℓ/s–turbopumps. The measured pressures in the different pumping stages were in good accordance to calculated values. The apparatus is now prepared for the transport to its final ring position in the center of the western straight section. The preliminary interaction chamber and adjacent beam pipes are ready as well. In the first tests with a nitrogen jet, scheduled for the coming weeks, it is planned to scan the density profile of the jet by means of electron scattering. The large 4-stage roots blower (3300 ℓ/s pumping speed at 10^{-2} mbar), which is necessary to attain the maximum target density in the order of 10^{14} molecules/cm^2, is in house. Final assembly will be done on its final position on the concrete cover above the ESR as soon as the latter is complete. The control unit of the jet apparatus is connected to the control system via the standard vacuum controller.

Particle and X-Ray Detectors

Two special linear feedthroughs for position sensitive particle detectors, containing vacuum tight stainless steel pockets with 100 μm thick particle windows, are already installed in front of the horizontal beam scrapers in the northern arc of the ESR. Another is going to be mounted in the scraper station of the southern arc. The prototype of a suitable multiwire detector was recently tested with success using 150 MeV/u Ne-ions out of the SIS. The detector can be inserted into the pocket without influencing the ring vacuum and shall be removed during baking out of the vacuum system.

Two Si-Li–X-ray detectors with special supports for the installation in the electron cooler are complete. Similar to the particle detectors and for the same reason, they are separated from the UHV by stainless steel pockets with beryllium windows, allowing the detection of X–ray energies as low as a few keV. A similar X-ray window is provided at the preliminary interaction chamber of the internal target. The windows are still behind schedule, because the welding of the Be-sheets turned out to be somewhat complicated. Nevertheless, X–ray spectra should be available during the first tests with the cooling electron beam and the internal gas jet, at least by using stainless steel windows.

References

[1] G. Moritz, F. Klos, B. Langenbeck, Y. M. Sun, K. Zweig; *Magnetic Field Measurements of the ESR Main Magnets*; this report

[2] K. Beckert, S. Cocher, B. Franzke, U. Schaaf; *Status of the ESR Schottky Diagnosis System*; this report

[3] N. Angert, W. Bourgeois, H. Emig, B. Franzke, A. Kritzer, B. Langenbeck, K. D. Leible, G. Moritz, T. Odenweller, H. Schulte, P. Spädtke, B. H. Wolf; *Status of the Electron Cooler*; this report

[4] P. Spädtke, F. Klos, B. Langenbeck, G. Moritz, K. Zweig; *Magnetic Field Measurements of the Electron Cooler*; this report

[5] T. Odenweller, M. Chen, J. R. Dang, B. Langenbeck, G. Moritz; *A System to Measure Field Harmonics in the Electron Cooler Solenoid*; this report

[6] G. Jöst, K. D. Leible, H. Schulte, P. Spädtke, B. Wolf; *The Linear Test Facility for the Electron Cooler*; this report

[7] P. Spädtke; *Operating Program for the Electron Cooler*; this report

[8] P. Raabe, W. Heinrich, H. L. Hartnagel; *Beam Signal Detection in Stochastic Cooling Systems Using Electrode Array Pickups*; this report

[9] F. Nolden; *Beam Electrode Interactions in Stochastic Cooling*; this report

Status of the Electron Cooler

N.Angert, W.Bourgeois, H.Emig, B.Franzke, A.Kritzer, B.Langenbeck, K.D.Leible,
G.Moritz, T.Odenweller, H.Schulte, P.Spädtke and B.H.Wolf
GSI-Darmstadt

The final assembly of the electron cooler started in November, when all magnet measurements and correction procedures have been finalised. A description of the 320 kV electron cooler was given in a previous report[1] and in ref.2. A sectional view is shown in fig. 1.

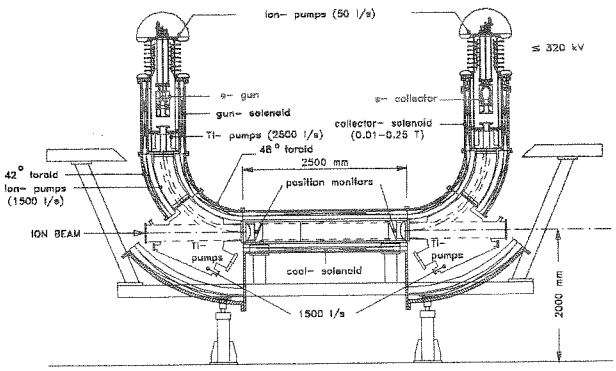


Fig. 1: 320 kV electron cooler for ESR

Magnets: The 3D field mapping of the cooler magnets was rather time consuming. In six different positions of the electron cooler the field was measured. Then field flux and lines from the cathode to the collector were calculated[3] in order to define the path of the electron beam.

For the fine correction of the transversal field errors of the cooling solenoid below $\Delta B / B \; 10^{-3}$a separate field measurement was done. The correction procedure is described elsewhere in this report[4]. Steering coils for gun, collector and cooling sections have been designed and ordered together with the dipole correction coils of the toroidal field.

Gun and Collector: Extensive tests were carried out at the linear test set up[5]. High voltage tests up to 220 kV have been performed without beam. With electron beam the set-up was operated up to 50 kV at 5A. A detailed report is given elsewhere[6].

Vacuum: All vacuum parts are in house and leak proofed. The cooling section is assembled with position monitors and drift tubes and mounted inside the solenoid. The integrated ion pumps and the titanium supplimation pumps are mounted. The production of the drifttubes in the toroid sections was retarded by the delayed field mapping. They will be installed into the vacuum chambers in January 1990. The bake out jackets and the water cooled heat shields are delivered and mounted around the vacuum chambers. A bakeout test at 280° C will be done end of January for the toroid and cooling sections.

Power Supplies and Controls: All power supplies for the high voltage platform were tested at the linear test set-up and controlled by the VAX-computer system. A basic operation program for the cooler was developed and tested. For routine operation of the cooler additional software has to be developed to make the adjustment of the cooler easy, safe and clearly monitored.

Faraday Cage and Installation: The faraday cage was finished in spring. Its screening effect is ≤ 50 dB at doors etc. and < 70 dB in general. The ventilation and dehumidification of the faraday cage are delayed to mid 1990. This will limit the electron energy to 200 keV. The power installation is accomplished and the 50 kW, 320 kV insulating transformer installed with all the rf-filter elements. The high voltage platform is built up. The water installation is ready for the connection of the cooler.

References

[1] N.Angert et al.; Scientific report GSI 88-1, p.379 (1988).

[2] N.Angert et al.; Electron cooling at GSI, Proc. of the First European Part. Acc. Conf., Rome, 1988.

[3] P.Spädtke et al., this scientific report.

[4] T.Odenweller et al., this scientific report.

[5] N.Angert et al., scientific report GSI 89-1, p.396 (1989)

[6] H.Schulte, this scientific report.

[7] P.Spädtke, this scientific report.

Status of the ESR Schottky-Diagnosis-System

K. Beckert, S. Cocher, B. Franzke, U. Schaaf
GSI - Darmstadt

The planned system will allow on-line measurements of normal Schottky spectra (longitudinal and transverse) and of beam transfer functions, yielding information on a lot of beam parameters (revolution frequency and energy of particles, betatron tune and chromaticity, synchrotron frequency and rf-amplitude, emittance and particle distributions) and providing also data on the ring itself (stability limits, wall impedance, field error effects, working line). In the case, that transversely unstable modes should occur an active feedback system will be used to damp these oscillations.

A more detailed description of this complex has already been given elsewhere [1,2]. The present contribution describes only the most important changes which resulted from discussions during the last two years, and summarizes the actual situation.

Based on experiences gained during first Schottky measurements at SIS it has been decided to instal a dedicated pickup in the ESR as soon as possible. This new monitor has a considerable greater length than the position monitors; its coupling impedance will be 50 Ω, and it can be used in the electrostatic mode as well as in the stripline mode. These changes lead to a much higher sensitivity and therefore allow the detection of smaller signals. The design of the monitor has been completed, and it will be manufactured during spring 1990.

To control the electronics at the beam line the possibilities offered by the ESR/SIS control system will be used instead of the formerly planned multiprogrammer unit.

A substantial improvement of the analyzing capacity will be achieved by using the DSA 602, a fast digitizer, which allows the recording of very short transient events with excellent time resolution. The time spectra will then be Fourier transformed and evaluated on a HP9000/340C+ computer equipped with a lot of convenient graphics features. This opens up a completely new group of measurements in addition to the normal spectrum analyzer, the FFT-analyzer and the network-analyzer.

Since it is fairly complicated to satisfy the phase relation in feedback applications for different operation modes by using only one monitor another solution was necessary. A method developed in CERN will be adopted. By applying the signals from two pickups to the kicker, the phase angle of the feedback signal can be varied. The signal levels from the two pickups are individually adjusted with the correct settings obtained from the beam transfer function. To achieve the large necessary bandwidth, the signal travel time between pickups and kicker has to correspond to the time of flight of the particles.

A diagram of the planned equipment is shown in Fig.1 . The above mentioned devices are all available; the necessary software will be written during the next month and years; the required electronics has been developed and ordered and will be available by the end of March 1990.

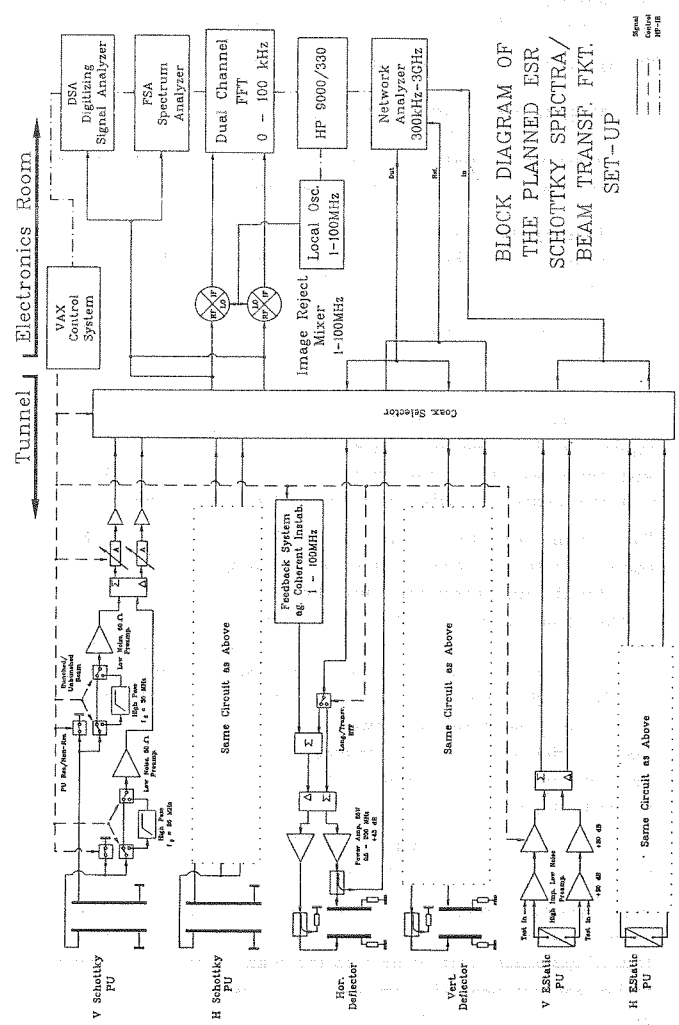


Fig.1 Equipment for Schottky Diagnostics.

References

[1] K.Beckert, B.Franczak,GSI 88-1,p.378

[2] K.Beckert,U.Schaaf,GSI-Nachrichten 12-88,p.16-21

Magnetic Field Measurements for the Electron Cooler

P. Spädtke, F. Klos, B. Langenbeck, G. Moritz, K .Zweig
GSI - Darmstadt

The magnetic field distribution of the electron cooler has been measured using the magnet measuring device described in[1]. For that purpose the cooling solenoid, the toroids and the gun solenoid have been mounted together in a horizontal setup. The correction coils between the solenoid and the toroid, between the 42^0 and 48^0 toroids and the dipole field coils were included in this set-up.

The aim of these measurements were, similar to[2]:

Verifying the quality of the magnetic field.

Tracking the path of the electron beam within the cooler, especially within the fringing field regions.

Finding the correct currents for the different power supplies to produce the homogeneous field along the path of the electron beam.

Field errors — especially in the cooling section — should be detected to be compensated with correction coils.

The specified accuracy (10^{-4} in the cooling section and 10^{-3} in the toroidal sections) require a careful alignement of the probe head with three orthogonal hall probes by autocollimation. Together with the measurements[4] the accuracy has been verified.

Due to time restrictions it was not possible to measure the whole volume for the tracking simulation. To minimize the necessary time for the measurements, only the magnetic field components on the surface of closed volumes have been measured. Typically, these boxes were 2 m long with a cross section of 12 cm × 12 cm. Their location were choosen such to cover all the path of the electron beam. Six main boxes have been measured in this way (gun -, collector-, two toroid and two cooler regions), see Fig. 1. The magnetic field components were measured on each surface in mesh units of 2 cm. Even with these restrictions each of these measurements took about two hours.

Inside these volumes the magnetic field can be calculated, applying the Laplace equation to each magnetic field component[3].

Each measured volume has its own local coordinate system. The transformation matrix was determined from the mechanical location of the cooler with respect to the mapper coordinate system which has not been changed during the measurements. These geodatic measurements have been made by the GSI survey group. Applying the correct transformation the overlap region of adjacent boxes could be found sufficiently well.

If the components of the magnetic field components are known, the field lines can be calculated by simple integration. The field lines has been traced from the gun to the collector, through-out the magnetic system.

It is possible to move the field tubes in the cooling section slightly by changing the current within the toroids. On the other side this would cause a change of the electron beam diameter within this section and should be avoided therefore.

The knowledge of the direction of the field line is essential, because the electrons are bound to these field lines. In case of a low energy electron beam (< 50 keV) we do not need dipole fields within the toroidal section. For higher energies the $v_{\parallel} \times B_{\perp}$ drift can cause heating of the electron beam.

For some of these boxes measurements were done with different currents in different coils, this allow us to calculate the exact current in the toroids and the correction coils to achieve a homogeneous field along the electron beam.

The measured fields can also be used to determine the necessary corrections for the ion beam in the ESR-ring optic (steerer and correction solenoid).

The developement of the correction coils within the cooling system was made with a multipole analysis of the field[4] instead of using these measurements.

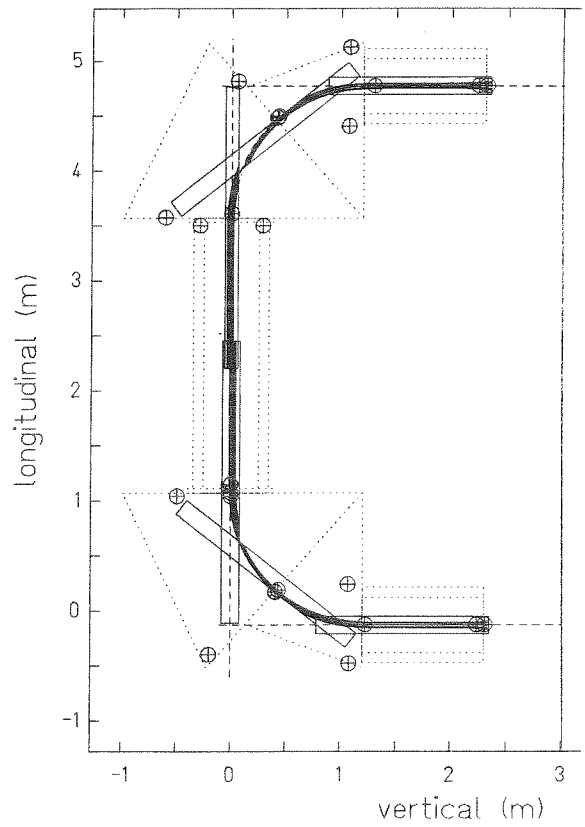


Fig. 1: Arrangement of the boxes (solid lines) within the electron cooler (dotted line). The field lines were calculated without applying the exact transformation.

Literatur

[1] G. Moritz et. al.; Performance of the Three-dimensional Magnet Measuring, GSI Scientific Report 1988, p.217 (1989)

[2] A. Wolf et. al.; CERN, EP Internal Report 84-01.

[3] P. Spädtke and S. Wipf; KOBRA3, GSI-89-09 (1989).

[4] B. Langenbeck et. al.; this report.

A System to Measure Magnetic Field Harmonics in the Electron Cooler Solenoid.

B. Langenbeck, G. Moritz, T. Odenweller; GSI
Dang Jian Rong, IMP Lanzhou, P.R. of China
Chen Miao, SINR Shanghai, P.R. of China

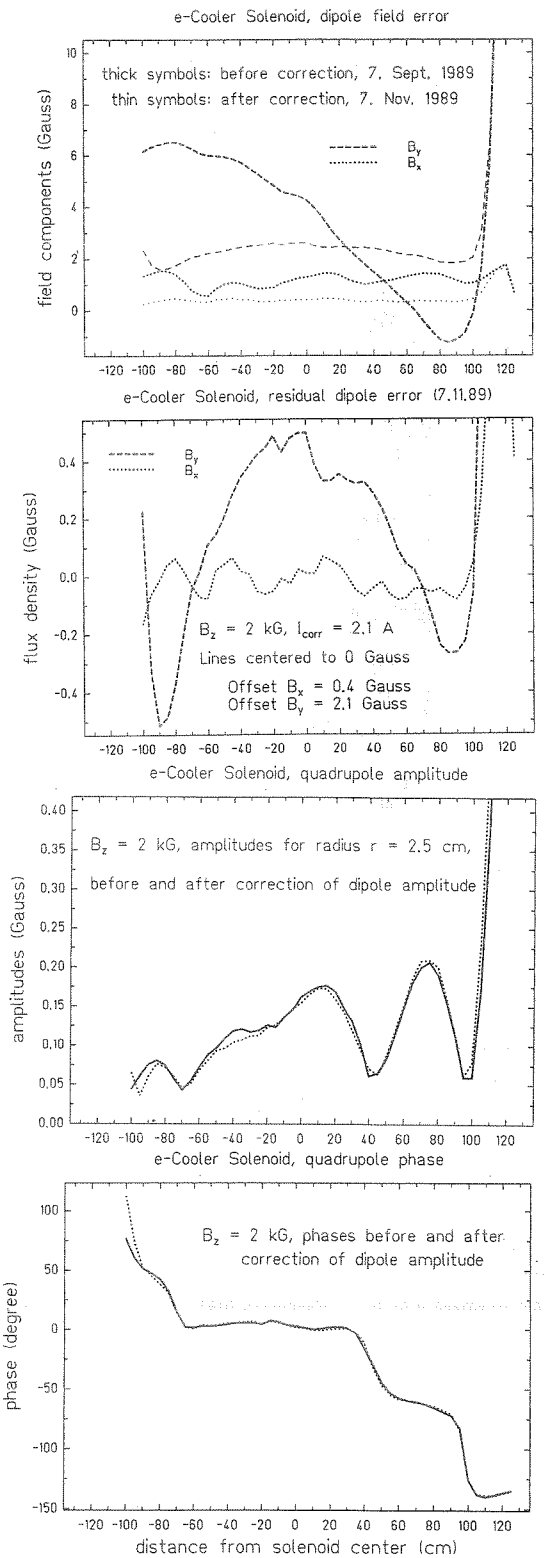
To assure an efficient function of the Electron Cooling device of the ESR[1] tight tolerences were imposed upon the quality of the magnetic field especially of the Cooler Solenoid. Field errors must not be larger than 10^{-4}. But, to keep purchase costs low, it was decided to specify for the manufacturer much weaker tolerances, 10^{-3} to 10^{-2}, and to compensate field errors later with the help of small correcting windings during the field measurements.

For these measurements we prepared a system which allows a determination of the local field harmonics along the axis of the solenoid. The radial field components at each position were determined as a function of the azimuth with the help of a Hall probe, which was moved at a constant radius around the axis. The measured values were submitted to a Fourier Analysis which gave us amplitudes and phases of the harmonics. Knowing these it is possible to eliminate each multipole with the help of a single set of correcting windings (and a single power supply) by choosing the local number of windings and their orientation properly. Details will be given in a GSI Report which is in preparation[2].

A constant value of the Fourier Analysis (A_0), i.e. a radial field component independent from the angle of probe rotation, can have three different reasons. First, it could be due to a variation of the solenoidal field itself along the axis ($B_{rad} \sim dB/dz$). In this case a correction would be necessary if the amplitude is out of tolerances. Alternatively, it can be caused by either an offset of the Hall probe electronic or by a misalignment of the probe, i.e. if it was not carefully aligned perpendicular to the solenoidal field direction. Because a discrimination of the causes is difficult, we decided to rely for the correction of the solenoidal field error on the measurements earlier done with an axially oriented probe[3], which are insensitive to small alignment errors. Nevertheless, Fourier Analysis eliminated two important measurement error sources.

A constant value of the horizontal and/or vertical dipolar field components along the solenoid (dipole components are easily extracted from the amplitude A_1 and phase α_1) is, if present, caused by a small angle between the axis of the solenoid coil and the mechanical axis of the Cooler setup. The latter was used as a reference during alignment of the measurement system. During several measurement runs after dis- and remounts of the Cooler- and measurement setup such fields were reproducible only within ±2 Gauss, which is 0.1% of the longitudinal flux density. We refer this to unavoidable alignment imperfections. The Cooler solenoid will, therefore, contain special dipole coils to steer the field direction.

The following four figures show some results of the measurements and what could be achieved by adding above mentioned correcting windings. As one can see, the horizontal dipole component B_x could be flattened to ±0.1 Gauss (at 2 kG axial flux density), and was stable after dis- and remount. On the other hand, the vertical component was, even after a second correcting measure, reproducible only within ±0.5 Gauss. This we refer to small mechanical deformations of the solenoid when the toroidal sectors were attached to the system. (the Cooler of GSI is built up vertically). The last two figures show the quadrupole field error, which was constant during the manipulations of the system. The relative amplidude is within $\pm 10^{-4}$ inside the good field region. We did, therefore, not attempt a correction. Higher harmonics are negligible, too.



[1] N. Angert et al., Electron Cooling at GSI, Proc. EPAC, Rome (1988)
[2] T. Odenweller
[3] P. Spädtke, this Report, and
J. Hofmann, Beschr. von Korr.-Spulen f. das Axialfeld des Kühlsol., GSI-Studentenpr. 1989

The Linear Test Facility for the Electron Cooler

G. Jöst, K. Leible, H. Schulte, P. Spädtke, B. Wolf
GSI - Darmstadt

To test the gun and the collector of the electron cooler [1] under realistic conditions in advance of the cooler commissioning a linear test facility was assembled from the complete gun and collector section. Both parts were flanged together and mounted vertically on a 3 m high platform, with the gun at the top.

The resulting linear beam path length from gun cathode to the collector pot was approx. 1.6 m and the grounded drift tube in the centre (from main acceleration to deceleration gap) was 70 cm long (Fig.1).

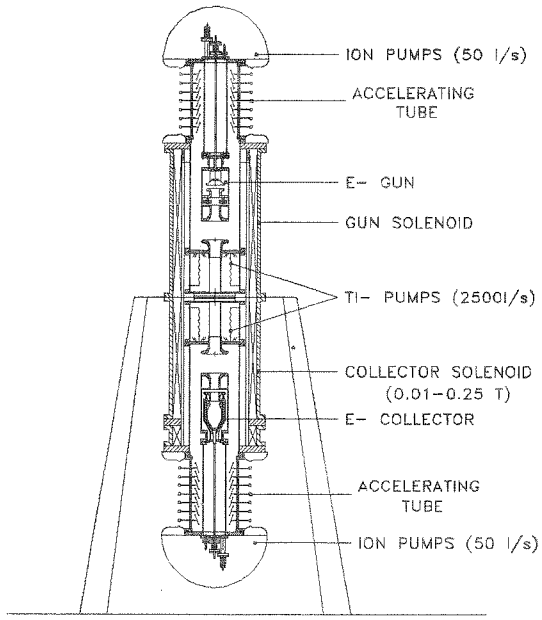


Fig. 1: Test Assembly

We started investigations with magnetic field measurements and pyrometric measurements of the cathode temperature versus heating power. Next we shot a weak (c.100 μA) pilot beam onto a phosphor target to visually confirm the straightness of the beam path. An estimate of the power distribution inside the collector was obtained (with some mA of beam current) by a special five-ring- arrangement in place of the normal inner surface of the collector. We found a fair agreement with previous computer simulations.

Then the gun was equipped with a fresh cathode, the collector was installed and the tank pumped down to a pressure around 10^{-8} mbar by a small turbopump.

There followed a series of extensive high voltage tests (without e-beam): In the beginning serious difficulties were encountered with penning discharges (especially at high magnetic fields: 1-2.5 kG) and it took a tedious period of conditioning and cleanup to reach nominal voltage on all inner electrodes. The gun to ground was tested to 100 kV and the collector was conditioned to 220 kV. The current drain at this voltage was some hundred μA (including the current over the voltage dividing resistor) and lead shrouds were necessary to shield the emanating x-rays.

A thorough bakeout (200^0 C, 30 h) of the whole system then brought us down to the 10^{-9} mbar range, where we startet outgassing of the new cathode. It was again a time-consuming job to keep the pressure below 10^{-7} mbar. After reaching the activation temperature (1200^0 C) of the cathode, the heating power was reduced and the internal titanium pump (2 x 2500 l/s nom.) fired.

The system was then disconnected from the turbopump and with four additional (50 l/s) sputter ion pumps (for noble gas pumping) the pressure dropped to approx. 2 x 10^{-10} mbar which was the base pressure for the following beam experiments.

Although there were no serious problems with the gun or the collector we only slowly increased the beam current from a few milliamps to the ampere range always keeping the pressure below 10^{-8} mbar. With increasing current, degassing of the collector was always less problematic than the gas load from the gun, but normally cleanup was quick and the pressure came down again to some 10^{-10} mbar. Clearly the system showed some sort of conditioning or training: a current level once reached normally could be reproduced the next day within minutes. A longer shutdown period required a more careful startup. Therefore, preceeding and following cooler operation it seems advisable to keep a standby beam of an amp or so running at a voltage between 50 and 100 kV.

The maximum current and voltage level reached at the test stand was 5 A at 50 kV which was close to the limits of our isolation transformer. The gun perveance came out as 1.85 μPerv (1.85 A @ 10 kV anode voltage) compared to a calculated 1.95. At the thermal load of approx. 20 kW the pressure in the collector chamber was well below 5 x 10^{-10} mbar.

One aim of the tests was to look for a loss current to ground. Although there was some doubt if a linear test arrangement could give reliable results concerning collector efficiency it came as a surprise that even at 5 A, the beam induced load to the HV power supply was less than 10 μA (the resolution of the digital amperemeter).

Unfortunately that does not mean that the collector is perfect. We deliberately caused beam reflection by varying the srceen and collector voltage. Thereby the load to the anodes (gun and collector) increased from microamperes to milliampere values (dependent on the magnetic field strength) but loss to ground was not detected. Thus with our electrode geometry (anodes: 60 mm diam.; drift tube: 80 mm diam.) current loss to ground cannot be used to obtain information on collector efficiency.

The current to the screen electrode was always near zero with some indication of a reverse current in the 1 μA range. This could be a hint of an ion current signaling some space charge compensation, though the onset of beam reflection shows that it cannot be of appreciable amount.

In summary, gun and collector seem to work as expected and if the losses are not dramatically worse in the cooler, the gas load can easily be handled by the internal pumps. No information was obtained (or expected) on beam quality, i.e. electron temperature. This must be left to the cooler experiments.

Finally, the test stand has been successfully operated by computer control[2].

References

[1] N. Angert et al.; this report

[2] P. Spädtke; this report

Operating Program for the Electron Cooler

P. Spädtke, GSI - Darmstadt

For the operation of the electron cooler a group of about twenty power supplies must be controlled. These power supplies are from different type and are located on different potentials. However, for the operating they must be seen as one machine with complicate properties. For that purpose a remote control program has been developed. The necessary hardware has been designed at GSI and was described in [1]. The structure of the special hardware arrangement is shown in Fig. 1.

Four different power supply families are involved, which require four control units (SE):

SE 1 controls the HV-power supplies for the drift tubes in the cooling section and within the toroid.

SE 2 controls the power supplies located at the HV-platform (electron gun and collector supplies).

SE 3 controls the HV-power supply itself.

SE 4 controls the power supplies for the magnetic field (solenoid, toroid, correction coils and steerer).

All power supplies on the platform and the high voltage generator itself are linked by fibre optics, which transform the serial MIL-bus from ground to high potential.

The software on the lower level side (EQM's and USR's) was taken from existing software, which was available at GSI. Only a few modifications were necessary, especially for the HVN1000 modules[2]. These modules are designed to make available voltage and current signals simultaneously, as well as providing all the other standard functions.

The high level control software requires a VAX-station, which provides a graphic interface (DEC-windows). The use of this software has two main advantages:

1 It provides the programmer with tools which can be used in the program very easily. These tools are, for example, push buttons, windows, menus or sliders which are set with the help of a pointing device (a mouse).

2 The usage of different programs becomes easier for the operator because the interaction with the program is standarized.

The program itself has the following features:

Automatic start up or shut down of the cooler.

Manual setting of each individual power supply.

Periodical update of the status.

Generating a database for typical settings.

Online display of all important data of the cooler.

The standard operation of the electron cooler, namely to start the machine or to shut it down can be done automatically, as can electron-current or energy changes without interacting with each power supply individually. In these standarized procedures precautions are included, to prevent the incorrect setting of operation parameters.

The archive function provides the option to store (or to restore) a favourable setting.

Nevertheless, the possibility exists to set each power supply seperately. These changes are made either with a slider moved by the mouse or by a increment/decrement button.

First tests of hard- and software have been successful.

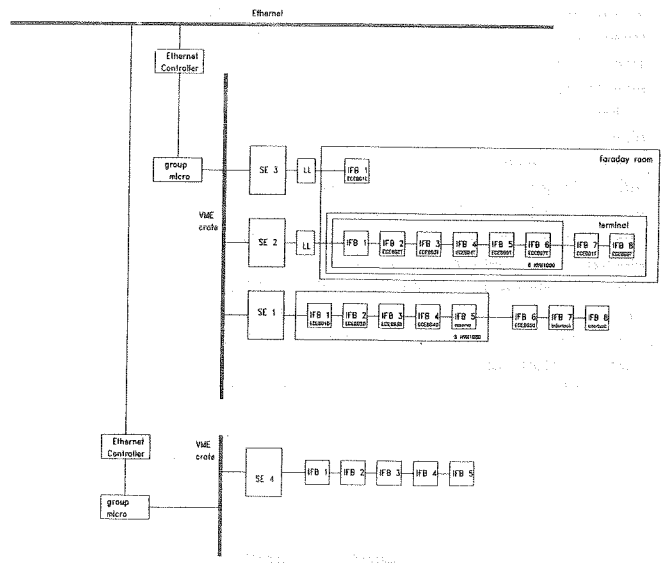


Fig. 1: Structure of the control hardware.

Literatur

[1] R. Steiner; SIS Control System Status, GSI Scientific Report 1986, (GSI 87-1), p.333.

[2] W. Meufels, K. Poppensieker; Computerized Control System for Experiments, GSI Scientific Report 1988, (GSI 89-1), p.337.

Beam Signal Detection in Stochastic Cooling Systems Using Electrode-Array Pickups ^{G}

P. Raabe, W. Heinrich, H.L. Hartnagel
Institut für Hochfrequenztechnik, Technische Hochschule Darmstadt

Introduction

The electrical properties of beam signal-pickup devices are of great interest in optimizing stochastic cooling systems as under construction at ESR [1]. The transfer characteristics, coupling efficiency and sensitivity as functions of beam position and frequency become fundamental parameters of the system design. The need for a compact and broad band ESR coupling device for signal detection in the GHz range led to the arrangement of 4 horizontal electrodes in a rectangular beam pipe , as shown in Fig.1. No vertical electrodes are used because of rf-stacking after stochastic beam cooling. Each electrode works as a quarter wave directional-coupler loop. It forms a parallel-plane transmission line with a characteristic impedance Z_L matching the 50 ohm system outside the pickup device.

Taking into account low relativistic beam velocities ($\beta_{ESR} \approx 0.76$), significant longitudinal electric fields exist in the pickup structure due to the mismatch of beam velocity v_B and phase velocity c_0 of the transmission lines. Deriving the geometrical pickup sensitivity from a two-dimensional electrostatic model (conformal mapping, including the restriction of infinitely thin electrodes) would neglect the resulting dislocation current at high frequencies. Furthermore, in reality the amplitudes of the induced conductive currents become frequency dependent for $v_B < c_0$. In this case, the static approach of calculating the signal coupling has to be replaced by more accurate methods. Therefore, we present here a theoretical investigation of electromagnetic beam interaction with electrode-array pickup devices based on a full-wave analysis in frequency domain.

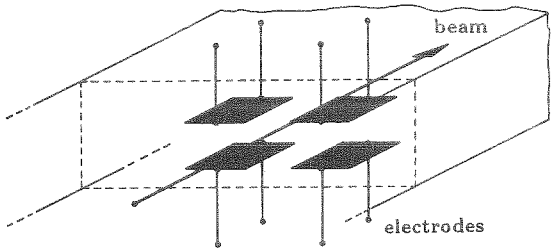


Fig. 1: Electrode-array pickup (principle)

Analysis

Assuming longitudinal beam propagation $\sim exp[j(\omega t - k_{z_B} z)]$ with $k_{z_B} = \omega / v_B$ inside a perfectly conducting pickup structure of infinite length, the resulting electromagnetic field distribution is calculated using a special mode-matching technique [2,3]. The excited fields are analytically expanded into the well-known eigenfunctions of the waveguide structure, which is subdivided into areas of rectangular shape. Integration of the tangential magnetic field yields the conductive currents of electrodes and inner wall as functions of beam position, frequency and pickup geometry.

Due to the proximity of plates, signal cross-talk occures. Thus, the 'beam-free' electrode array can be characterized as a system of coupled transmission lines, requiring an electrical termination network. Matching can be described by the 4×4 matrix equation $[Z]_{(0)} = [Y_{PU}]^{-1} = [Z]_{(l)}$. Here $[Z]_{(0)}$ and $[Z]_{(l)}$ characterize the external impedance networks at the input and output ports of the pickup device. The admittance matrix $[Y_{PU}]$ is derived from the coupling capacitances between the electrodes by means of the solution of the two-dimensional Laplace equation in the transverse plane of the pickup geometry.

Assuming the total conversion of the beam-induced plate currents into TEM-waves at the input and output ports of a pickup device with fixed length l, i.e. neglecting the excitation of higher order waveguide modes, the transfer characteristics and pickup frequency response can then be calculated using common theory of electrical transmission lines.

Results

- Amplitudes of induced plate currents change significantly with varying frequency and beam velocity, see Fig.2.
- At system frequencies (0.9-1.6GHz), dislocation currents in the transverse pickup plane are not negligible for central beam positions, exceeding 10 percent of beam current intensity at f=1.5GHz and $\beta = 0.76$.
- Due to the special arrangement of plates, the geometrical sensitivity curves are nonlinear.
- Separate termination of each pickup line does not correspond to electrical matching due to the spatial proximity of the electrodes and signal cross-talk.
- The transfer characteristics of the electrodes, working as directional couplers as shown in Fig.3, are particularly influenced by the frequency-dependent signal coupling (Fig.2). Maximizing the output signal at mid frequency (1.25GHz) requires pickup electrode lengths l even shorter than $\lambda/(2(1+1/\beta))$.

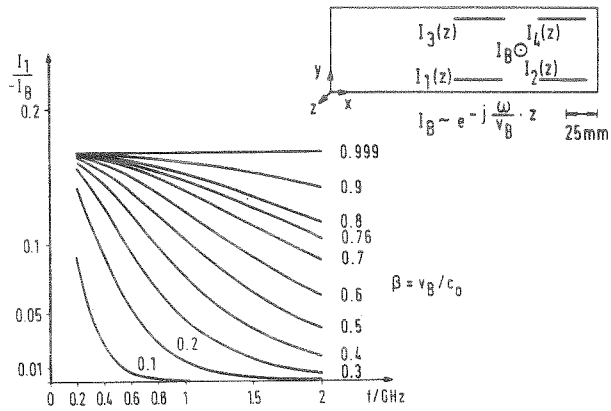


Fig. 2: Signal coupling as a function of frequency

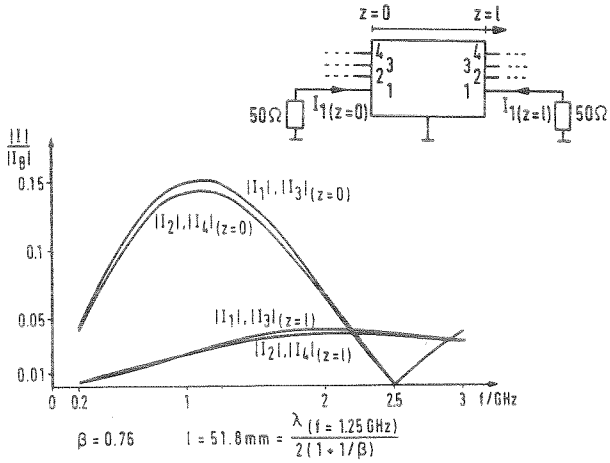


Fig. 3: Frequency response of a quarter-wave pickup device

References

[1] F. Nolden et al., EPAC Rome 1988, p.579
[2] G. Piefke: Feldtheorie III. Bibliograph. Inst., Mannheim 1977
[3] R. Mittra et al., IEEE MTT-28 (1979) 36

Beam-Electrode Interactions in Stochastic Cooling

F. Nolden, GSI - Darmstadt

The beam-electrode interaction in stochastic cooling systems can be deduced completely, once the effective accelerating voltage $U_K(x,z,\Omega)$ along a path with transverse coordinates (x,z) is known, presuming that an rf voltage $V_K(\Omega)$ is applied at the input ports of the device:

$$U_K(x,z,\Omega) = S(x,z,\Omega)V_K(\Omega)$$

The quantity S in this equation is called sensitivity.

The strength of transverse kicks can be uniquely deduced from the longitudinal sensitivity, using the the Panofsky - Wenzel theorem [2]:

$$\Delta x' = \frac{iq}{\Omega p_0}\frac{\partial U_K}{\partial x} = \frac{iv_0}{\Omega}\frac{1}{U_K}\frac{\partial U_K}{\partial x}\frac{\Delta p}{p_0}$$

The transverse kicks are proportional to the *transverse gradient* of the *longitudinal* electric field. They tend to be the less effective the higher the frequency. Furthermore, transverse kicks to an extended beam are necessarily accompanied by longitudinal kicks of varying strength, usually largest at the beam edges. For example, with $v_0 = 0.75c$ and a frequency of 1 GHz, a transverse kick of 3.6 mrad in the beam center leads to a momentum kick of 10^{-3} at a beam radius of 1 cm. There is a phase shift of 90^0 beween the transverse and momentum kicks.

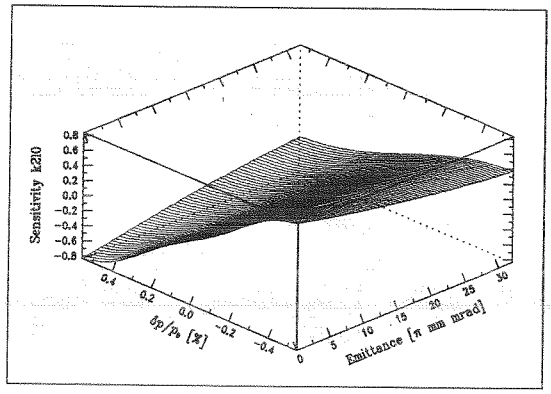
The reciprocity theorem [1] guarantees that pick-ups and kickers of equal geometry can be described by means of the same sensitivity. Given a longitudinal beam current density j_s in the device, the voltage V_P at the output port is

$$V_P(\Omega) = -\frac{Z}{2}\int dx\,dz S(x,z,\Omega)j_s(x,z,\Omega)$$

In order to simplify the discussion, let us now assume zero vertical emittance. The strength of the signal at the output ports of a pick-up depends on both the betatron amplitudes and on the form of the sensitivity S. Up to a phase, the signal due to a single particle is

$$\frac{q\omega Z}{2}\sum_{m=-\infty}^{+\infty}\sum_{l_x=-\infty}^{+\infty}\bar{S}^{l_x}(x_\beta^{\max},x_\delta,\Omega)\,\delta\left(\Omega-(m+l_xQ_x)\,\omega\right)$$

where ω is the particle revolution frequency, and Q_x is the betatron tune.



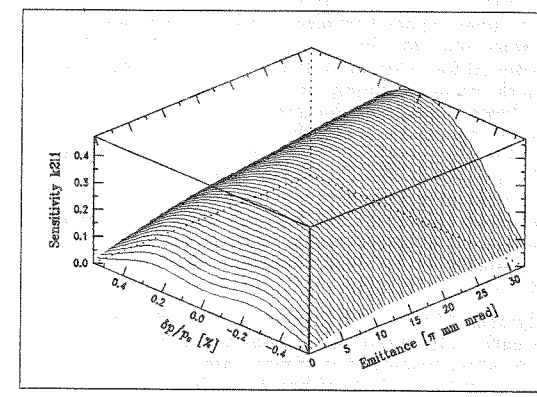
Midband sensitivity S^0 of ESR dipole electrode (zero order sideband or momentum signal)

The sensitivity coefficients $\bar{S}$ depend on the shift x_δ of the closed orbit due to the dispersion D and on the maximum betatron amplitude $x_\beta^{\max}$. They can be evaluated from the horizontal Fourier transform $S(k_x,\Omega)$ of S in two steps: First, calculate the coefficients [1]

$$S^{l_x}(x_\beta^{\max},x_\delta,\Omega) = \int\frac{dk_x}{2\pi}S(k_x,\Omega)J_{l_x}\left(k_x x_\beta^{\max}\right)e^{ik_x x_\delta}$$

These are related to derivatives of S which are averaged over the range of betatron oscillations. With small betatron oscillations, they are approximately given by

$$S^{l_x}(x_\beta^{\max},x_\delta,\Omega) \approx \frac{\left(x_\beta^{\max}\right)^{l_x}}{(2i)^{l_x}l_x!}\frac{\partial^{l_x}}{\partial x^{l_x}}S(x,z,\Omega)\Big|_{x=x_\delta,z=0}$$



Midband sensitivity S^1 of ESR dipole electrode (first order sideband or transverse signal)

However, it has turned out not to be sufficient to calculate the response at specific sidebands by just performing a *spatial* average. Indeed, the betatron motion makes the *times of arrival* at the electrodes oscillate. The amplitude τ of these oscillations is

$$\tau = \frac{Dx_\beta^{\max}}{v_0\beta_x}$$

if the slopes of the beta and dispersion functions are negligible. It plays a role if one cools at sufficiently high frequencies. Then, the effective sensitivities are given by

$$\bar{S}^{l_x} = \sum_{r=-\infty}^{\infty} i^r J_r(\Omega\tau)S^{l_x-r}(x_\beta^{\max},x_\delta,\Omega)$$

Recently, a field theoretical model for our electrodes has been designed leading to an improved understanding of our electrode sensitivities, particularly in the frequency domain [3].

If S is sufficiently linear, the higher order sidebands with $|l_x| > 1$ do not play a significant role for cooling. However, in the ESR with its excellent signal to noise ratio with very heavy ions, we expect to see second order sidebands in the Schottky spectra and use them for diagnostic purposes.

References

[1] J. Bisognano, C. Leemann, in Physics of High Energy Accelerators, Fermilab School 1981, AIP Conf. Proc. 87 (1982)

[2] G. Lambertson, in Physics of High Energy Accelerators, SLAC Summer School 1985, Fermilab Summer School 1984, AIP Conf. Proc. 153

[3] P. Raabe, H.G. Hartnagel, W. Heinrich, this report

Filamentation of Phase Space and Coherent Noise

I. Hofmann
GSI Darmstadt

Injection of a bunched beam into a storage ring leads to the formation of filaments in longitudinal phase space, if the beam is allowed to coast freely. It is generally assumed that this microscopic filamentary structure can be described after some time by a continuous, smoothely varying distribution function. The question is of interest how this transformation occurs in reality. This problem is also related to Liouville's theorem, which states that the area actually covered in (here the longitudinal) phase space remains constant. Obviously any kind of longitudinal instability, like the microwave instability, would disintegrate the ordered filamentary structure. We suggest, however, another mechanism for breakup of filamentation, which works even if the beam current is below the microwave threshold. The mechanism presented here is self-amplification of noise due to electrostatic coupling of space charge waves on neighbouring filaments. At saturation this leads to phase space turbulence, which eventually is washed out after some time by phase mixing. The result of this turbulence are coherent fluctuations, which can cause strong coherent signals within the usual incoherent Schottky band. The momentum width of the beam remains unchanged, unless there is a simultaneously appearing microwave instability, since this unstable process only affects the microscopic structure of the phase space distribution.

The process is closely related to the two-stream or multiple-stream instability known in plasma physics for a plasma made up of individual beams/1/. We have analyzed the dispersion relation of a somewhat idealized system of filaments and compared it with more realistic results from computer simulation with a particle-in-cell code/2/.

Analytical Model of Filament Perturbations

After sufficiently many revolutions the local picture of the beam in momentum space is that of many almost parallel filaments originating from the individual bunches. The width of a filament and its distance to the next neighbour is shrinking with time. We simplify this picture by assuming that all filaments are identical and separated by equal momemtum gaps. Moreover, we ignore the coherent momentum variation over the whole length of a filament for the analytical model. This is justified after sufficiently many revolutions when the momentum variation of a filament over a characteristic wavelength of perturbation and growth time is negligible.

Such a stationary pattern of M filaments can be described by a distribution function of longitudinal velocities (in the moving frame)

$$f_0(v) = \frac{n_0}{M} \sum_{j=1}^{M} \delta(v - v_j) \qquad (1)$$

where n_0 is the total line density. The number of filaments (M) at some location, i.e. the bunch overlap, is given by the ratio of debunched length l over initial length: $M = l/l_0$. Note that l is given by the time T that is allowed for debunching (ignoring the initial length): $l = \Delta_0 T$ with Δ_0 the intitial total velocity spread related to the momentum spread according to: $\Delta_0/2 \equiv \Delta v = \beta c \eta \Delta p/p$.

We have considered a perturbed distribution function $f(v,z,t) = f_0 + f_1$ satisfying Vlasov's equation. For the perturbation we have assumed a plane wave dependence $e^{i(kz-\omega t)}$, linearized Vlasov's equation and solved the resulting equation for the distribution of Eq.1 with the appropriate Poisson equations/2/. By solving the resulting dispersion relation we have found that instability occurs (i.e. $\mathrm{Im}\omega > 0$) if the number of filaments exceeds a threshold given by

$$M_{thr} = \frac{\Delta_0^2}{\omega_p^2 \eta \pi^2 R_{beam}^2 g/4} \qquad (2)$$

with ω_p the plasma frequency and $g = 1 + 2ln R_{pipe}/R_{beam}$.

Computer Simulation

We have used the particle-in-cell simulation code SCOP-RZ /3/, which traces particles in 6d phase space and solves Poisson's equation in rotational symmetry (r,z) with infinite conductivity boundary conditions on a cylindrical pipe. For the solution of Poisson's equation a density is calculated on a mesh in r,z with 39x512 nodes. The simulation is performed with 32.000 particles representing a beam sample of a given length, which is assumed as periodically continued over the circumference of the ring.

The initial configuration (Fig.1) consists of equally spaced bunches (i.e. a single turn injection) of length equal to 3 times the pipe diameter and radius 1/3 of the pipe diameter. An important quantity is the initial intensity and momentum width of the bunches. In our example the intensity was chosen so high that a considerable momentum blow up occurs during debunching (after the first frame). We have used scaled units, which can be easily descaled to real units in the following example: if we interpret all lengths in Fig.1 in centimeters and time units in microseconds , the injected momemtum spread is $\pm 2 * 10^{-3}$ for $\beta = 0.023$.

For our example we have the analytical estimate $M_{thr} \approx 4$. For the simulation it is noted from Fig.1 that the first evidence for an instability appears in the frame at $T = 1500$, where about twice as many filaments exist as predicted analytically for the threshold. Hence, there is good agreement. The instability has started from the central filaments in velocity space, which is not surprising, since they are somewhat more intense than the outer ones. In the final frame all filamentary structure is completely broken up into a coarse-grained phase space distribution. At this point coherent fluctuations of density are still considerable, which should be observable by strong coherent Schottky signals ("pseudo-Schottky noise/4/.

References

1.Th.H.Stix, "The Theory of Plasma Waves", McGraw- Hill, New York, 1963

2.I.Hofmann, GSI preprint GSI-89-32, to be published in Part. Acc.(1990)

3.I.Hofmann and I.Bozsik, Proc. of the Symp. on Accelerator Aspects of Heavy Ion Fusion, GSI Darmstadt, 1982, p.181 (1982)

4.D.Boussard in Proc. CERN Accelerator School, Oxford, 1985, p.416 and private communication

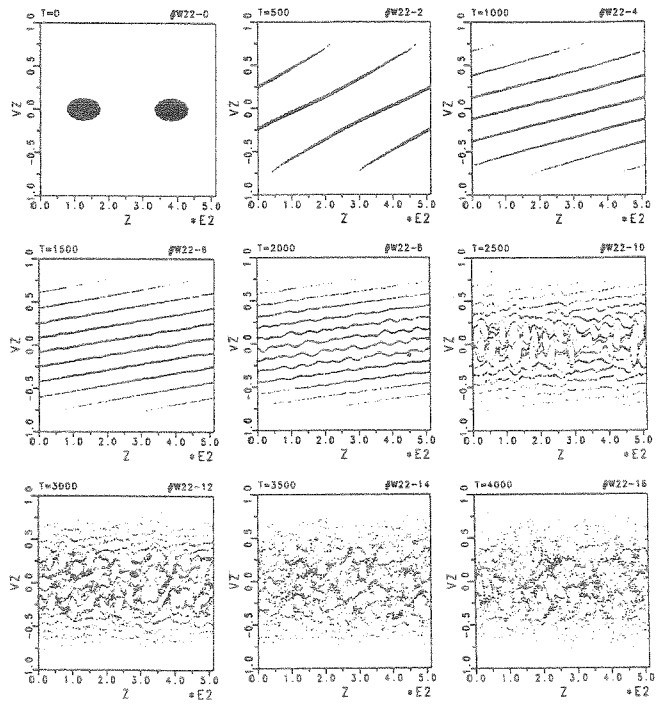


Fig.1 Computer simulation of debunching (space charge dominated) with filamentation instability and development of phase space turbulence. Frames shown are projections into longitudinal phase space at subsequent time steps

Observation of a Dip in the Momentum Distribution of a Coasting Beam

I. Hofmann
GSI Darmstadt

A dip in the momentum distribution of a stored ion beam may appear in processes of resonant removal of particles from a part of momentum space or from the beam as a whole. This might occur during extraction by a nonlinearity (via the chromaticity), laser cooling or dielectronic recombination in the electron cooling section. Such a dip would become unstable, if it could be produced in a sufficiently short time. In this case an exponentially growing coherent oscillation appears at the frequency corresponding to the dip, which has the effect of filling the dip until it is stable. In the case of a stable dip it is interesting to note that it leads to anomalous behaviour of the Schottky power spectrum, which will be shown by numerical examples.

Analytical Solution for a Dip-Distribution

For orientation we present a simple analytical model starting from the well-known dispersion relation /1/ for the frequency ω of longitudinal electrostatic modes at harmonic p. For a distribution function of single particle frequencies, $g_0(\Omega)$, it can be written as:

$$1 + i\frac{I\eta eZ}{Am_pc^2\gamma\beta^2}Z_\parallel \int_{-\infty}^{\infty} \frac{\partial g_0(\Omega)/\partial\Omega}{\omega - p\Omega} d\Omega = 0 \qquad (1)$$

It is easiest to take for g_0 a piecewise constant function. Such a function has no Landau damping, hence a resistive part in the coupling impedance always leads to instability. This makes the constant distribution somewhat unfavorable, if one is comparing its stability threshold with that of smooth distributions. As we are only interested in approximate expressions for the destabilizing effect of a dip (ignoring any resistive effects) with rather sharp edges, we limit the evaluation to such a piecewise constant function. We assume the distribution of frequencies has a total width of Δ around the central frequency Ω_0, with a small dip of width δ centered at the dip frequency Ω_g. In this case Eq.1 can be solved analytically. In the limit of small dip width the two pairs of eigenfrequencies are:
$\omega_{1,2} = p\Omega_0 \pm p\frac{\Delta}{2}(1+P)^{1/2}$, which is not affected by the dip in lowest order, and

$$\omega_{3,4} = p\Omega_g \pm p\frac{\Delta}{2}\left\{\frac{\delta^2}{\Delta^2} - \frac{\delta/\Delta}{P^{-1} + (1 - 4(\Omega_g - \Omega_0)^2/\Delta^2)^{-1}}\right\}^{1/2} \qquad (2)$$

For convenience we have introduced a dimensionless "intensity parameter" $P \equiv -i\frac{I\eta eZ\Omega_0^2}{2\pi Am_pc^2\gamma\beta^2(\Delta/2)^2}\frac{Z_\parallel}{p}$. It is helpful here to note the relationship of P with the Keil-Schnell threshold for the microwave instability. By keeping in mind that $\Delta/\Omega_0 = -\eta\Delta p/p$ we readily see from Ref.2 that this threshold is given by $|P| = 0.5$. The second pair of solutions is responsible for the dip instability, if the term in the square root is negative. Assuming that the dip is close to the center of the distribution we can simply write this criterion as

$$\frac{\delta}{\Delta} < \frac{P}{P+1} \qquad (3)$$

We conclude that the dip is always unstable, if it is small. In the high-intensity limit (i.e. close to the Keil-Schnell threshold with $P \approx 1$) practically any dip is unstable. In the low-intensity limit ($P << 1$) only dips with $\delta/\Delta < P$ are unstable.

Anomalous Schottky spectrum for a dip

In this section we show the numerical results for a Gaussian momentum distribution with a dip, also of Gaussian shape, which we assume for convenience at the center of the main distribution. We have found that for the Gaussian dip the result depends on the depth of the dip. In figs.1-2 we show the results for variable intensity and depth of the dip. We note that the current in the example of fig.2 (0.4 emA) is still about an order of magnitude below the Keil-Schnell threshold for $\Delta p/p = 10^{-4}$. Is is noted that for the higher density of fig.2 a dip in the momentum distribution is reflected by a peak in the Schottky spectrum. This anomalous behaviour can be related to a shrinking of the stability domain due to the dip. At the boundary of stability Landau damping is changed to anti-damping due to a reversal of the sign of the gradients of the distribution function, which leads to the above described dip instability; on the stable side it leads to enhanced fluctuation power. If the dip goes to zero, the Schottky peak disappears since there are no particles at this frequency to produce noise. We conclude that this effect is important for diagnozing resonant removal of particles.

References:
1. V.K.Neil and A.M.Sessler, Rev. Sci. Instr. 36, 429, (1965)
2. G.Guignard, CERN 77-10 (1977)

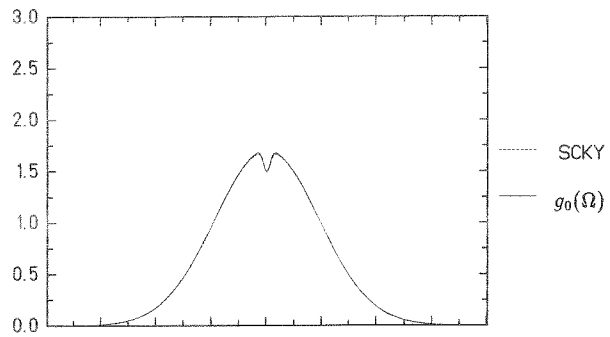


Fig.1 Momentum distribution and Schottky power for small dip in beam: Ne^{10+}, 100 MeV/u, $\Delta p/p = 10^{-4}$, I=10eμA

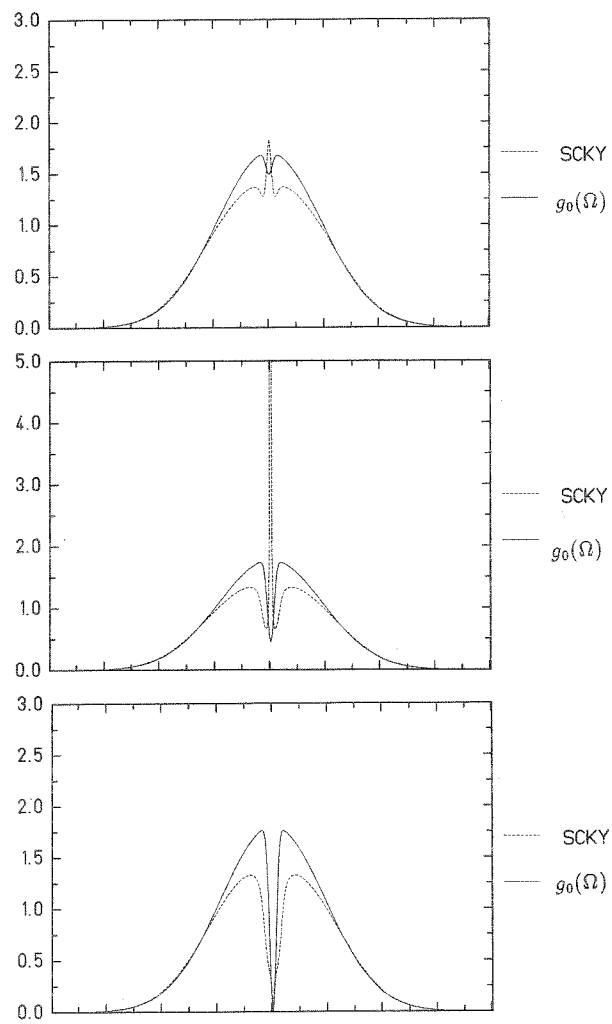


Fig.2 Variable dip depth with current increased to I=400eμA

A Method to Determine Momentum Distribution and Impedance for Cooled Beams

I. Hofmann
GSI Darmstadt
A.N. Talysin and P.R. Zenkevich
ITEP Moscow

For beams with low phase space density the distribution function is given directly by the Schottky noise spectrum. It has been shown that for cooled beams the beam transfer function (BTF) and Schottky spectra lead to the correct distribution function only if the coupling impedance is known with some accuracy (this is discussed along with further references in Ref.1). The required accuracy is the larger the closer the beam is to its limit of stability, in which case the form of the Schottky spectrum is dominated by the presence of coherent signals. Here we present a procedure, which can be implemented on-line for evaluation of measured data. The BTF is a complex quantity (amplitude and phase) which contains information about the distribution function as well as the coupling impedance and is defined as inverse response:

$$\frac{1}{r_{\|}} = i\frac{\beta^2\gamma Amc^2/e}{\eta q I}\{\int \frac{\partial\Psi_0/\partial\omega}{\Omega - p\omega}d\omega\}^{-1} + Z_{\|} \qquad (1)$$

The imaginary part of the dispersion integral D in Eq.1 is identical to $\frac{\pi}{p}\partial\Psi_0/\partial\omega$. We could then calculate Ψ_0 from the measured $r_{\|}$ according to Eq.1 if $Z_{\|}$ were known. This problem of both quantities unknown can be solved by using the Schottky spectrum as additional information. One starts from a guessed value for $Z_{\|}$, calculates the distribution function from Im D and compares it with the distribution function obtained from the Schottky power spectrum (as discussed in Ref.1)

$$P = \Psi_0/|\epsilon|^2 \qquad (2)$$

The required dielectric function is calculated from the dispersion integral:

$$\epsilon = 1 - iZ_{\|}\frac{\eta q I}{\beta^2\gamma Amc^2/e}\int \frac{\partial\Psi_0/\partial\omega}{\Omega - p\omega}d\omega \qquad (3)$$

The true impedance is found by searching the minimum of

$$I = \int |\Psi_{schottky} - \Psi_{btf}|^2 d\omega \qquad (4)$$

Numerical results

We have written a computer program which first creates the "measured" BTF and Schottky power from an input distribution and impedance. For the example of Fig.1 we have chosen a Gaussian distribution cooled to such a low width that the stability diagram given by $\epsilon = 0$ (where the factor in front of the integral in Eq.3 is used as normalized impedance) is noticeably shifted by the impedance. The latter is assumed to have a relatively large resistive part ($ReZ = -1/4ImZ$). In real quantities this could be, for example, 13 emA of Ne^{10+} at 100 MeV/u, $\Delta p/p = 10^{-4}$ with ImZ= 1 kΩ, ReZ=250Ω. The relatively high phase space density is also reflected by a substantial suppression of the Schottky power spectrum shown in Fig.1. The variational procedure given by Eq.4 is shown in Fig.2, where we have plotted the functional $I(ReZ, ImZ)$ along horizontal and vertical lines going through the true value of the impedance. It is seen that the descent to the minimum is very steep along the Re Z as well as the Im Z direction. It must be noted, however, that a large statistical error in the Schottky spectra smears out the sharp minimum. We have tested this assuming 5 percent relative statistical error on the Schottky power and found that the minimum is still sufficiently well pronounced to be found (Fig.3). We conclude that the method is not disturbed by errors in the Schottky measurement of a few percent.

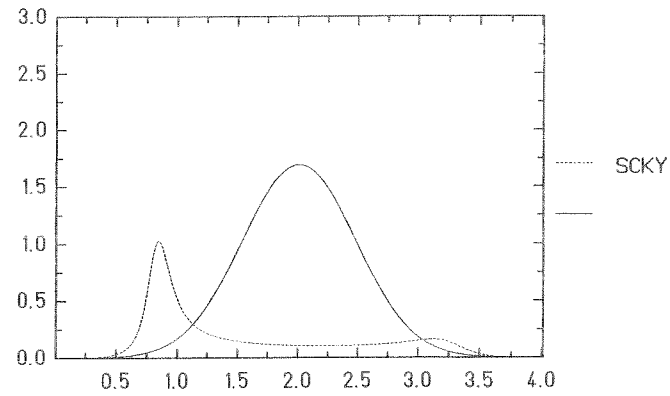


Fig.1 Distribution function and Schottky power

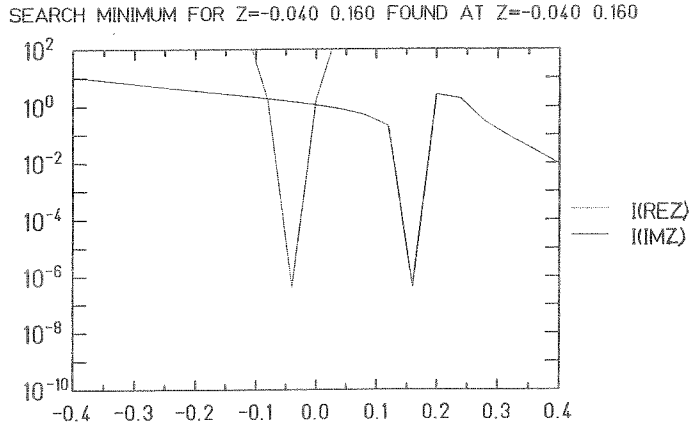


Fig.2 Minimum search with BTF and Schottky power evaluation

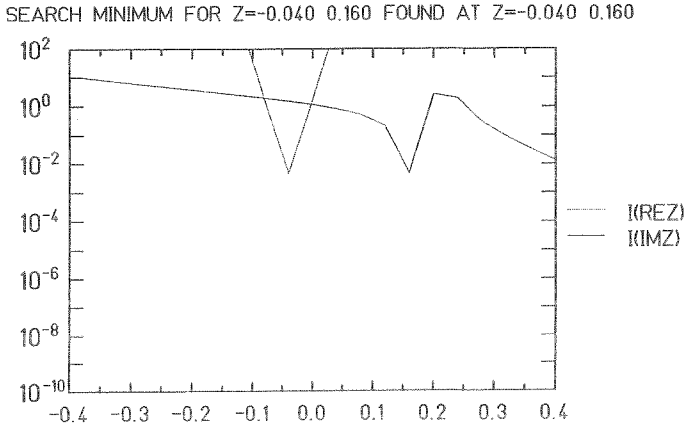


Fig.3 Same with ±5% statistical error added to true Schottky power. Note that the minimum search is well-defined if it is started from the side of vanishing impedance.

References

1. S.Cocher, I.Hofmann, to be published in Particle Accelerators, preprint GSI-89-61

Harmonic Dynamics of the Chain of Charged Disks

V.V. Avilov[1] and I. Hofmann
GSI Darmstadt
[1]Humboldt-fellow, permanent address: Landau Institute, Moscow

Theoretical consideration of a highly cooled heavy-ion beam predicts a transition to one-dimensional crystal structure if the number of particles in the machine is below a certain threshold[1]. From the dynamics of electron and laser cooling it is more obvious to expect extremely low longitudinal temperature, whereas the transverse might be much higher[2]. For this case it proposed here to use the model of charged disks rather than points for describibing the dynamical properties of the system. For this model it is also necessary that the transverse oscillation frequencies are much larger than the longitudinal ones. This is satisfied, if the period d of a one-dimensional lattice is much larger than the critical value corresponding to the loss of stability of a simple chain[1]. This rather anharmonic system may be described within the method of self-consisted phonon approximation[3]. In the description of a slow system (longitudinal phonons) we can can use the potential averaged over the motion of a fast subsystem (transversal motion). The effective potential of the transversal motion is $U_b = m\omega_b^2 r^2/2$ (where m is the ion mass, the betatron frequency ω_b which determines of the intensity of the external confining focusing force is assumed to be independent of the longitudinal coordinate z). The probability to find a particle at the distance r from the axis of the beam give us the charge destribution function at the coordinate r for every particle (Z is the ion charge)

$$\rho(r) = \frac{Zm\omega_b^2 \exp(-U_b(r)/T_i)}{2\pi T_i} \qquad (1)$$

if the charge density of the individual (harmonic) oscillator is averaged over a Boltzmann enscamble. Hence for the description of longitudinal phonons we can use the model of a chain of charged disks in wich the radial density of charges corresponds to Eq. (1). The effective potential of interaction $U(z)$ of two such disks can be evaluated by using the Fourier transform technique or explicitly in terms of the error function (see Fig.1)

$$U(z) = \frac{Z^2\pi^{1/2}}{2A} \exp(\frac{z^2}{4A^2}) \operatorname{erfc}(\frac{z}{2A}). \qquad (2)$$

where A is the effective amplitude of transversal oscillations $A = (T_i/m)^{1/2}/\omega_b$.

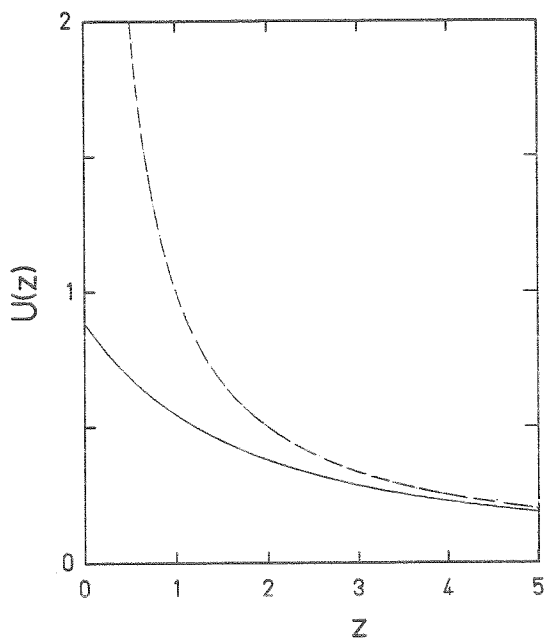


Fig.1 The potential of interaction of two charged disks (solid line) and two charged points (dashed line).

The dispersion relation for the phonon frequency $\omega(q)$ in a one-dimensional crystal with period d is

$$\omega^2(q) = \frac{2Z^2}{mA^3} \sum_{l=1}^{\infty} (1 - \cos(qld)) U''(ld) \exp(-ld/D) , \qquad (3)$$

where $\exp(-ld/D)$ describes the effective screening of the long-range Coulomb interaction within a metallic tube of the storage ring and D is of the order of the diameter of this tube. From Eq.(2) we have

$$\omega^2(q) = \frac{\pi^{1/2}Z^2}{4mA^3} \sum_{l=1}^{\infty} (1 - \cos(qdl))$$

$$((l\zeta)^2 \exp((l\zeta)^2/4) \operatorname{erfc}(l\zeta/2) - l\zeta/4) \exp(-ld/D) =$$

$$= \frac{Z^2}{mA^3} \int_0^{\infty} k^2 \exp(-k^2) \left(\frac{2}{\exp(k\zeta + d/D) - 1} - \right.$$

$$\left. - \frac{1}{\exp(k\zeta + d/D + iqd) - 1} - \frac{1}{\exp(k\zeta + d/D - iqd) - 1}\right) dk , \qquad (4)$$

where $\zeta = d/A$. Some typical profiles of $\omega(q)$ are shown on Fig.2. The characteristic feature of these profiles is that there exists at small q some linear dispersion region with $\omega \approx c_s q$, where the "sound velocity"

$$c_s = Z(\ln(D/A)/(md))^{1/2} . \qquad (5)$$

Outside this interval $\omega(q)$ reaches the saturation value $\omega_{pl} = (Z/A)/(2md)^{1/2}$. These two pecularities of the phonon spectrum also determine the spectrum of Schottky noise signal[4]. The measurements of the splitting of the two Brillouin peaks $\Delta F/F$ give us the value of $c_s = (\Delta F/F)(v_0/2)$,where v_0 is the velocity of the beam. The Eq.(5) gives us the possibility to determine A and hence T_i .These measurements are possible, in principle, at frequencies of the order of some MHz.

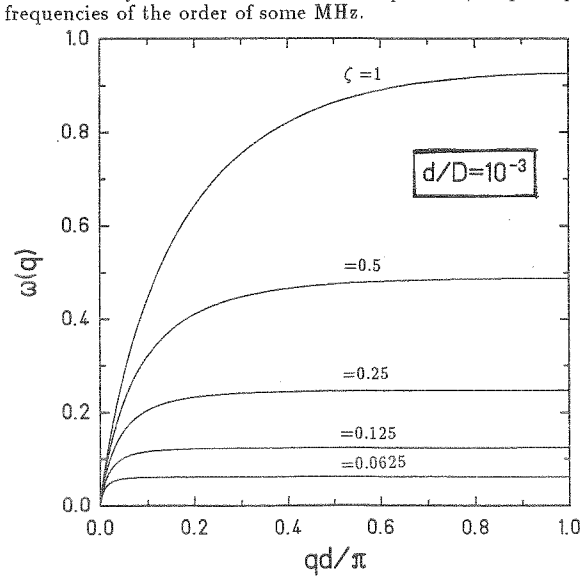


Fig.2 Typical profiles of $\omega(q)$ in units of $Z/(md^3)^{1/2}$ for some values of $\zeta = d/A$.

References
I. Hofmann, J. Struckmeier, Proc. Workshop on Crystalline Ion Beams, Eds. R.W.Hasse, I.Hofmann, D.Liesen, 1988, GSI-89-10
I. Hofmann, J. Struckmeier, S. Cocher, Proc. European Part. Accel. Conf., Rome, 1988, p.201
N.S. Gillis, N.R. Werthamer, T.R. Koehler, Phys. Rev., 165, N3, 951 (1968)
S. Chattopadhay, CERN 84-11 (1984)

Large Amplitude Vibrations of the Coulomb String[G]

Rainer W. Hasse - GSI Darmstadt

Static calculations[1] showed that the possible existence of crystalline structures of a highly cooled heavy-ion beam in a storage ring hinges crucially on the particle density and on the final beam temperature. Molecular dynamics calculations reveiled that full crystallization is achieved at[2] $\Gamma \approx 170$, where Γ is the ratio of Coulomb energy to temperature but an ordered liquid state exists already at[1] $\Gamma \approx 10$. However, at low particle densities, one expects that the particles under the influence of a harmonic transverse confining force align along the beam axis to form a Coulomb string even at higher temperature.

Here we study the stability of the Coulomb string under large amplitude longitudinal (β) and transverse (ρ) vibrations where at rest particles are spaced by the distance d. In the following, lengths are measured in units of d, frequencies in units of

$$\sqrt{\frac{Z^2e^2}{md^3}} = \frac{Z \cdot 370}{(d/\mu\mathrm{m})^{3/2}}\ \mathrm{MHz},$$

where Ze, m are the charge and mass of an ion, and energies per particle in units of

$$\frac{Z^2e^2}{d} = \frac{Z^2 \cdot 1.44}{(d/\mu\mathrm{m})}\ \mathrm{meV}.$$

The particle density is then characterized by the parameter $\lambda = (3/2\omega_\beta)^{1/3}$ as a function of the betatron-frequency ω_β, or of the plasma frequency $\omega_p = \sqrt{2}\,\omega_\beta$.

The modes of vibration can be classified by a mode number M or wave number $q = 2\pi/M$ and the parity Π according to cosine- or sine-like vibrations in longitudinal (z) or transverse (r) directions,

$$z_j = j + \beta \cdot \left\{ \begin{matrix} \cos \\ \sin \end{matrix} \right\}(jq)\ ,$$
$$r_j = \rho \cdot \left\{ \begin{matrix} \cos \\ \sin \end{matrix} \right\}(jq) \quad \text{for} \quad \Pi = \left\{ \begin{matrix} + \\ - \end{matrix} \right\}. \qquad (1)$$

For example, $M = 1^+$ is a pure translation, for $M = 1^-$ and 2^- all particles are at rest and $M = 2^+$ is the lowest interisting mode, the zigzag mode. According to the symmetry of q in eq.(1), the intervals $0 \le q \le \pi$ or $2 \le M \le \infty$ suffice. The longitudinal amplitude is limited due to the fact that countermoving particles touch. For instance,

$$\beta_{2^+}^{\max} = 1/2, \quad \beta_{M\to\infty}^{\max} = 1/q,$$

but the transverse amplitude ρ, of course, is unlimited.

The Coulomb potential generated by the particles reads

$$\Phi_{M^\Pi}(\beta,\rho) = \frac{3\mu^*}{4\lambda^3} + \frac{2}{P}\sum_{i=1}^{\infty}\sum_{j=1}^{P}\left(\left[(i-\beta S)^2 + \rho^2 S^2\right]^{-1/2} - 1/i\right),$$

where the summation extends only over even numbers i+j. Here

$$S = 2\sin(iq/2)\cdot\left\{ \begin{matrix} \cos \\ \sin \end{matrix} \right\}(jq/2) \quad \text{for} \quad \Pi = \left\{ \begin{matrix} + \\ - \end{matrix} \right\}$$

and P is the period of the sublattice in z-direction which is finite if the mode $M = P/Q$ is a rational number of two relative primes P, Q. The effective mass is given by

$$\mu^* = \frac{1}{P}\sum_{j=1}^{P}\left\{ \begin{matrix} \cos^2 \\ \sin^2 \end{matrix} \right\}(jq) = \left\{ \begin{matrix} 0 \\ 1 \\ 1/2 \end{matrix} \right\} \quad \text{for} \quad M^\Pi = \left\{ \begin{matrix} 2^- \\ 2^+ \\ \text{else} \end{matrix} \right\}.$$

The frequencies in this potential can be obtained from

$$\omega = \frac{\pi}{\sqrt{2}}\left[\int_0^x \mathrm{d}x'\left(\Phi(x) - \Phi(x')\right)^{-1/2}\right]^{-1},$$

where $x = \beta, \rho = 0$ for longitudinal and $x = \rho, \beta = 0$ for transverse vibrations.

In the small amplitude (harmonic) limit the eigenfrequencies are degenerate in parity. The longitudinal frequencies read[3]

$$\omega_{\|M^\pm} = \sqrt{8\sum_{j=1}^{\infty}(\sin^2 jq/2)/j^3}.$$

For instance,

$$\omega_{\|2^\pm} = \sqrt{7\zeta(3)}, \quad \omega_{\|M\to\infty} = q\sqrt{2\log(1/q)},$$

where $\zeta(n)$ is the Riemann zeta-function. The transverse frequencies, on the other hand, depend on the density λ and $\omega_{\perp 2^\pm}$ vanishes at the critical $\lambda^{\mathrm{crit}} = [3/7\zeta(3)]^{1/3} = 0.709$ where the string ceases to be the energetically lowest configuration (the transition to the zigzag structure[1]). They follow from the dispersion relation

$$\omega_\|^2 + 2\omega_\perp^2 = \omega_p^2.$$

For large amplitudes, the transverse frequencies remain rather independent of amplitude whereas the longitudinal ones increase rapidly, see Fig.1. The potential energy β *vs.* ρ exhibits a saddle point, see Fig.2. Thermal energies which drive the system over this saddle, cause particles to change places in the string and, thus, can destroy the ordered string structure. In a wide range of densities the saddle energies are of the order of one, see Fig. 3. Hence cooling powers $\Gamma \gtrsim 1$ suffice to preserve the string. other modes, although lower in frequency, have higher saddles.

[1] R.W.Hasse, J.P. Schiffer, preprint; Proc. Workshop on Crystalline Ion Beams, Wertheim/Main, Oct. 1988, GSI report 89-10, p.33
[2] W. Slattery, G. Doolen, H. DeWitt, Phys. Rev. A21 (1980) 2087
[3] V.V. Avilov, priv. comm.

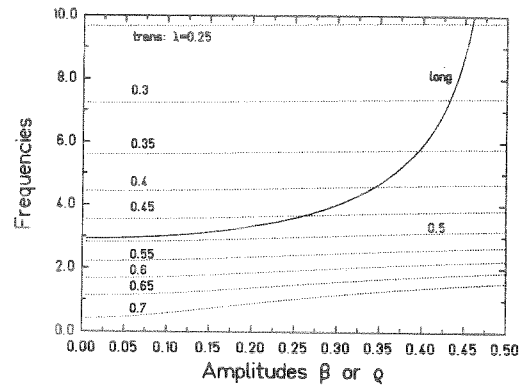


Fig.1: Longitudinal (full line) and transverse (dotted lines for different densities λ) eigenfrequencies of the $M^\Pi = 2^+$ - zigzag mode *vs.* amplitude.

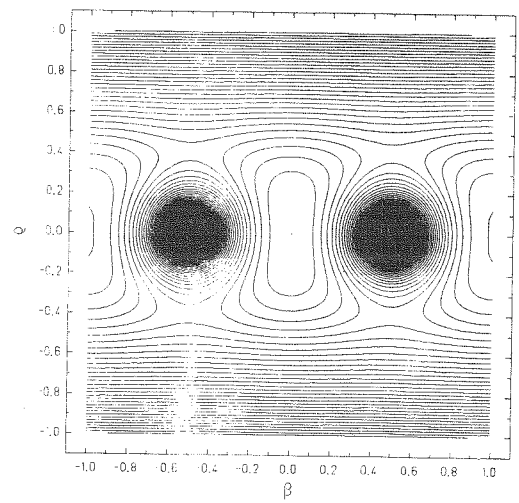


Fig.2: Potential energy map for longitudinal (β) and transverse (ρ) $M = 2^+$ vibrations. The ground state has zero energy and contour lines are spaced by 0.05 energy units.

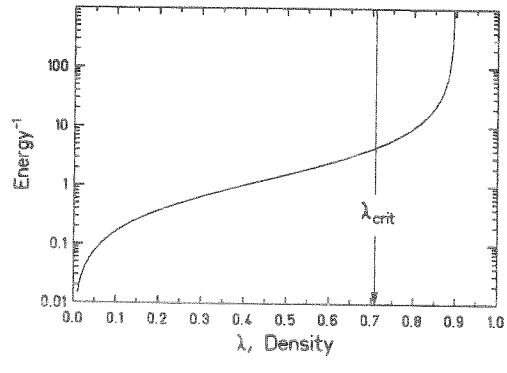


Fig.3: The reciprocal saddle point energies for $M = 2^+$ vibrations.

HEAVY ION BEAMS FOR THE GENERATION OF HIGH ENERGY DENSITY IN MATTER

7. HEAVY ION BEAMS FOR THE GENERATION OF HIGH ENERGY DENSITY IN MATTER

PAGE

Energy Loss of Heavy Ions in a Dense Z-Pinch Plasma 369
K.-G. Dietrich, E. Boggasch, D.H.H. Hoffmann, K. Weyrich, H. Wahl

Heavy Ion and Laser Induced Plasma 370
K. Mahrt-Olt, J. Jacoby, K.-G. Dietrich, D.H.H. Hoffmann, A. Golubev, B. Sharkov, A. Shumshurov, N.G. Borisenko

Effects of Radiation in Xenon Targets Irradiated with Heavy Ion Beams 371
V. Schneider, K.-J. Lutz, J.A. Maruhn

Simulation of RFQ Experiments with Xenon Targets 372
V. Schneider, K.-J. Lutz, J.A. Maruhn

Focusing the SIS - Ne^{3+}-Beam 373
B. Heimrich, M. Winkler, H. Wollnik

Development of Plasma Lenses for Focusing of Heavy Ion Beams 374
E. Boggasch, K.-G. Dietrich, D.H.H. Hoffmann, H. Wahl,

Voltage Unflatness of Multi-Module Split Coaxial RFQ Linac Cavities 375
Y. Oguri, R.W. Müller

PROFIL - a Program for the Design of Split-Coaxial RFQ Linacs 376
R.W. Müller

Energy Loss of Heavy Ions in a Dense Z-Pinch Plasma B

K.-G. Dietrich, E. Boggasch, D.H.H. Hoffmann, K. Weyrich, H. Wahl
GSI Darmstadt and Max-Planck-Institut für Quantenoptik, Garching

The main goal of last years activities on the z-pinch experiment was the extension of the energy loss data for heavy ions in plasma to a regime of higher plasma densities. With the experimental setup described last year [1] we measured the stopping power of a hydrogen plasma for Pb and U ions at an energy of 1.4 MeV/u. A major progress was achieved by optimizing the parameters of the discharge (hydrogen pressure and voltage) for a maximum transmission of the beam.

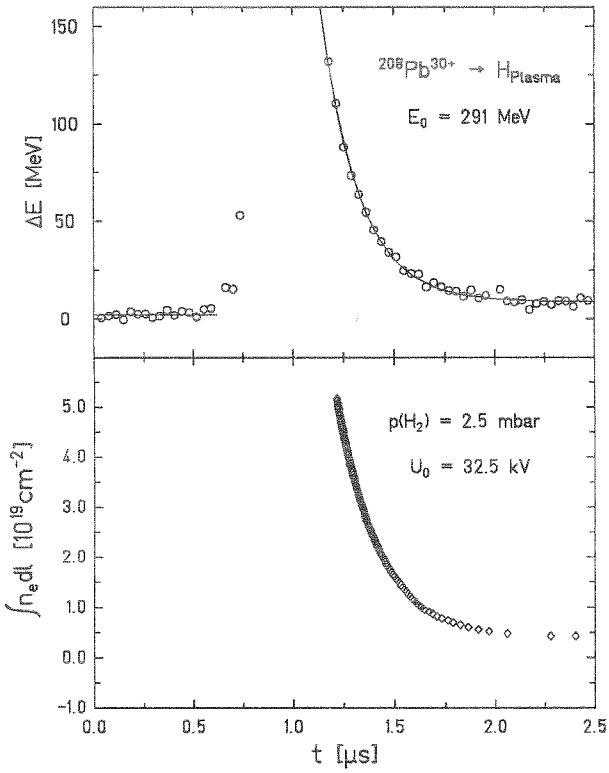


Fig. 1: Energy loss of Pb ions in the plasma (top) and the corresponding areal density of free electrons (bottom).

The upper part of fig. 1 shows the observed energy loss of Pb ions as a function of time (time zero arbitrary). The data points up to 600 ns correspond to the energy loss in the cold hydrogen gas. When the pinch reaches the beam axis the energy loss rises very steeply and we cannot follow it to the most dense phase of the plasma. For times above 1μs the energy loss during the reexpansion of the plasma is displayed. The maximum energy loss detected was about 130 MeV which is 45% of the incident energy. The experimental limit is mainly given by the time of flight method which fails at larger energy losses although we already reduced the time of flight distance from 8m to 4m.

The lower part of fig. 1 shows the free electron density determined by on-axis Mach-Zehnder interferometry. This diagnostic method also fails in the most dense phase because the light of the Ar ion laser is completely absorbed. However, in the expanding phase areal densities up to 5.5x$10^{19}cm^{-2}$ were measured.

Note that the maximum of energy loss and diagnosed free electron density have been increased by factors of 4.5 and 2 respectively compared to the data presented last year [1].

Plasma temperature was determined by spectroscopy of the emitted plasma light. At an areal density of 5x$10^{19}cm^{-2}$ the temperature is about 5eV. For the whole range between 1 and 2.5μs the temperature is high enough to guarantee a degree of ionization of more than 99%.

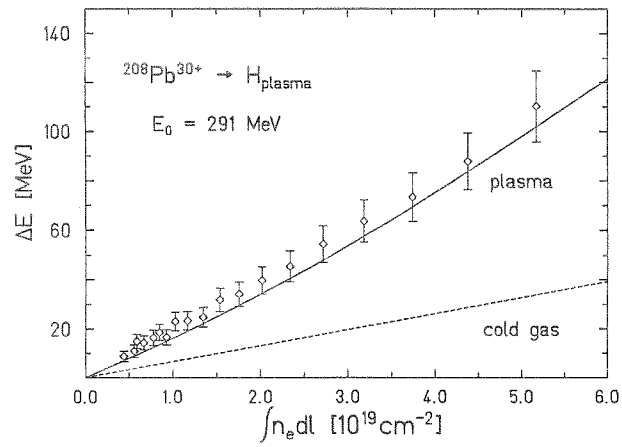


Fig. 2: Energy loss as a function of the plasma density.

In fig. 2 the energy loss as a function of plasma density is displayed. We find an enhancement of nearly a factor of 3 compared to the cold gas value (taken from [2]). The data is compared to a calculation in the standard stopping power model which takes into account the higher Coulomb logarithm and the higher charge state of the ions in the plasma as well. The evolution of the charge state was modeled by a Monte-Carlo simulation where all important charge exchange cross sections were put in. The agreement of the calculation with our data is very good. This experiment is therefore the hitherto best evidence for the higher effective charge of heavy ions in a completely ionized plasma as it has been predicted theoretically.

The whole equipment has been moved to the large experimental hall at the end of the UNILAC where we want to continue our experiment with ions up to 6 MeV/u. Also foreseen is a direct measurement of the ion charge state after its passage through the plasma.

References

[1] K.-G. Dietrich et al., GSI-report 89-21, 1989, p. 6
[2] L.C. Northcliffe and R.F. Schilling, Nucl. Data Tables, A7 (1970) 223

Heavy Ion and Laser Induced Plasma[B]

K. Mahrt-Olt, J. Jacoby, K.-G. Dietrich, D.H.H. Hoffmann (GSI-Darmstadt & MPQ-Garching)
A. Golubev, B. Sharkov, A. Shumshurov (ITEP-Moscow)
N.G. Borisenko (Lebedev Institute-Moscow)

Within the project "High Energy Density in Matter" various experiments are performed with the RFQ-preaccelerator MAXILAC at GSI and with a CO_2-Laser at ITEP-Moscow. Many different kinds of targets were used, providing the material to be heated to plasma conditions. Gas puff targets [1], foam targets, and solids covered a density regime of four orders of magnitude.

During the measurements described here, Kr^+ projectiles (beam current: 4 mA) from MAXILAC [2] were used to diagnose the line integrated gas density of the gas puff target. With a time of flight system (TOF) the energy loss of the unfocused beam below the Laval nozzle was measured. The target was filled with Argon at a prepressure of 40 to 50 bar. A phase probe positioned behind the Laval nozzle delivered the start signals and a fast Faraday cup provided the stop signals coming synchronously with the RFQ micropulse structure of 13.5 MHz. The energy loss is estimated by the shift of the micropulse signals, measured with and without gas. With the data for energy loss given in Reference [3] the gas density – averaged over a beam diameter of 2 mm at a target length of 5.6 mm measured 2 mm below the nozzle – is estimated to be 0.4 mg/cm^3. With a beam diameter of 13 mm at a target length of 16 mm measured 10 mm below the nozzle the averaged density results to 0.15 mg/cm^3.

The foam targets consist of carbon, hydrogen and some oxygen are used in a density range from 0.3% to 80% of solid density. When the targets were heated with the full intensity Kr^+ beam the spectral analysis showed only a weak radiation intensity in the visible region. Thus, an analysis with an optical spectrometer was not possible. An investigation with a photodiode (spectral cut off at 150 nm) and successive insertion of filters (180 nm, 370 nm, 550 nm) showed that the main radiation (> 90%) lies below 180 nm.

Carbon-, tantal- and titan-hydrid served as solid targets. With a streak camera spectral and time resolved images [4] were taken. The comparison of the time behavior from solids and foams shows that the light emission of foams starts immediately with the beam, whereas the radiation for solids was delayed [5] for about 300 μs. Space resolved pictures show clusters flying away from the surface of carbon and titan with velocities from 10 to 30 m/s. The investigation of the spectrum with and without H_β-filter shows that a big part of the radiation is concentrated at the H_β line. Wavelength resolved streaks show a very broad spectrum of the heated carbon targets close to the surface of the target. With increasing distance (0 - 0.4 mm) from the surface more and more structure in the H_β region is resolved.

At the ITEP-Moscow a CO_2-Laser (λ = 10.6 μm) with an energy of 4 J during 100 ns is used to heat similar targets as those used at GSI to plasma conditions. A particle spectrometer was used for energy and charge state detection of the outgoing plasma ions to diagnose the target. In addition, an optical diagnostics with a spectrometer (27 cm focal length, $\Delta\lambda$ = 200 - 800 nm) and streak camera coupled to an image analysis system was performed. The foam targets showed using the low resolution, low dispersion grating (300 gr/mm) a rather complicated spectrum. But while using the high resolution grating (2400 gr/mm) several CII, CIII and CIV lines could be resolved. The detected Stark broadening of the H_β line versus time is shown in figure 1.

From the tables of Griem [6] the free electron density could be evaluated from this line broadening (figure 2). This density is averaged over the line of sight parallel to the target surface 0.5 mm in front of it. The laser heated solid carbon targets showed strong carbon lines in the UV region from CI, CII and CIV. From line ratios of these lines it is possible to determine the plasma temperature and its time dependence.

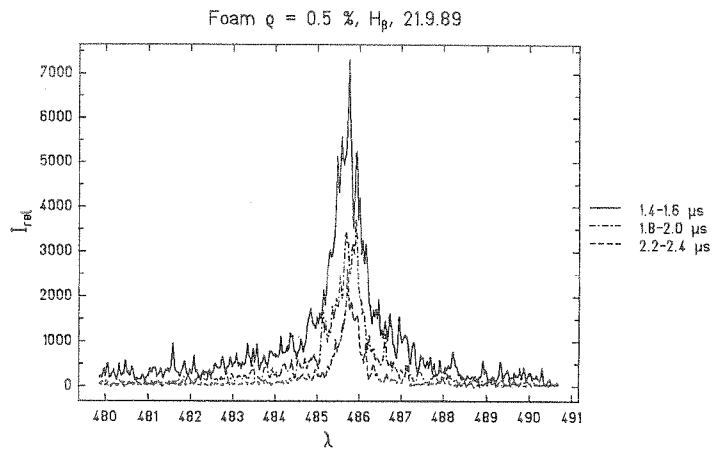


Figure 1: Stark broadening of the H_β line measured from a foam target versus time.

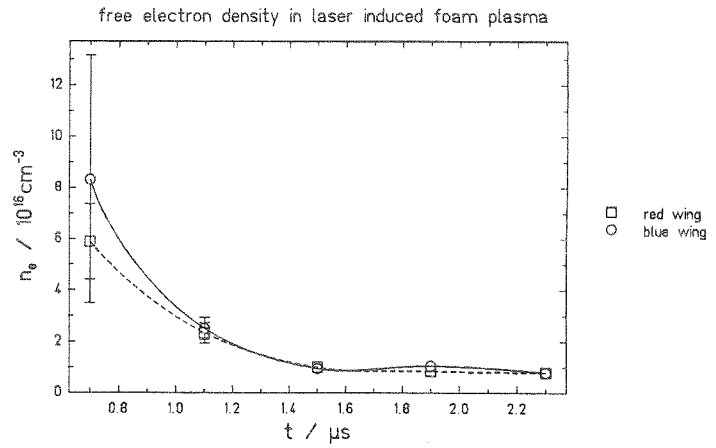


Figure 2: Electron density evaluated from the Stark broadening of the H_β line.

References

[1] J. Jacoby: Nucl. Instr. and Meth. A282, 94 (1989)

[2] R.W. Müller, P. Spädtke, R. Keller, J. Klabunde, A. Schönlein, Y. Oguri, A. Warwick: GSI-87-1 Scientific Report 1986, 379 (1987)

[3] L.C. Northcliffe, R.F. Schilling: Nucl. Data A7, 233 (1970)

[4] J. Jacoby: Thesis, Universität Heidelberg; GSI-89-24 Report (1989)

[5] J. Jacoby, R.W. Müller, D.H.H. Hoffmann, H. Wahl, K. Weyrich, B. Heimrich, M. Winkler, H. Wollnik, S. Maurmann: Nucl. Instr. and Meth. A278, 82 (1989)

[6] H.R. Griem: Spectral Line Broadening by Plasmas, Academic Press, New York (1974)

Effects of Radiation in Xenon Targets Irradiated with Heavy Ion Beams [B]

V. SCHNEIDER, K.-J. LUTZ, and J. A. MARUHN
Institut für Theoretische Physik der Universität Frankfurt

One of the principal mechanisms determining the attainable temperatures in irradiated gas targets is the emission of radiation. The coefficient of thermoconductivity κ entering the heat flux $\vec{J} = -\kappa\vec{\nabla}T$ is mainly given by the sum of the electronic (κ_e) and radiative (κ_r) components. The electronic contribution is calculated according to the Spitzer formula. In the determination of the radiative contribution the diffusion limit has been assumed leading to the relation $\kappa_r \propto (\rho K_R)^{-1} T^3$. K_R is the Rosseland mean opacity (taken from the corresponding SESAME opacity tables), ρ and T are target density and temperature respectively. The effects of surface radiation have been neglected because beam, target, and time scales are chosen in such a way that surface heating does not become important.

For the simulations the beam was assumed to be a 45 keV/u Krypton beam with a mean specific deposition power of 1–10 GW/g. The beam focus is round with a radius of 1.5 mm. The radial intensity profile has a parabolic shape. One macropulse of the beam is formed by a series of parabolically shaped micropulses with a width of 10 ns and a micropulse separation of 70 ns. The targets simulated were cylindrical Xenon targets (density of 11 mm length and a diameter of 6.5 mm. For the Xenon targets the gas density was 10^{-3} g/cm^3, corresponding to a pressure of 0.6 bar.

Fig. 1 shows the temperature profiles at different times and for various values of the mean opacity. The peak temperature, reached in the center of the target, varies monotonically with opacity and depends sufficiently sensitively on it, so that a measurement of the peak temperatures should allow the determination of the opacity. The experimental value (Jacoby 1989) is approximately $T_{\max} = 0.7$eV, so that an opacity of less than 10^4cm^2/g is indicated.

The radial profiles of the radiated power roughly follow the temperature profiles, so that we only show a sample for $J = 40$ in fig. 2. Apparently a measurement of the temperature distribution in the target allows quite detailed conclusions about the energy deposition and shock wave propagation, once the information about the mean opacity is sufficiently precise.

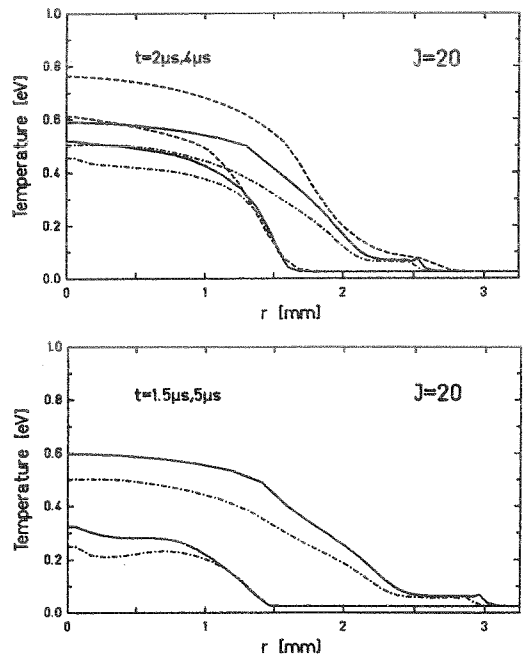


Fig. 1: Radial temperature profiles for $J = 20$ in the Xenon target simulation with different values of the Planck mean opacity. In both plots the distinct groups of curves correspond to different times, the mean temperature increasing with time. The opacity values are 0 (dashed curves), 1 (solid curves), and 3×10^4cm^2/g (dash-dotted curves), respectively.

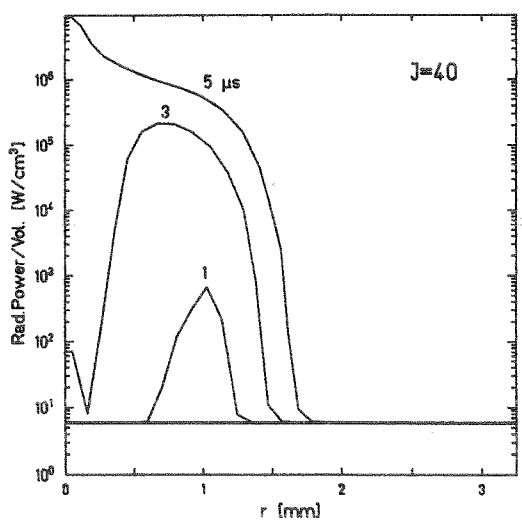


Fig. 2: Radial profile of radiated power in the Xenon target, calculated for a Planck mean opacity of 10^4cm^2/g.

References

Jacoby J. 1989: Thesis, to be published as GSI-Report

Simulation of RFQ Experiments with Xenon Targets [B]

V. SCHNEIDER, K.-J. LUTZ, and J. A. MARUHN
Institut für Theoretische Physik der Universität Frankfurt

Previous simulations of the hydrodynamic flow in gas targets irradiated by intense heavy ion beams were extended, assuming beam and target parameters selected specifically to correspond to the experiments carried out by Jacoby (Jacoby 1989). The numerical method is based on a time-marching partially implicit scheme for arztrarily moving grid vertices (Cloutman, Dukowitz, Ramshaw & Amsden 1982). Lagrangian grids are used throughout to obtain a high resolution of discontinuities and compression waves occuring in the simulations.

For the simulation the beam was assumed to be a 45 keV/u Krypton beam with a mean specific deposition power of 1–10 GW/g (1 GW/g for the results shown). The beam focus is round with a radius of 1.5 mm. The radial intensity profile has a parabolic shape. One macropulse of the beam is formed by a series of parabolically shaped micropulses with a width of 10 ns and a micropulse separation of 70 ns. The duration of the macropulse is long enough that it could be assumed to be turned on for the full duration of the simulations. For comparison some simulations were also carried out for a box-shaped beam and uniform macropulse.

The targets are cylindrical tubes of 11 mm length and a diameter of 6.5 mm. The gas density was 10^{-3} g/cm^3, corresponding to a pressure of 0.6 bar. The Planck mean opacity for the plots shown here was 10^4cm^2/g.

In the plots, the z-axis is the beam axis, and they are positioned such that the beam direction is to positive z. Because of the axial symmetry it suffices to plot one side of the target. Boundary conditions are fixed walls at the radial boundary and free expanding surfaces in the z-direction.

Fig. 1 shows density contour lines for a simulation of the experiments of Jacoby. Volume radiation with a mean opacity from the SESAME tables was included, and the equation of state was taken from the Saha model. The main difference to previous simulations are a three times higher gas density and a specific deposition lower by a factor of ten, which allow the shock wave to propagate also in the beam direction, whereas in those simulations it was overtaken by the beam.

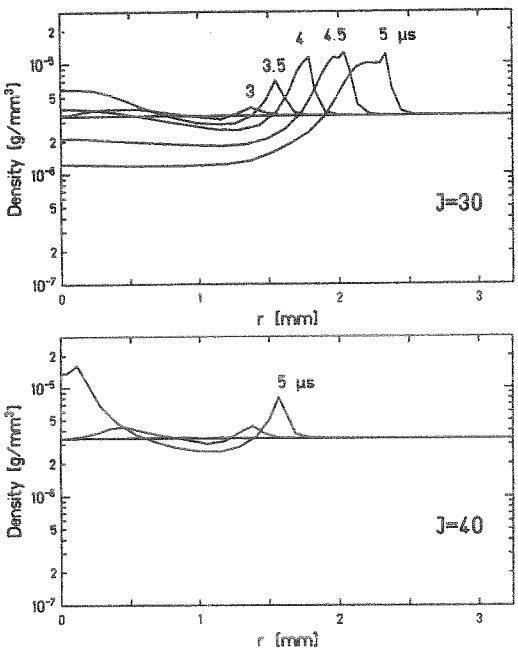


Fig. 2: Density profiles along Lagrangian grid lines $J = 30$ (top) and $J = 40$ (bottom).

Again the contour lines clearly exhibit the "hole drilling" effect, which allows the beam to propagate further into the target in the region of the rarefaction wave. A new an interesting effect becomes visible in the upper part of the figure: the hole drilling effect in this region also makes a shock wave propagating towards the central axis possible, and because of the cylindrical convergence this leads to an enhanced compression.

This effect is exhibited much more clearly in fig. 2, which shows two cuts through the density distribution roughly horizontally in the upper region of the target (the Lagrangian coordinate J runs from 1 at the lower end of the target through 50 at the upper end).

References

Cloutman L.D., Dukowitz J.K., Ramshaw J.D. & Amsden A.A. 1982: LASL Report LA-9294-MS

Jacoby J. 1989: Thesis, to be published as GSI-Report

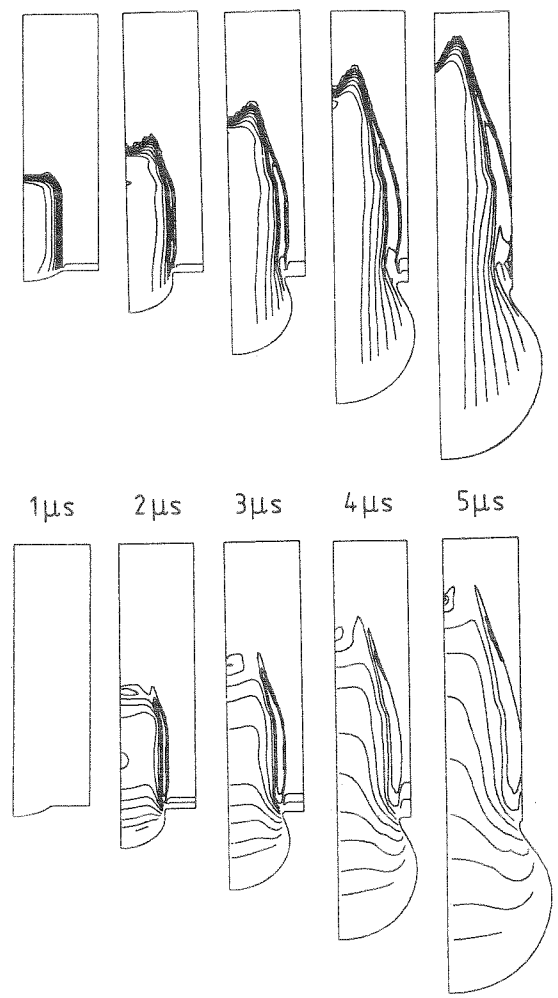


Fig. 1: Contour lines for temperature and density in a Xenon target with a pressure of 0.6 bar irradiated by a 1 GW/g beam coming from below in the plots. The upper row shows the temperature and the lower one the density.

Focusing the SIS–Ne^{3+} –$Beam^{B}$

B.Heimrich, M.Winkler, H.Wollnik
2. Physikalisches Institut, Universität Giessen, 6300 Giessen

To use the SIS facility for the investigations of hot dense matter we have calculated a final focusing system with GIOS [1]. According to these calculations the system should focus the intense heavy ion beam from the SIS accelerator to a spot size of about 100 μm radius [2]. The parameters of the focusing elements of this system are listed in Table 1.

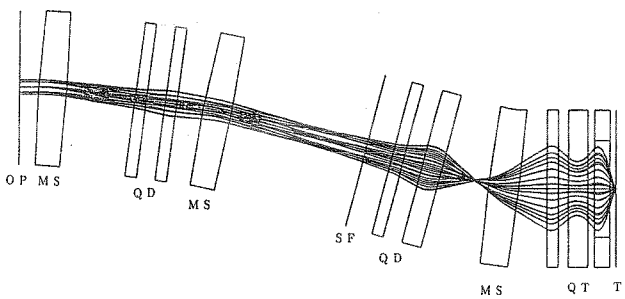


Figure 1: Overview of the final focus beam guidance system.

M S : Magnetic Sector
M Q : Magnetic Quadrupole
O P : Takeover Point
S P : Stripper Point
T : Target

At first the SIS–accelerator will accelerate Ne^{3+} ion's to a magnetic rigidity of about 18 Tm and a beam current of about 0.2 A. Thirteen meters upstream from the takeover point in the beam line, we plan to strip the ion's fully by passing them through a thin foil, in order to reduce the ohterwise required too strong magnetic flux densities in the last focusing quadrupole triplet [3] since in this case the magnetic rigidity is decreased to about 6 Tm. However the beam current increases to about 0.72 A which causes larger space–charge problems. Figure 2a shows a contour plot of the focused spot size which has an elliptical structure generated by second order image abberations in the sector fields of our final focusing system.

element	aperture radius	length	flux density
7.5°–dipole	40 mm	R=11.25 m	1.59 T
quadrupole	65 mm	600 mm	0.195 T
quadrupole	65 mm	600 mm	0.401 T
7.5°–dipole	40 mm	R=11.25 m	1.59 T
quadrupole	65 mm	600 mm	0.140 T
quadrupole	65 mm	1000 mm	0.259 T
15°–dipole	40 mm	R=6.25 m	0.859 T
quadrupole	65 mm	600 mm	0.298 T
quadrupole	65 mm	1000 mm	0.451 T
quadrupole	40 mm	800 mm	0.672 T

Table 1: Characteristic Data of the Focusing System

To create hot dense plasma it is necessary to make use of the highest available deposited beam power. Therefore it is of importance to increase the transmission of ions, which will be focused onto the final beam spot. This should be possible if the image abberations of the system can be reduced. For this purpose we made additional calculations by theoretically inserting higher–order magnetic elements in the beam line.

We observed some effects by introducing a magnetic hexapole behind the final magnetic sector field. With an effective length of 300 mm and an aperture radius of 65 mm for the hexapole we calculate a raise of ion transmission at the target from about 52% up to approximately 60%. Here the magnetic flux density of the hexapole should be 0.01T which is easily achieviblable. The effect is also perceptible at the contour plot of the spot size, which is more circular with a hexapole component than without (compare Fig. 2a and Fig. 2b).

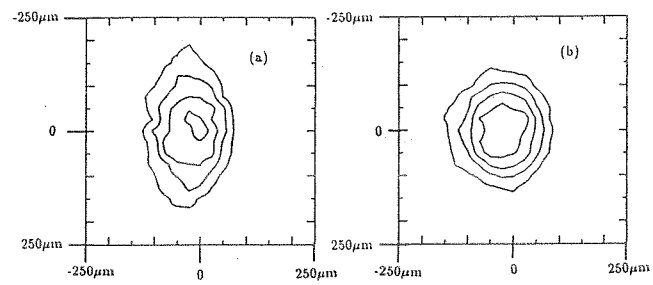


Figure 2: Calculated intensity distribution at the final focus with (a) and without (b) an magnetic hexapole component. The intensity is given for 20, 40, 60 and 80% of the maximum value.

Another possibility to decrease the focus spot area is to add another focusing element. We have theoretically inserted a z–pinch plasma lens between the final focusing triplet and the focus point. Such a plasma lens has the property to focus the beam in both directions perpendicular of propagation of the ion beam. With a length of 100 mm, an aperture radius of 12 mm and an magnetic flux density of about 10 T for the plasma lens at the outside of the plasma cylinder the calculations reduced the focus radius by about a factor 2.

References

[1] H. Wollnik, J. Brezina and M. Berz, Nucl. Instr. and Meth. A 258 (1987) 408
[2] B.Heimrich et.al.; Proc. Nucl. Instr. and Meth., in print
[3] I. Hofmann, Report GSI 88–1, ISSN 0174–0814 (1988) 404

Development of Plasma Lenses for Focusing of Heavy Ion Beams B

E. Boggasch, K.-G. Dietrich, D.H.H. Hoffmann, H. Wahl
GSI Darmstadt and Max-Planck-Institut für Quantenoptik, Garching

The investigation of heavy-ion-beam-produced hot dense plasmas is an interesting and challenging research area relevant to inertial fusion. Heavy ion beams strongly focused onto targets are necessary to achieve a notable deposition power in matter [1]. Besides conventional focusing systems consisting of electric and magnetic quadrupoles also plasma lenses are presently under discussion as attractive focusing devices [2, 3].

For this kind of lenses the plasma serves as an almost transparent current-carrying and space-charge-neutralizing medium. If a homogeneous current density distribution is obtained it will result in a linearly rising magnetic field. In contrary to quadrupoles these cylindrically symmetric "wire lenses" provide simultaneous focusing in both planes with very high field gradients of several hundred Tesla per meter. One possibility for producing the plasma is realized by a z-pinch discharge. Driven by the strong magnetic force during a pulsed high-current discharge an uniform axial plasma column is formed (fig. 1).

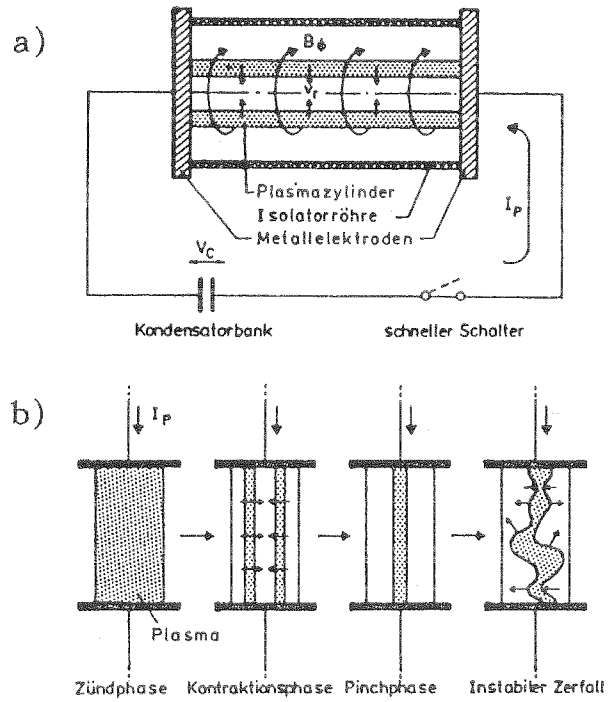


Fig. 1. a) Schematic set-up of a dynamic z-pinch experiment
b) Sketch of plasma movement in a dynamic z-pinch

Plasma lenses based on z-pinch discharges have been successfully used earlier for focusing of high-energy charged particle beams at Berkeley [4] and Brookhaven [5]. At CERN a plasma lens designed for antiproton collection is presently being tested off-line and is planned to be installed in the target area of the Antiproton Collector Ring in 1991 [3]. A significant increase of captured antiprotons and decrease of accumulation time is anticipated.

With the completion of the SIS facility at GSI high-energy heavy ion beams with energies over 300 MeV/u will become available for target experiments. Strong focusing is needed to reduce the beam size to small spots of less than 200 μm diameter. The parameters of a plasma lens suited for focusing a typical SIS beam are summarized and compared to the CERN plasma lens values in tab. 1.

Tab. 1. Parameter values of a future SIS Plasma lens compared to the existing CERN antiproton plasma lens

	SIS/ESR	CERN
particle	heavy ions	antiprotons
rigidity (Tm)	6.8 (300 MeV/u , I^{53+})	11.8
max. conv./div. angle (mrad)	100	70
current (kA)	450	400
length (mm)	105	250
diameter (mm)	20	40
max. magn flux density (T)	9	4
field duration (ns)	100	500
transv. emittance (mm mrad)	10π	210π
spotsize (mm)	0.1	3

The CERN lens will capture a large emittance diverging beam, whereas a SIS lens has to focus a low emittance, almost parallel beam. Lens aberrations caused by non-linear field distribution limit the performance, especially of a focusing lens, with respect to minimum spot size. Therefore accurate magnetic field measurements inside the plasma region are essential for a successful lens development. The field distribution inside the CERN plasma lens prototype has been determined by small inductive coils [7].

In addition to direct field measurement an alternative method will be pursued at GSI. Starting in 1990, focusing experiments will be performed using the UNILAC heavy ion beam together with a scaled-down plasma lens set-up. The effect of magnetic field distributions of different discharge regimes and plasma lens concepts can be tested on-line by simultaneous observation of the downstream beam profile. These experiments will provide further information needed for design and construction of a future SIS plasma lens.

References

[1] B.Heimrich et al., Nucl. Instr. Meth., **A278**, 202 (1989)
[2] B.Heimrich et al., GSI report 89-21, p.10 (1989)
[3] Special Seminar on Plasma Focusing and Plasma Lenses, GSI, 17,18 January 1990
[4] W.K.H.Panofsky and W.R.Baker, Rev. Sci. Instr. **21**, 445 (1950)
[5] E.B.Forsyth, L.M.Ledermann, J.Sunderland, IEEE Trans. Nucl. Sci. **12**, 872 (1965)
[6] B.Autin et al., IEEE Trans. Plasma Sci., **PS-15**, 226 (1987)
[7] E.Boggasch, Dissertation, Universität Erlangen, (1987)

Voltage Unflatness of Multi-Module Split Coaxial RFQ Linac Cavities

Y. Oguri
Tokyo Institute of Technology, Tokyo, Japan

R. W. Müller
GSI, Darmstadt

The split coaxial linac structure has been invented in 1978 for the application as a resonator of a heavy-ion RFQ linac.[1] It has been applied as a 5-module stack in the 45 keV/u RFQ linac MAXILAC of GSI for the acceleration of Xe^{+} and U^{++} ions. Another example is developed at INS in Tokyo.[2]

The structure is well suited for long RFQ linacs at low RF freqencies because of its inherent voltage flatness and good power economy or shunt impedance. So far an easy-to-handle formalism for calculating flatness errors due to local capacity errors did not exist. This is needed if very long stacks (e. g., of 14 or 19 modules as they are conceived for the UNILAC high-current injector) are to be designed. Also, a discussion about beam-excited modes played a role here: beam mismatch is seen by the cavity as a capacity error pattern. But from the results of this study the importance of effects of this type can be ruled out.

Fig. 1 shows the basic principle of one module. It is a coaxial system whose inner conductor is split into (practically four) segments. The focusing/accelerating electrodes present capacitive loads to these segments. Because the partial capacities of the segments to the outer conductor are inversely proportional to the voltages on them, no net capacitive current transits, and due to the tapered inductances the voltage difference between the segments is exactly flat.

Of course, local capacity errors change this: "capacity attracts voltage". Within one module a localized capacity error will excite a standing wave of sinusoidal distribution.[3] The wavelength of this wave is about 20 m for MAXILAC. For a stack of modules, however, this is not true; transition from one module to the next breaks the wave.

The calculation of the selfinductances L_1 and L_2 and the mutual inductance L_{12} of a piece ds of the split conductors was done with an analytical potential ansatz which ends in the summation of converging serieses. With good precision the result is

$$L_1 = (\mu_0/2\pi)\{(s/s_0)^2F+\ln(R_a/R_i)\}ds$$
$$L_2 = (\mu_0/2\pi)\{((s_0-s)/s_0)^2F+\ln(R_a/R_i)\}ds$$
$$L_{12} = (\mu_0/2\pi)\{-(s(s_0-s)/s_0^2)F+\ln(R_a/R_i)\}ds$$

where s_0 is the module length, R_a and R_i the outer and inner conductor radius, and F a shape factor for the gap width; $F \approx 0.8$ for a wide range of realistic gap widths. With these inductances and the capacity C'ds of the system eight-pole (4*4 elements) matrices connecting voltages and currents at both ends of the interval ds can be written. Multiplying them from s=0 to $s=s_0$ corresponds to integrating the voltages and currents through the module. For instance, with the "tuned" parameters $R_a/R_i=3.511$; $C'=30.9\ \varepsilon_0$; $s_0=1.4$ m and f=13.689 MHz (the eigenfrequency), we have for the sequence U_1, U_2, I_1, I_2 a matrix M. M has some symmetry properties, but none of the elements is 1 or -1.

If it is the matrix of a "even" module, we have $U_{2i}=U_{1e}=0$ at the (broad) ends of the segments. Using these conditions and giving U_{1i} and I_{1i}, we can calculate I_{2i}, I_{1e}, U_{2e} and I_{2e} from linear algebraic equations. So initial conditions can be given for the calculation of voltages and currents for any module stack, if the 4*4 matrices are known.

Fig. 2 shows an example of voltage and current distributions when a five-module stack is operated at a 3% too low frequency. This is one of the rare cases where we could detect a considerable unflatness. The voltage rises monotonously by 50% towards the feeding end, where a big inductive current has to be fed in from the feeding amplifier. For periodically variing capacity errors of the same magnitude (6%) no unflatness can be seen in the scale of this figure. The split coaxial structure is extremely insensitive against capacity errors.

The eight-pole matrix M can be transformed into a four-pole matrix N (2*2 elements) since $U_{2i}=U_{1e}=0$, and I_{2i} and I_{1e} can be eliminated. The new four-pole matrix N connects linearly (U_{1i}, I_{1i}) with (U_{2e}, I_{2e}):

$$N = \begin{pmatrix} m_{21}-m_{11}m_{24}/m_{14} & m_{23}-m_{13}m_{24}/m_{14} \\ m_{41}-m_{11}m_{44}/m_{14} & m_{43}-m_{13}m_{44}/m_{14} \end{pmatrix}$$

where m_{ij} are the elements of the 4*4 matrix M. For our (tuned) example we obtain

$$N = \begin{pmatrix} -1 & -20.4*i\Omega \\ 0 & -1 \end{pmatrix}$$

the matrix of an equivalent circuit as shown in fig. 3. Beyond the interior of a single module the structure does not have a waveguide behaviour. Analysis of the matrices of detuned modules reveals that there is a resonator hidden in the circuit, as shown in fig. 4.

References

1. R. W. Müller, GSI-79-7
2. N. Tokuda et al., INS-Rep.-794
3. R. W. Müller, GSI-89-04

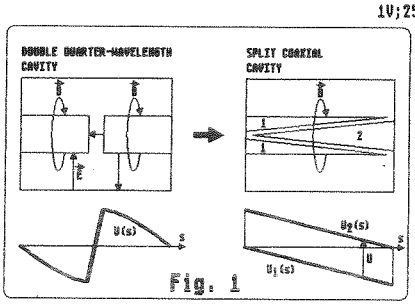


Fig. 1

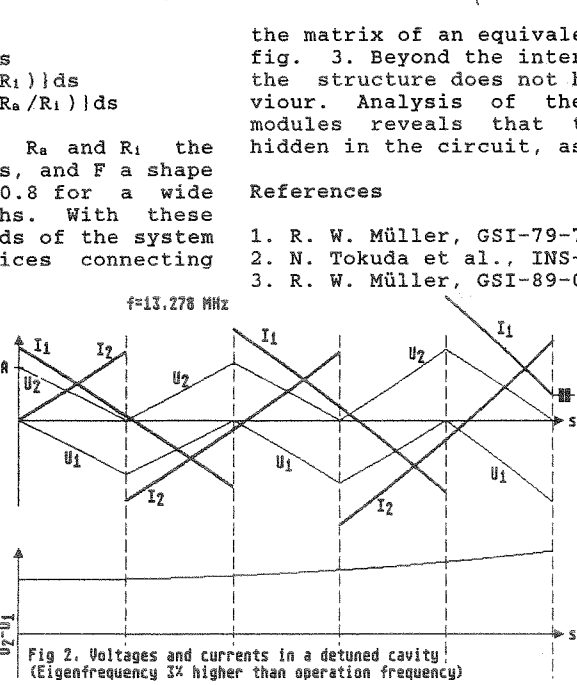


Fig 2. Voltages and currents in a detuned cavity (Eigenfrequency 1% higher than operation frequency)

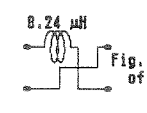


Fig. 3. Equ. circuit of a tuned module

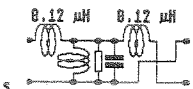


Fig. 4 ....and of a detuned module

PROFIL - a Program for the Design of Split-Coaxial RFQ Linacs

R. W. Müller
GSI, Darmstadt

In order to make the design of the high-current injector for UNILAC more flexible, a Basic program has been written which comprises data and experience of the construction of MAXILAC I and generates designs with different parameters at a high level of design reliability.

The design of a split-coaxial linac structure is straight-forward if the following data are given:

Data required	given by	other possible data sources
Gradient coeff. $1-B_0$, B_2; long. amplitude coeff. A_1 as fct. of $\beta\lambda/R$	ELTROG calcul. using the rod and frame shapes of MAXILAC I ("Profile B")	calculations for continual hyperbolic electrodes, modulation depth m given
C'/ε_0 as a function of $\beta\lambda/R$	model meas. and measurements on MAXILAC I	new measurements, or conformal mapping plus measured add. terms

Table I

In the present version the data listed in the central column of table I are used, splined between reference points. Here $1-B_0$ and B_2 mean the Fourier coefficients of the transverse gradient, and A_1 the basic Fourier component of the potential on the axis. ELTROG is a three-dimensional potential relaxation program which is needed for the determination of the above-mentioned field coefficients if the electrodes are not of hyperbolic shape. Of course, ELTROG can be used for any shape of electrodes, but for preliminary design studies the MAXILAC I shaping (represented by two simple parameter formulae) is used, because besides the generation of new data also new measurements of C' would be required.

The profile is generated sectionwise:
- $\beta\lambda$ for the end of a section is given;
- $\cos\varphi_s$ is determined so that the longitudinal bucket has a given, normally constant, size;
- an ansatz $\beta\lambda=(\beta\lambda)_e((z+z_0)/L)^\Gamma$ is made, and Γ and L are determined so that the equation of motion is fulfilled; $z-z_0$ is the position of the cell with length $\beta\lambda$; simple formulas are available[3] which contain the basic (unmodulated) transverse phase advance σ_{00} of a channel of width R rather than voltage, particle mass and charge etc.;
- all other data for individual $\beta\lambda$ periods follow from interpolation formulae.[3]

If the section intervals $(\beta\lambda)_e-(\beta\lambda)_i$ are chosen not too large, the method generates very smooth profiles and gives a quick survey over the total system length and cell number. The quality of the design is checked by a calculation of the motion of axis particles (no space charge forces) with different starting phases (routine LONGBEW). Also, the RF cavities are completely designed by the program PROFIL.

The same procedure has been applied for the design of the first split-coaxial design A (but still with a different electrode shaping)[1] which was used for the first Frankfurt proton model accelerator,[2] and for profile B which was used in MAXILAC I.[3]

Discussion of Alternatives

Table II lists three alternatives for the high-current injector conceived to increase the current of UNILAC. All of them operate at a frequency of 27.1 MHz because this is better adapted to UNILAC (no buckets remaining free, somewhat smaller longitudinal emittance than with the originally conceived frequency of 13.55 MHz). The beam brightness and density are higher at the transport limit; the total beam intensity is not lower only because the operating voltage (Kilpatrick number) has been chosen somewhat higher than in Profile B. This is justified by operating experience with MAXILAC I which could easily be operated above the Xe^+ voltage level without sparking.

The first line (D3) presents a conventional solution. An alternative (E2) has been developed because a shorter RFQ linac would allow the use of the old UNILAC injectors (see second line).

A very interesting alternative has recently been proposed by Ratzinger.[4] Progress and better understanding of ECR ion sources promise adequate multi-charged ion currents at least in pulsed operation. If this is true, only the first Wideröe tank of UNILAC would have to be replaced by a better structure (Tank W1 has a focusing structure which is weaker than in W2 to W4). Moreover, adiabatic beam bunching is needed. For this purpose, the third line of table II gives a preliminary design (F2). It is preliminary because, for the final design, a new electrode shaping ought to be found which reduces the structure length slightly. Even if the particle current out of the ECR sources is lower than that of CHORDIS bucket-field sources, the big gain is that stripping at 216 keV/u is not necessary. (Of course, this choice is the optimum only with the boundary condition of already existing machines, the choice would be different for an inertial-confinement fusion driver.)

The discussion about the best high-current injector is not at all finished as long as solutions are found which are potentially better, or at least cheaper, than foregoing ones.

References

1. R. W. Müller, GSI-79-7 (1979).
2. J. Müller, Untersuchungen an HF-Quadrupol-Beschleunigerstrukturen. Diss. Univ. Frankfurt 1983.
3. R. W. Müller, Parameter des RFQ-Prototyps für schwere Ionen (Design B). Unpublished internal paper, 1980.
4. U. Ratzinger, Überlegungen zur Entwicklung einer gepulsten ECR-Quelle und zu ihren Einsatzmöglichkeiten in Synchrotroninjektoren. GSI-UNILAC-INT/89-3.

Profile name	Heaviest ion	Inj. energy keV/u	Final energy keV/u	f MHz	Ap. radius mm	U*q/A kV/u	Kilp. number	I_{1m} *q/A mA/u	Number of SC modules	Length m	R_p kΩ
D3	Xe^+, U^{++}	2.011	216	27.1	3.6	1.05	2.7	0.25	19	29.7	15.4
E2	Kr^+, U^{+++}	3.421	216	27.1	5.0	2.026	3.0	0.7	14	19.0	25.1
F2	U^{+++}	11.644	216	27.1	10	8.105	2.65	6.0	7	8.3	33.6

Table II. Three alternatives proposed for the UNILAC high-current injector

ANNEX

8. ANNEX

PAGE

8.1 SCIENTIFIC ACTIVITIES OUTSIDE GSI 379

8.1.1 PUBLICATIONS 379
8.1.2 CONFERENCE CONTRIBUTIONS 388
8.1.3 SEMINARS AT OTHER INSTITUTES 400
8.1.4 LECTURES AND COURSES 403

8.2 SCIENTIFIC ACTIVITIES WITHIN GSI 404

8.2.1 MEETINGS, WORKSHOPS AND RESEARCH SEMINARS 404
8.2.2 SEMINARS AT GSI 404
8.2.3 GSI-REPORTS 408
8.2.4 GSI-PREPRINTS 409
8.2.5 VISITING GROUPS AT GSI 413

8.3 SCIENTIFIC COMMITTEES, DIRECTORATE AND PERSONAL 414

8.4 SCIENTIFIC COOPERATIONS 416

8.5 AUTHOR INDEX 418

8.1 SCIENTIFIC ACTIVITIES OUTSIDE GSI

8.1.1 Publications

(Permanent GSI staff members are underlined)

P. Armbruster, G. Münzenberg
Creating Superheavy Elements
Scientific American, Vol. 260, No. 5 (1989)

E.A. Bakkum, P. Decowski, K.A. Griffioen, R.J. Meijer, R. Kamermans
Impact Parameter Dependence of Incomplete Fusion Between 10 and 20 MeV/Nucleon
Phys. Rev. C39, 2094 (1989)

H.W. Barz, B.L. Friman, J. Knoll, H. Schulz
Nuclear Matter-Quark Matter Phase Diagram with Strangeness
Phys. Rev. D40, 157 (1989)

D. Berdichevsky, A. Lukasiak, W. Nörenberg, P. Rozmej
Diabatic Shifts and Fluctuations of Heavy-Ion Fusion Barriers
Nucl. Phys. A499, 609 (1989)

D. Berdichevsky, A. Lukasiak, W. Nörenberg and P. Rozmej
Diabatic Hindrance of Heavy-Ion Fusion
Nucl. Phys. A 502, 395 (1989)

H.F. Beyer, D. Liesen, O. Guzman
On the Total Recombination Between Cooling Electrons and Heavy Ions
Part. Accel. 24, 163 (1989)

T.S. Biro
QCD in the Hartree-Approximation
Ann. Phys. 191, 1 (1989)

T.S. Biro
Color Correlations and Confinement
Phys. Lett. B228 16 (1989)

T.S. Biro, W. Cassing, M. Durand
O(4)-Vacuum Invariance and Deconfinement
Phys. Lett. B232, 10 (1989)

M. Biyajima, G.N. Fowler, N. Suzuki, R.M. Weiner, G. Wilk
Forward-Backward Multiplicity Distribution in a Two-Component Model
Z. Phys. C44, 11 (1989)

B. Blättel, V. Koch, K. Weber, W. Cassing, U. Mosel
Transverse Momentum Analysis in the Relativistic BUU Approach
Nucl. Phys. A495, 381c (1989)

J.H. Blanke, B. Fricke, D. Heinemann, W.-D. Sepp, B. Thies, T. Göbenli, P.H. Heckmann, G. Müller, E. Träbert,
Study of the 3d-4f and 3d-5f Quartet and Doublet Transitions of Doubly Excited Three-Electron Ions, experiment and MCDF Theory Along the Isoelectronic Series
Z.Phys. D13, 1 (1989)

R. Bock
Overview of the German Program on High Energy Density Produced by Heavy Ion Beams
Nucl. Instr. and Meth. in Phys. Res. A278, 7 (1989)

R. Bock
Heavy Ion Inertial Fusion
J. de Phys., Coll. C1, Tome 50, 489, (1989)

R. Bock et al.
Source Parameters Deduced from Bose-Einstein Correlations of Two and Three Soft Pions in Symmetrie Heavy-Ion Interaction at 650 A MeV
Z. Phys. A333, 193 (1989)

R. Bock et al.
A Study of $K^0_S\lambda\bar{\lambda}$ production in 60 and 200 GeV per nucleon OAu and pAu collisions with a streamer chamber detector at the CERN SPS
Z. Phys. C43, 25 (1989)

A. Bohnet, N. Ohtsuka, J. Aichelin, R. Linden, A. Faessler
Quantum Molecular-Dynamics Approach to Heavy-Ion Collisions with Brueckner G-Matrix Cross Sections
Nucl. Phys. A494, 349 (1989)

H. Bokemeyer, H. Folger
The Part of Targets in Heavy-Ion Positron Spectroscopy
Nucl. Inst. and Meth. in Phys. Res. A282, 40 (1989)

H. Bokemeyer, P. Salabura, D. Schwalm, K.E. Stiebing
Correlated Electron-Positron Emission in Heavy Ion Collisions
in: Test of Fundamental Laws in Physics, Editions Frontiers, 77 (1989) (eds.: O. Fackler, J. Tran Thanh Van)

P.F. Bortignon, R.A. Broglia, A. Bracco, W. Cassing, T. Dossing, W.E. Ormand
Collisions and Mean Field Fluctuations in the Relaxation of Giant Resonances in Hot Nuclei
Nucl. Phys. A495, 155c (1989)

R. Brandt, G. Dersch, E.M. Friedlander, G. Haase, V.S. Butsev, M.I. Krivopustov, B.A. Kulakov, E. Ganssauge, W. Schulz, E.-J. Langrock, F. Pille
Untersuchung des abnormalen Verhaltens relativistischer Fragmente aus Schwerionenreaktionen (in Russisch)
Isotopenpraxis, 25, 434 (1989)

G. Breitbach, G. Koch, S. Koch, W. Kühn, A. Ruckelshausen, V. Metag, R. Novotny, S. Rieß, D. Habs, D. Schwalm, E. Grosse, H. Ströher
Dominance of Nucleon-Nucleon Bremsstrahlung in Mass-Asymmetric Heavy Ion Collisions at 15 MeV/u,
Phys. Rev. C40, 2893 (1989)

J.P. Briand, P. Indelicato, A. Simionovici, V. San Vicente, D. Liesen, D. Dietrich
Spectroscopic Study of Hydrogenlike and Heliumlike Xenon Ions
Europhys. Lett. 9, 225 (1989)

M. Brügger, K. Lützenkirchen, S. Polikanov, G. Herrmann, M. Overbeck, N. Trautmann, A. Breskin, R. Chechik, Z. Fraenkel, U. Smilansky
Search for Strange Matter by Rutherford Backscattering
Nature 337, 434 (1989)

K.A. Bugaev, M.I. Gorenstein, B. Kämpfer, V.I. Zhdanov
Generalized Schock Adiabatics and Relativistic Nuclear Collisions

G.A. Chandler, M.H. Chen, D.D. Dietrich, P.O. Egan, K.P. Ziock, P.H. Mokler, S. Reusch, D.H.H. Hoffmann
Precision X-Ray Crystal Spectroscopy of Neonlike Gold
Phys. Rev. A39, 565 (1989)

M. Cubero, M. Schönhofen, M. Gering, M. Sambataro, H. Feldmeier, W. Nörenberg
The Nuclear Equation of State in Quantum Hadrodynamics and Pion Yields in Heavy-Ion Collisions
Nucl. Phys. A495, 347c (1989)

H.H. Cui, W. Ke, J. Zhou, W. Lu, R. Brandt
Study on the Interaction of 960 MeV A ^{238}U-Ions with Light Nuclei (in Chinese)
J. of High Energy Phy. and Nucl. Phys. (China) 13, 199 (1989)

G.D. Deco, R.D. Rivarola
Pair Production with Electron Capture in Relativitic Heavy Ion Collisions
J. Phys. B22, 1043 (1989)

G. Deco, N. Grün
Asymptotic Behaviour of Distored-Wave Models for Ionisation at Relativistic Energies
J. Phys. B22, 1357 (1989)

G. Deco, N. Grün
Capture from the Vacuum in Ion-Ion Collisions at Relativistic Energies
J. Phys. B22, 3709 (1989)

C. Deutsch, G. Maynard, R. Bimbot, D. Gardes, S. Della-Negra, M. Dumali, B. Kubica, A. Richard, M.F. Rivet, A. Servajean, C. Fleurier, A. Sanba, D.H.H. Hoffmann, K. Weyrich, H. Wahl
Ion Beam-Plasma Interaction: A Standard Model Approach
Nucl. Inst. and Meth. in Phys. Res. A278, 38 (1989)

R. Dörner, J. Ullrich, H. Schmidt-Böcking, R.E. Olson
Three-Body Interactions in Proton Helium Angular Scattering
Phys. Rev. Lett., 63, 147 (1989)

M. Durand, J. Knoll
Quenching Effects in Photon Production
Nucl. Phys. A496, 539 (1989)

B. Eichler, C. Frink, G. Herrmann, N. Trautmann
Fast Volatilization of Some Lanthanide and Actinide Elements from Titanium Surfaces
Fresenius Z. Anal. Chem. 335, 656 (1980)

D.G. Ellis, I. Martinson, E. Träbert
Intercombination Transitions in Heavy Ions
Comm. At. Mol. Phys. 22, 241 (1989)

H. Emling, I. Ahmad, P.J. Daly, B.K. Dichter, M. Drigert, U. Garg, Z.W. Grabowski, R. Holzmann, R.V.F. Janssens, T.H. Khoo, W.C. Ma, M. Piiparinen, M.A. Quader, I. Ragnarsson, W.H. Trzaska
Lifetime Measurements of Terminating and Collective High-Spin States in ^{155}Dy and ^{156}Dy
Phys. Lett. B217, 33 (1989)

Ch. Ender, R. Männer, P. Bauer
Multiprocessor Data Acquisition System for High Event Rates at the Heidelberg/Darmstadt Crystall Ball
IEEE Trans. on Nucl. Sci. 36, 5 (1989)

H.G. Essel, J. Hoffmann, M. Richter, H. Sohlbach, W. Spreng
An Integrated Data Acquisition and Analysis System at GSI
IEEE Trans. Nucl. Sci. 36, No. 5, 1523 (1989)
(Proc. of the 6th Conf. on Real-Time Computer Applications in Nuclear Particle, and Plasma Physics, Williamsburg, USA, May 15-19, 1989)

A. Faessler, M. Rashdan, M. Ismail, N. Ohtsuka, W. Wadia
Nuclear Shapes and Interaction Potentials of Two Colliding ^{208}Pb Nuclei at Finite Temperature
Z. Phys. A333, 153 (1989)

H. Feldmeier, M. Schönhofen, M. Cubero
The Relativistic Vlasov Equation with Non-Radiating Meson Fields
Nucl. Phys. A495, 337c (1989)

D.E. Fields, K. Kwiatkowski, D. Bonser, R.W. Viola, V.E. Viola, W.G. Lynch, J. Pochodzalla, M.B. Tsang, C.K. Gelbke, D.J. Fields, and S. Austin
Non-Equilibrium Versus Equilibrium Emission of Complex Fragments from Hot Nuclei
Phys. Lett. B220, 356 (1989)

R. Fleischhauer, W. Scheid
Coulomb and Photo Cross Sections for Nucleon Emission by Relativistic Heavy Ions and Applications to ^{40}Ar on ^{89}Y
Nucl. Phys. A493, 583 (1989)

R. Fleischhauer, W. Scheid
Corrections of Semiclassical Virtual Photon Numbers in Coulomb Scattering for energy Loss of Projectile
Nucl. Phys. A504, 855 (1989)

H. Folger, W. Hartmann, J. Klemm, W. Thalheimer
Uranium Targets Sandwiched Between Carbon Layers for Use on Target Wheels and on a Wobbler in Heavy-Ion Bombardments
Nucl. Inst. and Meth. in Phys. Res. A282, 73 (1989)

B.L. Friman
Strangeness in Ultra-Relativistic Heavy-Ion Collisions
Nucl. Phys. A498, 161c (1989)

H.W. Gäggeler, D.T. Jost, A. Türler, P. Armbruster, W. Brüchle, H. Folger, F.P. Heßberger, S. Hofmann, G. Münzenberg, V. Ninov, W. Reisdorf, M. Schädel, K. Sümmerer, J.V. Kratz, U. Scherer, M.E. Leino
Cold Fusion Reactions with ^{40}Ca
Nucl. Phys. A502, 561c (1989)

H.W. Gäggeler, D.T. Jost, A. Türler, P. Armbruster, W. Brüchle, H. Folger, F.P. Heßberger, S. Hofmann, G. Münzenberg, V. Ninov, W. Reisdorf, M. Schädel, K. Sümmerer, J.V. Kratz, U. Scherer, M.E. Leino
Cold Fusion Reactions with ^{48}Ca
PSI-Bericht Nr. 29 (1989)

M. Gai, J.F. Ennis, D.A. Bromley, H. Emling, F. Azgui, E. Grosse, H.J. Wollersheim, C. Mittag, F. Riess
Enhanced E1 Deexcitation in ^{218}Ra and the Evolution of Reflection Asym. at Moderate Spins
Phys. Lett. B215, 242 (1988)

D. Gardès, R. Bimbot, M. Dunmail, B. Kubica, A. Richard, M.F. Rivet, A. Servajean, C. Fleurier, A. Sanba, D. Hong, C. Deutsch, G. Maynard, D.H.H. Hoffmann, K. Weyrich, K.G. Dietrich
Experimental Investigation of Beam-Plasma Interactions Enhanced Stopping Power - Plasma Lens Effect
Rad. Effects and Defects in Solids 110, 49 (1989)

K. Geiger, M. Grabiak, O. Graf, S. Graf, W. Greiner, C. Hofmann, D.C. Ionescu, B. Müller, J. Reinhardt, T. de Reus, K. Rumrich, A. Schäfer, A. Scherdin, S. Schramm, G. Soff
Theoretical Considerations Concerning the GSI Positron Experiments
in: Test of Fundamental Laws in Physics Editions Frontiers 107 (1989) (Eds.: O. Fackler, J. Tran Thanh Van)

J. Gerl, Ch. Ender, D. Habs, W. Korten, E. Schulz, D. Schwalm
Observation of the Ground-State Band of ^{234}Th (^{18}O, ^{16}O) Reactions
Phys. Rev. C39, 1145 (1989)

J. Gerl, W. Korten, D. Habs, D. Schwalm, H.J. Wollersheim
Spectroscopy and Reaction Mechanism of the System $^{90}Zr \rightarrow {}^{232}Th$ in the Vicinity of the Coulomb Barrier
Z. Phys. A334, 195 (1989)

I. Giese
Writing PHIGS Applications with PL/1
SEAS Proceedings AM 1989, Amsterdam, The Netherlands

P. Glässel, R. Schmid-Fabian, D. Schwalm, D. Habs, U. v. Helmolt
^{252}Cf Fission Revisted - New Insights into the Fission Process
Nucl. Phys. A502, 317 (1989)

B. Grabez, P. Vater, R. Brandt
A New Methode for Identification of ions in a CR-39 Detector
Nucl. Inst. and Meth. in Phys. Res. B42, 286 (1989)

M. Grabiak, W. Greiner, B. Müller, G. Soff, P. Koch
Electroweak Physics at Ultrarelativistic Heavy Ion Colliders
J. Phys. G15, L25 (1989)

O. Graf, J. Reinhardt, B. Müller, W. Greiner, G. Soff
Angular Correlations of Coincident Electron-Positron Pairs Produced in Heavy-Ion Collisions with Nuclear Time Delay
Phys. Rev. Lett. 61, 2831 (1988)

K. Gramlich, N. Grün, W. Scheid
Coupled-Channel Calculations with Gauss-Type Orbitals for Charge Transfer and Ionisation in Collisions of the $(He\text{-}He)^{2+}$ System
J. Phys. B22, 2567 (1989)

K.A. Griffioen, B.J. Gluckman, R.J. Meijer, P. Decowski, R. Kamermans
Deducing the Initial Properties of Hot Nuclei Formed in Central Heavy-Ion Collisions
Phys. Rev. C40, 1647 (1989)

D.H.E. Gross, G. Klotz-Engmann, H. Oeschler
Relative Velocities Between Fragments - A Key Quantity in Multifragmentation
Phys. Lett. B224, 29 (1989)

R.K. Gupta, W. Scheid
Nuclear Polarization Effects due to Classical Dynamics of two Colliding ^{238}U Nuclei with frictional Forces
Phys. Rev. C40, 1653 (1989)

D. Habs
Spectroscopy in the Second Minimum
Nucl. Phys. A502, 105 (1989)

D. Habs
Simple Treatment of Ordered Beams, Spectroscopy and Collisions of Few-Electron Ions
Porc. of the Study Conf. SCOFEI, Bucharest, Aug. 1888, World Scientific Singapore (1989)

D. Habs, W. Baumann, J. Berger, P. Blatt, A. Faulstich, P. Krause, G. Kilgus, R. Neumann, W. Petrich, R. Stokstad, D. Schwalm, E. Szmola, K. Welti, A. Wolf, S. Zwickler, E. Jaeschke, D. Krämer, G. Bisoffi, M. Blum, A. Friedrich, C. Geyer, M. Grieser, H.W. Heyng, B. Holzer, R. Ihde, M. Jung, K. Matl, W. Ott, B. Povh, R. Repnow, M. Steck, M. Steffens, S. Dutta, T. Kühl, D. Marx, S. Schröder, M. Gerhard, R. Grieser, G. Huber, R. Klein, M. Krieg, N. Schmidt, R. Schuch, J.F. Babb, L. Spruch, W. Arnold, A. Noda
First Experiments with the Heidelberg Test Storage Ring TSR
Nucl. Instr. and Meth. in Phys. Res. B43, 390 (1989)

R.W. Hasse, H.A. Borgwaldt, E. Aker
Benchmarking on Supercomputers with a Highly Vectorized ADI Code
in: Algorithms, Computer Systems and User Experience, Elsevier 177 (1989) (Eds.: C.A. Brebbia, A. Peters)
(Proc. Int. Conf. on Application of Supercomputers in Engineering, Southampton, UK, Sept. 1989)

Z. He, J. Wu, W. Nörenberg
Evaporation of Particles from Hot Nuclei
Nucl. Phys. A489, 421 (1988)

J. Heilmann, H. Rink
DNA Strand Break Induction, Rejoining and Repair in Cultured Mammalian Cells after Irradiation with Accelerated Heavy Charged Particles
in: Frontiers in Radiation Biology, Balaban Publ. u. Verlag Chemie, Tel Aviv und Weinheim, 1989 (Ed.: E. Riklis)

B. Heimrich, H. Nestle, M. Winkler, H. Wollnik, J. Jacoby, R.W. Müller, D.H.H. Hoffmann
Final Focusing Lenses to Produce Hot Dense Matter
Nucl. Instr. and Meth. in Phys. Res. A278, 202 (1989)

D. Heinemann, B. Fricke, D. Kolb
Finite Element Method for the Accurate Solution of Diatomic Molecules
in: Numerical Determination of the Electronic Structure of Atoms, Diatomics and Polyatomic Molecules
NATO-AIP-Series C271, 275 (1989)

P.A. Henning, B.L. Friman
Dynamical Instabilities in Heavy-Ion Collisions
Nucl. Phys. A490, 689 (1988)

P.A. Henning, Ch. Becker, A. Lang, U. Winkler
Thermo Field Dynamics and the Generation of Bosonic Coherent States
Phys. Lett. B217, 211 (1989)

G. Herrmann
A Historical Target: Ammonium Diuranate
Nucl. Instr. and Meth. in Phys. Res. A282, 301 (1989)

G. Herrmann
Discovery and Confirmation of Fission
Nucl. Phys. A502, 141c (1989)

R. Herrmann, G. Plunien, W. Greiner, W. Scheid
Collective Spin from the Linearization of the Schrödinger Equation in Multidimentional Riemannian Spaces Used in Collective Nuclear Models
Mod. Phys. A4, 4961 (1989)

F.P. Heßberger, S. Hofmann, G. Münzenberg, K.-H. Schmidt, P. Armbruster, R. Hingmann
Nucl. Inst. and Meth. in Phys. Res. A274, 522 (1989)

F.P. Heßberger, H. Gäggeler, P. Armbruster, W. Brüchle, H. Folger, S. Hofmann, D. Jost, J.V. Kratz, M.E. Leino, G. Münzenberg, V. Ninov, M. Schädel, U. Scherer, K. Sümmerer, A. Türler, D. Ackermann
The New Nuclide ^{225}U
Z. Phys. A333, 163 (1989)

F.P. Heßberger, H. Gäggeler, P. Armbruster, W. Brüchle, H. Folger, S. Hofmann, D. Jost, J.V. Kratz, M.E. Leino, G. Münzenberg, V. Ninov, M. Schädel, U. Scherer, K. Sümmerer, A. Türler, D. Ackermann
The New Nuclide ^{225}U
Z. Phys. ;us.A333, 111 (1989)

D.H.H. Hoffmann, J. Meyer-ter-Vehn, R.W. Müller, I. Hofmann, R. Bock, R. Arnold
Beam-Plasma Interaction Experiments at GSI: An Experimental Program to Study High Energy Density in Matter by Means of Intense Heavy Ion Beams
Nucl. Instr. and Meth. in Phys. Res. A278, 44 (1989)

I. Hofmann
RF Linac and Storage Ring - Perspectives of Heavy Ion Fusion Studies at GSI
Nucl. Inst. and Meth. in Phys. Res. A278, 271 (1989)

I. Hofmann, J. Struckmeier, S. Cocher
Perspectives of Ultracold and Crystalline Ion Beams Cooled by Electrons
Proc. of the Europ. Part. Acc. Conf., Rome, June 7-11, 201 (1989)

S. Hofmann, P. Armbruster, G. Berthes, T. Faestermann, A. Gillitzer, F.P. Heßberger, W. Kurcewicz, G. Münzenberg, K. Poppensieker, H.J. Schött, I. Zychor
The New Nuclei ^{162}Os and ^{156}Ta and the N=84 Alpha Emitting Isomers
Z. Phys. A333, 107 (1989)

J. Homolka, W. Schott, W. Wagner, W. Wilhelm, R.D. Bent, M. Fatyga, R.E. Pollock, M. Saber, R.E. Segel, P. Kienle
Measurements of the $^{12}C(^{3}He,\pi^{+})^{15}N$ Reaction Cross Section near the Threshold
Phys. Rev. C38, 2686 (1988)

G. Huber, S. Schröder, R. Klein, M. Gerhard, R. Grieser, M. Krieg, A. Karafillidis, T. Kühl, A. Faulstich, W. Petrich, V. Balykin, D. Habs, R. Neumann, D. Schwalm, A. Wolf
Partial Laser Cooling and Saturation Spectroscopy on 9 MeV $^{7}Li^{+}$-Ions in a Storage Ring
Proc. of the 9th Int. Conf. on Laser Spectroscopy 'NICOLS'89, Academic Press (1989)

G. Hubricht, E. Träbert
A Position-Sensitive X-Ray Detector for an X-ray/Ion Coincidence Experiment
Phys. Scripta 39, 581 (1989)

E.K. Hulet, J.F. Wild, R.J. Dougan, R.W. Lougheed, J.H. Landrum, A.D. Dougan, P.A. Baisden, C.M. Henderson, R.J. Dupzyk, R.L. Hahn, M. Schädel, K. Sümmerer, G.R. Bethune
Spontaneous Fission Properties of ^{258}Fm,^{259}Md, ^{260}Md,^{258}No, and ^{260}[104]: Bimodal fission
Phys. Rev. C40, 770 (1989)

D.C. Ionescu, J. Reinhardt, B. Müller, W. Greiner, G. Soff
Reply on 'Comments on Non-Linear Interactions and Poly-Positronium Bound States'
J. Phys. G15, 931 (1989)

M. Ismail, M. Rashdan, A. Faessler, R. Linden, N. Ohtsuka, W. Wadia
Relativistic Effects on the Optical Potential of Deformed U+U Nuclei
Nucl. Phys. A496, 795 (1989)

J. Jacoby
Targets for Heavy Ion Beams for Beam-Plasma Interaction Research
Nucl. Instr. and Meth. in Phys. Res. A282, 94 (1989)

J. Jacoby, R.W. Müller, D.H.H. Hofmann, H. Wahl, K. Weyrich, B. Heimrich, M. Winkler, H. Wollnik, S. Maurmann
RFQ-Experiments with Intense Heavy-Ion Beams
Nucl. Instr. and Meth. in Phys. Res. A278, 82 (1989)

R.K. Jain, S.K. Bose, K.K. Dwivedi
Measurement of Heavy Ion Ranges in Complex Medium Using a Solid State Nuclear Track Detector
J. Phys. D22, 1025 (1989)

J. Kiefer
Heavy Ion Effects on Cells: an Approach to Theoretical Understanding
in: Terrestrial Space Radiation and its Biological Effects, Plenum Press, 117 (1989)

J. Kiefer, H. Straaten
Quantitative Interpretation of Heavy Ion Effects: Models for the Biolocal Effects of Heavy Ions
Adv. Space Res. 9, (10)21 (1989)

P. Kienle
Strong Field Atomic Processes
Europhys. News, 20, 97 (1989)

P. Kienle
Studies of Radioactive Decays of Completely Ionized Nuclei in a Heavy Ion Storage Ring
Nucl. Instr. and Meth. in Phys. Res. A271, 277 (1988)

P. Kienle
Electron-Positron-Paircreation in Heavy Ion Collisions
Physics Scripta T23, 123 (1988)

P. Kienle,
Quasiatoms
1990 McGraw-Hill Yearbook of Science and Technology

G. Klotz-Engmann, H. Oeschler, J. Stroth, E. Kankeleit, Y. Cassagnou, M. Conjeaud, R. Dayras, S. Harar, R. Legrain, E.C. Pollacco, C. Volant
Properties of Binary Fission and Multifragmentation
Nucl. Phys. A499, 392 (1989)

J. Knoll, C. Guet
Sum Rules at Finite Temperature and the Limitation of Kinetic Particle-Production Models
Nucl. Phys. A494, 334 (1989)

J. Knoll
Is the Quark-Gluon Plasma Detectable from Flavour Signals?
Nucl. Phys. A496, 539 (1989)

G. Koch, G. Breitbach, V. Metag, S. Tschesche, R. Beck, U. Dittmayer, R. Gothe, F. Kalleicher, M. Schmitz, B. Schoch, J. Vogt, S. J. Hall, J. D. Kellie, J. C. Mc-George, D. Branford, H. Ströher
Cross Sections and Angular Distributions for $^{12}C(\gamma, \pi^{0})$
Phys. Lett. B218, 143 (1989)

G. Koch, G. Breitbach, V. Metag, S. Tschesche, R. Beck, R. Gothe, B. Schoch, J. D. Kellie, J. C. Mc-George, S. J. Hall, H. Ströher
Differential Cross Sections for Coherent and Incoherent Neutral Pion Photoproduction from Calcium
Phys. Rev. Lett. 43, 498 (1989)

W. König, E. Berdermann, F. Bosch, S. Huchler, P. Kienle, C. Kozhuharov, A. Schröter, S. Schuhbeck and H. Tsertos
On the Momentum Correlation of $(e^{+}e^{-})$ Pairs Observed in U+U and U+Pb Collisions
Phys. Lett. B218, 12 (1989)

E.A. Koop, G. Feige, L. Schmidt, H. Junclas, R. Brandt, G. Ingold, D.C. Hoffman
Direct Measurement of the Neutron Emission in Complete and Incomplete ^{12}C-Induced Fusion Reactions
Phys. Rev. C39, 687 (1989)

M. Kost
Biological Action of Ion Irradiation on Individual Yeast Cells
in: Terrestrial Space Radiation and its Biological Effects, Plenum Press, 197 (1989)

M. Krämer, B. Blank, E. Bozek, E. Ditzel, E. Kankeleit, G. Klotz-Engmann, C. Müntz, H. Oeschler, M. Rhein, P. Senger
Phys. Rev. C40, 1662 (1989)

D. Kraft, K.E. Stiebing, K. Bethge, E. Schmidt,
H. Bokemeyer, H. Folger
Fast Determination of Structure, Homogeneity, and Composition of Targets for Heavy Ion Experiments from Backscattering and Pixe with 1.6 MeV Protons
Nucl. Instr. and Meth. in Phys. Res. A282, 199 (1989)
(Proc. of INTDS & IAEA-INDC Conf., Darmstadt, FRG, 1988)

J. Kramp, J. Gerl, D. Habs, D. Schwalm, P. Thirolf
The Search for Resonances in the $e^+e^- \rightarrow n\gamma$ System
in: Test of Fundamental Laws in Physics, Editions Frontiers, 171 (1989) (Eds.: O. Fackler, J. Tran Thanh Van)

J. V. Kratz, H. P. Zimmermann, U. W. Scherer, M. Schädel, W. Brüchle, K. E. Gregorich, C. M. Gannett, H. L. Hall, R. A. Henderson, D. M. Lee, J. D. Leyba, M. J. Nurmia, D. C. Hoffman, H. Gäggeler, D. Jost, U. Baltensperger, Ya Nai-Qi, A. Türler, Ch. Lienert
Chemical Properties of Element 105 in Aqueous Solutions: Halide Complex Formation and Anion Exchange into Triisooctyl Amine
Radiochim. Acta 48, 121 (1989)

W. Krötz, A. Ulrich, B. Busch, G. Ribitzki, J. Wieser
Emission of Vacuum Ultraviolet Radiation from Neon Excimers Excited by a Heavy Ion Beam
Appl. Phys. Lett. 55, 2265 (1989)

W. Kühn, R. Ruckelshausen, R.D. Fischer, G. Breitbach, H.J. Hennrich, V. Metag, R. Novotny, R.V.F. Janssens, T.L. Khoo, D. Habs, D. Schwalm, B. Haas, R.S. Simon
Nuclear-Structure Dependence of Heavy-Ion Fusion Partial-Wave Distributions
Phys. Rev. Lett. 62, 1103 (1989)

R. Kulessa, R. Bengtsson, H. Bohn, H. Emling, T. Faestermann, F. v. Feilitsch, E. Grosse, W. Nazarewicz, D. Schwalm, H.J. Wollersheim
Angular Momentum Dependence of the Quadrupole Deformation in ^{182,184,186}W
Phys. Lett. B218, 421 (1989)

S. Laubach, P. Schwalbach, M. Hartick, E. Kankeleit, G. Klingelhöfer, R. Sielemann
Time-Differential Mößbauerspectroscopy of ^{57}Fe in Silicon after Coulomb Excitation by Pulsed Heavy Ion Beams
Z. Phys. B75, 173 (1989)

S. Laubach, M. Hartick, B. Keck, E. Kankeleit, G. Klingelhöfer, P. Schwalbach, R. Sielemann
Time Differential Mößbauerspectroscopy with ^{75}Fe after Coulomb Excitation by Pulsed Heavy Ion Beams
Hyperfine Interactions 47, 570 (1989)

D. Liesen
Electron Cooling Rings
in: Physics of Highly-Ionized Atoms, Plenum Press 1989 (Ed.: R. Marrus) (Proc. of the Conference Atomic Physics of Highly-Ionized Atoms', Cargèse, Corsica, June 1988)

Th. Lippert, N. Grün, W. Scheid
Production of Dileptons by Bremsstrahlung During the Stopping of Relativistic Heavy Ions
Mod. Phys. A4, 4221 (1989)

R. Maass, K.-E. May, W. Scheid
Inversion of Elastic Scattering Phase Shifts Calculated with Algebraic Scattering Theory
Phys. Rev. C39, 1201 (1989)

R. Männer, Ch. Ender, W. Ludwig, P. Bauer, A. Wurz
Multiprocessor Data Acquisition and Analysis with the Heidelberg Polyp System, Hardware and Software for Real Time Process Control
Elesevier Science Publ. BV, North Holland, IFIP 1989 (Eds.: J. Zalewski, W. Ehrenberger)

R. Marrus, A. Simionovici, P. Indelicato, D. Dietrich, P. Charles, J.P. Briand, K. Finlayson, F. Bosch, D. Liesen, F. Parente
Measurement of the 2^3P_0-2^3P_1 Fine Structure Splitting in Heliumlike Ag^{45+}
Phys. Rev. Lett. 63, 502 (1989)

R. Marrus, P. Charles, P. Indelicato, L. de Billy, Ch. Tazi, J.P. Briand, A. Simionovici, D. Dietrich, F. Bosch, D. Liesen
The Lifetime of the 2^3S_1 State of Heliumlike Xenon (Xe^{52+})
Phys. Rev. A39, 3725 (1989)

K.-E. May, E. Scheid
The Inverse Scattering Problem in Nuclear Heavy-Ion Physics at Fixed Angular Momentum with Bound States
Nucl. Phys. A499, 200 (1989)

G. Mehler, G. Soff, K. Rumrich, W. Greiner
K-Shell Ionization in Relativistic Ion-Atom Collisions
Z. Phys. D13, 193 (1989)

R.J. Meijer
Central Collisions between ^{28}Si Nuclei at 12.4, 19.7 and 30.0 MeV/Nucleon
Thesis, University of Utrecht, The Netherlands, 1989

F. Melchert, E. Salzborn, I. Hofmann, R.W. Müller, V.P. Shevelko
Beam Intensity Losses in the Storage Rings
Nucl. Instr. and Meth. in Phys. Res. A278, 65 (1989)

J.C.C. van Melle, G.J. van Nieuwenhuizen, R.J. Meijer, P. Box, P. Decowski, R. Kamermans
Pulse Shape Analysis of CsI(tl)-PD Signals Induced by 6-20 MeV α-Particles
Nucl. Instr. and Meth. in Phys. Res. A277, 584 (1989)

R. Menegazzo, H. Güven, J. Styczen, N. Roy, P. Kleinheinz, D. Schardt, R. Barden, G. Walter, A. Huck, G. Marguier, J. Blomqvist and the ISOLDE Collaboration
Gamow-Teller Strength and Particle-Phonon States in ^{149}Dy from Decay of its $11/2^-$ and $1/2^+$ ^{149}Ho Parents
Z. Phys. A334, 525 (1989)

J. Meyer, W.-D. Sepp, B. Fricke, A. Rosen
Computation of Relativistic Symmetry Orbitals for Finite Double-Point Groups
Comp. Phys. Comm. 54, 55 (1989)

B. Milek, W. Nörenberg, and P. Rozmej
Quantum Chaos in the Two-Center Shell Model
Z. Phys. A 334, 233 (1989)

U. Milkau, D. Bohle, A. Richter
Search for the Mixed-Symmetry $J^\pi = 1^+$ and 2^+ States in ^{110}Pd with Inelastic Electron Scattering
Nucl. Phys. A499, 517 (1989)

P.H. Mokler, S. Reusch, Th. Stöhlker
Heavy-Ion Beam Tailoring Using Dielectronic Recombination
Nucl. Instr. and Meth. in Phys. Res. A278, 93 (1989)

P.H. Mokler, S. Reusch, Th. Stöhlker, R. Schuch, M. Schulz, G. Wintermeyer, Z. Stachura, A. Warczak, A. Müller, Y. Awaya, T. Kambara
Resonant Transfer and Excitation in Swift, Heavy Few-Electron Projectiles
Rad. Effects and Defects in Solids 110, 39 (1989)

G. Möller, E. Träbert, V. Lodwig, C. Wagner, P.H. Heckmann, J.H. Blanke, A.E. Livingston, P.H. Mokler
Experimental Transition Probability for the E1 Intercombination Transition in Be-Like Xe $^{50+}$
Z. Phys. D11, 333 (1989)

K. Momberger, N. Grün, W. Scheid, U. Becker
Angular Distribution of Electrons Emitted from 1s½ and 2s½ States in Relativistic Heavy-Ion Collisions
J. Phys. B22, 3269 (1989)

B. Morgenstern, W. Nörenberg
Dissipative Fluid Dynamics
Nucl. Phys. A492, 93 (1989)

D.J. Morrissey
Systematics of Momentum Distributions from Reactions with Relativistic Ions
Phys. Rev. C39, 460 (1989)

A. Müller
Targets Consisting of Free Charged Particles
Nucl. Instr. and Meth. in Phys. Res. A282, 80 (1989)

B. Müller, J. Reinhardt, O. Graf, S. Graf, C. Ionescu, S. Schramm, M. Grabiak, W. Greiner, A. Schäfer, G. Soff
Theoretical Attempts to Explain the GSI Positron Peaks
in: AIP 189, 479 (1989) (Eds.: W. Johnson, P. Mohr, J. Sucher)
(Proceedings of the Conference on 'Relativistic, Quantum Electrodynamics, and Weak Interactions Effects in Atoms')

G. Münzenberg, F.P. Heßberger, W. Faust, H. Folger, S. Hofmann, K.-H. Schmidt, H.-J. Schött, P. Armbruster
Nucl. Instr. and Meth. in Phys. Res. A282, 28 (1989)

G. Münzenberg
Heavy Element Production and Limits to Fusion
Nucl. Phys. A502, 571c (1989)

G. Münzenberg, P. Armbruster, S. Hofmann, F.P. Heßberger, H. Folger, J.G. Keller, V. Ninov, K. Poppensieker, A.B. Quint, W. Reisdorf, K.-H. Schmidt, J.R.H. Schneider, H.-J. Schött, K. Sümmerer, I. Zychor, M.E. Leino, D. Ackermann, U. Gollerthan, E. Hanelt, W. Morawek, D. Vermeulen, Y. Fujita, T. Schwab
Element 107
Z. Phys. A333, 163 (1989)

G. Münzenberg Status and Prospects for the Production and Investigation of Heavy Elements
Proc. Int. Symposium on Advanced Nuclear Energy Research JAERI, Tokyo, Japan 135 (1989)

T. Matulewicz, E. Grosse, H. Emling, H. Grein, R. Kulessa, F.M. Baumann, G. Domogala, H. Freiesleben
Response of CsI(Tl) and Pb-Glass Detectors to Neutrons Below 22 MeV
Nucl. Instr. and Meth. in Phys. Res. ;us.A276, 501 (1989)

T. Murakami, T.K. Nayak, W.G. Lynch, K. Swartz, Z. Chen, D.J. Fields, C.K. Gelbke, Y.D. Kim, M.R. Maier, J. Pochodzalla, M.B. Tsang, H.M. Xu, and F. Zhu
A Position Sensitive High Resolution Hodoscope for Particle Unstable Intermediate Mass Fragments
Nucl. Instr. and Meth. A275, 112 (1989)

T.K. Nayak, T. Murakami, W.G. Lynch, K. Swartz, D.J. Fields, C.K. Gelbke, Y.D. Kim, J. Pochodzalla, M.B. Tsang, F. Zhu, and K. Kwiatkowski
Fragmentation Products with Non-Statistical Excited State Populations
Phys. Rev. Lett. 62, 1021 (1989)

W. Neu, R. Neugart, E.-R. Otten, G. Passler, K. Wendt, B. Fricke, E. Arnold, H.-J. Kluge, G. Ulm
Quadrupole Moments of Radium Isotopes from the 7p $^2P_{3/2}$ Hyperfine Structure in Ra II
Z. Phys. D11, 105 (1989)

K. Niita, T.S Biro, W. Cassing, A.L. de Paoli, U. Mosel, M. Schäfer
Particle Production within a Selfconsistent Transport Approach to Heavy-Ion Collisions
Nucl. Phys. A495, 91c (1989)

K. Niita, W. Cassing, U. Mosel
Hard Photon Production within a Selfconsistent Transport Approach to Heavy-Ion Collisions
Nucl. Phys. A504, 391 (1989)

M. Okolowicz, M. Ploszajczaj, S. Drozdz, E. Caurier
Giant Dipole Resonances in Hot Nuclear Matter in a Model of Self-Relaxing Mean Field
Nucl. Phys.A501, 289 (1989)

R.E. Olson, J. Ullrich, H. Schmidt-Böcking
Multiple-Ionization Collision Dynamics
Phys. Rev. A39, 5572 (1989)

R.E. Olson, J. Ullrich, R. Dörner, H. Schmidt-Böcking
Single- and Double-Ionization Cross Sections for Angular Scattering of Fast Protons by Helium
Phys. Rev. A40, 2843 (1989)

U. Ornik, F.W. Pottag, R.M. Weiner
High-Energy Heavy-Ion Reactions and Relativistic Hydrodynamics in Three Dimensions
Phys. Rev. Lett. 63, 2641 (1989)

A. Palmeri, S. Aiello, A. Badala, R. Barbera, G.S. Pappalardo, L. Bimbot, F. Reide, N. Willis, H. Oeschler
Charged Pions from the Isotopes ^{58,64}Ni by 201 MeV Protons
Phys. Rev. C40, 1081 (1989)

G. Pantis, R. Linden, N. Ohtsuka, W. Wadia
Effect of 3-α States in ^{12}C-^{12}C Scattering
Nucl. Phys. A499, 209 (1989)

Z. Patyk, A. Sobiczewski, P. Armbruster, K.-H. Schmidt
Shell Effects in the Properties of the Heaviest Nuclei
Nucl. Phys. A491, 267 (1989)

U. Post, U. Mosel
Selfconsistent Mean Field Wavefunctions of Nucleon and Delta for the Cranked Chiral Soliton Bag
Nucl. Phys. A499, 789 (1989)

G. Plunien, B. Müller, W. Greiner, G. Soff
Nuclear Polarization Contribution to the Lamb-Shift in Heavy Atoms
Phys. Rev. A39, 5428 (1989)

J. Pochodzalla, R.J. Charity, U. Lynen, H. Sann, W. Trautmann, R. Trockel
Possibility of Transient Effects During the Emission of Intermediate Mass Fragments
Phys. Rev. 40, 2918 (1989)

J. Pochodzalla, W. Trautmann, U. Lynen
Sensitivities of the Relative Velocity Between Fragments on the Decay Mechanism
Phys. Lett. B232, 41 (1989)

S. Polikanov
Meson, Hyperon, and Antiproton Induced Fission
Nucl. Phys. A502, 195c (1989)

F. Pougheon, V. Borrel, J.C. Jacmart, R. Anne, C. Détraz, D. Guillemaud-Mueller, A.C. Mueller, D. Bazin, R. Del Moral, J.P. Dufour, F. Hubert, M.S. Pravikoff, G. Audi, E. Roeckl, B.A. Brown
Beta-Delayed Proton Decay of ^{28}S
Nucl. Phys. A500, 287 (1989)

K. Rashid, B. Fricke, J.H. Blanke, J.-P. Desclaux
Ground State Correlation Energy of the Be-Sequence for Z = 4-20 in MCDF Approximation
Z.Phys. D11, 99 (1989)

T. Reitz
On the Validity of the Cranking Model for 2^+-Vibrations
Z. Phys. A332, 137 (1989)

T. Reitz, U. Mosel
Ion-Ion Optical Potentials in a Relativistic Model
Nucl. Phys. A501, 877 (1989)

T. de Reus, U. Müller-Nehler, G. Soff, J. Reinhardt, S. Graf, B. Müller, W. Greiner
Coupled-Channel Results for Atomic Excitations in Intermediate-Energy Heavy-Ion Collisions
Phys. Rev. C40, 752 (1989)

U. Reuter, F. Hagelberg, S. Kremeyer, H.-J. Simonis, K.-H. Speidel, M. Knopp, W. Karle, J. Cub, P.N. Tandon, J. Gerber
Large Transient Magnetic Fields for Single Electron O-Ions on a 10fs Time Scale
Phys. Lett. 230B, 16 (1989)

H. Riege, E. Boggasch
High-Power, High-Current Pseudospark Switches
IEEE Trans. Plasma Sci., PS-17, 775 (1989)

E. Roeckl
Nuclear Structure Data from Charged-Particle Decay Spectroscopy: Some Recent Results
J. Phys. Soc. Jpn. 58, Suppl. 509 (1989)
(Proc. 5th Int. Conf. Clustering Aspects in Nucl. and Subnucl. Systems, Kyoto, 1988)

W. Rösch, W. Cassing, H. Gemmecke, R. Gentner, K. Keller, L. Lassen, W. Lücking, A. Richter, R. Schreck, G. Schrieder
Preequilibrium Emission in Central Collisions of the Mass-Symmetric System $^{40}Ar + ^{40}Ca$ at 20 MeV/u
Nucl. Phys. A496, 141 (1989)

B. Rumler, N. Trautmann, G. Herrmann
Chemistry at Low Concentrations: Astatine at a Level of 10^8 to 10^3 Atoms
Radiochimica Acta 47, 91 (1989)

K. Rumrich, W. Greiner, G. Soff, K.-H. Wietschorke, P. Schlüter
Continuum States of the Two-Centre Dirac Equation
J. Phys. B22, 165 (1989)

W. Ruster, F. Ames, H.-J. Kluge, E.-W. Otten, D. Rehklau, F. Scheerer, G. Herrmann, C. Mühlbeck, J. Riegel, H. Rimke, P. Sattelberger, N. Trautmann
A Resonance Ionization Mass Spectrometer as an Analytical Instrument for Trace Analysis
Nucl. Instr. and Meth. in Phys. Res. A281, 547 (1989)

K. Rykaczewski, K.-L. Gippert, N. Kaffrell, R. Kirchner, O. Klepper, V.T. Koslowsky, W. Kurcewicz, W. Nazarewicz, E. Roeckl, E. Runte, D. Schardt, W.-D. Schmidt-Ott, P. Tidemand-Petersson
Investigation of Neutron-Rich Rare-Earth Nuclei Including the New Isotopes ^{177}Tm and ^{184}Lu
Nucl. Phys. A499, 529 (1989)

K. Rykaczewski, A. Plochocki, I.S. Grant, H. Gabelmann, R. Barden, D. Schardt, J. Zylicz, G. Nyman
The Gamow-Teller Beta Decay of ^{100}Cd
Z. Phys. A332, 275 (1989)

P. Sattelberger, M. Mang, G. Herrmann, J. Riegel, H. Rimke, N. Trautmann, F. Ames, H.-J. Kluge
Separation and Detection of Trace Amounts of Technetium
Radiochim. Acta 48, 165 (1989)

A. Saxena, K.K. Dwivedi, E. Reischwein, G. Fiedler
Energy-Loss Measurement of ^{132}Xe in Lead by a Nuclear Track Technique
Nucl. Instr. and Meth. in Phys. Res. B36, 276 (1989)

M. Schädel, W. Brüchle, E. Jäger, E. Schimpf, J. V. Kratz, U.W. Scherer, H. P. Zimmermann
ARCA II - A New Apparatus for Fast, Repetitive HPLC Separations
Radiochim. Acta 48, 171 (1989)

A. Schäfer, G. Soff, P. Indelicato, B. Müller, W. Greiner
Prospects of an Atomic Parity Violation Experiment in U^{90+}
Phys. Rev. A40, 7362 (1989)

M. Schäfer, T.S. Biro, W.Cassing, U. Mosel
e^+e^--Production in Proton-Neutron Collisions
Phys. Lett. B221, 1 (1989)

W. Scheid, H. Hora
On Electron Acceleration by Plane Transverse Electromagnetic Pulses in Vacuum
Laser and Particle Beams 7, 315 (1989)

J. Schirmer, J. Gerl, D. Habs, D. Schwalm
γ-Decay of the Superdeformed Shape Isomer in ^{236}U
Phys. Rev. Lett. 63, 2196 (1989)

J.M. Schmidt, G. Soff, P.J. Mohr
Higher-Order Vacuum Polarisation Corrections in Muonic Atoms
Phys. Rev. A40, 2176 (1989)

R. Schmidt, B. Kämpfer, H. Feldmeier, O. Knospe
Relativistic Effetcs in Molecular Dynamics Simulations of Heavy-Ion Reactions
Phys. Lett.B229, 197 (1989)

H. Schmidt-Böcking, J. Ullrich, R. Schuch, R.E. Olson, R. Dörner
Electronic Transitions in Highly Charged Ion-Atom Collisions
Nucl. Instr. and Meth. in Phys. Res. B43, 272 (1989)

M. Schönhofen, M. Cubero, M. Gering, M. Sambataro, H. Feldmeier, W. Nörenberg
The Nuclear Equation of State in Effective Relativistic Field Theories and Pion Yields in Heavy Ion Collisions
Nucl. Phys. A504, 875 (1989)

M. Schönhofen, M. Cubero, H. Feldmeier, W. Nörenberg
On the Relation between Pion Yields and the Nuclear Equation of State in a Self-Consistent Treatment
World Scientific, Singapore, 200 (1989) (Eds.: W.Q Shen, J.Y. Liu, L.X. Ge)
(Proc. of the Int. Summer School on 'Heavy Ion Reaction Theory', Lanzhou, P.R. of China)

P. Schuck, G. Chanfray, W. Nörenberg
Is the σ Field in the σ-ω Model Related to a Pion Pair Coherent State?
Nucl. Phys. A495, 355c (1989)

P. Schuck, R.W. Hasse, J. Jaenicke, C. Grégoire, B. Rémaud, F. Sébille, E. Suraud
Semiclassical and Phase Space Approaches to Dynamic and Collisional Problems of the Nucleus
Prog. Part. Nucl. Phys. 22, 181 (1989)

G. Schütz, M. Knülle, R. Wienke, W. Wilhelm, W. Wagner, P. Kienle, R. Frahm
Spin-Dependent Photoabsorption at the L-Edges of Ferromagnetic Gd and Tb Metal
Z. Phys. B73, 67 (1988)

G. Schütz, R. Frahm, P. Mautner, R. Wienke, W. Wagner, W. Wilhelm, and P. Kienle,
Spin-Dependent Extended X-Ray Absorption Fine Structure: Probing Magnetic Short-Range Order
Phys. Rev. Lett. 22, 2620 (1989)

G. Schütz, R. Wienke, W. Wilhelm, W. Wagner, R. Frahm, P. Kienle
Spin-Dependent absorption at the K- and $L_{2,3}$-Edges in Ferromagnetic $Fe_{medium.80}^{large.Pt_{20}}$ Alloy.
Physica B158, 284 (1989)

G. Schütz, R. Wienke, W. Wilhelm, W. Wagner, R. Frahm, P. Kienle, R. Zeller
Strong Spin-Dependent Absorption at the $L_{2,3}$-Edges of 5d-Impurities in Iron
Z.Phys. B75, 495 (1989)

G. Schütz, R. Frahm, R. Wienke, W. Wilhelm, W. Wagner, P. Kienle
Spin-Dependent K- and L-Absorption Measurements
Rev.Sci.Instr. 60, 1661 (1989)

H. Schulte, B. Jäckel, R.A. Esterlund, M. Knaack, W. Westmeier, A. Rox, P. Patzelt
Dynamic Contributions to Symmetric Fragmentation Processes
Phys. Lett. B232, 37 (1989)

M. Schulz, S. Datz, P.F. Dittner, J.P. Giese, H.F. Krause, P.D. Miller, H. Schöne, J.K. Swenson, C.R. Vane, R. Schuch, E. Justiniano, M. Benhenni, S.M. Shafroth, P.H. Mokler, S. Reusch
Transfer and Excitation Processes Studied in H-Like S and Li-Like and H-Like F Colliding with H_2
Nucl. Instr. and Meth. in Phys. Res. B40/41, 154 (1989)

P. Schwalbach, M. Hartick, U. Imkeller, E. Kankeleit, S. Laubach, M. Menningen, R. Sielemann
Implantation of Coulomb Excited ^{57}Fe into Silicon and MnF_2
Hyperfine Interactions 47, 573 (1989)

G. Soff
Higher-Order Vacuum Polarization Charge Densities for Spherical Symmetric External Potentials
Z. Phys. D11, 29 (1989)

G. Soff, P.J. Mohr
Influence of Vacuum Polarization Corrections of the Order $\alpha(Z\alpha)$ and $\alpha(Z\alpha)^3$ in Hydrogen-Like Uranium
Phys. Rev. A40, 2174 (1989)

G. Soff, J. Rafelski
Radiative Muon Capture in Light Atoms
Z. Phys.D14, 187 (1989)

G. Soff, J. Reinhardt, T. de Reus, K.-H. Wietschorke, S. Graf, A. Schäfer, P. Schlüter, U. Müller, B. Müller, W. Greiner
Positrons Produced in Heavy Ion Collisions - Vacuum Decay - a New Particle - or Something Else?
Journ. of the Madras University B50, 1 (1987) (erst jetzt erschienen)

P. Spädtke
Computer Modeling
in: The Physics and Technology of Ion Sources, J. Wiley & Sons, ISBN 0-471-85708-4, (Ed.: I.G. Brown)

K.-H. Speidel, M. Knopp, W. Karle, J. Cub, M.-L. Dong, H.-J. Simonis, F. Hagelberg, U. Reuter, S. Kremeyer, J. Gerber, P.N. Tandon
Transient Magnetic Fields for Highly Stripped Ions Transversing Ferromagnetic Solids
Hyp. Int.51, 817 (1989)

K.-H. Speidel, M. Knopp, W. Karle, M.-L. Dong, J. Cub, U. Reuter, H.-J. Simonis, P.N. Tandon, J. Gerber
Heavy Ion Beam Induced Attenuations of Transient Magnetic Fields
Phys. Lett. 227B, 16 (1989)

K.-H. Speidel, M. Knopp, J. Cub, W. Karle, J. Cub, U. Reuter, H.-J. Simonis, F. Hagelberg, J. Gerber, P.N. Tandon
Strong Dynamic Perturbations of Transient Magnetic Fields in Ferromagnetic Fe and Gd Under Heavy Ion Bombardment
Rad. Effects and Defects in Solids 110, 173 (1989)

A. Steinhof, K.H. Behr, A. Brünle, E. Roeckl, E. Boaretto, M. Paul, D. Fink, G. Hollos, W. Kutschera
Electromagnetic Isotope Enrichment for Accelerator Mass Spectrometry of ^{41}Ca
Nucl. Instr. and Meth. in Phys. Res. B43, 73 (1989)

A. Steinhof, H. Folger, W. Henning, M. Müller, A. Paic, E. Roeckl, D. Schüll
Charge State Distribution of Potassium and Calcium Ions, and Full-Stripping Probabilities in Carbon Foils for Medium-Heavy Fast Ions
Nucl. Instr. and Meth. in Phys. Res. B36, 93 (1989)

K.E. Stiebing, D. Kraft, P. Salabura, K. Bethge, H. Bokemeyer, H. Folger
Influence of Heavy Ion Bombardment on the Structure of Targets for Atomic and Nuclear Interaction Studies
Nucl. Instr. and Meth. in Phys. Res. A282, 206 (1989)
(Proc. of INTDS & IAEA-INDC Conf., Darmstadt, FRG, 1988)

B. Szweryn, W. Brüchle, B. Schausten, M. Schädel
Radiochemical Separations of Target-Like Reaction Products from Au-, Pt-, and Th-Targets after Irradiation with GeV Protons
Radiochim. Acta 47, 33 (1989)

J.L. Tain, B. Rubio, P. Kleinheinz, D. Schardt, R. Barden, J. Blomqvist
Two-Nucleon Excitation in $^{148}_{66}Dy_{82}$ from Gamow-Teller Decay of the $^{148}_{67}Ho_{81}$ 6^- Isomer
Z. Phys. A333, 29 (1989)

A. Thiel, W. Greiner, J.Y. Park, W. Scheid
Structures due to the Nuclear Landau-Zener Effect in the $^{17}O + ^{12}C$ Scattering within the Molecular Particle-Core Model
J. Phys. G15, 1833 (1989)

A. Thiel, Th. Lippert, N. Grün, W. Scheid
Cross Sections for Photons Produced in the Stopping Phase in Relativistic Heavy-Ion Collisions
Nucl. Phys. A504, 864 (1989)

B. Thies, W.-D. Sepp, B. Fricke
Many-Electron Coupled Channel Calculations for the System F^{8+}-Ne
J. de Phys. C1, 193 (1989)

B. Thies, W.-D. Sepp, B. Fricke
Many-Electron Relativistic Calculation and Interpretation of Atomic Processes in Time Dependent Heavy Ion Scattering
Phys. Lett. A139, 161 (1989)

B. Thies, W.-D. Sepp, B. Fricke
Relativitic Many-Electron Coupled-Channel Calculations in Heavy Ion Scattering
in: Spectr. and Coll. of Few-Electron Ions (World Scientific, Singapore, 1989)
(Eds.: M. Ivascu, V. Florescu, V. Zoran)

N. Trautmann, H. Folger
Preparation of Actinide Targets by Electrodeposition
Nucl. Inst. and Meth. in Phys. Res. A282, 102 (1989)

N. Trautmann, G. Herrmann, C. Mühleck, P. Peuser, H. Rimke, P. Sattelberger F. Ames, H.-J. Kluge, E.-W. Otten, D. Rehklau, W. Ruster
Laser Resonance Ionization Mass Spectrometry as a Sensitive Analytical Method for Actinides and Technetium
Isotopenpraxis 24/6, 217 (1988)

R. Trockel, K.D. Hildenbrand, U. Lynen, W.F.J. Müller, H.J. Rabe, H. Sann, H. Stelzer, W. Trautmann, R. Wada, E. Eckert, P. Kreutz, A. Kühmichel, J. Pochodzalla, D. Pelte
Onset of Multifragment Emission in Heavy-Ion Collisions
Phys. Rev. C39, 729 (1989)

H. Tsertos
Search for Resonant Bhabha Scattering at MeV Energies
Nucl. Instr. and Meth. in Phys. Res. A284, 54 (1989)

H. Tsertos
Comment on Electron Peaks in e^+ + Th, U, and Ta Interactions
Phys. Rev. C40 1839 (1989)

H. Tsertos, C. Kozhuharov, P. Armbruster, P. Kienle, B. Krusche, K. Schreckenbach
High-Sensitivity Measurements of the Excitation Function for Bhabha Scattering at MeV Energies
Phys. Rev. D40, 1397 (1989)

J. Ullrich, R.E. Olson, H. Berg, S. Kelbch, R. Dörner, C. Kelbch, H. Schmidt-Böcking, S. Hagmann, P. Richard, M. Prior, A.S. Schlachter
Multiple Ionization and Collision Dynamics in High-Energy Uranium-Rare Gas Collisions
Nucl. Instr. and Meth. in Phys. Res. B40/41, 149 (1989)

J. Ullrich, R.E. Olson, R. Dörner, V. Dangendorf, S. Kelbch, H. Berg, H. Schmidt-Böcking
Influence of Ionised Electrons on Heavy Nuclei Angular Differential Scattering Cross Sections
J. Phys. B22, 627 (1989)

J. Ullrich, R. Olson, H. Schmidt-Böcking, S. Schmidt, R. Dörner, V. Dangendorf, H. Berg
Multiple Ionisation and Collective Electron Emission in Mev/u Uranium-Ion Rare Gas Collisions
J. de Phys. Coll. C1, Tome 50 (1989)

J. Ullrich, R. Olson, H. Berg, S. Kelbch, R. Dörner, C. Kelbch, H. Schmidt-Böcking, S. Hagmann, P. Richard, M. Prior, F. Schlachter
Multiple Ionisation and Collision Dynamics in High-Energy Uranium - Rare Gas Collisions
in: 'Spectroscopy and Collisions of Few-Electron Ions', World Scientific (Eds.: M. Ivascu, V. Floyescu, V. Zoran)
(Proceedings of the Study Conference SCOFEI 88, Bucharest, Romania, Aug. 29 - Sept. 2, 1988)

A. Ulrich, B. Busch, W. Krötz, G. Ribitzki, J. Wieser
Emission of Light from Matter Excited by Heavy Ion Beams
Nucl. Instr. and Meth. in Phys. Res. A278, 72 (1989)

S.J. Wang, W. Cassing
Extended Relativistic Mean Field Theory and Relativistic Transport Equations
Nucl. Phys. A495, 371c (1989)

Th. Weber, W. Wilke, H. J. Emrich, R. D. Heil, Th. Kihm, U. Kneissl, K. T. Knöpfle, U. Seemann, F. Steiper, H. Ströher
Evidence for Different Fission Fragment Mass Aymmetries for Specific Nuclear Excitations Studied in (e, e'f) and (γ,f) Reactions
Nucl. Phys. A502, 279c (1989)

K. Weyrich, D.H.H. Hoffmann, J. Jacoby, H. Wahl R. Noll, R. Haas, H. Kunze, R. Bimbot, D. Gardès, M.-F. Rivet, C. Deutsch, C. Fleurier
Energy Loss of Heavy Ions in a Hydrogen Discharge Plasma
Nucl. Instr. and Meth. in Phys. Res. A278, 52 (1989)

J.B. Wilhelmy, M. Begemann-Blaich, T. Blaich J. Boissevain, M.M. Fowler, A. Gavron, B.V. Jacak, P.S. Lysaght H.C. Britt, D.J. Fields, L.F. Hansen, R.G. Lanier, D.J. Massoletti, M.N. Namboodiri, B.A. Remington, T.C. Sangster, G.L. Struble, M.L. Webb, Y.D. Chan, A. Dacai, A. Harmon, J. Leyba, J. Pouliot, R.G. Stokstad, O. Hansen, M.J. Levine, C.E. Thorn, W. Trautmann, B. Dichter, S. Kaufman, F. Videbaek, Z. Fraenkel, G. Mamane, D. Cebra, G.D. Westfall
Fission in Intermediate Energy Heavy Ion Reactions
Nucl. Phys. A502, 601c (1989)

G. Wintermeyer, V. Dangendorf, M. Gabr, T. Kambara, P.H. Mokler, S. Reusch, H. Schmidt-Böcking, R. Schuch, I. Tserruya
K- to K-Shell Charge Transfer in Close Collisions of H-Like Kr Ions on Mo
J. de Phys. C1, 175 (1989)

H. Wu, M. Greiner, D.-H. Feng
Collective Spin in Nuclear Dynamical Symmetry
Phys. Rev. C39, 1059 (1989)

H.M. Xu, W.G. Lynch, C.K. Gelbke, M.B. Tsang, D.J. Fields, M.R. Maier, D.J. Morrissey, T.K. Nayak, J. Pochodzalla, D.G. Sarantities, L.G. Sobotka, M.L. Halbert, and D.C. Hensley
Complex Fragments Emitted in Particle Stable States for the ^{32}S + medium.^{nat}Ag Reaction at E/A = 22.3 MeV
Phys. Rev. C40, 186 (1989)

8.1.2 Conference Contributions

Amsterdam, The Netherlands: SEAS Meeting, 25.-29.09.1989

I. Giese
Writing PHIGS Applications with PL/1

Amsterdam, The Netherlands: 3rd Coll. on Atomic Spectra and Oscillator Strengths for Astrophysics and Fusion Research, 28.-31.0 .1989

E. Träbert, G. Möller, A.E. Livingston, P.H. Heckmann
Wavelength and Lifetime Measurements on Intercombination Lines of Ag XVIII, Ag XVII and Ag XVI (zn I, Ga I, and Ge I-like)

Anaheim, USA: APS-Division of Plasma Physics Annual Meeting, 13.-17.11.1989

M.J. Rhee, E. Boggasch
High Brightness Electron Beam Produced by a Pseudospark Discharge

Arad, Israel: 6th Int. Conf. on Recent Progress in Many Body Theory, 05.-10.11.1989

M. Kleber
Nonadiabatic Tunneling Through a Time-Dependent Barrier

Asilomar, USA: Fall Meeting of the American Physical Society, Division of Nuclear Physics, 12.-14.10.1989

E. Roecki
Recent Studies of Exotic Nuclei at the UNILAC and Plans for SIS Experiments

Aussois, France: 10ème Session d'Etudes Biennale de Physique Nucléaire, 06.-10.03.1989

S. Hofmann
Heavy Elelemnts Research and the Future at SIS

D. Schardt
Decay Study of Very Neutron-deficient Nuclei Near ^{100}Sn and ^{146}Gd

Bad Herrenalb, FRG: 25. Symp. für Theoretische Chemie, 03.-06.09.1989

L. Yang, D. Heinemann, D. Kolb
Anwendungen und Optimierung Finiter Elemente Rechnungen

Bad Honnef, FRG: Int. Workshop on Nuclear Structure of the Zirconium Region, 24.-28.04.1989

R. Barden, H. Gabelmann, I.S. Grant, R. Kirchner, O. Klepper, G. Nyman, A. Plochocki, G.-E. Rathke, E. Roecki, K. Rykaczewski, D. Schardt, J. Szerypo, J. Zylicz
Gamow-Teller Beta Decay of Even Nuclides Near ^{100}Sn

Bad Honnef, FRG: Europhysics Industrial Workshop, 10.-13.10.1989

B.H. Wolf
High Energy Ion Implantation Facilities at GSI

Bad Honnef, FRG: Chaotic Phenomena in Nuclei and Atoms, 16.-18.10.1989

W. Nörenberg
Dissipation and Fluctuation in Heavy-Ion Collisions as an Example of Chaotic Motion

Baltimore, USA: American Phys. Soc. Spring Meeting, 01.-04.05.1989

A. Sandoval
Distributions in Rapidity and Transverse Momentum and Two Particle Correlations from Oxygen and Sulphur Induced Reactions

Berkeley, USA: Int. Conf. on Ion Sources, 10.-14.07.1989

P. Spädtke
The Influence of Axial Magnetic Fields on the Extraction of an Ion Beam from a Plasma Source

D.M. Rück, H. Emig, P. Spädtke, B.H. Wolf, B.R. Nielsen, B. Torp
High Current Ion Beams of Metallic Elements

B.H. Wolf, J. Bossler, H. Emig, K.D. Leible, M. Müller, D.M. Rück, P. Spädtke
Development and Operation of Heavy Ion Sources at GSI

Berkeley, USA: 1st Int. Conf. on Radioactive Nuclear Beams, 16.-18.10.1989

C. Broude, G. Goldring, M. Hass, N. Takahashi, S. Hofmann, F.P. Heßberger, V. Ninov
A Parity Violation Experiment with a Separated Beam of Tc Isomers

G. Münzenberg
The GSI Projectile Fragment Separator

G.D. Sprouse, A. Berger, J. Das, T. Lauritsen, J. Schecker, F. Xu, J. Billowes, C.H. Holbrow, T. Kühl, S. Dutta, F. Heßberger, S. Hofmann, R. Kirchner, O. Klepper, D. Marx, V. Ninov, U. Dinger, G. Huber, R. Menges, S. Schröder
Laser Spectroscopie of Beams of Unstable Nuclei

K. Sümmerer, D.J. Morrissey
Systematics of Fragmentation Cross-sections: Empirical Descriptions and Microscopic Calculations

Berkeley, USA: Workshop on Highly Charged Ions, New Physics and Advanced Techniques, March 1989

R.A. Esterlund, B. Jäckel, M. Knaack, H. Schulte, W. Westmeier, P. Patzelt
Dynamic Components in ^{40}Ar-induced Fissionlike Reactions

P. Glässel, R. Schmid-Fabian, D. Schwalm, D. Habs, U. v. Helmolt
^{252}Cf Fission Revisted

D. Habs
First Experiments with the Heidelberg Test Storage Ring

E. Träbert
Intercombination and Forbidden Transitions in Beam-Foil Spectra of Highly-Ionized Ag and Xe

Berlin, FRG: Fifty Years Research in Nuclear Fission, 03.-07.04.1989

H.W. Gäggeler, D.T. Jost, A. Türler, P. Armbruster, W. Brüchle, H. Folger, F.P. Hessberger, S. Hofmann, G. Münzenberg, V. Ninov, W. Reisdorf, M. Schädel, K. Sümmerer, J.V. Kratz, U.W. Scherer, M.E. Leino
Cold Fusion Reactions with ^{48}Ca

D. Habs
Spectroscopy of the Second Minimum

G. Herrmann
Discovery and Confirmation of Fission

G. Münzenberg
Heavy Element Production and Limits to Fusion

W. Nörenberg
Diabatic Hindrance of Heavy-Ion Fusion

S. Polikanov
Meson, Hyperon, ad Antiproton Induced Fission

Th. Weber, W. Wilke, H. J. Emrich, R.D. Heil, Th. Kihm, U. Kneissl, K.T. Knöpfle, U. Seemann, F. Steiper, H. Ströher
Evidence for Different Fission Fragment Mass Aymmetries for Specific Nuclear Excitations Studied in (e, e'f) and (γ,f) Reactions

Bloomington, USA: The Genetics and Molecular Biology of Arabidopsis, 12.-15.10.1989

A.R. Kranz
Genetic Stress and Risk Induced by Heavy Ions in Arabidopsis

Bonn, FRG: Spring Meeting of the German Physical Society, Nuclear Physics Section, 13.-17.03.1989

J. van Aarle, W. Westmeier, R. Brandt, P. Patzelt, J.F. Wild, E.K. Hulet
Prompt Neutron Emission in the Spontaneous Fission of 260 Md

P. Armbruster
Neue Wege zur Elementherstellung

J. Bacelar, A. Balanda, M. de Boer, J. Hinnefeld, H. Kaper, J. van Klinken, W.J. Meiring and S.J. van der Werf, F.W.H. de Boer, H. Bokemeyer, D. Kraft and K.E. Stiebing
Search for Resonant Bhabba Scattering in the MeV Region

H. Backe, M. Begemann-Blaich, M. Dahlinger, M. Kiüver, W. Konen, P. Kosmadakis, J. Stroth, K. Bethge, S. Mojumder, K.E. Stiebing, H. Bokemeyer, P. Senger, P. Glässel, D.v.Harrach und P. Fröbrich
Messung der Kernkontaktzeiten

E. Berdermann, F. Bosch, S. Huchler, P. Kienle, W. Koenig, C. Kozhuharov, A. Schröter, S. Schubeck, H. Tsertos
Über die Impulskorrelation der in U+U und U+Pb Stößen emittierten (e^+e^-)-Paare

T.S. Biro, U. Kalmbach, U. Mosel, T. Schäfer
Sea-Effekte im Chiralen Soliton Bag Modell

T.S. Biro
Color-Transport-Theorie

B. Blättel, V. Koch, K. Weber, W. Cassing, U. Mosel
Das relativistische BUU-Modell - Resultate und Verbesserungen

B. Blank, E. Bozek, E. Ditzel, H. Friedemann, H. Jäger, E. Kankeleit, G. Klotz-Engmann, M. Krämer, V. Lips, C. Müntz, H. Oeschler, A. Piechaczek, M. Rhein, I. Schall, C. Wille
Elektronen- und Positronenspektroskopie bei Schwerionenstößen

H. Bokemeyer, H. Folger, K. Bethge, K. Sakaguchi, P. Salabura, K.E. Stiebing, T. Cowan, J.S. Greenberg, J. Schweppe, H. Backe, D. Schwalm
Systematic Investigation of the Narrow Positron Elektron Sum Energy Lines

E. Bozek, E. Kankeleit, H. Oeschler, M. Rhein, I. Schall
Plastikszintillator - Photodioden - Anordnung für schwere Ionen

K. Th. Brinkmann, H. Freiesleben, H. Gassel, J. Kiesewetter
Eine Ionisationskammer mit intergriertem Parallelplattenlawinenzähler für Orts- und Zeitmessung

R. Brockmann
Particle Spectra in Oxygen and Sulphur Induced Reactions at Energies of 60 - 200 GeV per Nucleon

T. Brohm, H.-G. Clerc, U. Gollerthan, E. Hanelt, W. Morawek, V. Ninov, W. Schwab, J.-P. Dufour, F.-P. Heßberger, M. Montoya, G. Münzenberg, K.-H. Schmidt, R.S. Simon
Massenbestimmung von ^{178}Pt und ^{175}Ir über Q-Wert-Messung bei der Fusionsreaktion $^{89}Y + ^{90}Zr$

M. Cubero, M. Schönhofen, H. Feldmeier, W. Nörenberg
The Relativistic Vlasov Equation with Non-Radiating Meson Fields

R. Fleischhauer, W. Scheid
Theoretische Untersuchungen zur Coulombstreuung mit relativistischen Schwerionen

J. Friese, H.J. Körner, C. Schießl, W. Wagner, K. Zeitlhack
PIN-Photodiodes as Charged Particle Detector

J. Friese, H.J. Körner, W. Wagner, K. Zeitlhack
A Detection System for Heavy Projectile Fragments

H. Gäggeler, D. Jost, A. Türler, M.E. Leino, P. Armbruster, W. Brüchle, H. Folger, F.P. Heßberger, S. Hofmann, G. Münzenberg, V. Ninov, M. Schädel, K. Sümmerer, J.V. Kratz, U.W. Scherer
Bestimmung der partiellen Elektron Capture- und Spontanspaltungshalbwertszeiten von ^{254}No

J. Gerl, D. Schwalm
Designstudien für Composite-γ-Detektoren höchster Effizienz im Rahmen des EURO-Ball Projektes

U. Gollerthan, H.-G. Clerc, T. Brohm, M. Horz, H.-H. Schmidt, W. Schwab, R.S. Simon
Komplette Beschreibung der Abdampfung geladener Teilchen von $^{179}Au^*$ mit dem statistischen Modell

W. Greiner, W. Scheid, R. Herrmann, G. Plunien
Kollektiver Spin

G. Haase, R. Brand
Some Theoretical Remarks Concerning the Unusual Behaviour of Relativistic Projectile Fragments at Large Lab Angles

F. Hagelberg, H.-J. Simonis, P.N. Tandon, K.-H. Speidel, M. Knopp
Spinaustauschstreuung als Mechanismus der Polarisationsübertragung auf Ionen beim Durchflug durch Ferromagnetika

M. Heck, H. Barth, R. Brandt, V.S. Butsev, G. Haase, M.I. Krivopustov, B.A. Kulakov, E.-J. Langrock, D. Molzahn, F. Pille
On the Measurement of the Neutron Dosis Behind Experimental Concrete Schieldings Produced in the Interaction of 44 GeV C-12 with Cu and Graphite Targets

S. Hlavac, R.S. Simon
Verschlechterung von BaF_2-Signalen durch Verzögerungskabel

K.H. Kampert
Schock-Kompression im Kern-Kern-Stoß

H. Keller, E. Roeckl, D. Schardt, R.S. Simon, C.F. Liang, P. Paris, K. Becker
Ein summationsfreies Spektrometer für Positronen im MeV-Bereich

J. Kiefer
Mutagenität geringer Strahlendosen

H. Klein, J. Gerl, Ch. Ender, H.W. Heyng, W. Korten, D. Schwalm G. Klotz-Engmann, V. Lips, H. Oeschler, J. Stroth, E. Kankeleit, Y. Cassagnou, M. Conjeaud, R. Dayras, S. Harar, R. Legrain, E. Pollacco, C. Volant
Multifragmentation: Anzeichen eines gleichzeitigen Aufbruchs

Untersuchungen von Transferreaktionen am System $^{18}O \rightarrow {}^{232}Th$ mit dem Kristallkugelspektrometer

M. Knaack, R.A. Esterlund, B. Jäckel, H. Schulte, W. Westmeier, P. Patzelt
Search for Dynamic Contributions to Fissionlike Processes for $^{40}Ar + {}^{165}Ho$

M. Knaack, B. Jäckel, R.A. Esterlund, H. Schulte, W. Westmeier, P. Patzelt
Dynamic Contributions to Fissionlike Processes for $^{40}Ar + {}^{181}Ta$

J. Knoll, C. Guet, M. Durand
Grenzen kinetischer Produktionsmodelle, aufgedeckt durch neue Summenregeln

C. Kozhuharov, H. Tsertos, P. Armbruster, P. Kienle, B. Krusche, K. Schreckenbach
Präzise Vermessung der Anregungsfunktion für Bhabha-Streuung um 1.8 MeV/cm^2

J. Kramp, J. Gerl, D. Habs, D. Schwalm, P. Thirolf
Suche nach Resonanzen im System $e^+e^- \rightarrow n\gamma$

Th. Lippert, N. Grün, W. Scheid
Leptonenpaarerzeugung durch Bremsstrahlung in relativistischen Schwerionenkollisionen

V. Lips, E. Kankeleit, G. Klotz-Engmann, H. Oeschler, Y. Cassagnou, M. Conjeaud, R. Dayras, S. Harar, R. Legrain, E. Pollacco, C. Volant
Korrelationen von Spaltung und intermediären Fragmenten im System ^{40}Ar auf ^{232}Th

R. Maaß, W. Scheid
Beschreibung der Resonanzstrukturen in der $^{24}Mg + {}^{24}Mg$-Streuung

S. Margetis, W. Heck, H. Ströbele, C. Guerra, A. Sandoval, D. Vranic and NA35 Collaboration
Transverse Energy Systematics for Oxygen and Sulphur Induced Collisions at 200 and 60 GeV per Nucleon

A. Marinov, S. Gelberg, D. Kolb
Evidence for very Asymetric Fission Process Observed in the $^{35}Cl + {}^{197}Au$ Reaction

K.-E. May, R. Maaß, W. Scheid
Inversion der elastischen Streuphasen für $^{16}O + {}^{28}Si$ aus der algebraischen Streutheorie mit dem modifizierten Newton-Verfahren

R.S. Mayer, S. Hlavac, R.S. Simon
Lichtsammlung in BaF_2-Kristallen mit TAPS Geometrie

R. Menegazzo, M. Pliparinen, P. Kleinheinz, D. Schardt, C.F. Liang
Are $H_{11/2}O^+$-Proton Pairs Present in the Groundstate of ^{147}Tb ?

N. Ohtsuka, R. Linden, H. Müther, A. Fässler, M. El Shabshiry
Nucleus-Nucleus Optical Potential Based on Dirac-Brueckner Theory for Nuclear Matter

J. Peter, A. Müller, K.E. Stiebing, K. Bethge, H. Bokemeyer, H. Folger, E. Grosse, P. Senger,
Ein Magnetspektrometer zum Nachweis von Elektronen im Bereich $E \geq 20$ MeV

W. Reisdorf, M. Schädel, R. Bellwied, J.V. Kratz, R. Künkel, B. Kohlmeyer
Vollständige Reaktionsstudie im System $^{124}Sn + {}^{96}Zr$ bei einer Einschußenergie zwischen statischer und dynamischer Fusionsbarriere

P. Reiter, J. Gerl, D. Habs, D. Schwalm, P. Thirolf
Eigenschaften des statistischen Zerfalls von Dy-Compoundkernen

K. Rykaczewski, T. Bartsch, A. Plochocki, J. Zylicz, R. Barden, O. Klepper, D. Schardt, J. Szerypo, I.S. Grant, H. Gabelmann, P. Hill
Beta Decay of the Proton-Rich Nucleus ^{98}Cd

M. Schäfer, T.S. Biro, W. Cassing, U. Mosel
Photonen- und Dileptonen-Produktion in Proton-Neutron Stößen

U.W. Scherer, C. Frink, G. Herrmann, J.V. Kratz, N. Trautmann, M. Schädel, K.J. Moody, W. Brüchle, K. Sümmerer, G. Wirth, H. Gäggeler
Massenfluß in den Reaktionen $^{40}Ar + {}^{233}U$, ^{235}U,^{238}U an der Barriere

E. Schmidt, D. Kraft, K.E. Stiebing, K. Bethge, H. Bokemeyer, H. Folger
Nachweis von Wasserstoff in Targets

E. Schneider
Biologische Wirkung schwerer Ionen

H. Schulte, B. Jäckel, R.E. Esterlund, M. Knaack, W. Westmeier, A. Rox, P. Patzelt
Influence of the Mass-Energy Surface on Fissionlike Processes

E. Schulz, J. Gerl, U. v. Helmolt, C. Klatt, W. Korten
Ein neues Verfahren zur Ortsauslese von Parallelplattenzählern

R.S. Simon
Rotation Alignment in Actinide Nuclei

H.-J. Simonis, S. Kremeyer, F. Hagelberg, U. Reuter, P.N. Tandon, M. Knopp, K.-H. Speidel, W. Karle, J. Gerber
Zeitdifferentielle Messungen zum Nachweis der Elektronen-Spin-Polarisation von Ionen beim Austritt aus ferromagnetischen Oberflächen ins Vakuum

K.-H. Speidel, M. Knopp, W. Karle, J. Cub, M.-L. Dong, U. Reuter H.-J. Simonis, P.N. Tandon, J. Gerber
Ionenstrahl-Induzierte Abschwächungen transienter Magnetfelder von ^{28}Si- und ^{62}Ni-Ionen in Fe und Gd

K.-H. Speidel, M. Knopp, W. Karle, J. Cub, M.-L. Dong, U. Reuter, H.-J. Simonis, P.N. Tandon, J. Gerber
Transiente Magnetfelder als experimentelle Methode der Kernphysik unter neuen Aspekten

A. Steinhof, K.H. Behr, A. Brünle, E. Roeckl, E. Boaretto, M. Paul, D. Fink, G. Hollos, W. Kutschera
Elektromagnetische Isotopenanreicherung für ^{41}Ca Beschleuniger-Massenspektroskopie

H. Ströher
Photoproduktion und Restwechselwirkung neutraler Pionen in komplexen Kernen

J. Thiel, Th. Lippert, N. Grün
Photonenproduktion durch klassische Bremsstrahlung bei relativistischen Kern-Kern-Stößen

F.W. Vedder, W. Scheid
Untersuchungen der Potentialenergiefläche des superschweren Kerns mit Z = 108

G. Wirth, W. Brüchle, F. Wo, E. Jäger, K. Sümmerer, F. Funke, J.V. Kratz, N. Trautmann
Suche nach langen Wechselwirkungszeiten im U + Au System nahe der Coulomb-Barriere

A. Zielke, R. Maaß, W. Scheid
Streupotentiale in der Algebraischen Streutheorie

Bordeaux, France: 3rd European Conf. on Atomic and Molecular Physics, 03.-07.04.1989

J.H. Blanke, B. Fricke, P.H. Heckmann
Quintett States of Doubly-Excited Three-Electron Ions

G. Deca, N. Grün
Double Electron Capture in Alpha Helium Collisions at High Energies

R. Dörner, J. Ullrich, R. Olson, S. Nemat, H. Schmidt-Böcking
Experimental Determination of the Complete Transverse Momentum Balance in Singly Ionising 500 KeV Proton on He Collisions

A. Faulstich, W. Petrich, D. Habs, R. Neumann, D. Schwalm, A. Wolf, S. Schröder, G. Huber, M. Dutta, T. Kühl, D. Marx
Laser Colling of $^{9}Be^{+}$ at the TSR

B. Fricke, K. Rashid, J.H. Blanke, J.-P. Desclaux
Ground State Correlation Energy of the Be-Sequence for Z = 4-20 in MCDF Approximation

M. Gerhard, R. Grieser, G. Huber, R. Klein, M. Krieg, S. Schröder, N. Schmidt, M. Dutta, T. Kühl, D. Marx, F. Nicle, H. Orth, A. Faulstich, W. Petrich, D. Habs, R. Neumann, D. Schwalm, A. Wolf
Laser Spectroscopy in Heavy-Ion Storage Rings

K. Gramlich, N. Grün, W. Scheid
Coupled Channel Calculations with Gaussian Basis Function for Charge Transfer and Ionization in $(He\text{-}He)^{2+}$ Collisions

P.H. Mokler, S. Reusch, Th. Stöhlker, Y. Awaya, T. Kambara, A. Warczak, Z. Stachura, R. Schuch, G. Wintermeyer, M. Schulz, A. Müller
Resonant Transfer and Excitation (RTE) in $_{32}Ge^{31+} \rightarrow H_2$ Collisions

G. Möller, J.H. Blanke, V. Lodwig, C. Wagner, E. Träbert, P.H. Heckmann, A.E. Livingston, P.H. Mokler
Fast-Ion Beam Observation of M1 Transitions within the Ground-State Configurations of Highly Charged Xenon Ions

K. Momberger, G. Deco, N. Grün, W. Scheid
First Order Perturbation Claculations of K-Shell Ionization in Relativistic Heavy Ion Collisions

H. Sharabati, J. Ullrich, R. Dörner, V. Dangendorf, K. Bethge, R. Olson, H. Schmidt-Böcking
Multiple Ionisation in Fast Proton on Neon Collisions

B. Thies, P. Kürpick, W.-D. Sepp, B. Fricke, D. Heinemann, D. Kolb
Multi-Electron Interpretation of Coupled-Channel Calculations for Heavy Systems

P. Zimmerer, N. Grün, W. Scheid
Trajectory Method for the Time-Dependent Thomas-Fermi Equation

Bormio, Italy: XXVII Winter Meeting on Nuclear Physics, 23.-27.01.1989

W. Greiner, W. Scheid
The Collective Spin of Nuclear Surface Vibrations

U. Lynen
The Onset of Multifragment Decay

R.J. Meijer, P. Box, P. Decowski, K.A. Griffioen, R. Kamermans, G.J. van Nieuwenhuizen, H.W. Wilschut, A. Goini, C. Morand, A. Demeyer, D. Guinet
Central Collisions Between ^{28}Si Nuclei at 12.4, 19.7 and 30.0 MeV per Nucleon

U. Mosel
Relativistic Transport Theory for Heavy-Ion Reactions

K. Niita, T.S. Biro, W. Cassing, A.L. De Paoli, U. Mosel, M. Schäfer
Particle Production in Heavy-Ion Collisions from 20 MeV/u to 2 GeV/u

Bratislava, Czechoslovakia: Hadron Structure 89, 25.-29.09.1989

A. Eklund
Global and Local Fluctuations in Ultrarelativistic Heavy-Ion Interactions

Bretton Woods, USA: 9th Int. Conf. on Laser Spectroscopy, 18.-23.06.1989

G. Huber, S. Schröder, R. Klein, M. Gerhard, R. Grieser, M. Krieg, A. Karafillidis, T. Kühl, A. Faulstich, W. Petrich, D. Habs, R. Neumann, D. Schwalm, A. Wolf and the TSR Group
Partial Laser Cooling and Saturation Spectroscopy on 9 MeV $^{7}Li^{+}$-Ions in a Storage Ring

S. Dutta, R. Kirchner, O. Klepper, T. Kühl, D. Marx, U. Dinger, G. Huber, D. Knussmann, R. Menges, S. Schröder, G. Sprouse
Laser Spectroscopy of Neutron Deficient Lead and Thallium Isotopes: Systematics of Nuclear Radii in the Z = 82 Region

Brussels, Belgium: 22nd Annual Meeting of the Europ. Soc. of Radiat. Biology, 11.-16.09.1989

T. Kranert, J. Kiefer
Mutation Induction in V79 Cells by Low Dose Rate α-Irradiation

Budapest, Hungary: Int. Workshop on Theoretical Physics of the Hungarian Academy of Sciences, 12.-16.06.1989

T.S. Biro
Sea-Effects in the Chiral Bag Model

J. Knoll
Quantum Limits of Particle Production

U. Mosel
Covariant Transporttheory for Heavy Ions

G. Wolf
Pion and Dilepton Production at SIS Energies

Budapest, Hungary: Workshop on Relativistic Heavy Ion Physics, 13.-16.06.1989

R.Bock
Physics at SIS/ESR

Budapest, Hungary: Int. Conf. on the Application of Mößbauereffect, 04.-08.09.1989

S. Laubach, P. Schwalbach, M. Hartick, B. Keck, E. Kankeleit, R. Sielemann
Implantation of Coulomb Excited ^{57}Fe

on Buffalo, USA: 16th IEEE Int. Conf. on Plasma Science, 22.-24.05.1989

R. Bock
Present and Future Experiments on Heavy Ion Beam Plasma Interaction and on Beam Dynamics

E. Boggasch, M.J. Rhee
Pseudospark as an Electron Beam Source

Caen, France: 1. Int. Symp. on Swift Heavy Ions in Matter, 16.-19.05.1989

P.H. Mokler, S. Reusch, Th. Stöhlker, R. Schuch, M. Schulz, G. Wintermeyer, Z. Stachura, A. Warczak, A. Müller, Y. Awaya, T. Kambara
Resonant Transfer and Excitation in Swift, Heavy Few-Electron Projectiles

G. Wintermeyer, V. Dangendorf, M. Gabr, T. Kambara, P.H. Mokler, S. Reusch, H. Schmidt-Böcking, R. Schuch, I. Tserruya
Investigation of Quasimolecular- and K- X-Ray Production in Close Collisions of H-Like Kr Ions on Mo

Caen, France: Meeting on 'Rare' Particle Production in Heavy-Ion Collisions, 'Journees Theoriciens GANIL', 12.-16.12.1989

J. Knoll
Quantum Limits of Photon Production

G. Wolf
Dilepton and K^+-Production at Intermediate Energies

Chicago, USA: Particle Accelerator Conference, 20.-23.03.1989

D. Böhne
Status Report on the SIS/ESR Project

E. Boggasch, T. Fine, M.J. Rhee
The Pseudospark as an Electron Beam Source

T.A. Fine, E. Boggasch, M.J. Rhee
Current Measurement in a Gas Filled Drift Tube

Ch. Ender
The Polyp Multi Processor System

P. Kienle
Perspectives of Cooled Radioactive Beams

T. Shea, E. Boggasch, M.J. Rhee
Current Measurement in a Gas Filled Drift Tube

Copenhagn, Denmark: Workshop on Nuclear Physics, Nov. 1989

W. Nörenberg
Diabatic Approach to Collective Motion and Dynamical Hindrance of Heavy-Ion Fusion

W. Nörenberg
Quantum Chaos and Dissipation in Nuclei

Cordobang, GDR: 20th Spring Symposium on High Energy Physics, 17.-22.04.1989

H.R. Schmidt
Ultrarelativistic Heavy-Ion Collisions

Dallas, Texas/USA: Symposium on Nuclear Dynamics and Nuclear Disassembly, Annual ACS Meeting 10.-14.04.1989

W. Trautmann, K.D. Hildenbrand, U. Lynen, W.F.J. Müller, H.J. Rabe, H. Sann, H. Stelzer, R. Trockel, R. Wada, E. Eckert, P. Kreutz, A. Kühmichel, J. Pochodzalla
Reactions at the Threshold to Multifragment Decay

Darmstadt, Germany: Projektsymposium Radiotherapie mit Schwerionen, 12.5.1989

P. Kienle
Wissenschaftliches Programm der GSI und das Strahlentherapieprojekt

Dourdan, France: Symp. on the 10th Anniversary of Projectile Fragmentation in the Study of Nuclei Far from Stability, 01.-04.12.1989

E. Roeckl
Deacy Spectroscopy of Far Unstable Nuclei Using MeV/u to GeV/u Heavy-Ion Projectiles

K. Sümmerer, D.J. Morrissey
Systematics of Fragmentation Cross-Sections

Dubna, USSR: Int. Conf. on Selected Topics in Nuclear Structure, 20.-24.6.1989

E. Roeckl
Beta-Decay Studies of Heavy-Ion Produced Nuclei with Large Proton and Neutron Excess

Dubna, USSR: International School-Seminar on Heavy Ion Physics, 03.-12.10.1989

R. Bock
Progress at GSI and 4π-Detectors for Charged Particle Detection

D. Habs
Experiments on Atomic and Fundamental Physics with the Heidelberg Test Storage Ring

S. Hofmann
Experiments for Production of Heavy Elements at Darmstadt

M. Schädel
Radiochemical Studies of the Transactinide Elements

D. Schwalm
Fusion Studies with the Crystal Ball

Durango, USA: Anomalous Absorption Conf., 19.-23.06.1989

D.H.H. Hoffmann
Beam Plasma Interaction Experiments

Eilat, Israel: Nuclear Physics at the Red Sea, Europhysics Study Conference, 08.-13.01.1989

P. Kienle
Electron-Positron Pair Creation in Heavy Ion Collisions

D. Schwalm
On the Deformation of Actinide Nucei

Erice, Italy: Higgs Particle(s) - Physics Issues and Experimental Searches in High and Low Energy Collisions, 15.-26.7.1989

P. Kienle
The Present Status of the Electron Positron Pair Creation Experiments in Heavy Ion Collisions and in Bhabha Scattering

Erice, Italy: Int. School of Quantum Electronics, 14th Course, Optoelectronics for Environmental Science, 03.-09.09.1989

F. Ames, H.-J. Kluge, E.-W. Otten, B.M. Suri, A. Venugopalan, G. Herrmann, J. Riegel, H. Rimke, P. Sattelberger, N. Trautmann, R. Kirchner
Trace Analysis of Plutonium and Technetium by Resonance Ionization Mass Spectrometry Using an Atomic Beam and a Laser Ion Source

Essen, FRG: Spring Meeting of the German Physical Society, Molecular Physics Section, 06.-10.03.1989

Th. Häuser, W. Scheid
Analytische Untersuchungen zur Emission von Ionen aus dem Laser-Brennpunkt

D. Heinemann, B. Fricke
Grid-optimierte molekulare Finite Elemente Rechnungen

H. Hora, L. Cicchitelli, W. Scheid
Beschleunigung von Teilchen mit Lasern ohne Plasmahintergrund

W. Krötz, A. Ulrich, B. Busch, G. Ribitzki, W. Seebeck, J. Wieser
Messung von Ratenkonstanten für die Bildung und den Zerfall von Ne_2-Excimeren

W. Seebeck, N. Machlitt, A. Ulrich, G. Ribitzki, J. Wieser
Untersuchung der Lichtemission einer überlasteten Funkenstrecke

W.-D. Sepp, B. Fricke, D. Heinemann
Relativistische Dirac-Fock-Slater Rechnungen mit frei wählbarer frozen-Core Näherung

A. Ulrich, J. Wieser, B. Busch, W. Krötz, G. Ribitzki, W. Seebeck
Untersuchung der Lichtemission von Edelgasen bei der Anregung mit einem Schwerionenstrahl

L. Yang, D. Heinemann, D. Kolb, B. Fricke
Möglichkeiten zur Optimierung der Methode der Finiten Elemente

Gaithersburg, USA: 7th American Phys. Soc. Top. Conf. on Atomic Processes in Plasma, 02.-05.10.1989

E. Träbert
Intercombination Transition Probabilities in two Electron Spectra

Gauhati, India; 6th Nat. Sem. on Solid State Nuclear Track Detector, 16.-18.03.1989

K.K. Dwivedi
Studies on Fusion-Fission Reactions by a Nuclear Track Technique

K.K. Dwivedi
Cross-Section of Elastic Scattering in $^{238}U + ^{nat}U$ (12.0 MeV/u) Reaction

S. Gosh, K.K. Dwivedi
Registration of ^{132}Xe Tracks in Hostaphan Stacks

S. Gosh, K.K. Dwivedi
Heavy Ion Tracks in Muscovite Mica

J. Raju, S. Gosh, A. Saxena, K.K. Dwivedi
Interaction of 350 MeV ^{90}Zr Ions

J. Raju, S. Gosh, A. Saxena, K.K. Dwivedi
Measurement of Heavy Ion Tracks in CR-39

J. Raju, S. Gosh, A. Saxena, K.K. Dwivedi
Calibration of CR-39 and ZnP-Glass with ^{90}Zr Ions

A. Saxena, K.K. Dwivedi
Energy Loss and Mean Ranges of 1.678 GeV ^{93}Nb in Ni and Ta

Geilo, Norway: 8th Nordic Meeting on Intermediate and High Energy Nuclear Physics, 03.-07.01.1989

H.A. Gustafsson
Heavy Ions at CERN and Brookhaven. An Overview.

Gif-sur-Yvette, France: Production de Mesons Lourds et D'etrangeté dans les Noyaux, 16.-17.03.1989

E. Grosse
Mesons from Colliding Nuclei

A.L. De Paoli, K. Niita, W. Cassing, U. Mosel
Eta-Production in Heavy-Ion Collisions

Giens, France: Colloque Ganil 22.-26.05.1989

U. Lynen
Multifragment Emission at Intermediate Energies

Grenoble, France: Int. Workshop on Fundamental Physics with Slow Neutrons, 08.-11.03.1989

H. Tsertos
Search for Resonant Bhabha Scattering at MeV Energies

Grenoble, France: Workshop on the Relativistic Many-Body Problem in Atomic Physics, Oct. 1989

B. Fricke, B. Thies, W.-D. Sepp
Many-Electron Relativistic Calculations of Time-Dependent Heavy-Ion Scattering

G. Soff
Theoretical Atomic Physics for the SIS Project at GSI

Groningen, The Netherlands: Informal Workshop on Physics with a Magnetic Spectrograph, 10.-13.09.1989

H. Freiesleben
How Useful are High-Resolution Studies for the Investigation of Heavy-Ion Reactions ?

Hannover, FRG: Annual Meeting of the German Genetics Society, 18.-20.05.1989

M. Pickert, U. Bork, A.R. Kranz
Genetischer Treffbereich und biologischer Schaden von Schwerionenstrahlung bei Arabidopsis Thaliana (L.) Heynh.

Haugesund, Norway: 6th Nordic Meeting on Nuclear Physics, 11.-15.8.89

H.A. Gustafsson
Global and Collective Phenomena observed in Nuclear Collisions at Ultrarelativistic Energy

J. Idh
Global and Local Fluctuations in Distributions from Ultrarelativistic Heavy-Ion Interactions

P. Kienle
Experimental Status of Pair Production

Heidelberg, FRG: SIS-Theorie-Treffen, 29.06.-01.07.1989

M. Herrmann
Paarproduktion in endlichen dynamischen Systemen

V. Koch, B. Blättel, W. Cassing, A. Lang, U. Mosel, K. Weber
Relativistic Transport Model for Heavy-Ion Collisions

K. Weber, B. Blättel, W. Cassing, V. Koch, A. Lang, U. Mosel
Retardation and Radiation in the Relativistic BUU-Model

Hirschegg, Austria: XVII Int. Workshop on Gross Properties of Nuclei and Nuclear Excitations, 16.-21.01.1989

T.C. Awes, R.L. Ferguson, F.E. Obenshain, F. Plasil, G.R. Young, S. Pratt, Z. Chen, C.K. Gelbke, W.G. Lynch, J. Pochodzalla, H.M. Xu
Extended Emission Sources Observed via Two-Photon Correlations

H.W. Barz, B. Kämpfer, B. Lukacs, G. Wolf
Interpenetrating Nuclei

T.S. Biro, W. Cassing, U. Mosel, K. Niita, G. Wolf
Non-Equilibrium γ-Production in Heavy-Ion Collisions

B. Blättel, V. Koch, K. Weber, W. Cassing, U. Mosel
New Results from the Relativistic BUU-Approach

W. Cassing, T.S. Biro, B. Blättel, V. Koch, U. Mosel, M. Schäfer, S.J. Wang
Towards Selfconsistent Relativistic Transport Theories

J. Knoll
Quenching Effects in Photon Production

H.R. Schmidt
A New Component of the Collective Flow in Relativistic Heavy-Ion Collisions

M. Schönhofen, H. Feldmeier, M. Cubero
The Relativistic Vlasov Equation with Non-Radiating Meson Fields - Results

A. Ulrich
VUV Emission from Matter Excited by Heavy Ion Beams

Holzhau, GDR: Spring School, 27.-31.03.1989

E. Grosse
Pions and Photons from Nuclear Collisions

W. Nörenberg
Towards a Covariant Transport Theory

H. Oeschler
Dynamics of Dissipative Collisions Determined from δ-Electron Spectra

J. Pochodzalla, R. Charity, U. Lynen, H. Sann, W. Trautmann, R. Trockel
On the Possibility of Transient Effects During the Emission of Intermediate Mass Fragments

R.S. Simon
The Photon Spectrometer TAPS

Honolulu, USA: 9th. Int. Conf. on Vacuum Ultraviolet Radiation Physics (VUV9), 17.-21.07.1989

E. Träbert, A.E. Livingston, G. Möller, P.H. Heckmann
Wavelength and Lifetime Measurements on Forbidden and Intercombination Lines in the EUV Spectra of Swift Foil-Excited Highly Charged Ions

Honolulu, USA: The 1989 Int. Chemical Congress of the Pacific Basin Societies, 17.-22.12.1989

M. Schädel
The non Ta-Like Behaviour of Element 105

Iguazu Falls, Argentine: XII Workshop on Nuclear Physics, 28.08.-01.09.1989

J. Gerl
Heavy Ion Transfer Reactions on ^{232}Th Studies with the Crystall Ball Spectrometer

Islamabad, Pakistan: 3rd Regional Conf. in Mathematical Physics, 18.-24.02.1989

D. Kolb
Finite Element Methode in Quantum Applications

Islamabad, Pakistan: 3rd Einstein Seminar, 25.-27.02.1989

D. Kolb
The Early Einstein

Karlsruhe, FRG: 2nd Karlsruhe Int. Conf. on Anal. Chem. in Nucl. Techn. 05.-09.06.1989

M. Ganz, H. Barth, M. Fuest, S. Heise, C.D. Zhao, P. Vater, R. Brandt
Determination of an Upper Limit Concentration in Granites, Obtained from 'Kontinental Tiefbohrung'

M. Ganz, H. Barth, M. Fuest, S. Heise, C.D. Zhao, P. Vater, R. Brandt
The Application of Nuclear Track Filters to the Liquid-Liquid Extraction of Actinides in Analytical Procedures

G. Haase, M. Heck, R. Brandt
The Observation of an Unusual Behaviour of Relativistic Projectile Fragments at Large Lab Angles

Kopervik, Norway: 6th. Nordic Meeting on Nuclear Physics 10.-15.08.1989

J. Pochodzalla
Multifragment Emission at Intermediate Energies: Prologue to Multifragmentation ?

La Biodala, Isola d'Elba, Italy: 4th. Pisa Meeting on Advanced Detectors, 21.-25.05.1989

G. Vasileiadis, R. Boucler, W. Dominik, A. Gougas, A. Ljubicic, M. Mongelli, E. Nappi, G. Paic, A. Petridis, A. Sandoval, E. Schmoetten, D. Vranic, N. Zaganidis
Development of a RICH Detector for Ultra-Relativistic Heavy-Ion Collisions

Ladenburg, FRG: Workshop on the Kinetic Description of Nucleus-Nucleus Collisions, 17.-18.04.1989

J. Knoll
Sum-Rules for Photon Production

V. Koch
Relativistic Transport Model for Heavy-Ion Collisions

U. Lynen
The Use of the ALADIN Spectrometer for the Investigation of Multifragmentation

K. Niita
Nonrelativistic VUU and Particle Production

H.R. Schmidt
Some Data on Multifragmentation

M. Schönhofen, H. Feldmeier, M. Cubero
Relativistic Molecular Dynamics and the Relativistic Vlasov Equation with Non-Radiating Meson Fields

W. Trautmann
Systematics of Multifragment Decay

Laguna Beach, USA: 2nd Int. Conf. on High Density Pinches, 26.-28.04.1989

E. Boggasch, M.J. Rhee
Experimental Study of Pseudospark-Produced Electron Beams

La Hulpe, Belgium: ICX Seminar Large Systems /Large Scale Computing Conference, 17.-19.05.1989

M. Krämer
Experiences with Parallel FORTRAN

La Thuile, Valle d'Aosta, Italy: Multiparticle Dynamics, A Dialogue between Experiment and Theory, 20.-22.03.1989

I. Lund
Fluctuations in the density of charged particles in 200 AGeV 160+(C, Au) collisions

Leipzig, GDR: Workshop über ausgewählte Probleme der Kern- und Radiochemie, 13.-16.09.1989

W. Brüchle
Untersuchungen zu Eigenschaften des Elementes 103 in wässriger Lösung

J.V. Kratz
Untersuchungen zu den Eigenschaften des Elementes 105 in wässriger Lösung

J.V. Kratz
Extraktionsstudien tetra- und pentavalenter Ionen in verschiedenen Amin-Mineralsäure-Systemen

M. Schädel
ARCA II - Ein automatisiertes diskontinuierliches Trennverfahren zur Actiniden und Transactinidentrennung

N. Trautmann
SISAK3 - ein on-line Trennverfahren mit Minizentrifugen

N. Trautmann
Thermochromatographie von Platinelementen

Leningrad, USSR: Int. Conf. '50th Anniversary of Nuclear Fission', 16.-20.10.1989

H. Folger
The Fissioning Target in the Experiment of O. Hahn and F. Straßmann in Comparison with Targets and Set-Ups of Competing Groups

D. Schwalm, J. Gerl, D. Habs, J. Schirmer
γ-Decay of the Fission Isomer ^{236}U

Les Arcs, France: VIII. Moriand Workshop, Tests of Fundamental Laws in Physics, 21.-28.01.1989

H. Bokemeyer, P. Salabura, D. Schwalm, K. Stiebing
Correlated e^+e^- Emission in Heavy Ion Collisions

P. Kienle
Electron-Positron Paircreation in Heavy Ion Collisions Investigated with 'Orange'-Spectrometer

J. Kramp, J. Gerl, D. Habs, D. Schwalm, P. Thirolf
The Search for Resonances in the $e^+e^- \rightarrow n\gamma$ System

I. Lund
Fluctuations in the density of charged particles in 200 AGeV 160+(C, Au) collisions

M. Rhein, B. Blank, E. Bozek, E. Ditzel, H. Friedemann, H. Jäger, E. Kankeleit, G. Klotz-Engmann, M. Krämer, V. Lips, C. Müntz, H. Oeschler, A. Piechaczek, I. Schall, C. Wille
Electron-Positron Coincidence Experiment at the TORI Spectrometer

P. Salabura
e^+e^- Resonances: Monte Carlo Calculations for EPOS

D. Schwalm
Experimental Findings of the EPOS collaboration $e^+(+e^-)$ Lines from Heavy Ion Collisions

K.S. Stiebing
e^+e^- Resonances: Future Experimental Projects

Les Houches, France: Nuclear Matter and Heavy Ion Collisions 07.-16.02.1989

E. Grosse
Photons, Subthreshold Pions and Kaons from Heavy Ion Collisions

K.H. Kampert
Relativistic Heavy-Ion Collisions: The experimental Situation

P. Kienle
Status of the SIS/ESR-Project at GSI

V. Koch
Pisobars in Relativistic Heavy-Ion Collisions

U. Lynen
Time Scales for the Emission of Intermediate Mass Fragments

M. Schönhofen, H. Feldmeier, M. Cubero
Relativistic Molecular Dynamics and the Relativistic Vlasov Equation

Lake Arrowhead, USA: UCLA-Workshop on Advanced Accelerator Concepts, 09-13.01.1989

L. Cicchitelli, H. Hora, W. Scheid
Acceleration of Charged Particles by Lasers in Vacuum

Lake Yamanaka, Japan: Int. Conf. on Strongly Coupled Plasmas, 29.08.-02.09.1989

I. Hofmann
Dynamical Properties of a Beam OCP in a Storage Ring for Heavy Ions

Lillehammar, Norway: NATO Advanced Workshop on Physics and Applications of Hollow Glow Switches, 17.-21.07.1989

M.J. Rhee, E. Boggasch
Emittance Measurement of a Pseudospark-Produced Electron Beam

Lindenfels, FRG: Workshop on Atomic Physics Experiments at SIS/ESR, 26.-28.04.1989

A. Müller
Dielectronic Recombination

Manhattan, USA: Int. Sem. on Ion Atom Collisions, ISIAC XI, 03.-04.08.1989

P.H. Mokler
Resonant Transfer and Excitation into Highly Charged Heavy Projectiles

Miami Beach, USA: American Chemical Society, 198th Nat. Meeting, 10.-15.10.1989

G. Münzenberg, P. Armbruster
Towards Superheavy Nuclei - Status and Prospects for the Production and Investigation of Heavy Elements

Mittelberg, Austria: Arbeitstagung über "Energiereiche atomare Stöße, 22.-27.01.1989

H. Backe, K. Bethge, H. Bokemeyer, T. Cowan, H. Folger, J.S. Greenberg, K. Sakaguchi, P. Salabura, D. Schwalm, J. Schweppe, K.E. Stiebing
Monoenergetische Paaremission aus superschweren Stoßsystemen

J.H. Blanke, B. Fricke, P.H. Heckmann, G. Möller
Quintettzustände von dopplet-angeregten Ionen mit vier Elektronen

G. Deco, N. Grün
Doppelladungsaustausch in Ion-Atom-Kollisionen im Hochenergiebereich

G. Kilgus, D. Habs, E. Szmola, A. Wolf, R. Schuch
Messung von Umladungsprozessen am TSR

B. Kraus, K.-H. Schartner, F. Folkmann, A.E. Livingston, P.H. Mokler
The '5m-Grazing-Incidence' Spectrometer at GSI

A.E. Livingston, E. Träbert, G. Möller, P.H. Heckmann, C. Wagner, J.H. Blanke
Interkombinationsübergänge in der N=4 Schale von hochionisiertem Silber

S. Mannervik, R.T. Short, D. Sonnek, S. Träbert, G. Möller, V. Lodwig, P.H. Heckmann, J.H. Blanke, K. Brand
Ein gebundener dreifach-angeregter Zustand des Lithium-Atoms

P.H. Mokler, S. Reusch, A. Warczak, Z. Stachura, T. Kambara, R. Schuch, M. Schulz, G. Wintermeyer, A. Müller
Resonanter Elektroneneinfang in wasserstoffähnliche Ge^{31+} Projektile

G. Möller, E. Träbert, J.H. Blanke, V. Lodwig, C. Wagner, P.H. Heckmann, A.E. Livingston, P.H. Mokler
Beobachtung von verbotenen (M1) und Interkombinationsübergängen (E1) in hochionisiertem Xenon

S. Mojumder, H. Backe, K. Bethge, H. Bokemeyer, M. Dahlinger, W. Konen, P. Kosmadakis, P. Senger, J. Stroth
Überhöhte Elektronenausbeute in zentralen U+Pd Stößen bei 6.1 MeV/u

R. Neumann
Laserexperimente am Heidelberger Testspeicherring

K. Rashid, B. Fricke, J.H. Blanke, J.-P. Desclaux
Korrelationsenergie der Be-Sequenz für schwere Elemente in MCDF-Näherung

E. Szmola
Zerstörungsfreier Profilmonitor zur Untersuchung schneller Ionenstrahländerungen im TSR

J. Thiel, Th. Lippert, N. Grün, W. Scheid
Photonenproduktion durch klassische Abbremsung in relativistischen Kern-Kern-Stößen

B. Thies, W.-D. Sepp, B. Fricke
Viel-Elektronen-Rechnungen und Interpretation der zeitabhängigen relativistischen Schwerionenstreuung

E. Träbert, G. Möller, V. Lodwig, P.H. Heckmann, J.H. Blanke
Satelliten zur Li II $1s^2\ {}^1S_0$ -1s2p $^1p^o_1$ Linie

A. Warczak, C. Kozhuharov, A.E. Livingston, P.H. Mokler, S. Reusch, Z. Stachura, Th. Stöhlker, A. Szymanski
Evidenz für den resonanten Zweielektroneneinfang bei gleichzeitiger Elektronenanregung

L. Yang, D. Heinemann, D. Kolb
Optimierung atomarer Finite Elemente Rechnungen

Monterey, USA: 9th Int. Conf. on Laser Interaction and Related Plasma Phenomena, 06.-10.11.1989

F. Caspers, L. Cicchitelli, H. Haseroth, H. Hora, E. Jensen, A. Scharmann, W. Scheid, E. Wilson
Acceleration of Electrons to TeV Energy by Lasers in Vacuum

Monterey, USA: 2nd Int. Conf. on Chemistry and Migration Behaviour of Actinides and Fission Products in the Geosphere, 06.-10.11.1989

M. Ganz, H. Barth, M. Fuest, D. Molzahn, R. Brandt
Natural Plutonium Traces within the Geosphere, i.e. the Depth of the Continental Crust

Montreal, Kanada: Int. Symp. on Weak and Electromagn. Interact. in Nuclei (WEIN), 1989

G. Koch, V. Metag, R. Beck, B. Schoch, H. Ströher
Photoproduction of Neutral Pions from Complex Nuclei

M. Pfeiffer, G. Koch, V. Metag, R. Beck, R. Gothe, B. Schoch, M. Wilhelm, H. Ströher
Direct Observation of Incoherent π^0-Photoproduction

Munich, FRG: Results of the Feasibility Studies of the ^{205}Tl Solar Neutrino Experiment, 24.11.1989

P. Kienle
Status of SIS and ESR

Münster, FRG: Spring Meeting of the German Physical Society, Solid State Physics Section, 03.-07.04.1989

P. Schwalbach, M. Hartick, U. Imkeller, E. Kankeleit, B. Keck, G. Klingelhöfer, S. Laubach, M. Menningen, R. Sielemann, B. Stahl
In-Beam-Mößbauerspektroskopie: ^{57}Fe in Silizium, GaAs und $LiNbO_3$

New London, USA: 1989 Gordon Research Conference, 12.-16.06.1989

Effects on Nuclear Structure in the Stability and Formation of the Heaviest Elements

New York, USA: 16th Int. Conf. on the Physics of Electronic and Atomis Collisions (ICPEAC), 26.07.-01.08.1989

G. Deco, K. Momberger, N. Grün
Ionization in Relativistic Ion-Atom Collisions

G. Deco, K. Momberger, N. Grün
Pair Production in Ion-Ion Collisions at Relativistic Energies

R. Dörner, K. Dexheimer, J. Euler, R. Koch, H. Schmidt-Böcking, R. Seip, J. Ullrich
L-Subshell Ionisation Probabilities and Alignment for 1 MeV p-Sm

C. Kelbch, S. Hagmann, O. Jagutzki, G. Kraft, R. Mann, R.E. Olson, U. Ramm, S. Schmidt, H. Schmidt-Böcking, J. Ullrich
Unexpected Structures in the Doubly Differential Cross Sections for Electron Emission in 1.4 MeV U^{33+}-Rare Gas Collisions

A. Müller
Resonant Recombination and Autoionization in Electron-Ion Collisions

R.E. Olson, J. Ullrich, R. Dörner, V, Dangendorf, S. Kelbch, K. Berg, H. Schmidt-Böcking
Angular Scattering of Energetic Uranium Ions by Neon

J. Ullrich, R. Dörner, R. Olson, H. Schmidt-Böcking
Ionisation Dynamics in Proton-Helium Collisions

A. Wolf et al.
First Atomic Physics Experiments with Cooled Ion Beams at the Heidelberg Heavy-Ion Ring TSR

New York, USA: XVI Int. Conf. on the Physics of Electronic and Atomic Collisions, 26.07.-01.08.1989

W.G. Graham, K.H. Berkner, E.M. Bernstein, M.W. Clark, H. Crawford, B. Feinberg, M. Flores, L. Greiner, R.J. McDonald, P.H. Mokler, T.J. Morgan, W. Rathbun, A.S. Schlachter, J.A. Tanis
The Search for RTE in 30 - 38 GeV Collisions of U^{89+} with Carbon Foils

S. Reusch, P.H. Mokler, A. Warczak, Z. Stachura, T. Kambara, R. Schuch, M. Schulz, G. Wintermeyer, A. Müller
The Two-Photon Decay of the $^1S_0$ State in $_{32}Ge^{30+}$ Produced by Resonant Transfer and Excitation

S. Reusch, P.H. Mokler, A. Warczak, Z. Stachura, T. Kambara, R. Schuch, M. Schulz, G. Wintermeyer, A. Müller
Resonant Transfer and Excitation in Hydrogenic Ge-Projectiles

R. Schuch, E. Justiniano, M. Schulz, P.H. Mokler, S. Reusch, S. Datz, P.F. Dittner, J. Giese, P.D. Miller, H. Schöne, T. Kambara, A. Müller, Z. Stachura, R. Vane, A. Warczak, G. Wintermeyer
RTE of Hydrogen-Like and Lithium-Like Ions

A. Warczak, Z. Stachura, A. Szymanski, Th. Stöhlker, C. Kozhuharov, A.E. Livingston, P.H. Mokler, S. Reusch
Evidence for Resonant Two-Electron Capture and Excitation

Oarai, Ibaraki, Japan: Int. Symp. on Advanced Nucl. Energ. Res., 15.-16.02.1989

G. Münzenberg
Status and Prospects for the Production and Investigation of Heavy Elements

Obernai, France: Workshop on Nuclear Structure of Light Nuclei Far From Stability - Experiment and Theory, 27.-29.11.1989

H. Geissel, P. Armbruster, K.-H. Behr, B. Blank, A. Brünle, H.G. Burkard, K. Burkard, H.-G. Clerc, M. Chen, J. P. Dufour, B. Franczak, Y. Fujita, J. J. Gaimard, E. Hanelt, R. Kirchner, O. Klepper, B. Langenbeck, G. Münzenberg, F. Nickel, K. Poppensieker, M.S. Pravikoff, E. Roecki, D. Schardt, K.-H. Schmidt, H.J. Schött, Th. Schwab, B. Sherrill, K. Sümmerer, H. Wollnik
The Projectile-Fragment Separator FRS at GSI: Status and Planned Experiments

J. Szerypo, D. Bazin, B.A. Brown, D. Guillemaud-Mueller, H. Keller, R. Kirchner, O. Klepper, D. Morrissey, E. Roecki, D. Schardt, B. Sherrill
The Beta-Decay of ^{48}Mn: Improved Data on Gamow-Teller Quenching

Osaka, Japan: The XXIII Yamada Conference on Nuclear Weak Process and Nuclear Structure, 12.-15.06.1989

R. Barden, T. Batsch, H. Gabelmann, I.S. Grant, P. Hill, R. Kirchner, O. Klepper, G. Nyman, A. Plochocki, G.-E. Rathke, H. Ravn, E. Roecki, K. Rykaczewski, D. Schardt, J. Szerypo, J. Zylicz

Gamow-Teller Beta Decay of Even-Even Nuclei Near ^{100}Sn

Paris, France: Symp. on the Auger Effect, 30.-31.03.1989

P.H. Mokler, S. Reusch
The Time Reversal of the Aufer Effect and its Relevance in Atomic Collisions

Peniscola, Spain: NATO Advanced Study Institute, Int. Advanced Courses on 'The Nuclear Equation of State', 21.05.-03.06.1989

G. Batko, T.S. Biro, W. Cassing, U. Mosel, M. Schäfer, T. Wolf
Dilepton Production in Heavy-Ion Collisions

B. Blättel, V. Koch, A. Lang, K. Weber, W. Cassing, U. Mosel
The Relativistic BUU Approach - Analysis of Retardation Effects and Thermal Properties

W. Greiner, W. Scheid
The Collective Spin of Nuclear Surface Vibrations

E. Grosse
Meson and Photon Production in Heavy Ion Collisions

H.H. Gutbrod
Heavy Ion Experiments at CERN SPS

P. Kienle
The SIS/ESR-Project at GSI - Present and Future

B. Kämpfer, G. Wolf, B. Lukacs, B.W. Barz
Description of the Nuclear Stopping Process within the Anisotropic Thermo-Hydrodynamics

K.H. Kampert
Fragment Flow and Squeeze-Out of Hot and Dense Nuclear Matter

Th. Lippert, J. Thiel, N. Grün, W. Scheid
Photon and Lepton Production by Bremsstrahlung in Relativistic Heavy Ion Collisions

H. Loehner
Photon and Meson Production in Heavy Ion Reactions at CERN

A.M. Poskanzer
A History of Central Collisions at the Bevalac

H.R. Schmidt
Stopping at CERN

Piriac-sur-Mer, France: 5èmes Journées d'Etudes Saturne 16.-20.05.1989

W. Trautmann, E. Berdermann, B. Berthier, C. Cerruti, C.K. Gelbke, J. Hubele, P. Kreutz, G.J. Kunde, S. Leray, R. Lucas, U. Lynen, U. Milkau, C. Ngô, C.H. Pinkenburg, J. Pochodzalla, G. Raciti, H. Sann
Results Obtained for Heavy-Ion Reactions at Saturne

Praque, CSSR: VIIIth Int. Conf. on Hyperfine Interactions, 14.-19.08.1989

U. Dinger, S. Dutta, J. Eberz, G. Huber, R. Kirchner, O. Klepper, T. Kühl, D, Marx, R. Menges, S. Schröder, G. Sprouse
Laser Spectroscopy of Radioactive Lead and Thallium Isotopes

P. Ganal, T. Butz, W. Karle, K.-H. Speidel, A. Lerf
Suppression of the Charge Density Waves in 1T-TaS_2 by 70 MeV O^{6+} Bombardment

K.-H. Speidel
New Aspects of Trancient Magnetic Fields

K.-H. Speidel, J. Cub, M. Knopp, H.-J. Simonis, H.-J. Wollersheim, P. Egelhof, H. Emling, H. Grein, W. Henning, R. Holzmann, R.S. Simon, R. Schmidt, N. Gollwitzer
Measurements of Transient Magnetic Fileds on Single-Electron Ni-Ions

K.-H. Speidel, M. Knopp, W. Karle, J. Cub, P.N. Tandon, U. Reuter, H.-J. Simonis, S. Kremeyer, F. Hagelberg
Large Dynamic Perturbations of Transient Magnetic Fields Induced by Heavy Ion Beams

H.-J. Simonis, S. Kremeyer, F. Hagelberg, U. Reuter, M. Knopp, K.-H. Speidel, J. Cub, W. Karle, P.N. Tandon, J. Gerber
Plunger Measurements on Highly Stripped O-Ions as Tool for Detecting Electron Polarization on Emergence from Thin Ferromagnetic Layers

Rio de Janeiro, Brasil: Int. Workshop on Relativistic Aspects of Nuclear Physics, 28.-30.08.1989

U. Mosel
The Relativistic BUU Approach - Analysis of Retardation Effects and Thermal Properties

Rome, Italy: 10thSymp. of Microdosimetry, 21.-26.05.1989

J. Kiefer
Estimation of Proximity Functions for Ion Tracks

M. Kost, J. Kiefer
Biological Action of Heavy Ion Irradiation on Individual Yeast Cells

E. Schneider, M. Kost, M. Schäfer
Inactivation Cross Sections of Yeast and Bacteria Exposed to Heavy Ions at Low Energy ($\leq$600 keV/u)

Saclay, France: Journées des Theoriciens SATURNE III 23.-24.11.1989

U. Milkau, E. Berdermann, B. Berthier, C. Cerruti, A. Demeyer, E.-M. Eckert, D. Guinet, K.D. Hildenbrand, J. Hubele, P. Kreutz, G.J. Kunde, S. Leray, P. Lhénoret, R. Lucas, U. Lynen, C. Mazur, W.F.J. Müller, C. Ngô C.H. Pinkenburg, J. Pochodzalla, H.J. Rabe, G. Raciti, M. Ribrag, H. Sann, H. Stelzer, E. Tomasi, W. Trautmann, R. Trockel, R. Wada
Fragment Emission in the Reaction $^{40}Ar + ^{197}Au$ at E/A = 30 and 200 MeV

Salzburg, Austria: Dreiländertagung Elektronenmikroskopie, 10.-16.09.1989

J. Vetter
Über Kernspurkanäle induzierte durch Schwerionen bei hoher Energie

San Diego, USA: Int. Symp. on Optical and Optoelectronic Applied Science and Engineering, 06.-11.08.1989

B. Kraus, K.H. Schartner, F. Folkmann, A.E. Livingston, P.H. Mokler
The GSI - 5m Grazing Incidence Spectrometer

San Francisco, USA: Annual meeting of the American Physical Society, 15.-19.01.1989

A. Thiel, C. Borchert, W. Greiner, J.Y. Park, W. Scheid
Coupled Channel Calculations for the $^{17}O + ^{13}C$ Scattering

Santander, Spain: Nuclear Physics in the Nineties, European Facilities, 31.7.4.8.1989

P. Kienle
SIS/ESR - a New Heavy Ion Accelerator Facility at GSI
First Experiments at SIS/ESR

Sao Paulo, Brasil: International Nuclear Physics Conference, 20.-26.08.1989

P. Armbruster
Transactinide Elements

P. Kienle
Physics with Stored and Colled Heavy Ion Beams

G. Koch, V. Metag, R. Beck, B. Schoch, H. Ströher
Photoproduction of Neutral Pions from Complex Nuclei

U. Mosel
Hard Particles as Probes for Hot and Compressed Nuclear Matter

Th. Weber, W. Wilke, H. J. Emrich, R. D. Heil, Th. Kihm, U. Kneissl, K. T. Knöpfle, U. Seemann, F. Steiper, H. Ströher
Evidence for Different Fission Fragment Mass Aymmetries for Specific Nuclear Excitations Studied in (e, e'f) and (γ,f) Reactions

G. Wirth, W. Brüchle, Fan Wo, K. Sümmerer, F. Funke, J.V. Kratz, N. Trautmann
Nuclear Reactions in Collisions of Very Heavy Ions at Energies Below and Near the Barrier

Schleching, Austria: XX. Expertentreffen der Kernphysik, 22.02.-02.03.1989

B. Blättel
Eine relativistische Transporttheorie zur Beschreibung von Schwerionenkollisionen

W. Cassing
Dynamik von Schwerionenreaktionen im Mittelenergiebereich

J. Knoll
Produktion harter Photonen und Summenregeln

W. Trautmann
Reaktionen hochenergetischer schwerer Ionen

Surrey, UK: Low Energy Ion Beam Conference 5, 03.-06.04.1989

D. Rück
High Current Metallic Ion Beams

Tashkent, USSR: International Conference 'Actinides-89', 24.-29.09.1989

W. Brüchle
Aqueous Chemistry With Element 105

G. Herrmann, N. Trautmann
Recent Developments in Rapid Radiochemical Separations of Heavy Elements

Tashkent, USSR: Int. Astronautical Academy Symp. 'Man in Space', 02.10.1989

J. Kiefer
Radiation Hazards in Space: the Need for New Concepts

Tokyo, Japan: 12th Symp. on Ion Sources and Ion Assisted Technology, 05.-07.07.1989

B.H. Wolf
Intense High Energy Metal Ion Beams

Tsukuba, Japan: Workshop on Reaction Mechanism of Intermediate Energy Heavy-Ion Collisions, 29.-30.06.1989

K. Niita
Particle Production in Heavy-Ion Collisions from 20 MeV/u to 2 GeV/u

Varenna, Italy: 'Enrico Fermi' Int. Summer School on High-Pressure Equations of State , 25.07.-04.08.1989

J. Pochodzalla
Multifragmentation: A Probe for Hot Expanding Nuclei

R.M. Weiner
Equations of State in Nuclear, Hadronic and Quark-Gluon Matter

Varenna, Italy: 2nd Workshop on Inertial Confinement Fusion by Heavy Ion Beams, 25.-27.10.1989

I. Hofmann
Non-Liouvillean Pulse Compression

R. Bock
Status of the SIS/ESR Facility at GSI and its Perspective for the German H.I.I.F. Program

Villigen, Switzerland: Workshop on Applications of Heavy Ions in Atomic Nuclear, Solid State Physics, Chemistry and Biology, 16.06.1989

J.V. Kratz
Chemical Properties of Element 105

P.H. Mokler
Atomic Physics Research Possible at the ECR-Cyclotron

Wertheim, FRG: Workshop on Crystalline Ion Beams, 04-07.10.1989

T. Kühl, S. Dutta, D. Marx, G. Huber, S. Schröder, B. Fricke, A. Faulstich, W. Petrich, D. Hahn, R. Neumann, D. Schwalm, A. Wolf
Precision Optical Spectroscopy of the Ground State Fine- und Hyperfine Structure of Highly Charged Ions as a Diagnostic Tool

Williamsburg, USA: VIth Conf. on Real-Time Computer Applications in Nuclear, Particle and Plasma Physics, 15.-19.05.1989

Ch. Ender, R. Männer, P. Bauer
Multiprozessor Data Acquisition System for High Event Rates at the Heidelberg-Darmstadt Crystall Ball

H.G. Essel, J. Hoffmann, M. Richter, H. Sohlbach, W. Spreng
An Integrated Data Acquisition and Analysis System at GSI

Windsor, Canada: 1989 Annual Meeting of the Division of Atomic, Molecular and Optical Physics (DAMOP), 17.-19.05.1989

E. Träbert
Intercombination and Forbidden Transitions in Delayed Beam-Foil Spectra

R. Bock
Status and Perspectives on Heavy Ion Inertial Fusion

Zakopane, Poland: XXIV School on Physics, Selected Topics in Nuclear Structure, 16.-22.4.1989

S. Hofmann
New Results on Heavy Elements Research and Plans for the Future

P. Kienle
Electron-Positron Pair Creation in Heavy Ion Collisions

P. Schwalbach
In Beam Mößbauer Spectroscopy: Implantation of ^{58}Fe into Semiconductors and Insulators

8.1.3 Seminars at other Institutes

P. Armbruster
Neues über die schwersten Elemente und Atomkerne
University of Würzburg, FRG, 16.01.1989

P. Armbruster
Schalen- und Clustereffekte bei der Erzeugung überschwerer Elemente
University of Tübingen, FRG, 01.02.1989

T.S. Biro
Die Farbstruktur des Vakuums
TU Wien, Austria, 19.06.1989

T.S. Biro
Gluon Mass and Confinement
LBL Berkeley, Berkeley, USA, 15.08.1989

T.S. Biro
The Collor Structure of the Vacuum
University of Marburg, 25.10 1989

T.S. Biro
Gluon Mass and Deconfinement
University of Frankfurt, 03.11.1989

B. Blättel
Eine relativistische Transporttheorie für Schwerionenkollisionen bei SIS-Energien
GSI, Darmstadt, FRG, 04.10.1989

D. Böhne
Stochastische Kühlung
University of Frankfurt, Inst f. Angew. Phys., FRG, 20.01.1989

D. Böhne
Stochastische Kühlung
TU München, Inst. f. Hochfrequenztechnik, FRG, 27.01.1989

D. Böhne
Stand der Technik bei Teilchenbeschleunigern
VDE Symposium Vakuum Elektronik, Garmisch Partenkirchen, FRG, 10.05.1989

D. Böhne
SIS Commissioning
Accel. and Fusion Division, LBL Berkeley, USA, 11.08.1989

W. Cassing
Relativistic Heavy-Ion Collisions and the Equation of State
University of Milano, Italy, 05.04.1989

W. Cassing
Teilchenproduktion in mittelenergetischen Schwerionenreaktionen
University of Tübingen, FRG, 12.06.1989

W. Cassing
Teilchenproduktion in Kernreaktionen
KFA Jülich, FRG, 29.06.1989

W. Cassing
Relativistische Schwerionenstöße und Observablen für die Zustandsgleichung der Kernmaterie
ZfK Rossendorf, GDR, 21.08.1989

M. Cubero
The Relativistic Vlasov Equation with Non-Radiating Meson Fields
University of München (LMU and TU), FRG, 21.02.1989

B. Fricke, E. Johnson
On the Chemical Prediction of Element 104 and 105
University of Mainz, FRG, 02.02.1989

B. Fricke
Vielelektronenrechnung und Interpretation im Ion-Atom-Stoß
University of Frankfurt, FRG, 24.04.1989

B. Fricke
Gekoppelte-Kanäle-Rechnungen auf der Basis selbstkonsistenter Dirac-Fock-Slater Matrixelemente
DFG-Kolloquium, Bielefeld, FRG, 08.05.1989

B. Fricke
Elektronendichte am Kernort und deren Berechnung
University of Mainz, FRG, 28.06.1989

B. Fricke
MCDF-Calculations in Very Heavy Atoms
Oak Ridge, USA, 26.10.1989

B. Fricke
Time-Dependent Calculations of Heavy-Ion Processes
Manhattan, USA, 02.11.1989

B. Fricke
Eine PC-Datei für theoretische atomare Daten
DFG-Kolloquium, Jülich, FRG, 06.11.1989

B.L. Friman
Dynamical Instabilities in Heavy-Ion Collisions
Abo Akademi, Abo, Finland, 22.05.1989

S. Glückert
Aufgaben der Datenverarbeitung in einer Großforschungseinrichtung
GMD, Heidelberg, FRG, 12.04.1989

E. Grosse
Pions and Photons from Nucleus-Nucleus Collisions
University of Mainz, FRG, 19.04.1989

E. Grosse
The Experimental Program at SIS
Michigan State University, USA, 25.08.1989

H.H. Gutbrod
Heavy Ion Experiments at the CERN SPS
Beijing, P.R. of China, 02.06.1989

R.W. Hasse
Kristallstrahlen
University of Giessen, FRG, Mai 1989

R.W. Hasse
Moderne Methoden der Kernforschung
Wetterauische Gesellschaft für die gesamte Naturforschung, Hanau, Oktober 1989

W. Henning
Beschleuniger-Massenspektrometrie: Gemeinsame Aspekte von Totem Meer, Sonnenneutrinos und Funden aus dem Pleistozän
Gesamthochschule Kassel, FRG, 02.02.1989

W. Henning
Beschleuniger-Massenspektrometrie: Gemeinsame Aspekte von Totem Meer, Sonnenneutrinos und Funden aus dem Pleistozän
University of Bayreuth, FRG, 14.11.1989

G. Herrmann
Vor fünf Jahrzehnten: Von den 'Transuranen' zur Kernspaltung
University of Mainz, FRG, 13.06.1989

G. Herrmann
Die schwersten chemischen Elemente
University of Münster, FRG, 14.06.1989

G. Herrmann
Vor fünf Jahrzehnten: Von den 'Transuranen' zur Kernspaltung
University of Bonn, FRG, 22.06.1989

G. Herrmann
Vor fünf Jahrzehnten: Von den 'Transuranen' zur Kernspaltung
University of Frankfurt, FRG, 28.06.1989

G. Herrmann
Five Decades Ago: From the 'Transuranics' to Nuclear Fission
Institute Curie, Paris, France, 09.11.1989

G. Herrmann
Synthese schwerster chemischer Elemente - Ergebnisse und Perspektiven
University of Siegen, FRG, 19.12.1989

F.P. Heßberger
Erste Experimente zur Untersuchung hochangeregter CN am SHIP
University of Marburg, FRG, 26.01.1989

I. Hofmann
Kristalline Ionenstrahlen
University of Erlangen, FRG

Ch. Jung
One-Dimensional Nuclear Dynamics in QHDI
ISN, Grenoble, France, 10.11.1989

J. Kiefer
Mutation Induction by Heavy Ions
Joint Inst. for Nucl. Res., Dubna, USSR, 15.06.1989

J. Kiefer
Cellular Effects of Heavy Ions
Centre de Biophysique Moleculaire, CNRS, Orleans, France, 10.03.1989

P. Kienle
Neues aus der Schwerionenphysik
Physikalischer Verein, Frankfurt, FRG, 15.03.1989

M. Kleber
Time-Dependent Tunneling Through Potential Barriers
The Weizmann Institute of Sciences, Rehovot, Israel, 07.02.1989

M. Kleber
Classical and Qunatum Theory of the Fermi Accelerator
The Weizmann Institute of Sciences, Rehovot, Israel, 28.03.1989

O. Klepper
Studies of Unstable Nuclei with the GSI On-Line Mass Separator
JAERI, Tokai-Mura, Japan, 16.06.1989

O. Klepper
Nuclei Far from Stability. Recent Results Obtained at the GSI On-Line Mass Separator
Tohoku University, Sendai, Japan, 20.06.1989

O. Klepper
Gamow-Teller β-Decays of Even-Even Nuclei Near ^{100}Sn
RIKEN, Tokyo, Japan, 22.06.1989

G. Klotz-Engmann
Transition from Binary Fission to Multifragmentation
Inst. of High-Energy Physics, Dubna, USSR, 15.11.1989

J. Knoll
Limitation de la Production des Photons par des Regles des Sommes Quantiques
CNRS, Strasbourg, France, 11.05.1989

J. Knoll
Summenregeln zur Photonproduktion
University of Erlangen, FRG, 31.05.

J. Knoll
Grenzen kinetischer Photonen Produktion durch quantenmechnaische Summenregeln
University of Tübingen, FRG, 05.06.1989

V. Koch
A Relativistic Transport Theory for Heavy-Ion Collisions
TU München, FRG, 21.11.1989

D. Kolb
Pollution and the Ozon Drama
Islamabad, Pakistan, 07.03.1989

D. Kolb
Optimierung und weitere Anwendungen der Finite Elemente Methode
DFG-Kolloquium, Bielefeld, FRG, 08./09.05.1989

M. Krämer
Erfahrungen mit Vektor- und Parallelverarbeitung
TH Darmstadt, FRG, 09.11.1989

M. Krämer
Experiences with Parallel FORTRAN
Wiss. Zentrum IBM, Heidelberg, FRG, 17.-18.04.1989

D. Liesen
Energien und Lebensdauern in Wenig-Elektronen-Systemen
TUM and LMU, München, FRG, 03.11.1989

H. Loehner
Photon and Meson Production in Heavy Ion Reaction at CERN
University of Utrecht, The Netherlands, 24.02.1989

P.H. Mokler
Die Zeitumkehr des Auger Effektes in der Stoßphysik
University of Giessen, FRG, 13.11.1989

U. Mosel
Teilchenerzeugung in Schwerionenreaktionen
University of Heidelberg, FRG, 26.06.1989

U. Mosel
Teilchenerzeugung in Schwerionenreaktionen
HMI Berlin, FRG, 03.07.1989

U. Mosel
Hard Particle Production in Intermediate Energy Heavy-Ion Collisions
University of Washington, USA, 20.07.1989

U. Mosel
Hochenergetische Stöße zwischen Atomkernen
University of Tübingen, FRG, 06.12.1989

G. Münzenberg
Erzeugung und Nachweis der schwersten Elemente
University of Kaiserslautern, FRG, 31.01.1989

G. Münzenberg
On the Road to Superheavy Elements
JAERI, Tokai-mura, Japan, 17.02.1989

G. Münzenberg
On the Road to Superheavy Elements
Cycl. Rad. Center, Tohoku University, Sendai, Japan, 18.02.1989

G. Münzenberg
Status and Prospects for the Production and Investigation of Heavy Elements
Tokyo Metropolitan University, Kyoto, Japan, 20.02.1989

G. Münzenberg
Status and Prospects for the Production and Investigation of Heavy Elements
INS University of Tokyo, Japan, 21.02.1989

G. Münzenberg
The New Experimental Facilities for Relativistic Heavy Ions and the Projectile Fragment Separator at GSI
RIKEN, Tokyo, Japan, 22.02.1989

G. Münzenberg
The New Experimental Facilities for Relativistic Heavy Ions and the Projectile Fragment Separator at GSI
RNCP, Osaka, Japan, 25.02.1989

G. Münzenberg
Die schalenstabiliserten schweren Elemente
Deutscher Verein zur Förderung des math. und naturw. Unterrichts, Darmstadt, FRG, 21.03.1989

G. Münzenberg
Der projektil-Fragmentseparator bei GSI und das Experimentierprogramm
ZfK Rossendorf, GDR, 08.11.1989

K. Niita
Hard Photon Production in Heavy-Ion Collisons
Texas A&M University Cyclotron Institute, USA, 16.05.1989

K. Niita
Particle Production in Heavy-Ion Collisons from 20 MeV/A to 2 GeV/A
Oak Ridge National Laboratory, USA, 01.06.1989

K. Niita
Particle Production in Heavy-Ion Collisons from 20 MeV/A to 2 GeV/A
Michigan State University, USA, 14.06.1989

K. Niita
Particle Production in Heavy-Ion Collisons from 20 MeV/A to 2 GeV/A
Tohoku, University, Sendai, Japan, 26.06.1989

K. Niita
Hard Photon Production in Heavy-Ion Collisons
RIKEN, Saitama, Japan, 22.06.1989

K. Niita
Hard Photon Production in Heavy-Ion Collisons
Tsukuba University, Japan, 27.06.1989

K. Niita
Particle Production in Heavy-Ion Collisons from 20 MeV/A to 2 GeV/A
Tokyo Institute of Technology, Japan, 11.09.1989

K. Niita
Particle Production in Heavy-Ion Collisons from 20 MeV/A to 2 GeV/A
Tokyo Metropolitan University, Japan, 22.09.1989

K. Niita
Particle Production in Heavy-Ion Collisons from 20 MeV/A to 2 GeV/A
INS, Tokyo, Japan, 26.09.1989

W. Nörenberg
Physik am neuen Beschleuniger SIS/ESR bei GSI
TU Dresden, GDR, 30.03.1989

W. Nörenberg
Towards a Covariant Transport Theory: Some Studies on Relativisitic A-A Collisions
JINR, Dubna, USSR, 24.08.1989

W. Nörenberg
Diabatic Hindrance of Heavy-Ion Fusion
University of Leningrad, USSR, 1989

H. Oeschler
Fission Binaire et Multifragmentation
GANIL, Caen, France, 26.09.1989

H. Oeschler
The New Koan Spectrometer at SIS
Inst. of High-Energy Physics, Dubna, USSR, 15.11.1989

H. Oeschler
Dynamics of Dissipative Collisions Determined from δ-Electron Spectra
Joint Inst. for Nucl. Res., Lab. of Nucl. React., Dubna, USSR, 16.11.1989

H. Oeschler
The New Kaon Spectrometer at SIS
Joint Inst. for Nucl. Res., Lab. of Nucl. React., Dubna, USSR, 17.11.1989

F. Plasil
WA80 Results
Michigan State University, USA, Nov.1989

A.M. Poskanzer
The Collective Flow of Nuclear Matter
US Navy Postgraduate School of Monteray, USA, 21.07.1989

M. Richter
Datenaufnahme bei der GSI
CANU-Arbeitstreffen, Bad Honnef, FRG, 19.12.1989

D. Rück
Hochstromionenquellen
Gesamthochschule Kassel, FRG, 08.06.1989

A. Sandoval
Future Relativistic Heavy-Ion Experiments at CERN
University of Frankfurt, FRG, 12.07.1989

M. Schäfer
Photon and Dilepton Production in Nucleon-Nucleon Collisions
LBL Berkeley, Berjkeley, USA, 22.08.1989

D. Schardt
Studies of Exotic Nuclei - Recent Results from the GSI On-line Mass Separator and Future Possibilities at SIS/ESR
Instituto de Fisica Corpuscular, Valencia, Spain, 24.01.1989

D. Schardt
Exotic Nuclei Studies at the GSI Projectile Fragment Separator
Michigan State University, East Lansing, USA, 17.06.1989

D. Schardt
Das Strahlentherapieprojekt am Schwerionensynchrotron der GSI
ZfK, Rossendorf, GDR, 08.11.1989

D. Schardt
Protonen- und Gammaspektroskopie neutronenarmer seltener Erden um N=82
ZfK, Rossendorf, GDR, 09.11.1989

G. Soff
Radiative Capture of Muons in Light Atoms
Dept. of Physics, University of Arizona, Tucson, USA, Febr. 1989

G. Soff
The GSI Positron Peaks - Recent Investigations
Nat. Inst. of Standards and Technology, Giathersburg, USA, 07.03.1989

H. Ströher
Photoproduction of Neutral Pions at the Mainz-Microtron
Inst. f. Theor. Phys., University of Pavia, Italy, 12.01.1989

H. Ströher
Photoproduktion neutraler Mesonen mit monochromatischen Photonen
University of Giessen, FRG, 30.11.1989

P. Vater
Production and Application of Nuclear Track Microfilters
Joint Inst. for Nucl. Res., Dubna, USSR, 28.09.1989

G. Wirth
Kernreaktionen bei der Wechselwirkung sehr schwerer Ionen unterhalb und nahe der Barriere
TH Darmstadt, FRG, 02.02.1989

G. Wirth
Kernreaktionen in Stößen sehr schwerer Atomkerne unterhalb und nahe der Coulombbarriere
University of Mainz, FRG, 05.07.1989

H.J. Wollersheim
Search for the 2-Octupole-Phonon Multiplet in ^{208}Pb
MPI Heidelberg, FRG, 27.10.1989

8.1.4 Lectures and Courses

P. Armbruster
Seminar '50 Jahre Kernspaltung'
(TH Darmstadt, FRG)

R. Brockmann
Instrumentation in Ultra-Relativistic Heavy-Ion Experiments (I-IV)
(Winter School on Quark-Gluon Plasma, Puri, India, Dec. 5-16, 1989)

B.L. Friman and P.A. Henning
Theorie der Fermi Flüssigkeiten
(TH Darmstadt, FRG)

N. Grün, G. Herrmann, H. Löb, V. Metag, P.H. Mokler, A. Müller, E. Salzborn, A. Scharmann, K.-H. Schartner, W. Scheid
Seminar über Atomphysik
(University of Giessen, FRG)

G. Herrmann
Einführung in die Kernchemie
(University of Mainz, FRG)

G. Herrmann
Kernchemisches Praktikum I
(University of Mainz, FRG)

G. Herrmann
Kernchemisches Praktikum II
(University of Mainz, FRG)

I. Hofmann
Einführung in die Plasmaphysik
(University of Frankfurt, FRG)

I. Hofmann
Intensity Limits in Storage Rings
(CERN Acc. School, Uppsala, Sweden, Sept. 18-29, 1989)

I. Hofmann
Crystalline Ion Beams
(CERN Acc. School, Uppsala, Sweden, Sept. 18-29, 1989)

D. Kolb
Finite Element Method in Quantum Applications
(PINSTECH, Islamabad, Pakistan, 19.02.-23.03.1989)

D. Liesen
Gruppenunterricht zur Physik II
(University of Heidelberg, FRG)

P. Malzacher
Graphische Datenverarbeitung
(Fachhochschule Darmstadt, FRG)

P.H. Mokler, A. Müller, E. Salzborn, K.-H. Schartner
Seminar über experimentelle Methoden der Atompkysik
(University of Giessen, FRG)

P.H. Mokler, K.-H. Schartner
Ergänzungen zur Technischen Physik I
(University of Giessen, FRG)

P.H. Mokler, A. Müller, E. Salzborn, K.-H. Schartner, J. Kiefer
Seminar über Wechselwirkungem von Schwerionenstrahlen mit Materie
(University of Giessen, FRG)

G. Münzenberg
Mittelenergiephysik-Experimente am SIS
(University of Giessen, FRG)

W. Nörenberg, P.A. Henning
Theoretische Kernphysik
(TH Darmstadt, FRG)

G. Soff
Kosmologische Modelle
(University of Frankfurt, FRG)

G. Soff
Pfadintegrale
(University of Frankfurt, FRG)

K. Winkelmann
Rechnerarchitektur
(Fachhochschule Darmstadt, FRG)

8.2 SCIENTIFIC ACTIVITES WITHIN GSI

8.2.1 Meetings, Workshops and Research Seminars

10.05.	Research Seminar	21.08.-13.10.	Students Program
12.05.	Biology Workshop	05./06.09.	Biology
09.06.	1.4 Decades of 1.4 MeV/u Beam	28./29.09.	Research Seminar
27./28.06.	Experimentausschuß-Sitzung	19./20.10.	Laser Workshop
10.-14.07.	Scholars Program	05./6.12.	Experimentausschuß-Sitzung

8.2.2. Seminars at GSI

10.01.
E. Jaeschke, Heidelberg
TSR - Ein Kühlring für schwere Ionen

11.01.
G. Bertsch, East Lansing
Static Path Approximation for Nuclear Level Densities

13.01.
K.V. Shitikova, Moscow
The Hyperspherical Functions Method and its Application to Heavy Ion and Quark Physics

17.01.
K. Winkelmann, Darmstadt
UNIX - einige Grundlagen

17.01.
M. Huyse, Leuven
Decay and Reaction Studies with Radioactive Ion Beams

18.01.
M. Fuchs, Geneva
Transputer: Grundlagen und Anwendungen

24.01.
P.J. Crutzen, Mainz
Ozonloch

25.01.
H. Pilkuhn, Universität Karlsruhe
On the Connection between One- and Two-time Relativistic Equations of Motion in Atomic Physics

25.01.
B. Franzke, Darmstadt
Der Experimentier-Speicherring: Konzept, gegenwärtiger Status und Aktivitäten 1989

31.01.
A. Ertem, Frankfurt
Integrierte Netzwerke

31.01.
W. Paul, Bonn
Lebensdauer und Gewicht des Neutrons

01.02.
B. Kämpfer, Dubna/Darmstadt
Phenomenological Models for the Confinement Transition

01.02.
H. Homeyer, Berlin
Dynamik von Aufbruchsreaktionen

02.02.
M. Martin, Berlin
Multioktav Breitbandverstärker 50 kHz bei 8 GHz

08.02.
P.F. Bortignon, Mailand
Properties of Nuclear Excitation at Finite Temperature

08.02.
K. Sümmerer, Darmstadt
Spallation von Gold mit GeV-Protonen - ein Testfall für die Fragmentation schwerer Kerne bei SIS ?

09.02.
R.W. Hasse, Darmstadt
Rechnungen zu kristallinen Strahlen im Speicherring

14.02.
H. Sohlbach, Darmstadt
Das Konzept des SIS/ESR Datenaufnahmesystems

15.02.
G. Kraft, Darmstadt
Biophysik-Experimente und das Strahlentherapie-Projekt bei GSI

15.02.
B. Milek, Dubna
Some Investigations Concerning Quantum Chaos

15.02.
T. Ishikawa, Darmstadt
Study of Hypernuclei with Stopped Kaons

16.02.
K.H. Warum, Seligenstadt
Warum CASE (Computer Aided Software Engineering)?

21.02.
S. Gralla, Darmstadt
Neue Konzepte in der Textverarbeitung

22.02.
T. Schlagel, Urbana
Classical Simulations of Heavy-ion Collisions

22.02.
R. Menges
Laserspektroskopie an radioaktiven Isotopen aus Schwerionen-Reaktionen

28.02.
Fa. SUN
Ein Konzept des offenen Systemnetzwerkes

01.03.
W.H.A. Hesselink, Amsterdam
Angular Momentum and Temperature Dependences of the Giant Dipole Resonance

06.03.
T. Yamazaki, Tokyo
Deeply Bound π^--States and Pion Transfer Reactions

07.03.
H. Göringer, Darmstadt
Ein interaktives Testsystem für PL/I (PLITEST) - ein Tutorial

08.03.
R. Schmidt, Dresden
Atomic Cluster Physics from the Viewpoint of Nuclear Physics

08.03.
P. Salabura, Cracow/Frankfurt
Neuer Ergebnisse der EPOS-Messungen zur korrelierten Elektronen-Positronen-Emission in Schwerionenstößen

14.03.
R. Thieme, Darmstadt
Das neue ISPF 2.3.0

15.03.
J. Virgin, Frankfurt
Das Datenbanksystem DB2, ein Überblick

16.03.
F. Nolden, Darmstadt
Strahlwechselwirkung mit Hochfrequenz-Pickups und Kickern

22.03.
B. Schürmann, München
An Introduction to Artificial Neural Systems

05.04.
Hanna, Stanford
Decay of the Giant Resonance Excited by Pion Single Charge Exchange

05.04.
R.J. Charity, Darmstadt
Complex Fragment Emission at Bombarding Energies between 10 and 20 MeV/u

12.04.
D. Guillemaud-Mueller
Recent GANIL Experiments on Production and Decay of Neutron-Rich Isotopes, Using ^{48}Ca Beam

14.04.
P. Elderon, Santa Teresa
On the Debugging Tools PLITEST and INSPECT

18.04.
W. Kynast, Darmstadt
AWK - ein MS-DOS und UNIX Tool

18.04.
J. Stachel, Stony Brook
Recent Results from the Relativistic Heavy Ion Experiment E814 at BNL

19.04.
K. Weyrich, Darmstadt
Experimentelle Bestimmung des Energieverlustes von Schwerionen in einem Wasserstoffplasma

20.04.
H. Poth, Darmstadt
Gleichgwicht Elektronenkühlung-stochastische Heizung

25.04.
U. Meyer, Darmstadt
Das Reich der Netze

25.04.
I.M. Khalatnikov, Moscow
Inflationary Cosmology

26.04.
M. Schädel, Darmstadt
Experimente zur Chemie der schwersten Elemente

02.05.
A.E. Livingston, Indiana
Fine Structure Spectroscopy of Highly Ionized Atoms

03.05.
A. Steinhof, Darmstadt
Beschleunigermassenspektroskopie von ^{41}Ca am UNILAC and am Rehovot-Tandem

09.05.
M. Krämer, Darmstadt
Erfahrungen mit Parallel FORTRAN

09.05.
K. Kleinknecht, Mainz
Erste Beobachtung der direkten CP-Verletzung in K^0-Zerfällen

10.05.
V. Toneev, Moscow
Relativistic Heavy-ion Collisions in an Independent Quark-Gluon String Model: Dynamics and Nuclear Effects

10.05.
H. Wipf, Darmstadt
Wasserstoff in Metallen

11.05.
U. Blell, Darmstadt
Ein neues Programm zur Berechnung 3-dimensionaler elektrischer Strömungsfelder

17.05.
E.A. Remler, Williamsburg
A 'Pure' Classical String Model for Ultrarelativistic Hadronic Collisions - Status Report

17.05.
K. Takahashi
Bound-State β Decay

18.05.
K. Takahashi, Bruxelles
Shell-Model Calculations of the Beta-Strength Function

18.05.
N. Cerf, Bruxelles
Alpha-Decay: Forgotten in Astrophysics?

18.05.
M. Kondo, Osaka
Recent Developments and New Accelerator Plans at RCNP

23.05.
W. Ahner, Darmstadt
Kinematik und Geometrie von SI-Reaktionen

23.05.
R. Neumann, Heidelberg
Erste Laserexperimente am Heidelberger Testspeicherring

24.05.
R.J. Meijer, Darmstadt
Central Collisions of ^{28}Si + ^{28}Si at Energies up to 30 MeV/Nucleon

24.05.
V.M. Strutinsky, Kiev
Macroscopics and Microscopics in Nucleu: Volume and Density Dynamics

30.05.
K. Mahrt, Darmstadt
Experimente mit intensiven SI-Strahlen in Materie

30.05.
V.M. Strutinsky, Kiev
Macroscopic and Microscopic Descriptions in Nuclear Physics ... and Elsewhere

31.05.
V.A. Karnaukhov, Dubna
FASA - a 4π Fragment Detector at the Dubna Synchrophasotron

06.06.
U. Milkau
Fragmentation und Feuerballemission bei SI-Stößen

06.06.
B. Lenk, Urbana
The Acuracy of the Vlasov-Nordheim Equation in Heavy-ion Collisions: Comparison to an Exact Model in the Classical Limit

06.06.
W. Hofmann, Heidelberg
Teilchenerzeugung in Hochenergiereaktionen

07.06.
W. Bauer, East Lansing
Role of the Delta in Pion- and Photon-spectra

07.06.
M. Richter, Darmstadt
Perspektiven der Datenaufnahme bei GSI

13.06.
O. Siart
Die Library Look Aside (LLA) Facility

13.06.
H. Wessels, Darmstadt
Kollektive Phänomeme in Experimenten mit SI von ca. 1 GeV/u

13.06.
J. Bille, Heidelberg
Lasertomographie am Auge

14.06.
J. Diaz-Alonso, Paris
Screening of the Pion Exchange Part of the NN Interaction in Relativistic Nuclear Matter

14.06.
R. Wada, College Station
Light Particle Emission as a Probe of Hot Nuclei

15.06.
U. Schaaf, Darmstadt
Überlegungen zur Schottky-Diagnose und erste Messungen am SIS

20.06.
B. Rittenhouse, Darmstadt
Simulation of Advanced Instrumentation - The GSI PHIGS Shell

20.06.
A. Wolf, Heidelberg
Uhren in beschleunigter Bewegung

20.06.
E. Recknagel, Konstanz
Metal Clusters

21.06.
E. Oset, Valencia
Production of Pion Modes in Relativistic Heavy Ion Collisions

21.06.
D. Böhne, Darmstadt
SIS Inbetriebnahme

27.06.
Y.-Z. Zuo, Beijing
Relativistic Mean Field Theory: From the Optical Potential to Heavy Ion Collision Dynamics

27.06.
B.A. Arbuzov, Protvino
The Conventional QED Interpretation of the e^+e^-Narrow Resonances

28.06.
M. Poszajczak, Darmstadt
Large N Quantum Mechanics and the Classical Limits

28.06.
W. Dünnweber, München
Interferometrie mit koinzidenten Neutronen

04.07.
H. Bloos, Frankfurt
Das automatische Cartridge-System MRX5400

04.07.
F. Urban, Darmstadt
Teilcheninterferometrie

04.07.
W. Greiner, Frankfurt
Quantenelektrodynamik starker Felder: Fakten, Fiktionen und eine mögliche Erklärung

05.07.
G. Chanfray, Lyon
Collective High-Energy Spin-Isospin Modes in Nuclei

05.07.
S. Schröder, Mainz
Laser-Experimente am TSR: Spektroskopie von 9 MeV $^7Li^+$

11.07.
E. Boggasch, München
Z-Pinch Plasma Linsen zur Fokussierung hochenergetischer geladener Teilchen

11.07.
N. Pfaff, Wiesbaden
Die ESA-Architektur

11.07.
D. Dubbers, Grenoble
Teichenphysik mit langsamen Neutronen

12.07.
A. Stahlhofen, Bonn
Interplay between Atomic, Molecular and Nuclear Forces in Muon Catalysed Fusion

18.07.
G. Kilgus, Heidelberg
Messungen zur dielektronischen Rekombination am TSR Heidelberg

19.07.
T. Matsui, MIT
Implications of J/ψ Suppression in Ultrarelativistic Nucleus-Nucleus Collisions

20.07.
K. Sato, Chiba
RF Accelerating System and Bunch Beam Monitoring System in Synchrotrons (TARN II)

24.07.
K. Sato, Chiba
The HIMAC Project

25.07./26.07.
R. Malfliet, Groningen
The Dynamics of Medium Effetcs in Relativistic Kinetic Theories

05.09.
Herr König, Frankfurt
Das automatische Kassettensystem COMPAREX 6388 ACL

13.09.
G. Kraft, Darmstadt
Information über geplante und laufende Teilchentherapie-Projekte

20.09.
N. Orr, Caen
Light Exotic Nuclei - A View from the Antipodes

20.09.
W. Kühn, Giessen
Photonen als Sonde für den Stoßparameter in Schwerionenreaktionen

21.09.
J. Finger, Bonn
Systemarchitektur und Betriebssystem (Suprenum)
Parallelisierungskonzept und Anwendersoftware

27.09.
W. König, Darmstadt
Spektroskopie von Schwerionen-induzierten Paaren mit der Doppelorange
Neue Ergebnisse zur Bhabha-Streuung

04.10.
B. Milek
The Kicked Rotator with Separable Perturbation: Onset of Quantum Chaos?

04.10.
B. Blättel, Giessen
Eine relativistische Transportheorie für Schwerionenkollisionen bei SIS-Energien

10.10.
V. Bunakov, Heidelberg
Direct Mechanism of Fast Light Particle Emission in Heavy Ion Collisions

11.10.
I. Rotter, Dresden
Resonanzen und Fluktuationen in Kernreaktionsquerschnitten

11.10.
D. Böhne, Darmstadt
Medizinbeschleuniger

18.10.
P. Mohr, Gaithersburg
The Lamb-shift in High-Z Atoms

25.10.
W. Enghardt, Dresden
Positronenemissionstomographie in Rossendorf

25.10.
M. Pfützner, Darmstadt
A Puzzle of the Internal Bremsstrahlung Accompanying the Forbidden Electron Capture Decay

31.10.
I. Giese, Darmstadt
graPHIGS-Anwendungen unter PL/1

31.10.
A. Bykov, Leningrad
Total γ-absorption Spectroscopy
a) Recent Results for β-decay
b) A New BGO-BaF_2 Spectrometer

01.11.
M. Herrmann, Darmstadt
Space-time Effects in the Decay of Strings by Pair Production

01.11.
D. Blaschke, Rostock
J/ψ Suppression and Quark-matter Formation within the String-flip Model

01.11.
G. Paic, Geneva
A Ring Imaging Cerenkov Detector for Ultra Relativistic Heavy Ion Collisions

07.11.
A. Möller, Darmstadt
Ein neues HELP bei GSI

07.11.
H. Miller, Pretoria
Phase Transition in Nuclei and Hadronic Matter

08.11.
G. Klotz-Engmann, Darmstadt
Übergang von binärer Spaltung zur Multifragmentation

10.11.
Yu. Oganessian, Dubna
Plans at Dubna to Study Exotic Nuclei

10.11.
J. Zylicz, Warsaw
Quenching of Gamow-Teller Strength

14.11.
S. Tesch, Dresden
Streuung und Fragmentation leichter Kerne im GeV-Gebiet

14.11.
L.H. Andersen, Aarhus
e^--Ion Recombination Measurements in an Electron Cooler; Dielectronic and Radiative Recombination

15.11.
J. Zofka, Prag
Hypernuclei and their Production in Relativistic Heavy-ion Collisions

16.11.
Th. Härder, Kaiserslautern
Grenzen und Erweiterungsmöglichkeiten relationaler Datenbanksysteme
P. Mossak, Darmstadt
Ein Entity-Relationship-Datenbanksystem in der Praxis

21.11.
U. Meyer, Darmstadt
Neues vom Reich der Netze

21.11.
G. Bartosz, Lodz
Spin-label Studies of Radiation Effects on the Erythrocyte Membrane

21.11.
J.-P. Dufour, Bordeaux-Gradignan
New Results on the Study of Isotopes at the Limits of Nuclear Binding

27.11.
M. Soyeur, Saclay
Relativistic Transport Theory of Fluctuating Fields for Heavy-ion Collisions

28.11.
H.-G. Ortlepp, Dresden
Das 4π-Detektorprojekt PHOBOS am VIK Dubna

28.11.
H. Wollnik, Giessen
Direkte Massenmessungen kurzlebiger Nuklide an FRS und ESR - physikalisches Konzept und technische Realisierung

28.11.
I. Tanihata, RIKEN
Exotic Behaviour of Neutron-Rich Nuclei: Studies with Radioactive Beams

29.11.
J. Knoll, Darmstadt
Quantenmechanische Grenzen für die Produktion harter Photonen

30.11.
J.C. Gauthier, Paris
K_α-Absorptionsspektroskopie in Laser-erzeugten Plasmen

30.11.
Th. Weiland, Darmstadt
Elektromagnetisches Design von Beschleunigerkomponenten

05.12.
H. Göringer, P. Malzacher, Darmstadt
MVS/ESA Anwendungen: Die 'Data Window Services'

06.12.
G.J. Kunde, Heidelberg
Emissionstemperaturen und Quellradien in der Reaktion $^{40}Ar + {}^{197}Au$ bei E/A = 200 MeV

07.12.
Braun-Munzinger, Stony Brook
Recent Results of the Experiment E 814 at the AGS in Brookhaven

08.12.
W. Seidel, Dresden
Detektorenentwicklungen in Rossendorf

11.12.
A. Bialas, Cracow
Intermittence and Multiparticle Dynamics

12.12.
P. Malzacher, Darmstadt
MVS/ESA Anwendungen in FORTRAN Programmen

12.12.
G. Roche, Clermont Ferrand
Lepton Pair Production and Proton-Nucleus and Nucleus-Nucleus Collisions between 1 and 5 A GeV

13.12.
W. Mayer, Kassel
Ein Rastertunnelmikroskop zur Untersuchung biologischer Objekte und technischer Oberflächen

19.12.

A. Reuter, Stuttgart
Verteilte Datenbanksysteme - Entwicklungsstand und ihre Bedeutung für die Praxis

19.12.
R. Vogt, Livermore
J/ψ Suppression in Hadron-Nucleus and Nucleus-Nucleus Collisions

19.12.
J. Rafelski, Tucson
Kalte Fusion

8.2.3 GSI-Reports

89 - 1
Scientific Report 1989

89 - 2
F + E Programm 1989

89 - 3
Th. Happ
Spektroskopische Untersuchungen nach quasielastischen Stößen im System $^{208}Pb + {}^{232}Th$ bei einer Einschußenergie von 17 MeV/u

89 - 4
R.W. Müller
The Split Coaxial Linac Structure and its RF Modes

89 - 5
K. Weyrich
Untersuchungen zum Energieverlust von Schwerionen in einem Wasserstoffplasma

89 - 6
R. Menges
Kollineare Laserspektroskopie an radioaktiven neutronenarmen Blei- und Thalliumisotopen

89 - 7
B. Heimrich
Feinfokussierung intensiver Schwerionen zur Erzeugung heißer dichter Materie

89 - 8
R. Bellwied
Korrelation zwischen Transfer und Fusion in Schwerionenkollisionen an der Coulombbarriere

89 - 9
P. Spädtke, S. Wipf
KOBRA 3 - A Code for the Calculation of Space-Charge-Influenced Trajectories in 3-Dimensions

89 - 10
R.W. Hasse, I. Hofmann,. D. Liesen (eds.)
Proc. of the Workshop on Crystalline Ion Beams
(Wertheim, Fed. Rep. of Germany, Oct. 4-7, 1988)

89 - 11
A. Steinhof
Messung natürlicher ^{41}Ca-Konzentrationen

89 - 12
A. Schröter
Optimierung und Ausbau der GSI-Doppelorangen-Apparatur zur Untersuchung von in Schwerionenstößen emittierten $(e^+ e^-)$-Paaren

89 - 13
U.E. Trebus
Production, Transport and Charge Capture Measurements of Highly Charged Recoil Ions

89 - 14
R. Herrmann
Einführung des Spinfreiheitsgrades im Riemannschen Raum kollektiver Modelle

89 - 15
1.4 Decades of 1.4 MeV/u Heavy Ion Beams
(GSI Darmstadt, Fed. Rep. of Germany, June 9, 1989)

89 - 16
W. Schmidt
Die Rolle der Viskosität im hydrodynamischen Modell hochenergetischer Schwerionenreaktionen

89 - 17
G. Plunien
Kernpolarisation in schweren Atomen und superschweren Quasiatomen

89 - 18
U.W. Scherer
Untersuchungen zur Synthese und chemischen Charakterisierung sehr schwerer Elemente

89 - 19
M. Rufa
Kerne, Hyperkerne und Neutronensterne in einem relativistischen Mean-Field Modell

89 - 20
J. Rau
Supersymmetrie

89 - 21
R. Bock, I. Hofmann, J. Meyer-ter-Vehn (Editors)
High Energy Density in Matter Produced by Heavy Ion Beams
(Annual Report 1988)

89 - 22
A.B. Quint
Untersuchungen zur Fusion schwerer symmetrischer Systeme

89 - 23
A.B. Quint
Appendix: Investigations of the Fusion of Heavy Symmetric Systems

89 - 24
J. Jacoby
Untersuchungen zur Erzeugung hoher Energiedichte in Materie mit intensiven Schwerionenstrahlen

89 - 25
K. Geiger
Glueballs und ihre Eigenschaften im Rahmen eines erweiterten Bag Modells

89 - 26
H. Wituschek
Modifikation einer Ionenquelle zur ionenstrahlgestützten Beschichtung von Bauteilen

89 - 27
G. Münzenberg
Wie weit sind wir auf dem Weg zu den superschweren Kernen?

89 - 28
J. Häusler
Eigenschaften von Spiralresonatoren

89 - 29
A. Gerhard
Felddurchschlag in elektrischen Hochfrequenzfeldern (Sparking)

89 - 30
H. Geissel, P. Armbruster, K.-H. Behr, B. Blank, A. Brünle, H.G. Burkard, K.-H. Burkard, H.-G. Clerc, M. Chen, J.P. Dufour, B. Franczak, Y. Fujita, J.J. Gaimard, E. Hanelt, R. Kirchner, O. Klepper, B. Langenbeck, F. Nickel, K. Poppensieker, M.S. Pravikoff, E. Roecki, D. Schardt, K.-H. Schmidt, Th. Schwab, H.J. Schött, B. Sherrill, K. Sümmerer, H. Wollnik, G. Münzenberg
The Projectile Fragment Separator FRS at GSI

89 - 31
Ch. Hofmann
Elektron-Positron-Winkelkorrelation bei der Paarkonversion

8.2.4 GSI-Preprints

89 - 1
G. Soff, P.J. Mohr
Influence of Vacuum Polarization Corrections of Order $\alpha(Z\alpha)$ and $\alpha(Z\alpha)^3$ in Hydrogen-Like Uranium

89 - 2
P.-G. Reinhard
The Relativistic Mean-Field Description of Nuclei and Nuclear Dynamics

89 - 3
R. Albrecht, T.C. Awes, C. Baktash, P. Beckmann, F. Berger, R. Bock, G. Claesson, G. Clewing, L. Dragon, R.L. Ferguson, A. Franz, S. Garpman, R. Glasow, H.A. Gustafsson, H.H. Gutbrod, K.H. Kampert, B.W. Kolb, P. Kristiansson, I.Y. Lee, H. Löhner, I. Lund, F.E. Obenshain, A. Oskarsson, I. Otterlund, T. Peitzmann, S. Persson, F. Plasil, A.M. Poskanzer, M. Purschke, H.G. Ritter, R. Santo, H.R. Schmidt, T. Siemiarczuk, S.P. Sorensen, E. Stenlund, G.R. Young
Transverse Momentum Distributions of Neutral Pions from Central and Peripheral ^{16}O + Au Collisions at 200 A GeV

89 - 4
I. Lund, R. Albrecht, T.C. Awes, C. Baktash, P. Beckmann, F. Berger, R. Bock, G. Claesson, L. Dragon, R.L. Ferguson, A. Franz, S. Garpman, R. Glasow, H.A. Gustafsson, H.H. Gutbrod, K.H. Kampert, B.W. Kolb, P. Kristiansson, I.Y. Lee, H. Löhner, F.E. Obenshain, A. Oskarsson, I. Otterlund, T. Peitzmann, S. Persson, F. Plasil, A.M. Poskanzer, M. Purschke, H.G. Ritter, R. Santo, H.R. Schmidt, T. Siemiarczuk, S.P. Sorensen, E. Stenlund, G.R. Young
Fluctuations in Multi-Particle Production and γ/π^0-Ratios in 200 A GeV ^{16}O + Au Collisions

89 - 5
T. Peitzmann, R. Albrecht, T.C. Awes, C. Baktash, P. Beckmann, F. Berger, R. Bock, G. Claesson, G. Clewing, L. Dragon, A. Eklund, R.L. Ferguson, A. Franz, S. Garpman, R. Glasow, H.A. Gustafsson, H.H. Gutbrod, J. Idh, K.H. Kampert, B.W. Kolb, P. Kristiansson, I.Y. Lee, H. Löhner, I. Lund, F.E. Obenshain, A. Oskarsson, I. Otterlund, S. Persson, F. Plasil, A.M. Poskanzer, M. Purschke, H.G. Ritter, R. Santo, H.R. Schmidt, T. Siemiarczuk, S.P. Sorensen, E. Stenlund, G.R. Young
Correlations of Neutral Pions in Ultra-Relativistic Heavy Ion Collisions

89 - 6
I. Hofmann
RF Linac and Storage Ring-Perspectives of Heavy Ion Fusion Studies at GSI

89 - 7
P.A. Henning
On the Treatment of Initial Correlations in Quantum Field Theory of Non-Equilibrium States

89 - 8
J.M. Schmidt, G. Soff, P.J. Mohr
Higher-Order Vacuum Polarization Corrections in Muonic Atoms

89 - 9
M. Durand, J. Knoll
Quenching Effects in Photon Production

89 - 10
Th. de Reus, U. Müller-Nehler, G. Soff, J. Reinhardt, St. Graf, B. Müller, W. Greiner
Coupled-Channel Results for Atomic Excitations in Intermediate-Energy Heavy-Ion Collisions

89 - 11
K. Rykaczewski, K.-L. Gippert, N. Kaffrell, R. Kirchner, O. Klepper, V.T. Koslowsky, W. Kurcewicz, W. Nazarewicz, E. Roeckel, E. Runte, D. Schardt, W.-D. Schmidt-Ott, P. Tidemand-Petersson
Investigation of Neutron-rich Rare-earth Nuclei Including the New Isotopes ^{177}Tm and ^{184}Lu

89 - 12
R. Bock, K.G.R. Doss, H.H. Gutbrod, I. Lund, H.G. Ritter, T. Siemiarczuk, W. Wislicki
Source Parameters Deduced from Bose-Einstein Correlations of Two and Three Soft Pions in Symmetric Heavy-Ion Interactions at 650 A MeV

89 - 13
H.W. Barz, B.L. Friman, J. Knoll, H. Schulz
Nuclear Matter - Quark Matter Phase Diagram with Strangeness

89 - 14
P. Schuck, G. Chanfray, W. Nörenberg
Is the σ Field in the σ - ω Model Related to a Pion Pair Coherent State?

89 - 15
R. Kulessa, R. Bengtsson, H. Bohn, H. Emling, T. Faestermann F. von Feilitsch, E. Grosse, W. Nazarewicz, D. Schwalm, H.J. Wollersheim
Angular Momentum Dependence of the Quadrupole Deformation in ^{182,184,186}W

89 - 16
B.S. Ishkhanov, I.M. Kapitonov, P. Rozmej, K.V. Shitikova
Configurational Splitting of Dipole Giant Resonance of Nuclei with Mass Number 23-26

89 - 17
G. Mehler, G. Soff, K. Rumrich, W. Greiner
K-Shell Ionization in Relativistic Ion-Atom Collisions

89 - 18
W. Kraft-Weyrather, G. Kraft, S. Ritter, M. Scholz, J.A. Stanton
The Preparation of Biological Targets for Heavy-Ion Experiments up to 20 MeV/u

89 - 19
S. Schmidt, J. Euler, C. Kelbsch, S. Kelbsch, R. Koch, G. Kraft, R.E. Olson, U. Ramm, J. Ullrich, H. Schmidt-Böcking
Double Differential Stopping Powers of 1.4 MeV/u U^{33+} in Ne and Ar Derived from Electron Production and Multiple Ionization Cross Sections

89 - 20
K.V. Shitikova, P. Rozmej
Method of the Hyperspherical Functions and its Application to Heavy Ion and Quark Physics

89 - 21
H. Tsertos, C. Kozhukarov, P. Armbruster, P. Kienle, B. Krusche, K. Schreckenbach
High-Sensitivity Measurements of the Excitation Function for Bhabha Scattering at MeV Energies

89 - 22
S. Cwiok, A. Sobiczweski
Potential Energy and Fission Barriers of Superheavy Nuclei Calculated in Multidimensional Deformation Space

89 - 23
B. Kämpfer, M.I. Gorenstein, O.P. Pavlenko
Correlations between Dilepton Yields and Pion Multiplicities as Probe of the Deconfinement Transition

89 - 24
J. Okolowicz, M. Ploszajczak, S. Drozdz, E. Caurier
The Monopole and Quadrupole Vibration of a Hot Nucleus

89 - 25
B. Milek, W. Nörenberg, P. Rozmej
Quantum Chaos in the Two-Center Shell Model

89 - 26
K.A. Bugaev, M.I. Gorenstein, B. Kämpfer, V.I. Zhdanov
Generalized Shock Adiabatics and Relativistic Nuclear Collisions

89 - 27
M. Schönhofen, H. Feldmeier, M. Cubero
The Relativistic Vlasov Equation with non-Radiating Meson Field-Results

89- -28
E. Caurier, S. Drozdz, J. Okolowicz, M. Ploszajczak
The Time-Dependent Variational Description of Nuclear Transition Probabilities

89 - 29
WA80 Collaboration
Fluctuations and Intermittency in 200 A GeV ^{16}O + (C, Au) Reactions

89 - 30
J. Okolowicz, M. Ploszajczak, S. Drozdz, E. Caurier
Giant Dipole Resonances in Hot Nuclear Matter in the Model of Self-Relaxing Mean-Field

89 - 31
P. Kienle
Status of the SIS/ESR-Project at GSI

89 - 32
I. Hofmann
Filamentation of Phase Space and Coherent Noise for Beams Injected into Storage Rings

89 - 33
H. Tsertos
Search for Resonant Bhabha Scattering At MeV Energies

89 - 34
W. Henning
The Research Program at SIS/ESR

89 - 35
P. Bozek, M. Ploszajczak
Dispersion Relation for Hot Gluonic Matter from the BBGKY Hierarchy

89 - 36
H.H. Gutbrod, A.M. Poskanzer, H.G. Ritter
Plastic Ball Experiments

89 - 37
J.V. Kratz, H.P. Zimmermann, U.W. Scherer, M. Schädel, W. Brüchle, K.E. Gregorich, C.M. Gannett, H.L. Hall, R.A. Henderson, D.M. Lee, J.D. Leyba, M.J. Nurmia, D.C. Hofman, H. Gäggeler, D. Jost, U. Baltensperger, N.-Q. Ya, A. Türler, Ch. Lienert
Chemical Properties of Element 105 in Aqueous Solutions: Halide Complex and Anion Exchange into Triisoctyl Amine

89 - 38
M. Schädel, W. Brüchle, E. Jäger, E. Schimpf, J.V. Kratz, U.W. Scherer, H.P. Zimmermann
ARCA II - A New Apparatus for Fast, Repetitive HPLC Separations

89 - 39
R.W. Hasse, H.A. Borgwardt, E. Aker
Benchmarking on Supercomputers with a Highly Vectorized ADI Code

89 - 40
G. Herrmann
Discovery and Confirmation of Fission

89 - 41
R. Bock
Status and Perspectives of Heavy Ion Inertial Fusion

89 - 42
A. Steinhof, K.H. Behr, A. Brünle, E. Roeckl, E. Boaretto, M. Paul, D. Fink, G. Hollos, W. Kutschera
Electromagnetic Isotope Enrichment for Accelerator Mass Spectrometry of ^{41}Ca

89 - 43
G. Soff, J. Rafelski
Radiative Muon Capture in Light Atoms

89 - 44
D.H. Rischke, B.L. Friman, B.M. Waldhauser, H. Stöcker, W. Greiner
Shock Discontinuities around the Confinement-Deconfinement Transition in Baryon-Rich Dense Matter

89 - 45
R. Schmidt, B. Kämpfer, H. Feldmeier, O. Knospe
Relativistic Effects in Molecular Dynamics Simulations of Heavy-Ion Collisions

89 - 46
A. Schäfer, G. Soff, P. Indelicato, B. Müller, W. Greiner
Atomic Parity Violation in U^{90+}

89 - 47
G. Münzenberg
Heavy Element Production and Limits to Fusion

89 - 48
J. Szerypo, R. Barden, L. Kalinowski, R. Kirchner, O. Klepper, A. Plochocki, E. Roeckl, K. Rykaczewski, D. Schardt, J. Zylicz
Low-Lying Levels in :medium^{114}In and a Problem of Spin-Mixing in Hyperfine Fields

89 - 49
H. Bokemeyer, P. Salabura, D. Schwalm, K.E. Stiebing (EPOS Collaboration)
Correlated Electron-Positron Emission in Heavy-Ion Collisions

89 - 50
M. Schönhofen, M. Cubero, M. Gering, M. Sambataro, H. Feldmeier, W. Nörenberg
The Nuclear Equation of State in Effective Relativistic Field Theories and Pion Yields in Heavy-Ion Collisions

89 - 51
D. Berdichevsky, A. Lukasiak, W. Nörenberg, P. Rozmej
Diabatic Hindrance of Heavy-Ion Fusion

89 - 52
V.D. Toneev, A.S. Amelin, K.K. Gudima
The Independent Quark-Gluon String Model for Heavy-Ion Collisions at Ultrarelativistic Energies

89 - 53
H.W. Barz, B.L. Friman, J. Knoll, H. Schulz
Strangeness Production in Ultra-relativistic Heavy-Ion Collisions

89 - 54
B. Blank, J.-J. Gaimard, H. Geissel, G. Münzenberg K.-H. Schmidt, H. Stelzer, K. Sümmerer, H.-C. Clerc, E. Hanelt, B. Voss, D. Bazin, R. del Moral, J.-P. Dufour, A. Fleury, M.S. Pravikoff
First Application of the Momentum-Loss Achromat to the Isotopic Separation of Relativistic Projectile Fragments

89 - 55
G. Soff, J. Rau, M. Grabiak, B. Müller, W. Greiner
Production of Supersymmetric Particles and Higgs Bosons in ultra-relativistic Heavy-Ion Collisions

89 - 56
E. Lubkiewicz, H. Emling, H. Grein, R. Kulessa, R.S. Simon, H.J. Wollersheim, Ch. Ender, J. Gerl, D. Habs, D. Schwalm
Measurement of g-Factors in ^{160}Yb by a Gamma-Gamma Coincidence Technique

89 - 57
M. Oberbeck, Al. Breskin, M. Brügger, R. Chechik, Z. Fraenkel, G. Herrmann, K. Lützelkirchen, S. Polikanov, N. Trautmann, Th. Wilpert
A Heavy-Ion Identification System for the Detection of rare Events

89 - 58
A. Warczak, Y. Stachura, A. Szymanski, Th. Stöhlker, C. Kozhuharov, A.E. Livingston, P.H. Mokler, S. Reusch
Evidence for Resonant Two Electron Capture and Excitation in Collisions of H-like Ge with Ne

89 - 59
R. Albrecht, T.C. Awes, C. Baktash, P. Beckmann, F. Berger, R. Bock, G. Claesson, G. Clewing, L. Dragon, A. Eklund, R.L. Ferguson, A. Franz, S. Garpman, R. Glasow, H.A. Gustafsson, H.H. Gutbrod, J. Idh, K.H. Kampert, B.W. Kolb, P. Kristiansson, I.Y. Lee, H. Löhner, I. Lund, F.E. Obenshain, A. Oskarsson, I. Otterlund, T. Peitzmann, S. Persson, F. Plasil, A.M. Poskanzer, M. Purschke, H.G. Ritter, R. Santo, H.R. Schmidt, T. Siemiarczuk, S.P. Sorensen, E. Stenlund, G.R. Young
Transverse Energy Production in the Target Fragmentation Region in ^{16}O-Nucleus Reactions at 60 and 200 A GeV

89 - 60
K. Depta, W. Greiner, J.A. Maruhn, H.J. Wang, A. Sandulescu, R. Herrmann
On the Necking-In Process in Cluster Decays

89 - 61
S. Cocher, I. Hofmann
On the Stability and Diagnostics of Heavy Ions in Storage Rings with High Phase Density

89 - 62
S. Drozdz, P.Kaminski, M. Ploszajczak, E. Caurier
On a Validity of Adiabatic Approach to the Tunneling Phenomena

89 - 63
W. Henning
Physics at SIS/ESR

89 - 64
P. Oblozinsky
Absence of Parity Effects in Preequilibrium γ Emission

89 - 65
P. Armbruster
Transactinide Elements

89 - 66
J. Pochodzalla, W. Trautmann, U. Lynen
Sensitivities of the Relative Velocity Between Fragments on the Decay Mechanism

89 - 67
M. Herrmann, J. Knoll
Space-Time Effect in the Decay of Strings by Pair-Creation

89 - 68
J. Pochodzalla, R.J. Charity, U. Lynen, H. Sann, W. Trautmann, R. Trockel
Possibility of Transient Effects during the Emission of Intermediate Mass Fragments

89 - 69
S. Ritter, W. Kraft-Weyrather, M. Scholz, G. Kraft
Influence of Radiation Quality on Heavy Ion Induced Chromosome Aberrations in V79 Cells

89 - 70
F. Kraske, S. Ritter, M. Scholz, M. Schneider, G. Kraft U. Weisbrod, E. Kankeleit
Directed Irradiation of Mammalian Cells by Single Charged Particles with a Given Impact Parameter

89 - 71
J. Stanton, G. Taucher-Scholz, M. Schneider, G. Kraft
Comparison between Indirect and Direct Effects for High and Low LET Radiations in SV40 DNA Strand Break Induction

89 - 72
M. Schädel
Radiochemical Studies of the Transactinide Elements

89 - 73
P. Kienle
Physics with Stored and Cooled Heavy Ion Beams

89 - 74
P. Bozek, M. Ploszajczak
Transport Equations and Features of the Long Wavelength Oscillation of the Quark-gluon Plasma

89 - 75
S.Y. Luo, I. Hofmann
Dynamics of a One-dimensional Coulomb Chain in a Storage Ring

89 - 76
J. Rau, B. Müller, W. Greiner, G. Soff
Production of Supersymmetric Particles in Ultrarelativistic Heavy-Ion Collisions

89 - 77
K. Geiger, B. Müller, W. Greiner
(η - η' - ι)-Mixing, Decay and Production Mechanisms

89 - 78
K.-H. Schmidt, B. Blank, J.-J. Gaimard, H. Geissel, G. Münzenberg, H. Stelzer, K. Sümmerer, H.-G. Clerc, E. Hanelt, M. Steiner, B. Voss, D. Bazin, R. del Moral, J.-P. Dufour, A. Fleury, F. Hubert, M.S. Pravikoff
Experiments for the Isotope Separation of Secondary Beams with the Momentum-Loss Achromat

89 - 79
Th. Schwab, H. Geissel, P. Armbruster, A. Gillibert, W. Mittig, R.E. Olson, K.B. Winterbon, H. Wollnik, G. Münzenberg
Energy and Angular Distributions for the Ar Ions Penetrating Solids

89 - 80
G. Münzenberg, H. Geissel, P. Armbruster, K.-H. Behr, B. Blank, K.H. Burkard, H.-G. Clerc, M. Chen, J.P. Dufour, B. Franczak, J.-J. Gaimard, E. Hanelt, R. Kirchner, O. Klepper, B. Langenbeck, F. Nickel, K. Poppensieker, M.S. Pravikoff, E. Roeckl, D. Schardt, K.-H. Schmidt, H.-J. Schött, Th. Schwab, B. Sherrill, K. Sümmerer, H. Wollnik
The GSI Projectile-Fragment Separator - Status and Planned Experiments

89 - 81
G. Herrmann
Vor fünf Jahrzehnten: Von den 'Transuranen' zur Kernenergie

89 - 82
B.E. Fischer, C. Mühlbauer
Micro-Tomography by Heavy Ions

89 - 83
S. Hofmann
Experiments for Production of Heavy Elements at Darmstadt

89 - 84
E. Caurier, S. Drozdz, J. Okolowicz, M. Ploszajczak
Geometrical Versus Semiclassical Quantization

89 - 85
U.W. Scherer, W. Brüchle, M. Brügger, C. Frink, H. Gäggeler, G. Herrmann, J.V. Kratz, K.J. Moody, M. Schädel, K. Sümmerer, N. Trautmann, G. Wirth
Reactions of ^{40}Ar with ^{233}U, ^{235}U, and ^{238}U at the Barrier

89 - 86
H. Feldmeier
Fermionic Molecular Dynamics

8.2.5 Visiting Groups at GSI 1989

17.01.	Justus Liebig Schule, Darmstadt	19
18.01.	Heinrich-Kleier-Schule, Frankfurt	28
18.01.	Studenten der Univ. Gießen	35
19.01.	Goethe Gymnasium, Neu Isenburg	13
23.01.	Starkenburg Gymnasium, Heppenheim	16
25.01.	Ziehen-Schule, Frankfurt	40
26.01.	Bert-Brecht-Schule, Darmstadt	15
30.01.	Telekommunikations Techniker	20
31.01.	Hilda Gymnasium, Koblenz	53
08.02.	Eichwald Gymnasium, Schwalbach	29
08.02.	Studenten Univ. Mainz	20
13.02.	Studenten Univ. Gießen	42
17.02.	Studenten Univ. Heidelberg	25
20.02.	Gymnasium Coburg	30
22.02.	Studenten Univ. Frankfurt	11
24.02.	Merck Schule, Darmstadt	27
27.02.	Gymnasium Höhr-Grenzhausen	25
28.05.	Studenten Univ. München	60
02.03.	Landrat-Gruber-Schule, Dieburg	29
02.03.	Wanderverein Gernsheim	45
07.03.	Arbeitskreis Schule-Wirtschaft	18
09.03.	Technologie Transfer Treffen, AGF	30
11.03.	Familienkreis Weiterstadt	19
14.03.	Odenwaldclub Niederramstadt	32
15.03.	Gymnasium Deggendorf	20
15.03.	Netzbetriebspersonal der EVU	38
21.03.	Verein für Förderung von Math. und Naturwiss.	48
22.03.	Verein für Förderung von Math. und Naturwiss.	35
29.03.	FH der Deutschen Bundespost	25
03.04.	Fernmeldetechnisches Zentralamt, Darmstadt	13
04.04.	Kommunalpolitische Jugendwoche, Darmstadt	20
04.04.	Gymnasium Rheinstetten	16
05.04.	Gymnasium Lahnstein	28
07.04.	Gymnasium Karlsruhe	32
11.04.	Öffentlichkeitsarbeiter der EVU	18
12.04.	Gymnasium Heusenstamm	17
13.04.	Justus-Liebig-Schule, Darmstadt	14
13.04.	Victoria Schule, Darmstadt	15
14.04.	Lise-Meitner-Gymnasium, Böblingen	28
17.04.	Gymnasium Groß Gerau	26
18.04.	Englisches Gymnasium, Heidelberg	10
19.04.	Gymnasium Babenhausen	18
20.04.	Gymnasium Johaneum, Herborn	33
21.04.	Eleonoren Gymnasium, Darmstadt	20
21.04.	Gymnasium Seligenstadt	15
21.04.	Fa. Zentfrenger	8
24.04.	Schuldorf Bergstraße	16
25.04.	FH Wiesbaden	30
25.04.	Gymnasium Frankenberg	25
26.04.	Gymnasium Bad Homburg	18
26.04.	Gymnasium Frankfurt	18
27.04.	Gymnasium Taunsstein	38
27.04.	Gymnasium Königstein	12
28.04.	Studentengruppe "Mensa"	15
02.05.	Gymnasium Gernsheim	32
10.05.	American High School, Frankfurt	50
11.05.	Gymnasium Neustadt	21
11.05.	Studenten Mainz	12
12.05.	Workshop Strahlentherapie	100
17.05.	Schiller Schule, Frankfurt	9
18.05.	Handwerkskammer Rhein Main	20
23.05.	Gymnasium Gladenbach	12
24.05.	Studenten Wiesbaden	18
31.05.	Laborleiter der Fa. Merck, Darmstadt	8
01.06.	Gymnasium Neckargmünd	25
06.06.	VHS Darmstadt	11
14.06.	Herder Schule, Gießen	14
16.06.	Architekten und Ingenieurverein, Darmstadt	20
21.06.	Studenten, Univ. Frankfurt	15
22.06.	GSI-Mitarbeiter	100
27.06.	Viktoria Schule, Darmstadt	23
28.06.	Friedrich-List-Schule, Ulm	30
28.06.	Studenten Univ. Frankfurt	20
03.07.	Berufliche Schule, Bensheim	15
03.07.	Gymnasium Marburg	23
04.07.	A. Delp Schule, Dieburg	20
04.07.	Kinder von GSI-Mitarbeitern	12
05.07.	Univ. Konstanz	38
06.07.	Univ. Tübingen	50
10.07.	Darmstäder Schulen	25
10.07.	Edith Stein Schule, Darmstadt	19
13.07.	Bad-Zwischenahn Gymnasium	20
14.07.	FTZ Darmstadt	17
20.07.	Studenten Darmstadt	30
26.07.	Soldaten des Arbeitskreises 'Gott und Welt'	29
27.07.	Energieconsulting Heidelberg	18
21.08.	Freiwillige Feuerwehr Wixhausen	5
23.08.	Studentenprogramm	35
29.08.	Merck Darmstadt	8
06.09.	Biophysics Workshop	12
15.09.	Gymnasium in Dänemark	50
20.09.	Gymnasium Marburg	64
21.09.	Friedensgemeinde Darmstadt	16
22.09.	FFW Wixhausen	18
25.09.	Verein Teli	24
27.09.	Zahnärztliche Gesellschaft Hessen	45
28.09.	Int. School Frankfurt	35
02.10.	Studenten	11
04.10.	Sportgemeinschaft Arheilgen	28
05.10.	Arbeitsamt Darmstadt	9
12.10.	VHS Darmstadt	11
14.10.	Wetterauische Gesellschaft für Naturforschung	20
18.10.	Rechenzentrum	13
19.10.	Workshop Laserspektroskopie	30
25.10.	Delegation aus der UdSSR	12
25.10.	Wandergruppe TSG Arheilgen	42
07.11.	Albert Einstein Schule, Groß Bieberau	19
07.11.	Gesamtschule Groß Biberau	18
10.11.	Gymnasium Niederolm	8
13.11.	Berufsschule Bensheim	45
14.11.	Techniker Schule, Weilburg	25
16.11.	Phys. Committee of the Swedish Res. Council	11
16.11.	EDV-Mitarbeiter Bundesbahn Frankfurt	21
17.11.	Chemiker TH Darmstadt	20
21.11.	Stipendiaten der K. Adenauer Stiftung	10
24.11.	Chemiker Hoechst	9
06.12.	Heidemannschule, Rüsselsheim	14
07.12.	Studenten aus Darmstadt	13
08.12.	Math.-Tech. Assistenten	12
12.12.	Rudi-Stephan-Gymnasium, Worms	24
14.12.	FH Wiesbaden	10
15.12.	Kernsteiner Schule, Bad Homburg	20
19.12.	FH Wiesbaden	12
19.12.	Informatik Kreis	60
20.12.	Heinrich-Lanz-Schule, Mannheim	23
20.12.	Deutsche und französische Studenten	23
21.12.	Eleonorenschule, Darmstadt	22
21.12.	Werner von Siemens Schule, Frankfurt	40
	40 small groups	240
	Visitors	3390

8.3 SCIENTIFIC COMMITTEES, DIRECTORATE AND PERSONNEL

Scientific Directorate

P. Kienle (Chairman, Scientific Director), R. Bock (Vice-Director), H.O. Schuff (Administrative Director), D. Böhne, W. Henning

Scientific Council (external)

D. Schwalm (Heidelberg, Chairman), V. Metag (Giessen, Vice-Chairman), P.G. Hansen (Aarhus, Denmark), H. Hartnagel (Darmstadt), H. Hoffmann (Geneva, Switzerland), J. Hüfner (Heidelberg), P. Paul (Stony Brook, USA), H. Schindler (Erlangen), B. Wiik (Hamburg), S. Witkowski (Garching), G. Zimmer (Duisburg), C. Zupancic (Garching)

Users Committee (until June 1989)

S. Skorka (Garching, Chairman), P. Kleinheinz (Jülich, Vice-Chairman), P. Armbruster (GSI), W. Cassing (Gießen), B. Fricke (Kassel), H. Gäggeler (Würenlingen, Switzerland), B. Haas (Strasbourg, France), W. Henning (GSI), K. Hildenbrand (GSI), D. Hilscher (Berlin), P. Mokler (GSI), K.H. Speidel (Garching)

Scientific and Technical Division Leaders

N. Angert (UNILAC Accelerator), P. Armbruster (Atomic Physics and Nuclear Chemistry II), R. Bock (Nuclear Physics I), D. Böhne (New Projects and Technical Operation), W. Henning (Nuclear Physics II), G. Herrmann (Nuclear Chemistry I), U. Lynen (Nuclear Physics III), W. Nörenberg (Theory Group)

Scientific Committee (internal)

H.-D. Liesen (Chairman), H. Ahrens (Vice-Chairman), Armbruster (until Oct. 1989), N. Angert, K. Blasche, H. Emling, H. Essel, S. Glückert, G. Herrmann, P. Kienle, G. Kraft, U. Lynen, G. Münzenberg (since Oct. 1989), W. Nörenberg, M. Richter, C. Riedel, W. Rösch, W. Trautmann, D. Wilms

Experiment Board (since July 1989)

H.-J. Körner (Garching, Chairman), J. Kluge (Mainz, Vice-Chairman), P. Armbruster (GSI), P. Braun-Munzinger (Stony Brook), D. Harder (Göttingen), W. Henning (GSI), Ch. Ngô (Gif-sur-Yvette), J. Meyer-ter-Vehn (Garching), J. Remillieux (Villeurbanne), R. Schuch (Stockholm), J. Specht (Heidelberg), H. Stöcker (Frankfurt)

Guest Scientists and Consultants

F. Azgui (Algeria), T. Bartsch (Poland), G. Chanfray (France), R.-J. Charity (Australia), M. Chen (P.R. of China), J.-R. Dang (P.R. of China), J. Diaz-Alonso (Spain), J.-M. Eisenberg (USA), Z. Fodor (Hungary), R. Freifelder (USA), B.L. Friman (Finland), K. Geiger (Fed. Rep. of Germany), A. Gerhard (Fed. Rep. of Germany), M. Gering (South Africa), M. Godlewski (Poland), C. Guerra (Mexico), O. Gustafsson (Sweden), J. Häuser (Fed. Rep. of Germany), S. Hlavac (Poland), H. Iiponen (Finland), T. Ishikawa (Japan), E. Jennewein (Fed. Rep. of Germany), B. Kämpfer (Fed. Rep. of Germany), V. Karnaukhov (USSR), A. Kondeja (Poland), A. Kugler (CSSR), R. Kulessa (Poland), W. Kurcewicz (Poland), M. Leino (Finland), G.-S. Li (P.R. of China), W.-S. Li (P.R. of China), Z. Li (P.R. of China), Z.-A. Liu (P.R. of China), A.E. Livingston (USA), E. Lubkiewicz (Poland), I. Lund (Sweden), S. Luo (P.R. of China), T. Matulewicz (Poland), R.-J. Meijer (The Netherlands), B. Milek (German Democratic Republik), D. Miskowiec (Poland), P. Oblozinsky (CSSR), G. Paic (Yugoslavia), J. Park (USA),

Z. Patyk (Poland), M. Paul (Israel), K. Pena (Poland), M. Pfützner (Poland), H. Pilkuhn (Fed. Rep. of Germany), M. Ploszajczak (Poland), Y. Qian (P.R. of China), H. Poth (Fed. Rep. of Germany), W. Prokopowicz (Poland), Y. Qian (P.R. of China), E. Remler (USA), R. Rittenhouse (USA), P. Rozmej (Poland), K. Rykaczewski (Poland), P. Salabura (Poland), M. Samek (Poland), C. Sastri (India), R. Schmidt (German Democr. Rep.), D. Shao (P.R. of China), K. Shitikova (USSR), R. Shyam (India), J. Skalski (Poland), A. Sobiczewski (Poland), G. Soff (Fed. Rep. of Germany), J.-A.-L. Stanton (Australia), Y.-M. Sun (P.R. of China), J. Szerypo (Poland), M.-H. Tanaka (Japan), K. Teh (Malaysia), V. Toneev (Poland), H. Tsertos (Greece), A. Tucholski (Poland), A. Vass (Hungary), W. Walus (Poland), Y.-D. Wang (P.R. of China), Y.-H. Wang (P.R. of China), G.-M. Welke (Fed. Rep. of Germany), G.-H. Wu (P.R. of China), M. Xie (P.R. of China), G.-J. Xu (P.R. of China), W.-P. Xu (P.R. of China), W.-F. Yang (P.R. of China), J. Zawadzki (Poland), W. Zhao (P.R. of China), D.-Q. Zhou (P.R. of China), X.-Z. Zhu (P.R. of China), Y.-Z. Zhuo (P.R. of China)

Scientific Personnel

W. Ahner, H. Ahrens, R. Albrecht, N. Angert, P. Armbruster, R. Barden, K. Beckert, E. Berdermann, H. Beyer, B.-A. Blank, K. Blasche, R. Bock, H. Bokemeyer, F. Bosch, R. Brockmann, W. Brüchle, S. Buchhaupt, P. Buck, M. Cubero, L. Dahl, K.-G. Dietrich, O. Echt, P. Egelhof, H. Eickhoff, H. Emling, M. Emmerling, H.-G. Essel, H. Feldmeier, J.-G. Festag, M. Feyerabend, K.-D. Finlayson, B. Fischer, B. Fleischmann, H.-A. Folger, B. Franczak, B. Franzke, M. Fuchs, H. Geissel, J. Glatz, S. Glückert, A. Gobbi, H. Göringer, S. Gralla, E. Grosse, A. Gruber, U. Grundinger, H. Grunenberg, H.-H. Gutbrod, Th. Haberer, D. Hartwig, E.-M. Heck, P. Henning, W. Henning, G. Herrmann, M. Herrmann, N. Herrmann, R. Herrmann, F.-P. Hessberger, K. Hildenbrand, D. Hoffmann, I. Hofmann, S. Hofmann, J. Hubele, J. Jacoby, W. Jacoby, K. Kaspar, H.-J. Keller, H. Keller, A. v. Kienlin, R. Kirchner, J. Klabunde, O. Klepper, J. Knoll, P. Koczon, I. Koenig, W. Koenig, B. Kolb, C. Kozhuharov, M. Krämer, W. Kraft-Weyrather, G. Kraft, F. Kraske, U. Krause, T. Kühl, R. Künkel, B. Langenbeck, H.-D. Liesen, V. Lindenstruth, K. Lützenkirchen, U. Lynen,

P. Malzacher, R. Mann, D. Marx, R.-S. Mayer, U. Meyer, T. Milkau, P.-H. Mokler, G. Moritz, M. Müller, R.W. Müller, W. Müller, G. Münzenberg, R. Neumann, F. Nickel, V. Ninov, W. Nörenberg, F. Nolden, Th. Odenweller, H. Orth, U. Orth, A. Peters, J. Pfennig, G. Plunien, S. Polikanov, K. Poppensieker, H.-U. Post, H.-B. Prange, A.B. Quint, U. Ratzinger, W. Reisdorf, S. Reusch, M. Richter, C. Riedel, S. Ritter, E. Roeckl, D.-M. Rück, M. Rufa, A. Sandoval, H.-J. Sann, T. Sann, V. Schaa, U. Schaaf, M. Schädel, D. Schall, D. Schardt, R. Schicker, H.R. Schmidt, K.H. Schmidt, R. Schmidt, W. Schmidt, M. Schneider, M. Schönhofen, M. Scholz, D. Schüll, H. Schulte, P. Senger, O. Siart, G. Siegert, R. Simon, H. Sohlbach, R. Spohr, W. Spreng, R. Steiner, A. Steinhof, H. Stelzer, T. Stöhlker, P. Strehl, H. Ströbele, H. Ströher, J. Struckmeier, K. Sümmerer, G. Taucher-Scholz, K. Tinschert, Ch. Trautmann, W. Trautmann, U. Trebus, C. Treffert, J. Ullrich, F.-J. Urban, J. Vetter, M. Weber, A. Weiss, J.-P. Wessels, K. Weyrich, K. Winkelmann, G. Wirth, B. Wolf, H.-J. Wollersheim,

Technical and Administrative Staff

F. Achenbach, K. Adelberger, J. Ahrens, G. Aker, J. Alt, W. Amann, R. Appel, G. Augustinski, E. Babinsky, E. Babinsky, M. Balloff, K.-H. Behr, E. Benz, H.-J. Benz, L. Bernhardt, H. Bingel, U. Blell, W. Bleuel, H. Blinn, F. Blumert, F. Bock, W. Bock, W. Bock, D. Böhne, E. Bohlaender, P. Borisch, I. Bormet, R. Bormet, J. Bossler, W. Bourgeois, K. Bräuer, H. Brandis, G. Breitenberger, W. Brenger, H. Britz, A. Brünle, N. Brunner, C. Bruske, D. Büttner, K.-H. Burkard, H.-G. Burkhard, A. Busch, J-P. Clain, H. Dächert, H. Damm, H.-W. Daues, J.-R. Dengler, G. Dick, I.-M. Diedrich, R. Diehl, R. Döring, R. Dünkel, H. Dunker, O. Eberhardt, H. Eckhardt, H. Egger, M.-F. Eick, G. Eidmann, G. Eisold, E. Eitel, H. Emig, W. Enders, J. Engel, S. Engel, G. Englert, F. Ertan, H. Fischer, M. Fradj, P.-W. Frank, G.-R. Freiwald, P. Freudenberger, E. Fritsch, R. Fritsche, G. Fröhlich, B. Froitzheim, H.-F. Fuchs, R. Gärtner, H. Gaiser, K.-D. Ganser, A. Gasper, M. Gassner, H. Gebhardt, B. Geck, E. Gerbig, O. Gerhardt, I. Giese, H. Gilbert, W. Gockel, R. Goetz, V.-G. Gomez, H. Graf, H. Graf, K. Graf, H. Grein, D. Grimm, G. Grimm, H. Grösch, J. Grösser, H. Gross, J. Gross, T. Günel, J.L. Gundlach, B. Gutermuth, W. Gutowski, T. Gyoerffy, E. Häcker, D. Hager, W. Hahn, J.-Ch. Hahne, P. Hahne, P. Hahnel, W. Hambruch, H. Hammal, E. Hammann, H. Hardel, M. Hartung, O.-P. Hartmann, R. Hartmann, W. Hartmann, W. Hartmann, R.W. Hasse, L. Hechler, T. Heinbüchner, H. Heller, H. Helms, M. Hener, D. Henke, H. Hewig, J. Hey, K. Hill, F. Himmelmann, C. Hoffmann, J. Hoffmann, R.-H. Hoffmann, N. Hofmann, R. Holzmann, L. Horas, H. Horneff, A.-L. Hotop, R. Hotz, W. v.d.Hoya, W. Huber, W. Hüller, G. Hutter, G. Ickert, W. Ille, K. Illert, E. Jäger, V. Jäger, H. Jakobi, S. Jansen, G.-K. Jöst, R. Johaenntges, R. Jung, P. Kainberger, G. Kaiser, R. Kaiser, E. Kammer, R. Kammer, W. Kappel, W. Kaufmann, E. Kehr, F. Keil, M.-M. Khaouli H.-R. Kiesewetter, N. Kischnick, A. Kissler, G. Klappich, B. Klar, H. Klecker, L. Kleim, H. Klemm, J. Klemm, S. Klemm, A. Klöckner, F. Klos, J. Klosa, K.-D. Knapp, K. Knies, W. Köthe, K. Kohl, K. Kohl, P. Kohn, U. Kopf, W. Krall, H. Kraus, I. Kraus, St. Kredel, K-R. Kress, W. Kreuzer, H. Krichbaum, J. Krieg, A. Kritzer, R. Krug, G. Kube, K. Kucharczyk, H. Kühn, J. Kühtz, K.-K.-B. Küper, G. Kunz, W. Kunz, H.-P. Kurz, E. Labinsky, H. Lameli, G. Langer, H. Larem, G. Ledl, B. Lehn, K.-D. Leible, S. Leichtweiss, E. Leiser, G. Leidel, H. Leiser, W. Leiser,

F. Lembke, G. Lenz, H. Leonhardt, G. Lerch, H.-P. Liebold, L. Liebschwager, N. Lohneis, A. Loos, D. Loos, A. Lorenz, W. Losert, M. Ludwig, G. Lücker, J. Lühning, S. Lüttges, H. Mader, K.-H. Mader, E. Magnussen, E. Malwitz, I. Malwitz, H.-G. Manns, M. Marquardt, H.-G. Martens, U.-N. Marx, W. Marx, K.-H. Matthöfer, R. Mayr, H. Meder, B. Melchior, K. Metz, W. Meufels, E. Mitz, A. Möller, K. Möller, K. Mömerzheim, R. Montay-Bettermann, A. Morhardt, P. Moritz, C.H. Mühle, A. Müller, B. Müller, B. Müller, W. Müller, A. Muhn, H. Neff, K.-H. Neff, W. Neuhäuser, A. Nicklas, A. Niebur, W. Niebur, D. Nitsch, G. Noä W. Obermeier, G. Otto, G. Pabst, J. Palm, W. Panschow, F. Peldzinski, H. Penninger, K. Petrich, E.-L. Pfaff, I. Pfaff, K.-L. Pfaff, E. Pfeng, P. Pfizenmaier, A.-S. Pflanz, A. Pitzen, H. Pons, I. Poppert, A. Przybyla, W. Quick, D. Quis, S. Raiss, H. Ramakers, A. Rass, E. Rass, H. Reeg, W. Rehm, S. Remeli, H. Riesner, D. Rochna, Ch. Röder, D. Röder, H. Röder, H. Rödl, E. Röhricht, W. Rösch, K.-D. Roessler, M. Romig, K. Rost, G.-A. Rudolph, R. Rulfs, K. Salzer, W. Salzer, J.-W. Sauer, H.-W. Schäfer, F. Schäffer, J. Schäffer, B. Schausten, H. Schiemann, E. Schimpf, H.-J. Schlitt, A. Schlossarek, I. Schmadel, D. Schmalz, G. Schmelig, H.-G. Schmidt, W. Schmidt, L. Schmiedler, R. Schmitt, M. Schneider, M. Schneider, N. Schneider, W. Schneider, H.-J. Schött, B. Schreiber, H. Schütz, H.-O. Schuff, H. Schulze, R. Schulze, R. Schumann, G. Schunk, B. Schuster, W. Schuth, G. Schwarz, R. Schwarz, V. Schwarz, R. Schwedhelm, G. Schweipert, A. Schwinn, S. Selent, H. Sitta, G. Sobainsky, H. Sondershaus, P. Spädtke, H. Spika, A. Spitaler, A. Stagno, K. Stallmann, E. Stenger, R. Stenner, M. Stevens, J. Störmer, A. Stork, M. Stork, W. Stork, I. Strehl, K. Streich, G. Stubenrauch, E. Sturm, K.-H. Stutz, A. Suderleith, K. D. Süssbrich, D. Svrcina, W. Thalheimer, S. Thiel, R. Thieme, R. Thomitzek, E. Thurau, H. Titzschker, I. Türk, G. Tufo, H. Ullrich, H.-G. Valter, E. Veith, H. Vilhjalmsson, R. Vincelli, W. Vinzenz, P. Völger, H. Vogel, U. Vogel, D. Vogt, S. Voltz, D. Volz, R. Vrtal, V. Wagner, K. Waitz, K.-H. Wannemacher, I.-H. Warsow, R. Weber, G. Weidlich, E. Weigand, J. Weinert, P.-W. Weinreuter, L. Weiss, H. Weitzel, D. Wendt, E. Werkmann, R. Werkmann, H. Wesp, Ch.-K. Wetzel, J. Wiessmann, G. Wilde, S. Wilhelm, D. Wilms, H. Wirth, W. Wissing, H. Wörner, A. Wolf, R. Zecher, V. Zelba, A. Zennia, H. Ziegler, A. Ziem, E. Zilch, S. Zipprich, A. Zschau, K. Zweig

8.4 Scientific Cooperations

(from contributions to this report)

FEDERAL REPUBLIC OF GERMANY

University of Bayreuth
Hahn-Meitner-Institut, Berlin
University of Bochum
University of Bonn
Fachhochschule Darmstadt
Technische Hochschule Darmstadt
University of Erlangen
University of Frankfurt
University of Freiburg
MPI für Quantenoptik, Garching
University of Gießen
University of Göttingen
Deutsches Krebsforschungszentrum, Heidelberg
MPI für Kernphysik, Heidelberg
Strahlenklinik, Heidelberg
University of Heidelberg
University of the Saarland, Homburg
Kernforschungsanlage Jülich
University of Kassel
University of Köln
Deutsche Forschungs- und Versuchsanstalt für Luft- und Raumfahrt, Köln
Gesellschaft für hausbiolog. Forschung, Mainz
University of Mainz
University of Marburg
MPI München
Technische University of München
University of München
University of Münster
University of Oldenburg
University of Siegen
University of Stuttgart
University of Tübingen
University of Würzburg

GERMAN DEMOCRATIC REPUBLIC

ZfK Rossendorf, Dresden
Technische Hochschule Leipzig

ALGERIA

CDTN Algier

CANADA

Chalk River

PEOPLE'S REPUBLIC OF CHINA

University of Beijing
Institute of Modern Physics, Lanzhou
SINR Shanghai

DENMARK

University of Aarhus
Niels Bohr Institute Copenhagen
University Hospital of Copenhagen
Danfysik, Jyllinge
Riso National Laboratory, Roskilde

ENGLAND

Daresbury Laboratory (SERC)
Ruhterford Appleton Laboratory

FINLAND

University of Helsinki
University of Jyväskylä

FRANCE

GANIL, Caen
LPC Clermont-Ferrand
Centre d'Etudes Nucléaires de Bordeaux, Gradignan
CEN Grenoble
ILL Grenoble
ISN Grenoble
University of Paris Sud, Orsay
Ecole Polytechnique, Palaiseau
University P. et M. Curie, Paris
Centre d'Etudes Nucléaires, Saclay
Centre de Recherche Nucléaire, Strasbourg
University of Villeurbanne

GREECE

University of Athens
University of Thessaloniki

HUNGARY

University of Budapest
University of Debrecen

INDIA

Guru Nanak Dev University, Amritsar
VECC-BARC, Calcutta
University of Hissar
Department of Applied Physics, Kurukshetra
North-Eastern Hill University, Shillong

ISRAEL

University of Jerusalem
Weizmann Institute, Rehovot

ITALY

University of Bari
University of Catania
University of Florence
University of Legnaro

JAPAN

Osaka University
Institute of Technology, Tokyo

THE NETHERLANDS

University of Amsterdam
University of Groningen
Noordwijk
University of Utrecht

PAKISTAN

Gomal University
PINSTECH, Islamabad
University of Peshawar

POLAND

Jagellonian University, Cracow
Astronomical Observatory, Frombork
Pedagogical University, Kielce
University of Lodz
Institute of Technology, Warsaw
University of Warsaw

PORTUGAL

University of Lisboa

ROMANIA

Institute of Phys. and Nucl. Eng., Bucharest

SPAIN

IFIC Valencia
University of Barcelona

SWEDEN

University of Lund
University of Stockholm

SWITZERLAND

CERN, Geneva
PSI Villigen
University of Bern

UNITED SOVIET SOCIALIST REPUBLIC

Joint Institute for Nuclear Research, Dubna
ITEP, Moscow
Landau Institute, Moscow
Lebedev Physical Institute, Moscow

UNITED STATES OF AMERICA

Angelo State University
Argonne National Laboratory
A&M University, Texas
Lawrence Berkeley Laboratory
Harvard University, Cambridge
University of Illinois, Champaign
Duke University, Durham
Michigan State University, East Lansing
University of Florida
Nuclear Bureau of Standards, Gaithersburg
Notre Dame, Indiana
Los Alamos National Laboratory
Kansas State University, Manhattan
Oak Ridge National Laboratory
University of Pennsylvania
North Carolina State University, Raleigh
Pacific Northwest Laboratory, Richmond
University of Missouri, Rolla
State University, Rutgers
Yale University, New Haven

YUGOSLAVIA

Boris Kidric Institute, Belgrade
Rudjer Boskovic Institute, Zagreb
University of Kragujevac

8.5 Author Index

Ackermann, D. 23, 31, 32
Adloff, J.C. 38, 46, 268
Adzic, P.R. 44
Ahmad, W. 234
Ahner, W. 274, 307
Aichelin, J. 99, 100, 101
Akpa, T. 187
Alard, J.P. 267
Albrecht, R. 302, 303
Andersen, L.H. 150
Anders, F. 197
Andreev, I.V. 115
Angert, N. 148, 200, 335, 337, 354
Anicin, I.V. 44
Anne, R. 257
Anton, A. 139
Appelhans, H. 192
Appenheimer, M. 292
Armbruster, P. 22, 255, 259, 260
Arnold, W. 289, 293
Audouard, A. 215, 218
Augerat, J. 267
Augustin, J. 122, 158
Averback, R.S. 221
Avilov, V.V. 365
Azgui, F. 298

Backe, H. 130, 300
Baechler, J. 52, 60
Bahr, M. 299
Balanda, A. 277
Balanzat, E. 215, 218
Ballhause, P. 207
Balog, K. 261
Baltensperger, U. 245
Baltes, P. 274, 282
Balykin, V. 151, 152, 153
Barbu, A. 221
Barden, R. 11, 17
Barreau, G. 15, 16
Barth, R. 35
Bartke, J. 52
Bartosz, G. 181
Barz, H.W. 112, 113
Bastid, N. 267
Batko, G. 92, 94
Batsch, T. 302
Baumann, A. 292
Baumann, F.M. 281
Baum, W. 16
Bazin, D. 12, 49
Beckert, K. 347, 348, 355
Becker, R. 148
Behr, K.-H. 255, 262
Beiersdorf, S. 33
Bellm, D. 40
Berdermann, E. 48, 50, 129
Berger, F. 299
Bergmann, M. 281
Berg, F.-D. 313
Berg, H. 140, 280
Bernhardt, J. 277
Berthier, B. 48, 50
Bessler, U. 338
Bethge, K. 130, 277, 300
Beyer, H.F. 143
Biagi, F. 267
Bialkowska, H. 52
Bilwes, B. 38
Bilwes, R. 38
Bing, L. 137
Biro, T.S. 93, 121
Bischoff, E. 235
Blaettel, B. 91, 96, 97, 98
Blaich, T. 269, 311
Blanke, J.H. 146, 167
Blank, B. 49, 255
Blasche, K. 201
Blell, U. 341
Bleuel, W. 340
Blomqvist, J. 17
Blum, V. 123
Bock, R. 37, 52, 58, 60, 209
Boehne, D. 200, 201
Boer de, J. 21
Bogdanski, P. 212
Boggasch, E. 369, 374
Bokemeyer, H. 130, 277, 300
Boonstra, A.L. 290, 291, 292
Borchert, Ch. 86
Borisenke, N.G. 370
Bork, U. 196
Bosch, F. 129, 132, 144
Bosch, U. 29
Bossler, J. 336, 337
Bouffard, S. 212, 213, 218
Bourgeois, W. 354
Box, P.F. 43
Brandt, R. 225, 227, 230, 231, 232, 233, 234, 235, 301
Braunshausen, G. 219, 220
Breitbach, G. 24, 41
Brentano von, P. 21
Breskin, A. 286
Briand, J.P. 144
Brill, D. 274, 276

Brinkmann, K.-Th. 281
Brockmann, R. 52, 58, 59, 274
Brohm, T. 23, 255, 279
Broude, C. 13
Brown, B.A. 12
Bruechle, W. 22, 26, 27, 28, 239, 240, 241, 242, 243, 244, 245
Bruegger, M. 26
Bruenle, A. 255
Brummund, N. 290, 291
Bruske, C. 257
Brutscher, J. 342
Buecker, H. 188, 194, 195
Buehler, J. 178
Burkard, H.-G. 255
Burkard, K.-H. 255, 257
Bursill, L.A. 219, 220
Busch, B. 154
Butorac, S. 83

Carjan, N. 15
Casini, G. 36, 37
Cassing, W. 40, 91, 92, 93, 94, 96, 97, 98
Cerruti, C. 47, 48, 50, 265, 266
Chakarvarti, S.K. 236
Chamberod, A. 218
Charity, R.J. 37, 38, 42
Charles, P. 144
Chase, S.I. 52
Chaubey, P.P. 224
Cheblukov, Yu.N. 209
Chechik, R. 286
Chen, M. 255, 357
Cleff, B. 137
Clerc, H.-G. 23, 49, 255, 258, 249
Clewing, G. 299
Cline, D. 20
Cocher, S. 347, 348, 355
Coffin, J.P. 265, 266
Combes, I. 265
Connell, S. 132
Cowan, T. 130
Cremer, C. 185
Cremer, T. 185
Crouau, M. 267
Cubero, M. 95
Cub, J. 18
Cwiok, S. 88
Czosnyka, T. 20

Dahlinger, M. 300
Dahl, L. 337
Dangendorf, V. 286
Dang, J.R. 357
Daudon, F. 267
Daues, H.W. 278
Debeauvais, M. 45, 46
Decowski, P. 43
Deitinghoff, H. 337, 339
Del Moral, R. 49
Demeyer, A. 43, 47, 48
Dengler, J. 302
Derado, I. 52, 55
Derreth, Ch. 108
Dersch, R. 301
Deslattes, R.D. 143
Dietrich, D.D. 144
Dietrich, K.-G. 369, 370, 374
Ditzel, E. 35
Djuric, N. 148
Doan, T. 16
Doerner, R. 140, 141, 142
Dominik, W. 60
Dorste, Ch. 20
DuBois, R.D. 140
Duering, J. 226
Dufour, J.-P. 49, 255
Dunlop, A. 216, 217, 218, 221
Dupieux, P. 267
Dural, J. 217
Durrani, F. 234
Dwivedi, K.K. 222, 223, 224

Eckardt, V. 52, 58
Eckert, E.-M. 47, 48
Egelhof, P. 18, 21, 34, 269, 298
Egger, H. 317
Eidmann, G. 302
El Shabshiry, M. 100
Ellert, C. 151
Elze, Th.W. 269
Emig, H. 337, 343, 344, 346, 354
Emling, H. 18, 20, 21, 34, 269, 272, 288
Enders, G. 42, 134, 289
Enders, W. 148
Ender, Ch. 316
Engel, A. 93
Ensinger, W. 207
Ernwein, R. 265
Eschke, J. 52, 60
Eska, G. 229
Essel, H.G. 302, 304, 307, 308, 309

Esterlund, R.A. 25, 33
Faessler, A. 99, 100, 101, 104
Faestermann, T. 296
Fahlander, C. 20, 21
Fan, Z.-J. 231
Faulstich, A. 151
Favucci, C. 52
Feldmeier, H. 102, 103
Feng, R. 87
Ferber, H. 206
Ferenc, D. 52
Fernandez, F. 45, 46
Feuerstrack, F. 255

Finlayson, K.D. 143, 144
Fintz, P. 265, 266
Fischer, B.E. 200, 201, 208
Fischer, W. 207
Fleischmann, B. 62
Flentje, M. 178
Fleury, A. 49
Folger, H. 14, 22, 29, 130, 240, 255, 258, 277
Folkmann, F. 147
Forberich, E. 141
Fradj, M. 257
Franczak, B. 200, 255
Frankenberg-Schwager, M. 187
Frankenberg, D. 187
Franzke, B. 352, 354, 355
Fraysse, L. 267
Freiesleben, H. 269, 281, 287
Freifelder, R. 36, 37, 38, 42, 311
Fricke, B. 164, 165, 166, 167, 168
Friedemann, H. 35
Friedrich, J. 337, 338
Friese, J. 283, 284, 297
Friman, B.L. 95, 112, 113
Frink, C. 26
Fritzsche, R. 304, 308, 309
Froh, J. 282
Fromhold, Th. 293
Fuchs, G. 215, 218
Fuchs, M. 62
Fuessel, K. 177
Fujita, Y. 261
Funke, F. 27, 28

Gabelmann, H. 11
Gademann, G. 200
Gaeggeler, H.W. 22, 26, 240, 245
Gaertner, H. 181, 198, 204
Gaimard, J.-J. 49, 89, 255
Gaiser, H. 255
Galin, J. 38
Gannett, C.M. 245
Ganz, M. 231, 232, 233
Gassel, H. 281
Gassen, H.G. 192
Gazdzicki, M. 52, 55
Gebauer, H.-J. 52
Geissel, H. 49, 200, 255, 257, 259, 260, 261
Gelberg, S. 14
Gelbke, C.K. 50
Gentner, R. 40
Georget, Y. 257
Gerhard, M. 152, 153
Gerl, J. 133, 134
Geschke, O. 210
Gierlik, E. 43
Giese, I. 324, 328
Gillibert, A. 259, 260
Gillitzer, A. 296
Giorni, A. 43
Gladysz, E. 52
Glasow, R. 299
Glatz, A. 264
Glatz, J. 337
Glueckert, S. 317
Gnirs, M. 37, 38, 39
Gobbi, A. 36, 37, 38, 41, 42
Gober, M.K. 239, 240, 241, 246
Goebel, R. 293
Goepfert, A. 16
Goeringer, H. 322
Goldring, G. 13
Gollerthan, U. 23
Gollwitzer, N. 18
Golubev, A. 370
Gosh, S. 222, 223, 224
Gougas, A. 60
Grabez, B. 225
Graf, K. 337
Graf, O. 155
Graf, S. 158
Grant, I. 11
Granzer, F. 226
Greenberg, J.S. 130
Gregorich, K.E. 245
Greinert, R. 183
Greiner, W. 81, 82, 83, 86, 90, 105, 108, 109, 110, 114, 122, 123, 124, 155, 156, 157, 158, 159, 160
Grein, H. 18, 20
Grieser, R. 152, 153
Griffioen, K.A. 43
Groeneveld, K.O. 226
Grosse, E. 34, 274, 276, 277
Gruen, N. 161
Guerra, C. 52, 63
Guerreau, D. 38
Gugulski, B. 270
Guillaume, G. 265, 266
Guillemaud-Mueller, D. 12
Guinet, D. 43, 47, 48
Guo, S.-L. 228, 231, 232
Gustafsson, H.A. 299
Gutbrod, H.H. 59, 75, 76, 77, 299
Gutermuth, B. 336

Haberer, T. 200, 201
Habs, D. 24, 133, 134, 149, 150, 151, 152, 153, 332
Hackel, S. 165
Haffner, M. 82
Hagel, K. 42, 289
Hagmann, S. 138, 140
Hall, H.L. 245
Hammal, H. 302, 303
Hanelt, E. 23, 49, 255, 258, 279
Hansen, O. 52, 55

Hansen, P.-G. 271
Hao, X.-H. 231, 232
Harbich, R. 187
Hardel, H. 302
Harris, J.W. 52, 58
Hartick, M. 203
Hartmann, G. 200
Hartnack, C. 90
Hartnagel, H.L. 360
Haselbauer, J. 148
Hasse, R.W. 366
Hass, M. 13
Hauber, E. 21
Hausmann, A. 277
Heckmann, P.H. 146, 167
Heck, W. 52, 60, 63
Heeg, P. 15
Heerd, S. 269, 288
Heilmann, J. 180
Heimrich, B. 373
Heinemann, D. 165, 166
Heine, F. 296
Heinrich, W. 210, 360
Hellmann, N. 191
Henderson, R.A. 245
Henning, W. 18, 21, 34, 42, 269, 274, 277, 298, 330
Hennrich, H.-J. 24
Henze, M. 197
Hernandez-Benavides, T. 60
Herrmann, G. 26, 331
Herrmann, M. 111
Herrmann, N. 36, 37, 38, 264, 311
Hertzog, D.W. 299
Hessberger, F.P. 13, 22, 23, 30, 31, 32, 33
Heyer, G. 107
Hieber, L. 182
Hildenbrand, K.D. 36, 37, 38, 41, 42, 47, 48, 281, 289
Hiller, H. 283
Hilscher, D. 40
Hirayoshi, Y. 229
Hoch, T. 106
Hoelker, G. 299
Hoffmann, D.H.H. 209, 369, 370, 374
Hoffmann, J. 302, 306
Hoffmann, M. 52, 60
Hoffman, D.C. 245
Hoflund, G.B. 206
Hofmann, Ch. 156
Hofmann, I. 362, 363, 364, 365
Hofmann, N. 336
Hofmann, S. 13, 22, 295
Holzmann, R. 18, 21, 34, 269, 272
Hornecker, F. 265
Horneck, G. 188
Horz, M. 23
Hoshino, S. 206
Houpert, C. 214
Hubele, J. 50, 268
Hubert, F. 49
Huber, G. 151, 152, 153
Huettermann, J. 190
Hue, R. 257
Hughes, S.A. 299
Humanic, T. 52
Humbert, F. 271
Hunzinger, M.O. 265
Hussain, G. 232
Hutter, G. 335

Ickert, G. 269
Idh, J. 299
Ihorst, M. 324
Indelicato, P. 143, 144
Ionescu, D.C. 157
Ishikawa, T. 129
Ismail, M. 100

Jacoby, J. 370
Jaeckel, B. 25, 33
Jaeger, E. 27, 28, 262
Jaeger, H. 274, 282
Jaenicke, J. 99
Jaeschke, E. 149, 150, 151
Jagutzki, O. 140
Jahnke, U. 38
Jelenkovic, B. 148
Jennewein, E. 148
Joest, G. 358
Johaenntges, R. 257
Johannsen, L. 271
Johnson, F. 168
Jokic, S. 45, 46
Jonson, B. 271
Jost, D.T. 22, 240, 245
Jousset, J.C. 215, 218
Judge, S.M. 131
Julien, R. 21
Jundt, F. 265, 266

Kabana, S. 52, 55, 56
Kadija, K. 52, 55
Kaempfer, B. 102
Kaiser, K. 21
Kalmbach, U. 121
Kamermans, R. 43
Kampert, K.H. 75, 76, 77, 299
Kankeleit, E. 35, 179, 202, 203, 282, 294
Karabarbounis, A. 52, 60
Karczmarczyk, W. 20
Kassing, R. 205
Katscher, U. 124
Keck, B. 203
Kehr, E. 177
Keidel, R. 52, 61, 64, 314

Keitz von, A. 109
Kelbch, C. 138, 140
Kellerer, A.M. 182, 183
Keller, H. 11, 12, 19
Keller, J.G. 269, 287, 288, 311
Keller, K. 40
Keller, O.L., Jr. 168
Khan, E.U. 234, 301
Khan, H.A. 228, 232
Khaouli, M. 336
Kiefer, J. 184, 187, 193
Kienle, P. 129, 131
Kienlin von, A. 298
Kiesewetter, J. 281
Kilgus, G. 149, 150
Kimoundri, U. 45
Kipper, A. 342
Kirchner, R. 11, 12, 19, 29, 247, 255, 257
Klabunde, J. 148, 335, 337
Kleber, M. 162
Kleinheinz, P. 17, 19
Kleinod, M. 148
Klein, H. 81, 82
Klein, H. 337
Klein, R. 151, 152, 153
Klepper, O. 11, 12, 19, 29, 255
Klingelhoefer, G. 202, 203
Klingler, H. 269
Klos, F. 356
Klotz-Engmann, G. 35
Knaack, M. 25, 33
Kneissel, W. 287
Kneissl, U. 289, 293
Kneissl, W. 269
Knoedler, B. 255, 279
Knoll, J. 111, 112, 113
Knopp, M. 18
Knospe, O. 102
Koch, R. 138
Koch, V. 91, 96, 97, 98
Koczon, P. 274, 311
Koeber, E. 230
Koenig, I 129
Koenig, R. 269, 287
Koenig, W. 129
Koepf, M. 296
Koerner, H.-J. 34, 154, 284, 297
Kohlmeyer, B. 274, 275, 281
Kohn, P. 322
Kolasinski, A. 11
Kolb, B.W. 59, 75, 76, 77
Kolb, D. 14, 85, 165, 166
Koncul, M. 60
Konrad, W. 274, 275
Koschel, P. 29
Koshkarev, D.G. 209
Kosiec, J. 52, 57, 62
Kosmadakis, P. 300
Kost, M. 193
Kovacs, A. 240
Kowalski, M. 52
Kozhuharov, Ch. 145
Kozhuharov, C. 129, 135, 136
Kraemer, D. 149, 150, 151
Kraemer, M. 311, 323, 325
Kraft-Weyrather, W. 175, 176, 177, 200
Kraft, D. 130, 277, 300
Kraft, G. 138, 175, 176, 177, 179, 181, 186, 189, 190, 191, 199, 200, 201
Kramp, J. 133
Kranert, T. 184
Kranz, A.R. 196
Kraske, F. 175, 176, 179
Kratz, J.V. 22, 26, 27, 28, 239, 240, 241, 245, 246, 269, 331
Krause, P. 332
Kraus, B. 147
Kraus, G. 34
Kreutz, P. 48, 50, 268
Krichbaum, H. 336
Krieg, M. 152, 153
Kristensen, M. 151
Kritzer, A. 354
Krmpotic, D.M. 44
Kroetz, W. 154
Krusche, B. 131
Kuehl, Th. 151, 152, 153, 191
Kuehmichel, A. 47, 52, 53, 57, 62
Kuehn, W. 24, 41, 42, 289, 292, 313
Kuerpick, P. 164
Kukoc, A.H. 44
Kulessa, R. 20, 21, 34, 269, 270
Kunde, G.J. 48, 50
Kurz, H.P. 336
Kutschera, W. 330
Kynast, W. 325, 326, 327

Lahanas, M. 52
Lambrecht, D. 269
Langenbeck, B. 200, 201, 255, 340, 354, 356, 357
Lange, J.S. 287
Lange, S. 269
Langrock, E.-J. 230
Lang, A. 96, 97
Lang, S. 229
Lassen, L. 40
Laubach, S. 203
Lauritsch, G. 123
Lee, D.M. 245
Lee, J.-Y. 52, 56
Lehmann, M. 40
Leible, K.D. 354, 358
Leifels, Y. 269, 311
Leino, M.E. 22
Lenz, G. 175, 176, 179, 193
Leray, S. 48, 50

Leroux, B. 15, 16
Lesueur, D. 215, 217, 218
LeVine, M. 52, 60
Lhénoret, P. 47, 48
Liang, C.F. 19
Liebold, H.P. 302
Lienert, Ch. 245
Liesen, D. 137, 143, 144
Lindemann, K. 261
Lindenstruth, V. 311
Linden, R. 99, 104
Lips, V. 35
Liu, Z.A. 285
Livingston, A.E. 135, 136, 145, 146, 147
Li, J.D. 245
Ljubicic, A., Jr. 52, 60
Loebner, K.E.G. 261
Loehner, H. 290, 291
Loos, A. 302
Lorenz, W.J. 200, 201
Loyd, D. 140
Lubkiewicz, E. 269, 270
Luboeinski, A. 197
Lucas, R.J. 47, 48, 50, 323
Luehning, J. 285
Luettgen, A. 31, 32
Luetzenkirchen, K. 331
Lutz, K.-J. 371, 372
Lynen, U. 47, 48, 50, 268, 285

Madland, D.G. 106
Madlung, J. 338
Maguire, C.F. 265, 266
Mahrt-Olt,K. 370
Maier, K. 132
Major, J. 132
Malzacher, P. 322, 328
Manakos, P. 106, 107
Mannel, T. 107
Manns, M. 322
Mann, R. 277
Mansoor, K. 234
Margetis, S. 52, 63
Marinov, A. 14, 85
Marrus, R. 144
Martens, H.-G. 302, 305
Maruhn, J.A. 81, 82, 83, 123, 124, 371, 372
Maruyama, T. 101
Mary, P. 212
Marzo de, C. 52
Mattiello, R. 109
Maurenzig, P.R. 37, 38
Mayade, S. 267
Mayer, R. 42
Mayer, W. 198
Mazur, C. 47, 48
Meczynski, W. 19
Mehler, G. 159
Meier, J. 298
Meijer, R.J. 43, 285
Meissner, F. 29
Menegazzo, R. 19
Mennigmann, H.D. 188
Metag, V. 24, 41, 42, 289, 292, 313
Metzger, S. 208
Meufels, W. 302, 305, 309
Meyer, U. 317, 329
Micke, U. 188
Milkau, U. 48, 50, 268
Millon, G. 60
Miskowiec, D. 274, 276
Mittig, W. 259, 260
Moeller, A. 327
Moeller, G. 146
Moemerzbach, K. 302
Mokler, P.H. 135, 136, 137, 145, 146, 147, 148, 286
Molzahn, D. 230
Momberger, K. 161
Mongelli, M. 60
Montarou, G. 267
Moody, K.J. 26
Morand, C. 43
Morawek, W. 23, 31, 32
Morel, P. 267
Morillo, J. 217
Moritz, G. 255, 354, 356, 357
Morrissey, D. 12
Mosel, U. 91, 93, 94, 96, 97, 98
Mount, C.K. 206
Muehlhans, R. 41
Mueller A.C. 257
Mueller, A. 148, 149
Mueller, B. 110, 114, 122, 155, 156, 157, 158, 160
Mueller, G. 202
Mueller, I. 148
Mueller, M.M. 330, 335, 336, 337, 345
Mueller, R.W. 209, 375, 376
Mueller, W.F.J. 47, 48, 311
Muentz, Ch. 35, 274, 282, 293
Muenzenberg, G. 22, 200, 255, 259, 260, 261
Muhn, A. 302, 303
Murnick, D.E. 154
Music, M. 151
Mutterer, M. 15, 16

Napiorkowski, P. 20
Nappi, E. 52, 60
Nast-Linke, U. 16
Nazarewicz, W. 88
Nazarov, V.M. 209
Nestor, C.W., Jr. 168
Neumann, R. 151, 152, 153, 191, 332
Neumann-Cosel von, P. 40
Neunlist, R. 265

Ngô, C. 47, 48, 50
Nickel, F. 255
Nicklas, A. 337
Nieuwenhuizen van, G.J. 43
Niita, K. 92, 94
Nikolaus, B.A. 106
Nilsson, T. 271
Ninov, V. 13, 22, 30, 31, 32, 33
Noerenberg, W. 84, 87, 95
Nolden, F. 347, 348, 361
Noll, A. 210
Novotny, R. 24, 41, 42, 289, 292
Nurmia, M.J. 245
Nyman, G. 271

Oberstedt, A. 40
Oberstedt, S. 15
Odenweller, TH. 354, 357
Odyniec, G. 52
Oelert, W. 14
Oeschler, H. 35, 274, 282, 294
Oguri, Y. 375
Ohl, T. 107
Ohtsuka, N. 99, 100, 101, 404
Olmi, A. 37, 38, 42
Olson, R.E. 135, 138, 141, 142, 259, 260, 280
Overbeck, M. 331

Paic, G. 52, 60
Panagiotou, A.D. 52, 60
Pantis, G. 104
Pan, O. 342
Parente, F. 144
Paris, P. 19
Parizet, M.J. 267
Pascard, H. 214
Patyk, Z. 78, 79, 80
Patzelt, P. 25, 33
Paul, M. 330
Pedersen, J. 140
Peilert, G. 105
Peise, J. 292
Pelte, D. 37, 38, 41, 264
Pena, K. 270
Penninger, H. 175, 176, 179
Perelygin, V.P. 301
Petrich, W. 151, 152, 153
Petridis, A. 52, 60
Petrovici, M. 37, 38
Peuto, A.R. 209
Pfaffenberger, R. 154
Pfeiffer, M. 292
Pfennig, J. 52, 57, 62
Pfuetzner, M. 11, 255
Pickert, M. 196
Piechaczek, A. 35
Pinilla, C. 328
Pinkenburg, C.H. 48, 50

Piper, A. 61, 64, 314
Plisch, B. 230
Plochocki, A. 11
Pochodzalla, J. 47, 48, 50, 268
Poeppl, H. 274, 275
Polai, W. 35
Polikanov, S. 331
Polley, L. 120
Poppensieker, K. 148, 255, 274, 302, 305
Popp, S. 185
Posa, F. 52, 60
Poskanzer, A.M. 75, 76, 77
Post, U. 304, 307, 322, 325, 326
Pravikoff, M.S. 89, 255
Prior, M. 140
Proebstel, U. 148
Proft, M. 269
Prokopowicz, W. 269, 270
Przybyla, A. 302
Przybyla, T. 59
Puehlhofer, F. 52, 61, 64, 274, 275, 314
Pugh, H.G. 52, 58
Purschke, M. 299

Qassoud, D. 267
Quick, W. 285
Quis, D. 302

Raabe, P. 360
Rabe, H.J. 47, 48
Raciti, G. 48, 50
Rafelski, J. 163
Raha, S. 116, 119
Rahmani, A. 267
Rai, G. 52
Raju, J. 222, 223, 224
Ralarosy, J. 45, 46
Rami, F. 38, 265, 266
Ramm, U. 199
Randrup, J. 105
Ranieri, A. 52
Raschke, A. 290, 291
Rasmusson, J. 257
Ratzinger, U. 337, 340, 341
Rauch, W. 52, 58
Rau, J. 114
Reimold, D. 37, 38
Reinhardt, J. 110, 155, 156, 158
Reinhardt, R. 21
Reinhard, P.-G. 123
Reinhold, J. 284
Reisdorf, W. 22
Remm, B. 185
Renfordt, R. 52, 54, 58, 59, 274
Renner, W. 82
Reusch, S. 136
Rhein, M. 35, 293, 294
Ribitzki, G. 154

Ribrag, M. 47, 48
Richard, P. 140
Richter, A. 40, 271
Richter, M. 302, 304, 306, 309, 310
Riess, S. 313
Riisager, K. 271
Rink, H. 180
Rittenhouse, R. 328
Ritter, H.G. 75, 76, 77
Ritter, S. 175, 176, 177, 179, 200
Roeckl, E. 11, 12, 19, 29, 255, 257, 330
Roehrich, D. 52, 53, 54, 56, 57, 62
Roesch, W. 40
Roland, G. 57
Rommel, M. 230
Rosen, A. 166
Rothard, H. 52, 53, 54
Rothmann, Th. 175, 176, 179
Rozmej, P. 84
Rubio, B. 17
Rudolf, D. 268
Rudolf, G. 38, 268
Rudskoygh, I.V. 209
Rueck, D.M. 204, 206, 207, 343, 344, 346
Rueschmann, R. 300
Rumrich, K. 159, 160
Runge, K. 52
Runne, M. 268
Rykaczewski, K. 11, 19, 29, 255, 257

Saettel, M.A. 265
Sailer, K. 110
Sakaguchi, K. 130
Salabura, P. 130
Saler, S. 205
Sampsonidis, D. 46
Sandoval, A. 52, 60, 62, 274
Sann, H. 47, 48, 50, 268, 285
Santo, R. 299
Sastri, C. 331
Savinel, G. 267
Saxena, A. 222
Schaaf, U. 347, 348, 355
Schaedel, M. 22, 26, 239, 240, 241, 242, 243, 244, 245, 262
Schaefer, A. 110, 190
Schaefer, M. 93, 94, 188, 194, 195
Schall, D. 179, 302, 304, 306, 307, 308, 322
Schall, I. 35, 294
Schardt, D. 11, 12, 17, 19, 200, 255
Schartner, K.-H. 139, 147
Schausten, B. 241, 242, 243, 244
Scheid, W. 86, 161
Scheitler, G. 162
Schempp, A. 337, 338, 339, 342
Schennach, S. 148
Scherer, U.W. 22, 26, 241, 245, 246
Schicker, R. 75, 76, 274
Schiessl, Ch. 34, 297
Schiffer, J.P. 34
Schimpf, E. 262
Schindler, E. 328
Schlachter, A.S. 140
Schlei, B. 274, 275
Schlesier, R. 264
Schmadel, I. 349
Schmidt-Boecking, H. 138, 140, 141, 142, 199, 277, 280, 286
Schmidt-Ott, W.-D. 29
Schmidt, E. 53
Schmidt, H.-G. 302, 309
Schmidt, H.R. 75, 76, 77
Schmidt, K.-H. 23, 49, 89, 255, 258, 279
Schmidt, N. 152, 153
Schmidt, R. 18, 59, 102, 269, 299, 311
Schmitt, E. 52, 57
Schmitz, C. 194, 195
Schmitz, M. 292
Schmitz, N. 52, 58
Schmoetten, E. 60
Schnabel, D. 81, 82
Schneider, E. 184, 193
Schneider, I. 52, 57
Schneider, M. 179, 186, 189
Schneider, V. 124, 371, 372
Schnell, J. 261
Schoenfeld, Th. 110
Schoenhofen, M. 95
Schoen, W. 181
Schoett, H. 255
Scholz, M. 175, 176, 177, 178, 179
Schreckenbach, K. 131
Schrieder, G. 40, 271
Schroeder, L.S. 52
Schroeder, S. 151, 152, 153
Schroeter, A. 129
Schuch, R. 149, 150
Schuell, D. 281, 330
Schuettauf, A. 268
Schulte, H. 25
Schulte, H. 354, 358
Schulze, R. 302
Schulze, Th. 134
Schulz, H. 112, 113
Schwab, Th. 200, 255, 259, 260, 261
Schwab, W. 23
Schwalbach, P. 202, 203
Schwalb, O. 42, 289
Schwalm, D. 24, 130, 133, 134, 149, 150, 151, 152, 153, 316, 332
Schweppe, J. 130
Seeger, A. 132
Seidel, W. 285
Seifert, H. 261
Selvaggi, G. 52
Senger, P. 34, 274, 276, 277, 300

Sepp, W.-D. 164
Seyboth, P. 52, 55, 58
Seyerlein, J. 52, 58
Sharkov, B. 370
Shepard, K. 298
Sherrill, B. 12, 255
Sher, A. 234
Shin, Y. 274, 276
Shumshurov, A. 370
Siart, O. 317
Sicre, A. 16
Sigray, P. 151
Simionovici, A. 144
Simonis, H.-J. 18
Simon, R.S. 18, 19, 21, 42, 273
Singh, P. 236
Skalski, J. 80
Skrzypczak, E. 52
Smida, J. 183
Sobiczewski, A. 78, 79, 80
Soff, G. 114, 155, 156, 159, 160, 163
Sohlbach, H. 281, 302, 306
Sorensen, R.H. 210
Sorge, H. 109
Spaedtke, P. 148, 343, 344, 346, 354, 356, 358, 359
Speer, J. 281, 330
Speidel, K.-H. 18
Spies, H. 269, 288
Spies, W. 148
Spinelli, P. 52, 60
Spohr, R. 212, 213, 214, 215, 217, 218, 219, 220, 221, 229
Spreng, W. 302, 304, 307
Srebrny, J. 20
Stachura, Z. 135, 136, 137
Stahlhacke, B. 192
Stahl, B. 203
Stanton, J.A. 186, 189
Staudte, R. 300
Steck, M. 149, 150
Stefanini, A.A. 37, 38, 42
Steiner, M. 49, 255, 279
Steinhof, A. 330
Steiper, F. 289
Stelzer, H. 37, 38, 47, 48, 49, 200, 255, 278, 282
Stelzer, K. 269, 288
Stenner, R. 340
Stephan, R. 198
Stetsenko, S.G. 301
Stiebing, K.E. 130, 274, 277, 300
Stiel, E. 331
Stock, R. 52, 53, 54, 55, 56, 57, 58, 60, 62, 63, 274, 276
Stoecker, H. 90, 105, 109
Stoehlker, Th. 135, 136, 145
Stork, M. 336
Strehl, P. 335
Stroebele, H. 52, 53, 54, 55, 56, 63, 274, 276
Stroth, J. 300
Strottman, D.D. 106
Studer, F. 214
Sturm, E. 302
Suemmerer, K. 22, 26, 27, 28, 49, 255
Szerypo, J. 11, 12
Szymanski, A. 135, 136

Tahseen, R. 234
Tain, J.L. 17
Takahashi, N. 13
Talysin, A.N. 364
Tanaka, M. 36
Tanis, J.A. 140
Taucher-Scholz, G. 186, 189
Teh, K. 311
Teitelbaum, L. 52
Terasawa, M. 148
Tezkratt, R. 265, 266
Theobald, J.P. 15, 16
Thiel, A. 86
Thiel, S. 175, 176
Thiermann, J. 192
Thies, B. 164
Thirolf, P. 133
Thomas, A. 52, 55
Thoma, K. 204
Thomé, L. 215, 218
Tischler, B. 265
Tomasi, E. 47, 48
Tonse, S. 52
Toprek, D. 44
Torp, B. 344
Toulemonde, M. 212, 213, 214
Traebert, E. 146
Trautmann, C. 229
Trautmann, N. 26, 27, 28, 239, 331
Trautmann, W. 47, 48, 50, 268
Trockel, R. 47, 48
Troetscher, J. 261
Troltenier, D. 83
Truebenbacher, V. 298
Trutschler, K. 182
Trzaska, M. 51, 264
Tserruya, I. 286
Tsertos, H. 129, 131
Tucker, T.C. 168
Tuerler, A. 22, 240, 245

Ullrich, J. 140, 141, 142, 145, 277, 280
Ulrich, A. 154
Uwira, O. 148

Vasileiadis, G. 52, 60
Vasiliev, N.A. 209

Vasiliou, M. 60
Vater, P. 225, 227, 230, 231, 232, 233, 234, 235, 301
Venema, L.B. 290, 291
Vesztergombi, G. 52, 62
Vetter, J. 209, 210, 212, 213, 214, 215, 217, 218, 219, 220, 221, 229
Vetter, T. 93
Vieira, D. 261
Viyogi, P. 299
Voelkel, K. 274
Vogt, D. 343
Volkmann, H. 204
Voss, B. 23, 49, 255, 279
Vranic, D. 52, 60
Vukanovic, R.B. 44

Wada, R. 47, 48
Wagner, C. 146
Wagner, M. 148, 149
Wagner, P. 265, 266
Wagner, W. 34, 296, 297
Wahl, H. 369, 374
Waldhauser, B. 124
Walus, W. 34, 269, 270, 274, 276
Wang, Y.-L. 228, 231, 232
Wannenmacher, M. 175, 176, 178, 200, 201
Wanner, B. 151, 152, 153
Warczak, A. 135, 136, 137
Weber, K. 91, 96, 97
Weber, K.J. 187
Weber, M. 257
Weber, T. 289
Weckenmann, J. 255, 258
Weiner, R.M. 115, 116, 118, 119
Wendel, M.H. 120
Wenig, S. 52, 53, 54
Wensveen, M. 60
Wessels, J. 36, 37, 38, 42
Westmeier, W. 25, 33
Weyrich, K. 369
Widmann, E. 132
Wieser, J. 154
Wiese, C. 179, 186, 189
Wilhelm, W. 283
Wilk, G. 116, 117, 118, 119
Wilms, D. 335
Wilschut, H.W. 43, 290, 291, 292
Winkelmann, K. 317, 322, 323, 325
Winkelmann, T. 261
Winkler, M. 373
Winkler, U. 41, 264
Winterbon, K.B. 259, 260
Wirowski, R. 21
Wirth, G. 26, 27, 28
Wituschek, W. 346
Wlodarczyk, Z. 116, 117, 118
Woerner, A. 268
Wolfenstetter, H. 264
Wolf, A. 149, 150, 151, 152, 153, 332
Wolf, B.H. 148, 343, 344, 346, 354, 358
Wolf, G.K. 92, 94, 207, 346
Wollersheim, H.-J. 18, 20, 21, 34, 269, 272
Wollnik, H. 255, 259, 260, 261, 373
Wouters, J. 261
Wo, F. 27, 28
Wu, G. 87

Yang, L. 165
Ya, N.-Q. 245

Zaganidis, N. 60
Zamani, M. 45, 46
Zeitelhack, K. 284
Zenkevich, P.R. 364
Zhao, C.-D. 227, 233, 235, 301
Zhu, T.-C. 228, 232
Zimmermann, H.P. 239, 240, 241, 245
Zoeller, C. 16
Zupancic, M.T. 44
Zweig, K. 356
Zwicker, S. 332
Zylicz, J. 11, 19

ALADIN Collaboration 271
CIRIL 211
DIOGENE Group 51
FRS Collaboration 271
KaoS Collaboration 274, 276, 282
KAON Collaboration 275
L.A.N.D. Collaboration 270, 271, 272, 287, 288
NA35 Collaboration 53, 54, 55, 56, 57, 58, 59, 61, 62, 63, 64, 314
TAPS Collaboration 273, 289, 290, 291, 292, 313
TSR Group 152, 153
WA80 Collaboration 59, 65, 66, 67, 68, 69 70, 71, 72, 73, 74, 315
4π Collaboration 263